

Bernhard Wunderlich

## **Thermal Analysis of Polymeric Materials**

Bernhard Wunderlich

# **Thermal Analysis of Polymeric Materials**

With 974 Figures

 Springer

**Prof. Dr. Bernhard Wunderlich**

200 Baltusrol Road

Knoxville, TN 37922-3707

USA

*wunderlich@chartertn.net*

Library of Congress Controll Number: 2004114977

**ISBN 3-540-23629-5 Springer Berlin Heidelberg New York**

This work is subject to copyright. All rights are reserved, whether the whole or part of the material is concerned, specifically the rights of translation, reprinting, reuse of illustrations, recitation, broadcasting, reproduction on microfilm or in any other way, and storage in data banks. Duplication of this publication or parts thereof is permitted only under the provisions of the German Copyright Law of September 9, 1965, in its current version, and permission for use must always be obtained from Springer. Violations are liable to prosecution under the German Copyright Law.

Springer is a part of Springer Science+Business Media

springeronline.com

© Springer-Verlag Berlin Heidelberg 2005

Printed in The Netherlands

The use of general descriptive names, registered names, trademarks etc. in this publication does not imply, even in the absence of a specific statement, that such names are exempt from the relevant protective laws and regulations and therefore free for general use.

Cover design: KünkelLopka, Heidelberg

Production: LE-TeX Jelonek, Schmidt & Vöckler GbR, Leipzig

Typesetting by the author

Printed on acid-free paper

2/3130/yl – 5 4 3 2 1 0

---

# Preface

*Thermal analysis* is an old technique. It has been neglected to some degree because developments of convenient methods of measurement have been slow and teaching of the understanding of the basics of thermal analysis is often wanting. *Flexible, linear macromolecules*, also not as accurately simply called *polymers*, make up the final, third, class of molecules which only was identified in 1920. Polymers have never been fully integrated into the disciplines of science and engineering. This book is designed to teach thermal analysis and the understanding of all materials, flexible macromolecules, as well as those of the small molecules and rigid macromolecules. The macroscopic tool of inquiry is thermal analysis, and the results are linked to microscopic molecular structure and motion.

Measurements of *heat* and *mass* are the two roots of quantitative science. The macroscopic heat is connected to the microscopic *atomic motion*, while the macroscopic mass is linked to the microscopic *atomic structure*. The macroscopic units of measurement of heat and mass are the joule and the gram, chosen to be easily discernable by the human senses. The microscopic units of motion and structure are the picosecond ( $10^{-12}$  seconds) and the ångström ( $10^{-10}$  meters), chosen to fit the atomic scales. One notes a factor of 10,000 between the two atomic units when expressed in “human” units, second and gram—with one gram being equal to one cubic centimeter when considering water. Perhaps this is the reason for the much better understanding and greater interest in the structure of materials, being closer to human experience when compared to molecular motion.

In the 19<sup>th</sup> century the description of materials could be based for the first time on an experiment-based atomic theory. This permitted an easy recognition of the differences between *phases* and *molecules*. Phases are macroscopic, homogeneous volumes of matter, separated from other phases by well-defined boundaries, and molecules are the constituent smallest particles that make up the phases. As research progressed, microphases were discovered, initially in the form of colloidal dispersions. More recently, it was recognized that phase-areas may be of nanometer dimensions (nanophases). On the other hand, flexible macromolecules have micrometer lengths or larger. Particularly the nanophases may then have structures with interfaces that frequently intersect macromolecules, giving the materials unique properties.

Finally, the classical phases, gases, liquids, and solids, were found to be in need of expansion to include mesophases and plasmas. The discussion of history in the first lecture shows the tortuous path scientific discovery takes to reach the present-day knowledge. Easier ways can be suggested in hindsight and it is vital to find such simpler approaches so to help the novice in learning. In this book on “Thermal Analysis of Polymeric Materials” an effort is made to discover such an easy road to understand the large, flexible molecules and the small phases, and to connect them to the small molecules and macroscopic phases which are known for much longer.



Since the goal of this book is to connect the new knowledge about materials to the classical topics, but its size should be restricted to two to three semesters' worth of learning, several of the standard classical texts were surveyed by the author. Only when a topic needed special treatment for the inclusion of thermal analysis or macromolecules, was this topic selected for a more detailed discussion in this book. The knowledge in polymer science, in turn, often improves the understanding of the other types of molecules. A typical example is discussed in the first lecture when describing the classification-scheme of molecules. With this approach, the learning of materials science, as a whole, may be less confusing. A series of six additional examples of such improvement of the understanding is given on pg. VII.

The study of "Thermal Analysis of Polymeric Materials" is designed to accomplish two goals: First, the learning of the new subject matter, and second, to stimulate a review of the classical topics. Naturally, one hopes that in the future all topics are included in the main educational track. This joining of the physics, chemistry, and engineering of small and large molecules with thermal analysis is of urgency since most students must in their career handle polymeric materials and deal with the application of some type of thermal analysis. A list of short summaries of the seven chapters of the book is given below for a general orientation and to allow for reading, starting at different entry points:

*Chapter 1 Atoms, Small, and Large Molecules* is designed to enhance the understanding and history of the development of knowledge about small and large molecules. Furthermore, the nomenclature, description, and characterization of linear macromolecules by basic theory and experiment are summarized.

*Chapter 2 Basics of Thermal Analysis* contains definitions of systems, flux, and production and the following thermodynamic functions of state which are needed for the description of thermal analysis results: heat capacity, enthalpy, entropy, and free enthalpy.

*Chapter 3 Dynamics of Chemical and Phase Changes* is a summary of the syntheses by matrix, stepwise, step, and chain reactions. It also contains information on emulsion polymerizations, cross-linking, gelation, copolymerization, and decomposition. Kinetics of nucleation, crystallization, and melting, as well as glass transitions are chosen as representative of the dynamics of phase changes.

*Chapter 4 Thermal Analysis Tools* contains a detailed description of thermometry, calorimetry, temperature-modulated calorimetry (TMC), dilatometry, thermomechanical analysis (TMA), dynamic mechanical analysis (DMA), and thermogravimetry (TGA).

*Chapter 5 Structure and Properties of Materials* covers the solid states (glasses and crystals), mesophases (liquid, plastic, and condic crystals), and liquids. Also treated are multi-phase materials, macroconformations, morphologies, defects and the prediction of mechanical and thermal properties.

*Chapter 6 Single Component Materials* provides detailed descriptions of phase diagrams with melting, disordering, and glass transitions. In addition, the effects of size, defects, strain on transitions and properties of rigid amorphous and other intermediate phases are treated in the light of thermal and mechanical histories.

*Chapter 7 Multiple Component Materials*, finally covers our limited knowledge of chemical potentials of blends, solutions, and copolymers. The Flory-Huggins equation, phase diagrams, solvent, solute, and copolymer effects on the glass, melting, and mesophase transitions are the major topics.

This book grew out of the two three-credit courses "Physical Chemistry of Polymers" and "Thermal Analysis" at The University of Tennessee, Knoxville (UTK). First, the lectures were illustrated with overhead foils, generated by computer, so that printouts could be provided as study material. In 1990 these

overheads were changed to computer-projected slides and the textbook “Thermal Analysis” was published (Academic Press, Boston). In 1994, a condensed text was added to the slides as lecture notes. A much expanded computer-assisted course “Thermal Analysis of Materials” was then first offered in 1998 and is a further development, enabling self-study. The computer-assisted course is still available via the internet from our ATHAS website ([web.utk.edu/~athas](http://web.utk.edu/~athas)) and sees periodic updates. It is the basis for the present book. A short version of the ATHAS Data Bank, a collection of thermal data, is included as Appendix 1. A treatise of the theory of “Thermophysics of Polymers” was written by Prof. Dr. Herbert Baur in 1999 (Springer, Berlin) and can serve as a companion book for the theoretical basis of the experimental results of “Thermal Analysis of Polymeric Materials.”

The book contains, as shown above, a critically selected, limited series of topics. The field of flexible macromolecules is emphasized, and the topics dealing with small molecules and rigid macromolecules, as well as the treatment of mechanical properties, are handled on a more elementary level to serve as a tie to the widely available, general science and engineering texts.

### ***Topics that are Different for Polymers and Small Molecules***

The structure of a macromolecular substance is characterized by a diversity of molecular shapes and sizes, as is discussed in Chap. 1. These are items unimportant for small molecules. Chemically pure, small molecules can be easily obtained, are of constant size and often are rigid (i.e., they also are of constant shape).

Classically, one treats phases of two components as ideal, regular, or real solutions. Usually, however, one concentrates for the non-ideal case only on solutions of salts by discussing the Debye-Hückel theory. Polymer science, in turn, adds the effect of different molecular sizes with the Flory-Huggins equation as of basic importance (Chap. 7). Considerable differences in size may, however, also occur in small molecules and their effects are hidden falsely in the activity coefficients of the general description.

The comparison of the entropy of rubber contraction to that of the gas expansion, on one hand, and to energy elasticity of solids, on the other, helps the general understanding of entropy (see Chap. 5). Certainly, there must be a basic difference if one class of condensed materials can be deformed elastically only to less than 1% and the other by up to 1,000%.

The kinetics of chain reactions of small molecules is much harder to follow (and prove) than chain-reaction polymerization. Once the reaction is over, the structure of the produced macromolecule can be studied as permanent documentation of the reaction (see Chaps. 1 and 3).

The notoriously poor polymer crystals described in Chap. 5 and their typical microphase and nanophase separations in polymer systems have forced a rethinking of the application of thermodynamics of phases. Equilibrium thermodynamics remains important for the description of the limiting (but for polymers often not attainable) equilibrium states. Thermal analysis, with its methods described in Chap. 4, is quite often neglected in physical chemistry, but unites thermodynamics with irreversible thermodynamics and kinetics as introduced in Chap. 2, and used as an important tool in description of polymeric materials in Chaps. 6 and 7.

The solid state, finally, has gained by the understanding of macromolecular crystals with helical molecules, their defect properties, mesophases, small crystal size, glass transitions, and rigid-amorphous fractions (Chaps. 5 and 6).

### General References

The general references should be used for consultation throughout your study of *Thermal Analysis of Polymeric Materials*. You may want to have the textbooks at hand which you own, and locate the other reference books in the library for quick access. Frequent excursions to the literature are a basis for success in learning the material of this course.

*Typical books on polymer science are (chemistry, physics, or engineering):*

1. Rodriguez F, Cohen C, Ober CK, Archer L (2003) Principles of Polymer Systems, 5<sup>th</sup> ed. Taylor & Francis, New York.
2. Stevens MP (1989) Polymer Chemistry, 2<sup>nd</sup> ed. Oxford University Press, New York.
3. Billmeyer, Jr. FW (1989) Textbook of Polymer Science, 3<sup>rd</sup> ed. Wiley & Sons, New York.

*Typical physical chemistry texts are:*

4. Atkins PW (1998) Physical Chemistry, 6<sup>th</sup> ed. Oxford University Press, Oxford.
5. Mortimer RG (1993) Physical Chemistry. Benjamin/Cummings, Redwood City, CA.
6. Moore WG (1972) Physical Chemistry, 4<sup>th</sup> ed. Prentice Hall, Englewood Cliffs, NJ.

*As mentioned above, the companion book treating the theory of the subject is:*

7. Baur H (1999) Thermophysics of Polymers. Springer, Berlin.

*Reference books for numerical data on polymers and general materials are:*

8. Brandrup J, Immergut EH, Grulke EA, eds (1999) Polymer Handbook. Wiley, New York, 4<sup>th</sup> edn.
9. Lide DR, ed (2002/3) Handbook of Chemistry and Physics, 83<sup>rd</sup> ed. CRC Press, Boca Raton, FL. (Annual new edns.)

*For detailed background information on any type of polymer look up:*

10. Mark HF, Gaylord NG, Bikales NM (1985–89) Encyclopedia of Polymer Science and Engineering, 2<sup>nd</sup> ed; Kroschwitz JI ed (2004) 3<sup>rd</sup> ed. Wiley, New York. Also available with continuous updates via the internet: [www.mrw.interscience.wiley.com/epst](http://www.mrw.interscience.wiley.com/epst)

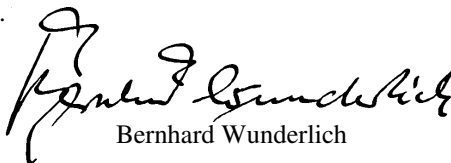
*For more advanced treatises on physical chemistry, you may want to explore:*

11. Eyring H, Henderson D, Jost W (1971–75) Physical Chemistry, An Advanced Treatise. Academic Press, New York.
12. Partington JR (1949–54) An Advanced Treatise on Physical Chemistry. Longmans, London.

### Acknowledgments

This book has grown through many stages of development. At every stage the book was shaped and improved by many participating students and numerous reviewers. Research from the *ATHAS* Laboratory described in the book was generously supported over many years by the Polymers Program of the Materials Division of the National Science Foundation, present Grant DMR-0312233. Several of the instrument companies have helped by supplying information, and also supported acquisitions of equipment. Since 1988 the *ATHAS* effort was also supported by the Division of Materials Sciences and Engineering, Office of Basic Energy Sciences, U.S. Department of Energy at Oak Ridge National Laboratory, managed and operated by UT-Battelle, LLC, for the U.S. Department of Energy, under contract number DOE-AC05-00OR22725. All figures were originally newly developed and drawn for the computer course “Thermal Analysis of Materials” and have been adapted or were newly generated for the present book.

Knoxville, TN, January 2005



Bernhard Wunderlich

---

# Contents

<b>Preface</b> .....	V
Topics that are Different for Polymers and Small Molecules .....	VII
General References .....	VIII
Acknowledgments .....	VIII
<b>1 Atoms, Small, and Large Molecules</b>	
1.1 Microscopic Description of Matter and History of Polymer Science	
1.1.1 History .....	1
1.1.2 Molecular Structure and Bonding .....	3
1.1.3 Classification Scheme for Molecules .....	6
1.1.4 The History of Covalent Structures .....	9
1.1.5 The History of Natural Polymers .....	9
1.1.6 The History of Synthetic Polymers .....	11
1.2 Nomenclature	
1.2.1 Source- and Structure-based Names .....	13
1.2.2 Copolymers and Isomers .....	22
1.2.3 Branched, Ladder, and Network Polymers .....	24
1.2.4 Funny Polymers .....	25
1.3 Chain Statistics of Macromolecules	
1.3.1 Molecular Mass Distribution .....	27
1.3.2 Random Flight .....	31
1.3.3 Mean Square Distance from the Center of Gravity .....	32
1.3.4 Distribution Functions .....	33
1.3.5 Steric Hindrance and Rotational Isomers .....	37
1.3.6 Monte Carlo Simulations .....	40
1.3.7 Molecular Mechanics Calculations .....	41
1.3.8 Molecular Dynamics Simulations .....	43
1.3.9 Equivalent Freely Jointed Chain .....	47
1.3.10 Stiff Chain Macromolecules .....	47
1.4 Size and Shape Measurement	
1.4.1 Introduction .....	50
1.4.2 Light Scattering .....	50
1.4.3 Freezing Point Lowering and Boiling Point Elevation .....	58
1.4.4 Size-exclusion Chromatography .....	62
1.4.5 Solution Viscosity .....	63
1.4.6 Membrane Osmometry .....	65
1.4.7 Other Characterization Techniques .....	66
<b>References</b> .....	68

<b>2</b>	<b>Basics of Thermal Analysis</b>	
2.1	Heat, Temperature, and Thermal Analysis	
2.1.1	History .....	71
2.1.2	The Variables of State .....	75
2.1.3	The Techniques of Thermal Analysis .....	76
2.1.4	Temperature .....	79
2.1.5	Heat (The First Law of Thermodynamics) .....	81
2.1.6	The Future of Thermal Analysis .....	84
2.2	The Laws of Thermodynamics	
2.2.1	Description of Systems .....	88
2.2.2	The First Law of Thermodynamics .....	90
2.2.3	The Second Law of Thermodynamics .....	91
2.2.4	The Third Law of Thermodynamics .....	94
2.2.5	Multi-component Systems .....	96
2.2.6	Multi-phase Systems .....	98
2.3	Heat Capacity	
2.3.1	Measurement of Heat Capacity .....	101
2.3.2	Thermodynamic Theory .....	104
2.3.3	Quantum Mechanical Descriptions .....	106
2.3.4	The Heat Capacity of Solids .....	111
2.3.5	Complex Heat Capacity .....	117
2.3.6	The Crystallinity Dependence of Heat Capacities .....	118
2.3.7	ATHAS .....	121
2.3.8	Polyoxide Heat Capacities .....	128
2.3.9	Heat Capacities of Liquids .....	131
2.3.10	Examples of the Application of ATHAS .....	134
	Polytetrafluoroethylene .....	134
	Poly(oxybenzoate- <i>co</i> -oxynaphthoate) .....	134
	Large-amplitude motions of polyethylene .....	136
	Polymethionine .....	136
	MBPE-9 .....	137
	Liquid selenium .....	138
	Poly(styrene- <i>co</i> -1,4-butadiene) .....	139
	Hypothetical entropy of the liquid at absolute zero of temperature .....	140
	Starch and water .....	142
	Conclusions .....	144
2.4	Nonequilibrium Thermodynamics	
2.4.1	Flux and Production .....	147
2.4.2	Melting of Lamellar Crystals .....	148
2.4.3	Experimental Data .....	154
2.4.4	Internal Variables .....	155
2.4.5	Transport and Relaxation .....	158
2.4.6	Relaxation Times .....	159
2.5	Phases and Their Transitions	
2.5.1	Description of Phases .....	162

2.5.2	Phases of Different Sizes .....	167
2.5.3	Mesophases .....	169
2.5.4	Mesophase Glasses .....	175
2.5.5	Thermodynamics and Motion .....	176
2.5.6	Glass Transitions .....	178
2.5.7	First-order Transitions .....	181

<b>References</b> .....	184
-------------------------	-----

### **3 Dynamics of Chemical and Phase Changes**

3.1	Stepwise and Step Reactions	
3.1.1	Stepwise Reactions .....	189
3.1.2	Mechanism of Step Reactions .....	193
3.1.3	Examples .....	196
3.1.4	Conditions .....	198
3.1.5	Reaction Rates .....	200
3.1.6	Lithium Phosphate Polymerization .....	201
3.2	Chain and Matrix Reactions	
3.2.1	Mechanism of Chain Reactions .....	206
3.2.2	Kinetics .....	212
3.2.3	Equilibrium .....	214
3.2.4	Chain Reactions without Termination .....	215
3.2.5	Emulsion Polymerization .....	217
3.2.6	Matrix Reaction .....	218
3.3	Molecular Mass Distributions	
3.3.1	Number and Mass Fractions, Step Reactions .....	219
3.3.2	Number and Mass Fractions, Chain Reactions .....	221
3.3.3	Step Reaction Averages .....	224
3.3.4	Chain Reaction Averages .....	225
3.4	Copolymerization and Reactions of Polymers	
3.4.1	Chain Reaction Copolymers .....	227
3.4.2	Step Reaction Copolymers .....	229
3.4.3	Gelation .....	230
3.4.4	Decomposition .....	231
3.4.5	Polymer Reactions .....	233
3.5	Crystal and Molecular Nucleation Kinetics	
3.5.1	Observation of Nucleation and Crystal Growth .....	238
3.5.2	Evaluation of Nucleation Rates .....	240
3.5.3	Mathematical Description of Primary Nucleation .....	242
3.5.4	Heterogeneous Nucleation .....	246
3.5.5	Secondary Nucleation .....	249
3.5.6	Molecular Nucleation .....	253
3.6	Crystallization and Melting Kinetics	
3.6.1	Linear Melting and Crystallization Rates .....	255
3.6.2	Directional Dependence of Crystallization .....	256
3.6.3	Diffusion Control of Crystallization .....	257

3.6.4	Growth of Spherulites .....	259
3.6.5	Avrami Equation .....	260
3.6.6	Nonisothermal Kinetics .....	263
3.6.7	Experimental Data .....	264
	<b>References</b> .....	276
<b>4</b>	<b>Thermal Analysis Tools</b>	
4.1	Thermometry and Dilatometry	
4.1.1	Principle and History of Thermometry .....	279
4.1.2	Liquid-in-glass Thermometers .....	283
4.1.3	Resistance Thermometers and Thermocouples .....	285
4.1.4	Applications of Thermometry .....	290
4.1.5	Principle and History of Dilatometry .....	291
4.1.6	Length, Volume, and Density Measurement .....	293
4.1.7	Applications of Dilatometry .....	298
4.2	Calorimetry	
4.2.1	Principle and History .....	304
4.2.2	Isothermal and Isoperibol Calorimeters .....	307
4.2.3	Loss Calculation .....	310
4.2.4	Adiabatic Calorimetry .....	312
4.2.5	Compensating Calorimeters .....	314
4.2.6	Modern Calorimeters .....	317
4.2.7	Applications of Calorimetry .....	319
	Purity analysis .....	319
	Thermochemistry .....	320
	Thermodynamic functions of three allotropes of carbon .....	325
	Thermodynamic functions of paraffins .....	327
4.3	Differential Scanning Calorimetry	
4.3.1	Principle and History .....	329
4.3.2	Heat-flux Calorimetry .....	331
4.3.3	Power Compensation DSC .....	335
4.3.4	Calibration .....	338
4.3.5	Mathematical Treatment .....	340
4.3.6	DSC Without Temperature Gradient .....	344
4.3.7	Applications .....	349
	Heat capacity .....	349
	Finger printing of materials .....	350
	Quantitative analysis of the glass transition .....	354
	Quantitative analysis of the heat of fusion .....	355
4.4	Temperature-modulated Calorimetry	
4.4.1	Principles of Temperature-modulated DSC .....	359
4.4.2	Mathematical Treatment .....	362
4.4.3	Data Treatment and Modeling .....	369
4.4.4	Instrumental Problems .....	373
4.4.5	Heat Capacity Measurement .....	385
4.4.6	Glass Transition Measurement .....	388

4.4.7	First-order Transition Analysis .....	396
4.4.8	Chemical Reactions .....	402
4.5	Thermomechanical Analysis, DMA and DETA .....	
4.5.1	Principle of TMA .....	404
4.5.2	Instrumentation of TMA .....	406
4.5.3	Applications of TMA .....	408
4.5.4	Principles and Instrumentation of DMA .....	412
4.5.5	Applications of DMA .....	419
4.5.6	DETA .....	424
4.6	Thermogravimetry .....	
4.6.1	Principle and History .....	428
4.6.2	Instrumentation .....	430
4.6.3	Standardization and Technique .....	437
4.6.4	Decomposition .....	438
4.6.5	Coupled Thermogravimetry and Differential Thermal Analysis .....	439
4.6.6	Applications of Thermogravimetry .....	443
	Calcium oxalate/carbonate decomposition .....	444
	Lifetime prediction .....	446
	Summary of Chapter 4 .....	448
	<b>References</b> .....	450
<b>5</b>	<b>Structure and Properties of Materials</b> .....	
5.1	Crystal Structure .....	
5.1.1	Introduction .....	455
5.1.2	Lattice Description .....	457
5.1.3	Unit Cells .....	457
5.1.4	Miller Indices .....	458
5.1.5	Symmetry Operations .....	460
5.1.6	Helices .....	463
5.1.7	Packing in Crystals .....	468
5.1.8	Packing of Helices .....	471
5.1.9	Selected Unit Cells .....	474
5.1.10	Isomorphism .....	481
5.1.11	Crystals with Irregular Motifs .....	483
5.2	Crystal Morphology .....	
5.2.1	Crystal Habit .....	486
5.2.2	Molecular Macroconformation .....	486
5.2.3	Fold Length .....	488
5.2.4	Lamellar Crystals .....	493
5.2.5	Dendrites and Spherulites .....	497
5.2.6	Fibers .....	503
5.2.7	Isometric Crystals .....	508
5.3	Defects in Polymer Crystals .....	
5.3.1	Materials Properties .....	512
5.3.2	Crystallinity Analysis .....	512
5.3.3	Summary of Defect Types .....	516



5.3.4	Supercomputer Simulation of Crystal Defects .....	524
5.3.5	Deformation of Polymers .....	530
5.3.6	Ultimate Strength of Polymers .....	533
5.4	Transitions and Prediction of Melting	
5.4.1	Transitions of Macromolecules .....	536
5.4.2	Crystals of Spherical Motifs .....	538
5.4.3	Crystals of Non-spherical Motifs .....	541
5.4.4	Crystals of Linear Hydrocarbons .....	542
5.4.5	Crystals of Macromolecules .....	544
5.5	Mesophases and Their Transitions	
5.5.1	Multiple Transitions .....	547
5.5.2	Classes of Mesophases .....	551
5.5.3	Jump-motion in Crystals .....	555
5.5.4	Conformational Disorder .....	558
5.5.5	Examples .....	561
	Summary of the section on morphology .....	571
5.6	Melts and Glasses	
5.6.1	Structure of the Amorphous Phase .....	572
5.6.2	Properties of the Amorphous Phase .....	574
5.6.3	Viscosity .....	575
5.6.4	Energy Elasticity .....	578
5.6.5	Entropy Elasticity .....	579
5.6.6	Viscoelasticity .....	583
	<b>References</b> .....	586
<b>6</b>	<b>Single Component Materials</b>	
6.1	The Order of Transitions	
6.1.1	Review of Thermodynamics, Motion, and Reversibility .....	591
6.1.2	First Order Phase Transition .....	593
6.1.3	Glass Transitions .....	597
	The hole model of the glass transition .....	598
	Enthalpy relaxation .....	599
	The kinetics of the number of holes .....	600
	Effect of the size of the phase on the glass transition .....	605
	Rigid-amorphous fraction, RAF, in semicrystalline polymers .....	607
	Differences in $T_g$ by DSC and DMA .....	609
6.2	Size, Extension, and Time Effects During Fusion	
6.2.1	Melting of Polyethylene .....	611
6.2.2	Reversible Melting and Poor Crystals .....	624
	Poly(oxyethylene) .....	624
	Polyterephthalates .....	628
	Polynaphthoate .....	634
	Polycarbonate .....	637
	Poly(phenylene oxide) .....	639
	Poly( $\epsilon$ -caprolactone) .....	641
	Polypropylenes .....	644

Decoupling of segments of polymer chains .....	649
Poor crystals .....	652
6.2.3 Annealing and Recrystallization Effects .....	655
6.2.4 Melting of Poly(oxymethylene) .....	666
6.2.5 Melting of PEEK .....	668
6.2.6 Melting of Fibers .....	672
6.3 Analysis of the Sample History Through Study of the Glass Transition .....	
6.3.1 Time and Temperature Effects .....	682
6.3.2 Modeling of the Glass Transition .....	686
6.3.3 Pressure and Strain Effects .....	689
6.3.4 Crystallinity Effects .....	693
6.3.5 Network Effects .....	698

<b>References</b> .....	701
-------------------------	-----

## **7 Multiple Component Materials**

7.1 Macromolecular Phase Diagrams .....	
7.1.1 Phase Diagrams .....	706
7.1.2 Flory-Huggins Equation .....	709
7.1.3 Upper and Lower Critical Temperatures .....	712
7.1.4 Phase Diagrams with Low-mass Compounds .....	714
7.1.5 Phase Diagrams with Low-mass Homologs .....	717
7.1.6 Block Copolymers .....	723
7.2 Melting Transitions of Copolymers .....	
7.2.1 Theory of Copolymer Melting and Crystallization .....	725
7.2.2 Applications .....	733
LLDPE .....	733
POBcoON .....	743
7.2.3 Melting Transitions of Block Copolymers .....	747
7.2.4 Melting Transitions of Regular Copolymers .....	756
7.3 Glass Transitions of Copolymers, Solutions, and Blends .....	
7.3.1 Theory of Glass Transitions .....	759
7.3.2 Glass Transitions of Solutions .....	763
7.3.3 Glass Transitions of of Copolymers .....	766
7.3.4 Glass Transitions of Block Copolymers .....	768
7.3.5 Glass Transitions of Multi-phase Systems .....	772

<b>References</b> .....	774
-------------------------	-----

## **Appendices**

A.1 Table of Thermal Properties of Linear Macromolecules and Related Small Molecules—The ATHAS Data Bank .....	777
A.2 Radiation Scattering (Essay by W. Heller) .....	801
A.3 Derivation of the Rayleigh Ratio .....	806
A.4 Neural Network Predictions .....	811

A.5	Legendre Transformations, Maxwell Relations, Linking of Entropy and Probability, and Derivation of (dS/dT) .....	813
A.6	Boltzmann Distribution, Harmonic Vibration, Complex Numbers, and Normal Modes .....	815
A.7	Summary of the Basic Kinetics of Chemical Reactions .....	817
A.8	The ITS 1990 and the Krypton-86 Length Standard .....	818
A.9	Development of Classical DTA to DSC .....	820
A.10	Examples of DTA and DSC under Extreme Conditions .....	824
A.11	Description of an Online Correction of the Heat-flow Rate .....	831
A.12	Derivation of the Heat-flow Equations .....	835
A.13	Description of Sawtooth-modulation Response .....	837
A.14	An Introduction to Group Theory, Definitions of Configurations and Conformations, and a Summary of Rational and Irrational Numbers ...	848
A.15	Summary of Birefringence and Polarizing Microscopy .....	850
A.16	Summary of X-ray Diffraction and Interference Effects .....	851
A.17	Optical Analog of Electron Double Diffraction to Produce Moiré Patterns .....	852
<b>Substance Index</b> .....		855
<b>Subject Index</b> .....		875

# Atoms, Small, and Large Molecules

## 1.1 Microscopic Description of Matter and History of Polymer Science

### 1.1.1 History

At the beginning of the 19<sup>th</sup> century the description of matter attained, what one would call today, a scientific basis. Dalton<sup>1</sup> supported the atomic theory with experiments permitting the development of modern chemistry. The book "A New System of Chemical Philosophy," describes this new approach. In Fig. 1.1, an excerpt is displayed. Chapters I and II give a summary of the contemporary understanding of nature by analyzing heat and mass, the two basic building-blocks of any material. Chapter I displays the theory of the *caloric* as it was generally

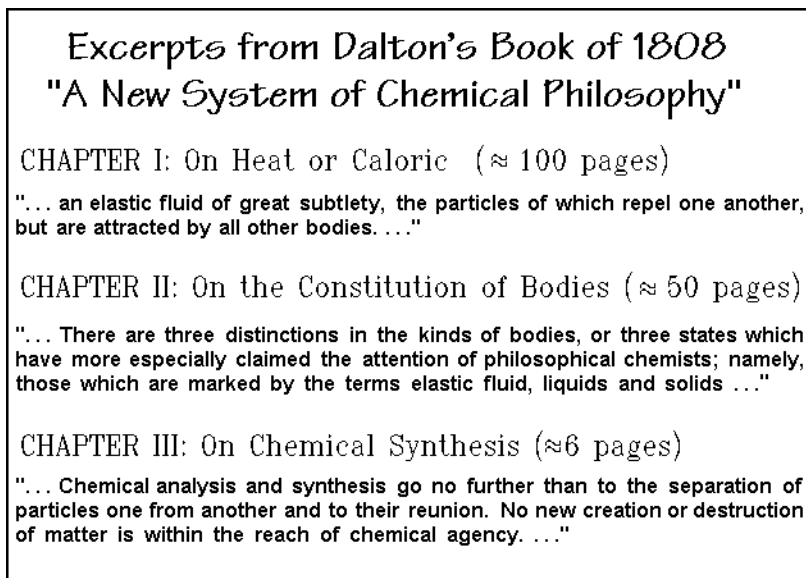


**Fig. 1.1**

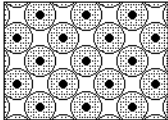
---

<sup>1</sup> John Dalton (1766–1844) founded the experiment-based atomic theory. In 1798 he was elected to be a Member of the Literary and Philosophical Society of Manchester, England. There, he read on Oct. 21, 1803 the communication on the "Chemical Atomic Theory."


accepted in the early 19<sup>th</sup> century. Heat was assumed to be an indestructible fluid that occupies spaces between the molecules of matter, as illustrated with the schematic at the top of Fig. 1.2 for gases. The schematic does not agree with today's picture of a gas which calls for mobile molecules that collide with each other (see Sect. 2.5.1). It, however, permitted quantitative measurements as discussed in more detail in the description of heat and temperature in Sect. 2.1.1.

**Excerpts from Dalton's Book of 1808**  
**"A New System of Chemical Philosophy"**

Gas:



molecule •

caloric 

Reaction:  $aA + bB \rightleftharpoons cC + dD$

Conclusion:

**Molecules of matter consist of atoms held together by chemical bonds**

Dalton's formula for sugar:  
 (1H, 4C, 20)

1 alcohol + 1 carbonic acid  
 (still far from the true molecular structure  $C_{12}H_{22}O_{11}$ , sucrose)

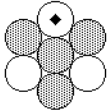


**Fig. 1.2**

Chapter II of Dalton's book gives a description of the three classical phases of matter in terms which we still recognize today, except that in modern science one calls the *elastic fluids* of the quotation in Fig. 1.1, gasses. Only Chap. III has stood the test of time and is the basis of the fame of Dalton: "Molecules of matter consist of atoms, held together by chemical bonds" (see Fig. 1.2). Although Dalton's chemical formula of sugar in Fig. 1.2 is not up to the present knowledge in composition and structure, the principle is correct. Molecules are made up of one or more atoms. Note also from the lengths of the chapters in Dalton's book that it seems, as is common in most human endeavors, that the more one knows about a subject, the fewer words are needed for its description.

Another point to be made in connection with Dalton's writings is the distinction between phases and substances (molecules). It will be shown later in the book that large molecules may reach the size of phases. On the other hand, phases that were initially thought to be macroscopic in size, may also be very small in form of microphases and nanophases, as will be detailed in Sect. 2.5. Sufficiently large molecules may then reside at the same time in more than one phase. Many of the special properties of crystalline flexible polymers, for example, are based on the smallness of their phases, and this will be a major item of discussion in the various chapters of the book.

### 1.1.2 Molecular Structure and Bonding

In order to understand molecules, there is a need for a brief review of atoms and the bonding which holds the atoms in a molecule. A characterization of the atomic structure is given by the configuration of its valence electrons, the electrons available for bonding in the outer shells of the atoms, and the electronegativity,  $X_A$ , as demonstrated in Fig. 1.3. The electronegativity is a measure of the ability to attract an electron pair, needed for covalent bonding [1]. It is approximately the average between the electron affinity (the energy gained or lost when adding an electron) and the ionization energy (the energy needed to remove an electron), and adjusted with data from bond energies. The electronegativity has a scale from zero to four and permits an estimation of covalent bond energy.

The range of atomic radii of the different atoms is not very large, still, the differences in sizes are of importance for the fitting of atoms to molecules, and furthermore for the packing of molecules into liquids and crystals, as will be

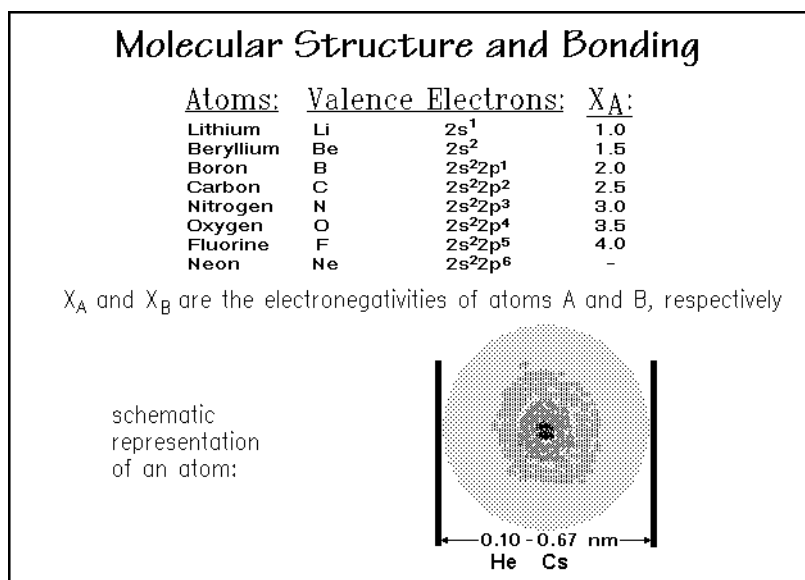


**Fig. 1.3**

discussed below. Negative ions often exceed the given range of sizes, and positive ions may be smaller. The small range of atomic radii is also the reason for the excitement created when close-to-spherical fullerenes were discovered [2] which are molecules consisting of carbon atoms only, such as  $C_{60}$  and  $C_{70}$ . For the structure of  $C_{60}$  and its thermal properties see Sect. 2.5.3. These spheres of  $\approx 1.0$  nm diameter may act also as building blocks of *pseudo molecules*. It is interesting to imagine, how nature would change with changes in atomic size and also shape.

The joining of atoms to molecules requires interactions that keep the atoms bound together, at least long enough for identification, as pointed out in Fig. 1.4. This statement is an operational definition of a bond. Operational definitions were

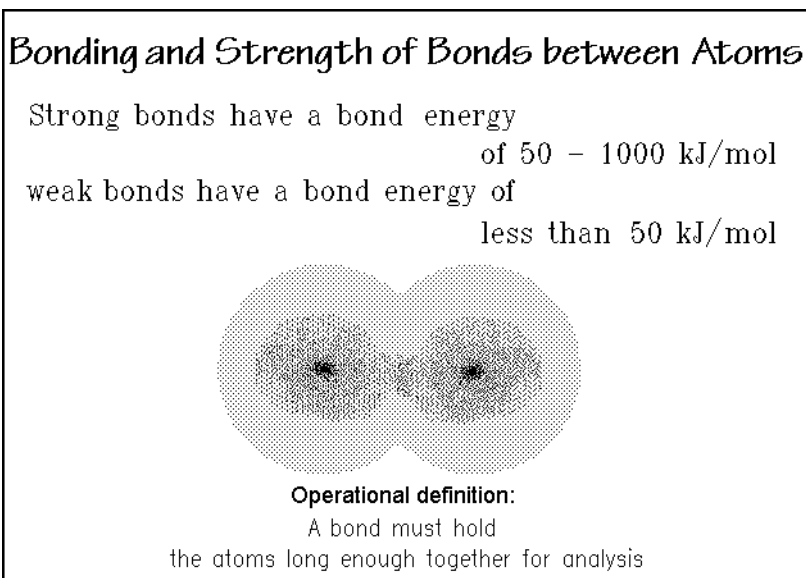


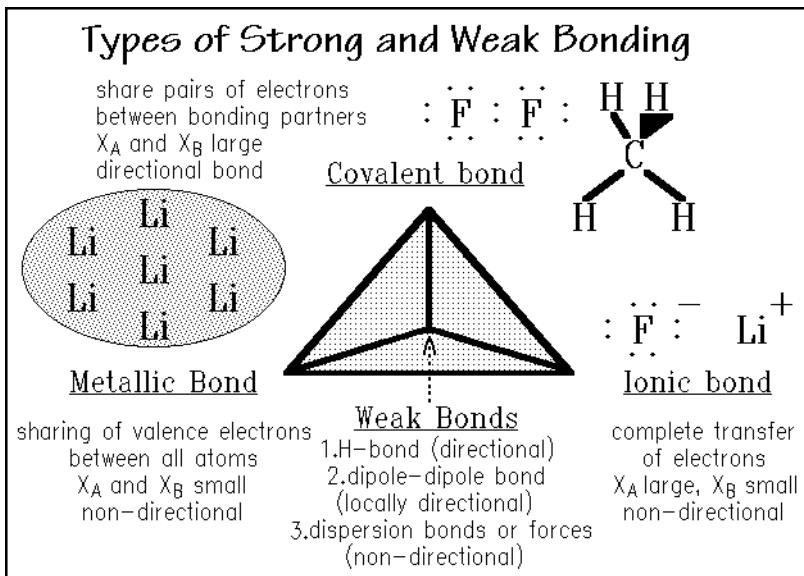
**Fig. 1.4**

suggested by Bridgman<sup>1</sup> as a means to give precise, experiment-based information, even when the phenomenon to be described is not fully understood. This will be made use of, for example, to clarify difficult subjects, such as: Where is the borderline between solids and liquids? A topic that will be tackled in Sect. 1.1.3 and leads to a surprising and not conventional result.

For the description of molecules in Fig. 1.4, one expects some correlation between the life-time of a bond and its strength. Often one judges the strength of a bond by its bond energy. Checking a large number of experimentally measured bond energies, it becomes obvious that there are only two well-separated classes of bonds when describing atoms, ions, and molecules, namely strong bonds and weak bonds. Bond energies in the range of 50 kJ mol<sup>-1</sup>, that would be called intermediate, are rarely observed. Different types of bonding involve different interactions and displacements of the electrons of the bonding partners.

The strong bonds are classified as covalent, ionic, or metallic. Figure 1.5 illustrates the covalent bonds for fluorine, F<sub>2</sub>, and methane, CH<sub>4</sub>. The bonds involve sharing of electrons between the bonding partners. Important in the description of a covalent bond is its directiveness, governed by the molecular orbital that contains the electron pair. Most of the bonds of interest in polymer science involve hybrid bonds of s and p orbitals (molecular orbitals are described by combinations of atomic orbitals, see also Fig. 1.3). Because of the close approach of the atoms in a covalent bond and the frequent involvement of only s and p orbitals in bonding, coordination numbers, CN, of one to four are most frequent.

<sup>1</sup> Percy Williams Bridgman (1882–1961), Professor at Harvard University, was awarded the Nobel Prize for Physics in 1946 for his studies of materials at very high temperatures and pressures.

**Fig. 1.5**

Moving the (valence) electrons during bonding from one atom (of low  $X_B$ ) to another (of higher  $X_A$ ), leads to ionic bonds. Figure 1.5 shows the example of lithium fluoride, LiF, a salt with strong ionic bonds. The major bonding is caused by Coulomb attraction between the positive ions and their negative counterparts which extend into all directions of space. Important for the assembly of large aggregates of ions is this absence of any directiveness. It must be recognized, however, that only negative ions in contact with positive ions lead to a strong attraction. Ions of equal charges repel each other. There are, thus, strict rules of the alternation of charges, which limits the CN between oppositely charged ions usually to between four and eight, depending on the size-ratio of the ions.

The metallic, strong bonds are shown in Fig. 1.5 for the example of lithium, Li. In this case the electrons are not concentrating in an identifiable bond, but are shared in a band structure. Such arrangement makes the bonds, as in the LiF non-directive, but it also removes all packing restrictions. Metals can thus pack most closely, often with a CN of 12. The most dense materials are found among the heavy metals (osmium, iridium, platinum, and gold have densities of 19–22 g cm<sup>-3</sup>, compared to water with the density of 1.0 g cm<sup>-3</sup>).

The three types of strong bonds and their intermediates, such as polar covalent bonds are found at the base of a tetrahedron in Figure 1.5, called the Grimm tetrahedron. The Grimm tetrahedron summarizes all types of bonds and its intermediates. The additional weak bonds are collected at the top of the tetrahedron and are discussed in more detail when needed. The directionality of weak bonds is of importance for the understanding of structures held together only temporarily and also, for example, the crystal of the linear macromolecules, discussed in Chap. 5. The polymer crystals have low melting temperatures because of these weak bonds and the influence of the flexibility of the chains, as will be quantified in Sect. 5.4.



### 1.1.3 Classification Scheme for Molecules

In early classifications of types of molecules, one differentiated between organic and inorganic molecules. The former was thought to need the intervention of a living organism for their formation, the latter, not. Already in 1828 it was, however, discovered (accidentally) by Wöhler<sup>1</sup> that urea, a typical *organic* molecule ( $\text{H}_2\text{N}-\text{CO}-\text{NH}_2$ ), could be made in the laboratory from ammonium cyanate, an *inorganic* molecule ( $\text{ONC}-\text{NH}_4$ ). With the blurred division between organic and inorganic molecules, it became the custom to distinguish biological molecules as truly organic molecules. Today one can even synthesize or modify biological molecules, removing much of the original usefulness for such classification.

A better classification makes use of the sizes of molecules, dividing them into small molecules and macromolecules, as is indicated in Fig. 1.6 [3]. The importance of large molecules, or macromolecules, was shown by Staudinger<sup>2</sup> about 80 years ago. Following his suggestion, any molecule with more than 1000 atoms or a molar mass of more than 10,000 Da should be called a macromolecule. This operational definition is quite useful since there are not many molecules that are known with about 1000 atoms. Most are either much larger or much smaller.

To complete this classification of Fig. 1.6, a further subdivision into flexible and rigid macromolecules is advantageous. Flexible macromolecules are of main interest

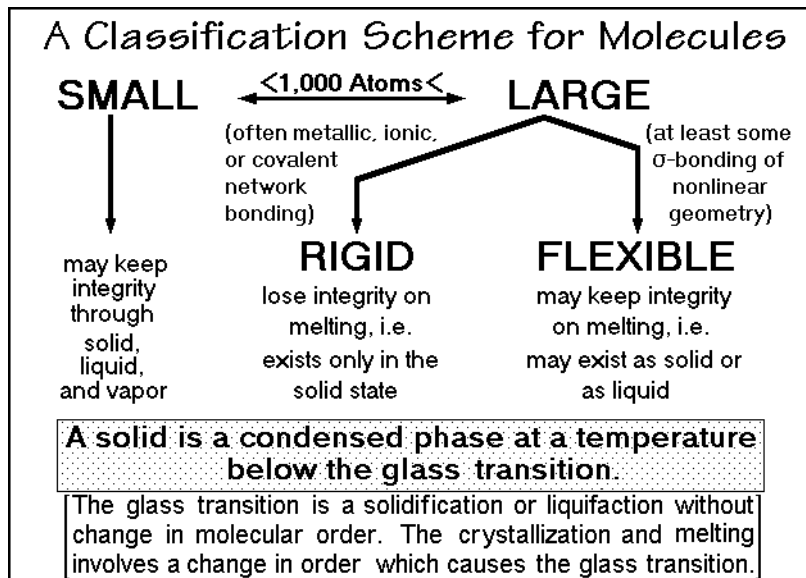


Fig. 1.6

<sup>1</sup> Friedrich Wöhler (1800–1882) Professor at the Universities of Heidelberg and Göttingen in Germany.

<sup>2</sup> Hermann Staudinger (1881–1965) Professor at the University of Freiburg, Germany, Nobel Prize for Chemistry in 1953.

to the discussions in this book and are usually, but not so precisely, just called *polymers*. The term *plastics* is often applied colloquially to the low-melting, polymeric materials. The polymers also are the macromolecules Staudinger introduced to chemistry as the last class of new molecules. The flexibility of such molecules is caused by internal rotation about at least some sigma bonds of proper geometry (see Sect. 1.3). Missing flexibility makes a macromolecule rigid. Rigid macromolecules are usually of the size of the phase, and make the distinction between phases and molecules superfluous and unwieldy. The molecule of a single crystal of 100 g, for example, reaches a molar mass of about  $6 \times 10^{19}$  metric tons.

Chemistry is the science dealing with synthesis, reactions, and properties of all substances, but traditionally small molecules have become the main focus. After the discovery of X-ray diffraction, rigid macromolecules have become the primary substances of interest to material science and solid state physics. The *new*, flexible macromolecules fell between these fields and have only slowly been accepted into the various academic disciplines. Presently polymer science is most prominently taught in material science courses, less in chemistry, and least in physics.

The key distinction between the three classes of molecules just described is summarized in the center of Fig. 1.6. Small molecules may appear in the solid, liquid, and gaseous phases without decomposition, while rigid macromolecules keep their bonding (molecular integrity) only to nearest neighbors in the solid state. Due to internal rotation, the flexible macromolecules can attain sufficient intramolecular disorder to melt (or dissolve) without breaking strong bonds. This property is at the root of many of the useful properties of polymers, as will be discussed throughout the book. The three classes of molecules are thus very distinct in their phase behavior.

No large molecules can be evaporated thermally without decomposition. If one tries to place flexible macromolecules into the gas phase by evaporation of the solvent molecules from a dispersion of droplets of a solution with only one macromolecule per droplet, the macromolecules become solid microphase particles and collect at the bottom of the container. Typical examples of single polymer glass phases and crystals are shown in Chap. 5.

A preliminary, operational definition of the solid state is given within the box of Fig. 1.6. It will be expanded upon and linked to the material properties throughout the book. For materials, the transitions between solid and liquid are basic and determine their utility. Similarly, the evaporation characteristics need to be known to choose a molecule for a given application. The new classification scheme for molecules of Fig. 1.6 is, thus, much more useful than the earlier, arbitrary distinction that relied upon the ability or inability of living organisms to synthesize a particular substance. The bottom brackets give a rather unique explanation of the glass transition which is detailed in Sect. 2.5.

Figure 1.7 contains a listing of small molecules, flexible macromolecules, and rigid macromolecules. The small molecules are the compounds of traditional chemistry, they are limited at the size of about 1000 atoms, as indicated in Fig. 1.6. As also pointed out in Fig. 1.6, they are often stable in all three phases, gas, liquid, and solid. One can see the importance of the different phases from terminology in use for hundreds of years. The compound  $\text{H}_2\text{O}$  has three names, steam, water, and ice, which link it to its phases, a practice not carried to any other compound. Perhaps the

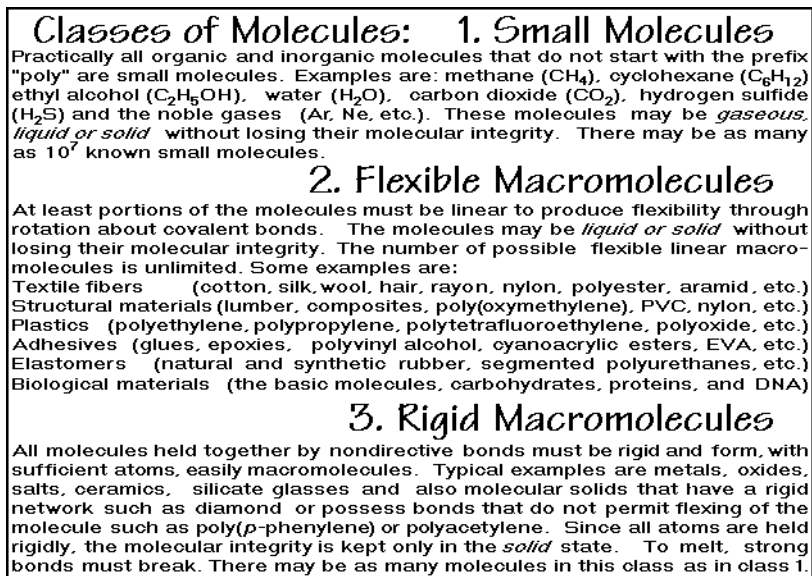


**Fig. 1.7**

difference between molecules and phases was understood by the time other important molecules were identified in detail.

Next, a series of flexible macromolecules is listed in Fig. 1.7 together with their applications. At sufficiently high temperatures they form mobile, random coils in a liquid state, as will be described in Sect. 1.3. On cooling, they become solid, either by crystallization (although they usually crystallize only partially) or by formation of a glass. These transitions are discussed in much more detail in Chaps. 2 and 5. If the flexible macromolecules are cross-linked, they show rubber elasticity, another unique polymer property, detailed in Sect. 5.6.5. Both, small molecules and flexible macromolecules must contain directive strong bonds, as shown in the Grimm tetrahedron of Fig. 1.5. These directive bonds connect the atoms to a molecule to a closed structure. Non-directive bonds with enough atoms, in contrast, lead to three-dimensional, unlimited, open aggregates and, thus, rigid macromolecules.

Rigid macromolecules, the last group in Fig. 1.7, are often not recognized as separate molecules because of their enormous size. The molecule determines the size of the phase or vice versa. A single crystal of NaCl is naturally a single molecule. It is thus more important to know the structure, shape, and defects of the crystal than the mass of the macromolecule. The chemical formula refers only to the smallest unit describing the material and refers to a formula mass, not the molar mass. Similarly, the flexible macromolecules are represented by the formula of their repeating unit, not the full molecule, as will be discussed in Sect. 1.2. On fusion or sublimation, rigid macromolecules lose their integrity, as discussed above, and break into smaller units. A sodium chloride melt is thus not a liquid of small NaCl molecules, but rather a dynamic aggregate of positive sodium and chloride ions that constantly changes the bonding to their neighbors. Only in the gas phase are strongly polar, small NaCl molecules detectable.

### 1.1.4 The History of Covalent Structures

The historic development of knowledge about polymer science is rather surprising in that it took so long to recognize the existence of flexible macromolecules. This delay occurred despite the great importance of polymers to man. Flexible linear macromolecules are not only a key compound in material science, they are also the basic molecules of life in the form of proteins, nucleic acids, celluloses, and starches. Polymeric materials can be stronger than metals, be more (rubber-) elastic than any other substance, be among the best insulators of heat and electricity, but if properly chosen, can also conduct electricity. Polymeric adhesives, films, fibers, and packaging have thoroughly affected our way of life. Polymers provide the many enzymes, which govern the chemical reactions basic to life, supply the molecules that store and govern genetic information, and create the supporting structural basis of biological systems.

All flexible macromolecules must contain at least a sequence of linear, covalently bonded atoms. The understanding of the cylindrically symmetric, directed, covalent bonds (sigma bonds) was thus the first step towards polymer science. This step was already taken in 1858 by Kekulé<sup>1</sup> as shown in Fig. 1.8. The detailed structures of large aggregates of atoms (macromolecules) could next be analyzed in detail after X-ray diffraction was fully understood. Major steps in the development of X-ray analysis of macromolecules are listed in the figure. First, rigid macromolecules such as metals, salts, minerals, and ceramics were analyzed. This was followed by many polymer crystal structures and even globular proteins.

The general reference to the book by Flory<sup>2</sup> contains a brief, expert summary of the history of knowledge about polymers and is a treatise on polymer physical chemistry. (See also the list of general references for this section). The delay in development of polymer science due to the misunderstanding of colloid science (microphases) is discussed next.

### 1.1.5 The History of Natural Polymers

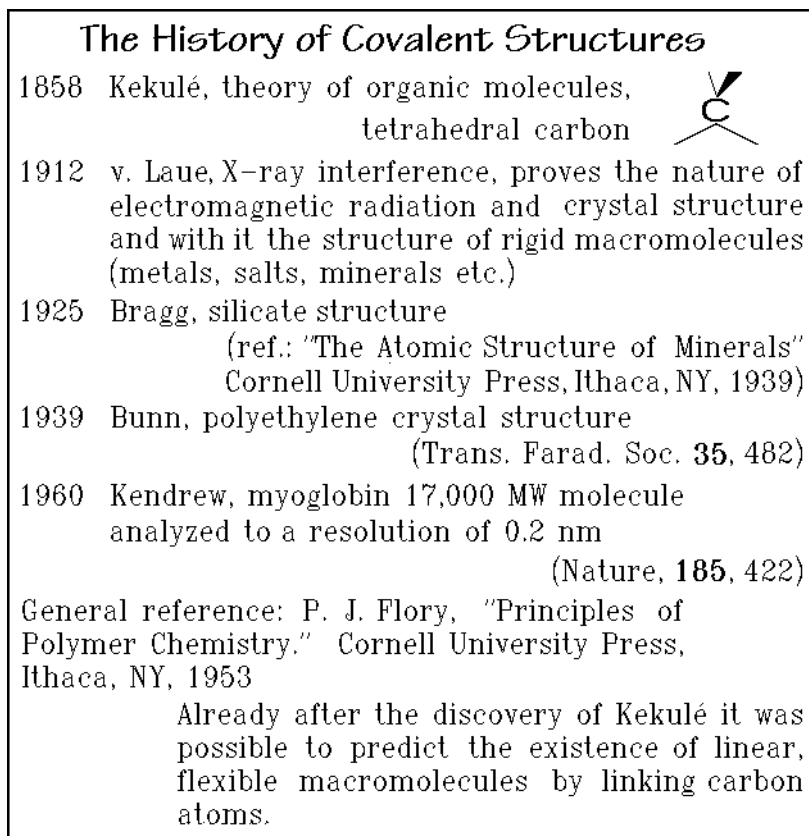
Naturally occurring polymers, as listed in Fig. 1.9, have always been present in nature and should have led to the early discovery of flexible, linear macromolecules. In retrospect, the observation of Gough, shown in Fig. 1.9, is already a hint at the thermodynamics of rubber elasticity, as will be shown in Chap. 5. The fact, that on extension polymers increase in temperature is an indication of a decrease in entropy. This contrasts the energy-elasticity of metals, which leads to constant or slightly decreasing temperatures on extension, indicative of unchanged or slightly increasing entropy on reversible extension (see Sect. 5.6).

Further development was, however, slowed with the discovery of colloids, as indicated in Fig. 1.9. The radii of colloidal particles are  $10^{-4}$ – $10^{-6}$  cm. Today one

---

<sup>1</sup> August Kekulé (1829–1896) Professor at the University of Bonn, Germany.

<sup>2</sup> Paul John Flory (1910–1985) Professor at Stanford University, Nobel Prize for Chemistry, 1974 for work in the field of synthetic and natural macromolecules.

**Fig. 1.8**

would call phases of such dimensions microphases (with less than one micrometer in size,  $10^{-4}$  cm) or nanophases (when approaching one nanometer in size  $10^{-7}$  cm). Flexible macromolecules are by themselves already in the range of colloidal dimensions, i.e., they may be longer than the diameter of a microphase. Many of the properties of polymers are due to the possibility that a single molecule may, thus, be part of more than one phase and cause strong interactions across the phase boundaries.

On the example of natural rubber listed in Fig. 1.9 it can be seen how the knowledge about colloids has hindered the development of polymer science. The series of the listed experiments should have made it increasingly clear that rubber consists of long-chain molecules. Instead, it was concluded at the turn of the 19<sup>th</sup> to the 20<sup>th</sup> century that there exists no single molecule with the polymer structure, but that rubber is a colloidal phase of weakly attached rings. Covalently bonded molecules of colloidal dimensions were thought to be impossible. The assumption that the basic rubber molecules were rings was needed to account for the simple  $C_5H_8$  stoichiometry. Macromolecules are a typical example of the difficulties one has to change prevalent opinion, even in the natural sciences.

The History of Natural Polymers	
Natural polymers: mainly	
	polysaccharides (starches and celluloses)
	proteins (copolymers of some 21 amino acids)
	nucleic acids (phosphate-sugar-base copolymers)
	rubber and related polymers (isoprene polymers)
1805	Gough, rubber heats on stretching (Proc. Lit. and Phil. Soc. Manchester 2nd Series, 1, 288)
1861	Graham, development of Colloid Science, terminated progress towards polymer science. Each large molecule was assumed to be an aggregation of small molecules.
Example: Rubber	
(polyisoprene $\text{ICH}_2\text{-C(CH}_3\text{)=CH-CH}_2\text{-I}_x$ )	
1826	Faraday, empirical formula $\text{C}_5\text{H}_8$
1860	Williams, isoprene by distillation (decomposition)
1882	Raolt's Law: MW of up to 30,000 from f.p. lowering
1904	Harries: $\text{=CH-CH}_2\text{-CH}_2\text{-C(CH}_3\text{)=}$
	(identification of levulinic aldehyde $\text{H-C-CH}_2\text{-CH}_2\text{-C(CH}_3\text{)=}$ and
	levulinic acid $\text{HO-C-CH}_2\text{-CH}_2\text{-C(CH}_3\text{)=}$ on ozone decomposition)
Still, rings were assumed to make up the rubber	

Fig. 1.9

### 1.1.6 The History of Synthetic Polymers

The many synthetic polymers or flexible macromolecules are practically all new molecules on earth, and as with any new substance, there may be a hazard to the environment on its introduction in large volume. Fortunately, as soon as one becomes aware of problems with a specific polymer, a remedy can be found by altering the polymer produced because of the multitude of available macromolecules, as described in Chap. 3. The enormous usefulness of the materials by far outweighs any of the temporary problems that have been created and will arise in the future. The use of polymers has changed technology on a similar scale as the availability of cheap iron some 200 years ago, which was the major root of the industrial revolution (1750–1900).

The history of synthetic polymers started with the analysis of sticky and tar-like residues left after organic syntheses. A typical example was the early work on poly(ethylene glycol) shown in Fig. 1.10. The logical progress to polymer science would have been faster if microphases and molecules would have been better distinguished, as is suggested in the figure. Only in 1920, through the large effort of

The History of Synthetic Polymers	
Story of tars and undistillable residues	
1860 – 1863	Lourenço, on poly(ethylene glycol)s: noted increasing viscosity with $n$ , and concluded the sticky residue would have $n \approx \infty$ $\text{HO}-(\text{C}_2\text{H}_4-\text{O})_n\text{H}$ $n < 7$ separable by distillation
1894	Vorländer assigned increasing ring sizes to the polymers, thus postponing the development of polymer science
1920	Staudinger: proposed chain formulae for polystyrene, poly(oxymethylene), and rubber $(\text{CH}_2-\underset{\text{C}_6\text{H}_5}{\text{CH}})_n$ $(\text{O}-\text{CH}_2)_n$ $(\text{CH}_2-\underset{\text{CH}_3}{\text{C}}=\text{CH}-\text{CH}_2)_n$
1929	Carothers: polyesters and nylons polyester: $(\text{R}_a-\text{O}-\text{CO})_n$ or $(\text{O}-\text{R}_a-\text{O}-\text{CO}-\text{R}_b-\text{CO})_n$ nylon (polyamide): $(\text{R}_a-\text{NH}-\text{CO})_n$ or $(\text{NH}-\text{R}_a-\text{NH}-\text{CO}-\text{R}_b-\text{CO})_n$ $\text{R}_{a,b} = (\text{CH}_2)_{a,b}$
1930 – 1950	Chain statistics (Kuhn, Flory) large-scale industrial production, rubber elasticity understood
1950 – 1970	Stereospecific polymers, copolymers, solid state (crystallinity)
1970 – 2000	Complex polymers, mesophase polymers, high-strength polymers, high-temperature polymers conductivity in polymers, micro- and nanophase separation

Fig. 1.10

Staudinger [4], was it finally established without doubt, that flexible, linear macromolecules are a new class of molecules as was described in Sect. 1.1.3. With the discovery of this new class of molecules the overall description of all molecules is possible as summarized in Figs. 1.6 and 7.

Once discovered and understood, the number of new polymers and knowledge about them grew rapidly. Some of the milestones are listed also in Fig. 1.10. The growth of new information on polymers went parallel with the enormous growth of the polymer industry. It is surprising that the traditional academic disciplines were very slow in including the new body of knowledge about molecules into their field of interest. In fact, many of the premier universities in the world still do not have polymer chemistry or physics in their curriculum. Much of the early progress of polymer physical chemistry and physics was thus left to the organic chemists who made the new molecules and the material and textile engineers who had to support the new industrial uses. The basics of nomenclature and structure, as well as descriptions of the molecular size-distribution and the experiments needed to experimentally characterize the molecular sizes of the flexible macromolecules are discussed in the remaining sections of this chapter.

## 1.2 Nomenclature

### 1.2.1 Source- and Structure-based Names

Flexible macromolecules were identified in Fig. 1.6 within the framework of all possible molecules, and the historical development of the science of the field was sketched. The present topic is nomenclature. Without mastery of the basic nomenclature it is difficult to talk about any new subject matter, much less is it possible to learn its intricacies. For this reason, one must go through the drudgery of learning the needed names and rules by rote. Without such drill, future discussions will have to be at a much lower level. When discussing macromolecules, their name *and* their structure must be in ones mind in order to understand their behavior. Only then, for example, can there be a link between the question of flexibility, reaction mechanisms, and crystallization to the bonds and atoms that are affected.

The rules of nomenclature are set by the International Union of Pure and Applied Chemistry (IUPAC) [5]. When a new polymer has been made, a need to name it arises, even before the structure is known. This is done by giving the polymer a source-based name, as indicated in Fig. 1.11. For example, the polymer made by polymerization of methyl methacrylate is called poly(methyl methacrylate). The monomer name is simply added to the word poly (Gk. πολύς = many; note that

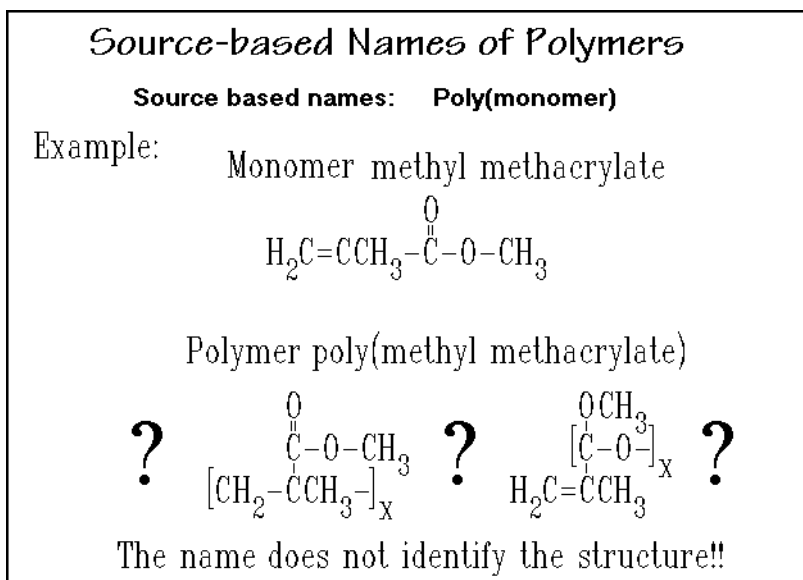


**Fig. 1.11**

monomer stems from μέρος = single, and μέρος = part). If the name of the monomer consists of only one word, the parentheses can be omitted, as for example in polyethylene or polypropylene. Often this simple, source-based name, once given, remains in common usage. One notices immediately that some basic knowledge of



nomenclature of small molecules is required to deduce the polymer composition, and then to speculate about the possible structure.

In the case of methyl methacrylate and most other monomers, several different polymers could be made by different reactions, as will be discussed in Chap. 3. A structure-based name, thus, would be helpful in distinguishing polymers and understanding the special properties of the different macromolecules even if they arise from the same monomer.

The structure-based names are designed to give a precise link of the name to the structure. The rules are summarized in Fig. 1.12. Basic is the identification of the constitutional repeating unit (CRU). If there is no repetition of the structure within

**Structure-based Names of Polymers**

**Structure based names: Poly(CRU)**

- 1. Identify the CRU (constitutional repeating unit)**
- 2. Orient the CRU**
- 3. Name the CRU**
- 4. Add end-groups if needed**

**Orientation:**  
start with highest seniority chain atom, go to next  
and write the name left-to-right

**Seniority list:**

- 1. heterocyclics**
- 2. hetero atoms (O, S, Se, Te, N, P, As, Sb, Bi, Si, Ge, Sn, Pb, B, Hg, ...)**
- 3. carbocyclics**
- 4. carbon only**

**The principle of minimizing free valences overrides the seniority rules.**

Fig. 1.12

a macromolecule, a structure-based name may not be feasible, as has been experienced in efforts to name the enormous variety of proteins of which some examples are given in Chap. 3. First, the CRU must be identified by finding the repetition scheme of the molecular architecture along the linear molecule. Naturally, one could start with any atom in the backbone of the molecule and identify the CRU by the beginning of the next repetition cycle. To eliminate accidental multiplicity of names derived from beginning the naming from different atoms, a seniority list has been set up to fix the proper starting atom as is listed at the bottom of Fig. 1.12. Next, the CRU must be oriented properly. The name of an O-C sequence in a CRU is different from C-O. The appropriately chosen and oriented CRU can then be named. The names are based on the established rules of organic chemistry which can be looked up in any textbook. One needs, thus, to know a list of common diradicals that give the CRU when linked together. Finally, the end groups may have to be specified to complete the name of the molecule in the case of shorter molecules, as illustrated in Fig. 1.14, below.

To illustrate these rules, a seemingly simple molecule is shown in Fig. 1.13 and the naming process is followed step by step. The structural formula being developed, the  $(\text{CRU})_x$  must indicate the continuation of the backbone bonds. This can be done by extending the bond through the parentheses,  $(\text{CRU})_x$ , an awkward way for typing. An easier way is chosen by placing the bond on the left fully outside of the parentheses and on the right fully inside the parentheses,  $-(\text{CRU}-)_x$ . The left bond can then be omitted since it is not part of the repetition scheme of the CRU. Figure 1.13 shows that there are a total of six possible arrangements of CRUs starting with different atoms and going in the two different directions. The seniority list of Fig. 1.12 eliminates all but two.

**Example of Finding a Structure-based Name**

...-CHF-CH<sub>2</sub>-O-CHF-CH<sub>2</sub>-O-CHF-CH<sub>2</sub>-O-CHF-CH<sub>2</sub>-O-...

Possible arrangements:

$(\text{O}-\text{CH}_2-\text{CHF}-)_x$	$(\text{CH}_2-\text{O}-\text{CHF}-)_x$	$(\text{CHF}-\text{CH}_2-\text{O}-)_x$
$(\text{O}-\text{CHF}-\text{CH}_2-)_x$	$(\text{CH}_2-\text{CHF}-\text{O}-)_x$	$(\text{CHF}-\text{O}-\text{CH}_2-)_x$

Eliminated due to seniority rule:

$(\text{O}-\text{CH}_2-\text{CHF}-)_x$	<del><math>(\text{CH}_2-\text{O}-\text{CHF}-)_x</math></del>	<del><math>(\text{CHF}-\text{CH}_2-\text{O}-)_x</math></del>
$(\text{O}-\text{CHF}-\text{CH}_2-)_x$	<del><math>(\text{CH}_2-\text{CHF}-\text{O}-)_x</math></del>	<del><math>(\text{CHF}-\text{O}-\text{CH}_2-)_x</math></del>

Final arrangement:

Pick the name that results in the smallest sum of the numerals

$(\text{O}-\text{CHF}-\text{CH}_2-)_x$  poly(oxy-1-fluoroethylene)

**Fig. 1.13**

One additional rule, that of the smallest sum of numerals that are found in the name is to be added to find the name of the polymer: poly(oxy-1-fluoroethylene), as shown in the box of Fig. 1.13. Its monomer could be either a substituted ethylene epoxide or an ethylene glycol. The name of the not chosen CRU is poly(oxy-2-fluoroethylene) with the larger numeral in its name.

Figure 1.14 gives a short list of diradicals which are frequently found in polymers. Note that the name of the polymer should also be short. If there exists an acceptable name for a longer diradical, this name should be used. The diradical propylene should thus not be named (methylmethylene)methylene. Longer sequences of CH<sub>2</sub>-groups are called trimethylene, tetramethylene, etc. Naturally, ethylene, trimethylene etc. are not permitted as the only diradical in a CRU, such polymers are all poly(methylene)s. The structure-based names are always enclosed in parentheses, even if the diradical is a single word, as in poly(butenylene).

Next, a much more complicated example is illustrated in Fig. 1.14. Poly(vinyl butyral) is produced by making poly(vinyl alcohol) and then reacting it with

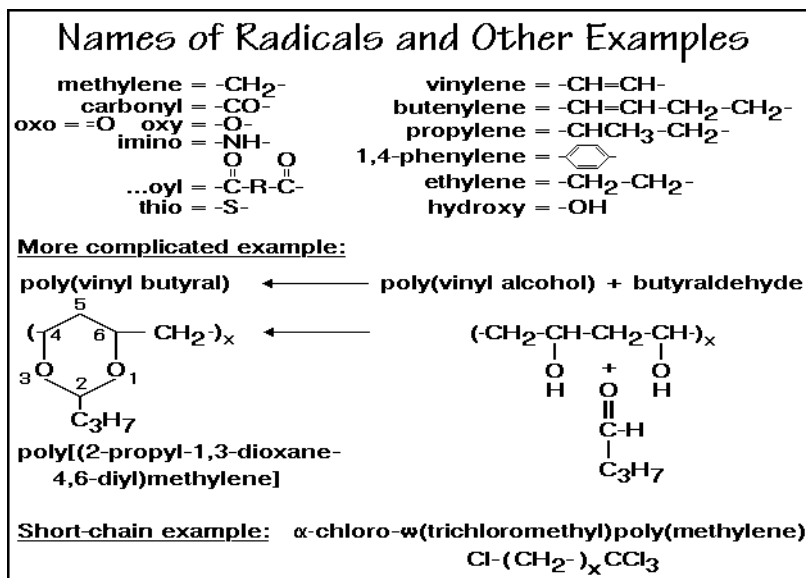


Fig. 1.14

butyraldehyde. The source-based name does not tell the structure. The rather complicated structure-based name can be deduced from the structure in the figure.

The chain ends can be identified also as shown in Fig. 1.14. This naming is needed in case the properties of a macromolecule are influenced by its end groups or the molecule is short enough to change its overall composition due to the ends. The left chain end is preceded by the first letter of the Greek alphabet ( $\alpha$ ) and the right end, by the last ( $\omega$ ).

Besides the source- and structure-based names, trade names are in common usage because of their convenient brevity. Unfortunately, commercial polymers may have been changed by copolymerization (see below), contain additives to enhance handling or performance, and may even change in composition with time as improvements are made in the product. When using trade names, always identify them as such with a trademark sign: <sup>TM</sup> or <sup>®</sup>, then give the trade name holder, as well as the IUPAC name of the polymer and list deviations from the pure polymer, if they are known.

Often polymer names are cumbersome and one may want to use an abbreviated letter code, as are listed in Table 1.1. The shorter the letter code, the easier are accidental duplications possible. It is, thus, again necessary to identify a letter code with the IUPAC name. For example, the full statement that should identify the polymer PTFE in a publication is PTFE = polytetrafluoroethylene (source-based name), poly(difluoromethylene) (structure-based name), Teflon<sup>®</sup> (trade name of the DuPont Company).

With this simple set of rules of nomenclature one can name a large number of macromolecules. To make this chore more interesting, one should not only learn names, but connect the various polymers to their well-known uses. Perhaps the most difficult polymer to find an application for when looking through handbooks is a

polymer you see almost every day. It is poly(vinyl butyral), used as the inner layer in safety glass (automobile windshields) and used as the complex example of naming in Fig. 1.14. Its structure is also given in Fig. 1.17, below.

**Table 1.1.** List of frequently used abbreviations of names of polymers

ABS	acrylonitrile/buta-	PMI	poly(methacrylimide)
	diene/styrene rubber	PMMA	poly(methyl methacrylate)
CPE	chlorinated polyethylene	PMP	poly(4-methyl pentene-1)
CTA	cellulose triacetate	POB	polyoxybenzoate
EPS	expanded polystyrene (foam)	POM	poly(oxymethylene)
HIPS	high-impact polystyrene	PP	polypropylene
HDPE	high-density (linear)	PPO	poly(phenylene oxide)
	polyethylene	PPOX	poly(propylene oxide)
LDPE	low-density (branched)	PPP	poly- <i>p</i> -phenylene
	polyethylene	PPS	poly(phenylene sulfide)
LLDPE	linear, low-density	PPT	poly(propylene terephthalate)
	polyethylene	PPX	poly- <i>p</i> -xylylene
PAA	poly(acrylic acid)	PS	polystyrene
PAN	polyacrylonitrile (fiber)	PTFE	polytetrafluoroethylene
PB	poly(1-butene)	P3FE	polytrifluoroethylene
PBI	polybenzimidazole	PVAC	poly(vinyl acetate)
PBS	butadiene/styrene copolymer	PVAL	poly(vinyl alcohol)
PBTP	poly(butylene terephthalate)	PVB	poly(vinyl butyral)
PC	polycarbonate	PVC	poly(vinyl chloride)
PDMS	polydimethylsiloxane	PVF	poly(vinyl fluoride)
PE	polyethylene	PVF <sub>2</sub>	poly(vinylidene fluoride)
PEG	poly(ethylene glycol)	SAN	styrene/acrylonitrile
PEO	poly(ethylene oxide)		copolymer
PET	poly(ethylene terephthalate)	SBR	styrene/butadiene rubber
PI	polyimide	UHMPE	ultrahigh molar mass
PIB	polyisobutene		polyethylene
PMA	poly(methyl acrylate)	XLPE	cross-linked polyethylene

Figures 1.15 to 1.18 show a standard frame for name and structure information. The first example is polyethylene. Note, that in this case source-based and structure-based names have different CRUs, causing problems in assessing molar quantities. The subsequent 19 structures are for other, frequently used polymers. Structure and nomenclature should be studied. At the same time, one should find out where one has heard about this particular macromolecule.

A number of the displayed polymers can be constructed of diradicals that represent different isomers (Gk. ἴσος = equal, μέρος = part). From the structure of polypropylene, for example, it can be seen that the methyl group can be located in front of the screen (d, as drawn) or in back (l). As long as the end-groups of the molecule can be neglected, the two possible polymer molecules can be superimposed by rotation about an axis vertical within the screen, i.e., the two molecules are not true isomers. If the configurations change along the chain, special problems arise with nomenclature and properties (see also Fig. 1.20, below).

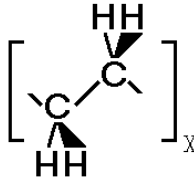
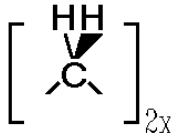
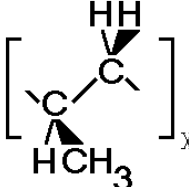
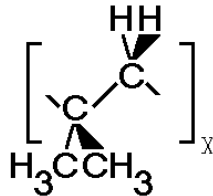
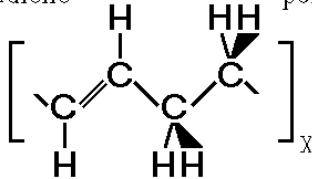
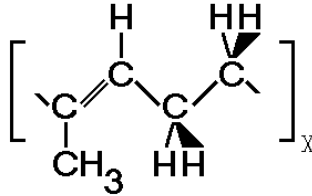
Names of Common Polymers I [Source and structure-based nomenclature]	
Source-based Name:	Structure-based Name:
polyethylene	poly(methylene)
	
polypropylene	poly(propylene)
	
(possibility of stereo-isomers, d or l position of the -CH <sub>3</sub> )	
polyisobutylene	poly(1,1-dimethylethylene)
	
polybutadiene	poly(1-butenylene)
	
(possibility of <i>cis</i> and <i>trans</i> isomers)	
polyisoprene	poly(1-methyl-1-butenylene)
	
(possibility of <i>cis</i> and <i>trans</i> isomers)	

Fig. 1.15

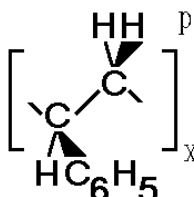
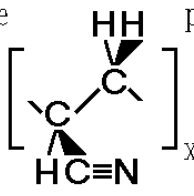
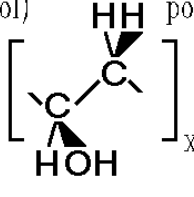
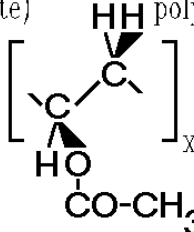
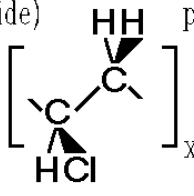
Names of Common Polymers II [Source and structure-based nomenclature]	
Source-based Name:	Structure-based Name:
polystyrene	poly(1-phenylethylene)
	
(possibility of stereoisomers, d or l position of the -C <sub>6</sub> H <sub>5</sub> )	
polyacrylonitrile (PAN)	poly(1-cyanoethylene)
	
(possibility of stereoisomers, d or l position of the -C≡N)	
poly(vinyl alcohol)	poly(1-hydroxyethylene)
	
(possibility of stereoisomers, d or l position of the -OH)	
poly(vinyl acetate)	poly(1-acetoxyethylene)
	
(possibility of stereoisomers, d or l position of the -O-CO-CH <sub>3</sub> )	
poly(vinyl chloride) (PVC)	poly(1-chloroethylene)
	
(possibility of stereoisomers, d or l position of the -Cl)	

Fig. 1.16

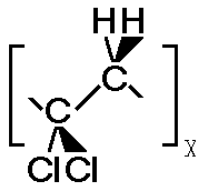
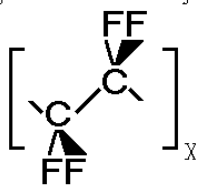
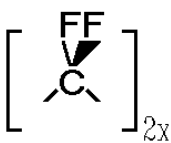
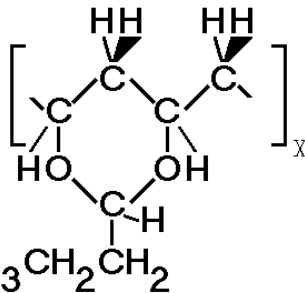
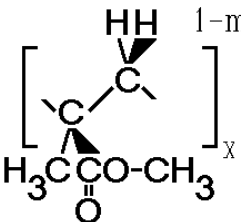
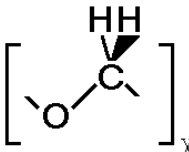
Names of Common Polymers III [Source and structure-based nomenclature]	
Source-based Name:	Structure-based Name:
poly(vinylidene chloride)	poly(1,1-dichloroethylene)
	
polytetrafluoroethylene (PTFE)	poly(difluoromethylene)
	
	poly[(2-propyl-1,3-dioxane-4,6-diyl)methylene]
poly(vinyl butyral)	
poly(methyl methacrylate) (PMMA)	poly[1-(methoxycarbonyl)-1-methylethylene]
	 <p>(possibility of stereoisomers)</p>
polyformaldehyde	poly(oxymethylene) (POM)
	

Fig. 1.17

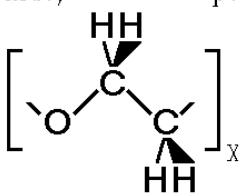
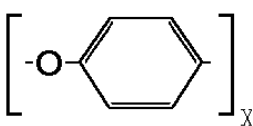
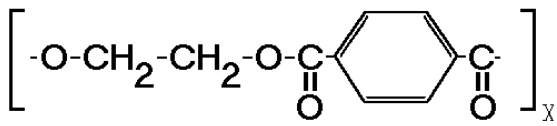
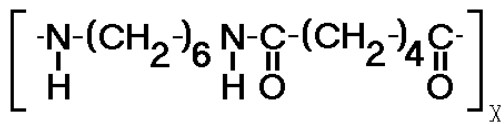
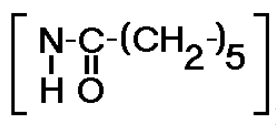
Names of Common Polymers IV [Source and structure-based nomenclature]	
Source-based Name:	Structure-based Name:
poly(ethylene oxide) (PEO)	poly(oxyethylene) (POE)
	
poly(phenylene oxide)	poly(oxy-1,4-phenylene)
	
poly(ethylene terephthalate) (PET)	poly(oxyethyleneoxyterephthaloyl)
	
poly(hexamethylene adipamide) (nylon 6,6)	poly(iminohexamethyleneiminoadipoyl)
	
polycaprolactam (nylon 6)	poly[imino(1-oxohexamethylene)]
	
<p><b>Reference:</b> Brandrup, Immergut, and Grulke, "Polymer Handbook," Wiley, New York, 1999.  Source-based name: Poly(monomer) (no () if the monomer name is one word only)  Structure-based name: Poly(CRU) (CRU = constitutional repeating unit)</p>	

Fig. 1.18



Figure 1.15 shows polyisobutylene, a vinylidene polymer with symmetric substitution, and thus without stereoisomers. *Cis* and *trans* isomers are possible in butenylene polymers. Two examples are at the bottom of Fig. 1.15. They are not interconvertible by rotating of the molecule. Shown in the figures are the *trans* isomers ( $\backslash \quad /$ ). In the *cis* isomers the backbone chain continues on the same side of the double bond ( $\_ \quad /$ ). In Figs. 1.16 and 1.17 a series of vinyl and vinylidene polymers are shown. The above-mentioned PTFE, poly(vinyl butyral), and poly(methyl methacrylate) are given, starting in Fig. 1.17. Polyoxides are drawn at the bottom of Fig. 1.17, and the top of Fig. 1.18. Poly(ethylene terephthalate) and two aliphatic polyamides (nylon 6,6 and nylon 6) round out Fig. 1.18. The 20 polymers just looked at should serve as an initial list that must be extended many-fold during the course of study of thermal analysis of polymeric materials.

### 1.2.2 Copolymers and Isomers

If a linear macromolecule is made up of more than one repeating unit, one calls the molecule a copolymer, in contrast to homopolymers with only one CRU. The repeating units of polymers may be fixed during synthesis, or they may still change after polymerization. Examples of the former are most vinyl polymers, examples for the latter, polyesters and polyamides. The vinyl polymers usually decompose irreversibly on heating, while the polyesters and polyamides can interchange chain segments under proper conditions (ester and amide interchange). For full description, it is thus advantageous to know the reaction kinetics of the different monomer units (see Chap. 3).

Copolymers can be distinguished as random or regular as illustrated in Fig. 1.19. The nomenclature requires simply the syllable *-co-* between the names of the two

<b>Copolymers</b>		(analogous to alloys, but much greater multiplicity)
A. Random Copolymers		-A-A-A-B-B-A-B-A-B-B-A
poly(ethylene- <i>co</i> -propylene)		
B. Regular Copolymers		
a. alternating	<i>alt</i>	-A-B-A-B-A-B-A-B-A-B-A
b. block	<i>block</i>	-A-A-A-A-A-A-A-B-B-B-B
c. graft	<i>graft</i>	-A-A-A-A-A-A-A-A-A-A
		$\downarrow$ (B-) <sub>n</sub> $\downarrow$ (B-) <sub>n</sub> $\downarrow$ (B-) <sub>n</sub>
poly(isobutylene- <i>alt</i> -tetrafluoroethylene)		
poly(styrene- <i>block</i> -isoprene)		
		[polyisoprene = 1,4-poly(2-methyl butadiene)]

Fig. 1.19

repeating units (source or structure based). If a random copolymer does not deviate from randomness within any molecule and between molecules, full characterization is possible by giving just the mole fractions of the components, if not, characterization is very difficult. Often copolymers are compared erroneously to alloys. There exists, however, a big difference, the possible permanence of the arrangement along the chain of the two or more components of copolymers. This leads to a much larger multiplicity of copolymers than alloys. The different sequences will also give special effects in the thermodynamics (see Chap. 7).

The regular copolymers require additional structure information. Three simple examples are listed with their nomenclature in Fig. 1.19. While alternating copolymers also need only information on the concentration for full characterization, more detail is needed for block and graft copolymers. The number and length of the blocks or grafted chains and their possible distributions within and between the molecules must be known for full structural characterization.

Many different regular arrangements of two or more components within a molecule can be envisioned. In fact, the multiplicity is practically unlimited and a systematic study of all possible molecules is impossible. A goal for the material scientist is thus to understand copolymer behavior to such a degree that an optimized structure can be predicted before synthesis is attempted.

The number of possible polymers is increased further by the many isomers. Isomers have the same number of atoms in each of their repeating units, but arranged in different structures. A simple type of isomer is the positional isomer, observed in most vinyl polymers as indicated at the top of Fig. 1.20. Fortunately the reaction mechanism prefers often one of the isomers (usually the head-to-tail isomer) to such a degree that the concentration of the other one is small. Uncontrolled isomerization causes a loss of regularity, similar to that in random copolymers. The irregular

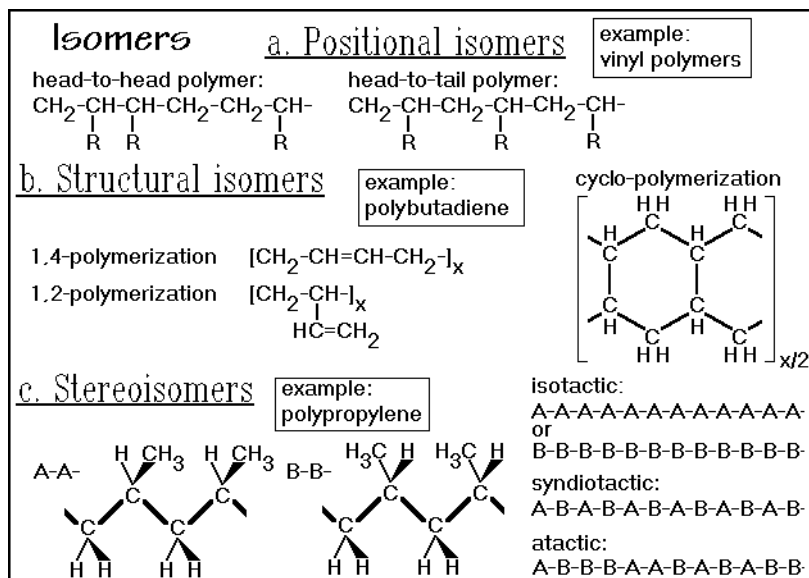


Fig. 1.20

molecules have often a low crystallinity and with it comes a loss of mechanical properties (see Chap. 5).

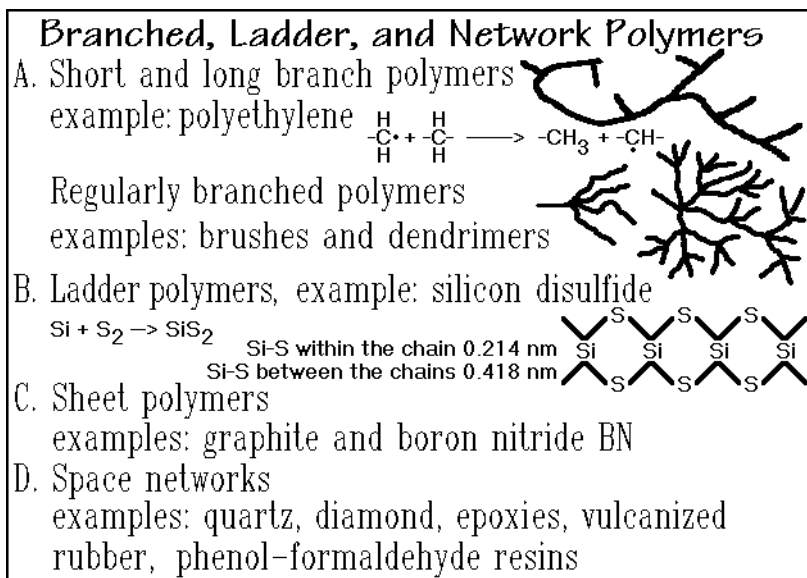
Besides different positional placement of monomers, it is possible to grossly change the structure on polymerization. Three structural isomers are given for the butadiene polymerization in Fig. 1.20. The 1,2-polybutadiene can, as a vinyl polymer, also have head-to-tail and head-to-head positional isomers. The 1,4-polybutadiene allows, in addition, *cis* and *trans* isomers, as discussed along with the names of the polymers in Fig. 1.15. Even the cyclopolymerized polybutadiene may have several structural isomers of different conformations.

Stereoisomers are drawn in Fig. 1.20 for the two possible isotactic forms of polypropylene. The term isotactic indicates that all repeating units are identical (Gk. ἴσος = equal, τακτός = ordered). Each second chain atom of polypropylene is a chiral center. Writing this center:  $L-HC^*CH_3-R$ , one can see that the tetrahedrally coordinated carbon  $C^*$  has four different substituents as long as the left and right continuations of the chain (L and R) are different. The two isomers are mirror images of each other with the mirror plane parallel to the screen (see Fig. A-13.2). As was pointed out above, for long homopolymers, L and R are sufficiently equal that the two isomers are superimposable by rotation. Changing the chirality randomly along the chain gives rise to an atactic isomer (Gk. α = privative, i.e., atactic = not tactic). This disordered polymer is, again, unable to crystallize. In addition, an unlimited number of specific, longer, regular sequences are possible. In Fig. 1.20 only the syndiotactic isomer is indicated (Gk. συν = together). Although interesting molecules may be among the more involved, regular isomers, they are difficult to make.

### 1.2.3. Branched, Ladder, and Network Polymers

Branched, ladder, and network polymers deviate from the linear macromolecules discussed up-to now. In order to remain fusible and plastic, the molecule must contain sufficient segments that are flexible and linear. Even without branches, linear molecules may have insufficient flexibility to melt. The linear poly(*p*-phenylene), for example, is a rigid macromolecule (class 3 of Sect. 1.1.3), because rotation about its bonds does not change the molecular shape. One must thus watch in such molecules that sufficient flexibility exists for plastics applications.

The question of nomenclature can be solved only in the simplest cases. In Fig. 1.21 a possible shape for a branched polyethylene is drawn. The branches are introduced during free-radical polymerization (see Chap. 3). By hydrogen abstraction, one chain is terminated, and somewhere else a new radical is introduced that can add a new run of monomers. A specially favorable configuration is the ring configuration of six atoms at the end of a growing molecule that leads by back-biting to short branches of four carbon atoms. To characterize the structure, the number, length, and position of the branches need to be known. For most molecules this information cannot be included in the nomenclature. Branched polyethylene is usually only named by recognition of its low density after crystallization (low-density polyethylene). For characterization of low-density polyethylene, the distribution of branches must be identified within *and* between the molecules.

**Fig. 1.21**

The regularly-branched polymers separate at fixed points and present special shapes that can be used to modify surfaces. The three-dimensional dendrimers [6] form a sphere with an interesting space-filling character which depends on the chemical structure of the chains and branch points.

The ladder, sheet, and some of the space network polymers shown are listed under letters B, C, and D in Fig. 1.21. They are often rigid, and are thus class 3 macromolecules (see Sect. 1.1.3). The flexible molecules of interest, however, are difficult to make with a specific structure so that they can be named (for a ladder polymer, see the isomers of polybutadiene in Fig. 1.20). Even epoxies and rubbers are usually so poorly characterized, that precise naming is impossible.

### 1.2.4 Funny Polymers

The *funny* attribute of the molecules in this group is some unusual feature that can produce shapes with special properties. The following listing is by no means complete and should serve only as an inducement to think about other possible funny polymers. Together with linear macromolecules and branched, ladder and network polymers they make the building blocks for an unlimited number of shapes which have barely been studied. Figure 1.22 illustrates some complicated structures. The first example illustrates a rotaxane [7]. It consists of a normal polymer backbone on which unconnected, mobile rings are threaded (example: cyclic molecules of oxyethylene repeating units). The properties of such polymers should be linked to the restrictions induced by the two components on each other and the ease of slippage of the rings along the chain.

The mesogens that are introduced in the main-chain and side-chain of the molecules shown as items 2 and 3 are rigid, elongated or disc-like groups. They are

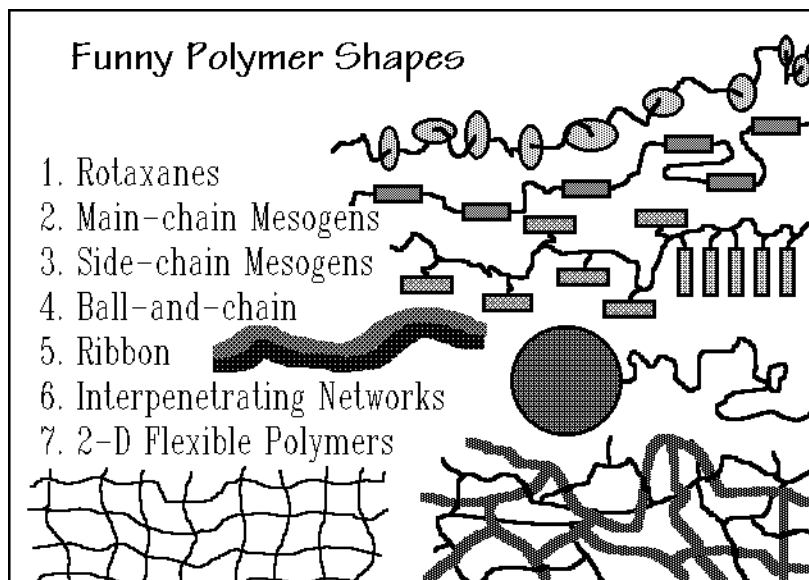


Fig. 1.22

incorporated in flexible polymers to enhance liquid-crystal-like behavior as is discussed in Sects. 2.5.3 and 5.5). Since liquid crystals align their mesogens spontaneously when being cooled below a certain transition temperature, these linear macromolecules can straighten spontaneously from their random-coil shape. On further cooling into the solid state, these molecules may retain the once produced partial order or crystallize further. In this way strong fibers can be made because of a more perfect alignment of the molecules along the fiber axis on spinning. An example of such a material is Kevlar<sup>®</sup> (trade name DuPont), source-based name poly(*p*-phenylene terephthalamide), and the structure-based name is poly(imino-1,4-phenylene-iminoterephthaloyl).

The ball-and-chain polymer has been proposed to be made by attaching, for example, a fullerene ( $C_{60}$ , see Sect. 2.5.3) to a polymer chain. This shows that there are no limits to the structures to which chains can be attached. Adding flexible chains to rather rigid structures can enhance the solubility of the often poorly soluble rigid molecules and change the processing and the physical properties.

The ribbon polymer is related to the less-flexible ladder and sheet polymers discussed before. One might expect very much different viscous behavior of such molecules in the melt. The interpenetrating networks [8] can have interesting elastic properties since each network may respond differently and interact with the other. The two-dimensional flexible polymers have recently been explored. They also belong to the sheet-like polymers.

Very specific properties, thus, can be achieved with these funny polymers. The question of nomenclature, however, is for most of them formidable. New rules or naming must be formulated to satisfy the goal to have not only an empirical name for a polymer, but to be able to systematically link a name to the chemical structure of the macromolecule.



polymer, it is necessary to know at least the first two moments. Rarely does one derive more than three, and it will turn out that knowing one moment only is not very helpful. Some moments are directly accessible by experiment as discussed in Sect. 1.4.

The definitions of moments, as can be found in many mathematics texts, are listed in Fig. 1.24. The moments  $v$  and  $\mu$  have the dimension of the  $r^{\text{th}}$  power of the abscissa, the moments  $\alpha$  are dimensionless. More details about the first four moments are given in the figure. The first moment is the common average, more precisely characterized as the abscissa of the center of gravity of the distribution curve. One should also note the connection between the second moment or variance about the mean,  $\mu_2$ , with the commonly known standard deviation,  $\sigma$ .

The equation relating the variance to the second moment and the arithmetic mean can be derived from the following simple considerations:

$$\begin{aligned}\mu_2 &= \frac{1}{N} \sum N_x (x - v_1)^2 \\ &= \frac{1}{N} \left[ \sum N_x x^2 - 2N v_1^2 + v_1^2 \sum N_x \right] = v_2 - v_1^2.\end{aligned}$$

The first equation is the definition of the second moment about the mean as given in Fig. 1.24. This is followed by carrying out the squaring [note  $(1/N) \sum N_x x = v_1$  and  $\sum N_x = N$ ].

The second moment, variance, or dispersion,  $\mu_2$ , as well as the standard deviation,  $\sigma$ , are all measures of the breadth of the distribution. The distribution can then be further characterized by the skewness,  $\alpha_3$ . It retains the sign of the deviations from the mean and indicates, as the name suggests, the departure from a balanced distribution about the mean, but counting, because of the third power, larger

<b>Definitions of the Various Moments</b>	
$v_r = (1/N) \sum N_x (x - x_0)^r$	$r^{\text{th}}$ moment about $x_0$
$\mu_r = (1/N) \sum N_x (x - \bar{x})^r$	$r^{\text{th}}$ moment about the mean $\bar{x}$
$\alpha_r = (1/N) \sum N_x \left( \frac{x - \bar{x}}{\sigma} \right)^r$	$r^{\text{th}}$ moment about the mean $\bar{x}$ in terms of the standard deviation $\sigma = \sqrt{\mu_2}$
$v_1 =$ arithmetic mean (abscissa of the center of gravity)	
$v_1 = \bar{x}$	$\mu_1 = \alpha_1 = 0$
$\mu_2 = v_2 - v_1^2$	variance, dispersion (about the mean)
$\alpha_2 = 1$	
$\alpha_3 = \mu_3 / \sigma^3$	skewness (asymmetry about the mean)
$\alpha_4 = \mu_4 / \sigma^4$	kurtosis (flatness, for a Gaussian $\alpha_4 = 3$ )

**Fig. 1.24**

deviations more heavily. The kurtosis, finally is again considering positive and negative deviations about the mean equally (because of the fourth power). The greater influences of the larger deviations make it an overall measure of the flatness of the distribution.

<b>Number Averages of the Molecular Mass Distributions</b>		
Number Average:	$N = \sum_1^{\infty} N_X$	$N$ = number of molecules
$n_X = N_X / \sum_1^{\infty} N_X$	$N_0 = \sum_1^{\infty} N_X x$	$N_X$ = number of x-mers $N_0$ = number of repeating units
$\bar{M}_n = \sum_1^{\infty} n_X M_X = M_0 N_0 / N$		$n_X$ = number fraction
$\bar{M}_n = M_0 \sum_1^{\infty} N_X x / N = M_0 v_1$		$M_{X,0}$ = corresponding masses

**Fig. 1.25**

The next step involves the application of the mathematical moments to the special needs of macromolecular mass distributions. Figure 1.25 shows how to express the distribution of molecules of length  $x$  ( $x$ -mers) and the total number of molecules. The number-average molecular mass  $\bar{M}_n$  is derived in the figure. It is the ordinary average. Figure 1.25 also illustrates the link of the number-average molecular mass to the first moment  $v_1$ . Its limitation for a full characterization of a broad molecular mass distribution can be seen by calculating  $\bar{M}_n$  for a mixture of an equal number of moles of molar mass 10,000 and 1,000,000 Da. This leads to an  $\bar{M}_n$  of only 505,000, despite the fact that the lower-mass polymer is only about 1% of the mass of the mixture. If the mass (or volume) of the molecules determines a property, knowing  $\bar{M}_n$  is not very useful.

A mass-average molecular mass,  $\bar{M}_w$ , is derived in Fig. 1.26. It is proportional to the second moment. The above mixture of equal mole fractions of largely different molar masses yields a mass-average molar mass,  $\bar{M}_w$ , of 990,198. This is a better representation of the molecules in the mixture than given by  $\bar{M}_n$ . Since most applications in polymer science deal with effects that scale with molar mass or volume and not number of molecules, it is more important to know  $\bar{M}_w$  than  $\bar{M}_n$ . The second equation for  $\bar{M}_w$  lists a more detailed expression. You may want to check all four equations for the one most suitable for a given calculation. Finally Fig. 1.26 introduces the term polydispersity, a measure of the disparity between the size of molecules in the mixture.



### Mass Averages of the Distributions

Mass Average:  $M = N_0 M_0 = \sum_i N_X M_X$   $M$  = mass of all molecules

$w_X = N_X M_X / \sum_i N_X M_X$   $\bar{M}_w = \sum_i w_X M_X$   $M_X$  = mass of x-mers

$$\bar{M}_w = M_0 \sum_i N_X x^2 / N_0 = M_0 (v_2 / v_1)$$

$$= M_0 [(1/N) \sum_i N_X x^2] / [(1/N) \sum_i N_X x]$$

$M_0$  = mass of a repeating unit

$$\text{Polydispersity} = \bar{M}_w / \bar{M}_n = v_2 / v_1^2$$

$$= [(1/N) \sum_i N_X (x - \bar{x})^2] / [(1/N) \sum_i N_X x]^2$$

$w_X$  = mass fraction  
 $N_X, N_0$  = numbers of molecules

**Fig. 1.26**

Some polymers have a polydispersity close to two, polydispersities as large as 10 or 20 are found in molecules grown by free radical reactions (see Chap. 3). A polydispersity of 1.0 signals that all molecules are of the same length. A mixture of equal masses of molecules of molar masses of 10,000 and 1,000,000 Da gives a polydispersity of 25.5 ( $\bar{M}_n = 19,802$ ,  $\bar{M}_w = 505,000$ ). Additional examples for two-components polymer mixtures are worked in Fig. 1.27.

### Example Calculations of Averages

Assuming  $M_1 = 10$  Da (1 mole = 10 g) and  $M_2 = 1,000,000$  Da (1 mole = 1 metric ton). This enormous disparity in size causes difficulties when attempting to handle solutions.

1. Calculation for equal molar solutions:

$$\bar{M}_n = \text{total mass/total molecules} = 1,000,010/2 = 500,005$$

$$\bar{M}_w = \sum w_X M_X = (10/1,000,010) \times 10 + (10^6/1,000,010) \times 10^6$$

$$= 999,990$$

$$\bar{M}_w / \bar{M}_n = 2.0$$

2. Calculation for solutions of equal masses:

$$\bar{M}_n = 2,000,000/100,001 = 20 \quad (N_1 = 100,000; N_2 = 1)$$

$$\bar{M}_w = 0.5 \times 10 + 0.5 \times 10^6 = 500,005$$

$$\bar{M}_w / \bar{M}_n = 25,003$$

3. Calculation for a 9 : 1 molar ratio:

$$\bar{M}_n = 1,000,090/10 = 100,009$$

$$\bar{M}_w = (90/1,000,090) \times 10 + (10^6/1,000,090) \times 10^6 = 999,910$$

$$\bar{M}_w / \bar{M}_n = 10$$

**Fig. 1.27**

### 1.3.2 Random Flight

The next statistics problem in characterizing a flexible, linear macromolecule is to describe its overall shape (see also Fig. A-13.3). Changing the rotation angle about the backbone bonds lets the molecule take on many shapes. This multiplicity of arrangements leads to high entropy and permits the appearance of polymers as liquids and in solutions (see Sect. 1.1.3). A simple estimate for the shape of a molecule is based on the statistical model of a random flight, a walk of  $x$  steps of constant length in three dimensions. One assumes that in this model for a molecule of  $x$  flexible bonds (and  $x + 1$  chain units) each bond- and rotation-angle is chosen randomly. Figure 1.28 illustrates how such a random coil is generated.

Treating each bond as a vector, an end-to-end-distance vector  $\vec{r}$  can be calculated. To simplify the rather lengthy computation for which all bond- and rotation-angles

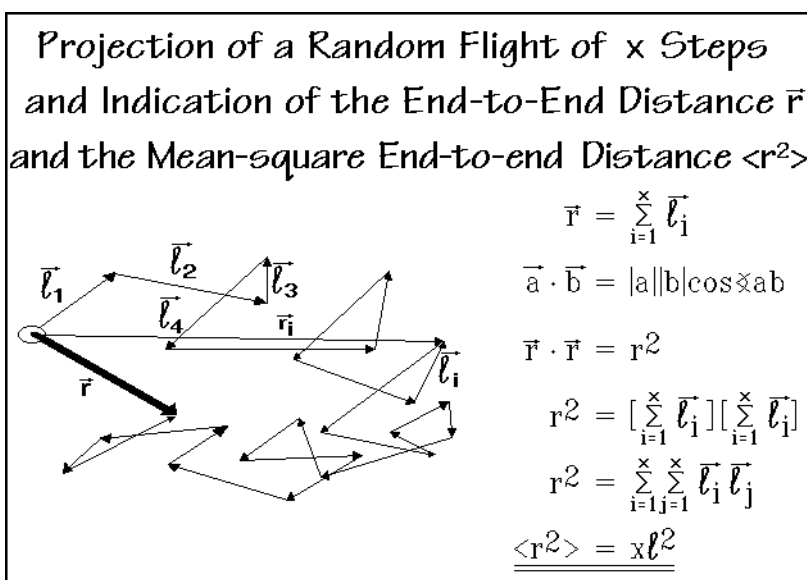


**Fig. 1.28**

must be known, one is usually satisfied with the mean square end-to-end distance  $\langle r^2 \rangle$ . A random choice for every angle has just as many positive as negative advances of the vector  $\vec{r}_i$ . The double sum for the square of  $r$ , a scalar quantity, retains thus, on averaging, only the terms  $\ell_i^2$  which have an angle of  $\angle ab = 0$  (i.e.,  $\cos \angle ab = 1.0$ ) and do not have negative counterparts. For polyethylene  $(\text{CH}_2)_n$ , with a number of bonds of  $x = 19,999$ , one can compute the root-mean-square end-to-end distance of:

$$\langle r^2 \rangle^{1/2} = 21.8 \text{ nm}$$

since the C-C bond length is 0.154 nm ( $M_w = 280,000$  Da). Fully extended, the molecule would be 141 times as long (contour length, assuming  $180^\circ$  bond angles).

This simple calculation gives an idea of the possible amount of coiling of the molecule. The root-mean-square end-to-end distance increases with the square root of the number of bonds, while the contour length grows linearly. To fully extend such random coil, one has to use a draw-ratio of 141×, much more than is usually possible in drawing of polymeric fibers for textile applications which is 5–10×. But note, that the gel-spun, high-molar-mass polyethylenes, which are discussed in Sect. 6.2.6 have a draw ratio of more than 100×.

### 1.3.3 Mean Square Distance from the Center of Gravity

The equation that defines a center of gravity is shown in Fig. 1.29. The sum of the vectors from the center of gravity to all elements of the object (assumed to be of equal mass) is zero. The figure shows the correlation of the vectors from the center of gravity of a macromolecule to the end-to-end vectors. The equation for the mean square distance from the center of gravity is illustrated, but not derived. The sums

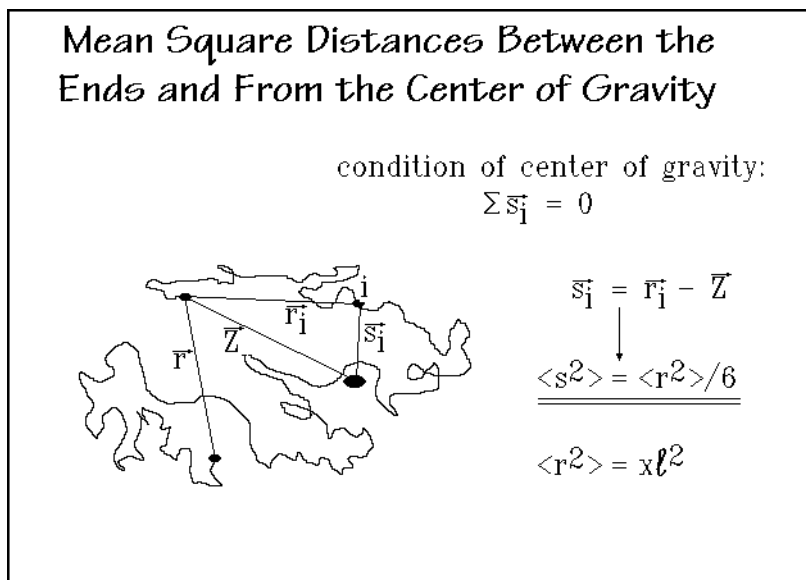


Fig. 1.29

are similar to the random-flight case, but it is somewhat more involved to reach the simple, final equation. There is no such obvious solution to the double sums of the vector products as in the derivation of the expression for  $\langle r^2 \rangle$ .

The density of matter within the random coil is a quantity that lets one better understand the nature of macromolecules. The overall conformation is also called the macroconformation (see Fig. 5.42). The density of a given molecule in a random coil macroconformation can be estimated by assuming that the coil locates in a spherical volume  $V$  with a radius of its root-mean-square end-to-end distance. Taking the example of the standard polyethylene of the previous section of molar mass 280,000 Da ( $4.65 \times 10^{-22}$  kg molecule<sup>-1</sup>) and  $\langle r^2 \rangle^{1/2} = 21.8$  nm, one finds that

$V = (4\pi/3)(21.8 \times 10^{-9})^3 = 4.34 \times 10^{-23} \text{ m}^3$ . Taking the ratio of mass to volume gives an average density within the random coil of  $10.7 \text{ kg m}^{-3}$  ( $10.7 \text{ g L}^{-1}$ ). This is about the density of air at ten times atmospheric pressure. Increasing the molar mass to 30,000 kDa would find matching air and polymer density of about  $1.0 \text{ g L}^{-1}$ . Note also, that the molecules in the melt have similar sizes as the random coils. To fill the space to a density of the melt of  $\approx 1 \text{ kg L}^{-1}$ , many molecules must invade the same space. Packing random coils so densely must lead to entanglements between the chains (see Sect. 5.6.1). These entanglements are typical for flexible polymers and give, for example, the reason for a large increase in viscosity as molar mass increases. They also cause problems for completion of crystallization from the melt (see Chap. 5).

### 1.3.4 Distribution Functions

The next step in the description of the chain statistics is an effort to find a functional expression for the distribution of the density of matter within a random coil of a single macromolecule. Assuming that the distribution of the end-to-end vectors of a macromolecule is Gaussian, one can establish a full distribution function, as shown in Fig. 1.30. The function  $W(\vec{r})$  represents the fractional probability to find a given end-to-end vector  $\vec{r}$  defined by its length *and* direction. The general Gaussian curve has only two constants,  $a$  and  $b$ :

$$W(\vec{r}) = a e^{-br^2}.$$

For our purpose it is easy to derive these constants because the integral over all probabilities must be 1.0 (normalization), and the mean-square end-to-end distance

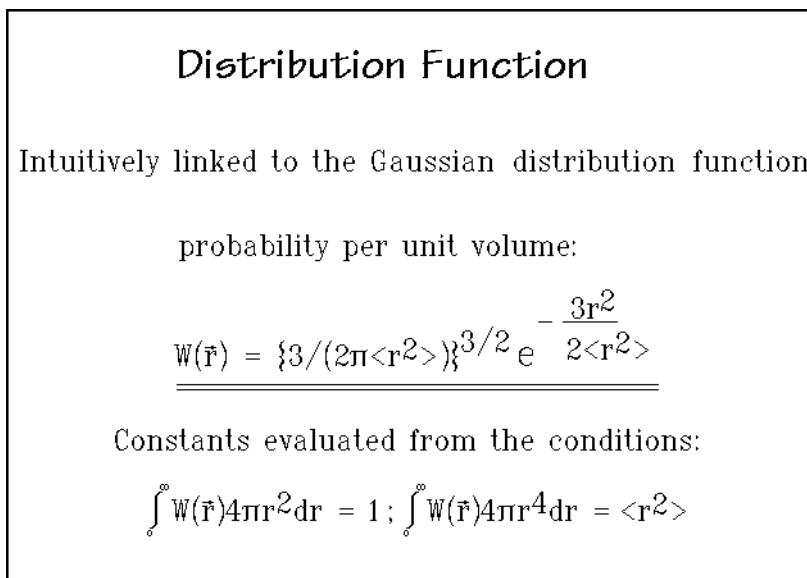


**Fig. 1.30**

must be  $\langle r^2 \rangle = x \ell^2$ , as computed before. The integrations for the proper values of  $a$  and  $b$  are written at the bottom of Fig. 1.30. They go over all vector orientations (yielding the multiplication with  $4\pi r^2$ ) and lengths  $dr$ .

The distribution function just derived is an expression for the probability that an end-to-end vector  $\vec{r}$  terminates in the volume element centered about the coordinates  $x, y, z$  (at the end of the vector  $\vec{r}$ ). Figure 1.31 is drawn for a random flight of 10,000 steps, each step being 0.25 nm, almost double the length of a chain segment of polyethylene. Because of bond restrictions that will be discussed later in this section,

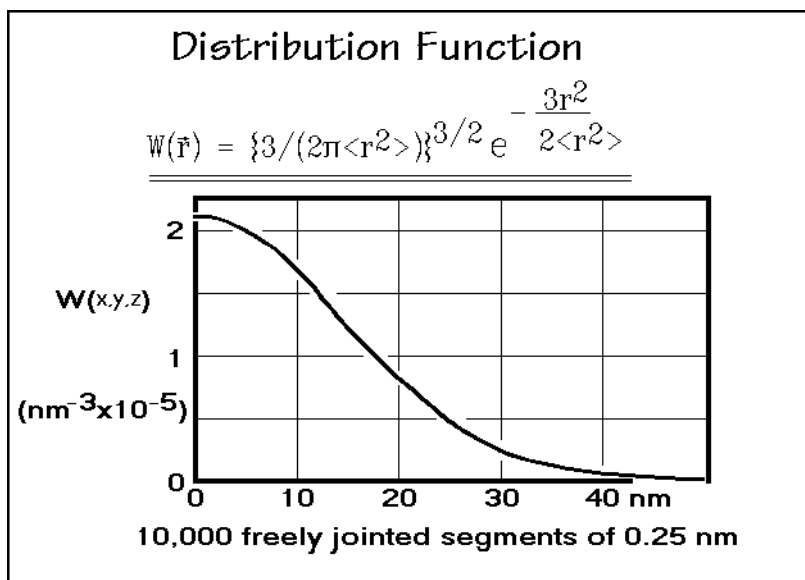


**Fig. 1.31**

the curve is close to the dimensions of the 280,000 Da polyethylene molecule described above. The general shape of the curve indicates that it is most probable that the two ends of the molecule meet ( $x = y = z = 0$ ) and for larger  $r$ ,  $W(x, y, z)$  continuously decreases. The probability to find an end-to-end vector of length  $r$ , regardless of the direction, is shown in Fig. 1.32. The number of vectors of length  $r$  is represented by the surface of a sphere with radius  $r$ , which is  $4\pi r^2$ , and yields a maximum when the exponential decrease of  $W(x, y, z)$  overtakes the second-power increase of the number of vectors.

The chain statistics can be brought closer to reality by a number of improvements to be discussed next. In Fig. 1.33 the results from the random flight model for a 280,000 Da polyethylene molecule are listed once more. Its ultimate extension is the 141 times larger contour length of 30.8  $\mu\text{m}$ . The distribution function of the previous figure gives, however, small probabilities for even longer separations which are physically impossible. An inverse Langevin function must be used to assess the extension of macromolecules and the retractive forces it produces. The inverse Langevin function reaches infinity for this force when  $r$  reaches the contour length of the molecule.

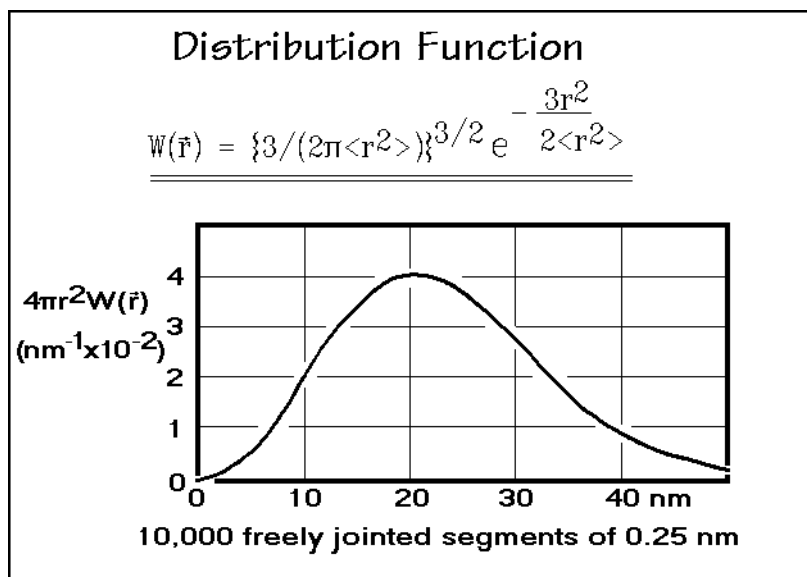


Fig. 1.32

The next improvements concern the bond angles,  $\alpha$ , and the rotation-angles about the bond,  $\eta$ . The bond angle is relatively constant in the different shapes of the molecule and close to the tetrahedral angle for  $sp^3$  bonds ( $\approx 109^\circ$ ), while the rotation angle has usually also only a limited range of change (see Sect. 1.3.5) and can be represented by the average of its cosine. Figure 1.33 illustrates the changes in the root-mean-square end-to-end distance due to these restrictions.

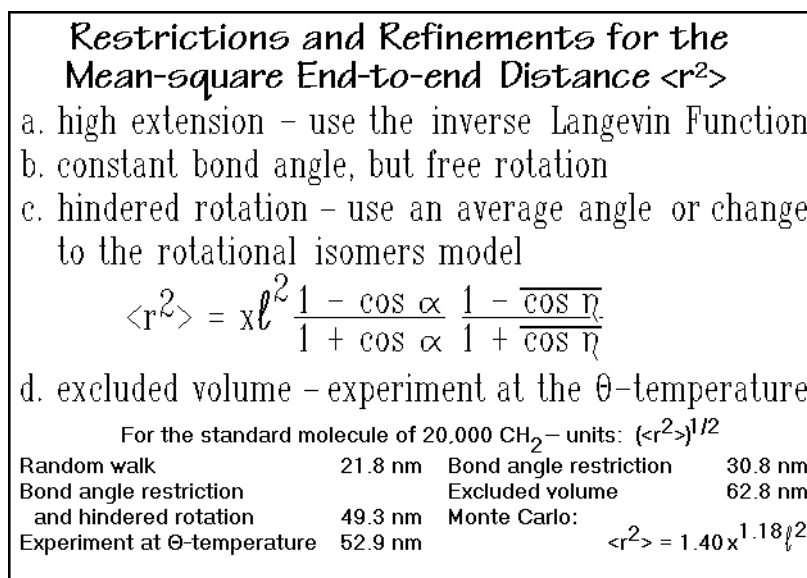


Fig. 1.33

This leaves as a final problem, the excluded volume. The excluded volume arises from the fact that a random flight can have unlimited revisits of any point in space, while a molecule modeled by the random flight would interfere with earlier segments at the same point. A certain volume of space is, thus, excluded for the remaining molecule, as indicated as entry d.

The summary of dimensions at the bottom of Fig. 1.33 demonstrates the effects of the various restrictions on the model compound. The random flight model gives for polyethylene already an answer within a factor of about 2.5. Comparison with the experiment is possible by analyzing the dimensions of a macromolecule in solution, as will be discussed in Chap. 7. One can visualize a solution by filling the vacuum of a random flight of the present discussion with the solvent molecules. The  $\theta$ -temperature listed as condition for the experiment is the temperature at which the expansion of the molecule due to the excluded volume is compensated by compression due to rejection of the solvent out of the random coil. This compensation of an excluded volume is similar to the Boyle-temperature of a real gas as illustrated in

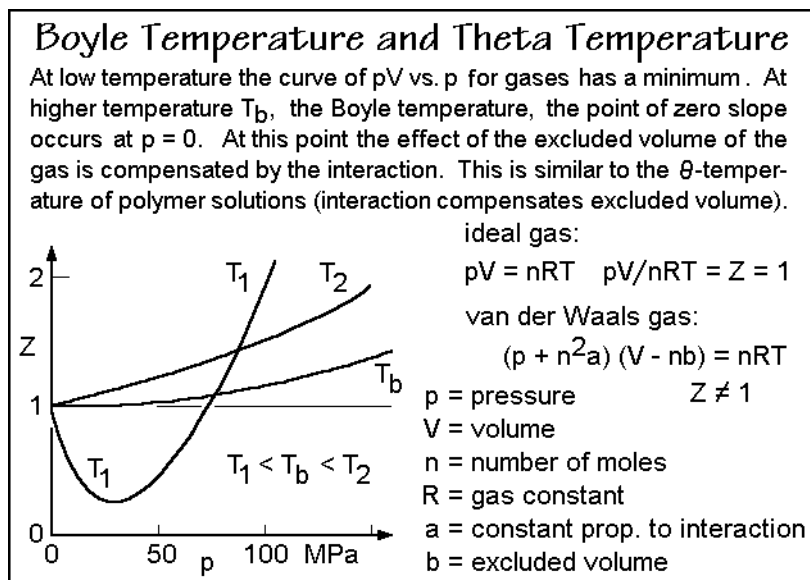


Fig. 1.34

Fig. 1.34. Not far from the  $\theta$ -temperature, polymer solutions undergo phase separation. An equation describing the excluded volume effect gained from Monte-Carlo simulation, is discussed in Sect. 1.3.6 and given in Fig. 1.39, below.

The discussion of the chain statistics permits one, thus, to have a more quantitative description of a flexible, linear macromolecule. The random coil of a sufficiently long molecule can be compared in mass-density and randomness to an ideal gas at atmospheric pressure. The elastic compression and expansion of gases are caused by changes in entropy. It will be shown below that corresponding behavior exists for the extension and contraction of random-coil macromolecules (entropy or rubber elasticity, see Sect. 5.6.5). Combining many random coils into a

condensed phase (liquid), entanglements start to dominate structure-sensitive properties such as the viscosity (see Fig. 3.5). Macromolecules which are less flexible lose their typical plastic behavior. Their melting temperature becomes higher, the rubber elasticity is less pronounced, and ultimately a rigid macromolecule results (see Sect. 1.2.4).

Further discussion of the properties of macromolecules will recognize the cooperative behavior. The repeating units (or parts of them) have limited independent mobility and remain linked to the overall molecule. In the crystallization of a metal, for example, any suitably positioned atom on a crystal surface can be added to the growing new phase. For polymers, in contrast, only sequential crystallization is possible. It is thus not only that the molecules must disentangle themselves from the other random coils and straighten to a certain degree, the proper sequence (and, in addition, often the proper direction) must be established for the addition of a given repeating unit to a crystal. The chain statistics of a flexible molecule is thus at the root of the special properties of polymers. It should also be remembered that many biological and inorganic compounds are macromolecules and even many small molecules are flexible! Neglecting the special effects based on molecular shape and flexibility severely limits not only the understanding of the behavior of polymeric and flexible materials.

The second part of the discussion of chain statistics will establish, in addition, the link between structure and mobility. While molecular structure has a length scale based on atomic dimensions of less than one nanometer ( $10^{-9}$  m), it will be shown that the atomic time scale is in the picosecond range ( $10^{-12}$  s). Both of these units must be recognized to make a link between the macroscopic and microscopic material properties.

### 1.3.5 Steric Hindrance and Rotational Isomers

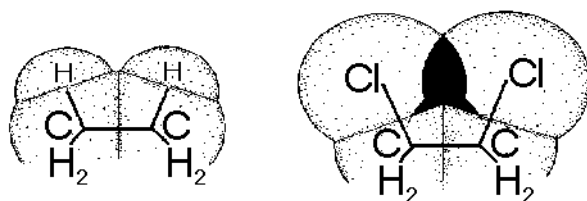
In this section, additional details on the conformations of macromolecules are given to further the understanding of flexible molecules. Details on computer simulation are presented to evaluate mobility. Increasingly stiff molecules are described to make the link to rigid macromolecules.

To begin the discussion, one can look at small molecules with two halves that can be rotated against each other about a sigma bond, a bond with cylindrical symmetry. The drawings of Fig. 1.35 are to scale, and, assuming the atomic sizes are fixed by the van der Waals radii, result in a solid atom model (see Fig. 4.23). The basic fact is that on overlapping, the electrons of different parts of the molecules show a strong repulsion at short distances. Strong steric hindrance to rotation for the dichloroethane, shown on the right, is obvious from the black area of overlap. Ethane, on the left, in contrast, shows no such steric hindrance. An analysis of the energy as a function of angle of rotation,  $U(\phi)$ , shows that even in ethane the rotation around the C-C-bond is not free, i.e., there is an intrinsic barrier to rotation. This barrier is particularly large for the sigma bonds of the small atoms of the second row of the periodic table (B, C, N, and O). The overall energy of rotation, thus, is written as:

$$U(\phi) = U_{\text{steric}} + U_{\text{intrinsic rotation}}$$



### Internal and Steric Hindrance on Rotation about a Cylindrically Symmetric Covalent Bond



A

B

$$U(\phi) = U_{\text{steric}} + U_{\text{rot.}}$$

(assume no changes in bond length or bond angle,  
as well as no charge or dipole effects)

**Fig. 1.35**

Additional contributions to this expression can arise from electric charges and dipoles. The dichloroethane in Fig. 1.35 would need, because of the strongly polar C-Cl bonds an extra term accounting for the repulsion between parallel dipoles.

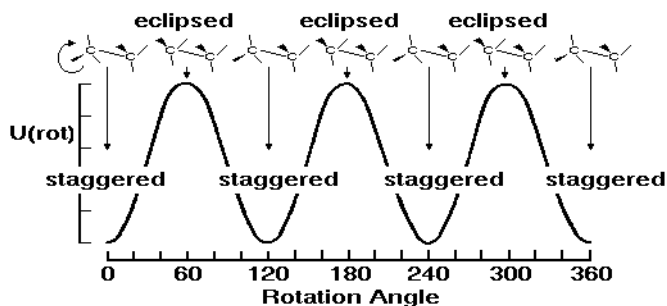
The angle  $\phi$  for the lowest energy is a compromise between the different energy contributions. Naturally, one assumes that bond lengths and angles are fixed when using this expression. Figure 1.36 shows the intrinsic hindrance to rotation in ethane.

### Rotational Isomers of Ethane

sp - orbital overlap for C, N, and O

$$U(\text{rot}) = (U^{(3)}/2)(1 - \cos 3\phi) + (U^{(6)}/2)(1 - \cos 6\phi) + \dots$$

intrinsic barrier of ethane = 12 kJ/mol



three indistinguishable rotational isomers

**Fig. 1.36**

As was discussed with Fig. 1.35, there should only be minimal steric hindrance between the hydrogen atoms on rotation. The three conformations of the molecule at the staggered positions at the angles of 0, 120, and 240° are energetically most stable. These are called the rotational or conformational isomers, but are indistinguishable because of the identical hydrogens. Energetically least favorable are the eclipsed positions at 60, 180, and 300°. For molecules with larger side-groups, the

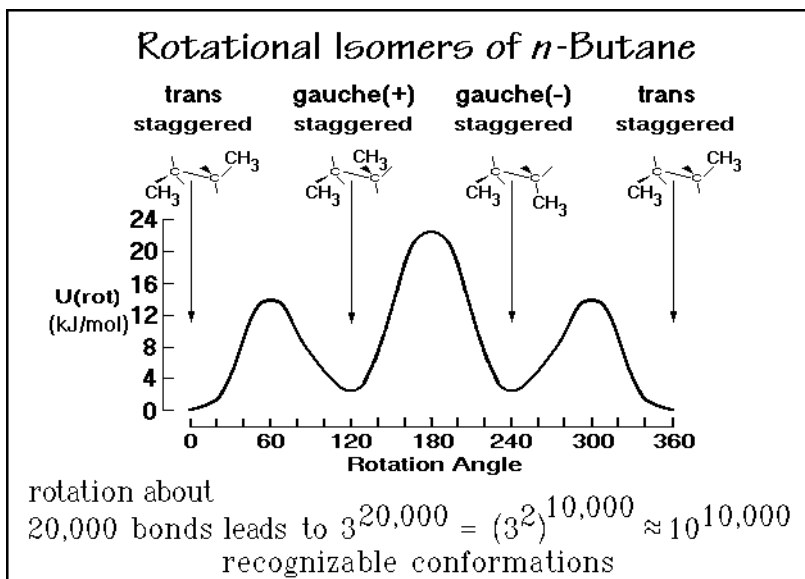


**Fig. 1.37**

steric hindrance must be added. The energetics of rotation about the center bond of *n*-butane is drawn in Fig. 1.37 as an example representing the shortest model-compound for polyethylene. The potential-energy curve still shows three low-energy conformations (rotational isomers), but these are now of different energy and distinguishable. The *trans* conformation is lowest in energy. Compared to the thermal energy  $(3/2)RT$ , about  $4 \text{ kJ mol}^{-1}$  at room temperature, the barriers to rotation can occasionally be surmounted, but most of the time one expects the molecule to take one of the three staggered conformations.

The number of possible shapes a polyethylene molecule can now be calculated easily by assuming that each bond must be in one of these three rotational positions. Then the statistics of the molecule is based on the conformational entropy per rotatable bond of this type,  $k \ln 3$ , where  $k$  is Boltzmann's constant (see Sect. 2.2.4 and Fig. A.5.4). Per mole of bonds  $k$  is replaced by  $R$ , the gas constant. For a molecule with  $n$  rotatable bonds,  $S_{\text{conformation}} = n \times 9.2 \text{ J K}^{-1} \text{ mol}^{-1}$ . The calculation at the bottom of Fig. 1.37 reveals that the different conformations possible for a macromolecule with 20,000 flexible backbone bonds and three rotational isomers per bond are more than astronomical. This large amount of disorder (entropy) is at the root of the special behavior of polymers. It permits melting of the macromolecule without breaking into small parts, and is the reason for entropy elasticity (viscoelasticity and

rubber elasticity), and also causes the special defects in polymer crystals, and the many thermodynamic nonequilibrium states (see Chaps. 5–7).

### 1.3.6. Monte Carlo Simulations

To understand the overall conformation of a large molecule, also called the macro-conformation, one can use computers and simulate the molecule with a Monte Carlo program. Figure 1.38 illustrates the Monte Carlo technique [9]. First, one chooses a lattice for the generation of the macromolecule. Figure 1.39 illustrates a two-dimensional square lattice with coordination number (CN) four. Then one places the first atom somewhere on the lattice. This leaves four choices for the placement of the second atom ( $w_N = 4$ ). Choosing one of these four possibilities leads to three as the number of choices for the third and most subsequent atoms, as shown in the figure.

#### The Principles of the Monte Carlo Technique

Any method for obtaining a statistical estimate of a desired quantity by random sampling is called a Monte Carlo technique after one of the quarters (sections) of the Principality of Monaco, famous for its gambling casino. In the most successful applications the desired quantity is, in fact, a statistical parameter, and the sampling is made from an artificial population that is in some sense a model of the physical system itself.

The example on the right shows a distribution of 100 sums of ten random numbers  $rn$ , each between 0 and 1. It fits a normal distribution.

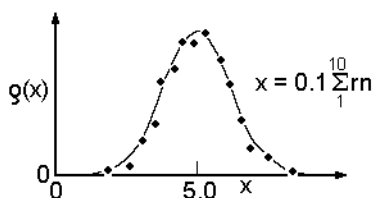


Fig. 1.38

When in the course of generating the molecule one chooses an already occupied position, the simulation is discarded. This permits the representation of the excluded volume problem mentioned in Sect. 1.3.4. In the computation of the probability in Fig. 1.39 this termination of chains because of excluded volume is recognized by the factor  $F_N$ . Results on 1123 surviving chains, generated on a tetrahedral lattice to simulate the conformations of a carbon backbone, are also given in Fig. 1.39 [10]. These data were also shown in Fig. 1.33 with the restriction and refinements of the random flight.

Many refinements and extensions of the Monte Carlo simulations are possible. More detailed information about the influence of the energetics of the *trans* and *gauche* conformations on the chain statistics can be obtained. In this case, one biases the probability of the choices of successive positions in favor of the *trans* conforma-

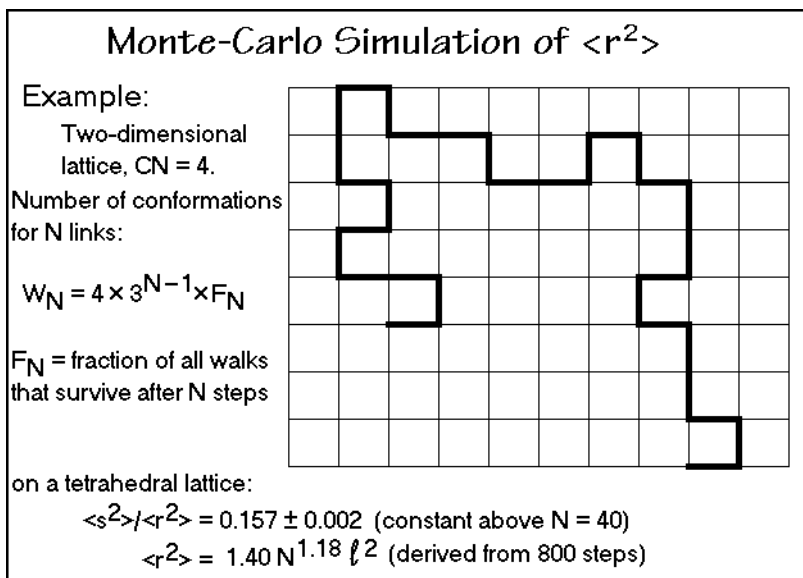


Fig. 1.39

tion, using the known energy minima of the conformational isomers. It is also possible to simulate kinetics of changes of given conformation by considering the possible choices for rotation about the bonds of a molecule. Again, the energetics must be incorporated in the model. Other examples of Monte Carlo simulations include diffusion about obstacles, motion of the different molecules in mixtures, and during the crystallization process [11]. Limits are the growing computational needs for large molecules, difficulties in linking the computation steps with actual time scales, and the poor representation of a crystal by the chosen rigid lattices.

### 1.3.7 Molecular Mechanics Calculations

Molecular mechanics calculations are designed to find the energy of a given conformation of a molecule,  $U(\phi)$ . Once the equation for the potential energy has been established, it can be minimized to identify the most stable macroconformation. For polyethylene, this conformation of minimum energy would obviously be the all-*trans*, extended-chain arrangement, i.e., it represents a zig-zag chain. In the calculation, all interactions important for the molecule must be included. Figure 1.40 is a typical example with parameters for the simulation by molecular mechanics of hydrocarbon molecules [13–15]. The equation in the figure considers steric hindrance, rotation, and valence angle distortion. Omitted is the less important change in bond length. Such simplifications are often included in the calculation to save computation time.

The term  $U_{\text{steric}}$  in Fig. 1.40 includes the van der Waals interactions between all atom pairs, including those involved in rotation and bending. The intrinsic hindrance to rotation is given by  $U_{\text{rot}}$ , as before for ethane. It is obvious that rotation about any one C–C-bond must overcome the barriers to rotation which is similar to the ones for

### Molecular Mechanics Calculation of the Rotational Isomer of Lowest Energy

$$U(\phi) = U_{\text{steric}} + U_{\text{rot.}} + U_{\text{val. angle}}$$

$$U_{\text{steric}} = \sum_i a_i \exp(-R_i/\rho_i) - bR_i^{-6}$$

$$U_{\text{rot.}} = (U^{(0)}/2)(1 - \cos 3\phi) + \dots$$

$$U_{\text{val. angle}} = \sum_j (K_j)(\Delta\theta_j)^2$$

minimize the  
overall energy

typical parameters:

$a_{\text{HH}} = 12.5$	MJ/mol	$a_{\text{CH}} = 58.6$	MJ/mol
$b_{\text{HH}} = 138$	mJ nm <sup>6</sup> /mol	$b_{\text{CH}} = 0.5376$	J nm <sup>6</sup> /mol
$\rho_{\text{HH}} = 0.0267$	nm	$\rho_{\text{CH}} = 0.0272$	nm
$a_{\text{CC}} = 222$	MJ/mol	$K_{\text{CCC}} = 418$	kJ/mol
$b_{\text{CC}} = 2.09$	J nm <sup>6</sup> /mol	$K_{\text{CCH}} = 218$	kJ/mol
$\rho_{\text{CC}} = 0.0278$	nm	$K_{\text{HCH}} = 314$	kJ/mol
$U(3) = 10.9 \text{ kJ/mol}$			

Fig. 1.40

*n*-butane; shown in Fig. 1.37, but in addition, for a sufficiently long molecule there may be other serious steric hindrance from atoms further along the chain of the molecule.

An example of an actual molecular mechanics calculation is shown for polyparaxylylene in Figs. 1.41 and 42 [12]. Both, a space-filling and a line representation of the low-energy conformation are displayed in Fig. 1.41. Molecular mechanics

### Example of a Molecular Mechanics Calculation of the Low-energy Conformations of Polyparaxylylene

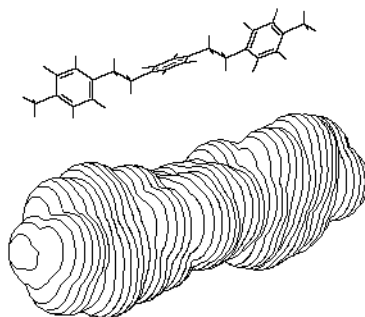
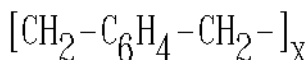
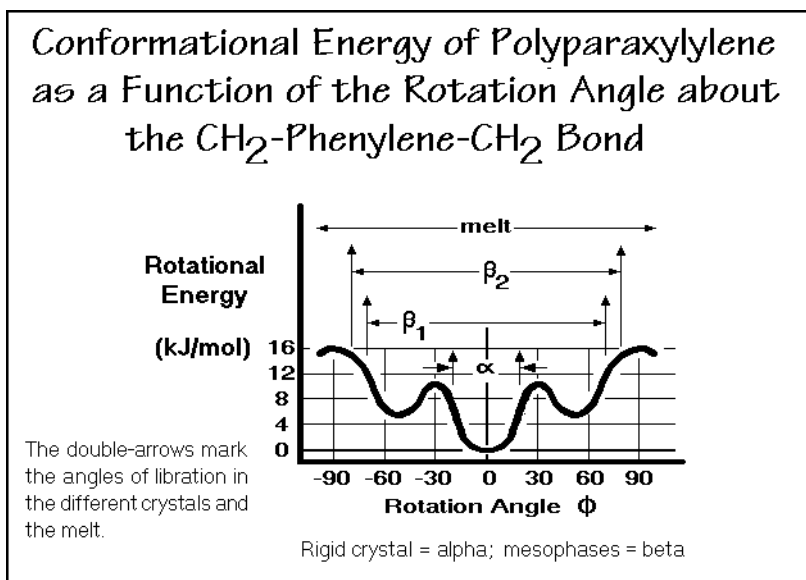


Fig. 1.41

calculations are of importance for the prediction of crystal structures. The molecules in crystals frequently have the conformation of lowest energy. The results of Fig. 1.42 can be used to interpret the rotations of the phenylene groups in different crystal polymorphs (see Chap. 5). Although low-energy reaction-paths from one conformation to another can be calculated with molecular mechanics, actual dynamics often takes other paths.



**Fig. 1.42**

### 1.3.8 Molecular Dynamics Simulations

The ultimate simulation of a molecule involves full molecular dynamics (MD), as can be derived by step-wise integration of the Hamiltonian,  $H$ , in Fig. 1.43. The first term of  $H$  represents the kinetic energy, the others, the potential energies. The sums go over all atoms,  $i$ , of the system. Illustrated are  $p$  chains of 100 atoms each. The representation of the potential energy is similar to the just completed molecular-mechanics treatment. The non-bonded (NB) van der Waals interaction is included only for the atoms not involved in the adjacent two, three, and four-body interactions (bond stretching, bending, and rotation, respectively), i.e., the short-range intra-molecular NB interactions are included in  $V_2$  to  $V_4$ . Furthermore, the Hamiltonian can be used to include static chains in the simulation. These contribute only to the NB interactions. If the full outermost ring of chains is immobilized, the simulation represents constant volume. Without static chains, it is close-to constant (zero) pressure. A set of parameters for paraffins and polyethylene are given in Fig. 1.44. These parameters are for the united-atom simplification that treats a CH<sub>2</sub>-group as a single unit of atomic mass 14.03 Da. This simplification saves computation time and does not affect many of the problems. The equations available for the MD simulation

### Molecular Dynamics Simulation

Hamiltonian for a crystal of  $p$  chains of 100 atoms each

$$H = \sum_{m=1}^p \left[ \sum_{i=100m-99}^{100m} \frac{p_{x_i}^2 + p_{y_i}^2 + p_{z_i}^2}{2M} + \sum_{i=100m-99}^{100m-1} V_2(r_{i,i+1}) \right. \\ \left. + \sum_{i=100m-99}^{100m-2} V_3(\theta_{i,i+1,i+2}) + \sum_{i=100m-99}^{100m-3} V_4(\tau_{i,i+1,i+2,i+3}) \right] \\ + V_{2NB}(R_{i,j}) + V_{2NB}(R_{i,k})$$

$m$  = chain index (from 1 to  $p$ )       $j$  = non-bonded dynamic  
 $i$  = dynamic chain atom      chain atom  
 (from 1 to  $100p$ )       $k$  = static chain atom

**Fig. 1.43**

are also listed in Fig. 1.44. These equations must be numerically integrated as a function of time, as indicated. The problem lies in the huge number of terms in the Hamiltonian. If 10,000 atoms interact with each other, one expects at least 100 million interaction terms that change at each instant. The supercomputers used in the discussed simulations could handle up to 100,000 atoms for times as long as about one nanosecond ( $10^{-9}$  s).

### Potential Energies and Computation Functions

$$V_2(r) = 334.72 \{ 1 - e^{-19.9(r-0.153)} \}^2$$

$$V_3(\theta) = 65.061 (\cos 113^\circ - \cos \theta)^2$$

$$V_4(\tau) = 8.3704 - 18.4096 \cos \tau + 26.78 \cos^3 \tau$$

$$V_{2NB}(R) = 1.9748 \{ (0.4335/R)^{12} - (0.4335/R)^6 \}$$

(potentials in kJ/mol, distances in nm, angles in degrees)

velocities:       $\partial q / \partial t = \partial H / \partial p$

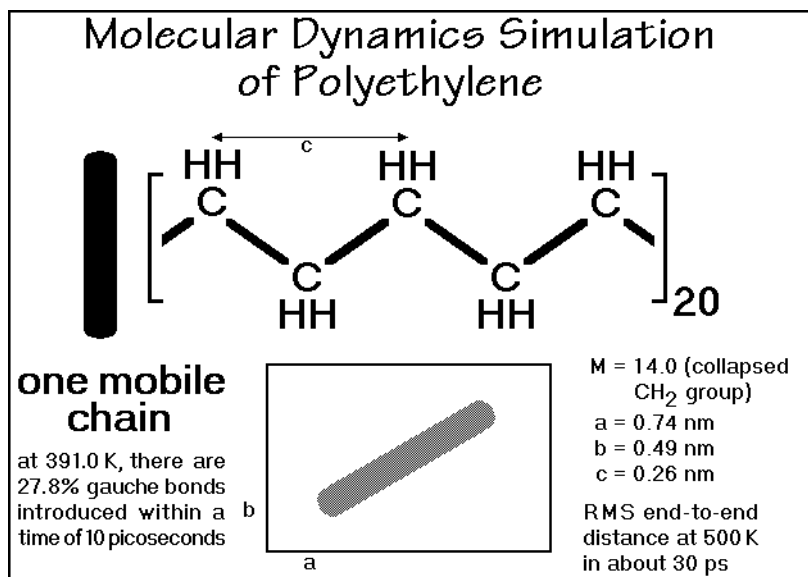
momenta:       $\partial p / \partial t = -\partial H / \partial q$

kinetic energy:  $3kT/2 = \sum_i \frac{p_i^2}{2M}$

integration:  $q(t + \Delta t) = 2q(t) - q(t - \Delta t) + [(\Delta t)^2 F(t)]/M$   
 or more accurate:

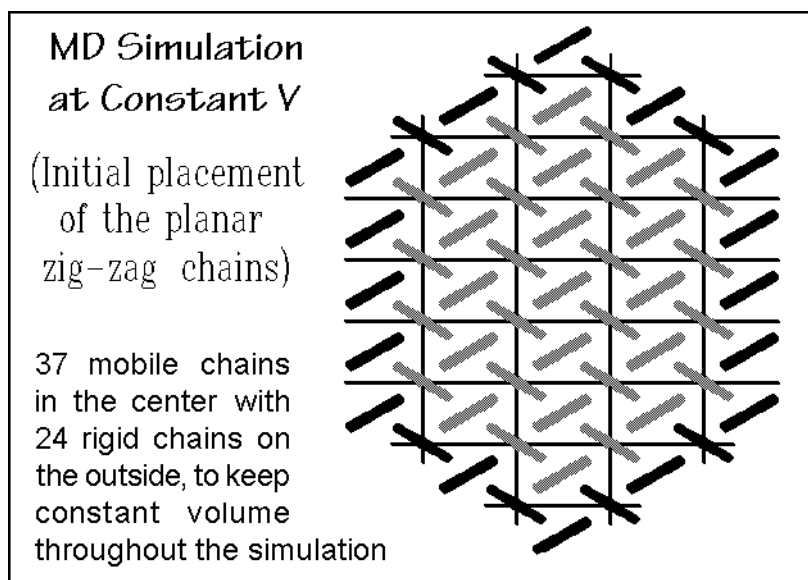
predictor-corrector-variable time step (variable order  $\leq 12$ )

**Fig. 1.44**

**Fig. 1.45**

The MD simulations of a single chain starting from the extended, planar, all-*trans* conformation are summarized in Fig. 1.45. It leads in about 30 ps to a random coil. The *gauche* conformations are to be compared to the equilibrium concentration of about 40% that is found in the melt or in solution.

Figure 1.46 shows an arrangement of 37 chains of a polyethylene crystal of 100  $\text{CH}_2$ -groups each at the beginning of a MD simulation. The chains are surrounded

**Fig. 1.46**



by 24 static chains to define a fixed volume. Next, a predetermined amount of kinetic energy is distributed randomly among the 3700 mobile  $\text{CH}_2$ -groups to raise the temperature to 80 K. After only few picoseconds mechanical and thermal equilibrium is approached and the atomic motion can be observed.

Figure 1.47 illustrates the initial state and two snapshots of the inner seven chains of a simulated crystal, 0.2 ps apart. Only the lower parts of the chains are drawn to better show the details. The x, y, and z axes of the projection correspond to the initial

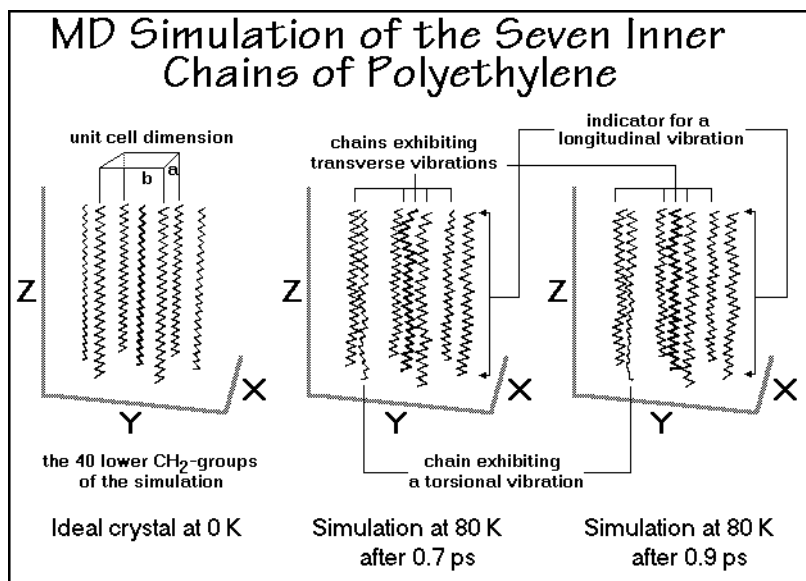


**Fig. 1.47**

a-, b-, and c-axes of the unit cell which is described in Chap. 5. All chains exhibit skeletal vibrations. It will be shown that these vibrations contribute much of the low-temperature heat capacity. Transverse deviations from the planar zig-zag chains are seen in most chains as soon as the simulation is initiated (marked at the top of the center figure). The wave-motion can be followed and is seen to travel up and down the chains (compare to the right figure). The second chain from the left displays a strong torsional oscillation, visible by the change in the appearance of the projection of the zig-zag chain. Finally, a check of the lengths of the chains reveals longitudinal vibrations. All possible skeletal vibrations can thus be identified in Fig. 1.47. Their frequencies range up to about  $1.8 \times 10^{13}$  Hz, a value derived from normal mode calculations which are discussed when analyzing heat capacities in Chap. 2 (see Fig. 2.7).

Figure 1.48 contains a block diagram of the distribution of the rotation angles  $\tau$  at higher temperatures. Oscillations of small amplitude represent the overwhelming part of the torsional vibrations. A small amount of large-amplitude deviations is found at an angle that is slightly smaller than the expected *gauche* conformations at 60 and 240°. (Note that the convention chosen for  $\tau$  is different from that of Figs. 1.36 and 37 by 180°,  $\tau_{\text{trans}} = 180^\circ$ ). The intermediate, eclipsed conformations

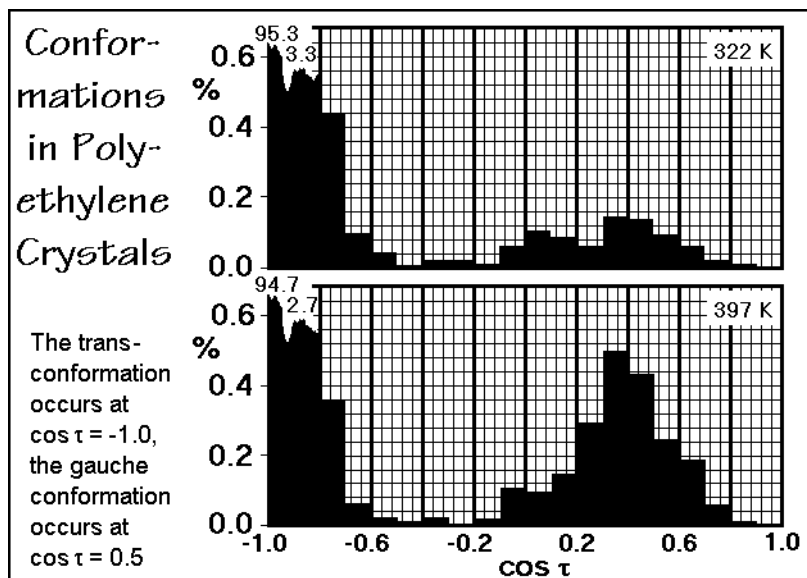


Fig. 1.48

are found only rarely. A detailed discussion of the *gauche* conformations which represent defects in polyethylene crystals, and their relation to crystal properties, will be given in Sect. 5.3.4.

### 1.3.9 Equivalent Freely Jointed Chain

To represent real, unperturbed polymer molecules with the much simpler random-flight formalism, Kuhn<sup>1</sup> introduced the equivalent, freely jointed chain by defining a longer segment that gives an identical mean square end-to-end distance with the same number of links  $x$  as a random flight of segments of length  $\ell$  would give [16]. The new, longer segment is called the Kuhn length,  $\ell_k$ . Results for some flexible molecules are given in Fig. 1.49. The equations permit an easy correlation between the two definitions, the Kuhn length, and an expansion ratio  $c$ . All listed polymers would be characterized as flexible. The values of  $\ell_k$  should be compared to the C–C bond length of 0.154 nm.

### 1.3.10 Stiff Chain Macromolecules

Four types of macromolecules of largely different Kuhn length are listed at the top of Fig. 1.50. Below this list, the repeating units which lead to molecules of different stiffness are drawn. The repeating units I and II can be found in most of the flexible molecules. Their inclusion in a polymer backbone introduces the angle in the structure which, together with a rather unhindered rotation about the connecting

<sup>1</sup> W. Kuhn (1899–1963) Professor at the University of Basel, Switzerland.

Equivalent Freely Jointed Chain			
random flight:			$\langle r^2 \rangle = x \ell^2$
real, unperturbed chain:			$\langle r_0^2 \rangle = c x \ell^2$
representation of the chain by a freely jointed chain of longer segment			
	$c$	$\ell_k \text{ (nm)}$	Kuhn length $\ell_k$
polyethylene	6.7	0.39	$\ell_k = \sqrt{c} \ell$
polystyrene	10.0	0.48	
polypropylene	5.7	0.37	
PMMA			expansion ratio $c$
atactic	6.9	0.40	
isotactic	9.3	0.47	
syndiotactic	7.0	0.41	
POE	4.0	0.31	$c = \langle r_0^2 \rangle / x \ell^2$
nylon 6.6	5.9	0.37	

Fig. 1.49

bonds, produces the flexibility. Some inorganic molecules, such as Si and Se, also can produce rather flexible macromolecules. Inclusion of occasional small, more rigid groups do not significantly increase the Kuhn length, such as is indicated by the aliphatic polyesters and amides (see the data for nylon 6.6 in Fig. 1.49).

The stiffest molecules are reached when the bond-angle between the backbone bonds is 180 degrees, such as in linking groups like III, XI, XII, and XV to XVII. For molecules such as polyparaphenylene, the Kuhn length approaches infinity and the molecules belong to the rigid macromolecules which are classified in Fig. 1.6 and in Fig. 1.7 a list representative is given.

To design molecules of different stiffness, one can couple the building blocks of Fig. 1.50. To produce flexibility, short and bent segments are required and steric hindrance due to bulky side groups must be small. Increasing the steric hindrance on rotation, lengthening the straight segments, and increasing the bond angle to 180°, and proper placement of crank-shaft-like segments (as IV–IX, XIII, and XIV) are the tools to tailor-make stiffer molecules. The 1,4-cyclohexylene repeating unit (X) has an internal mobility, known from the easy interchange between its chair and boat conformations.

To appreciate the multiplicity of polymer molecules and their conformations, one should review the following points: 1. The many ways the repeating units can be linked together. 2. The uncountable number of molar mass distributions and conformations each single sample can have. 3. The large numbers of different degrees of stiffness that can be produced, ranging from the most flexible polymer to linear, rigid macromolecules. Knowledge about these topics permits the design of new materials of optimum properties and leads to the understanding of the behavior of already known polymeric materials, the elusive goal of every modern material scientist.

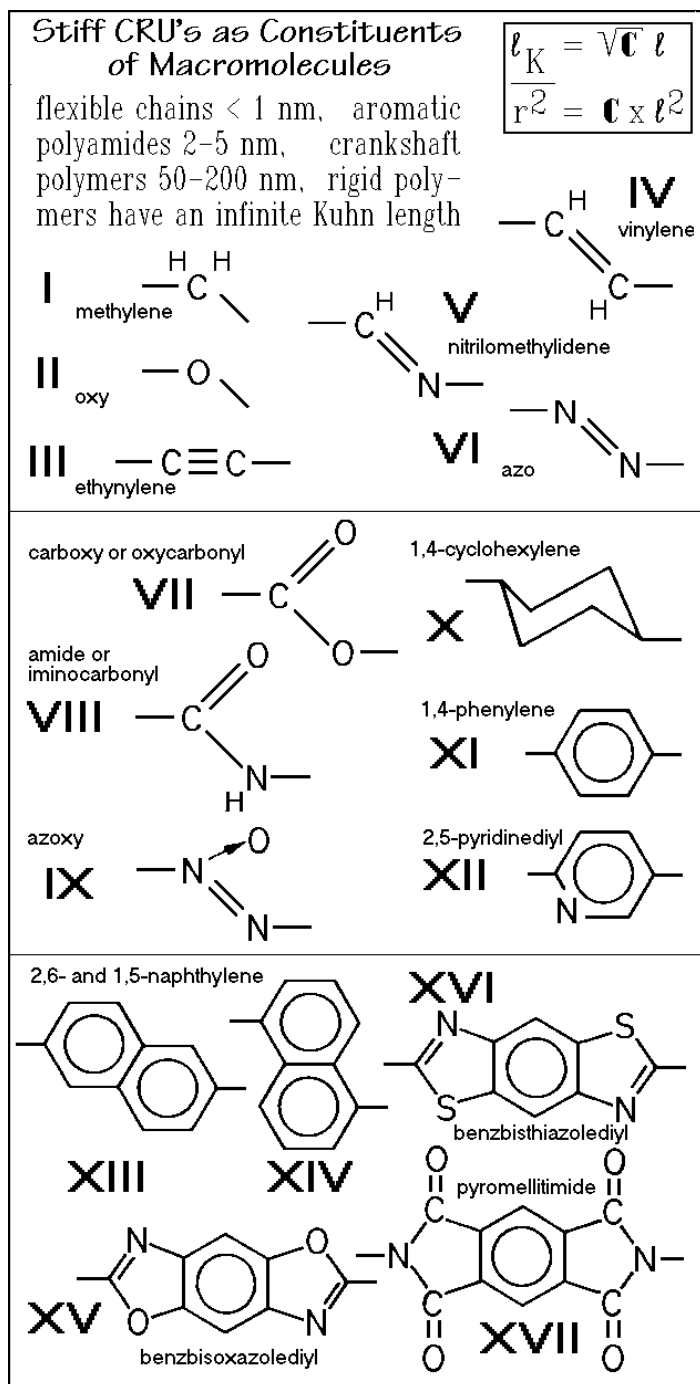
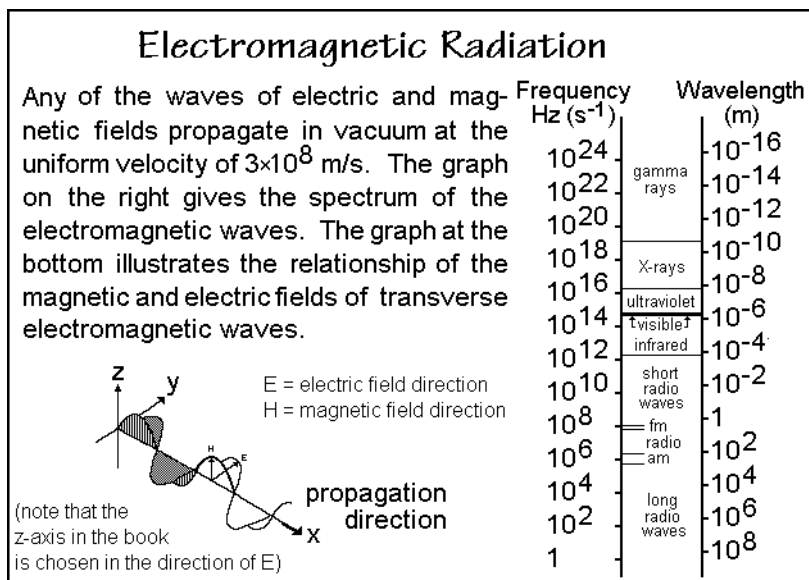


Fig. 1.50

## 1.4 Size and Shape Measurement

### 1.4.1 Introduction

In this last section of Chap. 1, experimental methods are discussed to obtain data for the characterization of macromolecular sizes and shapes. The scattering of light is selected as the major method. It provides three pieces of information, the molecular size, shape, and the interaction parameters of the macromolecule with solvents [17,18]. The scattering of light is thus a versatile technique. Furthermore, its theory describes also the scattering of other electromagnetic radiation, as is summarized in Fig. 1.51, and even the scattering of neutrons and electrons, as described in Fig. 1.72,



**Fig. 1.51**

below. Light scattering is only one of the twelve techniques mentioned in this section. Details are also given for the colligative properties, explained in Fig. 4.52 (freezing temperature, boiling temperatures, and osmotic pressure), the semiempirical techniques of membrane osmometry and size-exclusion chromatography, and also the solution viscometry. Five additional characterizations are mentioned at the end of the chapter (Sect. 1.4.7).

### 1.4.2 Light Scattering

Light is one of the basic experiences of man. Ancient speculations about its nature abound. Pythagoras, the Greek philosopher and mathematician of the 6<sup>th</sup> century BC, suggested that light travels in straight lines from the eye to the object and that the sensation of sight arises from the touch of the light rays on the object. This *feeling* with light is still anchored in our language. The verb to see is used in the active

### *Colligative Properties*

A colligative property depends on the number of molecules, not on their nature. The main examples of colligative properties are the pressure of an ideal gas ( $pV = nRT$ ), the depression of the freezing point of a solvent in the presence of a solute, the elevation of the boiling point by a solute and also the osmotic pressure. The latter three are used for  $M_n$  determination.

In all cases the properties are truly colligative only at the limit of infinite dilution, so that there is no effect of the substance-specific interaction contributing to the property.

Taking the gas as an example, one can describe its non-ideal properties by the van der Waals equation:

$$[p + a(n/V)^2][V - nb] = nRT$$

The constants  $a$  and  $b$  are molecule-specific and make thus the non-ideal pressure non-colligative. A large volume for a given  $n$  makes the changes from the ideal  $p$  and  $V$  negligible.

**Fig. 1.52**

voice. With present-day knowledge one must reverse the direction of the flow of information from the object to the eyes, i.e., to see should be passive.

The physical nature of light rays was a puzzle for many years. In the 17<sup>th</sup> and 18<sup>th</sup> centuries, theories about the wave nature (Huygens 1596–1687) and particle character (Newton 1643–1727) were proposed. By the 19<sup>th</sup> century the wave concept dominated, based on the precise descriptions of electromagnetic waves by Maxwell (1831–1879). Only in the 20<sup>th</sup> century could both concepts be joined by the discovery of matter waves (de Broglie, 1924). In the 19<sup>th</sup> century Richter developed as a first step of quantification the turbidity equation:  $\tau = (1/\ell) \ln(I_0/I)$ , where  $\ell$  is the length traveled by light of initial intensity  $I_0$ , and  $I$  is the reduced intensity due to turbidity  $\tau$ . The theory of light scattering as accepted today was then created by Lord Rayleigh<sup>1</sup> [19].

In our daily life, the scattering of light explains a number of well-known effects, listed in Fig. 1.53. The observations A–D are basic experiences. The wavelength dependence of the scattering of light ( $\propto \lambda^4$ ) causes the often brilliant colors of the sky, ranging from the blue sky overhead to the red evening sky. The coherence of scattered light permits interference of light scattered from different parts of objects as explained in Fig. 1.54. The size of the scattering centers can be linked to the observed intensities. Small water droplets in fog scatter so much that vision is completely obscured, while a much larger amount of water concentrated in bigger rain drops hinders vision only little. The dependency of light scattering on difference in polarizability,  $\alpha$ , which is proportional to the square of the refractive index,  $n$ ,

<sup>1</sup> John William Strutt (1842–1919), in 1873 he succeeded to the title Third Baron Rayleigh of Terling Place; professor at Cambridge University, England, Nobel Prize for Physics, 1904.

### The Scattering of Light

- A. Wavelength dependent (blue and red sky)
- B. Coherent scattering (leads to interference)
- C. Scattering center size dependent (fog, rain)
- D. Polarizability dependent (paper, air, and fat)
- E. Dependent on the number of scattering centers  
(only in dilute solution, otherwise extrapolate)
- F. Dependent on the shape of the scattering center  
(except if smaller than  $1/20$  wavelength,  $\approx 25$  nm)
- G. Dependent on the direction of observation from  
the scattering center (forward more than reverse)

**Fig. 1.53**

leads, for example, to the loss of scattering of light on adding grease to paper, making it translucent. Paper appears white because of the large difference in  $n$  between the cellulosic fibers of paper ( $n = 1.55$ ) and air located in the spaces between the fibers with  $n \approx 1.00$ . Replacement of air with fat ( $n = 1.46$ ) makes this difference in  $n$  disappear. Somewhat more advanced observation techniques are needed to detect the effects from E to G. The interference of light originating from different particles

### Interference of Waves

Interference is the variation of the wave amplitude with time or distance caused by superposition of two or more waves of the same or nearly the same frequency.

If the square of the sum of the resultant amplitude is more than the square of the waves A and B, the interference is constructive, if less, destructive. If two waves travel from a common source in two paths of different lengths, interference occurs. One can observe interference with electromagnetic, sound, water, and matter waves (such as neutrons and electrons).

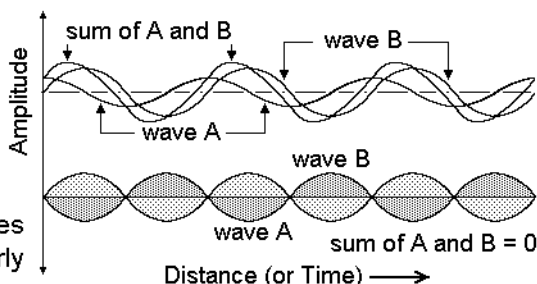


**Fig. 1.54**

leads to a decrease in scattering intensity from concentrated solutions. As soon as the particles of the scattering centers are larger than about 25 nm in different directions, the shape of the scattering centers becomes of importance and leads to different scattering intensities. Finally, the direction of observation of scattered light is of importance. All these factors must be explained by the theory of light scattering. If some of these phenomena are not fully familiar to you, check the popular composition by Heller, who taught at the University of Detroit in the 1960s, which has been reprinted as Appendix 2.

The experimental set-up for the scattering of light is shown in Fig. 1.55. The primary beam of light enters from the left and traverses the polymer solution contained in the cell C. The scattered light with an intensity  $i_\theta$  at an angle  $\theta$  to the

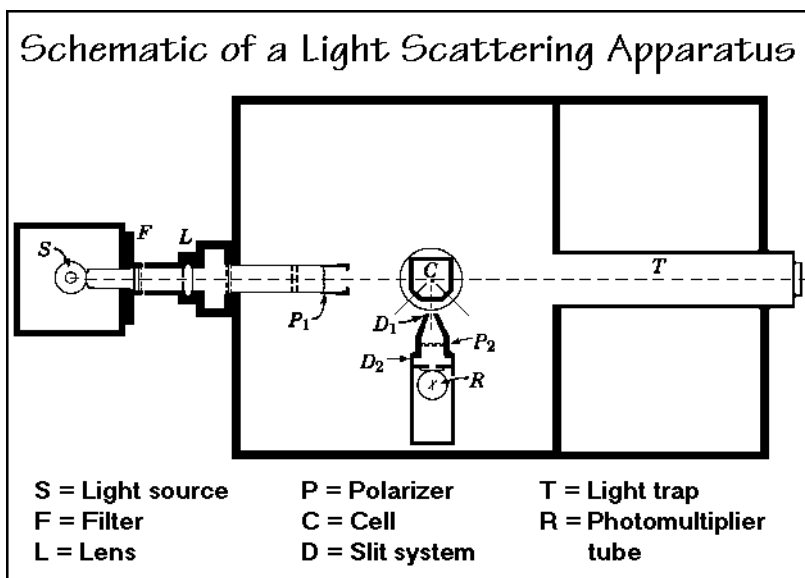


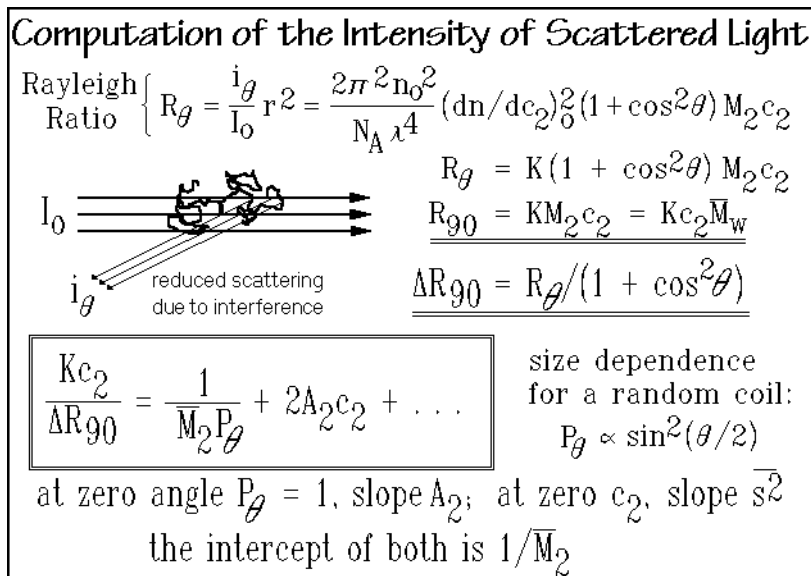
**Fig. 1.55**

incident light beam is measured with the photomultiplier tube R. Modern equipment uses laser light and employs computer analysis for the data treatment.

The experimentation requires also a sensitive differential refractometer to separately evaluate the change of the refractive index of the polymer solution with concentration. Producing clean solutions is a paramount experimental condition, since all foreign particles scatter light and reduce the accuracy of the measurement. Furthermore, stray light must be kept from the photomultiplier, accomplished by a light-proof enclosure and a light trap T to eliminate the residual light from the incident beam. The angular dependence is measured by rotating R to different positions. In the shown instrument, the angles  $\theta$  of 45, 90, and 135° are preset and match the cell walls.

Figure 1.56 illustrates the computation of the molar mass average,  $\bar{M}_w$  from the light-scattering results. The Rayleigh ratio  $R_\theta$  is the ratio of the scattered light intensity in direction  $\theta$  to the primary light intensity  $I_0$  at a distance  $r$  from the scat-



**Fig. 1.56**

tering center. Because of the somewhat lengthy nature of the detailed derivation of the Rayleigh ratio, it is given as Appendix 3. Figure 1.56 links the experimental Rayleigh ratio to the wavelength,  $\lambda$ , of the light used, the refractive index of the solvent,  $n_0$ , the change of  $n$  with polymer concentration  $c_2$ , the molar mass of the polymer  $M_2$ , the polymer concentration  $c_2$  (in  $\text{Mg m}^{-3}$ ), and the angle of scattering, expressed as  $\theta$ .

The Rayleigh ratio simplifies on collecting all constants, the independently measured refractive index, and its change with concentration into a constant,  $K$ . Even simpler is the result when measuring at  $\theta = 90^\circ$  when  $1 + \cos^2 \theta = 1$ . If more species of molecules with molar masses  $M_i$  and concentrations  $c_i$  are present, the mass-average is to be used. It is derived as follows from Sect. 1.2:

$$\sum M_i c_i = c_2 (\sum M_i c_i) / c_2 = c_2 (\sum w_i M_i) = c_2 \overline{M}_w.$$

The equations just presented have two shortcomings. They apply only under the conditions of a very dilute solution, so that the scattered light from different particles does not interfere (see Fig. 1.54), and the scattering particles themselves are less than 25 nm in size, so that the light scattered from different parts of the same molecule does not interfere either.

Both of the shortcomings caused by interference can be corrected by appropriate extrapolations. The first extrapolation is carried to zero concentration  $c_2$ , the second to zero scattering angle,  $\theta$ . Understanding these two extrapolations does permit the extraction of two additional characterization parameters of the polymer from the same light-scattering experiment. The first extrapolation yields the interaction parameter between polymer and solvent. The second extrapolation yields an estimate of the molecular shape.

The extrapolation of the light-scattering data as a function of concentration was first given by Debye<sup>1</sup> as shown in Fig. 1.57. One can write the equation for  $Kc_2/R_{90}$  as an expansion in powers of  $c_2$  by noting the similarity of the concentration

<h3 style="margin: 0;">Debye Equation for the Description of the Change of I with Concentration</h3>	
<p>Virial expansion of the osmotic pressure:</p> $\pi = RT \left( \frac{c}{M_2} + A_2 c^2 + A_3 c^3 + \dots \right)$ <p>ideally <math>\frac{\partial \pi / \partial c}{RT} = \frac{1}{M_2}</math> and <math>\frac{Kc_2}{R_{90}} = \frac{1}{M_2}</math></p> <div style="border: 1px solid black; padding: 10px; margin: 10px 0;"> <p>Debye Equation:</p> <math display="block">Kc_2/R_{90} = \left( \frac{1}{M_2} + 2A_2 c + 3A_3 c^2 + \dots \right)</math> </div> <p>On replacement of the second virial coefficient <math>A_2</math> with the result of the Flory-Huggins equation (Chapter 7) one obtains:</p> $Kc_2/R_{90} = (1/M_2) + 2(\bar{v}_2/v_1) \left( \frac{1}{2} - \chi \right) c_2 + \dots$	<p>Based on the virial equation of state (Clausius, 1875). It expresses <math>p</math> in powers of pressure or inverse volume. In the present case it has been expressed in terms of osmotic pressure and concentration. At <math>p</math> or <math>c \rightarrow 0</math> or at <math>v \rightarrow \infty</math> it reverts to the ideal gas law: <math>p = nRT</math> or <math>p = RTc/M</math></p>

**Fig. 1.57**

dependence of the osmotic pressure in a non-ideal solution to that of the inverse Raleigh ratio. The result is also listed in Fig. 1.56 for the case of terminating the expansion with the second term. The coefficient  $A_2$  (second virial coefficient) can be obtained from the slope of a plot of  $Kc_2/\Delta R_{90}$  vs.  $c_2$ . The bottom equation in Fig. 1.57 shows the changes necessary if one wants to describe polymer solution with the Flory-Huggins equation, discussed in Chap. 7.

The dependence of light-scattering data on the angle  $\theta$  is also mentioned in Fig. 1.53. It is accounted for by the factor  $P_\theta$  that corrects for the interference of the scattered light from different parts of the same molecule. The proportionality of factor  $P_\theta$  to the angle  $\theta$  is derived by summing of all contributions to the scattered light from the macromolecule. A detailed expression for the change of  $P_\theta$  with angle is given in Fig. 1.58 for several shapes. It can be derived from statistical considerations, leading to results as shown in the figure for the random coil, discussed in Sect. 1.3.

Separating the angular dependence found earlier for small particles by dividing the Rayleigh ratio by  $(1 + \cos^2 \theta)$ , one obtains  $\Delta R_{90}$ , which is still  $\theta$ -dependent because of the intermolecular interference. As expected, there is no reduction in the

<sup>1</sup> Peter JW Debye (1884–1966), born in Maastricht, The Netherlands. Taught physics at the Universities of Zürich, Utrecht, Göttingen, and Leipzig. Director of the Kaiser Wilhelm Institute for Theoretical Physics, Berlin, from 1935, and from 1940 Professor of Chemistry at Cornell University, Ithaca, NY. Nobel Prize for Chemistry in 1936 (work on atomic dipoles).

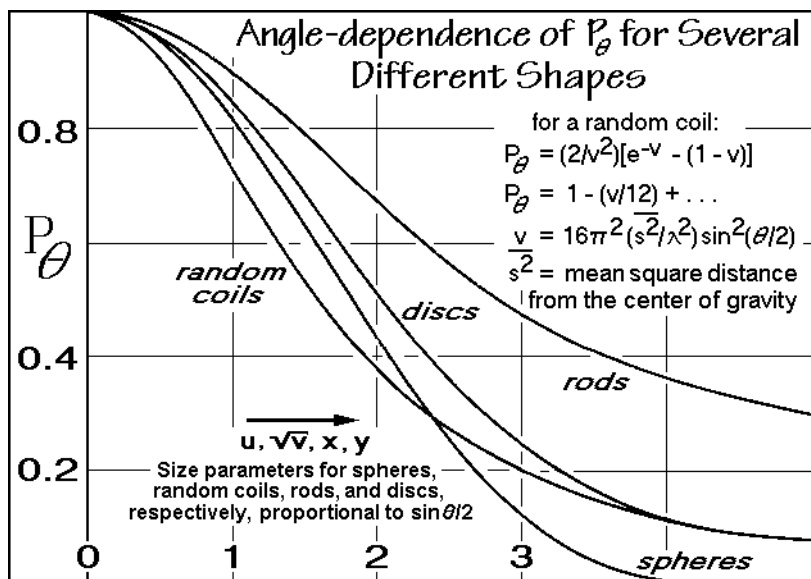


Fig. 1.58

forward scattering seen in Fig. 1.58 since all scattered light adds with the same phase as the incoming light. For the shape determination,  $P_\theta$  must be known quite precisely since the changes between discs, rods, random coils, spheres and other shapes can be quite small, as seen in the figure.

Typical light-scattering data for polystyrene in butanone are plotted in Fig. 1.59 in a method which was suggested originally by Zimm [20,21]. The abscissa is

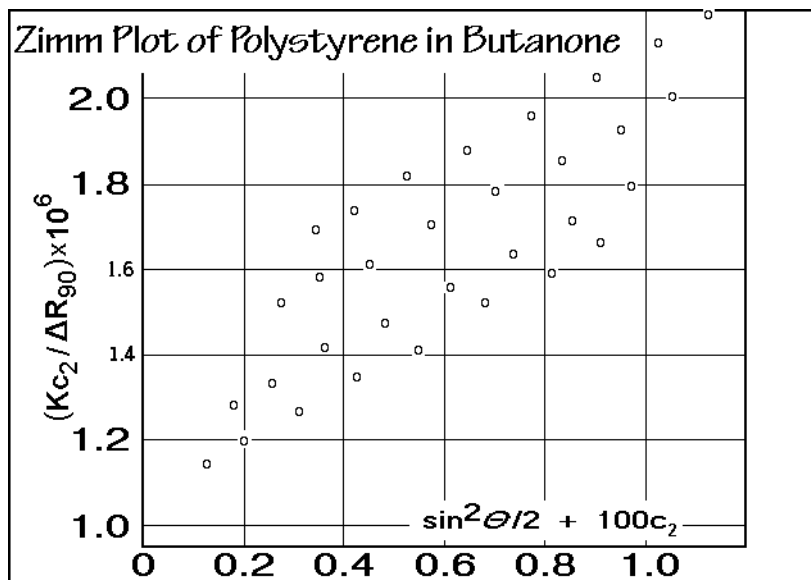


Fig. 1.59

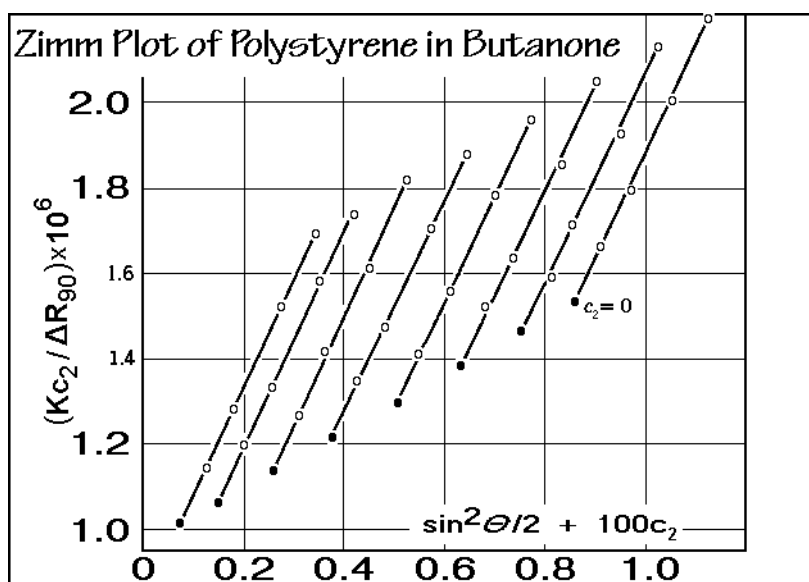


Fig. 1.60

proportional to the functional shape-dependence for a random coil,  $\sin^2 \theta/2$ , added to the concentration  $c_2$ , multiplied with an arbitrary constant  $k = 100$  (arbitrarily chosen so that the points are well separated). Next, in Fig. 1.60, all sets of data at the same scattering angle are extrapolated to zero concentration. The slopes of these lines are largely parallel. Extrapolating in addition to zero angle, as shown in Fig. 1.61, yields the so-called Zimm plot. The slope of the line of zero concentration is proportional

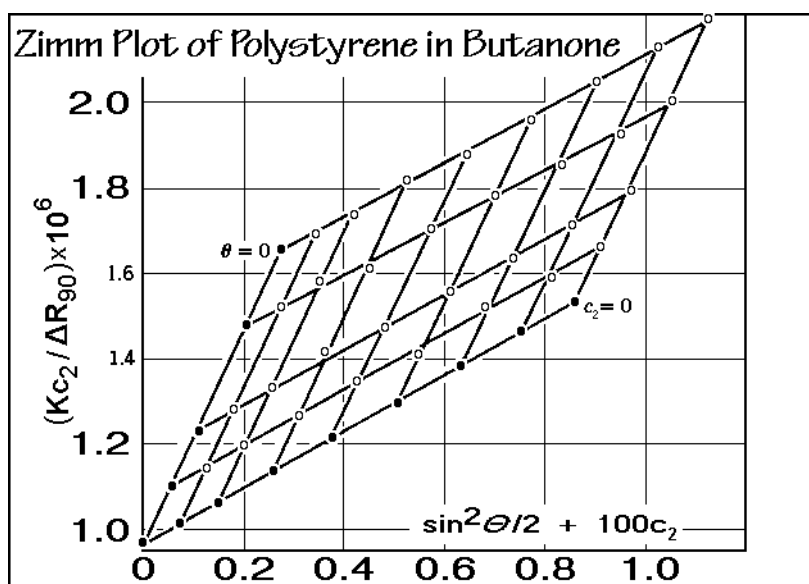


Fig. 1.61

to the mean square of the distance of the chain elements from their center of gravity ( $\langle s^2 \rangle^{1/2} = 46 \text{ nm}$ ); the slope of the line at zero scattering angle, which is proportional to the second virial coefficient ( $A_2 = 1.29 \times 10^{-4} \text{ m}^3 \text{ mol/kg}^2$ ); and the common intercept at zero concentration and angle, yields the inverse of the mass-average molar mass ( $\bar{M}_w = 1,030,000 \text{ Da}$ ).

Finally, the integration of the Rayleigh ratio over all angles can make the connection of the scattered light in direction  $\theta$  to the turbidity  $\tau$ , mentioned at the beginning of this section. The result is  $K/R_{90} = H/\tau$  with the constant  $H$  given by:

$$H = \frac{32\pi^3 n_o^2}{3N_A \lambda^4} \left( \frac{dn}{dc} \right)_o^2$$

This completes the discussion of light scattering. These data were the source of much of the information discussed in Sect. 1.3. Next, a series of other, somewhat simpler characterization techniques is discussed which can be used to determine average molar masses. With size-exclusion chromatography and ultracentrifugation, distributions can also be assessed.

### 1.4.3 Freezing Point Lowering and Boiling Point Elevation

The freezing point lowering and boiling point elevation of a low-molar-mass solvent due to the presence of a solute are colligative properties as described in Fig. 1.52, i.e., they are independent of the type of solute. One can thus use these properties to determine the molar mass of a polymeric solute. Figure 1.62 shows the appropriate equations and pressure-temperature phase diagram. The polymer mole fraction  $x_2$  is expressed in terms of heat of fusion ( $\Delta H_f$ ) or evaporation ( $\Delta H_v$ ), the freezing point lowering or boiling point elevation ( $\Delta T$ ) and the equilibrium melting or boiling temperatures ( $T_m^\circ$  or  $T_b^\circ$ ). The gas constant  $R$  is  $8.3143 \text{ J K}^{-1} \text{ mol}^{-1}$  and  $T$  is the temperature of measurement in kelvins. The equations can be derived easily, as is shown in the final result of Sect. 2.2.5 in Fig. 2.26, below.

Before the equations of Fig. 1.62 can be applied to experiments, they must be rewritten in terms of the measurable and known quantities, as is illustrated in Fig. 1.63. First the mole fraction is expressed in terms of concentration  $c_2$  in g per kg of solvent (note the difference from the  $c_2$  used in light scattering). On insertion for  $x_2$ , the heats of transitions are conveniently changed to the *latent heats* (J per kg of solvent). The mole fractions are available after the completed experiment.

The data treatment is illustrated in Fig. 1.64. Since ideal behavior is only expected at infinite dilution, the indicated extrapolation is necessary. This applies especially to macromolecular solutes. A list of values for  $RT_m^\circ L^{-1}$  for different solvents is shown at the bottom of the figure. It should be looked at in terms of the dimensionless variables  $\Delta T/T$ , the change in transition temperature in multiples of absolute temperature, and  $L/RT_{m,b}^\circ$ , the entropies of transition in multiples of  $R$ . The smaller the entropy change (larger  $RT_{m,b}^\circ/L$ ), the larger is  $\Delta T/T$ . Plastic crystal forming liquids, such as cyclohexane and camphor have a much smaller entropy of isotropization than rigid crystals of similar molecular structure (see Chap. 5) and are thus good solvents for freezing-point lowering experiments. Since the entropy of

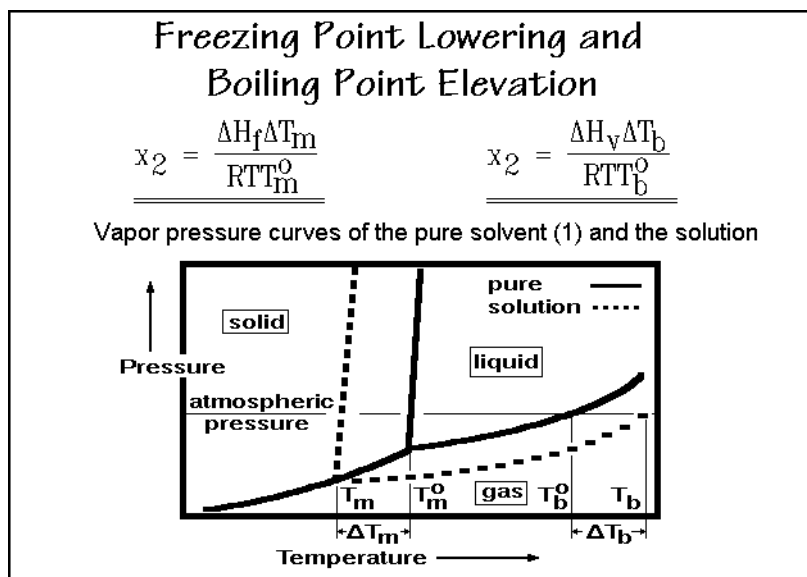


Fig. 1.62

evaporation is always larger than the entropy of fusion and does not change much for different solvents since all follow Trouton's rule (see Sect. 2.5.7), one needs higher precision of the thermometry for the determination of molar mass by boiling point elevation.

Figure 1.65 illustrates a differential ebulliometer for the measurement of boiling point elevations. This ebulliometer gives the precision which is required for

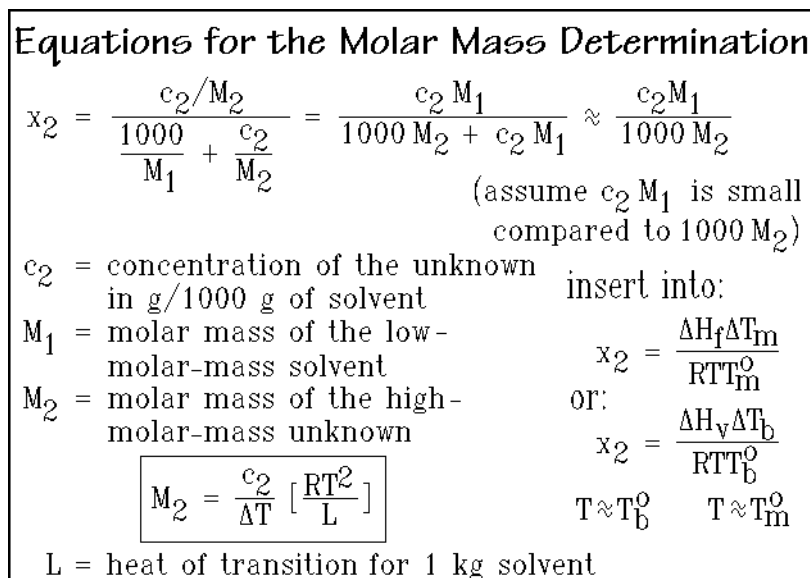


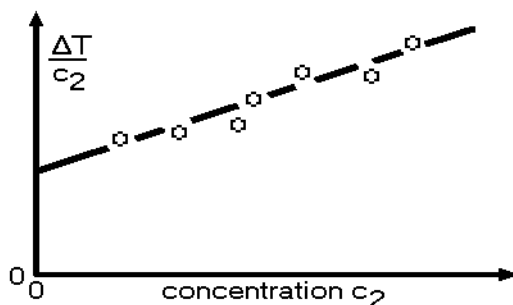
Fig. 1.63

## Data Treatment:

$$M_2 = \frac{c_2}{\Delta T} \left[ \frac{RT^2}{L} \right]$$

$$\lim_{c_2 \rightarrow 0} \frac{\Delta T}{c_2} = \frac{RT^2}{LM_2}$$

$$RT^2/L = RT/S$$



Typical values of  $RT^2/L$

Solvent	$T_m^0$ (K)	$RT_m^2/L$	$T_b$ (K)	$RT_b^2/L$
water	273.15	1.853	373.15	0.512
benzene	278.60	5.085	353.25	2.53
cyclohexane	279.65	20.5	354.15	2.79
camphor	451.55	40.0	--	--

Fig. 1.64

polymeric solutes. The upper bank of thermocouple reference junctions is kept at the boiling temperature of the pure solvent by being in the reflux stream of the condensed vapor (at  $T_b^0$ ). The measuring thermocouples are kept at the boiling point of the solution by having the solution flowing across their surface from the exit of the Cottrell pump that works like a percolator. The overheating, possible in the reservoir of solution, is thus kept low. There is no commercial ebulliometer, perhaps because

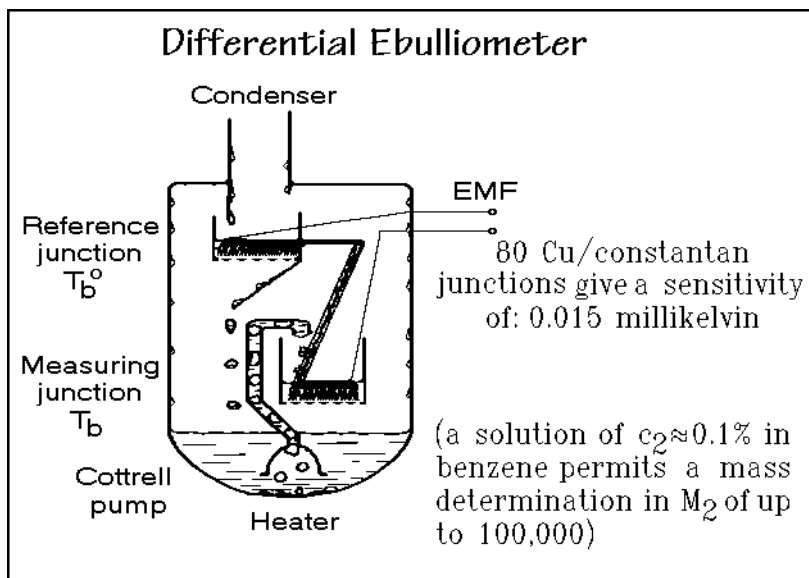
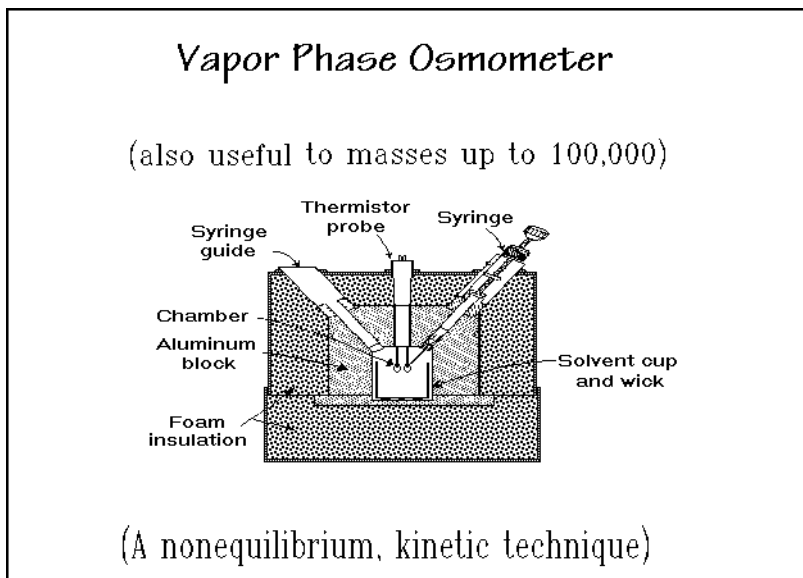


Fig. 1.65

of the success of an empirical method of measuring the differential evaporation and condensation of solvent vapor from pure solvent and from solution, the vapor phase osmometer shown in Fig. 1.66. With the indicated syringe a pure solvent drop is



**Fig. 1.66**

placed on one thermistor probe, and a solution drop on the other. The chamber is kept at the vapor pressure of the solvent, so that the measured  $\Delta T$  is proportional to the rate of excess condensation of solvent vapor on the solution droplet. Since the rates are not only dependent on the lower vapor pressure at the surface of the solution droplet, but also on the rates of mass diffusion and heat conduction,  $\Delta T$  must be calibrated with known standards.

Figure 1.67 shows a schematic of a simple, but effective set-up for cryoscopy, the method for the measurement of the freezing point lowering. Cryoscopy is perhaps the easiest of the molar mass determinations. The main prerequisites are a good temperature control and uniformity, corrections for the common supercooling observed on crystallization, and the usual extrapolation to infinite dilution. The thermodynamic equations are derived in Sect. 2.2.5, together with the equations needed for the ebulliometry.

The molar mass data for six typical polyethylene samples are listed in Fig. 1.68 [22]. They permit judgement of the routine precision for such experiments. Only ebulliometry and cryoscopy are absolute methods and need no calibration. Using the greatest possible precision, ebulliometry, vapor phase osmometry, and cryoscopy can be used up to 100,000 Da. Light scattering, also an absolute method, can readily measure up to 10,000,000 Da and give, in addition, information on the shape of the molecules, but may have difficulties with the lowest molar masses. The interaction parameter  $A_2$  could, in principle, be extracted from the concentration dependence of light scattering, ebulliometry, and cryoscopy data.



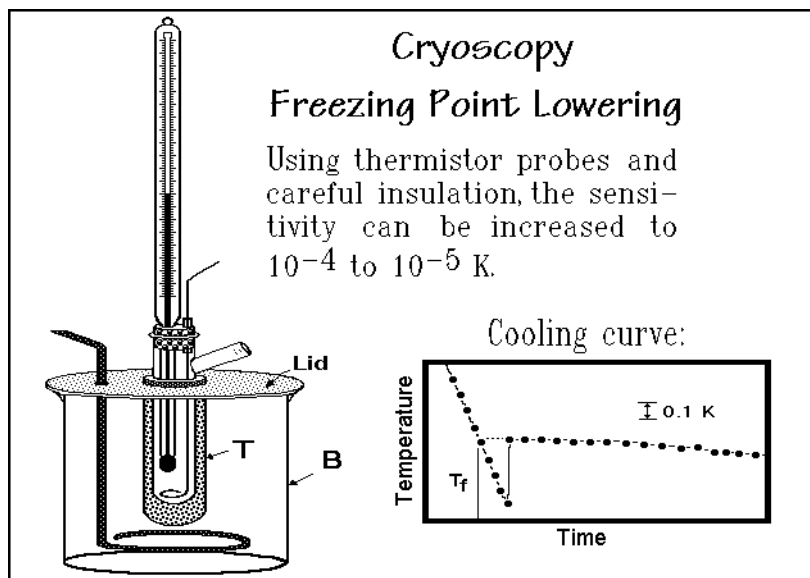


Fig. 1.67

Comparison of the Three Techniques of Molar Mass Determination for Six Low Molar Mass Polyethylenes			
	Sample 75	Sample 77	Sample 76
Ebulliometry	11,150	18,400	---
Vapor phase osmometry	11,000	18,800	16,300
Cryoscopy	10,700	19,100	13,300
	Sample 99H	Sample 99	Sample 99L
Ebulliometry	37,400 <sup>a</sup>	8,100 <sup>a</sup>	4,800 <sup>a</sup>
Vapor phase osmometry	38,400 <sup>b</sup>	8,600	3,500
Cryoscopy	40,600	8,100	3,320
<sup>a</sup> end-group analysis by IR <sup>b</sup> osmometry			

Fig. 1.68

#### 1.4.4 Size-exclusion Chromatography

Size-exclusion chromatography, also called by its older designation gel-permeation chromatography, permits the separation of different sizes of molecules by retarding the smaller ones longer than the larger ones while passing over a specially prepared

gel (for the description of gels, see Fig. 3.48, below). Figure 1.69 shows a schematic sketch of the process. The different fractions of the polymer appear at different times at the bottom of the column. The calibration is done with well-known, commercially

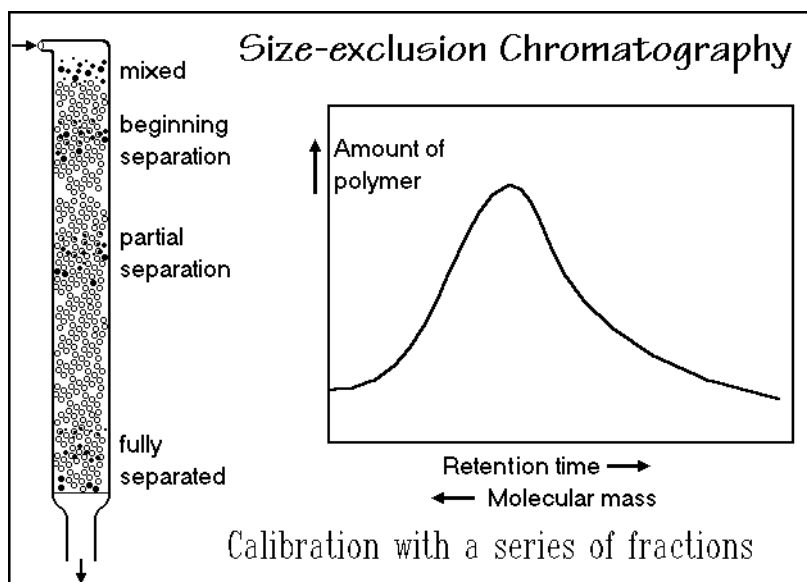


Fig. 1.69

available, polymer fractions. Polystyrene is often used, but different polymers may deviate considerably from a polystyrene calibration. Analyzing the emerging fractions with one of the absolute methods discussed above is the best calibration method. After the calibration, a full distribution curve of molecular sizes can be found, as indicated in the figure. This method goes thus far beyond the establishment of an average molar mass or a moment of the distribution as described in Sect. 1.1.3. At least number and mass average and polydispersity should be established. Besides analysis, preparative separation of a sample into narrow molar mass fractions is also possible.

### 1.4.5 Solution Viscosity

Solution viscosity was already recognized by Staudinger as a useful measure of the size of macromolecules. It is a measure of the extension of the molecule in solution. The larger the extension, the larger should be the contribution to the solution viscosity. Usually it is related empirically to the molar mass, although models have been developed to understand the results. Figure 1.70 shows a drawing of an Ubbelohde capillary viscometer. Constant temperature  $\pm 0.002$  K and efflux-times above 100 s are required. The viscosity  $\eta$  (measured in  $\text{Pa s} = \text{J cm}^{-3} \text{ s}^{-1}$ ) for a given viscometer is then proportional to the efflux time (see also Chap. 5). The viscometer is calibrated with two known liquids. Measurements are made at different concentrations  $c_2$  (in g/100 mL) to extrapolate to zero concentration. Three

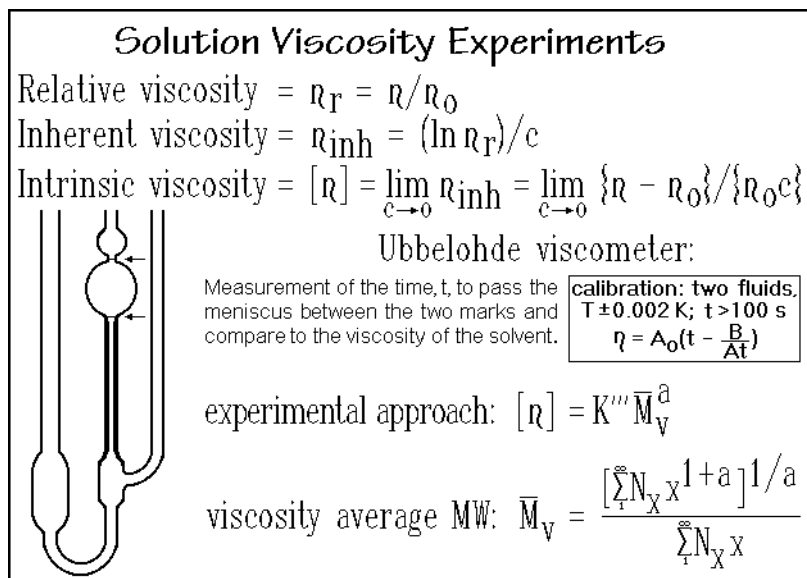


Fig. 1.70

commonly given viscosity measures are listed in the figure, where  $\eta_0$  is the solvent viscosity. The intrinsic viscosity suggests the extrapolation procedure for a measure of the influence of the polymer on the solvent viscosity.

Modeling polymer viscosity starts with calculating the effect of separate, solid spheres immersed in a solvent. The first result was already given by Einstein<sup>1</sup> in 1911 [23] ( $[\eta] = 2.5/\text{density of the solute in Mg/m}^3$ ). The energy dissipated by the spheres at the given concentration  $c_2$  each second per unit volume of solution is equal to the intrinsic viscosity. The next step is to go to the freely draining model for which more details are given in the discussion of melt viscosity in Sect. 5.6.6. One assumes that the macromolecule rotates as a whole through the action of the shear-gradient, but entraps no solvent. On summation of the frictional energy over all parts of the molecule assumed to be solid beads. This summation was first done by Debye [24,25], a proportionality to the mean-square end-to-end distance with an expansion factor  $\alpha^2$  results in the expression:

$$[\eta] = K' \langle r^2 \rangle \alpha^2.$$

At the  $\theta$ -temperature, the excluded volume effect is avoided ( $\alpha = 1.0$ , see Sect. 1.3.). Making some solvent to rotate with the molecule leads to the equivalent sphere model. In this case one assumes that a certain inner solid sphere of solvent is

<sup>1</sup> Albert Einstein (1879–1955), born in Ulm, Germany. He was recognized in his own time as one of the most creative intellects in human history. Einstein studied mathematics and physics at the ETH in Zürich until 1900 when he became a Swiss citizen. In 1905 he earned his Ph.D. from the University of Zürich. The later life was in Berlin (1914–33) and then Princeton, NJ. Nobel Prize for Physics in 1921 (for work on photoelectricity and theoretical physics).

entrapped by the macromolecule and rotates with it in the shear-gradient. The intrinsic viscosity is now decreased to the square-root dependence on the molar mass of the polymer,  $M_2$ :

$$[\eta] = K'' M_2^{1/2} \alpha^3.$$

Neither the limits of the freely-draining nor the equivalent sphere give, however, the proper proportionality. One uses thus an empirical approach by calibration with standards as indicated in Fig. 1.70. The exponent  $a$  is typically fractional, between 0.6 and 0.8. As a result, the viscosity average molar masses are neither of the averages discussed in Sect. 1.4.3. A special average is defined as given in Fig. 1.70. The viscosity average molar mass, written as  $\bar{M}_v$ , is closer to  $\bar{M}_w$  than to  $\bar{M}_n$ , as seen in the last line of the figure.

### 1.4.6 Membrane Osmometry

The osmotic pressure is again a colligative property and leads, thus, to an absolute molar mass and for a distribution of different species, a number-average molar mass, as summarized in Fig. 1.71. The pressure  $p$  of the ideal gas law is replaced by the osmotic pressure  $\pi$ ,  $w$  is the total mass dissolved, so that  $w/\bar{M}_n$  is the number of moles,  $n$  to give the link to  $pV = nRT$ .

Measurements became easier with rapidly equilibrating membrane osmometers with servo pressure control. The instrument senses differences in osmotic pressure based on the mass transport through the membrane. The pressure differential between solvent and solution is then controlled by increasing the solution level to hydrostatically counterbalance the osmotic pressure  $\pi$ . The success of the osmometry

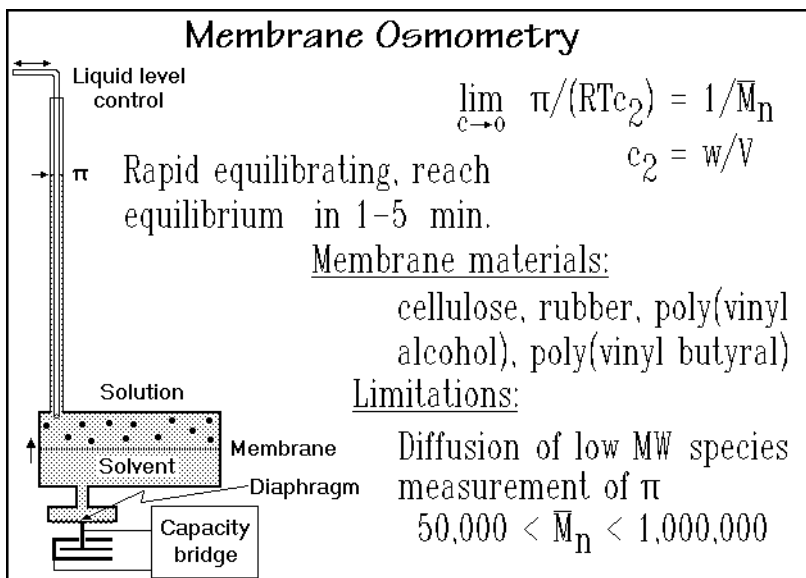


Fig. 1.71

rests with the quality of the membrane. It must not let small polymer molecules pass, but have free exchange of solvent. Best results have been obtained with molar masses above 50,000 Da.

### 1.4.7 Other Characterization Techniques

A series of additional characterization techniques for macromolecules is available. All should be familiar to the polymer scientist. Ultracentrifugation is a special technique, although in principle well understood, it is more difficult to make absolute measurements on synthetic polymers than for the more compact globular proteins for which the method was originally developed.

The scattering of neutrons is in several aspects similar to the earlier discussed light scattering, as is summarized together with the scattering of electrons in Fig. 1.72. It can be used to find molar mass, the shape of the molecule, and the interaction with the solvent. Of particular interest is the neutron scattering of polymers in solutions of their deuterated counterparts since the scattering diameter of hydrogen for neutrons is particularly large. With such experiments it could be shown that in

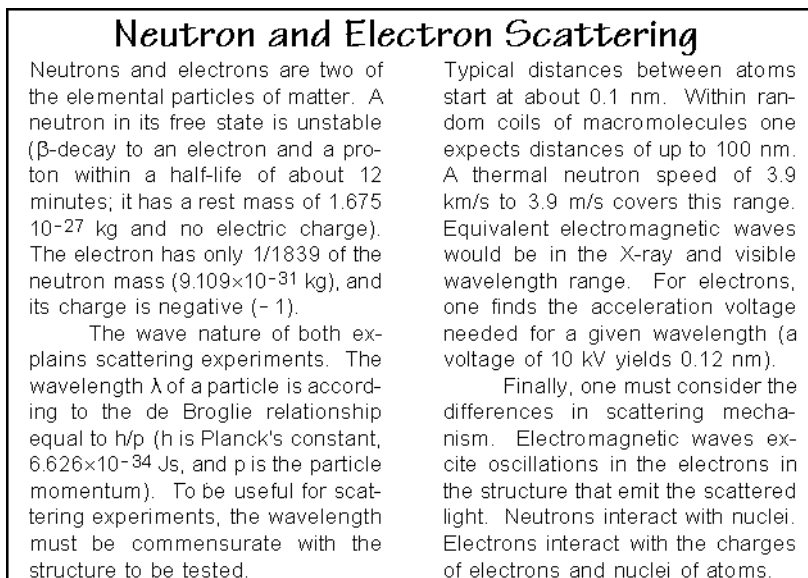


**Fig. 1.72**

the melt polymer molecules assume, indeed, shapes close to those calculated in Sect. 3 and found in solution at the  $\theta$ -temperature, i.e., they are unaffected by the excluded volume.

The end-group determination can be done with many analytical tools, such as infrared analysis, nuclear magnetic resonance, or the detection of radioactive end groups which were included during the synthesis. The end-group determination for the purpose of measurement of the molar mass of macromolecules, great precision is necessary.

Calorimetry and dilatometry were used to estimate super-high molar masses for some crystallizable polymers. For such high molar masses, crystallization is increasingly impeded and the fraction of the molecules able to crystallize has been calibrated with respect to molar mass for polytetrafluoroethylene [25,26].

Melt viscosity can also be used for molar mass estimates. The measurements are, however, somewhat less precise because of the high viscosities due to entanglements of the molecules, and it is inconvenient to work at the higher temperatures needed to melt the polymer. A frequent measurement is that of the melt index. A basic extrusion-capillary is used to determine the (mass) rate of flow of the polymer through a specified capillary under controlled conditions of temperature and pressure. Similarly, the Mooney viscometer gives a measure of the torque to revolve a rotor at constant speed in a polymer at constant speed, which is linked ultimately to molar mass. The Mooney viscometer has found application in the rubber industry as an empirical measure of molar mass. Somewhat more information on melt viscosity is given in Sect. 5.6.6.

A final tool is electron microscopy and atomic force microscopy. Both tools can image isolated molecules and an estimate of their volume can be made, which in turn, can be converted to molar mass with knowledge of the density. Both amorphous polymers as well as crystalline polymers have been analyzed. The main problem of this technique is the separation of the sample into single-molecule droplets or crystals [27] (see also Figs. 5.160 and 5.74, respectively).

This summary of the experimental evaluation of molecular sizes, interactions and shapes concludes the discussion of Atoms, Small, and Large Molecules. The major topics of this first chapter of the book were the identification of all types of molecules, the naming of macromolecules, and their characterization via molecular mass and chain statistics, as well as experimental molar mass and distribution determination. Several of the instruments described are classified as thermal analysis equipment and belong into the large field of thermometry, which will be treated in more detail in Sect. 4.1.

## References

### **General References**

**Sect. 1.1.** For the section on the microscopic description of matter, review your physical chemistry references. Examples are given in the General References of the Preface.

The book by Dalton J (1808) "A New System of Chemical Philosophy" is available in many reprints, for example, (1964) The Science Classics Library. The Citadel Press, New York.

A useful reference to the state of science at the beginning of the modern science era is: Lavoisier AL (1789) Elements of Chemistry. Paris. Frequently reprinted, for example, found in a Dover Publication as a paperback facsimile reprint (1965) New York (translation by Kerr R, 1790, Edinburgh).

A typical source of bibliographic information is Farber E, ed (1961) Great Chemists. Interscience Publ. New York. Much information can also be found in the electronically searchable Encyclopædia Britannica.

The history of polymer science can be followed best with the books: Morawetz H (1985) Polymers, The Origin and Growth of a Science. Wiley, New York; and Furukawa Y (1998) Inventing Polymer Science: Staudinger, Carothers, and the Emergence of Macromolecular Chemistry. University of Pennsylvania Press.

**Sect. 1.2.** A sufficiently detailed description of the IUPAC rules for naming polymers is given in: Brandrup J, Immergut, EH, Grulke EA, eds (1999) Polymer Handbook. Wiley, 3<sup>rd</sup> edn, New York. See also: International Union of Pure and Applied Chemistry (1991) Compendium of Macromolecular Nomenclature. Blackwell, Oxford; a summary of the nomenclature of inorganic and organic small and large molecules is given also in Lide DR, ed (2002/3) Handbook of Chemistry and Physics, 83<sup>rd</sup> edn. CRC Press, Boca Raton.

Collections of three- and four-letter abbreviations of polymers have been made by many organizations. IUPAC Division of Applied Chemistry, Plastics and High Polymer Section (1969) Recommendations for Abbreviations for Terms relating to Plastics and Elastomers. Pure Appl Chem 18: 583–589. Commission on Macromolecular Nomenclature (1974) List of Standard Abbreviations (Symbols) for Synthetic Polymer Materials. Pure Appl Chem 40: 475–476. For a collection of abbreviations accepted internationally by many organizations see also Elias HG, Pethrick RA (1984) Polymer Yearbook. Harwood Acad Publ, Chur, Switzerland.

To find out about extensive details for a polymer which is new to you, check: Mark HF, Gaylord, NG Bikales NM (1985–89) Encyclopedia of Polymer Science and Engineering. Interscience Publ., 2<sup>nd</sup> edn, New York. (A 12-volume 3<sup>rd</sup> edn is in preparation, Kroschwitz, ed (2003–2004) Wiley, New York.) It may also be sufficient to check your introductory polymer science text (see examples in the Preface).

**Sect. 1.3.** Use your basic reference books on mathematics, statistics, and vector analysis to support the concepts and derivations developed. Some examples are: (1960 and later) International Dictionary of Applied Mathematics. Van Nostrand, Princeton. Feller W (1950 and later) An Introduction to Probability Theory and Its Applications. Wiley, New York.

Mood AM (1959) *Introduction to the Theory of Statistics*. McGraw-Hill, New York.  
Hamming RW (1962 and later) *Numerical Methods for Scientists and Engineers*. Dover, New York.  
Coffin JG (1911 and later) *Vector Analysis*. Wiley, New York.

The early ideas about molecular mass distributions are well displayed in Flory PJ (1953) *Principles of Polymer Chemistry*. Cornell University Press, Ithaca.

A specially detailed book about molecular chain dimensions and rubber elasticity is by: Bueche F. (1962) *Physical Properties of Polymers*. Interscience, New York.

A Specialized book on molecular mass distributions is Peebles LH (1971) *Molecular Weight Distribution in Polymers*. Wiley Interscience, New York.

The classical texts on rotational isomers and the calculation of chain conformations are: Flory PJ (1966) *Statistical Mechanics of Chain Molecules*. Interscience, New York.  
Volkenstein, MV (1963) *Configurational Statistics of Polymeric Chains*. Engl translation, Interscience, New York.

For a general review of the molecular dynamics method see, for example: Klein ML (1985) *Computer Simulation Studies of Solids*. *Ann Rev Phys Chem* 36: 525–548. Suter U, Monnerie L eds (1994) *Atomistic Modelling of Physical Properties of Polymers*. Springer, Berlin (*Adv Polymer Sci*, vol 116).

A general collection of papers on simulations is given in: Roe RJ, ed (1991) *Computer Simulation of Polymers*. Prentice Hall, Englewood Cliffs.

**Sect. 1.4.** A number of books specializing on the techniques of polymer characterization are: White JR (1989) *Polymer Characterization*. Chapman and Hall, New York. Barth HG, Mays JW (1991) *Modern Methods of Polymer Characterization*. Wiley-Interscience, New York. Compton TR (1989) *Analysis of Polymers: An Introduction*. Pergamon Press, New York. Craver CD (1983) *Polymer Characterization*. *Am Chem Soc Washington DC (Advances in Chemistry Series 203)*.

### ***Specific References***

1. Pauling L (1960) *The Nature of the Chemical Bond*. Cornell University Press, 3<sup>rd</sup> edn, Ithaca, NY.
2. Kroto HW, Heath JR, O'Brien SC, Curl RF, Smalley RE (1985) C<sub>60</sub>: Buckminsterfullerene. *Nature* 318: 162–163.
3. The first write-up of the suggested classification of molecules including macromolecules was given in: Wunderlich B. (1980) *Macromolecular Physics*, Vol. III, Sect. 8.1.2. Academic Press, New York. See also a recent summary: Wunderlich B (1999) *A Classification of Molecules and Transitions as Recognized by Thermal Analysis*. *Thermochim Acta* 340/41: 37–52.
4. Staudinger H (1920) Über Polymerisation. *Ber* 53: 1073–1085.
5. IUPAC Commission on Macromolecular Nomenclature: (1976) *Nomenclature of Regular Single-stranded Organic Polymers*. *Pure Appl Chem* 48: 375–385; (1985) *Source-based Nomenclature for Copolymers*. *Ibid* 57: 1427–1440.
6. Newkome GR; Morefield CN; Vogtle F (2001) *Dendrimers*. Wiley, Chichester, UK, second edn.
7. Raymo, FM, Stoddart JF (1999) *Interlocked Macromolecules*. *Chem Rev* 99: 1643–1663.
8. Sperling LH, Fay JJ, Murphy CJ, Thomas DA (1990) *Interpenetrating Polymer Networks, The State of the Art*. *Makromol Chem Makromol Symp* 38: 99–113.
9. Lowry GG (1970) *Markov Chains and Monte Carlo Calculations in Polymers*. Marcel Dekker, New York.
10. Wall FT, Erpenbeck JJ (1959) *Statistical Computation of Radii of Gyration and Mean Internal Dimensions of Polymer Molecules*. *J Chem Phys* 30: 637–640.



11. Cheng SZD, Noid DW, Wunderlich B (1989) Molecular Segregation and Nucleation of Poly(ethylene oxide) Crystallized from the Melt. IV. Computer Modeling. *J Polymer Sci Part B Polymer Phys* 27: 1149–1160.
12. Miller KJ, Hollinger HB, Grebowicz J, Wunderlich B (1990) On the Conformations of Poly(*p*-xylylene) and its Mesophase Transitions. *Macromolecules* 23: 3855–3859.
13. Noid DW, Sumpter BG, Wunderlich B (1990) Molecular Dynamics Simulation of the Condis State of Polyethylene. *Macromolecules* 23: 664–669.
14. Sumpter BG, Noid DW, Wunderlich B (1990) Computer Experiments on the Internal Dynamics of Crystalline Polyethylene: Mechanistic Details of Conformational Disorder. *J Chem Phys* 93: 6875–6889.
15. Noid DW, Sumpter BG, Wunderlich B, Pfeffer GA (1990) Molecular Dynamics Simulations of Polymers: Methods for Optimal Fortran Programming. *J Comp Chem* 11: 236–241.
16. Kuhn W (1936) The Relationship Between Molecular Size, Statistical Molecular Shape, and Elastic Properties of Highly Polymerized Substances. *Kolloid Z* 76: 258–271.
17. Hughlin MB (1972) *Light Scattering from Polymer Solutions*. Academic Press, London.
18. Stacey KA (1956) *Light Scattering in Physical Chemistry*. Academic Press, New York.
19. Strutt JW (Lord Rayleigh) (1914) Diffraction of Light by Spheres of Small Relative Index. *Proc Roy Soc London (A)* 90: 219–225.
20. Zimm BH (1948) The Scattering of Light and the Radial Distribution Function of High-polymer Solutions. *J Chem Phys* 16: 1093–1099.
21. Zimm BH (1948) Apparatus and Methods for Measurement and Interpretation of the Angular Variation of Light Scattering; Preliminary Results on Polystyren Solutions. *J Chem Phys* 16: 1099–1116.
22. Data by Billmeyer, Jr. FW, Kokle, V (1964) The Molecular Structure of Polyethylene. XV. Comparison of Number-average Molecular Weights. *J Am Chem Soc* 86: 3544–3546.
23. Einstein A (1906) Eine neue Bestimmung der Moleküldimensionen. *Ann Phys* 19: 289–306 [correction *Ann Phys* (1911) 34: 591–592].
23. Debye P (1944) Light Scattering in Solutions. *J Appl Phys* 15: 338–342.
24. Debye P (1947) Molecular-weight Determination by Light Scattering. *J Phys Colloid Chem* 51: 18–32.
25. Suwa T, Takehisa M, Machi S (1973) Melting and Crystallization Behavior of Poly(tetrafluoroethylene). New Method for Molecular Weight Measurement of Poly(tetrafluoroethylene) Using a Differential Scanning Calorimeter. *J Appl Polymer Sci* 17: 3253–3257.
26. Sperati CA, Starkweather, Jr. HW (1961) Fluorine-containing Polymers. II. Polytetrafluoroethylene. *Adv Polymer Sci* 2: 465–495.
27. Bu H, Shi S, Chen E, Hu H, Zhang Z, Wunderlich B (1996) Single-molecule Single Crystals of Poly(Ethylene Oxide). *J Macromol Sci Phys B* 35: 731–747.

# Basics of Thermal Analysis

The basic, macroscopic theories of matter are equilibrium thermodynamics, irreversible thermodynamics, and kinetics. Of these, kinetics provides an easy link to the microscopic description via its molecular models. The thermodynamic theories are also connected to a microscopic interpretation through statistical thermodynamics or direct molecular dynamics simulation. Statistical thermodynamics is also outlined in this section when discussing heat capacities, and molecular dynamics simulations are introduced in Sect. 1.3.8 and applied to thermal analysis in Sect. 2.1.6. The *basics*, discussed in this chapter are designed to form the foundation for the later chapters. After the introductory Sect. 2.1, equilibrium thermodynamics is discussed in Sect. 2.2, followed in Sect. 2.3 by a detailed treatment of the most fundamental thermodynamic function, the heat capacity. Section 2.4 contains an introduction into irreversible thermodynamics, and Sect. 2.5 closes this chapter with an initial description of the different phases. The kinetics is closely linked to the synthesis of macromolecules, crystal nucleation and growth, as well as melting. These topics are described in the separate Chap. 3.

## 2.1 Heat, Temperature, and Thermal Analysis

The introductory discussion on thermal analysis begins with a brief outline of the history of the understanding of heat and temperature. Heat is obviously a macroscopic quantity. One can feel its effect directly with one's senses. The microscopic origin of heat, the origin on a molecular scale, rests with the motion of the molecules of matter discussed in Sect. 2.3. The translation, rotation, internal rotation, and vibration of molecules are the cause of heat. Temperature, in turn, is more difficult to comprehend. It is the intensive parameter of heat. Before we can arrive at this conclusion, several aspects of heat and temperature must be considered. A short description based on experiments is given in Sects. 2.1.5 and 2.1.4 and more details are found in Sects. 4.2 and 4.1.

### 2.1.1 History

The scheme of the elements of the ancient Greek philosophers of some 2500 years ago contained heat (fire) as one of the four basic elements. The other three elements were the phases, gas (air), liquid (water), and solid (earth) as discussed in Sect. 2.5 and Chap. 5. Figure 2.1 is an illustration of this ancient scheme. It is interesting that the logo of the International Confederation for Thermal Analysis and Calorimetry,

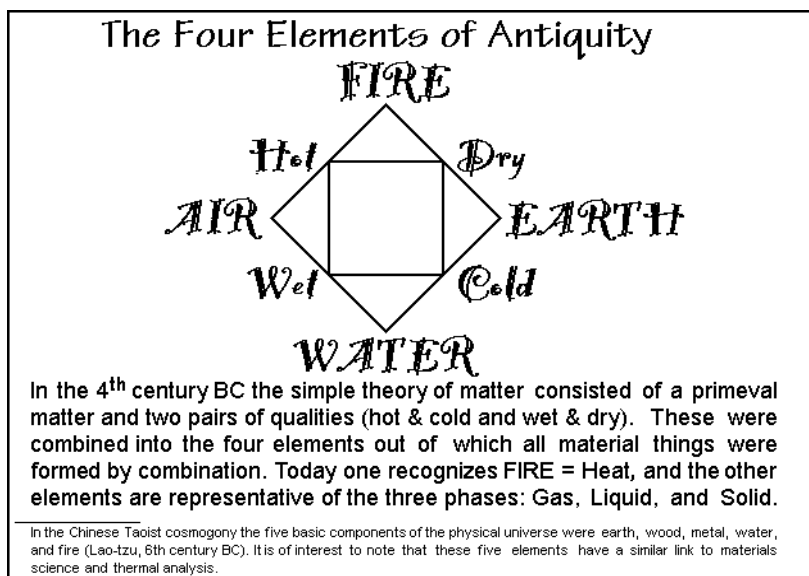


Fig. 2.1

ICTAC, described in Fig. 2.5, below, includes the center part of the scheme of Fig. 2.1. A first explanation of the phenomenon of heat that seems to better match the present knowledge can be found in the interesting writings of Bacon excerpted in Fig. 2.2. The molecular motion as we know it today was naturally not known then. Bacon, also, did not convince his peers. An important further development can be gained from the famous book by Lavoisier "Elements of Chemistry." Two of its

**Two Historical Statements about "Heat"**

Francis Bacon in "Novum Organum" (second book, aph. 20) he says that:  
(1620): "... the very essence of heat, or the substantial self of heat is motion and nothing else."

**ELEMENTS OF CHEMISTRY**

Translated by R. Kerr, Edinburgh, 1789, pages 4-6, about heat:

This substance, whatever it is, being the cause of heat, or, in other words, the sensation which we call *warmth* being caused by the accumulation of this substance, we cannot, in strict language distinguish it by the term *heat*; because the same name would then very improperly express both cause and effect....

A. Lavoisier  
(1789): .... Wherefore, we have distinguished the cause of heat, or that exquisitely elastic fluid which produces it, by the term of *caloric*. Besides, that this expression fulfils our object in the system which we have adopted, it possesses this farther advantage, that it accords with every species of opinion, since, strictly speaking, we are not obliged to suppose this to be a real substance; it being sufficient, as will more clearly appear in the sequel of this work, that it be considered as the repulsive cause, whatever that may be, which separates the particles of matter from each other; so that we are still at liberty to investigate its effects in an abstract and mathematical manner.

Fig. 2.2

paragraphs are reprinted in Fig. 2.2. In the first paragraph, Lavoisier<sup>1</sup> states the difficulties with respect to the word heat. Without knowledge about the origin of heat, he suggests the solution, copied in Fig. 2.2. He points out that after the introduction of the word *caloric* for the substance of heat, one can go ahead and investigate the effects of heat without inconsistency of nomenclature. Indeed, the calorimetric theory was well developed before full knowledge of heat as molecular motion was gained.

It is interesting that today one would not accept the ultimate experiments which at the end of the 19<sup>th</sup> century supposedly disproved the theory of the caloric. The main difficulty in the caloric theory was the explanation of friction. Friction seemed to be an inexhaustible source of caloric. For *measurement* Count Rumford in 1798 used a blunt drill “to boil 26.5 pounds of water.” The only effect on the metal was to shave off 4.145 grams. Next, he could prove that the capacity of heat of this powder, meaning the amount of heat to raise its temperature by a fixed amount, was identical to that of the uncut material. He argued that the fact that the powder had the same capacity for heat also proved that there was no *caloric* lost in shaving off the metal. This obviously is insufficient proof. The powder may have had the same capacity for heat, but it was not proven to have a smaller heat content. For a complete proof, one would have to reconvert the powder into solid metal and show that in this process there was no need to absorb caloric, a more difficult task. Count Rumford himself probably felt that his experiments were not all that convincing, because at the end of his paper he said, in a more offhand analysis: “In any case, so small a quantity of powder could not possibly account for all the heat generated, . . . the supply of heat appeared inexhaustible.” Finally, he stated, “Heat could under no circumstances be a material substance, but it must be something of the nature of motion.” So, one has the suspicion that Count Rumford knew his conclusions before he did the experiment.

The other experiments usually quoted in this connection were conducted by Humphry Davy<sup>2</sup> in 1799. He supposedly took two pieces of ice and rubbed them together. During this rubbing, he produced large quantities of water. Ice could, thus, be melted by just rubbing two pieces of ice together. Since everyone knows that one must use heat to melt ice, this was in his eyes proof that caloric could not be the reason for fusion and the “work of rubbing” had to be the cause of melting. The unfortunate part of this otherwise decisive experiment is that one could not repeat it under precise conditions. It is not possible to rub two pieces of ice together to produce water. The friction is too little. If one increases the friction by using pressure, the melting temperature is reduced, so that melting occurs by conduction of heat. One must again conclude that Davy got results he was expecting and did not analyze his experiment properly for conduction of heat, the probable cause of the melting. The experiments, however, were accepted by the scientific community, and since the conclusions seemed correct, there was little effort for further experiments.

---

<sup>1</sup> Antoine-Laurent Lavoisier, 1743–1794. Leading French Chemist of the 18<sup>th</sup> century. Well known for his development of the understanding of the reactions of oxygen. As a public administrator before the French Revolution, he was executed during the revolutionary terror.

<sup>2</sup> Sir Humphry Davy, 1778–1829. English Chemist and Fellow of the Royal Society who discovered sodium, potassium, and iodine and is known for his early work on electrolysis.

A mathematical theory of the caloric, seemingly in contrast to these experiments, was given by Carnot<sup>1</sup>, based on the efficiency of a reversible heat engine, which seemed to rest on the assumption of a conserved material of heat (the caloric). The qualitative arguments of Count Rumford and Davy, however, could finally be proven by the quantitative experiments of Joule<sup>2</sup> in the 1840s. From these experiments he inferred properly that heat was a state of motion, not a material. In the early 1850s this conflict to Carnot's findings was finally resolved by Kelvin<sup>3</sup> and Clausius<sup>4</sup>. Joule had correctly asserted that heat could be created and destroyed proportionally to the exchanged amount of mechanical, electrical, or chemical energy (first law of thermodynamics, the total energy of a system is conserved, see Sects. 2.1.5 and 2.2.2), but Carnot's result also holds, it rests not on the conservation of heat, but of entropy (under reversible conditions, the change in entropy is zero, second law of thermodynamics, see Sect. 2.2.3).

Since language is rarely corrected after scientific discovery of old errors, some of this confusion about heat is maintained in present-day languages. Several different meanings can be found in any dictionary for the noun "heat." A good number of these have a metaphorical meaning and can be eliminated immediately for scientific applications. Eliminating duplications and separating the occasionally overlapping meanings, one finds that there remain four principally different uses of the word heat. The first and primary meaning of heat describes the heat as a physical entity, energy, and derives it from the quality of being hot which, in turn, describes a state of matter. An early, fundamental observation was that in this primary meaning, heat describes an entity in equilibrium. Heat is passed from hot to cold bodies, to equilibrate finally at a common, intermediate, degree of hotness. In the seventeenth and the eighteenth century, this observation was the basis of the theory of the caloric, as described above. Heat was assumed to be an indestructible fluid that occupies spaces between the molecules of matter as sketched in Figure 1.2.

Turning to the other meanings of the word heat listed in most dictionaries, one finds that a degree of hotness is implied. This indicates that heat is still confused with its intensive parameter temperature. The example "the heat of this room is unbearable" is expressed correctly by saying "the temperature of this room is unbearable." The improper use of heat in this case becomes clear on recognizing that,

---

<sup>1</sup>Sadi Carnot, 1824, lived 1796–1832, French army officer and "constructor of steam engines."

<sup>2</sup>James P. Joule, 1818–1889, English physicist. He found that the energy of an electric current can produce either heat or mechanical work, each with a constant conversion factor.

<sup>3</sup>William Thomson, 1<sup>st</sup> Baron Kelvin of Largs, 1824–1907, Scottish engineer, mathematician, and physicist. Professor at the University of Glasgow, England. His major contributions to thermal analysis concern the development of the second law of thermodynamics, the absolute temperature scale (measured in kelvins) and the dynamic theory of heat.

<sup>4</sup>Rudolf Clausius, 1822–1888, Professor at the University of Bonn. German mathematical physicist who independently formulated the second law of thermodynamics and is credited with making thermodynamics a science.

depending on the matter inside the room, the same temperature can be produced by different amounts of heat. A more detailed description of the term temperature will be given in Sects. 2.1.4 and 4.1.

The third meaning of heat involves the quantity of heat. This reveals that heat actually is an extensive quantity, meaning that it doubles if one doubles the amount of material talked about. Doubling the size of an object will take twice the amount of heat to reach the same degree of hotness (temperature).

Finally, a fourth meaning connects heat with radiation. This meaning is not clearly expressed in most dictionaries. Again, turning to Lavoisier's "Elements of Chemistry," he wrote there: "In the present state of our knowledge we are not able to determine whether light be a modification of caloric, or caloric be, on the contrary, a modification of light." Very early, people experienced that the sun had something to do with heat, as expressed in terms like "the heat of the sun." The inference of a connection between heat and color also indicates a link between heat and radiation through expressions like red-hot and white-hot, as expressed in the physiological temperature scale described in Sect. 4.1. Today, one should have none of these difficulties since we know that heat is just one of the many forms of energy. The radiant energy of the sun, felt as heat, is the infrared, electromagnetic radiation. By absorption into matter, it is converted to heat, the energy of molecular motion.

As a result of not changing the use of language during the last 200 years, today each child is still first exposed to the same wrong and confusing meanings based on the centuries-old misconceptions. Only later and with considerable effort do some acquire an understanding of heat as the extensive, macroscopic manifestation of the microscopic molecular motion and temperature as its intensive parameter, perhaps best expressed by the ideal gas theory, described in Figs. 2.8 and 9.

### 2.1.2 The Variables of State

Six physical quantities are commonly used for the description of the state of matter, hence they are called variables of state. They are, with their SI units given in parentheses, the total energy,  $U$  (J), temperature,  $T$  (K), volume,  $V$  ( $\text{m}^3$ ), pressure,  $p$  (Pa), number of moles,  $n$  (mol), and mass,  $M$  (kg). The SI units are summarized in some more detail in Fig. 2.3 [1].<sup>1</sup> Of these variables of state, the quantities whose magnitudes are additive when increasing the system are called *extensive*, i.e., they double with doubling of the system. Quantities whose magnitudes are independent of the extent of the system are called *intensive*. Of the listed functions,  $T$  and  $p$  are intensive, all others are extensive. Furthermore, infinitesimal changes of the variables of state are indicated by the letter "d." For partial infinitesimal changes, as arise when restrictions are placed on the variables, one writes the symbol " $\partial$ " instead of "d." It signifies that in this case all but one variable of state are kept constant. When necessary, the variables kept constant are identified by subscripts.

---

<sup>1</sup> There are four simple rules to satisfy the SI rules: 1.) Use only SI units. 2.) Use only numerical values from 0.1 to 999. 3.) Scale other values by using prefixes such as  $k = 1,000$ ,  $M = 1,000,000$ ,  $m = 1/1,000$ ,  $\mu = 1/1,000,000$ . 4.) Use only one scaling prefix and use it only in the numerator.

## The International System of Units, SI Système International des Unités

The SI is the logical extension of the metric system of units that has been in use for about 200 years. It was adopted by the 11<sup>th</sup> General Conference on Weights and Measures (CGPM) in 1960. It is a coherent system of seven base units, one for each of the seven dimensionally independent quantities:

meter (m), kilogram (kg), second (s), ampere (A)  
kelvin (K), mole (mol), and candela (ca)

for length, mass, time, electric current, thermodynamic temperature, amount of substance, and luminous intensity, respectively.

The SI is a meter-kilogram-second-ampere system (MKSA), giving it marked advantages over the old MKS and the cgs systems it replaces. Contained in the SI system are also a number of other, single-named units: the radian and steradian (angle), and a series of derived units named after great scientists, mathematicians, and inventors, such as: the hertz (Hz, frequency), newton (N, force), pascal (Pa, pressure), joule (J, energy), watt (W, power), coulomb (C, quantity of electricity), volt (V, electrical potential, emf), siemens (S, electric conductance), ohm ( $\Omega$ , electrical resistance), farad (F, electrical capacity), weber (Wb, magnetic flux), henry (H, electric inductance), tesla (T, magnetic flux density).

**Fig. 2.3**

The first law of thermodynamics states simply that the total energy  $U$  is conserved, i.e., there can be no production or loss of energy, as discussed in more detail in Sects. 2.1.5 and 2.2.2. An identical conservation law exists for mass  $M$ . Both of these conservation laws must, however, be combined if the velocity of the described matter approaches the speed of light or during nuclear reactions. In these cases the ratio of  $U$  to  $M$  may change, but in a fixed ratio, given by:  $\Delta U/\Delta M = c^2$ , the Einstein equation, where  $c$  is the speed of light, a constant, and  $\Delta U$  and  $\Delta M$  signify the changes in energy and mass, respectively. For all topics of this book such speeds and nuclear processes are of no concern and one can use the independent laws of energy and mass conservation.

Heat,  $Q$ , and work,  $w$ , are two forms of energy that appear when energy is exchanged between systems. The heat and work are not stored as such in the system, i.e., one cannot allot definite parts of the energy content of a system to heat and work. Their infinitesimal changes depend on the path taken to accomplish the change, and are thus marked by a Greek " $\delta$ " instead of  $d$  or  $\partial$  which represent infinitesimal changes of state. The change  $\delta$  is used to express the overall change in total energy  $dU = \delta Q + \delta w$ . This equation represents the first law of thermodynamics. In words, it can be said that the sum of heat and work exchanged must equal the change in total energy  $U$ , the parts exchanged as heat and work may, however, be much different for different paths. The only condition is that their sum ( $= dU$ ) is the same for all paths.

### 2.1.3 Techniques of Thermal Analysis

Thermal analysis is the analytical technique that establishes the experimental data for the variables of state. Details about the definition of thermal analysis are given in Fig. 2.4. The six most basic thermal analysis techniques which allow the determina-

tion of the variables of state are (1) thermometry, (2) differential thermal analysis, DSC, (3) calorimetry, (4) thermomechanical analysis, TMA, (5) dilatometry, and (6) thermogravimetry, TGA. A determination of heat,  $Q$ , is possible by using (2) or (3), temperature,  $T$ , can be measured with (1), volume,  $V$ , is accessible through (5), and mass,  $M$ , is available from (6). Indirectly, it is possible to derive pressure,  $p$ , as stress in (4), the number of moles,  $n$  from (6) by combining the total mass with the molar mass, which is deduced from the molecular structure, the total energy,  $U$ , by integration of  $Q$  over temperature from 0 K to the temperature in question, and work,  $w$ , for example, as volume or extension work as  $p\Delta V$  or  $f\Delta l$ , where  $f$  is the force and  $\Delta V$  and  $\Delta l$  the volume expansion and extension in length, respectively, measured by using (4) and (5).

The term thermal analysis can be applied to any technique which involves the measurement of a physical quantity while the temperature is changed or maintained in a controlled and measured fashion as expressed in Fig. 2.4. Usually the temperature is, for simplicity, kept constant or increased linearly with time. Recently, it was found advantageous to superimpose a small modulation of the temperature to check for the reversibility of the measurement and to separate the calorimeter response from inadvertent gains or losses that do not occur with this modulation frequency (see Sect. 4.4). The professional organizations of thermal analysis are the International Confederation for Thermal Analysis and Calorimetry, ICTAC, and the North American Thermal Analysis Society, NATAS, described in some detail in Figs. 2.5 and 2.6, respectively. The most common journals dealing with thermal analysis techniques and results are *Thermochimica Acta* and the *Journal of Thermal Analysis and Calorimetry*.

Thermometry, is the simplest technique of thermal analysis. It becomes even more useful when time is recorded simultaneously. Such thermal analyses are called

### Definition of Thermal Analysis

The International Confederation for Thermal Analysis and Calorimetry (ICTAC) defines thermal analysis (TA) as a group of techniques in which a property of the sample is monitored against time or temperature while the temperature of the sample, in a specified atmosphere, is programmed. The program may involve heating or cooling at a fixed (or variable) rate of temperature change, or holding the temperature constant, or any sequence of these. Since hardly any measurement is worth doing if the temperature is not controlled, almost all measurements are some type of thermal analysis. Most important are the techniques measuring heat (calorimetry), volume (dilatometry), length (thermomechanical analysis), and mass (thermogravimetry). The basic theories to be used in thermal analysis are equilibrium and nonequilibrium thermodynamics and kinetics. For a general text see the two volumes of:

E. Turi, Ed., "Thermal Characterization of Polymeric Materials."  
Academic Press, New York, 1997.


Fig. 2.4



heating or cooling curves. Time is measured with a clock, temperature with a thermometer. Details of the thermometry techniques, as well as the cooling and heating curves, are discussed in Sect. 4.1.

The most basic thermal analysis technique is naturally calorimetry, the measurement of heat. The needed thermal analysis instrument is the calorimeter. Instrumentation, technique, theory and applications of calorimetry are treated in

### International Confederation for Thermal Analysis and Calorimetry




In 1968 an International Confederation for Thermal Analysis (ICTA) was organized with the "aim to promote international understanding and co-operation in this branch of science." It grew out of the first International Conference on Thermal Analysis (ICTA), held 1965 in Aberdeen Scotland. At the tenth ICTA held 1992 in Hatfield, England, the name was extended to include "and Calorimetry" in the designation. The next ICTAC is planned for the year 2004. The Society has a large number of affiliated regional and national societies. Its Scientific Commission addresses a series points of interest to thermal analysis. Some examples are: Nomenclature, Standardization, Education, Organizing (congresses), Calorimetry, Kinetics.

Fig. 2.5

### North American Thermal Analysis Society (NATAS)

Website: [www.natasinfo.org](http://www.natasinfo.org)



The North American Thermal Analysis Society, abbreviated NATAS, presents a regular and continuing program devoted to all aspects of the subject of thermal analysis. It provides communications among the members regarding the developments, techniques, equipment, meetings, and activities pertaining to thermal analysis. It provides a supporting affiliation to the International Confederation for Thermal Analysis and Calorimetry, ICTAC.

The society was founded in 1968. Its program includes an annual conference. In 2002 the 30<sup>th</sup> NATAS Conference was held in Pittsburgh, PA. The conference proceedings and a quarterly bulletin, the NATAS Notes, are the publications of the society. A Tutorial at the conference is part of the educational program. An increasing number of local thermal analysis sections are affiliated with NATAS. As an interested student of thermal analysis you should consider becoming a member.

Fig. 2.6

Sects. 4.2–4.4. Intermediate between thermometry and calorimetry is differential thermal analysis, or DTA. In this technique transition temperature information is derived by the qualitative changes in heats of transition or heat capacity. As the instrumentation of DTA advanced, quantitative heat information could be derived from temperature and time measurements. The DTA has in the last 50 years increased so much in precision that its applications overlap with calorimetry, as is shown in the discussion of the different forms of differential scanning calorimetry, DSC (Sects. 4.3 and 4.4).

The basic measurement of length or volume is called dilatometry if it is carried out at constant pressure or stress. Details are given in Sect. 4.1. When measuring stress as well as strain, the technique is called thermomechanical analysis, TMA. This technique is described in Sect. 4.5. Measurements can be made at constant or variable stress or strain, including periodic changes as in dynamic mechanical analysis, DMA, also discussed in Sect. 4.5. Finally, the thermal analysis technique to measure mass as a function of temperature and time is thermogravimetry, TGA. The technique is treated in Sect. 4.6.

Several more complicated thermal analysis techniques are mentioned from time to time, but are not described in detail because they involve additional specialization. Of particular interest are also the many thermal analysis techniques that involve the addition of time and temperature measurements to well-established analysis techniques, such as the various types of microscopy, any kind of scattering or spectroscopy, chromatography, mass spectroscopy, and nuclear magnetic resonance. Coupling of more than one of the mentioned techniques is naturally of additional advantage for a more complete materials-characterization. Of particular importance is the addition of the macroscopic thermal analysis with microscopic analyses leading to information on molecular structure and motion, as emphasized throughout this book. Additional techniques which are recognizable from their names are evolved gas analysis, emanation thermal analysis, thermoacoustimetry, thermobarometry, thermoelectrometry, thermoluminescence, thermomagnetometry, thermooptometry, thermoparticulate analysis, thermophotometry, thermorefractometry, and thermosonometry.

An Advanced Thermal Analysis scheme, the ATHAS scheme has been developed over the years and is described in Sect. 2.3.7. It was created to improve the quantitative aspects of thermal analysis and includes methods of data collection and evaluation (computation). Furthermore, it provides computer courses for distance learning, and a data bank of critically evaluated heat capacities of linear polymers and related compounds, both in downloadable information from the ATHAS website. An abbreviated data bank, of use in connection with the discussions in this book, is collected in Appendix 1.

### 2.1.4 Temperature

Temperature, as the intensive parameter of heat, could not be well understood until the cause of heat became clear (see Sect. 2.1.1). Early thermometers were based on the property of specific materials, such as their length or resistivity as described in Sect. 4.1. Figure 2.7 displays the mercury-in-glass thermometer, the most precise

liquid-in-glass thermometer which has been in use for the last 300 years (see Sect. 4.1.2). Such thermometers are still used extensively. For convenience of measurement, however, secondary thermometers are employed, thermometers which need a calibration at a known temperature.

The development of absolute temperatures began when quantitative experiments were made on the properties of gases. Boyle's law was long known. It states that for a given amount of gas the product of pressure and volume is constant for a given temperature, as summarized in Fig. 2.8. In 1802 Gay-Lussac found that gases expand linearly with temperature when measured with a mercury-in-glass thermometer. With these two observations it became possible to define a temperature that is independent

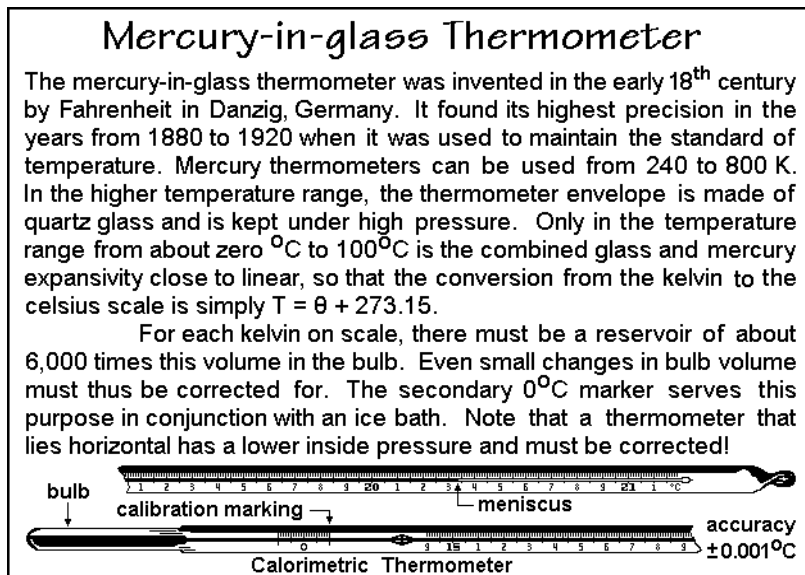


Fig. 2.7

of any particular material since all ideal gases behave identical. Today's value for the expansivity of an ideal gas is  $0.003661$  or  $1/273.15 \text{ K}^{-1}$ . With this knowledge one can define the gas temperature,  $T$ , as indicated in Fig. 2.8.

Even more interesting, one can relate the gas temperature easily to its microscopic description. Figure 2.9 illustrates that the translational kinetic energy of an ideal gas atom is the cause of pressure through the change of momentum of gas atoms on collision with the surface. Coupled with the ideal gas law, the temperature is connected to the average kinetic energy of the gas atoms (see also Sect. 2.1.6).

More fundamental is the thermodynamic temperature scale. It is based on the second law of thermodynamics which is discussed in Sect. 2.2. This temperature scale is defined such, to be identical to the gas temperature in the region where the gas temperature is measurable. The thermodynamic temperature scale is independent not only of any material property, but also of the state of matter. The zero of the thermodynamic temperature fixes the zero of thermal motion. For more details on thermometry, see Sect. 4.1.

### Development of the Gas-temperature Concept

Boyle's Law (1660):

$$pV = \text{constant}$$

$p$  = pressure  
 $V$  = volume  
 $\theta$  = temperature  
 $\alpha$  = expansivity  
 (expansion coefficient)

$$V = V_0(1 + \alpha\theta) \quad \text{Law of Gay-Lussac (1802)}$$

$$V = V_0(1 + \alpha t)$$

$$V = V_0 \frac{273.15 + t}{273.15}$$

$$V = \frac{V_0}{T_0} T \quad T = 273.15 + t$$

$t$  = celsius temperature

$$\alpha = 1/273.15$$

$V_0$  = volume at  $0^\circ\text{C}$

$T$  = kelvin temperature

$$T_0 = 273.15 \text{ K} = 0^\circ\text{C}$$

$n$  = # of moles

$$R = 8.3143 \text{ JK}^{-1}\text{mol}^{-1}$$

$$pV = nRT \quad \text{ideal gas law}$$

Fig. 2.8

### Link of $T$ of Gases to the Molecular Kinetics

translational kinetic energy  
 of a gas atom:

$$\frac{1}{2}mv^2$$

pressure:

$$p = \frac{N}{V} m \overline{v_x^2}$$

$$\overline{v^2} = \overline{v_x^2} + \overline{v_y^2} + \overline{v_z^2}$$

$$\overline{v_x^2} = \frac{1}{3} \overline{v^2}$$

$$pV = nRT = \frac{1}{3} N m \overline{v^2}$$

$p$  = pressure (Pa)

$V$  = volume ( $\text{m}^3$ )

$T$  = temperature (K)

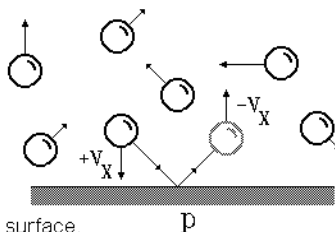
$n$  = # of moles

$$R = 8.3143 \text{ JK}^{-1}\text{mol}^{-1}$$

$N$  = # of molecules

$m$  = mass per molecule

$v$  = molecular velocity



The momentum change at the surface is  $2mv_x$ , producing the pressure, but note that only half the molecules have a  $v$ -component towards the surface.

Fig. 2.9

### 2.1.5 Heat (The First Law of Thermodynamics)

To follow the discussion of the history of the understanding of heat in Sect. 2.1.1 and the identification of heat as a part only of the conservation law of energy in Sect. 2.1.2, it is necessary to establish a description of the total energy  $U$ , and then connect

it to the description of heat. As pointed out above, heat becomes recognizable during energy transfer where  $dU$  is the sum of heat ( $\delta Q$ ) and work ( $\delta w$ ). The conservation of energy  $U$  is the content of the first law of thermodynamics, and the limits to the interconversion of heat and work are set by the second law of thermodynamics, as is discussed in Sect. 2.2.3.

Energy is a function of state (i.e., a state fixed by its variables of state). The change in energy  $dU$  is then the total differential that can be represented as a sum of the partial differentials, as given in Eq. (1) of Fig. 2.10. Each of the coefficients of the partial changes is accessible to measurement.

The description of heat,  $Q$ , in terms of the first law of thermodynamics and the ideal gas law is given by Eq. (2) of Fig. 2.10, written for the situation in which all work is the maximum volume work,  $-pdV$ , where  $p$  and  $V$  are the equilibrium pressure and volume of the system. The negative sign results from the fact that for an increase in volume the system must do some work (lose energy). If other types of work are done, such as electrical or elastic work, additional terms must be added to Eq. (2). Note that the chosen volume work,  $-pdV$ , is determined by the equilibrium pressure and volume, it is thus also fixed by the state of the material, i.e.,  $dQ$  is in this case also a function of state. As soon as the work lost is less, as happens when the opposing pressure on expansion is less than  $p$ , as in a partially free expansion against a piston, the corresponding heat exchanged is also less and must be written as  $\delta Q$ . For the evaluation of  $\delta Q$  under such (nonequilibrium) conditions, information about the actual opposing pressure must be provided.

Combining Eq. (1) with (2) results in Eq. (3). One can see that in this case the change of heat,  $dQ$ , can be expressed in three terms: the first is due to the change in temperature, the second due to the change in volume, and the third due to the change of the number of moles of substance in the system. A full characterization by thermal analysis would, thus, require calorimetry, dilatometry, and also thermogravimetry.

If one can keep the number of moles and the volume constant, terms 2 and 3 are zero because  $dV$  and  $dn$  are zero. The change in heat,  $dQ$ , is then expressed by the first term alone. These conditions of zero  $dV$  and  $dn$  are used so often that  $(\partial U/\partial T)_{V,n}$  has been given a new name, the heat capacity (heat capacity at constant volume and constant number of moles). Speaking somewhat more loosely, one can say that the heat capacity is the amount of heat, necessary to raise the temperature of the system by one kelvin at constant volume. The heat capacity that refers to one gram of the substance is the specific heat capacity. The older term specific heat is to be abandoned since it would refer to the integral quantity  $U$ . This is the type of error in nomenclature that led, for example, to the questionable interpretation of Count Rumford's experiment in Sect. 2.1.1.

There is no difficulty in keeping the number of moles constant during the measurement of heat by thermal analysis, but to keep the volume constant is easy for gases only. Solids and liquids develop enormous pressures when heated at constant volume. To allow easier experimentation, it would, thus, be better to use the variables of pressure,  $p$ , temperature,  $T$ , and number of moles,  $n$ , instead of volume, temperature, and number of moles. With these new variables, Eq. (1) takes on the form given by Eq.(5) in Fig. 2.10. To combine Eq. (5) with Eq. (2), one needs to express volume in the same variables as  $U$ . This is done in Eq. (6). When one now

### Development of the Concept of Heat (The First Law of Thermodynamics)

$$(1) dU = \left(\frac{\partial U}{\partial T}\right)_{V,n} dT + \left(\frac{\partial U}{\partial V}\right)_{T,n} dV + \left(\frac{\partial U}{\partial n}\right)_{T,V} dn$$

$$(2) dQ = dU + p dV$$

$$(3) dQ = \underbrace{\left(\frac{\partial U}{\partial T}\right)_{V,n} dT}_1 + \underbrace{\left[\left(\frac{\partial U}{\partial V}\right)_{T,n} + p\right] dV}_2 + \underbrace{\left(\frac{\partial U}{\partial n}\right)_{T,V} dn}_3$$

$$(4) \text{Definition of Heat Capacity: } C_V = \frac{dQ}{dT} = \left(\frac{\partial U}{\partial T}\right)_{V,n}$$

$$(5) dU = \left(\frac{\partial U}{\partial T}\right)_{p,n} dT + \left(\frac{\partial U}{\partial p}\right)_{T,n} dp + \left(\frac{\partial U}{\partial n}\right)_{T,p} dn$$

$$(6) dV = \left(\frac{\partial V}{\partial T}\right)_{p,n} dT + \left(\frac{\partial V}{\partial p}\right)_{T,n} dp + \left(\frac{\partial V}{\partial n}\right)_{T,p} dn$$

$$(7) dQ = \underbrace{\left[\left(\frac{\partial U}{\partial T}\right)_{p,n} + p\left(\frac{\partial V}{\partial T}\right)_{p,n}\right] dT}_1 + \underbrace{\left[\left(\frac{\partial U}{\partial p}\right)_{T,n} + p\left(\frac{\partial V}{\partial p}\right)_{T,n}\right] dp}_2 + \underbrace{\left[\left(\frac{\partial U}{\partial n}\right)_{T,p} + p\left(\frac{\partial V}{\partial n}\right)_{T,p}\right] dn}_3$$

H = enthalpy

$$(8a) H = U + pV \quad \Leftrightarrow \quad U = H - pV$$

$$(8b) H = U + pV - fl$$

$$(9) dQ = \left[\left(\frac{\partial H}{\partial T}\right)_{p,n} - p\left(\frac{\partial V}{\partial T}\right)_{p,n} + p\left(\frac{\partial V}{\partial T}\right)_{p,n}\right] dT + \dots$$

$$(10) dQ = \left(\frac{\partial H}{\partial T}\right)_{p,n} dT + \dots$$

$$(11) \text{Definition of Heat Capacity: } C_p = \frac{dQ}{dT} = \left(\frac{\partial H}{\partial T}\right)_{p,n}$$

$$(12) C_p - C_V = \left[\left(\frac{\partial U}{\partial V}\right)_{T,n} + p\right] \left(\frac{\partial V}{\partial T}\right)_{p,n}$$

**Fig. 2.10**

inserts Eqs. (5) and (6) into Eq. (2), to come up with an expression for  $dQ$ , one gets to the somewhat unhandy expression of Eq. (7). It consists of six quantities, to be compared to the simpler Eq. (3). Each of the three terms in Eq. (7) is made up of two quantities that must be known for evaluation. With such a complicated correlation, it is not convenient to define and use a heat capacity at constant pressure and composition as expressed in part 1 of Eq. (7).

To resolve this problem, one defines a new function of state out of the old one, the enthalpy,  $H$  [Eq. (8a) of Fig. 2.10]. Enthalpy is the internal energy,  $U$ , plus the product  $pV$ . The term  $pV$  represents the work needed to create a cavity of volume  $V$  to insert the sample in question at constant pressure  $p$ . If  $V$  changes during a process,  $\Delta U$  and  $\Delta H$  are different. Since solids and liquids change only a little in volume with temperature, the difference between  $U$  and  $H$  is usually small and can often be approximated (see Sect. 2.3.2). Liquids consisting of linear macromolecules need a somewhat special treatment since they may be rubbery and can take up large quantities of work on deformation. The state of extension is then of importance for the evaluation of  $U$ . As with volume, it is not experimentally easy to keep the length constant when changing temperature. For macromolecules it is therefore sometimes of value to define  $H$  as given by Eq. (8b), i.e., by subtracting a term for the work needed to extend the sample to length  $l$  against a constant force  $f$ . Equation (8b) will be used for the discussion of rubber elasticity in Chap. 6. Note that the terms  $p dV$  and  $f dl$  have opposite signs. Volume expansion leads to a loss of energy of the sample (work done by the sample), while on drawing a rubbery material, work has to be done on the sample (gain of energy by the sample).

Combining Eq. (8a) with Eq. (7), one can see that the first term in Eq. (7) changes to Eq. (9). The two  $p(\partial V/\partial T)$ -terms cancel, and the first term of Eq. (7) is now as simple as the first term in Eq. (3), so that one can define a second, more convenient heat capacity, this time, a heat capacity at constant pressure (and if necessary at constant extensive force). The two different heat capacities can easily be related to each other by insertion of the definitions in, for example, Eq. (3). The result of the derivation of such relationship is given as Eq. (12), it contains, as expected, the extra term of part I of Eq. (7).

Adding heat to a sample can also have an effect that does not increase the temperature. This heat is called a latent heat. It has its origin in a change of the structure of the sample as in a chemical reaction (heat of reaction) or a phase transition (heat of transition). The measurement of a latent heat is done by direct calorimetry as described in Chap. 4. Note that the latent heat is only the heat of reaction or transition if temperature,  $T$ , is constant; if not, heat capacity effects must be considered separately.

### 2.1.6 The Future of Thermal Analysis [2]

In the past, nature was either studied by experiment and a link to a simple, all-encompassing theory was sought. In the last three decades, however, methods evolved to simulate atomic motion with computers, as described in Sects. 1.3.6–8, and to predict properties by neural network techniques, as summarized in Appendix 4. Both techniques are neither theory nor experiment. The simulations let us *see* the changes in the microscopic structure in slow motion and give a base for the understanding of physical problems which at present are too complicated to fit into a simple theory. The neural network analysis, in turn, looks for a method to use implicit functional relationships between the properties of different substances which are too difficult to ascertain explicitly [3]. The method of Appendix 6, produces a computer program which then correlates the properties.

The molecular dynamics simulation for *thermal analysis* uses the classical equations of motion. Figures 1.43 and 44 illustrate the basic equations which introduce the model polyethylene crystals used for the simulation. A thermal analysis simulation with 192 chains of 50  $\text{CH}_2$ -units each is shown in Fig. 2.11 [2]. A fixed

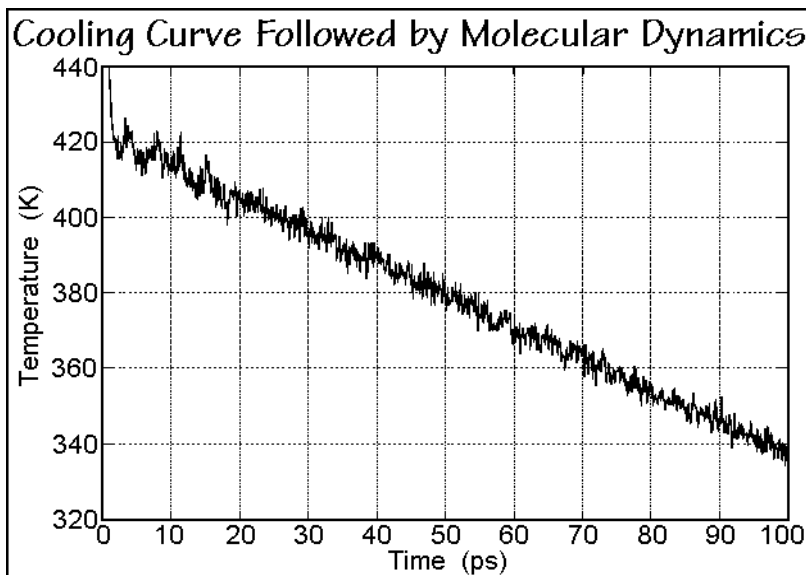


Fig. 2.11

amount of random kinetic energy, as expressed in Fig. 1.44, corresponding to a given temperature, was distributed over the 9600 atoms and followed as the motion develops. A cut-off of the non-bonded interaction at 1.0 nm leads to a continuous loss of energy, so that the crystal *cools*. This loss of energy is sufficiently slow to keep the crystal in thermal equilibrium and simulate a cooling curve in thermal analysis. Next, the total energy,  $U$ , is shown in Fig. 2.12. Both figures show the fluctuations typical for microscopic systems.

Knowing the changes in temperature and energy, permits the calculation of heat capacity as illustrated in Fig. 2.13 by averaging data over 6 ps time intervals. The error bars are strictly due to the averaging procedure. Since the simulation is done using classical mechanics, one finds heat capacities close to the Dulong-Petit limit of  $3R$  ( $\approx 25 \text{ J K}^{-1} \text{ mol}^{-1}$ , see Sect. 2.3). The decrease from this value, seen at low temperature, is difficult to discuss since the heat capacity is known to follow quantum mechanics (see Sect. 2.3). For comparison, the known vibrational heat capacity of  $\text{CH}_2$ - is drawn in Fig. 2.13 along with data for polyethylene.

More important is the increase in heat capacity above  $3R$  which is also seen in the experimental data. Figure 2.14 suggests that this increase is due to the formation of conformational defects (*gauche* conformations in the otherwise all-*trans* crystal, see Sect. 5.3). The simulation is in this case in close agreement with infrared experiments which assess the *gauche* concentration from its changed local vibrations.



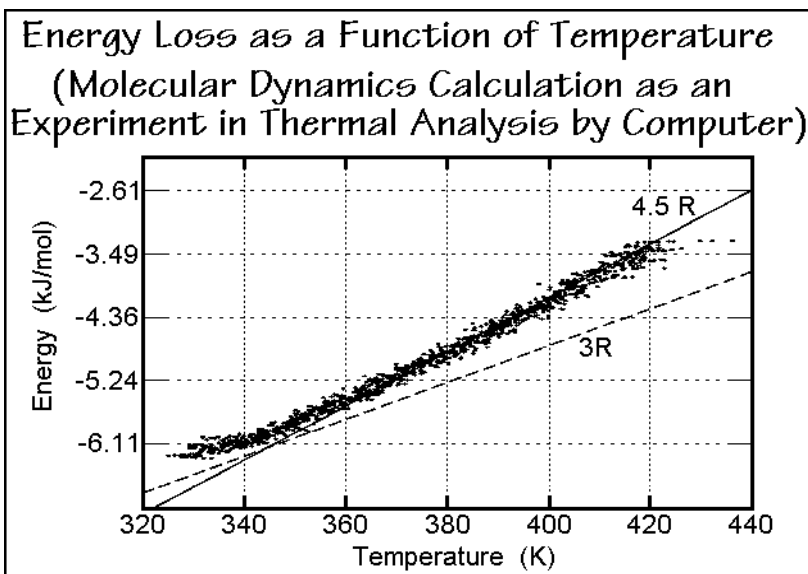


Fig. 2.12

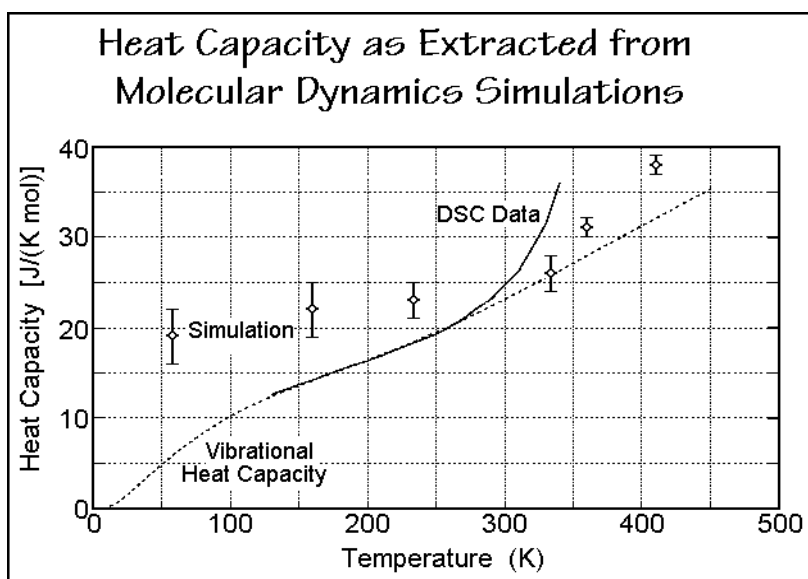


Fig. 2.13

Further, the number of double defects is listed in Fig. 2.15. Such double defects lead in Sect. 5.3 to an understanding of defect crystals and their deformation kinetics. The number of defects refers to the whole crystal. Assuming that the increase in heat capacity from 3 to 4.5 R in Fig. 2.14 is due to defect formation, it is possible to calculate the energy of defect formation as  $44 \text{ kJ mol}^{-1}$ .

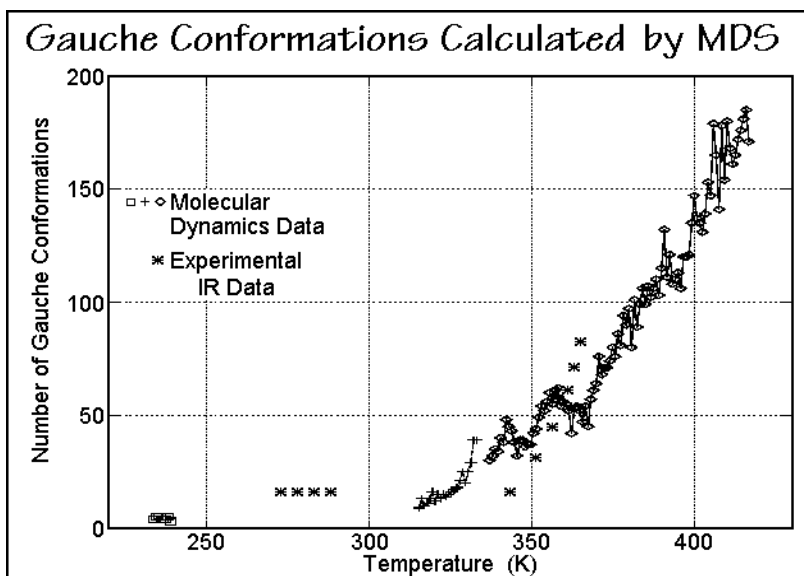


Fig. 2.14

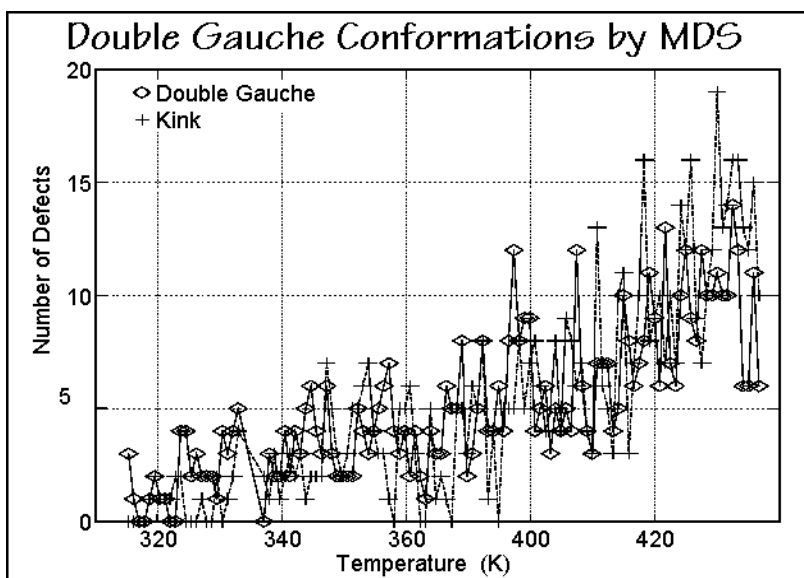


Fig. 2.15

These first thermal analysis simulations open the view how future macroscopic experiments may be directly connected to molecular structure and motion. Much progress is naturally needed to establish proper simulation parameters and to expand the low-temperature analyses to quantum-mechanical calculations.

With neural networks, as described in Appendix 4, the prediction of properties of unmeasured substances on the basis of data of known substances became possible (see introduction to Sect. 3.4). For thermal analysis, it has been possible to extend measured heat capacities at high temperatures into the region of low temperature where measurement is more difficult, as well as predict the theta-temperatures needed for the description of the vibrational heat capacities [4,5].

## 2.2 The Laws of Thermodynamics

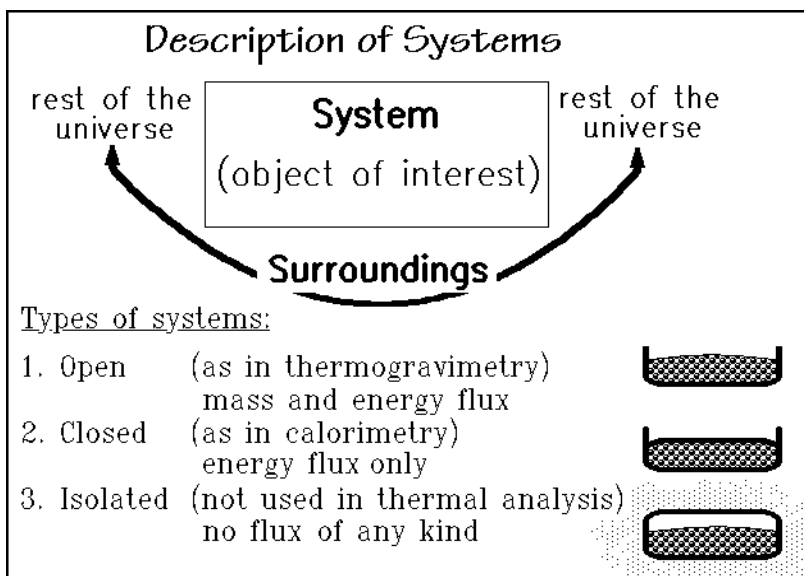
Only a brief introduction to thermodynamics is offered in this Section. It should serve as a refresher of prior knowledge and a summary of the important aspects of the material needed frequently for thermal analysis. It is a small glimpse at what must be securely learned by the professional thermal analyst. For an in-depth study, some of the textbooks listed at the end of the chapter should be used as a continual reference. This does not mean that without a detailed knowledge of thermodynamics one cannot begin to make thermal analysis experiments, but it does mean that for increasing understanding and better interpretation of the results, a progressive study of thermodynamics is necessary.

### 2.2.1 Description of Systems

To start with a thermodynamic description of an object of interest, it is best to define it as a *system* as illustrated schematically in Fig. 2.16. The system must be well delineated from its *surroundings* by real or imaginary boundaries. These surroundings are in the widest sense the rest of the universe. This makes the surroundings ill defined. One simply does not know the size, content, and behavior of the universe. For this reason, it is convenient to work with the system alone and separately assess and account for the effects of the surroundings.

To be sure what ensues within the system, one monitors carefully its state and its boundaries. All transport across the boundaries or creation which increases an extensive quantity within the system is counted as positive (+). All that is lost across the boundaries or within the system is counted as negative (-). This assignment of plus and minus is characteristic from the point of view of the scientists. They consider themselves as the spokespersons for the system. Engineers often have the opposite view since their responsibility is to make use of the products of a system. They will count quantities lost by the system as a gain. This double set of definitions causes confusion, but by now cannot be eliminated and requires care to avoid mistakes.

A term describing the transport across the boundaries is called *flux*, and the creation of any extensive quantity within the system is called *production*. Immediately, one recognizes that the conservation laws of mass and energy, which is discussed in Sect. 2.1.2, forbid their production. A final set of new terms is also shown in Fig. 2.16. It is a classification of the types of systems. The first type is an *open* system, represented by an open container, for example, as used for the sample placement in thermogravimetry. In such a system mass and energy flux may occur

**Fig. 2.16**

across the boundaries of the system to be analyzed. Across the boundaries of the system flows heat from the furnace, and mass can be lost by evaporation, or gained by interaction with the atmosphere. All changes in mass are recorded by a balance, as described in Sect. 4.6.

The second type of system, shown in Fig. 2.16 is the *closed* system. It does not permit exchange of matter, but energy may still be exchanged. A closed vessel can still be heated or cooled from the outside. Calorimetry is an example for a closed system in thermal analysis. The inner surface of the closed sample pan is the boundary of the system across which only heat flows. This heat is being measured, so that a controlled experiment is performed as discussed in Sects. 4.2–4.4.

The third type of system sketched in Fig. 2.16 is an *isolated* system. Neither energy nor matter, may pass across its system boundaries. Obviously, it is challenging to use an isolated system for measurement by thermal analysis.

From this initial discourse into the basics of thermal analysis, it can be learned that thermogravimetry should, for full system description, be coupled with calorimetry, so that both mass and energy changes can be followed. Calorimetry, in turn, is restricted to closed systems, since changes in the amount of matter within the system would distort the analysis. A simple rule for calorimetry is to check the sample weight after completion of each measurement to make sure the system was truly closed.

For a thermodynamic description of a system, there is one important set of additional requirements: The system must be in mechanical and thermal equilibrium. Equilibrium requires that the intensive variables, such as concentration, pressure, and temperature, are constant throughout the system. If the system is not in equilibrium, however, not all is lost. Analysis is still possible, but with a greater effort. One must then recognize that the overall system can be considered as being composed of many

subsystems as illustrated in Fig. 2.80, below. Each subsystem is a chosen portion of the system which in itself is in equilibrium, or at least sufficiently close to equilibrium that the error introduced by assuming it is, is negligible. Although one can now describe the nonequilibrium system in terms of the many subsystems, each subsystem must be analyzed separately for the description of the system as a whole. This is often a difficult task and may even become impossible for a large number of subsystems.

The extensive properties of the overall system that is not in equilibrium, such as volume or energy, are simply the sums of the (almost) equilibrium properties of the subsystems. This simple division of a sample into its subsystems is the type of treatment needed for the description of irreversible processes, as are discussed in Sect. 2.4. Furthermore, there is a natural limit to the subdivision of a system. It is reached when the subsystems are so small that the inhomogeneity caused by the molecular structure becomes of concern. Naturally, for such small subsystems any macroscopic description breaks down, and one must turn to a microscopic description as is used, for example, in the molecular dynamics simulations. For macromolecules, particularly of the flexible class, one frequently finds that a single macromolecule may be part of more than one subsystem. Partially crystallized, linear macromolecules often traverse several crystals and surrounding liquid regions, causing difficulties in the description of the macromolecular properties, as is discussed in Sect. 2.5 when nanophases are described. The phases become interdependent in this case, and care must be taken so that a thermodynamic description based on separate subsystems is still valid.

## 2.2.2 The First Law of Thermodynamics

A system in a given state can be described by a set of independent variables that must be known or established by experiment. The functions of state can then be represented by a mathematical relationship between this set of independent variables. Typical functions of state of importance for thermal analysis, such as total energy,  $U$ , temperature,  $T$ , volume,  $V$ , pressure,  $p$ , number of moles,  $n$ , and mass,  $M$ , are described in Sect. 2.1.2. More details about the first law are also given in Sect. 2.1.5 with Fig. 2.10. For example, the total energy of one mole of an ideal gas is a function of state fixed by only one variable, the temperature,  $T$ , since for an ideal monatomic gas the kinetic energy is equal to the total energy ( $U = 3RT/2$ , as seen in Fig. 2.9). A more general description of  $U$  is given by the differential function  $dU$ , listed as Eq. (1) in Fig. 2.10. For one mole of an ideal gas  $dn$  and  $(\partial U/\partial V)$  are zero, reducing the independent variables to  $T$  [ $(\partial U/\partial T)_{V,n} = 3R/2$  and  $dU = (3/2)RdT$ ]. Expanding this discussion to a general system of one component, three independent variables are expected. For systems of multiple components, additional concentration terms increase the number of variables.

Thermodynamics provides the framework of functions of state. All our experimental experience can be distilled into the three laws of thermodynamics (or four, if one counts the zeroth law, mentioned in the discussion of thermometry in Sect. 4.1). Not so precisely, these three laws have been characterized as follows [6]: In the heat-to-work-conversion game the first law says you cannot win, the best you

can do is break even. The second law says you can break even only at absolute zero of temperature, and the third law, finally, says you can never reach absolute zero. Indeed, one finds that it is difficult to win in thermodynamics. Somewhat more precisely, as discussed in Sect. 2.1.5, the first law is based on the fact that energy is conserved in experiments that concern thermal analysis. One can transfer energy from one system to another, but one cannot create or destroy it. Many thermal analysis experiments are based on the first law alone.

### 2.2.3 The Second Law of Thermodynamics

The second law of thermodynamics restricts the first law:  $dU = \delta Q + \delta w$  (see Sect. 2.1.5). From experience, it is not possible to arbitrarily subdivide  $dU$  among heat,  $\delta Q$ , and work,  $\delta w$ . Through the ages man has tried to make engines which convert more heat into work, either by violating the first law, or by dividing  $\delta Q$  and  $\delta w$  in favor of more work (perpetuum mobiles of the first and second kind, respectively). The frustration with the unattainable perpetuum mobile of the second kind has been gathered in the last century into the formulation of the second law. The formulation by Thomson (Lord Kelvin) is listed in Fig. 2.17.

**The Second Law of Thermodynamics**

"It is impossible to devise an engine which, working in a cycle, shall produce no effect other than the extraction of heat from a reservoir and the performance of an equal amount of work."

**(Thomson Statement)**

Entropy	$\frac{dQ_{\text{reversible}}}{T} = dS$
Helmholtz Free Energy	$dw_{\text{reversible}} = dF$

At constant temperature:

$dU = TdS + dF$

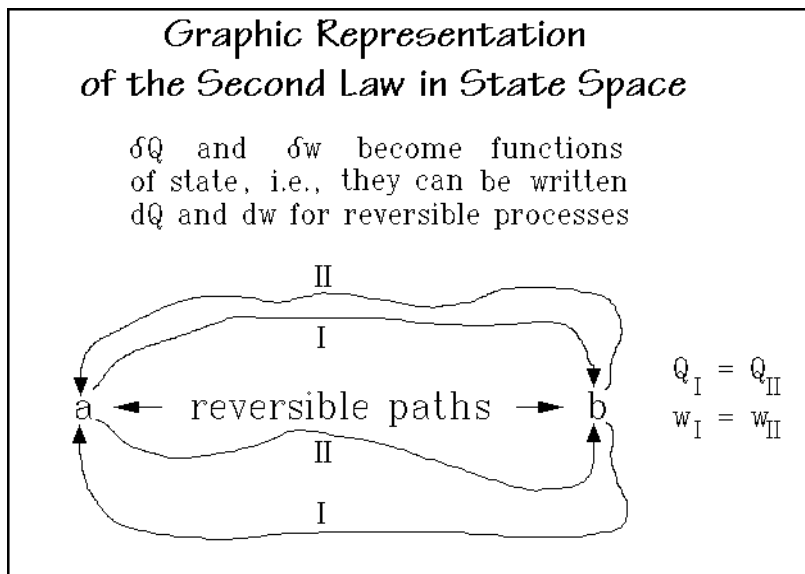
then,  $\delta Q$  and  $\delta w$  become functions of state, i.e., they can be written as  $dQ$  and  $dw$  for reversible processes

$$dS = \left(\frac{\partial S}{\partial T}\right)_{V,n} dT + \left(\frac{\partial S}{\partial V}\right)_{T,n} dV + \left(\frac{\partial S}{\partial n}\right)_{T,V} dn$$

$$dF = \left(\frac{\partial F}{\partial T}\right)_{V,n} dT + \left(\frac{\partial F}{\partial V}\right)_{T,n} dV + \left(\frac{\partial F}{\partial n}\right)_{T,V} dn$$

**Fig. 2.17**

To express the second law mathematically, one defines a new function of state, the entropy,  $S$ . The differential form of  $S$  is written in the figure. The reasoning behind this equation is simple. For all different reversible cycles between given states the heats exchanged must be identical and naturally, the same must be true for the different amounts of work. Figure 2.18 shows a schematic of two reversible cycles between  $a$  and  $b$  in the space of states. It is obvious that  $Q_I$  must be equal to  $Q_{II}$  and  $w_I$  equal to  $w_{II}$ . If this were not so, one could run the two cycles in opposite

**Fig. 2.18**

directions, converting each time  $Q_{II} - Q_I$  heat into  $w_I - w_{II}$  work. This means, one would do what the Thomson statement says cannot be done—namely, have an engine which does nothing but extract heat from a reservoir and perform an equal amount of work. Since experience tells us this cannot be so for reversible processes, heat and work must be functions of state and can be written as total differentials  $dQ$  and  $dw$ , as shown in Fig. 2.17. The ratio  $dQ_{\text{reversible}}/T$  defines the new, second-law function entropy,  $S$ , and  $w_{\text{reversible}}$  is, naturally, also a function of state, called the Helmholtz free energy,  $F$ . The total differentials,  $dS$  and  $dF$ , can be written as for the other functions of state, as also shown in Fig. 2.17. The first law of thermodynamics can, finally, be written as a second-law expression which holds only for reversible processes and at constant temperature, as shown by the boxed equation in the figure. The second law assigns thus limiting values to the amounts of heat and work that can be exchanged in a reversible process. Much of the present form of presentation of thermodynamics was derived towards the end of the last century by Gibbs<sup>1</sup> [7].

The just derived functions are awkward to use for thermal analysis as is the total energy in Fig. 2.10. The introduction of the enthalpy function was the solution. Figure 2.19 shows the use of  $H$  instead of  $U$  in connection with the second-law functions. It leads to the analogous expressions for the free enthalpy,  $G$ , replacing the free energy  $F$  (also called Gibbs free energy or function). The advantage of  $G$  lies, as with  $H$ , in its easy measurement at constant pressure. Since all functions used for the definition of  $H$  are functions of state, one can easily write the proper total differentials. The transformations needed for this change of variables are known as

<sup>1</sup> J. Willard Gibbs, 1839–1903. Theoretical physicist and chemist, introduced the theory of thermodynamics as key element into physical chemistry. He was appointed Professor of Mathematical Physics at Yale University in 1871.

### Derivation of the Second-law Expressions which Allow Easy Determination from Calorimetric Data at Constant Pressure

At constant temperature:

$$dH = TdS + dG$$

$$\text{Enthalpy } H = U + pV$$

$$\text{Free Enthalpy } G = H - TS$$

$$G = F + pV$$

$$dS = \left(\frac{\partial S}{\partial T}\right)_{p,n} dT + \left(\frac{\partial S}{\partial p}\right)_{T,n} dp + \left(\frac{\partial S}{\partial n}\right)_{T,p} dn$$

$$dG = \left(\frac{\partial G}{\partial T}\right)_{p,n} dT + \left(\frac{\partial G}{\partial p}\right)_{T,n} dp + \left(\frac{\partial G}{\partial n}\right)_{T,p} dn$$

From Legendre transformations and Maxwell relations:

$$-S = \left(\frac{\partial G}{\partial T}\right)_p \quad V = \left(\frac{\partial G}{\partial p}\right)_T \quad -S = \left(\frac{\partial F}{\partial T}\right)_V \quad -p = \left(\frac{\partial F}{\partial V}\right)_T$$

$$\frac{C_p}{T} = \left(\frac{\partial S}{\partial T}\right)_p \quad -V\alpha = \left(\frac{\partial S}{\partial p}\right)_T \quad \frac{C_V}{T} = \left(\frac{\partial S}{\partial T}\right)_V \quad \left(\frac{\partial p}{\partial T}\right)_V = \left(\frac{\partial S}{\partial V}\right)_T$$

**Fig. 2.19**

Legendre transformations and given in Appendix 5. Together with the Maxwell relations, the correlations at the bottom of Fig. 2.19 are derived.

To connect the verbal statement of the second law to a mathematical expression, one can use the Thomson engine, shown schematically in Fig. 2.20. The reversible engine is an isothermal, closed system; the system including the two dotted boxes, is isolated since there is no further contact with the surroundings. Heat,  $Q$ , is taken

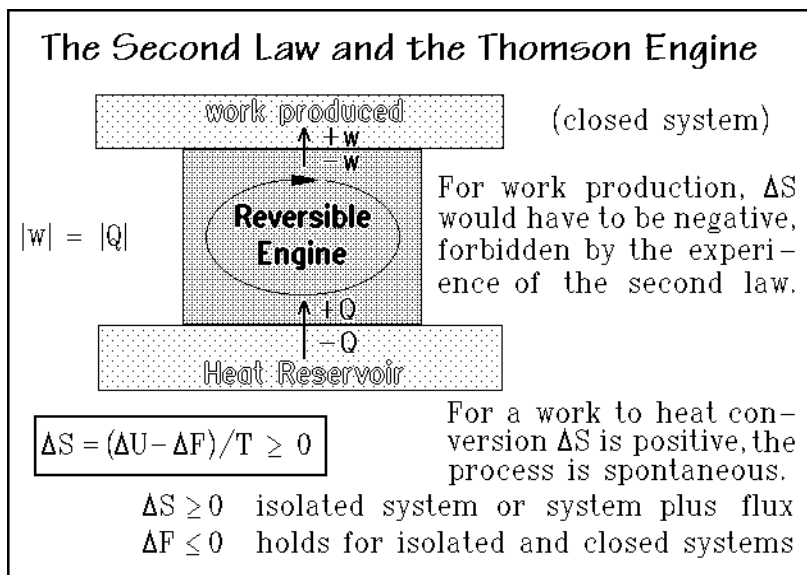


**Fig. 2.20**



from the heat reservoir and converted via the reversible engine into work. The engine regains the initial functions of state after one revolution in either direction. In the forward direction, as shown in the figure, the engine has after one cycle taken-in heat  $Q$  and produced (lost) work  $w$ . Such process is not possible according to the Thomson statement. The reversible engine has, by definition not changed its functions of state, including the entropy. The heat reservoir, however, lost  $Q$  and, thus, the entropy of the isolated system has decreased. The Thomson statement forbids such change ( $\Delta S < 0$ ). The Thomson statement permits, however, the reverse process of conversion of work into heat ( $\Delta S > 0$ ). The expression  $\Delta S \geq 0$  is, thus, also a statement of the second law. A process in an isolated system with a negative entropy change is forbidden (has never been observed). A positive change in  $S$  in an isolated system points to a permitted, irreversible process, and if there is no change in  $S$ , the process is reversible ( $\Delta S = 0$ ).

By use of the boxed equation in Fig. 2.20, one gets a measure of irreversibility of a process in both, isolated *and* closed systems which will form the basis of the irreversible thermodynamics discussed in Sect. 2.4. Since  $\Delta U$  under the given conditions is zero independent of the changes in the surroundings, the following must hold:  $\Delta F < 0$ . If, in turn,  $\Delta F = 0$ , the system is in equilibrium, and an increase in  $F$ ,  $\Delta F > 0$ , is forbidden by the second law.

## 2.2.4 The Third Law of Thermodynamics

The third law is particularly easy to understand if one combines the macroscopic entropy definition with its statistical, microscopic interpretation through the Boltzmann equation<sup>1</sup>  $S = k \ln W$ , as shown in Fig. 2.21. The symbol  $k$  is the Boltzmann constant, the gas constant  $R$  divided by Avogadro's number  $N_A$ , and  $W$  is the thermodynamic probability, representing the number of ways a system can be arranged on a microscopic level. Figure A.5.3 in Appendix 5 gives some additional information on the Boltzmann equation. One can state the third law then, as proposed by Nernst<sup>2</sup>, formulated by Lewis and Randall [8], and reprinted in Fig. 2.21. This statement sets a zero of entropy from which to count. For measurement by calorimetry, one can assume that a perfect crystal at absolute zero has zero entropy, since  $W$  for perfect order must be one, making the logarithm zero. Measuring the heat capacity,  $C$ , lets one determine the absolute entropy of such crystal at any other temperature by adding increments of  $C/T$ , as indicated in the second boxed equation in Fig. 2.21, and derived for heat capacities at constant volume and pressure in Appendix 5, Fig. A.5.4.

---

<sup>1</sup> Ludwig E. Boltzmann, 1844–1906. Physicist whose greatest achievement was in the development of statistical mechanics. After receiving a Ph.D. from the University of Vienna (1866) he held professorships at Vienna, Graz, Munich, and Leipzig. The equation  $S = k \ln W$  is carved above Boltzmann's name on his tombstone in the Zentralfriedhof of Vienna.

<sup>2</sup> Walter H. Nernst, 1864–1941. Professor of Physics in Göttingen and Berlin. He was one of the founders of modern physical chemistry. His formulation of the third law of thermodynamics gained him the 1920 Nobel Prize for Chemistry.

### The Third Law of Thermodynamics

#### Nernst Statement (as given by Lewis and Randall, 1923)

$$S = k \ln W$$

$$S = \int_0^T \frac{C}{T} dT$$

"If the entropy of each element in some crystalline state be taken as zero at the absolute zero of temperature, every substance has a finite, positive entropy; but at the absolute zero of temperature the entropy may become zero, and does so become in case of perfect crystalline substances."

$k$  = Boltzmann constant ( $R/N_A$ )

$W$  = Thermodynamic probability  
(number of ways a system  
can be arranged microscopically)

The third law sets a zero for the entropy so that, experimentally, measurement of heat capacity of a thermodynamically stable crystal can give the absolute entropy at any temperature  $T$ .

**Fig. 2.21**

The three laws of thermodynamics just summarized give the basis for all thermal analysis. Figure 2.22 illustrates the thermodynamic functions as they relate to the heat capacity and will be discussed in Sect. 2.3. Equation (1) is based on the first law alone, Eqs. (2) and (3) need the second law. With the third law, the entropy at zero kelvin is fixed, so that Eq. (2) leads to an absolute value for the entropy. The enthalpy is not known as an absolute value. By convention the enthalpy of all

### The Thermodynamic Functions Needed for the Interpretation of Calorimetric Results

$$(1) \quad H - H_0 = \int_0^T C_p dT \quad \text{enthalpy (or energy } U = \int_0^T C_v dT)$$

$$(2) \quad S = \int_0^T (C_p/T) dT \quad \text{entropy (or } S = \int_0^T (C_v/T) dT)$$

$$(3) \quad G = H - TS \quad \text{free enthalpy or Gibbs energy} \\ \text{(free energy: } F = U - TS)$$

with a completely known heat capacity

(and known heats of transition) the

thermodynamic properties of a material are known

$U, H \rightarrow$  total thermal motion and energy

$S \rightarrow$  disorder       $F, G \rightarrow$  stability

**Fig. 2.22**

elements in equilibrium at 298.15 K (25°C) is set to be zero. By thermochemistry the enthalpy of all compounds can then be determined, as discussed in Sect. 4.2.7.

Figure 2.23 displays the change of enthalpy and free enthalpy of polyethylene from zero kelvin, based on heat capacity data, described in Sect. 2.3.7, and heat of fusion measurements (see, for example, Sect. 4.3.7). There is no jump in free enthalpy at the melting temperature, only a change in the slope. The double arrow marks TS as the difference between H and G as shown in Fig. 2.22, Eq. (3).

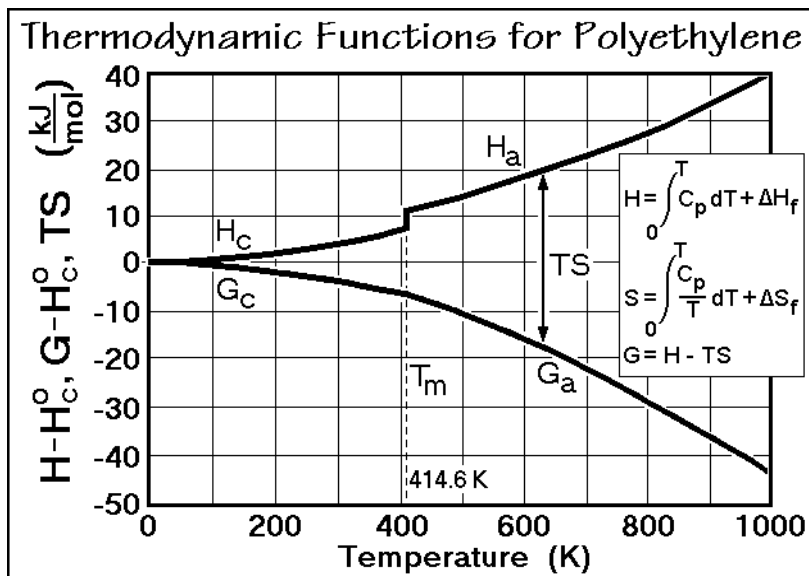


Fig. 2.23

## 2.2.5 Multi-component Systems

Multi-component systems have more than one type of molecule mixed within the system. For the description of the system one needs, thus, one more independent variable for each additional component. Gases always mix, i.e., an unlimited number of multi-component systems can be generated. Liquids still dissolve a variety of gases, other liquids, or even solids, but molecules with weaker interactions than in their respective pure states, may only mix to a limited degree. Common knowledge is that polar and non-polar molecules, like oil and water are immiscible. Although crystals sometimes also dissolve other solids, liquids, or gases, they do so to a lesser degree than the liquid state. Not only must the interaction between the different molecules be favorable for mixing, but the molecular geometry must also be proper to assemble mixed crystals. The mixing equations discussed next are for ideal solutions, i.e., systems that have colligative properties (see Fig. 1.52). Solutions that deviate slightly from the ideal case are called *regular solutions*. They have a small heat of mixing, but can still be approximated by an ideal entropy of mixing. *Real solutions* have a substantial heat of mixing and a nonideal entropy of mixing.

Macromolecules behave always as real solutions because of the size dependence of the mixing parameters which is approximated by the Flory-Huggins equation, described in Chap. 7. A correction for the mixing of small molecules in the presence of ions is given by the Debye-Hückel theory, not discussed in this book.

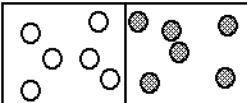
The ideal mixing process can be visualized by the expansion of two pure gaseous components of volumes,  $V_1$  and  $V_2$ , at an initial pressure  $p$  and temperature  $T$ , into the volume,  $V_t$ . Figure 2.24 represents the process schematically. Before mixing, two separate ideal gas equations describe the system (independent of the chemical nature of the molecules  $pV_1 = n_1 RT$  and  $pV_2 = n_2 RT$ , see Fig. 2.23). The pressures one would find if components 1 and 2 alone would occupy volume  $V_t$  are called the partial pressures  $p_1$  and  $p_2$ , respectively, so that one can write the overall gas equation as  $pV_t = n_1 RT = (p_1 + p_2) RT = (n_1 + n_2)RT$ . For ideal gases the mixing process occurs without change in internal energy as long as the number of moles of molecules  $n$  and the temperature  $T$  stay constant ( $dU = 0$ ). The change in enthalpy is also zero since  $dH = d[U + (pV = nRT)] = 0$ , so that the change in entropy  $dS = -dG/T$ . Under these conditions only volume work can be done, which leads to  $dG = pdV$  and:

$$(\partial S/\partial V)_{T,n} = p/T = nR/V,$$

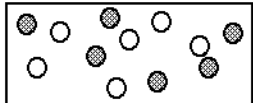
(see Fig. 2.19). Figure 2.24 illustrates the results on expansion of the given initial volumes  $V_1$  and  $V_2$  to  $V_t$ , and lists the final mixing equations that describe the change on mixing [Eqs. (1) and (2)]. The concentrations are expressed in terms of the mole fractions  $x_1$  and  $x_2$  which derive by insertion of the appropriate expressions for  $n_1$  and  $n_2$ . Since mole fractions are always smaller than one, the entropy on mixing is always positive and  $\Delta G$ , negative, i.e., the mixing process must always be spontaneous and can only be reversed by a negative interaction term  $\Delta H$ , not present in ideal gases.

**Ideal Multicomponent Gaseous System**

Mixing of Two Gases ( $\Delta H = 0$ ):



→



solvent:  $x_1 = n_1/(n_1 + n_2)$     solute:  $x_2 = n_2/(n_1 + n_2)$

Expansion of pure component 2 into the total volume  $V_t = V_1 + V_2$ :

$pV = nRT$      $\Delta S_2 = S_{V_{tot}} - S_{V_2}$

$(\partial S/\partial V)_{T,n} = nR/V$   
 $\Delta S_2 = n_2 R \ln(V_t/V_2)$

(1)  $\Delta S = -n_1 R \ln x_1 - n_2 R \ln x_2$

(2)  $\Delta G = RT(n_1 \ln x_1 + n_2 \ln x_2)$

Analogous equations can be written for component 1

**Fig. 2.24**

Because of the simplicity of the functions of state of the ideal gas, they serve well as models for other mixing experiments. Dilute solutions, for example, can be modeled as ideal gases with the empty space between the gas atoms being filled with a second component, the solvent. In this case, the ideal condition can be maintained as long as the overall interaction between solvent and solute is negligible. Deviations from the ideal mixing are treated by evaluation of the partial molar quantities, as illustrated on the example of volume,  $V$ , in Fig. 2.25. The first row of equations gives the definitions of the partial molar volumes  $V_A$  and  $V_B$  and shows the addition of their differentials. For ideal solutions the partial molar volumes are equal to the volumes in the pure states ( $V_A^\circ$  and  $V_B^\circ$ ). The first equation in the second row shows the obvious integration of  $dV$  to  $V$  without change in concentration. The total differential of  $V$ , derived after this integration can be compared, in turn, with the starting equation for  $dV$  in the first row. Both can only hold simultaneously if the boxed equation, the Gibbs-Duhem equation, is true. After measurement of  $V$  over the full concentration range, the construction and equations in Fig. 2.25 permits the full evaluation of the volume of the system. In the shown case there is an expansion on mixing, indicative of repulsion between the two types of molecules. Similar constructions can be made for other partial molar quantities of interest. More details, especially for solutions of polymers, are given in Sect. 7.1.

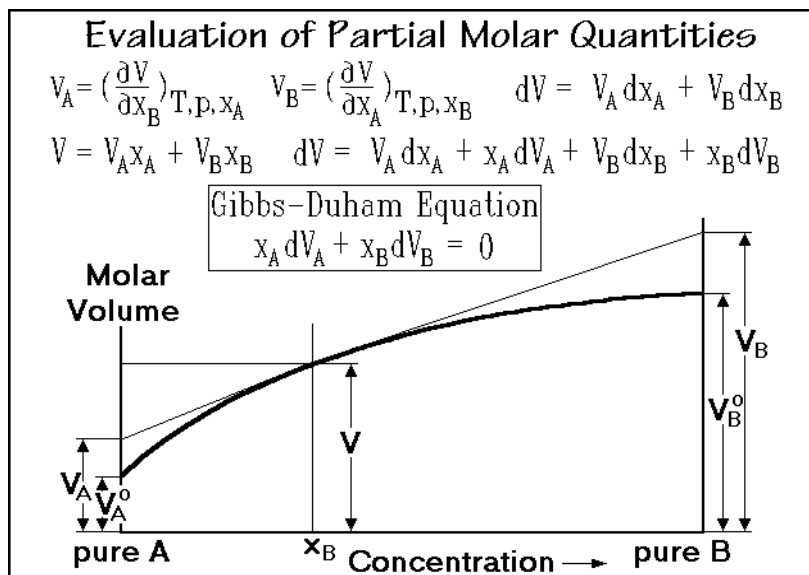


Fig. 2.25

### 2.2.6 Multi-phase Systems

Phases are described in Sect. 2.5. An equilibrium between phases involves the exchange of molecules (components) of different chemical nature or physical state. Two components of small molecules and two phases are treated in this section. Single and multi-phase systems of macromolecules are treated in Chaps. 6 and 7.

The description of phase equilibria makes use of the partial molar free enthalpies,  $\mu$ , called also chemical potentials. For one-component phase equilibria the same formalism is used, just that the enthalpies,  $G$ , can be used directly. The first case treated is the freezing point lowering of component 1 (solvent) due to the presence of a component 2 (solute). It is assumed that there is complete solubility in the liquid phase (solution, s) and no solubility in the crystalline phase (c). The chemical potentials of the solvent in solution, crystals, and in the pure liquid (o) are shown in Fig. 2.26. At equilibrium,  $\mu$  of component 1 must be equal in both phases as shown by Eq. (1). A similar set of equations can be written for component 2. By subtracting  $\mu_1^o$  from both sides of Eq. (1), the more easily discussed mixing (left-hand side, LHS) and crystallization (right-hand side, RHS) are equated as Eq. (2).

The mixing expression for the LHS of Eq. (2) is derived from Eq. (2) of Fig. 2.24. For dilute solutions  $\ln x_1$  is close to zero ( $x_1 \approx 1$ ), so that the series representing the logarithm of  $x_1$  in terms of  $x_2$  ( $x_1 = 1 - x_2$ ) can be represented by the first term alone, giving a very simple LHS of Eq. (2) written in Fig. 2.26. At larger concentrations, the full logarithm must be used.

<b>Phase Equilibrium of a Low Molar Mass Component</b>		
(1) $\mu_1^s = \mu_1^c$		
(2) $\mu_1^s - \mu_1^o = \mu_1^c - \mu_1^o$		$\mu_1^s = \left(\frac{\partial G^s}{\partial n_1}\right)_{T,p,n_2}$
LHS: change on mixing	RHS: change on crystallization	$\mu_1^c = G_1^c$
		$\mu_1^o = \text{pure solvent}$ ( $= G_1^o$ )
$(\partial G / \partial n_1)_{n_2} = RT \ln x_1$ $= RT \ln(1 - x_2)$		
$[\ln(1 - x_2) = -x_2 - x_2^2/2 - x_2^3/3 \dots]$ for small $x_2$ : $-x_2$		
LHS = $-RTx_2$		
RHS = $-\Delta H_f \Delta T_m / T_m^o$	$-\Delta G_f = -(\Delta H_f - T_m \Delta S_f)$ $(\Delta S_f = \Delta H_f / T_m^o)$	
$x_2 = \frac{\Delta H_f \Delta T_m}{RT_m^o}$	$-\Delta G_f = -\Delta H_f [1 - (T_m / T_m^o)]$	

**Fig. 2.26**

The RHS of Eq. (2) of Fig. 2.26 applies to the crystallization of pure 1 (one component, two-phase system). It is written as the reverse of fusion (f), which accounts for the minus sign in the expression for the RHS. Assuming that the change of entropy and heat of fusion with temperature is negligible over the range of freezing point lowering, a simple expression for the RHS is derived. The final equation linking  $x_2$  to the entropy of fusion of the solvent ( $\Delta H_f / T_m^o$ ) and the lowering of the melting temperature,  $\Delta T$ , is obtained by equating LHS with RHS.

Experimental use of the melting-point lowering can be made to determine molar concentrations, of importance for the molar-mass determinations (see Sect. 1.4), and

the heats of fusion (diluent method, see Sect. 7.1.4). Figure 2.27 illustrates the use of the freezing point lowering for the description of the left side of a eutectic phase diagram. Analogous expressions can be derived for the right side by replacing 1 with 2 in the equations. The two curved boundaries of the area of the melt are the liquidus lines. At the intersection of the two lines one finds the eutectic temperature where both crystals have the same freezing point lowering.

A similar expression as for the freezing point lowering can be derived for the boiling point elevation. The second phase is now the pure vapor phase ( $\mu_1^v$ ). This case of a pure vapor in contact with a liquid solution occurs for two major groups of components, macromolecules and ions. Polymeric components have negligible vapor pressures due to the large size of the molecule. Ions without solvent are rigid macromolecules (see Sect. 1.1), and also have negligible vapor pressure. In solution they are solvated to large aggregates, still without significant vapor pressure. On subtraction of  $\mu_1^o$ , the LHS of Eq. (2) of Fig. 2.26 is again the change on dissolution, while the RHS represents the evaporation of the pure solvent. Since the heat of crystallization is exothermic and the heat of evaporation ( $\Delta H_v$ ) endothermic, the changes in the phase transition temperatures are going in opposite directions. The experimental use of boiling point elevation for the molar mass determination of macromolecules is discussed in Sect. 1.4, along with other methods making use of colligative properties (Fig. 1.52).

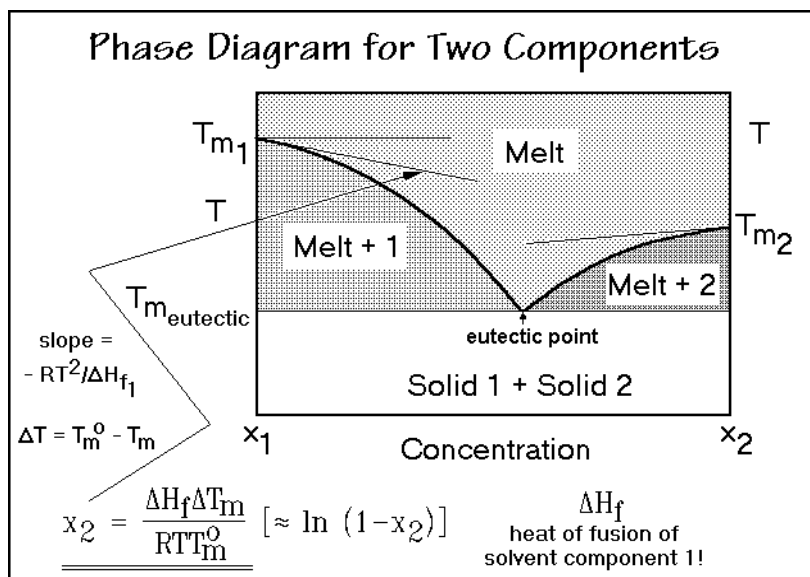


**Fig. 2.27**

A third case arises when a mixed gas is in equilibrium with immiscible pure liquid or solid phases. The vapor pressure of each condensed phase is then unaffected by the existence of the mixed vapor phase. Each pure condensed phase communicates only with its own partial pressure. This results in a total pressure that is the sum of the two vapor pressures, as illustrated above for ideal gas mixing:  $p_1 = n_1 RT/V$ , and

$p_2 = n_2RT/V_1$ . The effect is a higher total pressure above the two pure phases than without the second component. This effect is made use of, for example, in steam distillations. Boiling water carries, on distillation, the low vapor-pressure material to the condensate in the molar ratio of the vapor pressures of the two condensed phases.

## 2.3 Heat Capacity

Heat capacity is the basic quantity derived from calorimetric measurements, as presented in Sects. 4.2–4.4, and is used in the description of thermodynamics, as shown in Sects. 2.1 and 2.2. For a full description of a system, heat capacity information is combined with heats of transition, reaction, etc. In the present section the measurement and the theory of heat capacity are discussed, leading to a description of the Advanced THERMAL Analysis System, ATHAS. This system was developed over the last 30 years to increase the precision of thermal analysis of linear macromolecules.

### 2.3.1 Measurement of Heat Capacity

In a measurement of heat capacity, one determines the heat,  $dQ$ , required to increase the temperature of the sample by  $dT$ , as is shown in Fig. 2.28. Classically this is done with an adiabatic calorimeter (see Sect. 4.2) which allows no heat transfer to the surroundings of the calorimeter (Gk. ἀδιάβατος, not able to go through). Even today, adiabatic calorimetry is the most precise method of measurement in the temperature range from 10 to 150 K. In an adiabatic calorimeter [9] (see Fig. 4.33),

#### Equations to Measure Heat Capacities

Definition of Heat Capacity:  $C_p = \frac{dQ}{dT} = \left(\frac{\partial H}{\partial T}\right)_{p,n}$   
(see Sect. 2.1)

from adiabatic calorimetry (see Sect. 4.2):

$$c_p = \frac{\Delta Q_{\text{corrected}} - C' \Delta T_{\text{corrected}}}{m \Delta T_{\text{corrected}}}$$

from DSC (see Sect. 4.3):

$$mc_p = K \frac{\Delta T}{q} + (K \frac{\Delta T}{q} + C_p') \left( \frac{d\Delta T/dT_r}{1 - d\Delta T/dT_r} \right) \approx K \frac{\Delta T}{q}$$

from TMDSC (see Sect. 4.4):  $mc_p = \frac{A_\Delta}{A} \sqrt{\left(\frac{K}{\omega}\right)^2 + C_p'^2}$

Fig. 2.28

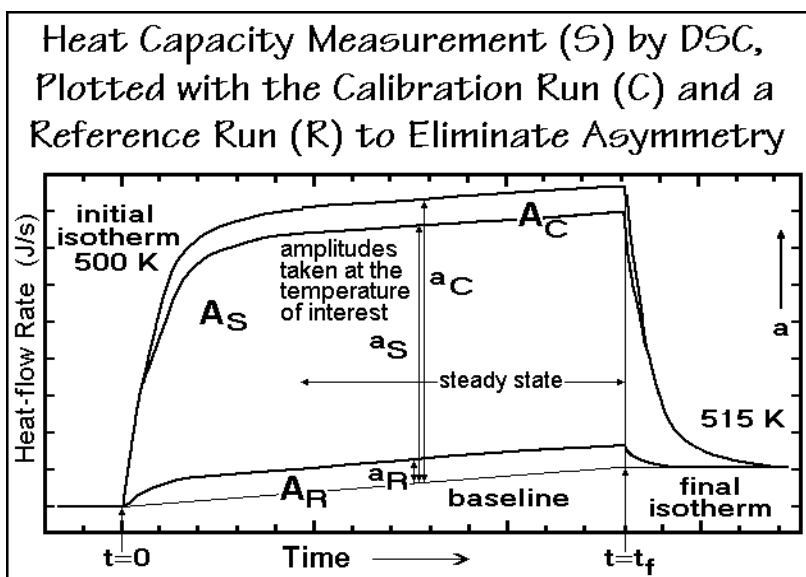


an attempt is made to follow step-wise temperature changes of an internally heated calorimeter in well-controlled, adiabatic surroundings. Due to heat loss caused by deviations from the adiabatic condition, corrections must be made to the heat added to the calorimeter,  $\Delta Q$ . Similarly, the measured temperature increase,  $\Delta T$ , must be corrected for the temperature drifts of the calorimeter. The calculations are summarized in Fig. 2.28 (see also Fig. 4.34). The specific heat capacity, written as  $c_p$  (in  $\text{J K}^{-1} \text{g}^{-1}$ ), is calculated by subtracting the heat capacity of the empty calorimeter, its *water value*  $C'$  (or, in Fig. 4.34,  $C^\circ$ ), and dividing by the mass of the sample,  $m$  (or  $W_{\text{unknown}}$ ). The evaluation of these corrections is time consuming, but at the heart of good calorimetry.

Modern control and technology of measurement permitted to miniaturize the calorimeter some 30–40 years ago and to measure down to milligram quantities in a differential scanning mode (DSC, see Sect. 4.3 [10]). In a symmetrical setup, the difference in extraneous heat flux can be minimized and the remaining imbalance corrected for. Under the usual condition where sample and reference calorimeters (often aluminum pans) are identical, and the reference pan is empty, one finds the heat capacity as shown in Fig. 2.28, where  $K$  is the Newton's-law constant;  $\Delta T$ , the temperature difference between reference and sample ( $T_r - T_s$ ), and  $q$ , the constant heating rate. The left equation is exact, the right approximation neglects the difference in heating-rate between reference and sample due to a slowly changing heat capacity of the sample. This limits the precision to  $\pm 3\%$ .

In the more recently developed temperature-modulated DSC (TMDSC, see Sect. 4.4 [11]), a sinusoidal or other periodic change in temperature is superimposed on the underlying heating rate. The heat capacity is now given by the bottom equation in Fig. 2.28, where  $A_\Delta$  and  $A$  are the maximum amplitudes of the modulation found in temperature difference and sample temperature, respectively, and  $\omega$  is the modulation frequency  $2\pi/\text{period}$ . The equation represents the reversing heat capacity. In case there is a difference between the result of the last two equations, this is called a nonreversing heat capacity, and is connected to processes within the sample which are slower than the addition of the heat or which cannot be modulated at all (such as irreversible crystallization and reorganization, or heat losses).

Figure 2.29 illustrates a measurement by DSC. Central is the evaluation of the calibration constant at every temperature. Three consecutive runs must be made. The sample run (S) is made with the unknown, enclosed in the customary aluminum pan and an empty, closely-matched reference pan. The width of the temperature interval is dictated by the change of the isothermal baseline with temperature. In the chosen example, the initial isotherm is at 500 K and the final, at 515 K. Typical modern instrumentation may permit intervals up to 100 K. Measurements can also be made on cooling instead of heating. When measurements are made on cooling, all calibrations must necessarily also be made on cooling, using liquid-crystal transitions which do not supercool on ordering. As the heating is started, the DSC recording changes from the initial isotherm at 500 K in an exponential fashion to the steady-state amplitude on heating at constant rate  $q$ . After completion of the run, at  $t_r$ , there is an exponential approach to the final isotherm at 515 K. The area between baseline and the DSC run is the integral over the amplitude, indicated as  $A_s$  in Fig. 2.30. A reference run (R) with a matched, second, empty aluminum pan instead of the sample

**Fig. 2.29**

yields the small correction area  $A_R$  which may be positive or negative and corrects for asymmetry. This correction can also be done online, as discussed in Appendix 11, below. Finally, a calibration run (C) with sapphire ( $Al_2O_3$ ) completes the experiment (area  $A_C$ ). The difference between the two areas,  $A_S - A_R$ , is a measure of the uncalibrated integral of the sample heat capacity, as indicated in Eq. (1). For a small temperature interval and constant heating rate  $q$ , it is sufficient to define an average

### Data Evaluation from the Runs in Fig. 2.29

- |  |                     |                                       |
|--|---------------------|---------------------------------------|
| 1. Sample run  | $A_S = \int a_S dt$ | (at constant<br>heating<br>rate $q$ ) |
| 2. Reference run   | $A_R = \int a_R dt$ |                                       |
| 3. Calibration run<br>[frequently C = Al <sub>2</sub> O <sub>3</sub> ] | $A_C = \int a_C dt$ |                                       |

$$(1) \int_0^{t_f} \dot{C}_p(S) q dt = \bar{C}_p(S) \Delta T = K[A_S - A_R]/q$$

$$(2) \int_0^{t_f} C_p(C) q dt = \overline{C_p}(C) \Delta T = K[A_C - A_R]/q$$

$$(3) \quad K'/q = \frac{W(C)\overline{c_p}(C)\Delta T}{A_C - A_B}$$

$$(4) \quad C_p(S) = K[a_S(T) - a_R(T)]/q$$

$$(5) \quad K/q = \frac{W(C)c_p(C)\Delta T}{a_C(T) - a_R(T)}$$

With the expression of Eq. (5) for  $K/q$ , Eq. (4) can be solved for the heat capacity of the sample,  $C_p(S)$  at temperature  $T$ .

**Fig. 2.30**

heat capacity to simplify the integral, as indicated. The uncalibrated heat capacity of  $\text{Al}_2\text{O}_3$  is similarly evaluated, as shown by Eq. (2). The proportionality constant,  $K'$ , can now be evaluated between Eqs. (1) and (2), as shown by Eq. (3). The specific heat capacity of sapphire,  $c_p(\text{Al}_2\text{O}_3)$ , is well known, and the sapphire mass used,  $W(C) = W(\text{Al}_2\text{O}_3)$ , must be determined with sufficient precision ( $\pm 0.1\%$ ) so as not to affect the accuracy of the measurement ( $\pm 1\%$  or better).

The initial and final exponential changes to steady state are sufficiently similar in area so that one may compute the heat capacities directly from the amplitudes  $a_s(T)$ ,  $a_R(T)$ , and  $a_C(T)$  at the chosen temperatures in the region of steady state. Equations (4) and (5) of Fig. 2.30 are outlines of the computations.

In a typical DSC a sample may weigh 20 mg and show a heat capacity of about  $50 \text{ mJ K}^{-1}$ . For a heating rate of  $10 \text{ K min}^{-1}$  there would be, under steady-state conditions, a lag between the measured temperature and the actual temperature of about 0.4 K. This is an acceptable value for heat capacity that changes slowly with temperature. If necessary, lag corrections can be included in the computation. The typical instrument precision is reported to be  $\pm 0.04 \text{ mJ s}^{-1}$  at 700 K. Heat capacities should thus be measurable to a precision of  $\pm 0.25\%$ , a very respectable value for such a fast-measuring instrument. For TMDSC the sample mass and modulation parameters must be chosen, so that the whole sample is modulated with the same amplitude (check with varying parameters).

### 2.3.2 Thermodynamic Theory

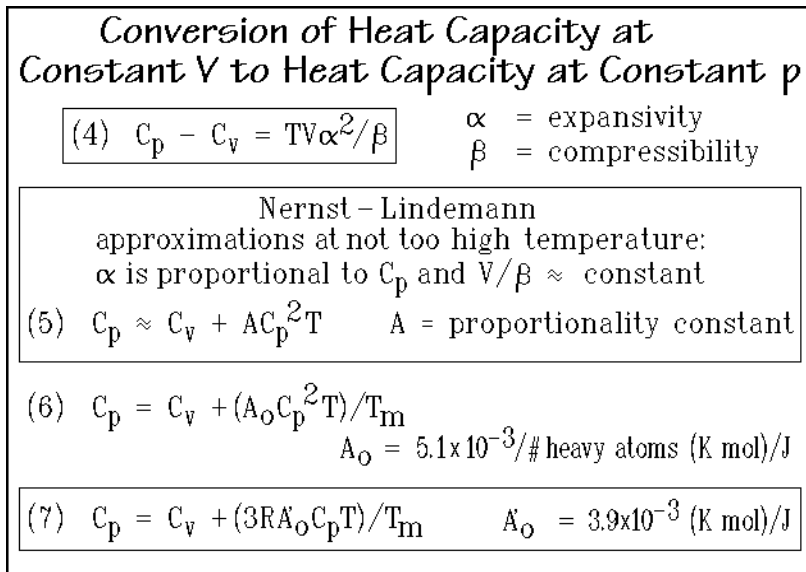
The importance of heat capacity becomes obvious when one looks at Eqs. (1–3) of Fig. 2.22. The quantities of enthalpy or energy, entropy, and Gibbs energy or free energy, are all connected to the heat capacity. Naturally, in cases where there are transitions in the temperature range of interest, the latent heats and entropies of these transitions need to be added to the integration, as shown in Fig. 2.23. The enthalpy or energy of a system can be linked to the total amount of thermal motion and interaction on a microscopic scale. The entropy of a system can be connected to the degree of order, and finally, the Gibbs energy (free enthalpy) or the Helmholtz free energy is related to the stability of the chosen system.

All experimental techniques lead to heat capacities at constant pressure,  $C_p$ . In terms of microscopic quantities, however, heat capacity at constant volume,  $C_v$ , is the more accessible quantity. The relationship between  $C_p$  and  $C_v$  is listed as Eq. (4) in Fig. 2.31 in continuation of Fig. 2.22. It involves several correlations, easily (but tediously) derivable from the first and second law expressions as will be shown next. To simplify the derivation, one starts assuming constant composition for the to be derived equation (no latent heats,  $dn = 0$ ). From the first law, as given by Eq. (3) of Fig. 2.10, one differentiates  $dQ$  at constant pressure. Since  $(\partial Q/\partial T)_p = C_p$  and  $(\partial U/\partial T)_v = C_v$ , this differentiation gives Eq. (12) of Fig. 2.10:

$$C_p = C_v + [(\partial U/\partial V)_T + p](\partial V/\partial T)_p.$$

Next, from the second law given in Fig. 2.17, one can write:

$$(\partial U/\partial V)_T = [(\partial(F + TS)/\partial V)_T = -p + T(\partial p/\partial T)_V].$$

**Fig. 2.31**

The expressions  $(\partial F/\partial V)_T = -p$  and  $(\partial S/\partial V)_T = (\partial p/\partial T)_V$  are derived in Fig. A.5.2. Combining the two equations via the common  $(\partial U/\partial V)_T$  terms, gives:

$$C_p = C_v + T(\partial V/\partial T)_p (\partial p/\partial T)_V .$$

The final step involves coefficient comparison for  $dT$  between the two expressions for  $dp$  that can be derived from the differential  $dV = (\partial V/\partial T)_p dT + (\partial V/\partial p)_T dp$  [Eq. (6) of Fig. 2.10] and  $dp = (\partial p/\partial T)_V dT + (\partial p/\partial V)_T dV$ . The comparison yields:

$$(\partial p/\partial T)_V = - [(\partial(V)/\partial T)_p]/(\partial V/\partial p)_T .$$

Insertion of the expressions for the expansivity,  $\alpha = (\partial V/\partial T)_p/V$ , discussed in Sect. 4.1, and the compressibility, which is  $\beta = -(\partial V/\partial p)_T/V$ , as discussed in Sect. 4.5, leads first to  $(\partial p/\partial T)_V = \alpha/\beta$  and then to the sought-after relationship of Eq. (4) of Fig. 2.31 which was to be proven. To establish  $C_p - C_v$ , one needs, thus, both the expansivity and the compressibility for all temperatures of interest.

Frequently, however, experimental data for expansivity and compressibility are not available over the whole temperature range, so that one knows  $C_p$ , but has difficulties evaluating  $C_v$ . At moderate temperatures, as usually encountered below the melting point of linear macromolecules, one can assume that the expansivity is proportional to  $C_p$ . In addition, it was found that volume divided by compressibility does not change much with temperature. With these two empirical observations one can derive the approximate Eq. (5) of Fig. 2.31, where  $A$  is a constant that needs to be evaluated only at one temperature. If even this is not available, there exists the observation made by Nernst and Lindemann for elements and ionic solids that Eq. (5) holds with a universal constant  $A_0$  ( $= 5.1 \times 10^{-3}$ , in  $\text{K mol J}^{-1}$ ;  $T_m$  = melting temperature). In the survey of Nernst and Lindemann  $A_0$  varied from  $2.4$  to  $9.6 \times 10^{-3} \text{ K mol J}^{-1}$ , showing that Eq. (6) is only a rough approximation and should be avoided,

if possible [12]. Furthermore, one must be careful to use the proper units,  $A_0$  refers to one mole of atoms or ions in the sample, so  $C_p$  and  $C_v$  must be expressed for the same reference amount. But, the difference between  $C_p$  and  $C_v$  remains small up the melting temperature, as seen in Fig. 2.51, below, for the polyethylene example. A rather large error in Eq. (6), thus, has only a small effect on  $C_v$ . For polyethylene, the difference becomes even negligible below about 250 K.

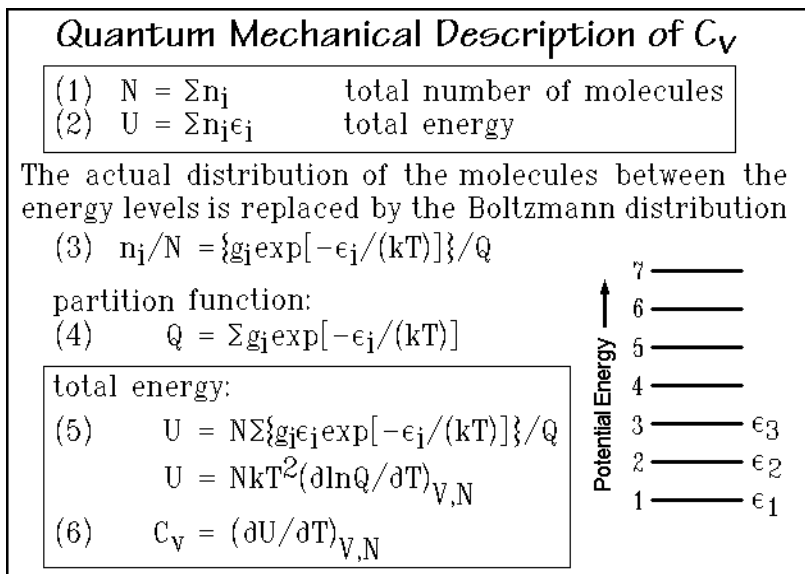
For organic molecules and macromolecules, the equivalent of the atoms or ions must be found in order to use Eq. (6). Since the equation is based on the assumption of classically excited vibrators, which requires three vibrators per atom (degrees of freedom), one can apply the same equation to more complicated molecules when one divides  $A_0$  by the number of atoms per molecule or repeating unit. Since very light atoms have, however, very high vibration frequencies, as will be discussed below, they have to be omitted in the counting at low temperature. For polypropylene, for example, with a repeating unit  $[\text{CH}_2-\text{CH}(\text{CH}_3)-]$ , there are only three vibrating units of heavy atoms and  $A_0$  is  $5.1 \times 10^{-3} / 3 = 1.7 \times 10^{-3} \text{ K mol J}^{-1}$ . Equation (7) of Fig. 2.31 offers a further simplification. It has been derived from Eq. (6) by estimating the number of excited vibrators from the heat capacity itself, assuming that each fully excited atom contributes  $3R$  to the heat capacity as suggested by the Dulong–Petit rule [13]. The new  $A_0'$  for Eq. (7) is  $3.9 \times 10^{-3} \text{ K mol J}^{-1}$  and allows a good estimate of  $C_v$  even if no expansivity and compressibility information is available [14].

### 2.3.3 Quantum Mechanical Description

In this section, the link of  $C_v$  to the microscopic properties will be derived. The system in question must, of necessity, be treated as a quantum-mechanical system. Every microscopic system is assumed to be able to take on only certain states as summarized in Fig. 2.32. The labels attached to these different states are 1, 2, 3, ... and their potential energies are  $\epsilon_1, \epsilon_2, \epsilon_3 \dots$ , respectively. Any given energy may, however, refer to more than one state so that the number of states that correspond to the same energy  $\epsilon_1$  is designated  $g_1$  and is called the degeneracy of the energy level. Similarly, degeneracy  $g_2$  refers to  $\epsilon_2$ , and  $g_3$  to  $\epsilon_3$ . It is then assumed that many such microscopic systems make up the overall matter, the macroscopic system. At least initially, one can assume that all of the quantum-mechanical systems are equivalent. Furthermore, they should all be in thermal contact, but otherwise be independent. The number of microscopic systems that are occupying their energy level  $\epsilon_1$  is  $n_1$ , the number in their energy level  $\epsilon_2$  is  $n_2$ , the number in their level  $\epsilon_3$  is  $n_3, \dots$ .

The number of microscopic systems is, for simplicity, assumed to be the number of molecules,  $N$ . It is given by the sum over all  $n_i$ , as shown in Eq. (1) of Fig. 2.32. The value of  $N$  is directly known from the macroscopic description of the material through the chemical composition, mass and Avogadro's number. Another easily evaluated macroscopic quantity is the total energy  $U$ . It must be the sum of the energies of all the microscopic, quantum-mechanical systems, making the Eq. (2) obvious.

For complete evaluation of  $N$  and  $U$ , one, however, needs to know the distribution of the molecules over the different energy levels, something that is rarely available. To solve this problem, more assumptions must be made. The most important one is

**Fig. 2.32**

that one can take all possible distributions and replace them with the most probable distribution, the Boltzmann distribution which is described in Appendix 6, Fig. A.6.1. It turns out that this most probable distribution is so common, that the error due to this simplification is small as long as the number of energy levels and atoms is large. The Boltzmann distribution is written as Eq. (3) of Fig. 2.32. It indicates that the fraction of the total number of molecules in state  $i$ ,  $n_i/N$ , is equal to the number of energy levels of the state  $i$ , which is given by its degeneracy  $g_i$ , multiplied by some exponential factor and divided by the partition function,  $Q$ . The partition function  $Q$  is the sum over all the degeneracies for all the levels  $i$ , each multiplied by the same exponential factor as found in the numerator.

The meaning of the partition function becomes clearer when one looks at some limiting cases. At high temperature, when thermal energy is present in abundance,  $\exp[-\epsilon_i/(kT)]$  is close to one because the exponent is very small. Then  $Q$  is just the sum over all the possible energy levels of the quantum mechanical system. Under such conditions the Boltzmann distribution, Eq. (3), indicates that the fraction of molecules in level  $i$ ,  $n_i/N$ , is the number of energy levels  $g_i$ , divided by the total number of available energy levels for the quantum-mechanical system. In other words, there is equipartition of the system over all available energy levels. The other limiting case occurs when  $kT$  is very much smaller than  $\epsilon_i$ . In this case, temperature is relatively low. This makes the exponent large and negative; the weighting factor  $\exp[-\epsilon_i/(kT)]$  is close to zero. One may then conclude that the energy levels of high energy (relative to  $kT$ ) are not counted in the partition function. At low temperature, the system can occupy only levels of low energy.

With this discussion, the most difficult part of the endeavor to connect the macroscopic energies to their microscopic origin is already completed. The rest is just mathematical drudgery that has largely been carried out in the literature. In order

to get an equation for the total energy  $U$ , the Boltzmann distribution, Eq. (3), is inserted into the sum for the total energy, Eq. (2). This process results in Eq. (5). The next equation can be seen to be correct, by just carrying out the indicated differentiation and comparing the result with Eq. (5).

Now that  $U$  is expressed in microscopic terms, one can also find the heat capacity, as is shown by Eq. (6) of Fig. 2.32. The partition function  $Q$ , the temperature  $T$ , and the total number of molecules  $N$  need to be known for the computation of  $C_v$ . Next,  $C_v$  can be converted to  $C_p$  using any of the expressions of Fig. 2.31, which, in turn, allows computation of  $H$ ,  $S$ , and  $G$ , using Eqs. (1), (2), and (3) of Fig. 2.22, respectively.

For a simple example one assumes to have only two energy levels for each atom or molecule, i.e., there are only the levels  $\epsilon_1$  and  $\epsilon_2$ . A diagram of the energy levels is shown in Fig. 2.33. This situation may arise for computation of the  $C_v$  contribution from molecules with two rotational isomers of different energies as shown in Fig. 1.37. For convenience, one sets the energy  $\epsilon_1$  equal to zero. Energy  $\epsilon_2$  lies then higher by  $\Delta\epsilon$ . Or, if one wants to express the energies in molar amounts, one multiplies  $\Delta\epsilon$  by Avogadro's number  $N_A$  and comes up with the molar energy difference  $\Delta E$  in  $\text{J mol}^{-1}$ . A similar change is necessary for  $kT$ ; per mole, it becomes  $RT$ . The partition function,  $Q$ , is now given in Eq. (7) of Fig. 2.33. The next step involves insertion of Eq. (7) into Eq. (5) of Fig. 2.32 and carrying out the differentiations. Equation (8) is the total energy  $U$ , and the heat capacity  $C_v$  is given by Eq. (9). The graph in Fig. 2.33 shows the change in  $C_v$  for a system with equal degeneracies ( $g_1 = g_2$ ). The abscissa is a reduced temperature—i.e., the temperature is multiplied by  $R$ , the gas constant, and divided by  $\Delta E$ . In this way the curve applies to all systems with two energy levels of equal degeneracy. The curve shows a relatively sharp peak at the reduced temperature at approximately 0.5. In this temperature

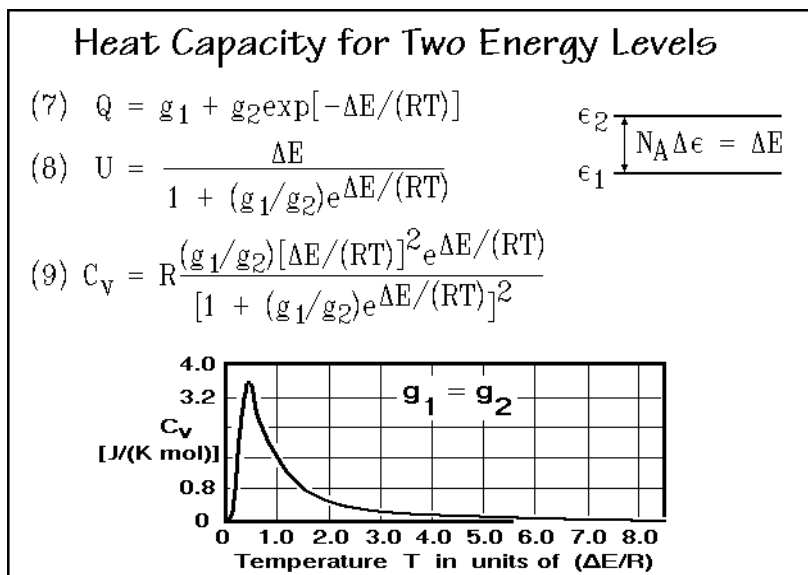


Fig. 2.33

region many molecules go from the lower to the higher energy level on increasing the temperature, causing the high heat capacity. At higher temperature, the heat capacity decreases exponentially over a fairly large temperature range. At high temperature (above about 5 in the reduced temperature scale), equipartition between the two levels is reached. This means that just as many systems are in the upper levels as are in the lower. No contribution to the heat capacity can arise anymore.

The second example is that of the harmonic oscillator in Fig. 2.34. The harmonic oscillator is basic to understanding the heat capacity of solids and summarized in Fig. A.6.2. It is characterized by an unlimited set of energy levels of equal distances, the first few are shown in Fig. 2.34. The quantum numbers,  $v_i$ , run from zero to infinity. The energies are written on the right-hand side of the levels. The difference in energy between any two successive energy levels is given by the quantity  $h\nu$ , where  $h$  is Planck's constant and  $\nu$  is the frequency of the oscillator (in units of hertz, Hz,  $\text{s}^{-1}$ ). If one chooses the lowest energy level as the zero of energy, then all

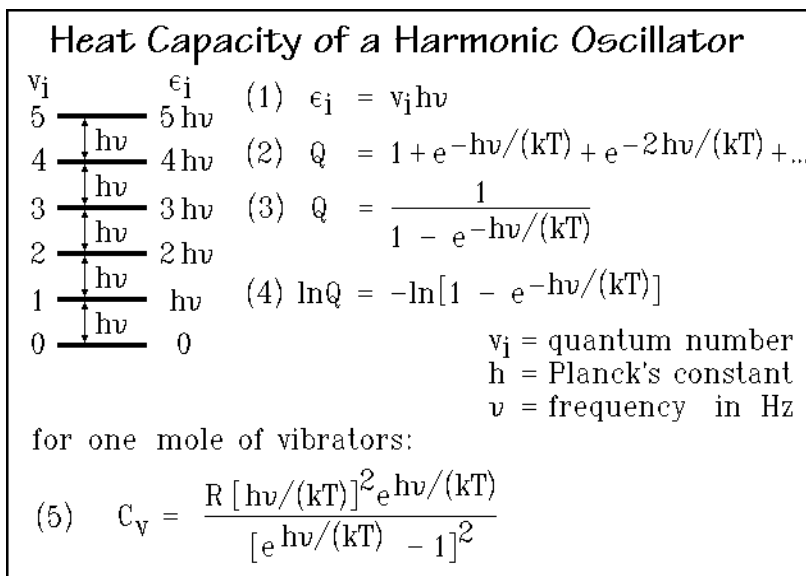


Fig. 2.34

energies can be expressed as shown in Eq. (1).<sup>1</sup> There is no degeneracy of energy levels in harmonic oscillators ( $g_i = 1$ ). The partition function can then be written as shown in Eq. (2). Equation (2) is an infinite, convergent, geometrical series, a series that can easily be summed, as is shown in Eq. (3). Now it is a simple task to take the logarithm of Eq. (3) and carry out the differentiations necessary to reach the heat capacity. The result is given in Eq. (5). It may be of use to go through these laborious steps to discover the mathematical connection between partition function and heat capacity. Note that for large exponents—i.e., for a relatively low

<sup>1</sup> The lowest energy level is  $\frac{1}{2} h\nu$  above the potential-energy minimum (zero-point vibration). Vibrators can exchange energy only in multiples of  $h\nu$ , so that level 0 is the lowest state.



temperature—Eq. (5) is identical to Eq. (9) in Fig. 2.33, which was derived for the case of two energy levels only. This is reasonable, because at sufficiently low temperature most molecules will be in the lowest possible energy levels. As long as only very few of the molecules are excited to a higher energy level, it makes very little difference if there are more levels above the first, excited energy level. All of these higher-energy levels are empty at low temperature and do not contribute to the energy and heat capacity. The heat capacity curve at relatively low temperature is thus identical for the two-level and the multilevel cases.

The heat capacity of the harmonic oscillator given by Eq. (5) of Fig. 2.34 is used so frequently that it is abbreviated on the far right-hand side of Eq. (6) of Fig. 2.35 to  $RE(\Theta/T)$ , where  $R$  is the gas constant, and  $E$  is the Einstein function. The shape of the Einstein function is indicated in the graphs of Fig. 2.35. The fraction  $\Theta/T$  stands for  $h\nu/kT$ , and  $h\nu/k$  has the dimension of a temperature. This temperature is called the Einstein temperature,  $\Theta_E$ . A frequency expressed in Hz can easily be converted into the Einstein temperature by multiplication by  $4.80 \times 10^{-11}$  s K. A

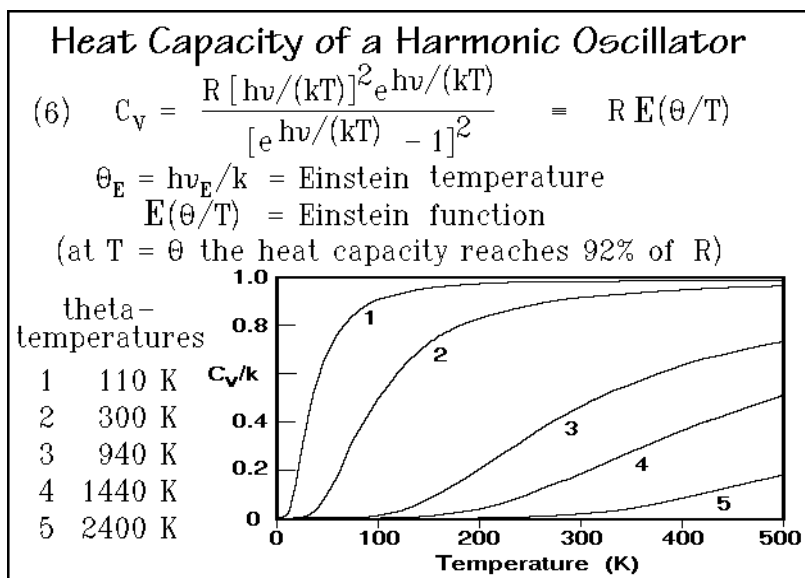


**Fig. 2.35**

frequency expressed in wave numbers,  $\text{cm}^{-1}$ , must be multiplied by  $1.4388$  cm K. At temperature  $\Theta$ , the heat capacity has reached 92% of its final value,  $R$  per mole of vibrations, or  $k$  per single vibrator. This value  $R$  is also the classical value of the Dulong–Petit rule. The different curves in Fig. 2.35 are calculated for the frequencies in Hz and Einstein temperatures listed on the left. Low-frequency vibrators reach their limiting value at low temperature, high-frequency vibrators at much higher temperature.

The calculations were carried out for one vibration frequency at a time. In reality there is, however, a full spectrum of vibrations. Each vibration has a heat capacity contribution characteristic for its frequency as given by Eq. (6). One finds that

because of vibrational coupling and anharmonicity, the separation into normal modes, to be discussed below, is questionable. The actual energy levels are neither equally spaced, as needed for Eq. (6), nor are they temperature-independent. There is hope, however, that supercomputers will ultimately permit more precise evaluation of temperature-dependent vibrational spectra and heat capacities. In the meantime, approximations exist to help one to better understand  $C_v$ .

### 2.3.4 The Heat Capacity of Solids

To overcome the need to compute the full frequency spectrum of solids, a series of approximations has been developed over the years. The simplest is the Einstein approximation [15]. In it, all vibrations in a solid are approximated by a single, average frequency. The Einstein function, Eq. (6) of Fig. 2.35, is then used with a single frequency to calculate the heat capacity. This Einstein frequency,  $\nu_E$ , can also be expressed by its temperature  $\Theta_E$ , as before. Figure 2.36 shows the frequency distribution  $\rho(\nu)$  of such a system. The whole spectrum is concentrated in a single frequency. Looking at actual measurements, one finds that at temperatures above about 20 K, heat capacities of a monatomic solid can indeed be represented by a single frequency. Typical values for the Einstein temperatures  $\Theta_E$  are listed in Fig. 2.36 for several elements. These  $\Theta$ -values correspond approximately to the heat capacity represented by curves 1–4 in Fig. 2.35. Elements with strong bonds are known as hard solids and have high  $\Theta$ -temperatures; elements with weaker bonds are softer and have lower  $\Theta$ -temperatures. Soft-matter physics has recently become an important field of investigation. Somewhat less obvious from the examples is that heavy atoms have lower  $\Theta$ -temperatures than lighter ones. These correlations are

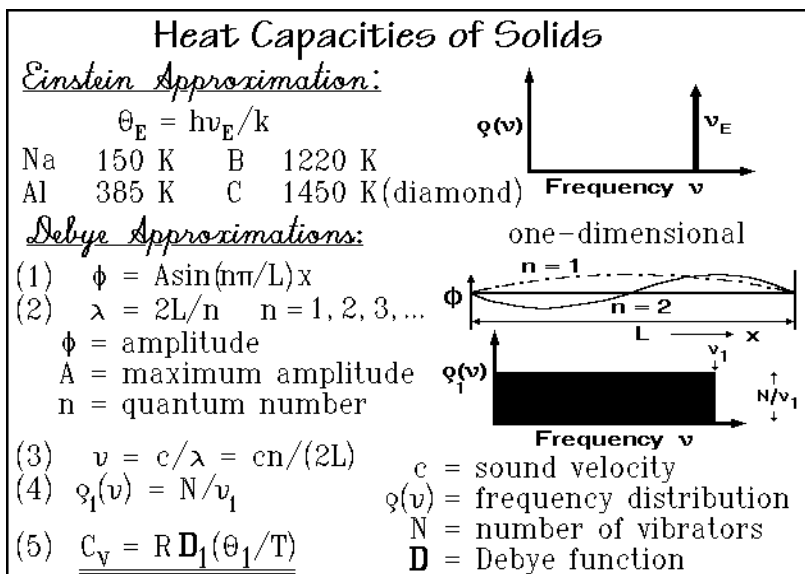


Fig. 2.36

easily proven by the standard calculations of frequencies of vibrators of different force constants and masses. The frequency is proportional to  $(f/m)^{1/2}$ , where  $f$  is the force constant and  $m$  is the appropriate mass.

The problem that the Einstein function does not seem to give a sufficiently accurate heat capacity at low temperature was resolved by Debye [16]. Figure 2.36 starts with the Debye approximation for the simple, one-dimensional vibrator. To illustrate such distribution, macroscopic, standing waves in a string of length,  $L$ , are shown in the sketch. All persisting vibrations of this string are given by the collection of standing waves. From the two indicated standing waves, one can easily derive that the amplitude,  $\phi$ , for any standing wave is given by Eq. (1), where  $x$  is the chosen distance along the string, and  $n$  is a quantum number that runs from 1 through all integers. Equation (2) indicates that the wavelength of a standing wave, identified by its quantum number  $n$ , is  $2L/n$ .

One can next convert the wavelength into frequency by knowing that  $v$ , the frequency, is equal to the velocity of sound in the solid,  $c$ , divided by  $\lambda$ , the wavelength. Equation (3) of Fig. 2.36 shows that the frequency is directly proportional to the quantum number,  $n$ . The density of states or frequency distribution is thus constant over the full range of given frequencies.

From Eq. (3) the frequency distribution can be calculated following the Debye treatment by making use of the fact that an actual atomic system must have a limited number of frequencies, limited by the number of degrees of freedom  $N$ . The distribution  $p(v)$  is thus simply given by Eq. (4). This frequency distribution is drawn in the sketch on the right-hand side in Fig. 2.36. The heat capacity is calculated by using a properly scaled Einstein term for each frequency. The heat capacity function for one mole of vibrators depends only on  $v_l$ , the maximum frequency of the distribution, which can be converted again into a theta-temperature,  $\Theta_l$ . Equation (5) shows that  $C_v$  at temperature  $T$  is equal to  $R$  multiplied by the one-dimensional Debye function  $D_l$  of  $(\Theta_l/T)$ . The one-dimensional Debye function is rather complicated as shown in Fig. 2.37, but can easily be handled by computer.

Next, it is useful to expand this analysis to two dimensions. The frequency distribution is now linear, as shown in Eq. (6) of Fig. 2.38. The mathematical expression of the two-dimensional Debye function is given in Fig. 2.37. Note that in Eq. (7) for  $C_v$  it is assumed that there are  $2N$  vibrations for the two-dimensional vibrator, i.e., the atomic array is made up of  $N$  atoms, and vibrations out of the plane are prohibited. In reality, this may not be so, and one would have to add additional terms to account for the omitted vibrations. The same reasoning applies for the one-dimensional case of Eq. (4) of Fig. 2.36.

For a linear macromolecule in space, a restriction to only one dimension does not correspond to reality. One must consider that in addition to one-dimensional, longitudinal vibrations of  $N$  vibrators, there are two transverse vibrations, each of  $N$  frequencies. Naturally, the longitudinal and transverse vibrations should have different  $\Theta_l$ -values in Eq. (5). For a two-dimensional molecule, there are two longitudinal vibrations, as described by Eq. (7) in Fig. 2.38, and one transverse vibration with half as many vibrations, as given in Eq. (6). As always, the total possible number of vibrations per atom must be three, as fixed by the number of degrees of freedom.

### Debye Approximations for Vibrators Coupled in One, Two, and Three Dimensions

$$\underset{\text{one-dimensional}}{\mathbf{D}_1(\Theta_1/T)} = (T/\Theta_1) \int_0^{(\Theta_1/T)} \frac{(\Theta/T)^2 \exp(\Theta/T)}{[\exp(\Theta/T) - 1]^2} d(\Theta/T)$$

$$\underset{\text{two-dimensional}}{\mathbf{D}_2(\Theta_2/T)} = 2(T/\Theta_2)^2 \int_0^{(\Theta_2/T)} \frac{(\Theta/T)^3 \exp(\Theta/T)}{[\exp(\Theta/T) - 1]^2} d(\Theta/T)$$

$$\underset{\text{three-dimensional}}{\mathbf{D}_3(\Theta_3/T)} = 3(T/\Theta_3)^3 \int_0^{(\Theta_3/T)} \frac{(\Theta/T)^4 \exp(\Theta/T)}{[\exp(\Theta/T) - 1]^2} d(\Theta/T)$$

Fig. 2.37

To conclude this discussion, Eqs. (8) and (9) of Fig. 2.38 represent the three-dimensional Debye function. The mathematical expression of the three-dimensional Debye function is also given in Fig. 2.37. Now the frequency distribution is quadratic in  $\nu$ , as shown in Fig. 2.38. The derivation of the three-dimensional Debye model is analogous to the one-dimensional and two-dimensional cases. The three-dimensional case is the one originally carried out by Debye [16]. The maximum frequency is  $\nu_3$

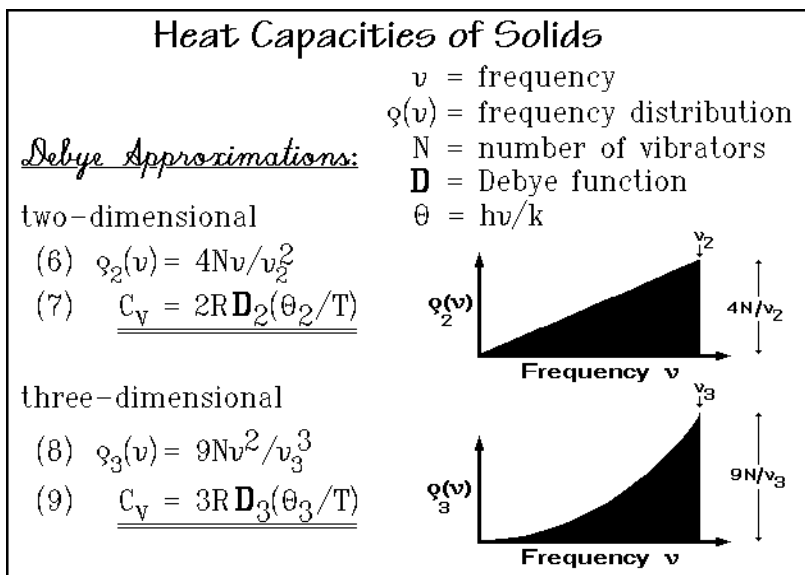


Fig. 2.38

or  $\Theta_3$ . At this frequency the total possible number of vibrators for N atoms,  $N_3$ , is reached. From the frequency distribution one can, again, derive the heat capacity contribution. The heat capacity for the three-dimensional Debye approximation is equal to  $3R$  times  $D_3$ , the three-dimensional Debye function of  $(\Theta_3/T)$ .

In Fig. 2.29 a number of examples of three-dimensional Debye functions for elements and salts are given [17]. A series of experimental heat capacities is plotted (calculated per mole of vibrators). Note that salts like KCl have two ions per formula

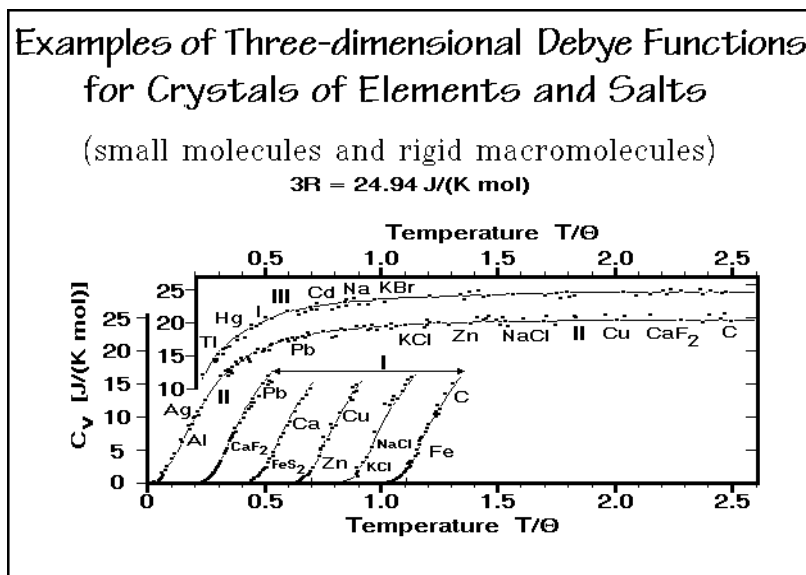


Fig. 2.39

mass (six vibrators) and salts like  $\text{CaF}_2$  have three (nine vibrators). To combine all the data in one graph, curves I are displaced by  $0.2 T/\Theta$  for each curve. For clarity, curve III combines the high temperature data not given in curve II at a raised ordinate. The drawn curves represent the three-dimensional Debye curve of Fig. 2.38, Eq. (9). All data fit extremely well. The Table in Fig. 2.40 gives a listing of the  $\Theta$ -temperatures which permit the calculation of actual heat capacities for 100 elements and compounds.

The correspondence of the approximate frequency spectra to the calculated full frequency distribution for diamond and graphite is illustrated in Fig. 2.41. The diamond spectrum does not agree well with the Einstein  $\Theta$ -value of 1450 K ( $3 \times 10^{13}$  Hz) given in Fig. 2.36, nor does it fit the smooth, quadratic increase in  $\rho(\nu)$  expected from a Debye  $\Theta$ -value of 2050 K ( $4.3 \times 10^{13}$  Hz) of Fig. 2.39. Because of the averaging nature of the Debye function, it still reproduces the heat capacity, but the vibrational spectrum shows that the quadratic frequency dependence reaches only to about  $2 \times 10^{13}$  Hz, which is about 1000 K. Then, there is a gap, followed by a sharp peak, terminating at  $4 \times 10^{13}$  Hz which is equal to 1920 K.

In Fig. 2.41 the frequency spectrum of graphite with a layer-like crystal structure is compared to 3-dimensional diamond (see Fig. 2.109, below). The spectrum is not

Debye Temperatures for Crystals of Fig. 2.39				
in K at $T \approx \Theta/2$				
Element	Element	Element	Element	Element
Ar 90	Cr 430	Hg 100	Ne 60	Si 630
Ag 220	Cs 45	I <sub>2</sub> 105	Ni 440	Sn(fcc) 240
Al 385	Cu 310	In 140	O <sub>2</sub> 90	Sn(tetr) 140
As 275	Dy 155	Ir 290	Os 250	Sr 170
Au 180	Er 165	K 100	Pa 150	Ta 230
B 1220	Fe 460	Kr 60	Pb 85	Tb 175
Be 940	Ga(trig) 240	La 130	Pd 275	Te 130
Bi 120	Ga(tetr) 125	Li 420	Pr 120	Th 140
C(dia) 2050	Gd 160	Mg 330	Pt 225	Ti 355
C(graph) 760	Ge 370	Mn 420	Rb 60	Tl 90
Ca 230	H <sub>2</sub> (para) 115	Mo 375	Re 300	V 280
Cd(hcp) 280	H <sub>2</sub> (ortho) 105	N <sub>2</sub> 70	Rh 350	W 315
Ce 110	D <sub>2</sub> 95	Na 150	Rn 400	Y 230
Cl <sub>2</sub> 115	He 30	Nb 265	Sb 140	Zn 250
Co 440	Hf 195	Nd 150	Se 150	Zr 240
Compound	Compound	Compound	Compound	Compound
AgBr 140	AuCu <sub>3</sub> (ordered) 200	CrCl <sub>3</sub> 100	KI 195	
AgCl 180	AuCu <sub>3</sub> (disord.) 180	Cr <sub>2</sub> O <sub>3</sub> 360	LiF 680	
Alums 80	BN 600	FeS <sub>2</sub> 630	MgO 800	
As <sub>2</sub> O <sub>3</sub> 140	CaF <sub>2</sub> 470	KBr 180	MoS <sub>2</sub> 290	
As <sub>2</sub> O <sub>5</sub> 240	CrCl <sub>2</sub> 80	KCl 230	NaCl 280	

Fig. 2.40

related to the 3-dimensional Debye function of Fig. 2.40 with  $\Theta = 760$  K. The quadratic increase of frequency at low frequencies stops already at  $5 \times 10^{12}$  Hz, or 240 K. The rest of the spectrum is rather complicated, but fits perhaps better to a two-dimensional Debye function with a  $\Theta_2$  value of 1370 K. The last maximum in the spectrum comes only at about  $4.5 \times 10^{13}$  Hz (2160 K), somewhat higher than the diamond frequencies. This is reasonable, since the in-plane vibrations in graphite

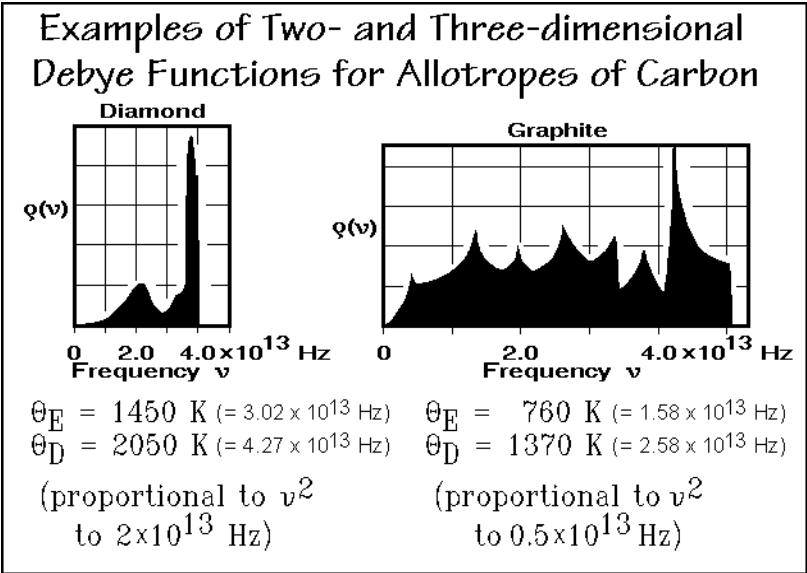


Fig. 2.41

involve C=C double bonds, which are stronger than the single bonds in diamond. A more extensive discussion of the heat capacities of various allotropes of carbon is given in Sect. 4.2.7.

In Fig. 2.42 results from the ATHAS laboratory on group IV chalcogenides are listed [18]. The crystals of these compounds form a link between strict layer structures whose heat capacities should be approximated with a two-dimensional Debye function, and crystals of NaCl structure with equally strong bonds in all three directions of space and, thus, should be approximated by a three-dimensional Debye function. As expected, the heat capacities correspond to the structures. The dashes in the table indicate that no reasonable fit could be obtained for the experimental data to the given Debye function. For GeSe both approaches were possible, but the two-dimensional Debye function represents the heat capacity better. For SnS and SnSe, the temperature range for data fit was somewhat too narrow to yield a clear answer.

As mentioned in the discussion of the two-dimensional Debye function, one needs to distinguish between the two longitudinal vibrations per atom or ion within the layer planes and the one transverse vibration per atom or ion directed at right angles to the layer plane. As expected, the longitudinal  $\Theta$ -temperatures,  $\Theta_l$ , are higher than the transverse ones,  $\Theta_t$ . The bottom three equations in Fig. 2.42 illustrate the calculation of heat capacity for all compounds listed. The experimental heat capacities can be represented by the listed  $\Theta$ -temperatures to better than  $\pm 3\%$ . The temperature range of fit is from 50 K, to room temperature. Above room temperature the heat capacities of these rather heavy-element compounds are close-to-fully excited, i.e., their heat capacity is not far from  $3R$  per atom. In this temperature range, precise values of the  $C_p - C_v$  correction are more important for the match of calculation and experiment than the frequency distribution. At higher temperatures, one expects that the actual vibrations deviate more from those calculated with the harmonic oscillator model.

### Examples of Two- and Three-dimensional Debye Functions for Group IV Chalcogenides

Substance	Crystal Structure	3-D $\Theta$	2-D $\Theta_l$	2-D $\Theta_t$
GeS	orthorhombic layer	-	505	200
GeSe	orthorhombic layer	(270)	345	185
GeTe	trigonal, distorted NaCl	205	-	-
SnS	orthorhombic layer	300	400	160
SnSe	orthorhombic layer	(230)	-	-
SnTe	cubic NaCl	175	-	-
PbS	cubic NaCl	225	-	-
PbSe	cubic NaCl	150	-	-
PbTe	cubic NaCl	130	-	-
GeS <sub>2</sub>	orthorhombic layer	-	705	175
GeSe <sub>2</sub>	hexagonal layer	-	480	100
SnS <sub>2</sub>	hexagonal layer	-	570	265

$$C_{v3-D}(AB) = 6RD_3(\Theta_3/T) \quad (\Theta\text{-temperatures in K})$$

$$C_{v2-D}(AB) = 4RD_2(\Theta_l/T) + 2RD_2(\Theta_t/T)$$

$$C_{v2-D}(AB_2) = 6RD_2(\Theta_l/T) + 3RD_2(\Theta_t/T)$$

Fig. 2.42

### 2.3.5 Complex Heat Capacity

In general, one can represent a complex number, defined in Fig. A.6.3 of Appendix 6 as  $z = a + ib$ , with  $i = \sqrt{-1}$ . A complex number can also be written as:

$$z = |z|e^{i\theta} = |z|(\cos\theta + i\sin\theta), \quad \text{with} \quad (1)$$

$$|z| = \sqrt{a^2 + b^2}; \quad \cos\theta = \frac{a}{|z|}; \quad \text{and} \quad \sin\theta = \frac{b}{|z|}. \quad (2)$$

For the description of periodic changes, as in modulated-temperature differential scanning calorimetry [19], TMDSC (see Sect. 4.4), or Fourier analyses, the introduction of complex quantities is convenient and lucid. It must be noted, however, that the different representation brings no new physical insight over the description in real numbers. The complex heat capacity has proven useful in the interpretation of thermal conductivity of gaseous molecules with slowly responding internal degrees of freedom [20] and may be of use representing the slow response in the glass transition (see Sect. 5.6). For the specific complex heat capacity measured at frequency  $\omega$ ,  $c_p(\omega)$ , with its real (reactive) part  $c_p'(\omega)$  and the imaginary part  $ic_p''(\omega)$ , one must use the following equation to make  $c_p''(\omega)$ , the dissipative part, positive:

$$c_p(\omega) = c_p'(\omega) - ic_p''(\omega). \quad (3)$$

The real quantities of Eq. (3) can then be written as:

$$c_p'(\omega) = c_p^e - \frac{\omega^2(\tau_{T,p}^e)^2 \Delta^e c_p}{1 + \omega^2(\tau_{T,p}^e)^2} \quad \text{and} \quad (4)$$

$$c_p''(\omega) = \frac{\omega \tau_{T,p}^e \Delta^e c_p}{1 + \omega^2(\tau_{T,p}^e)^2}, \quad (5)$$

where  $\tau_{T,p}^e$  is the Debye relaxation time of the system. The reactive part  $c_p'(\omega)$  of  $c_p(\omega)$  is the dynamic analog of  $c_p^e$ , the  $c_p$  at equilibrium. Accordingly, the limiting cases of a system in internal equilibrium and a system in arrested equilibrium are, respectively:

$$\omega \tau_{T,p}^e \ll 1; \quad c_p(\omega) = c_p'(\omega) = c_p^e, \quad \text{and} \quad (6)$$

$$\omega \tau_{T,p}^e \gg 1; \quad c_p(\omega) = c_p''(\omega) = c_{p,\infty}^e. \quad (7)$$

The internal degree of freedom contributes at low frequencies the total equilibrium contribution,  $\Delta^e c_p$ , to the specific heat capacity. With increasing  $\omega$ , this contribution decreases, and finally disappears.

The limiting dissipative parts,  $c_p''(\omega)$ , without analogs in equilibrium thermodynamics, are:

$$\omega \tau_{T,p}^e \ll 1; \quad c_p''(\omega) = \omega \tau_{T,p}^e \Delta^e c_p, \quad \text{and} \quad (8)$$

$$\omega \tau_{T,p}^e \gg 1 \quad c_p''(\omega) = \Delta^e c_p / \omega \tau_{T,p}^e, \quad (9)$$



so that the dissipative part disappears in internal equilibrium ( $\tau_{T,p}^e \rightarrow 0$ ) as well as in arrested equilibrium ( $\tau_{T,p}^e \rightarrow \infty$ ). Figure 2.43 illustrates the changes of  $c_p'(\omega)$  and  $c_p''(\omega)$  with  $\omega\tau_{T,p}^e$ .

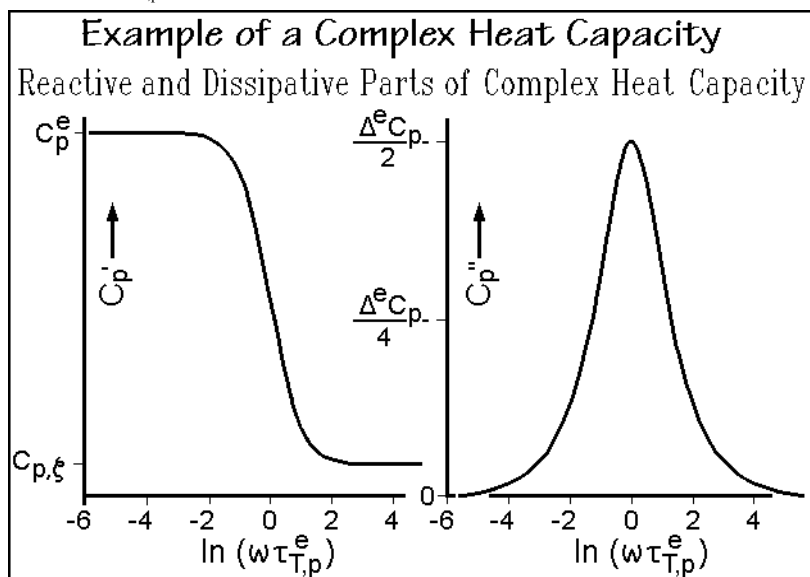


Fig. 2.43

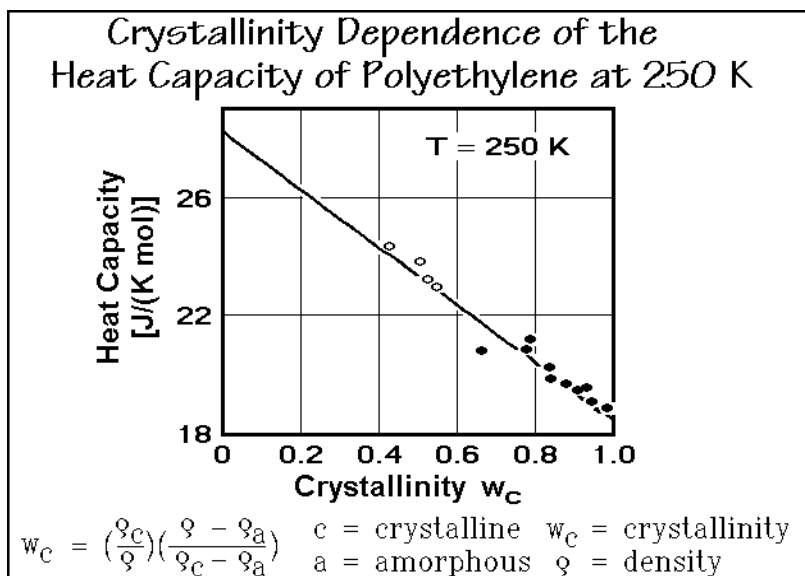
The dissipative heat capacity  $c_p''(\omega)$  is a measure of  $\Delta_i s$ , the entropy produced in nonequilibrium per half-period of the oscillation  $T(t) - T^e$ :

$$c_p''(\omega) = (1/\pi)(T^e/A_T)^2 \Delta_i s. \quad (10)$$

### 2.3.6 The Crystallinity Dependence of Heat Capacity

Several steps are necessary before heat capacity can be linked to its various molecular origins. First, one finds that linear macromolecules do not normally crystallize completely, they are semicrystalline. The restriction to partial crystallization is caused by kinetic hindrance to full extension of the molecular chains which, in the amorphous phase, are randomly coiled and entangled. Furthermore, in cases where the molecular structure is not sufficiently regular, the crystallinity may be further reduced, or even completely absent so that the molecules remain amorphous at all temperatures.

The first step in the analysis must thus be to establish the crystallinity dependence of the heat capacity. In Fig. 2.44 the heat capacity of polyethylene, the most analyzed polymer, is plotted as a function of crystallinity at 250 K, close to the glass transition temperature ( $T_g = 237$  K). The fact that polyethylene,  $[(CH_2-)_x]$ , is semicrystalline implies that the sample is metastable, i.e., it is not in equilibrium. Thermodynamics

**Fig. 2.44**

requires that a one-component system, such as polyethylene, can have two phases in equilibrium at the melting temperature only (phase rule, see Sect. 2.5).

One way to establish the weight-fraction crystallinity,  $w_c$ , is from density measurements (dilatometry, see Sect. 4.1). The equation is listed at the bottom of Fig. 2.44 and its derivation is displayed in Fig. 5.80. A similar equation for the volume-fraction crystallinity,  $v_c$ , is given in the discussion of crystallization in Sect. 3.6.5 (Fig. 3.84). Plotting the measured heat capacities of samples with different crystallinity, often results in a linear relationship. The plot allows the extrapolation to crystallinity zero (to find the heat capacity of the amorphous sample) and to crystallinity 1.0 (to find the heat capacity of the completely crystalline sample) even if these limiting cases are not experimentally available.

The graphs of Fig. 2.45 summarize the crystallinity dependence of the heat capacity of polyethylene at high and low temperatures. The curves all have a linear crystallinity dependence. At low temperature the fully crystalline sample ( $w_c = 1.0$ ) has a  $T^3$  temperature dependence of the heat capacity up to 10 K (single point in the graph), as is required for the low-temperature limit of a three-dimensional Debye function. One concludes that the beginning of the frequency spectrum is, as also documented for diamond and graphite in Sect. 2.3.4, quadratic in frequency dependence of the density of vibrational states,  $\rho(\nu)$ . This  $\nu^2$ -dependence does not extend to higher temperatures. At 15 K the  $T^3$ -dependence is already lost. The amorphous polyethylene ( $w_c = 0$ ) seems, in contrast, never to reach a  $T^3$  temperature dependence of the heat capacity at low temperature. Note that the curves of the figure do not even change monotonously with temperature in the  $C_p/T^3$  plot.

As the temperature is raised, the crystallinity dependence of the heat capacity becomes less; it is only a few percent between 50 to 200 K. In this temperature range, heat capacity is largely independent of physical structure. Glass and crystal

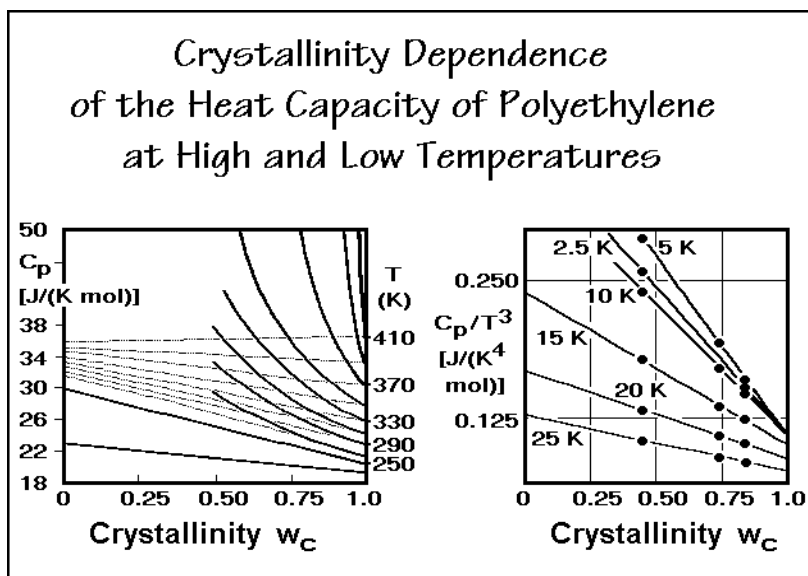
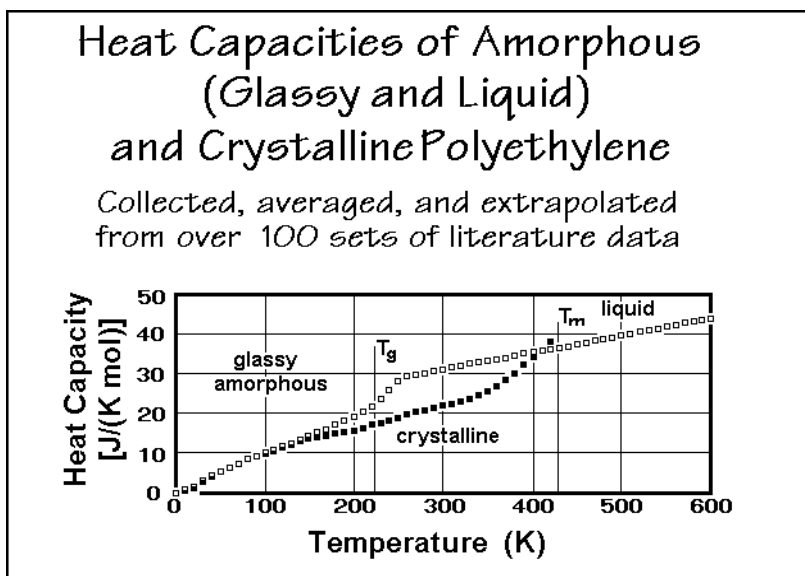


Fig. 2.45

have almost the same heat capacity. This is followed again by a steeper increase in the heat capacity of the amorphous polymer as it undergoes the glass transition at 237 K. It is of interest to note that the fully amorphous heat capacity from this graph agrees well with the extrapolation of the heat capacity of the liquid from above the melting temperature (414.6 K).

Finally, the left curves of Fig. 2.45 show that above about 260 K, melting of small, metastable crystals causes abnormal, nonlinear deviations in the heat capacity versus crystallinity plots. The measured data are indicated by the heavy lines in the figure. The thin lines indicate the continued additivity. The points for the amorphous polyethylene at the left ordinate represent the extrapolation of the measured heat capacities from the melt. All heat capacity contributions above the thin lines must thus be assigned to latent heats. Details of these apparent heat capacities yield information on the defect structure of semicrystalline polymers as is discussed in Chaps. 4–7.

Figure 2.46 illustrates the completed analysis. A number of other polymers are described in the ATHAS Data Bank, described in the next section. Most data are available for polyethylene. The heat capacity of the crystalline polyethylene is characterized by a  $T^3$  dependence to 10 K. This is followed by a change to a linear temperature dependence up to about 200 K. This second temperature dependence of the heat capacity fits a one-dimensional Debye function. Then, one notices a slowing of the increase of the crystalline heat capacity with temperature at about 200 to 250 K, to show a renewed increase above 300 K, to reach values equal to and higher than the heat capacity of melted polyethylene (close to the melting temperature). The heat capacity of the glassy polyethylene shows large deviations from the heat capacity of the crystal below 50 K (see Fig. 2.45). At these temperatures the absolute value of the heat capacity is, however, so small that it does not show up in Fig. 2.46. After

**Fig. 2.46**

the range of almost equal heat capacities of crystal and glass, the glass transition is obvious at about 240 K. In the melt, finally, the heat capacity is linear over a very wide range of temperature.

### 2.3.7 ATHAS

The quite complicated temperature dependence of the macroscopic heat capacity in Fig. 2.46 must now be explained by a microscopic model of thermal motion, as developed in Sect. 2.3.4. Neither a single Einstein function nor any of the Debye functions have any resemblance to the experimental data for the solid state, while the heat capacity of the liquid seems to be a simple straight line, not only for polyethylene, but also for many other polymers (but not for all!). Based on the ATHAS Data Bank of experimental heat capacities [21], abbreviated as Appendix 1, the analysis system for solids and liquids was derived.

For an overall description, the molecular motion is best divided into four major types. Type (1) is the vibrational motion of the atoms of the molecule about fixed positions, as described in Sect. 2.3.3. This motion occurs with small amplitudes, typically a fraction of an ångström (or 0.1 nm). Larger systems of vibrators have to be coupled, as discussed in Sect. 2.3.4 on hand of the Debye functions. The usual technique is to derive a spectrum of normal modes as described in Fig. A.6.4, based on the approximation of the motion as harmonic vibrators given in Fig. A.6.2.

The other three types of motion are of large-amplitude. Type (2) involves the conformational motion, described in Sect. 1.3.5. It is an internal rotation and can lead to a 360° rotation of the two halves of the molecules against each other, as shown in Fig. 1.37. For the rotation of a CH<sub>3</sub>-group little space is needed, while larger segments of a molecule may sweep out extensive volumes and are usually restricted

to coupled rotations which minimize the space requirement. Backbone motions which require little additional volume within the chain of polyethylene are illustrated by the computer simulations in Sect. 5.3.4.

The last two types of large-amplitude motion, (3) and (4), are translation and rotation of the molecule as a whole. These motions are of little importance for macromolecules since a large molecule concentrates only little energy in these degrees of freedom. The total energy of small molecules in the gaseous or liquid state, in contrast, depends largely on the translation and rotation.

Motion type (1) contributes  $R$  to the heat capacity per mole of vibrators (when excited, see Sect. 2.3.3 and 2.3.4). Types (2–4) add only  $R/2$ , but may also need some additional inter- and intramolecular potential energy contributions, making particularly the types (3) and (4) difficult to assess. This is at the root of the ease of the link of macromolecular heat capacities to molecular motion. The motion of type (1) is well approximated as will be shown next. The motion of type (2) can be described with the conformational isomers model, and more recently by empirical fit to the Ising model (see below). The contribution of types (3) and (4), which are only easy to describe in the gaseous state (see Fig. 2.9), is negligible for macromolecules.

The most detailed analysis of the molecular motion is possible for polymeric solids. The heat capacity due to vibrations agrees at low temperatures with the experiment and can be extrapolated to higher temperatures. At these higher temperatures one can identify deviations from the vibrational heat capacity due to beginning large-amplitude motion. For the heat capacities of the liquids, it was found empirically, that the heat capacity can be derived from group contributions of the chain units which make up the molecules, and an addition scheme was derived. A more detailed model-based scheme is described in Sect. 2.3.10.

After the crystallinity dependence has been established, the heat capacity of the solid at constant pressure,  $C_p$ , must be changed to the heat capacity at constant volume  $C_v$ , as described in Fig. 2.31. It helps in the analysis of the crystalline state that the vibration spectrum of crystalline polyethylene is known in detail from normal mode calculations using force constants derived from infrared and Raman spectroscopy. Such a spectrum is shown in Fig. 2.47 [22]. Using an Einstein function for each vibration as described in Fig. 2.35, one can compute the heat capacity by adding the contributions of all the various frequencies. The heat capacity of the crystalline polyethylene shown in Fig. 2.46 can be reproduced above 50 K by these data within experimental error. Below 50 K, the experimental data show increasing deviations, an indication that the computation of the low-frequency, skeletal vibrations cannot be carried out correctly using such an analysis.

With knowledge of the heat capacity and the frequency spectrum, one can discuss the actual motion of the molecules in the solid state. Looking at the frequency spectrum of Fig. 2.47, one can distinguish two separate frequency regions. The first region goes up to approximately  $2 \times 10^{13}$  Hz. One finds vibrations that account for two degrees of freedom in this range. The motion involved in these vibrations can be visualized as a torsional and an accordion-like motion of the  $\text{CH}_2$ -backbone, as illustrated by sketches #1 and #2 of Fig. 2.48, respectively. The torsion can be thought of as a motion that results from twisting one end of the chain against the other about the molecular axis. The accordion-like motion of the chain arises from the

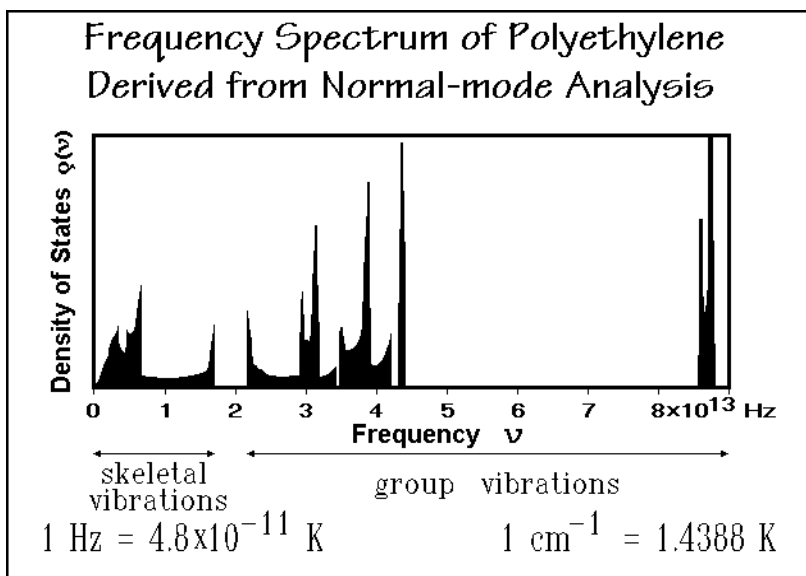


Fig. 2.47

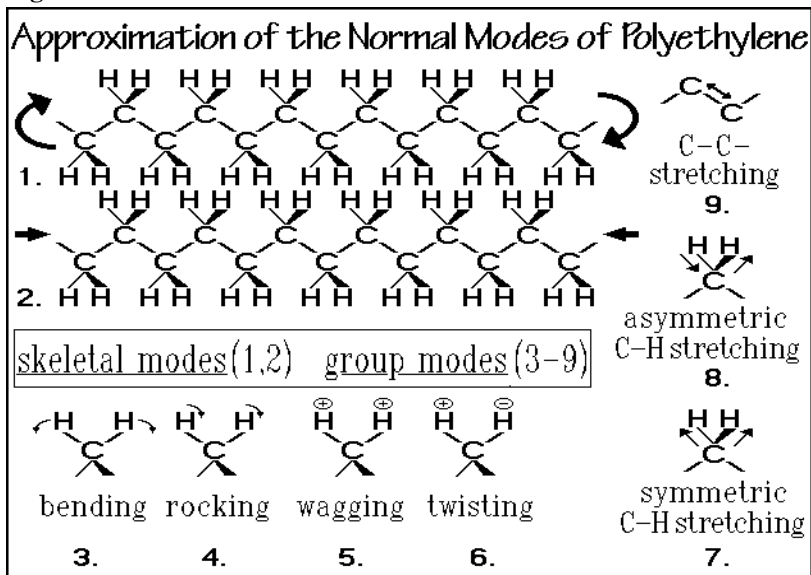


Fig. 2.48

bending motion of the C-C-C-bonds on compression of the chain, followed by extension. These two low-frequency motions will be called the skeletal vibrations. Their frequencies are such that they contribute mainly to the increase in heat capacity from 0 to 200 K. The gap in the frequency distribution at about  $2 \times 10^{13}$  Hz is responsible for the leveling of  $C_p$  between 200 and 250 K, and the value of  $C_p$  accounts for two degrees of freedom, i.e., is about  $16\text{--}17 \text{ J K}^{-1} \text{ mol}^{-1}$  or 2 R.

All motions of higher frequency will now be called group vibrations, because these vibrations involve oscillations of relatively isolated groupings of atoms along the backbone chain. Figure 2.48 illustrates that the C–C-stretching vibration (#9) is not a skeletal vibration because of the special geometry of the backbone chain. The close-to-90° bond angle between successive backbone bonds in the crystal ( $\approx 111^\circ$ , see Sect. 5.1) allows only little coupling for such vibrations and results in a rather narrow frequency region, more typical for group vibrations. In the first set of group vibrations, between 2 and  $5 \times 10^{13}$  Hz, one finds these oscillations involving the bending of the C–H bond (#3–6) and the C–C stretching vibration (#9). Type #3 involves the symmetrical bending of the hydrogens. The bending motion is indicated by the arrows. The next type of oscillation is the rocking motion (#4). In this case both hydrogens move in the same direction and rock the chain back and forth. The third type of motion in this group, listed as #5, is the wagging motion. One can think of it as a motion in which the two hydrogens come out of the plane of the paper and then go back behind the plane of the paper. The twisting motion (#6), finally, is the asymmetric counterpart of the wagging motion, i.e., one hydrogen atom comes out of the plane of the paper while the other goes back behind the plane of the paper. The stretching of the C–C bond (#9) has a much higher frequency than the torsion and bending involved in the skeletal modes. These five vibrations are the ones responsible for the renewed increase of the heat capacity starting at about 300 K. Below 200 K their contributions to the heat capacity are small.

Finally, the CH<sub>2</sub> groups have two more degrees of freedom, the ones that contribute to the very high frequencies above  $8 \times 10^{13}$  Hz. These are the C–H stretching vibrations. There are a symmetric and an asymmetric one, as shown in sketches #7 and #8. These frequencies are so high that at 400 K their contribution to the heat capacity is still small. Summing all these contributions to the heat capacity of polyethylene, one finds that up to about 300 K mainly the skeletal vibrations contribute to the heat capacity. Above 300 K, increasing contributions come from the group vibrations in the region of  $2\text{--}5 \times 10^{13}$  Hz, and if one could have solid polyethylene at about 700–800 K, one would get the additional contributions from the C–H stretching vibrations, but polyethylene crystals melt before these vibrations are excited significantly. The total of nine vibrations possible for the three atoms of the CH<sub>2</sub> unit, would, when fully excited, lead to a heat capacity of  $75 \text{ J K}^{-1} \text{ mol}^{-1}$ . At the melting temperature, only half of these vibrations are excited, i.e., the value of  $C_v$  is about  $38 \text{ J K}^{-1} \text{ mol}^{-1}$ , as can be seen from Fig. 2.46.

The next step in the analysis is to find an approximation for the spectrum of skeletal vibrations since, as mentioned above, the lowest skeletal vibrations are not well enough known, and often even the higher skeletal vibrations have not been established. To obtain the heat capacity due to the skeletal vibrations from the experimental data, the contributions of the group vibrations must be subtracted from  $C_v$ . A table of the group vibration frequencies for polyethylene can be derived from the normal mode analysis [22] in Fig. 2.47 and listed in Fig. 2.49. If such a table is not available for the given polymer, results for the same group in other polymers or small-molecule model compounds can be used as an approximation. The computations for the heat capacity contributions arising from the group vibrations are also illustrated in Fig. 2.49. The narrow frequency ranges seen in Fig. 2.47 are treated as

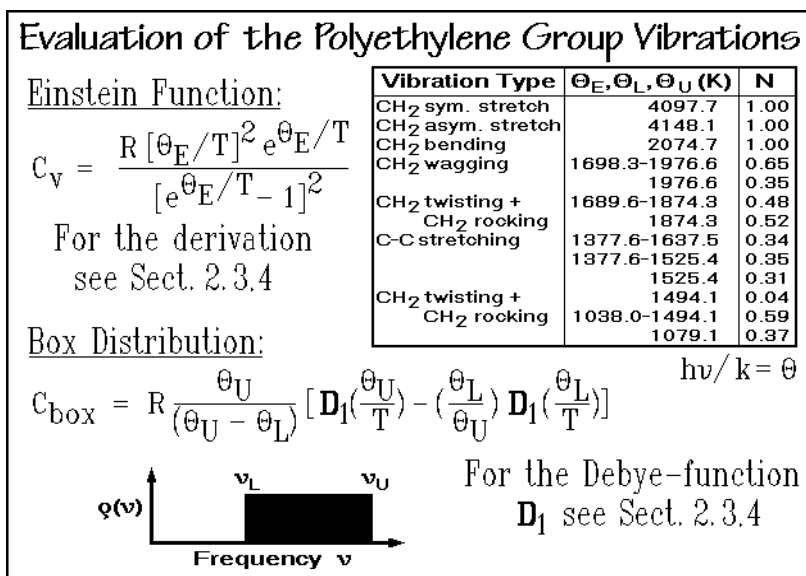


Fig. 2.49

single Einstein functions, the wider distributions are broken into single frequencies and box distributions as, for example, for the C–C-stretching modes. The lower frequency limit of the box distribution is given by  $\Theta_L$ , the upper one by  $\Theta_U$ . The equation for the box distribution can easily be derived from two adjusted one-dimensional Debye functions as shown in the figure.

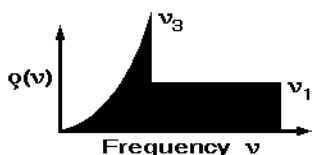
The next step in the ATHAS analysis is to assess the skeletal heat capacity. The skeletal vibrations are coupled in such a way that their distributions stretch toward zero frequency where the acoustical vibrations of 20–20,000 Hz can be found. In the lowest-frequency region one must, in addition, consider that the vibrations couple intermolecularly because the wavelengths of the vibrations become larger than the molecular anisotropy caused by the chain structure. As a result, the detailed molecular arrangement is of little consequence at these lowest frequencies. A three-dimensional Debye function, derived for an isotropic solid as shown in Figs. 2.37 and 38 should apply in this frequency region. To approximate the skeletal vibrations of linear macromolecules, one should thus start out at low frequency with a three-dimensional Debye function and then switch to a one-dimensional Debye function.

Such an approach was suggested by Tarasov and is illustrated in Fig. 2.50. The skeletal vibration frequencies are separated into two groups, the intermolecular group between zero and  $\nu_3$ , characterized by a three-dimensional  $\Theta$ -temperature,  $\Theta_3$ , and an intramolecular group between  $\nu_3$  and  $\nu_1$ , characterized by a one-dimensional  $\Theta$ -temperature,  $\Theta_1$ , as expected for one-dimensional vibrators. The boxed Tarasov equation shows the needed computation. By assuming the number of vibrators in the intermolecular part is  $N \times \Theta_3/\Theta_1$ , one has reduced the adjustable parameters in the equation from three ( $N_3$ ,  $\Theta_3$ , and  $\Theta_1$ ) to only two ( $\Theta_3$  and  $\Theta_1$ ). The Tarasov equation is then fitted to the experimental skeletal heat capacities at low temperatures to get  $\Theta_3$ , and at higher temperatures to get  $\Theta_1$ . Computer programs for fitting are available,



### Fitting of the Experimental, Skeletal Heat-capacity Contribution to the Tarasov Equation

$$C_{1,3} = R\{D_1(\theta_1/T) - (\theta_3/\theta_1)[D_1(\theta_3/T) - D_3(\theta_3/T)]\}$$



$$h\nu/k = \theta$$

$$N = N_1 + N_3$$

$$q(v) = N_1/(v_1 - v_3)$$

$$q(v) = 3N_3v^2/v_3^3$$

For the Debye-functions  
 $D_1$  and  $D_3$  see Sect. 2.3.4

crystalline polyethylene:

$$\theta_1 = 519 \text{ K}; \quad \theta_3 = 158 \text{ K}$$

glassy polyethylene:

$$\theta_1 = 519 \text{ K}; \quad \theta_3 = 80 \text{ K}$$

$$(v_3 \geq v \geq v_1) \quad (0 \geq v \geq v_3)$$

Fig. 2.50

giving the indicated  $\theta_3$  and  $\theta_1$ . Fitting with three parameters or with different equations for the longitudinal and transverse vibrations showed no advantages.

With the Tarasov theta-parameters and the table of group-vibration frequencies, the heat capacity due to vibrations can be calculated over the full temperature range, completing the ATHAS analysis for polyethylene. Figure 2.51 shows the results. Up to at least 250 K the analysis is in full agreement with the experimental data, and at

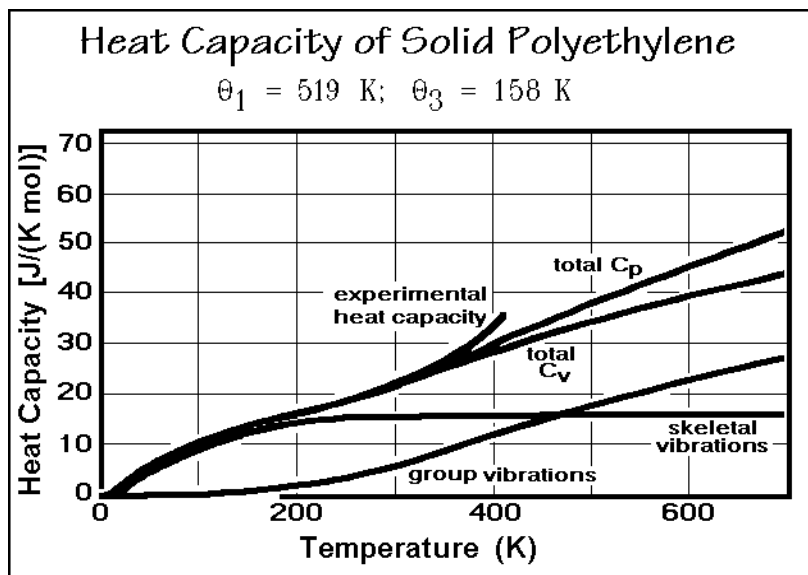


Fig. 2.51

higher temperatures, valuable information can be extracted from the deviations of the experiment, as will be shown below. A detailed understanding of the origin of the heat capacity of polyethylene, thus, is achieved and the link between the macroscopic heat capacity and the molecular motion is established.

Figure 2.52 shows a newer fitting procedure on the example of one of the most complicated linear macromolecules, a solid, water-free (denatured) protein [23]. The protein chosen is bovine  $\alpha$ -chymotrypsinogen, type 2. Its degree of polymerization is 245, containing all 20 naturally occurring amino acids in known amounts and established sequence. The molar mass is 25,646 Da. All group vibration contributions were calculated using the data for synthetic poly(amino acid)s in the ATHAS Data Bank, and then subtracted from the experimental  $C_v$ . The remaining experimental skeletal heat capacity up to 300 K was then fitted to a Tarasov expression for 3005 skeletal vibrators ( $N_s$ ) as is shown in 2.3.25. A  $20 \times 20$  mesh with  $\Theta_3$  values between 10 and 200 K and  $\Theta_1$  values between 200 and 900 K is evaluated point by point, and then least-squares fitted to the experimental  $C_p$ . It is obvious that a unique minimum in error is present in Fig. 2.52, proving also the relevance of the ATHAS for the

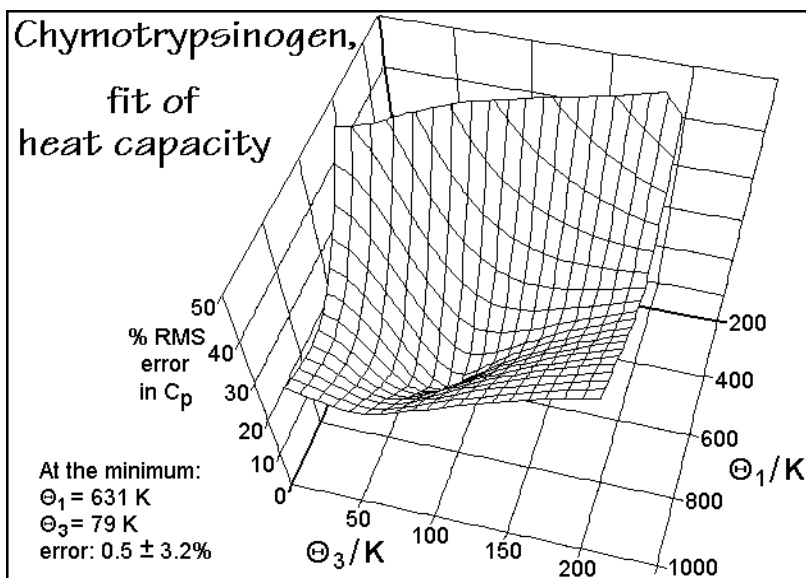


Fig. 2.52

evaluation of the vibrational heat capacities of proteins. An interpolation method was used to fix the global minimum between the mesh points.

Figure 2.53 illustrates the fit between calculation of the heat capacity from the various vibrational contributions and the experiments from various laboratories. Within the experimental error, which is particularly large for proteins which are difficult to obtain free of water, the measured and calculated data agree. Also indicated are the results of an empirical addition scheme, using the appropriate proportions of  $C_p$  from all poly(amino acid)s. All transitions and possible segmental melting occur above the temperature range shown in the figure.

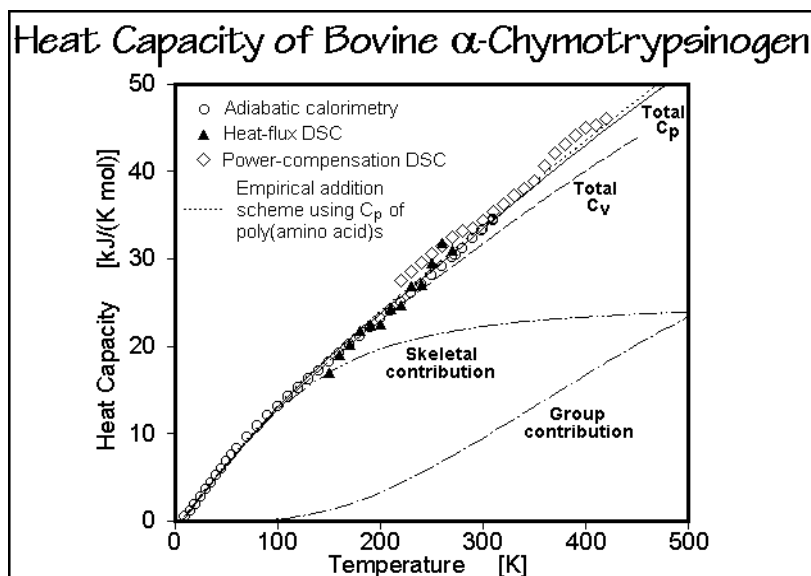


Fig. 2.53

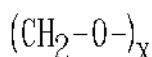
### 2.3.8 Polyoxide Heat Capacities

Besides providing heat capacities of single polymers, the ATHAS Data Bank also permits us to correlate data of homologous series of polymers. The aliphatic series of polyoxides is an example to be analyzed next. An approximate spectrum of the group vibrations of poly(oxymethylene), POM ( $\text{CH}_2\text{-O-}$ )<sub>x</sub>, the simplest polyoxide, is listed in Fig. 2.54. The  $\text{CH}_2$ -bending and -stretching vibrations are similar to the data for polyethylene, PE ( $\text{CH}_2$ -)<sub>x</sub>. The fitted theta-temperatures are given also in the figure. Note that they are calculated for only two modes of vibration. The missing two skeletal vibrations, contributed by the added O- group, are included (arbitrarily) in the list of group vibrations since they are well known.

The table of group vibration frequencies with their  $\Theta$ -temperatures and the number of skeletal vibrators,  $N_s$ , with their two  $\Theta$ -temperatures permits us now to calculate the total  $C_v$  and, with help of the expressions for  $C_p - C_v$ , also  $C_p$ . Figure 2.55 shows the results of such calculations, not only for POM and PE in the bottom two curves, but also for a larger series of homologous, aliphatic polyoxides. The calculations are based on the proper number of group vibrations for the number of O- and  $\text{CH}_2$ - in the repeating unit from Fig. 2.54:

PO8M	= poly(oxyoctamethylene)	$[\text{O}-(\text{CH}_2)_8]_x$
POMO4M	= poly(oxymethyleneoxytetramethylene)	$[\text{O}-\text{CH}_2-\text{O}-(\text{CH}_2)_4]_x$
PO4M	= poly(oxytetramethylene)	$[\text{O}-(\text{CH}_2)_4]_x$
PO3M	= poly(oxytrimethylene)	$[\text{O}-(\text{CH}_2)_3]_x$
POMOE	= poly(oxymethyleneoxyethylene)	$[\text{O}-\text{CH}_2-\text{O}-(\text{CH}_2)_2]_x$
POE	= poly(oxyethylene)	$[\text{O}-(\text{CH}_2)_2]_x$

### The Evaluation of Polyoxide Heat Capacities, Starting with Poly(oxymethylene)



Two skeletal  
and 10 group  
vibrations

$$\theta_1 = 232 \text{ K}$$

$$\theta_3 = 117 \text{ K}$$

Vibration Type	$\theta_E, \theta_L, \theta_U$ (K)	N
CH2 symm. stretch	4284.7	1.00
CH2 asym. stretch	4168.2	1.00
CH2 bending	2104.5	1.00
CH2 wagging	2018.6	1.00
CH2 twisting	1921.9	1.00
CH2 rocking	1524.7	0.20
	1707.2	0.24
	1524.7-1707.2	0.56
C-O stretching	1385.1	0.22
	1632.1	0.11
	1385.1-1632.1	0.67
	1304.6	1.00
chain bending	869.7	1.00
	655.0	0.23
	359.7-440.2	0.29
	359.7-655.0	0.48

Fig. 2.54

### Computed Heat Capacities of a Series of Solid Polyoxides

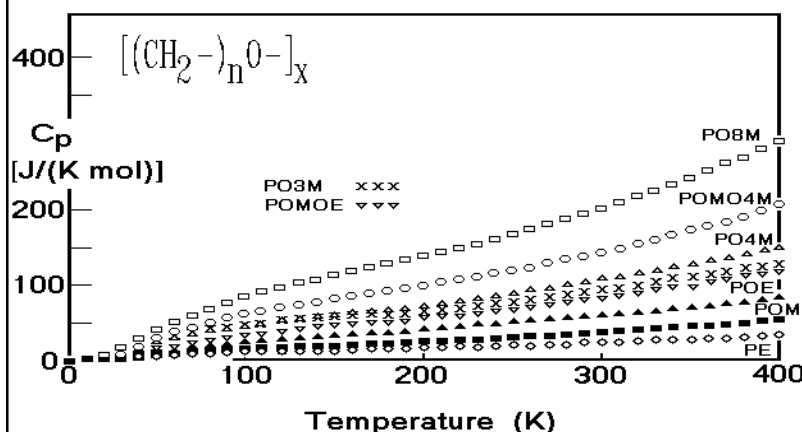


Fig. 2.55

The more detailed analysis of the heat capacities of the solid, aliphatic polyoxides is summarized in the next two figures. Figure 2.56 displays the deviations of the calculations from the experiment. Although the agreement is close to the accuracy of the experiment ( $\pm 3\%$ ), some systematic deviation is visible. It is, however, too little to interpret as long as no compressibility and expansivity data are available for

### Deviations of the Computed Heat Capacities of the Previous Figure from the Experiment

$$\Delta = [C_p(\text{computed}) - C_p(\text{measured})]/C_p(\text{measured})$$

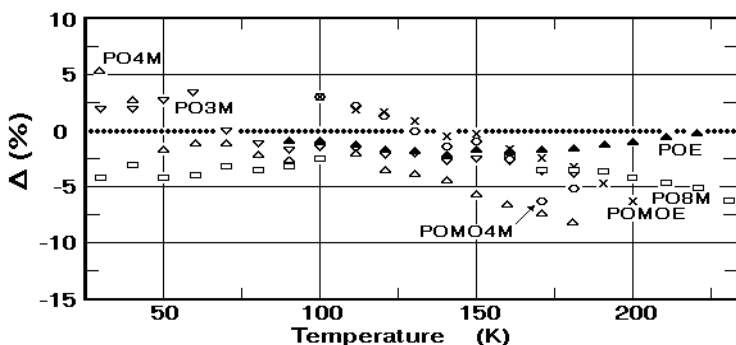


Fig. 2.56

a more precise  $C_p$  to  $C_v$  conversion. Figure 2.57 indicates that the  $\Theta_1$  and  $\Theta_3$  values are changing continuously with chemical composition. It is thus possible to estimate  $\Theta_1$  and  $\Theta_3$  values for intermediate compositions, and to compute heat capacities of unknown polyoxides or copolymers of different monomers without reference to measurement. An interesting observation is that the  $\Theta_1$ -values are not very dependent on crystallinity (see also Fig. 2.50 for polyethylene). The values for  $\Theta_3$ , in contrast,

### Change of Theta-temperatures of Solid Aliphatic Polyoxides with Composition

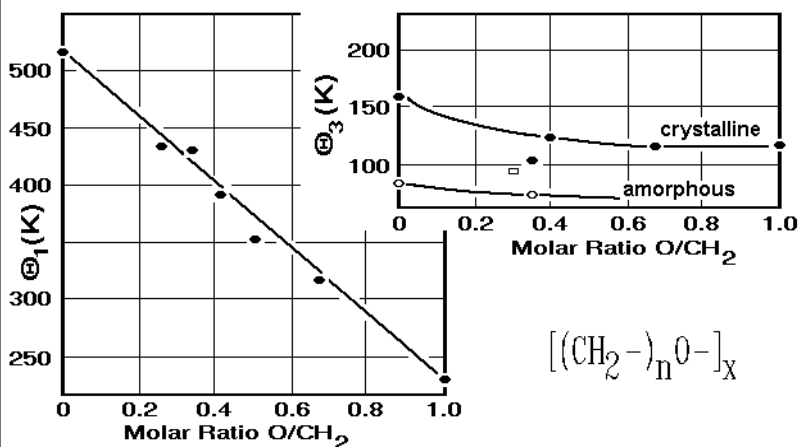


Fig. 2.57

are as much as double as high for the crystalline polymers than for the glassy ones. Since the  $\Theta_3$  values are, however, relatively small, the skeletal contributions are usually close-to-fully excited above room temperature.

Similar analyses were accomplished for more than 150 macromolecules. The data on  $N$ ,  $\Theta_1$ , and  $\Theta_3$  together with the ranges of experimental  $C_p$  data, are collected in the ATHAS Data Bank and summarized in Appendix 1. The precision of these computed heat capacities is in general better than  $\pm 5\%$ , close to the experimental accuracy.

The strict additivity of the heat capacity contributions of the group vibrations, and the continuous change in  $\Theta_1$  with chemical composition, led to the development of addition schemes for heat capacities. As long as the contribution which corresponds to the backbone grouping of a polymer is known empirically, it is possible to estimate heat capacities of such polymers and copolymers. The just completed discussion of the Tarasov analysis indicates that, indeed, the group vibrations are additive, but that for the low-temperature heat capacities deviations are to be expected as long as the intermolecular skeletal vibrations are not fully excited. In this case it is possible to estimate  $\Theta_3$  from similar substances for an improved estimate.

### 2.3.9 Heat Capacities of Liquids

The heat capacities of liquids are much more difficult to understand. The motion involves now also large-amplitude rotations and translations. Since, however, in the liquid state polymers are usually in equilibrium, measurements are more reproducible, as is shown in Fig. 2.58 using the example of poly(oxymethylene), POM. The graph is a direct copy of 36 runs of differently treated poly(oxymethylenes). The almost vertical approach of some curves to the liquid  $C_p$  is caused by the end of melting of crystallized samples. All curves superimpose when the samples are liquid.

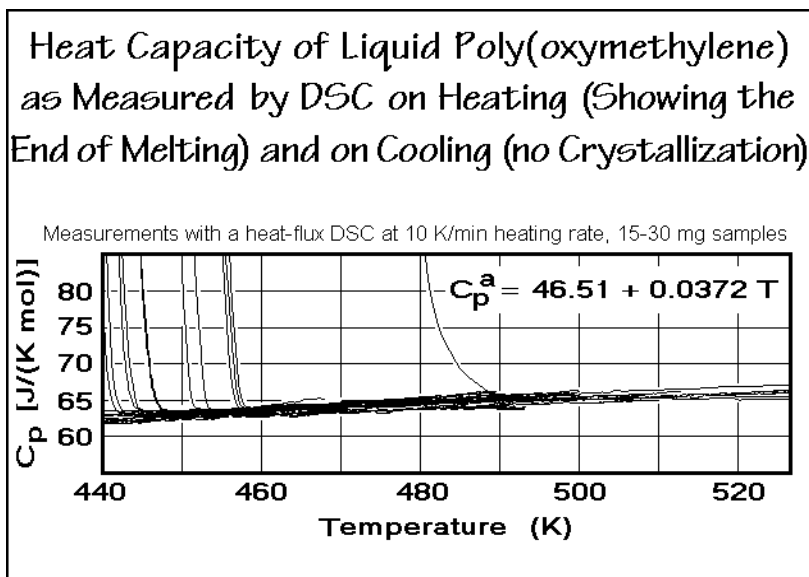


Fig. 2.58

The addition scheme of group contributions helps to connect larger bodies of data for liquid polymers. In the liquid state one is always at a sufficiently high temperature so that the intermolecular skeletal vibrations are fully excited so that additivity holds for both the intramolecular skeletal vibrations and the group vibrations. Figure 2.59 shows the experimental data for the liquids for the same series of polyoxides as analyzed for the solid state. The equation in the top of the graph represents all the thin lines, while the thick lines represent the experimental data. The equation for  $C_p^a$  was arrived at by least-squares fitting of all experiments and seems more precise than any of the separate experiments.

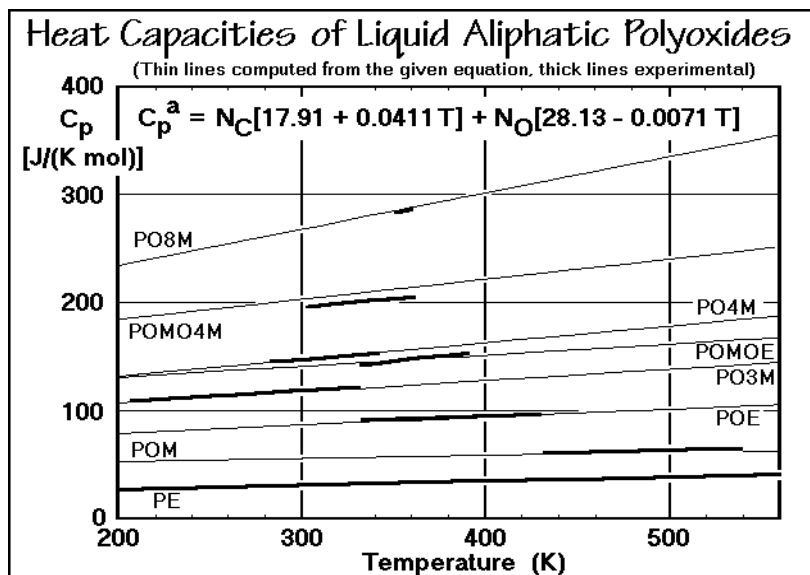


Fig. 2.59

Other examples of the heat capacities of homologous series of liquid polymers are given in Figs. 2.60 and 2.61 for aliphatic nylons and polyesters. The nylons are indicated by their number of carbon atoms in the repeating units (see Sect. 1.2). The names of the polyesters are abbreviated as follows:

PHMS	= poly(hexamethylene sebacate)	$[(CH_2)_6OCO-(CH_2)_8COO-]$
PPDL	= polypentadecanolactone	$(CH_2)_{14}COO-$
PES	= poly(ethylene sebacate)	$[(CH_2)_2OCO-(CH_2)_8COO-]$
PTDL	= polytridecanolactone	$(CH_2)_{12}COO-$
PUDL	= polyundecanolactone	$(CH_2)_{10}COO-$
PTMA	= poly(trimethylene adipate)	$[(CH_2)_3OCO-(CH_2)_4COO-]$
PTMS	= poly(trimethylene succinate)	$[(CH_2)_3OCO-(CH_2)_3COO-]$
PCL	= poly( $\delta$ -valerolactone)	$(CH_2)_5COO-$
PVL	= poly( $\delta$ -valerolactone)	$(CH_2)_4COO-$
PBL	= poly( $\gamma$ -butyrolactone)	$(CH_2)_3COO-$
PPL	= poly( $\beta$ -propiolactone)	$(CH_2)_2COO-$
PGL	= polyglycolide	$(CH_2)COO-$

Again, single equations represent all data for each, the liquid aliphatic nylons and polyesters. The overall error using all experimental data is less than for any single measurement. It is typical for the data taken by DSC that over larger temperature regions a slope develops which introduces a systematic error. For higher quality data, the temperature range of measurement should be limited, as was suggested in Sect. 2.3.1.

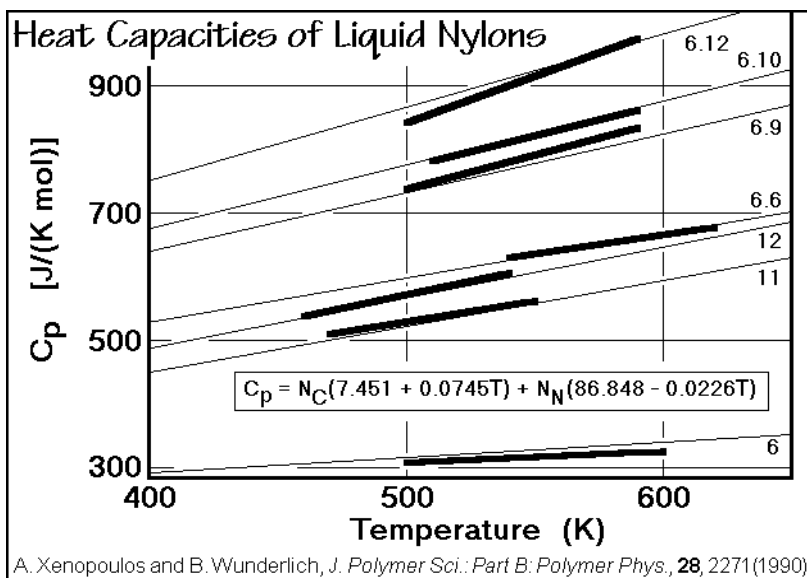


Fig. 2.60

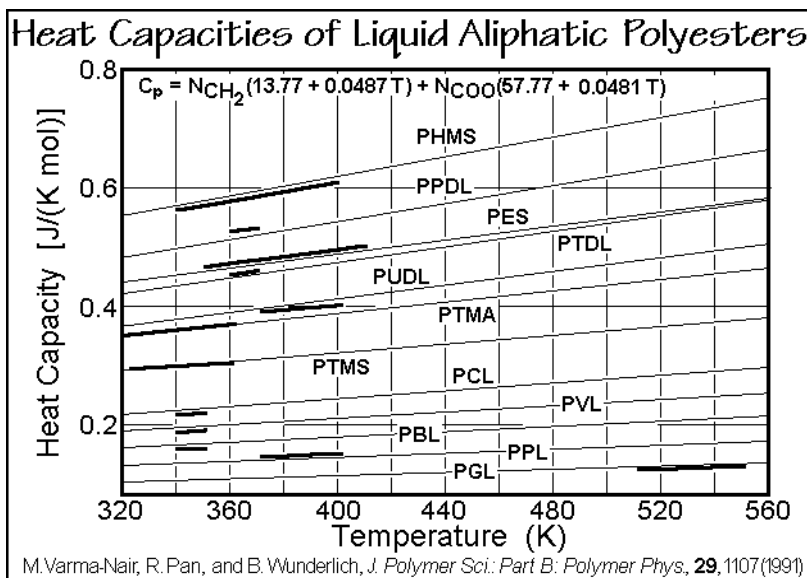


Fig. 2.61



### 2.3.10. Examples of Application of ATHAS

The application of the ATHAS has produced a large volume of critically reviewed and interpreted heat capacity data on solid and liquid homopolymers. This knowledge is helpful in the determination of the integral thermodynamic functions which are also part of the data bank. Even of greater importance is the help these basic data give in the separation of nonequilibrium enthalpy and heat capacity effects as will be illustrated in a number of examples.

**Polytetrafluoroethylene.** Figure 2.62 shows the analysis of the heat capacity of crystalline polytetrafluoroethylene (PTFE). The comparison between calculation and measurement is given in Fig. 2.63. As in the case of the polyoxides, it is also possible to predict heat capacities of all less fluorinated polyethylenes. The measured sample

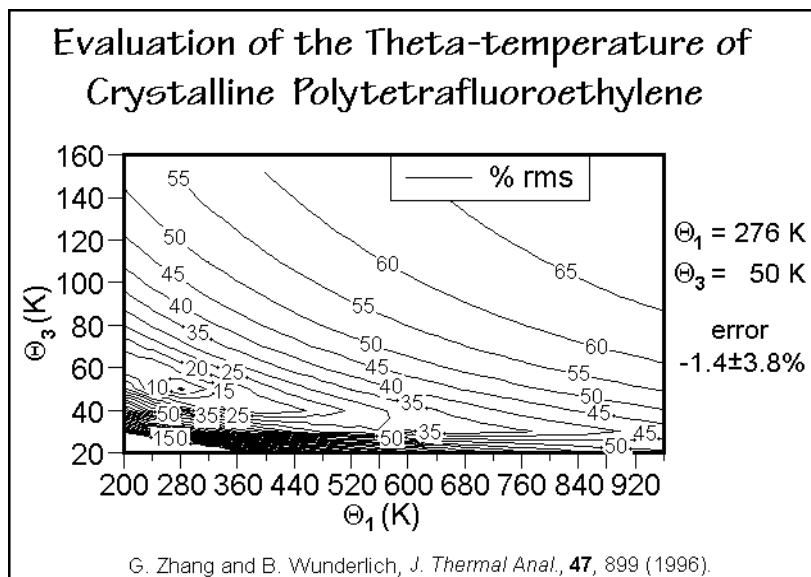


**Fig. 2.62**

was almost completely crystalline, but it is obvious from the graph that there are two rather broad endotherms superimposed on the heat capacity curves. The room temperature transition is particularly broad. It represents a crystal-to-condis-crystal transition, discussed in Sect. 2.5. Without the computed heat capacity as a baseline, it is impossible to separate the heat of transition quantitatively from the heat capacity. Based on these data it was possible to show that the entropies of transition, when added, give a similar value ( $9.6 \text{ J K}^{-1} \text{ mol}^{-1}$ ) as the entropy of fusion of polyethylene ( $9.9 \text{ J K}^{-1} \text{ mol}^{-1}$ ). The high temperature of the appearance of liquid PTFE is thus due to the disorder in the crystal, not a lesser entropy in the melt.

**Poly(oxybenzoate-co-oxynaphthoate).** Figure 2.64 represents an even more complicated polymer system. In this case the macromolecule is the random copolymer poly(oxybenzoate-co-oxynaphthoate), a high-strength material (Vectra<sup>TM</sup>).

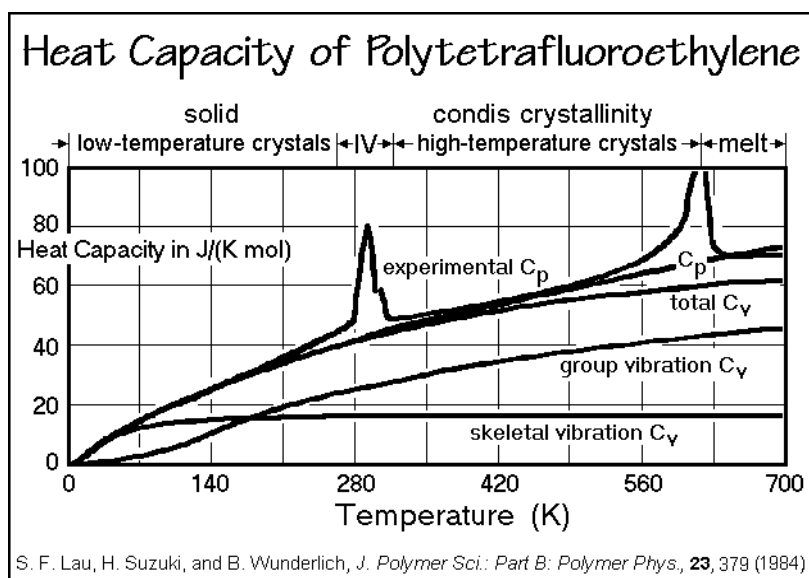


Fig. 2.63

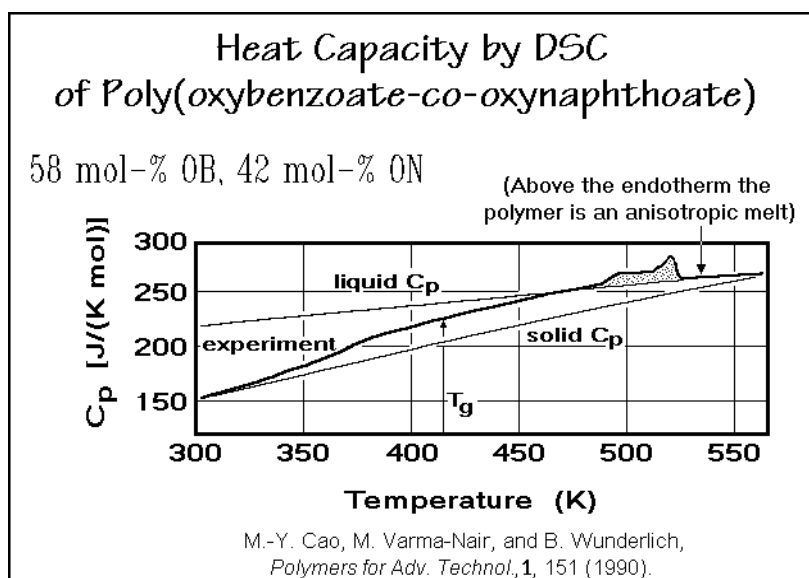
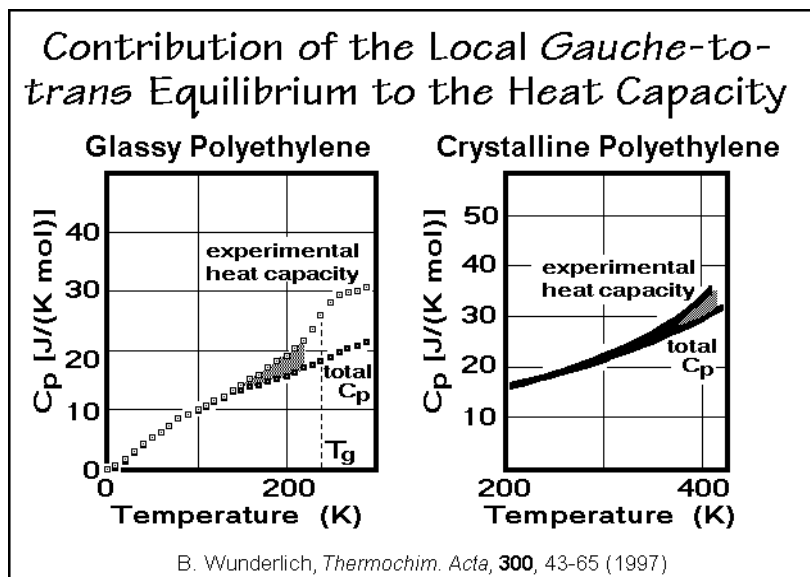


Fig. 2.64

The graph shows a rather small endotherm and a broad, possibly two-stage glass transition which stretches over more than 100 K. Without precise computation of the liquid and solid heat capacities, it would not have been possible to identify the glass transition and provide important characteristics for the practical application of the polymer. The broad glass transition is caused by the small amount of ordering in the

copolymer that produced a nanophase-separated structure with each molecule traversing many different nanophases. A similar broadening of the glass transition is found for all semicrystalline polymers (see Sect 6.3.4).

**Large-amplitude motions of polyethylene.** The increasing deviation from the glassy or crystalline vibrational heat capacity of polyethylene with temperature was already noted in Figs. 2.46 and 2.51. In Fig. 2.65 these two effects are compared side-by-side. The glassy polyethylene shows local *gauche-trans* exchanges down to almost 100 K. With mechanical measurements this has been identified as the  $\gamma$ -transition. This small increase in heat capacity has also been mistaken as the glass transition, which, however, is clearly seen at 237 K. A similar increase in heat capacity occurs for the crystalline polyethylene. It could also be linked to the local formation of dynamic *gauche*-defects in the crystals (see Sects. 5.3 and 5.5). One expects that these small increases in heat capacity are indicative of the possibility of plastic deformation. Many other polymers have similar gradual beginnings of the increase in heat capacity at the glass transition and also before melting.



**Fig. 2.65**

**Polymethionine.** Figures 2.66 and 2.67 illustrate the analysis of the heat capacity of anhydrous, solid polymethionine, a synthetic poly(amino acid) with the structural formula  $[\text{CH}(\text{CH}_2-\text{CH}_2-\text{S}-\text{CH}_3)-\text{CO}-\text{NH}-]_x$ . This is only one of the 20 poly(amino acids) that can be made out of the naturally occurring amino acids and were analyzed for the data bank (see Appendix 1). These data form the basis for the addition scheme of protein heat capacities. Of particular interest is the positive deviation starting at room temperature or maybe even earlier. It was suggested that this increase in heat capacity may be connected with a glass transition involving the side groups of the polymer. Confirmation of this suggestion is still pending and could have important implications for the understanding of proteins.

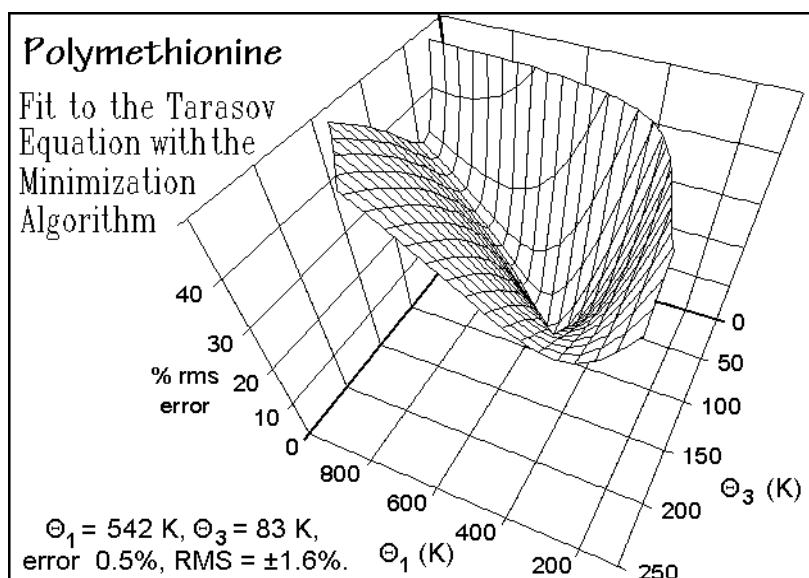


Fig. 2.66

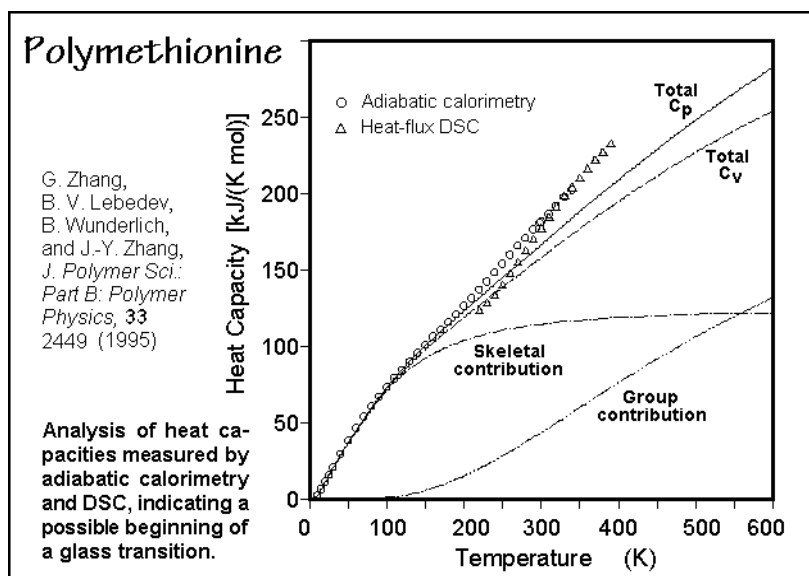


Fig. 2.67

**MBPE-9.** Macromolecules that contain aliphatic and aromatic sequences in their backbone structure have special possibilities to exist as liquid crystals or as condisc crystals (see Sect. 2.5). The thermal analysis of a polyether based on the semi-flexible mesogen 1-(4-hydroxyphenyl)-2-(2-methyl-4-hydroxyphenyl)ethane is copied in Fig. 2.68. The computed vibration-only heat capacity is reached somewhat

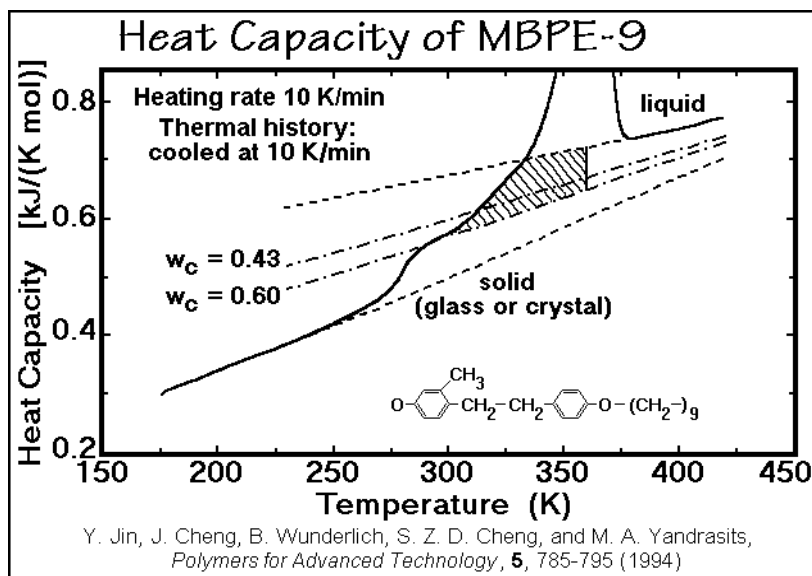


Fig. 2.68

below the glass transition, but above the glass transition the heat capacity does not reach the computed value expected from the crystallinity derived from the heat of fusion ( $w_c = 0.43$ ). One assumes that there is some rigid-amorphous fraction present. Furthermore, the entropy of fusion indicates considerable conformational disorder in the crystal that freezes in its own *glass transition*, indicated by the cross-hatched area. The rigid-amorphous phase is discussed in Sects. 6.1.3 and 6.3.4.

**Liquid selenium.** The heat capacity of liquid selenium, which is also a linear macromolecule, illustrates the effect of a chemical equilibrium. The heat capacity for many liquid, linear macromolecules increases linearly with temperature, despite the fact that one expects an exponential increase in  $C_v$  from the vibrational contributions of the C-H-bending and -stretching vibrations. To understand this observation, one has to remember that a decreasing heat capacity contribution with temperature results from the changes of the heat capacity from vibrational motion to rotational motion. Also the hole-theory of liquids, discussed in Sect. 6.1.3, includes a decrease in the hole contribution to the heat capacity since it is calculated similar to the case of two energy states, (see Fig. 2.33). The maximum in heat capacity occurs close to the glass transition temperature. The subsequent decrease seems to be able to compensate most of the vibrational increases in heat capacity for a considerable temperature range. Looking now at the heat capacity of the monatomic, liquid selenium, one finds that there are no group vibrations to produce the exponential increase in  $C_p$  and, indeed, the heat capacity of the liquid Se decreases with temperature from the glass-transition temperature. The decrease in  $C_p$  is nonlinear. At high temperature, however,  $C_p$  increases again. These changes in heat capacity with temperature are specific to Se, and an explanation is given in Fig. 2.69. Curve 1 represents the experimental data, curve 2, the vibrational contributions as derived from the crystalline vibrational spectrum. The difference between curves 1 and 3

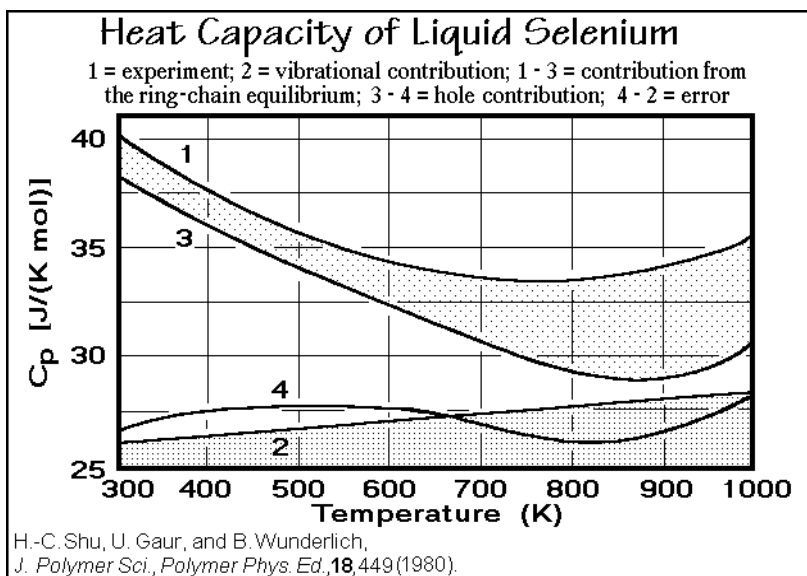
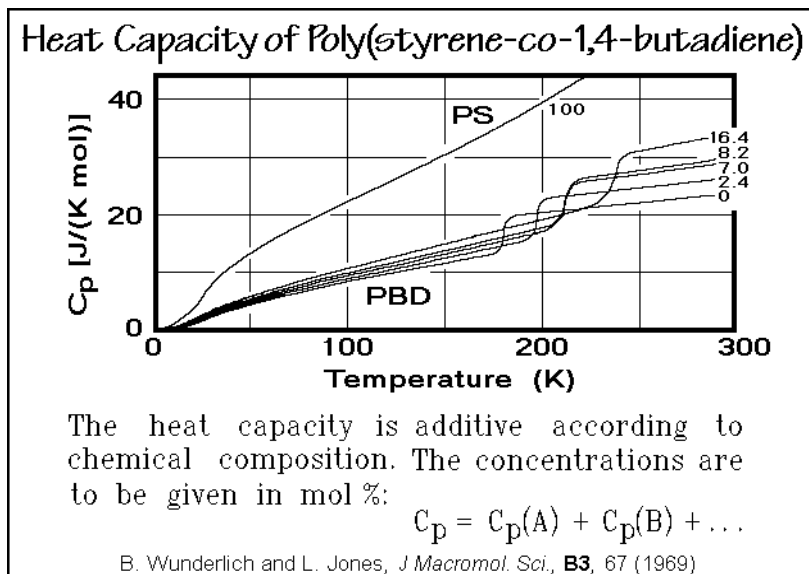


Fig. 2.69

represents the special contribution to the heat capacity that arises from the ring-chain equilibrium, i.e., from a chemical reaction. The melt of selenium consists of very long macromolecules  $(\text{Se-})_x$  and rings (mainly  $\text{Se}_8$ ). The two components are in a temperature-dependent chemical equilibrium, and the difference between curves 1 and 3 is an estimate of the heat of reaction per kelvin of a temperature increase for this process. Finally, the difference between curves 3 and 4 is an estimate of the heat capacity due to the hole equilibrium. It decreases with temperature, as expected. The agreement between curves 4 and 2 is, finally, a measure of the quality of the model that was chosen for the interpretation of the change of heat capacity with temperature. Selenium represents thus a case where a chemical heat of reaction (latent heat) is included in the measurement of heat capacity.

From the addition scheme of heat capacities, it is possible to deduce the heat capacity of another, hypothetical, monatomic polymeric chain, namely  $(\text{O-})_x$ . Its heat capacity is estimated by subtracting the  $(\text{CH}_2)_C$  contribution to the heat capacity from the total heat capacities of the polyoxides which are shown in Fig. 2.59. As in the Se heat capacities, the heat capacities of  $(\text{O-})_x$  decrease with temperature.

**Poly(styrene-co-1,4-butadiene).** To describe heat capacities of copolymers, it is naturally impossible to measure each and every composition. But since the heat capacities in the solid state at temperatures above, perhaps 100 K, are close-to-additive with respect to composition, and the same is true for the liquid states, estimates can be made of the heat capacities of all copolymers. Figure 2.70 shows the additivity of the heat capacities of poly(styrene-co-1,4-butadiene). These measurements were done many years ago by adiabatic calorimetry, and it was possible later to derive the heat capacity of the copolymers from their molar composition and the heat capacities of the constituent homopolymers. As indicated in the equation, it is also possible to add more than two components. A conspicuous

**Fig. 2.70**

feature of the 1,4-polybutadiene and copolymer heat capacities is the increase in temperature of the glass transition with styrene composition. The glass transition of pure polystyrene occurs at 373 K. The changes of glass transition temperature with concentration are discussed in Chap. 7. Comparing now the heat capacity measured by calorimetry with the heat capacity calculated from the addition scheme, one finds an error between 0 and 4% from 10 K to the beginning of the glass-transition region. But even above the glass-transition temperature, the additivity works well. The errors are less than 5%. Note that for the addition scheme contributions of both components, the butadiene as well as styrene, must be taken as their liquid heat capacities as soon as the copolymer glass-transition temperature has been exceeded. Position and breadth of the glass transition has to be predicted from other considerations.

**Hypothetical entropy of the liquid at absolute zero of temperature.** This topic was raised many years ago when extrapolating the heat capacity of the liquids in Figs. 2.59–61 to absolute zero and estimating the entropy, as outlined in Fig. 2.23. Since the heat capacity of the (metastable) liquid below the melting temperature is higher than that of the crystal, the step in entropy seen in Fig. 2.23 becomes less and finally reaches zero at the so-called Kauzmann temperature, 145 K for polyethylene. The third law of thermodynamics in Sect. 2.2.4, however, is hard to be reconciled with an amorphous structure of an entropy smaller than zero. The glass transition which intervenes below 237 K slows the structure rearrangements required for the liquid, so that the measured heat capacity drops and leaves a positive entropy of 2.59 J K<sup>-1</sup> mol<sup>-1</sup> at zero kelvin. Experimentally, thus, the entropy of the liquid at zero kelvin cannot be reached, but what if one could make sufficiently slow experiments to follow the liquid to low temperatures would the entropy be positive? Figure 2.71 suggests that these linear extrapolations of the liquid heat capacities of polymers shown in Figs. 2.46 and 2.59–61 are not correct at such low temperatures. The heavy

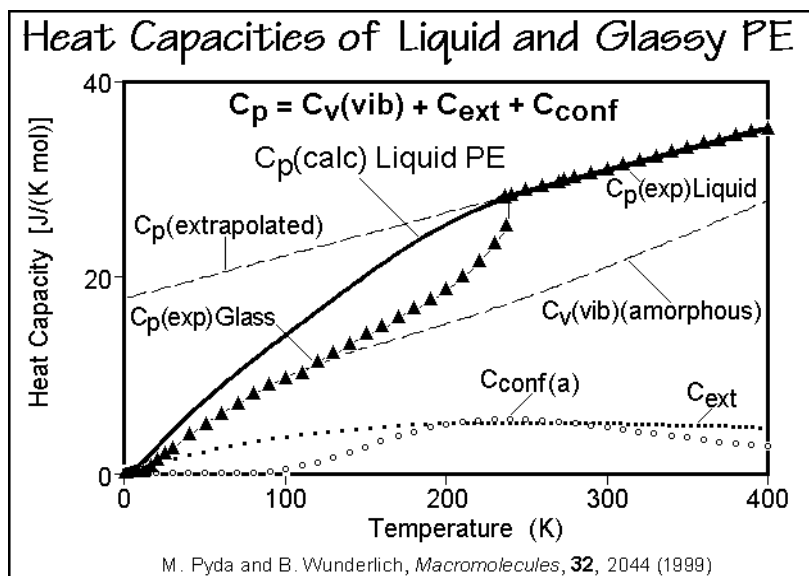


Fig. 2.71

black line was calculated accounting for the conformational energy difference, cooperativity along the chain, and the external contribution which can be approximated by  $C_p - C_v$ . All three contributions are indicated in the figure. At high temperature, the fit to the experimental data of Fig. 2.46 is quite perfect, but the extrapolation below the glass transition temperature is far from linear. Figure 2.72 shows the corresponding entropy calculation. Instead of a negative entropy at zero

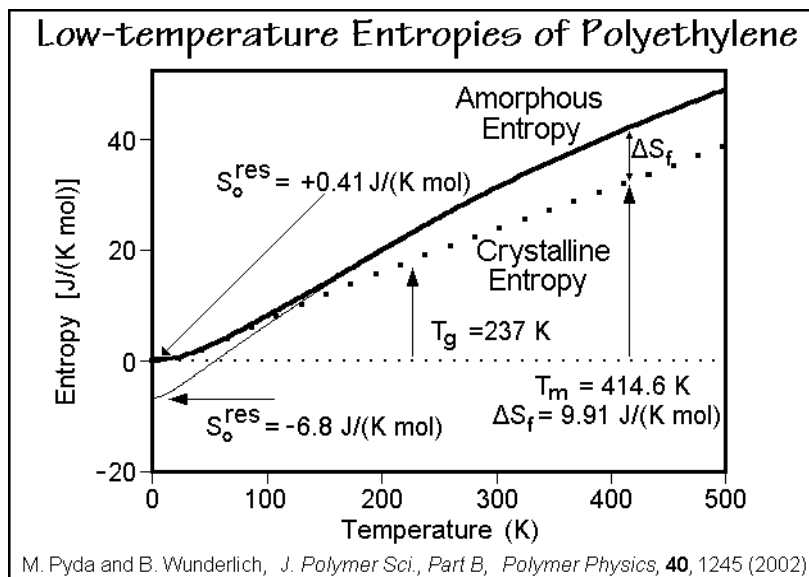
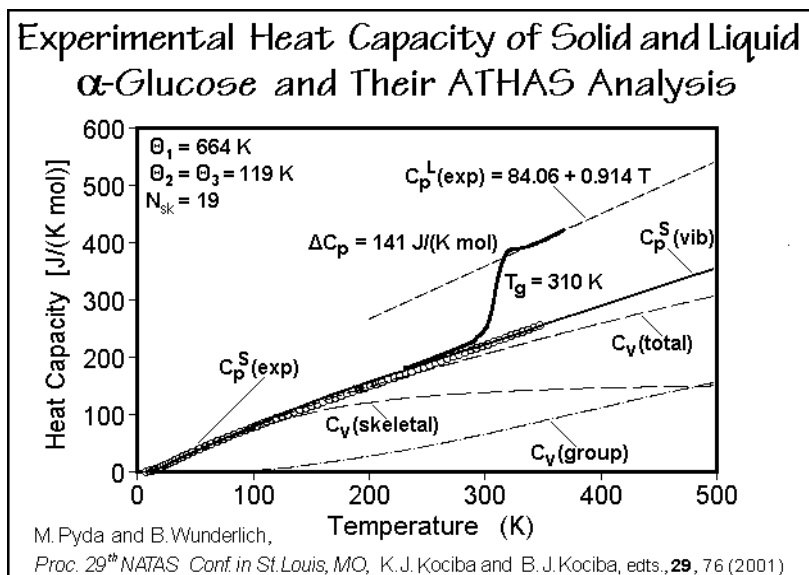


Fig. 2.72



kelvin of  $-85 \text{ J K}^{-1} \text{ mol}^{-1}$  which a linear extrapolation of  $C_p$  would have given, one reaches now  $-6.8 \text{ J K}^{-1} \text{ mol}^{-1}$ . A minor correction for the external contribution which is based on experiments at high temperature to account for the decrease in the conformational motion yields the indicated residual entropy at zero kelvin of  $+0.41 \text{ J K}^{-1} \text{ mol}^{-1}$ . This refutes, at least for polyethylene, what is called the Kauzmann paradox, a negative entropy at zero K. Note, that the free enthalpy  $G$  has no such problem. The free enthalpy of the liquid is identical to that of the crystal at the equilibrium melting temperature as shown in Fig. 2.23. Relative to the crystal, it increases when approaching zero kelvin, where it reaches  $+2.1 \text{ kJ mol}^{-1}$ , indicating a substantial metastability of the liquid. The heat of fusion at the melting temperature is  $4.11 \text{ kJ mol}^{-1}$ , and it decreases at zero kelvin to half of this value.

**Starch and water.** The final example of the analysis of heat capacities of linear macromolecules concerns the biological carbohydrates. Figure 2.73 illustrates as a first step the standard ATHAS analysis of the small molecule glucose, a key building block of the carbohydrates. Although glucose is not a linear polymer, the fitting to a vibrational skeletal and group-vibration spectrum is possible for the solid (glassy) state, and the melt yields a straight-line temperature dependence of the heat capacity as seen for the linear macromolecules in Figs 2.46 and 59–61. Using in a first step the heat capacity of liquid glucose as an estimate for the heat capacity of liquid starch, a polymer made out of glucose monomers with repeating 1,4-glucopyranose links, a similar heat capacity analysis is possible as displayed in Fig. 2.74. Besides the basic thermodynamic information available from the heat capacity information on amorphous, glassy starch, one can see that there is an increase of the heat capacity above room temperature. From the experience gathered in this section, one might interpret this increase in heat capacity as the beginning of the glass transition when compared to the polyethylene displayed in Fig. 2.46. The starch starts decomposing



**Fig. 2.73**

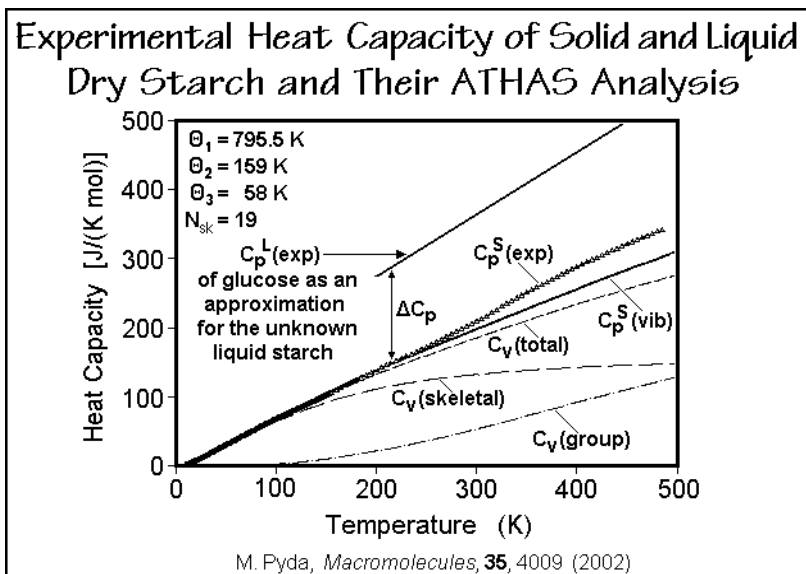


Fig. 2.74

on heating long before the glass transition is completed and the heat capacity has reached the level expected for starch from the liquid glucose. Adding water to the starch, an important process in the food industry, the results of Fig. 2.75 have been obtained. The beginning of the glass transition of the starch is moved to lower temperature and in addition to the transition already seen in the amorphous, glassy starch, there is a second step in the glass transition, also not reaching the expected

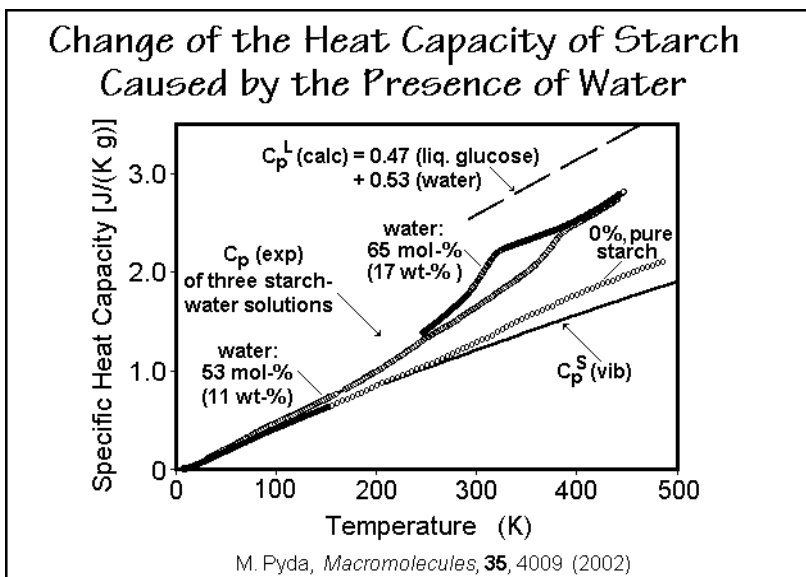
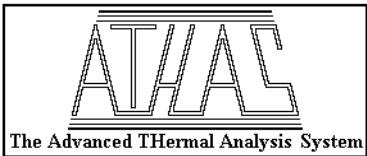


Fig. 2.75

heat capacity as derived from the glucose. Above 450 K, thus, there must be a third step in the devitrification of starch and water system. The next step in this analysis is the identification of the molecular motion responsible for the stepwise increase in large-amplitude motion, this research is not completed yet. Furthermore, the phase diagram of the partial molar quantities needs to be evaluated for all thermodynamic functions, as outlined in Fig. 2.25.

**Conclusions.** The heat capacity is one of the few macroscopic quantities with a well-understood link to the microscopic molecular motion. The Advanced Thermal Analysis System displayed in Fig. 2.76 allows to establish empirical addition schemes



The Advanced THERmal Analysis System

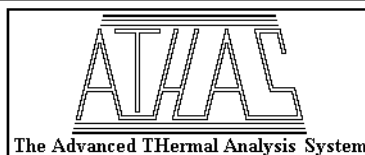
The Advanced THERmal Analysis System was developed in the 1980's to be able to interpret the heat capacities of linear macromolecules more precisely. In the solid state, the heat capacity is described by contributions from the vibrations of an approximate spectrum. Any deviation is a sign of additional processes, usually conformational disordering or motion. In the liquid state extensive addition schemes based on group contributions have been developed to judge heat of fusion baselines and increases in heat capacity on devitrification at  $T_g$ .

General descriptions: B. Wunderlich and S. Z. D. Cheng, *Gazz. Chim. Italiana*, **116**, 345 (1986); B. Wunderlich, *Shin Netsu Sokuteino Shimo*, **1**, 71-100 (1990); B. Wunderlich, *Pure Appl. Chem.*, **67**, 1919 (1995). Experimental data: ATHAS data bank, request newest copy from the author: U. Gaur, S.-F. Lau, H.-C. Shu, B. B. Wunderlich, M. Varma-Nair, and B. Wunderlich, *J. Phys. Chem. Ref. Data*, **10**, 89, 119, 1001, 1051 (1981); **11**, 313, 1065 (1982); **12**, 29, 65, 91 (1983); and (1990), **20**, 349-404 (1991). See also our Internet address: [web.utk.edu/~athas](http://web.utk.edu/~athas)

**Fig. 2.76**

to compare similar structures and permit estimation of heat capacities of unknown materials. Figure 2.77 summarizes such addition schemes and their limits at low temperature were shown above in Sect. 2.3.7 to be caused by the nonlinear sum of the skeletal vibrations. A second step in ATHAS is the evaluation of the baseline of vibration-only heat capacity from the analysis of low-temperature solids of linear macromolecules, as well as related monomers. The key to this analysis is the separation of the frequency spectrum into group vibrations whose frequencies are experimentally available from Raman and IR data without calorimetric input, and skeletal vibrations, which can at present only be fitted to experimental data using two or three fitting parameters, the theta temperatures of Fig. 2.50. Figure 2.78 gives a schematic of the handling of the experimental data and the generation of the parameters for the calculations needed for the extrapolation into temperature ranges not available experimentally. The changes in the types of motion from the expected data can be found with the help of a fast, quantitative thermal analysis described in Chap. 4. Based on the accumulation of calorimetric data and evaluation together with kinetic information discussed in Chap. 3 and structural information discussed in

## Addition Scheme of Heat Capacities



The addition scheme of heat capacities rests on the additivity of the heat capacities of the backbone atom groupings and perhaps also side groups. The discussions in the text have shown that above 50 to 100 K this addition scheme works reasonably well and can be made use of, to estimate heat capacities for the many polymers and also copolymers not measured. The heat capacity of a poly(pentamethylene terephthalate) (PPT) could thus be calculated in the following way:

$$C_p(\text{PPT}) = 5x C_p(\text{CH}_2-) + 2x C_p(\text{CO-O-}) + C_p(\text{C}_6\text{H}_4-).$$

Reference and tables: U. Gaur, M.-Y. Cao, R. Pan, and B. Wunderlich, *J. Thermal Anal.*, **31**, 421 (1986); and part II: R. Pan, M.-Y. Cao, and B. Wunderlich, *J. Thermal Anal.*, **31**, 1319 (1986).

Fig. 2.77

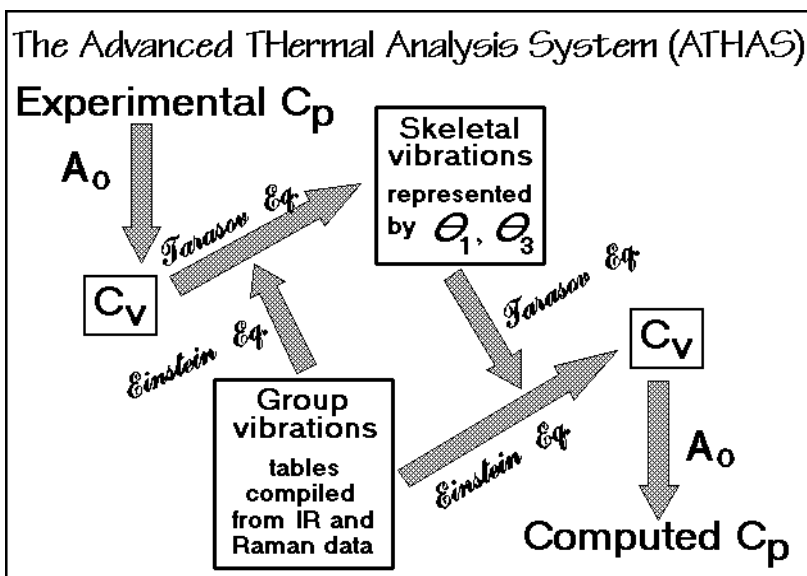
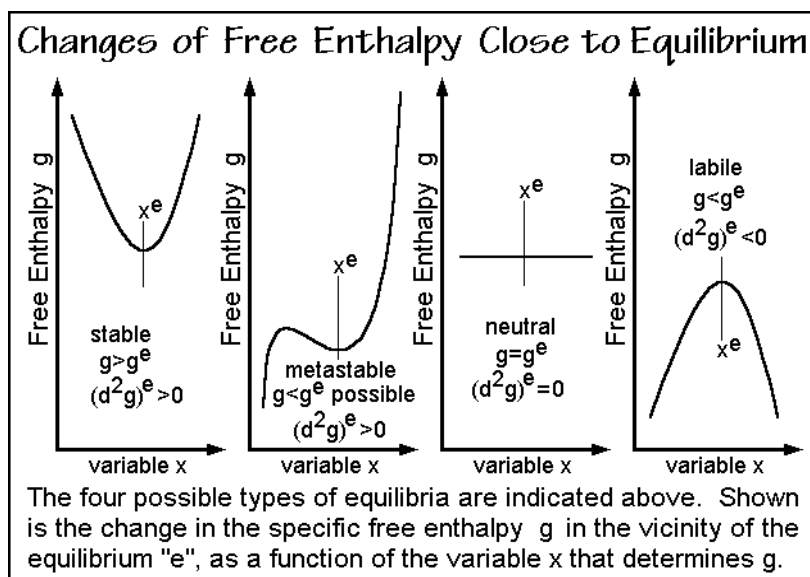


Fig. 2.78

Chap. 5, it is possible to interpret the behavior of polymeric materials as is described in more detail on-hand of a larger series of examples in Chaps. 6 and 7. The understanding of polymeric materials at this level has the goal to predict properties before samples become available, a result of great importance because of the unlimited number of macromolecules possible.

## 2.4 Nonequilibrium Thermodynamics

For the understanding of thermal analysis, it is necessary to recognize that most encountered polymeric systems are not in equilibrium, may be micro- or nanophase separated, and could even be not homogeneous. In order to describe such situations, one has to turn to nonequilibrium, irreversible thermodynamics. Functions of state such as entropy and free enthalpy are defined for systems in global equilibrium. Some others, such as mass, volume, and total energy, on the other hand, are largely indifferent to equilibrium. They need special treatment to be used for the description of nonequilibrium situations which arise when deviating from the free enthalpy minimum characteristic for equilibrium, as shown in Fig. 2.79. The four possible functional forms of the free enthalpy lead to stable, metastable, neutral, and labile equilibria.



**Fig. 2.79**

The next step of importance is the description of inhomogeneous systems in terms of local equilibria. This process involves the division of the system to be described into subsystems, as discussed in Sect. 2.2.1, and shown in the upper half of Fig. 2.80. This is to be followed by the description of the system as a function of time as an additional variable. Following the system as a function of time allows the study of the kinetics of the processes seen when approaching equilibrium. Finally, it may be necessary to identify additional, internal variables to describe the nonequilibrium states as a function of time. The kinetics of polymers may be sufficiently slow to decouple consecutive steps. For very slow responses, it may lead to arrested equilibria, such as seen in materials below their glass transitions as described in Sect. 2.4.4. The following Section makes use of the just summarized concepts in an attempt to achieve a depiction of the nonequilibrium state of macromolecules.

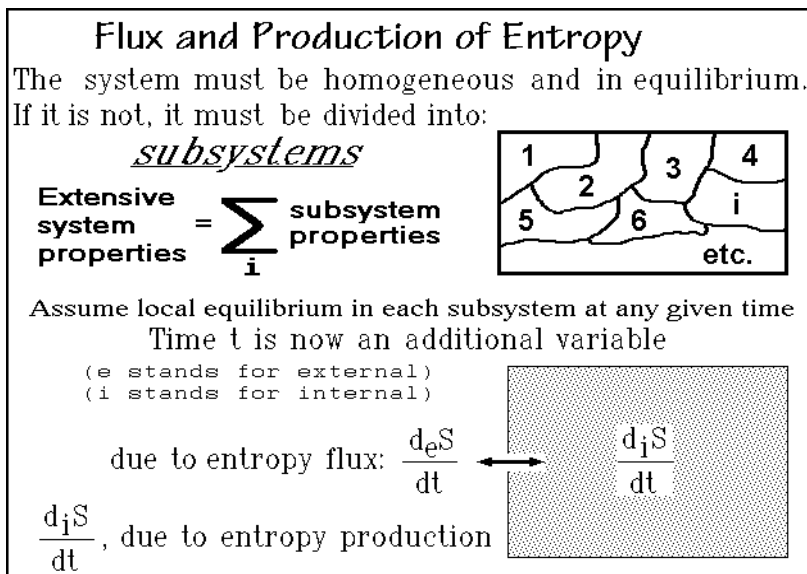


Fig. 2.80

### 2.4.1 Flux and Production

To describe the overall change of entropy in a system or subsystem with time,  $dS/dt$ , one makes a division into a term due to entropy flux,  $d_e S/dt$ , which gives the flow across the boundary, and to entropy production,  $d_i S/dt$ , which gives the internal entropy changes. The sketch in the lower part of Fig. 2.80 illustrates this statement. Equation (1) in Fig. 2.81 expresses the time dependence of the total rate of change of entropy of the system in terms of the flux and production. Calorimetry can give information on the heat-flow rate,  $dQ/dt$ , at constant temperature and pressure as it changes the entropy of a closed system described in Fig. 2.16. Since the temperature of the closed system is constant within the boundaries during  $dt$ , the heat flux can be considered reversible. The overall irreversibility caused by a higher temperature outside the boundaries, needed to bring about the heat flux, is pushed outside of the boundary and, thus, is of no importance to the description of the system.

For the open system of Fig. 2.16, one must express the entropy-flow rate as written in Eq. (2) of Fig. 2.81. Besides the entropy change due to the heat flux, there is an entropy change due to the flux of matter. The matter flux of component  $i$  is expressed by its flow-rate term,  $d_e n_i/dt$ . The matter flux can be measured, for example, by thermogravimetry as listed in Fig. 2.16. Each flux of matter across the boundary of the system,  $d_e n_i$ , needs to be multiplied with the partial molar change in the corresponding entropy,  $S_i^*$  [ $= (\partial S/\partial n_i)_{T,p}$ , see Fig. 2.19], to obtain the total contribution to  $d_e S/dt$ . The change in partial molar entropy must be known, or be measured independently by heat capacity measurements, for example, from zero kelvin to  $T$ , as outlined in Figs. 2.22 and 2.23.

<b>Flux and Production of Entropy</b>	
<p>(1) <math>\frac{dS}{dt} = \frac{d_e S}{dt} + \frac{d_i S}{dt}</math>            terms due to: flux + production</p> <p>(2) <math>\frac{d_e S}{dt} = \frac{1}{T} \frac{dQ}{dt} + \sum_i S_i^* \frac{d_e n_i}{dt}</math>            from heat flux + matter flux            calorimetry + thermogravimetry</p> <p>(3) <math>d_i S &gt; 0</math>            for spontaneous processes            (second law result)</p> <p>(4) <math>d_i U = 0</math></p> <p>(5) <math>d_i M = 0</math>            conservation laws for            energy and mass</p>	<div style="border: 1px solid black; padding: 5px; margin-bottom: 10px;">             for an open system              at constant T and p:  <math>\frac{d_e n_i}{dt} =</math>              rate of flux of matter              across the boundary           </div> <div style="border: 1px solid black; padding: 5px;"> <math>S_i^* =</math> molar change in entropy              due to flux of one mole              of substance i into the              system or subsystem    <math>Q =</math> heat  <math>T =</math> system temperature           </div>

**Fig. 2.81**

More difficult is the evaluation of the rate of entropy production  $d_i S/dt$ . Entropy production cannot be measured directly, but one can make a number of general statements about it using the second law of thermodynamics treated in Figs. 2.17–2.20. Note that by separating the flux terms, one can treat the remaining production as being the changes in a hypothetical isolated system without flux. This hypothetical isolated system behaves like a small universe, meaning that the overall entropy statements of the second law apply:  $d_i S$  must increase for a spontaneous process as written in Eq. (3) of Fig. 2.81. A constant  $_i S$  indicates equilibrium ( $d_i S = 0$ ), and a negative  $d_i S$  has not been observed. In irreversible processes there is always an entropy production.

Other production terms are also restricted. The change  $d_i U$ , for example, must always be zero, since energy is conserved. All changes of  $U$  must come from flux across the boundary. Similarly, the change in mass,  $d_i M$ , must be zero. One cannot produce new mass. Equations (4) and (5) are expressing these conservation laws for energy and mass.

With this description of open and closed systems, melting and reorganization of lamellar crystals is treated next as an example of the irreversible thermodynamics of defect polymer crystals and their melting [24]. The added variable for the description of lamellae is the shape of the crystal. A more general treatment of internal variables is given in Sect. 2.4.4, and the detailed time-dependence of the processes is discussed in Sects. 2.4.5 and 2.4.6.

## 2.4.2 Melting of Lamellar Crystals

Most macromolecular, lamellar crystals are only about 10 nm thick (see Sect. 5.2), i.e., their surface area is about  $200 \text{ m}^2 \text{ g}^{-1}$ . For any reasonable specific surface free energy, such a large surface will lead to a sizeable metastability, overshadowing most

other defect contributions. The melting kinetics of such thin, lamellar crystals, is discussed further in Sect. 3.6, and a larger set of experimental data on melting of polymer crystals is given in Sect. 6.2. The sketch of Fig. 2.82 shows schematically a diagram for the flux of heat into a closed calorimeter as used for thermal analysis,

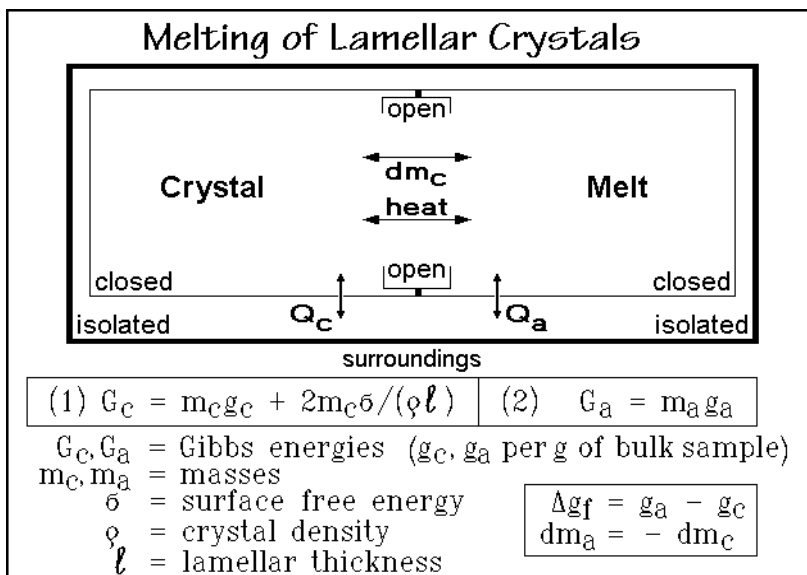


**Fig. 2.82**

and the production term caused by changing the crystal-to-melt ratio by flux across an open, internal boundary between crystal lamellae and melt. The lamellar crystal is the system with a total free enthalpy of  $G_c$ . As long as the lamellae in the sample are of the same thickness, have large lateral dimensions (so that the surfaces on the sides can be neglected), and are free of temperature and pressure gradients, all crystals can be described together as a single system or subsystem. If this were not so, one would have to sum over different subsystems, by either making measurements for every subsystem, a perhaps impossible task, or by deconvolution of the observed heat of fusion (see, Chap. 6, Fig. 6.3).

The amorphous part of the usually semicrystalline polymer and the melt produced on fusion are assumed to be coalesced to a single, amorphous system or subsystem with the free enthalpy  $G_a$ . If this were not so, additional amorphous subsystems would have to be introduced, and, if these subsystems are small, their surface effects would have to be considered via their area and the specific surface free energies. This leads, again, to experimental problems that are difficult to resolve.

The whole sample, consisting of crystals and melt, is enclosed in the sample holder of the calorimeter (see Sects. 4.2–4.4), making it the overall closed system, isolated from the surroundings. As melting progresses, mass is transferred in Fig. 2.82 from the left to the right. On crystallization, the mass transport goes in the opposite direction. The heat transport across the open boundary is minimal since it is assumed that the calorimeter remains at constant temperature.



The heat exchange into the crystalline system from the outside is given by  $Q_c$ , the heat exchange to the amorphous system by  $Q_a$ . The lamellar crystals are described by the overall free enthalpy of Eq. (1) in Fig. 2.82, with  $m_c$  representing the mass of the lamellar crystal;  $g_c$ , the specific free enthalpy per gram of bulk crystal;  $\ell$ , the lamellar thickness;  $\rho$ , the density; and  $\sigma$ , the specific surface free energy. The side surface areas are, as suggested above, negligible. The amorphous system has a free enthalpy  $G_a$ , simply described by  $m_a g_a$ , as shown by Eq. (2). The free enthalpy of the amorphous subsystem is, thus, assumed to be described by an extrapolation of  $G_a$  from above the melt.

On melting, the change in free enthalpy of the bulk crystal is given in Fig. 2.82 by the boxed expression  $\Delta g_f = g_a - g_c$ , where  $\Delta g_f$  represents the specific free enthalpy of fusion of a large crystal. One more simplifying fact arises from the schematic drawing. The change in mass of the amorphous system,  $dm_a$ , has to be equal to the negative of the change in mass of the crystalline system,  $dm_c$ . There is conservation of mass within the closed system. The infinitesimal entropy flux  $d_e S$  during melting is given next in Fig. 2.83. It is derived directly from the heat flow, measured by thermal analysis.

**Melting of a Single Lamella  
at Constant Pressure  $p$  and Temperature  $T$   
in the Time Interval  $dt$**

$$d_e S = (dQ_c + dQ_a)/T \quad (\text{flux term, measurable by thermal analysis})$$

$$\Delta g_f = \Delta h_f - T\Delta s_f = \Delta h_f - T\Delta h_f/T_m^0 = \Delta h_f \Delta T/T_m^0$$

$$d_i S = \underbrace{\frac{\Delta g_f dm_c}{T}}_{\text{melting term}} - \underbrace{\frac{2\sigma dm_c}{T\phi\ell}}_{\text{reorganization}} + \frac{2m_c\sigma d\ell}{T\phi\ell^2}$$

**1. large  $\ell$  :**  
 equilibrium melting and crystallization.  $d_i S = 0$   
 crystallization with supercooling.  $d_i S > 0$   
 melting with superheating.  $d_i S > 0$

**2. small  $\ell$  :**  
 reorganization only.  $d_i S > 0$   
 crystallization and melting.  $d_i S > 0$   
 zero entropy production melting.  $d_i S = 0$

**Fig. 2.83**

Making use of Eqs. (1) and (2) of Fig. 2.82, it is possible to derive the overall entropy production  $d_i S$  as shown by the boxed equation in the center of Fig. 2.83. It is caused by the flux between the two subsystems of Fig. 2.82. For the derivation one assumes that the entropy of melting,  $\Delta s_f$ , does not change with temperature from its equilibrium value ( $\Delta h_f/T_m^0$ ) and writes that  $\Delta g_f$  is simply  $\Delta h_f \Delta T/T_m^0$  as shown in Fig. 2.83 with  $\Delta T = T_m^0 - T$ . The entropy production  $d_i S$  is, in contrast to  $d_e S$ , not directly measurable, but to keep the temperature constant, all enthalpy changes due to melting or crystallization were compensated by flux  $Q_a$  and  $Q_c$ .

The first two terms of entropy production in Fig. 2.83 describe the melting ( $dm_c < 0$ ) or crystallization ( $dm_c > 0$ ) as a flux across the internal boundary. Term  $\Delta g_f dm_c / T$  is the bulk-entropy change. Since on melting the surface of the lamella decreases, one has to introduce the loss in surface area, expressed by the second term  $[-2\sigma/(T\rho\ell)]dm_c$ . Overall, this term is positive on melting ( $dm_c < 0$ ) and negative on crystallization ( $dm_c > 0$ ).

The last term in the equation for  $d_i S$  of Fig. 2.83 is the entropy production term for the crystalline subsystem due to a change in thickness of the lamella by  $d\ell$ . For the present discussion this is the only change assumed to be possible on annealing. This simplification is based on the experience that annealing to larger fold length is often the most important type of reorganization. If there are other changes, such as a decrease in concentration of nonequilibrium defects, one would simply expand the equation by the appropriate terms.

The three terms of  $d_i S$  must obey the restrictions of the second law of thermodynamics: The entropy production can be zero or positive, but never negative. Crystals with a large  $\ell$  are treated first (list 1 in Fig. 2.83). In this case the last two terms of  $d_i S$  are negligible because they contain  $\ell$  in the denominator [i.e.,  $d_i S = (\Delta g_f / T) dm_c$ ]. This equation applies to perfect crystals with negligible surface areas. On melting and crystallization of such crystals under equilibrium conditions  $d_i S$  is zero since  $\Delta g_f$  is zero at the equilibrium melting temperature ( $T = T_m^\circ$ ). Equilibrium melting and crystallization is, as expected, always a zero-entropy-production process. The total entropy of transition is provided by the measurable entropy flux  $(dQ_c + dQ_a)/T_m^\circ$  (upper box of Fig. 2.83). The equilibrium melting can be visualized by the intersection of  $G_c$  and  $G_a$  in the free-enthalpy diagram of Fig. 2.84.

Whenever one crystallizes with supercooling, i.e., below  $T_m^\circ$ ,  $\Delta g_f$  is positive since  $\Delta h_f$  and  $\Delta T$  are positive and  $dm_c$  is positive, resulting in a positive  $d_i S$ . There is an entropy production, an indication that the process is permitted by the second law and can proceed irreversibly by a downward transition between corresponding free enthalpy curves shown in Figure 2.85. A quite similar heat flux  $dQ_c + dQ_a$  as in the equilibrium melting leads in this case to an entropy production because  $T < T_m^\circ$ . Similarly, if one melts with superheating, i.e., melting occurs above  $T_m^\circ$ ,  $\Delta g_f$  is negative, but  $dm_c$  is also negative so that  $d_i S$  is positive again. Melting under conditions of superheating is thus also permitted by the second law. Melting with supercooling or crystallization with superheating are, in contrast, both forbidden because of the resulting negative  $d_i S$ , in good accord with experience.

For the description of thin lamellae, as listed in group 2 of Fig. 2.83, all three terms for the entropy production,  $d_i S$ , must be considered. First, one assumes that there is no overall crystallization or melting, i.e.,  $dm_c = 0$ . A process that leads to changes in crystal thickness,  $d\ell$ , is reorganization or annealing. Only if  $d\ell$  is positive, is  $d_i S$  positive and allows spontaneous reorganization with entropy production. The reorganization can also be recognized in a free enthalpy diagram as given in Fig. 2.86. Lamellar crystals can only increase in thickness or stay the same, a fact commonly born out by experience. A few observed cases of thinning of lamellae are caused by a tilting of the chains in the crystal with a decreasing specific surface free energy or a change in defect concentration, overcompensating the increase in surface area. The second case is described for polyethylene in Sect. 6.2.1 with Fig. 6.34.

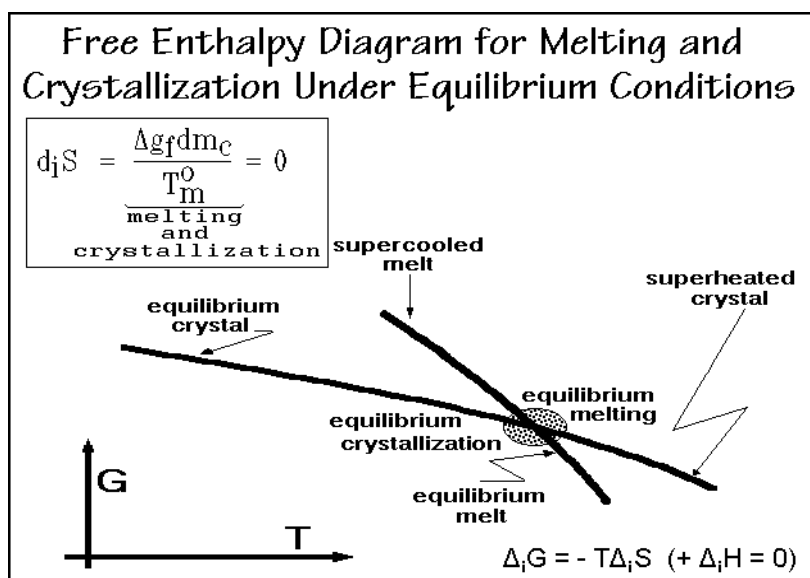


Fig. 2.84

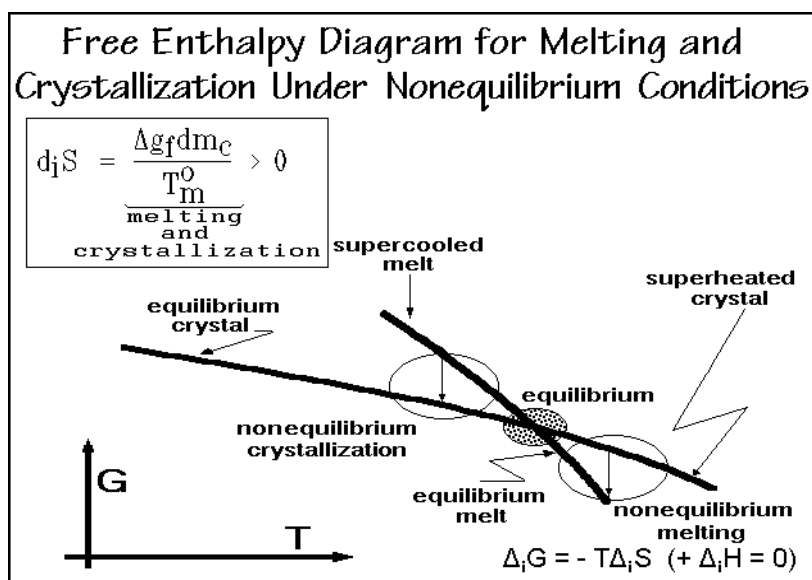


Fig. 2.85

Crystallization and melting of thin lamellae without reorganization ( $d\ell = 0$ ) show important differences from equilibrium melting and crystallization. Crystallization and melting is governed by the first two terms on the right-hand side of  $d_i S$  of Fig. 2.83  $[(\Delta h_f \Delta T / T_m^0) - \{2\sigma / (T\rho\ell)\}]$ . The second term,  $\{2\sigma / (T\rho\ell)\}$  is always positive, i.e., crystallization with a positive  $dm_c$  can only occur at a temperature

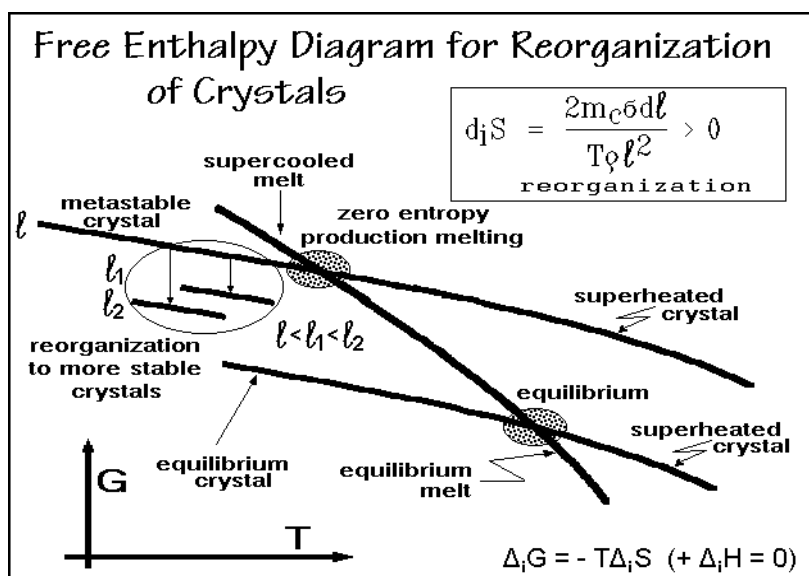


Fig. 2.86

below the equilibrium melting temperature to make  $(\Delta h_f \Delta T / T_m^\circ)$  sufficiently positive to give an entropy production. Similarly, melting can already occur at a temperature lower than the equilibrium melting temperature. Both cases are illustrated in the free enthalpy diagram of Fig. 2.87. The temperature where the two melting terms are equal is of prime importance for thermal analysis. It indicates a second zero-entropy-production melting, i.e., the  $d_i S$  term is zero, although it does *not* refer to an

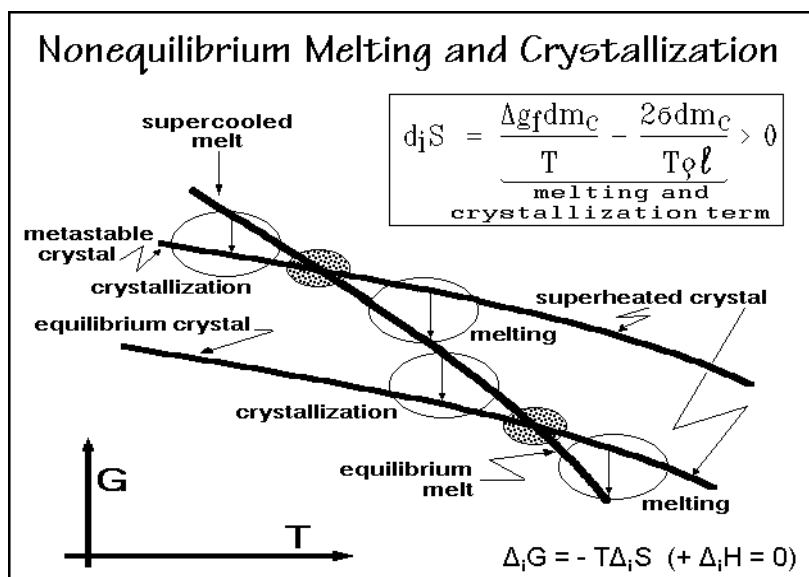


Fig. 2.87

equilibrium process. The metastable lamellae melt directly into a melt of equal metastability. The metastability of the melt is caused by being below the equilibrium melting temperature, at  $T_m$  of a thin crystalline lamella with a large surface free energy. Such melting looks superficially like equilibrium melting. The difference between the two zero-entropy-production cases is easily seen in the free enthalpy diagram of Fig. 2.4.88. Since heat capacities of crystals of different stability are usually similar (see Sect. 2.3), metastable free enthalpy curves are often parallel to equilibrium curves and can be superimposed by shifting from one  $T_m$  for zero-entropy-production melting to another.

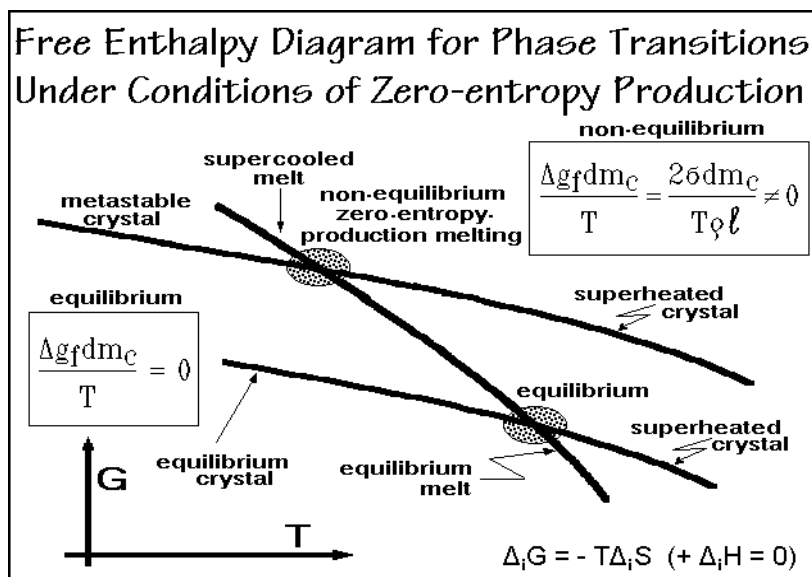


Fig. 2.88

### 2.4.3 Experimental Data

Experimental use of the zero-entropy production melting temperatures allows a study of metastable crystals. Crystallization, in contrast, always requires a supercooling due to crystal and molecule nucleation, as is discussed in Sects. 3.5 and 3.6. It is a simple matter to derive the equation for the zero-entropy-production melting temperature from the equation for  $d_i S$ , derived in the previous section (Fig. 2.83) and shown once more in Fig. 2.89. The measurable lowering in melting temperature from equilibrium,  $\Delta T$ , is given by the easily derived Gibbs-Thomson equation which contains the surface free energy  $\sigma$  and the lamellar thickness  $\ell$ . If one of the two latter quantities is known, the other can be calculated.

Thermal analysis data on lamellar crystals of polyethylene over a wide range of thicknesses are plotted in Fig. 2.90. The Gibbs-Thomson equation is a good mathematical description of the observed straight line and can be used to calculate the equilibrium melting temperature by setting  $\ell = \infty$  ( $T_m^\circ = 414.2$  K). Also, the ratio of the surface free energy to the heat of fusion can be obtained from the equation.

### Experimental Data for the Melting of Lamellar Crystals of Polyethylene

For zero entropy production:

$$0 = d_i S = \underbrace{\frac{\Delta g_f d m_c}{T}}_{\text{melting term}} - \underbrace{\frac{2\sigma d m_c}{T\phi l}}_{\text{reorganization}} + \frac{2m_c\sigma dl}{T\phi l^2}$$

If there are no crystallization, reorganization, and superheating:

$$\frac{\cancel{\Delta g_f d m_c}}{\cancel{T}} = \frac{\cancel{2\sigma d m_c}}{\cancel{T\phi l}}$$

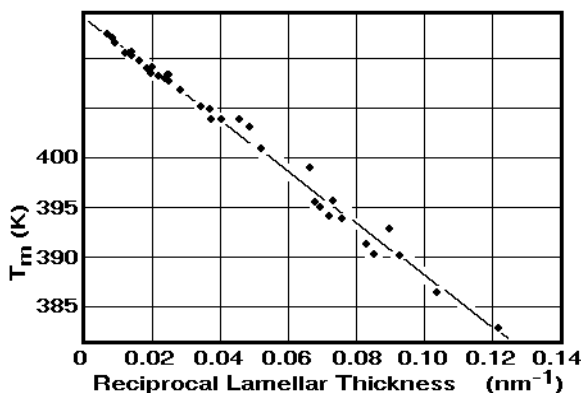
$$\Delta g_f = 2\sigma/\phi l$$

so that with  $\Delta g_f = \Delta h_f \Delta T / T_m^0$ :

$$\Delta T = (2\sigma T_m^0) / (\Delta h_f \phi l) \quad \text{Gibbs-Thomson equation}$$

Fig. 2.89

### Experimental Data for the Melting of Lamellar Crystals of Polyethylene



$$T_m = 414.2 \left(1 - \frac{0.627}{l}\right) \quad l \text{ in nm, error } \pm 0.8 \text{ K}$$

Fig. 2.90

#### 2.4.4 Internal Variables

The following treatment applies to homogeneous systems with constant mass. The dissipative, time-dependent effects are caused in such homogeneous systems by disturbance of the equilibrium of the internal, molecular degrees of freedom. The

internal, molecular degrees of freedom,  $\zeta_i$ , often do not appear in the description of the system because of existing relations to the fixed internal equilibrium, to be shown as Eq. (15), below. To better understand the processes, however, it is useful to first consider the variables  $\zeta_i$  explicitly. In the case of a glass transition, a single  $\zeta$  can be linked to the concentration of the microscopic vacancies in a liquid (number of holes,  $N_h$ , see Sects. 5.6 and 6.3). Similarly, the surface area of metastable crystals, as described in the previous two sections, could be expressed by a single  $\zeta$ . The actual time-dependence of the change of  $\zeta$  will be discussed in Sect. 2.4.6, the present discussion will deal with the equilibrium of a single internal variable  $\zeta$ .

The starting point for the description of the system considered is the Gibbs fundamental equation, Eq. (1), shown in Fig. 2.91 in terms of the specific quantities:

<b>Introduction of an Internal Variable</b>		
Gibbs equation with T, p, and $\zeta$ as independent variables:		
(1) $g(T, p, \zeta) = h(T, p, \zeta) - Ts(T, p, \zeta)$		
From Fig. 2.19 one can write:		
(2) $s = -\left(\frac{\partial g}{\partial T}\right)_{p, \zeta}$	(3) $h = g - T\left(\frac{\partial g}{\partial T}\right)_{p, \zeta}$	
Total differentials:		
(4) $dg = \left(\frac{\partial g}{\partial T}\right)_{p, \zeta} dT + \left(\frac{\partial g}{\partial p}\right)_{T, \zeta} dp + \left(\frac{\partial g}{\partial \zeta}\right)_{T, p} d\zeta$		
(5) $dh = \left(\frac{\partial h}{\partial T}\right)_{p, \zeta} dT + \left(\frac{\partial h}{\partial p}\right)_{T, \zeta} dp + \left(\frac{\partial h}{\partial \zeta}\right)_{T, p} d\zeta$		
(6) $ds = \left(\frac{\partial s}{\partial T}\right)_{p, \zeta} dT + \left(\frac{\partial s}{\partial p}\right)_{T, \zeta} dp + \left(\frac{\partial s}{\partial \zeta}\right)_{T, p} d\zeta$		
Partial molar quantities:		
(7) $a = -\left(\frac{\partial g}{\partial \zeta}\right)_{T, p}$	(8) $\sigma = \left(\frac{\partial s}{\partial \zeta}\right)_{T, p}$	(9) $\eta = \left(\frac{\partial h}{\partial \zeta}\right)_{T, p}$

**Fig. 2.91**

free enthalpy,  $g$ , enthalpy,  $h$ , and entropy,  $s$ , per unit mass, written in lower-case letters, compare to Fig. 2.19 and also [19]. Temperature,  $T$ , pressure,  $p$ , and the internal variable  $\zeta$  are the mutually independent variables. Also listed in the figure are the expressions for  $s$ , Eq. (2), and  $h$ , Eq. (3), and the total differentials with respect to the independent variables, Eqs. (4)–(6). The partial molar quantities of  $g$ ,  $s$ , and  $h$  with respect to  $\zeta$  at constant  $T$  and  $p$  are shown as Eqs. (7)–(9) and named:  $a$ ,  $\sigma$ , and  $\eta$ , respectively. The partial molar free enthalpy “ $a$ ” is commonly called the *activity* and has the significance of a driving force (see Sect. 2.4.6).

Equation (10) of Fig. 2.92 is the Gibbs equation for the corresponding partial quantities at constant  $T$  and  $p$ . At internal equilibrium (designated by the superscript “e”)  $a^e = 0$ , which leads to Eq. (11) and fixes one of the independent variables. At equilibrium, one can write with help of Eq. (10) and Eq. (12) the Eqs. (13) and (14) since  $da = 0$ . Finally, one can derive the change of the internal variable with temperature at equilibrium and constant pressure, as shown in Eq. (15).

(10)	$a = T\sigma - \eta$	Partial molar Gibbs equation
At equilibrium:		
(11)	$\zeta = \zeta^e(T, p)$	$(a^e = 0 \text{ and } T\sigma^e = \eta^e)$
(12)	$da = \left(\frac{\partial a}{\partial T}\right)_{p, \zeta} dT + \left(\frac{\partial a}{\partial p}\right)_{T, \zeta} dp + \left(\frac{\partial a}{\partial \zeta}\right)_{T, p} d\zeta$	
(13)	$\left(\frac{\partial a}{\partial T}\right)_{p, \zeta}^e = -\left(\frac{\partial^2 g}{\partial T \partial \zeta}\right)^e = -\left(\frac{\partial^2 g}{\partial \zeta \partial T}\right)^e = \sigma^e$	
From Eq. (7) (left) and Eq. (2) (right)		
(14)	$\left(\frac{\partial a}{\partial \zeta}\right)_{T, p}^e = -\left(\frac{\partial^2 g}{\partial \zeta^2}\right)_{T, p}^e$	
From Eq. (7). Inserting Eqs. (13) and (14) into Eq. (12) at constant p gives Eq. (15).		
(15)	$\left(\frac{\partial \zeta}{\partial T}\right)_p^e = \frac{\sigma_{T, p}^e}{\left(\frac{\partial^2 g}{\partial \zeta^2}\right)_{T, p}^e}$	Change of the internal variable maintaining internal equilibrium

**Fig. 2.92**

The specific heat capacity at constant pressure can be written as shown in Fig. 2.93, based on the relationship derived in Fig. 2.19. Insertion at constant pressure into Eq. (6) for  $ds$  (from Fig. 2.91) leads to the connection to the internal degree of freedom  $\zeta$ . The first term of the right-hand side of Eq. (16) is the heat capacity of the so-called arrested equilibrium ( $\zeta = \text{constant}$ ). This specific heat capacity is measured when the change in temperature occurs sufficiently fast that the

<b>Specific Heat Capacity at Arrested and Internal Equilibrium</b>	
From Fig. 2.91:	
(6)	$ds = \left(\frac{\partial s}{\partial T}\right)_{p, \zeta} dT + \left(\frac{\partial s}{\partial p}\right)_{T, \zeta} dp + \left(\frac{\partial s}{\partial \zeta}\right)_{T, p} d\zeta$
The heat capacity can be defined, as shown in Fig. 2.19, and given in Eq. (16). Insertion of $(ds/dT)_p$ from Eq. (6) and using Eq. (8) of Fig. 2.91 for $\sigma$ yields:	
(16)	$c_p = T \left(\frac{ds}{dT}\right)_p = T \left(\frac{\partial s}{\partial T}\right)_{p, \zeta} + T\sigma \left(\frac{d\zeta}{dT}\right)_p$
(17)	$c_{p, \zeta} = T \left(\frac{\partial s}{\partial T}\right)_{p, \zeta}$
Specific heat capacity at arrested equilibrium at a constant $\zeta$	
(18)	$c_p^e = c_{p, \zeta}^e + \Delta^e c_p$
Specific heat capacity at internal equilibrium, $\Delta^e c_p$ = contribution of the internal degree of freedom	

**Fig. 2.93**



internal degree of freedom cannot follow ( $\dot{\zeta} \ll \dot{T}$ ) and also if the internal degree of freedom is frozen ( $\dot{\zeta} = 0$ , because  $L \rightarrow 0$ ; see Sect. 2.4.6). For the example of the glass transition, this is the specific heat capacity of the solid,  $c_p^\circ$  (see Sects. 5.6 and 6.3). In internal equilibrium, one measures the specific heat capacity as expressed in Eq. (18), where  $\Delta^\circ c_p$  is the specific heat-capacity contribution of the internal degree of freedom  $\zeta$ .

## 2.4.5 Transport and Relaxation

Time-dependent processes are usually divided into transport phenomena and relaxation phenomena. The transport phenomena cause a move towards equilibrium by transport of, for example, heat, momentum, or mass if there is a difference in the corresponding intensive variables, temperature, pressure, or composition, respectively. Figure 2.94 shows a table of these common transport processes. Naturally there may also be changes of more than one intensive variable at one time. In this case the description of the overall transport processes is more complicated than represented next.

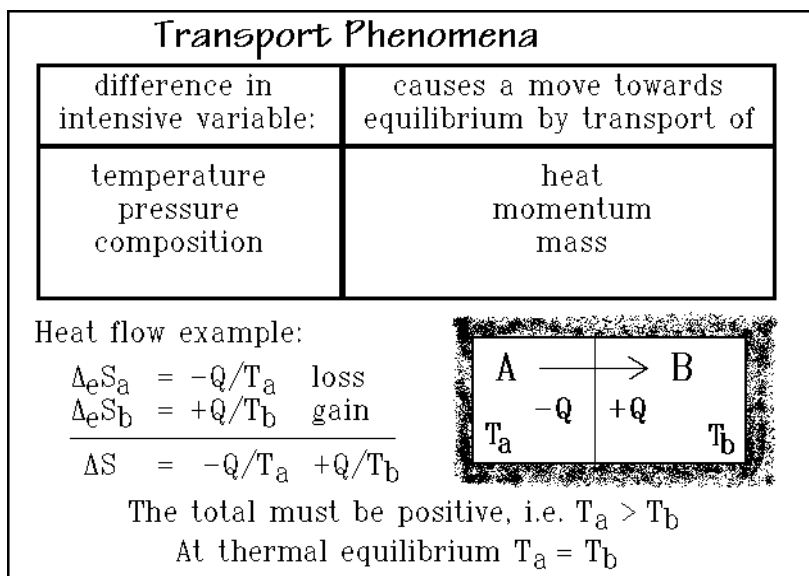


**Fig. 2.94**

For a transport process to occur, neighboring systems must have different intensive variables. Again, the actual irreversible process is pushed into the boundary between the systems. As an example, the description of heat flow is given in Fig. 2.94. One sets up a hot system, A, next to a colder system, B, both being isolated from the surroundings. The object is to follow the transport of an amount of heat  $Q$  in a given time span from A to B, which are closed towards each other. The entropy change in A is  $-Q/T_a$ , a loss. The entropy change in B is  $Q/T_b$ , a gain. The overall change in entropy,  $\Delta S$ , must, according to the second law, be positive for a

spontaneous process, i.e., cause an entropy production. This happens whenever  $T_a$  is larger than  $T_b$ , as assumed in the figure. Heat flow in the opposite direction would be forbidden by the second law. Note that the absolute magnitude of the heat flux  $Q$  is the same in both systems, but the entropies are different.

Relaxation phenomena do not produce any transport, but they do produce a change in an internal degree of freedom, as discussed in Sect. 2.4.4. An internal degree of freedom may be the degree of order of a system. An example of a system with different degrees of order is a carbon monoxide crystal. Two possible structures are  $C=O$   $C=O$   $C=O$   $C=O$ , and  $C=O$   $C=O$   $O=C$   $C=O$ . Another example of an internal degree of freedom is the surface area of small crystals, discussed in Sects. 2.4.2 and 2.4.3. The thermodynamic description of these internal degrees of freedom is given in Sect. 2.4.4 and the time-dependence is discussed in Sect. 2.4.6.

### 2.4.6 Relaxation Times

In this section we assume a nonequilibrium process occurs in a homogeneous system. The process is caused by the disturbance of a single internal degree of freedom  $\zeta$  (see Sect. 2.4.4 for the description of internal degrees of freedom). The independent variables  $T(t)$ ,  $p(t)$ , and  $\zeta(t)$  are directly dependent on time,  $t$ . The changes with time,  $T \equiv dT/dt$  and  $p \equiv dp/dt$ , are given by the external perturbation.

The change of the internal variable with time,  $\dot{\zeta} \equiv d\zeta/dt$ , can be given by a dynamic law as shown in Eq. (1) of Fig. 2.95, where  $a(T, p, \zeta)$  is the so-called affinity which has the meaning of a driving force, and  $L$  is the so-called phenomenological coefficient or coupling factor. The first-order kinetics expression, as it is discussed in Chap. 3 for chemical reactions, is shown as Eq. (2) for comparison. The constant  $\tau$  is the inverse of the rate constant  $k$  and has the dimension of time. It is called the

<b>Relaxation Times</b>	
	$\zeta$ = Grk. zeta, internal variable
	All other variables, $T$ , $p$ , $n$ , etc. are kept constant.
(1) $\frac{d\zeta}{dt} = -L \left( \frac{\partial g}{\partial \zeta} \right) = La$	For $a$ and $\zeta$ see Figs. 2.91 and 2.92, $a = -(\partial g / \partial \zeta)_{T,p}$
(2) $\frac{dN}{dt} = \frac{1}{\tau} (N^e - N)$	$L$ = Phenomenological coefficient
	$\tau$ = Relaxation time
First term of the Taylor expansion about equilibrium:	
(3) $a = a^e + \left( \frac{\partial a}{\partial \zeta} \right)_{T,p}^e [\zeta(t) - \zeta^e]$	( $a^e = 0$ )
(4) $\left( \frac{d\zeta}{dt} \right) = L \left( \frac{\partial^2 g}{\partial \zeta^2} \right) [\zeta^e - \zeta(t)]$	<div style="border: 1px solid black; padding: 5px; display: inline-block;"> Relaxation time:  (5) <math>1/\tau_{T,p}^e = L \left( \frac{\partial^2 g}{\partial \zeta^2} \right)_{T,p}^e</math> </div>

**Fig. 2.95**

relaxation time. The concentration is expressed by the number of species  $N$ , and  $N^e$  corresponds to  $N$  at equilibrium, so that  $(N^e - N)$  is the distance from equilibrium and expresses the driving force. Close to the internal equilibrium, designated by the superscript  $^e$ , a connection between these two equations can be made. One develops  $a(T, p, \zeta)$  into a Taylor series and obtains Eq. (3) of Fig. 2.95. Insertion of Eq. (3) into Eq. (1) yields Eq. (4). By comparison of the coefficients, one can derive an expression for the relaxation time in terms of the thermodynamic functions as given in Eq. (5). This correspondence only applies close to equilibrium, as the derivation reveals. The correspondence is based on the linear term of the Taylor expansion. In actual applications, neither the relaxation-time of Eq. (2) nor (5) need to be constant. This is particularly true if  $T$  and  $p$  are not kept constant, as indicated.

Next, one can make a connection with the discussion of the internal variables of Sect. 2.4.4. Figure 2.96 illustrates the connection between the change of the internal variable with temperature at constant pressure, Eq. (15), and the just derived relaxation time at equilibrium of given  $T$  and  $p$ , Eq. (5). This relaxation time is also called the Debye relaxation time. Because of the positive curvature at equilibrium drawn in Fig. 2.79, the Debye relaxation time must be  $\geq 0$ .

Relaxation Times	
(15) $\left(\frac{\partial \zeta}{\partial T}\right)_p^e = \frac{\sigma_{T,p}^e}{\left(\frac{\partial^2 g}{\partial \zeta^2}\right)_{T,p}^e}$	Change of the internal variable maintaining internal equilibrium Equation (15) from Fig. 2.92
Debye Relaxation time: (5) $1/\tau_{T,p}^e(T,p) = L\left(\frac{\partial^2 g}{\partial \zeta^2}\right)_{T,p}^e$	Relaxation time: (6) $1/\tau_{T,p}(T,p,\zeta) = L\left(\frac{\partial^2 g}{\partial \zeta^2}\right)_{T,p}$
By insertion in Eq. (12) of Fig. 2.92	Assuming $L$ is constant:
(7) $\dot{a} = \left(\frac{\partial a}{\partial T}\right)_{p,\zeta} \dot{T} - \frac{1}{L \tau_{T,p}} \dot{\zeta}$	(8) $\ddot{\zeta} = L \dot{a}$
(9) $\ddot{\zeta} + \frac{1}{\tau_{T,p}} \dot{\zeta} = L \left(\frac{\partial a}{\partial T}\right)_{p,\zeta} \dot{T}$	Nonlinear differential equation for the determination of the internal variable as a function of $t$ .

**Fig. 2.96**

Analogous to the Debye relaxation time, one can introduce the relaxation time of Eq. (6) in Fig. 2.96. This new relaxation time describes also processes further from equilibrium, but it depends on  $\zeta$ , as indicated. In nonequilibrium  $T$ ,  $p$ , and  $\zeta$  are variables that are independent of each other. At constant  $p$  one must set  $(d\zeta/dT)_p = \dot{T}/\dot{\zeta}$ . For the change of the affinity with respect to time at constant pressure Eq. (7) follows from Eqs. (12) and (6). If, furthermore, the coupling factor  $L$  is constant, Eqs. (7) and (8) yield at constant pressure the nonlinear differential equation for the determination of the internal variable  $\zeta(t)$ , given as the boxed Eq. (9), where  $\dot{T}$  is the

external perturbation of the system. The right side of Eq. (9) expresses also the external force which acts on the internal, molecular degree of freedom. As first integral of Eq. (9) one finds Eq. (10) in Fig. 2.97, with the dimensionless, relative variable of time defined as Eq. (11).

<b>Integration of the Relaxation Time</b>	
$(9) \quad \ddot{\zeta} + \frac{1}{\tau_{T,p}} \dot{\zeta} = L \left( \frac{\partial a}{\partial T} \right)_{p,\zeta} \dot{T}$	Nonlinear differential equation for the determination of the internal variable as a function of $t$ .
Integral:	
$(10) \quad \dot{\zeta}(t) = e^{-\lambda_{T,p}(t)} \left[ \dot{\zeta}(0) + L \int_0^t \left( \frac{\partial a}{\partial T} \right)_{p,\zeta} e^{\lambda_{T,p}(t')} \dot{T}(t') dt' \right]$	
Using equilibrium as reference state and making the deviations from $T^e$ small:	
$(11) \quad \lambda_{T,p}(t) = \int_0^t \frac{dt'}{\tau_{T,p}}$	$(12) \quad \lambda_{T,p}(t) = - \frac{t}{\tau_{T,p}^e}$
$(13) \quad \dot{\zeta}(t) = L \sigma_{T,p}^e e^{-t/\tau_{T,p}^e} \int_0^t e^{t'/\tau_{T,p}^e} \dot{T}(t') dt'$	
Solution of the linear differential equation that holds close to equilibrium	

**Fig. 2.97**

If one assumes the internal equilibrium,  $^e$ , as the initial state,  $\dot{\zeta}(0)$  becomes zero. Furthermore, taking this internal equilibrium as the reference state and assuming that the deviations from  $T^e$  are small, one can relate all coefficients in Eqs. (9) and (10) to this equilibrium state and consider them to be approximately constant. Equation (10) becomes then a linear differential equation. Its simple integral can be written as Eq. (13). Equation (12) is the easy-to-handle variable of time in terms of the relaxation time.

This description suffices for a first introduction into irreversible thermodynamics. More information is contained in the general references, listed below. In Chap. 3, it will become obvious that the kinetic processes can also be described with detailed, microscopic models of the process. A larger number of applications of the free enthalpy diagrams for crystallization, reorganization, and fusion, discussed in Sect. 2.4.2 will be shown in Chap. 6. The kinetic expressions which can be derived from detailed molecular models, as described in Chap. 3, are used more frequently than the kinetics as it can be derived from the irreversible thermodynamics. One, however, must always be aware that the agreement of a microscopic model with macroscopic experiments is not necessarily proof of the mechanism, while a disagreement is always a reason for either improving or discarding the chosen microscopic model. The just derived kinetic equations based on irreversible thermodynamics are free of any molecular model and are best applied when the linear differential equation holds.

## 2.5 Phases and Their Transitions

Traditionally a phase is defined in thermodynamic terms as a state of matter that is uniform throughout, not only in chemical composition, but also in physical state. In other words, a phase consists of a homogeneous, macroscopic volume of matter, separated by well-defined surfaces of negligible influence on the phase properties. Domains in a sample, which differ in composition or physical states, are considered different phases. The basic elements of the phases are the atoms and molecules as discussed in Sect. 1.1.3.

A first description will be given of classical (Sects. 2.5.1 and 2.5.5) and mesophases (Sects. 2.5.3 and 2.5.4). It will be shown in Sect. 2.5.2 that sizes of the phases can change from macroscopic ( $> \text{one } \mu\text{m}$ ) to microscopic ( $< \text{one } \mu\text{m}$ ), to nanophases of only a few nm. Figure 2.98 shows an early suggestion of nanophase structures in polymer fibers [26]. Obviously, one must analyze, to what level such small agglomerations of matter can still function as a phase. When dealing with one component (molecule or part of a molecule of one of the three classes of Chap. 1), one may recognize as many as 57 different phase descriptions [27], based on the constituent molecule, type of phase, and phase size (see Sect. 2.5.2). Finally, an initial insight into phase transitions will be offered in Sects. 2.5.6 and 2.5.7.

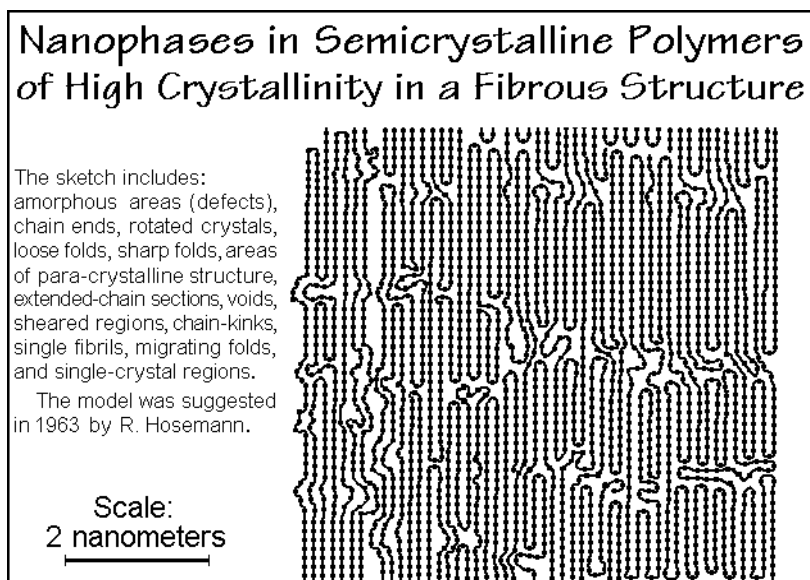


**Fig. 2.98**

### 2.5.1 Description of Phases

A definitive link between the microscopic and macroscopic description of matter can be given for gases, the most dilute phase as is shown in Figs. 2.8 and 2.9. A schematic representation of a gas frozen in time with indication of the velocity vectors is shown in Fig. 2.99. A graph of the macroscopic, functional relationship

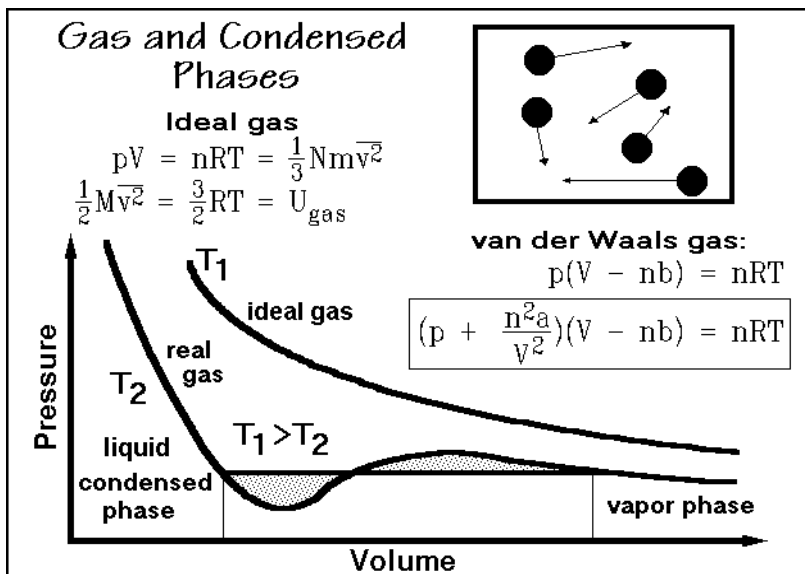


Fig. 2.99

between volume,  $V$ , and pressure,  $p$ , at constant temperature,  $T$ , is also given. The constant  $R$  is the universal gas constant ( $8.3143 \text{ J K}^{-1} \text{ mol}^{-1}$ ). It is rather easy to derive this ideal gas law using the microscopic model of Fig. 2.9. This model of a gas reveals that  $pV$  is also equal to  $(1/3)Nm\overline{v^2}$ , the right half of the top equation in Fig. 2.5.2. The microscopic parameters are  $N$ ,  $m$ , and  $v$ , as listed in Fig. 2.1.9, with the volume,  $V$ , having a microscopic as well as macroscopic meaning.

The ideal gas law, as a function of state, does not explain the existence of condensed states of matter, and even for gases, it represents the experimental data only for a dilute gas, i.e., at low  $p$  and high  $T$ . The basic conditions on which the ideal gas law was derived were: (1) The molecules of an ideal gas should be negligible in volume, (2) have no interactions with the other molecules, and (3) collide elastically. To describe a *real* gas, the first two conditions must be changed to correspond to the experiment. A simple model which can be used for the description of real gases was proposed by van der Waals<sup>1</sup> in 1881. First, he assumed that the molecules, though small, exclude a certain fraction of the total available volume,  $V$ , from motion for themselves. At atmospheric pressure, this excluded volume is typically only 0.1%, but at 100 times atmospheric pressure, the excluded volume is as much as 10%. The correction term for the excluded volume,  $b$ , is summarized in Fig. 2.100, and expressed with the equation at the top-right in Fig. 2.99. This correction does not change the nature of the gas equation. A simple shift in the volume coordinate by  $nb$  leads to the ideal gas curve, similar to the curve shown for the temperature  $T_1$ .

<sup>1</sup> Johannes D. van der Waals, 1837–1923, Professor of Physics at the University of Amsterdam, The Netherlands, received the Nobel Prize in Physics in 1910 for his research on the gaseous and liquid states of matter (van der Waals equation).

### Calculation of van der Waals Excluded Volumes

The excluded volume for the center of gravity of molecule B due to the presence of molecule A is 8 times its molar volume (the lightly shaded area) or 4 times the molar volume per one molecule:

$$\text{molar volume: } V = \frac{4}{3} r^3 \pi$$

$$\text{excluded volume: } \frac{1}{2} \left[ \frac{4}{3} (2r)^3 \pi \right] = 4V = b$$

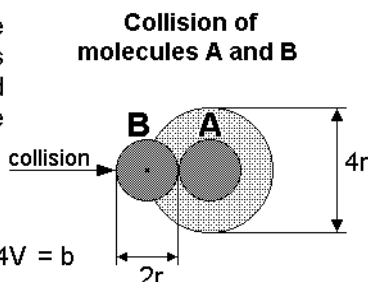


Table of some representative van der Waals constants: (a in $\text{m}^6 \text{Pa mol}^{-2}$ and b in $\text{cm}^3 \text{mol}^{-1}$ )	$\text{H}_2$	a = 0.0248	b = 26.61
	CO	a = 0.1505	b = 39.85
	$\text{H}_2\text{O}$	a = 0.5526	b = 30.49
	$\text{CO}_2$	a = 0.3510	b = 42.67
	$\text{CH}_4$	a = 0.2279	b = 42.78

**Fig. 2.100**

The second correction accounts for weak interactions between the molecules. It is done with the constant, a, modifying the measured pressure, p. If one wants to describe a state where molecules are condensed, they must be held together by some interactions which cannot be neglected. Interactions between pairs of molecules are always proportional to the square of concentration, so it is best to give the correction term the form  $a(n/V)^2$  and add it to the pressure. The reduction of pressure when molecules attract each other is perhaps obvious if one considers that the molecules that collide with the surface are being attracted away from the surface by the other molecules of the gas. The resulting equation correcting for both the excluded volume and the intermolecular interaction is the van der Waals equation, the boxed equation of Fig. 2.99. The constants, a and b, are different for every gas.

A typical isotherm of a van der Waals equation is drawn in Fig. 2.99 at low temperature  $T_2$ . At the high temperature  $T_1$ , the p-V curve is still similar to the ideal gas curve. The effect of the interaction is small (because of the large kinetic energy of the molecules) and nb is small relative to the large V. At  $T_2$ , one finds a pressure region where three different volumes exist as solution to the van der Waals equation, a first indication that there may be more than just the gaseous state.

If one draws at  $T_2$  a horizontal so that the dotted areas above and below the p-V curve are equal, as illustrated in Fig. 2.99, one can show that the two marked states at the ends of the horizontal are equally stable. They are in equilibrium. One can give proof of the stability by using the free enthalpy, discussed in Sect. 2.2. For the moment it is sufficient to know that the two end points are in thermodynamic equilibrium and all intermediate states along the p-V curve are metastable or unstable (they have a higher free enthalpy). The van der Waals equation leads, thus, at certain temperatures and pressures, to the description of two phases in equilibrium, a small-volume, condensed phase (the liquid), and a large-volume, dilute gas phase (the

vapor). With the introduction of an interaction between the molecules, it is thus possible to understand the connection between liquids and gases. Unfortunately the constants  $a$  and  $b$ , specific for any one gas, change also with temperature and pressure, limiting the use of the van der Waals equation.

The next step is to use the understanding of the gaseous and liquid states on the microscopic and macroscopic levels to connect to the other condensed states. It is easy to visualize that the liquid is a condensed gas, i.e., neighboring molecules touch frequently, but still move randomly, similar to the gas with all possible forms of large-amplitude motion, summarized in Sect. 2.3.7. Next, one can imagine what happens when the temperature is lowered. The large-amplitude motion must continually decrease and finally stop. As the translational and rotational motion decreases, the liquid becomes macroscopically more viscous. Finally, the large-scale motion becomes practically impossible. Thermal motion continues below this temperature only through vibration. The molecules cannot change their position and the substance becomes solid. In the given case it is an amorphous glass (Gk. ἄ-μορφη, without form). The structure is the same as that of a liquid, but the changes in position, orientation, and conformational isomeric state of the molecules have stopped. Such a liquid-to-solid transformation occurs at the glass transition temperature,  $T_g$ .

To connect liquids to crystals (from Gk. κρύσταλλος, ice), one notes that often molecules are so regular in structure that they order on cooling above the glass transition. In this case, the liquid phase undergoes a more drastic change when solidifying. On crystallization and melting, thus, one finds two changes in the nature of the phase. On crystallization, an ordering occurs, which results in a decrease in entropy, and, helped by the closer packing in the crystal, the large-amplitude motion stops, i.e., a glass transition takes place, as was suggested already in Fig. 1.6.

Figure 2.101 illustrates an early picture of the microscopic structure of a crystal, drawn many years before Dalton's insight into the atomic structure of matter displayed in Chap. 1. At that time there was no knowledge about the shape and size of the molecules. Figure 2.102, in contrast, is a reprint of an early electron micrograph of a crystal with large motifs, where the regular crystalline arrangement can be seen directly. For more detailed description of crystals, see Sect. 5.1.

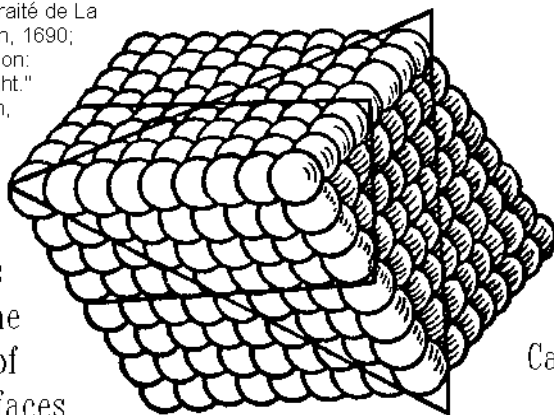
To round out the discussion of the different states of matter, a schematic summary is given in Fig. 2.103. The four classical phases are listed—gas, melt (liquid), crystal and glass (solids). The main difference between the mobile (fluid) and solid phases are the presence or absence of the three types of large-amplitude motion described in Sect. 2.3.7. In special circumstances, as are addressed in Sect. 2.5.3, not all the large-amplitude motions are frozen. The resulting phase is then intermediate, it is a mesophase (from Gk. μέσος, in the middle). The possible mesophases are: Liquid crystals (LC, orientationally ordered and mobile liquids), plastic crystals (PC, positionally ordered crystal with local rotational disorder and mobility), and condensation crystals (CD, conformationally disordered and mobile crystals with positional and orientational order). These mesophases are, thus, characterized by an increase of disorder relative to a crystal *and* by the presence of distinct amounts of large-amplitude molecular motion. On the right-hand side of Fig. 2.103 the possible transitions between these phases are marked and some empirical rules describing the



### Early Speculation about a Crystalline Structure

Atomic arrangement of calcite as proposed in 1690

C. Huygens, "Traité de La Lumière." Leiden, 1690;  
English translation:  
"Treatise on Light."  
S. P. Thompson,  
U. Chicago  
Press,  
1912,



The planes  
indicate the  
locations of  
major surfaces

$\text{CaCO}_3$

**Fig. 2.101**

### Early Direct Image of a Crystal

Electron micrograph  
of a replica  
of a crystal of  
Tobacco Necrosis  
Virus, by Wyckoff  
and Labaw (1958)

(*J. Ultrastructure Research*, **2**, 8)

The size of the motifs is  
about 15 nm in diameter.  
(Note the "defect" on the  
crystal surface.)

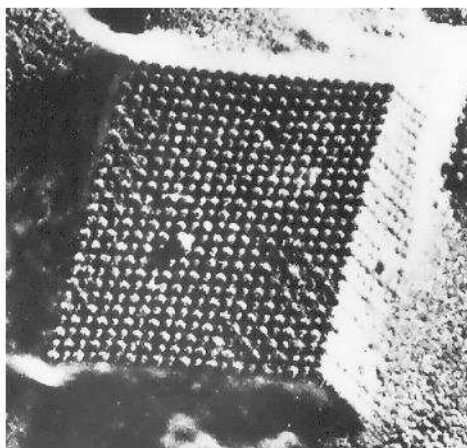


**Fig. 2.102**

changes in entropy which are coupled with the disordering are listed. Details about these data are presented in Sect. 5.4. Usually these transitions are first-order transitions (see Sect. 2.5.7). All mesophases, when kept for structural or kinetic reasons from full crystallization on cooling, display in addition a glass transition, as is indicated on the left-hand side of Fig. 2.103. The glass transition leads to a glass

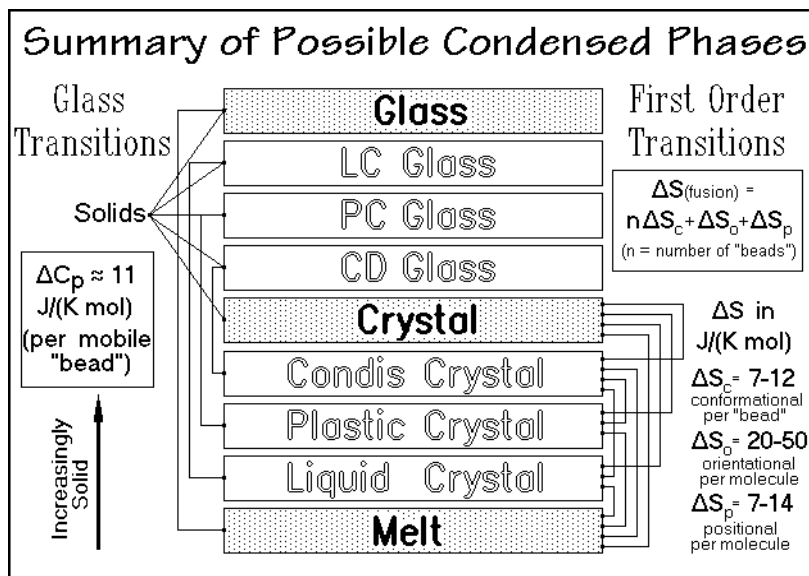


Fig. 2.103

with mesophase order, but without the large-amplitude motion. The recognition of mesophases and mesophase glasses as states of intermediate order and their study by thermal analysis has become of great importance for the understanding of the multitude of materials. The empirical rule of change of the heat capacity when going through a glass transition, is described in Sect. 2.5.6.

### 2.5.2 Phases of Different Sizes

It was noted about 150 years ago that the properties of phases change when their dimensions decrease to the micrometer scale. This observation was first made after the discovery of colloids. Today, such small phases are better called microphases [27]. In microphases, the effect of the surfaces cannot be neglected. Surface free energies and charges (surface potentials) govern the properties and stability (or metastability) of the microphases. Similarly, in Fig. 1.6 it is shown that molecules may be classified into three types, small, large and flexible, and large and rigid. In this section the changes of phase size and molecular size are analyzed briefly.

When forming a crystal via nucleation and growth, as described in Sects. 3.5 and 3.6, the linear growth rates in the various crystallographic directions determine the initial, usually metastable, crystal shape. Linear, flexible macromolecules, for example, chain-fold to lamellar crystals with much faster growth in the crystallographic *a*- and *b*-directions than in direction *c*, along the chain direction, as outlined in Fig. 2.104. The folds accumulate in the *ab*-surface (see Sect. 5.2). By limiting the available material to a few macromolecules, the initial liquid takes the shape of a small droplet with a micrometer diameter, and the crystal is also a microphase, as assumed in the figure. On annealing, the initial, kinetically-determined morphology

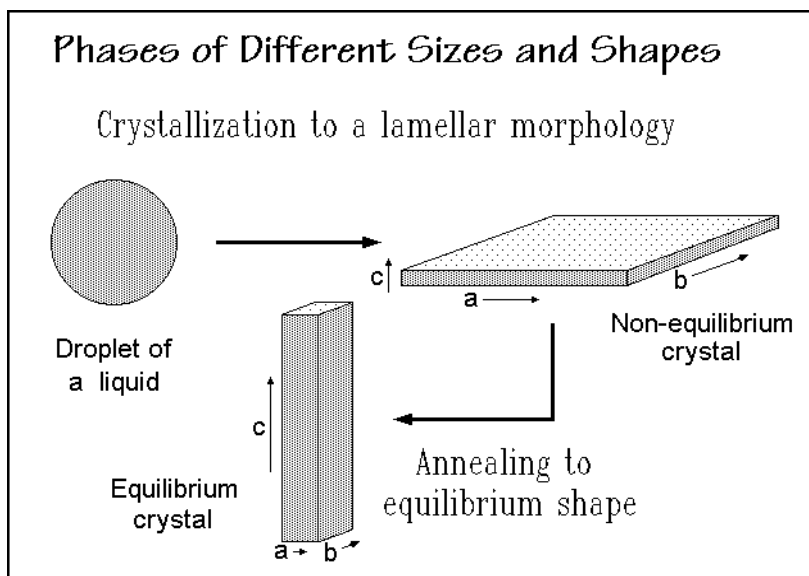


Fig. 2.104

(shape) may approach equilibrium, as shown in the sketch at the bottom. The major rearrangement of the molecules within the crystal requires sufficient mobility, as has been observed, for example, in the condensation mesophase of polyethylene. The equilibrium crystal must have a minimum of the positive surface free energy. Based on this principle, Wulff devised in 1901 a construction to establish the equilibrium shape (Wulff construction). By drawing normals from a point within the crystal to the various possible surfaces with lengths proportional to the surface free energy, the innermost complete body of these surfaces is the equilibrium shape. The proper volume can be achieved by adjusting the lengths without changing the proportions. The equilibrium polymer crystal should have, thus, its large dimension at right angles to the high energy fold surface  $ab$ , as indicated in Fig. 2.104.

New properties arise when the molecular sizes increase to the dimensions of the phase, as for example in the case of a typical polyethylene of 500,000 Da. It has a contour length of  $2.8\ \mu\text{m}$  and can easily cross microphase boundaries. This traversing of the surface makes neighboring phases interact strongly, in contrast to the weak interactions by intermolecular forces (see Fig. 1.5).

The lower limit of the size of crystals of macromolecules may be as small as 2 nm and must then be called a *nanophase* as displayed in Fig. 2.98. The noncrystalline material surrounding the macromolecular crystals, containing folds, chain ends, noncrystallizable repeating units, and tie molecules, has similarly small phase dimensions. In nanophases the opposing surfaces of a phase area are sufficiently close to interact so that no bulk phase exists anymore. Macromolecules traversing a nanophase will strongly link the surfaces; but even weaker forces, such as caused by polarity at the interface, or by charges in the surface, may bridge nanophases and may give rise to special properties of the nanophases. For characterization, nanophases need a detailed study of composition, physical state, molecular structure,

and molecular motion. The macromolecules can now traverse not only one, but several or many phase domains and influence the macroscopic properties.

The limit of nanophases towards smaller sizes occurs at perhaps one nanometer. Two causes exist for this limit: The increasing loss in homogeneity due to the inherent molecular structure and their fluctuations in energy makes the recognition of a homogeneous phase impossible; and for copolymers, the decreasing gain in enthalpy on mixing due to the larger surface contribution relative to the entropy loss on phase separation makes the nanophase unstable compared to a solution.

This short summary illustrates that three size-ranges must be considered for each type of phase (macrophases, microphases, and nanophases). In addition, the phase structure may be different for each of the three types of molecules. This leads to a total of nine possible situations for each of the nine condensed phases shown in Fig. 2.103. Of the 81 combinations, 57 have been suggested to be possible at the beginning of Sect. 2.5 [27]. Thermal analysis is the main technique to distinguish and identify this multitude of different systems.

### 2.5.3 Mesophases

The term mesophase, introduced in Sect. 2.5.1, was first coined in 1922 by Friedel to describe mainly liquid crystals which are known since 1888. They are related to liquids, but maintain a certain degree of orientational order, as shown schematically in Fig. 2.105. A list of characteristic properties of liquid crystals is given in the left column of Fig. 2.107, below. In the examples shown in Fig. 2.105, the liquid crystalline order is due to an elongated, rod-like or flat, board or disk-like segment of the molecules, the mesogen. The left example in Fig. 2.105 is a two-dimensional representation of a nematic liquid crystal (Gk. νήμα, thread, from the thread-like interference patterns of nematic liquid crystals under the polarizing microscope). The nematic phase shows orientation of the mesogens in only one direction. The right example is a macromolecular smectic liquid crystal (Gk. σμέγμα, soap). In this case the limited orientational order is in two dimensions. The example is of a polymer that has a mesogen included in the otherwise flexible chain. For example, CH<sub>2</sub>-sequences can link the mesogens and providing the mobility needed to give a liquid-crystalline character. A typical example of a mesogen is shown at the bottom of Fig. 2.105. The orientation in the liquid crystals gives rise to the birefringence and its high mobility allows the use of liquid crystals in display devices.

Soaps and lipids are also liquid crystals. These molecules consist of two parts that would be phase-separated, if not connected by strong bonds. In the pure state these molecules arrange such that the junction between their two incompatible segments form an interface (I) between two phase areas, for example, in sodium stearate, a soap: Na<sup>+</sup> OOC-(I)(CH<sub>2</sub>)<sub>16</sub>-CH<sub>3</sub>, and in lipids as seen in Fig. 2.106. The domain size of these phases is about one nanometer in the direction of the molecule, i.e., they are nanophases. On crystallization, the molecules of the liquid crystals have to pack closely, which is not always possible for more complicated structures, so that glasses are common low-temperature phases for such molecules. For the soaps and lipids, a nanophase-separation remains in the crystals. Sometimes the two types of nanophases within the overall crystal undergo separate phase transitions.

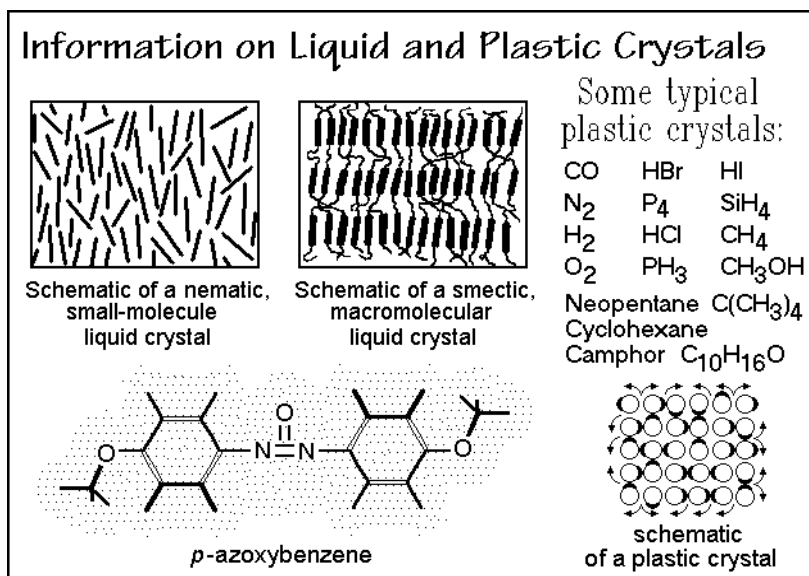


Fig. 2.105

Plastic crystals are more closely related to the classical crystals. They have full positional order as shown in the sketch in Fig. 2.105. The plastic crystal consist, however, of molecules (their mesogens) that are almost spherical and can start to rotate within the crystal at a given transition temperature. Figure 2.107 contains a list of typical properties of plastic crystals and allows a comparison to liquid crystals. The plastic crystalline state was first recognized in the 1930's. Most plastic crystals

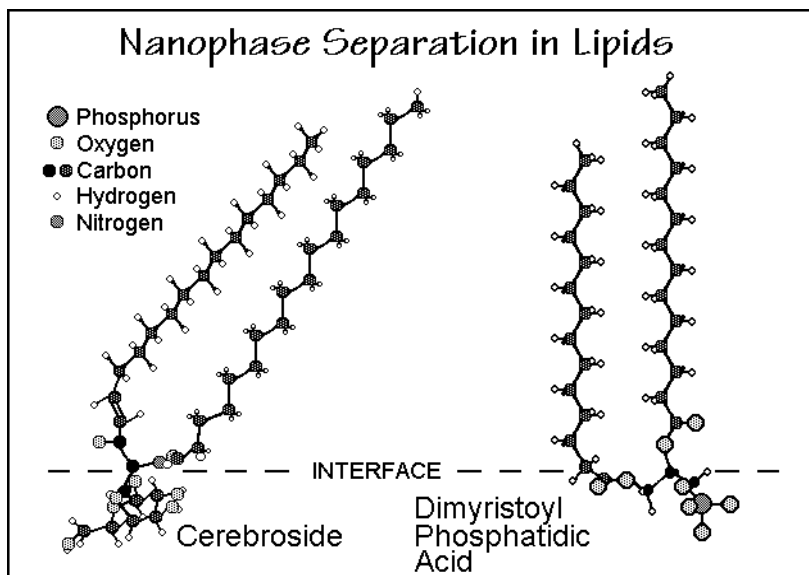


Fig. 2.106

Characteristics of the Three Mesophases		
Liquid Crystals	Plastic Crystals	Condis Crystals
1. "liquid"	1. "plastic"	1. "solid"
2. birefringence	2. no birefringence	2. birefringence
3. small $\Delta S_f$ often 2-5 J/(K mol)	3. fixed, molar $\Delta S_f$ of 7-14 J/(K mol)	3. $\Delta S_f = 7-12$ J/(K mol) for each rotatable bond
4. 100% crystalline	4. 100% crystalline	4. limited crystallinity for macromolecules
5. small and large mols.	5. small molecules only	5. small and large mols.
6. no positional order, some orientational order	6. positional order, no orientational order	6. positional order and orientational order
7. full conformational disorder (as in the melt)	7. full conformational disorder (similar to the melt)	7. partial or full confor- mational disorder
8. mesogen shape: rod, board, or disc	8. mesogen shape: close to spherical	8. rotational isomers that keep the chains largely parallel

Fig. 2.107

have a cubic crystal structure. Due to the rotation of the molecules in the crystal, their actual symmetry is averaged to a sphere, eliminating both the birefringence and causing an entropy of fusion similar to the metals and noble gases which have spherical motifs (see Sects. 5.4 and 5.5). Cubic crystals have also many slip planes and with rotating, weakly bound molecules, the crystals easily deform, they are plastic. Metals with similar crystal structures and spherical motifs, but stronger bonding, still show ductility, but no plastic-crystal behavior. Both liquid and plastic crystals show conformational mobility and disorder if the basic molecule is flexible, i.e., can change to different conformational isomers.

Conformationally disordered crystals (condis crystals) were discovered in the 1980's. They show positional and orientational order, but are partially or fully conformationally mobile. The condis crystals complete the comparison of mesophases in Figs. 2.103 and 2.107. Linear, flexible molecules can show chain mobility that leaves the position and orientation of the molecule unchanged, but introduces large-amplitude conformational motion about the chain axis. Again, the symmetry of the molecule is in this case increased. Condis crystals have often a hexagonal, columnar crystal structure. Typical examples of condis crystals are the high-temperature phase of polyethylene, polytetrafluoroethylene, *trans*-1,4-polybutadiene, and the low-temperature phases of soaps, lipids and other liquid-crystal forming, flexible molecules.

Figure 2.108 illustrates the chemical structure and a thermal analysis curve of a typical small molecule with liquid-crystal and condis-crystal phases, OOBPD. The mesogen is the rigid bisoxybenzalphenylenediamine. Two flexible octyl groups enable conformational disorder by rotation about the C-C and O-C bonds. The letter N represents the nematic phase, letters C, I, G', and H' the increasingly better ordered smectic phases, and K designates condis phases. Note that phase K<sub>3</sub> has still not

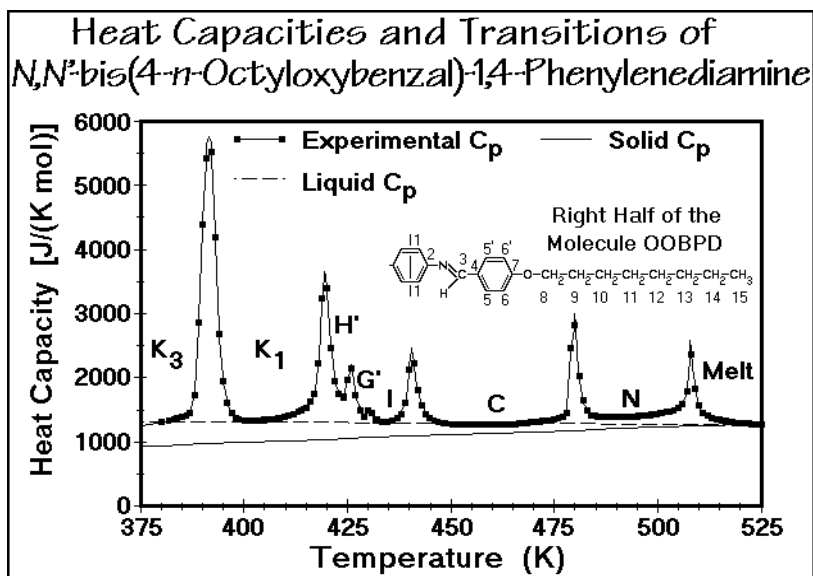


Fig. 2.108

reached the heat capacity expected for the solid crystalline or glassy state indicated by the thin, bottom line (vibration-only crystalline heat capacity, see Sect. 2.3). Since no further crystallization occurs, a glass transition is expected and is seen in thermal analysis at about 350 K. More details about this compound are given in Sect. 5.5.4.

Fullerene,  $C_{60}$ , is an example of a molecule with a plastic-crystal phase. Its structure is given in Fig. 2.109 together with the other two allotropes of carbon,

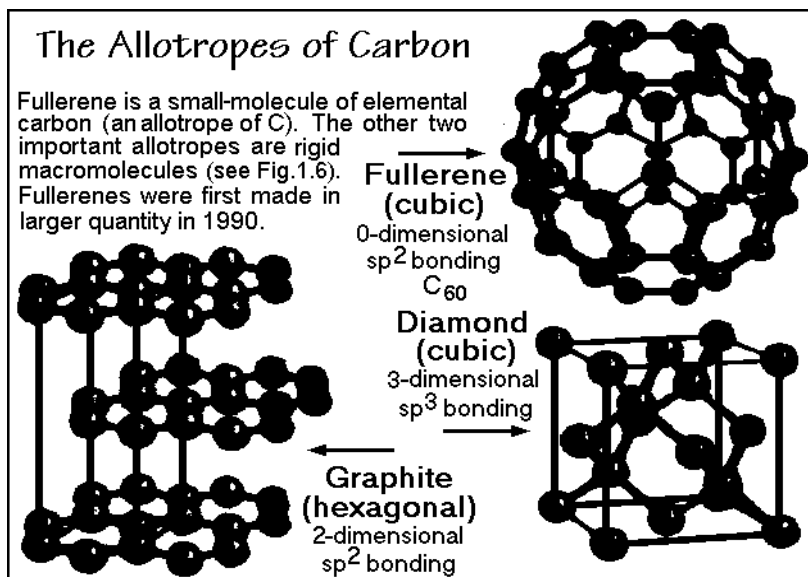


Fig. 2.109

diamond and graphite. Its calorimetry is discussed in Sect. 4.2.7 (see also Figs. 2.39–41). Figure 2.110 is a thermal analysis trace (DSC, see Sect. 4.3). The transition starts rather broad and then becomes sharp as full rotation becomes possible. More details about this transition are available through  $^{13}\text{C}$  nuclear magnetic resonance experiments. Figure 2.111 is a recording of the spin-lattice relaxation time  $T_1$ . It is a measure of the rotation of the molecule. Three models

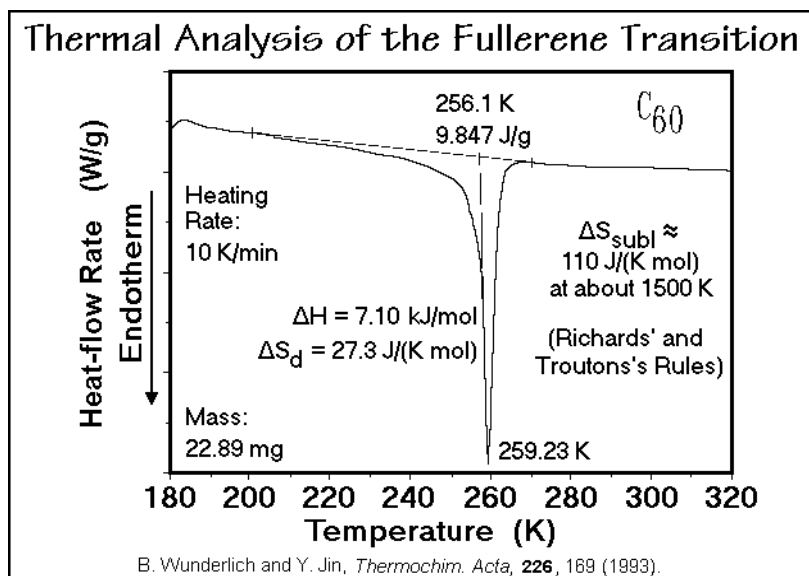


Fig. 2.110

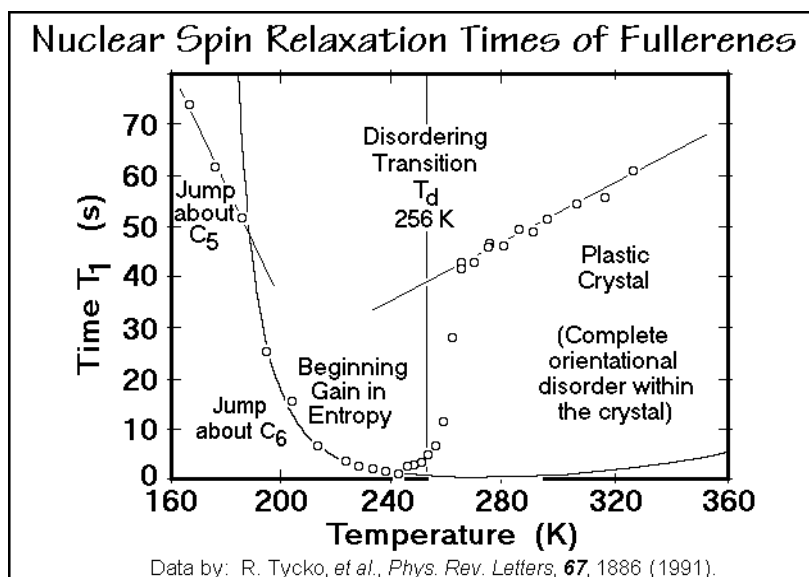


Fig. 2.111



were fitted to the data: (1) molecular motion about the five-fold symmetry axis  $C_5$  (see Sect. 5.1.5 for a discussion of symmetry), (2) motion about the incomplete, six-fold axis,  $C_6$ , and (3) full rotation. Since there is no change in heat capacity (entropy) in the lowest temperature region of Fig. 2.111, motion (1) must be a jump between indistinguishable states of lower energy and longer residence time. This agrees with the symmetry axis  $C_5$ , best seen in Fig. 5.37. The mechanism (2) is energetically only slightly more difficult, but the symmetry is incomplete and produces disorder, i.e., the entropy (heat capacity) increases. Stage (3), finally, leads orientational disorder.

Polytetrafluoroethylene and *trans*-1,4-polybutadiene are two examples of macromolecular condense crystals. The heat capacity of polytetrafluoroethylene is shown in Fig. 2.63, that of *trans*-1,4-polybutadiene is illustrated in Fig. 2.112. Both polymers

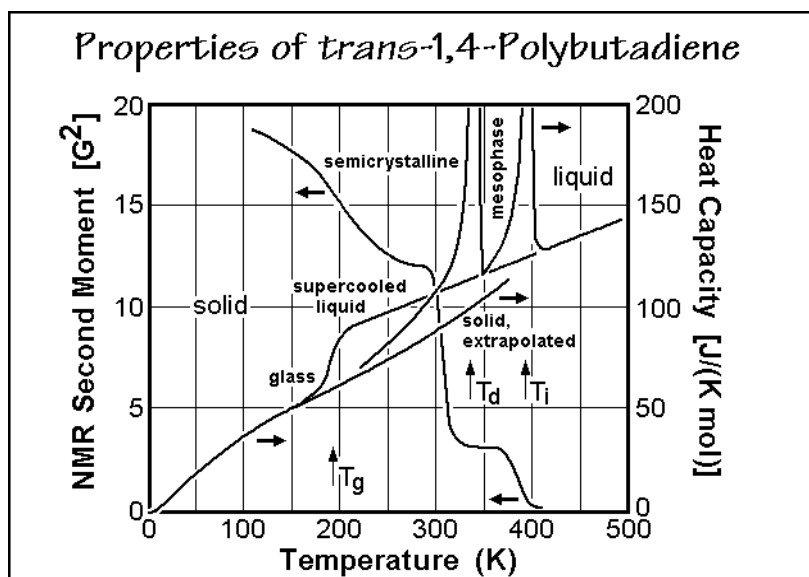


Fig. 2.112

have two endothermic transitions. At low temperature they show an endotherm at the disordering temperature,  $T_d$ , on going from the crystal to the condense phase, then they ultimately melt at  $T_i$  (isotropization temperature). In Fig. 2.112 the motion of *trans*-1,4-polybutadiene is characterized with  $^1H$  solid-state NMR, using the line width of the signal as a measure of mobility. The line width can be modeled quantitatively in terms of its second moment ( $G^2$ ). The first narrowing is due to the glass transition of the not-crystallized, amorphous fraction of the semicrystalline polymer, the second, due to the conformational mobility gained at  $T_d$ , the third to final melting (isotropization) at  $T_i$ .

Figure 2.113 indicates with an entropy plot that only the *trans* isomer of the 1,4-butadienes displays a stable mesophase. The crystals of the *cis* isomer have a more helical structure which packs less well in the crystal and needs much more space to rotate into a conformationally disordered structure. As a result of this different structure, the *cis* polymer melts at a lower temperature, and in one step.

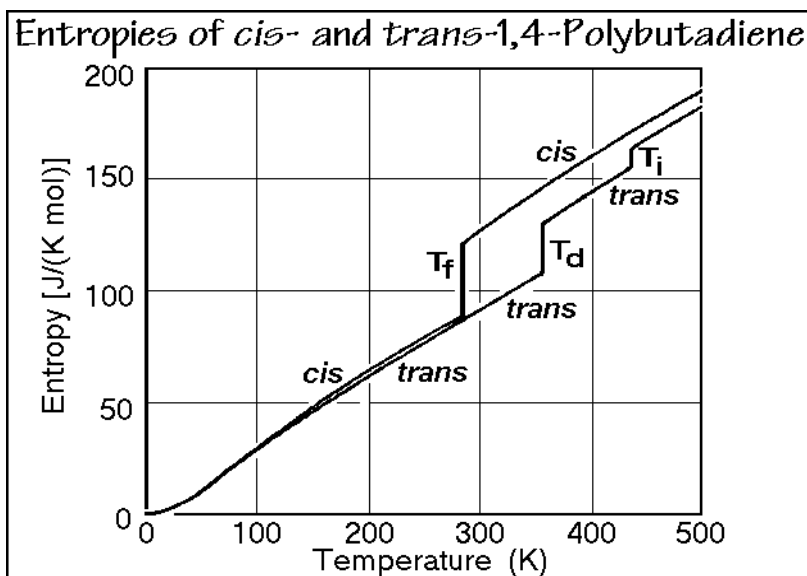


Fig. 2.113

### 2.5.4 Mesophase Glasses

All mesophases have some large-amplitude type of motion. On cooling the mesophases have two paths to the solid state as seen in Fig. 2.103. Either the mesophase orders to the crystal state, or the large-amplitude motion changes to the corresponding vibrations without change of order. In the second case there is no entropy of transition to the solid state (see Sect. 2.5.6), only the heat capacity changes to the vibration-only case, discussed in Sect. 2.3. The mesophase glass differs from the amorphous glass by possessing the order of the mobile mesophase. Each mesophase, thus, has a corresponding glass, as was discussed in Sect. 2.5.1 and shown in Fig. 2.103. Liquid crystal glasses were seen already in the 1930's [28].

Liquid crystals are quite similar to the liquids in their mobility, their glass transition is similar to the glass transition of an amorphous liquid. Figure 2.114 shows a special example. The monomer of the chosen polymer, acryloyloxybenzoic acid, does not have a liquid crystalline phase. On polymerization, an amorphous liquid results that changes with time to a liquid crystal on dimerization of the oxybenzoic acid side-group via hydrogen bonds. The thermal analysis of Fig. 2.114 shows in its upper trace a sample quenched to the amorphous glass before ordering. A normal glass transition occurs on heating, followed by ordering to the liquid crystal at  $T_o$ . On the second cooling, the LC glass is formed, which, on reheating (bottom trace) shows a glass transition of similar magnitude, but at higher temperature because of the dimerization. Glass transitions also have been observed for plastic crystals and condic crystals. Depending on the degree of cooperation necessary between neighboring molecules, narrow or broad glass transition regions result. For some additional information, see Sect. 5.5.

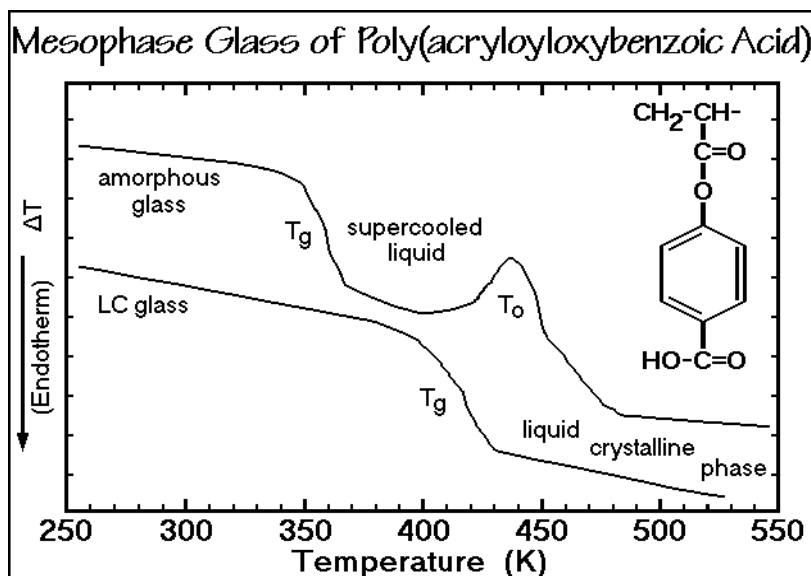
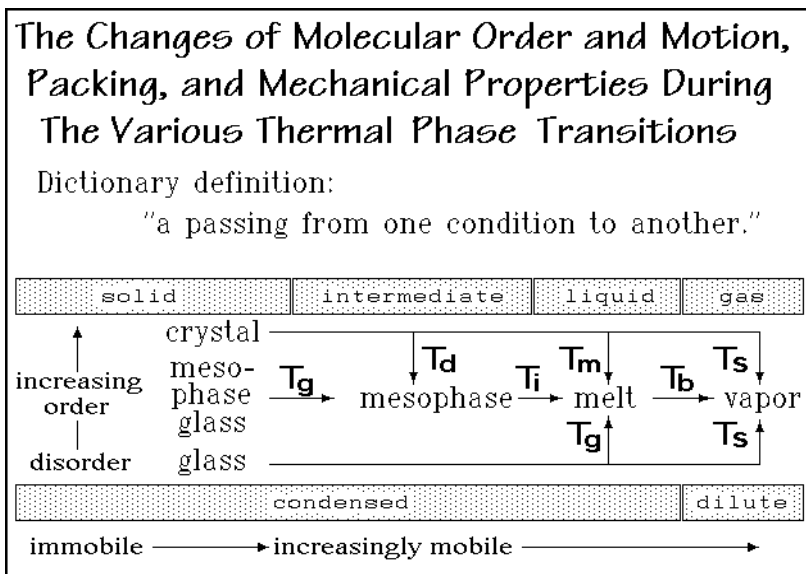


Fig. 2.114

### 2.5.5 Thermodynamics and Motion

Thermodynamics and motion can be used as a base for an operational definition of the solid state. A solid is a phase below its glass- or melting-transition temperature where the molecular motion is almost completely restricted to small-amplitude vibrations. Both transitions are easily determined by thermal analysis (the operation). Recently it has become possible by simulation on supercomputers to establish the link from the microscopic thermal motion of macromolecules to the macroscopic thermal analysis. By solving the equation of motion, one can produce a detailed movie of molecular motion (see Sect. 1.3.4, Fig. 1.47). At high temperature, conformational disorder is seen, i.e., the crystal can change to a condense state. Note that even the conformational motion occurs in a picosecond time scale (see Sect. 5.3.4).

The meaning of the word transition is not specific. In Fig. 2.115 a dictionary definition is listed, which states: *Transition* means just a passing from one condition to another. The basic transitions of interest to thermal analysis are described in the classification scheme of Fig. 2.103. In the bottom half of Fig. 2.115 the properties of the condensed phases are reviewed and their transitions identified. On the left side, the solid states are characterized by their order. The mobility and degrees of packing are listed at the bottom, and the physical states above the diagram. The mobile mesophases appear at higher temperatures via glass transitions (at  $T_g$ ) or disordering transitions (at  $T_d$ ). The liquid phase (melt) is reached with an additional transition, the isotropization (at  $T_i$ ), or by bypassing the mesophases from the glass via a glass transition (at  $T_g$ ) or a one-step melting from the crystal (at  $T_m$ ). The liquid is still a condensed phase, meaning that the constituent motifs, the atoms, ions, or molecules, are more or less touching. The gas phase is dilute, in contrast to the condensed

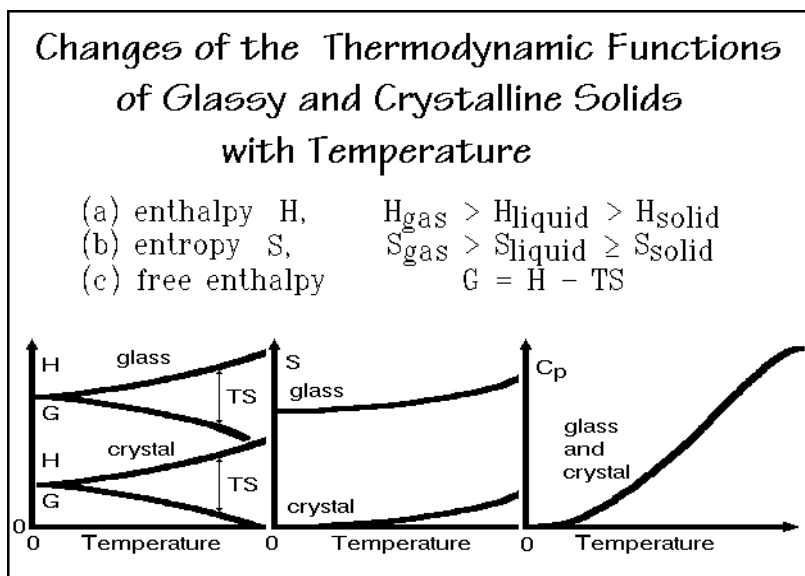
**Fig. 2.115**

phases. Large empty spaces exist between the motifs. Its connection to the condensed phases is shown in Fig. 2.115 by boiling from the liquid phase (at  $T_b$ ) or the direct transition from the solids by sublimation (at  $T_s$ ).

The motions observed for a specific material are dependent on the molecular structure. Spherical atoms cannot exist as mesophases, except when included as a solvent (as in lyotropic liquid crystals). Only small, rigid molecules can exist as plastic crystals, while condensation crystallinity is reserved for flexible molecules. Since all degrees of freedom are at low temperature vibrational with a limiting heat capacity of  $3R$  per mole of atoms, and all large-amplitude motion decreases to  $R/2$  per degree of freedom when losing the potential energy contribution, one would expect that the heat capacity decreases at every transition to higher-temperature phases that possess more large-amplitude motion. The experimental data are not in agreement with this prediction (see Sect. 2.3). The main reason for the often observed increase in heat capacity at glass and disordering transitions is the need of additional potential energy to create the increased volume for the large-amplitude motion.

The macroscopic, thermodynamic description of states is achieved through their major functions and variables of state listed in Fig. 2.116. One can deduce from the microscopic picture of the states of matter that the enthalpy of the gas must be largest, and of the solid, smallest. The larger the packing density, the stronger are the interactions between the motifs decreasing the enthalpy. On transition to a new, higher-temperature phase, this interaction must be overcome by an endothermic heat of transition.

The magnitude of the entropy can also be estimated from the microscopic description. One expects the entropy of the gas to be largest because of the large disorder in this dilute state. The crystal, on the other hand, because of its order, should have the smallest entropy; in fact, the third law of thermodynamics sets the

**Fig. 2.116**

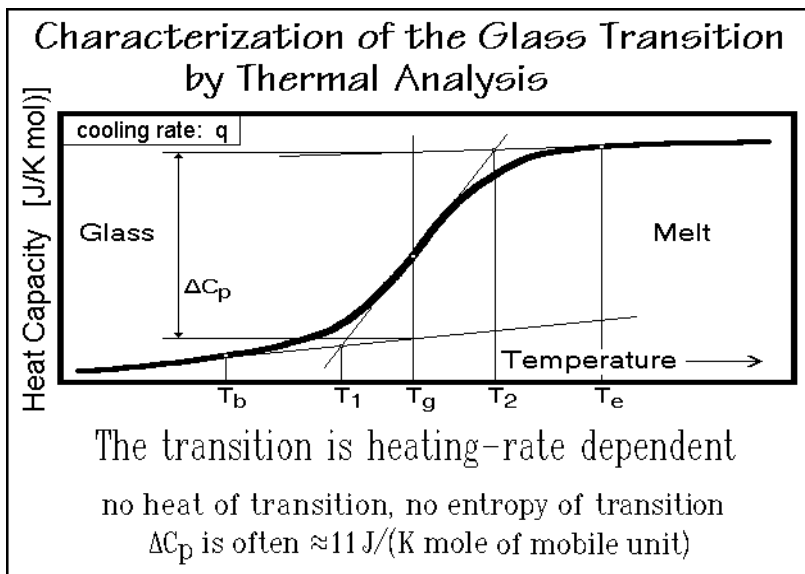
entropy of an ideal, equilibrium crystal equal to zero at the absolute zero of temperature (Sect. 2.2.4). The free enthalpy, finally, can be derived from enthalpy and entropy as shown. Its significance lies in the fact that it tells which state is most stable at a given temperature as shown in Figs. 2.84–88.

The temperature dependencies of enthalpy, free enthalpy, entropy, and heat capacity of glasses and crystals are schematically indicated in the three drawings at the bottom of Fig. 2.116 (see also Fig. 2.23). Enthalpy, entropy, and heat capacity increase with temperature, while the free enthalpy decreases. The reasons for the trends of these functions with temperature can be derived from a detailed understanding of heat capacity (see Sects. 2.3). The link between heat capacity and enthalpy is obvious from its definition (Fig. 2.10). Entropy is similarly related to heat capacity in Fig. 2.19 (see also Fig. 2.22). The free enthalpy is then fixed by  $G = H - TS$ .

### 2.5.6 Glass Transitions

The glass transition is a much more subtle transition than melting or evaporation. In Fig. 2.117 the change in heat capacity on going through the glass transition temperature is drawn after a typical polymer. There is a jump in the heat capacity, but there is no indication of a heat of transition. If there is no heat of transition, there can also be no entropy of transition.

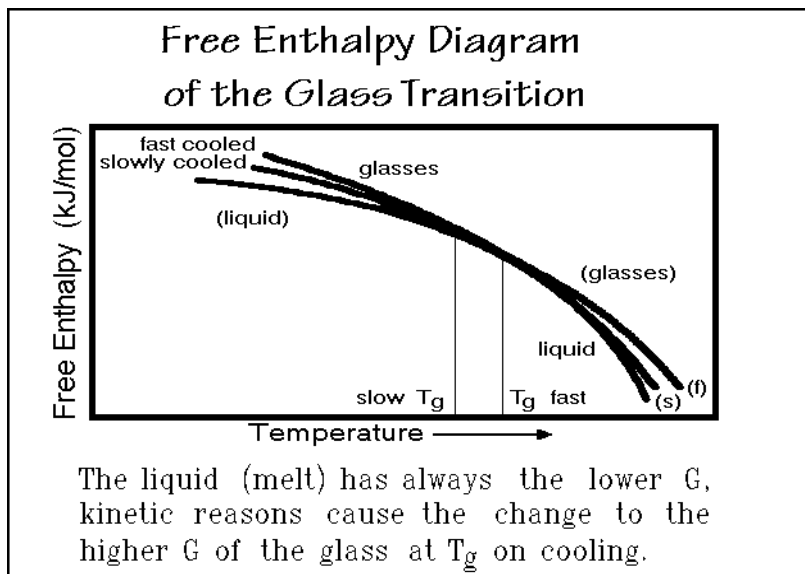
The increase in heat capacity  $\Delta C_p$  always occurs over a temperature range of 5 to 20 K, and the jump is often  $11 \text{ J K}^{-1} \text{ mol}^{-1}$  of mobile units in the liquid. This means, for a monatomic liquid the decrease in heat capacity at the glass transition is  $\approx 11 \text{ J K}^{-1} \text{ mol}^{-1}$ . Macromolecules, such as polyethylene,  $(\text{CH}_2)_x$ , change in heat capacity by approximately  $11 \text{ J K}^{-1} (\text{mol of chain atom})^{-1}$  (see Appendix 1). To describe the glass transition, the temperature of half-vitrification,  $T_g$ , should be

**Fig. 2.117**

specified, i.e., the temperature at which the heat capacity is midway between that of the liquid and glassy states. This temperature usually corresponds closely to the point of inflection in the heat capacity, and also to the breaks in the enthalpy or volume versus temperature curves at the glass transition (see Sect. 6.3). To specify the range of the glass transition, the beginning of the transition,  $T_b$ , the end,  $T_e$ , the extrapolated beginning,  $T_1$ , and the extrapolated end,  $T_2$ , should be given in addition to  $T_g$ ,  $\Delta C_p$ , and the cooling rate,  $q$ , as is indicated in the figure. All seven parameters empirically characterize the glass transition. The transition temperature,  $T_g$ , alone is a poor characterization.

A study of large lists of glass transition temperatures reveals that the ratio of the melting temperature to the glass transition temperature is often (but not always) between 1.5 and 2.0. The glasses of small molecules, such as water and ethyl alcohol, fulfill this rule also. Their ratios are 1.91 and 1.64, respectively. The glass transition, thus, is reached at a much lower temperature than the melting transition, so that for materials applications, crystalline substances should be preferred. Again, exceptions are known. Poly(oxy-2,6-dimethyl-1,4-phenylene) (PPO<sup>TM</sup>, General Electric) has a  $T_g$  of 482 K and a  $T_m$  of 580 K (ratio 1.20), sufficiently low that on partial crystallization,  $T_g$  increases due to strain caused by the small crystals, and  $T_m$  decreases because of the small size of the crystals, so that  $T_g$  may exceed  $T_m$  (see the rigid amorphous fraction of PPO in Sect. 6.2.2). Similar closeness of  $T_g$  and  $T_m$  is observed in long-side-chain polymethacrylates, where the glass transition is fixed by the backbone of the polymer and the melting transition by its side-chain length.

From the measurement of heat capacity one can derive the free enthalpy as drawn schematically in Fig. 2.118. Since the heat capacity of the liquid is always larger than the heat capacity of the glass (see 2.117), the free-enthalpy curve of the liquid must have the larger curvature since  $(\partial^2 G / \partial T^2)_p = -C_p / T$  (see Fig. 2.19) and when

**Fig. 2.118**

extrapolated to below  $T_g$ , it lies lower than the glass free enthalpy. At the glass temperature, both free enthalpies are equal, i.e., the two curves touch. In addition, the slopes of the curves are identical because of their identical heat capacities (see Sect. 2.3).

The question that one must answer is then: How is it possible for such a glass transition actually to occur, since  $G$  of the liquid is less and becomes equal to  $G$  of the glass only at  $T_g$ ? In order to stay in equilibrium, it should be forbidden to cross from  $G_{\text{liquid}}$  to  $G_{\text{glass}}$  at  $T_g$ . This paradox can be resolved only by knowing that below  $T_g$  the liquid state does not exist. Microscopically,  $T_g$  is the temperature where the liquid-like large-amplitude motion stops. The nature of the stopping precludes supercooling on cooling, and similarly, superheating on heating. Whenever the experimental time is too short for the molecules to readjust to the changes in temperature, one reaches the glass transition. This time-dependence is an indication that the transition does not occur under equilibrium conditions. Different cooling rates produce different glasses, and each glass will have a different free enthalpy.

In contrast to the well-defined equilibrium crystals, there exist a multitude of glasses of the same chemical structure, differing only in the cooling or annealing history. Also, an analogous extrapolation of the liquid and solid free enthalpies beyond the transition temperature, as possible for crystals is not permitted as implied by the parentheses in Fig. 2.118.

A detailed discussion of the dependence of the glass transition not only on cooling, but also on heating is given in Sect. 6.3. For the present, it suffices to suggest that a recorded glass transition corresponds only to a glass cooled at a given rate, i.e., with a fixed thermal history. For full specification of a glass transition, the cooling rate or other experimental parameters of the thermal history, and possibly also mechanical and electrical history must be specified.

### 2.5.7 First-order Transitions

First-order transitions are characterized by an enthalpy and entropy of transition. All transitions indicated on the right side of the list of classical phases and mesophases in Fig. 2.103 are usually assumed to be first-order transitions. In some cases, especially when involving mesophases or flexible polymers, these transitions are not as sharp as one would expect for first-order transition as discussed below. Common reasons that can broaden first-order transitions are impurities (additional components, see Chap. 7) and a distribution of phases with different perfections (see Chap. 6).

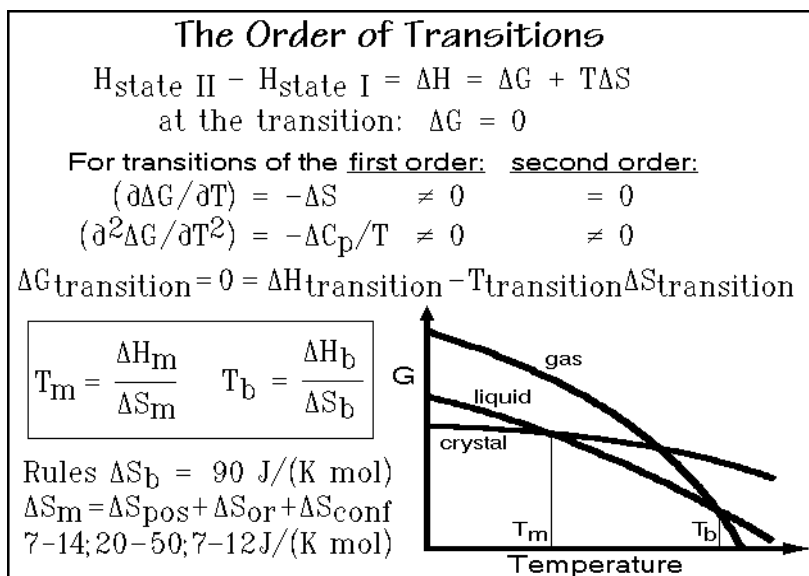
In the case where two phases are in contact and at equilibrium, the stability of both phases must be equal. This requires that the two free enthalpies per mole,  $G'$ , must be the same at the given temperature and pressure. In addition, any infinitesimal change  $dG'$  of each phase must also be equal so that the equilibrium is stable as suggested in Fig. 2.79. These conditions of equilibrium between phases I and II are written at the top of Fig. 2.119. By equating expressions similar to those derived for the free enthalpy in Fig. 2.19, additional information for the phase transitions can be obtained. Since the changes  $dG$  are expressed per mole, there is no change in the number of moles,  $n$ , and each side of the equation has only two terms. This equation allows only one independent choice between the two variables  $T$  and  $p$ —i.e., if two phases are in contact and in equilibrium, there is only one degree of freedom for a one-component system. This statement is called the *phase rule* and can be written more general as:  $P + F = C + 2$ , where  $P$  is the number of phases,  $F$  is the degrees of freedom,  $C$  is the number of components, and 2 represents the two variables  $p$  and  $T$ . For a one-component system, no degrees of freedom or independently adjustable variables are possible for three phases in contact. The third phase would give rise to another equation between, let us say, phases II and III, of the same type as written for phases I and II. Two equations with two variables permit computation of both variables. There is thus no degree of freedom. In a  $p$ - $T$  diagram this situation is represented by a point (a triple point) (see also Sects. 2.3.5 and 2.3.7 and Sect. 1.4.3).

The definition of components for linear macromolecules is somewhat complicated. One must distinguish between processes that occur with parts of molecules, i.e., strongly coupled components which must keep their positions within the molecule (as in copolymers, see Sect. 3.4), and processes with whole molecules, i.e., where there exist only weakly bound components that can easily segregate. More details about multi-component systems are given in Chap. 7.

The most far-reaching transitions are melting and evaporation. They involve the loss of order in the case of melting, and the change from a condensed to a dilute state in the case of evaporation. All other transitions are of lesser magnitude. In Fig. 2.119 it is indicated how the enthalpy changes in going from state I to state II. To stay in equilibrium during a transition, the change in Gibbs energy,  $\Delta G$ , must be zero.

The derivatives of  $\Delta G$  with respect to temperature, on the other hand, do not have to be zero. This suggests a way to characterize the transitions thermodynamically. Ehrenfest suggested that a transition for which  $(\partial\Delta G/\partial T) (= -\Delta S$ , see Fig. 2.19) is not equal to zero be called a first-order transition [25]. A second-order transition would analogously have the first derivative  $(\partial\Delta G/\partial T)$  equal to zero, but the second derivative  $(\partial^2\Delta G/\partial T^2)$  would not equal zero. The second derivative of  $\Delta G$  is equal



**Fig. 2.119**

to  $-\Delta C_p/T$ , as shown in Fig. 2.119. This condition is superficially fulfilled in a glass transition at a fixed time scale, but the time-dependence of  $T_g$  indicates that the transition should not be considered an equilibrium transition.

To discuss melting and evaporation, one can make use of the schematic drawing of the free enthalpy in Fig. 2.119, which applies to a one-component, pure substance. At low temperature the crystalline state is most stable. The crystals are stable up to the melting temperature,  $T_m$ . At this temperature, the crystal must change to the liquid, in order to remain stable. The change of state is connected with a change in the slope of  $G$ —i.e., the transition must be of first order. The system changes states with a discontinuity in entropy as well as enthalpy. Increasing the temperature further, the limit of stability of the liquid is reached at the boiling temperature  $T_b$ . Here again, on going from the liquid to the gas there is a change in the slope of  $G$ , so that it is also a first-order transition with an entropy and enthalpy of evaporation.

To describe the thermodynamic equilibrium behavior at the transition, one can write the boxed equations in Fig. 2.119. Inspection of these equations shows that thermometry, discussed in Sect. 4.1, can give a characterization of a material if there is information on either the heats or entropies of transition. Some help for interpretation comes from the fact that related materials have similar changes in disorder—the entropies of transition are similar for structurally related materials.

Richards's rule, for example, which applies to solids that melt by producing spherical, mobile motifs, such as noble gases and metals, says that the entropy of melting,  $\Delta S_m$ , is somewhere between 7 and 14  $\text{J K}^{-1} \text{mol}^{-1}$ . A similar empirical rule exists for the boiling point, known as Trouton's rule. Normal boiling materials have an entropy of boiling,  $\Delta S_b$ , of approximately 90  $\text{J K}^{-1} \text{mol}^{-1}$ . A more detailed empirical rule for the entropy of melting is listed at the bottom of Fig. 2.119 (see also Fig. 2.103). Three types of disorder make up the change on fusion: positional (pos),

orientational (or), and conformational (conf). The approximate contributions to  $\Delta S$  are listed in brackets. The first term represents Richards's rule. It is the only contribution for spherical motifs. Irregular motifs can, in addition, show orientational disorder, and thus gain an extra  $20\text{--}50\text{ J K}^{-1}\text{ mol}^{-1}$  on fusion. Flexible molecules have a third contribution to the entropy of fusion of  $7\text{--}12\text{ J K}^{-1}\text{ mol}^{-1}$  for each flexible bead within the molecule (for details see Sects. 5.4 and 5.5).

The boiling transition is simpler to describe since the vapor is close to an ideal gas without interactions between the molecules. The heat of evaporation is also called the cohesive energy, a quantity that can be related to many properties of liquids as well as solids. The cohesive energy density, CED, given in kJ per mole of molecules or repeating units, is often used to characterize the energetics of crystals.

Gradual or multiple equilibrium transitions need a sequence of states with differences in interaction and disorder such that  $\Delta H/\Delta S$  is lower than  $T_m$ . For spherical motifs it takes, however, a relatively larger amount of energy than entropy to introduce a phase with partial disorder, i.e.,  $\Delta H/\Delta S$  is usually larger than  $T_m$ . But note, that a small amount of equilibrium disorder may be introduced as isolated defects (see Sect. 5.3). For other shapes of motifs or types of large-amplitude motion, the changes of  $\Delta H$  and  $\Delta S$  may be such as to permit gradual transitions or multiple phases. For example, the internal rotation of a  $-\text{CH}_3$  group in polypropylene starts gradually, producing little disorder and no recognizable transition. The mesophase transitions in Fig. 2.103, in turn, are linked to special mesogens or low-energy, large-amplitude motion that produces a relatively big disorder. Under such conditions the free enthalpy curve has a relatively lower level of  $G$  and a larger slope ( $\partial G/\partial T = S$ ) in the  $G$ -vs.- $T$  diagram. Figure 5.120 is a summary  $G$  vs.  $T$  diagram comparing the metastable states (see Sect. 2.4) along with mesophases (see Sect. 2.5.3) and also strained melts (see Sect. 5.6).

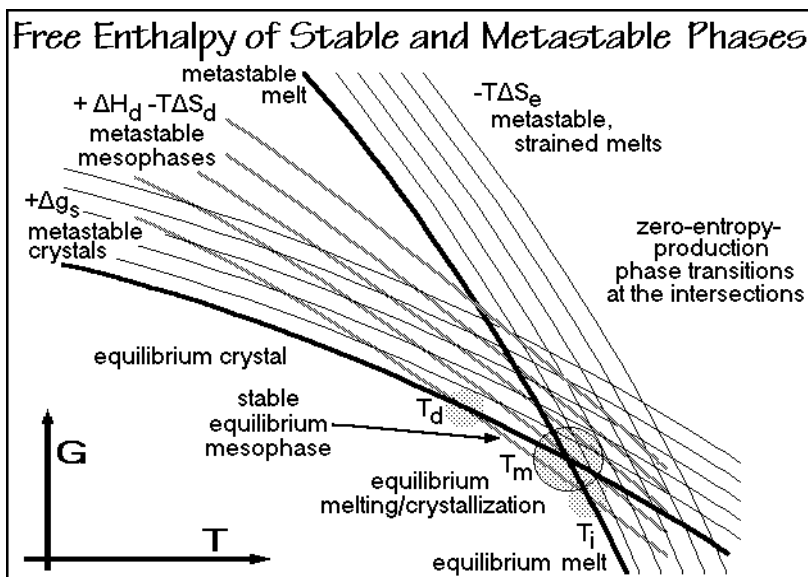


Fig. 2.120

## References

### General References

**Sect. 2.1.** For an extensive discussion of temperature and heat and its history see, for example, the entries “Heat” and “Thermometry” in the “Encyclopædia Britannica.” Particularly extensive are the articles in the earlier editions, starting with the famous eleventh edn of 1910. (Encyclopædia Britannica Inc, Chicago).

Some of the early experiments can be found in: Thompson B, Count Rumford (1789) *Phil Trans* 88: 80; Davy J (1839–40) *The Collected Works of Sir Humphry Davy*. London; see also Joule JP, Thomson W (1854) *Phil Trans Roy Soc*, London 144: 355. For the work of Gay-Lussac see Schimank H (1951) *Naturwissenschaften* 38: 265.

The basic thermodynamics can be reviewed on hand of any of the standard texts of physical chemistry, such as Atkins PW (1998) *Physical Chemistry*, 6<sup>th</sup> ed, Oxford University Press, Oxford.

**Sect. 2.2.** Advanced texts and reference books on thermodynamics are, for example: Eyring H, Henderson D, Jost W (1971–75) *Physical Chemistry, an Advanced Treatise*. Academic Press, New York, Vols I–IX; Partington JR (1949–54) *An Advanced Treatise on Physical Chemistry*. Longmans, London, Vols I–V.

The handling of heat and work as two forms of energy in the thermodynamic description of a system has been recognized as one of the difficulties in understanding thermal analysis. It has been suggested to eliminate work as a separate energy by Barrow GM (1988) *Thermodynamics Should be Built on Energy—not on Heat and Work*. *J Chem Ed* 65: 122–125.

Specific books on the second law are those of Bent HA (1965) *The Second Law, An Introduction to Classical and Statistical Thermodynamics*. Oxford University Press, New York; or Atkins PW (1984) *The Second Law*. Freeman, San Francisco.

For an advanced treatment of heat capacity see: Blackman M (1955) *The Specific Heat of Solids*. In Flügel S, ed, *Encyclopedia of Physics*, Vol VII, Part 1. Springer, Berlin.

**Sect. 2.3.** Extensive data-tables on heat capacities are found in:

- a. Hellwege KH, ed (1956–71) in Landolt-Boernstein, *Zahlenwerte und Funktionen*. Springer, Berlin, 6<sup>th</sup> ed, Vol II, Parts 1–5; continued as New Series, Group IV, *Macroscopic and Technical Properties of Matter*.
  - b. Touloukian YS, Ho CY, eds (1970–79) *Thermophysical Properties of Matter, The TPRC Data Series*. IFI/Plenum, New York, Vols 4–6, *Specific Heat*.
  - c. Lide DR, ed (2002/3) *Handbook of Chemistry and Physics*, 83<sup>rd</sup> ed. CRC Press, Boca Raton, FL (annual new editions).
  - d. Pyda M, Wunderlich B (1999) *Heat Capacities of High Polymers*, in Immergut EH, Grulke EA, eds. *Polymer Handbook*. Wiley, 4<sup>th</sup>, revised edn pp VI/483–520.
- Tables of the one, two, and three-dimensional Debye functions are available, respectively:
- a. Wunderlich, B (1962) *J Chem Phys* 37: 1207.
  - b. Gaur U, Pultz G, Wiedemeier H, Wunderlich B (1981) *J Thermal Anal* 21: 309.
  - c. Beatty JA (1926/27) *J Math Phys (MIT)* 6: 1.

Tables of the Einstein function can be found, for example, in Sherman J, Ewell RB (1942) *J Phys Chem* 46: 641.

Closed-form approximations to the Debye functions have been published by Pan R, Varma-Nair M, Wunderlich B (1990) *J Thermal Anal* 36: 145.

More detailed descriptions of heat capacities of polymers can be found in: Wunderlich B, Baur H (1970) *Adv Polymer Sci* 7: 151–368; Perepechko I I (1980) *Low Temperature Properties of Polymers*. Pergamon Press, Oxford.

For ATHAS descriptions and data see the website: [web.utk.edu/~athas](http://web.utk.edu/~athas). For Journal articles see: Wunderlich B (1995) *Pure Applied Chem* 67: 1019–1026; Wunderlich B (1997) *Thermochim Acta* 300: 43–65. A detailed discussion of the match between heat capacities and the low-frequency vibrational spectrum is given by: Bu H-S, Cheng SZD, Wunderlich B, (1987) *J Phys Chem* 91: 4179–4188.

Details for the ATHAS calculations are given in: Pyda M, Bartkowiak M, Wunderlich B (1998) *Computation of Heat Capacities of Solids Using a General Tarasov Equation*. *J. Thermal Anal Calorimetry* 52: 631–656. Zhang G, Wunderlich B (1996) *A New Method to Fit Approximate Vibrational Spectra to the Heat Capacity of Solids with Tarasov Functions*. *J Thermal Anal* 47: 899–911. Noid DW, Varma-Nair M, Wunderlich B, Darsey JA (1991) *Neural Network Inversion of the Tarasov Function Used for the Computation of Polymer Heat Capacities*. *J Thermal Anal* 37: 2295–2300. Pan R, Varma-Nair M, Wunderlich B (1990) *A Computation Scheme to Evaluate Debye and Tarasov Equations for Heat Capacity Computation without Numerical Integration*. *J Thermal Anal* 36: 145–169. Lau S-F, Wunderlich B (1983) *Calculation of the Heat Capacity of Linear Macromolecules from  $\Theta$ -Temperatures and Group Vibrations*. *J Thermal Anal* 28: 59–85. Cheban YuV, Lau SF, Wunderlich B (1982) *Analysis of the Contribution of Skeletal Vibrations to the Heat Capacity of Linear Macromolecules*. *Colloid Polymer Sci* 260: 9–19.

The original papers on the development of the Tarasov functions are: Tarasov VV (1950) *Zh Fiz Khim* 24:111; (1953) *ibid* 27: 1439; (1965) *ibid* 39: 2077; (1955) *Dokl. Akad. Nauk SSR* 100: 307.

For a description of the theory of heat capacities of liquid macromolecules, see: Loufakis K, Wunderlich B (1988) *J Phys Chem* 92: 4205–4209; and Pyda M, Wunderlich B (1999) *Macromolecules* 32: 2044–2050.

The development of the thermodynamic data on polyethylene and polyoxide crystals and melts is documented in the following publications: Wunderlich B, Dole M (1957) *J Polymer Sci* 24: 201; Wunderlich B (1962) *J Chem Phys* 37: 1203, 1207, 2429; Grebowicz J, Suzuki H, Wunderlich B (1985) *Polymer* 26: 561; Suzuki H, Wunderlich B (1985) *J Polymer Sci, Polymer Phys Ed* 23: 1671.

**Sect. 2.4.** More detailed descriptions of irreversible thermodynamics can be found in: Prigogine I (1961) *Introduction to Thermodynamics of Irreversible Processes*. Interscience, New York; Guggenheim EA (1959) *Thermodynamics*. North-Holland Publ Co., Amsterdam; DeGroot SR, Mazur P (1962) *Nonequilibrium Thermodynamics*. North Holland Publ., Amsterdam; DeGroot SR (1963) *Thermodynamics of Irreversible Processes*. North Holland Publ, Amsterdam; Yourgrau W, van der Merve A, Raw G (1982) *Treatise on Irreversible and Statistical Thermophysics*. Dover, New York, corrected reprint of the 1966 edition by Macmillan Co., New York; Baur H (1984) *Einführung in die Thermodynamik der irreversiblen Prozesse*. Wissenschaftliche Buchgesellschaft, Darmstadt; Gyarmati I (1970) *Nonequilibrium Thermodynamics*. Springer, Berlin, 1970.

For a discussion of the melting of polymer lamellae see: Wunderlich B (1980) *Macromolecular Physics*. Vol 3, Crystal Melting. Academic Press, New York.

For a discussion of the use of irreversible thermodynamics for the description of the glass transition, see: Baur H, Wunderlich B (1998) *J Thermal Anal Calorimetry* 54: 437.

**Sect. 2.5.** General discussions of the classical phases and their transitions can be found in your favorite physics, chemistry, or physical chemistry text. Liquid crystals are treated by: DeGennes PG (1974) *The Physics of Liquid Crystals*. Clarendon Press, Oxford; Brown GH (1975) *Advances in Liquid Crystals*. Academic Press, New York; Gray GW (1962) *Molecular Structure and the Properties of Liquid Crystals*. Academic Press, New York. Plastic crystals by: Sherwood N, ed. (1979) *The Plastically Crystalline State (Orientationally-disordered Crystals)*. Wiley, Chichester. For the condis state see: Wunderlich B, Möller M, Grebowicz J, Baur H (1988) *Conformational Motion and Disorder in Low and High Molecular Mass Crystals*. Springer Verlag, Berlin (*Adv Polymer Sci* Vol 87).

The term mesomorphic order was first proposed by: Friedel MG (1922) *Les Etats Méso-morphes de la Matétière*. *Ann Phys (Paris)* 18: 273. The discovery of liquid crystals occurred by Reinitzer F (1888) *Beiträge zur Kenntnis des Cholesterins Monatshefte* 9: 421. The naming goes back to: Lehmann O (1904) *Flüssige Kristalle*. Engelmann, Leipzig; see also Kelker H (1973) *History of Liquid Crystals*. *Mol Cryst Liq Cryst* 21: 1. The name conformationally disordered crystals was first suggested by: Smith GW (1975) *Plastic Crystals, Liquid Crystals and the Melting Phenomenon. The Importance of Order*. In Brown GH, ed. *Advances in Liquid Crystals*, Vol 1. Academic Press, New York. The first detailed comparison of all three mesophase types and the general diagram of Fig. 2.103 was given by: Wunderlich B, Grebowicz J (1984) *Thermotropic Mesophases and Mesophase Transitions of Linear, Flexible Macromolecules*. *Adv Polymer Sci* 60–61: 1.

Transitions are treated in the general physical chemistry references of Sect. 2.3. See also: Ubbelohde AR (1965 and 1978) *Melting and Crystal Structure*. Oxford University Press, London, and *The Molten State of Matter, Melting and Crystal Structure*. Wiley, New York; Boyer RF (1977) *Transitions and Relaxations*, in *Enc Polymer Sci and Technol Suppl* 2. Wiley, New York; an update was given in the second edition of the encyclopedia by Bendler JT (1989) under the same title, Vol 7, p 1.

For the rules of entropies of transition see: Richards JW (1897) *Chem News*: 75: 278; Trouton F (1884) *Philos Mag* 18: 54—Because of the great similarity of all gases, Trouton's rule is more general than Richards's rule. The tendency of Trouton's constant to be higher for higher boiling substances is largely eliminated if one determines the constant for a fixed vapor concentration, as discussed by Hildebrand JH (1915) *J Am Chem Soc* 37: 970 ( $113 \text{ J K}^{-1} \text{ mol}^{-1}$  at concentrations of  $0.005 \text{ mol L}^{-1}$ ). For an early description and classification of conformational defects in crystals, see Wunderlich B (1980) *Macromolecular Physics*, Vol 3, *Crystal Melting*. Academic Press, New York.

For a recent discussion of the assignment of the glass transition, see Syler RJ, ed (1994) *On the Assignment of Glass Transition Temperatures Using Thermomechanical Analysis*. ASTM Symposium, Atlanta, March 4–5, 1993, ASTM STP 1249, Am Soc Testing of Materials, Philadelphia. For the rules of  $\Delta C_p$  see: Wunderlich B (1960) *J Phys Chem* 64: 1052. For larger lists of macromolecular glasses see Athas Data Bank in Appendix 1, where also an approximation of the mobile sections (beads) of the repeating units are given in column 3. For large numbers of glass transition temperatures see: Lee WA, Rutherford RA (1999) in Brandrup J, Immergut EH, Grulke EA, eds, *Polymer Handbook*. 4<sup>th</sup> edn Wiley, New York.

### **Specific References**

1. Mills I, Cvitaš Y, Homann K, Kallay N, Kuchitsu K, eds (1993) *Quantities, Units and Symbols in Physical Chemistry*. Blackwell Science, Oxford.
2. The discussion of the "Future Thermal Analysis" is largely based on the article Kreitmeier SN, Liang, GL, Noid DW, Sumpter BG (1996) *Thermal Analysis via Molecular Dynamics Simulation*. *J Thermal Anal* 46: 853–869.

3. Wasserman PD (1989) *Neural Computing, Theory and Practice*, Van Nostrand Reinhold, New York.
4. The application of neural networks to are described by Noid DW, Varma-Nair M, Wunderlich B, Darsey, JA (1991) Neural Network Inversion of the Tarasov Function Used for the Computation of Polymer Heat Capacities. *J Thermal Anal* 37: 2295–2300.
5. Darsey JA, Noid DW, Wunderlich B, Tsoukalas L (1991) Neural-Net Extrapolations of Heat Capacities of Polymers to Low Temperatures. *Makromol Chem Rapid Commun* 12: 325–330.
6. Moore WG (1972) *Physical Chemistry*. Fourth Ed, p vi, Prentice-Hall, Englewood Cliffs, NJ.
7. Bumstead HA, Gibbs Van Name R (1906) *The Scientific Papers of J. Willard Gibbs*. Longmans, Green and Co. Reprinted by Dover Publications, New York, 1961.
8. Lewis GN, Randall M (1923) *Thermodynamics*, p 448. McGraw–Hill, New York; revised second ed by Pitzer KS, Brewer L (1961) p 130.
9. A modern adiabatic calorimeter is described by: Gmelin E, Rödhammer P (1981) Automatic Low Temperature Calorimetry for the Range 0.3–320 K. *J Phys E, Instrument*. 14: 223–238.
10. Höhne GWH, Hemminger WF, Flammersheim H-J (2003) *Differential Scanning Calorimetry*. 2<sup>nd</sup> edn, Springer, Berlin.
11. Reading M (1993) Modulated Differential Scanning Calorimetry—A New Way Forward in Materials Characterization. *Trends in Polymer Sci* 1(8): 248–253.
12. For the original paper on the Nernst-Lindemann approximation see: Nernst W, Lindemann FA (1911) Spezifische Wärmen und die Theorie der Energieeinheiten. *Z Electrochem* 17: 817–827.
13. For the original paper on the Dulong-Petit rule see: Petit AT, Dulong PL (1819) *Recherches de la Théorie de la Chaleur*. *Ann Chim Phys* 10: 395–413.
14. Pan R, Varma M, Wunderlich B (1989) On the  $C_p$  to  $C_v$  Conversion for Solid Linear Macromolecules II. *J Thermal Anal* 35: 955–966.
15. Einstein A (1907) Die Plancksche Theorie der Strahlung und die Theorie der spezifischen Wärme. *Ann Physik* 22: 180–190 (corrections p 800).
16. Debye P (1912) Zur Theorie der spezifischen Wärme. *Ann Physik* 39: 789–839.
17. Schrödinger E (1926) in Geiger H, Scheel K, eds, *Handbuch der Physik*. Springer, Berlin, Vol 10, p 275.
18. Gaur U, Pultz G, Wiedemeier H, Wunderlich B (1981) Analysis of the Heat Capacities of Group IV Chalcogenides using Debye Temperatures. *J Thermal Anal* 21: 309–326.
19. Baur H, Wunderlich B (1998) About Complex Heat Capacities and Temperature-modulated Calorimetry. *J Thermal Anal and Calorimetry* 54: 437–465.
20. See for example: Hirschfelder JO, Curtis CF, Bird RB (1954) *Molecular Theory of Gases and Liquids*. Wiley, New York (§11.4b).
21. The experimental data of the ATHAS Data Bank are published under the title: Heat Capacity and Other Thermodynamic Properties of Linear Macromolecules. Gaur U, Shu H-C, Mehta A, Wunderlich B (1981) I. Selenium. *J Phys Chem Ref Data* 10: 89–117; Gaur U, Wunderlich B (1981) II. Polyethylene. *Ibid* 10: 119–152; III. Polyoxides. *Ibid* 10: 1001–1049; IV. Polypropylene. *Ibid* 10: 1051–1064; Gaur U, Wunderlich B (1982) V. Polystyrene. *Ibid* 11: 313–325; Gaur U, Lau S-F, Wunderlich BB, Wunderlich B (1982) VI. Acrylic Polymers. *Ibid* 11: 1065–1089; Gaur U, Wunderlich BB, Wunderlich B (1983). VII. Other Carbon Backbone Polymers. *Ibid* 12: 29–63; Gaur U, Lau, S-F, Wunderlich BB, Wunderlich B (1983) VIII. Polyesters and Polyamides. *Ibid* 12: 65–89; Gaur U, Lau S-F, Wunderlich B (1983) IX. Aromatic and Inorganic Polymers. *Ibid* 12: 91–108; Varma-Nair M, Wunderlich B (1991) X. Update of the ATHAS 1980 Data Bank. *Ibid* 20: 349–404.

22. Barnes J, Fanconi B (1978) Critical Review of Vibrational Data and Force Field Constants for Polyethylene. *J Phys Chem Ref Data* 7: 1309–1321.
23. Zhang G, Gerdes S, Wunderlich B (1996) Heat Capacities of Solid Globular Proteins. *Macromolecular Chem Phys* 197: 3791–3806.
24. Wunderlich B (1964) A Thermodynamic Description of the Defect Solid State of Linear High Polymers. *Polymer* 5: 125–134; The Melting of Defect Polymer Crystals. *Ibid* 5: 611–624.
25. Ehrenfest P (1933) Phase Changes in the Ordinary and Extended Sense Classified According to the Corresponding Singularities of the Thermodynamic Potential. *Proc Acad Sci, Amsterdam* 36: 153–157, Suppl 75b, Mitt Kammerlingh Onnes Inst, Leiden.
26. Hosemann, R (1963) Crystalline and Paracrystalline Order in High Polymers. *J Appl Phys* 34: 25–41.
27. Chen W, Wunderlich B (1999) Nanophase Separation of Small and Large Molecules. Invited feature article *Macromol Chem Phys* 200: 283–311.
28. Glasses obtained on cooling of liquid crystalline mesophases were first described by: Vorlaender, D (1933) Remarks on Liquocrystalline Resins and Laquers. *Trans Farad Soc* 29: 907–910.

## Dynamics of Chemical and Phase Changes

The field of dynamics belongs into physical chemistry and deals with the kinetics of making and breaking of bonds in molecules and changes in phases. For macromolecules the basic processes are the syntheses, alteration, and decompositions of polymers and the crystallization and melting. To some degree the kinetics of the glass transition is also of interest. The polymerization kinetics is divided into four major types, as described in Sects. 3.1 and 3.2 (stepwise, step, matrix, and chain reactions). These syntheses lead to different molecular mass distributions, as described in Sect. 3.3. Once a macromolecule is made, its decomposition and its modification by polymer reactions can also be studied in Sect. 3.4 using kinetics, along with facts about polymerization, copolymerization, and cross-linking. Crystal nucleation, molecular nucleation, crystal growth and melting are used to illustrate the kinetics of phase changes in Sects. 3.5 and 3.6. Information on the time-dependence of the glass transition is given in Sects. 5.6, 6.1, and 6.3. Crystallization and melting of flexible macromolecules are often, but not always, free of reorganization of strong bonds. Crystallization during polymerization [1] and decomposition during melting provides connections between flexible and rigid macromolecules (see Sect. 1.1).

### 3.1 Stepwise and Step Reactions

#### 3.1.1 Stepwise Reactions

Syntheses of pure macromolecules are common in biochemistry, but rare for synthetic polymers. In a pure substance all molecules have the same composition and structure. Most syntheses of polymers, however, give a rather broad range of molecular lengths and may also introduce randomly placed isomers and comonomers, as described in Chap. 1 and discussed in more detail in this chapter. The biological molecule ribonuclease, as a well-studied example, is from a class of proteins that functions as an enzyme to control catalytically the transfer of phosphorus containing groups to cleave ribonucleic acids. Its chemical structure is written as  $C_{575}H_{901}O_{193}N_{171}S_{12}$ , making it a rather small macromolecule. The structure consists of a chain of 17 different amino acids from the 20 commonly found in nature. Of these, none occur in blocks longer than three identical amino acids. The general structure is  $H_2N-(CR_iH-CO-NH-)_{123}CR_jH-CO-OH$ , where  $i$  and  $j$  represent the side-groups of the different amino acids. All of its different amino acids are arranged in an identical sequence within each ribonuclease molecule, so that all molecules are of identical length and have a molar mass of 13,682 Da. Figure 3.1 displays the sequence





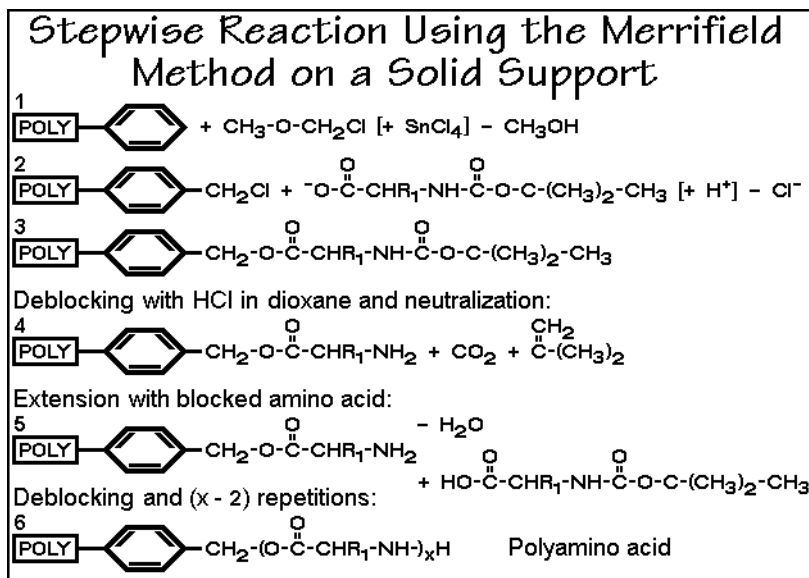


Fig. 3.2

produces methyl alcohol and attaches the methylene chloride group onto a styrene repeating unit of the gel, as shown. In step 2, the active group reacts with a blocked amino acid. The blocking hinders the addition of additional amino acids in the polymerization step 2 and stops the reaction at point 3. After each step of the reaction, the separation of the reactants is rather simple. The product of interest is attached to the network, and all excess reactants and side-products can be flushed by rinsing the gel. After rinsing of all excess chemicals, step 4 in Fig. 3.2 shows how deblocking produces the reactive, attached amino acid. Extension by one additional amino acid is now possible in step 5. Repeating the deblocking, step 4, and extension, step 5 for (x - 2) times, produces a polymer with the designed sequence of x amino acids, shown as the equation in step 6. The final step consists of the recovery of the polymer by cleaving it off the gel with HBr. The Merrifield reaction scheme permits automation of the stepwise reactions with computer control of each step and switching to preselected, different amino acids. Still, a limited yield remains, but can be helped by using longer sequences as starting material or reactant. This technique and related methods are used today for generating unique, short polyamino acids [4].

An oligomer is a molecule made of a number of repeating units, too short to be called a macromolecule which needs to have more than 1000 atoms (Gk. *ὀλίγος* = few, *μέρος* = part). In Fig. 3.3 several methods for the synthesis of oligomers are suggested. The illustrated example has been used to make longer paraffins as model compounds for polyethylene [5,6], several other series of oligomers have also been prepared [7-9]. As the chain-length increases, the initial monomers change to higher-boiling oligomers, and finally become solid.

A specially interesting method for making oligomers is the etching of lamellar crystals with well-defined thickness, as mentioned in Fig. 3.3. Chain-folded crystals of polymers are described in Sect. 5.2. Their lamellar surfaces consist of folds, loose

### Synthesis of Oligomers

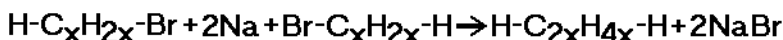
Oligomers have several repeating units linked to a molecule much shorter than a macromolecule.

Synthesis methods:

1. Stepwise reaction.
2. Low molecular mass polymerization and separation.
3. Etching of lamellar crystals, etc.

Example:

#### Paraffins



methane to butane.....gaseous

pentane to octadecane.....liquid

hexacontane..... 375 K melting pt.

longest oligomer made  $\text{C}_{320}\text{H}_{642}$

for long paraffins start

with long "monomer", to

reduce number of steps

and to simplify separation

**Fig. 3.3**

ends, and ties to other crystals and the remaining amorphous phase. All these materials etch faster than the crystal interior. It is, thus, possible by etching to get oligomers with lengths of the crystal thickness in the chain direction [9]. Applications have been, for example, the production of microcrystalline powders [10] and the study of the length for beginning of chain folding in polymer crystals [11].

Oligomers are too short to have typical polymer properties, but they establish the important relationship of the properties as a function of molecular length when going from a small molecule to its corresponding macromolecule. As long as the oligomer is rather short, it can still form, for example, equilibrium crystals and give, thus, a reliable extrapolation of the equilibrium melting temperature that otherwise may not always be available. For example, Fig. 3.4 shows schematically how the melting temperatures of paraffin crystals approach that of polyethylene. The crystal structure changes little in the basic lateral packing of the chains, but there is a decreasing effect from the chain ends. Note that little change occurs after one reaches the polymer molecular mass range ( $> 10,000$  Da). The equation listed gives a good empirical fit to the experimental data.

Quite different is the change of viscosity,  $\eta$ , plotted in Fig. 3.5. As soon as a length of about 1,000 mobile backbone units,  $z$ , designated as number of beads, is reached,  $\eta$  increases faster with molar mass. This is due to entanglements of the molecules, a typical polymer property. The viscosity is a property which does not reach a limiting value when macromolecular dimensions are reached. A similar dependence on length as for the melting exists for the glass transition temperature,  $T_g$ , displayed in the bottom half of Fig. 3.5 for the example of polystyrene. At  $T_g$ , the large-amplitude molecular motion of the viscous liquid stops. Macroscopically, the liquid becomes a solid with mainly vibrational motion, as is discussed in Sect. 2.5. More details about the entanglements and glass transition are given in Chaps. 5–7.

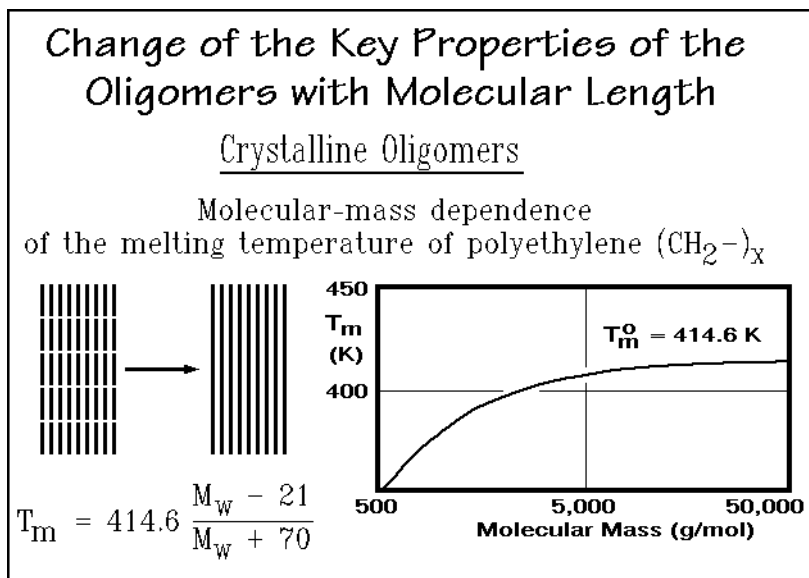


Fig. 3.4

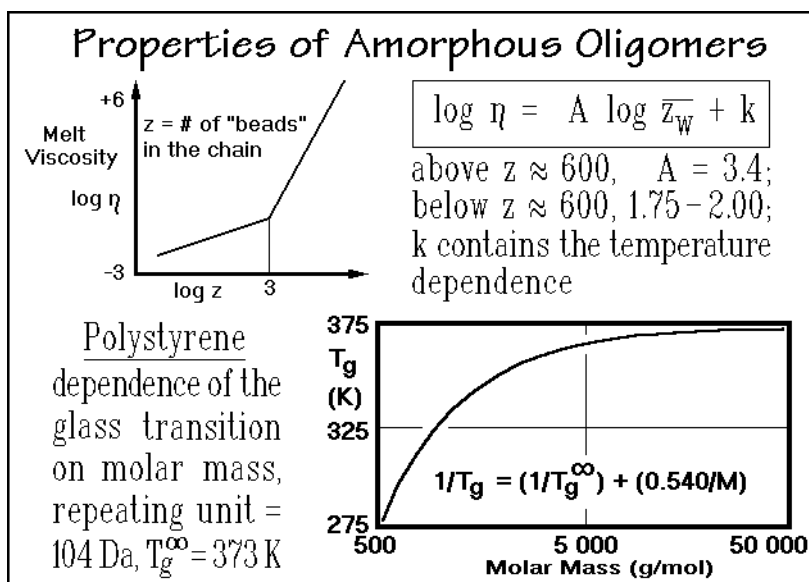


Fig. 3.5

### 3.1.2 Mechanism of Step Reactions

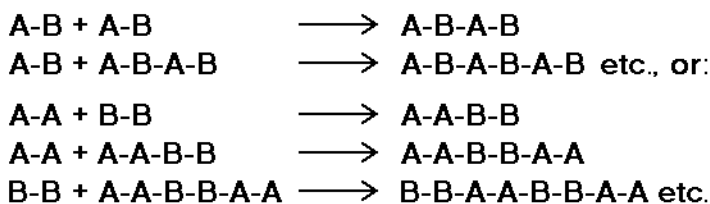
In Sect. 3.1.1 it was established that polymerization reactions must have high precision in repetition in order to yield macromolecules. The two most common reactions for such high-yield polymerizations are step-growth and chain-growth polymerizations.

These two reactions have largely different reaction paths and lead to different molar-mass distributions which are often rather broad and must be described using the techniques derived in Sect. 1.3. Step-growth polymerization is treated in the remaining part of this Sect. 3.1, chain-growth polymerization is covered in Sect. 3.2.

Figure 3.6 illustrates an idealized, kinetic reaction scheme of a step reaction. Molecules of all lengths are at all times able to extend. In reality, the forward reaction is usually able to reverse and to depolymerize or to connect the chain ends to rings.

### General Mechanisms of Step Reactions

One way of two to yield precise molecular composition is the reaction of bifunctional monomers:



qualitatively: 1. all molecules are active at all times  
 2. broad molecular mass distribution  
 3. slow build-up of large molecules  
 4. quick loss of monomer to dimer etc.  
 5. formation of small and large rings

Fig. 3.6

Assuming a chemical group A can react only with a second group B, as for an alcohol and an acid on esterification, one can think of two types of such polymerizations. One occurs with identical monomers with oppositely reacting groups on the ends of each molecule, as in A-B, shown in the top two reaction schemes of Fig. 3.6, the other occurs between two different monomers, each with two identical groups on its ends, as shown in the second three reactions of Fig. 3.6. The five major characteristics of step-reaction polymerizations are listed at the bottom of Fig. 3.6 and will be detailed next. Point 5 is particularly troublesome since it will lead to an inactive molecule.

A simple example of the beginning of a step-growth polymerization is outlined in Fig. 3.7. A purely kinetics-controlled reaction is assumed, as in Fig. 3.6. The scheme of Fig. 3.6 allows no reverse reaction, and for Fig. 3.7, ring formation is also excluded, so that only oligomer chains are produced. Under these conditions, the indicated 16 monomer molecules can be connected with 15 bonds to each other, i.e., they do not polymerize completely. The sequence of steps is indicated by the different shadings of the bonds. After step 1, 25% of the reaction is completed (solid bonds). Only few dimer molecules have been produced, but the monomer weight fraction is already cut in half, as shown in the first column of the table. There is no indication of oligomers or polymers in the distribution of *mers* listed in the figure.

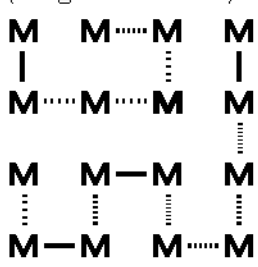
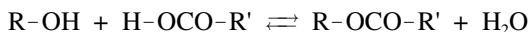
Step-growth Polymerization	Step 1	Step 2	Step 3	Step 4
	p=0.25	p=0.50	p=0.75	p=0.875
	8 M <sub>1</sub>	3 M <sub>1</sub>	0 M <sub>1</sub>	0 M <sub>1</sub>
	4 M <sub>2</sub>	3 M <sub>2</sub>	1 M <sub>2</sub>	0 M <sub>2</sub>
	0 M <sub>3</sub>	1 M <sub>3</sub>	1 M <sub>3</sub>	0 M <sub>3</sub>
16 possible bonds (ring formation) 	0 M <sub>4</sub>	1 M <sub>4</sub>	0 M <sub>4</sub>	0 M <sub>4</sub>
	0 M <sub>5</sub>	0 M <sub>5</sub>	1 M <sub>5</sub>	0 M <sub>5</sub>
	0 M <sub>6</sub>	0 M <sub>6</sub>	1 M <sub>6</sub>	1 M <sub>6</sub>
	M <sub>7</sub>	0 M <sub>7</sub>	0 M <sub>7</sub>	0 M <sub>7</sub>
				0 M <sub>8</sub>
				0 M <sub>9</sub>
				1 M <sub>10</sub>
<div style="border: 1px solid black; padding: 5px; display: inline-block;">             still no macromolecules made unless the monomer is large           </div>				

Fig. 3.7

Step 2 is shown after half of the reaction is over. Larger molecules have now appeared, and the weight fraction of monomers is less than 0.2. Still, one is far from having made polymer molecules. The early decrease in monomer concentration and the late appearance of polymers is typical for the step-growth mechanism.

Step 3 of the schematic of Fig. 3.7 has the reaction completed to 75%. Monomer molecules have now disappeared, and all molecules are different, i.e., a broad molar-mass distribution has developed, again typical of step-growth polymerization. Larger oligomers are still absent. In the last step of this simple example, 14 of the 16 possible bonds are made (87.5%). Now, larger oligomer molecules appear, illustrating the importance to drive step-growth reactions almost to completion. In the above mentioned esterification, completion is forced by removing the produced water:



The statistics of the step-growth polymerizations in Fig. 3.6 is rather easy to develop. If type A-B monomers are the reactants, one sets their initial number equal to  $N_0$ . To use the same  $N_0$  for the reaction of A-A with B-B, one must begin the reaction in the second case with precisely equal numbers of  $N_0/2$  of each monomer. The number of molecules in the reaction mixture,  $N$ , is then always the number of A-units that remain unreacted. The fractional conversion,  $p$ , and the degree of polymerization,  $\overline{DP}$ , can then be calculated as shown in Fig. 3.8. The number-average molar mass can also be calculated using the formalism of Fig. 1.25.

The table in Fig. 3.8 is calculated for a relatively large repeating unit, ethylene terephthalate ( $M_0 = 192.16$  Da, 22 atoms) and illustrates that at least 99% completion is necessary to drive the reaction to a range of lengths required for linear macromolecules. A  $\overline{DP}$  of 100 is a macromolecule of 2,200 atoms and a molar mass of about 20,000 Da, both values typical for a polyester which is industrially useful.

### Statistics of the Random Step Reaction

Equal concentration of A-A and B-B ( $N_0/2$ ) or  $N_0$  of A-B

**At any time the number of molecules  $N$  is equal to the number of remaining A (or B) functional groups. Reacted groups =  $N_0 - N$ .**

Fractional conversion:

$$p = (N_0 - N)/N_0 = \text{reacted A/total A}$$

$$N = N_0(1 - p)$$

Example: PET

Degree of polymerization:

$$\overline{DP} = N_0/N = 1/(1 - p)$$

$$M_0 = 192.16$$

Number average molar mass:

$$\overline{M}_n = M_0/(1 - p)$$

p	$\overline{DP}$	$\overline{M}_n$
0.25	1.33	256.2
0.50	2.00	384.3
0.75	4.00	768.6
0.875	8.00	1597.3
0.990	100.0	19216.0

Fig. 3.8

### 3.1.3 Examples

A number of examples of step-growth polymerizations are given in the following figures. Figure 3.9 illustrates examples of aliphatic polyesters of type A-A and A-B. These are a group of very flexible molecules (see Sect. 1.4). A consequence of the

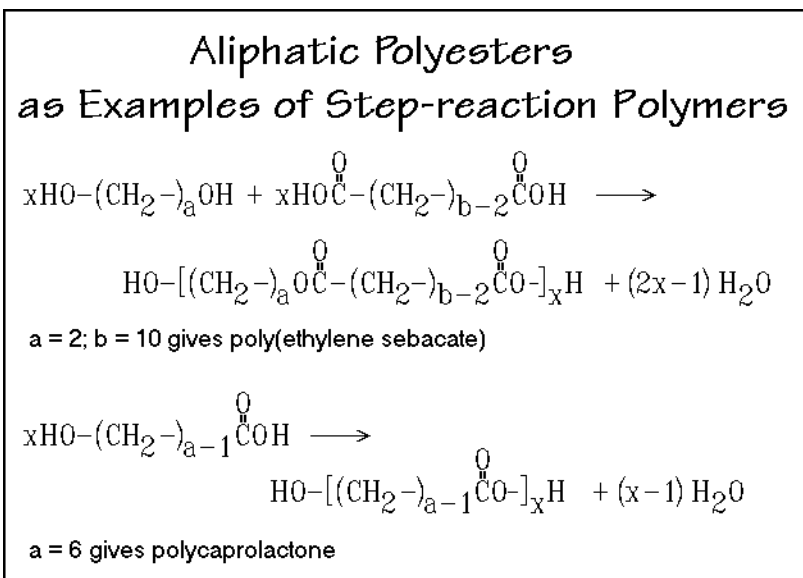
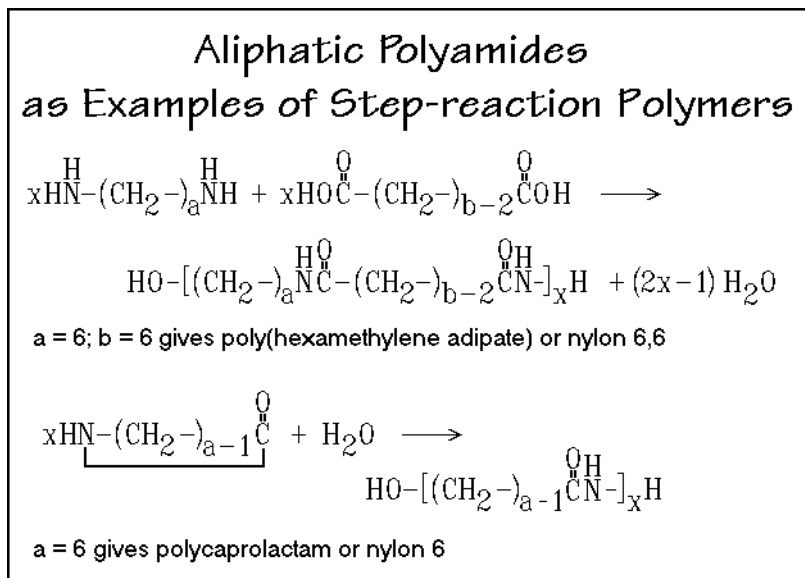


Fig. 3.9

flexibility are relatively low melting temperatures, such as 356.2 K for poly(ethylene sebacate) and 342.2 K for polycaprolactone. Because of the ease of making such polyesters, they were among the first polymers studied. The structurally similar aliphatic polyamides in Fig. 3.10, were the first fully synthetic fibers (nylons, originally trade name of du Pont de Nemours and Co., 1938<sup>1</sup>). Their greater utility, compared to the polyesters, lies in their higher melting temperatures when compared to the corresponding polyesters (574 K for nylon 6,6 and 533 K for nylon 6).



**Fig. 3.10**

The reaction for the A-B monomer starts with a ring-opening, using one molecule of water. This is to be followed by the step-reaction condensation with loss of one water, so that over the full polymerization only one water per molecule is added, as shown. Caprolactam, however, polymerizes better directly in a chain reaction after being initiated with HCl, i.e., it should then be discussed in Sect. 3.2.

The aromatic polymers in Fig. 3.11 are less flexible than their aliphatic counterparts due to the rigid phenylene groups. Increases in  $T_m$  are the result (see Sect. 5.4). Poly(*p*-phenylene terephthalate) (Kevlar<sup>®</sup>) is a high-strength material. The polycarbonates, polyureas, and polyurethanes in Fig. 3.12 round out this group of step-growth polymers. As before, aliphatic and aromatic segments can be included in the structures of monomers to tailor-make polymers of proper flexibility and strength.

A special step polymerization involves an acyclic diene metathesis polymerization, ADMET [12]. A diene,  $\text{CH}_2=\text{CH}(-\text{CH}_2)_n-\text{CH}=\text{CH}_2$ , sets up a condensation equilibrium, evolving ethylene in the presence of an ADMET catalyst and allows polymerization. Substituted dienes can produce precisely branched polymers [13].

<sup>1</sup> Wallace Hume Carothers, 1896–1937. American chemist who developed nylon, the first synthetic macromolecular fiber at the du Pont de Nemours & Company in Wilmington, DE.



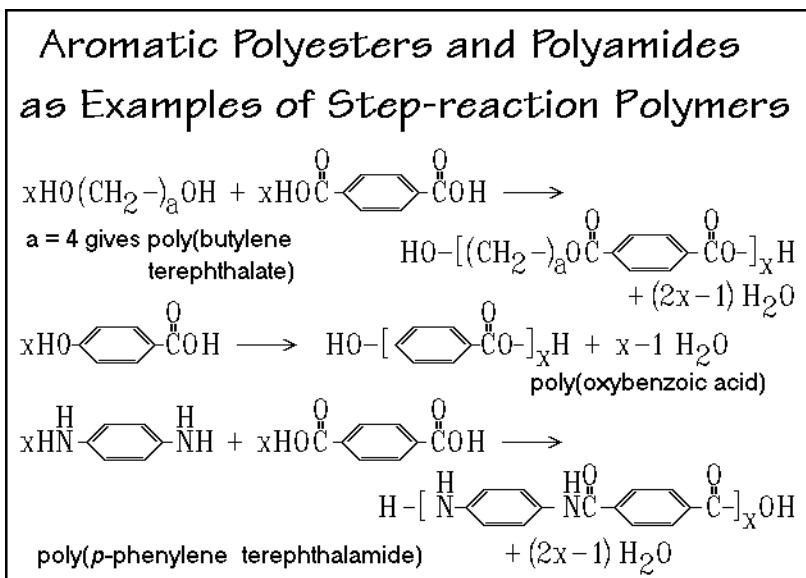


Fig. 3.11

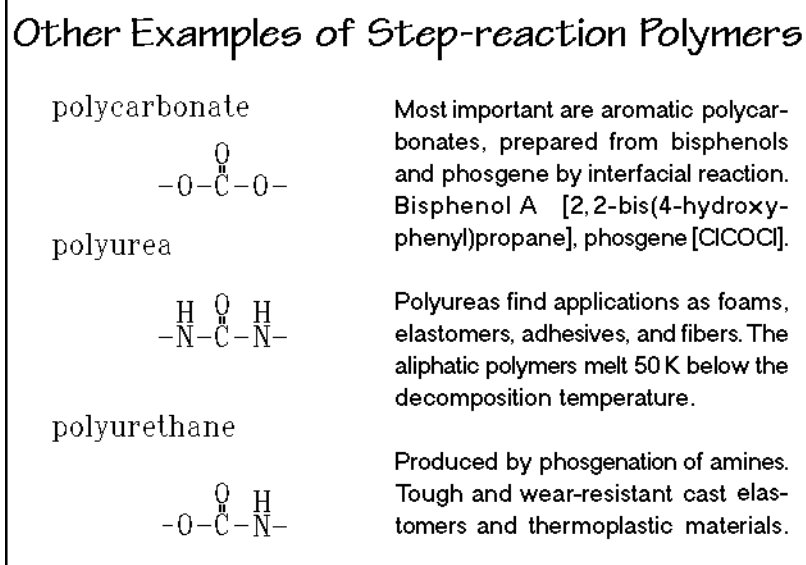


Fig. 3.12

### 3.1.4 Conditions

The conditions for step-growth polymerization are summarized in Fig. 3.13. The much more stringent conditions than customary in general organic syntheses that must be satisfied to produce macromolecules are listed as points a to d. Limits to the molar mass are not only set by incomplete polymerization reactions, as expressed by the

**Conditions for Step-reaction Polymerization**  
a: High conversion; b: Exact equivalence (no impurities);  
c: Absence of side reactions; d: Absence of ring formation.

**Inexact equivalence:** assume  $N_a/N_b = r \leq 1$

$$\overline{DP} = \frac{N_o}{N} = \frac{1+r}{2r(1-p) + (1-r)}$$

$$\overline{DP} \approx \frac{1+r}{1-r}$$

$$N_o = (N_a/2) + (N_b/2)$$

$$N = N_a(1-p) + (N_b/2) - (N_a/2)$$

Example: 1.0 mol % excess of component B-B:  $r = 0.99$   
 $\overline{DP} = 1.99/0.01 = 199$

**Impurity:** assume  $N_1$  moles

$$\overline{DP} = \frac{N'_o}{N'} = \frac{N_o + N_1}{N_o(1-p) + N_1}$$

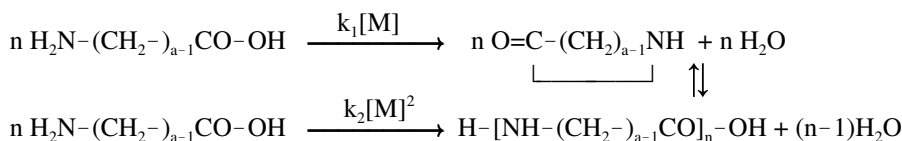
Example: 1 mol % benzoic acid to a terephthalic acid monomer,  $p = 0.99$ .  
 $\overline{DP} = 1.01/0.02 = 50.5$ , instead of 101

**Ring formation:** 
 $R = \frac{\text{cyclic monomer}}{\text{linear polymer}} = \frac{k_1[M]}{k_2[M]^2} = \frac{\text{constant}}{[M]}$

Fig. 3.13

fractional completion,  $p$ , or the degree of polymerization,  $\overline{DP}$ , but can also be set by inexact equivalence of the numbers of A-A and B-B molecules, impurities with only one active chain end, side reactions, and ring formation. Next, Fig. 3.13 shows the change in the degree of polymerization on deviation from equivalence of A- and B-groups (for equivalence  $N_a/N_b = r = 1.000$ ). From the example given, it is clear that 99% purity and reaction to completion ( $p = 1.00$ ) are needed for the production of macromolecules of acceptable size. Another limiting effect is the influence of impurities that can prevent molecules from further growth. The result is obviously similar to the nonequivalence of -A and -B. One mol % of impurity cuts the DP in half under the given conditions. The addition of a controlled amount of impurity, coupled with reaction conditions that fix  $p$  (usually close to 1.0) can be used in industrial polymerizations to control the overall molar mass.

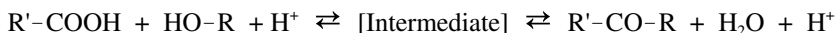
Strain-free, small rings, such as caprolactam or caprolactone, have a high rate constant,  $k_1$ , for their formation. On equilibration with the chain reaction, they lead to a fixed ratio of rings to chains,  $R$ , as is shown at the bottom of Fig. 3.13:



High rates of polymer formation call for a high monomer concentration  $[M]$  to favor initially the intermolecular reaction, written at the bottom, over the top cyclization reaction. As will be shown in the next section, the intramolecular cyclization is a reaction of first order, while a typical ester or amide formation, under the given conditions, is of second or third order.

### 3.1.5 Reaction Rates

The reaction mechanisms and rates involved in polymerizations and their temperature dependence are similar to reactions involved in small-molecule dynamics which are briefly reviewed in Appendix 7, Fig. A.7.1. Figure 3.14 represents an example of a reaction that involves a third-order mechanism, an esterification:



where R' can be the continuing polymer chain and R the to be added monomer. The reaction intermediate can be seen in the figure. The forward reaction leads to the connection of the two reactants (polymerization), while the reverse reaction (saponification) would be involved in a depolymerization. The same basic reaction is also discussed in Sect. 3.4 in connection with the treatment of transesterification, a reaction that can change the structure of once polymerized macromolecules.

The rate expression takes into account that three parts that must come together to form the reaction intermediate, the alcohol, acid, and catalyst ( $H^+$  in the chosen case). The evaluation of the reaction rate is particularly simple if all reactants are present at equal concentration,  $c$ . Since the  $[-A]$  and  $[-B]$  concentrations in step reaction polymerizations are always closely equal, and  $[H^+]$  may be kept constant by fixing its concentration, the pH, the reaction can also be analyzed as a second-order process as also shown in Fig. 3.14. These expressions will be used in Sect. 3.1.6 for the description of the  $LiH_2PO_4$  polymerization.

The left and right tables at the bottom of Fig. 3.14 list the changes of the rate constants with chain length for esterification and saponification, respectively. Only if structural changes are made less than 3–5 atoms from the reactive site, does one find significant changes in the rate constants of the esterification. The methyl alcohol rate

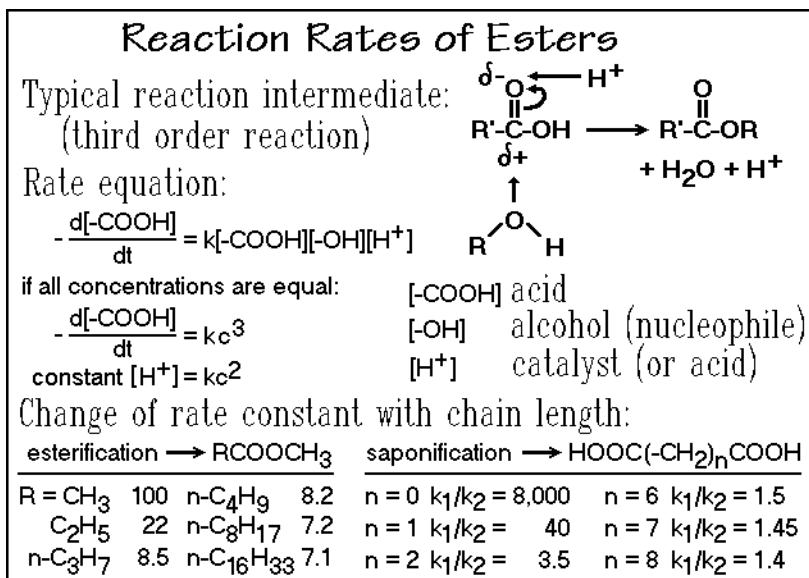


Fig. 3.14

constant is normalized to 100. In most cases the monomers are, however, already long enough that one or two rate constants are sufficient to model the overall polymerization. A similar result is seen for the saponification to the diacid. The ratio  $k_1/k_2$  signifies the rate of losing the first and second ester group.

Figure 3.15 summarizes the energetics of the reaction. Of importance is the higher potential energy reached by the activated state which is one key factor in the determination of the reaction rate via its activation energy  $E_a$ .

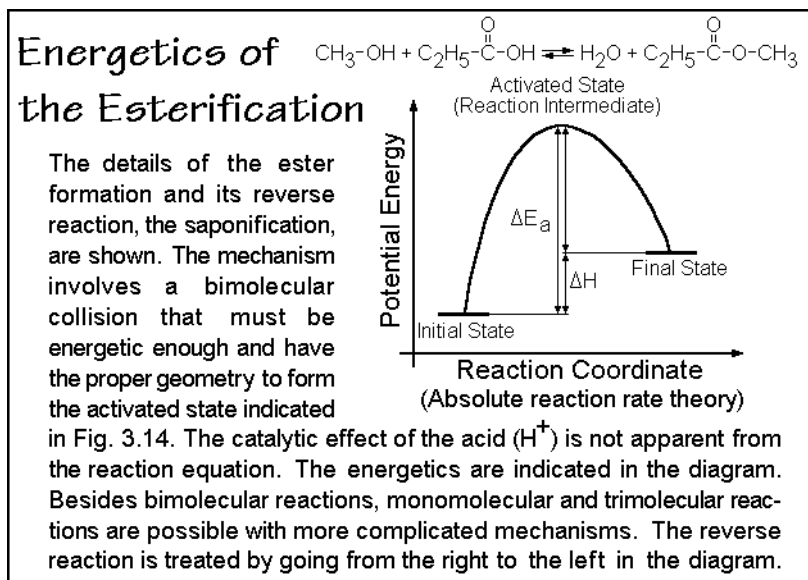


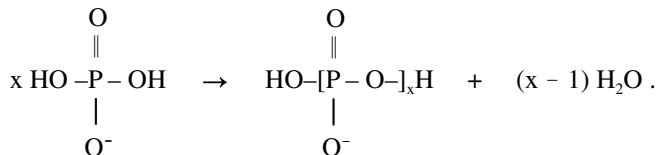
Fig. 3.15

### 3.1.6 Lithium Phosphate Polymerization

The step-growth polymerization of dibasic lithium phosphate is discussed next as an example of a polymerization reaction followed by immediate crystallization to the polymer, studied largely by thermal analysis [14,15]. It illustrates that not only organic molecules can be flexible macromolecules, but also inorganic ones. The two major techniques used for the analysis are differential scanning calorimetry (DSC, see Sect. 4.3) and thermogravimetry (TGA, see Sect. 4.6). The reaction equation is:



The reaction product, the polymeric phosphate (formerly called metaphosphate) has a high melt viscosity, as expected for a polymer. The step-reaction polymerization becomes clearer when following the fate of the dihydrogen phosphate ion:



The DSC heating-trace in Fig. 3.16 shows several complications during the nonisothermal reaction. First, there is the melting endotherm of the  $\text{LiH}_2\text{PO}_4$  monomer, beginning at about 470 K ( $\Delta T$  in the endothermic direction is proportional to the consumed heat to raise temperature). In addition to the fusion, other endothermic effects are due to the evaporation of water evolved in the chemical reaction. The TGA trace of Fig. 3.17 registers the changes in mass, and records quantitatively the

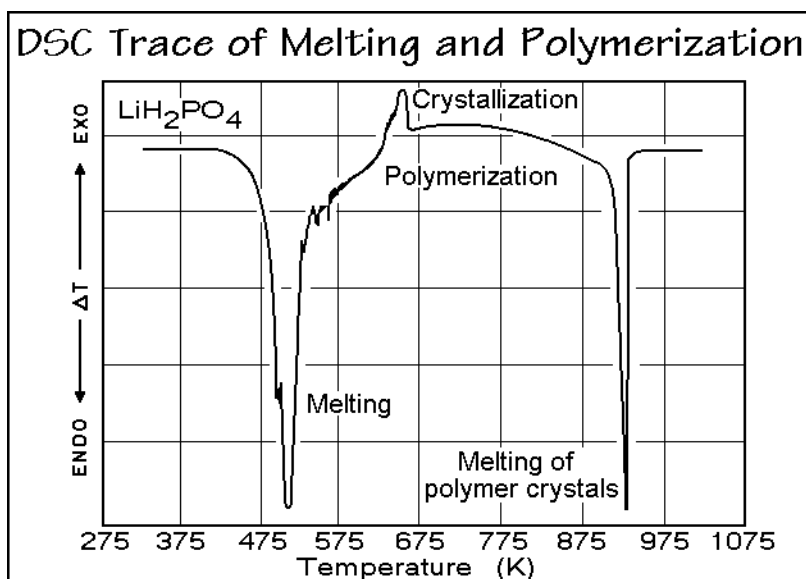


Fig. 3.16

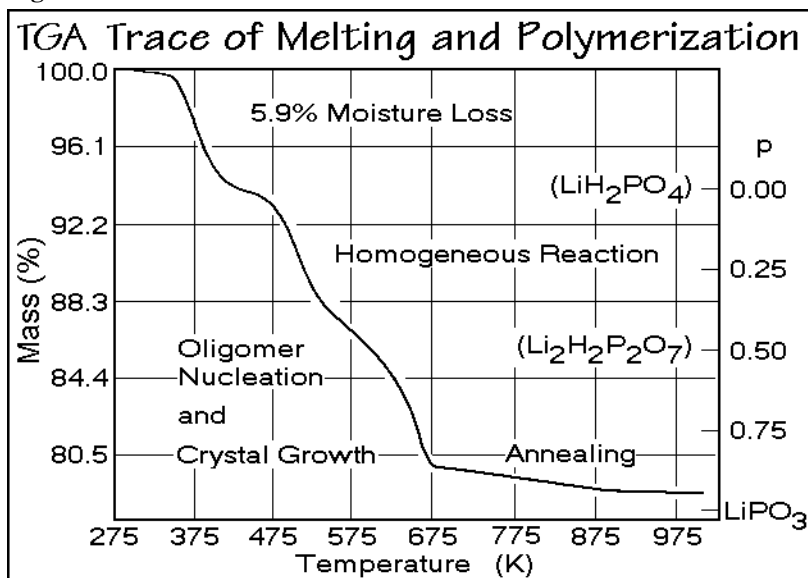


Fig. 3.17

progress of the chemical reaction. The initial moisture loss, shown in Fig. 3.17 can be removed by drying the monomer before the heating. The small exotherm in 3.16 comes from crystallization, and the final endotherm, at about 900 K, indicates melting of the polymer,  $\text{LiPO}_3$ . The TGA trace of Fig. 3.17 indicates that after the moisture loss the reaction proceeds in two stages, and is followed by slow annealing (crystal perfection). This process is clarified with an isothermal TGA run at 573 K of a dried monomer of sufficient quality to establish the kinetics of the polymerization. Figure 3.18 is the result and is of sufficient quality to establish the reaction kinetics.

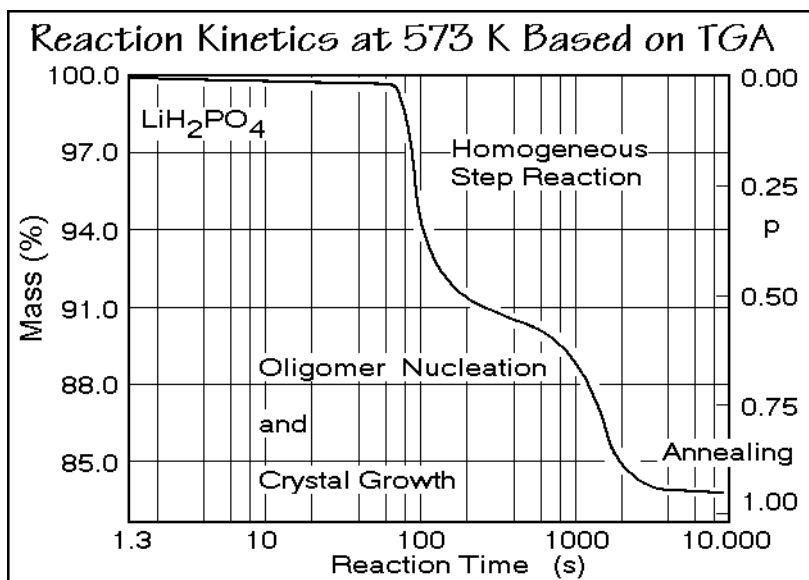


Fig. 3.18

As is typical for step-growth polymerizations, each molecule in the reaction mixture has two reactive  $-\text{OH}$  groups, and for each  $\text{H}_2\text{O}$  molecule lost, one bond is formed. Furthermore,  $[\text{H}^+]$  is also proportional to  $[-\text{OH}]$  if no external acid is added. In Fig. 3.19 a kinetics is assumed, similar to the just discussed third-order esterification ( $n = 3$ ). This assumption is next shown to fit the measured data. Writing for the concentration  $[\text{POH}] = [\text{POH}]_0(1 - p)$ , where  $[\text{POH}]_0$  is the initial concentration ( $= 2M_0$ ) and  $p$  the fractional progress of the polymerization, one can see that the rate of polymerization  $dp/dt = k[\text{POH}]_0^2(1 - p)^3$ . The connection to the boxed equation is given by  $k' = k[\text{POH}]_0^2$ . Also, written is the temperature-dependence of  $k'$  as described in Fig. A.7.2.

Since the TGA-trace in Fig. 3.18 indicates that the fast reaction is complete at  $p = 0.5$ , one expects that the rate constant  $k_a$  for the formation of a dimer is larger than  $k_b$  for further polymerization as suggested in the summary at the bottom of Fig. 3.14. Assuming that only the monomer-to-dimer rate is faster than the rest of the polymerization, a full set of kinetic equations as indicated in Fig. 3.20 can be solved. The monomer concentration decreases due to the formation of dimers (with a rate constant  $k_a$ ) and all other species that react need the rate constant  $k_b$ . Analogously other

### Detailed Discussion of the Reaction Rate

$$\text{Reaction rate} = -\frac{d[\text{P-OH}]}{dt} = k[\text{P-OH}]^n$$

$$dp/dt = k M_0^{n-1} (1-p)^n$$

$$dp/dt = k' (1-p)^3$$

$$k' = A e^{-E_a/(RT)}$$

$$p = \frac{M_0 - [\text{P-OH}]}{M_0}$$

$$[\text{P-OH}] = M_0(1-p)$$

$n$  = order of the reaction

$[\text{P-OH}]$  = concentration of -OH on the phosphates

$[\text{P-OH}]_0 = 2M_0$ , initial concentration

$p$  = degree of progress of the reaction

Assume  $n = 3$  in analogy to reactions of organic acids

**Fig. 3.19**

equations can be written for any oligomer of mass  $M_x$ , as shown. Concentration  $[M_2]$ , for example, increases when two monomers react with rate constant  $k_a$ , and decreases for any other species reacting with the dimer  $M_2$ .

The reaction equations of Fig. 3.20 were written for oligomer lengths of up to 30 repeating units and then fitted to the thermogravimetry experiment shown in Fig. 3.18. The reverse reactions, the depolymerizations, were neglected, which is permissible in

### Kinetics for the Polymerization

$$\frac{\Delta[M_1]}{\Delta t} = -2k_a[\text{P-OH}][M_1]^2 - k_b[\text{P-OH}][M_1]\{[M_2] + [M_3] + \dots\}$$

$$\frac{\Delta[M_2]}{\Delta t} = k_a[\text{P-OH}][M_1]^2 - k_b[\text{P-OH}][M_2]\{[M_1] + 2[M_2] + \dots\}$$

$$\frac{\Delta[M_3]}{\Delta t} = k_b[\text{P-OH}]\{[M_1][M_2] - [M_3]\{[M_1] + [M_2] + 2[M_3] + \dots\}\}$$

$$\frac{\Delta[M_4]}{\Delta t} = k_b[\text{P-OH}]\{[M_1][M_3] + [M_2]^2 - [M_4]\{[M_1] + [M_2] + \dots\}\}$$

$\vdots$

$\vdots$

$\vdots$

$\vdots$

$\vdots$

Experimental data:

$$573 \text{ K} \quad k_a = 7.5 \cdot 10^{-4}$$

$$563 \text{ K} \quad k_a = 5.5 \cdot 10^{-4}$$

$$549 \text{ K} \quad k_a = 2.9 \cdot 10^{-4}$$

$$k_b = 3.5 \cdot 10^{-6} \text{ (l}^2\text{mol}^{-2}\text{s}^{-2}\text{)}$$

$$k_b = 3.0 \cdot 10^{-6} \text{ (l}^2\text{mol}^{-2}\text{s}^{-2}\text{)}$$

$$k_b = 1.9 \cdot 10^{-6} \text{ (l}^2\text{mol}^{-2}\text{s}^{-2}\text{)}$$

**Fig. 3.20**

the initial stages of the reaction. The experimental data from the best fits at the early reaction times are shown at the bottom of Fig. 3.20. As expected, the rate constant  $k_a$  is much larger than the rate constant  $k_b$ . As the reaction starts, almost only the dimer is formed. In fact, in similar reactions of the sodium salt,  $\text{NaH}_2\text{PO}_4$ , it is possible to cause a sufficient build-up of the concentration of the dimer that it crystallizes and slows the reaction further.

Figure 3.21 illustrates the changes of the concentrations of the species with time for the experimental data with the faster monomer reactivity. The line  $4 \rightarrow \infty$  combines tetramers and larger molecules. The concentration of every species, except the monomer, has a maximum which shifts to later times for longer molecules. As before, ring-formation has been neglected to make the kinetics manageable.

The progress of the reaction at 573 K, as evaluated in Fig. 3.20, is shown in Fig. 3.22. Going back to the DSC-trace in Fig. 3.16 a complication arises indicated by the crystallization exotherm. After about 800 s, oligomers start to crystallize. The volume fraction of the crystallized polymer is given by  $v^c$  as measured by optical microscopy. The two phases which are now present consist of pure polymerized phosphate and the homogeneous melt with concentrations as suggested in Fig. 3.21. As the crystallization progresses, the higher oligomers and polymers are increasingly extracted from the melt, i.e., the degree of polymerization decreases below the value  $p$  calculated from the homogeneous phase of the reaction. The experimental data, recalculated for the depleted liquid phase (●), are added in Fig. 3.22 under the assumption that mainly dimers add to the growing macromolecules after they are nucleated in the solid state as oligomers. The data fit perfectly up to about 1,000 s. At times longer than 1,000 s, the reaction seems to reverse. More about the continuing crystallization during polymerization is discussed in Sects. 3.5 and 3.6.

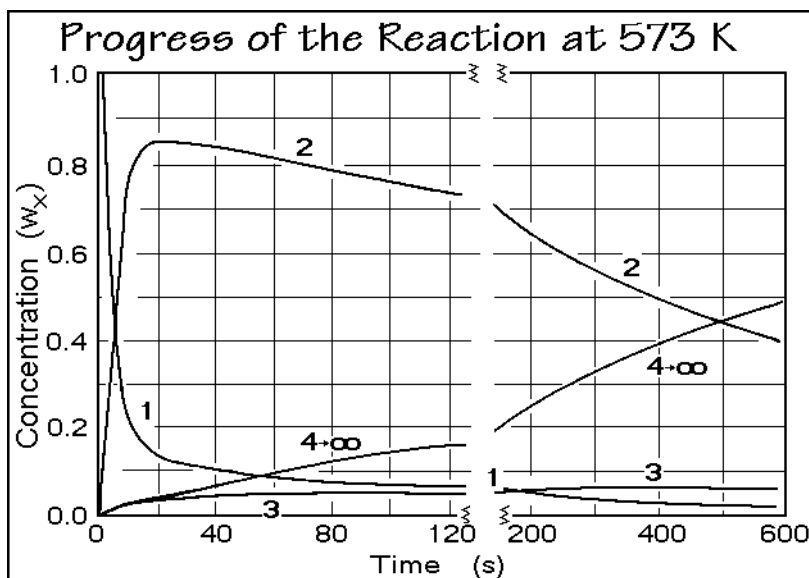


Fig. 3.21



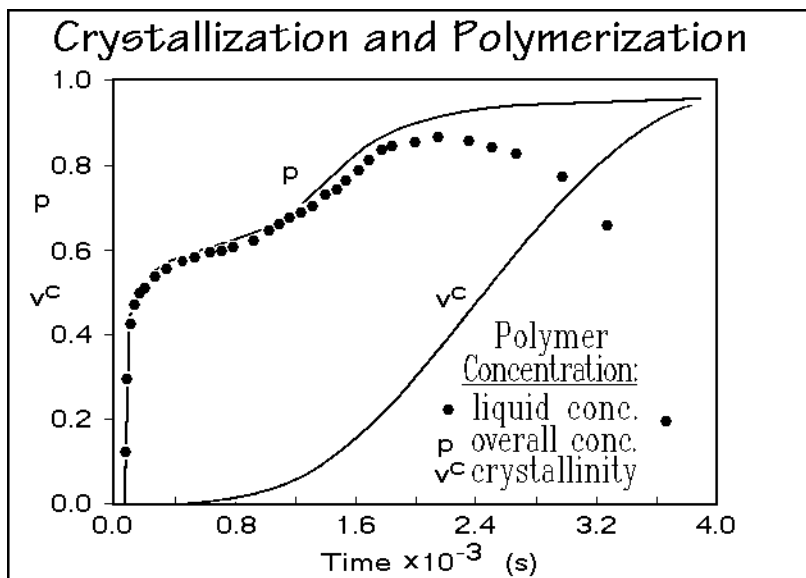


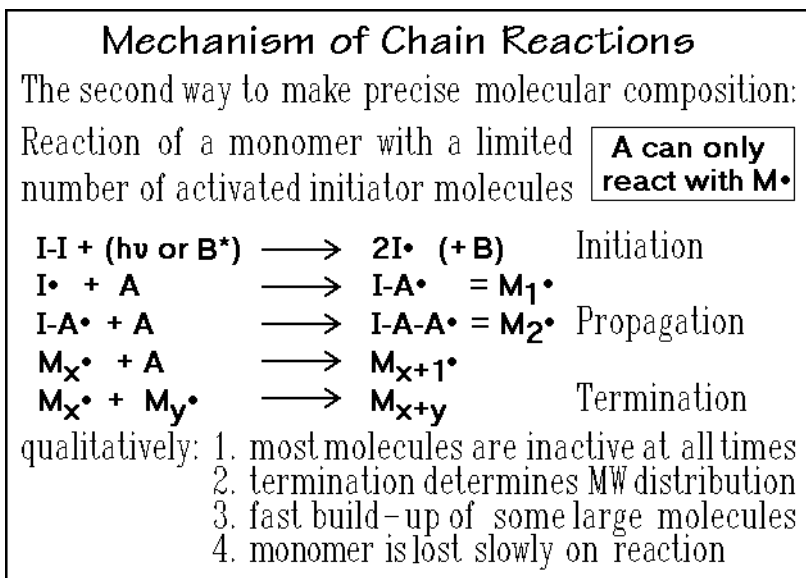
Fig. 3.22

## 3.2 Chain and Matrix Reactions

### 3.2.1 Mechanism of Chain Reactions

Chain-growth polymerization is the other important polymerization process besides the step reactions, discussed in Sect. 3.1. The condition for the reaction is given in Fig. 3.23. The mechanism of the reaction involves a small number of active molecules,  $M^\bullet$ . Only these active molecules support further polymerization of the monomers, A. The chemical composition is maintained by a continued chain of the same reactions of A with  $M^\bullet$ . The illustration of the mechanism refers to a free radical polymerization. Initiation, propagation, and termination are the three stages of the reaction.

The initiator, I-I, is homolytically broken into two free radicals by either absorption of a photon,  $h\nu$ , or by collision with another molecule,  $B^\bullet$ . In either case there must be sufficient energy to break the center bond of the initiator. Once formed, each free radical, written as  $I^\bullet$ , can start a polymerization reaction by adding monomer molecules. The first step leads to the free radical monomer,  $I-A^\bullet$ , also written as  $M_1^\bullet$ . The next step of the reaction produces a free radical called  $M_2^\bullet$ . Each step of the chain reaction has up to this point its own specific rate constant. Addition of further monomers goes, however, substantially with the same rate, so that one can write during the main growth period of the molecule for each step the fourth reaction equation in Fig. 3.23, where  $x$  is the degree of polymerization. Ultimately, the reaction may be stopped by a termination reaction of the chain. The example of the termination reaction shown is a combination of two free radicals. The special case for

**Fig. 3.23**

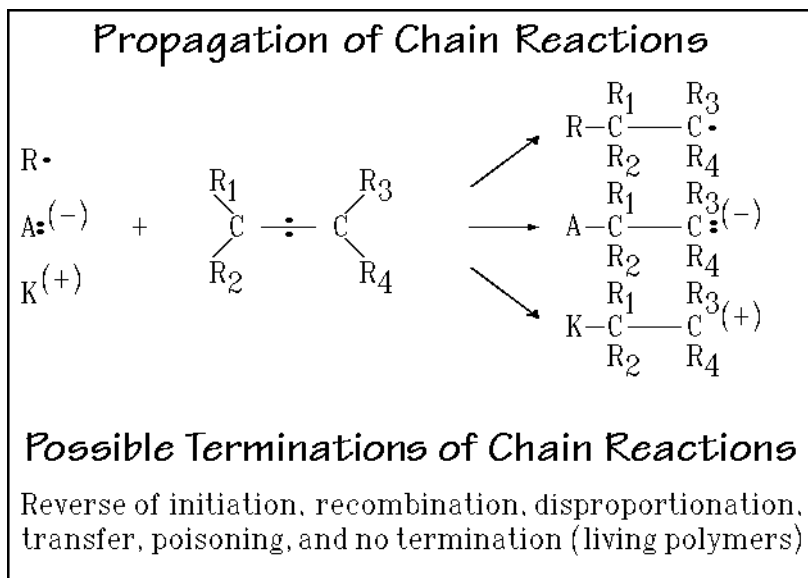
reactions that may have no termination is treated in Sect. 3.2.4. Most important is that during a chain reaction polymerization occurs only on the free-radical sites, i.e., most molecules are inactive at any given time, while during the step reaction all molecules remain active at all times. The other points at the bottom of Fig. 3.23 follow directly from the mechanism.

Three typical free radical initiation reactions are summarized in Fig. 3.24. In the free radical initiation the center part of the initiator, azobisisobutyronitrile, can eject a stable nitrogen molecule. This gives the driving force to produce the two active free radicals. Before recombination, the free radicals can accomplish the thousands of propagation steps necessary to produce a macromolecule.

Another type of chain reaction is possible by ionic initiation. Both, positive and negative ions may start polymerization reactions (cationic and anionic polymerization). The existence of ions in solution is illustrated in Fig. 3.24 (B = base, M = metal). The interaction with the solvent plays an important role in the activity of the catalyst. In the covalent combination, no reactivity is expected. As the ions separate, they become increasingly available for reaction. While one of the ions supports the reaction, the other, the counterion, is in the vicinity and may also affect the rate of reaction. Since cationic initiators accept a pair of electrons, one finds these among the Lewis acids. Anionic initiators donate an electron pair, so they are Lewis bases.

A third type of chain reaction is based on coordination catalysts. A most common example of such initiation is given in the Ziegler-Natta catalyst described in Fig. 3.24. A coordination complex may be formed on a crystal surface or in solution. The monomer is inserted into the active site, as is illustrated in the reaction sequence of propylene polymerization on a  $TiCl_3$  crystal surface, as described on Figs. 3.26 and 27, below. The geometry of the various ligands of the complex may direct the incoming monomer in such a way that a stereospecific polymerization is possible.



**Fig. 3.25**

is the ease of their termination. Anionic polymerization may be kept virtually free from termination due to the relative stability of the anion, as is discussed in Sect. 3.2.4 on chain reactions without termination. Cationic polymerization, on the other hand, may be terminated by any of a large number of reactions known for the organic cation. Poisoning of the active chain is a common termination reaction for all ionic polymerizations. Stringent conditions exist for all ionic reactions as well as the coordination reactions to keep out poisons such as oxygen and moisture.

Coordination reactions are insertion reactions. They may occur on single sites of a dissolved catalyst such as metallocenes [16,17], used for making stereospecific polypropylene or uniform polyethylene copolymers. Multiple sites are found on heterogeneous reactions, i.e., the reactions take place on surface sites of crystals. Most well-known is the Ziegler-Natta<sup>1</sup> polymerization [18], for which a recipe is given in Fig. 3.24. The schematic indicates one of the active sites on an  $TiCl_3$  crystal which acts by absorbing triethyl aluminum on one vacancy and the monomer on the other. By insertion of the adsorbed monomer between the Al and the  $-C_2H_5$  on the solid surface, the polymer grows by insertion, as illustrated for propylene in Figs. 3.26 and 3.27. Since the geometries of the reaction intermediates are quite restrictive, it is possible to direct the monomer in such a way to yield pure stereoisomers when using catalysts of proper design (for the description of isomers see Sect. 1.2). The discovery of synthetic routes to stereospecific macromolecules was one of the milestones to modern polymer science, as mentioned in Sect. 3.1. Due to the high regularity of the

<sup>1</sup> Karl Ziegler (1898–1973, German chemist, Director of the Max Planck Institute for Coal Research at Mülheim an der Ruhr); Giulio Natta (1903–1979, Italian chemist, Professor at the Milan Polytechnic and Research Director of Industrial Chemistry). Both shared in 1963 the Nobel Prize for their work on polymerization.

substituents  $R_1$  to  $R_4$  in pure stereoisomers, they may crystallize and produce solid structural materials. Without this regularity, the same macromolecules remain liquid or rubbery down to the glass transition temperature. The requirements of structural regularity for crystallization and the temperatures found for glass and melting transitions are discussed in Chap. 5.

Table 3.1, finally, introduces a summary for many monomers which are polymerizable by chain reactions. Listed are their ability to polymerize by free radical (R), cationic (C), anionic (A), or coordination reaction (Crd). Syntheses for many common macromolecules are found in this list. Now it is time to use this list to check the 22 polymers for the proper source-based and structure-based names, as in Sect. 1.2. Also, it is a suitable time to review the common applications, and properties of these polymers as known from the introductory chapter on polymer science.

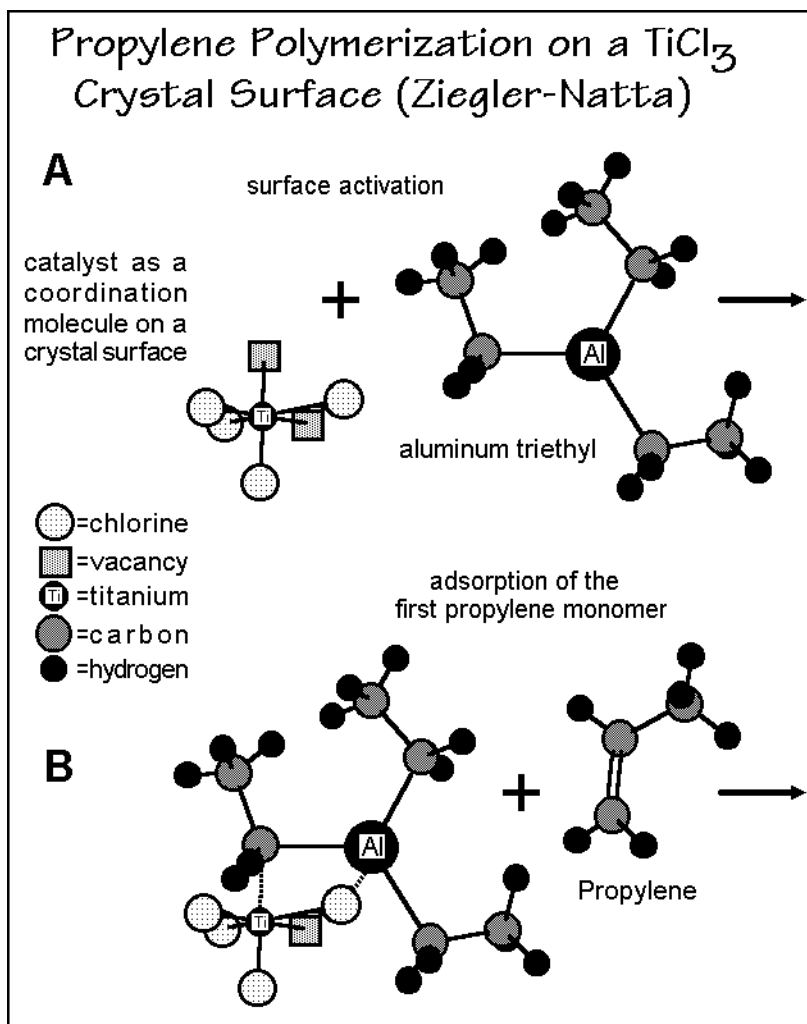


Fig. 3.26

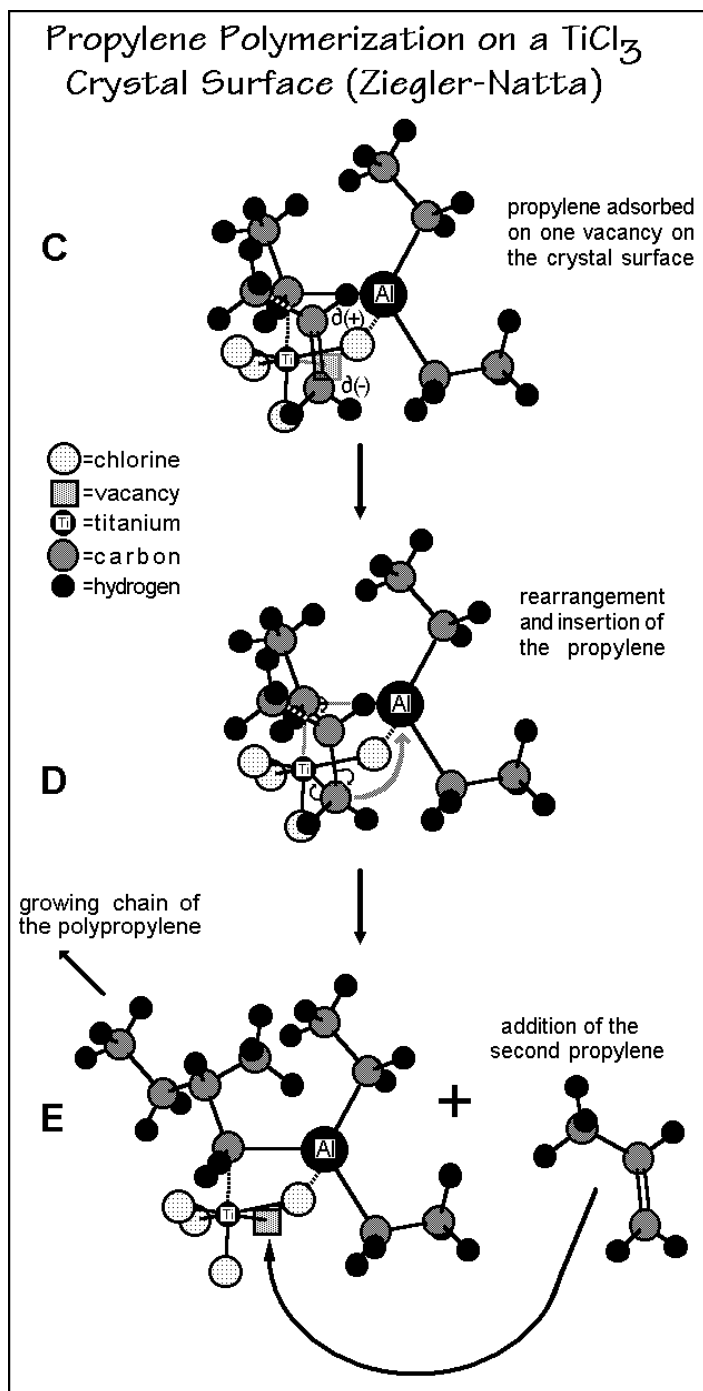


Fig. 3.27

**Table 3.1.** Reaction types for the polymerization of various monomers

Monomer Name and Formula		R <sup>a</sup>	C <sup>b</sup>	A <sup>c</sup>	Cr <sup>d</sup>
ethylene	H <sub>2</sub> C=CH <sub>2</sub>	+	+	[+]	+
propene	H <sub>2</sub> C=CH-CH <sub>3</sub>	-	-	-	+
butene	H <sub>2</sub> C=CH-CH <sub>2</sub> -CH <sub>3</sub>	-	-	-	+
isobutene	H <sub>2</sub> C=C(CH <sub>3</sub> ) <sub>2</sub>	-	+	-	-
1,3-butadiene	H <sub>2</sub> C=CH-CH <sub>2</sub> =CH <sub>2</sub>	+	[+]	+	+
isoprene	H <sub>2</sub> C=C(CH <sub>3</sub> )-CH=CH <sub>2</sub>	+	[+]	+	+
styrene	H <sub>2</sub> C=CHC <sub>6</sub> H <sub>5</sub>	+	+	+	+
α-methyl styrene	H <sub>2</sub> C=C(CH <sub>3</sub> )C <sub>6</sub> H <sub>5</sub>	+	+	+	+
vinyl chloride	H <sub>2</sub> C=CHCl	+	-	-	+
vinylidene chloride	H <sub>2</sub> C=CCl <sub>2</sub>	+	-	+	-
vinyl fluoride	H <sub>2</sub> C=CHF	+	-	-	-
tetrafluoroethylene	F <sub>2</sub> C=CF <sub>2</sub>	+	-	-	+
vinyl ether	H <sub>2</sub> C=CH-O-R	-	+	-	+
vinyl ester	H <sub>2</sub> C=CH-O-CO-R	+	-	-	-
acrylic ester	H <sub>2</sub> C=CH-CO-O-R	+	-	+	+
methacrylic ester	H <sub>2</sub> C=C(CH <sub>3</sub> )-CO-O-R	+	-	+	+
acrylonitrile	H <sub>2</sub> C=CH-C≡N	+	-	+	+
methacryl amide	H <sub>2</sub> C=C(CH <sub>3</sub> )-CO-NH <sub>2</sub>	+	-	+	+
aldehydes	HRC=O	-	+	+	?
ketones	R <sub>1</sub> R <sub>2</sub> C=O	-	+	+	?
N-vinyl carbazole	H <sub>2</sub> C=CH-NC <sub>12</sub> H <sub>8</sub>	+	+	-	?
N-vinyl pyrrolidone	H <sub>2</sub> C=CH-NC <sub>4</sub> H <sub>6</sub> O	+	+	-	?

<sup>a</sup> Free radical polymerization;<sup>b</sup> Cationic polymerization;<sup>c</sup> Anionic polymerization;<sup>d</sup> Coordination catalysis.

### 3.2.2 Kinetics

The kinetics of chain-reaction polymerization is illustrated in Fig. 3.28 for a free radical process. Analogous equations, except for termination, can be written for ionic polymerizations. Coordination reactions are more difficult to describe since they may involve solid surfaces, adsorption, and desorption. Even the crystallization of the macromolecule after polymerization may be able to influence the reaction kinetics. The rate expressions, as given in Appendix 7, Fig. A7.1, are easily written under the assumption that the chemical equations represent the actual reaction path. Most important is to derive an equation for the kinetic chain length,  $\bar{v}$ , which is equal to the ratio of propagation to termination-reaction rates. This equation permits computation of the molar mass distribution (see also Sect. 1.3). The concentration of the active species is very small and usually not known. First one must, thus, eliminate  $[M\bullet]$  from the rate expression, as shown in the figure. The boxed equation is the important equation for  $\bar{v}$ .

Figure 3.29 displays a schematic plot of the change in monomer concentration with time  $d[A]/dt$ . First there is an increase in reaction rates as more new radicals are produced by initiation. Next, a steady state is achieved as new radicals form as fast





available to absorb the heat of reaction. Chain transfer and any other of the possible termination reactions would invalidate the simple reaction kinetics. To consider other terminations, they must be known, along with their kinetic parameters. Precipitation may occur if the polymer is not soluble in the monomer or solvent used for the polymerization. The precipitation may remove the active radicals by incorporation in the solid. The gel effect is special for polymers. As the molar mass (and viscosity) increases sufficiently, termination may slow since chain ends cannot diffuse together. This results in an increase in  $d[A]/dt$  and molar mass.

### 3.2.3 Equilibrium

In case the reverse of the polymerization, the depolymerization, is significant, a more complicated kinetics describes the chain reactions. Figure 3.30 shows the scheme. If rates of the forward and reverse reactions become the same, equilibrium is reached. The equilibrium temperature is called the ceiling temperature,  $T_c$  (at a given concentration or vapor pressure  $[A]$ ). Standard thermodynamics applies to this equilibrium (see Chap. 2). On depolymerization, the entropy of the system,  $S$ , increases because the number of molecules increases. With a positive  $\Delta S$ , a  $T_c$  must exist at sufficiently high temperature, since one can write:  $\Delta G = \Delta H - T\Delta S$ , where  $\Delta G$  is the Gibbs function or free enthalpy and  $\Delta H$ , the enthalpy of the reaction.

For a kinetic argument, one notices that the temperature dependence of the reaction rate given in Fig. A.7.2 is described by the Arrhenius equation, written for polymerization,  $p$ , and depolymerization,  $d$ , as:

$$k_p = A_p e^{-E_p/RT} \quad \text{and} \quad k_d = A_d e^{-E_d/RT}$$

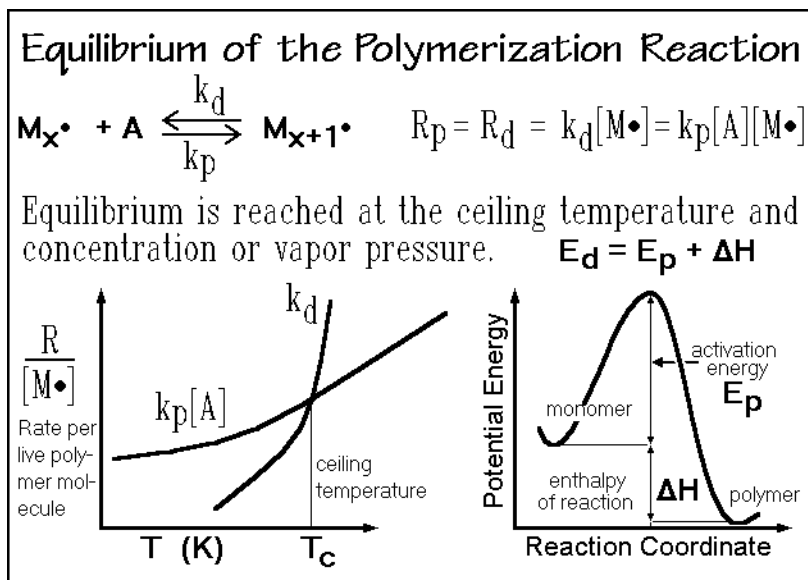


Fig. 3.30

where  $A$  is the reaction-specific, pre-exponential factor, and  $E$  represents the activation energies. The approximate connection between the activation energies of polymerization and depolymerization is shown in Fig. 3.30 together with the energetics of the transition state. At equilibrium  $\Delta G = 0$ ,  $R_p = R_d$ , and  $[A] = [A]_{eq}$ . The left sketch in Fig. 3.30 shows a schematic of the change of the rate constants of the forward and reverse reactions based on the above equations. Because of the larger activation energy of the depolymerization, there must be a point of intersection (at  $T_c$ ) above which the polymer is not stable for the given  $[A]$  and the polymer unzips from the chain ends. Note that this “loss of molecular integrity” was a characteristic of rigid macromolecules on melting and evaporation (see Sect. 1.1). For flexible macromolecules, melting is often possible without decomposition. A notable exception is poly(oxyethylene), where the decomposition must be retarded by blocking the unzipping by protection of the molecule with different end groups or by copolymerization with stable monomers.

### 3.2.4 Chain Reactions without Termination

A chain reaction without termination produces so-called living polymers. Even if on polymerization the initial monomer is used up, a new monomer can be added in a second step and the polymerization restarted as long as the active sites are not destroyed. The reaction became possible when initiation of vinyl polymerization with anionic mechanism was discovered by Szwarc in 1956 [19]. The process is easy to understand. A fixed number of initiator molecules,  $N_i$  is added to the monomer under conditions that eliminate termination (i.e., in the absence of water and oxygen). Figure 3.31 illustrates living polymerization with 10 initiator and 42 monomer molecules. Without termination, the reaction stops when all monomers are used up.

The evaluation of the molecular length distribution is a simple probability problem. For other types of polymerizations the molecular mass distributions are discussed in Sect. 3.4. In the present case, adding  $N_o$  monomer molecules to  $N_i$  initiator molecules yields an average (kinetic) chain length of  $v$  repeating units (plus the initiator residue). The probability that a given  $x$ -mer is made, is simply the mole fraction,  $n_x$ , and expressed by the binomial expression defined in Fig. 3.32 and written in the top boxed equation of Fig. 3.31. Its meaning can be understood by noting that the chance that  $x$  bonds are made in a given sequence is  $(1/N_i)^x$  and the chance that the remaining  $N_o - x$  bonds are not made in the given sequence, is  $[1 - (1/N_i)]^{N_o-x}$ . Since one is satisfied to know how often an  $x$ -mer is made regardless of the reaction sequence, the product of these very small chances must be multiplied with the number of all possible ways of arranging the  $N_o$  monomers, namely  $N_o!$ , and divided by the number different ways an  $x$ -mer can be made out of  $N_o$  monomers.

The Poisson distribution written in the bottom boxed equation of Fig. 3.31 approaches the binomial molar mass distribution for the case that  $p$  is small and the average kinetic chain length  $v = N_o/N_i$  is large, a condition approached for most living polymers. It is an equation that can be calculated much more easily than the binomial distribution. Analyzing the Poisson distribution, one finds that polymerizations without termination lead to rather narrow molar mass distributions as discussed in Sect. 3.3 with Figs. 3.39–41.



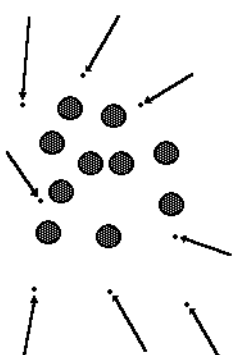
### 3.2.5 Emulsion Polymerization

Emulsion polymerizations are carried out in one liquid phase dispersed within another. The monomer or a solution of the monomer is dispersed with the aid of an emulsifier in the homogeneous phase and polymerized, for example, with free radical initiators. The product is a colloidal dispersion of the polymer. Since dispersions have lower viscosity than the melt, they can be handled much better. Also, the temperature control is easier. Typical emulsion polymers are poly(methyl methacrylate), poly(methacrylic acid), polystyrene, and poly(vinyl chloride). Two special applications of emulsion polymerization are the making of well-defined dispersion particles that may contain only one or few polymer molecules, and the possibility to make better defined molecular sizes by controlling the growth periods.

Figure 3.33 lists a recipe for emulsion polymerization of polystyrene in a water dispersion of monomer droplets and soap micelles [20]. The reaction is started by light-sensitive, water-soluble initiators, such as benzoyl peroxide. If one compares the sizes of the dispersed droplets, one notices that the small soap micelles that contain also styrene in their interior are most likely to occasionally initiate a polymerization of the monomer on absorption of a free radical. Once initiated, the reaction continues until a second free radical molecule enters the micelle. Then the reaction is terminated, until a third radical starts another molecule. Monomers continuously add to the micelles, so that the polymerization continues. Keeping the free radical generation constant, a relatively narrow molar mass distribution can be obtained.

The precision of the molar mass is further enhanced with periodic initiation with intermittent illumination. During the dark period, the droplets with a growing radical produce a molecule of mass determined by the length of the dark period. During the light period, all growing molecules are terminated by the excess of free radicals.

### Emulsion Polymerization with Sharp MW



1. 2% soap solution,  $\approx 5 \text{ nm } \varnothing$ ,  $10^{18} \text{ droplets per cm}^3$
2. monomer droplets  $\approx 1.5 \text{ } \mu\text{m } \varnothing$ ,  $10^{11} \text{ per cm}^3$ , do not capture radicals
3. stabilizer
4. initiator, generates  $10^{17} \text{ radicals per second and cm}^3 \text{ in the water phase}$

**initiation:**  
 $I_2 \xrightarrow{h\nu} I\cdot + I\cdot$

$I\cdot + A \longrightarrow M_1\cdot$   
 $M_x\cdot + A \longrightarrow M_{x+1}\cdot$   
 $M_x\cdot + I\cdot \longrightarrow M_x$

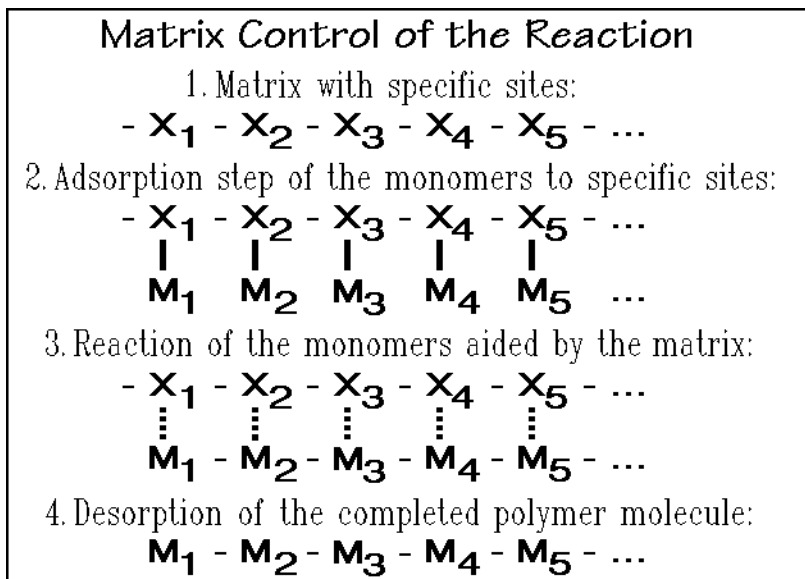
Intermittent initiation starts and stops polymerization by diffusion of many or no radicals into each droplet so that at any time 50% droplets grow and 50% are dead.

Fig. 3.33

### 3.2.6 Matrix Reactions

The chain-reaction polymerizations in Sects. 3.2.4 and 3.2.5 are methods that can be used to make narrower molar mass distributions than are possible with step reactions or chain reactions with random termination. This problem of producing “pure polymers” was mentioned above when discussing the step-wise reaction in Sect. 3.1.

Matrix polymerization is known from the biopolymerization of globular proteins and represents the ultimate in precision of not only molecular length, but also composition. A messenger RNA, attached to a ribosome, serves as the matrix (template) for protein syntheses. A matrix is shown schematically in Fig. 3.34. The



**Fig. 3.34**

specific monomers,  $M_x$ , can be absorbed only on the matrix sites indicated in step 1. Once adsorbed to these specific sites, as depicted in step 2, polymerization can begin in a matrix-controlled sequence as indicated in step 3. The matrix places the monomers not only into proper sequence, it also activates them for reaction. Step 3, furthermore, indicates that on polymerization the adsorption is weakened due to the change in molecular structure, so that the completed molecule is easily removed as seen in step 4, freeing the matrix for a new polymerization. The protein synthesis is not spontaneous. It needs the driving force (loss of free enthalpy) of a coupled reaction of adenosine triphosphate, ATP, to adenosine diphosphate, ADP, to execute the polymerization. A schematic of the ATP structure is shown in Fig. 3.35. Matrix control of polymerization of synthetic polymers remains, at present, of little importance for the production of homopolymers and copolymers, but provides a goal in the quest for more precise macromolecules for special applications and specificity. Initial efforts to make use of biological matrices of bacteria which have been altered to polymerize a specific set of synthetic monomers have been successful.

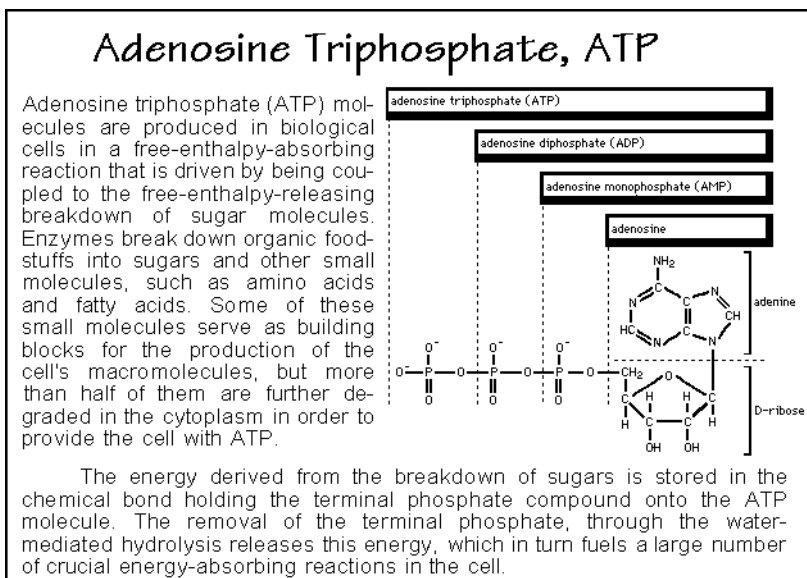


Fig. 3.35

### 3.3 Molecular Mass Distributions

#### 3.3.1 Number and Mass Fractions, Step Reaction

In the present section, quantitative molecular mass distribution and the equations for their averages will be derived. The basics of the description of mass distributions are discussed in Sect. 1.3 with Figs. 1.24 to 1.26, and the experimental methods of measurement are treated in Sect. 1.4.

Figure 3.36 gives the schematic of the step reaction, as discussed in Sect. 3.1. It must be noted, that considering only the forward reactions is a gross simplification, as discussed in the  $\text{LiPO}_3$  example of Sect. 3.1.6. Even more important, the chain-to-ring, ring-to-chain, and ring-to-ring reactions should be included. When in time, all reactions have reached thermodynamic equilibrium, all monomers should have ended up in a broad distribution of large rings since a large ring must be more stable than an equivalent chain with two active ends. When simplifying step polymerization to the idealized kinetics by treating chain-to-chain reactions only, i.e., assuming that all other reactions are negligible, the mole fraction of mers of length  $x$  is easy to find. It is simply the chance that a molecule taken randomly out of the mixture of all molecules has the length  $x$ . The number of molecules  $N$ , that make up the mixture at a given conversion is defined in Fig. 1.25, and linked to the probability,  $p$ , in Fig. 3.36. The initial number of monomer molecules is given by  $N_0$  and the molar mass of the repeating unit is  $M_0$ , leading to a number-average molar mass of  $\bar{M}_n = M_0/(1 - p)$ , as seen from  $\bar{M}_n$  in Fig. 1.25 and insertion of the expression for  $N/N_0$ . Because of the time-dependent approach to equilibrium of all reactions, the distributions from Fig. 3.36 cannot be precise, and are in need of comparison with experiments.

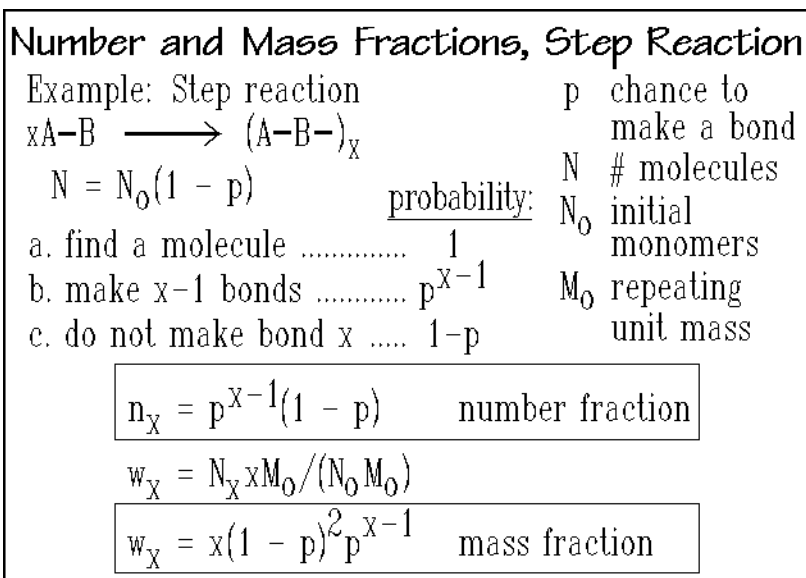


Fig. 3.36

The compound probability for the chance to randomly pick a specified molecule contains three factors in Fig. 3.36. a. The chance to find a molecule ( $= 1$  since it is assumed that we have already picked one of the molecules—note that each molecule has the same chance of being picked, independent of size!). b. The probability that  $x - 1$  bonds are made between its constituent repeating units ( $= p^{x-1}$ , needed so that the molecule is an  $x$ -mer). c. The probability that the  $x^{\text{th}}$  bond is not made [ $= (1 - p)$ , since one additional bond would lead to an  $(x + 1)$ -mer]. The probability to have a randomly chosen molecule which is an  $x$ -mer is the product of the three factors. It is also equal to the number or mole fraction of  $x$ -mers,  $n_x$ . The mass fraction is calculated from the equation for the mass fraction in Fig. 1.26. The result in Fig. 3.36 is derived by inserting the appropriate expressions, knowing that  $N_x = n_x N$ .

Next, one can follow the development of the molecular mass distribution for the step reaction as the reaction proceeds from pure monomers,  $p = 0$ , reaching almost completion,  $p = 0.99$ . Figure 3.37 shows a sequence of steps in the reaction. As already suggested in Sect. 3.1, the monomer concentration decreases quickly, but macromolecules develop very slowly. By the time the reaction is to 60% completed, the dimer is most common, as indicated by the maximum in the distribution curve. As  $p$  reaches 80%, the maximum has moved to the tetramer and pentamer. Only when driving the reaction close to completion is the most common species a true macromolecule, as shown in Fig. 3.38. Typical step-reaction polymers, such as the polyesters and polyamides of Sect. 3.1 are often reaching higher molar masses only because of the relatively large molar mass of the monomer. Also, note that the distribution of molecular masses is rather broad, leading to low concentrations of each individual species. To represent Fig. 3.37, it was necessary to multiply the scale of the ordinate of Fig. 3.37 by a factor of  $4 \times 10^4$ . In Sect. 3.3.3 it will be shown that the polydispersity of the step-reaction approaches two on completion of the reaction.

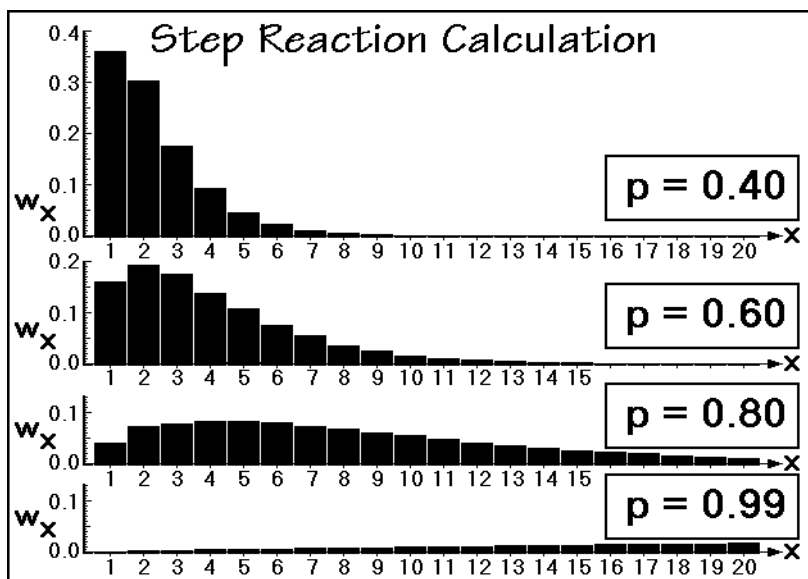


Fig. 3.37

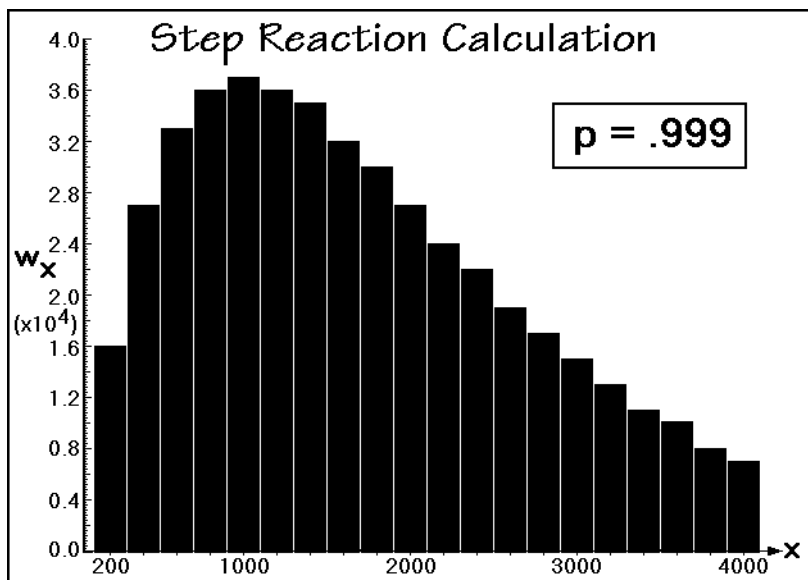


Fig. 3.38

### 3.3.2 Number and Mass Fractions, Chain Reactions

The molecular mass distribution of chain reactions was treated in Fig. 3.31 for living polymers. All active chain ends have in this case the same chance to add a new monomer. If all initiations have occurred at the same time, the chances are equal for



each molecule to reach an average length  $\bar{v}$ . The mole fraction  $n_x$  is then approximated by the Poisson distribution given in Fig. 3.31. For all other types of chain reactions the details of initiation, transfer, and termination determine the distribution, as will be described below. The number of  $x$ -mers  $N_x$  and the mass fraction  $w_x$  can be written as shown in Fig. 3.39 ( $N_x = N_i n_x$ , where  $N_i$  is the number of initiator molecules). In the derivations,  $n_x$  refers to the mole fraction of molecules of  $x$  monomers. To account for the initiator,  $x$  must be replaced by  $x - 1$  since the presence of the initiator unit is certain, and the new  $x$ -mer definition agrees with the molecules of the step-reaction example in Fig. 3.36. The initiator mass may be taken equal to the monomer mass, neglected, or it can be corrected for.

Figure 3.39 displays the change in molecular mass distribution after 40% of the assumed 900 initially present monomer molecules have reacted on the 100 initiator sites, i.e., the average chain length is 4.60 chain repeating units. Note that it is also

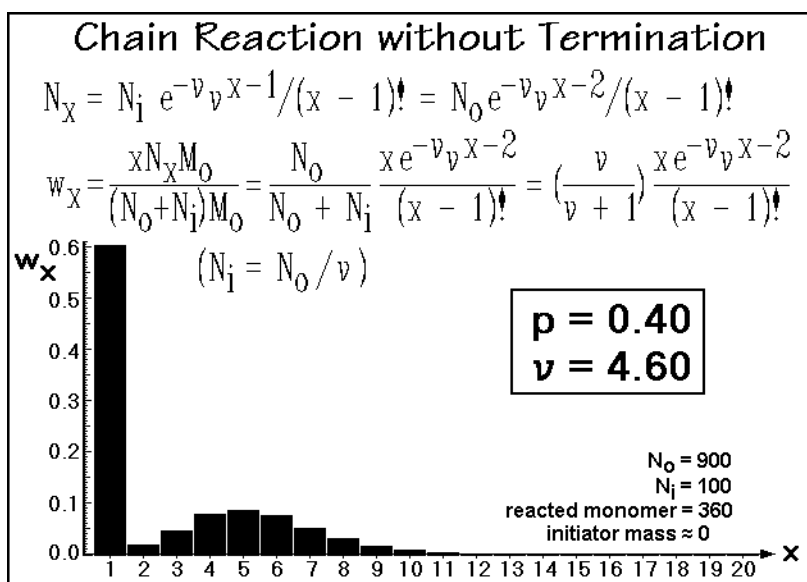


**Fig. 3.39**

assumed that the initiator mass is negligible. Naturally, the residual monomer is the predominant species. Further reaction steps are displayed in Fig. 3.40. Besides the shift of the distribution of oligomers to longer molecule lengths, there is, in contrast to the step reaction of Fig. 3.37, a much slower decrease in monomer. As long as the reaction is incomplete ( $p < 1.0$ ), considerable monomer remains. The amount of unreacted monomer is given by  $(1 - p)N_0$ , and one can compute the average chain length,  $\bar{v}$ , as shown in Fig. 3.39. By disregarding the unreacted monomer,  $\bar{v}$  can be computed for polymerized molecules only (by summing from  $x = 2$  and replacing  $N_0$  with the reacted monomer,  $N_0 p$ ). Beyond the monomer concentration, the oligomer distribution develops as in the step reaction, but it is much narrower. One notices the initial, quick development of dimers and trimers, which, at later time, decrease in mass fraction as longer molecules begin to dominate. Note, that while the step reaction is

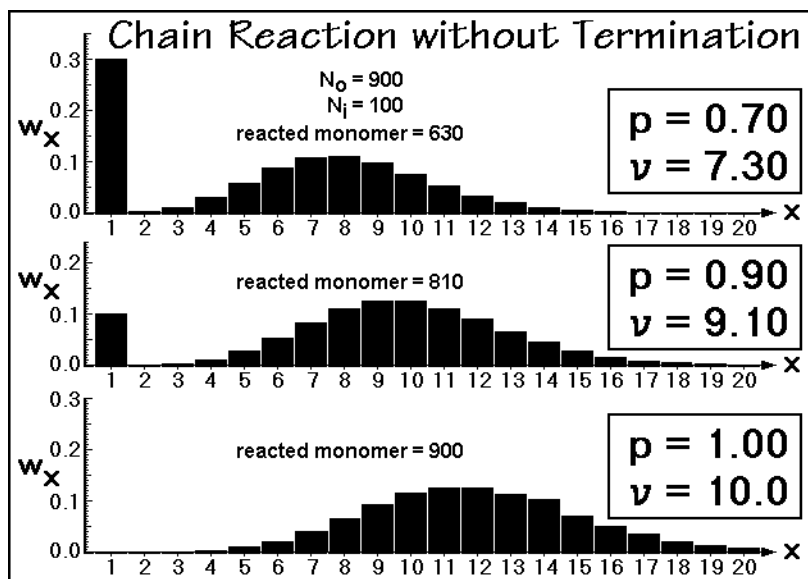


Fig. 3.40

never complete, so that  $p$  is an important characteristic. The final sample of a chain reaction is always completed. Figure 3.41 illustrates a chain reaction for  $v$  equal to 2,000. Compared to the step reaction of Fig. 3.40, the distribution is very narrow. The scale of  $w_x$  is much less expanded and the scale of  $x$  compressed. In Sect. 3.3.3 it will be shown that the polydispersity of this chain-reaction polymer approaches one on completion of the reaction. (Figure 3.41 illustrates a polydispersity of 1.0005.)

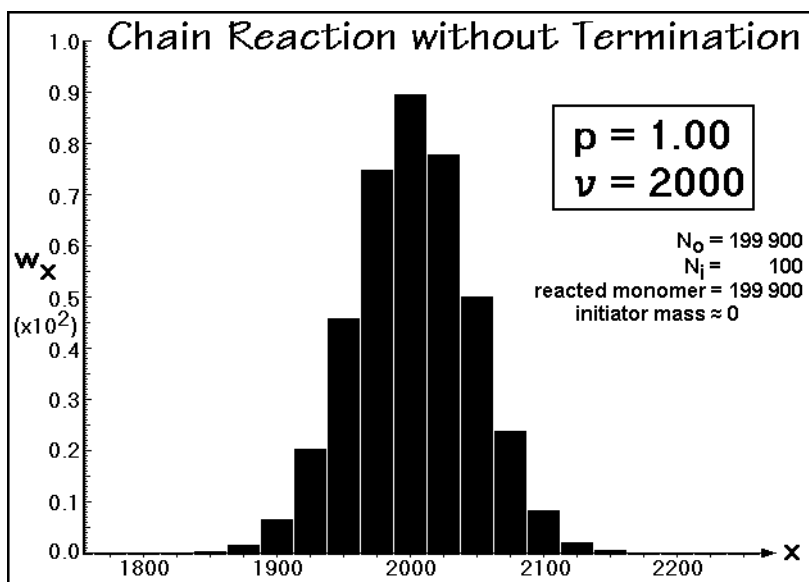


Fig. 3.41

### 3.3.3 Step Reaction Averages

The next two sections contain a discussion of the computations needed to evaluate average molar masses from the derived distributions of Sects. 3.3.1 and 2. The derivations are simple, but lengthy, so that it is given for the first example only, using an abbreviated summary. The characterization of the molar mass distributions is given by the polydispersity  $\bar{M}_w/\bar{M}_n$  as discussed in Sect. 1.3 (Fig. 1.26). It approaches 2.0 for the broad molecular mass distributions of the step reactions as  $p$  becomes 1.0, and should be close to 1.0 for living polymers of sufficiently high molar mass. In the latter case, the high molar mass is achieved by low initiator concentration and completion of the reaction. Actual samples may, however, show a much higher polydispersity. Particularly chain reactions with complicated initiation, termination, and transfer reactions may show polydispersities as high as 20 or more, as will be shown below.

First, Fig. 3.42 shows how to start from the equations of Fig. 3.8 to evaluate the simple equation for the number average molar mass of a step reaction. More difficult is to establish the mass average molecular mass. Starting from the mass-distribution

**Mass Averages for Step Reactions**

Degree of polymerization:  $\overline{DP} = N_0/N = 1/(1 - p)$

Number average molecular mass:

$$\overline{M}_n = M_0 \overline{DP}$$

$$\overline{M}_n = M_0/(1 - p)$$

Weight average molecular mass:

$$\overline{M}_w = \sum w_x M_x = \sum x^2 (1 - p)^2 p^{x-1} M_0$$

$$\sum x^2 p^{x-1} = \sum d(xp^x + c)/dp$$

$$= \sum d(xp^x + c)/dp$$

$$= \sum d[p d(p^x + c')/dp]/dp$$

$$= \frac{d}{dp} [p \frac{d}{dp} (p \sum p^{x-1} + c')]$$

since  $\sum p^{x-1} = 1 + p + p^2 + p^3 + \dots = 1/(1 - p)$ ,  
the sum can easily be differentiated to  
 $(1 + p)/(1 - p)^2$ , which leads to the final Eq.:

$$\overline{M}_w = M_0(1 + p)/(1 - p)$$

Fig. 3.42

equation of Fig. 3.36, one needs to sum over all species of  $x$ , as shown in Fig. 3.42. This sum is a geometric series that can be written as:

$$\overline{M}_w = M_0(1 - p)^2 [1 + 4p + 9p^2 + \dots]$$

The sum in brackets,  $\sum x^2 p^{x-1}$ , can, however, only easily be summed for large values of  $x$  and without the factor  $x^2$ . To achieve the latter, one writes the differential of the integral of  $x^2 p^{x-1}$  as shown in the second line of the derivation. The integration constants,  $c$ , disappear when ultimately the differentiations are carried out. The first

integration reduces the factor  $x^2$  to  $x$  and yields, after reorganization and a second differentiation and integration, the sum  $\sum p^{x-1}$  which can be evaluated easily for large values of  $x$ , as shown in the boxed part of Fig. 3.42. Next, the two differentiations are carried out. The resulting equation is quite simple, proving the approach of the polydispersity,  $\overline{M}_w/\overline{M}_n$ , to the value of two as soon as the degree of completion of the reaction approaches one. This polydispersity of two was suggested above as a characteristic of the step reaction.

### 3.3.4 Chain Reaction Averages

To assess molecular mass distributions of chain reactions, considerably more detail must be known about the mechanism than in the case of step reactions. As the reactions progresses, the length distribution of the polymer molecules changes increasingly from the simple case of fixed number of initiator molecules without termination, described above for the living polymers. Constantly some initiator is newly activated and growing molecules are terminated. One can compute a kinetic chain length only during the short time period of steady state in Fig. 3.29, as illustrated in Fig. 3.43. The chain length is the ratio of propagation to termination rates as

**Mass Averages for Chain Reactions**

From Fig. 3.28 kinetic chain length  $v = k_p^2 [A]^2 / \{2k_t R_p\}$

probability of  
termination:  $(1 - p) = \frac{2k_t [M\bullet]^2}{k_p [A][M\bullet] + 2k_t [M\bullet]^2} = \frac{2}{2 + v}$

The averages are, however, changing as  $v$  is changing with time.

Distribution:  $n_x = (1 - p)^2 [p^{y-1}] [p^{x-y-1}] (x - 1)$

$\left[ \begin{smallmatrix} N = N_0(1 - p)/2 \\ N_x = N n_x \end{smallmatrix} \right]$	$n_x = (x - 1) p^{x-2} (1 - p)^2$	$w_x = x N_x / N_0 = (1/2) x (x - 1) p^{x-2} (1 - p)^3$
probabilities:	coupling of two chains	y units in first chain    enough in the second for x    number of ways to make x out of different lengths y

Fig. 3.43

defined in Sect. 3.2. The probability of termination,  $1 - p$ , is shown for the case of termination by coupling of two molecule radicals. It is the termination rate divided by all reaction rates at the given moment. Analogous equations must be written for other termination and transfer reactions. The key point remains that even if the mechanism is known, the averages will change with time. One can approach a steady state that produces a fixed molecular mass distribution only in a flow reactor with constant monomer addition, polymer removal, and initiator replenishment. The

computation of the distribution of the mole fractions of molecules of length  $x$  is, again, based on a probability argument, as displayed in the last two lines of Fig. 3.43 and can be compared to the similar equations for the step reaction in Fig. 3.36.

The top equation in Fig. 3.44 lists the number and mass averages for chain reactions terminated by the combination of two growing molecule-radicals as described in Fig. 3.43. The derivation of the equation must be done in the same way as illustrated for the step reaction in Fig. 3.42. The next example, shown in Fig. 3.44, applies to termination by chain transfer (see Sect. 3.2). In this case the termination

**Mass Averages for Chain Reactions**

$$\overline{M}_n = 2M_0/(1 - p) \quad \overline{M}_w = M_0(2 + p)/(1 - p)$$

For termination by chain transfer only, double as many molecules are produced and  $p$  is treated as in a step reaction:

$$\overline{M}_n = M_0/(1 - p) \quad \overline{M}_w = M_0(1 + p)/(1 - p)$$

Without termination, the averages are derivable from the Poisson distribution:

$$\overline{M}_n = M_0(1 + v) \quad \overline{M}_w = M_0(v + 2)$$

Note that the computed polydispersities  $M_w/M_n$  range at  $p = 1$  from 1 to 2 only.  
Experimentally observed values may easily be 20 or more. Why?

**Fig. 3.44**

removes one polymer molecule but starts at the same time a new one. Again, the derivations of  $n_x$  and  $w_x$  are done as before and the summation is the same as for the step reaction in Fig. 3.42. The final averages are those derivable from the Poisson distribution which describes living polymers. Again, the limitations of the just derived equations must be kept in mind.

### 3.4 Copolymerization and Reactions of Polymers

The multiplicity of possible linear macromolecules is enormously increased by copolymerization, i.e., by polymerizing more than one monomer. Because it is possible to vary concentration as well as placement of the various monomers, as discussed in Sect. 1.2, there are unlimited numbers of different polymers, and it is impossible to ever produce all polymers of promise to check their properties and pick optimum materials. One must develop the ability to predict polymer properties before making the actual molecules. This prediction capability is one of the key goals of the study of polymers. It must start with a critical evaluation of data of the physical

properties of all known polymers and the development of prediction schemes. Most well-known are the property tables of van Krevelen, based on the addition of contributions from the constituent chemical groups [21]. If the connection between properties and chemical structure is not fully known, it is still possible to predict the properties using neural network computations as shown in Appendix 4 [22,23]. With such networks it is possible to develop predictions based on all present knowledge in an area. A prediction of properties of copolymers with neural network techniques has been described [24].

### 3.4.1 Chain Reaction Copolymers

The kinetic propagation reaction equations for radical copolymerization of two monomers,  $M_1$  and  $M_2$ , are written in Fig. 3.45. The complications due to additional, different monomers, as well as transfer, reverse, and termination reactions increase the numbers of equations and rate constants, so that the resulting reaction equations are unhandy, and it needs much experimental work to establish the rate constants. Also, the computational effort to solve the many equations becomes excessive.

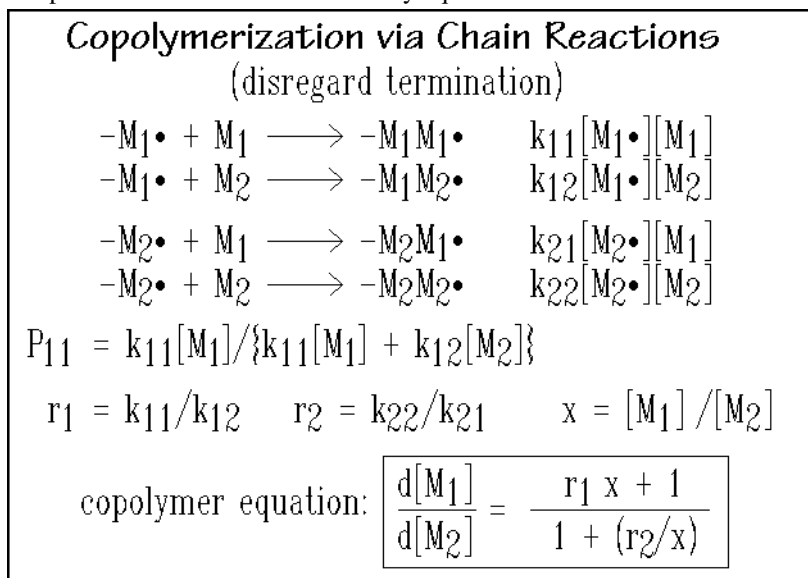


**Fig. 3.45**

For the two different monomers, there are four propagation reactions in Fig. 3.45. The chance that  $-M_1\bullet$ , the free radical terminating a chain ending in  $M_1$ , reacts with the same monomer  $M_1$  is  $P_{11}$ . The chance to continue with monomer  $M_2$ , is  $P_{12}$  which equals  $(1 - P_{11})$ . The analogous probabilities for  $-M_2\bullet$  are  $P_{22}$  and  $P_{12} (= 1 - P_{22})$ . The probabilities are equal to the rates of the appropriate reaction divided by the sum of both possible rates, as indicated in Fig. 3.45 for  $P_{11}$ . Three more definitions are given in Fig. 3.45, two for the reactivity ratios,  $r_1$  and,  $r_2$ , and the third, for the monomer ratio  $x$ , also called the feed ratio ( $x = f_1/f_2$ ). The basic copolymer equation is shown in the box at the bottom, where  $d[M_1]/d[M_2] = F_1/F_2$  is the composition ratio.

The copolymer equation is derived for the steady state when both,  $[M_1\bullet]$  and  $[M_2\bullet]$  do not change with time. Steady state requires also that there are the same number of conversions of molecular radical ends  $-M_1\bullet$  to  $-M_2\bullet$  and vice versa, and there are equal rates of change of  $M_1\bullet$  to  $M_2\bullet$  and vice versa, i.e., the second and third rate expressions of Fig. 3.45 must be equal:  $k_{12}[M_1\bullet][M_2] = k_{21}[M_2\bullet][M_1]$ .

Dividing the top rates of Fig. 3.45, considering  $r_1 = k_{11}/k_{12}$  and  $r_2 = k_{22}/k_{21}$  and using the equality, above, the ratio  $d[M_1]/d[M_2]$  is the copolymer equation, looked for:

$$\frac{d[M_1]}{d[M_2]} = \frac{r_1 \frac{[M_1]}{[M_2]} + 1}{1 + \frac{[M_2]}{[M_1]}} = \frac{r_1 x + 1}{1 + \frac{r_2}{x}} = \frac{F_1}{F_2}.$$

The copolymer equation represents the composition ratio of the copolymer produced at the given instant and is rewritten in Fig. 3.46. The final correlation between composition ratio,  $F_1/F_2$ , and the feed ratio,  $x = f_1/f_2 = [M_1]/[M_2]$ , can be reorganized, as also given in Fig. 3.46. For a reaction in a continuous flow reactor in steady state, one can thus predict the composition of the copolymer from the monomer feed ratio. In a batch reaction, in contrast, the composition changes continuously.

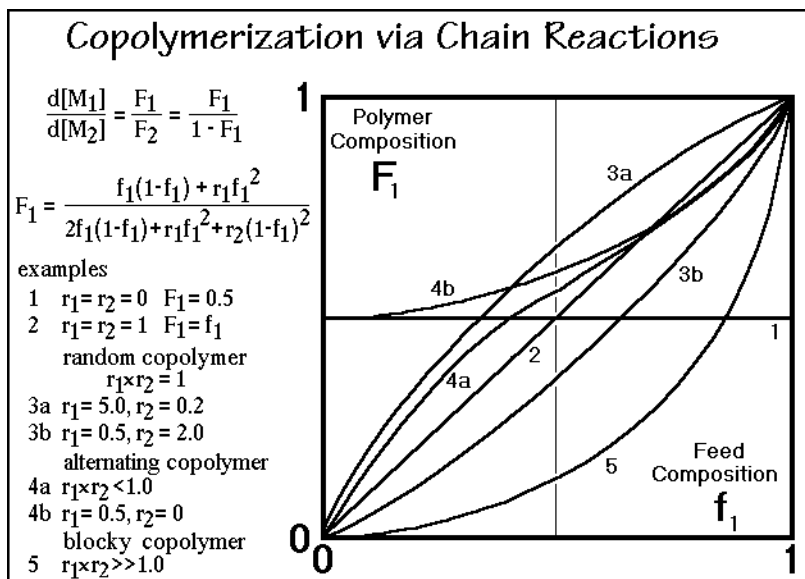


Fig. 3.46

In the plots included in Fig. 3.46 some typical copolymer-feed/composition diagrams are compared. The horizontal line of example 1 represents the case of copolymerization when both reactivity ratios are zero. Irrespective of the feed composition, the polymer composition has a 0.5 mole fraction of both components. The reaction leads to a strictly alternating copolymer since  $-M_1\bullet$  cannot be followed by  $M_1$  ( $r_1 = 0$ ). The same holds for  $-M_2\bullet$  ( $r_2 = 0$ ). A copolymer that fulfills this

requirement can be made of tetrafluoroethylene,  $\text{CF}_2=\text{CF}_2$ , and isobutylene,  $\text{CH}_2=\text{C}(\text{CH}_3)_2$ .

The kinetics of example 2 shows no preference between the two monomers. The resulting copolymer is azeotropic, meaning that feed and composition are always equal ( $F_1 = f_1$ ). An example is found in 1,3-butadiene,  $\text{CH}_2=\text{CH}-\text{CH}=\text{CH}_2$ , polymerizing with isoprene,  $\text{CH}_2=\text{C}(\text{CH}_3)-\text{CH}=\text{CH}_2$ .

Random copolymers are always found if the product  $r_1 \times r_2 = 1$ , i.e., both monomers have the same preference for monomer 1 over 2 ( $k_{11}/k_{12} = k_{21}/k_{22}$ ). The examples 3a and 3b are two possible random copolymers with opposite reactivity-ratios  $r_1$  and  $r_2$ . A typical random copolymer can be made of 1,3-butadiene,  $\text{CH}_2=\text{CH}-\text{CH}=\text{CH}_2$ , and styrene,  $\text{CH}_2=\text{CH}-\text{C}_6\text{H}_5$ .

To produce a copolymer with alternating tendency, the product  $r_1 \times r_2$  must be  $< 1$ . The examples 4 are two typical representatives. Note the tendency to approach curve 1 when  $f_1$  is 0.4 in case 4a, and  $f_2 = 0$ , in case 4b. An example copolymerization of this type is methyl methacrylate,  $\text{CH}_2=\text{C}(\text{CH}_3)-\text{CO}-\text{O}-\text{CH}_3$ , copolymerized with styrene,  $\text{CH}_2=\text{CH}-\text{C}_6\text{H}_5$ .

Example 5 in Fig. 3.46, finally, is characteristic for a tendency to make blocky copolymers. In this case  $r_1 \times r_2 \gg 1$ , as is found in poly(propylene-*co*-styrene). Once a given radical is formed, it prefers to add the same monomer rather than to switch to the other.

In all these cases the copolymers are not precisely of the same composition and sequence lengths from molecule to molecule, as could result from a stepwise reaction (see Sect. 3.1). Distributions of sequence lengths exist in all these copolymers and could, again, be calculated from the reactivity ratios. Figure 3.46 summarizes the wide variety of composition diagrams possible.

### 3.4.2 Step Reaction Copolymers

Step reaction copolymers tend to be more or less random. Even with different monomer reactivities that lead initially to non-random copolymers, randomization is ultimately helped by interchange reactions that can proceed after the initial polymerization. Figure 3.47 illustrates the interchange of chain segments by transesterification. One molecule has the chain-ends  $R_1$  and  $R_2$ , the other  $R_3$  and  $R_4$ . After the reaction, the ends are exchanged.

Three stages of the reaction-sequence are shown at the bottom of the figure which are similar to the initial polymerization shown in Fig. 3.14. The slow parts of the reaction involve the molecular movements. First is the addition of the catalyst, such as  $\text{H}^+$  which initiates the shift in the electron configuration, and the approach of the two chains to be interchanged. The electronic rearrangements, labeled 2, 3 and 4, are fast, lead to a distribution of the charge,  $\partial^+$ , and ultimately produce the reaction intermediate with a rather symmetric partial bonding. On removal of the original  $\text{H}^+$ , the molecules may separate either with their old structure, or, with electron shifts 5 and 6 to the new molecules  $R_1-\text{COO}-R_4$  and  $R_2-\text{COO}-R_3$ , as shown. In this way, it is also possible to produce random copolymers by melting the homopolymer components and keeping them for a sufficiently long time at high temperature to interchange the repeating units. This type of reaction is of importance to remember when



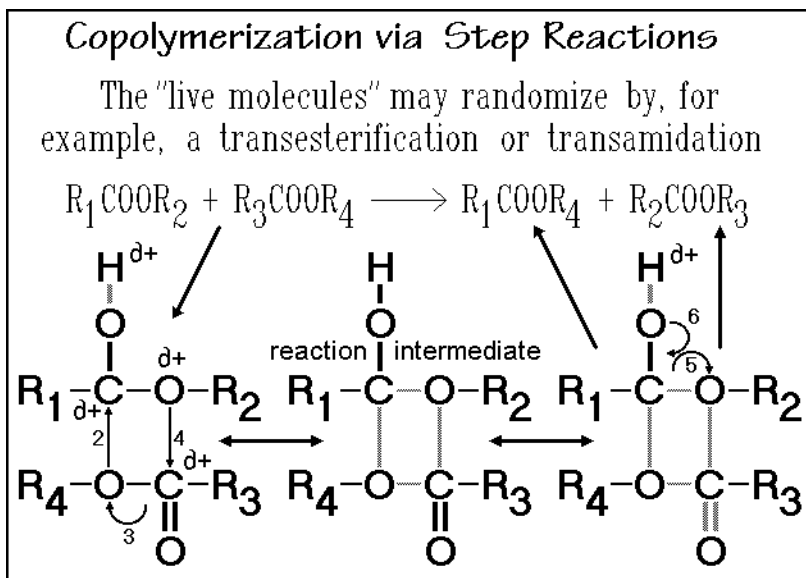


Fig. 3.47

discussing compatibility of step-reaction polymers in Chap. 7. If interchange reactions are possible, compatibility may be achieved by forming a copolymer. Similarly, an initially random copolymer may develop blocky sequences if one of the components may preferentially crystallize at a temperature where ester-interchange is possible. Crystallization removes the longer sequences of  $\xi$  identical repeating units with a mole fraction if  $n_{\xi} = P_{11}^{\xi-1}(1 - P_{11})$ . The interchange reaction can, then, recover these sequences, which, in turn, permits further crystallization and leads to a blocky copolymer. Homopolymers can, similarly, remove hindrances to crystallization by interchange reactions on folds and tie molecules of crystal surfaces discussed in Chap. 5. This interchange reaction limits the integrity of the molecules that was assumed to exist in flexible, linear macromolecules and points thus at the existence of intermediate compounds in the classification scheme of molecules of Sect. 1.1.3.

### 3.4.3 Gelation

Polymerizations lead to linear macromolecules only if the monomers are strictly bifunctional. Monofunctional molecules were shown in Fig. 3.13 to limit the molecular length of step-growth polymers. Adding monomers with a higher functionality than,  $f = 2$  to bifunctional monomers leads to network formation with structures as discussed in Sect. 1.2. A sudden gel formation is illustrated in Fig 3.48. Gel formation is marked by the appearance of a macroscopic network. The network has a practically infinite molar mass. In polymerizations from the pure monomer the network is swollen by monomer, oligomers, and linear and branched polymer molecule. In polymerization from solution, the solvent makes up a large number of the small molecules. As the polymerization continues, most or all of the polymerizable material joins the network. A gel can hold a large number of small

### Summary of the Gel Structure and Formation

Gels are cross-linked polymer networks swollen by a liquid. The properties of a gel depend strongly on the interaction of the two components and the degree of cross-linking of the network. The liquid prevents the network from collapsing and the network keeps the liquid contained. The network is usually <10% of the total mass of the gel. Gel formation occurs first at the gel point when the molar mass distribution becomes infinitely broad. At this point some low molar mass molecules can still be extracted. The change in properties through the gel point are shown on the right. The cross-links can be chemical or physical.

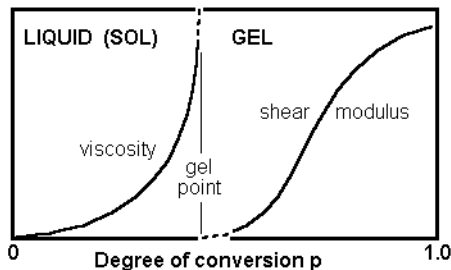


Fig. 3.48

molecules, such as monomers and/or solvents, because of the large volume of a coiled macromolecule and its low-mass density which was estimated from the random coil dimensions calculated in Sect. 1.3.

The gel formation can be linked to the functionality,  $f$ , and a branching coefficient,  $\alpha$ . The branching coefficient  $\alpha$  gives the probability that a specific functional group (of functionality  $> 2$ ) is connected to another branch point. One can deduce from statistical reasoning that a gel appears at a critical branching coefficient,  $\alpha_c$ . For  $f = 3$ , a gel appears when  $\alpha_c$  is 0.5, i.e., there is a 50% chance that each branch is connected to another branch point. The network structure depends on the concentration of branch points and the degree of polymerization.

Gels can also form by physical cross-linking. Most common are the entanglements in a concentrated polymer solution that can lead to a gel. Further enhancement of gel formation is possible by bonding between the molecules by hydrogen bonding or polar interaction.

Special gelation is based on phase separation within polymer solutions. If the separating phase exists as small, solid particles (crystal or glass), it may represent a cross-link of very high functionality. Even the typical semicrystalline polymer can be characterized as tightly cross-linked, nanophase-separated gels, as will be discussed in Chap. 5.

### 3.4.4 Decomposition

Decomposition can be looked upon as the reverse reaction of synthesis. Polymers with a ceiling temperature can simply show a reverse of the polymerization reaction as seen in Fig. 3.30. Figure 3.49 represents typical thermogravimetry traces for the decomposition of poly(methyl methacrylate), PMMA, and polytetrafluoroethylene,

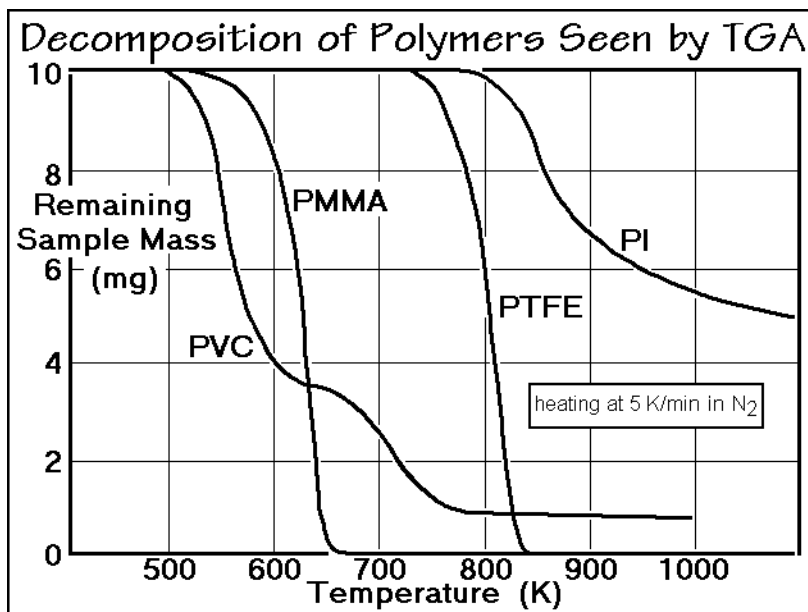
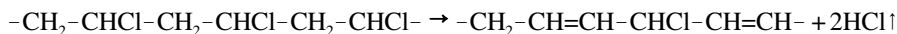


Fig. 3.49

PTFE. Both polymers yield mainly monomer on heating. Note that this process is nothing else but the sublimation or evaporation, common when heating small molecules or rigid macromolecules. In fact, PTFE is a good laboratory source of tetrafluoroethylene which is pure enough to be repolymerized on a cold surface, particularly in the presence of a free radical catalyst.

The reversal of polymerization, however, is not the norm for polymer decomposition. Most polymers show decomposition to multiple products. Especially in the presence of oxygen is there always a chance of oxidation, or even self-sustaining burning. Such reactions are better called pyrolysis than decomposition. The thermogravimetry is for this reason usually done in an inert atmosphere, such as nitrogen, unless oxidation is to be studied.

The poly(vinyl chloride), PVC, of Fig. 3.49 decomposes in two steps. In the first it loses most of its chloride as HCl between two neighboring carbon atoms:



In the second pyrolysis step, the polymer breaks up into many small molecules. (Note that the Cl trapped by two double bonds, as shown in the reaction sequence, above, cannot react as easily as a Cl next to a  $\text{CH}_2$ -group as exists in uninterrupted sequences of  $\text{CH}_2-\text{CHCl}-$ ). The remaining mass after pyrolysis consists of highly cross-linked carbon in the form of char.

The aromatic polyimide (PI) of Fig. 3.49 is a relatively stable polymer, such as a polypyromellitimide, that is usable for high-temperature applications such as needed for insulation. It finally decomposes to small fragments that carry away most H-atoms and leave highly cross-linked, high-carbon chars.

### 3.4.5 Polymer Reactions

Nine examples of reactions after polymerization are selected in this section. Further details of these industrially important reactions should be looked-up in the General References given in the Preface, as is also proposed for all other examples of materials mentioned in this book, and partially illustrated for the following reactions.

The first example is the well-known conversion of the easily polymerized poly(vinyl acetate), PVAc,  $\text{CH}_2\text{-CH(OCOCH}_3\text{)-}$ , by hydrolysis to the technologically important poly(vinyl alcohol), PVA,  $\text{CH}_2\text{-CHOH-}$ . Figure 3.50 lists the chemical

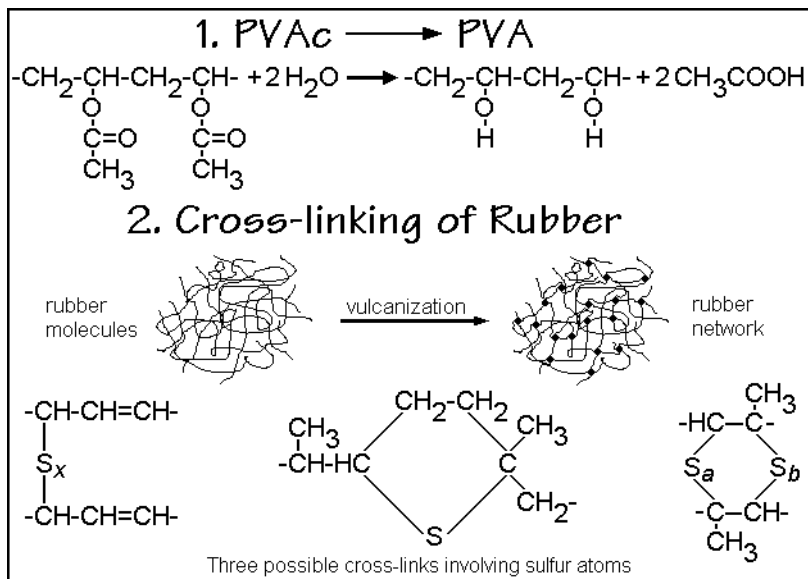


**Fig. 3.50**

equation of the process. Poly(vinyl acetate), the reactant, is an amorphous polymer with a glass transition temperature of 305 K. It is produced in megaton quantities and used as polymerized for emulsions, water-based paints, adhesives, and paper coatings. Its monomer is made by oxidative addition of acetic acid to ethylene and polymerized using free radical initiators in bulk, solution, or emulsion. Dependent on molar mass, the polymer may be a viscous liquid or brittle solid. It is not soluble in water, but in ethanol, propanol, or butanol containing 5–10% of water. It is water-sensitive, but does not hydrolyze at a neutral pH. The product of the hydrolysis, the poly(vinyl alcohol), is the largest-volume, synthetic, water-soluble polymer. Its main uses are in fibers, adhesives, production of poly(vinyl butyral) described in Fig. 1.14, textile and paper sizing, cold-water soluble bags, films, and packaging, water thickening agents and drag reducers. The properties of PVA vary considerably with the production conditions. The crystals have a melting temperature of 538 K and the amorphous PVA has a glass transition temperature of 358 K. The polymer is solvent, oil, and grease resistant and has a high tensile strength and good oxygen barrier properties when dry.

The second example of a polymer reaction is the industrial cross-linking of rubber by vulcanization sketched in Fig. 3.50. The process was invented already in 1839 by C. N. Goodyear<sup>1</sup> without knowledge of its chemical structure. Natural rubber is *cis*-poly(1-methyl-1-butenylene) or polyisoprene with a low glass transition temperature of about 210 K. Its structure and those of other rubbers are given in Fig. 1.15. The addition of sulfur in the form of S<sub>8</sub> rings and heating causes the vulcanization. Of the listed cross-links in Fig. 3.50, only the left example is an efficient network former. The sulfur introduces about 1 cross-link for each of 50 S-atoms used. Modern vulcanization involves activators and accelerators for increased efficiency. The detailed mechanism is rather complicated and not fully understood.

Other cross-linking reactions are shown in Fig. 3.51. They can lead to products that can be shaped by melting the flexible macromolecules (plastics) and then fixing the shape by cross-linking, approaching a rigid macromolecule as seen in

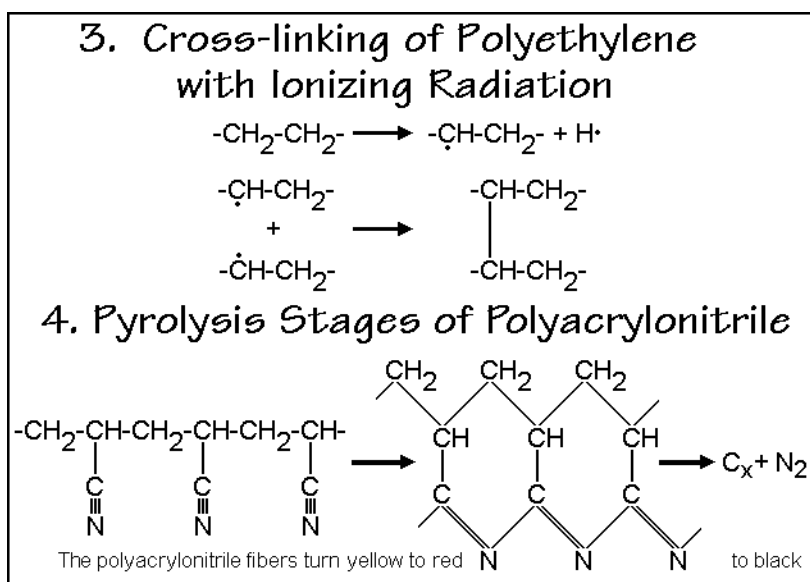


**Fig. 3.51**

Fig. 1.6. Reaction 3 involves ionizing radiation in form of X-rays, gamma rays, or electrons which impart high energy to a polymer to break bonds, producing ionic or free radical fragments of the molecules. The most common radiation sources are <sup>60</sup>Co for gamma rays of 1.25 MeV and electron accelerators (0.1–10 MeV). These energies compare to typical bond energies of only 100 to 1000 kJ (= 1–10 eV). Reaction 3 illustrates the cross-linking of polyethylene, started by the production of free radicals (top reaction). Two free radicals of different molecules can then combine in a cross-link, as seen in the second reaction. The cross-linking is most efficient in the liquid state in order to have enough mobility in the chain segments to be combined.

<sup>1</sup> Charles N. Goodyear, 1800–1860. The American inventor of the vulcanization cross-linking process which made possible the commercial use of rubber as one knows it today.

Semicrystalline polyethylenes cross-link only in the amorphous regions. After sufficient cross-linking, the polymer does not flow any more. Typical polymers that can be cross-linked similarly are polypropylene, polystyrene, polyacrylates, and poly(vinyl chloride). Uses of the cross-linked polymer include wire and cable insulation, heat-shrinkable films and tubing.

Polyacrylonitrile, PAN,  $\text{CH}_2\text{--CH}(\text{C}\equiv\text{N})\text{--}$ , leads on pyrolysis over an intermediate stage to complete carbonization, as depicted in Fig. 3.51. The final product is used to make strong carbon fibers. The polyacrylonitrile fibers turn yellow to red on the formation of the ladder structure shown in the figure. On final carbonization the fiber turns black and consists of graphite-like structures. The carbon fibers have found many applications due to their high tensile modulus in the fiber direction and their, compared to metals, low weight. They are used as fiber reinforcement in epoxy matrices. Typical applications range from aircraft and aerospace to industrial, transportation, and recreational equipment.

The fifth polymer reaction is an example of grafting to structures described in Sect. 1.2. This reaction can be used to change the nature of a macromolecule by adding side-chains as shown schematically in Fig. 3.52. It allows, for example, compatibilization with other polymers (see Chap. 7) or the attachment of groups that

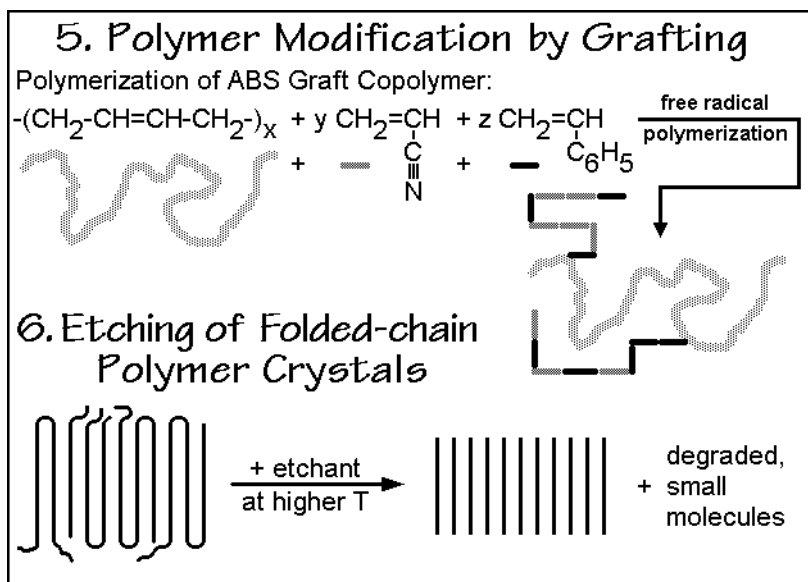


Fig. 3.52

change the physical properties. The grafted side-chain may be thermodynamically incompatible with the main-chain and leads then to multi-phase polymers. The morphology of the heterophase polymers is composition dependent and may also be affected by thermal history and precipitation conditions. Typical examples of graft copolymers are high-impact polystyrene (HIPS, styrene, polymerized in the presence of rubber, such as 1,4-polybutadiene), acrylonitrile-butadiene-styrene copolymers (ABS), and cellulose grafts. The ABS example is done by free radical polymerization

of acrylonitrile and styrene in the presence of 1,4-polybutadiene, as shown in Fig. 3.52. Free radicals attack on the remaining double bonds 1,4-polybutadiene crates graft sites for the copolymerization. Some free copolymer forms besides the graft.

The bottom reaction of Fig. 3.52 involves the chemical etching of semicrystalline hydrocarbons such as polyethylene and polypropylene. The surfaces, including the amorphous sections of the molecules are degraded oxidatively to low-mass fragments using, for example, ozone, permanganates, or nitric acid. The fold surfaces and strained sections in the amorphous fraction are broken and transformed into oxidized chain ends. The amorphous parts and surfaces of a semicrystalline polymer are, thus, removed first and a microcrystalline powder remains and can be analyzed more easily than when surrounded by amorphous material. The microcrystalline powders have found industrial applications. This reaction is also used to oxidize nonpolar polymer films to make them hydrophilic, so that they can be wetted for printing. Similar to the hydrocarbons, the molecular backbone of polyesters and polyamides can be broken by hydrolysis. These reactions can be done in the presence of water at elevated temperature with or without a catalyst. Contrasting these degradations are dissolutions with solvents, which lead to removal of whole molecules from the sample.

Ionomer production involving saponification of ester side-chains, such as in polyacrylates in the presence of NaOH, are shown in Fig. 3.53 as polymer reaction 7. The

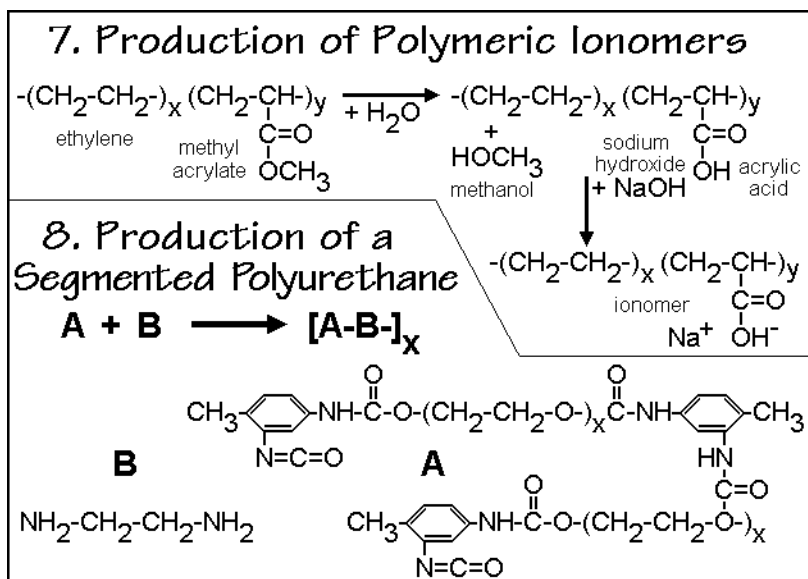


Fig. 3.53

pendent ionic groups interact to form ion-rich nanophases dispersed in the nonpolar polymer matrix and create a cross-linked system. Typical ionomers are copolymers with ionized groups on about 1–10% of the repeating units. A common route to the ionomer is the modification of the preformed polymer, such as the introduction of a sulfonate group in polystyrene, or as shown in the example for reaction 7, the saponification of the poly(methyl acrylate-co-ethylene) followed by neutralization of

the carboxylic acid with NaOH. This example is patterned after the DuPont Surlin® polymer. Properties such as modulus and tensile strength increase with ionic content. At higher ionic content microphase separation may occur, indicated by two glass transitions, one for the matrix phase, the other for the ion-rich phase.

Segmented polyurethanes with nanophase-separated hard and soft segments, linked together after prior partial polymerization, followed by joining of the molecules are summarized as reaction 8 in Fig. 3.53. The initial copolymer (A) is a polyurethane listed in Fig. 3.12, made, for example of poly(oxyethylene) of molar mass 3,000 with  $x \approx 68$ , reacted with an excess of 2,4-toluenediisocyanate. This prepolymer is then extended with some ethylene diamine (B) which reacts the remaining diisocyanates with urea bridges. The resulting segmented polyurethane consists of the urea-connected *hard segments* (HN-CO-NH-C<sub>2</sub>H<sub>4</sub>-HN-CO-NH-) and the remaining ethylene-oxide *soft segments* with embedded isolated urethane groups. These segmented polyurethanes are elastomers known for their good abrasion and solvent resistance. As fibers they have high elasticity and are used for stretch-fabrics which have largely replaced rubber latex threads. The hard segments are in the glassy state, micro- or nanophase separated from the segments that remain liquid (rubbery).

Polymer-supported chemistry, summarized in Fig. 3.54, is a large new field of chemistry involving polymer molecules. It is proving to be an important advance in modern chemistry. The reactant, byproduct, or catalyst can be attached to a polymer gel (see Fig. 3.48), which permits clean separation of the product by simply washing-out the small molecules. The open structure of the gel permits easy access to the active sites. An example of such reaction was given before in the Merrifield synthesis (see Fig. 3.2). Various gels with specific functional groups are listed in Fig. 3.54. With these tools a large number of chemical reactions can be undertaken. Note that this type of chemical reaction mimics biochemical reactions in living systems and may

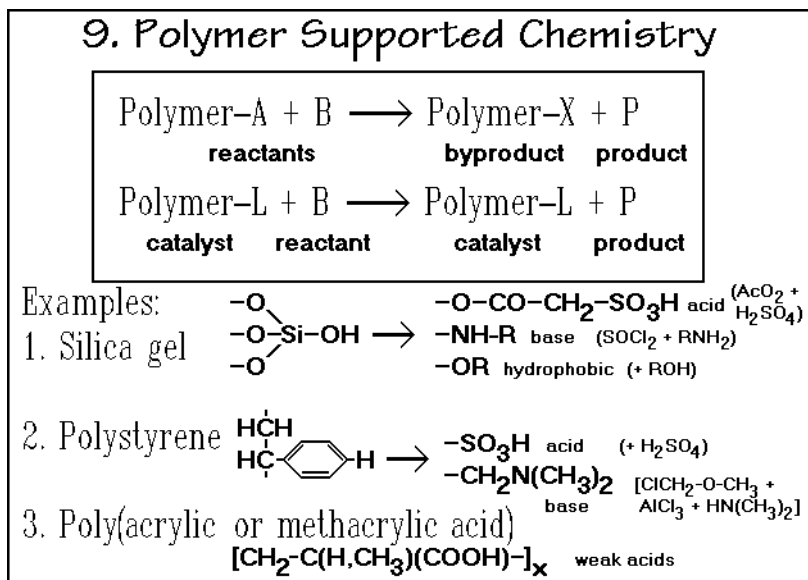


Fig. 3.54



help to rid chemical industry of many of the problems found in side-product separation and lead to cleaner processes.

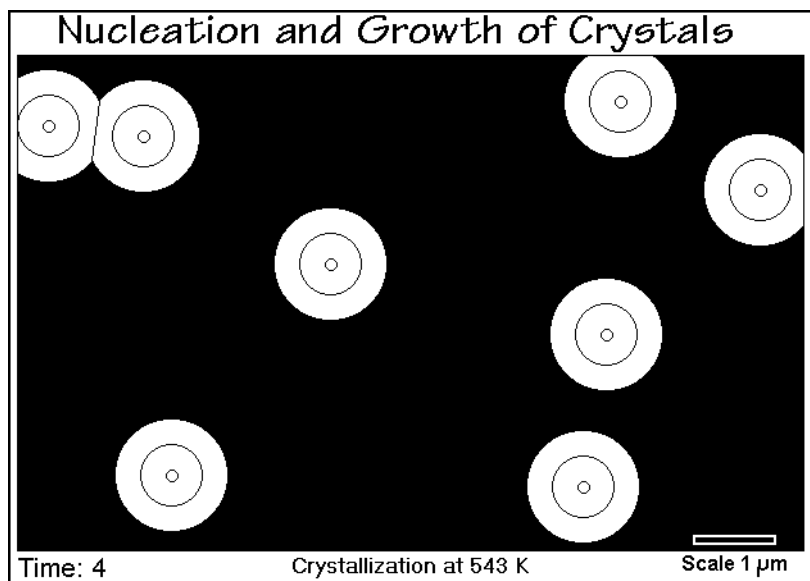
Naturally, only a short summary of the many reactions that lead to the complicated polymer structures can be given here. It must be noted that modern research in polymer science needs a close cooperation between the synthesis of new structures and the characterization of the achieved molecular and phase structures produced and their properties. Of main interest are in this connection the developments of particular phase aggregates such as were first found in proteins. Different small areas within globular proteins are different in polarity, capability of hydrogen bonding, and charge distribution. Sufficiently large differences between such domains can lead to nanometer-size phase separation, a phase separation occasionally referred-to in the different examples of polymer reactions that link incompatible molecular segments. These different phase domains take on special functions in the overall structure, such as giving strength or elasticity, setting up precise geometries and affinities for attraction of small molecules from a surrounding solution, and ultimately enhance reactions between the absorbed molecules. Such phase structures are still poorly understood, but lead to increasing numbers of new and useful materials.

## 3.5 Crystal and Molecular Nucleation Kinetics

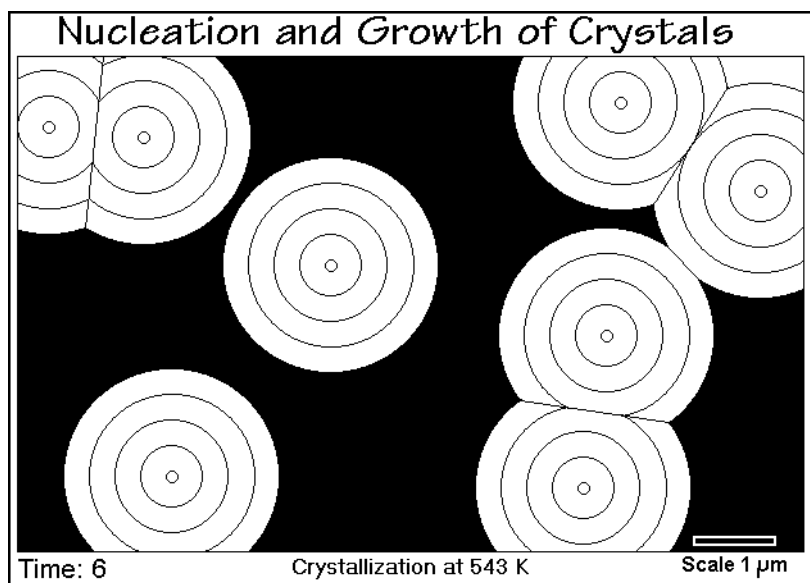
### 3.5.1 Observation of Nucleation and Crystal Growth

Crystallization and melting kinetics describe the dynamics of the transitions between random and ordered phases. A *crystal* is an aggregate of many motifs that satisfy a common ordering principle, the repetition scheme, defined in Sect. 5.1. Much is known about the crystallization step since it is often sufficiently slow to be studied. The melting kinetics, on the other hand, is frequently as fast as the conduction of the heat of fusion into the samples, and thus assumed to occur instantaneously. For linear macromolecules, one finds the crystallization usually to be incomplete, and the melting kinetics slow enough to be measured. The kinetics of crystallization differs from the chemical reaction kinetics discussed in Sects. 3.1. Any two reactant molecules can collide in a simple chemical reaction, and rearrange to the product. Before crystallization can occur, however, the melt or solution has to overcome a nucleation barrier. Furthermore, once in the crystalline state, there may still be the possibility of rearrangements to improve the initial, imperfect crystal. As a result, one must discuss crystallization at least in three stages: nucleation, growth, and perfection. There is a similarity of a chain-reaction polymerization to a crystallization in one dimension where nucleation is equal to the initiation of the reaction described in Sect. 3.2. The nucleation steps are treated in this section, details about crystallization and melting in Sect. 3.6, crystal perfection is also a topic in Chap. 5. Little quantitative information is available about crystal perfection, but it is evident in many thermal analyses.

Figure 3.55 illustrates a typical spherulitic crystallization in progress. The black background simulates the empty field of view of a polarizing microscope when looking at an isotropic melt. Time-step 4 is shown in the figure. Step 1 is the

**Fig. 3.55**

induction time before nucleation occurs and is not visible with an optical microscope. As soon as the growing crystals are large enough they appear as small, birefringent dots in step 2 and subsequently grow until they impinge. Such first impingement can be seen in the upper left corner of Fig. 3.55 where two neighboring crystals ran into each other between steps 3 and 4. After sufficient impingements, the crystal growth slows down, as is obvious in Fig. 3.56 which reproduces time step 6. It is interesting

**Fig. 3.56**

to note that the lines of intersection of neighboring crystals are straight. This is a consequence of nucleation of all crystals at the same time and at equal crystal growth rates. Figure 3.57 illustrates the crystallization, completed to impinging spherulites.

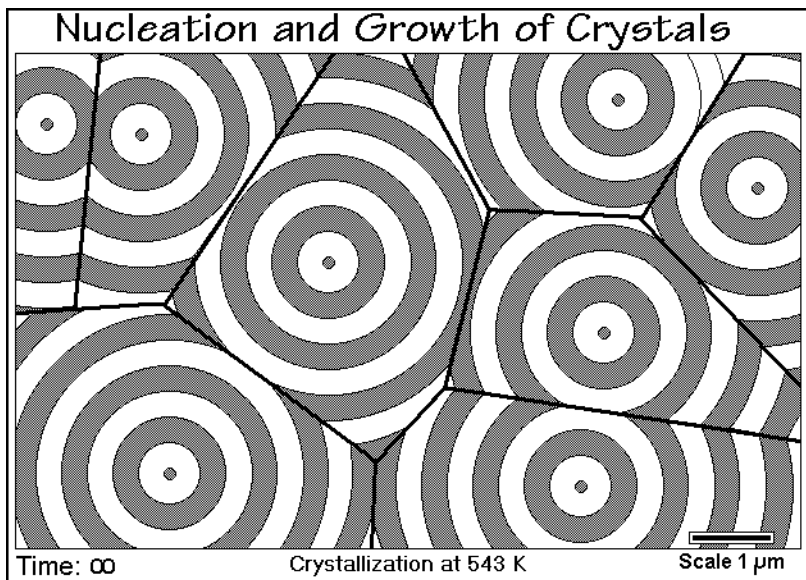


Fig. 3.57

Quite clearly information about the number of nuclei, their moment of appearance, and the subsequent crystal growth rate can be gained from such a microscopic picture. If the produced crystals are of larger than micrometer size, a microscopic inspection of the completed crystallization, or even better a video taping of the overall process, should be part of the thermal analysis of the crystallization process. More about the detailed crystallization kinetics will be discussed in Sect. 3.6.

### 3.5.2 Evaluation of Nucleation Rates

Nucleation of a crystal is called primary nucleation and is assumed to be one of two types. Most common is heterogeneous nucleation, also called athermal nucleation (Gk.  $\alpha$ - $\theta\acute{\epsilon}\rho\mu\eta$  = no change with heat or temperature, a misnomer, as shown in Fig. 3.63, below). It is thought to arise from preexisting nuclei, left over small crystals from prior, incomplete melting or dissolution, named self-nucleation, or foreign, solid particles. For heterogeneous nucleation one expects a constant number of nuclei that grow when the crystallization temperature is reached. Homogeneous nucleation is the second type of crystallization, often described as thermal nucleation. The number of nuclei increases with time in the volume not yet crystallized. On cooling, the nucleation rate increases first, then decreases as the glass transition is approached.

Figure 3.58 displays the results of a typical nucleation experiment. The data can be obtained, for example, with optical microscopy by counting the number of small crystals as a function of time in a given volume element. Easiest is to evaluate a video

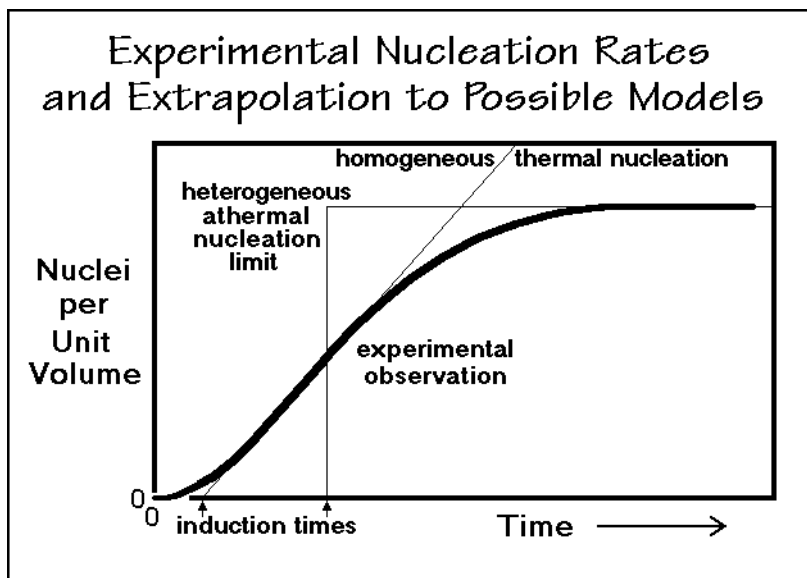


Fig. 3.58

recording of the crystallization of a sample of known thickness. There is a short induction time where no crystals grow and no viable nuclei seem to exist. Next, the number of nuclei increases to a fixed number, pointing to the presence of heterogeneous nuclei.

The data of Fig. 3.58 do not fully fit into the simple scheme of nucleations outlined above. The induction time is not explained, and indeed, little is known about it. Constant numbers of heterogeneous nuclei are only reached after some time, indicating that the initial nucleation proceeds similar to homogeneous nucleation, then reach saturation, not expected for homogeneous nucleation, but easily explained by the exhaustion of preexisting nuclei which become active only after a certain time at the given temperature. In case of fast crystal growth, nucleation might not extend to times permitting to see the finite number of nuclei, and thermal nucleation may be assumed by mistake. The data that need to be extracted from such experiment are:  $N$ , the number of nuclei,  $t_0$ , the induction time, and  $b$ , the rate constant for nucleation. The experimental observations of Fig. 3.58 were modeled after  $\text{LiPO}_3$ , which crystallizes after polymerizing, as discussed in Sect. 3.1.6.

Assuming athermal nucleation for the data treatment, the results for the  $\text{LiPO}_3$  nucleation at different temperatures are listed in Table 3.2. The number of nuclei does not vary substantially over the very large range of supercooling. The induction time seems to increase with supercooling. A detailed explanation of the mechanism cannot be given since the molecules could have undergone active interchange reactions with another temperature dependency (see Sect. 3.1). Finally, the data should also be fitted to a thermal nucleation model, i.e., the homogeneous nucleation limit  $N$  would not have been taken to be constant, but would vary with time as  $N = b(t - t_0)$ . Obviously this approximation would only be useful if considerable impingement of the crystals would have begun before the nucleation is leveling-off, which was not the case. The

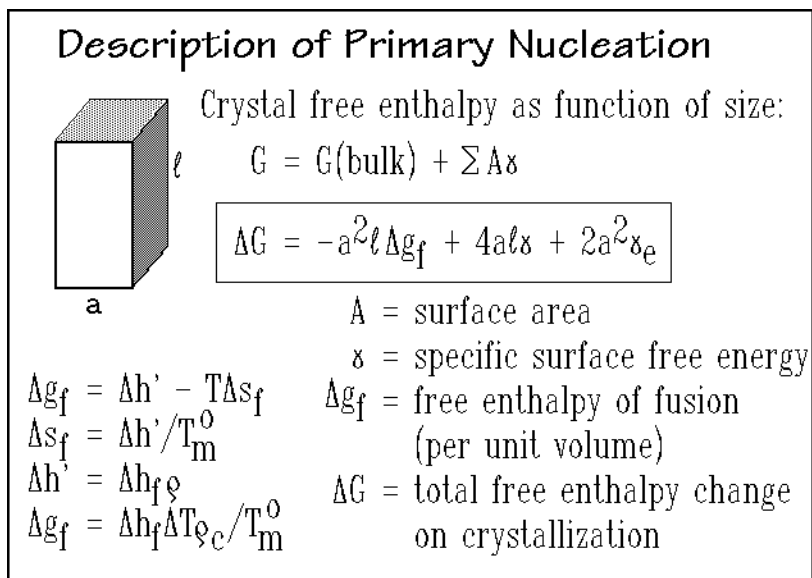
**Table 3.2.** Nucleation data for  $\text{LiPO}_3$  crystallization from the  $\text{LiH}_2\text{PO}_4$  melt

Temperature (K)	Nuclei ( $\#/\text{cm}^3$ )	Nucleation Time (s)
848	$0.5 \cdot 10^8$	?
793	$1.2 \cdot 10^8$	?
713	$1.6 \cdot 10^8$	?
648	$6.9 \cdot 10^8$	?
573	$2.4 \cdot 10^8$	165
568	$4.3 \cdot 10^8$	226
563	$4.7 \cdot 10^8$	245
553	$8.3 \cdot 10^8$	317
549	$5.3 \cdot 10^8$	360

conclusion that heterogeneous nucleation is a better model for the  $\text{LiPO}_3$  crystallization can also be derived from the morphology of the crystals grown. The  $\text{LiPO}_3$  crystal morphology is spherulitic as described in Sect. 5.2.5, as is also depicted in Fig. 3.57. All spherulites are nucleated at about the same time which causes straight lines of impingement. Spherulites nucleated at largely different times would have had hyperbolic lines of impingement.

### 3.5.3 Mathematical Description of Primary Nucleation

The thermodynamic description of a nucleus as a small crystal is given in Fig. 3.59. It shows a drawing of a prismatic nucleus with a quadratic cross-section,  $a$ . Its free enthalpy,  $G$ , can be expressed as a function of dimensions  $a$  and  $\ell$ , where the length  $\ell$  is taken always along the molecular chain axis. The term  $-a^2\ell\Delta g_f$  represents the bulk

**Fig. 3.59**

free enthalpy of crystallization which is the negative of the free enthalpy of fusion,  $\Delta g_f$ , and  $\gamma$  and  $\gamma_e$  are the surface free energies (per unit area). The change of  $\Delta g_f$  into an expression containing the heat of fusion  $\Delta h_f$  (per unit mass), the supercooling  $\Delta T$  ( $= T_m^\circ - T$ ), crystal density  $\rho_c$ , and equilibrium melting temperature  $T_m^\circ$  are indicated in the figure. This expression will also be used extensively in the discussion of the thermodynamics of defect crystals (Chap. 5).

Figure 3.60 illustrates the change in free enthalpy of a nucleus with dimensions  $a$  and  $\ell$ , and with parameters typical for polyethylene in units of  $10^{-20}$  J. The lines of equal value lead to a saddle point at  $\Delta G^* = +10$  ( $= 10^{-19}$  J) and a volume,  $a^2\ell$ , of  $10 \text{ nm}^3$ . At the saddle point a critical nucleus size has been reached ( $a^*$ ,  $\ell^*$ , and  $\Delta G^*$ ). The equations for the slopes of the saddle surface and the critical parameters are listed in the figure. The critical parameters are easily computed by recognizing that at the saddle point both slopes are zero. Any increase beyond the size of the critical nucleus decreases the free enthalpy, i.e., the nucleus becomes more stable. Smaller nuclei are called embryos, and beyond  $\Delta G = 0$ , a nucleus is a stable crystal that can now grow without further hindrance. One expects, however, additional complications as crystallization proceeds. The crystallizing entities are not small, rigid spheres, but are repeating units of a flexible, linear macromolecule that needs to have the proper conformation for crystallization. One of these complications is molecular nucleation, treated at the end of this section.

The change of  $\Delta G$  for a given shape is shown schematically in the bottom graph of Fig. 3.60 for different temperatures and as a function of a single size parameter, i. Close to the melting temperature the temperature dependence of the free enthalpy curve is caused mainly by the change of  $\Delta g_f$  with temperature. At  $T_m^\circ$ , the equilibrium melting temperature, no crystallization is possible since  $\Delta g_f$  is zero and  $\Delta G_i$  can never become negative. With decreasing temperature the critical nucleus becomes smaller

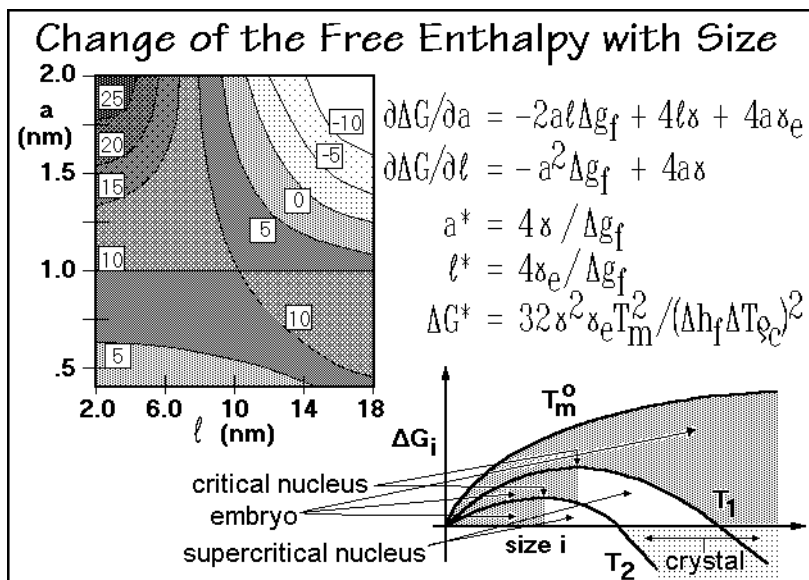


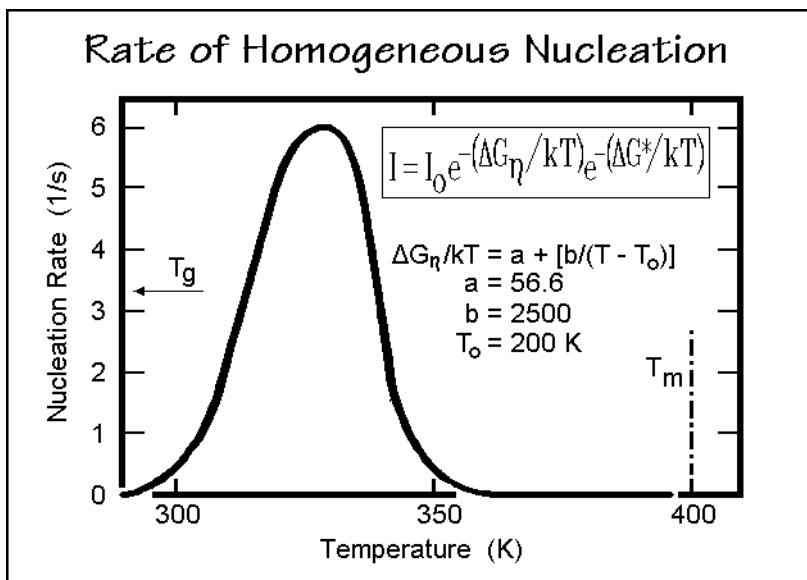
Fig. 3.60

**Table 3.3.** Critical nucleus dimensions,  $\ell^*$ , in nm.

$\Delta T$ (K)	Surface Free Energy ( $\mu\text{J cm}^{-2}$ )						
	0.1	0.5	1.0	1.5	5.0	10.0	20.0
0.1	76.5	382.4	764.8	1,147.2	3,824	7,648	15,209
1.0	7.6	38.2	76.5	114.7	382	765	1,521
10.0	0.8	3.8	7.6	11.5	38	76	153
25.0	0.3	1.5	3.0	4.5	15	31	61
50.0	0.2	0.8	1.5	2.3	8	15	31
100.0	0.1	0.4	0.8	1.2	4	8	15
150.0	0.1	0.2	0.5	0.8	3	5	10

and the nucleation rate speeds up, as can be deduced from the data of Table 3.3 which are calculated for a range of possible surface free energies and supercoolings,  $\Delta T$ . Typical fold-surface free energies are  $5 \mu\text{J cm}^{-2}$  and side-surface free energies are  $0.5 \mu\text{J cm}^{-2}$ . The calculations for Table 3.3 made use of heats of fusion of  $200 \text{ J g}^{-1}$ , densities of  $1.0 \text{ g cm}^{-3}$ , and  $T_m^o = 400 \text{ K}$ , typical for polyethylene-like polymers.

The rate of nucleation,  $I$ , has been estimated by Turnbull and Fisher [25] from the shape of  $\Delta G_i$  and the influence of local viscosity, governed by a free enthalpy  $\Delta G_\eta$ . In Fig. 3.61 this equation is listed. The rate  $I_0$  applies to the case that nucleation is unhindered. The first exponent of the equation expresses retardation of nucleation due to viscosity effects with the given parameters (see Sect. 5.6). It stops nucleation as the glass transition temperature is approached. The nucleation described is homogeneous nucleation and creates a continuous stream of new crystals in the remaining melt or solution. For polymers it takes a supercooling of about 50 K to overcome the

**Fig. 3.61**

nucleation barrier with an observable rate. The curve drawn for homogeneous nucleation is calculated for polymers with  $\gamma = 0.5 \mu\text{J cm}^{-2}$ ,  $\gamma_e = 5 \mu\text{J cm}^{-2}$ ,  $T_m^0 = 400 \text{ K}$ ,  $\Delta h_f = 210 \text{ J g}^{-1}$ ,  $\rho_c = 1.00 \text{ g cm}^{-3}$ ,  $I_0 = 6.2 \times 10^{-12} \text{ s}^{-1}$ . The nucleation rate  $I$  is expressed in nuclei per second for one mole of elements that can crystallize in a single step and is not expected to be more precise than one order of magnitude. Nucleation stops when approaching the glass or the melting transitions.

It is rather difficult to obtain experimental confirmation of the just derived expressions. One must have a melt or solution free of inadvertent heterogeneous nuclei. This was attempted by subdividing the crystallizing phase into small droplets. Each droplet has then only a small chance to contain a heterogeneous nucleus. Experimental data for homogeneous nucleation of polyethylene melt are displayed on the left side of Fig. 3.62. The polyethylene droplets of 1–3  $\mu\text{m}$  diameter were dispersed in silicon oil and observed under a polarizing microscope on cooling at  $0.17 \text{ K min}^{-1}$ . Four different regions of nucleation are obvious. Until 15 K of supercooling none of the droplets crystallized. Then a small number of droplets crystallized with the help of heterogeneous nuclei. Typically these were the larger droplets. A second stage of heterogeneous nucleation occurred at about 30 K supercooling. These nuclei are less efficient and need additional supercooling to develop into critical nuclei. The homogeneous nucleation range is then found at more than 45 K supercooling where ultimately all droplets crystallize.

The right figure gives more quantitative kinetics, gained from isothermal experiments. The fraction of droplets crystallized,  $n/n_0$ , can then be estimated from:

$$n/n_0 = 1 - \exp(-Ivt)$$

where  $v$  is the volume of the droplet and  $t$  the time. From the half-time,  $t = \tau_{1/2}$  [ $= 1.649/(Iv)$ ], it is then possible to estimate the surface free energies contained in

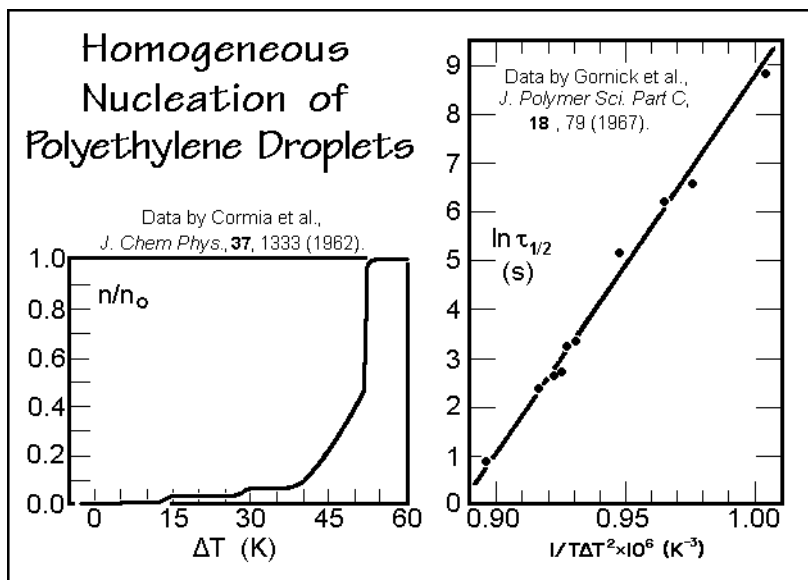


Fig. 3.62



$\Delta G^*$  ( $\gamma^2 \gamma_e \approx 11 \times 10^{-18} \text{ J}^3 \text{ cm}^{-6}$ ). Other polymers may need much larger supercooling for homogeneous nucleation than the just analyzed polyethylene. Typical examples are 105 K for polypropylene, 100 K for nylon 6, 70 K for poly(oxyethylene), and 68 K for poly(oxyethylene).

### 3.5.4 Heterogeneous Nucleation

Experimentally one usually observes not homogeneous, but heterogeneous nucleation. This is nucleation where small particles initiate crystallization. Instead of the interfacial surface free energy to the melt or solution preventing nucleation, the crystallization is now either unhindered or only restricted by the interfacial free energy with the heterogeneous nucleus. Analogous equations as for homogeneous nucleation can be derived for the latter case, but are difficult to verify because of insufficient knowledge of the interfacial free energies and the influence of the surface geometry.

Figure 3.63 illustrates a typical heterogeneous nucleation experiment for a melt of polypropylene. For a given amount of seeding material the number of active nuclei does not stay constant, but increases logarithmically with supercooling. For macromolecules, the effect of seeding disappears long before the melting temperature is reached. Even self-seeding does not cause crystal growth close to the melting temperature (see Sect. 3.6). Figure 3.64 shows some solution-grown, self-seeded polyethylene crystals as published originally by Keller and Willmouth [26]. The seeds are visible in the center of most of the lamellar crystals. Note, the crystals that grow under these conditions have the lattice orientation fixed by the seed. Figure 3.65 illustrates the growth of poly(oxyethylene) on a single-crystal surface of NaCl. Clearly the crystal order of the NaCl surface affects the alignment of the subsequently grown polymer crystals. This transmittal of order is called epitaxy. The term epitaxy

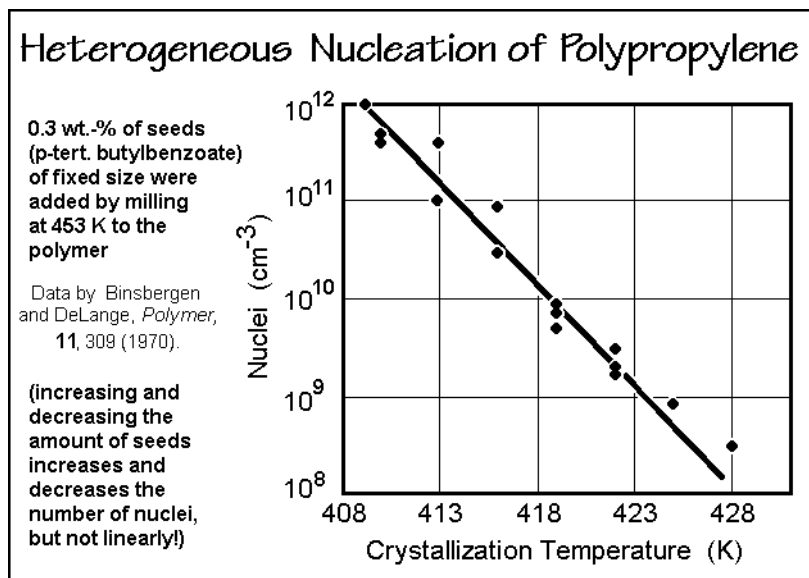
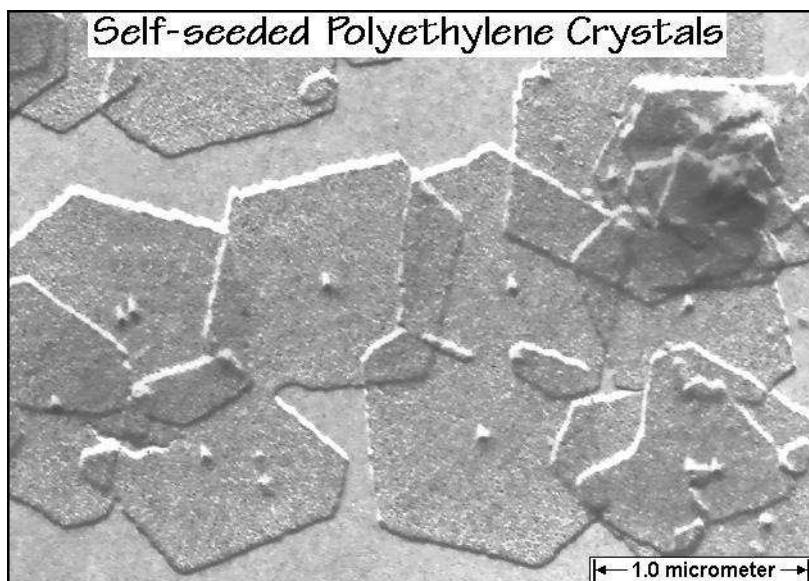
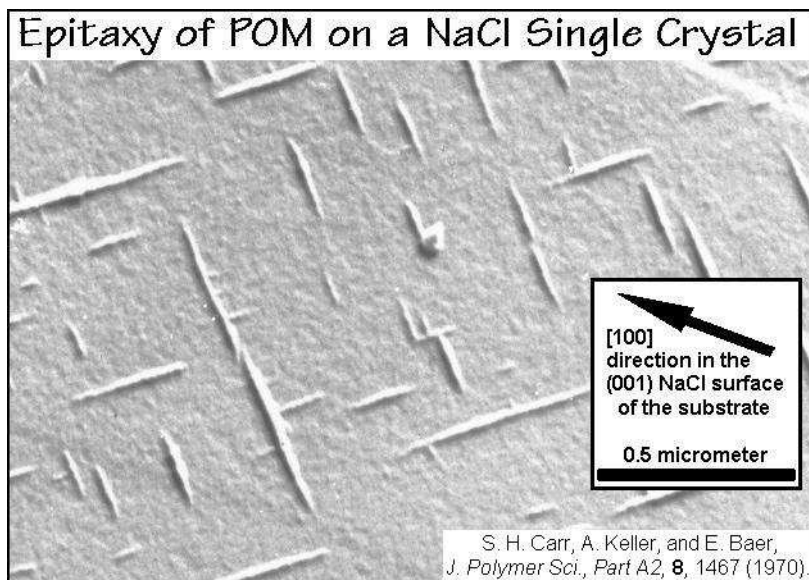


Fig. 3.63

**Fig. 3.64**

(Gk. ἐπί, on, upon; and τάξις, order, arrangement) is generally applied to oriented growth of one crystalline substance on another. Because of the long-chain nature of linear macromolecules, the initial adsorption of the polymer occurs such, that the chain axis lies in the surface. Even a limited matching of the structure of the substrate can then lead to the growth of well-aligned crystals, as seen in Fig. 3.65. The poly(oxymethylene) chains are oriented as shown by the arrow in the figure, along the

**Fig. 3.65**

S. H. Carr, A. Keller, and E. Baer,  
*J. Polymer Sci., Part A2*, **8**, 1467 (1970)

direction [110] of the equally-charged ions,  $\text{Na}^+$  and  $\text{Cl}^-$ . Both of these experiments illustrate possible mechanisms of heterogeneous nucleations that need to be investigated for the evaluation of the nucleation kinetics.

The quantitative influence of self-nucleation is shown in Fig. 3.66 for the case of crystallization of poly-1-butene with crystal form II when followed by dilatometry.

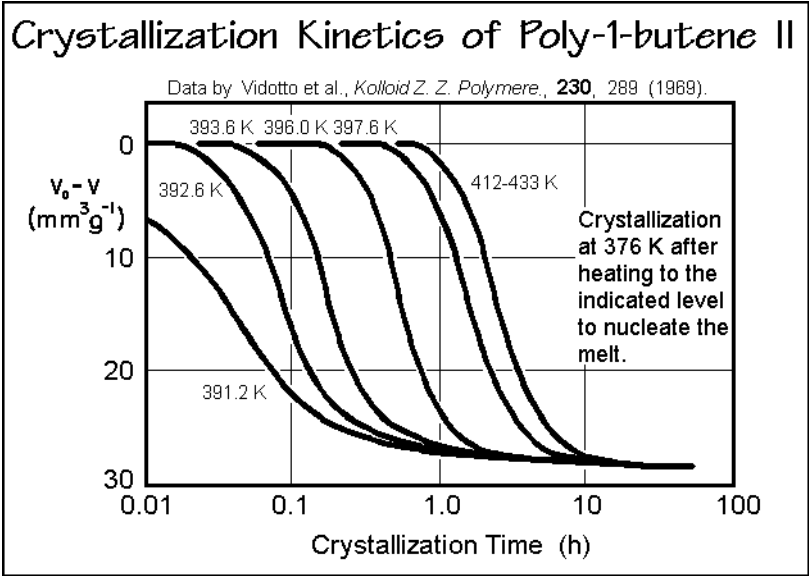


Fig. 3.66

Various amounts of self-nuclei were produced by heating the samples above the melting point. All self-nuclei are destroyed only above 402 K, and the constant crystallization kinetics is established with the remaining foreign nuclei. Table 3.4 contains a list of the crystallization peak temperatures by DSC on cooling of

**Table 3.4.** Crystallization peak temperatures of seeded polypropylene by DSC.

Seed Material:	Cryst. Peak (K):	Seed Material:	Cryst. Peak (K)
No seed	379	Ca(benzoate) <sub>2</sub>	389
AgNO <sub>3</sub>	380	Na m-benzoate	391
Pb(benzoate) <sub>2</sub>	381	Na caproate	391
Na 1-naphthoate	381	Na o-methylbenzoate	392
Na <sub>2</sub> SO <sub>4</sub>	383	Ba(benzoate) <sub>2</sub>	394
Al <sub>2</sub> O <sub>3</sub>	384	Na p-hydroxybenzoate	395
Na m-benzoate	384	Li benzoate	398
Na acetate	385	Na <sub>2</sub> 1,2-cyclohexane	
Na formate	386	dicarboxylate	401
Pyrex glass	386	Na cyclohexane	
Na octanate	386	carboxylate	403
Na nitrobenzoate	387	Na benzoate	404
Na <sub>2</sub> oxalate	388	Na p-methylbenzoate	405

polypropylene at  $12.5 \text{ K min}^{-1}$  when adding different seed materials (0.25%, milled at 423 K for 5 min). With such experiments large numbers of heterogeneous nucleating agents can be quickly assessed.

### 3.5.5 Secondary Nucleation

Experimental data on melt crystallization are summarized in Fig. 3.67 in form of the linear crystal growth rate,  $v$ . All linear crystal growth rates go exponentially to zero when the temperature approaches the melting temperature, pointing to a nucleation which is similar as developed in the Figs. 3.51–61. These experiments, thus, provide strong evidence that some kind of secondary nucleation must be found to account for the crystal growth of macromolecules [27].

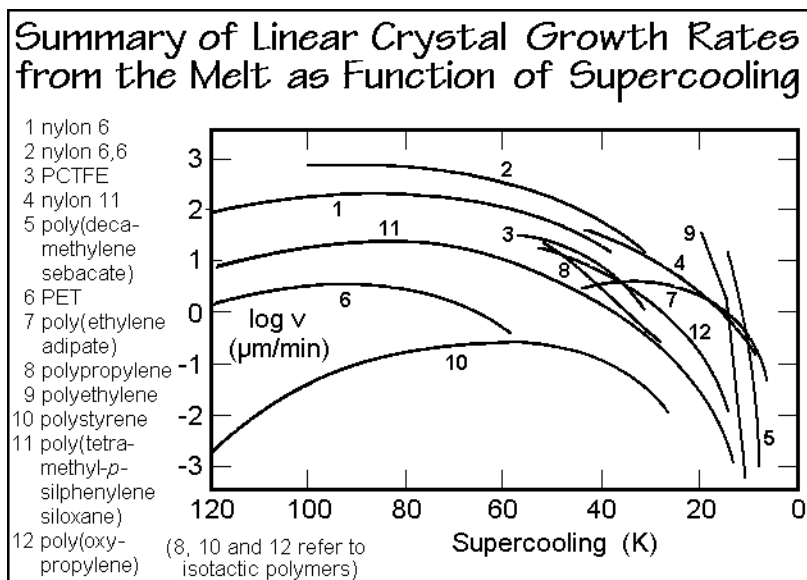


**Fig. 3.67**

For crystallization of small molecules, one can easily expand the mathematical description of primary nucleation to secondary nucleation by making use of the so-called Kossel crystal, shown in Fig. 3.68. Addition or removal of a crystallizing motif (assumed to be a cube) on different positions on the crystals gives different enthalpy contributions. During this process, however, surface area has also been removed or newly created. Only position “3” creates as much surface area of the crystal as it removes and has no surface contribution. Addition to positions 1 and 2 increases the surface area by 5 and 4 units, respectively, and thus leads to nucleation barriers. Addition to 4 and 5 decreases the surface area by 2 and 1 unit, respectively. These positions are quickly filled because of the decrease in surface area and yield a molecularly smooth surface. For secondary nucleation one assumes that growth continues with a given rate as long as positions of type 3 are available. Additional growth must then be nucleated by creating growth at a number of positions like 1 and

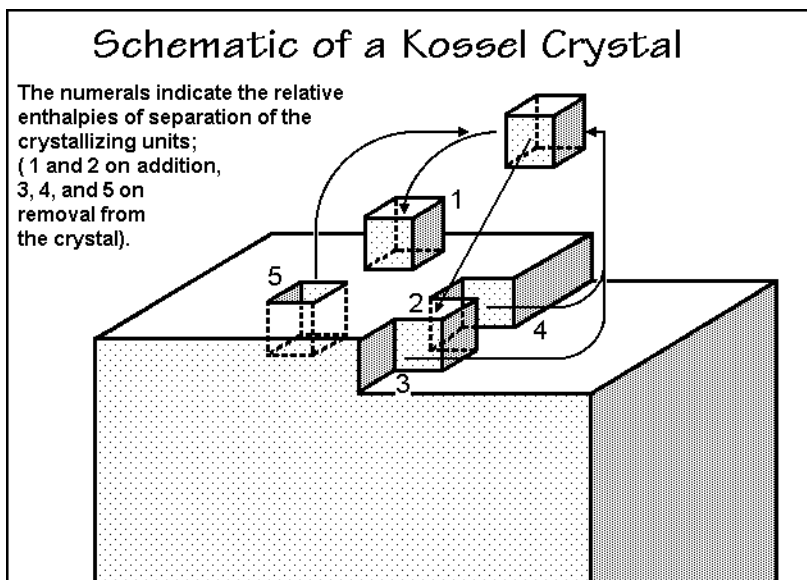


Fig. 3.68

2 on one of the smooth surfaces before the next layer can be grown. The linear crystal growth rate is given by the number of new layers nucleated per second.

Although this model does not fit well for macromolecules since it neglects the interconnection between the crystallizable units along the molecule, it has been used to develop nucleation models as shown in Fig. 3.69. As soon as a ledge is created on the surface, growth is assumed to occur by adding new molecular segments (stems)

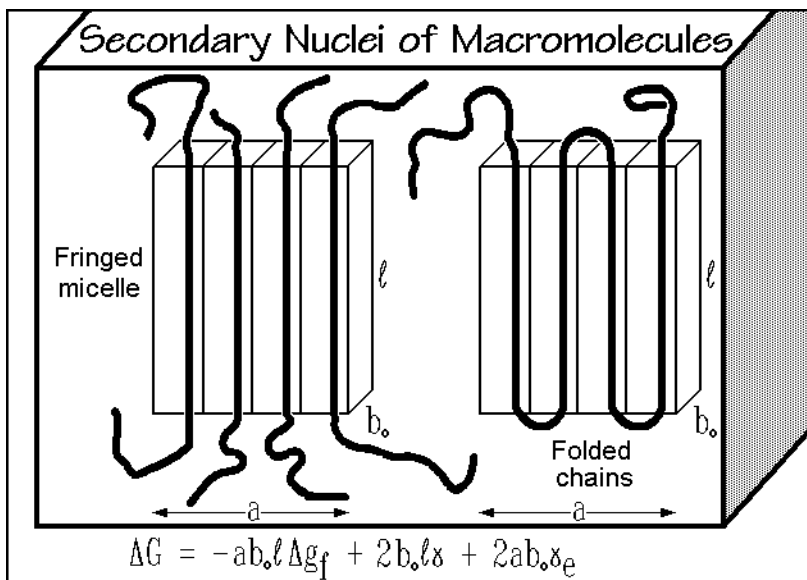


Fig. 3.69

without a further nucleation barrier. On a smooth growth surface, the free energy for formation of such a ledge is given by the equation at the bottom of Fig. 3.69. The possible differences between the fringed micellar and chain-folded chain conformations of Sect. 5.2 need to be taken into account by different surface free energies,  $\gamma_e$ .

Figure 3.70 shows the derivation of the equations needed to describe such secondary nucleation, along the same path as the equations for primary nucleation in Figs. 3.59–60. As for primary nucleation in Fig. 3.60, the system starts at the lower

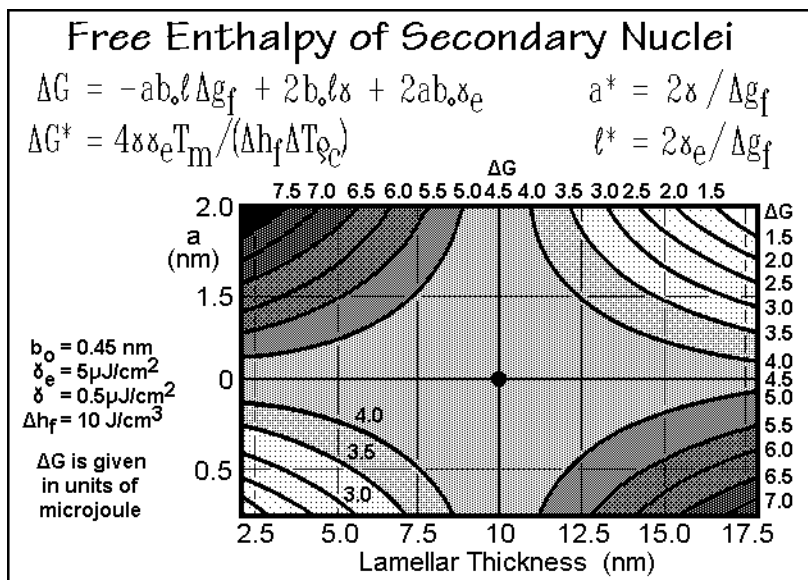


Fig. 3.70

left corner in the free-enthalpy graph and must cross the saddle point to reach the negative free enthalpy for continued growth. Using the same parameters as for the primary nucleation, the barrier to crystal growth due to secondary nucleation is lower, thus the rate of nucleation is higher, as shown in Fig. 3.71. One must consider when going to lower temperatures, that one needs only one primary nucleus per crystal, but very many secondary nuclei. The approach to similar nucleation rates when reaching the glass transition means not only that all nucleation stops at the glass transition, but that at the lower temperature, primary nucleation becomes more effective relative to secondary nucleation. Indeed, one observes faster overall crystallization due to enhanced primary nucleation when heating from the glassy state and crystallizing at low temperature than on cooling from the melt. Such low-temperature crystallization is called *cold crystallization*.

Two final points need to be made about secondary nucleation. First, that screw-dislocation defects, described in more detail in Sect. 5.3, produce indestructible secondary nuclei for growth on top of the fold surfaces of polymer lamellae. This surface would otherwise be inactive for further growth and restrict polymer crystals to single lamellae (see Chap. 5). An example of a series of screw dislocations is shown in Fig. 3.72 on the example of poly(oxyethylene) of 6,000 molar mass grown

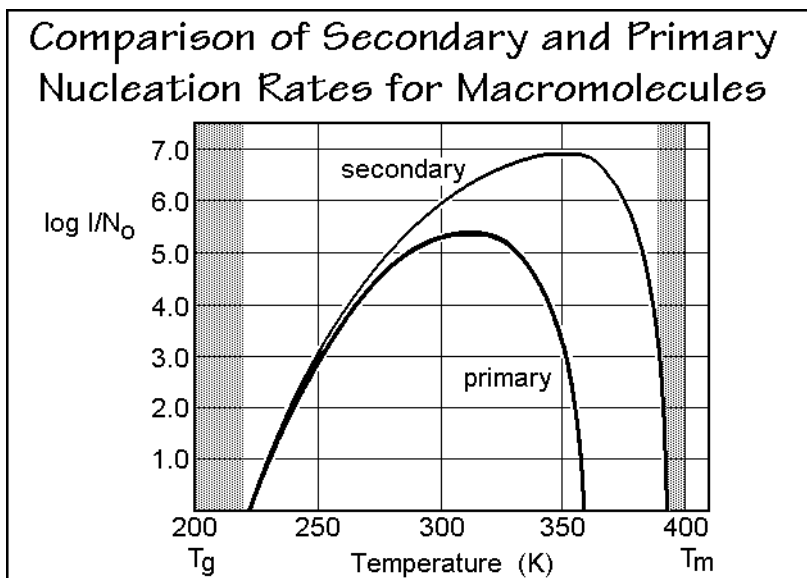


Fig. 3.71

at 332.6 K [28]. These screw dislocations continuously initiate new lamellae at their tops and bottoms without need of nucleation. Their growth, once initiated, should thus avoid the secondary nucleation and cause different linear-crystal-growth kinetics. Experimentally such kinetics, however, was only observed for small molecules.

Next, the rate of completion of a layer on the side surface of a lamella (growth face) and the rate of renewed nucleation seems not in the proper ratio with the simple

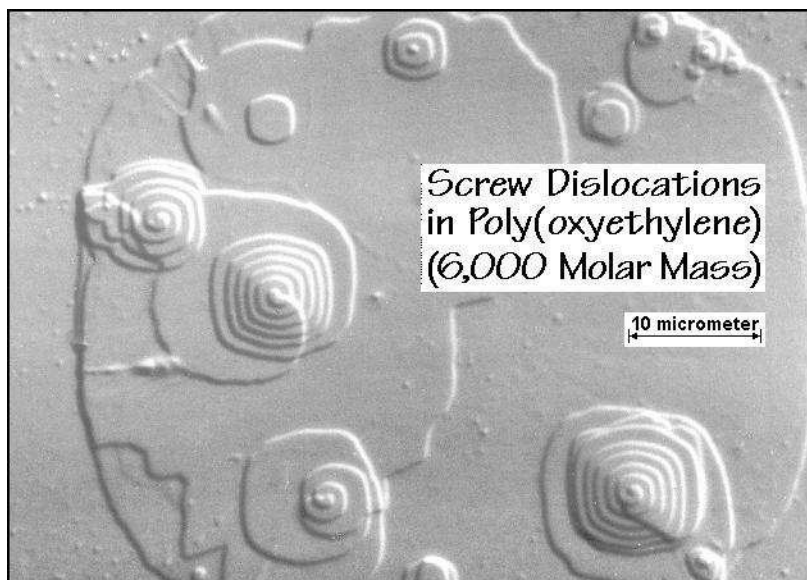


Fig. 3.72

models shown to yield smooth surfaces. A rough surface, however, does not need secondary nucleation. Finally, the crystal structure of many polymers, as described in Sect. 5.1, is such that polymer crystal surfaces are inherently rough, causing smaller surface-free energies than assumed. Experiments of nucleation on rough lamellar surfaces have also shown no preference for steps in the surface for nucleation. All these points cast doubt on the usefulness of the concept of secondary nucleation.

Naturally, one can also propose a tertiary nucleation step for starting growth on a smooth ledge as seen at position 2 in Fig. 3.68. Its nucleation barrier would be even smaller than for secondary nucleation and even less likely to slow the crystal growth significantly.

### 3.5.6 Molecular Nucleation

The concept of molecular nucleation was developed to explain some observations not in agreement with the above model of crystallization limited by secondary nucleation [29]. In Fig. 3.73 the molecular length is plotted which is rejected by a crystal growing from the melt or from solution (curves 1 and 2, respectively). These data were obtained by measuring the molar mass of the noncrystallized molecules of a

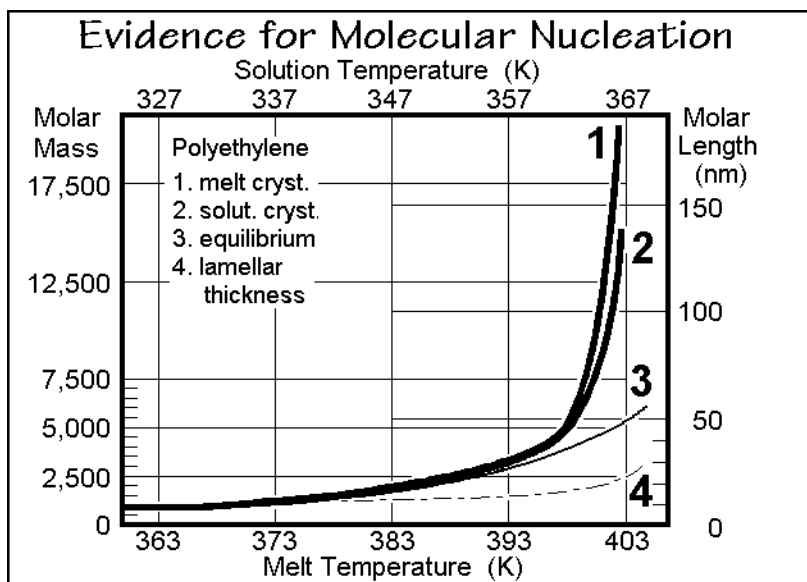


Fig. 3.73

broad molar mass distribution [30]. The surprise is that this length does not agree with the equilibrium melting temperature given as curve 3 and discussed in more detail in Sect. 7.1.5. A reversible selection of molecular lengths occurs, thus, below the equilibrium melting temperature. This is only possible if a reversible process occurs at this lower temperature. The process with a reversible crossing over a free-enthalpy barrier is assumed to be the molecular nucleation which must occur before a chain can grow onto the crystal surface as shown in Fig. 3.74. The molecular nucleation



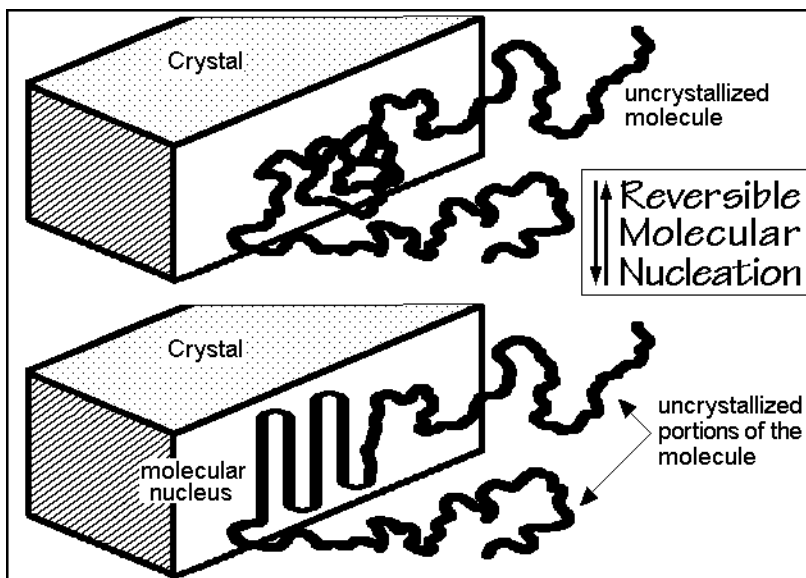


Fig. 3.74

contrasts crystal nucleation and seems unique for macromolecules. Crystallization of any single repeating unit out of the molecule onto a smooth crystal surface is unlikely since this fixing at a single point would restrict the molecule as a whole, i.e., the decrease in entropy of the molecule cannot be compensated by the heat of crystallization of the single repeating unit. The increase in free enthalpy describing molecular nucleation is similar to the formalism for the secondary nucleation, just that the molecular nucleus is decoupled at the points of junctions to the chain ends which are part of the amorphous phase. A molecule shorter than the critical or supercritical nucleus size can in this case not crystallize, while longer molecules can easily complete the crystallization by decreasing after molecular nucleation the free enthalpy of the molecule with every additional step into the region of stability, similar as shown in the schematic of Fig. 3.60.

The lower limit of molecular length which needs molecular nucleation on melt crystallization was explored for paraffins and polyethylenes by DSC and TMDSC described in Sects. 4.3 and 4.4. Figure 3.75 illustrates the supercooling necessary for measurable crystallization. The broader molecular mass fractions of polyethylene are marked by labels like PE1150, where the number gives the average molar mass in Da. A critical length of about 75 chain atoms can be derived for polyethylene.

This concludes the discussion of the nucleation dynamics of macromolecules. It shows that the usually assumed constant number of heterogeneous nuclei and linearly increasing number of homogeneous nuclei is a simplification, and secondary nucleation as the basis for crystal growth is a doubtful concept. Finally, molecular nucleation is not a well enough understood concept to quantitatively explain facts such as the molar mass dependence of crystallization. The further work needed to understand the basis of nucleation in polymers is a big challenge for new research in solid-state polymer science.

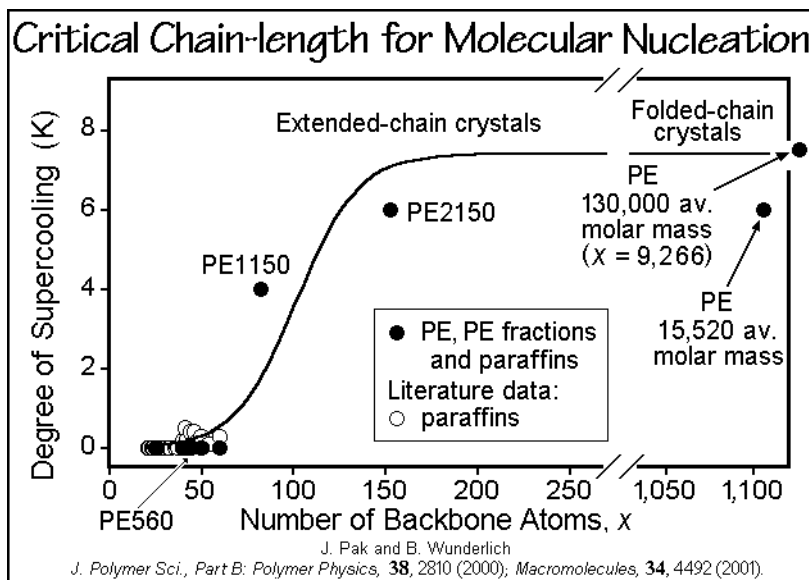


Fig. 3.75

## 3.6 Crystallization and Melting Kinetics

### 3.6.1 Linear Melting and Crystallization Rates

Crystal growth and melting is represented schematically in Fig. 3.76. The effect of primary nucleation, discussed in Sect. 3.5, is eliminated in the experiments by retaining crystals during the analysis. Small molecules, such as monomers, have a slope of the growth rate that does not reach zero on going through the equilibrium melting temperature,  $T_m^0$ . The slope is determined by the surface roughness or number of screw dislocations which provide secondary nucleation sites (see Sect. 3.5.5) and account for mechanisms, further influenced by crystal geometry. A check of the reversibility seen in Fig. 3.76 can be made with temperature-modulated differential scanning calorimetry, TMDSC. As an example, reversible melting of In is described in Sect. 4.4.7 (Figs. 4.106–109).

The continuity of the change of growth rates at  $T_m^0$  is interrupted as soon as primary, secondary, or molecular nucleation is necessary. The curves labeled oligomer and polymer in Fig. 3.76 show a region of zero growth rate due to molecular nucleation. Secondary nucleation would produce a smaller hindrance to crystal growth. Despite that there should be no reversible melting for flexible oligomers and macromolecules, TMDSC could show some reversibility based on local equilibria within the global metastable structure. Finally, it is possible to see a reduction of the metastability gap when nonequilibrium crystals of lower melting temperature,  $T_m$ , grow on cooling. Specific data will be discussed in Sect. 3.6.7. Also shown in Fig. 3.76 is the magnitude of a typical temperature modulation in TMDSC.

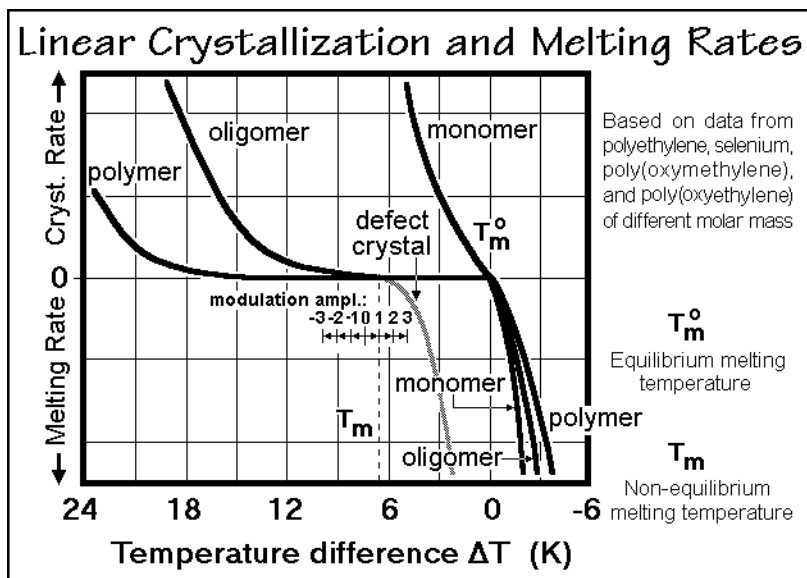


Fig. 3.76

This short introduction to possible paths and mechanisms of melting and crystallization indicates how difficult it is to develop a detailed kinetics that links the molecular mechanism to the observed, macroscopic kinetics. Considerable molecular scale information is needed for the interpretation of the macroscopic thermal analysis data. Few data on melting rates are available for polymers, due to the tendency of large crystals to superheat [31], and small crystals to melt very fast.

### 3.6.2 Directional Dependence of Crystallization

The directional dependence of the crystal shape is sketched in Fig. 3.77. With differences in the linear growth rates,  $v$ , in different crystallographic directions, different crystal shapes are produced. The three-dimensional sketch is given for different growth rates along three rectangular crystallographic directions  $a$ ,  $b$ , and  $c$ . Assuming that no other growth is possible, the simple tetragonal crystal results. A somewhat more complicated, monoclinic crystal shape is illustrated in the bottom sketch and photograph of the figure for the example of a single crystal of gypsum. More details about the shape or morphology of crystals are given in Sect. 5.2. The linear increase of size with time at right angles to the chain direction is documented in Fig. 3.78 for a folded-chain crystal of polyethylene grown from dilute solution. After about 11 days the crystallization is completed and the final crystal size is reached, determined in this case by the number of nuclei and the total crystallizable material available. The shape, however, is the result of the different rates of growth. In the analyzed case of chain folding, no crystal thickening occurred in the chain direction with the exception of some thickening due to screw-dislocation growth, as seen in Fig. 3.72. For polyethylene crystallization from solution at high temperatures, the growth faces are  $\{110\}$  planes, giving the shape shown in Fig. 5.5.2.

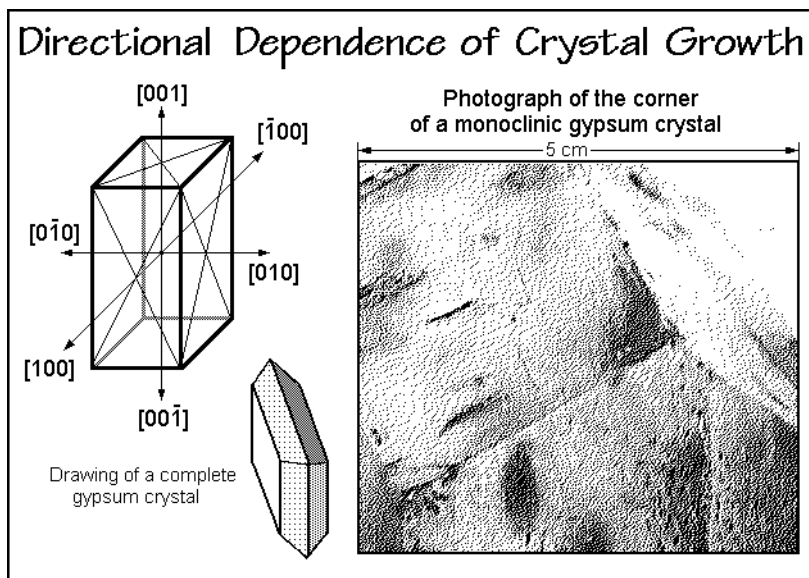


Fig. 3.77

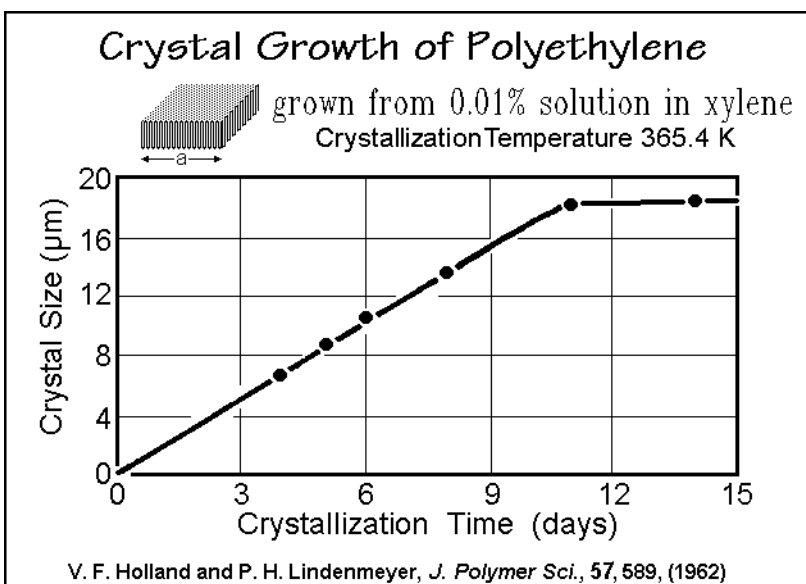


Fig. 3.78

### 3.6.3 Diffusion Control of Crystallization

Using the same polymer solution as in Fig. 3.78 for analysis of the crystal growth at lower temperature, the growth rate slows with time, as shown in Fig. 3.79. The crystal growth slows because the diffusion limits the number of crystallizable molecules in

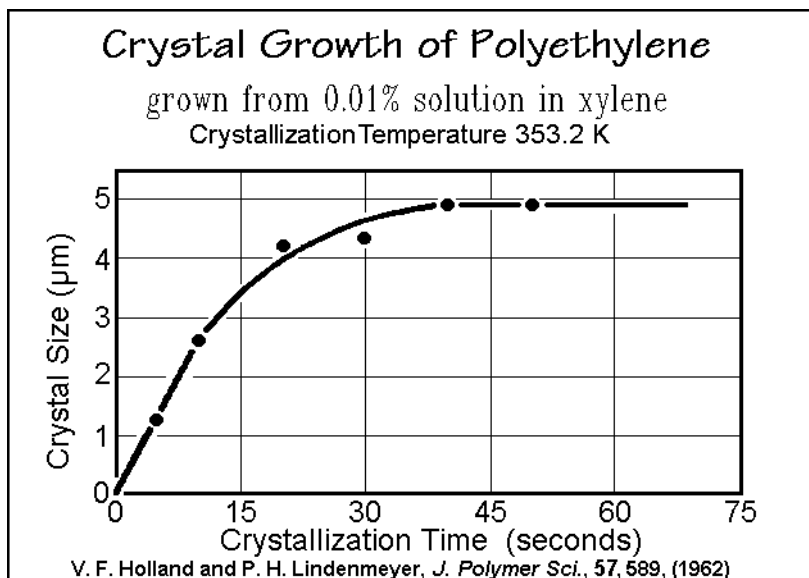


Fig. 3.79

the vicinity of the crystal surface. Similarly, crystal growth may be slowed on crystallization from the melt, if the heat of crystallization cannot be conducted away fast enough and the temperature at the interface increases and slows crystallization.

The solvent concentration,  $s$ , changes with distance,  $n$ , from the crystal and with time,  $t$ , until steady state is reached, as indicated on the left in Fig. 3.80. The equation for  $s$  involves a competition of the growth of the crystal in direction of lower solvent

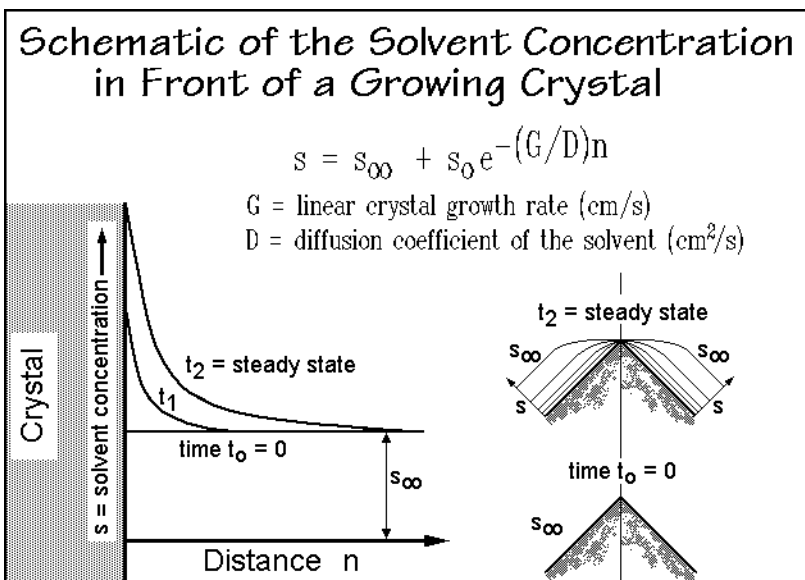
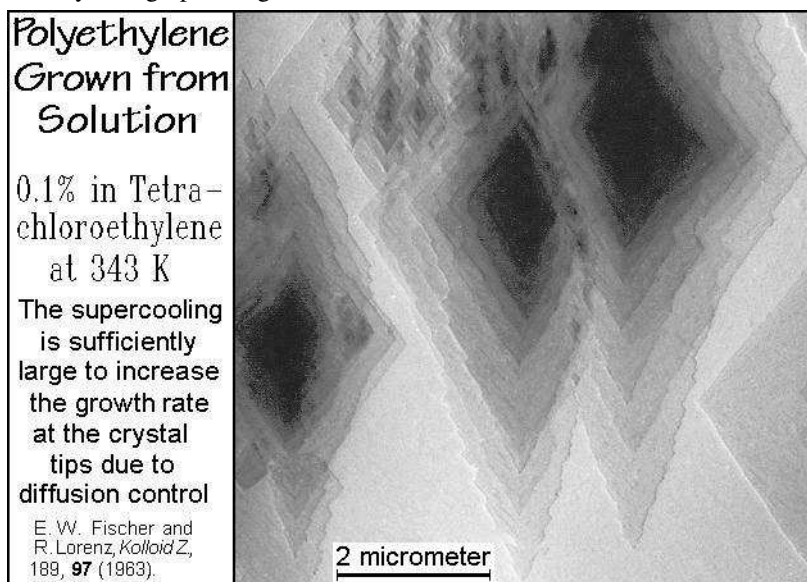


Fig. 3.80

concentration and the build-up of solvent due to the slow diffusion. The distance ( $s - s_{\infty}$ ) is a measure of the influence of the diffusion on crystal growth. The two sketches on the right suggest that diffusion control leads to faster crystal growth at corners of crystals and produces a dendritic morphology described in Sect. 5.2.5. In Fig. 3.81 an electron micrograph of polyethylene crystals with growth spirals in the center is given where the true crystallographic angle at the crystal tips is narrowed from its crystallographic angle of  $67^\circ$  due to diffusion control.



**Fig. 3.81**

### 3.6.4 Growth of Spherulites

Diffusion or thermal conductivity limitation may change the crystal morphology to such a degree that the dendritic morphology grows in all directions with approximately the same rate, namely that of the fastest growing apex. The electron micrograph of Fig. 3.82 shows the development such fast-growing tips in many directions. Additional discussion of dendritic crystal morphologies are given in Sect. 5.2.5 and an assessment of spherulites was given recently [32].

At sufficient supercooling, the spherulitic superstructure may be described with only one growth rate,  $v_a$ , as shown in Fig. 3.83. The increase in crystal volume,  $V$ , is given by the second equation and allows the computation of the enthalpy evolved by multiplication with the product of density and specific heat of fusion ( $\Delta h_f$  in  $\text{J g}^{-1}$ ). With nucleation data, the crystallization rate of the whole sample can be computed and linked to growth rates measured by dilatometry or calorimetry. Results for the  $\text{LiPO}_3$  crystallization, which is discussed in Sect. 3.1.6, are also listed in Fig. 5.83 [15]. The changes of the growth rate with temperature are given in the table. Note that the crystallization of the polymer is in this case coupled with the polymerization reaction [1], and increases with temperature.

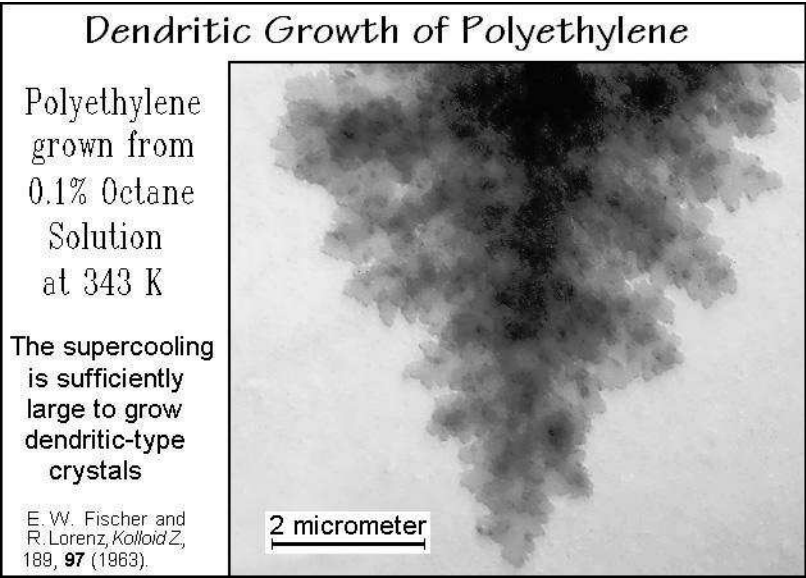


Fig. 3.82

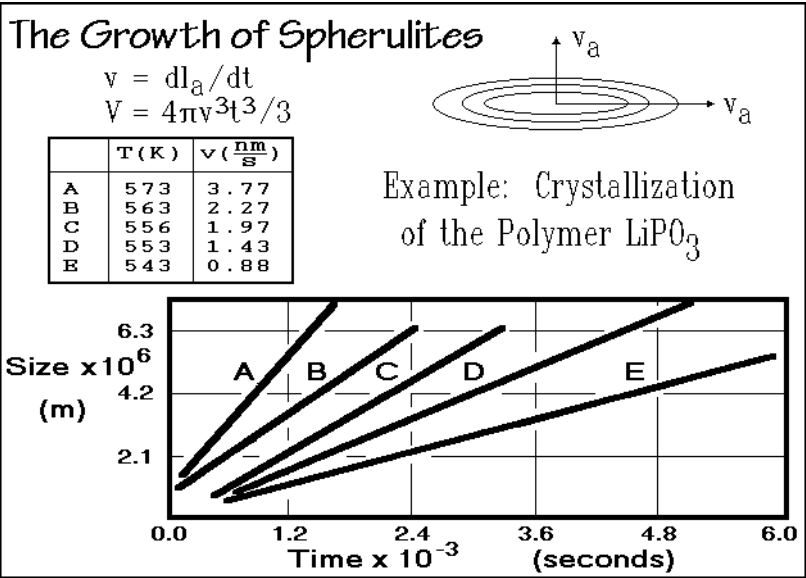


Fig. 3.83

**3.6.5 Avrami Equation**

Knowing from the microscopic analysis the number of athermally growing nuclei and the linear crystal growth rate, it is easy to calculate the initial volume fraction,  $v_c$ , crystallized at time  $t$ . This volume fraction is needed for the link of the crystallization

data to dilatometry (see Sect. 4.1) or heat of crystallization (see Sects. 4.2–4.4). In Fig. 3.84 the total volume  $V_i$  of crystal  $i$ , and the sum over all crystals are computed for a crystal morphology as shown in Fig. 3.57. This calculation, using Eq. (2), is

<b>Derivation of the Avrami Equation</b>		
(1) $V_i = 4\pi v^3 t^3 / 3$		volume of crystal $i$
(2) $V_{\text{c total}} = \sum V_i = 4N\pi v^3 t^3 / 3$		total crystal volume
(3) $V_\varrho = V_{\text{c}} \varrho_{\text{c}} + V(1 - v_{\text{c}}) \varrho_{\text{a}}$		(free growth approximation)
(4) $v_{\text{c}} = V_{\text{c total}} / V$		$V$ = volume at time $t$
(5) $v_{\text{c}} = \frac{\varrho - \varrho_{\text{a}}}{\varrho_{\text{c}} - \varrho_{\text{a}}}$		$\varrho$ , $\varrho_{\text{a}}$ , and $\varrho_{\text{c}}$ represent the densities of the overall sample, the amorphous and crystalline phase, all at time $t$
Poisson equation:		$P$ = chance of an event not occurring
(6) $P = e^{-x}$		$P = (1 - v_{\text{c}})$
(7) $x = 4N_0\pi v^3 t^3 / 3$		$x$ = average chance
Avrami equation:		$N_0$ = nuclei per unit volume
(8) $(1 - v_{\text{c}}) = \exp[-4N_0\pi v^3 t^3 / 3]$		

**Fig. 3.84**

called the free growth approximation of crystallization. It applies to the initial time period before significant impingement of neighboring crystals occurs, as can be seen from a comparison of Figs. 3.55 and 3.56. The dependence of the volume on the third power of time given in Eq. (1) accounts for the fast increase in crystallization with time. In case the nucleation is thermal, more complicated equations must be derived. At present, one usually uses only linear increases of nuclei with time and, if needed, an additional induction time as seen in Fig. 3.58.

Next, the equation for the evaluation of the crystallized volume-fraction is derived in Eqs. (3–5) of Fig. 3.84. Equation (5) is also used to compute the volume fraction crystallinity of semicrystalline polymers from dilatometric experiments (see Sect. 4.1). The more common mass-fraction crystallinity is derived in Sect. 5.3.1. Simple density determinations as a function of time can, according to Eq. (5), establish the overall progress of crystallization.

The last step is the evaluation of the impingement of the crystals as observed in Figs. 3.56 and 3.57. It is based on the Poisson equation, written as Eq. (6) in Fig. 3.84, which gives the probability that a point in the melt is not overrun by a growing, spherical crystal, i.e., remains melted ( $P = 1 - v_{\text{c}}$ ). The exponent  $x$  is the average chance, or the expectation value, simply the free growth approximation referred to the unit volume. Adding all together gives the Avrami equation, Eq. (8). Figure 3.85 shows the influence of  $n$  in the generalized Avrami equation. Experiments for the  $\text{LiPO}_3$  crystallization at different temperature are shown in Fig. 3.86 [15]. As long as the model used for nucleation and growth, and the assumptions that go into the



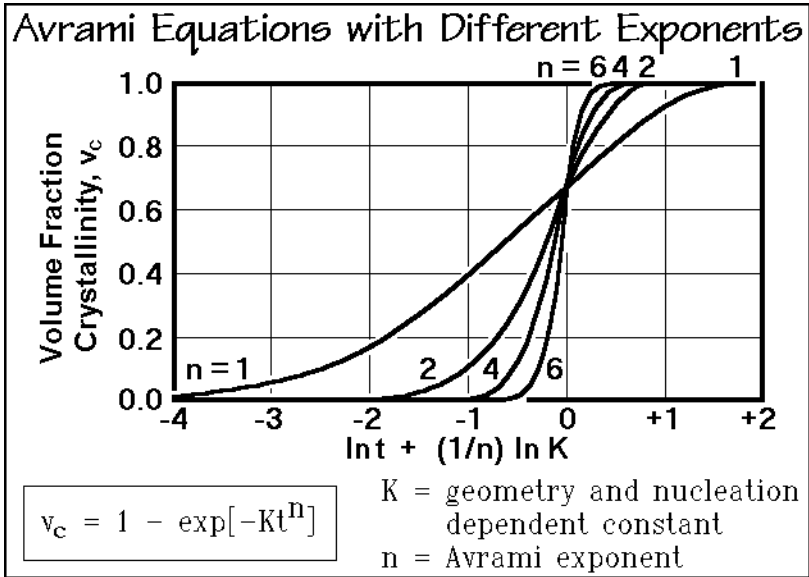


**Fig. 3.85**

Avrami equation hold, Eq. (8) agrees well with the data. Figure 3.86 was computed from the crystal-growth rates listed in Fig. 3.83 and the constant numbers of nuclei of Table 3.2. With these data it was possible to compute the overall curves shown in Fig. 3.22 for  $v_c$ , using  $n = 3$ , and thus, complete the discussion of the complicated case of simultaneous  $\text{LiPO}_3$  polymerization, a chemical reaction, with overlapping crystallization, a physical phase transition.

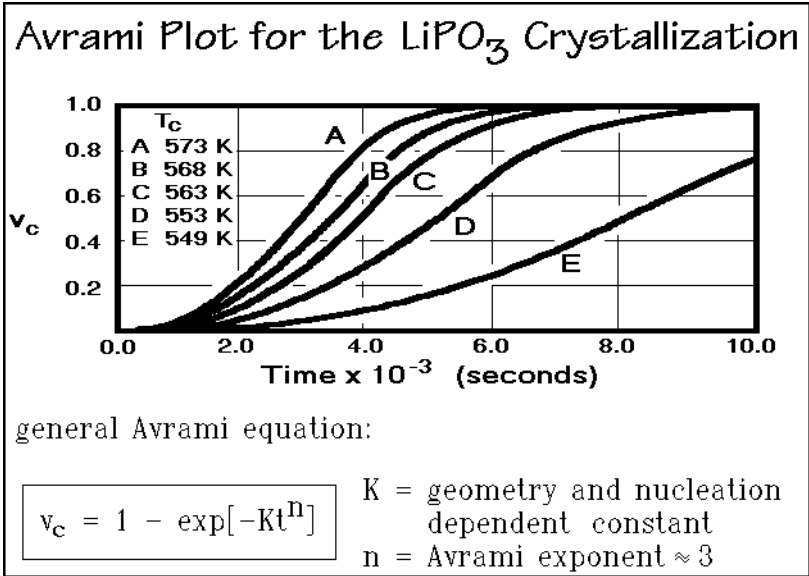


**Fig. 3.86**

Although the Avrami equation is derived for a very specific model, it is often generalized, as shown by the equation in Fig. 3.85. However, only when based on the Poisson equation can one expect a true link between experiment and crystallization model. In case the nucleation increases linearly with time, the Avrami exponent increases to four for a spherulitic crystallization. Often it is assumed that growth of lamellar and fibrillar morphologies can also be described with  $n$  changed to two and one (athermal nucleation) or three and two (thermal nucleation), respectively. In these cases, however, the condition that  $x$  is the free growth approximation in the unit volume is not fulfilled and geometric effects and the influence of the growth direction must be considered in evaluation of  $P$  in Fig. 3.84.

### 3.6.6 Nonisothermal Kinetics

An advantage for thermal analysis would be gained if one could evaluate crystal growth and chemical reactions with changing temperature in nonisothermal experiments. The simple kinetic models described in this chapter can be extended, making use of the change of reaction rates with temperature, as described by the Arrhenius equation described in Appendix 7, Fig. A.7.2. Figure 3.87 indicates the change of the rate constant with temperature, governed by an activation energy.

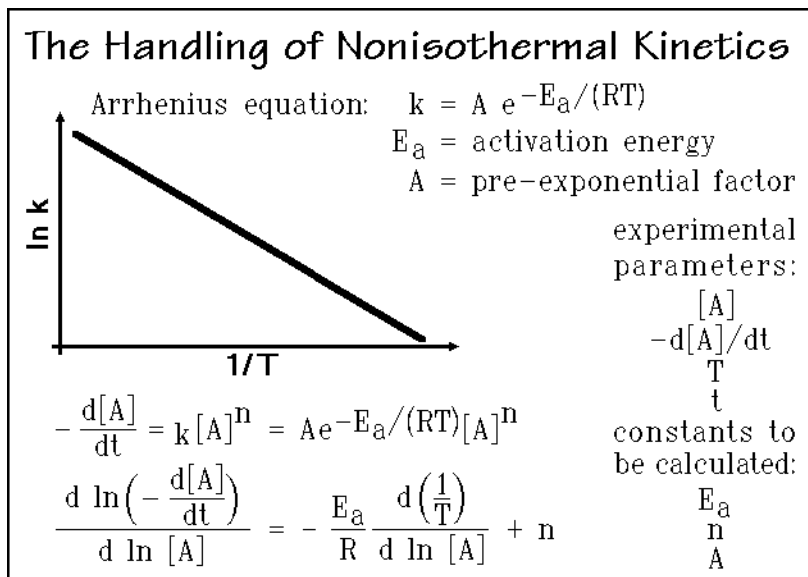


Fig. 3.87

Insertion of the Arrhenius equation into the rate expression leads to an expression for the decrease in concentration  $-d[A]/dt$ . Taking the logarithm of both sides of the equation removes the exponential, and additional differentiation leads to the second equation with the activation energy, pre-exponential factor, and order of the reaction expressed in terms of measurable quantities. This analysis is known under the name Freeman-Carroll method [33].

Although the method is straightforward, it has several problems. First, it is cumbersome to handle the equation without computerized data analysis. Perhaps most serious, however, is that the mechanism to be described may change with temperature. In addition, the equation shows little sensitivity to changes in  $E_a$ ,  $n$ , and  $A$ , making the evaluation of the data uncertain. To apply such analysis to the Avrami equation is even more unpredictable because of the two different dynamics involved, crystal nucleation and growth. Even in thermogravimetry where this method is frequently applied, one often finds changing data for different heating rates, indicative that the kinetics does not follow the Freeman-Carroll equation (see Sect. 4.6.6).

### 3.6.7. Experimental Data

In this section experimental results are discussed, concerned with analyses of melting and crystallization kinetics, as well as reversibility of the phase transition. The frame of the discussion is set by Fig. 3.76, which will be supported by experimental data on poly(oxyethylene). The thermal analysis tools involved are TMDSC, optical and atomic-force microscopy, DSC, adiabatic calorimetry, and dilatometry. Most of these techniques are described in more detail in Chap. 4. Results from isothermal crystallization, and reorganization are attempted to be fitted to the Avrami equation. This is followed by a short remark on crystallization regimes; and finally some data are presented on the polymerization and crystallization of trioxane crystals.

As suggested in Sect. 3.6.1, TMDSC, detailed in Sect. 4.4, is a new and effective tool to analyze the nature of the melting/crystallization transition [34]. Figure 3.88 shows with quasi-isothermal measurements that melting/crystallization is largely irreversible for well-crystallized, extended-chain poly(oxyethylene) molecules of 5,000 molar mass. Such results are expected from Fig. 3.76. In the quasi-isothermal

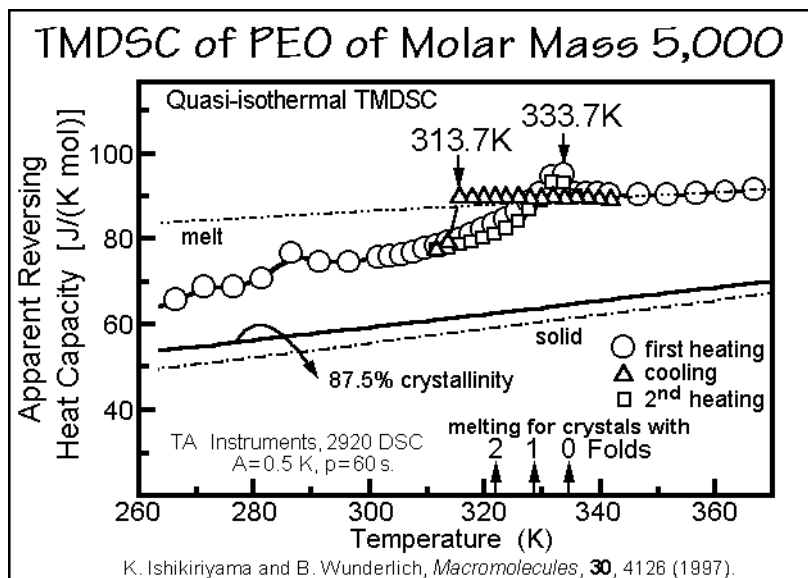


Fig. 3.88

experiments, the temperature is modulated with an amplitude,  $A$ , of  $\pm 0.5$  K at a series of constant base temperatures. Data are taken after steady state is reached. At steady state, melting has been completed and practically no heats of transition are seen. Only the apparent heat capacity indicates the increasing fusion or crystallization as the temperature is changed. The higher heat capacity measured relative to the expected value calculated for 87.5% crystallinity marked in the figure may be largely due to beginning conformational motion within the crystals, as described in Sect. 2.3.7. Figure 3.89 shows a comparison of the quasi-isothermal TMDSC with a standard DSC trace of the same sample which records both, the reversible and irreversible effects. A large difference in scale is necessary to display the full melting peak.

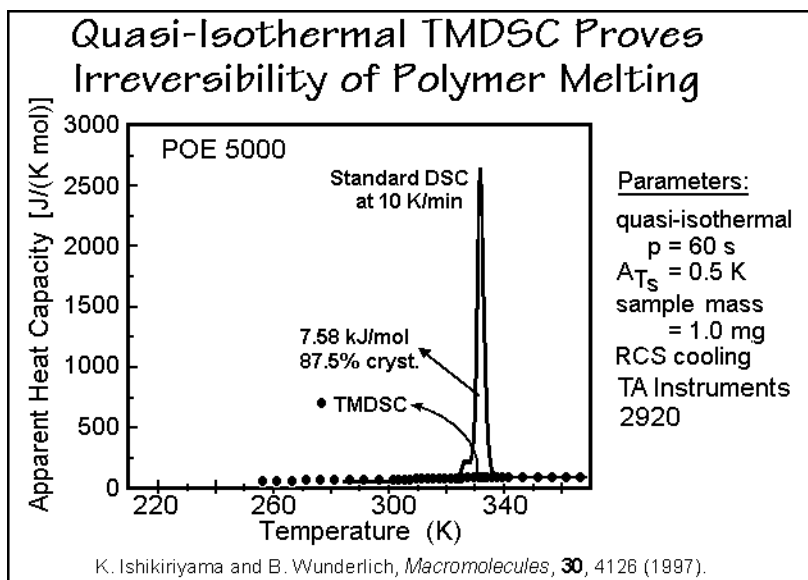


Fig. 3.89

Figure 3.90 shows a plot of the modulated temperature versus the heat-flow rate for a low-molar-mass poly(oxytetramethylene), POTM650, molar mass 650. The comparison to an identical measurement in the melt which shows no latent heat effects allows an analysis of the range of crystallization and melting. The crystallization and melting ranges join at point A. To the left and right of temperature A, some reversible melting is indicated with symmetrical rates, as expected from Fig. 3.76. A supercooling,  $\Delta T$ , of about 2.4 K can be seen due to primary nucleation (see Sects. 3.5.3–4). The broad melting and crystallization range is probably due to slow diffusion of the crystallizable species to and from the proper crystal and the reorganization (annealing) which may occur immediately after initial crystal growth.

Data on the supercooling of aliphatic polyoxides in Fig. 3.91 can be compared to the paraffin and polyethylene data used for the illustration of the limits of molecular nucleation in Fig. 3.75. In the same range of chain length all three polymers, polyethylene, PE, poly(oxyethylene), POE, and POTM, decrease in amount of supercooling due to molecular nucleation. The polyoxides, however, show a second

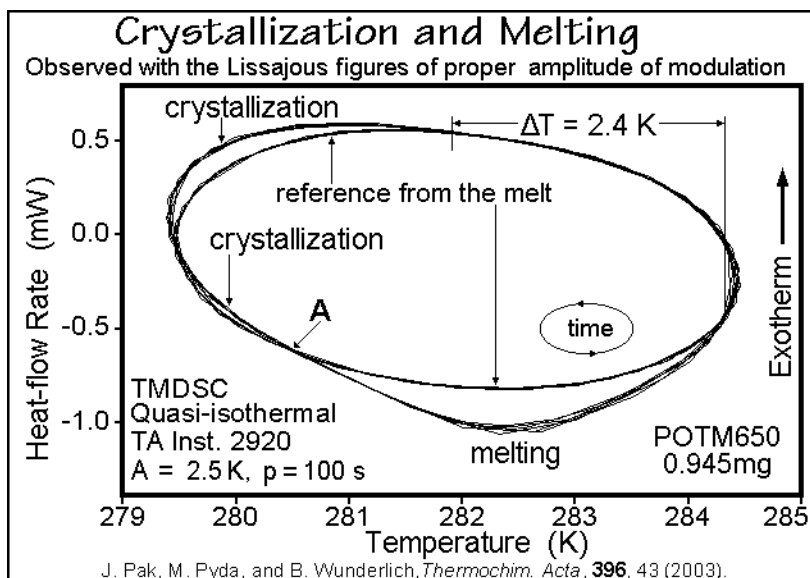


Fig. 3.90

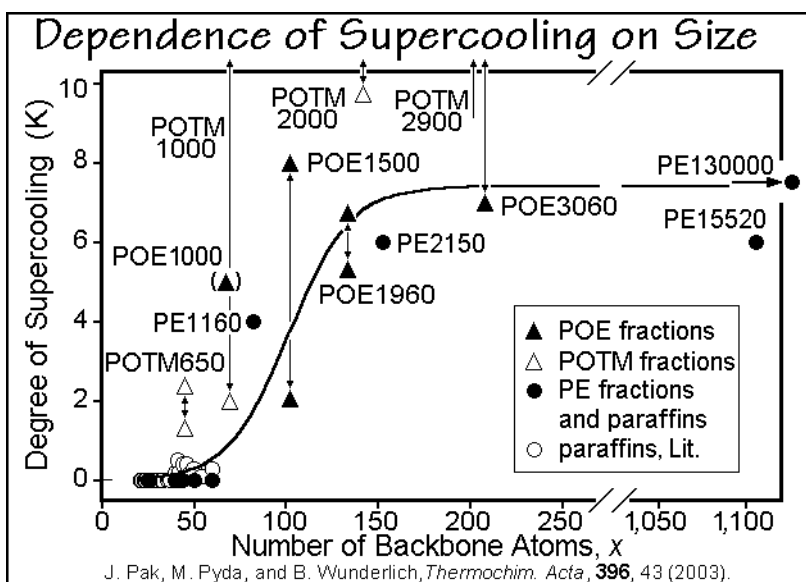


Fig. 3.91

series of higher supercooling which is due to primary nucleation seen in experiments where all crystals melt before cooling as illustrated in Fig. 3.90. The polyethylenes and paraffins do not need primary nucleation in typical crystallization experiments by DSC, so that only the lower values of supercooling show.

A similar comparison of DSC and quasi-isothermal TMDSC for poly(ethylene terephthalate) is given in Fig. 3.92. The reversible melting is substantial and seems to contradict the schematic of melting developed with Fig. 3.76. More will be said about this topic in Chaps. 4–7 in connection with the description of temperature modulation in the melting range. The picture that has developed from this thermal analysis is that the globally metastable, semicrystalline, and flexible polymers in their

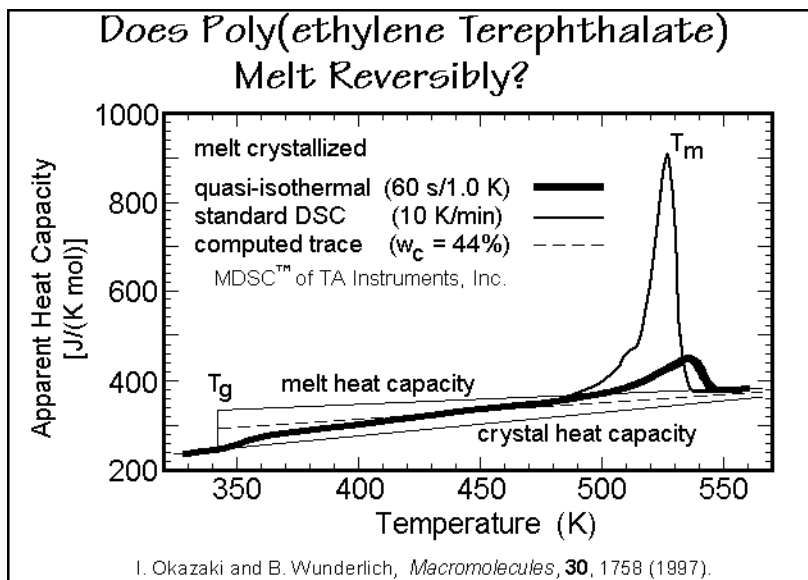


Fig. 3.92

chain-folded macroconformation have a nanophase structure which supports local equilibria [1]. A condition for such a picture is that the long molecules must have decoupled molecular segments at the phase boundary which can crystallize and melt independently of the rest of the molecule.

Thermal analysis experiments, which prove the existence of molecular segments which melt independently of the rest of the molecule, are shown in Fig. 3.93. A double melting peak is seen in the identical reference DSC traces 'a' after crystallization at 400 K. Next, the samples were extracted at different temperatures 'b' to 'd', cooled quickly, dried, and then analyzed by DSC again. The extractions should have removed all molecules that were above their dissolution temperature which changes with molar mass parallel to the melting temperature (see Fig. 3.73). The weights of material removed are listed in parentheses. At low temperature, only molecules of low molar mass are extracted and the corresponding low-temperature peak in 'a' has disappeared. On extractions 'c' and 'd', increasing amounts of unextractable segments are proven. These segments melt at lower temperature because of the poorer crystallization after extraction, compared to the melt crystallization at 400 K.

The melting and crystallization rates of oligomers and polymers were first measured by microscopy in the presence of remaining crystal, to eliminate nucleation effects. Figure 3.94 illustrates data for poly(oxyethylene) as a function of molar mass. On extrapolation to monomer dimensions, the metastability gap disappears and one

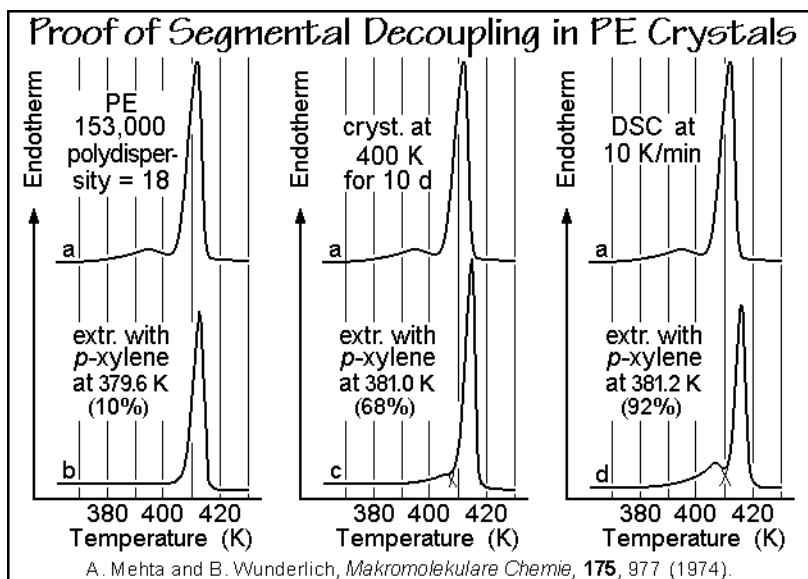


Fig. 3.93

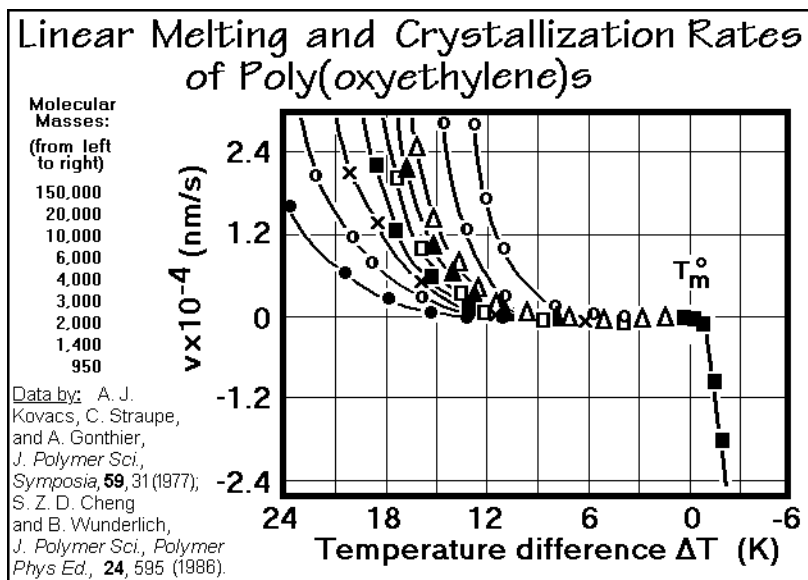
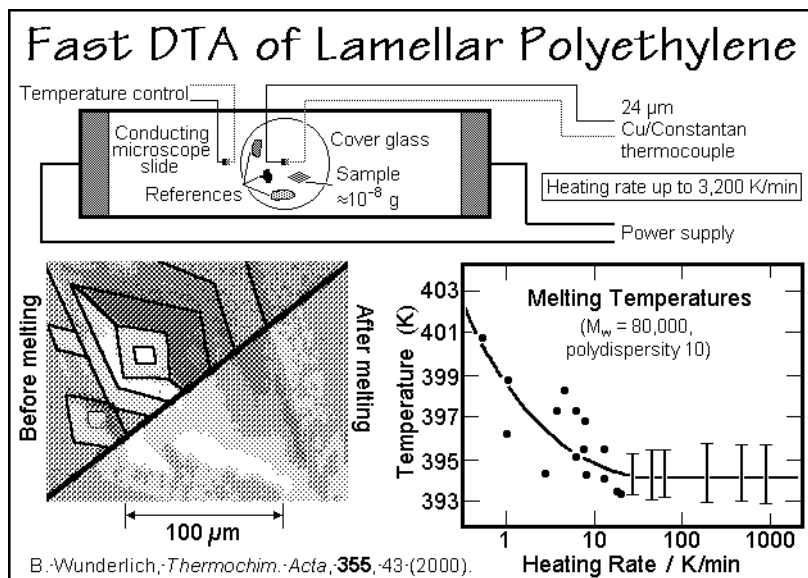


Fig. 3.94

reaches the same behavior as shown schematically in Fig. 3.76, and observed for crystals of small, rigid motifs and oligomers below the critical length of Fig. 3.91.

Fast optical microscopy can also be used for the study of reorganization during melting. Figure 3.95 illustrates an electrically-conducting, fast-heatable, tin-oxide-coated slide on which a folded-chain polyethylene growth spiral is deposited (left).

**Fig. 3.95**

On melting, it forms the droplet shown below the divide on the right. Plotting the temperatures of melting as a function of heating-rate gives the results of the graph at the bottom right. Only on heating faster than  $75 \text{ K min}^{-1}$ , the melting temperature is constant, signaling that then the crystals melt without reorganization, while on slower heating, they perfect and give a higher  $T_m$ . Although no quantitative reorganization rates were obtained, one can identify the zero-entropy-production case, where imperfect crystals melt without change in metastability (see Sects. 2.5 and 6.2).

A direct study of the melting of small regions has recently become available as a microcalorimeter, based on an atomic force microscope, AFM, as shown schematically in Fig. 3.96. For more details about the operating principle see also Appendix 10 (Fig. A.10.5). The platinum wire tip serves as a heater and simultaneously as a thermometer. Together with an identical reference tip it can serve as a DTA (see Sect. 4.3). At the same time the AFM can produce a topographical image. Figure 3.97 illustrates how it is possible to image the melting produced by setting the AFM tip at a preselected point of a growth spiral of solution-grown polyethylene and heating to melt. Further development of this special instrumentation may give direct information on the thermal behavior of microphase and nanophase structures as was proposed in a general discussion of modern thermal analysis [35].

A quantitative, isothermal measurement of the crystallization kinetics, usable for analysis by the Avrami method, is illustrated in Fig. 3.98 by the upper left curve. Similar curves can be generated by dilatometry or adiabatic calorimetry as described in Sects. 4.1 and 4.2. At time zero, one assumes that the isothermal condition has been reached. The dotted segments of the heat-flow response are then proportional to the heat of crystallization evolved in the given time intervals and can be converted directly into the changes of the mass fraction of crystallinity after calibration or normalization to the total heat evolved. An independent crystallinity determination



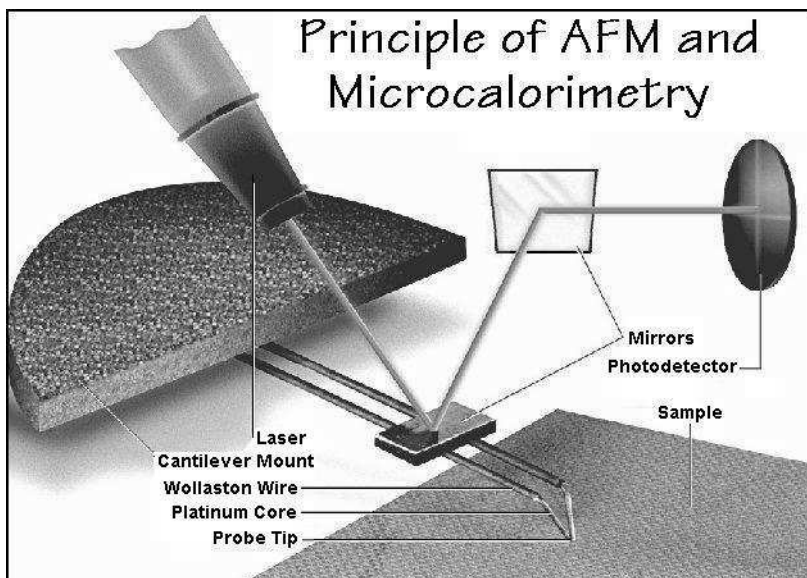


Fig. 3.96

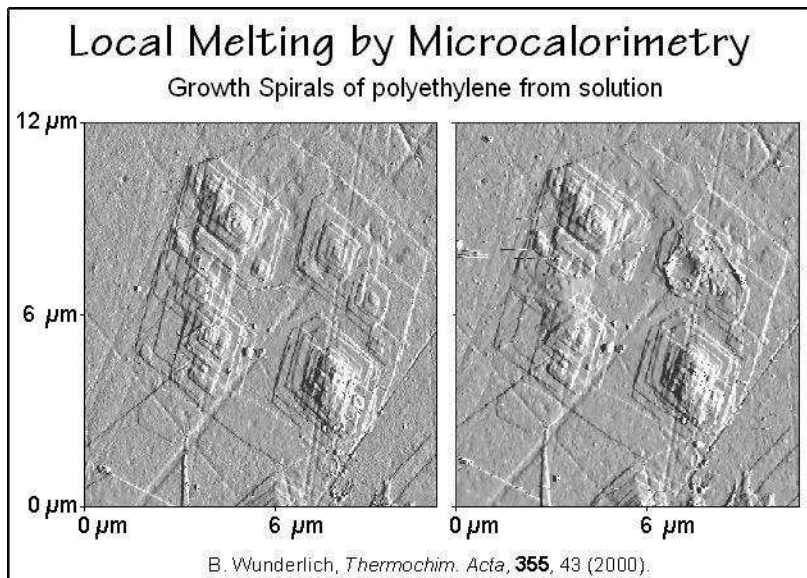


Fig. 3.97

is possible for the completely crystallized sample. A detailed development of the calculation of crystallinity from DSC data is given in Sect. 4.4.7.

The curves in the lower right of Fig. 3.98 illustrate a point-by-point determination of not only the crystallinity, but also the nature of the crystallization as a function of time. The example polymer is a poly(oxy-1,4-phenylene-oxy-1,4-phenylene carbonyl-1,4-phenylene) or simply poly(ether ether ketone), PEEK. After the given time at the

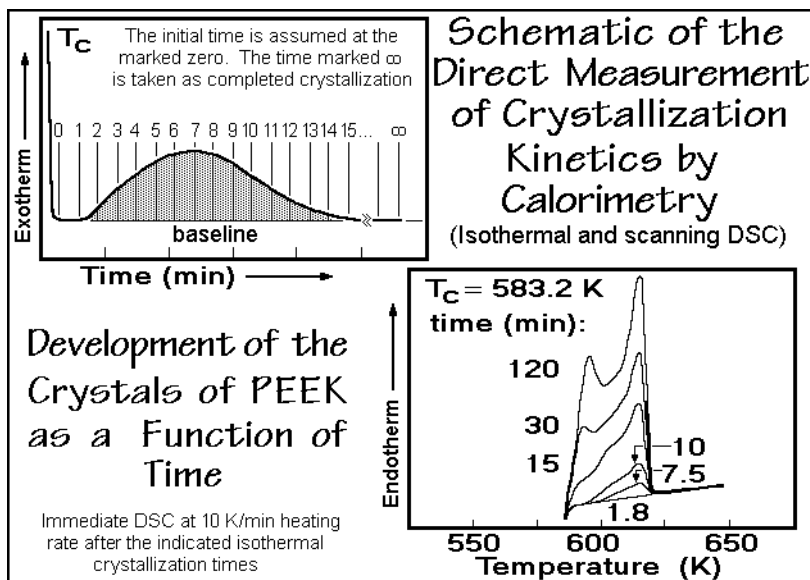


Fig. 3.98

crystallization temperature, the sample is heated directly under DSC conditions and the heat of fusion is used for crystallinity evaluation. The changing curve-shape indicates that reorganization is possible at the crystallization temperature. The initial crystals have a melting temperature of about 600 K, but increase quickly in perfection. Only after about 10 min does a secondary crystallization of poorer crystals develop with a peak which moves to a higher  $T_m$  with time.

Data on the development of crystallinity, obtained by adiabatic calorimetry are depicted in Fig. 3.99. Note, that for the Avrami analysis the crystallinity must be calculated in volume fraction,  $v_c$ , while the heat of fusion is usually expressed in weight-fraction,  $w_c$ , as displayed in Figs. 3.84 and derived in Fig. 5.80, respectively. The correlation between the two crystallinities is given by:

$$v_c = \frac{\rho - \rho_a}{\rho_c - \rho_a} = w_c \frac{\rho}{\rho_c}$$

where  $\rho$ ,  $\rho_a$ , and  $\rho_c$  are the densities of the sample, amorphous phase, and crystal. Since copolymers do not crystallize completely, one normalizes the data, as shown in the right graph of Fig. 3.99. This normalization corresponds to the assumption that the spherulites are of the same low crystallinity throughout their volume, and the space between the spherulites is filled with pure amorphous phase. This is a postulate that must be verified, for example by electron microscopy and X-ray diffraction. Especially later crystallization stages may involve new growth within the lamellar stacks of the spherulite or creation of whole new stacks changing the structure [36].

From the slope on the right graph of Fig. 99 an Avrami exponent of 3.2 results, close to the value expected for athermal nucleation followed by spherulitic growth, but because of the many assumptions that went into the derivation of the Avrami equation still not proven without a detailed structural analysis.

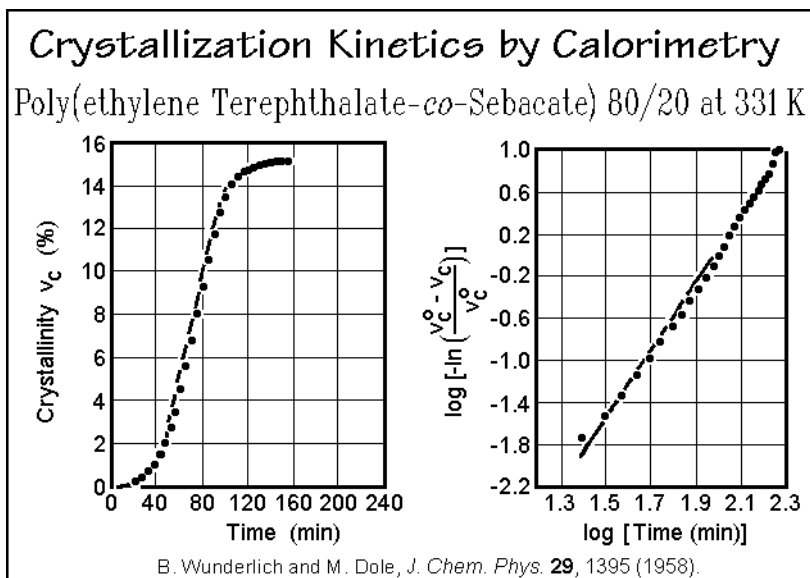


Fig. 3.99

Results from extensive dilatometric measurements of the crystallization of polyethylene from the melt are shown in Fig. 3.100. Without normalization, the data for different molar masses are first matched to Avrami curves of different exponents. Higher molar masses seem to fit better to lower exponents, but deviate earlier from the calculated curves. At later times the crystallization is not described by the Avrami expression. It is then governed by secondary crystallization within the spherulites.

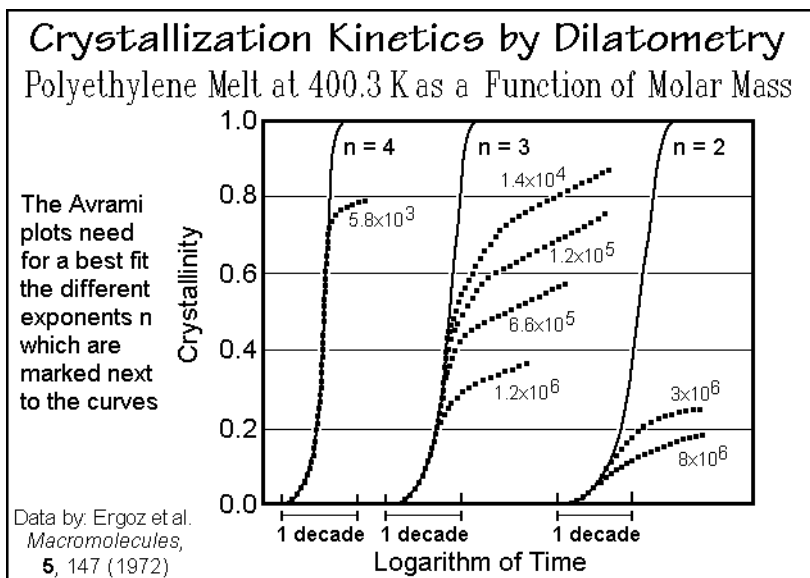
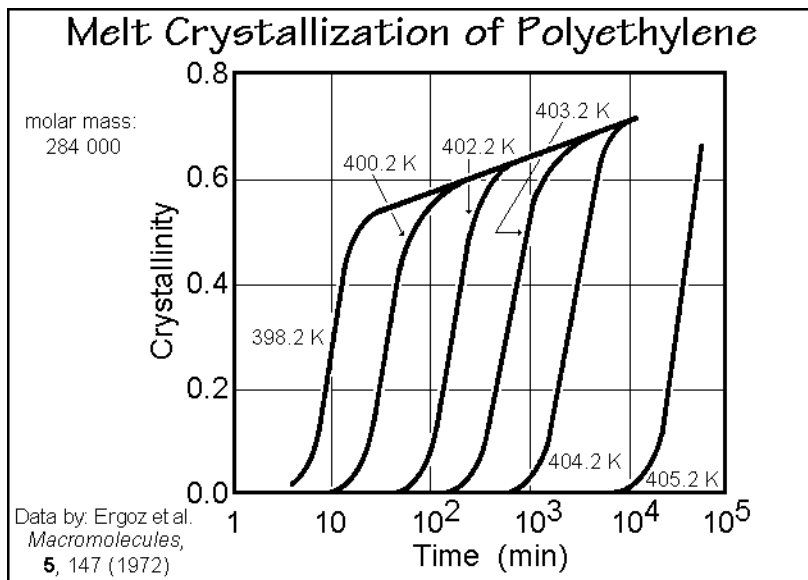


Fig. 3.100

It is interesting to note that the deviations from the Avrami expression occur at a level that is given by the limit of applicability of the free growth approximation in Fig. 3.55. Similar data for a single molar mass, but at different temperatures, are shown in Fig. 3.101. All crystallizations seem to approach a common limit, but deviate at different temperatures from the Avrami equation.

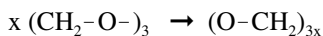


**Fig. 3.101**

Linear growth rates for polyethylene gained from microscopy are shown in Fig. 3.102. The break in the curve is attributed to a change in the secondary or molecular nucleation mechanism. At low temperature, one assumes multiple nucleations to occur during the growth of a given patch on the surface (regime 2), while at high temperature, nucleation occurs only once for the same patch (regime 1) [37]. The observed slopes correspond to the expected changes in growth-rate, the absolute values, however, do not [38].

Dilatometric data by measurement of stress decay on fibers are shown in Fig. 3.103 for extension ratios  $\alpha$  from one (no extension) to six. Besides the increase in rate of crystallization on stretching, one finds a decrease of the Avrami exponents from 3.5 to 1.3 with increasing extension ratio. The nature of the crystal morphology is changing from spherulitic to fibrillar as  $\alpha$  increases.

A final crystallization mechanism concerns, as in the earlier described  $\text{LiPO}_3$  case, crystallization coupled with polymerization. The example is the change of trioxane rings to poly(oxymethylene) chains within single crystals of the cyclic monomer trioxane:



Electron microscopy permitted the detailed study of this process. Figure 3.104 illustrates the dynamics of the polymerization. Note that the density of the growing

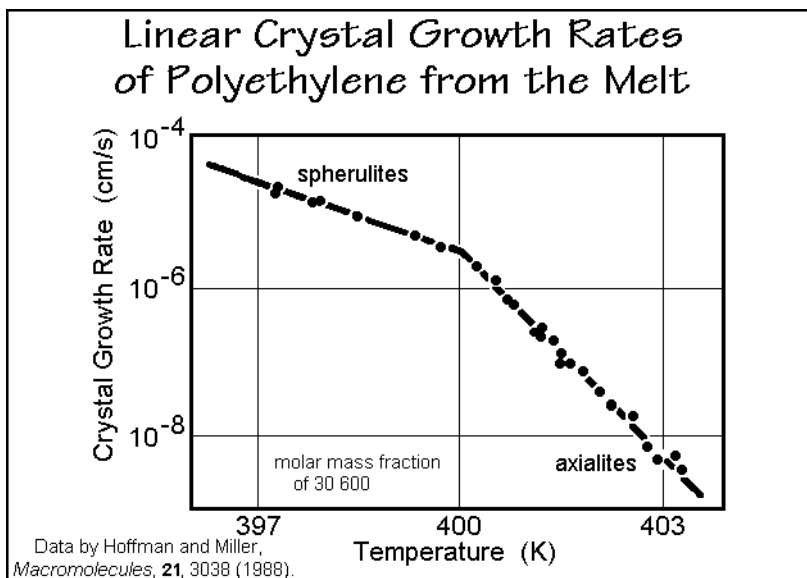


Fig. 3.102

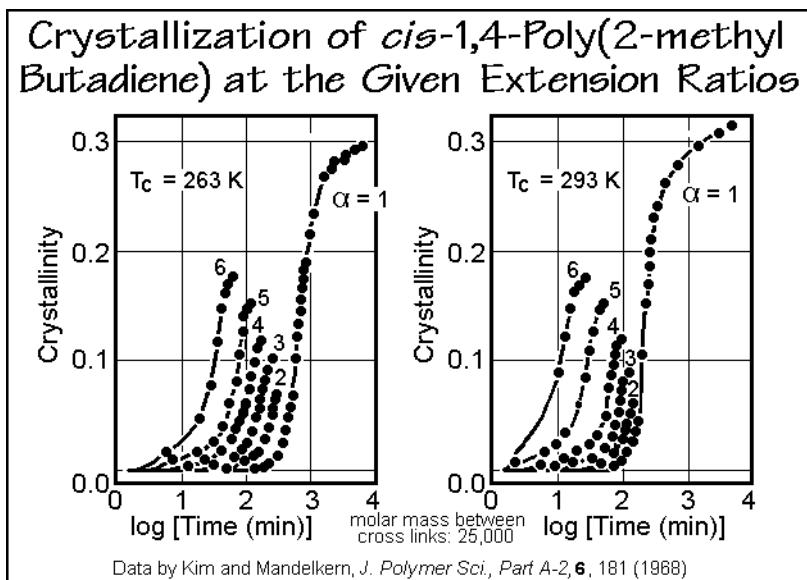


Fig. 3.103

polymer within the trioxane crystal is larger than the monomer. As a result, cavities are produced, which permit easy mass transport to the growing chain end. Once nucleated, the fibrillar polymer crystals may grow to the end of the monomer crystal. The nucleation was achieved at liquid nitrogen temperature by irradiation with X-rays. At this temperature further chemical reaction does not occur. On warming to 323 K,

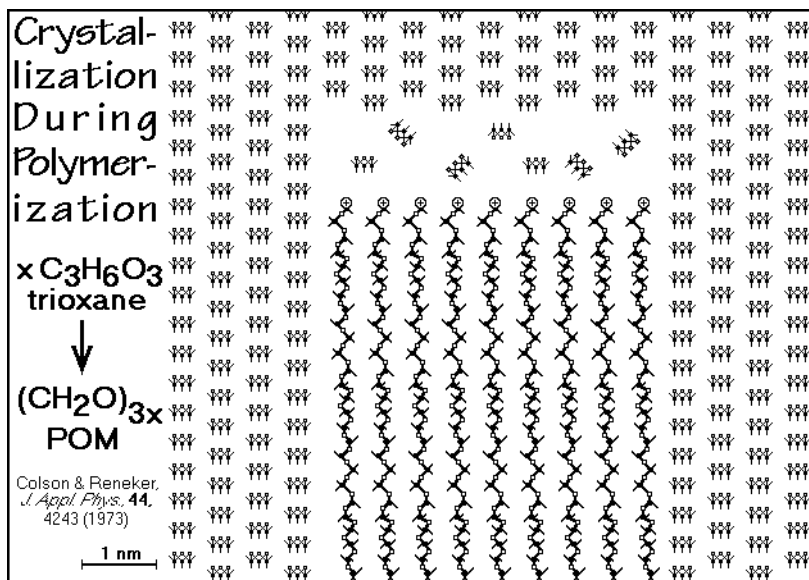


Fig. 3.104

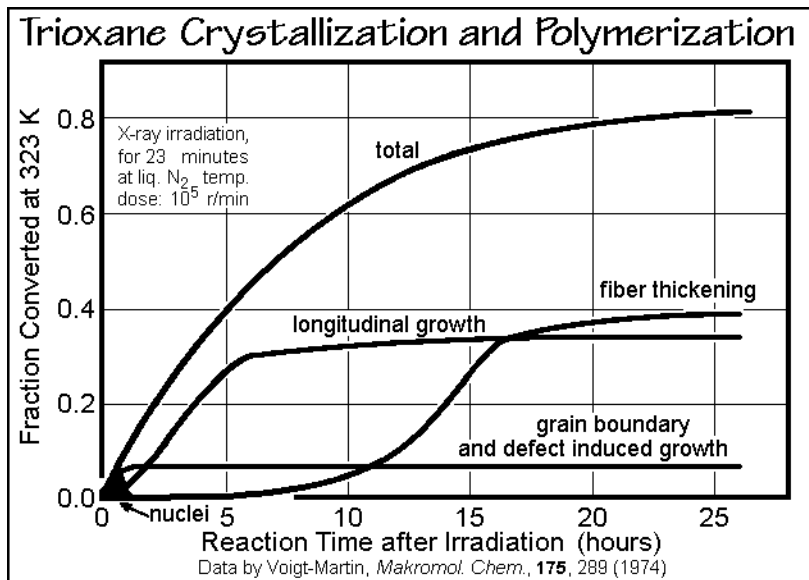


Fig. 3.105

it demonstrates the special nature of flexible macromolecules. Finally, the nucleation process was shown to be of importance for the initiation of a crystal, as well as the addition of a new macromolecule to a crystal when accepting the concept of molecular nucleation. This summary of data demonstrates the utility of the various forms of thermal analysis for the analysis of the crystallization and melting of polymers.

## References

### General References

**Sect. 3.1–3.** For general texts on the chemistry of synthesis of polymers see: Lenz RW (1967) *Organic Chemical Synthesis of High Polymers*. Interscience, New York; Odian G (1991) *Principles of Polymerization*. Wiley, New York, 3<sup>rd</sup> edn; Saunders JK (1973) *Organic Polymer Chemistry*. Chapman and Hall, London; Allcock H R, Lampe FW (1980) *Contemporary Polymer Chemistry*. Prentice-Hall, Englewood Cliffs; Rempp P, Merrill EW (1990) *Polymer Synthesis*. Hüthig and Wepf, Heidelberg. Also, use your introductory polymer science texts and the reference books listed in the General References in the Preface.

Specific books on reaction kinetics of small molecules are: Gardiner WC (1969) *Rates and Mechanics of Chemical Reactions*. Benjamin, New York; Bamford CH, Tipper CF (1969–1986) *Comprehensive Chemical Kinetics*, Vols 1–26. Elsevier, Amsterdam; Laidler KL, Keith J (1987) *Chemical Kinetics*, 3<sup>rd</sup> edn. Harper and Row, New York.

The problems of interaction of crystallization and polymerization of Sect. 3.2.2 are reviewed in Wunderlich B (1976) *Macromolecular Physics*, Vol 2, Crystal Nucleation, Growth, Annealing. Academic Press, New York, Chap VI.

The matrix control is treated, for example, in: Ingram, VM (1965) *The Biosyntheses of Macromolecules*. Benjamin, New York; and information on ribonuclease can be found in: Spakman DH, Stein WH, Moore S (1960) *J Biol Chem* 235: 648.

Specific sources on molecular mass distributions are: Flory PJ (1953) *Principles of Polymer Chemistry*, Chaps 3, 8 and 9. Cornell University Press, Ithaca; Peebles LH (1971) *Molecular Weight Distributions in Polymers*. Wiley-Interscience, New York. The problem of ring formation is treated by: Jacobson H, Stockmeyer WH (1950) *Intramolecular Reaction in Polycondensation*. I. The Theory of Linear Systems. *J Chem Phys* 18: 1600–1606; and Jacobson H, Beckmann CO, Stockmeyer WH (1950) , II. Ring-chain Equilibria in Polydecamethylene Adipate. *J Chem Phys* 18: 1607–1612.

More recent experiments proving the presence of very large rings in step reactions and a discussion of the role of ring formation in step polymerization are summarized by: Kricheldorf HR (2003) *The Role of Ring-ring Equilibria in Thermodynamically Controlled Polycondensation*, *Macromol Symp* 199: 15–22; see also other papers in the same issue and the introduction: *What Does Polycondensation Mean?* *Ibid* pp 1–13.

The recently developed living polymerization in polycondensation is reviewed by: Yokozawa T, Yokoyama A (2004) *Chain-growth Polycondensation: Living Polymerization Nature in Polycondensation and Approach to Condensation Polymer Architecture*. *Polymer J (Japan)* 36: 65–83 (in English). Examples are found for polyamides (2000) *J Am Chem Soc* 122: 8313–2314. Polyesters: (2003) *Macromolecules* 36: 4328–4336. Polyethers (2001) *J Am Chem Soc* 123: 9902–9903. Polythiophenes (2004) *Macromolecules* 37: 1169–1171. Several block copolymers can be found in the publications (2002) *J Am Chem Soc* 124: 15158–15159; and (2003) *J Polymer Sci, Part A: Polymer Chem* 41: 1341–1346.

Use your basic reference books on mathematics and vector analysis to support the reading on molar mass distributions. Some examples are the (1960–) *International Dictionary of Applied Mathematics*. Van Nostrand, Princeton, NJ; Feller W (1950–) *An Introduction to Probability Theory and Its Applications*. Wiley, New York; Mood AM (1950) *Introduction to the Theory of Statistics*. McGraw-Hill, New York; Hamming RW (1962–) *Numerical Methods for Scientists and Engineers*. Dover, New York.

**Sect. 3.4.** The references are to be supplemented with those listed for Sects. 3.1–3. Check there for examples of many polymer reactions.

More information on copolymerization is available through: Ham GE, ed (1964) *Copolymerization*. Wiley-Interscience, New York; Nashay A, McGrath JE (1977) *Block*

Copolymers: Overview and Critical Survey. Academic Press, New York; Cowie JMG, ed (1985) Alternating Copolymerization. Plenum Press, New York.

Three specific sources for information on pyrolysis are: Madorsky SL (1964) Thermal Degradation of Organic Polymers. Wiley-Interscience, New York; Kelen T (1983) Polymer Degradation. Van Nostrand-Reinhold, New York; Halim HS, ed (2000) Handbook of Polymer Degradation, 2<sup>nd</sup> edn. Dekker, New York.

For polymer reactions, see: Carraher, Jr. CE, Moore JA, eds (1983) Chemical Reactions on Polymers. American Chem. Soc. Symposium Series, Plenum Press, New York; Hodge P, Sherrington DC, eds (1980) Polymer-supported Reactions in Organic Synthesis. Wiley-Interscience, New York.

**Sect. 3.5 and 6.** The lecture follows closely the ideas which are described in much greater detail in: Wunderlich B (1976 and 1980), Macromolecular Physics, Vol. 2, Crystal Nucleation, Growth, Annealing, and Vol. 3, Crystal Melting. Academic Press, New York.

Some more specific articles on unsolved problems in polymer crystallization can be found in the proceedings of three international discussion meetings: (1979) Special issue of the Farad Disc Chem Soc 68; Dosi  re M, ed (1993) Crystallization of Polymers. NATO ASI Series, C, Vol 405, Kluwer Academic Publishers, Dordrecht, Netherlands; (2002) Proceedings of the International Symposium on Polymer Crystallization in Mishima, Japan, June 9–12, partially published (2003) Journal of Macromolecular Science, Physics Ed, vol B42.

Additional sources for information on crystallization and nucleation are: Hoffman JD, Davies GT, Lauritzen, Jr. JI (1976) The Rate of Crystallization of Linear Polymers with Chain Folding. In Hannay, NB, Treatise on Solid State Chemistry. Plenum, New York; Mark JE, Eisenberg A, Graessley WW, Mandelkern, L, Samulski, ET, Koenig, JL, Wignall, GD (1993) Physical Properties of Polymers, 2<sup>nd</sup> ed. ACS Washington DC. Also, look up the Polymer Handbook, and the Enc Polymer Sci and Eng listed in the Preface.

### Specific References

1. Wunderlich B (1968) Crystallization During Polymerization. Fortschr Hochpolymeren Forsch (Adv Polymer Sci) 5: 568–619.
2. Stuart JM, Young JD (1969) Solid Phase Peptide Synthesis. Freeman, San Francisco.
3. Atherton R, Sheppard RC (1989) Solid Phase Peptide Synthesis: A Practical Approach. IRL Press, Oxford.
4. Rothe M, Dunkel W (1967) Linear Cyclic Oligomers. XXIII. Synthesis of Monodisperse Oligomers of  $\epsilon$ -Aminocaproic Acid up to a Degree of Polymerization of 25 by the Merrifield Method. J Polymer Sci, Letters 5: 589–593.
5. Heitz W, Wirth Th, Peters W, Strobl G, Fischer EW (1972) Synthesis and Properties of Monodisperse *n*-Paraffins up to  $C_{140}H_{282}$ . Macromol Chem 162: 63–79.
6. Bidd I, Whiting, MC (1985) The Synthesis of Pure *n*-Paraffins with Chain-lengths between One and Four Hundred. J Chem Soc, Chem Comm 9: 543–44.
7. Dr  scher M, Wegner G (1978) Poly(ethylene Terephthalate). A Solid State Condensation Process. Polymer 19: 43–47.
8. Kovacs AJ, Buckley CP (1975,1976) Melting Behavior of Low Molecular Weight Poly(ethylene oxide). I Extended Chain Crystals. Prog Colloid Polymer Sci 58: 44–52; II. Folded Chain Crystals, Colloid Polymer Sci 254: 695–715.
9. Keller A, Udagawa Y (1970) Preparation of Long-chain Paraffins from Nitric Acid Degradation Products of Polyethylene; Consequences for Polymer Crystal Studies. J. Polymer Sci., Part A2, 8: 19–34.
10. Battista OA (1975) Microcrystal Polymer Science. McGraw-Hill, New York.
11. Ungar G, Stejny J, Keller A, Bidd I Whiting MC (1985) The Crystallization of Ultralong Paraffins: The Onset of Chain Folding. Science 229: 386–389.
12. O’Gara JE, Wagener KB, Hahn SF (1993) Acyclic Diene Metathesis (ADMET) Polymerization. Synthesis of Perfectly Linear Polyethylene. Makromol Chem Rapid Commun 14: 657–662.
13. Smith JA, Brzezinska KR, Valenti DJ, Wagener KB (2000) Precisely Controlled Methyl Branching in Polyethylene via Acyclic Diene Metathesis (ADMET) Polymerization. Macromolecules 33: 3781–3784.
14. Benkhoucha R, Wunderlich B (1978) Crystallization During Polymerization of Lithium Dihydrogen Phosphate. Part I. Nucleation of the Macromolecular Crystal from the



- Oligomer Melt. Part II. Crystal Growth by Dimer Addition. *Z allgem anorg Chem* 444: 256–276.
15. Benkhoucha R, Wunderlich CC, Wunderlich B (1979) Melting and Crystallization of a Polyphosphate. *J Polymer Sci, Polymer Phys Ed*, 17: 2151–2162.
  16. Ewen JA, Jones RL, Razawi AJ, Ferrara JD (1988) Syndiospecific Propylene Polymerization with Group IVB Metallocenes *J Am Chem Soc* 110: 6255–6256.
  17. Coates GW (2000) Precise Control of Polyolefin Stereochemistry Using Single-site Metal Catalysts. *Chem Rev* 100: 1223–1252.
  18. Boor J, Jr (1979) *Ziegler-Natta Catalysts and Polymerization*. Academic Press, New York.
  19. Szwarc M (1968) Carbanions, Living Polymers, and Electron Transfer Processes. Interscience, New York; see also: (1983) *Living Polymers and Mechanisms of Anionic Polymerization*. *Adv Polymer Sci* 49: 1–175.
  20. Bianchi JP, Price FP, Zimm BH (1957) Monodisperse Polystyrene. *J Polymer Sci* 26: 27–38.
  21. van Krevelen DW ed (1997) *Properties of Polymers: Their Correlation with Chemical Structure; Their Numerical Estimation and Prediction from Additive Group Contributions*, 3<sup>rd</sup> edn. Elsevier, Amsterdam.
  22. Wasserman PD (1989) *Neural Computing*. Van Nostrand-Reinhold, New York
  23. Hect-Nielson R (1990) *Neurocomputing*. Addison-Wiley, New York.
  24. Sumpter BG, Noid DW (1996) On the Design, Analysis, and Characterization of Materials Using Computational Neural Networks. *Ann Rev Mater Sci* 26: 223–277.
  25. Turnbull D, Fisher JC (1949) Rate of Nucleation in Condensed Systems. *J Chem Phys* 17: 71–73.
  26. Keller A, Willmouth FM (1970) Self-seeded Crystallization and its Potential for Molecular Weight Characterization. I. Experimentation on Broad Distributions. *J. Polymer Sci, Part A2* 8: 1443–1456.
  27. Armistead K, Goldbeck-Wood G (1992) Polymer Crystallization Theories. *Adv Polymer Sci Vol* 100: 219–312.
  28. Photograph, courtesy of Kovacs A (1973).
  29. Wunderlich B, Mehta A (1974) Macromolecular Nucleation. *J Polymer Sci, Polymer Phys Ed* 12: 255–263.
  30. Mehta A, Wunderlich B (1975) A Study of Molecular Fractionation during the Crystallization of Polymers. *Colloid and Polymer Sci* 253: 193–205.
  31. Hellmuth E, Wunderlich B (1965) Superheating of Linear High-Polymer Polyethylene Crystals. *J Appl Phys* 36: 3039–3044.
  32. Bassett DC (2003) Polymer Spherulites: A Modern Assessment. *J Macromol Sci, Physics B42*: 227–256.
  33. Freeman ES, Carroll B (1958) The Application of Thermoanalytical Techniques to Reaction Kinetics. The Thermogravimetric Evaluation of the Decomposition of Calcium Oxalate Monohydrate. *J Chem Phys* 62: 394–397.
  34. The results on reversible crystallization and melting are reviewed in: Wunderlich B (2003) Reversible Crystallization and the Rigid Amorphous Phase in Semicrystalline Macromolecules. *Progress in Polymer Science* 28/3: 383–450.
  35. Wunderlich B (2000) Temperature-modulated Calorimetry in the 21<sup>st</sup> Century. *Thermochim Acta* 355: 43–57.
  36. Zachman HG, Wutz, C (1993) Studies of the Mechanism of Crystallization by Means of WAXS and SAXS Employing Synchrotron Radiation, in Dosi re M, ed. *Crystallization of Polymers*. NATO ASI Series, C, Vol 405, Kluwer Academic Publishers, Dordrecht, Netherlands pp 403–414.
  37. Armistead JP, Hoffman JD (2002) Direct Evidence of Regimes I, II, and III in Linear Polyethylene Fractions as Revealed by Spherulitic Growth Rates. *Macromolecules* 35: 3895–3913.
  38. Point JJ, Janimak JJ (1993) An Evaluation of the Theories of Regimes of Nucleation Controlled Crystal Growth as Applied to Polymers. *J Cryst Growth* 131: 502–517.

## **Thermal Analysis Tools**

All basic techniques of thermal analysis treated in this chapter are already mentioned in Sect. 2.1.3, together with a number of further, less basic techniques. The thermal analysis tools are grouped according to the variables they are designed to determine, as is summarized in Fig. 2.4. The International Confederation for Thermal Analysis and Calorimetry, ICTAC, and the regional North American Thermal Analysis Society, NATAS, are the scientific organizations concerned with this field of science (see Figs. 2.5 and 6) and their proceedings contain a continuous record of thermal analysis [1,2]. Thermometry and dilatometry are treated in Sect. 4.1. They are the techniques most prominently represented by the mercury-in-glass thermometer, shown in Fig. 2.7 and the measurement of length, shown in Fig. 4.12, below. Section 4.2 contains a general description of calorimetry. Thermometry can be coupled, next, with the measurement of time by taking heating and cooling curves as seen, for example, in Fig. 4.9, below, and Fig. 1.67. These simple thermal analyses are the forerunners of DTA and DSC, popular techniques of thermal analysis, treated in Sects. 4.3 and 4.4. The measurement of length leads in Sect. 4.5 under conditions of changing temperature and a fixed force is thermomechanical analysis, TMA, which on adding force modulation leads to dynamic mechanical analysis, DMA. Also treated in Sect. 4.5 is DETA. Section 4.6 deals, finally, with measurement of mass with changing temperature and time.

### **4.1 Thermometry and Dilatometry**

#### **4.1.1. Principle and History of Thermometry**

The most common method of temperature measurement is contact thermometry, as demonstrated in Fig. 4.1. One brings a thermometer, C, a system with a known thermal property, into intimate contact with the to be measured system, A. Next, thermal equilibration is awaited. When reached, the temperatures of A and C are equal. The use of C as a contact thermometer is based on the fact that if the two systems A and B are in thermal equilibrium with C they must also be in thermal equilibrium with each other. This statement is sometimes called the zeroth law of thermodynamics. It permits to use B with a known temperature to calibrate C, and then use C for measurement of the temperature of system A. A calibration with B can be made at a fixed temperature of a phase transition without degree of freedom, as given by the phase rule of Sect. 2.5.7. Less common are methods of temperature measurement without a separate thermometer system. They make use of the sample itself. For example, the temperature of the sample can be determined from its length, the speed of sound within the sample, or the frequency of light emitted.

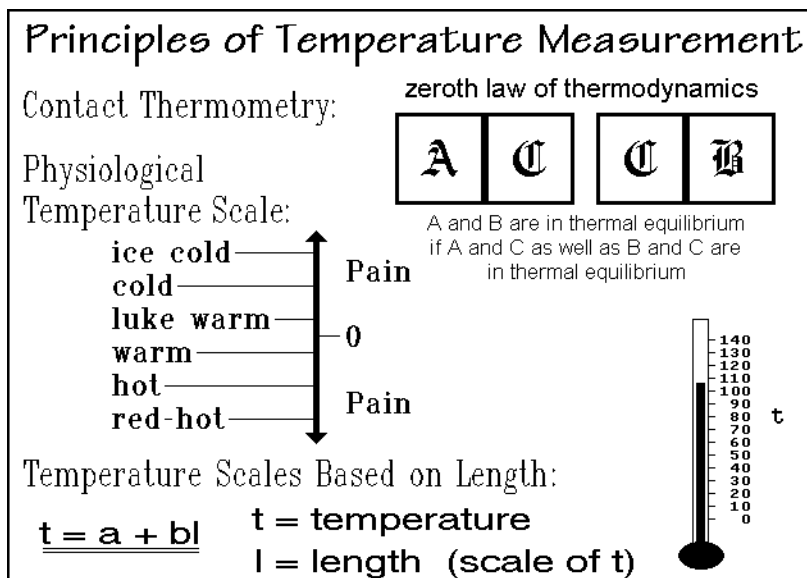


Fig. 4.1

Everyone is born with the ability to recognize temperature by contact through the degree of pain. No pain feels comfortable. This is the zero of the physiological temperature scale of Fig. 4.1. Cold and ice-cold show increasing degrees of pain in one direction, warm, hot, and red-hot, in the other. This temperature scale is, however, not very precise and has, in addition, no direction: It is impossible to distinguish pain caused by low temperature from pain caused by high temperature.

The first accurate temperature measurements were made in the 17<sup>th</sup> century in Florence, Italy. The thermometers capable of such precision measurement consisted of a partially liquid-filled, closed capillary and bulb, as indicated in the sketch in the lower right of Fig. 4.1. The change in length of the liquid thread in the capillary is proportional to the change in temperature. The equation in the figure gives a linear scale of temperature in terms of length. The constants  $a$  and  $b$  must be determined by calibration with systems B. All other temperatures are then given by interpolation.

Further historical development of thermometry was seen during the 18<sup>th</sup> century with the invention of various temperature scales. In principle, one can choose any function of length for a definition of temperature, but certainly, one wants to make it as easy as possible, and transferable from one thermometer type to another. The first significant suggestion for a temperature scale was made by Newton<sup>1</sup>. He said, the freezing point of water should be given the temperature zero degrees and body temperature should be 12 degrees higher. The interval of 12 degrees was thought to be useful because it can easily be subdivided into whole parts.

<sup>1</sup> Sir Isaac Newton, 1642–1727, English physicist and mathematician at Cambridge University 1669–1701, the central figure of the scientific revolution of the 17<sup>th</sup> century. Most well known for his exploration of light (*Opticks*, 1704), forces, gravity and motion (*Philosophiae Naturalis Principia Mathematica*, 1687), and mathematics (*Arithmetica Universalis*, 1707).

The next important scale was developed in 1714 by Fahrenheit<sup>1</sup>. He found freezing of pure water difficult to reproduce. The water frequently becomes undercooled. A saturated solution of a salt, such as  $\text{NH}_4\text{Cl}$ , has much more constant freezing temperature. So, Fahrenheit chose this lower temperature as his zero. He then chose body temperature to be  $96^\circ$ , which resulted in a more convenient, eight times finer division than proposed by Newton. Fahrenheit was a famous instrument maker and also introduced mercury as a liquid with reproducible, simple thermal properties. On further experimentation with the freezing of ice, he found that if the water was seeded with crystals, the freezing point was reproducible. So it was not very much later that Fahrenheit's scale was actually based on the freezing of water. At the same time, the upper value of the scale was also changed, namely to the boiling point of water, a more reproducible fixed point than body temperature. Since the old scale had already been adopted, the freezing point of water was given the value  $32^\circ$  and the boiling point of water the value  $212^\circ$ , giving the well-known scale with a fundamental interval of  $180^\circ\text{F}$ . The scale found wide acceptance, especially in English-speaking countries. The advantage of the Fahrenheit scale is its convenient subdivision for the description of the weather, the feel of water for washing and bathing, in cooking and baking, refrigeration, and for the evaluation of the body temperature, the most important uses of thermometry in daily life. We still like to give weather information in Fahrenheit's degrees because the scale is fine enough that there is no need of any decimals, and also because the values of negative temperatures are not very important, they just signify extreme cold.

Another scale was developed in France by Réaumur in 1730. It was based on experiments that showed the even expansion of an 80/20 wt-% mixture of water and ethyl alcohol. Réaumur found that this mixture expands exactly 80 parts per thousand between the ice and steam points. Thus, he invented the scale which showed the freezing of water at zero and boiling  $80^\circ$ .

A fourth scale was developed in 1742 by Celsius<sup>2</sup>. He chose the freezing of water as  $0^\circ$  and boiling as  $100^\circ$ . The celsius scale, finally won out among the over 30 empirical temperature scales because of the general change to the decimal system. For many years now, it has been accepted internationally as the mercury-in-glass scale of temperature, designated as  $^\circ\text{C}$ . Today it is also part of the International Temperature Scale, ITS 1990 [3], described in Appendix 8, the most precise empirical temperature scale. The sometimes used name of centigrade is not internationally recognized and should be avoided, just as the term micron for micrometer or the abbreviation cc for  $\text{cm}^3$  are not accepted.

All empirical Hg-based temperature scales have limitations. First, they are only usable within the range where mercury is liquid, from a low temperature of  $-39^\circ\text{C}$  to

---

<sup>1</sup> Daniel Gabriel Fahrenheit, 1686–1736, German physicist and instrument maker, best known for inventing the mercury-in-glass thermometer (1714) and developing the Fahrenheit temperature scale. Born in Danzig, Pol. Gdansk, he spent most of his life in the Netherlands.

<sup>2</sup> Anders Celsius, 1701–1744, Professor of astronomy at the University of Uppsala, Sweden. In 1742 he described his thermometer in a paper read before the Swedish Academy of Sciences.

a high of 356.6°C. Some extension of this range is possible by alloying with a solute to decrease the melting temperature, and by increasing the pressure above the liquid to increase the boiling temperature. Even more serious, however, is the fact that this temperature is based on the specific differential properties of mercury and glass. One cannot expect to get, in this manner, simple relationships between temperature and fundamental properties for other materials.

In Fig. 4.2 the progress to modern temperature scales as made in the 19<sup>th</sup> century is reviewed. The development began when quantitative experiments were made on the expansivity,  $\alpha$ , of gases as discussed together with the ideal gas law in Fig. 2.8. Gases were found by Gay-Lussac<sup>1</sup> to expand linearly with temperature when measured with a mercury-in-glass thermometer. All gases, when extrapolated to sufficiently low pressure, follow the same relationship and have the same value for the expansivity. With this knowledge one can define the gas temperature,  $T$ , as indicated. The gas temperature is limited only by the availability of gases. At very low temperatures, about 3–4 K, only very dilute gases are available, and at very high temperatures, such as above 5,000 K, there exist no containers which can hold the gases for measurement. Otherwise, no specific materials' properties are involved in the temperature measurement.

A final temperature scale is the thermodynamic or kelvin temperature. It is based on the second law of thermodynamics as discussed in Sect. 2.2.3. The temperature scale was defined by Joule and Thomson in 1854 in such a way that it is identical to the gas temperature scale in the region where the gas temperature is measurable. The

### Gas Temperature Scale

$V = V_0(1 + \alpha t)$ $V = V_0 \frac{273.15 + t}{273.15}$ $V = \frac{V_0}{T_0} T \quad T = 273.15 + t$	$t$ = celsius temperature $\alpha = 1/273.15$ $V_0$ = volume at 0°C $T$ = kelvin temperature $T_0 = 273.15 \text{ K} = 0^\circ\text{C}$
--	---

### Thermodynamic Temperature Scale

thermodynamic temperature = gas temperature  
 in the region of existence of the gas temperature

1854 J. P. Joule and W. Thomson

Temperature:  $T = (\partial U / \partial S)_{n,V}$  kelvin K

Time: second s  
(proper fraction of the ephemeris year 1900  
 matched closely by the Cesium 133 clock)

**Fig. 4.2**

<sup>1</sup> Joseph-Louis Gay-Lussac, 1778–1850. One of the great scholars of France. Student and later Professor of the École Polytechnique in Paris, France. His gas-laws are fundamental for the understanding of the molecular nature and chemistry of gases (1808).

thermodynamic temperature scale is independent not only of any materials' property, but also of the state of matter. The zero of the thermodynamic temperature fixes the zero of thermal motion of the molecules, as illustrated in Fig. 2.9. Through the connection of temperature with radiation laws, it is easily possible to measure temperatures of millions of kelvins, as pointed out in Appendix 8. The easy correlation between the celsius and kelvin scales comes from the accidental fact that the mercury-in-glass scale is practically linear in terms of the kelvin scale from 0 to 100°C. At higher temperatures, this accidental linearity does not hold. At 300°C, for example, the deviation is close to 30 degrees.

### 4.1.2 Liquid-in-glass Thermometers

A typical liquid-in-glass thermometer, capable of high precision thermometry is the mercury thermometer shown in Fig. 2.7. The variables of state needed for thermometry are temperature and time. The SI unit of temperature is the kelvin (K) or the degree celsius (°C), as summarized in Figs. 2.3 and Appendix 8. At the bottom of Fig. 4.2 a further concise connection of temperature to the second law of thermodynamics is given. Finally, time, the other variable often used in thermometry is listed in the figure. The unit of time is the second, and its abbreviation is s, not sec. For all practical purposes the unit is the well-known ephemeris second (from Gk. ἐφ-ημέρος, for the day), representing the proper fraction of the year 1900. The SI unit of time is chosen to match this time interval as closely as possible with the cesium-133 clock, described in Fig. 4.3 (atomic clock). The second is, thus, independent of astronomical time. Common combinations of time-temperature measurements are the cooling and heating curves illustrated in Fig. 1.67, above, and 4.8, below, respectively.

Only for low-temperature and inexpensive thermometers does one use other liquids than mercury in liquid-in-glass thermometers, such as alcohol or petroleum distillates. The mercury-in-glass thermometer has a useful range from about 240 to 800 K. With thermometers of smaller range, as are used in calorimetry, a precision of  $\pm 0.0001$  K has been reported. For many applications the precision required is, however, less than  $\pm 0.01$  K. The highest precision in Hg-in-glass thermometers was reached between the years of 1880 and 1920 when these thermometers were used to maintain the standard of temperature. Note, the scale of a thermometer can be read to one tenth of the markings, if need be, by using a magnifier for estimating the position of the meniscus.

The basic technique of temperature measurement with the liquid-in-glass thermometer is to provide intimate contact with the to-be-measured system, wait until the exponential approach to thermal equilibrium has reached an acceptable error, and if needed, make corrections for the heat flow from the to-be-measured system.

A number of errors in the mercury-in-glass thermometer need to be considered. Most are connected with irreversible or slowly reversing bulb contractions and are coupled with time and immersion effects. From the differential expansivity of mercury and glass, one can calculate that the volume within the capillary corresponding to one kelvin on the scale of the thermometer must communicate with 6,000 times this volume in the bulb of the thermometer to register the proper change of temperature. The most important limitation of the absolute accuracy of a thermometer, thus, resides in the precision to which the volume of the bulb can be maintained.

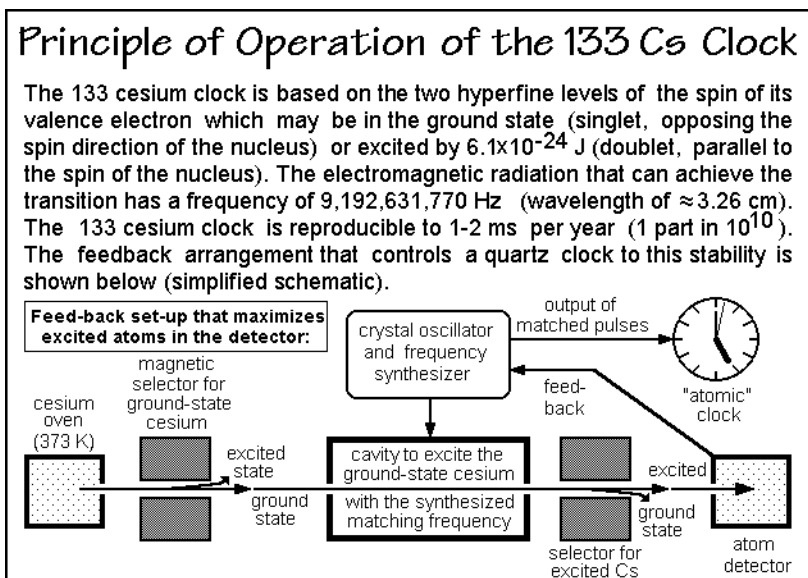


Fig. 4.3

The most bothersome effect is the irreversible contraction of the glass after the bulb is blown. It continues for many years and may cause effects of 1–2 scale divisions. To eliminate this effect, all liquid-in-glass thermometers must be calibrated from time to time at one temperature, usually the ice point. The same correction is then added to all measured temperatures (see Fig. 2.7).

A shorter time effect is the hysteresis of the thermometer. On heating it takes a thermometer bulb several minutes to reach its final volume, but on cooling, it may take many hours. The slow hysteresis effect involves 1–2 scale divisions for every 100 K of temperature change. It is best avoided by using the thermometer only in the heating mode. When cooling is necessary, temperature changes should be kept as small as possible.

Finally, every contact thermometer has a thermometer lag due to the time for heat conduction. It takes a certain time for the heat to flow into or out of the thermometer. For a typical laboratory thermometer with a bulb of size  $4.9 \times 25 \text{ mm}$ , filled with mercury, this effect has a time constant of 1–2 s to reach half of the initial temperature difference. Thus, if one wants an accuracy of 0.001 times the initial temperature difference, one must wait for a period of 10 such half-times.

Since the temperature measurement is dependent on the volume of the bulb, pressure differentials across the bulb walls must be kept constant. Typically the indicated temperature changes by one scale division when the pressure differential across the bulb changes by one atmosphere (0.1 MPa). One should thus always use the thermometer in the same position since the mercury inside the thermometer is a major pressure source for the bulb. Changing a thermometer with a 350-mm-long mercury thread from the horizontal to the vertical position, changes the pressure by 0.05 MPa or 0.5 scale divisions. Naturally, special precautions are needed, for example, when measuring water temperatures at great depths, as in oceanography.

The immersion effect is the largest and most common of all the causes of error, one which always must be corrected for. The drawing on the left in Fig. 4.4 illustrates a thermometer immersed only partially and the use of the correction equation. A length of  $n$  degrees on the scale of the mercury column is outside of the bath. The

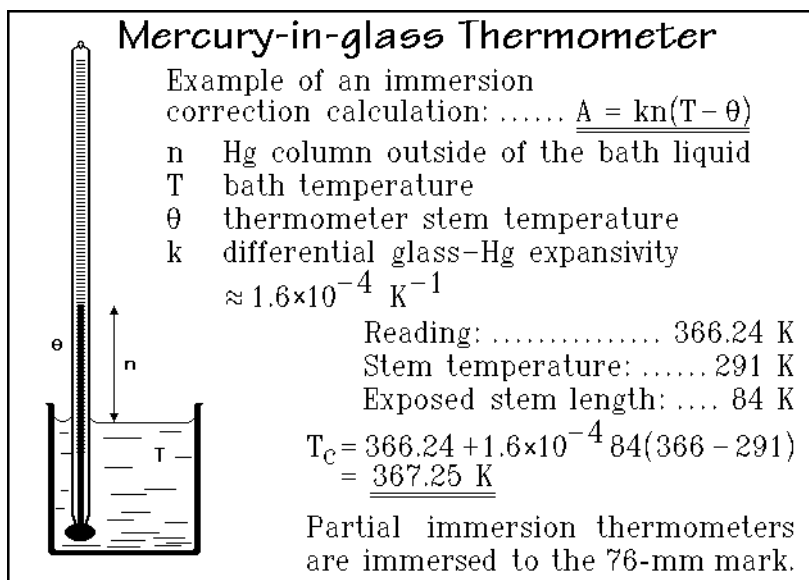


Fig. 4.4

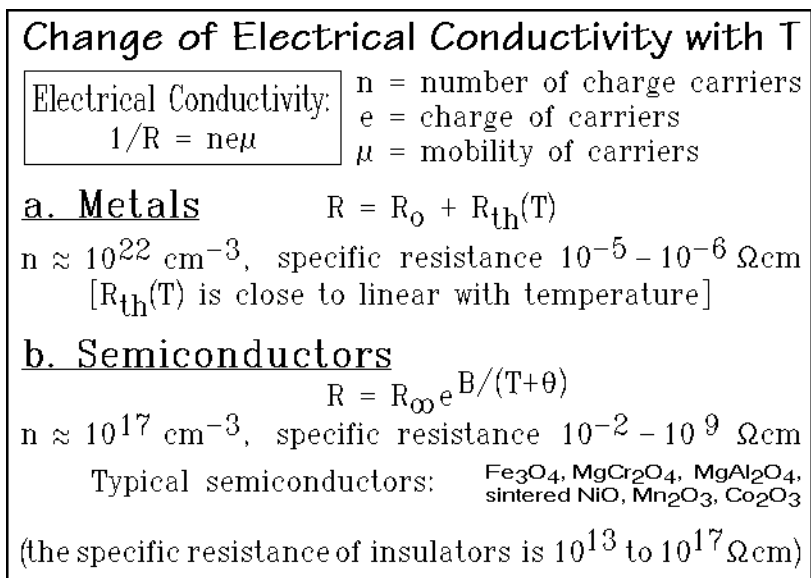
bath temperature itself is  $t$ ,  $k$  is the differential glass and mercury expansion coefficient, which can usually be set to be equal to  $1.6 \times 10^{-4} \text{ K}^{-1}$ , and  $\theta$  is the temperature of the stem, usually room temperature. The correction that must be added to the thermometer reading because of only partial immersion is shown in the example to be more than one degree! Obviously such a big error must always be corrected for.

In some thermometers, the so-called partial immersion thermometers, these corrections have been made at the factory. A partial immersion thermometer can be recognized by an engraved mark 76 mm from the bottom of the bulb. Such thermometers must always be immersed to this mark, and the stem must be kept at room temperature in order to have a precise reading. A partial immersion thermometer which is not immersed to its immersion mark, or which does not have the emerging stem at room temperature, still needs to be corrected by an expression analogous to that shown for total immersion thermometers. A final note of caution: no temperature measurement is possible if the bulb is not safely immersed to the beginning of the constant-diameter capillary.

### 4.1.3 Resistance Thermometers and Thermocouples

Metals, as well as semiconductors have been used as resistance thermometers. As given in Fig. 4.5, the conductivity depends upon the number of charge carriers  $n$ , their charge  $e$ , and their mobility  $\mu$ . The mobility of the electrons is impeded by the



**Fig. 4.5**

increasing atomic vibration amplitudes at higher temperatures. The resistance increases almost linearly with temperature. The best-known resistance thermometers are made of platinum. They are also used for the maintenance of the international temperature scale, ITS 90, as shown in Appendix 8. Over a wide temperature range, the change of its resistance is 0.4% per degree. In order to make a platinum resistance thermometer, a wire is wound noninductively. Most conveniently, the total resistance is made to be  $25.5 \text{ } \Omega$  at  $273.15 \text{ K}$ . Under this condition, the resistance of the thermometer will change by about  $0.1 \text{ } \Omega \text{ K}^{-1}$ . The best precision that has been achieved with platinum resistance thermometers is  $\pm 0.04 \text{ K}$  at  $530 \text{ K}$  and  $\pm 0.0001 \text{ K}$  at  $273.15 \text{ K}$ . It decreases to  $\pm 0.1 \text{ K}$  at  $1700 \text{ K}$ .

Semiconductor properties are also summarized in Fig. 4.5. The conduction mechanism of semiconductors is more complicated. At low temperatures, semiconductors have a very high resistance because their conductance band is empty of electrons. As the temperature increases, electrons are promoted out of the relatively low-lying valence band into the conductance band, or they may also be promoted from impurity levels into the conductance band. It is also possible that positive holes, created by the electrons promoted out of the valence band, carry part or all of the current. All these effects increase the conductance with increasing temperature by creating mobile charge carriers that more than compensate the decrease in mobility with increasing temperature. Semiconductors, thus, have over a wide temperature range the opposite dependence of resistance of metals on temperature. Typically, one may have as many as  $10^{17}$  charge carriers per cubic centimeter at room temperature, and the specific resistance may vary from  $10^{-2}$  to  $10^{+9} \text{ } \Omega \text{ cm}$ . The temperature coefficient of the resistivity may be ten times greater than that of a metal resistance thermometer. Semiconductor thermometers can be built in many shapes. Frequently they are very small beads, so that their heat capacity and thermal lag are small. They

may also be made in form of large disks, so that they can average the temperature over a larger object.

The principle of resistance measurement involves a dc Wheatstone bridge, as in the sketch of Fig. 4.6. The calculations show how the lead resistances,  $R_C$  and  $R_T$ , can be eliminated in precision thermometry by performing two measurements (a and b) with reversed leads connected to the bridge circuit. The measured resistances are represented by  $R_D$ , the unknown resistance by  $R_X$ .

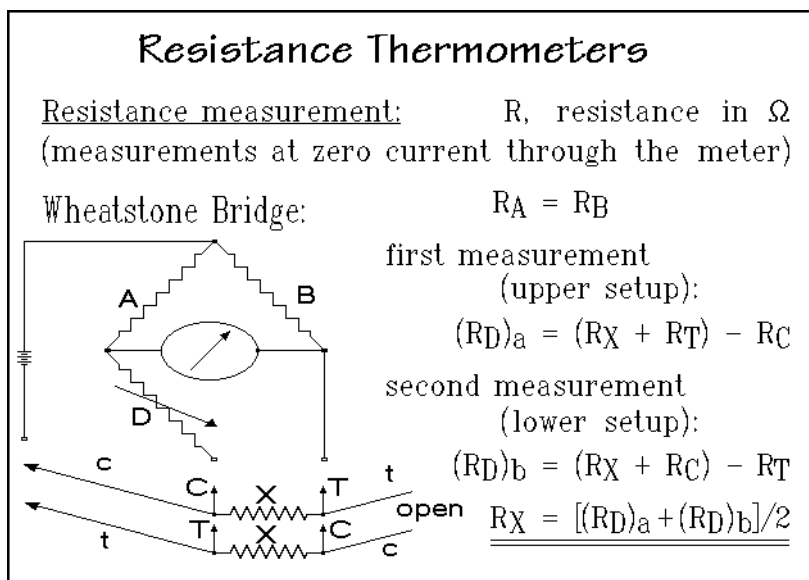


**Fig. 4.6**

A third type of frequently-used thermometer is the thermocouple. The thermocouple is based on the Seebeck effect (see also Fig. 4.36). At the contact points of two dissimilar metals a potential difference is created because some of the electrons in the material of the lower work function drift into the metal with the higher work function. The work function is the energy needed to remove one electron from a metal surface, i.e., from its Fermi level—usually measured in eV. One can think of the metal with the higher work function as holding the electrons more tightly. When a circuit of two different materials is set up, as is shown in the top drawing in Fig. 4.7, and a voltmeter is inserted in one of the branches, one observes no voltage as long as the two junction points are at equal temperature. The potential difference created in one junction by the drift of electrons from the low-work-function to the high-work-function metal is exactly opposite to the potential difference created in the other junction. If, however, the two junctions are kept at different temperatures, one observes a voltage or electromotive force (emf),  $E_{AB}$ . This electromotive force can be used to measure the temperature difference between the junction points of the thermocouple.

The table in Fig. 4.7 lists the change in the emf per kelvin of temperature difference for a number of well-known thermocouples. Copper–constantan thermocouples, which have been given the letter T by the Instrument Society of

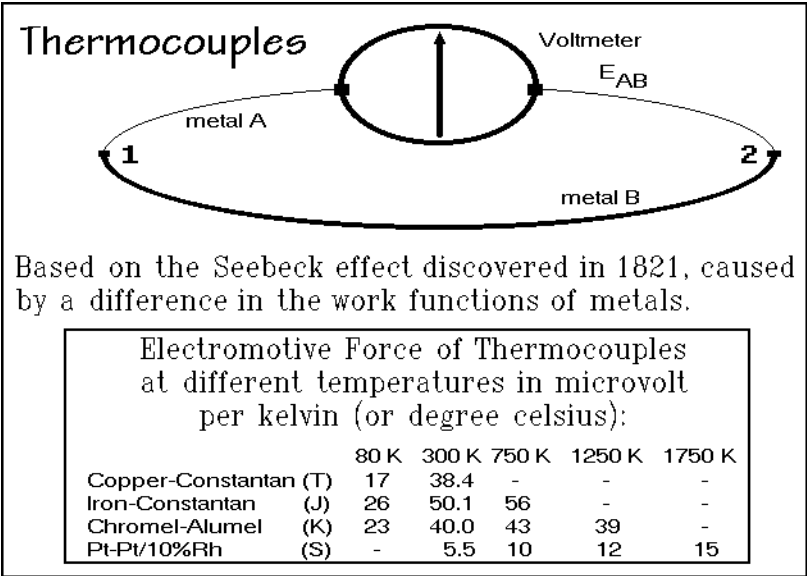


Fig. 4.7

America, are used frequently because of their reproducible temperature-to-emf relation. The chromel–alumel thermocouple (K) can be used all the way up to 1600 K. Its main advantage lies in the fact that the emf per kelvin of temperature change is relatively constant between 300 and 1250 K. A reading of the emf can in this way easily be converted into temperature. A voltmeter can be supplied with a linear scale, reading in K (or °C). Figure 4.8 illustrates how the emf of the thermocouples can be

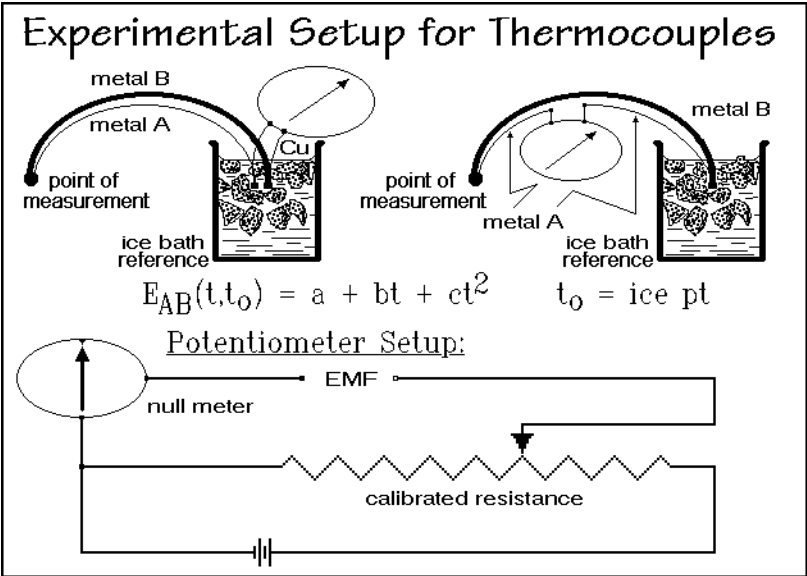


Fig. 4.8

expressed mathematically. The three constants  $a$ ,  $b$ , and  $c$  must be fitted at fixed points of the ITS 90 which are listed in Fig. A.8.1.

The main difficulty in high-precision temperature measurements with thermocouples is the introduction of spurious voltages by metal junctions outside of the measuring and reference junctions. In Fig. 4.8 two typical measuring circuits are sketched. The right circuit overcomes most of the difficulties by using only thermocouple metals for the circuit (including any switches and connectors!). One only has to watch that the two connections to the measuring instrument are at the same temperature and that no additional thermal emf is introduced inside the meter. The second circuit in Fig. 4.8 eliminates the need to carry the thermocouple wires to the measuring instrument by changing from thermocouple material to normal conductance copper in the reference ice bath. In this arrangement all subsequent Cu/Cu junction potentials cancel.

The measuring of the emf must naturally be carried out in such a way that practically no current flows. This can be done by bucking the thermocouple emf with an identical potential of a calibrated potentiometer and reading the position of zero current. At the bottom of Fig. 4.8 the circuit diagram is given for such a potentiometer. Today electronic voltmeters draw practically no current and potentiometers are becoming old-fashioned. A modern, high-impedance voltmeter can, in addition, be digital and be already calibrated for a given thermocouple. Also, it is possible to eliminate the reference junction at  $t_0$  by providing an appropriate counter-emf. But note that the condition of temperature constancy on all dissimilar metal junctions, up to and including the voltmeter, remains.

The discussion of the experimental aspects of temperature measurement is concluded with a listing of some additional instruments which offer promise for special applications:

**Quartz thermometer** (measurement of the frequency of an oscillator, controlled by a quartz crystal with linear temperature dependence—resolution 0.0001 K, range 200 to 500 K).

**Pyrometer** (measurement of the total light intensity or the intensity of a given, narrow frequency range to obtain the temperature—absolute thermometer, used in the maintenance of ITS 90 as given in Appendix 8. The calibration needs to be done at one temperature only).

**Bimetallic thermometer** (bimetallic strip which shows a deflection due to differential expansivity that is proportional to temperature—frequently used for temperature control by coupling the bimetallic strip to a mechanical switch to control the chosen device).

**Vapor pressure thermometer** (pressure measurement above a liquid in contact with the unknown system—particularly useful at low temperatures where other types of thermometers may not be applicable, see also Appendix 8 for the application of vapor pressure thermometers in the maintenance of the ITS 90).

**Gas thermometer** (measurement of  $p$  and  $V$ , followed by calculation of  $T$  through the gas laws—see Figs. 2.8, 2.99, and 4.2).

**Noise thermometer** (measurement of random noise caused by thermal agitation of electrons in conductors, detected by high amplification of the signal).

### 4.1.4 Application of Thermometry

Several typical thermometry applications are treated in connection with the molar mass determination of macromolecules in Sect. 1.4.3 and in a study of melting with optical and atomic force microscopy in Figs. 3.95–97. The evaluation of phase diagrams involves often the recording of time-temperature curves. A cooling curve to find the crystallization temperature is illustrated in Fig. 1.67. A heating curve is shown in Fig. 4.9, together with the corresponding phase diagram and Newton's law of temperature change on heating. The sample with its thermometer, initially at a

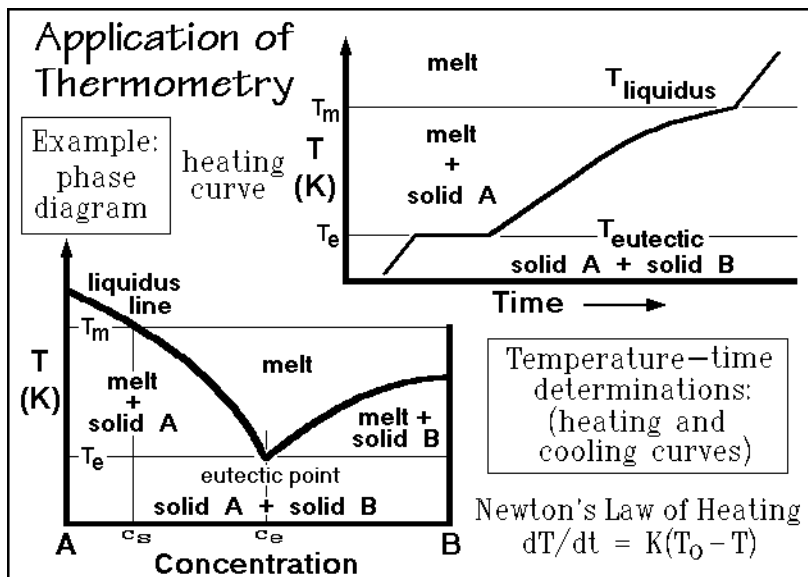


Fig. 4.9

temperature  $T_1$ , is inserted with a reproducible thermal resistance into a constant temperature bath at  $T_0$ , as shown in Fig. 1.67. For small changes in temperature difference,  $K$  of Newton's law remains constant. The heat exchanged,  $dQ$ , during the change in temperature,  $dT$ , during the time interval,  $dt$ , can be expressed as given in Fig. 2.10. Without any change in composition,  $n$ , one can write:

$$dQ = (\partial H / \partial T)_n dT = C_p dT$$

where  $C_p$  is the heat capacity of the system at temperature  $T$ . Equating  $dT$  with the  $dT$  of the Newton's law expression in Fig. 4.9, one can get an expression for the heat-flow rate,  $dQ/dt$ :

$$dQ/dt = C_p K (T_0 - T) .$$

If a pure sample undergoes a first-order phase transition, as described in Sect. 2.5, its temperature remains constant until the heat of transition is absorbed or evolved, but one can assume that the heat-flow rate is the same as without transition. At constant temperature,  $T$ , one can then write:

$$dQ = L(\partial n / \partial t)_T K(T_o - T) dt$$

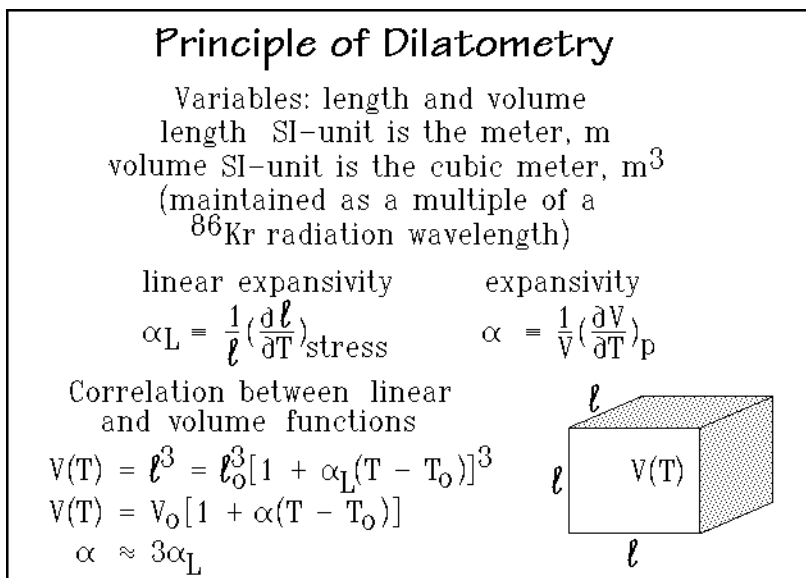
where  $L$  is the latent heat coupled to the change in  $n$ . This equation describes the heating curve at the eutectic temperature. Above the eutectic temperature, both heating and melting occur. In this case, both partial differentials must be properly combined, as suggested in Fig. 2.10 ( $dH = C_p dT + Ldn$ ). The changing amount of melting with temperature accounts for the changing slope between the eutectic and the liquidus temperature in Fig. 4.9. A special complication arises with the crystallization illustrated in Fig. 1.67, where a certain amount of supercooling is necessary to nucleate the crystallization of the sample (see Sect. 3.5). The equilibrium melting/crystallization is passed to lower temperature, followed by self-heating to equilibrium, once nucleated, as indicated by the dashed line in Fig. 1.67.

The heating curve of the two-component sample in Fig. 4.9 has a eutectic phase diagram (see Chap. 7). In addition, the heating curve indicates a heating apparatus that delivers a constant heat input as a function of time. In the first part of the experiment the temperature-increase is linear, indicating a constant heat capacity. Whenever the eutectic temperature,  $T_{\text{eutectic}}$  is reached, the temperature is constant, it increases only after all B-crystals are melted, along with enough A crystals to give the eutectic concentration  $c_e$ . Beyond the eutectic temperature, the slope of the temperature-versus-time curve is less than before since melting of A crystals continues, increasing the concentration of A in the melt from the eutectic concentration to the overall concentration,  $c_s$ , given by the liquidus line. At the liquidus temperature,  $T_{\text{liquidus}}$ , melting of A is completed and the original slope of the temperature increase is resumed. A simple thermometry experiment, thus, permits the measurements of two temperatures,  $T_{\text{eutectic}}$  and  $T_{\text{liquidus}}$ , and fixes two points in the phase diagram. Starting with different concentrations, the complete phase diagram can be mapped. When calibrating  $K$ , it may even be possible to evaluate heat capacity and latent heat, i.e., perform calorimetric experiments. Because of the different parts in the heating-curve apparatus in Fig. 1.67, all with different thermal conductivities and heat capacities, progress in calorimetry by scanning experiments was only made after developing differential techniques, described in Sects. 4.3 and 4.4.

#### 4.1.5 Principle and History of Dilatometry

A dilatometer is an instrument to measure volume or length of a substance as a function of temperature (from L. *dilatare*, to extend, and *metrum*, a measure). The SI unit of length is the meter, which is maintained as a multiple of a krypton-86 radiation wavelength described in Appendix 8 and listed in Fig. 4.10. From the present best value of the pole-to-pole circumference of the earth of  $40.009160 \times 10^6$  m one can see that originally the meter was chosen to make this circumference come out to be  $4 \times 10^7$  m. Such a definition changes, however, with time since measurements of the circumference of the earth are improving steadily and natural changes may occur.

The unit for volume is the cubic meter. For density measurements this makes an unhandy, large sample, but one may remember that the  $\text{g/cm}^3$  is numerically identical to the SI unit  $\text{Mg/m}^3$ . For the present discussion, the experimental pressure is assumed to be constant and, if not indicated otherwise, is the atmospheric pressure (0.1 MPa).

**Fig. 4.10**

Dilatometry under varying forces are the subject of thermomechanical analysis (TMA) and dynamic mechanical analysis (DMA), described in Sect. 4.5. The mass, needed for density measurement is always determined by weighing and is described in the discussion of thermogravimetry, TGA, in Sect. 4.6.

The change of length and volume with respect to temperature is described by the expansivities  $\alpha_L$  and  $\alpha$ , respectively, as written in Fig. 4.10. Both are frequently positive, but macromolecular crystals have often a close to zero or negative  $\alpha_L$  in the chain direction. The best known, exceptional substance with a negative volume expansivity is water from the melting temperature 273 up to 277 K. The correlation between the linear and volume expansivities is shown at the bottom of the figure for the case that  $\alpha_L$  is the same in all directions of space. The volume of the cube as a function of temperature can then be expressed in terms of the linear and volume expansivities, as shown at the bottom of Fig. 4.10. The quantity  $\ell_o$  is the length of the cube at the temperature  $T_o$ . Recognizing that terms higher than the first power in  $\alpha_L$  are small and can be neglected, one can see that  $\alpha \approx 3\alpha_L$ .

The obvious length measurement is a side-by-side comparison with a standard meter, the obvious volume measurement, the evaluation of the content of a standard vessel. Early length measurements of this type were based on anatomical lengths. Naturally, the variation in human size was a basic problem that was solved either by averaging, or by arbitrary choice. The sixteenth century woodcut of how to produce a “right and lawful” rood is illustrated in Fig. 4.11. It shows that one should line up sixteen men, tall and short, “as they happen to come out of the church” after the service. One sixteenth of this rood was “the right and lawful” foot.<sup>1</sup> It is surprising

<sup>1</sup> The rood as an old English measure of length derives from the Dutch rood and German Rute, about 5 m, it is also related to the common surveyor’s measure, the rod of 16.5 feet.

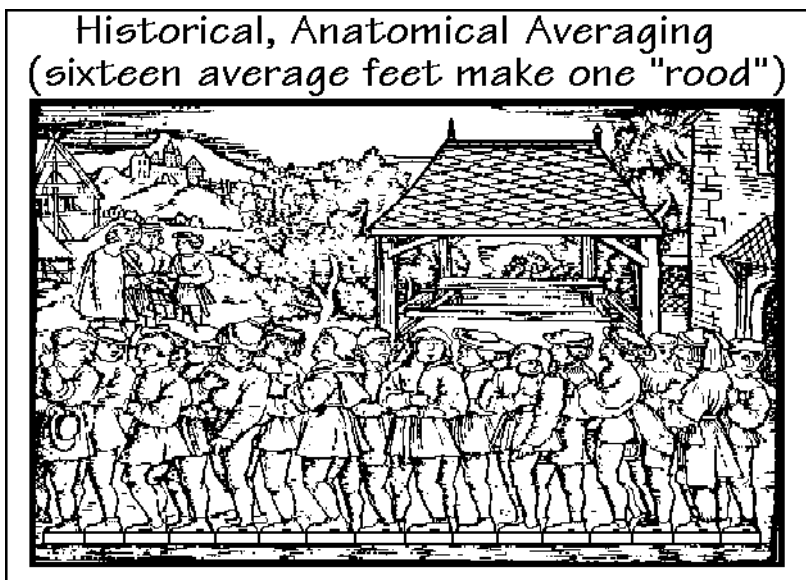


Fig. 4.11

how accurately historical standards could be reproduced. The Roman foot varied over several centuries by as little as 1/400 about the mean.

The establishment of volume standards is even more difficult. An interesting example is the ladder of units in use in Elizabethan England. It started with the smallest unit, the mouthful. Two mouthfuls gave the jigger, two of which, in turn, made a jack, and two of those were the jill. Two jills gave a cup, two cups a pint, two pints a quart, two quarts a pottle. Then follows the gallon, next the peck, the double peck, and the bushel. Doubling further, one gets, in sequence, to the cask, the barrel, the hogshead, the pipe, and finally, the tun. Many of these units had their own, fluctuating history. The mouthful, for example, was already in use as a unit in ancient Egypt. It is mentioned in the Papyrus Ebers as the basic unit for mixing medicines (the ro, equal to  $15 \text{ cm}^3$ ). It may be difficult, however, to calibrate a barrel with 8192 mouthfuls. The volume tun has the same root as the mass unit ton. When referring to water, their sizes are similar. The present-day metric ton represents  $10^6 \text{ cm}^3$  of water and leads to a size of the mouthful of  $15.3 \text{ cm}^3$ . Even mouths seem not to have changed much over the centuries. The connection between mass and volume was the most difficult branch of metrology. Hundreds of units have been described, each pointing to a different method of dilatometry.

#### 4.1.6 Length, Volume, and Density Measurement

The easiest length measurement involves direct placement of the sample against a standard meter as shown at the top of Fig. 4.12. Help in reading the divisions of the standard scale can be given by optical magnification or by designing a micrometer screw that allows one turn of the screw to be divided into 360 degrees, readable perhaps to a fraction of one degree. The length shown can be read as 22.45 units.



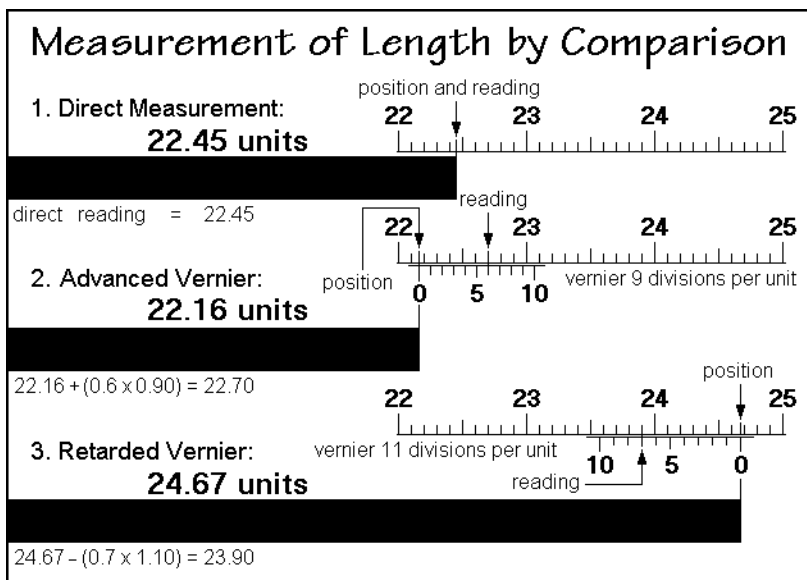
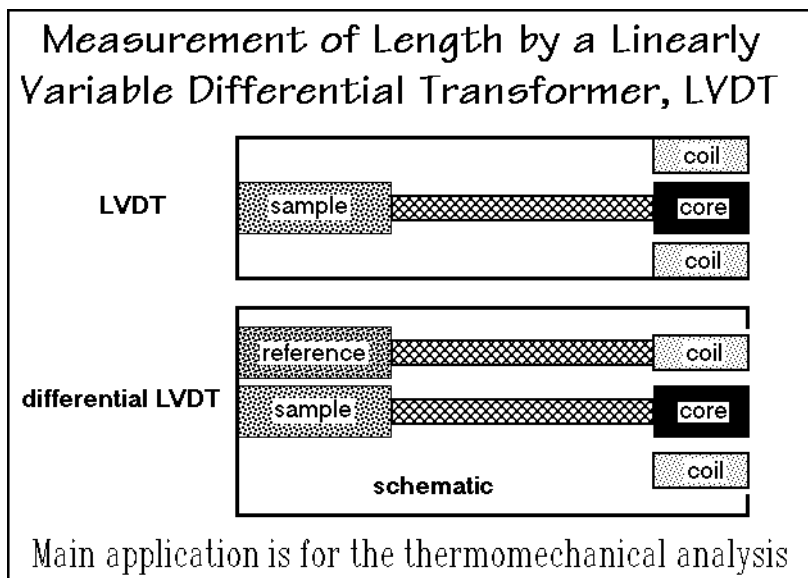


Fig. 4.12

A further refinement is given by the vernier which was invented by Pierre Vernier in 1631. Figure 4.12 shows examples of the use and construction of an advanced and a retarded vernier. The example lengths in the figure are of 22.16 and 24.67 units. One can see, that the advanced, linear vernier has 10 divisions for an interval of 0.9 units, and the retarded vernier, similarly, has 10 divisions for an interval of 1.1 units. The object to be measured is lined up with the zero position of the vernier and then the length is read at the exactly matching divisions. The calculations in the figure show the validity of the method. Similarly, one can construct angular verniers which, in addition, can be coupled with a micrometer screw for an even more precise length measurement.

For higher precision, the scale is magnified with an optical microscope. Accuracies of  $0.2 \mu\text{m}$  are possible in this way. Precision techniques for subdivision of scales and special instruments for comparisons have been developed. The highest precision can be reached by observing differences in interference fringes, set up by monochromatic light between the ends of the objects to be compared. For the maintenance of the standard meter a precision of  $1$  in  $10^8$  is possible as mentioned in Appendix 8.

For the thermomechanical analyses described in Sect. 4.5, which require measurement of small changes in length, and similar applications, an electrical measurement of length is chosen. It involves a linearly variable differential transformer, LVDT. A change in the position of the core of the LVDT, which floats without friction in the transformer coil, results in a linear change in output voltage. For length measurement, the sample is placed as indicated in the top sketch of Fig. 4.13. Variations in the length due to changes in temperature, force, or structure can then be registered. To eliminate the changes in length of the rods connected to the

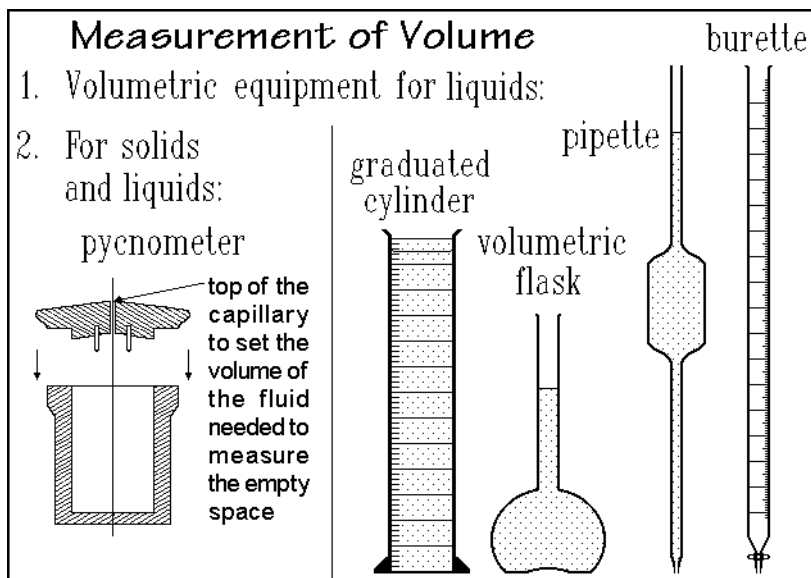
**Fig. 4.13**

LVDT due to temperature changes, a differential setup may be used, as indicated in the bottom sketch. A reference sample is connected to the coil, so that only the differential expansion of the sample is registered. Quartz is used frequently for the construction of the connecting rod and also as reference material. It has a rather small expansivity when compared to other solids as can be seen from Table 4.1. Another material of interest is Invar, an alloy, developed to have a low expansivity.

Four types of experimental setups for volume and density measurements are given in Figs. 4.14 and 4.15. Rarely is it possible to make a volume determination by finding the appropriate lengths. Almost always, the volume measurement will be based on a mass determination, as described in Sect. 4.6. For routine liquid volume measurements, common in chemistry laboratories, one uses the Type 1 volumetric equipment in the form of calibrated cylinders and flasks, pipettes, and burettes, as well as the Type 2 pycnometers. These instruments are calibrated at one temperature only and either for delivery of the measured liquid, as in case of burettes and pipettes, or the volume contained, as in case of volumetric flasks and pycnometers. Calibrations are done by weighing a calibration liquid delivered when emptying, or weighing the instrument filled with the liquid and correcting for the container weight.

**Table 4.1.** Typical Linear Expansivities for Solids

Material	$\alpha_L (\times 10^6 \text{ K}^{-1})$	Material	$\alpha_L (\times 10^6 \text{ K}^{-1})$
Quartz	0.6	Aluminum	25
Platinum	9	Diamond	1.3
Supra Invar (63% Fe, 32% Ni, 5% Co, 0.3% Mn)	0.1	NaCl	40
Benzoic acid	170	Polyethylene (crystal)	94.5

**Fig. 4.14**

To determine the bulk volume of a solid, one uses a calibrated pycnometer as shown in Fig. 4.14. After adding the weighed sample, the pycnometer is filled with mercury or other measuring fluid and brought up to the temperature of measurement. The excess measuring fluid is brushed off and the exact weight of the pycnometer, sample and measuring fluid is determined. From the known density of the measuring fluid and the sample weight, the density of the sample is computed. Today one hesitates to work with mercury without cumbersome safety precautions, but other liquids or gas pycnometers do not quite reach the Hg precision.

Figure 4.15 illustrates on the left as instruments of Type 3 a dilatometer usable over a wider temperature range at atmospheric pressure. It consists of a precision-bore capillary, fused to a bulb containing the sample, indicated as black, irregular shapes. The spacers are made out of glass to act as thermal insulators during the sealing of the dilatometer by the glass blower. The dilatometer is then evacuated through the top ground-glass joint, and filled with mercury. The whole dilatometer is, next, immersed in a constant-temperature bath, and the mercury position in the 30-cm-long capillary is read with a cathetometer. The change in sample volume between a reference temperature and the temperature of measurement is calculated using the indicated equation where  $\Delta V_g$  is the volume change due to the glass or quartz of the dilatometer and spacers. Routine accuracies of  $\pm 0.001 \text{ m}^3/\text{Mg}$  can be accomplished. The equation in Fig. 4.15, however, gives only changes from a fixed reference temperature. One, thus, must start with a sample of known density at the reference temperature to evaluate the absolute volume as a function of temperature.

To the right, Fig. 4.15 illustrates Type 4 instrumentation, a particularly easy method of density determination at a fixed reference temperature, the density gradient method. Figure 4.16 depicts the analysis method. The sample, checked for uniformity and freedom from attached air bubbles, is placed in a density gradient column, and its

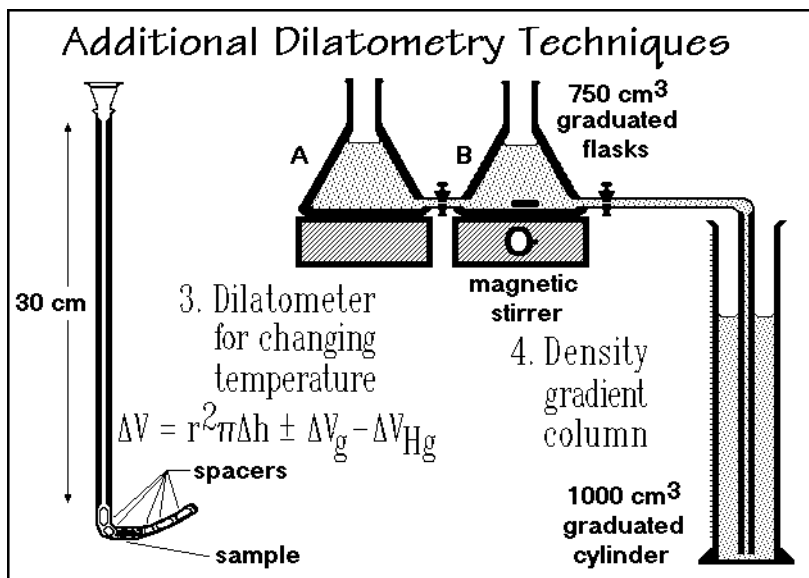


Fig. 4.15

floatation height is measured by a cathetometer. The two Erlenmeyer flasks A and B contain a heavy and a light, miscible liquid, respectively. The cylinder is slowly filled through the capillary from the bottom up. Stirring in flask B is sufficiently rapid to fully mix the liquid in flask B. The first liquid delivered to the cylinder is thus the light liquid. As the meniscus in B drops, heavy liquid out of A is mixed into B and the liquid delivered at the bottom of the density gradient column gets denser. After

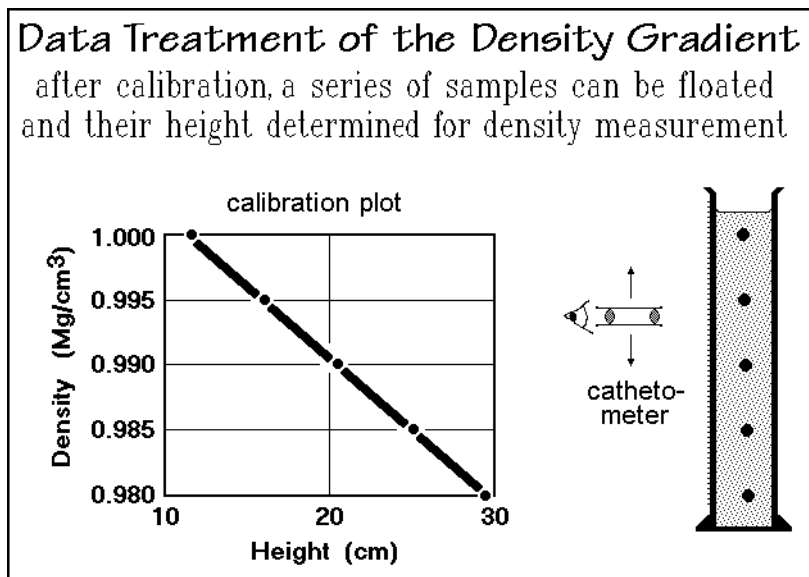


Fig. 4.16

filling, one waits for a few hours to establish a stable density gradient. Once established, the gradient slowly flattens out by diffusion, but usually it is usable for several weeks. The calibration of the density gradient is shown in the left graph of Fig. 4.16. The points in the graph are established by finding the height of glass floats of calibrated density. The floats can be precise to  $\pm 0.0001 \text{ Mg m}^{-3}$ . The height of a floating piece of sample can easily be measured to  $\pm 0.5 \text{ mm}$ , which means that four-digit accuracy in density is possible.

#### 4.1.7 Application of Dilatometry

A typical length measurement by thermomechanical analysis, TMA (see Sect. 4.5), is shown in Fig. 4.17 on the change in dimensions of a printed circuit board made of an epoxy-laminated paper. Measurements of this type are important for matching the expansivities of the electronic components to be fused to the board, so that strain and

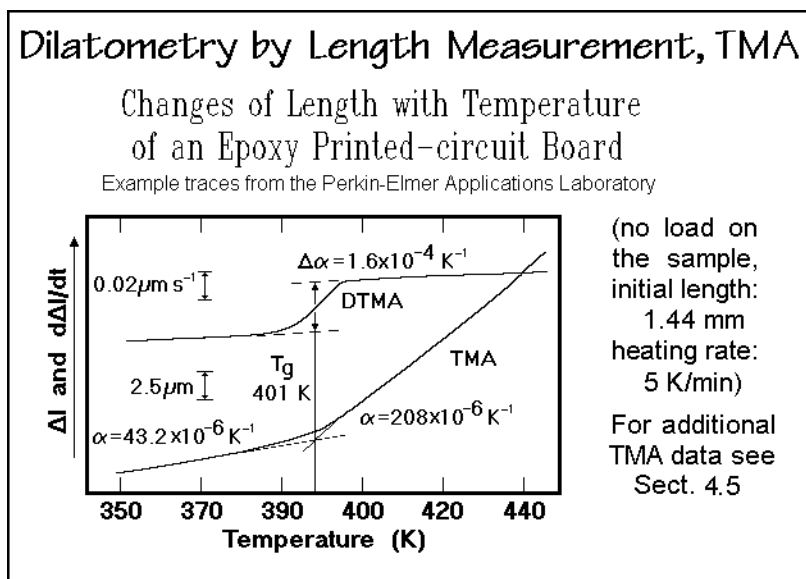


Fig. 4.17

eventual fracture of the printed metal can be avoided. The measurement is made in this case under zero load, so that the bottom curve directly gives the change in length relative to a reference length. The derivative, simultaneously recorded, yields the expansivity after changing from time to temperature. The glass transition at 401 K is easily established, and quantitative expansivities are derived, as is shown.

Figure 4.18 illustrates volume dilatometry of an extended-chain, high-crystallinity polyethylene sample (see also Chap. 6). A close to equilibrium melting is observed by such slow dilatometry with equipment illustrated on the left of Fig. 4.15.

The dilatometry at different pressures leads to a full p-V-T phase diagram. Linear macromolecules in the liquid state can reach equilibrium and have then been successfully described by a single p-V-T diagram. The semicrystalline and glassy

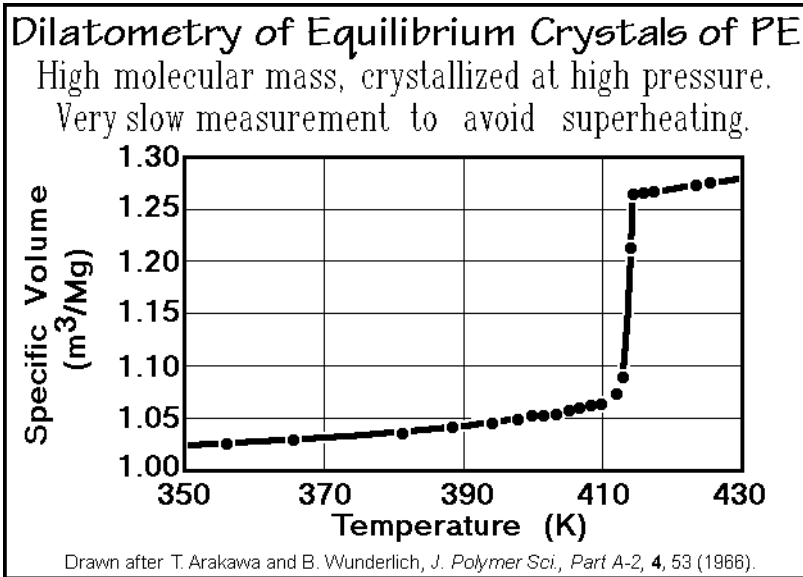


Fig. 4.18

states are usually not in equilibrium and have considerable difficulties in being represented in the multitude of nonequilibrium states, as is described in Chaps. 6 and 7. Figure 4.19 shows a typical p-V-T diagram for liquid polypropylene. Empirically the data can be fitted to the Tait equation, known to be useful for the description of many liquids. Both constants in this equation,  $v_o(T)$  and  $B(T)$ , are exponential functions of temperature.

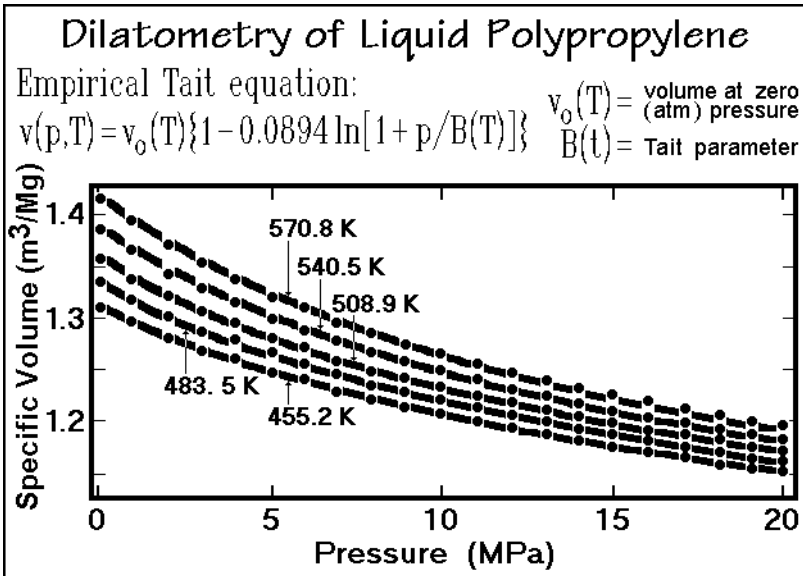
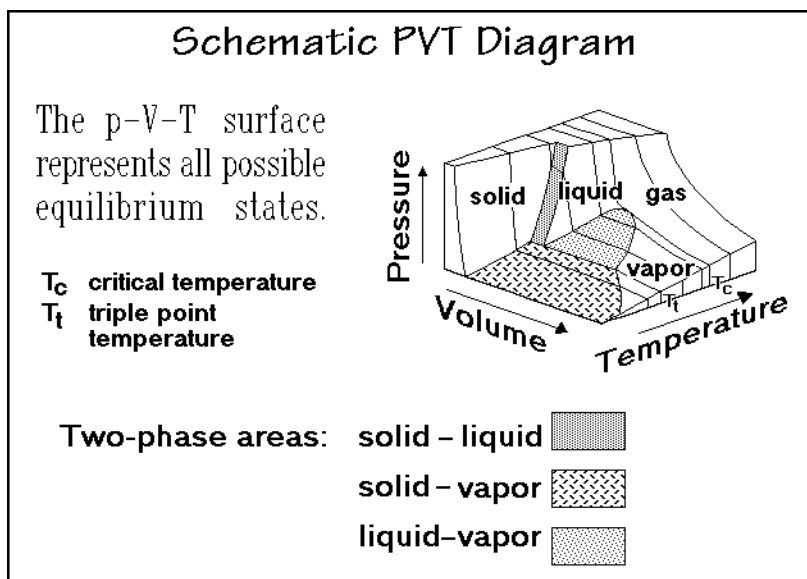


Fig. 4.19

A schematic, three-dimensional, one-component, p-V-T diagram is reproduced in Fig. 4.20. Its surface represents all possible equilibrium states of the system. The gas area, especially at high temperature and volume, is well described by the ideal gas law, at lower temperatures, the van der Waals equation is applicable as seen in Fig. 2.99.



**Fig. 4.20**

The critical point can be derived mathematically from the van der Waals equation by identifying the temperature for the p-V curve with a single horizontal tangent.<sup>1</sup> At the critical point, all gases are in corresponding states, i.e., they behave similarly. Above the critical temperature there is a continuous change from the liquid to the gaseous state. The liquid-to-gas transition can thus occur either below  $T_c$  via a first-order transition with an abrupt change in volume, enthalpy, and entropy, or above  $T_c$  with continuous changes in the thermodynamic functions.

Figure 4.21 displays the projections of the three-dimensional diagram of Fig. 4.20 into the pressure-volume and pressure-temperature planes. Such curves are used to characterize the equilibrium phase behavior of a one-component system. The diagram on the right is simple, it collapses the two-phase areas into lines. The left diagram shows the details of the two-phase areas and the critical point. At  $T_4$  a van der Waals curve is seen, as in Fig. 2.99. More detailed descriptions of the phase equilibria are given in Sect. 2.5. Actual data for the system of ice and water are reproduced in Fig. 4.22. The most fascinating is perhaps the behavior of ice-I, the common ice at atmospheric pressure. It is larger in volume than water and, thus, has according to the Clausius-Clapeyron equation a decreasing melting temperature with pressure (see Sect. 5.6). This trend is reversed with ice III, V, VI, and VII. Many of the geological and biological developments on Earth are based on this abnormal behavior of ice.

<sup>1</sup>  $V_c = 3b$ ;  $p_c = a/(3V_c^2) = a/(27b)$ ;  $T_c = 8p_c V_c / (3R) = 8a / (27Rb)$ ; volume  $V$  is for one mole.

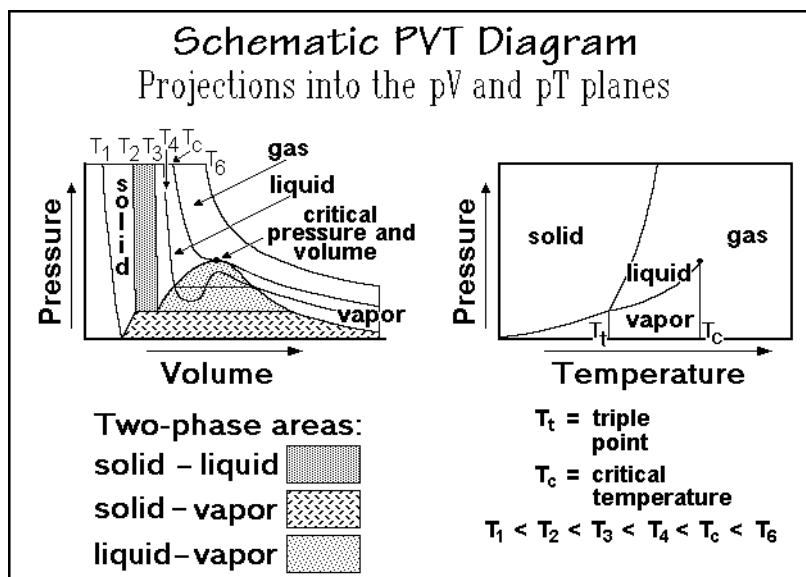


Fig. 4.21

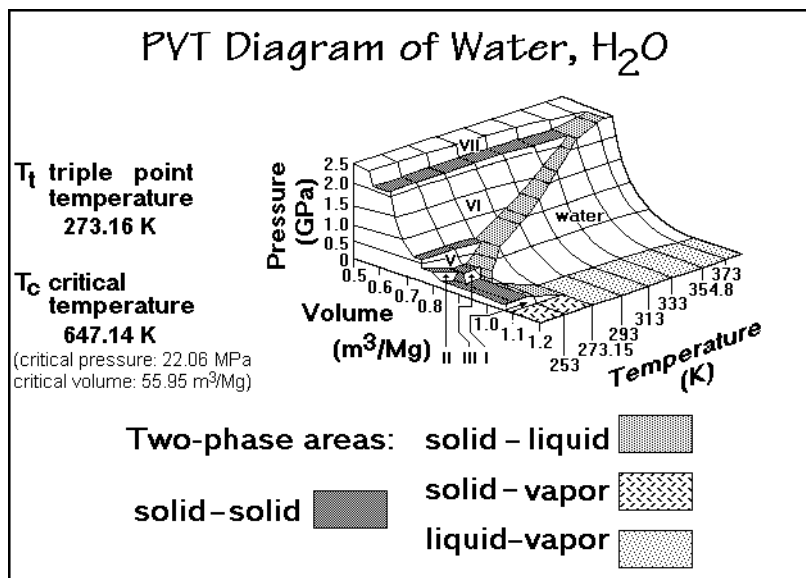


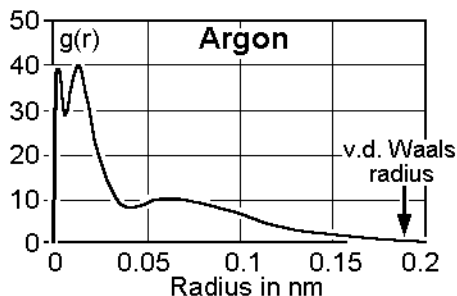
Fig. 4.22

To allow a better understanding of the condensed phase, the volume of a sample can be divided into two parts: the van der Waals volume,  $V_w$ , which represents the actual volume of the molecules or ions in the hard-sphere approximation, taken from Fig. 4.23, and the total, experimental volume  $V$ . It must be remembered that the van der Waals radius depends somewhat on the forces that determine the approach of the



## Solid Sphere Approximation of an Atom

The atomic radius is not well defined, as can be seen from the plot of the radial electron distribution function of argon. The K, L, and M electron shells are clearly visible, but there is no zero of the probability to find the electron at some radius.



To model the atom as a "hard" sphere, one measures the distance two atoms approach in a collision or the spacing they assume in a crystal, the van der Waals radius. Naturally, the van der Waals radius changes for different approaches of the atoms, but it permits an easy modeling of the packing of atoms and molecules in crystals and in the liquid.

Fig. 4.23

atoms considered. For similar types of crystals and liquids, however, the hard-sphere approximation of the atoms is useful. The ratio of these two volumes gives the packing fraction,  $k$ , as listed in in Fig. 4.24. A large packing fraction  $k$  means that the molecules are well packed; a low  $k$  indicates a large amount of empty space. Restricting the discussion for the moment to identical spherical motifs, one can easily compute that the highest packing fraction is 0.74. Such close packing of spheres leads

## Packing Fractions

$$k = V_W/V$$

$V_W$  = v.d.Waals volume

$V$  = actual volume

Three-dimensional packing fractions:

close pack of spheres (CN = 12) = 0.74

random pack of spheres = 0.64

irregular pack (CN = 3) = 0.22

close pack of rods (CN = 6) = 0.91

regular pack of rods (CN = 4) = 0.79

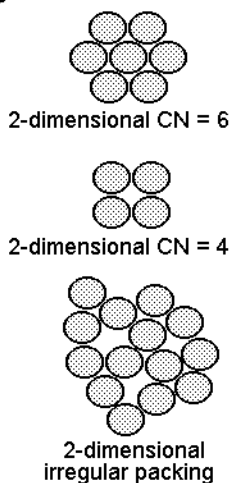


Fig. 4.24

to a coordination number, CN, of 12 nearest neighbors. The resulting crystal structure is a cubic, close-packed crystal or one of the various trigonal or hexagonal close packs. By placing the spheres randomly, but still packed as closely as possible, the packing fraction drops to 0.64. An irregular pack with a coordination number of three, the lowest possible coordination number without building a structure which would collapse, yields a very open structure with  $k = 0.22$ . Packing of spherical molecules in the condensed phase could thus vary between 0.22 and 0.74.

The packing fraction of rods is another easily calculated case. It could serve as a model for extended-chain, linear macromolecules. Motifs of other, more irregular shapes are more difficult to assess. The closest packing of rods with circular cross section reaches a  $k$  of 0.91 with a coordination number of six. Packing with coordination number four reduces  $k$  to 0.79. A random heap of rods which do not remain parallel can result in quite low values for  $k$  which should also depend on the lengths of the rods.

Making further use of packing fractions, one may investigate the suggestion that at the critical point the packing fraction is at its minimum for a condensed phase, and that at the glass transition temperature, packing for the random close pack is perhaps approached, while on crystallization closest packing is achieved via the cubic or hexagonal close pack. Unfortunately such a description is much too simplistic. An additional accounting for differences in interaction energies and the more complicated geometry of actual molecules is necessary for an understanding of the various phases of matter. Volume considerations alone can only give a preliminary picture. At best, molecules with similar interaction energies can be compared. Looking at the packing fractions of liquid macromolecules at room temperature, discussed in Sect. 5.4, some trends can be observed. A packing fraction of 0.6 is typical for hydrocarbon polymers. Adding  $>\text{N}-\text{H}$ ,  $-\text{O}-$ ,  $>\text{C}=\text{O}$ ,  $-\text{CF}_2$ ,  $>\text{S}$  or  $>\text{Se}$  to the molecule can substantially increase the packing fraction.

It is also of interest to compare the expansivity, the derivative of the extensive quantity volume, to specific heat capacity, the derivative of the extensive quantity enthalpy. A detailed discussion of heat capacity is possible by considering harmonic oscillations of the atoms (see Sect. 2.3). A harmonic oscillator does not, however, change its average position with temperature. Only the amplitudes of the vibrations increase. To account for the expansivity of solids, one thus, must look at models that include the anharmonicity of the vibrations. Only recently has it been possible to simulate the dynamics of crystals with force fields that lead to anharmonic vibrations (see Figs. 1.44–48). Despite this difference, the expansivity and heat capacity for liquids and glasses behave similarly (see Sect. 2.3). The reason for this is the larger influence of the change in potential energy (cohesive energy) with volume.

This concludes the discussion of thermometry and dilatometry. The tools to measure temperature, length, and volume have now been analyzed. The tools for measurement of heat, the central theme of this book, will take the next three sections and deal with calorimetry, differential scanning calorimetry, and temperature-modulated calorimetry. The mechanical properties which involve dilatometry of systems exposed to different and changing forces, are summarized in Sect. 4.5. The measurement of the final basic variable of state, mass, is treated in Sect. 4.6 which deals with thermogravimetry.

## 4.2 Calorimetry

Calorimetry involves the measurement of the extensive quantity heat. Its name derives from the middle of the 18<sup>th</sup> century when heat was called the “caloric,” as described in Sects. 1.1.1 and 2.1.1. As the main thermal-analysis method, calorimetry is discussed in this and the following two sections, covering classical calorimetry in Sect. 4.2, differential scanning calorimetry (DSC) in Sect. 4.3, and the more recent temperature-modulated calorimetry (TMC) in Sect. 4.4.

### 4.2.1 Principle and History

The SI unit of heat, as well as of work and energy is the joule, J as summarized in Fig. 2.3. Its dimension is expressed in  $[\text{kg m}^2 \text{s}^{-2}]$ . Heat and work describe the energy exchanged between thermodynamic systems, as discussed in Sect. 2.1.5 with the equation  $\delta q + \delta w = dU$ . An earlier, empirical unit, the “calorie,” was based on the specific heat capacity of water ( $1 \text{ cal}_{\text{thermochemical}} = 4.184 \text{ J}$ ). Since the early 20<sup>th</sup> century, however, energy, heat, and work are more precisely determined in joules, making the calorie a superfluous unit. The calorie is not part of the SI units and should be abandoned. All modern calorimetry is ultimately based on a comparison with heat generated by electrical work.

Almost all calorimetry is carried out at constant pressure, so that the measured heat is the change in enthalpy, as discussed in Chap. 2. The thermodynamic functions that describe a system at constant pressure are listed in Fig. 4.25. These functions contain the small correction caused by the work term  $\delta w = p dV$ . The free enthalpy,  $G$ , also called Gibbs function or Gibbs energy replaces the Helmholtz free energy and is used as measure of thermodynamic stability (see Sect. 2.2.3). The added  $pV$  term in these functions represents the needed volume-work for creation of the space for the system at the given, fixed pressure  $p$ . As indicated in Fig. 4.25, the  $pV$ -term is small. A difference of 0.1 J raises the temperature of one  $\text{cm}^3$  of water by a little more than 0.02 K. In addition, many processes have only a small change in volume ( $\Delta V$ ). The force-times-length term,  $fl$ , provides a similar correction for work exchanged by tensile force during a calorimetric experiment as occurs on changing the length, or geometry in general, of a sample, which is rubber-elastic (see Sect. 5.6.5).

A calorimeter does not allow one to find the total heat content ( $H$ ) of a system in a single measurement, such as one can for other extensive quantities like volume by dilatometry in Sect. 4.1 or mass by thermogravimetry in Sect. 4.6. A calorimeter is thus not a total-heat meter. Heat must always be determined in steps as  $\Delta H$ , and then summed from a chosen reference temperature. The two common reference temperatures are 0 K and 298.15 K (25°).

Three common ways of measuring heat are listed at the top of Fig. 4.26. First, the change of temperature in a known system can be observed and related to the flow of heat into the system. It is also possible, using the second method, to follow a change of state, such as the melting of a known system, and determine the accompanying flow of heat from the amount of material transformed in the known system. Finally, in method three, the conversion to heat of known amounts of chemical, electrical, or mechanical energy can be used to duplicate or compensate a flow of heat.

### Basic Units for Calorimetry

Heat: joule J because most experiments are carried out at constant pressure, it is more convenient to use:

enthalpy,  $H$ , instead of total energy,  $U$

heat capacity at constant  $p$ ,  $C_p$ , instead of at constant  $V$ ,  $C_V$

Gibbs free energy,  $G$ , instead of Helmholtz free energy,  $F$

New Definitions:

$$H = U + pV \quad (-fl)$$

$$G = F + pV \quad (-fl)$$

For solids at atmospheric pressure the  $pV$ -term is small, relative to  $U$ . It represents the volume work to create the space needed to insert the sample (0.1 J per  $\text{cm}^3$  at atm. pressure). The  $fl$  term is only of use for rubber-elastic liquids.

**Fig. 4.25**

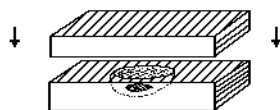
The prime difficulty of all calorimetric measurements is the fact that heat cannot be perfectly contained. There is no ideal insulator for heat. During the time one performs the measurement, there are continuous losses or gains from the surroundings. Even when a perfect vacuum surrounds the system under investigation, heat is lost and gained by radiation. Because of these heat-loss difficulties, experimental calorimetry has not received as much development as one would expect from its importance.

### Principle and History of Calorimetry

In calorimetry, heat measurements involve:

1. determination of temperature changes,
2. following of changes of state, or
3. comparison with chemical, electrical, or mechanical energy.

Experiment by J. Black 1760



$$(1) \quad W_{\text{water}} L = W_{\text{sample}} (h_1 - h_0)$$

Specific heat capacity:

$L$  = heat of fusion  
of water

$$(2) \quad c = \frac{h_1 - h_0}{T_1 - T_0} = \frac{W_{\text{water}} L}{W_{\text{sample}} (T_1 - T_0)}$$

**Fig. 4.26**

The earliest reasonably accurate calorimetry seems to have been carried out in the 18<sup>th</sup> century. In 1760 Joseph Black<sup>1</sup> described calorimetry with help of two pieces of ice, as sketched in Fig. 4.26. The sample is placed into the hollow of the bottom piece. A second slab is put on top. After the sample has acquired temperature-equilibrium at 273.15 K (0°C), the amount of water produced is mopped out of the cavity and weighed ( $W_{\text{water}}$ ). Equations (1) and (2) show the computation of the average specific heat capacity,  $c$ , from the latent heat of water,  $L$ . One expects the results are not of highest accuracy, although with care, and perhaps working in a cold room at about  $T_0$ , an accuracy of perhaps  $\pm 5\%$  might be possible. This is a respectable accuracy compared to the much more sophisticated calorimeters used today which often does not exceed  $\pm 1\%$ .

In 1781 de la Place published the description of a much improved calorimeter. A picture of it can be found in the writings of Lavoisier [4] and is shown in Fig. 4.27. The outer cavity,  $a$ , and the lid,  $F$ , are filled with ice to insulate the interior of the calorimeter from the surroundings. Inside this first layer of ice, in space  $b$ , a second

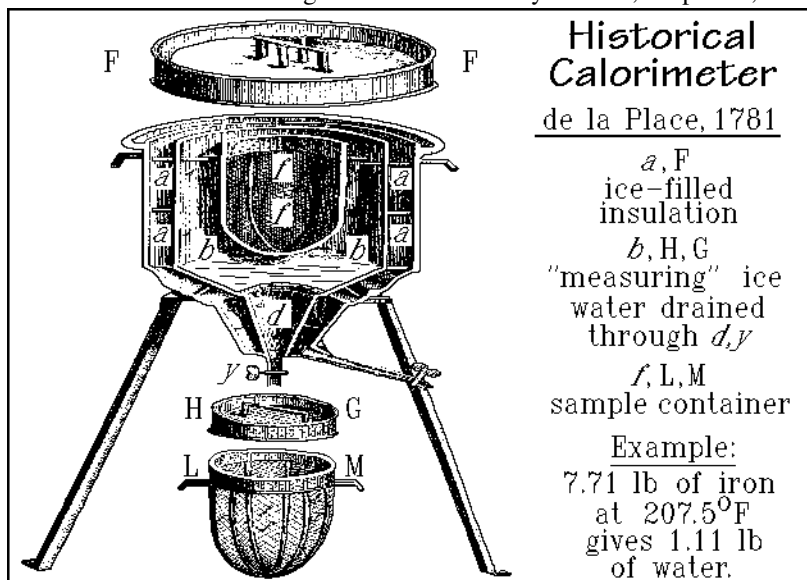


Fig. 4.27

layer of ice is placed, the measuring layer. Before the experiment is started, this measuring ice is drained dry through the stopcock,  $y$ . Then, the unknown sample in basket  $LM$ , closed with the lid  $HG$  and kept at a known temperature  $T_1$ , is quickly dropped into the calorimeter,  $f$ , and the lid,  $F$ , is closed. After 8–12 hours for equilibration of the temperature, the stopcock,  $y$ , is opened and the drained water,

<sup>1</sup> Joseph Black, 1728–1799. British chemist and physicist who discovered carbon dioxide, which he also found in air, and the concept of latent heat. He noticed that when ice melts, it takes up heat without change of temperature. He held a position as Professor of Chemistry and Anatomy at the University of Glasgow, Scotland and also practiced Medicine.

weighed. The heat that flowed from the sample to the measuring ice is thus measured as in the experiment of Black. At the bottom of Fig. 4.27, some of the experimental data are listed that were obtained by Lavoisier. This calorimeter was also used to determine the thermal effects of living animals such as guinea pigs.

#### 4.2.2 Isothermal and Isoperibol Calorimeters

The name calorimeter is used for the combination of sample and measuring system, kept in well-defined surroundings, the thermostat or furnace. To describe the next layer of equipment, which may be the housing, or even the laboratory room, one uses the term environment. For precision calorimetry the environment should always be kept from fluctuating. The temperature should be controlled to  $\pm 0.5$  K and the room should be free of drafts and sources of radiating heat.

Calorimeters can be of two types, 1. isothermal and isoperibol, or 2. adiabatic. Isothermal calorimeters have both calorimeter and surroundings at constant  $T_0$ . If only the surroundings are isothermal, the mode of operation is isoperibol (Gk. ἴσος, equal, περί-βάλλω, surround). In isoperibol calorimeters the temperature changes with time, governed by the thermal resistance between the calorimeter and surroundings. In adiabatic calorimeters, the exchange of heat between a calorimeter and surroundings is kept close to zero by making the temperature difference small and the thermal resistance large.

To better assess heat losses, twin calorimeters have been developed that permit measurement in a differential mode. A continuous, usually linear, temperature change of calorimeter or surroundings is used in the scanning mode. The calorimetry, described in Sect. 4.3 is scanning, isoperibol twin-calorimetry, usually less precisely called differential scanning calorimetry (DSC).

Perhaps the best-known isothermal phase-change calorimeter is the Bunsen<sup>1</sup> ice-calorimeter, invented in 1870 [5]. This calorimeter is strictly isothermal and has, thus, practically no heat-loss problem. The drawing in Fig. 4.28 shows the schematics. The measuring principle is that ice, when melting, contracts, and this volume contraction is measured by weighing the corresponding amount of mercury drawn into the calorimeter. The unknown sample is dropped into the calorimeter, and any heat exchange is equated to the heat exchanged with the measuring ice. Heat-loss or -gain of the calorimeter is eliminated by insulation with a jacket of crushed ice and water, contained in a Dewar vessel. An ice-calorimeter is particularly well suited to measure very slow reactions because of its stability over long periods of times. The obvious disadvantage is that all measurements must be carried out at 273.15 K, the melting temperature of ice. For a more modern version see [6].

Figure 4.29 represents an isoperibol drop calorimeter [7]. The surroundings are at almost constant temperature and are linked to the sample via a heat leak. The recipient is a solid block of metal making it an aneroid calorimeter (Fr. anéroïde, not using a liquid, derived from the Gk.). The solid block eliminates losses due to

---

<sup>1</sup> Robert Wilhelm Bunsen, 1911–1899. Professor of Chemistry at the University of Heidelberg, Germany. He observed in 1859 that each element emits light of a characteristic wavelength. These studies of spectral analysis led Bunsen to his discovery of cesium and rubidium.

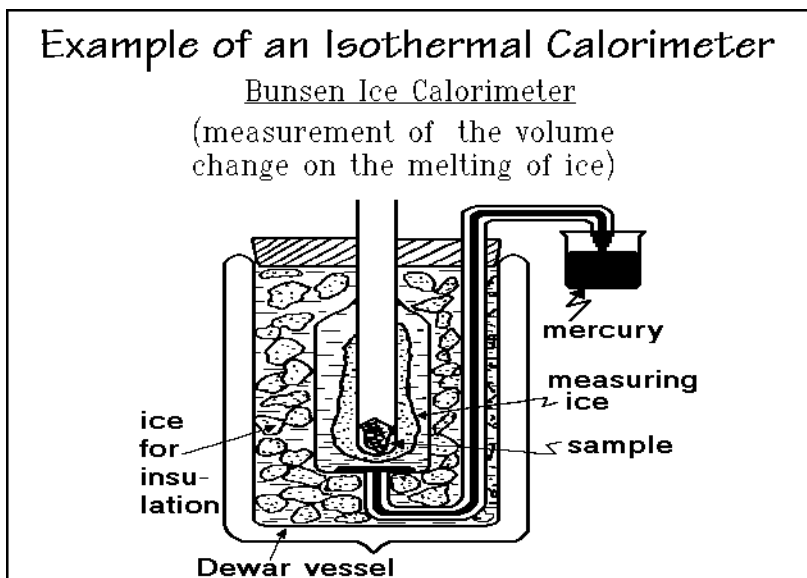


Fig. 4.28

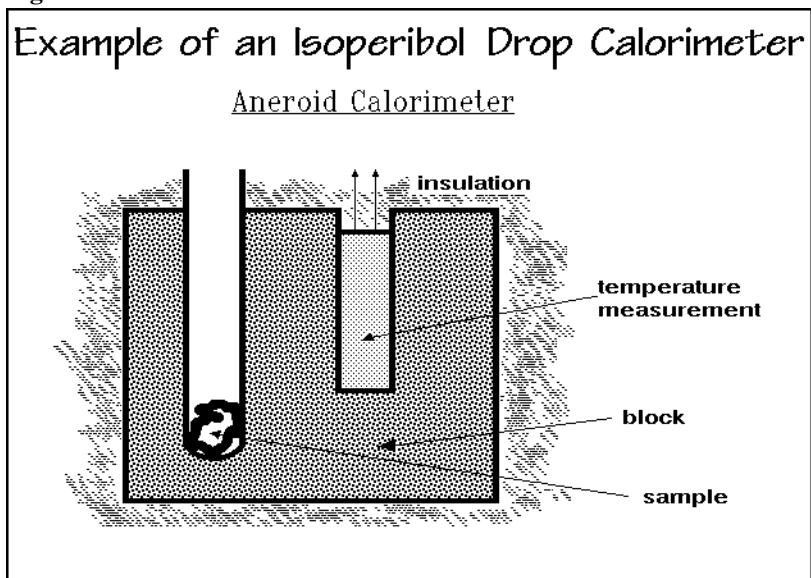


Fig. 4.29

evaporation and stirring that occur in a liquid calorimeter, as shown in Fig. 4.30. But its drawbacks are less uniformity of temperature relative to the liquid calorimeter and the need of a longer time to reach steady state.

For measurement, the sample is heated to a constant temperature in a thermostat above the calorimeter (not shown), and then it is dropped into the calorimeter, where heat is exchanged with the block. The small change in temperature of the block is

used to calculate the average heat capacity. Heats of reaction or mixing can also be measured by dropping one of the components into the calorimeter or breaking an ampule of one of the reactants to initiate the process. More advanced versions of this type of calorimeter involve compensation of heat flow, as shown in Sect. 4.2.5.

Figure 4.30 illustrates the liquid calorimeter. It also operates in an isoperibol manner. The cross-section represents a simple bomb or reaction calorimeter, as is ordinarily used for the determination of heats of combustion [8]. The reaction is carried out in a steel bomb, filled with oxygen and the unknown sample. The reaction is started by electrically burning the calibrated ignition wire. The heat evolved during

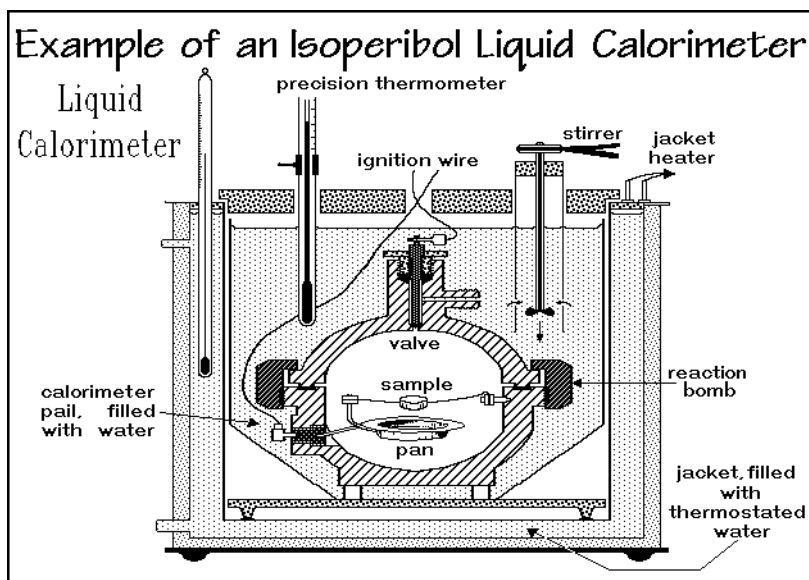


Fig. 4.30

the ensuing combustion of the sample is then dissipated in the known amount of water that surrounds the bomb, contained in the calorimeter pail. From the rise in temperature and the known *water value*,  $W$ , of the whole setup, the heat of reaction can be determined:

$$\Delta H = W\Delta T$$

where  $\Delta H$  is the heat of reaction and  $\Delta T$ , the measured increase in temperature. The water value is equivalent to the heat capacity of a quantity of water which equals that of the whole measuring system.

Much of the accuracy in bomb calorimetry depends upon the care taken in the construction of the auxiliary equipment of the calorimeter, also called the addenda. It must be designed such that the heat flux into or out of the measuring water is at a minimum, and the remaining flux must be amenable to a calibration. In particular, the loss due to evaporation of water must be kept to a minimum, and the energy input from the stirrer must be constant throughout the experiment. With an apparatus such as shown in Fig. 4.30 anyone can reach, with some care, a precision of  $\pm 1\%$ , but it is possible by most careful bomb calorimetry to reach an accuracy of  $\pm 0.01\%$ .



In both the aneroid and liquid calorimeters, a compromise in the block and pail construction has to be taken. The metal or liquid must be sufficient to surround the unknown, but it must not be too much, so that its temperature-rise permits sufficient accuracy in  $\Delta T$  measurement. The calibration of isothermal calorimeters is best done with an electric heater in place of the sample, matching the measured effect as closely as possible. To improve the simple calculation of the output of the aneroid and liquid calorimeters, a loss calculation must be carried out as described in the next section.

### 4.2.3 Loss Calculation

To improve the measured  $\Delta T$ , in isoperibol calorimetry, the heat losses must naturally be corrected for. Loss calculations are carried out using Newton's law of cooling, written as Eq. (1) in Fig. 4.31 (see also Fig. 4.9). The change in temperature with

<b>Loss Calculation:</b>	
by conduction and radiation:	$T$ = temperature
(1) $dT/dt = K(T_0 - T)$	$t$ = time
with added stirrer correction:	$K$ = constant
(2) $dT/dt = K(T_0 - T) + w$	$T_0$ = thermal head
(3) $R_i = K(T_0 - \bar{T}_i) + w$	$w$ = stirrer correction
(4) $R_f = K(T_0 - \bar{T}_f) + w$	$R$ = rate of temperature change
(5) $K = \frac{R_f - R_i}{\bar{T}_i - \bar{T}_f}$	(6) $w = \frac{R_i(T_0 - \bar{T}_f) - R_f(T_0 - \bar{T}_i)}{\bar{T}_i - \bar{T}_f}$
(7) $\Delta T_{\text{corrected}} = (T_3 - T_2) - \int_{t_2}^{t_3} (dT/dt)_{\text{no reaction}} dt$	
(8) define: $\frac{1}{(t_3 - t_2)} \int_{t_2}^{t_3} T dt = \bar{T}$	
	$\begin{bmatrix} \bar{T}_i = (T_1 + T_2)/2 \\ \bar{T}_f = (T_3 + T_4)/2 \end{bmatrix}$

**Fig. 4.31**

time,  $dT/dt$ , is equal to some constant,  $K$ , multiplied by  $T_0$ , the thermal head (i.e., the constant temperature of the surroundings), minus  $T$ , the measured temperature of the calorimeter. In addition, the effect of the stirrer, which has a constant heat input with time,  $w$ , must be considered in the liquid calorimeter in Eq. (2). The same term  $w$  also corrects any heat loss due to evaporation.

The graph in Fig. 4.32 and the data in Table 4.2 show a typical example of calorimetry with a liquid calorimeter. The experiment is started at time  $t_1$  and temperature  $T_1$ . The initial rate of heat loss is determined in the drift measurement. If the thermal head of the calorimeter,  $T_0$ , is not far from the calorimeter temperature, a small, linear drift should be experienced. The measurement is started at  $t_2$ ,  $T_2$ . This process may be combustion, mixing of two liquids, or just dropping a hot or cold sample into the calorimeter. A strong temperature change is noted between  $t_2$  and  $t_3$ .

This is followed by the period of final drift, between  $t_3$  and  $t_4$ . The experiment is completed at time  $t_4$  and temperature  $T_4$ .

The detailed analysis of the curve is continued in Fig. 4.32. The temperatures and times,  $T_2$ ,  $T_3$  and  $t_2$ ,  $t_3$ , respectively, are established as the points where the linear drifts of the initial and final periods are lost or gained. The equations for the initial and final drifts,  $R_i$  and  $R_f$ , are given by Eq. (3) and Eq. (4). They are used to evaluate Newton's law constant  $K$ , as shown by Eq. (5), and the stirrer correction  $w$ , as shown by Eq. (6). With these characteristic constants evaluated, the actual jump in temperature  $\Delta T$ , can be corrected. Now, the value of  $\Delta T_{\text{corrected}}$  is equal to the uncorrected temperature difference minus the integral over the rate of temperature-change given by New-

**Table 4.2** Data for Loss Calculation

t (min)	T (K)	(index)
0	301.1235	(1)
1	301.1255	-
2	301.1270	-
3	301.1290	-
4	301.1305	-
5	301.1320	-
6	301.1340	(2)
7	301.5340	-
8	301.9340	-
9	302.2290	-
10	302.3640	-
11	302.4770	-
12	302.4890	-
13	302.4890	(3)
14	302.4859	-
15	302.4810	-
16	302.4770	-
17	302.4730	-
18	302.4690	-
19	302.4650	(4)

ton's law (i.e., taken as if there had been no reaction). The integral goes from the time  $t_2$  to  $t_3$ , as shown in Eq. (7). If one now defines an average temperature,  $\bar{T}$ , as expressed by Eq.(8),  $\Delta T_{\text{corrected}}$  can be written as is shown in Fig. 4.32 as Eq. (9).

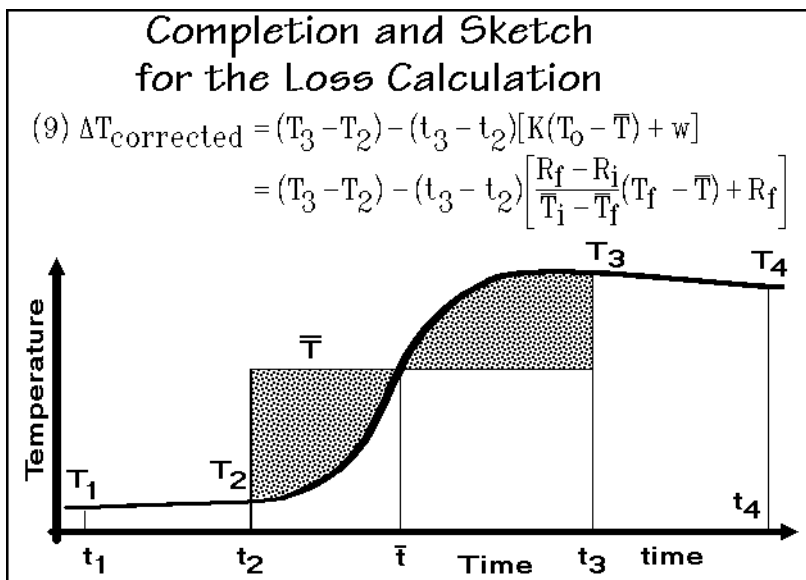


Fig. 4.32

Graphically,  $\bar{T}$  can be found by assuming that the heat losses change proportionally to the changes in the amplitude of the curve—i.e.,  $\bar{T}$  is fixed at a value that makes the two shaded areas of the figure equal in size (note that the thermal head,  $T_0$ , drops out of the calculation).

Several approximations are possible for the evaluation of  $\bar{T}$ . Often, it is sufficient to use the graphical integration just suggested, or to count the corresponding squares of the curve drawn on millimeter paper. If the heat addition is electrical, the temperature rise is close to linear, and the average time is the location of the average temperature. For heats of combustion, the rise in temperature is frequently exponential and can be integrated in closed form.

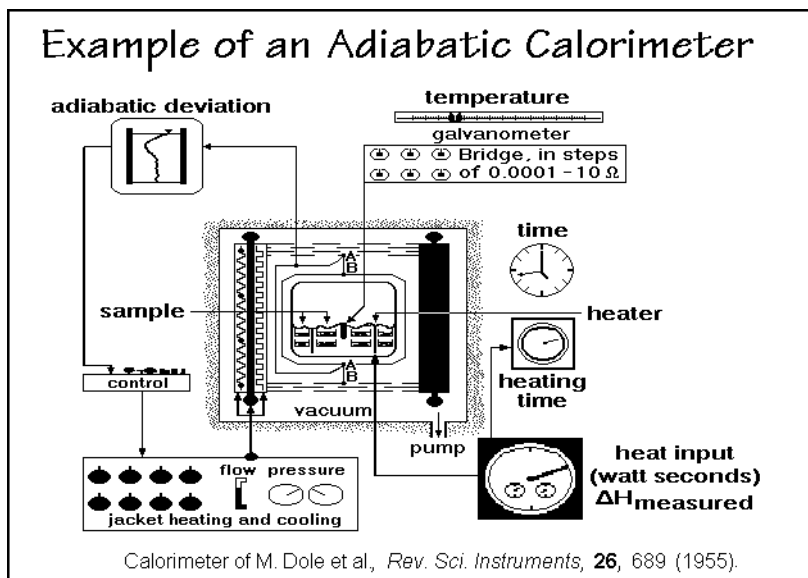
With all these corrections discussed, it may be useful to practice an actual loss calculation, using the data in Table 4.2 (answer:  $\Delta T = 1.3710$  K). If the temperature is measured with a calorimetric mercury-in-glass thermometer, an emergent stem correction becomes necessary if the thermometer extended out of the bath liquid. This emergent stem correction can be made as the last correction for the calculated  $\Delta T$ , using the equation derived in Fig. 4.4.

#### 4.2.4 Adiabatic Calorimetry

Figure 4.33 shows a sketch of an adiabatic calorimeter. With an adiabatic calorimeter an attempt is made to follow the temperature increase of an internally heated calorimeter raising the temperature of the surroundings so that there is no net heat flux between the calorimeter and surroundings. The electrically measured heat input into the calorimeter, coupled with the measurement of the sample temperature, gives the information needed to compute the heat capacity of calorimeter plus sample. If truly adiabatic conditions could be maintained, the heat input,  $\Delta H_{\text{meas}}$ , divided by the temperature change,  $\Delta T$ , would already be the heat capacity. Subtracting the heat absorbed by the empty calorimeter, its water value,  $C^\circ$ , completes the data analysis.

Adiabatic calorimeters have only become possible with advanced designs for electrical temperature measurement and the availability of regulated electrical heating. The first adiabatic calorimeter of this type was described by Nernst in 1911 [9]. Special equipment is needed for low-temperature calorimetry, below about 10 K as are described in Sect. 4.3. Modern calorimeters [10–13] are more automated than the adiabatic calorimeter shown in Fig. 4.33, but the principle has not changed from the original design by Nernst.

The shown calorimeter has an accuracy of  $\pm 0.1\%$  and a temperature range of 170 to 600 K. A sample of 100–300 g is placed in two sets of silver trays, one outside and one inside a cylindrical heater. In the middle of the sample, the tip of the platinum resistance thermometer can be seen. Sample trays, thermometer, and heater are enclosed in a rounded steel shell, which for ease of temperature equilibration is filled with helium of less than one pascal pressure. The shell is covered with a thin silver sheet on the outside, gold-plated to reduce radiation losses. The calorimeter is then hung in the middle of the adiabatic jacket, drawn in heavy black. This adiabatic jacket is heated by electrical heaters and cooled by a cold gas flow, as indicated by the dials of the instruments pictured on the left at the bottom. The whole assembly, calorimeter and adiabatic jacket, is placed in a sufficient vacuum to avoid convection.

**Fig. 4.33**

To measure the deviation from the ideal, adiabatic condition, the temperature difference between the calorimeter and the jacket, the adiabatic deviation, is continuously monitored between the points A and B ( $= T_A - T_B$ ). The heat losses as a function of the adiabatic deviation are measured and calibrated for each temperature ( $b_i$  and  $b_f$ ). The sample temperature is then determined with the platinum resistance thermometer, using a precision galvanometer and a Wheatstone bridge, indicated on the right in Fig. 4.33. The heat input into the sample,  $\Delta H_{\text{meas}}$ , is measured by the watt-hour meter, indicated on the bottom right (unit  $\text{Ws} \equiv \text{J}$ ). A typical experiment involves an increase in temperature in steps of between 1 and 20 K.

The loss and heat capacity calculations are indicated in Fig. 4.34. The curve represents the adiabatic deviation,  $T_A - T_B$ . During the initial isothermal period (up to  $T_i$ ), the drift  $R_i$  of the sample is followed with the platinum resistance thermometer as a function of time. The temperature difference between A and B is monitored continuously throughout the measurement. During the heating cycle (heater on) the temperature changes quickly, so that it cannot be determined. Temperature measurement is started again at  $T_f$ , as soon as a final, linear drift,  $R_f$ , is obtained.

This discussion of the measurement of heat capacity by adiabatic calorimetry gives insight into the difficulties and the tedium involved. Today, computers handle the many control problems, as well as the data treatment. The rather involved experimentation is the main reason why adiabatic calorimetry is not used as often as is required by the importance of heat capacity for the thermodynamic description of matter.

The main advantage of adiabatic calorimetry is the high precision. The cost for such precision is a high investment in time. For the measurement of heat capacities of linear macromolecules, care must be taken that the sample is reproducible enough to warrant such high precision. Both chemical purity and the metastable initial state must be defined so that useful data can be recorded.

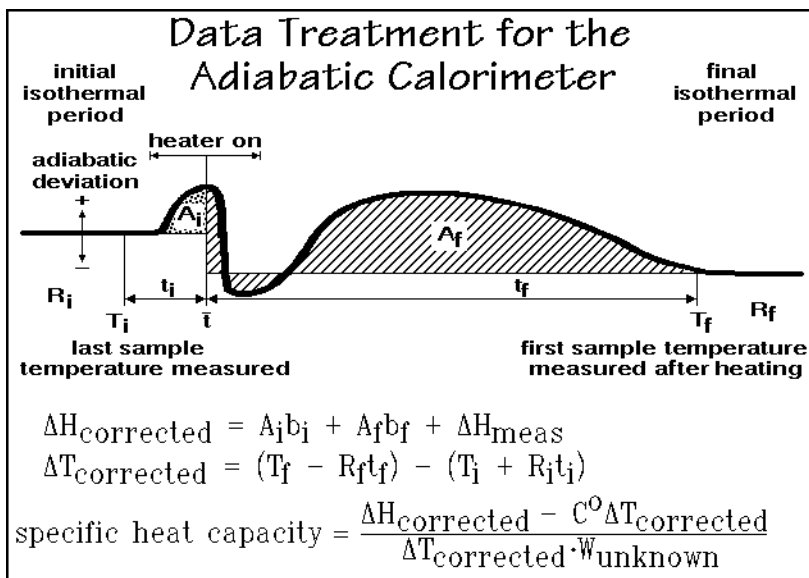


Fig. 4.34

#### 4.2.5 Compensating Calorimeters

Compensating calorimeters are constructed so that it is possible to compensate the heat effect with an external, calibrated heat source or sink. These calorimeters often operate close to isothermal conditions between the calorimeter and surroundings. Functionally the simplest of the compensating calorimeters is that designed by Tian and Calvet [14]. The schematic of Fig. 4.35 shows that the sample is contained in the central calorimeter tube that fits snugly into a silver socket, across which the heat exchange occurs. The heat generated or absorbed by the sample is compensated by the Peltier effect of hundreds of thermocouples. A short summary of the three thermoelectric effects, of which one is the Peltier effect, is given in Fig. 4.36 (see also Fig. 4.7 for the application of the Seebeck effect). If heat is generated in the calorimeter, the Peltier thermocouples shown in Fig. 3.35 are cooled. If heat is absorbed, the Peltier thermocouples are heated by reversing the current. These thermocouples are arranged in series, with one junction at the silver socket (calorimeter), and the other junction at the thermostated metal block (surroundings). The whole silver socket is covered evenly with the thermocouple junctions, as shown on the left-hand side of the drawing. In addition to the Peltier thermocouples, there is a set of measuring thermocouples, considerably smaller in number (approximately ten to twenty). These measuring thermocouples are interspersed between the Peltier thermocouples and are used to measure the temperature difference  $\Delta T$  between the silver socket and the metal block. In the figure, the measuring thermocouples are drawn separately on the right-hand side. The heat,  $\Delta Q$ , generated or absorbed by the Peltier effect is given by Eq. (1) where the Peltier coefficient is represented by  $\Pi$ ,  $i$  is the positive or negative current, and the time interval is  $\Delta t$ . The Peltier coefficient for

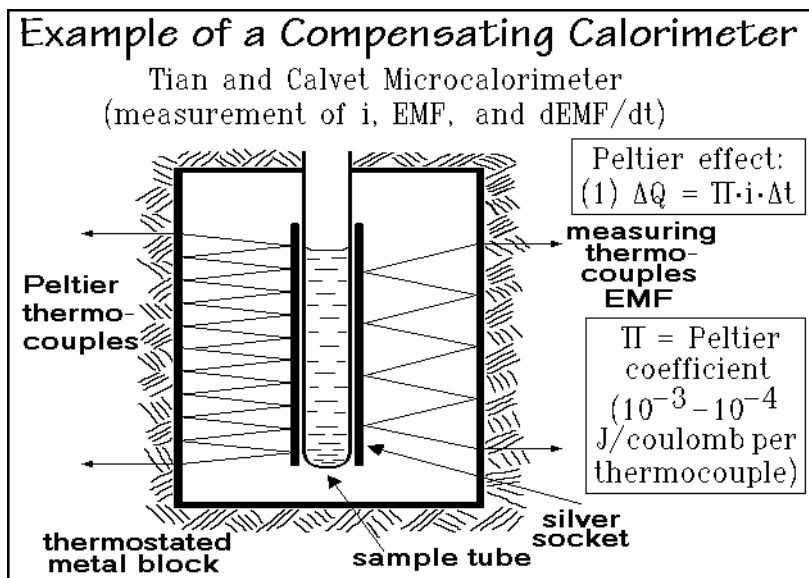


Fig. 4.35

### The Peltier Effect

This effect was discovered by J. C. A. Peltier in 1834 through calorimetry and is one of the three thermoelectric effects. It refers to a reversible heating or cooling which occurs at a contact point between two different conductors when current flows in a given direction:

$$\Delta Q = \Pi_{AB}(T)i\Delta t$$

where  $\Delta Q$  is the amount of heat in joules;  $\Pi_{AB}(T)$ , the temperature-dependent Peltier coefficient;  $i$ , the electric current in amperes; and  $\Delta t$ , the time-interval of measurement ( $i\Delta t$  = charge passed through the junction in As). If heat is absorbed, the Peltier coefficient is positive, it follows that  $\Pi_{AB}(T) = -\Pi_{BA}(T)$ .

The other two thermoelectric effects are the Seebeck effect,  $E_{AB}(T_1, T_2)$ , that gives the emf between the junctions at different temperatures of a circuit out of two different conductors, and the Thomson effect that refers to the reversible heat absorption which occurs when an electric current flows in a homogeneous conductor in which there is a temperature gradient,  $\Delta Q = \sigma_{TA}(T)(dT/dx)i\Delta t$ .

The three thermoelectric effects are related by the first law of thermodynamics:

$$E_{AB}(T_1, T_2) = \Pi_{AB}(T_1) - \Pi_{AB}(T_2) + \int_{T_1}^{T_2} [\sigma_{TA}(T) - \sigma_{TB}(T)]dT$$

Fig. 4.36

a single thermocouple is of the order of magnitude  $10^{-3}$  to  $10^{-4}$  J C<sup>-1</sup>. With this amount of reversible heat, the major heat effect in the calorimeter is compensated and thus measured directly.

The heat losses,  $\Phi$ , need to be discussed next on hand of Fig. 4.37. Obviously, the main heat loss should be through heat conducted by the thermocouples. If the

### Data Calculation from the Calorimeter

Heat loss  $\Phi$ :      (a) thermocouple wires ( $c\sum\Delta T$ )  
                          + (b) convection (approx.  $\delta\sum\Delta T$ )  
                          + (c) areas not covered ( $\epsilon\Phi$ )

from measuring thermocouples

$$(2) \quad \text{EMF} = \epsilon_o \sum \Delta T \quad \mathbf{C} = \text{heat capacity}$$

$$(3) \quad \text{EMF} = \frac{\epsilon_o}{c + \delta} (1 - \epsilon) \Phi \quad \text{of sample and water value}$$

$$(4) \quad \Delta H = \int (\Pi \cdot i) dt + \int \Phi dt + \mathbf{C}(dT/dt)dt$$

$$\int (\Pi \cdot i) dt = \text{Peltier compensation}$$

$$\int \Phi dt = \text{losses}$$

$$\mathbf{C}(dT/dt)dt = \text{calorimeter heating}$$

**Fig. 4.37**

temperature difference between the calorimeter and the surroundings is not exactly equal to zero, this heat loss is given by  $c\sum\Delta T$  (loss a). Another loss comes from the convection of air between calorimeter and surroundings. Again, one can assume that this convection loss is, at least approximately, proportional to the temperature difference  $\Delta T$  (loss b). Finally, a fraction of the losses must go through the areas which are not covered by thermocouples—for example, losses by radiation. These losses, as a catch-all, can be assumed to be a certain fraction of the total loss,  $\epsilon\Phi$  (loss c) as summarized in the figure.

All these heat losses can now be evaluated from the emf of the measuring thermocouples. The thermocouple emf is given in Eq. (2) of Fig. 4.37. It is equal to the thermocouple constant,  $\epsilon_o$ , multiplied by the sum of the temperature differences of all the measuring couples. Equation (3) is the final expression for the heat loss,  $\Phi$ , expressed in terms of the emf. It is arrived at by elimination of  $\sum\Delta T$  in (a) and (b), with help of Eq. (2), and the addition of (a), (b), and (c). All constants— $c$ ,  $\gamma$ , and  $\epsilon_o$ —have to be evaluated by calibration.

The overall calorimeter equation of the Calvet calorimeter is finally given by Eq. (4). The overall heat effect,  $\Delta H$ , is equal to the time integral over the Peltier compensation, the major effect to be measured, corrected for two factors: the time-integral over the just-discussed losses,  $\Phi$ , and, if the temperature does not stay exactly constant during the experiment, a correction term which involves the heat capacity of the calorimeter and the sample,  $\mathbf{C}$ . All three terms can be evaluated by the measurement of the Peltier current  $i$ , the measurement of the emf of the measuring thermocouples, and a measurement of the change of the emf with time. The last term is needed for the calculation of the heat capacity correction which is written in Eq. (4). The last two terms in Eq. (4) are relatively small as long as the operation is close to isothermal.

For larger temperature differences such calorimeters can also be used as heat-flux calorimeters, using only the last two terms in Eq. (4). Because of the small losses, Tian–Calvet calorimeters have found application for the measurement of slow, biological reactions.

#### 4.2.6 Modern Calorimeters

With the exception of the combustion calorimeters, not very many calorimeters have in the past been developed commercially. Calorimeters were usually built one at a time. Several of these unique calorimeters are described in the references. The choice of commercial calorimeters made in this section serves to illustrate the variety of available calorimeters.

A schematic of the operation of the Sinku Riku ULVAC SH-3000 adiabatic, scanning calorimeter is shown in Fig. 4.38. The calorimeter ① is detailed on the right. It is a miniaturization of the classical calorimeter in Fig. 4.30. The sample is indicated by 1. It is heated by supplying constant power, outlined in the block diagram on the

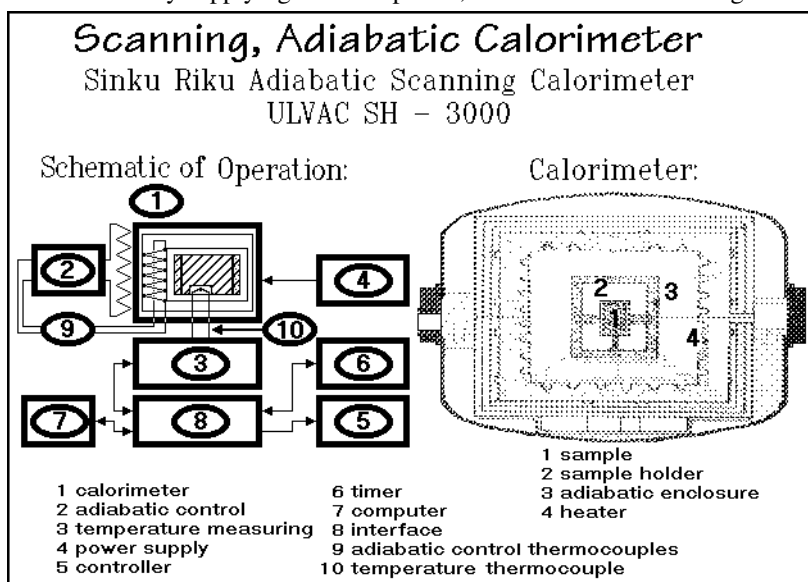


Fig. 4.38

left by ④. Temperature is measured by the block marked by ③. The rise in temperature of the sample holder, 2, inside the calorimeter is sensed by the thermocouple, ⑩. The adiabatic deviation is detected by the multi-junction thermocouple, marked ⑨ and controlled by ②. The adiabatic deviation is used to raise the temperature of the adiabatic enclosure 3, and heater 4 (right). The instrumentation ⑤ to ⑧, provide minicomputer control. Cooling water is provided to the surface of the calorimeter. The temperature range of the calorimeter is claimed to be 100 to 800 K with two different calorimeter models. The sample mass can be several grams. Adiabatic control is good to  $\pm 0.002$  K, and heat input is accurate to  $\pm 0.5\%$ .



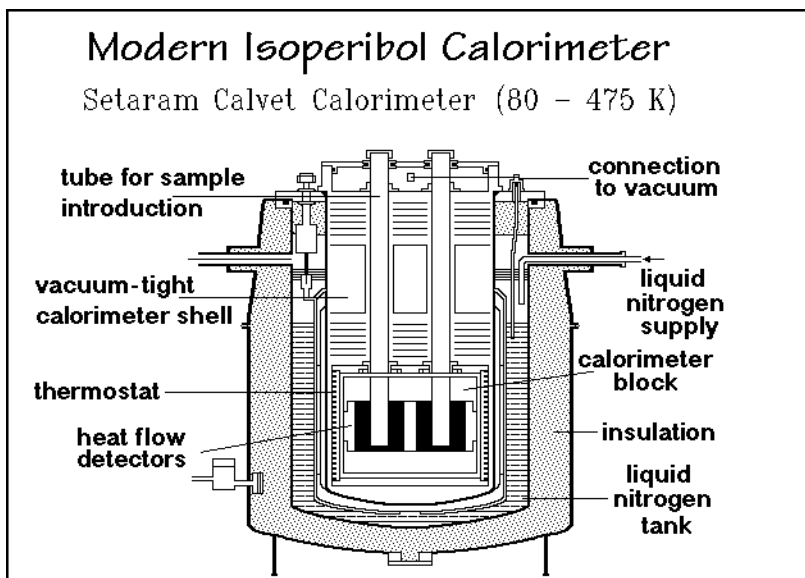
**Fig. 4.39**

Figure 4.39 illustrates a Calvet calorimeter, built by Setaram. A cross section through the low-temperature version of the calorimeter is shown. This instrument can operate between 80 and 475 K. Other calorimeters based on the same principle are available for operation up to 2000 K. The key features are the heat flow detectors which carry practically all heat to and from the sample. Although the Peltier effect could be used to quantitatively compensate heats evolved or absorbed, it is usually more precise to detect only the heat flow. The heating and cooling feature through the Peltier effect is then used for introducing initial temperature differences or for quick equilibration of sample and thermostat. The major feature of these Calvet calorimeters is their extremely good insulation. The special feature of the specific model is its ability to be cooled with liquid nitrogen. The temperature of the thermostat can be kept isothermal, or it can be programmed at rates from 0.1 to 1 K min<sup>-1</sup>. As little as 0.5  $\mu$ W of heat flow is detectable. The calorimetric sensitivity is 50  $\mu$ J. The cells may contain as much as 100 cm<sup>3</sup> of sample. These specifications make the calorimeter one of the most sensitive instruments, and make it suitable for the measurement of slow changes, as are found in biological reactions or dilute-solution effects.

In Fig. 4.40 a stirred liquid bench-scale calorimeter is displayed. It closely duplicates laboratory reaction setups. The information about heat evolved or absorbed is extracted from the temperature difference between the liquid return ( $T_J$ ) and the reactor ( $T_R$ ). This difference is calibrated with electric heat pulses to match the observed effect at the end of a chemical reaction. In a typical example, 10 W heat input gives a 1.0 K temperature difference between  $T_J$  and  $T_R$ . The sample sizes may vary from 0.3 to 2.5 liters. The overall sensitivity is about 0.5 W. The calorimeter can be operated between 250 and 475 K. Heat loss corrections must be made for the stirrer and the reflux unit. The block diagram in Fig. 4.40 gives an overview of the data handling.

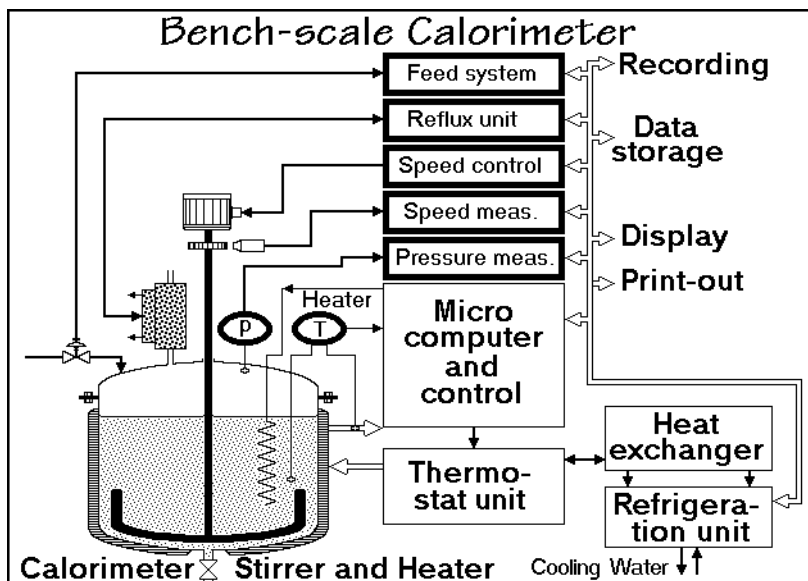


Fig. 4.40

#### 4.2.7 Applications of Calorimetry

Many applications of the various types of calorimetry described in Sects. 4.2–4.4 are given throughout the book. In this section four examples of calorimetric results are given: a) purity determination, b) determination of thermochemical functions by measurement and computation, c) and d) measurement of thermodynamic functions of carbon allotropes and paraffins.

**Purity Analysis** [15–18]. Purity analysis is an example of quantitative handling of a eutectic phase diagram with two components A and B. The analysis is based on the ideal mixing equation applied to the phase equilibrium of low-molar-mass compounds, as derived in Sect. 2.2.6 and expanded to macromolecules in Chap. 7 and shown in Fig. 4.41. The unknown impurity (B, component 2) is assumed not to crystallize together with the major phase (A, component 1). Its concentration  $x_2$ , the lowering of the melting point of the crystals A,  $\Delta T_m$ , and the fraction melted at any the given temperature,  $F$ , must be evaluated. Figure 4.41 shows in the top-left the equation needed to estimate the purity of the sample.

If half of A is melted ( $F = 0.5$ ), the concentration of the impurity is double the overall concentration  $x_2$ , and the freezing-temperature lowering,  $T_m^\circ - T_m$ , is double that at the liquidus line, the line in the phase diagram indicating the end of melting shown in Fig. 4.9. At the eutectic temperature all B and sufficient A melt, to reach the eutectic concentration with the corresponding increase in enthalpy as can be deduced from the upper diagram in Fig. 4.9. This is followed by a broad melting range of the remaining pure component A that ends at the liquidus line, as described by the equation and in Fig. 4.9 ( $F = 1$ ). For small impurities the beginning of melting is hard to find because of lack of equilibrium on crystallization, and the end of melting is not

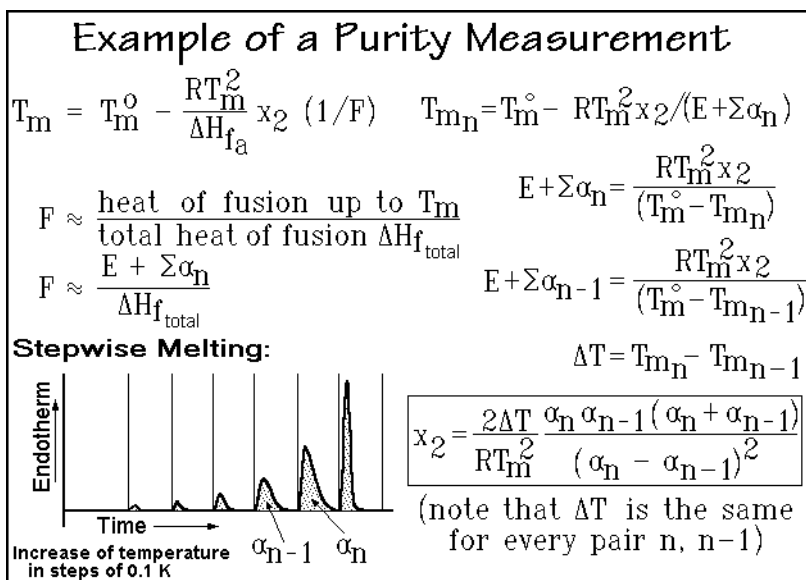


Fig. 4.41

easily detected, because of calorimeter-lag, particularly when using scanning calorimetry (see Sect. 4.3). These difficulties are removed by step-wise increasing of the temperature. After each melting step of, let us say 0.1 K, thermal equilibrium is awaited before one continues with the next step. The successive partial heats of fusion of A are  $\alpha_1, \alpha_2, \alpha_3$ , etc. The value of F, after melting the  $n^{\text{th}}$  fraction,  $\alpha_n$ , is then approximated as given in Fig. 4.41. The term E represents the unmeasured heat of fusion before the first step  $\alpha_1$  was made. The melting temperature after step n is given by the top right equation. Between any two successive steps,  $n-1$  and  $n$ , the remaining unknown E can then be eliminated as indicated in the boxed equation for  $x_2$ . To reach highest accuracy, the two steps should be close to, but not include, the final portion of the melting peak.

When using continuous DSC for purity determination, the data must be corrected for instrument lag and F must be corrected for the omitted portion E as shown in Fig. 4.42 for testosterone. Computer programs exist to optimize the fit to a linear curve. Over-correction would give a downward deviation instead of the upward deviation. This purity determination is only applicable if there is solubility of A and B in the melt, but no solubility of B in crystals of A (eutectic system).

**Thermochemistry.** Measurements of changes in enthalpy during chemical reactions are the basic tools of the branch of thermal analysis called thermochemistry. The thermodynamic description for a sample reaction of hydrogen with oxygen to water is given in Fig. 4.43. The top equation shows the differential change of the enthalpy with temperature, pressure, and composition, as discussed in Chap. 2. The integration of the enthalpy for the case of constant pressure and composition can be done with help of the experimental heat capacity  $C_p$ , obtainable by adiabatic calorimetry or DSC. The boxed chemical equation represents the reaction to be discussed. The next equation expresses the differential changes in H with composition

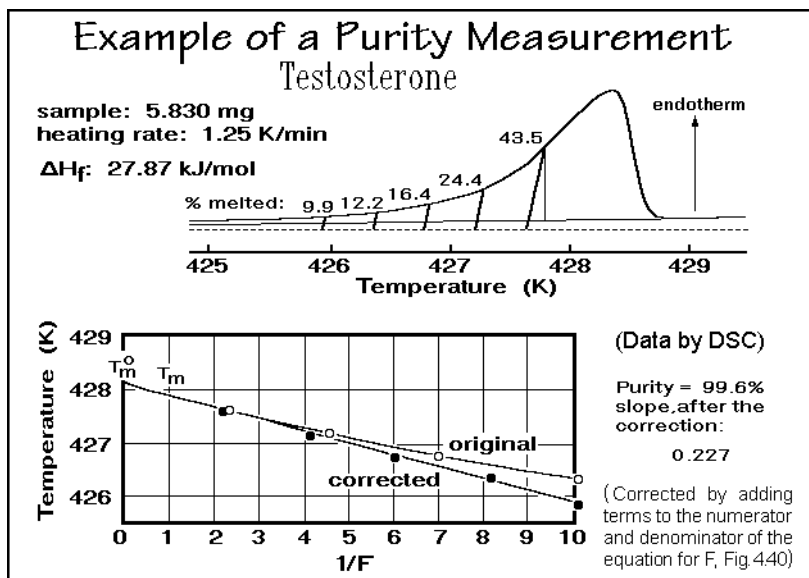
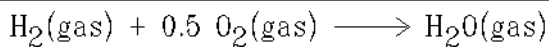


Fig. 4.42

### Thermochemical Calculations

$$dH = \left(\frac{\partial H}{\partial T}\right)_{p,n} dT + \left(\frac{\partial H}{\partial p}\right)_{T,n} dp + \sum_i \left(\frac{\partial H}{\partial n_i}\right)_{T,p, n \neq n_i} dn_i$$



at constant T and p:

$$dH = \left(\frac{\partial H}{\partial n_{\text{H}_2}}\right) dn_{\text{H}_2} + \left(\frac{\partial H}{\partial n_{\text{O}_2}}\right) dn_{\text{O}_2} + \left(\frac{\partial H}{\partial n_{\text{H}_2\text{O}}}\right) dn_{\text{H}_2\text{O}}$$

$$dn_{\text{H}_2} = 2.0 dn_{\text{O}_2} = -dn_{\text{H}_2\text{O}}$$

$$\Delta H(298) = -H_{\text{H}_2}^{\circ}(298) - 0.5H_{\text{O}_2}^{\circ}(298) + H_{\text{H}_2\text{O}}^{\circ}(298)$$

$H^{\circ}$  = partial molar enthalpy  $\partial H / \partial n$

$$\Delta H(298) = \Delta U(298) - 0.5RT = -241.83 \text{ kJ/mol}$$

$$\text{enthalpy of formation: } H_f^{\circ}(298)_{\text{H}_2\text{O}} = -241.83 \text{ kJ/mol}$$

Fig. 4.43

at constant T and p for the indicated reaction, usually measured by bomb calorimetry (Fig. 4.30). The correlations between the differential changes of the concentrations during the chemical reaction and the integrated change for one mole of gaseous water are given next. It is easy to calculate  $\Delta U$  from  $\Delta H$  as long as all gases can be treated as ideal gases (i.e.,  $pV = nRT$ ,  $p\Delta V = \Delta nRT$ ). The experimental data were taken at

298.15 K, the standard thermochemical reference temperature. The value of  $\Delta U(298)$  ( $= -240.59 \text{ kJ mol}^{-1}$ ) is only little different from  $\Delta H$ .

Absolute values for  $H^\circ$ , the partial molar enthalpies, are not known. For chemical changes of interest it is, however, not necessary to know the absolute value of  $H^\circ$  for the elements since the same value enters into the computations for all compounds containing the same element. One can thus fix  $H^\circ$  of the elements arbitrarily to any value. Simplest is to set  $H^\circ$  of the stable element at 298.15 K equal to zero. The  $\Delta H$  at 298 K and atmospheric pressure of a reaction leading from elements to a compound is then called the enthalpy of formation and written  $\Delta H_f^\circ(298)$ , as shown in Fig. 4.43. The enthalpies of formation are widely tabulated. Furthermore, since all enthalpies are functions of state, one can make a compound in any sequence of reactions and obtain the same heat of reaction, as long as the initial and final states are the same. By adding the appropriate enthalpies of reactions, one can also get the enthalpies of formation which are not directly measurable. Figure 4.44 illustrates the evaluation of the enthalpy of formation of ethane,  $\text{C}_2\text{H}_6$ , which cannot be made out of C and  $\text{H}_2$ . Enthalpies of formation at other temperature can be calculated using the appropriate

### Thermochemistry, Example Calculation

Evaluation of  $H_f^\circ(298)$  for ethane,  $\text{C}_2\text{H}_6$ :

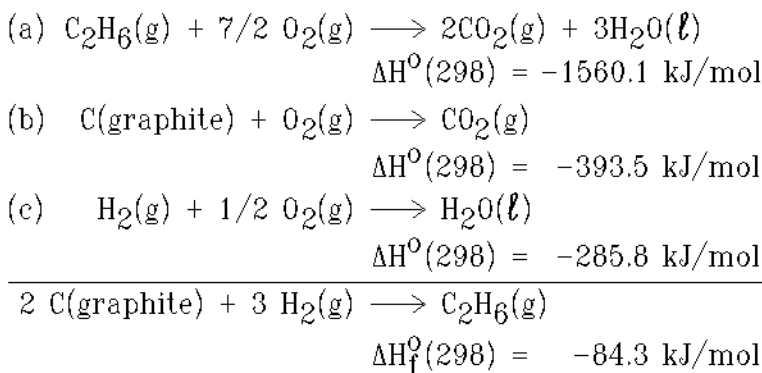


**Fig. 4.44**

heat capacities for the compounds as well as for the elements. The enthalpies of formation of elements at temperatures higher or lower than 298 K are not zero.

Typical thermochemical data are listed in Table 4.3. Note that the table contains data on free enthalpy and entropy, but  $\Delta H$  is easily computed from:  $\Delta H = \Delta G - T\Delta S$ . For wider ranges of temperature the heat capacity cannot be treated as a constant, as is discussed in Chap. 2. The data in Table 4.3 can also be used to compute equilibrium constants, as shown in any introductory text on physical chemistry. The combination of thermochemical measurements that produce heats of reaction at fixed temperatures and thermophysical measurements that yield heat capacities permits a

**Table 4.3.** Thermochemical Data at 298.15 K

Substance	$\Delta G_f^\circ$ kJ mol <sup>-1</sup>	$S^\circ$ J K <sup>-1</sup> mol <sup>-1</sup>	$C_p^\circ$ J K <sup>-1</sup> mol <sup>-1</sup>
Hydrogen, H <sub>2</sub> (g)	0.0	130.6	28.84
Sodium, Na (c)	0.0	51.0	28.41
Sodium chloride, NaCl (c)	-384.0	72.4	49.71
Sodium sulfate, Na <sub>2</sub> SO <sub>4</sub> ·10·H <sub>2</sub> O (c)	-3644.0	592.9	587.41
Sodium carbonate, Na <sub>2</sub> CO <sub>3</sub> (c)	-1047.7	136.0	110.50
Calcium, Ca (c)	0.0	41.6	26.27
Calcium oxide, CaO (c)	-604.2	39.7	42.80
Calcium carbonate, CaCO <sub>3</sub> (c)	-1128.8	92.9	81.88
Aluminum, Al (c)	0.0	28.3	24.34
Aluminum oxide, Al <sub>2</sub> O <sub>3</sub> (c)	-1576.4	51.0	78.99
Carbon C (diamond)	+2.9	2.4	6.06
Carbon C (graphite)	0.0	5.7	8.64
Carbon monoxide, CO (g)	-137.3	197.9	29.14
Carbon dioxide, CO <sub>2</sub> (g)	-394.4	213.6	37.13
Methane, CH <sub>4</sub> (g)	-50.8	186.2	35.71
Acetylene, C <sub>2</sub> H <sub>2</sub> (g)	+209.2	200.9	43.93
Methanol, CH <sub>3</sub> OH (l)	-166.3	126.8	81.60
Ethanol, C <sub>2</sub> H <sub>5</sub> OH (l)	-174.8	160.7	111.46
Oxygen, O <sub>2</sub> (g)	0.0	205.0	29.36
Water, H <sub>2</sub> O (l)	-237.2	69.9	75.30
Water, H <sub>2</sub> O (g)	-228.6	188.72	33.58
Chlorine, Cl <sub>2</sub> (g)	0.0	223.0	33.93
Hydrochloric acid, Hcl (g)	-95.3	186.7	29.12
Copper, Cu (c)	0.0	33.3	24.47
Copper oxide, CuO (c)	-127.2	43.5	44.40
Copper sulfate, CuSO <sub>4</sub> (c)	-661.9	113.4	100.80
Copper sulfate, CuSO <sub>4</sub> ·5H <sub>2</sub> O (c)	-1879.9	305.4	281.20
Iron, Fe (c)	0.0	27.2	25.23
Iron oxide, Fe <sub>2</sub> O <sub>3</sub> (c, hematite)	-741.0	90.0	104.60
Iron oxide Fe <sub>3</sub> O <sub>4</sub> , (c, magnetite)	-1014.2	146.4	--,--

full description of the energetics of systems at all temperatures. The pressure-dependence is usually of less importance, but can be treated in analogy to the temperature dependence by evaluation of  $(\partial H/\partial p)_{T,n}$  in addition to  $(\partial H/\partial T)_{p,n}$ .

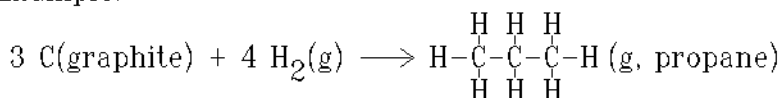
A simple method to obtain at least approximate heats of reaction for covalently bound molecules makes use of heats of atomization and bond energies, as outlined in Fig. 4.45. This method is particularly important for most small organic molecules and flexible, linear macromolecules, the main subjects of this course. To find the heat of reaction, the endothermic heats (+) of breaking all bonds of the reactants to make

## Calculations Based on Bond Energies

(assumes identical, covalent bonds in different molecules)

Procedure: A. Separate initial materials into atoms  
B. Reconnect into the final materials

Example:



$$\begin{array}{rcl} 1. \text{ atomize all:} & 3 \times 718.4 + 8 \times 217.9 & = \quad 3898 \text{ kJ} \\ 2. \text{ bond to propane:} & 2 \times 348 + 8 \times 413 & = -4000 \text{ kJ} \\ \text{heat of reaction:} & & \underline{\underline{-102 \text{ kJ}}} \\ \text{experimental value:} & & -104 \text{ kJ} \end{array}$$

**Fig. 4.45**

atoms are added to the exothermic heats (-) of reconnection of the atoms to form the products. This method is based on the assumption that covalent bonds have always the same bond energy, independent of the structure details, an assumption that is not always true. Table 4.4 contains a table of all common bonds and elements in covalent molecules, and Fig. 4.45 illustrates the calculation of the heat of reaction of propane. In case larger discrepancies occur, one can still use the table of Table 4.4 to discuss the deviation of the bonding from the norm. Poor fits are found for the following three examples: conjugated double bonds relative to isolated ones, differences between  $\text{>C=O}$  and  $\text{O=C=O}$ , and the presence of polar bonding.

**Table 4.4.** Heats of Atomization and Bond Energies

Element	Atomization	H-	C-	C=	C≡	N-	N=	N≡	O-	O=
H	217.9	436	413	-	-	391	-	-	463	-
C	718.4	413	348	615	812	292	615	891	351	728
N	472.6	391	292	615	891	161	418	946	-	-
O	247.5	463	351	728	-	-	-	-	139	485
F	76.6	563	441	-	-	270	-	-	185	-
Si	368.4	295	290	-	-	-	-	-	369	-
P	314.5	320	-	-	-	-	-	-	-	-
S	222.8	339	259	477	-	-	-	-	-	-
Cl	121.4	432	328	-	-	200	-	-	203	-
Br	111.8	366	276	-	-	-	-	-	-	-
I	106.6	299	240	-	-	-	-	-	-	-

<sup>a</sup> at atmospheric pressure, 101,325 Pa, and 298 K, in  $\text{kJ mol}^{-1}$  of atom or bond indicated.

**Thermodynamic Functions of Three Carbon Allotropes** [19]. Low temperature heat capacities of three allotropes of carbon are shown in Fig. 4.46. The data were derived from adiabatic calorimetry. Based on the discussion of heat capacities of Sect. 2.3 and the known chemical structure of the allotropes given in Fig. 2.109, the thermal behavior can be easily understood. Fullerene,  $C_{60}$ , is a small molecule. All strong bonds lie in the surface of the almost spherical molecule. The low-temperature heat

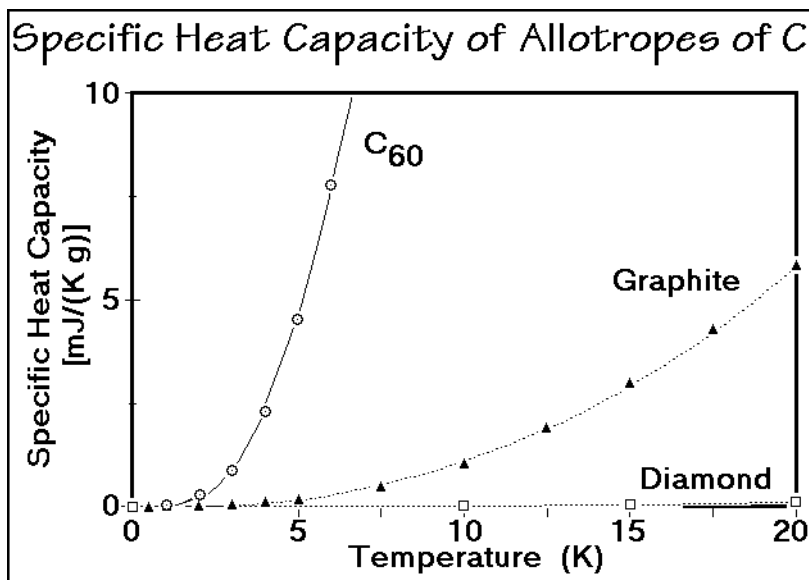


Fig. 4.46

capacity involves the molecules as a whole. Because of the weak interaction and the large mass of the  $C_{60}$  molecules, there are six low-frequency intermolecular vibrations per  $C_{60}$  that account for the high low-temperature specific heat capacity. Diamond, in contrast, consists of a continuous, tightly-bonded, three-dimensional network and has, as a result only a negligible low-temperature specific heat capacity. Graphite with its two-dimensional strong network is intermediate in specific heat capacity since some of the trans-planar vibrations are of low frequency and contribute also at low temperature to the heat capacity.

Figure 4.47 shows that at somewhat higher temperature, the specific heat capacities of graphite and  $C_{60}$  become almost equal. The surface structure of the fullerene and the layer-structure of graphite are quite similar, they consist of rings of conjugated double bonds. Diamond lags behind in gaining heat capacity because it lacks the low-frequency, intermolecular  $C_{60}$  and inter-planar graphite vibrations. Since the  $sp^3$  bonds are somewhat weaker than the conjugated double bonds, diamond ultimately gains the higher heat capacity at about 1000 K. At sufficiently high temperature, perhaps about 2000 K, all three allotropes must have the same heat capacity since they all have the same number of vibrational modes of motion. Dulong Petit's rule,  $C_V = 3R = 24.9 \text{ J K}^{-1} (\text{mol of carbon atom})^{-1}$  suggests the same vibrational heat capacity for all three carbon allotropes.



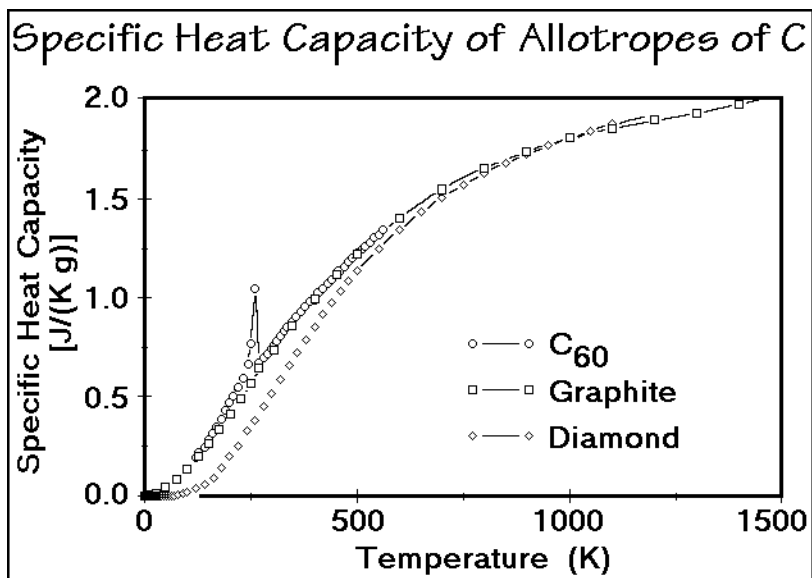


Fig. 4.47

Figure 4.47 shows that fullerene has an additional small transition at 256 K. Analysis of the entropy of transition of  $27\ J\ K^{-1}\ mol^{-1}$  and mobility by solid-state NMR proved a crystal to plastic-crystal transition as is described in Sect. 2.5.3. Fullerene is the plastic crystal material with the widest known temperature range. Its practical applications have not been fully explored. Figure 4.48, shows the integral thermodynamic functions that can be derived from the measured heat capacities.

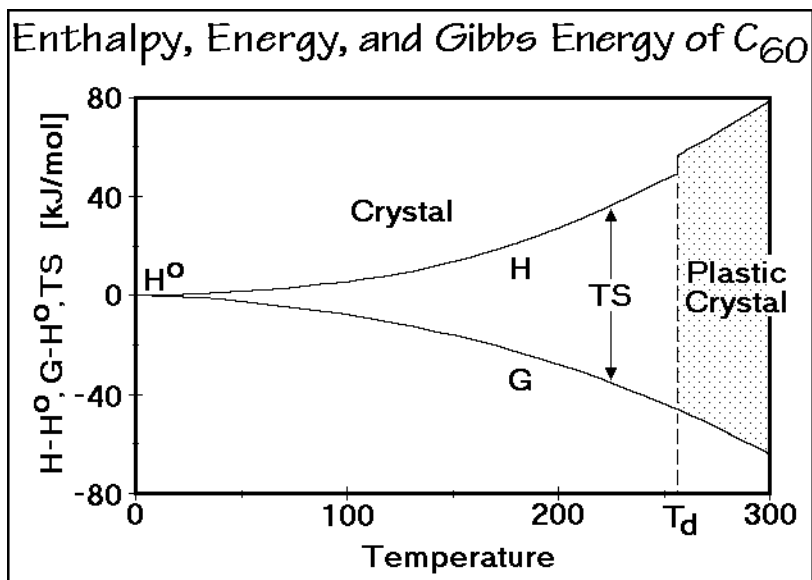


Fig. 4.48

**Thermodynamic Functions of Paraffins** [20]. Another example of heat capacity measurements by adiabatic calorimetry and DSC is given by the paraffins. Figure 4.49 illustrates heat capacities of some normal paraffins of short chain length  $C_xH_{x+2}$ . The drawn-out lines represent the computed heat capacities based on vibrational contributions fitted using the ATHAS system (see Sect. 2.3). Two observations can be made from these data. First, at higher temperature there is a constant increment in

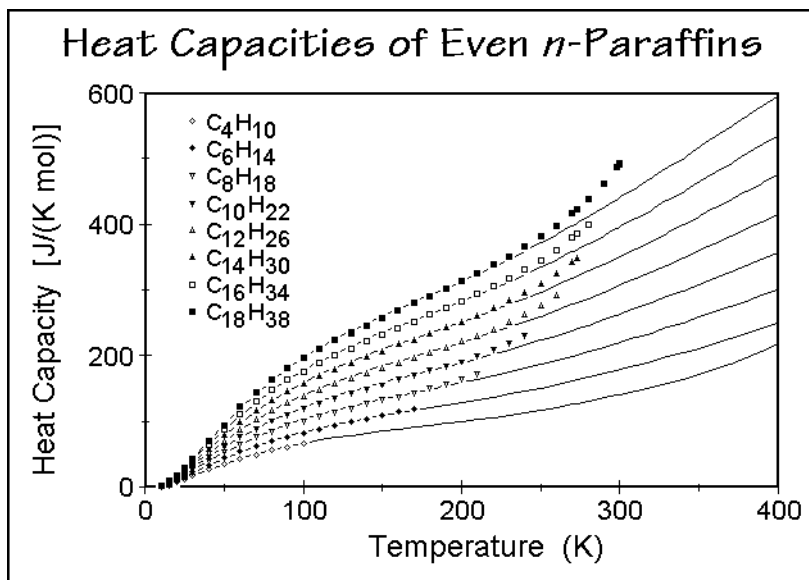


Fig. 4.49

heat capacity for each additional  $CH_2$ -group, second, the heat capacities increase beyond the computed vibrational contributions as they approach the melting and transition region. As in polyethylene, the increase is attributed to local, large-amplitude, conformational motion.

The heat capacity for a longer alkane, pentacontane,  $C_{50}H_{102}$ , is shown in Fig. 4.50 and integrated to the thermodynamic functions  $H$ ,  $G$ , and  $S$  in Fig. 4.51. This paraffin approaches the vibrational characteristics and thermodynamic behavior of polyethylene (see Sect. 2.3). The skeletal vibrations continuously approach those of polyethylene, while the group vibrations are practically the same for  $CH_2$ -groups in polyethylene and alkanes.

The use of the thermodynamic data for a discussion of stability of crystals is demonstrated in Fig. 4.52. The differences in crystal structure and melting temperatures of successive  $n$ -alkanes have been linked to the symmetries of odd and even  $CH_2$ -sequences. Note, that planar zig-zag chains of odd-numbered sequences of carbon atoms in a molecular backbone point with their final bonds into the same direction, while even ones point into opposite directions. Odd paraffins have an orthorhombic, rectangular layer-structure, while the even ones up to  $C_{24}H_{50}$  are triclinic with oblique layers. From structural analyses, orthorhombic crystals can accommodate even and odd chains without difference in packing density. The triclinic

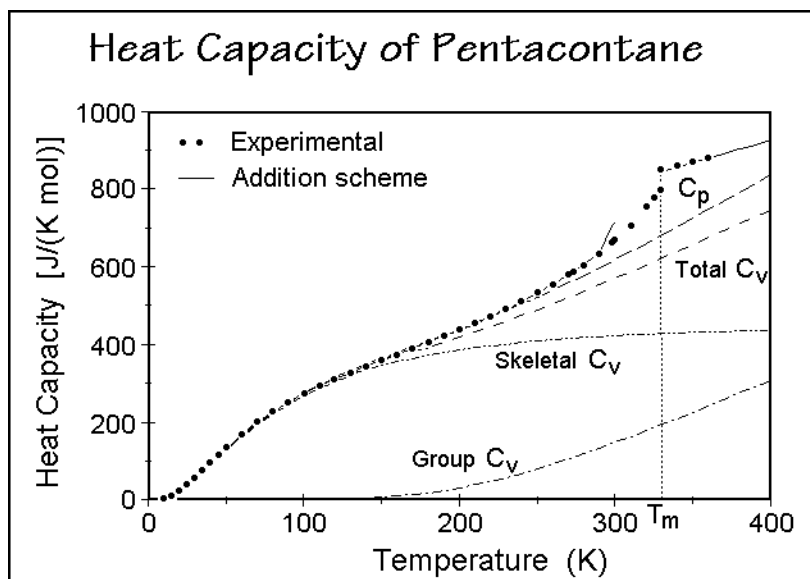


Fig. 4.50

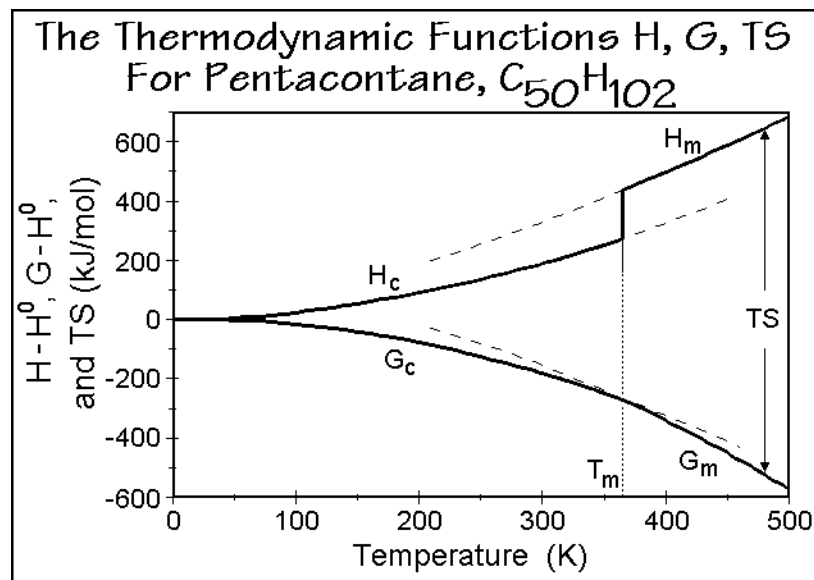


Fig. 4.51

crystals, in contrast, can only accommodate even molecules, but with a higher heat of fusion than the orthorhombic crystals. Figure 4.52 represents the thermodynamic reasoning for this odd/even effect. Structural requirements force the odd  $n$ -paraffins into the orthorhombic phase, which, in turn, requires a lower melting temperature to reach the common melt. For the even paraffins there is the structurally more favorable

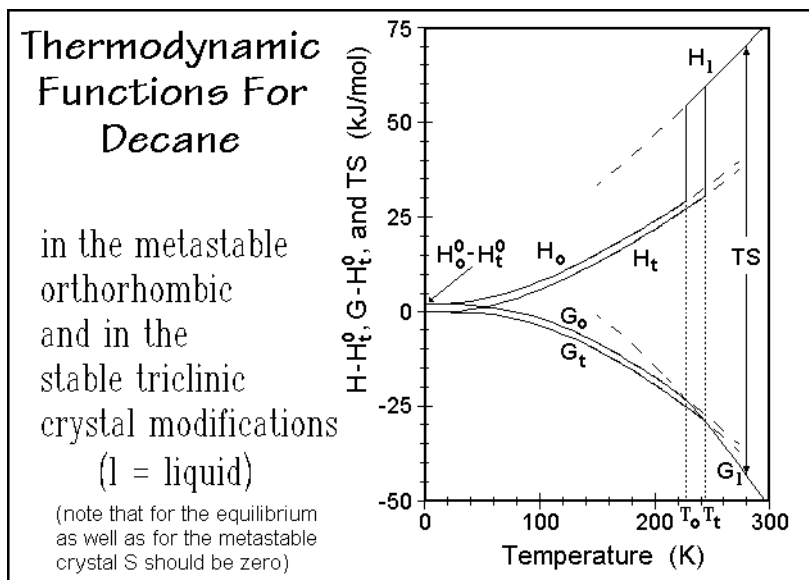


Fig. 4.52

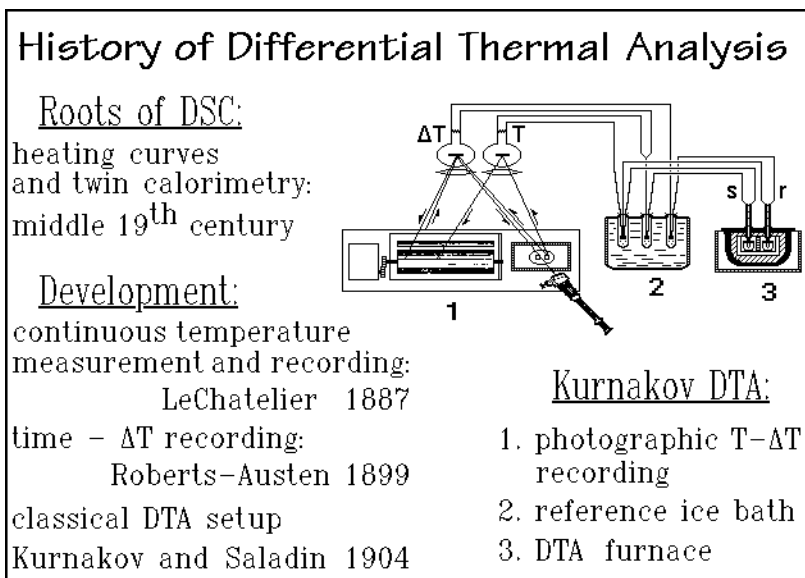
oblique packing, making the orthorhombic phase less stable, as shown in the figure. The skeletal vibration frequencies are lower in the orthorhombic crystal, but cannot overcome the heat of fusion effect.

## 4.3 Differential Scanning Calorimetry

### 4.3.1 Principle and History

Differential scanning calorimetry, DSC, is a technique which combines the ease of measurement of heating and cooling curves as displayed in Fig. 4.9 with the quantitative features of calorimetry (see Sect. 4.2). Temperature is measured continuously, and a differential technique is used to assess the heat flow into the sample and to equalize incidental heat gains and losses between reference and sample. Calorimetry is never a direct determination of the heat content. Measuring heat is different from volume or mass determinations, for example. In the latter cases the total amount can be established with a single measurement. The heat content, in contrast, must be measured by beginning at zero kelvin where the heat content is zero, and add all heat increments up to the temperature of interest.

In Fig. 4.53, a brief look is taken at the history of the DSC. Both, heating curves and calorimetry had their beginning in the middle of the nineteenth century. Progress toward a DSC became possible as soon as continuous temperature monitoring with thermocouples was possible (see Fig. 4.8), and automatic temperature recording was invented (see also Sect. 4.1). These developments led to the invention of differential thermal analysis, DTA. In Sect. 2.1.3 an introduction to thermal analysis and its instrumentations is given.

**Fig. 4.53**

Le Chatelier<sup>1</sup> seems to have been first to record temperature as a function of time in heating curves such as shown in Fig. 4.9. He used a mirror galvanometer to determine the thermocouple output and recorded the position of the galvanometer mirror on a photographic plate with a beam of light. Complete DTA, consisting of measurement of temperature difference,  $\Delta T$ , as a measure of the heat-flow rate, sample temperature,  $T_s$ , and time,  $t$ , was first performed at the beginning of the 20<sup>th</sup> century in the laboratories of Roberts–Austin, Kurnakov, and Saladin. The classical DTA setup of Kurnakov is shown in Fig. 4.53. The key elements of the DTA are, as today, the furnace for equal environment of reference and sample, a means to continuously measure  $T_s$  and  $\Delta T$ , and a recording device that also fixes the time,  $t$ , by being driven with a constant speed motor. The final output is a typical DTA plot of  $T_s$  and  $\Delta T$  versus  $t$ .

Very little further progress in instrumentation was made until the 1950s. A brief summary of the classical DTA and DSC operating system, instrumentation, rules of data treatment, and the differences between DSC and DTA are given in Appendix 9. The first milestone was reached by 1952 when about 1,000 research reports on DTA had been published. At that time, DTA was mainly used to determine phase diagrams, transition temperatures, and chemical reactions. Qualitative analysis (fingerprinting) was developed for metals, oxides, salts, ceramics, glasses, minerals, soils, and foods.

The second stage of development was initiated by the use of electronics in measurement and recording. It became possible to quantitatively measure the heat

<sup>1</sup> Henry-Louis Le Chatelier, 1850–1936, Professor of Chemistry at the University of Paris, France. Besides his work on thermocouples, he is best known for the principle of Le Chatelier, which predicts the direction on a chemical or physical change caused by a variation of temperature, pressure, or concentration.

flow, i.e., do calorimetry. The DTA used for quantitative measurement of heat was then called DSC, differential scanning calorimetry [21]. A higher accuracy in determining  $\Delta T$  and a decrease in heat losses through smaller sample sizes and faster heating rates were critical for the development of DSC. Next, the electronic data generation allowed the direct coupling with computers. Presently DSC is used in almost all fields of scientific investigation and has proven of great value for the analysis of metastable and unstable systems. By 1972 the annual number of research publications using DSC and DTA had reached 1,000, as many as were published in the first 50 years. The biannual reviews given by the journal *Analytical Chemistry* offer a quick introduction into the breadth and importance of DTA and DSC.

By now it is impossible to count the research papers dealing with DSC since it has become an accepted analysis technique and is not listed as a special research tool in the title or abstract. The main development of DSC since the 1990s has gone towards the improvement of computers and their software. Most recent was the invention of temperature-modulated DSC, discussed in Sect. 4.4 [22]. The effort spent on developing suitable computer software has, perhaps, slowed advances in the improvement of calorimeters by hiding instrumentation problems in data-treatment routines.

Key research papers in DSC are often presented in *Thermochimica Acta* and the *Journal of Thermal Analysis and Calorimetry*. Progress in DSC is also reported in the Proceedings of the International Conferences on Thermal Analysis and Calorimetry, ICTAC. The annual Proceedings of the Meeting of the North American Thermal Analysis Society, NATAS, are also a useful source of information.

### 4.3.2 Heat-flux Calorimetry

The principle of heat-flux calorimetry is illustrated with a schematic of a classical DTA in Appendix 9. Accuracies of heat measurements by DSC range from 10% to 0.1%. Temperature can be measured to  $\pm 0.1$  K. Typical heating rates vary between 0.1 and 200 K min<sup>-1</sup>. Sample masses can be between 0.05 and 100 mg. The smaller masses are suitable for large heat effects, such as chemical reactions (explosions), phase transitions, or when fast kinetics is studied. The larger masses are necessary for assessment of smaller heat effects as in studies of heat capacity or glass transitions. Sensitivities are hard to estimate, but effects as small as 1.0  $\mu\text{J s}^{-1}$  are observable.

A frequent confusion in reporting of data is that the direction of the endotherm may be plotted downwards or upwards. The first arises when plotting  $\Delta T = (T_s - T_r)$  instead of  $\Delta T = (T_r - T_s)$ . To avoid confusion, the endotherm or exotherm direction must be marked on DSC traces. Next, several modern, commercial, DSCs are introduced. They were selected because of their differences in design and performance. All these instruments are usable between 150 and 1000 K.

Special instrumentation exists for measurements under extreme conditions and is summarized in Appendix 10. A brief summary with references is given of very low and very high temperature measurements, high-speed DTA, DTA at very high pressures, and microcalorimetry in form of a DTA coupled with atomic force microscopy, AFM. Note that the term microcalorimetry is also used when small amounts of heat are measured for larger samples, as in the calorimeter of Fig. 4.39.

Slow calorimetry can be done isothermally by direct observation, as described in Sect. 4.2, and intermittently by checking the progress after appropriate time intervals, as in Figs. 3.98 and 4.41.

Figure 4.54 illustrates the measuring head of a modern heat-flux DSC of TA Instruments Inc., Type Q 1000 with the needed equation for data evaluation. The shown constantan body is solidly connected to the bottom of a measuring chamber

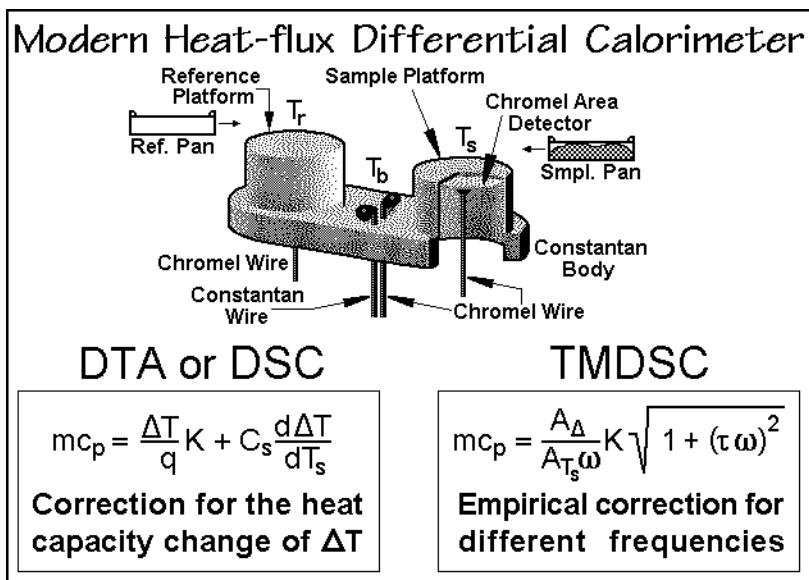


**Fig. 4.54**

made of silver which also permits a conditioned purge gas, usually nitrogen, to flow through. The internally heated furnace is connected to cooling rods and the controlled temperature is applied to the bottom of the chamber, producing a regulated temperature  $T_b$ . The sample and reference temperatures,  $T_s$  and  $T_r$  are measured separately with the chromel area detectors against the constantan reference wire shown in the figure. The heat-flow rate into the sample is proportional to  $\Delta T = T_r - T_s$  and corrected by software for the asymmetry in thermal resistance and capacitance to the reference and sample platforms, as well as for the heating rate imbalance. Appendix 11 gives more information on the online corrections developed for this calorimeter (Tzero™ method).

The heat-flow rate of the sample calorimeter, consisting of a pan and the sample, and the reference calorimeter, consisting usually of an empty pan, is governed by the rate of temperature change,  $q$  (in  $K \min^{-1}$ ), and the heat capacity,  $C_p$  (in  $J K^{-1}$ ). The heat capacity measured at constant pressure,  $p$ , and composition,  $n$ , can then be represented by  $C_p = (\partial H / \partial T)_{p,n}$ , with  $H$  being the enthalpy and  $T$ , the temperature. The overall heat capacity of the sample calorimeter is written as  $C_s = (mc_p + C_r)$ , where  $m$  is the sample mass,  $c_p$  is the specific heat capacity of the sample per unit mass, and  $C_r$  is the heat capacity of the empty calorimeter pan. The empty sample and reference pans are assumed to have the same heat capacity  $C_r$  so that in a differential measure-

ment  $mc_p$  can be established directly after calibration of  $K$ , the Newton's law constant. Corrections for remaining asymmetry are made by a baseline run with the two empty calorimeters which is then subtracted from the sample and calibration runs. The measurements consist, thus, of three separate runs over the same temperature range, namely, baseline, calibration, and sample run. The details of the mathematical description of the measurements are given in Sect. 4.3.5.

On the left of Fig. 4.55 the changes of the temperatures are illustrated for a standard DSC experiment. The data were calculated with  $K$  represented by  $C_r/20 \text{ J K}^{-1} \text{ s}^{-1}$  and using the Fourier equation of heat flow (see Sect. 4.3.5). The temperature of the constantan body,  $T_b$ , which is controlled by the heater starts at time

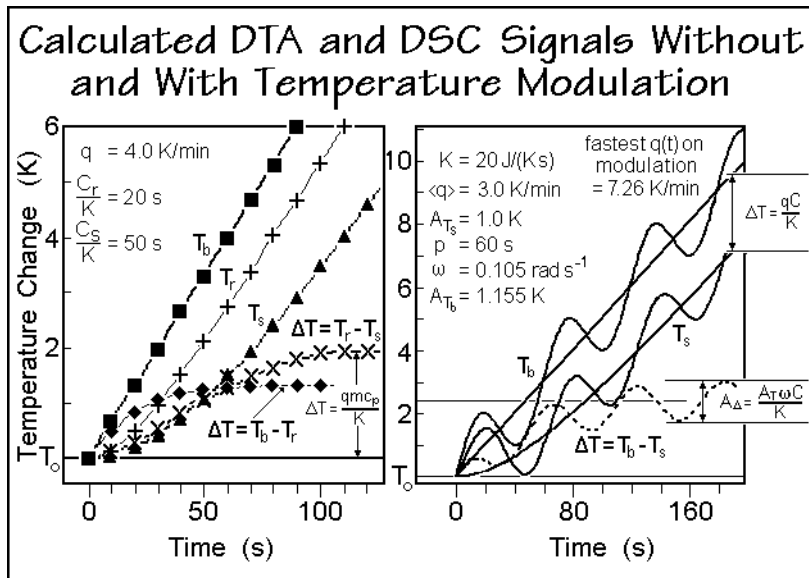


Fig. 4.55

zero with a linear increase. After about 100 s, the reference and sample temperatures reach a steady state, i.e., both change with the same heating rate,  $q$ , as the  $\Delta T$  become constant. At steady state, the heat capacity can then be represented as shown by the left equation in Fig. 4.54. The second term on the right-hand side is a small correction term, needed since the sample and reference calorimeters change their heat capacities differently with temperature, i.e.,  $T_r$  and  $T_s$  in Fig. 4.55 are not strictly parallel to  $T_b$ . This correction can be calculated and needs no further measurement. To have a negligible temperature gradient within the sample, also, is not a stringent condition as long as steady state is kept. A temperature gradient of 2.0 K across a sample of crystalline polyethylene, for example, will cause an error in the measurement of the magnitude of  $dc_p/dT$ , of about 0.3% at 300 K. This is less than the commonly accepted error for such measurements.

Modulating the temperature (see Sect. 4.4, TMDSC [22]) the measurement of  $c_p$  is just as easy as long as the condition of steady state and negligible temperature gradients within the sample can be maintained. In Fig. 4.55, the curves on the right



illustrate a temperature-modulated DSC, a TMDSC in a sinusoidal mode. One observes that the sinusoidal modulation reaches a constant average after a few cycles, and that the sliding averages over one modulation period yield the same curves as seen in standard DSC, and lead to the so-called *total* heat capacity. Next, a simple subtraction of these averages from their instantaneous values yields the pseudo-isothermal *reversing* signals, to be discussed in Sect. 4.4. A simple calculation of  $mc_p$ , using the equation on the bottom right of Fig. 4.54 without consideration of the correction term in the square root, is possible only if steady state is not lost during modulation, the temperature gradient within the calorimeters is negligible, and  $K$  is calibrated at the given frequency. The modulation amplitudes  $A_\Delta$  and  $A_{T_s}$  represent the reversing temperature difference and sample temperature and are obtained as the first harmonic of their Fourier-transform. The frequency,  $\omega$ , is given by  $2\pi/p$ , where  $p$  represents the modulation period in seconds. As long as the studied process is reversible, the total and the reversible  $C_p$  should be identical. Irreversible processes should not show in the reversing signal. The conditions for quantitative TMDSC are more stringent than for the standard DSC, because if even a small temperature gradient is set up within the sample during the modulation, each modulation cycle reverses this gradient and leads to smaller positive and negative heat-flow rates which depend on the unknown thermal conductivities. A negligible temperature gradient within the sample requires that the sample calorimeter oscillates in its entirety. An empirical solution to this problem is given in the right equation of Fig. 4.54 with  $\tau$  representing a characteristic time constant. This method is described in Figs. 4.94 and 4.95, below. For high frequencies,  $\tau$  becomes itself frequency dependent. With minor modifications and addition of the proper software, thus, any DSC can become a TMDSC. Even more important, any TMDSC can be used as a standard DSC by turning off the modulation. Most applications described in this Sect. 4.3 can usually be done better and faster by using standard DSC, and temperature modulation is the superior mode for most of the applications which are selected for discussion in Sect. 4.4.

Figure 4.56 shows a dual DSC cell with three measuring positions that can be used to make two measurements simultaneously. It is a further development of the DSC which is shown in Fig. A.9.2 as sketch A with only two measuring positions [23,24]. The temperature and temperature difference are measured with the chromel-alumel and chromel-constantan thermocouples. The heating block is made of silver for good thermal conductivity. The temperature range is 125 to 1000 K, the heating rate, 0.1 to 100 K min<sup>-1</sup>, the noise level is reported as  $\pm 5 \mu\text{W}$ , and the sample volume can be up to 10 mm<sup>3</sup>. Even more important than the capability to measure two samples simultaneously for comparison purposes is the ability to measure heat capacity in a single run by measuring a reference material and the sample at the same time. Full details and software, as well as a number of applications are given in the list of references at the end of the chapter [25].

A somewhat different DSC is shown in Fig. 4.57. The heating rate is controlled through the furnace temperature, as shown. The two sets of 28 thermocouples measure the heat-flow rates between the furnace and the pan for the sample and reference sides (thermopiles, vapor deposited on ceramics). The two central terminals bring the average  $\Delta T$  signal from the 56 thermocouples out to the computer, ready to be inserted into the equation on the left of Fig. 4.54.

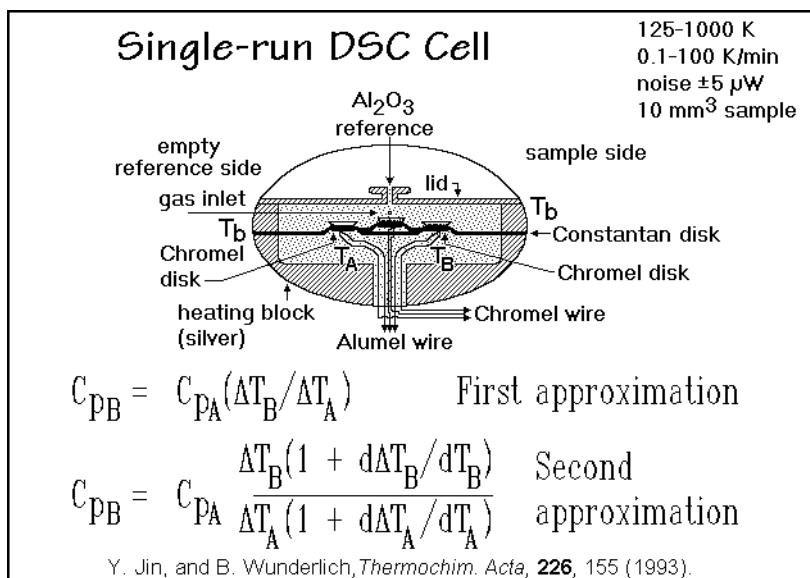


Fig. 4.56

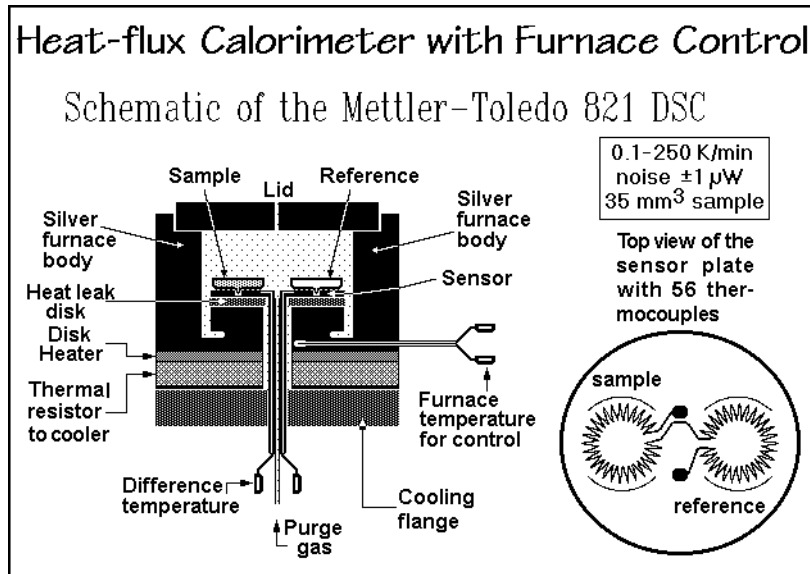
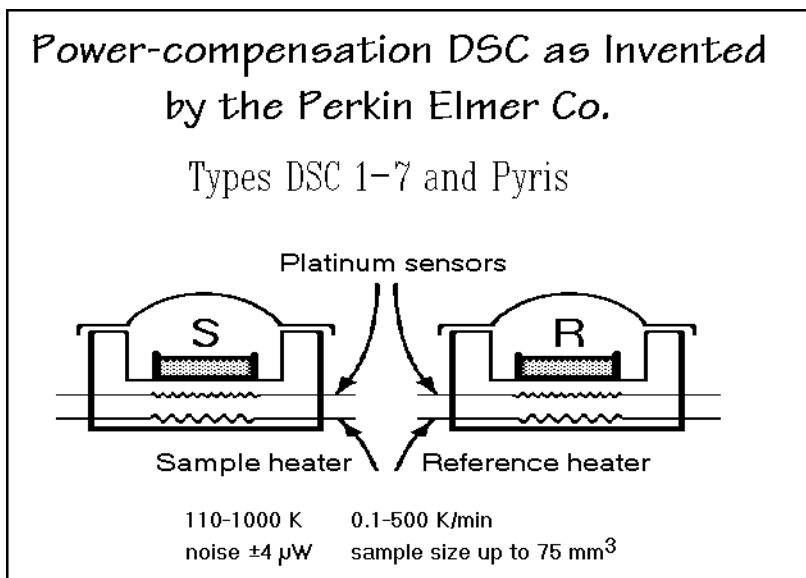


Fig. 4.57

### 4.3.3 Power Compensation DSC

A power compensation DSC uses a radically different measurement method. With its development in 1963, the name DSC was coined [21]. In Fig. 4.58 a schematic of sample and reference arrangement is drawn and some typical parameters are given.

**Fig. 4.58**

The sample and reference thermometers and heaters are platinum resistance thermometers (see Sect. 4.1). Instead of relying on heat conduction from a single furnace, governed by temperature difference, reference and sample are heated separately as required by their temperature and the temperature difference between the two furnaces. The two calorimeters are each less than one centimeter in diameter and are mounted in a constant temperature block. This instrument is, thus, a scanning, isoperibol twin-calorimeter (see Sect. 4.2).

The operation schematic is shown in Fig. 4.59. A programmer provides the average-temperature amplifier with a voltage that causes it to heat sample and reference calorimeters equally so that the average temperature increases linearly. The dotted line in the diagram of Fig. 4.60 represents this linear temperature increase of the average temperature,  $T_{\text{AV}}$ . If one assumes that initially both calorimeters are identical and the differential-temperature amplifier is not operating (open  $\Delta T$  loop), the temperatures of the reference,  $T_{\text{R}}$ , and sample,  $T_{\text{S}}$ , follow the solid, heavy line at the lower end of the diagram. If at time  $t_1$  the heat capacity of the sample calorimeter increases suddenly, the rate of change of the temperature of the sample calorimeter is reduced. At the same time, the rate of change of temperature of the reference calorimeter must increase to keep  $T_{\text{AV}}$  constant, as is shown by the lower and upper thin lines, respectively.

Mathematically this situation without a  $\Delta T$  loop is expressed by the upper three boxed equations in Fig. 4.60, where  $dQ_{\text{R}}/dt$  and  $dQ_{\text{S}}/dt$  are the heat-flow rates into the reference and sample calorimeters, respectively. The measured and true temperatures are represented by  $T^{\text{meas}}$  and  $T$ . For simplicity, one can assume that the proportionality constant  $K$  is the same for the sample and reference calorimeters. Differences are assessed by calibration. Both bottom equations are then equal to the power input from the average temperature amplifier,  $W_{\text{AV}}$  (in  $\text{W}$  or  $\text{J s}^{-1}$ ).

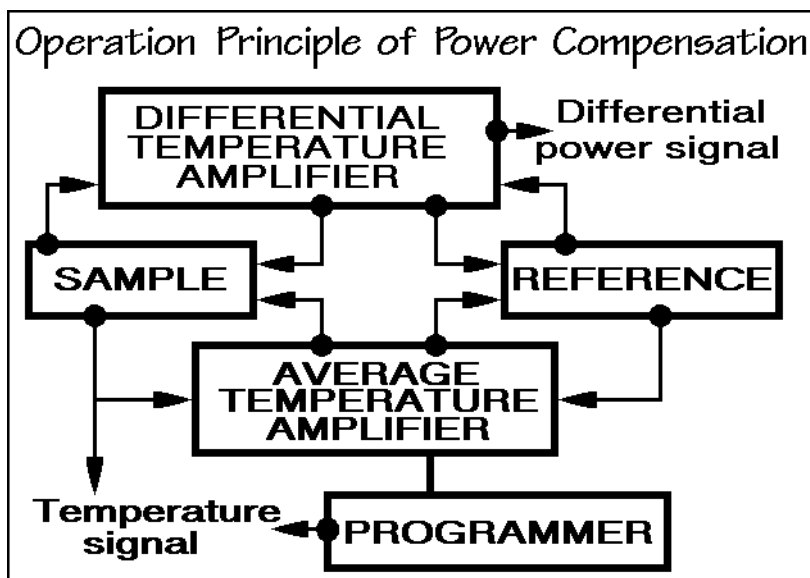


Fig. 4.59

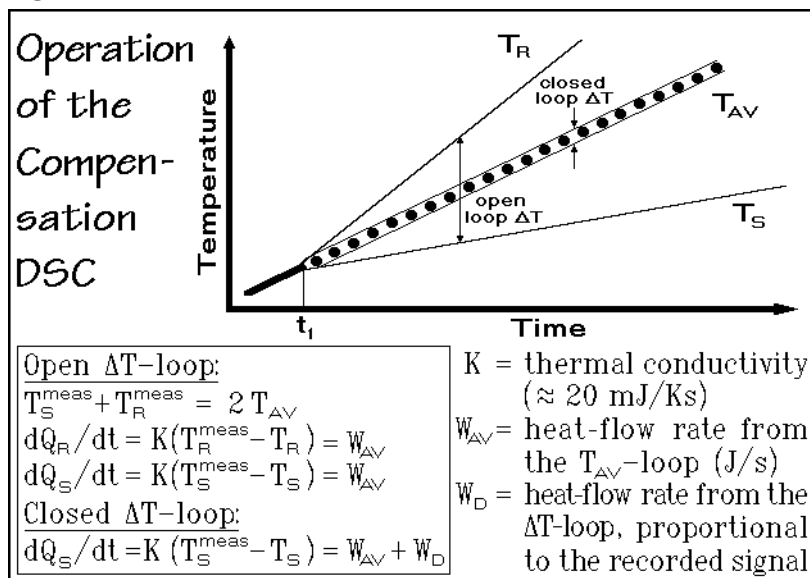


Fig. 4.60

The use of the upper, differential amplifier loop in Fig. 4.59 closes the  $\Delta T$  loop. The temperature-difference signal is directly amplified and a corresponding power is used to compensate the imbalance between the sample and reference calorimeter temperatures so that only a small temperature difference remains, as indicated in Fig. 4.60. This differential-power signal is also sent to the computer as  $W_D$ , the

differential heat-flow rate. The remaining temperature difference is in this way proportional to the differential power applied.

The mathematical description for the closed  $\Delta T$  loop is based on the equations of Fig. 4.60 which are rewritten as Eqs. (1) and (2) in Fig. 4.61. The amplifier gain,  $X$ , is introduced in Eq. (3). Combining Eqs. (1) and (2) yields Eq. (4), which one can reorganize into Eqs. (5) and (6) for  $\Delta T$  and  $W$ , respectively, the true differential

Final Operation Equations

$X = \text{amplifier gain in J/(Ks)}$

Closed  $\Delta T$ -loop

(1)  $W_{AV} = K(T_R^{meas} - T_R)$

(2)  $W_{AV} + W_D = K(T_S^{meas} - T_S)$

(3)  $W_D = X(T_R^{meas} - T_S^{meas}) = X\Delta T^{meas}$

(4)  $K(T_S^{meas} - T_S) = K(T_R^{meas} - T_R) + W_D$

(5)  $W_D = -K\Delta T^{meas} + (K\Delta T = W)$

(6)  $\Delta T^{meas} = (W - W_D)/K$

(7)  $W = W_D[(K/X) + 1] \approx W_D \text{ if } (K/X) \ll 1$

(8)  $\Delta T^{meas} = W/(K + X) \approx W/X \text{ if } K \ll X$

$W = K\Delta T$ , true differential heat-flow rate to establish equal temperature between the reference and sample.

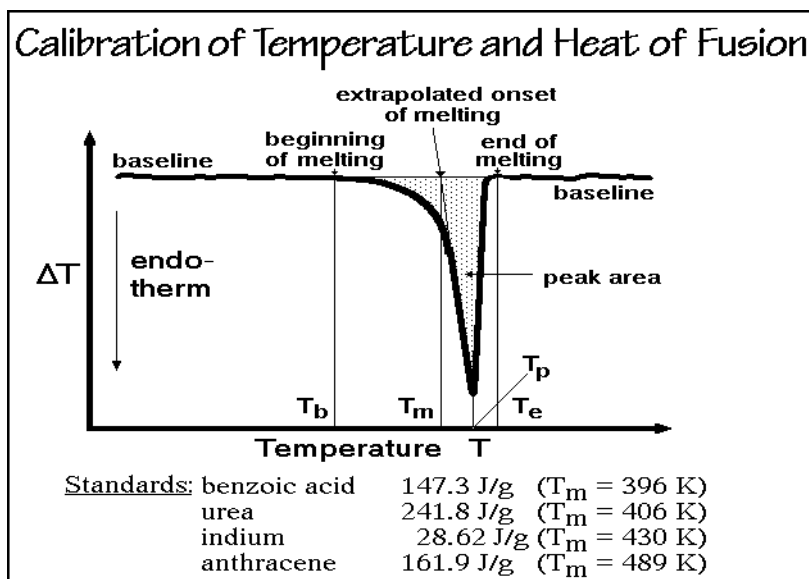
**Fig. 4.61**

temperature and power necessary for compensation calorimetry. The measured signal  $\Delta T^{meas}$  is made small by choosing a large  $X$ , as shown in Eq. (8), which can be derived by combining the equations indicated. It, however, cannot become zero, as required for true compensation calorimetry, since for zero  $\Delta T^{meas}$ ,  $W$  would also be zero. The “closed-loop” lines in Fig. 4.60 indicate that the measured caloric quantity of the power compensation DSC is also a temperature difference as in a heat-flux DSC.

One additional point needs to be considered. The commercial DSC is constructed in a slightly different fashion. Instead of letting the differential amplifier correct only the temperature of the sample calorimeter by adding power, only half is added, and an equal amount of power is subtracted from the reference calorimeter. This is accomplished by properly phasing the power input of the two amplifiers. A check of the derivations shows that the result does not change with this modification.

#### 4.3.4 Calibration

Differential scanning calorimetry is not an absolute measuring technique, calibrations are thus of prime importance. Calibrations are necessary for the measurement of temperature,  $T$  (in K); amplitude, expressed as temperature difference,  $\Delta T$  (in K) or as heat-flow rate,  $dQ/dt$  (in  $J\ s^{-1}$  or  $W$ ); peak area  $\Delta H$  (in J); and time,  $t$  (in s or min). Figure 4.62 shows the analysis of a typical first-order transition, a melting transition.

**Fig. 4.62**

The curve is characterized by its baseline and the peak of the (endothermic) process. Characteristic temperatures are, the beginning of melting,  $T_b$ , the extrapolated onset of melting,  $T_m$ , the peak temperature,  $T_p$ , and the point where the baseline is finally recovered, the end of melting,  $T_e$ . The beginning of melting is not a very reproducible point. It depends on the sensitivity of the equipment, the purity of the sample, and the degree to which equilibrium was reached when the sample crystallized. The extrapolated onset of melting is most reproducible if there is only a small temperature gradient within the sample and if the analyzed material melts sharply. The DSC curve should, under these conditions, increase practically linearly from an amplitude of about 10% of its deviation from the baseline up to the peak and show the heating rate as its slope when plotted against time or reference temperature. The extrapolation back to the baseline then gives an accurate measure of the equilibrium melting temperature,  $T_m$ .

If there is a broad melting range, it is better characterized by the melting peak temperature,  $T_p$ . It represents the temperature of the largest melting rate. The temperature of the recovery of the baseline  $T_e$  is a function of the design of the calorimeter. In Fig. 4.63 several reference materials are listed that may be used for temperature calibration to an accuracy of  $\pm 0.1$  K or better and for establishment of a link to the International Temperature Scale (ITS, see Appendix 8).

The next calibration concerns the area of the DSC trace or the amplitude at any one temperature. The peak area below the baseline in Fig. 4.62 can be compared with the melting peaks of standard materials such as the benzoic acid, urea, indium, or anthracene, listed at the bottom of the figure. The amplitudes measured from the baseline established in the heat-capacity mode of measurement are usually compared with the heat capacity of standard aluminum oxide in the form of sapphire. The heat capacity of sapphire is free of transitions over a wide temperature range and has been

Calibration of Temperature and $C_p$ using melting points or other first-order transitions		
cyclopentane	122.38 ●	●
cyclopentane	138.06 ●	GEFTA recommended
cyclopentane	179.72 ●	<i>Thermochimica Acta</i>
water	273.15 @	219, 333 (1993)
gallium	302.91 @	@
<i>p</i> -nitrotoluene	324.6 #	ITS 90 Fixed Point
naphthalene	353.4 #	
indium	429.75 @	
tin	505.08 @	#
lead	600.61 ●	Zone refined organic
zinc	692.68 @	compound (sublimes)

Heat-capacity table of  $\text{Al}_2\text{O}_3$  from 10 to 1650 K by:  
D. G. Archer, *J. Phys. Chem. Ref. Data*, 22, 1441 (1993).

Fig. 4.63

measured accurately by adiabatic calorimetry and reviewed by Archer in the reference listed at the bottom of Fig. 4.63. Although both calibration methods should give identical results, it is better to select the method that matches the application. For highest precision it is recommended to match the calibration areas or amplitudes with the measurement at a similar temperature.

A final calibration concerns time. Heating rates or modulations may not be constant over a wide temperature range, because of, for example, the effect of nonlinearity of the thermocouples (see Sect. 4.1). It is thus useful to occasionally check heating rate and modulation over the regions of temperature of interest. A good stopwatch is usually sufficient for this check.

Measurements at different heating rates may lead to different amounts of instrument-lag, i.e., the temperature marked on the DSC trace can only be compared to a calibration of equal heating rate and baseline deflection. A simple lag correction makes use of the slope of the indium melting peak when plotted vs. sample temperature as a correction to vertical lines on the temperature axis. In some commercial DSCs this lag correction is included in the analysis program. It must be considered, however, that different samples have different thermal conductivities and thermal resistances so that different lags are produced as shown, for example, in Fig. 4.94, for an analysis with TMDSC.

### 4.3.5 Mathematical Treatment

The mathematical treatment of calorimetry is complicated since there are no perfect insulators for heat. Even a vacuum is no barrier since radiation can transport heat, particularly at elevated temperatures. For this reason one uses differential techniques where reference and sample calorimeters are placed in symmetrical environments with

similar heat losses and gains. The differential measurement should then need only a small asymmetry correction. The heat-flux paths, however, are hard to assess mathematically, as is illustrated in Appendix 11 when describing a first attempt of making online corrections for heat-flow rates. Different DSCs require, in addition, different mathematical models. Finally, it must be observed that for the assessment of the time-dependence the thermal diffusivity must be known (see Fig. 4.65, below).

A schematic of a single DSC cell is given in Fig. 4.64. It is chosen to provide basic insight, and the results can be transferred to more involved calorimeters with appropriate changes in geometry, thermal resistances, and calibration constants. The

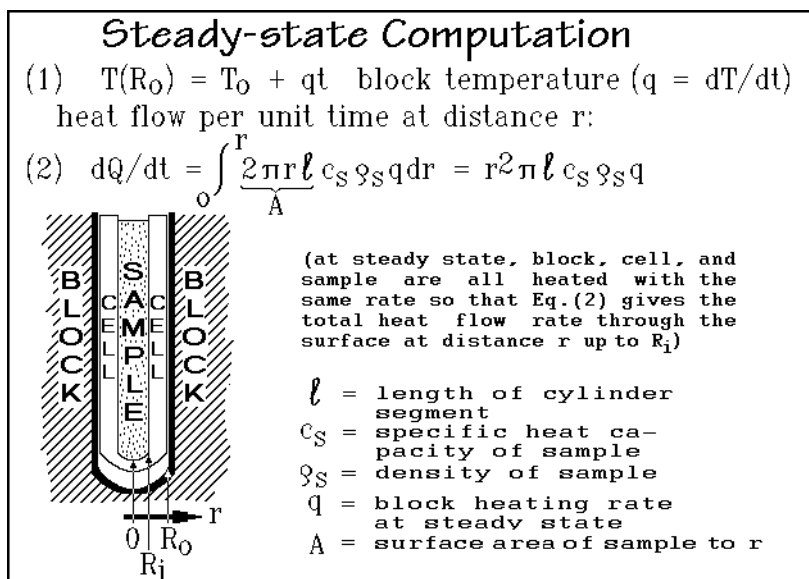


Fig. 4.64

cylindrical geometry in the center of the cell, chosen as an example, leads to a one-dimensional solution for the heat flow along the radius,  $r$ . The end-effects which occur for a length of one to two radii from the top and bottom are neglected. The radius  $R_i$  to the edge of the sample is assumed for all numerical calculations to be initially 4.0 mm. At  $R_0$ , the surface of the metal block is reached, with no further change in temperature to the heater. With a negligible temperature gradient within the sample, the heat capacity of the sample will be shown in Sect. 4.3.6 to determine the heat-flow rate at steady state, i.e., under conditions when the temperature of the calorimeter changes with the same rate  $dT/dt$  at all points. Only then can this problem be solved easily. First, however, the mathematical problem with a temperature gradient within the sample will be treated and then simplified.

Six conditions are set for the description. In case they are not fulfilled, further corrections need to be included in the presented calculations. (1) The thermocouples or resistance thermometers are assumed to be inert, meaning that they themselves do not contribute to the differential heat flow. (2) All material interfaces must be without thermal resistance. The main contacts are between the sample and cell, and from the



cell to the block. No effects due to these interfaces are included in the calculations. (3) There should be no or only negligible packing effects within the sample. (4) The heat capacity and thermal conductivity are assumed to be constant with temperature, or change so gradually that they do not create significant transients of their own. Major changes caused by thermal transitions within the sample are treated separately as distinct transients. (5) Only heat transfer by conduction or radiation is permitted. This assumption is necessary because one cannot assess heat transfer by the always irreproducible convection. (6) Sample and reference must be thermally independent of each other, so that there is no cross-flow of heat. Such cross-flow occurs for larger temperature differences between reference and sample placed too closely. In the calorimeter chosen for Fig. 4.64 there is no inert atmosphere. Most commercial DSCs work with purge gases which are prone to convection and cause then difficult to control heat losses or gains. For the typical commercial DSC this means that the gas flow should be as free of turbulence as possible (laminar flow, low flow-rate). The temperature of the gas should be that of the block, and its flow must be controlled and measured at the inlet *and* exit of the DSC. Inadvertent leaks, or too high flow rates, can cause major systematic errors.

The first step in the calculation is to describe the steady state which is reached when all parts of the calorimeter change temperature with the same rate  $q$  in  $\text{K min}^{-1}$ . The block temperature at the contact surface with the sample cell,  $T(R_o)$ , is governed by the controller as shown in Eq. (1) of Fig. 4.64. For convenience one sets  $T(R_o)$  at the beginning of the experiment equal to some constant temperature  $T_o$  and assumes that it rises linearly with the heating rate  $q$ . To calculate the heat flow into the sample at distance  $r$  to follow the steady-state heating rate  $q$ , one can set up Eq. (2) as the integral over  $dr$  from 0 to  $r$  of the surface of the cylinder,  $A$ , of length  $\ell$  ( $2\pi r\ell = A$ ). The heat exchanged per unit volume of the sample is  $c_s \rho_s q$  for the change in temperature,  $dT$ , per time-change,  $dt$ . With constant  $c_s$ ,  $\rho_s$ ,  $q$ , and  $\ell$ , the integration over the whole sample is easily completed. The right part of Eq. (2) illustrates the simple result of this integration.

The temperature gradient at any radius  $r$ , written as  $\text{grad } T = dT_1/dr$ , is connected with the heat-flow rate as given by Eq. (3) of Fig. 4.65. It derives from the boxed equation in Fig. 4.65, the one-dimensional form of the Fourier equation of heat flow. More details about the Fourier equation and its application are given in Appendix 13. Combining Eqs. (2) and (3) and integration from  $r$  to radius  $R_i$ , one gets the temperature difference between the outside of the sample at  $R_i$  and the position at distance  $r$  from the center, as given by Eq. (4). The temperature  $T_1(R_i)$  lags behind the block temperature by an amount given by a similar calculation using the geometry and thermal diffusivity of the cell. Under steady-state conditions, naturally, it also increases linearly with  $q$ .

Some typical parameters for DSC measurements are listed at the top of Fig. 4.66. The largest sample holder is assumed to have a radius of 0.4 cm. Such a sample holder would need on the order of magnitude of 1–2 g of materials. From Eq. (4) one can easily find the different temperature distributions that result from sample holders of different diameters. In order to keep the temperature gradient small, one may want to keep the heating rate between 1 and 5  $\text{K min}^{-1}$ . With a smaller sample holder of a 0.04 cm radius, a size requiring 1–2 mg of sample, the ordinate must be multiplied by

### Steady-state Computation

temperature gradient connected with the heat-flow rate:

$$(3) \quad \text{grad } T = dT_1(r)/dr = [(dQ/dt)/A]/\kappa_S$$

from insertion of Eq. (2) into:

Eq. for one-dimensional heat-flow rate

$$\left(\frac{dQ}{A dt}\right) = -\kappa \text{ grad } T \quad [J/(m^2 s)]$$

A = area, grad T =  $dT/dr$   
 $\kappa$  = thermal conductivity  
 $[J/(msK)]$

$\kappa_S$  = thermal conductivity of the sample

$k_S = \frac{\kappa_S}{c_S \rho_S}$  = thermal diffusivity

combination of Eqs. (2) and (3) and integration from  $r$  to  $R_i$ :

$$(4) \quad T_1(R_i) - T_1(r) = q \frac{R_i^2 - r^2}{4\kappa_S} = (qR_i^2/4\kappa_S)[1 - (r/R_i)^2]$$

temperature difference between sample surface and  $r$

Fig. 4.65

by 0.01. This means that for the same temperature lag in the center as before, the DSC can now be performed much faster at  $q \approx 100 \text{ K min}^{-1}$ . Such dimensions (and heating rates) are realized in many of the present-day DSCs. Furthermore, one can extrapolate to a design suitable for microgram or even nanogram samples which corresponds to  $r \approx 40$  and  $\approx 4 \mu\text{m}$ . Heating rates as high as  $10^4$  and  $10^6 \text{ K min}^{-1}$  should now be possible in these cases, as is discussed in Appendix 10.

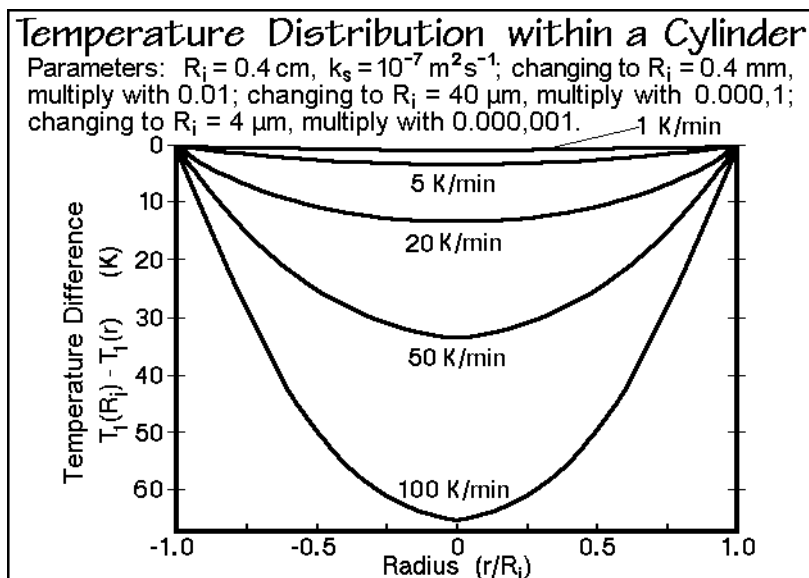


Fig. 4.66

### 4.3.6 DSC Without Temperature Gradient

The steady-state calculations have set the stage for computation of the DSC performance without, or better with negligible, temperature gradient within the sample. A temperature gradient within the sample pan should not exceed 2–3 kelvins for typical standard DSC experiments. The first two equations of Fig. 4.67 express the heat-flow rates into the sample and reference making use of Newton's law of cooling (see Fig. 4.9). The heat-flow rate,  $dQ/dt$ , is strictly proportional to the difference between block temperature,  $T_b$ , and sample temperature,  $T_s$ . The proportionality

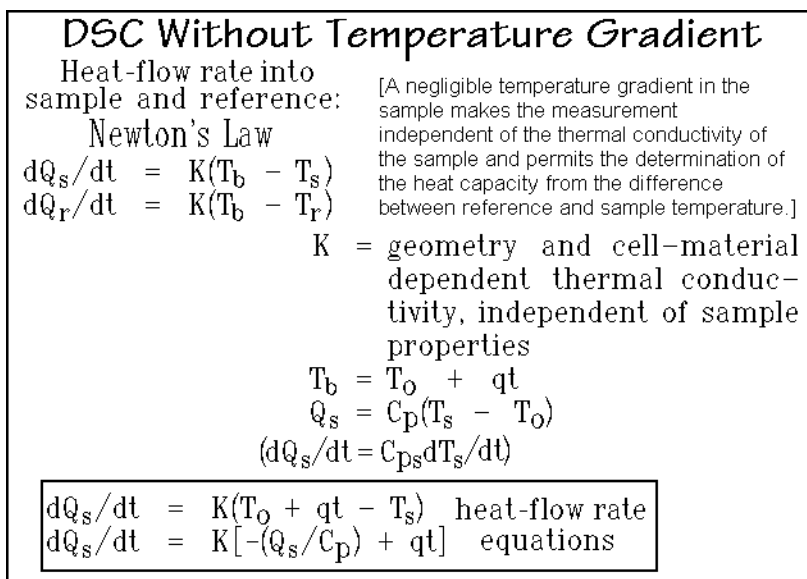
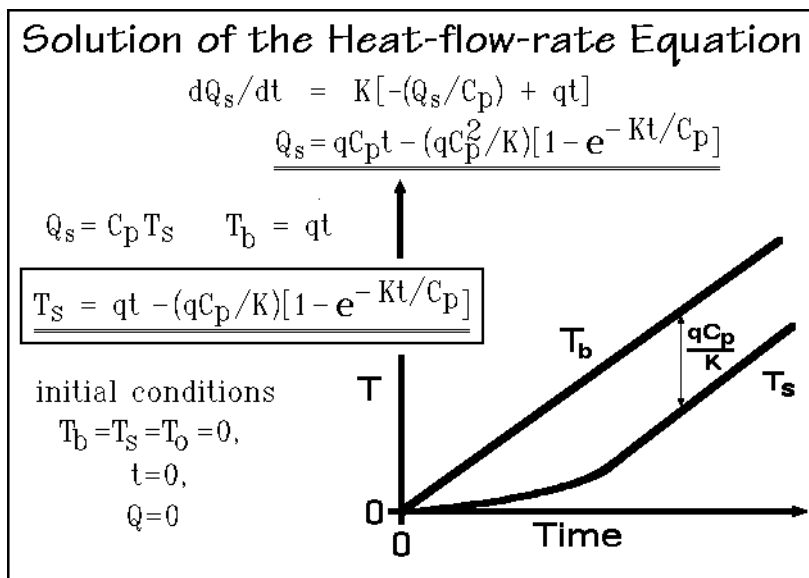


Fig. 4.67

constant,  $K$ , is dependent on the material of construction of the cell (or the heat-leak disk or cylinder), but under the chosen conditions of negligible temperature gradient within the sample, it is independent of the thermal diffusivity of the sample. Inserting the temperature of the block,  $T_b$ , and the total heat flow into the sample,  $Q_s$ , into the equation for heat-flow rate into the sample leads to the equations of Fig. 4.67. Similar equations can be written for the heat-flow rate into the reference. Choosing the initial conditions at time  $t = 0$   $T_b$ ,  $T_s$ , and  $T_o$  are all zero, the solution of the heat-flow-rate equations is given in Fig. 4.68. Instead of expressing the solution in terms of the heat  $Q$ , one can write an expression for the sample temperature as a function of time, as indicated, and drawn in the figure as an example.

The plot at the bottom of Fig. 4.68 shows the increase in block temperature,  $qt$ , and the change in sample temperature,  $T_s$ , in analogy to Fig. 4.55. Initially, at time zero, block and sample temperatures are identical. Then, as the experiment begins, the sample temperature lags increasingly behind  $T_b$  until steady state is reached. The difference between the block and sample temperatures at steady state is  $qC_p/K$ , a quantity which is strictly proportional to the heating rate and the heat capacity of the

**Fig. 4.68**

sample. The restriction of the sample to a small size, so that there is no temperature gradient within it, has led to a relatively simple mathematical description of the changes in temperature with time.

For the measurement of a constant heat capacity, the sketches of Fig. 4.55 and 4.68 show that only measurement of  $T_b$  and  $T_s$  is necessary. The value of  $K$  can be obtained by calibration. With this discussion, the principle of heat capacity measurement is already clarified. The further mathematical treatment of the DSC will show how to handle the calibration by using a differential set-up that is designed, as mentioned above, to minimize the effort to evaluate heat losses and gains.

The next stage in the mathematical treatment is summarized in Fig. 4.69. It models the measurement of a heat capacity that changes with temperature, but sufficiently slowly that a once achieved steady state is maintained. The changing heat capacity causes, however, different heating rates for sample and reference, so that the previous calculation cannot be applied. The two top equations express the temperature difference between the block and sample, and block and reference, respectively. They are derived simply from Newton's law expressed in temperature as seen in Fig. 4.68 after steady state has been achieved. The differences written show that further simplification is possible if the overall heat capacity of the sample calorimeter (pan and sample) is made to be equal to  $C_p' + mc_p$ , where  $C_p'$  is the heat capacity of the empty calorimeter (its water value),  $m$  is the sample mass, and  $c_p$  is the specific heat capacity of the sample in  $\text{J K}^{-1} \text{g}^{-1}$ . A further simplification is possible if one makes  $C_p'$  also the heat capacity of the reference calorimeter by using an empty pan of the same weight as the sample pan. This leads to the boxed Eq. (3). The equality of the heat capacities of the sample and reference holders are best adjusted experimentally ( $\pm 0.1 \text{ mg}$ ), otherwise, a minor complication in the mathematics is necessary, requiring knowledge of the different masses and the heat capacity of aluminum or other

<b>Measurement of Heat Capacity</b>	
$T_b - T_s = \frac{C_s}{K} \left( \frac{dT_s}{dt} \right) = \frac{C_p' + mc_p}{K} \left( \frac{dT_s}{dt} \right)$	$dQ = C_p dT$
$T_b - T_r = \frac{C_r}{K} \left( \frac{dT_r}{dt} \right) = \frac{C_p'}{K} \left( \frac{dT_r}{dt} \right)$	$dQ/dt = C_p dT/dt$
<hr/> <div style="display: flex; justify-content: space-between;"> <div style="width: 60%;"> <math display="block">(1) \quad \Delta T = T_r - T_s = \frac{C_s}{K} \left( \frac{dT_s}{dt} \right) - \frac{C_r}{K} \left( \frac{dT_r}{dt} \right)</math> <math display="block">(2) \quad \Delta T = T_r - T_s = \frac{C_s - C_r}{K} \left( \frac{dT_s}{dt} \right) - \frac{C_r}{K} \left( \frac{dT_r - dT_s}{dt} \right)</math> </div> <div style="width: 35%; border: 1px solid black; padding: 5px;"> <math display="block">(3) \quad \Delta T = T_r - T_s = \frac{C_p' + mc_p}{K} \left( \frac{dT_s}{dt} \right) - \frac{C_p'}{K} \left( \frac{dT_r}{dt} \right) \approx \frac{mc_p}{K} q</math> </div> </div>	
$C_p' = C_r = \text{heat capacity of the empty pan}$ $C_s = \text{heat capacity of the sample and pan}$ $m = \text{sample mass} \quad c_p = \text{sample specific heat capacity}$	

**Fig. 4.69**

calorimeter material. Checking the precision of several analyses with sample holders of different masses, it was found, in addition, that matching sample and reference sample pans gives higher precision than calculating the heat capacity effect of the different masses.

In Fig. 4.70 the expression for the heat capacity is completed by inserting the top equations into the equation for  $\Delta T$  of Fig. 4.69. The basic DSC equations contain the

<b>Reorganization to the Basic DSC Equation</b>	
at steady state: $dT_r/dt = q = dT_b/dt$	
$dT_s/dt = q dT_s/dT_r$	$d\Delta T/dT_r = 1 - [dT_s/(qdt)]$ $dT_s/dt = (1 - d\Delta T/dT_r)q$
$\Delta T = q \frac{C_p' + mc_p}{K} (1 - d\Delta T/dT_r) - \frac{C_p'}{K} q$	
$mc_p = K \frac{\Delta T}{q} + (K \frac{\Delta T}{q} + C_p') \left( \frac{d\Delta T/dT_r}{1 - d\Delta T/dT_r} \right)$	<div style="border-left: 3px double black; padding-left: 10px;">                         BASIC DSC EQUA- TIONS                     </div>
$mc_p = K \frac{\Delta T}{q} + (K \frac{\Delta T}{q} + C_p') (d\Delta T/dT_s)$	<div style="border-left: 3px double black; padding-left: 10px;">                         BASIC DSC EQUA- TIONS                     </div>
<div style="display: flex; align-items: center;"> <div style="text-align: center; margin-right: 10px;"> <math>\nwarrow</math> sample heat capacity <math>\nearrow</math> approximate heat capacity of the sample                         </div> <div style="text-align: center;"> <math>\underbrace{\hspace{10em}}</math> correction term, consisting of the product of the total heat capac- ity of sample and holder with a factor accounting for the different heating rates of r and s                         </div> </div>	

**Fig. 4.70**

assumptions that the change of reference temperature with time is in steady state, i.e.,  $dT_r/dt = q$ . Introducing the slope of the recorded baseline,  $d\Delta T/dT_r$ , one obtains a final equation that contains only parameters easily obtained, and furthermore, can be solved for the heat capacity of the sample as shown.

The correction term of the basic DSC equation has two factors. The factor in the first set of parentheses represents close to the overall sample and sample holder (pan) heat capacity,  $C_s$ . The factor in the second set of parentheses contains a correction accounting for the different heating rates of reference and sample. For steady-state (and constant heat capacity), a horizontal baseline is expected with  $d\Delta T/dT_r = 0$ ; the heat capacity of the sample is then simply represented by the first term. If, however,  $\Delta T$  is not constant, there must be a correction. Fortunately this correction is often small. Assuming the recording of  $\Delta T$  is done with 100 times the sensitivity of  $T_r$ , as is typical, then, for a  $\Delta T$  recording at a  $45^\circ$  angle the correction would be 1% of the overall sample and holder heat capacity. This error becomes significant if the sample heat capacity is less than 25% of the heat capacity of sample and holder. Naturally, it is easy to include the correction in the computer software. The online correction Tzero™, which is described in more detail in Appendix 11 accounts for this correction by separately measuring  $\Delta T$  and  $\Delta T_b = T_b - T_r$ . Similarly, the heat-flow rates measured in the DSC of Fig. 4.57 should automatically make this correction.

The second important measurement with a DSC is the determination of heats of transition. One uses the baseline method for this task. Of special interest is that during such transitions, steady state is lost. The sample undergoing the transition remains at the transition temperature by absorbing or evolving the heat of transition (latent heat). Figure 4.71 represents a typical DSC trace generated during melting. The temperature difference,  $\Delta T$ , is recorded as a function of time or reference temperature. The melting starts at time  $t_i$  and is completed at time  $t_f$ . During this time

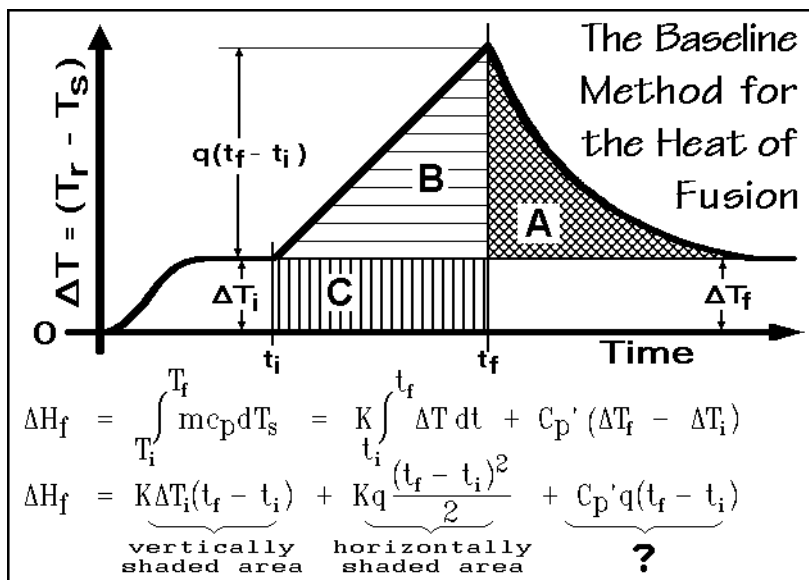


Fig. 4.71

span, the reference temperature increases at rate  $q$ , while the sample temperature remains constant at the melting point. The temperature difference  $\Delta T$ , thus, must also increase linearly with rate  $q$ . At the beginning of melting the temperature difference is  $\Delta T_i$ . At the end of melting, when steady state has again been attained, it is  $\Delta T_f$ , reaching the peak of the DSC curve.

The general integration of  $C_p$  to enthalpy goes over temperature, as shown in the top equation in Fig. 4.71. The second part of the top equation illustrates the insertion of the expression for  $mc_p$  from Eq. (3) of Fig. 4.69, changed to the variable time and partially integrated. The final integration to  $t_f$  is shown in the second equation of Fig. 4.71. The first term of the equation is  $K$  times the vertically shaded area, **C**, in the graph. The second term is the horizontally shaded area, **B**, multiplied by  $K$ . Again, the heat of fusion is not directly proportional to the area under the DSC curve up to the peak. There is, this time, a substantial third term,  $C_p'q(t_f - t_i)$ , marked with a “?”. An additional difficulty is that area **C** is not easy to obtain experimentally. It represents the heat the sample would have absorbed had it continued heating at the same steady-state rate as before. For its evaluation one needs the zero of the  $\Delta T$  recording which only is available by calibration for asymmetry (see Fig. 2.29).

Next, one may want to calculate the cross-hatched area, **A**. The calculation is carried out in Fig. 4.72. Area **A** represents the return to steady state and can be described by using the approach to steady state which was derived in Fig. 4.68. The result represents the first and the last term of the expression for  $\Delta H_f$  as it was given in Fig. 4.71. This means that under the conditions of identical  $\Delta T_i$  and  $\Delta T_f$ , one can make use of the simple baseline method for the heat of fusion determination: The heat of fusion,  $\Delta H_f$ , is just the area above the baseline in Fig. 4.71, multiplied with  $K$ , the calibration constant. If the baseline deviates substantially from the horizontal, corrections must be made which are discussed in Fig. 4.80, below.

**Completion of the Baseline**

cross hatched area:

$$A = \int_{t_i}^{t_\infty} [q(t_f - t_i) \exp\{-K(t - t_f)/(C_p' + mc_p)\}] dt$$

as in Fig. 4.68

$$A = \{q(t_f - t_i)(C_p' + mc_p)\}/K$$

assuming that  $\Delta T_i = \Delta T_f = mc_p q/K$ :

$$KA = \underbrace{K\Delta T_i(t_f - t_i)}_{\mathbf{C}} + \underbrace{C_p'q(t_f - t_i)}_{\mathbf{?}}$$

$$\Delta H_f = K \int_{t_i}^{t_f} \{\Delta T_i + q(t - t_i)\} dt + C_p'q(t_f - t_i)$$

$$\Delta H_f = Kq \underbrace{\frac{(t_f - t_i)^2}{2}}_{\mathbf{B}} + \underbrace{KA}_{\mathbf{A}}$$

Area **C** is not needed for the evaluation of the heat of fusion

**Fig. 4.72**

### 4.3.7 Applications

**Heat Capacity.** To make an actual heat capacity measurement, one must first do a calibration of the constant  $K$ . The procedure has been illustrated in Sect. 2.3.1 with Fig. 2.30. Three consecutive runs should be made. These allow to calculate the calibration constant  $K$  as given in Eq. (3) of Fig. 2.30:

$$K = C_p(\text{Calibrant})q/[a_c(T) - a_R(T)] \quad .$$

The three runs must agree within experimental error in their absolute amplitude of the initial and final isotherms. A deviation signals that the heat-loss characteristics of the calorimeters have changed. The only solution is then to start over. Such mishap occurs from time to time even with the greatest of care. Another important precaution is to keep the temperature-range for calibration sufficiently short to have a linear baseline, i.e., when halving the temperature range, the baseline change must be half. A well-kept DSC may permit temperature-ranges as wide as 100 K. The amplitudes,  $a$ , should be taken at intervals of 10 K, leading to a calibration table that agrees with typical heat capacity steps in data tables. Another hint for good quality DSC measurements is to adjust sample and calibrant amplitudes to similar levels and to choose the sample mass sufficiently high to minimize errors. Note, however, that too high amplitudes lead to instrument lags that may limit precision. This is even more important for TMDSC where the lag may become so large that the modulation is not experienced by the whole sample.

Figure 2.46 is an example of a heat capacity measurement of polyethylene. The data were first extrapolated to full and zero crystallinity, as discussed in Sect. 2.3.6, to characterize the limiting states of solid polyethylene (orthorhombic crystals and amorphous). The low-temperature data, below about 130 K, were measured by adiabatic calorimetry as described in Sect. 4.2. Besides the experimental data, the computed heat capacities from the Advanced THERmal Analysis System, ATHAS, can also be derived, as shown in Fig. 2.51 and summarized for many polymers in Appendix 1. This system makes use of an approximate frequency spectrum of the vibrations in the crystal. At sufficiently low temperature only vibrations contribute to the heat capacity and missing frequency information can be derived by fitting to the heat capacity. The skeletal vibrations are vibrations that involve the backbone of the molecule (torsional and accordion-like motion). Their heat capacity contribution is most important up to room temperature. The group vibrations are more localized (C-C and C-H stretching and C-H bending vibrations) and contribute mainly at higher temperature. A comparison of the computed and the measured heat capacity indicates deviations that start at about 250 K and signal other contributions to the heat capacity. For polyethylene this motion is conformational and of importance to understand the mechanical properties. This example illustrates the importance of good experimental heat capacity data. Only if  $C_p$  is known, is a sample well characterized.

Besides interpretation of the heat capacity by itself, the heat capacity,  $C_p$ , can also be used to derive the integral thermodynamic functions, enthalpy,  $H$ , entropy,  $S$ , and free enthalpy,  $G$ , also called Gibbs function:

$$H = \int C_p dT, \quad S = \int (C_p/T) dT, \quad G = H - TS \quad .$$



Polyethylene data are shown in Fig. 2.23. At the equilibrium melting temperature of 416.4 K, the heat of fusion and entropy of fusion are indicated as a step increase. The free enthalpy shows only a change in slopes, characteristic of a first-order transition. Actual measurements are available to 600 K. The further data are extrapolated. This summary allows a close connection between quantitative DSC measurement and the derivation of thermodynamic data for the limiting phases, as well as a connection to the molecular motion. In Chaps. 5 to 7 it will be shown that this information is basic to undertake the final quantitative step, the analysis of nonequilibrium states as are common in polymeric systems.

**Fingerprinting of Materials.** Changing to a less quantitative application, materials are characterized by their phase transition or chemical reactions in what has become known as fingerprinting. The measurements can be done by DTA with quantitative information on the transition temperature and made quantitative with respect to the thermodynamic functions by using DSC. The DSC is furthermore also able to measure kinetics parameters as shown in Fig. 3.98. The DTA curve of Fig. 4.73, taken as an unknown, is easily identified as belonging to amyl alcohol (DSC cell A of Fig. A.9.2, 2  $\mu$ l in air). At least two events are available for identification, the melting

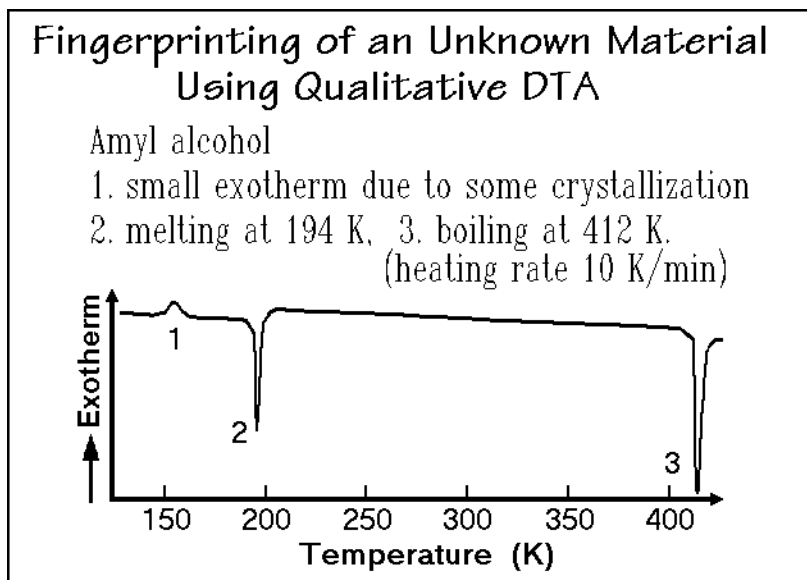
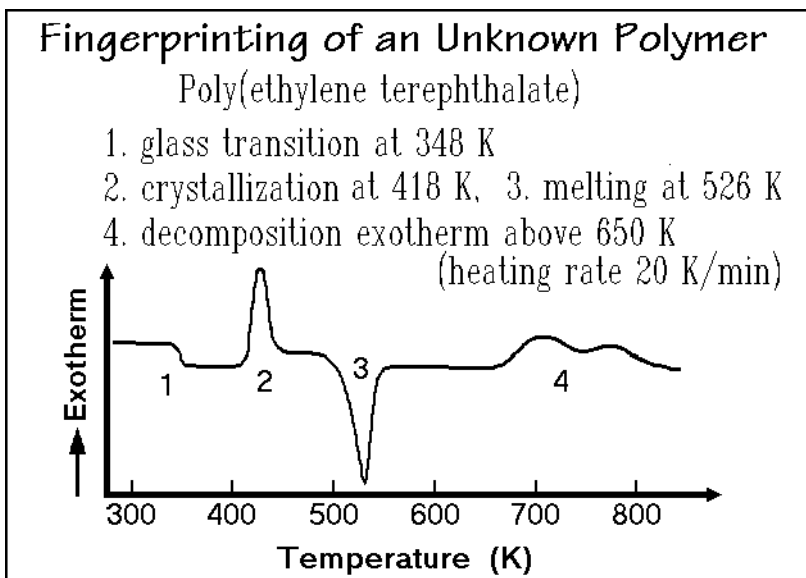


Fig. 4.73

(2) and the boiling (3). It helps the interpretation to look at the sample and know that it is liquid between (2) and (3) and has evaporated after (3). It is always of importance to verify transitions observed by DTA by visual inspection. The small exotherm (1) at about 153 K is due to some crystallization. It occurs on incomplete crystallization on the initial cooling, a typical behavior of alcohols.

The curve Fig. 4.74 represents a DTA trace, easily identified as belonging to poly(ethylene terephthalate) which was quenched rapidly from the melt to very low temperatures before analysis (DTA cell D of Fig. A.9.2, 10 mg of sample in  $N_2$ ).

**Fig. 4.74**

Under such conditions, poly(ethylene terephthalate) remains amorphous on cooling; i.e., it does not have enough time to crystallize, and thus it freezes to a glass. At point (1) the increase in heat capacity due to the glass transition can be detected. At point (2), crystallization occurs with an exotherm. Note that after crystallization the baseline drops towards the crystalline level. Endotherm (3) indicates the melting, and finally, there is a broad, exotherm with two peaks (4) due to decomposition. Optical observation to recognize glass and melt by their clear appearances is helpful. Microscopy between crossed polarizers is even more definitive for the identification of an isotropic liquid or glass. More details about this DSC trace will be discussed in Sect. 5.4.

Figure 4.75 refers to iron analyzed with a high-temperature DTA as sketched H in Fig. A.9.3. About 30 mg of sample were analyzed in helium. In this case several solid–solid transitions can be used for the characterization of the sample in addition to the fusion which is represented by endotherm four. As a group, these solid–solid transitions are characteristic of iron and can be usable for its identification. A more quantitative analysis may also allow to distinguish between the many variations of commercial irons.

The diagram in Fig. 4.76 is a DTA curve of barium chloride with two molecules of crystal water measured by high-temperature DTA (10 mg sample, in air). The crystal water is lost in two stages. Identification of these transitions is best through the weight loss and analysis of the chemical nature of the evolved molecules. Endotherm (3) is a solid-state transition. Either X-ray diffraction or polarizing microscopy can characterize it. Finally, anhydrous barium chloride melts at (4), proven by a loss of the particle character on opening the sample pan after cooling.

Figure 4.77 shows two qualitative DTA traces which can be used to interpret a chemical reaction between the two compounds. The chemical reaction can be

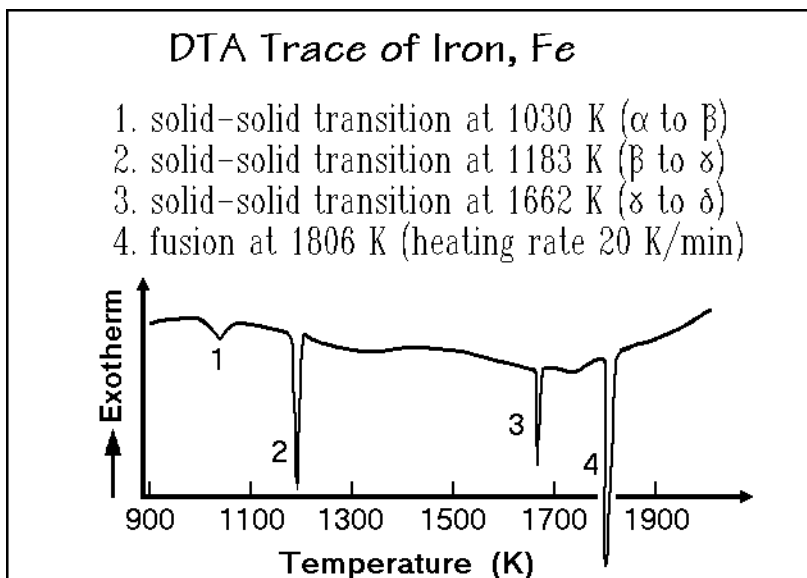


Fig. 4.75

performed either to identify the starting materials or to study the reaction between the substances. The top curve is a DTA trace of pure acetone (DSC type A of Fig. A.9.2, 1–5 mg of sample, static nitrogen). A simple boiling point is visible. The bottom trace is of pure *p*-nitrophenylhydrazine with a melting point, followed by an exothermic decomposition. The top of Fig. 4.78 is the DTA curve after mixing of both components in the sample cell. The chemical reaction leading to the product is:

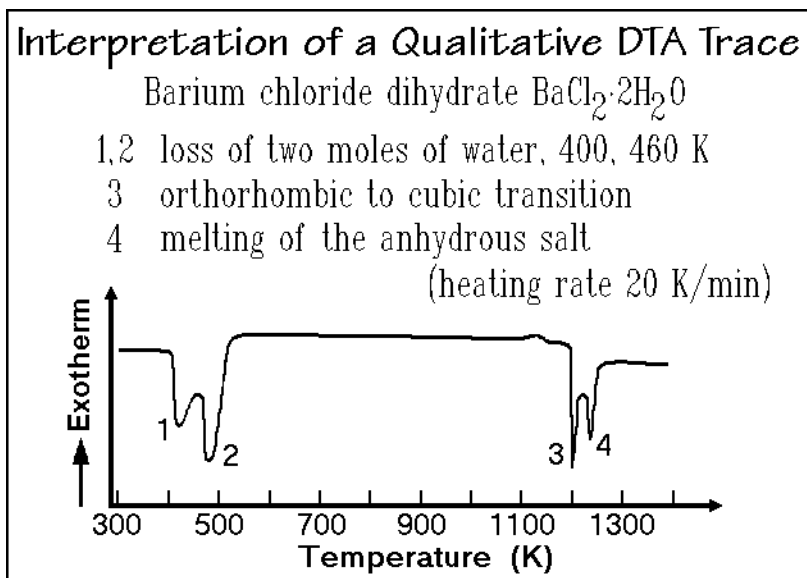


Fig. 4.76

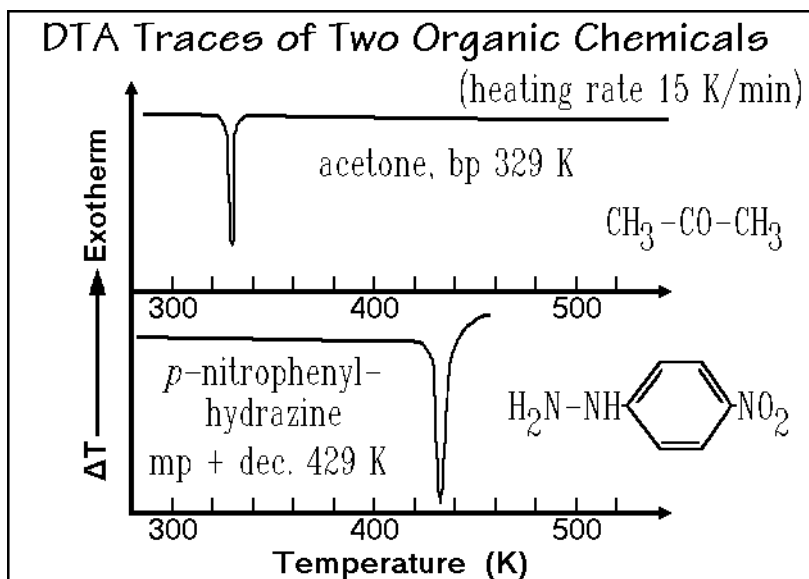


Fig. 4.77

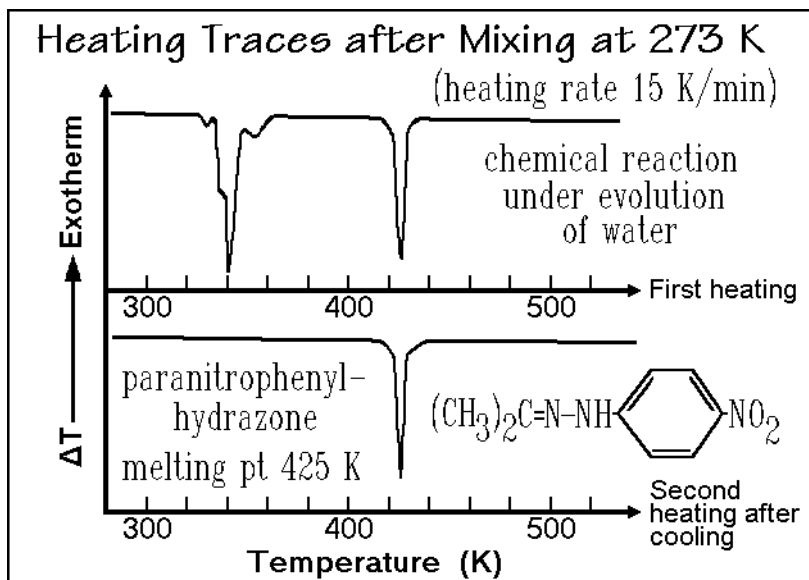
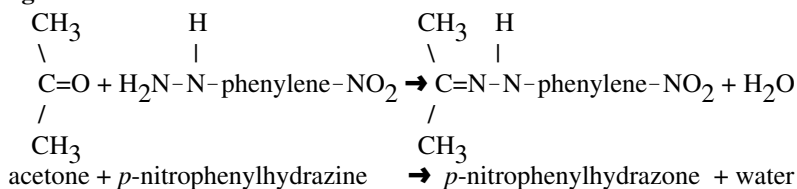
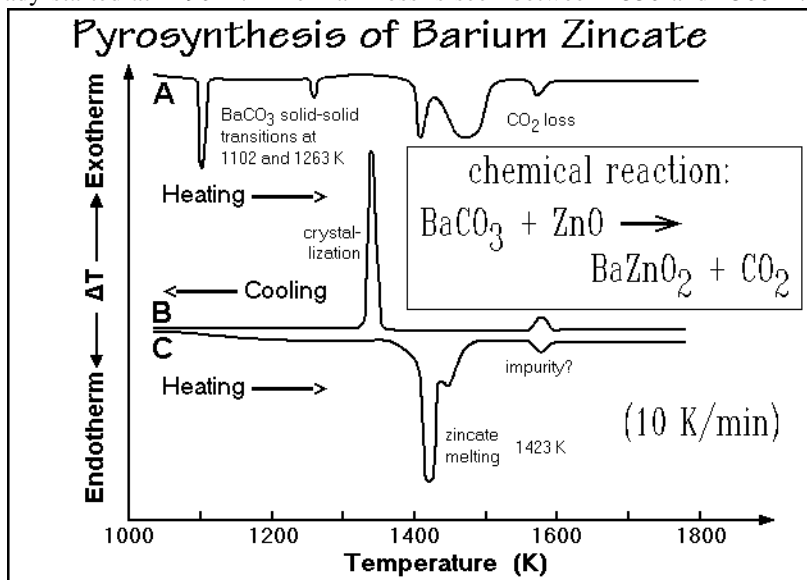


Fig. 4.78

The *p*-nitrophenylhydrazone has a different thermal behavior. It does not decompose in the range of temperature used for analysis and does not show the low boiling point of acetone. To date, little use has been made of this powerful DTA technique in organic chemical analyses and syntheses.

In Fig. 4.79 the DTA curves for the pyrosynthesis of barium zincate out of barium carbonate and zinc oxide are shown. The experiment was done by simultaneous DTA and thermogravimetry on 0.1 cm<sup>3</sup> samples in an oxygen atmosphere. Curve A is the heating trace of the mixture of barium carbonate and zinc oxide. The DTA curve is rather complicated because of the BaCO<sub>3</sub> solid–solid transitions. The loss of CO<sub>2</sub> has already started at 1190 K. The main loss is seen between 1350 and 1500 K. On



**Fig. 4.79**

cooling after heating to 1750 K, however, a single crystallization peak occurs at 1340 K (curve B). On reheating the mixture, which is shown as curve C, the new material can be identified as barium zincate by its 1423 K melting temperature. Unfortunately no explanation is given for the two small peaks at 1450 and 1575 K in the original research.

**Quantitative Analysis of the Glass Transition.** Cooling through the glass transition changes a liquid to a glassy solid. The transition occurs whenever crystallization is not possible under the given conditions. It is a much more subtle transition than crystallization, melting, evaporation or chemical reaction in that it has no enthalpy or entropy of transition. Only its heat capacity changes, as shown in Fig. 2.117. Characterization of the glass transition requires DSC data of high quality. At the glass transition, large-amplitude motion becomes possible on heating (devitrification), and freezes on cooling (vitrification). In contrast to the small-amplitude vibrational motion in solids, the large-amplitude motion involves translation and rotation, and for polymers, internal rotation (conformational motion). For more details on the glass transition, see also Chaps. 2 and 5–7. For characterization, one

finds first the glass-transition temperature,  $T_g$ , defined as the temperature of half-vitrification or devitrification. For homopolymers and other pure materials, the breadth of the transition, given by  $T_2 - T_1$ , and is typically 3–5 K. For polymers, blends, and semicrystalline polymers this breadth can increase to more than 100 K. The beginning, at  $T_b$ , and the end of the transition, at  $T_e$ , are also characteristically different from sample to sample. All five temperatures of Fig. 2.117 should thus be recorded together with the change in heat capacity,  $\Delta C_p$ , at  $T_g$ . Since the change into and out-of the glassy state follows a special, cooperative kinetics, the time-scale in terms of the heating or cooling rate needs to be recorded also (see Sects. 2.5.6 and 4.4.6).

A sample cooled more slowly vitrifies at lower temperature and stores in this way information on its thermal history. Reheating the sample gives rise to enthalpy relaxation or hysteresis as is described in Sect. 6.3. Only when cooling and heating rates are about equal is there only little hysteresis. Quantitative analysis of the intrinsic properties of a material and its thermal history is thus possible. Finally, it is remarked in Fig. 2.117 that it is possible to estimate from  $\Delta C_p$  how many units of the material analyzed become mobile at  $T_g$ . The DSC of the glass transition is thus a major source for characterization of materials.

**Quantitative Analysis of the Heat of Fusion.** The melting transition with its various characteristic temperatures and the enthalpy of fusion is discussed in Fig. 4.62 as a calibration standard for DSC. In Fig. 4.80 the case is treated where the simple baseline method of Fig. 4.71–72 is not applicable because of a broad melting range and a large shift in the baseline. In this case, the baseline must be apportioned properly to the already absorbed heat of fusion. This change in the baseline can be estimated by eye, as marked in the figure. The points marked 1/4, 1/2, 3/4, and the completion of melting are connected as the corrected baseline, if needed with a small correction for the time needed to reach steady state (lag correction). More quantitative is to use a computer program involving correction of the peak for lags (desmearing to the true progress of melting [26]) and quantitative deconvolution of the peak as indicated in the figure by Eq. (2) [27]. The recorded heat capacity that follows the peak is called the apparent heat capacity,  $C_p^{\#}$ . It is made up of parts of the crystal heat capacity, amorphous heat capacity, and the latent heat of fusion. In the case of polymers, the crystallinity is not 100% at low temperature, the samples are semicrystalline (see Chap. 5). The total measured heat of fusion is then also only a fraction of the expected equilibrium value.

Without measuring the heat capacity of the crystalline or semicrystalline sample, the change of crystallinity can be extracted by solving Eq. (3) [28]. The change of the heat of fusion with temperature needed for the solution is given in Eq. (1) and is available from the ATHAS Data Bank as summarized in Appendix 1. The needed quantity  $C_p^{\#} - C_{pa}$ , represents the difference between the measured curve and  $C_{pa}$  available from the DSC trace. Figure 4.81 illustrates the change in crystallinity of a complex block copolymer with two crystallizing species which is discussed in more detail in Sect. 7.3.3. At low temperature the sample which is phase-separated into a lamellar structure of the two components consists of glassy and crystalline phases in each lamella. Next, the oligoether goes through its glass transition without change in crystallinity. This is followed by the melting of the oligoether crystals, seen by the

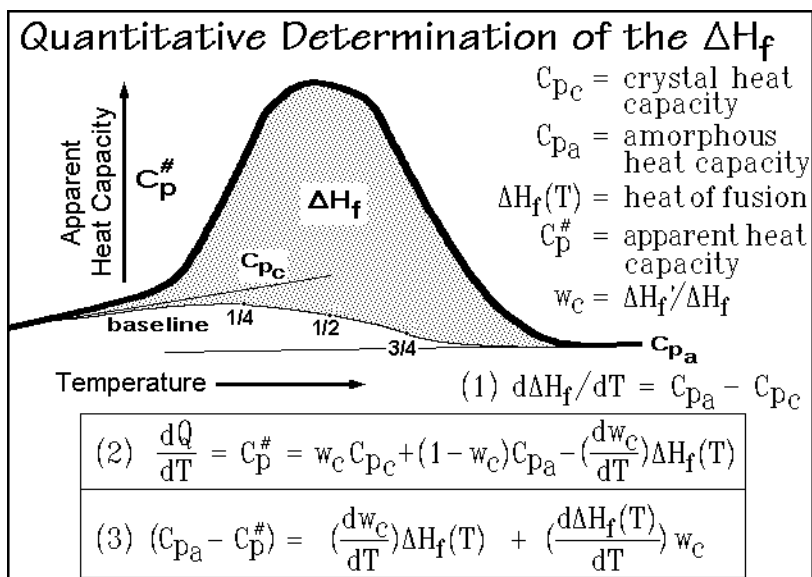


Fig. 4.80

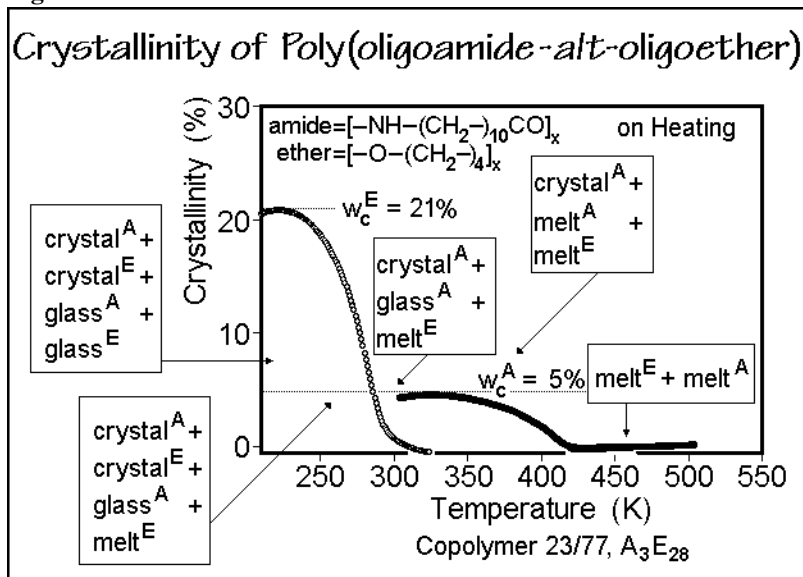


Fig. 4.81

decrease in oligoether crystallinity to zero. Next is the oligoamide glass transition, again without change in crystallinity, followed by melting of the oligoamide crystals, leading to the two-phase structure consisting of the melts of the two components. A total of six different phases, present in five different phase assemblies have in this experiment been analyzed quantitatively. The glass transitions are clearly visible in the heat-capacity traces of Sect. 7.3.3.

A final point to be made is the calibration of the onset temperature of melting with heating and cooling rates shown in Fig. 4.82. The instrument-lag for the power-compensated DSC of Fig. 4.58 changes by about 3.5 K on changing  $q$  by  $100 \text{ K min}^{-1}$ . On cooling, the In supercools by about 1 K. This can be avoided by calibrating with transitions that do not supercool, such as isotropizations of liquid crystals or by seeding using TMDSC (see Sect. 4.4.7). Figure 4.83 shows a similar experiment on

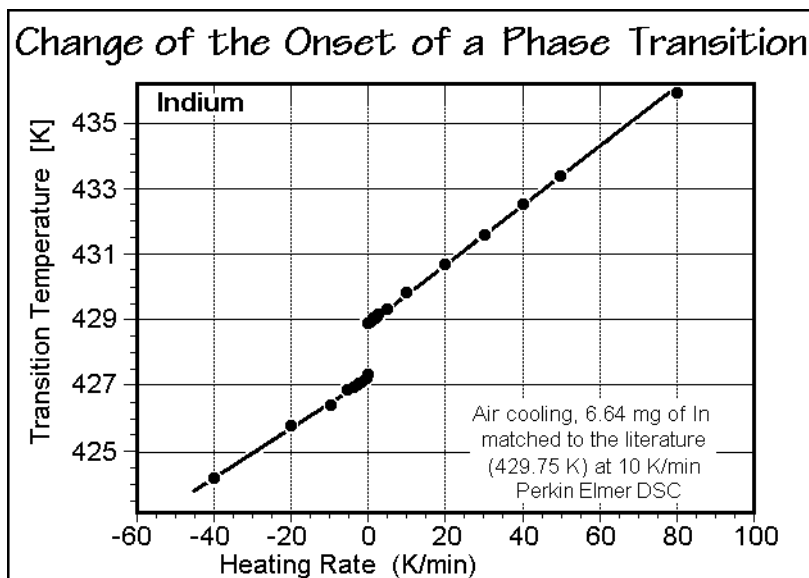


Fig. 4.82

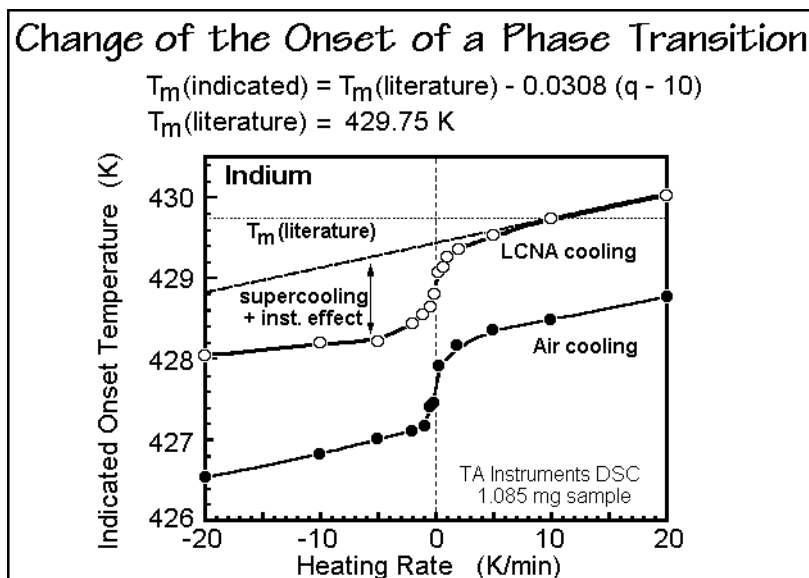
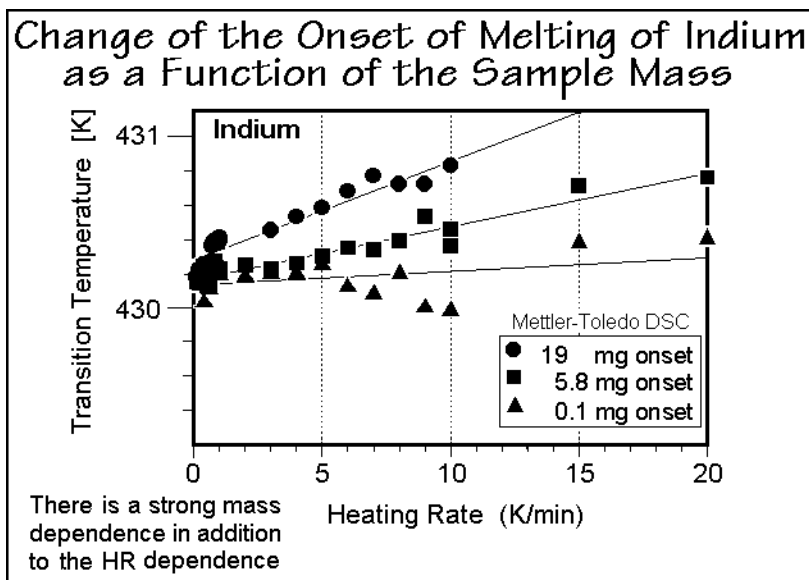


Fig. 4.83



a heat-flux DSC as shown in the sketch A of Fig. A.9.2, using different purge gases. The magnitude of change in the onset temperature of melting is similar to Fig. 4.82. The rounding in the vicinity of heating rate zero is a specific instrument effect and does not occur with the operating system of the power-compensated DSC in Fig. 4.82. When controlling the furnace temperature as in the heat-flux DSC of Fig. 4.57, there is a mass dependence of the onset of melting as illustrated in Fig. 4.84.



**Fig. 4.84**

Note, that some DSCs have a lag correction incorporated in their analysis software. Such corrections are, however, only approximations because of the changes with sample mass, heat conductivity, and environment as is pointed out on pg. 340, above. More applications of the DSC to the analysis of materials are presented in Sect. 4.4 as well as in Chaps. 6 and 7, below.

## 4.4 Temperature-modulated Calorimetry

A major advance in differential scanning calorimetry is the application of temperature modulation, the topic of this section. The principle of measurement with temperature modulation is not new, the differential scanning technique, TMDSC, however, is. This technique involves the deconvolution of the heat-flow rate into one part that follows modulation, the reversing part, and one, that does not, the nonreversing part. The term reversing is used to distinguish the raw TMDSC data from data proven to be thermodynamically reversible. Reversing may mean the modulation amplitude bridges the temperature region of irreversibility or the modulation causes nonlinear or nonstationary effects, as will be discussed in Sects. 4.4.3 and 4. The first report about TMDSC was given in 1992 at the 10<sup>th</sup> Meeting of ICTAC [1,22], see also Fig. 2.5.

### 4.4.1 Principles of Temperature-modulated DSC

In principle, any DSC can be modulated. As the details of construction of the DSC equipment vary, it may be advantageous to modulate in different fashions. One can modulate the block, reference, or sample temperatures, as well as the temperature difference (proportional to the heat-flow rate). For example, the temperature modulation of the Mettler-Toledo ADSC™ is controlled by the block-temperature thermocouple (see Fig. 4.57), while the modulation of the MDSC™ of TA Instruments in Fig. 4.85 is controlled by the sample thermocouple. Of special interest, perhaps, would be a modulated dual cell as shown in Fig. 4.56.

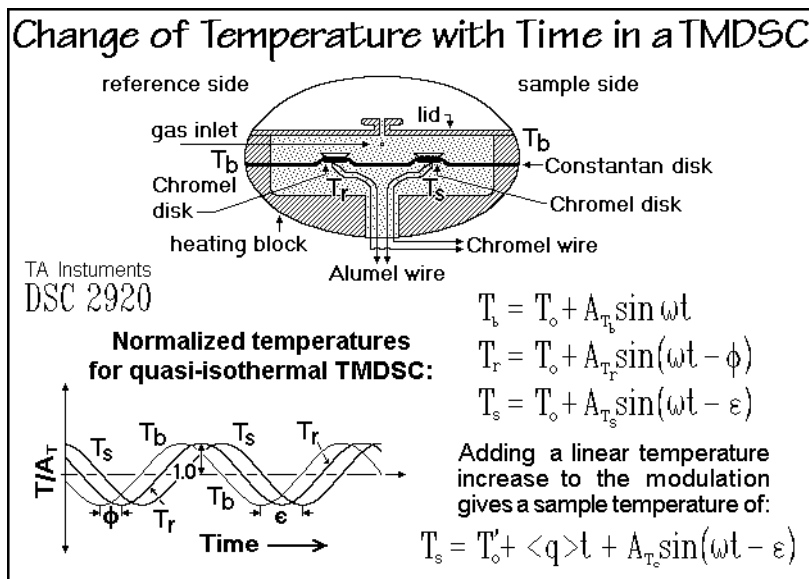


Fig. 4.85

In the following discussion, most calculations are patterned after the heat flux DSC as developed by TA Instruments. The actual software, however, is proprietary and may use a different route to the same results and also may change as improvements are made. Similarly, for other instruments the derived equations must be adjusted to the calorimeter used. A method to combine standard DSC and sawtooth modulation allows the simultaneous analysis of the standard DSC on linear heating and cooling segments and the averaged total response, and the evaluation of the reversing heat-flow rates from the Fourier harmonics of the sawtooth. Details about this versatile modulation are shown in Appendix 13, which also contains a detailed discussion of sawtooth modulation linked to the following description of TMDSC.

The major discussion will be based on the DSC shown in Fig. 4.85 which is a further development of the DSC A of Fig. A.9.2, i.e., TMDSC is an added choice of operation, not a new instrument. It will be advantageous to do some sample characterizations in the DSC mode, others in the TMDSC mode. It was noted in Sect. 4.3 that DSC could be used as a calorimeter or as DTA, similarly TMDSC can

be used as a precise, but often slow analysis tool with an average heating or cooling rate,  $\langle q \rangle$ , of  $0\text{--}1.0\text{ K min}^{-1}$  or as DSC with faster rates, typically  $5\text{--}50\text{ K min}^{-1}$ . Recording only temperature and qualitative heat flows, reduces the DSC to DTA. Most applications of Sect. 4.3 are best done by DTA and DSC (qualitative applications such as finger printing and quantitative determinations of heat capacity, heats of reaction and transition) while some of the latter are improved by TMDSC, additional measurements only are possible with TMDSC as described in Sects. 4.4.6–8.

A basic temperature-modulation equation for the block temperature  $T_b$  is written in Fig. 4.85, with  $T_0$  representing the isotherm at the beginning of the scanning. The modulation frequency  $\omega$  is equal to  $2\pi/p$  in units of  $\text{rad s}^{-1}$  ( $1\text{ rad s}^{-1} = 0.1592\text{ Hz}$ ) and  $p$  represents the length of one cycle in s. For the present, the block-temperature modulation is chosen as the reference, i.e., it has been given the phase difference of zero. The modulation adds, thus, a sinusoidal component to the linear heating ramp  $\langle q \rangle t$ , where the angular brackets  $\langle \rangle$  indicate the average over the full modulation cycle. If there is a need to distinguish the instantaneous heating rate from  $\langle q \rangle$ , one writes the former as  $q(t)$ . The modulated temperatures drawn in Fig. 4.85 are written for the quasi-isothermal mode of TMDSC, an experiment where  $\langle q \rangle = 0$ . The different maximum amplitudes  $A_{T_b}$ ,  $A_{T_r}$ , and  $A_{T_s}$  are used to normalize the ordinate in the graph, so that the phase differences  $\phi$  and  $\epsilon$  can be seen easily. The bottom equation in Fig. 4.85 is needed to represent the modulated temperature in the presence of an underlying heating rate  $\langle q \rangle \neq 0$ . Figure 4.55 in Sect. 4.3 shows the temperature changes with time in standard DSC and in TMDSC with a sinusoidal modulation and an underlying heating rate  $\langle q \rangle$ .

To illustrate the multitudes of possible modulations, the top row of Fig. 4.86 illustrates five segments that can be linked and repeated for modulation of the temperature. Examples of quasi-isothermal sinusoidal and step-wise modulations are

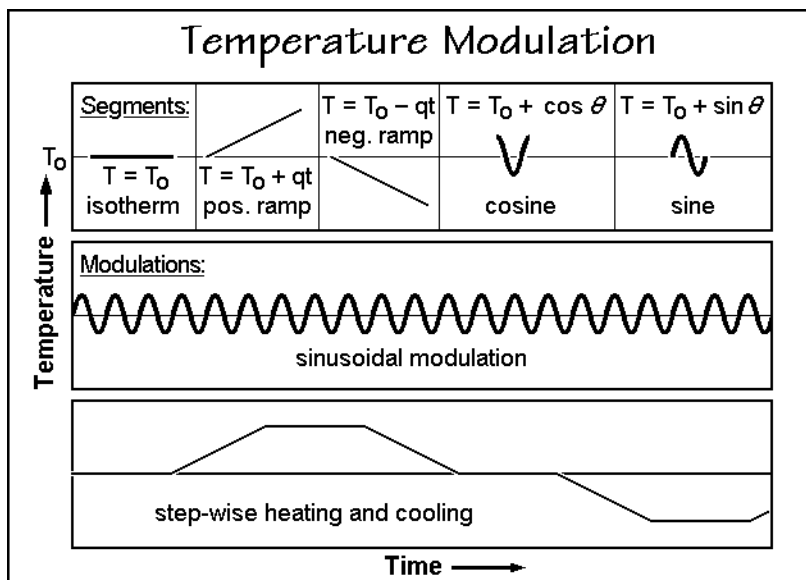


Fig. 4.86

shown at the bottom of Fig. 4.86. The sawtooth and two more complex temperature modulations are displayed in Fig. 4.87. The possible TMDSC modes that result from sinusoidal modulation are summarized in Fig. 4.88. For the analyses the curves are often represented by Fourier series. Their basic mathematics is reviewed in Appendix 13. Each of the various harmonics of a Fourier series of non-sinusoidal

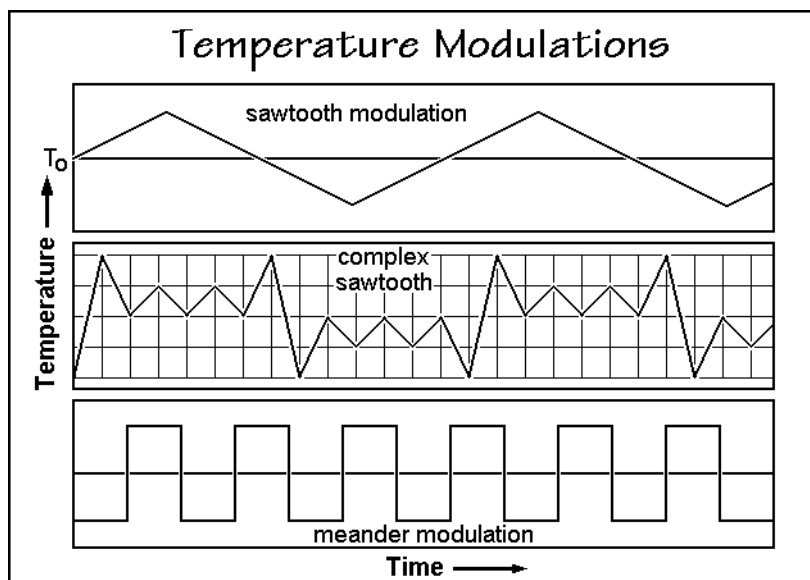


Fig. 4.87

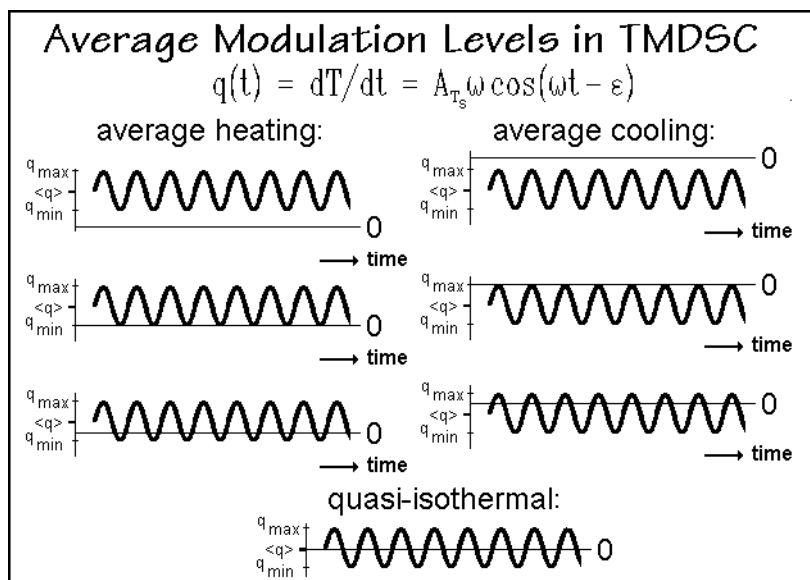


Fig. 4.88

modulation can be treated similar to the here discussed sinusoidal modulation, so that a single sawtooth, for example, can generate multiple-frequency experiments. Figure 4.89 illustrates the complex sawtooth of Fig. 4.87 which can be used to perform multi-frequency TMDSC with a standard DSC which is programmable for repeat segments of 14 steps [29]. Each of the five major harmonics possesses a similar modulation amplitude and the sum of these five harmonics involves most of the programmed temperature modulation, so that use is made of almost all of the temperature input to generate the heat-flow-rate response.

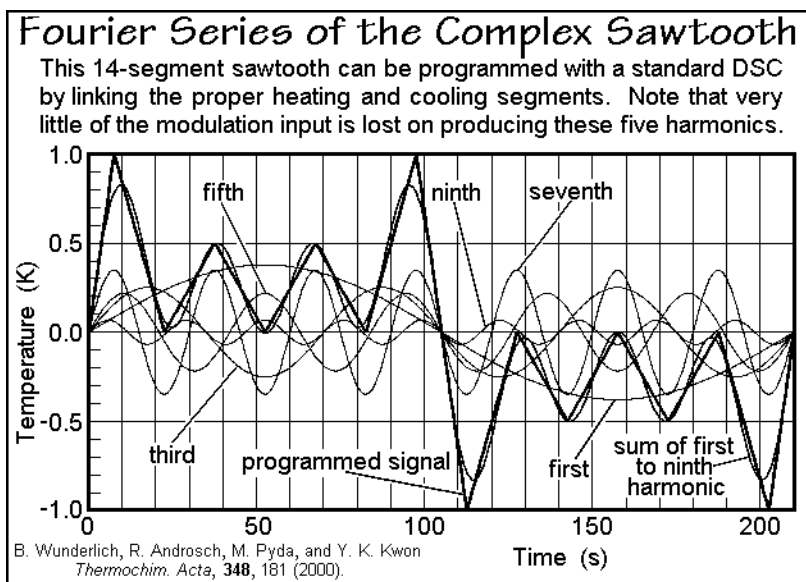


Fig. 4.89

#### 4.4.2 Mathematical Treatment

Next, a mathematical description of  $T_s$  is given for a quasi-isothermal run. This type of run does not only simplify the mathematics, it also is a valuable mode of measuring  $C_p$  as described in Sect. 4.4.5. In addition, standard TMDSC with  $\langle q \rangle \neq 0$  is linked to the same analysis by a pseudo-isothermal data treatment as described in Sect. 4.4.3.

Figure 4.90 summarizes the separation of the modulated sample temperature into two components, one is in-phase with  $T_b$ , the other,  $90^\circ$  out-of-phase, i.e., the in-phase component is described by a sine function, the out-of-phase component by a cosine function. The figure also shows the description of the time-dependent  $T_s$  as the sum of the two components. The sketch of the unit circle links the maximum amplitudes of the two components. Furthermore, the standard addition theorem of trigonometric functions in the box at the bottom expresses that  $T_s$  is a phase-shifted sine curve.

The additional boxed equation on the right side of Fig. 4.90 introduces a convenient description of the temperature using a complex notation. The trigonometric functions can be written as  $\sin \theta = (-i/2)(e^{i\theta} - e^{-i\theta})$  and  $\cos \theta = (1/2)(e^{i\theta} + e^{-i\theta})$  where  $i = \sqrt{-1}$ , so that  $\sin \theta + i \cos \theta = ie^{-i\theta}$ . The real part of the shown equation

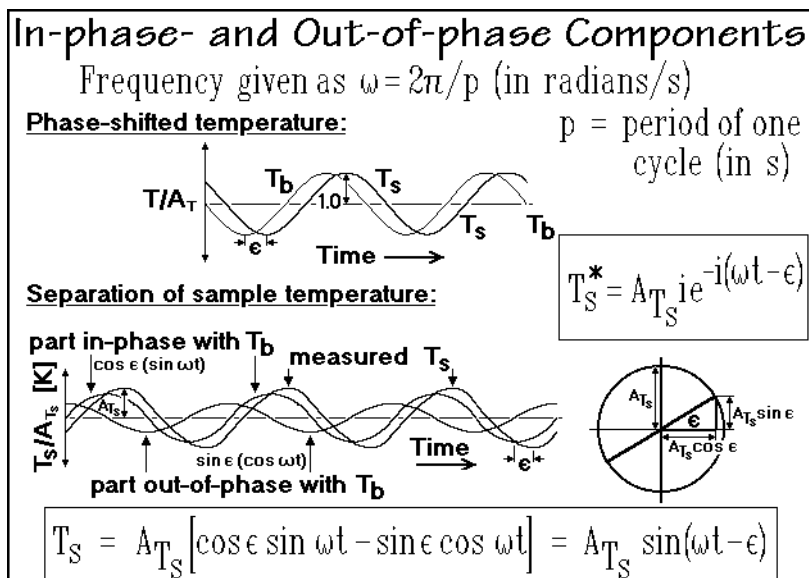


Fig. 4.90

represents then  $T_s$ . The chosen non-standard format of the complex number is necessary since at time zero  $T_s = T_r = T_b = T_o$  and  $\Delta T = 0$ . A phase-shift by  $\pi/2$  leads to the standard notation of complex numbers, given in Sect. 2.3.5 as Eqs. (1).

Naturally all these equations apply only to the steady state, illustrated by the right graph of Fig. 4.55. Its derivation is similar to the discussion for steady state in a standard DSC given in Fig. 4.68. One solves the differential equation for heat-flow rate, as in Fig. 4.67, but including also the term describing the modulation of  $T_s$ :

$$\frac{dQ}{dt} = K \left[ qt + A_{T_b} \sin \omega t - \frac{Q}{C_p} \right].$$

The solution of this differential equation can be found in any handbook and checked by carrying out the differentiation suggested. The terms in the first brackets of the solution are as found for the standard DSC in Fig. 4.68, the second bracket describes the settling of the modulation to steady state:

$$\vartheta = qC_p \left[ t - \frac{C_p}{K} (1 - e^{-Kt/C_p}) \right] + \frac{KA_{T_b}}{\left( \frac{K}{C_p} \right)^2 + \omega^2} \left[ \left( \frac{K}{C_p} \right) \sin \omega t - \omega \cos \omega t + \omega e^{-Kt/C_p} \right]$$

At sufficiently long time, steady state is reached ( $Kt \gg C_p$ ) and the equation reduces after division by  $C_p$  to the steady state temperature  $T(t) - T_o$ . It will then be applied in all further discussions, unless stated otherwise:

$$T(t) - T_o = qt - \frac{q C_p}{K} + \frac{A_{T_b} \left( \frac{K}{C_p} \right)}{\left( \frac{K}{C_p} \right)^2 + \omega^2} \left[ \left( \frac{K}{C_p} \right) \sin \omega t - \omega \cos \omega t \right] .$$

The next step is the analysis of a single, sinusoidal modulation in the DSC environment. In the top line of Fig. 4.91 Eq. (2) of Fig. 4.69 is repeated, the equation for the measurement of heat capacity in a standard DSC. The second line shows the needed insertions for  $T_s$  and  $\Delta T$  for the case of modulation. When referred to  $T_b$ , the phase difference of  $\Delta T$  is equal to  $\delta$  and its real part is the cosine, the derivative of the sine, as given by the top equation. Next, the insertion and simplification of the resulting equation are shown. By equating the real and imaginary parts of the equations separately, one finds the equations listed at the bottom of Fig. 4.91. These equations suggest immediately the boxed expression for  $C_s - C_r$  in Fig. 4.92.

**Analysis of Temperature Difference**

$$\Delta T = T_r - T_s = \frac{C_s - C_r}{K} \frac{dT_s}{dt} - \frac{C_r}{K} \frac{d(T_r - T_s)}{dt}$$

$$T_s^* = A_{T_S} i e^{-i(\omega t - \epsilon)} \quad \Delta T^* = A_{\Delta} e^{-i(\omega t - \delta)}$$

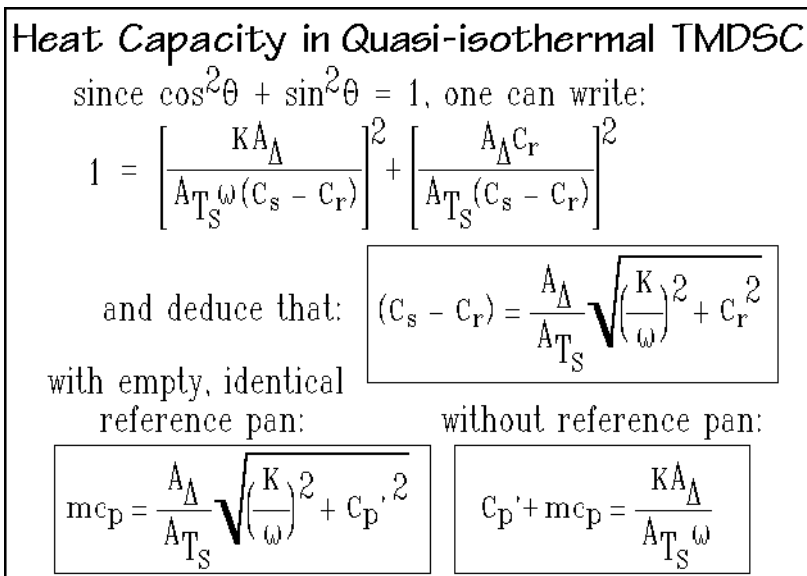
$$A_{\Delta} e^{-i(\omega t - \delta)} = \frac{C_s - C_r}{K} A_{T_S} \omega e^{-i(\omega t - \epsilon)} - \frac{C_r}{K} A_{\Delta} \omega i e^{-i(\omega t - \delta)}$$

$$e^{i(\epsilon - \delta)} = \frac{K A_{\Delta}}{A_{T_S} \omega (C_s - C_r)} - \frac{A_{\Delta} C_r i}{A_{T_S} (C_s - C_r)}$$

$$\sin(\epsilon - \delta) = \frac{A_{\Delta} C_r}{A_{T_S} (C_s - C_r)} \quad \cos(\epsilon - \delta) = \frac{K A_{\Delta}}{A_{T_S} \omega (C_s - C_r)}$$

**Fig. 4.91**

Several types of measurement can be made. First, one can use, as before, an empty pan as reference of a weight identical to the sample pan. The bottom equation of Fig. 4.92 suggests that in this case the sample heat capacity is just the ratio of the modulation amplitudes of  $\Delta T$  and  $T_s$  multiplied with a calibration factor that is dependent on the frequency and the mass of the empty pans. Standardizing on a single pan weight (such as 22 mg) and frequency (such as 60 s) permits measurements of the reversing heat capacity with a method that is not more difficult than for the standard DSC, seen in Figs. 2.28–30. Another simplifying experimental set-up is to use no reference pan at all. Figure 4.92 shows that in this case the pan-weight dependence

**Fig. 4.92**

of the calibration disappears. As a disadvantage, the measured quantity is, however, not the sample heat capacity directly, as before, but the measurement is the heat capacity of sample plus sample-pan.

More specific information was derived for the Mettler-Toledo DSC, as described in Figure 4.57 [30]. For the calculations, the DSC was modeled with an analog electrical circuit of the type shown in Appendix 11 for the elimination of asymmetry and pan effects. The Mettler-Toledo DSC is also of the heat-flux type, but the control-thermocouple is located close to the heater. The model considered the thermal resistances between heater and  $\Delta T$ -sensor,  $R$ , sensor and sample,  $R_s$ , and a possible cross-flow between sample and reference,  $R'$  [30]. Equations (1) and (2) in Fig. 4.93 show the equations which can be derived for the heat capacity,  $C_s^m$ , and the phase angle  $\delta$ . A series of quasi-isothermal measurements for different masses,  $m$ , and frequencies,  $\omega$  are shown in Fig. 4.93 for a sawtooth modulation. Uncorrected data for  $\delta$  and  $\omega$  are given by the open symbols. They were calculated using the bottom-right equation in Fig. 4.92. For the short periods with  $p$  less than 100 s, strong deviations occur. The known specific heat capacity of the aluminum sample is marked by the dotted, horizontal line. The constant, negative offset at long periods,  $p$ , was corrected by the usual calibration with sapphire ( $Al_2O_3$ ) with a constant shift over the whole frequency range. A value of  $35.38 \text{ mW K}^{-1}$  was found for  $K^*$  at 298 K. The deviations at small  $p$  were then interpreted with Eq. (1) making the assumption that they originate from the coupling between the various thermal resistance parameters. To determine  $\delta$ , Eq. (2) was fitted with the true specific heat capacity of the aluminum. The results of the fitting are indicated in Fig. 4.93 by the dashed lines. The value of  $R_s + R^2/(2R + R')$  of Eq. (2) has a sample-mass independent value of  $1.34/K^*$ . Finally, the corrected values for the specific heat capacities were calculated with Eq. (1) and marked in Fig. 4.93 by the filled symbols. All frequency and mass



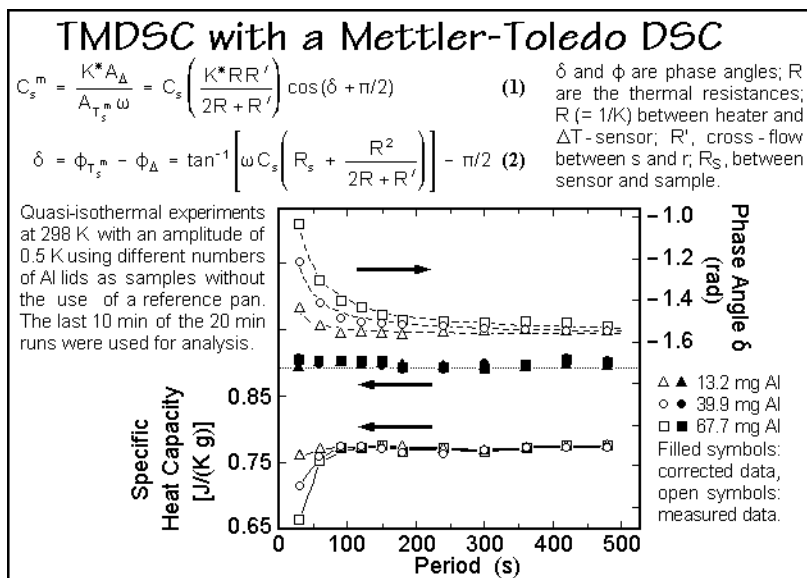


Fig. 4.93

dependence could be removed by this calculation. The RMS error of the data is 0.77%. Although measurements could now be made down to periods of about 20 s, the data evaluation is still cumbersome and not all thermal resistances one would expect to affect the data could be evaluated, such as the resistances within the sample pan and the heat supplied by the purge gas. If these latter effects cause significant changes or delays in the modulation, the parameters in the just discussed equations in Fig. 4.93 are just fitting parameters.

To find a universal equation which can be used to calibrate the data for different masses, frequencies, sample packing, and purge-gas configuration, the power-compensated DSC was employed [31]. Its operation is described in Figs. 4.58–61. Equation (1) in Fig. 4.94 repeats the approximate heat capacity determination from standard DSC using the total (averaged) heat-flow rate and rate of change of sample temperature (see Fig. 4.76,  $\langle HF \rangle = K \Delta T$ ,  $C_s - C_r = mc_p$ ,  $\langle q \rangle = q$ ). Equation (2) progresses to the quasi-isothermal, reversing heat capacity given in Fig. 4.92 at the bottom left. Finally, Eq. (3) shows the substitution of an empirical parameter,  $\tau$ , into the square root of the equation in Fig. 4.92 which can be calibrated. For very low frequencies,  $\tau$  approaches  $C_p/K$ , as expected from Fig. 4.92. This equation was introduced already in Fig. 4.54 as basic equation for the data evaluation.

The experiments on the left of Fig. 4.94 show the results for quasi-isothermal, sawtooth-modulated polystyrene as a function of period and amplitude (12 mg, at 298.15 K) [31]. The filled symbols were calculated using Eq. (1). Data were chosen when steady state was most closely approached, i.e., at the time just before switching the direction of temperature change or over the range of time of obvious steady state. The thin solid line is the expected heat capacity, the dotted lines mark a  $\pm 1\%$  error range. The bold line is an arbitrary fit to the open symbols. The different modulation amplitudes were realized by choosing different heating and cooling rates. The

modulation amplitude seems to have no influence on the dependence on period. The open symbols represent the reversing specific heat capacity. They were calculated using the amplitudes of the first harmonic of the Fourier fit of heat-flow rate and sample temperature to Eq. (2). In the case of the Fourier fit, the deviation from the true heat capacity starts at a period of  $\approx 96$  s. In the case of standard DSC, this critical value is shifted to  $\approx 48$  s. The influence of the sample mass was analyzed for Al. The data are shown on the right in Fig. 4.94. An increasing sample mass, as well as a shorter modulation period reduces the measured heat capacity. Again, the Fourier fit results in larger deviations from the expected value when compared to the heat capacity calculated by the standard DSC equation, Eq. (1).

Figure 4.95 illustrates the evaluation of the constant  $\tau$  as the slope of a plot of the square of the reciprocal of the uncorrected specific heat capacity as a function of the square of the frequency as suggested by Eqs. (2) and (3) of Fig. 4.94. Note that the calibration run of the sapphire and the polystyrene have different values of  $\tau$ . In

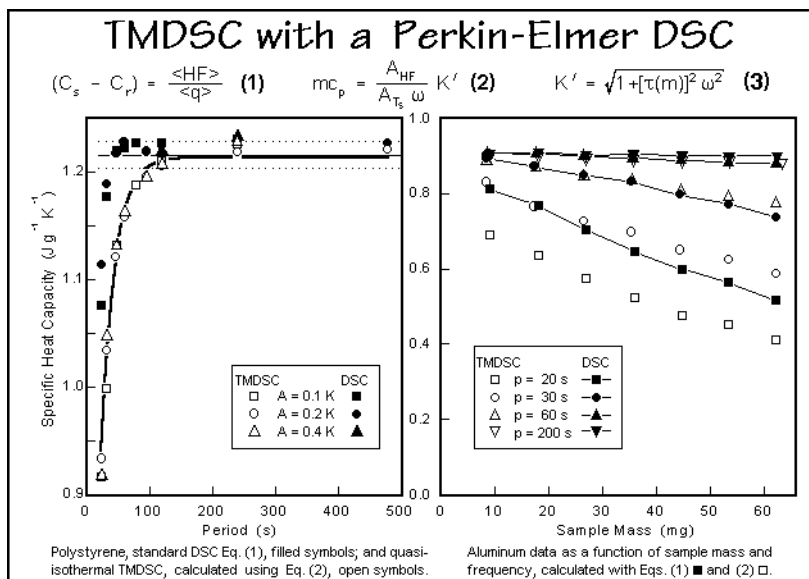


**Fig. 4.94**

addition, the asymmetry of the calorimeter must be corrected in a similar process as discussed in Sect. 4.4.4, again with a different value of  $\tau$ . Online elimination of the effects of asymmetry and different pan mass, as described in Appendix 11, should improve the ease of measurement. This method of analysis increases the precision of the reversing data gained at high frequency, and also the overall precision, since a larger number of measurements are made during the establishment of  $\tau$  as a function of frequency and spurious effects not following the modulation are eliminated.

A simplification of the multi-frequency measurements can be done by using not only the first harmonic of sawtooth modulation for the calculation of the heat capacity, but using several, as shown in Fig. 4.96 [32]. A single run can in this way complete many data points. As in Fig. 4.95, the lower frequencies have a constant  $\tau$ , while at

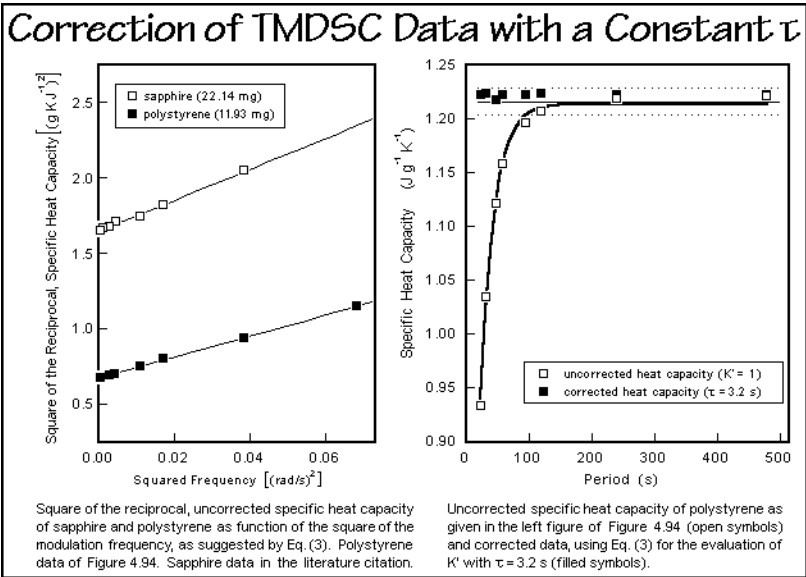


**Fig. 4.95**

higher frequency,  $\tau$  varies. Since the change of  $\tau$  with frequency is a continuous curve, rather high-frequency data should be usable for measurement. Since the higher harmonics in the sawtooth response have a lower amplitude, the complex sawtooth of Fig. 4.89 was developed with five harmonics of similar amplitudes [29]. A comparison of this type of measurement was made with all three instruments featured in this section in Figs. 4.57, 4.58, and 4.85 [33–35]. All data could be represented

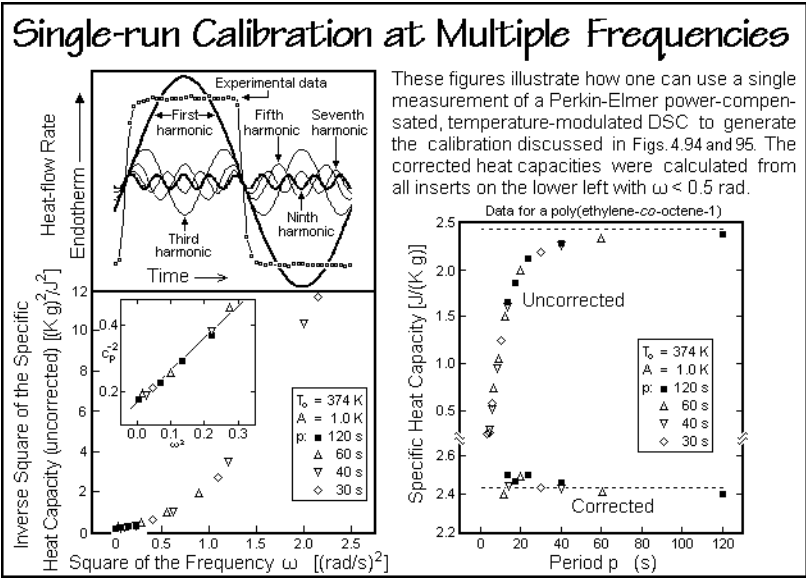


**Fig. 4.96**

with empirically found values of  $\tau$  and precision as high as  $\pm 0.1\%$  was approached, matching the typical precision of adiabatic calorimetry (see Sect. 4.2).

#### 4.4.3 Data Treatment and Modeling

The data treatment of TMDSC is summarized in Figs. 4.97 and 4.98. It uses the instantaneous values of  $\Delta T(t)$ , represented by curve **A** in Fig. 4.99 and involves their sliding averages ( $\langle \rangle$ ) over full modulation periods,  $p$ , as given by curve **B**. By subtracting this average from  $\Delta T(t)$ , based on curve **C**, a *pseudo-isothermal analysis* becomes possible. The averages contain none of the sinusoidal modulation effects and are called the *total heat-flow rate* ( $\langle HF(t) \rangle$  or  $\langle \Phi(t) \rangle$ , being proportional to  $\langle \Delta T(t) \rangle$ ). This analysis is strictly valid only, if there is a *linear response* of the DSC, i.e., doubling any of the variables in Fig. 4.54 ( $m$ ,  $q$ , and  $c_p$ , and also any latent-heat) doubles the response,  $\Delta T$ . In addition, the total quantity, **B**, must be *stationary*, i.e., change linearly or be constant over the whole period analyzed. The expression for the sample temperature,  $T_s(t)$ , is calculated analogously and should agree with the parameter set for the run, so that  $\langle T_s(t) \rangle$  is the total temperature calculated from the chosen underlying heating rate ( $= T(0) + \langle q \rangle t$ ). These averages make use of data measured over a time range  $\pm p/2$ , i.e., the output of TMDSC can only be displayed with a delay from  $t_0$ , the time of measurement of the calculated value.

Part 2 in Fig. 4.97 aims at finding the amplitude of curve **C**, the pseudo-isothermal response,  $\langle A_\Delta(t) \rangle$ , called the *reversing heat-flow rate*. Again,  $\langle A_{T_s}(t) \rangle$  is set as a run parameter and needs only a check that, indeed, it is reached. The amplitude  $\langle A_\Delta(t) \rangle$  is the first harmonic of the Fourier series for  $\Delta T(t)$ . The first step is the finding of **D** and **E**, where the capital letters indicate the corresponding curves in Figs. 4.99 to 4.102. Note: **D** =  $\langle A_\Delta \rangle \sin(\omega t - \delta) \sin \omega t$  and **E** =  $\langle A_\Delta \rangle \sin(\omega t - \delta) \cos \omega t$ . The

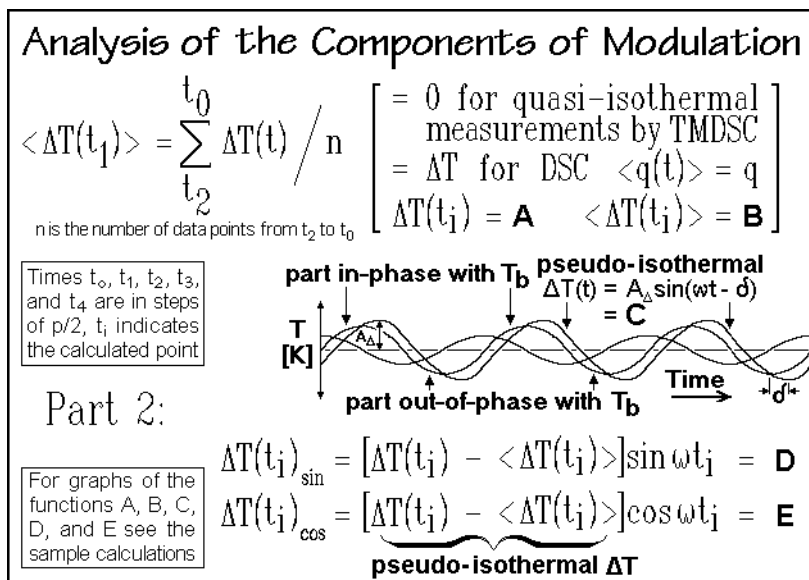


**Fig. 4.97**

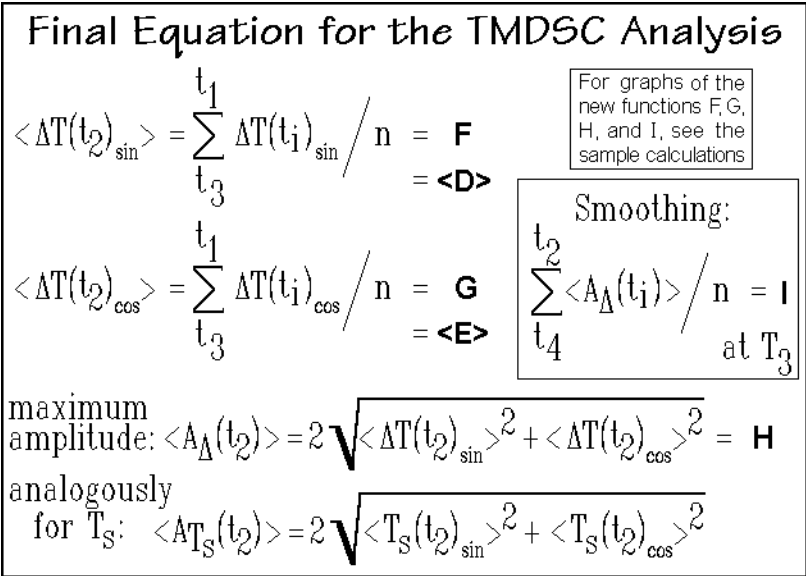


**Fig. 4.98**

value of  $\langle A_{\Delta} \rangle$  is then found from renewed averaging over one period, i.e., one forms  $\langle \Delta T(t_2)_{\sin} \rangle = (A_{\Delta}/2) \cos \delta = \langle \mathbf{D} \rangle = \mathbf{F}$ , and  $\langle \Delta T(t_2)_{\cos} \rangle = (A_{\Delta}/2) \sin \delta = \langle \mathbf{E} \rangle = \mathbf{G}$ , as shown in Fig. 4.98 and displayed in Fig. 4.99. The amplitude  $\langle A_{\Delta}(t_2) \rangle = \mathbf{H}$  is obtained from the sums of the squares of  $\mathbf{F}$  and  $\mathbf{G}$ . To further improve  $\mathbf{H}$ , smoothing is done by one more averaging, as shown in the box of Fig. 4.98. This yields the final output  $\mathbf{I}$ . The data used for  $\mathbf{I}$  cover two modulation periods and are displayed at  $t_3$ , 1.5

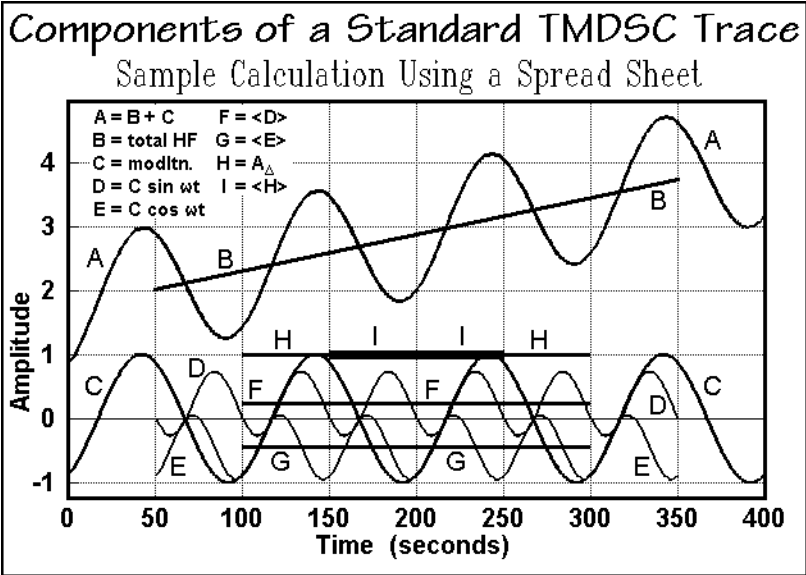


**Fig. 4.99**

periods later than the time of measurement  $t_0$ . All data between  $t_0$  and  $t_4$  are needed for the computation of this smoothed, reversing heat-flow amplitude  $\langle A_\Delta(t_3) \rangle$ .

The curves for the previous screens were modeled with a simple Lotus 1-2-3™ spreadsheet [36]. The input is a table of the to be analyzed heat-flow rate HF or temperature difference  $\Delta T$ . Since one can check through the columns of data for **A–I** for the propagation of any changes, this spreadsheet has proven a valuable tool for the prediction, analysis, and understanding of the results of TMDSC. Commercial mathematics packages which carry out Fourier analyses can as well be adapted to these calculations and also will give the higher harmonics without need of further programming. Several examples of data analyses are shown next.

Figure 4.100 is a similar analysis as in Fig. 4.99, except that at 200 s a sharp, 50% spike occurs in the heat-flow rate. The maximum reversing heat-flow-rate amplitude was chosen for all simulations to be 1.0, the phase lag  $\delta$  is  $45^\circ$  and  $p = 100$  s. Note that for clarity, the reversing, smoothed heat-flow rate **I** is moved by +1.0 in amplitude

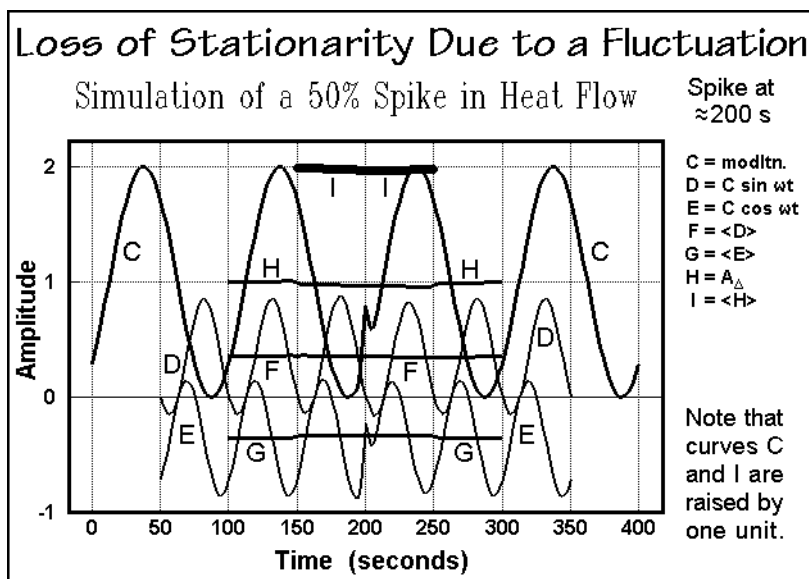


Fig. 4.100

in Fig. 4.100, and also in all the subsequent figures of this set of computations. The spike causes an instantaneous loss of stationarity which can be traced through the evaluation. The averaging steps smooth this effect greatly. If the spike is to be studied, as in the presence of a small amount of sharply melting material, the just completed data treatment is a poor choice. A detailed analysis of curve **C** in the time domain must then be made, as seen in Figs. 4.106–109, below.

In Fig. 4.101 an abrupt 50% increase in curve **C** starts at 300 s. An effect on the reversing heat-flow rate occurs only at the time of increase, broadened and smoothed by triple averaging. The constant change does not affect the measurement at a later time. The baseline shifts due to fluctuations in purge-gas flow or changes in temperature of the calorimeter environment are thus minimized.

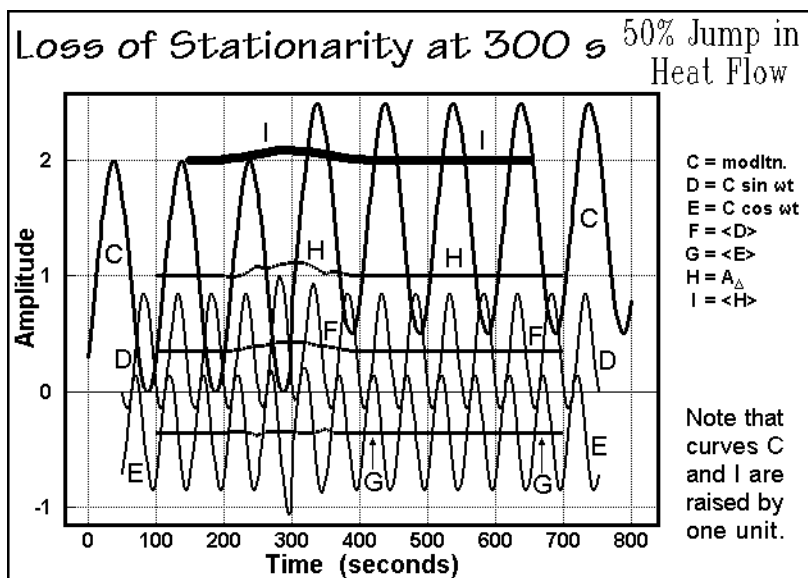


Fig. 4.101

In Fig. 4.102 a linearly increasing and an exponentially increasing heat-flow rate of many times the size of the effect to be measured, is added at 250 and 0 s in the top and bottom curves, respectively. The loss of stationarity is in these cases negligible, and a separation of reversing and nonreversing components is possible with high precision. Effects of this type are expected in samples that undergo irreversible

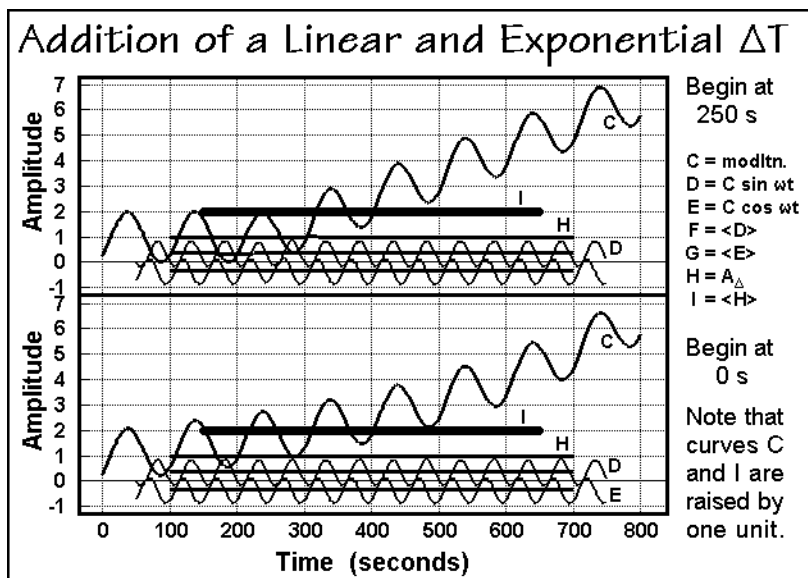


Fig. 4.102

chemical reactions or phase transitions. Despite the major disruption in the heat flow, TMDSC can still evaluate heat capacity quantitatively and follow, for example, the kinetics of the change of state.

These four examples, depicted in Figs. 4.100–103, illustrate the behavior of the heat-flow-rate response on analyzing various changes in the sample. The loss of stationarity, most clearly seen in Fig. 4.100 and 4.101, does not only affect the first harmonic, i.e., the reversing signal, but also the total signal, **B** in Fig. 4.99, which is not shown in the later figures. Because of the deviation from the sinusoidal response, the sliding average broadens the effect of the sharp peak at 200 s in Fig. 4.100 and the sharp jump in Fig. 4.101 over one whole modulation period. The total signal, thus, does not correspond to the actual effect, possibly broadened by instrument lag, but it is broadened additionally by the deconvolution. A separately run, standard DSC curve and the total heat-flow-rate curve of the TMDSC do not agree in shape, although the enthalpy, obtained by integration over time does ultimately reach the same value because of the conservation of heat. Specially clear examples of this broadening of the total heat-flow rate are illustrated in Figs. 4.108 and A.13.13, below.

The reversing signals **H** in Figs. 4.100 and 4.101, as the first harmonic of a Fourier series describing the actual response, do not represent the shapes of the response, but also, they do not give the proper magnitudes on integration since the higher harmonics are not considered. Proper analysis is reestablished after stationarity is reached again, or if the effect is gradual, as in Fig. 4.102, and the deviation from stationarity is negligible. The nonreversing signals, being calculated from **B** and **H**, contain the same errors due to nonstationarity, but note that Eq. (3) of Appendix 13 allows for a separate determination of the irreversible response.

#### 4.4.4 Instrumental Problems

Considerable calibration and care are needed not to exceed the conditions of steady state and negligible temperature gradients within the sample for the standard DSC, as discussed in Sect. 4.3.4–7. For TMDSC, additional points must be considered, as discussed in Sect. 4.4.3. The conditions of steady state may be relaxed to some degree, as long as linearity and stationarity are kept. Calibrations and checks of compliance with those conditions, thus, are also key to good TMDSC.

To compare the functioning of a TMDSC with that of a DSC, Fig. 4.103 gives data for three DSC runs and a matching TMDSC trace (TA Instruments, MDSC™ 2910). Plotted are the instantaneous (not averaged or smoothed) heating rates  $q(t)$  and heat-flow rates  $HF(t)$  (proportional to  $\Delta T$ ). The DSC was run at heating rates  $q = 3, 5$ , and  $7 \text{ K min}^{-1}$ , the TMDSC at  $\langle q \rangle$  of  $5 \text{ K min}^{-1}$ . These conditions result in a maximum  $q(t)$  of  $7.0$  and a minimum  $q(t)$  of  $3.0 \text{ K min}^{-1}$  for  $\langle q \rangle \pm A_{T_s} (2\pi/p)$ . Note that the time to reach steady state with TMDSC is longer than in a standard DSC. The four curves match well above  $340 \text{ K}$ . Typically, one should allow 2–3 min to reach steady state for the chosen calorimeter.

The next question to be answered is how large a modulation amplitude can one choose for a given experiment? In order to achieve maximum sensitivity, one wants to use maximum heating rates and large sample masses, but without creating undue temperature gradients within the sample. Figure 4.104 illustrates for two cooling



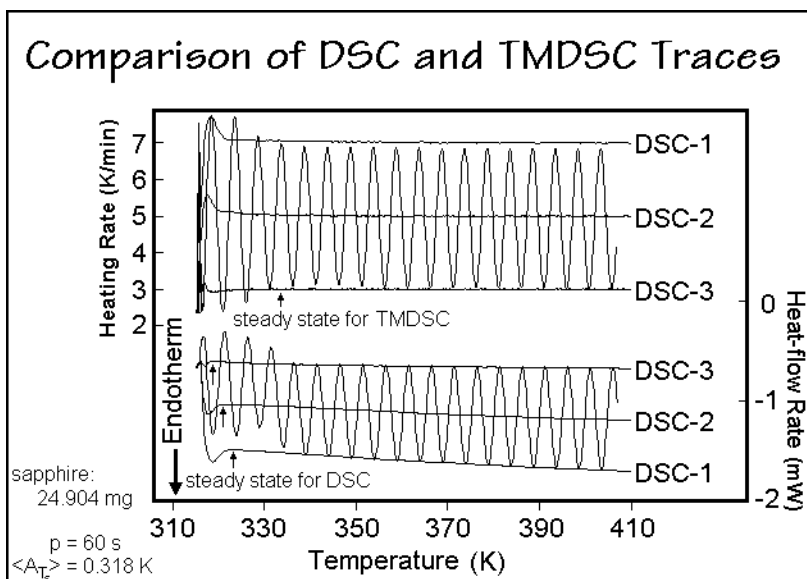


Fig. 4.103

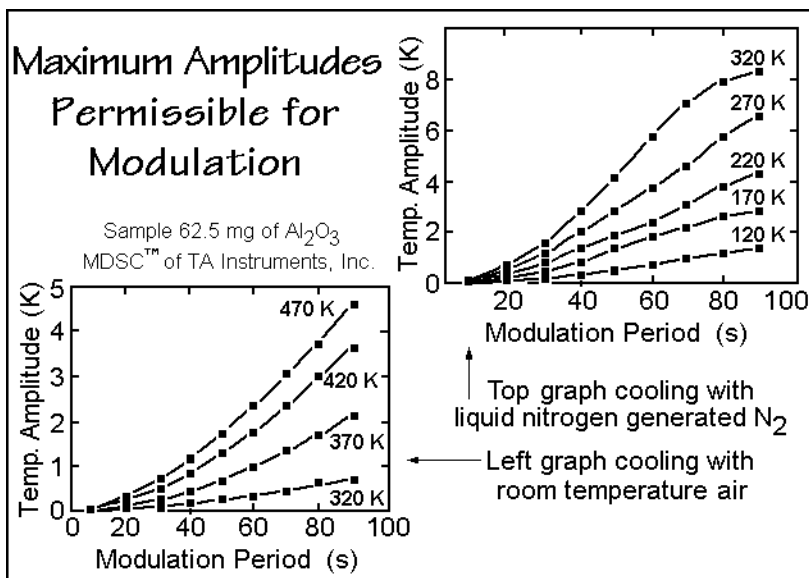
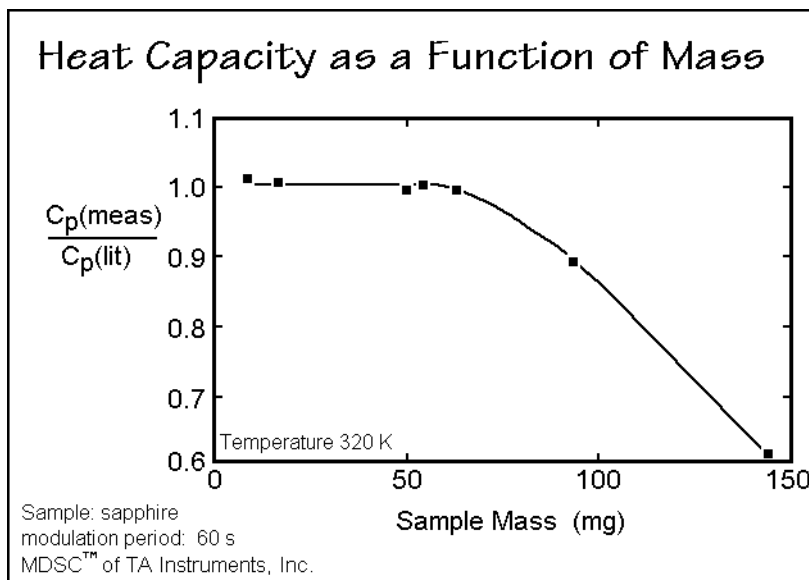


Fig. 4.104

conditions the maximum amplitudes that could be used at selected temperatures as a function of  $p$ . To use the figures, the amplitude for the lowest temperature of the run is picked and applied to the whole temperature scan, to make sure that the calorimeter can follow the chosen modulation over the chosen temperature range. One should generate these plots for each individual calorimeter and sample-type.

The effect of increasing sample mass on  $C_p$  is shown in Fig. 4.105. As the mass goes beyond the limit of negligible temperature gradient within the sample, part of the sample does not follow the modulation and thus, the linear response is lost. To find the proper conditions, one should run samples with different masses or do a full calibration of  $\tau$ , as shown in Figs. 4.93 to 4.96.



**Fig. 4.105**

An interesting experiment is the temperature calibration of TMDSC with indium. To understand the process, a direct analysis in the time domain is necessary, as shown in Fig. 4.106. The broken curve of the sample-sensor temperature indicates that the calorimeter was still controlled reasonably well. A magnification of the traces is given in Fig. 4.107. In the melting and crystallization ranges a temperature lag of up to 0.2 K can be seen when comparing the dash-dotted line for the programmed temperature with the solid line for the measured temperature. The small heat-flow-rate amplitudes only due to heat capacity can be noticed before and after the melting range (up to 5 min and above 14 min). To create the about 30-fold increase in  $\Delta T$  during melting and crystallization, the block- and reference-temperature modulations must have increased also by a factor of 30, a situation unique for controlling the modulation at the sample sensor. The first melting occurs at peak 1, close to  $T_s(t)$  for zero heating rate, and the last crystallization at peak 18, close to the same temperature (see Figs. 4.82 and 4.83). During melting, sufficient nuclei are seemingly left in these measurements to initiate crystallization with little or no supercooling.

The evaluation of the heat-flow-rate amplitude as modeled in Figs. 4.97–100 gives obviously an apparent heat capacity that yields on integration a too large reversing heat of fusion. An example of such evaluation is shown for a block-temperature-modulated TMDSC in Fig. 4.108. The maximum amplitude  $\langle A_{HF} \rangle$  (H in Figs. 4.99–102) remains high as long as melting and crystallization occurs. Similarly, the

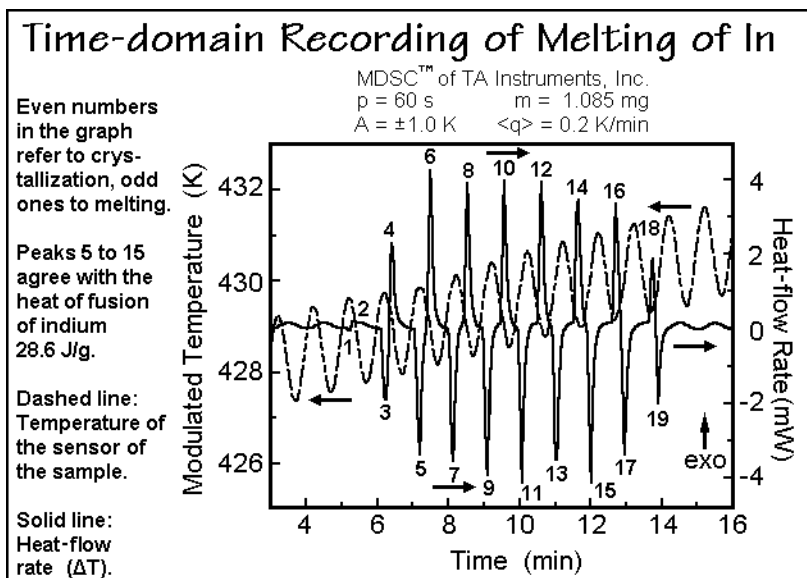


Fig. 4.106

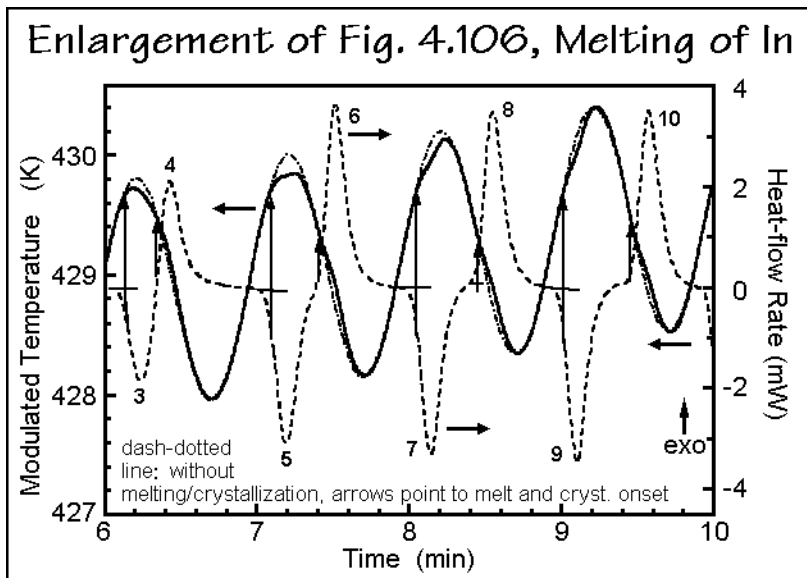
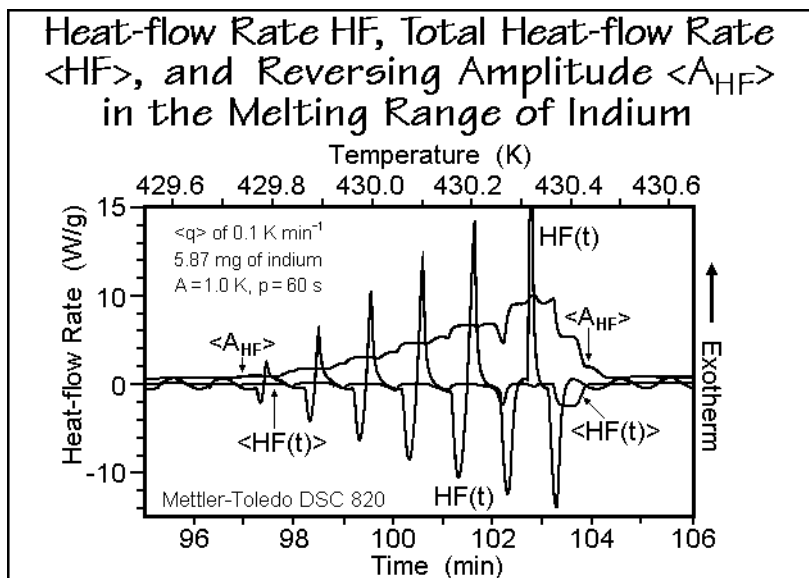
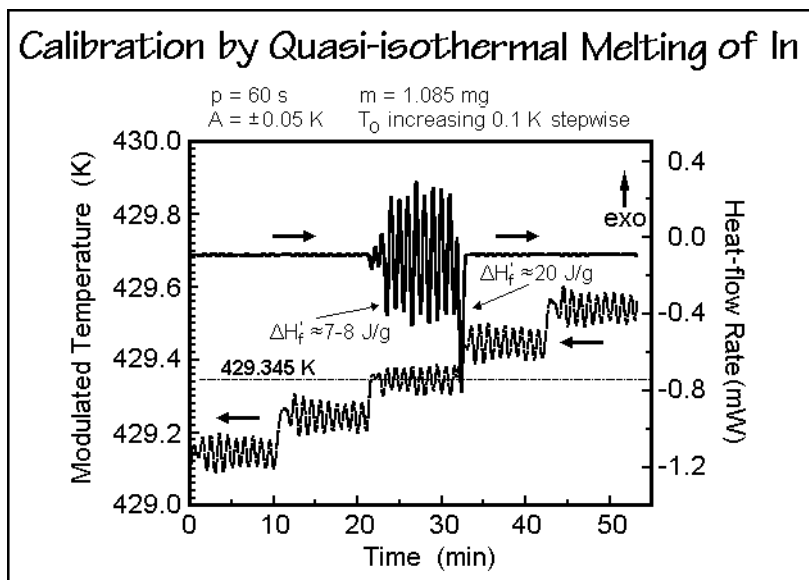


Fig. 4.107

total heat-flow rate  $\langle HF(t) \rangle$  is broadened over the whole melting and crystallization range, and even the largest maximum at the end of the melting is displaced to a higher temperature and broadened due to the averaging procedures. Only the time-domain recording of the heat-flow rate  $HF(t)$  can be interpreted as is seen in Figs. 4.107–108. After the last melting in peak 19 of Fig. 4.106, the melt supercools, as can also be seen

**Fig. 4.108**

in Figs. 4.82 and 4.83, i.e., no nuclei are left. This sequence of figures on melting of indium has shown that much can be learned about the melting and crystallization process by performing well-controlled TMDSC experiments. At the same time, the instrumental limitations become obvious when analyzing such a sharp-melting substance like indium. Figure 4.109 reveals the close control possible with the quasi-isothermal mode of analysis with very small modulation amplitudes. A step-wise

**Fig. 4.109**

increase in  $T_0$  of 0.1 K with a temperature modulation of  $\pm 0.05$  K brackets the melting point of indium. The figure reproduces five steps of the experiment. Only in the center step, melting occurs. Integrating the melting peaks in the time domain yields about 25% of the heat of fusion. The remaining  $20 \text{ J g}^{-1}$  can be detected on heating to the next quasi-isotherm (at about 30 min). The small modulation amplitude did not set up a large-enough temperature-gradient between  $T_b$  and  $T_s$  to conduct enough heat into the sample calorimeter for complete melting. The jump from the endotherm of partial melting to the exotherm goes with maximum speed (see also the enlarged Fig. 4.134, below). The observed melting temperature of  $429.34 \pm 0.05$  K agrees reasonably well with the expectation from Fig. 4.83 at  $\langle q \rangle = 0$ .

The use of the data treatment of Sect. 4.4.3 brings an additional problem into the quantitative analysis. By restricting the analysis to measurement of maximum amplitudes, one cannot distinguish between a positive or negative  $\Delta T$  or heat-flow rate. This can only be done by analyzing the data in the time domain, as with a standard DSC. As long as the difference in heat capacity between reference and sample is large, the problem is minor, because the sign of the differential heat flow is obvious. The baseline runs, however, with empty calorimeters to evaluate the asymmetry correction have very small amplitudes (see Fig. 2.29, amplitude  $a_R$ ) and may be just as often positive as negative. Figure 4.110 presents the results of an experiment to determine this cell asymmetry. A series of pairs of empty aluminum pans of different weights were run in quasi-isothermal experiments at 322 K, and then with the sample pan filled with 41.54 mg of sapphire, represented by open and filled circles, respectively. Negative and positive imbalances give positive heat capacities for correction. The sapphire run shows, because of its always higher heat capacity on the sample side, the expected increasing heat capacity with increasing weight of the empty sample pan. Only if the left empty run amplitudes are added and the right ones

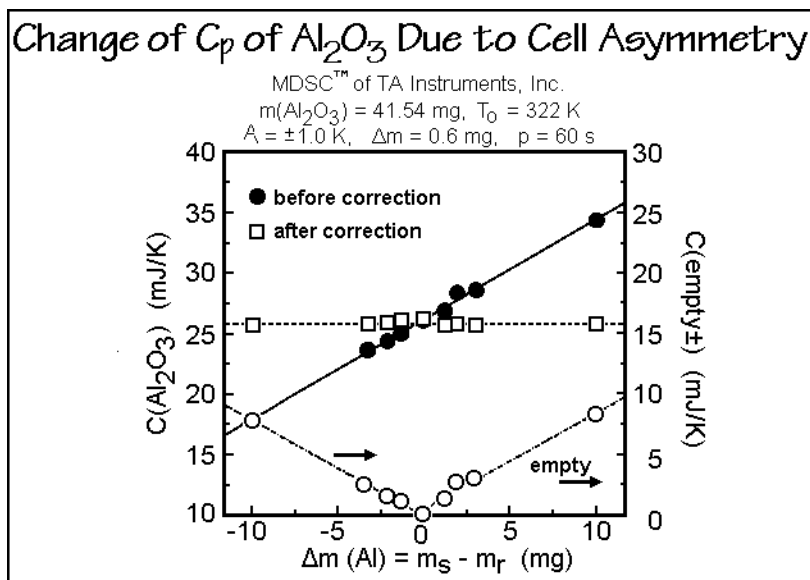


Fig. 4.110

subtracted is the correct heat capacity found for the heat capacity of the sapphire given by the open squares. The asymmetry measured extrapolates to an equivalent  $\Delta m$  of +0.6 mg. To resolve this problem, and to account for the change of the imbalance with temperature, it is suggested when using the method of Fig. 4.92 for heat capacity measurement, to overcorrect by using in the present case a two-milligram lighter reference pan for all runs to guarantee a positive  $C(\text{empty} \pm)$  at all temperatures.

Figure 4.111 illustrates the effect of the phase difference by comparing the determination of the corrected amplitudes in standard DSC and TMDSC for both, a positive and negative  $\Delta m$ , in the left and right schematics, respectively. The resulting phase difference between the  $\text{Al}_2\text{O}_3$  and empty run is clearly seen. Figure 4.112 shows the results of an actual TMDSC run in a plot of the observed phase angle for the data of Fig. 4.110. An asymmetry correction, thus, must involve either a correction in the time domain (possible in some commercial software), an over-correction as suggested with Fig. 4.110, or it may be possible to use the Tzero™ method of Appendix 11.

Another topic to establish a good TMDSC practice deals with Lissajous figures (or Bowditch curves), plots of the time-dependent heat-flow rate  $\text{HF}(t)$  or  $\Delta T(t)$  versus

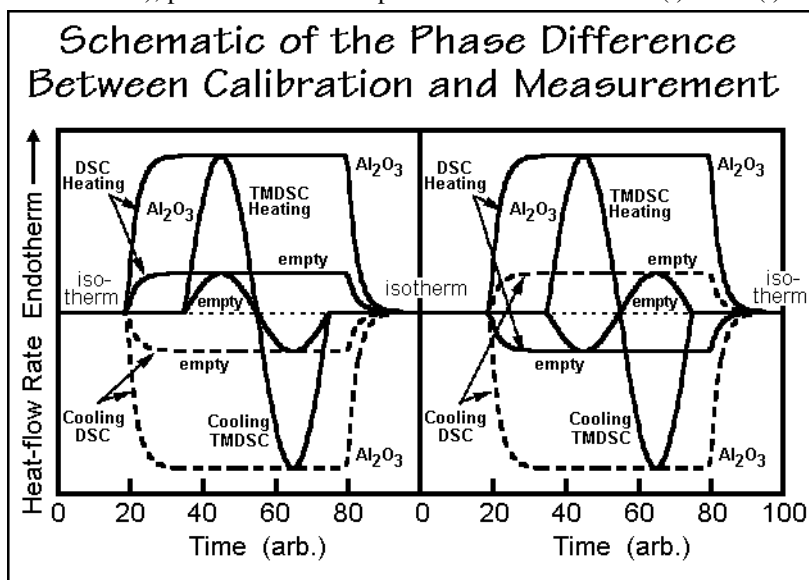


Fig. 4.111

$T_s(t)$ . For perfect steady-state without heat-flow or temperature drift, the phase-shifted, sinusoidal responses of identical frequency,  $\omega$ , should define ellipses. Rather perfect Lissajous figures of a quasi-isothermal TMDSC run in the glass transition region of poly(ethylene terephthalate) are displayed in Fig. 4.113. Only the last 10 minutes of 20-min runs are shown, eliminating the approach to steady state. Figure 4.114 shows long-time changes of the Lissajous figures of poly(oxyethylene) in the melting range. A small amount of melting and crystallization can be seen to build up with time on subsequent Lissajous figures (see also Chap. 6). Two further uses of Lissajous figures are given in the application sections, below, one in standard TMDSC

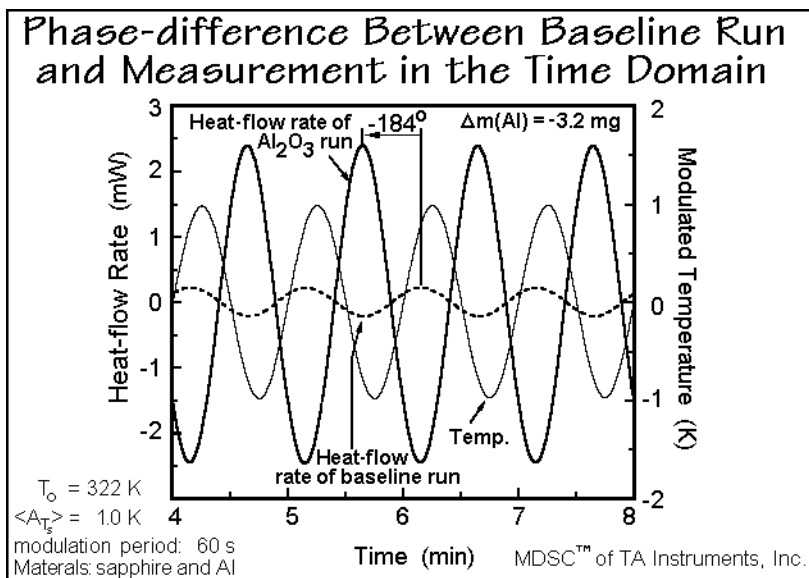


Fig. 4.112

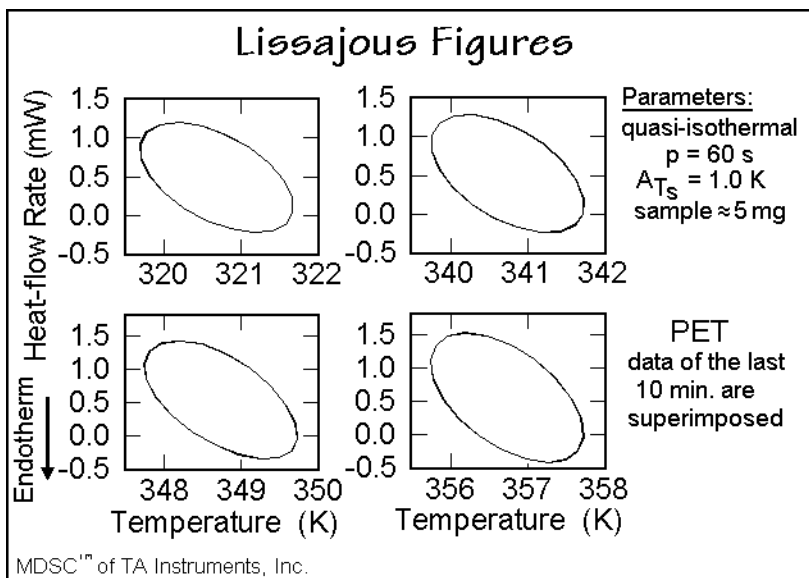


Fig. 4.113

for measurement of heat capacity with an underlying heating rate with Fig. 4.121, the other illustrating the effect of melting and crystallization in Fig. 4.135 where the indium melting is illuminated using the data of the Figs. 4.109 and 4.134. These examples point to the large amount of information that can be extracted by the interpretation of Lissajous figures.

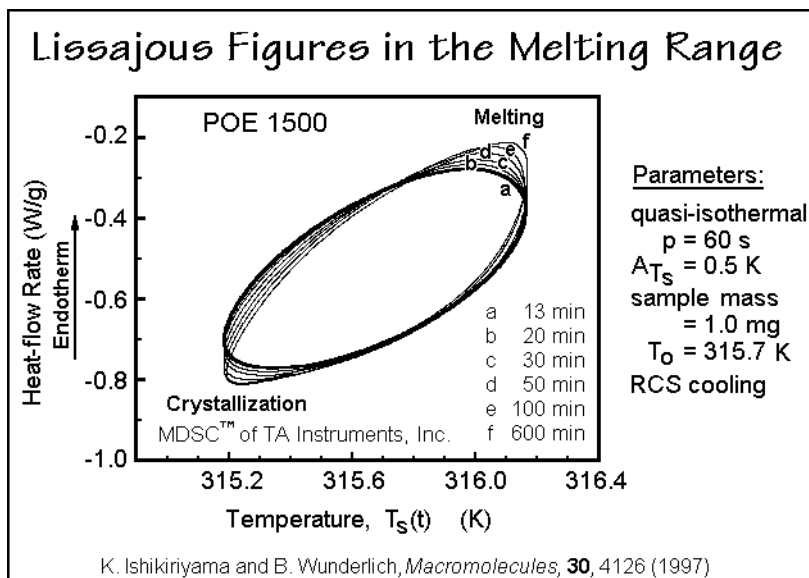


Fig. 4.114

Finally, the amplitude and frequency dependence of the TMDSC response is of interest. In Fig. 4.115, the dependence of the reversing, specific heat capacity of polycaprolactone with the repeating unit  $(-\text{CH}_2)_5\text{CO}-\text{O}$  is displayed as a function of modulation amplitude close to the melting peak [37]. The experimentation involved quasi-isothermal TMDSC at 334 K. Within the experimental error, no amplitude-dependence of the reversing specific heat capacity is seen, as is expected for a linear

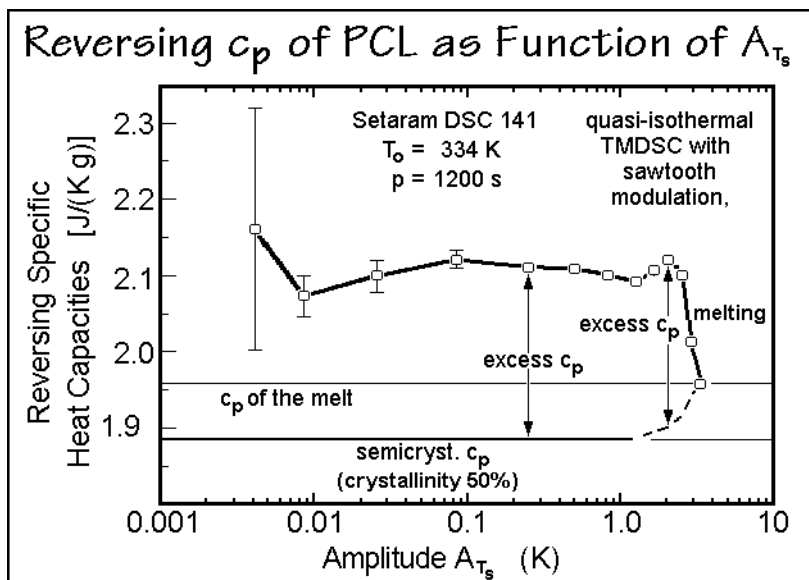


Fig. 4.115



response. Only at the highest amplitudes is the melting peak exceeded and the response decreases to the heat capacity of the liquid, as proven by the dashed line which follows the decreasing crystallinity.

The frequency dependence of the TMDSC response is shown in Fig. 4.116 [38]. The example polymer is nylon 6, polycaprolactam,  $[(-CH_2)_5-CO-NH]_x$ . The heat capacity at lower temperature shows no frequency dependence, but the apparent,

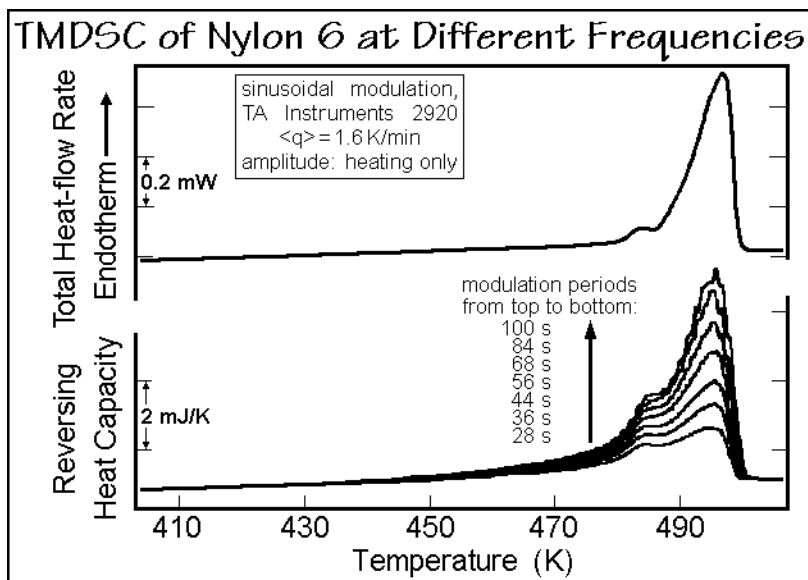


Fig. 4.116

reversing heat capacity in the melting range decreases drastically with frequency. The cause of this change with frequency is the time-dependence of the processes seen in the melting region. A detailed analysis was attempted using the measured phase lag between the modulation of the temperature and the heat-flow-rate response. All modulations were chosen such that the sample was exposed only to heating and no reversible crystallization should be seen. By extrapolation from outside the transition range, the phase lag due to the phase transformation of the sample was separated from the observed total phase lag which also includes delays due to thermal lags within the calorimeter and the sample. From the phase lag caused by the transition alone, one can calculate the complex heat capacity,  $C_p^*$ , as described in Sect. 2.3.5, Eq. (3):

$$C_p^* = C_p' - iC_p''$$

with  $C_p'$  representing the real or storage heat capacity and  $C_p''$ , the imaginary or loss heat capacity. The reversing heat capacity is then equal to the modulus or the absolute value of  $C_p^* = |C_p^*|$ . Next, the irreversible melting was modeled in [38] by a broad distribution of crystallites of different melting temperatures with the total melting rate represented by the time derivative of the total crystallinity. The latent heat-flow rate was analyzed as a function of modulation frequency and heating rate, using experiments of Fig. 4.116 for the underlying heating rate  $1.6 \text{ K min}^{-1}$ .

The frequency dependence yields information on the characteristic time of melting, and from its dependence on the underlying heating-rate, the superheating can be assessed. The extensive reorganization of the nylons, discussed in Chap. 6, provides an additional complication, adding an exotherm to the heat-flow rate, even during the heating-only modulation condition. Figure 4.117 depicts schematically the summation of the modulation effects on the basic heat capacity. Curve **a** represents the

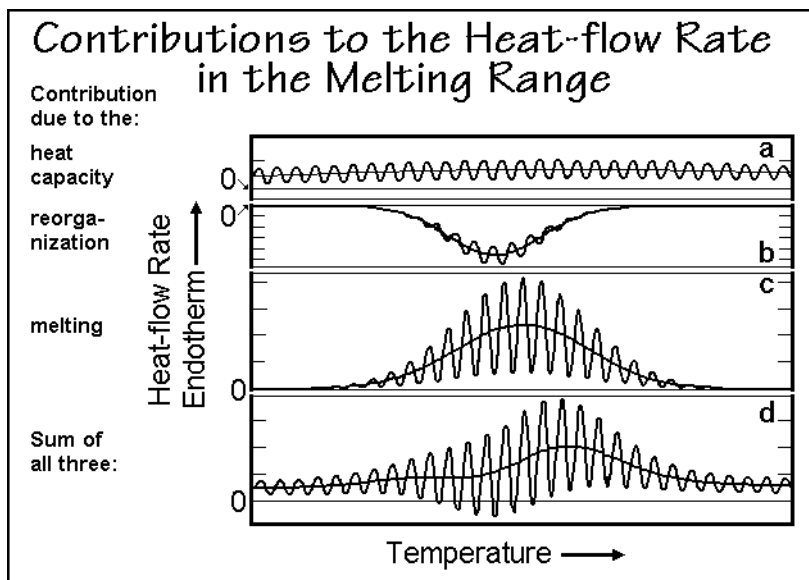


Fig. 4.117

contribution from the heat capacity, curve **b** the reorganization exotherm with a negligible modulation, and curve **c**, the melting endotherm. By a judicious choice of the parameters, the observed total heat-flow-rate curve of Fig. 4.116 can be matched. Forming now the total reversing heat-flow rate at zero frequency from the curve **d** in the figure, one obtains the mean endothermic heat-flow rate.

Plotting the normalized, imaginary versus the real (storage) heat capacity yields the Cole-Cole plot depicted in Fig. 4.118. The points are calculated from Fig. 4.116 at the various analyzed heating rates, making use of the phase angles. The half-circle was matched to the data points by adjusting the heat capacity (curve **a** of Fig. 4.117), the mean endothermic heat-flow rate (curve **c** of Fig. 4.117), and a single (Debye-type) relaxation time ( $\approx 7$  s). While for higher frequencies the curve is close to a semicircle, as expected for a single relaxation time, deviations become appreciable for lower frequencies at higher heating rates, an indication that then, the assumed steady state is lost. Similarly, it could be shown that higher harmonics should have been included in the analysis to account for nonlinearity of the response. The relaxation time showed an irregular dependence on temperature and an inverse square-root dependence on the heating rate. Figure 4.119, finally, summarizes the various heat-flow rates that can be extracted from this analysis. The total heat-flow rate is represented by the heavy line and is related to the standard DSC signal. The reversing heat-flow rates are frequency

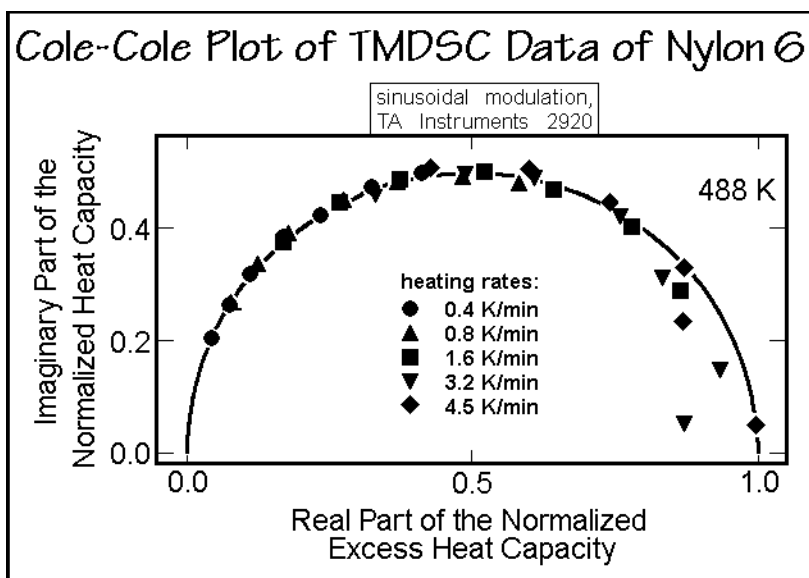


Fig. 4.118

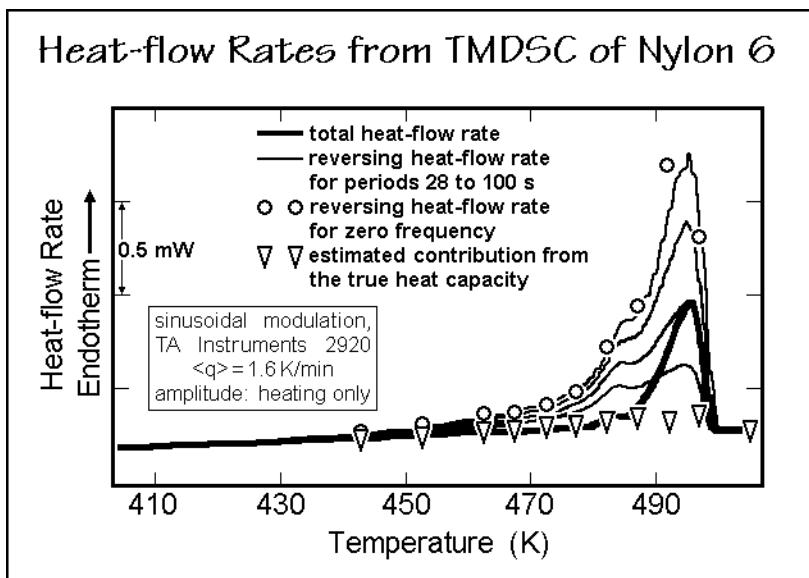


Fig. 4.119

dependent, as observed also for a number of other polymers [39]. At low frequency they exceed the total heat-flow rate because of the exotherm which is modulated only little. The endothermic, reversing heat-flow rate is given by the circles, and the reversible heat capacity by the triangles. The latter quantities were obtained by fitting the Cole-Cole circle.

### 4.4.5 Heat Capacities

The calculation method for heat capacity using the reversing signal of TMDSC is shown in Fig. 4.92. The total heat-flow rate can, in addition, be treated as for the standard DSC, illustrated in Figs. 2.28–30. For reversible processes both methods should give the same results. Differences may arise from instrumental problems, as discussed in Sect. 4.4.4 and in Sect. 4.3.4. If all precautions are taken, the reversing heat flow of TMDSC should be able to yield better data by rejecting spurious heat losses and irreversible heat flows. In Appendix 13 it is, furthermore, proven, that the ratio of  $A_{\Delta}$  to  $A_{T_s}$  can cancel the effect due to not reaching steady state, as long as the heat-flow rate is a linear response to the temperature modulation. Quasi-isothermal experiments are particularly well suited for establishing ideal measuring conditions. They take at least 10 min for each temperature, but note, that typical data tables for  $C_p$  need only one entry per 10 K. This time is then equivalent to continuous heating at  $1.0 \text{ K min}^{-1}$ . In addition, the averaging of the many data points in quasi-isothermal analysis eliminates all statistical errors. If data of high quality are needed for both, the reversing and the total  $C_p$ , it may be better to couple the quasi-isothermal TMDSC with the faster standard DSC mode at 10 to  $40 \text{ K min}^{-1}$ . Multiple runs are, however, needed for a high-quality DSC.

Figure 4.120 illustrates how the run parameters affect the quasi-isothermal TMDSC. As the modulation amplitude increases and causes a larger change in the heating rate  $q(t)$ , the heat capacity shows less noise (after discarding the initial irregularities). For  $A_{T_s} > 0.5 \text{ K}$  the precision is quite impressive. Figure 4.104 suggest that for the same conditions of modulation, periods, and temperature  $T_o$ , the limit of measurement is reached with an  $A_{T_s}$  of about 2 K.

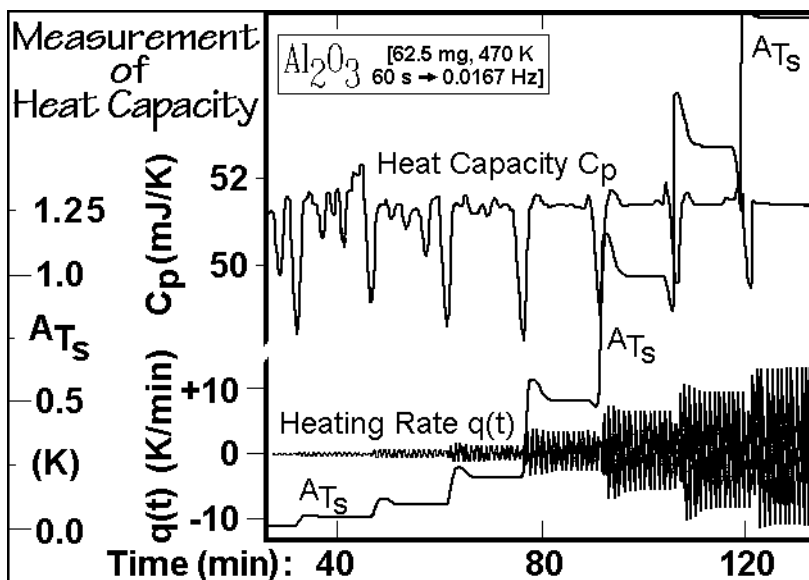
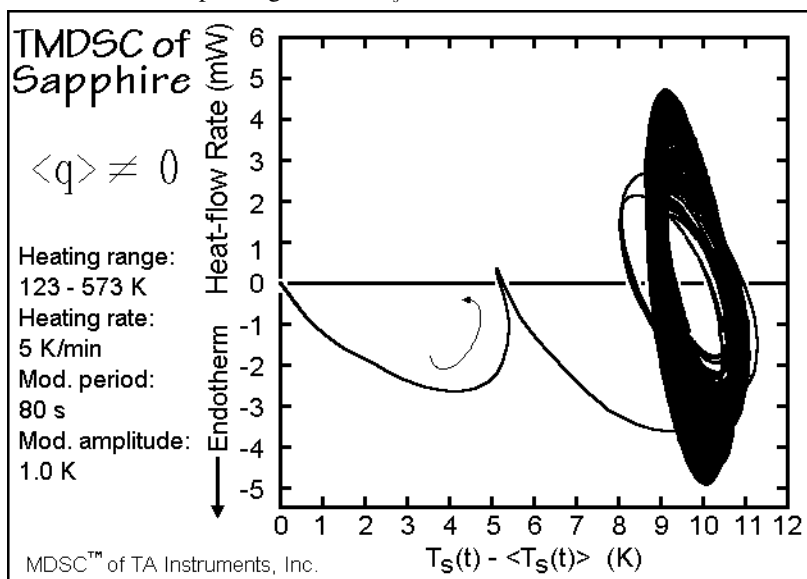


Fig. 4.120

Adding an underlying heating rate  $\langle q \rangle$  to the measurement leads to a Lissajous figure as is shown in Fig. 4.121. The computation using the pseudo-isothermal method of Sect. 4.4.3 implies the plotting of  $HF(t)$  versus  $T_s(t) - \langle T_s(t) \rangle$ . A similar plot is obtained when plotting versus  $dT_s/dt$ .



**Fig. 4.121**

The determination of heat capacities by using multiple modulation frequencies is illustrated above in detail using the Figs. 4.95–96. A precision of up to  $\pm 0.1\%$  has been reported with these measurements [33]. Such precision allows TMDSC to compete with adiabatic calorimetry described in Sect. 4.2. Although DSC and TMDSC are not able to reach as low temperatures as adiabatic calorimeters, they are able to reach up to 1,000 K, not possible for typical adiabatic calorimetry.

Figure 4.122 illustrates heat-flow data on TMDSC of quenched, amorphous poly(ethylene terephthalate). This figure is copied from the original MDSC™ Patent. The total heat-flow rate is similar as in a standard DSC trace. At least outside the transition regions, the thermodynamic heat capacity can be computed from the reversing heat-flow rate. A later, full evaluation on a similar experiment is shown in Sect. 4.4.7 with Figs. 4.136–139. When conditions of linearity, stationarity, and negligible temperature gradient within the sample for TMDSC are not violated, one can also obtain the nonreversing heat-flow rate from the difference between the total and the reversing HF. The heat capacity which is proportional to the reversing HF shows the typical increase at the glass transition (see Fig. 2.117). The hysteresis, as described in Sect. 6.3, is only seen in the total HF, as also shown in Sect. 4.4.6.

The cold crystallization starts at about 400 K at a supercooling not affected by modulation and registers as nonreversing. For separation of such nonreversing transitions, several modulation periods must occur across the transition, otherwise the pseudo-isothermal analysis would not develop the proper sinusoidal oscillations about  $\langle T_s \rangle$ , as can be seen from the modeling in Figs. 4.100–102 (loss of stationarity).

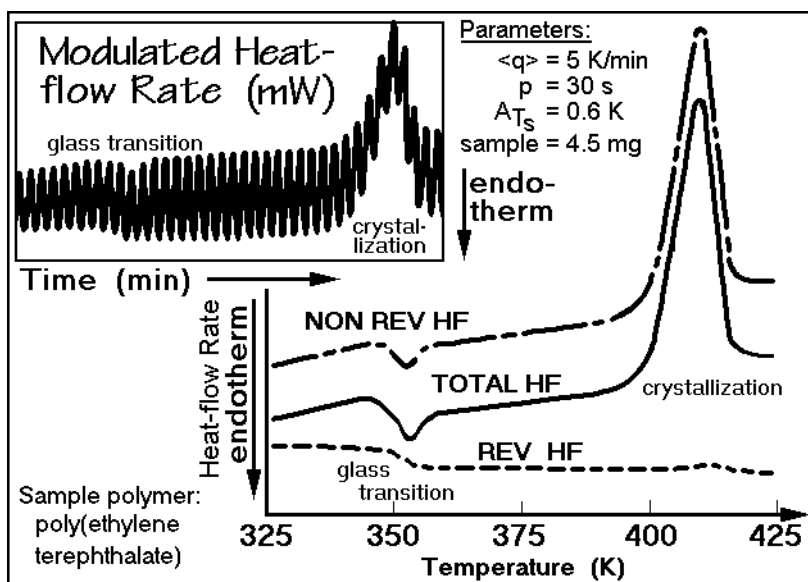


Fig. 4.122

The problem of maintaining modulation and keeping the other basic conditions of a DSC, makes for a difficult interpretation of a large transition over a narrow temperature range (see Sect. 4.4.7). Still, in many cases the nonreversing effects can be eliminated and heat capacities can be measured where no other method could succeed. If, in addition, the irreversible change to the new material produces a change in heat capacity, the kinetics of transformation can be followed by  $C_p$  measurement, as is illustrated in Sects. 4.4.7 and 4.4.8 (see Figs. 4.139 and 4.141). Melting of polymers is often more problematic. An attempt to separate melting and heat capacity is illustrated in Fig. 4.123 for a poly(oxyethylene) oligomer of 1,500 Da molar mass. This oligomer crystallizes about 8 K below  $T_m$  as seen from Fig. 3.91. The figure shows that melting is largely not followed by crystallization, and TMDSC can establish the heat capacity over much of the melting range. Additional information about TMDSC of the melting and crystallization of poly(oxyethylene) is given in Figs. 3.88 and 3.89, Fig. 4.114, and in Chap. 5.

A final data set of heat capacity measurements is shown in Fig. 4.124 for poly-*p*-dioxanone, a linear polymer with a repeating unit of  $\text{CH}_2\text{--CH}_2\text{--O--CH}_2\text{--COO--}$ . Data by adiabatic calorimetry (open circles), standard DSC (open squares), and quasi-isothermal TMDSC (filled circles) are plotted together. The sample for adiabatic calorimetry was initially semicrystalline, that for TMDSC, amorphous. The glass transition is visible at 264 K, and cold crystallization occurs at 345 K and melting at about 400 K. The adiabatic calorimetry seems to fail at high temperature, and the TMDSC discovers a small amount of reversible melting, to be discussed in Sect. 4.4.7. The interpretation of the heat capacities in terms of the molecular motion is indicated using the calculations described in Sect. 2.3. This graph illustrates the large amount of information the measurement of heat capacity can provide, and the good agreement between the various methods of measurement.

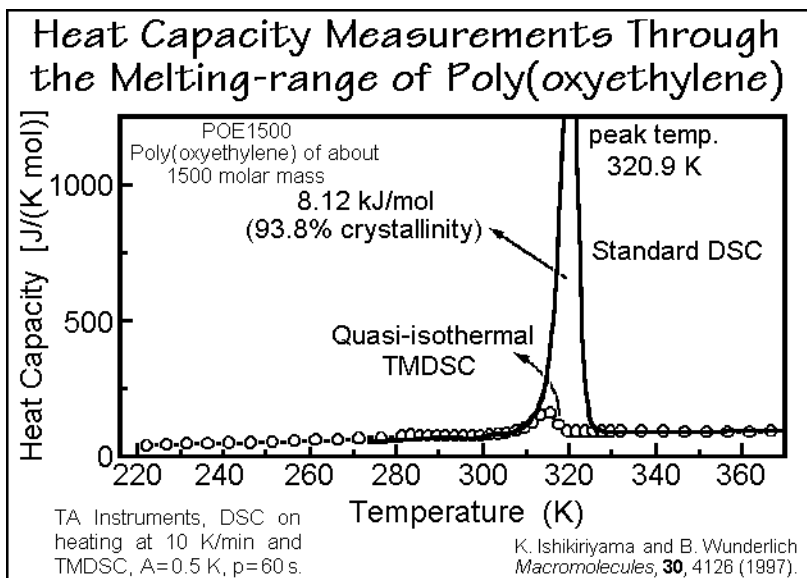


Fig. 4.123

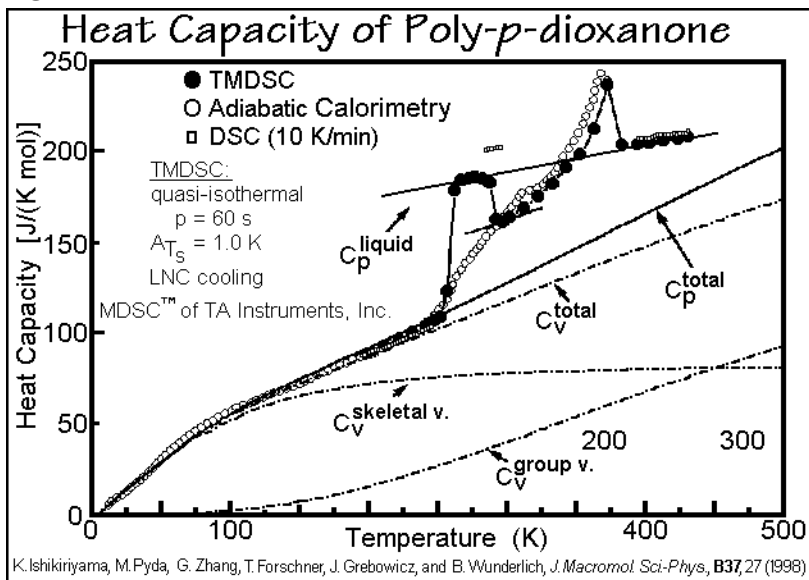


Fig. 4.124

#### 4.4.6 Glass Transition Measurement

An analysis of the glass transition of polystyrene by TMDSC is illustrated in Fig. 4.125. These measurements can be compared to the DSC results in Sect. 4.3.7. The left half of the figure shows besides the modulated heat-flow rate,  $\Delta T(t)$ , the three

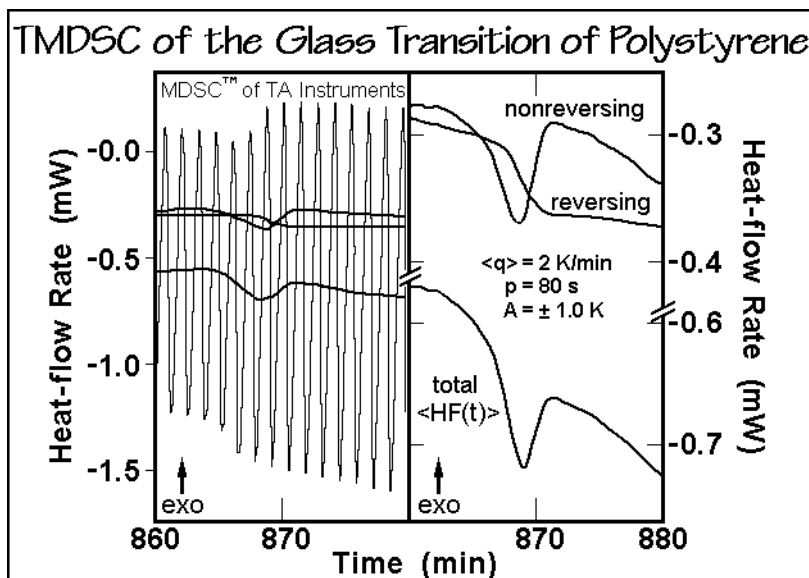


Fig. 4.125

computed output curves of the TMDSC (nonreversing, reversing, and total heat-flow rate, top-to-bottom). The total heat-flow rate,  $\langle HF(t) \rangle$ , is the appropriate average of  $HF(t)$  (proportional to  $\Delta T(t)$ , as discussed in Sect. 4.4.3). On the right, an enlarged graph of the left is shown, but without the instantaneous values of  $\Delta T(t)$ . The reversing heat-flow rate  $\langle A_{\Delta}(t) \rangle$  is proportional to the heat capacity, the *nonreversing heat-flow rate*, defined as  $\langle HF(t) \rangle - \langle A_{\Delta}(t) \rangle$ , indicates the existence of a hysteresis, an irreversible, slow drift of the sample towards equilibrium, caused by the thermal history and treated in more detail in Sect. 6.1.3. The TMDSC is able to approximately separate these two effects. It permits the simultaneous characterization of the glass transition and the thermal history, not possible by DSC.

Figure 4.126 illustrates that the reversing glass transition measurement is almost independent of the annealing (thermal) history. The still little-explored, small differences are an indication of the changes in relaxation kinetics on annealing of glasses. The corresponding nonreversing components are shown in Fig. 4.127. They permit the quantitative characterization of the thermal history of the glass as mentioned above, the differences, however, between the curves of Fig. 4.126 are not considered in this separation.

A preliminary explanation of the behavior of glasses is now attempted using the characterization of the transition in Figs. 2.117 and 2.118, and the quasi-isothermal TMDSC data. This is followed by extraction of quantitative data. At all temperatures the liquid represents equilibrium, illustrated by the heavy line in Fig. 4.128. On cooling at different rates, the glass transitions occur close to the intersections with the thinner enthalpy curves of the corresponding glasses. The heat capacity is equal to the slope of the enthalpy. Starting from a glass, any drift towards the liquid is irreversible and slows as the temperature decreases. Drifts from the liquid towards the glassy states are forbidden by the second law of thermodynamics (see Fig. 2.118).



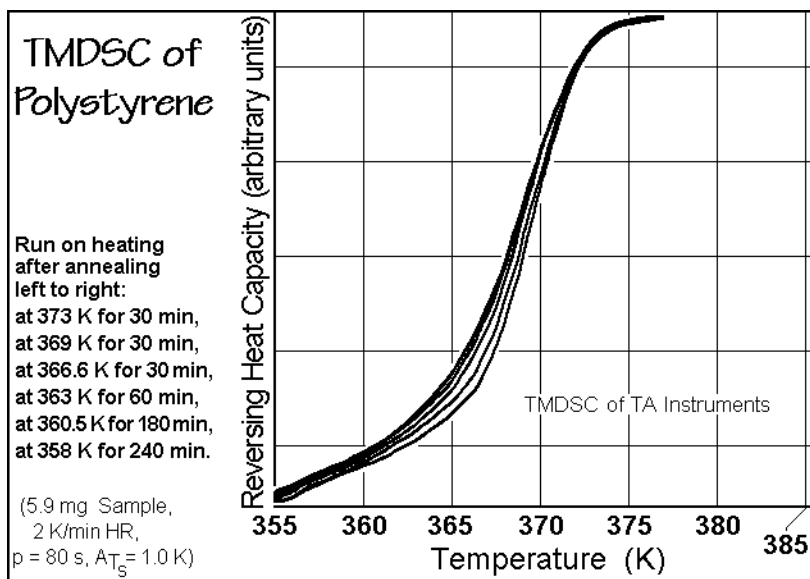


Fig. 4.126

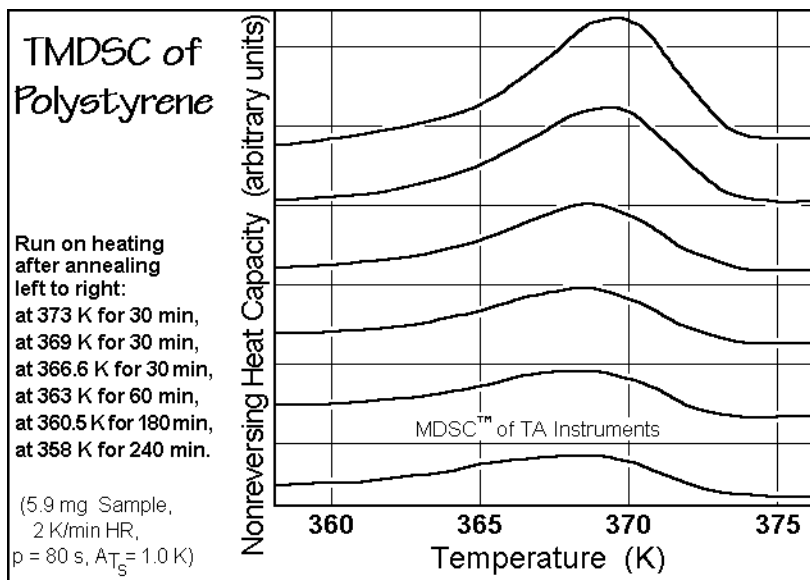


Fig. 4.127

Figure 4.128 illustrates that on cooling a liquid from high temperature, one measures the proper, reversible  $C_p$  of the liquid over a wide frequency and cooling rate range. On reaching  $T_1$  the large-amplitude molecular motion that characterizes the liquid has slowed so much, that it can only be followed by slow experiments. Fast modulation, on the other hand, elicits a glass-like response. On quickly cooling to  $T_2$ ,

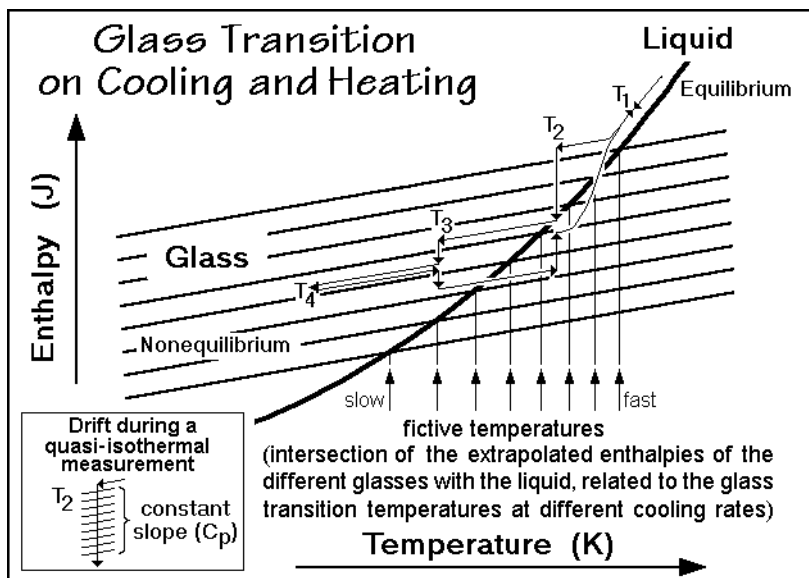


Fig. 4.128

to begin a quasi-isothermal TMDSC run, a glassy response is observed, characterized by the indicated fictive temperatures (see Sect. 6.3). With time, a slow, irreversible drift towards the liquid enthalpy continues as an exothermic enthalpy relaxation. The fast modulation measures, however, only the low-value of the vibrational  $C_p$  of a glass, as indicated by the insert. Even when ultimately the stable liquid is reached, relative to the time constant of the fast modulation, the large-amplitude motion is too slow to respond to the reversing temperature and only the vibrational  $C_p$  is measured. After further quenching to  $T_3$ , initially some annealing is possible toward an enthalpy corresponding to a lower fictive temperature. At  $T_4$ , the glass is finally in a fully metastable, arrested state and does not change with time. On reheating to  $T_3$ , annealing gives first some further exothermic relaxation, but heating to  $T_2$  produces a superheated glass that relaxes endothermically toward the liquid. Final heating to  $T_1$  shows superposition of the heat capacity and the irreversible enthalpy relaxation since now the time scales of measurement and relaxation are similar and one observes a hysteresis. The degree to which relaxation and reversible heat capacity are separable by TMDSC are shown next. Further details about the glass transition region in homopolymers, including the behavior of polystyrene and the quantitative assessment of hysteresis due to aging of the glass, are discussed in Sects. 6.1.3 and 6.3.

The TMDSC results, displayed in Figs. 4.125–127, illustrated for the first time a possible separation of the heat capacity and relaxation processes in the critical temperature range between  $T_b$  and  $T_c$ , defined in Fig. 2.117. We expect the reversing heat-flow rate to register the thermodynamic heat capacity, and the nonreversing heat-flow rate, the relaxation. The analysis will show to what degree this separation is possible. Because the time constants of the physical processes change rapidly with temperature, we will attempt first to approximate the kinetic parameters of the glass transition by quasi-isothermal TMDSC which involves only one time scale, expressed

by the modulation frequency,  $\omega$ , or period,  $p$ . This is followed by a look at the standard TMDSC with its two time scales defined by  $p$  and  $\langle q(t) \rangle$ . The description is more involved than described here and, thus, the superposition of the overlapping processes with different temperature as well as structure-dependent relaxation times are considered to be not well understood. More about the description of the glass transitions can be found in many places of this book, underlining the importance of the transition for the thermal analysis of polymeric materials. For major discussions see, in addition, the following Sects.: 2.5.6, 4.3.7, 5.6, 6.1.3, 6.3, and 7.3.

Figure 4.129 displays on the left some quantitative, quasi-isothermal data at different frequencies for amorphous poly(ethylene terephthalate), PET, but at equal

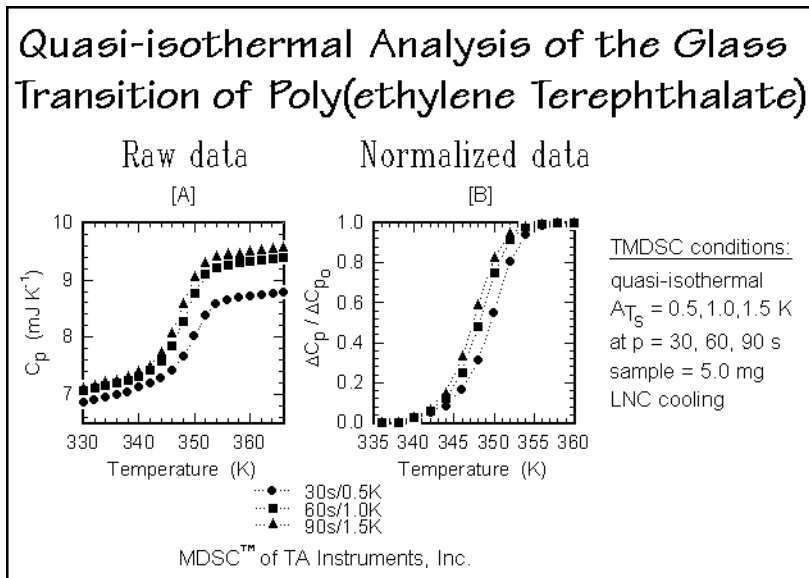
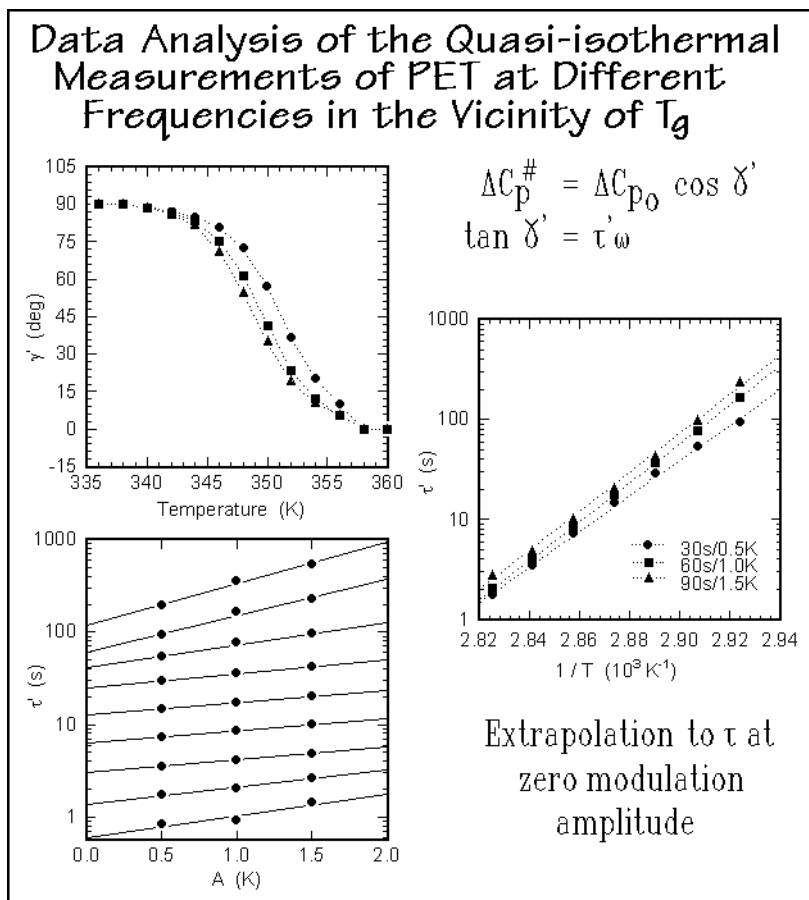


Fig. 4.129

maximum heating rates  $q(t)$  in the glass-transition region. Since for a kinetic analysis it is important to not lose steady state, the sample mass was reduced to 6 mg. To match the higher precision possible when measuring outside the glass transition region with larger sample masses, the raw data were calibrated internally by normalizing to the change of the heat capacity at the glass transition  $\Delta C_{p0}$ , as shown on the right side of the figure. Next, the equations of Fig. 4.130 are used to extract a phase angle  $\gamma'$  for the description of the frequency-dependent, apparent heat capacity,  $\Delta C_p^\#$ .

The simplest model for the representation of the glass transition, perhaps, is the *hole theory*. With it, the larger expansivity of liquids and the slower response to external forces is said to be due to changes in an equilibrium of holes. These holes are assumed to be all of equal size, and their number depends on temperature. The equilibrium number of holes at a given  $T$  is  $N^*$ , each contributing an energy  $\epsilon_h$  to the enthalpy. The hole contribution to  $C_p$  is then given under equilibrium conditions by:

$$C_p(\text{liquid}) = C_{p_0} + \epsilon_h \left( \frac{dN^*}{dT} \right) \quad (1)$$

**Fig. 4.130**

Creation, motion, and destruction of holes are cooperative kinetic processes and may be slow. This leads to deviations from Eq. (1) if the measurement is carried out faster than the kinetics allows. Applied to the glass transition, one can write and solve a simple, first-order kinetics expression [40] based on the equilibrium expression, above:

$$\left( \frac{dN}{dt} \right) = \frac{1}{\tau} (N^* - N) \quad (2)$$

where  $N$  is the instantaneous number of holes,  $t$  is the time, and  $\tau$ , a relaxation time. Details about the solution of Eq. (2) are described in Sect. 6.3.2. Similarly, one can derive an analogous relaxation time  $\tau'$  for the formation of holes from TMDSC experiments [41] as in Fig. 4.129. The process is illuminated by Fig. 130. The experimental relaxation times in the center graph are dependent on modulation amplitude, but can be extrapolated to zero amplitude, as seen in the bottom graph. At larger distance from equilibrium, however,  $\tau'$  does not remain a constant. Some five to ten kelvins above  $T_g$ , most liquids show no kinetic effects for typical DSC heating

or cooling rates ( $1\text{--}20\text{ K min}^{-1}$ ). The heat capacity is then equal to the slope of the liquid (see Fig. 4.128). On going through  $T_g$ , the glassy state is reached at different temperatures for different cooling rates. Each cooling rate corresponds to freezing a different number of holes, giving rise to the multitude of glasses with different enthalpies. The solution of Eq. (2) is rather complicated since both  $\tau$  and  $N^*$  are to be inserted with their proper temperature and (through the modulation) time dependence. In addition, the results of Figs. 4.126, above, and 4.133, below, reveal that  $\tau$  is also dependent on  $N$ , which makes  $\tau$  dependent on structure [41].

Figure 4.131 shows the integrated Eq. (2) at steady state of quasi-isothermal experiments such as in Fig. 4.130. The parameters  $A_\tau$  and  $A_N$  represent the amplitude contributions due to the change in  $N^*$  and  $\tau$ , and  $\beta$  and  $\gamma$  are phase shifts. The plotted  $(N - N_0)/N_0^*$  is proportional to the heat-flow rate (and thus  $\Delta C_p^\#$ ). The heavy curve, however, does not represent a sinusoidal response. The curve is higher by a constant amount ( $a = 0.0625$ ) and has a contribution of  $2\omega$ , double the modulation frequency, a second harmonic (curve b). Both these contributions are not included in the reversing heat-flow rate of the first harmonic (curve c). It, however, leads to an easy analysis of  $\gamma$  and  $\tau$ , as carried out in Fig. 4.132 [41]. Since the relaxation times change with modulation amplitude, they are extrapolated to zero amplitude and then used to calculate the apparent heat capacities shown on the right for a somewhat wider frequency range than the measurement. An extended range of frequencies would need a more detailed kinetic description. The pre-exponential factor  $B$  and the relaxation time, are strongly dependent on thermal history and determine the position of the glass transition and its breadth.

In Fig. 4.133 quasi-isothermal data of the filled circles are compared with standard TMDSC with the indicated underlying heating and cooling rates. As the underlying heating rate  $\langle q \rangle$  increases, the time scale of the modulation is approached, and the

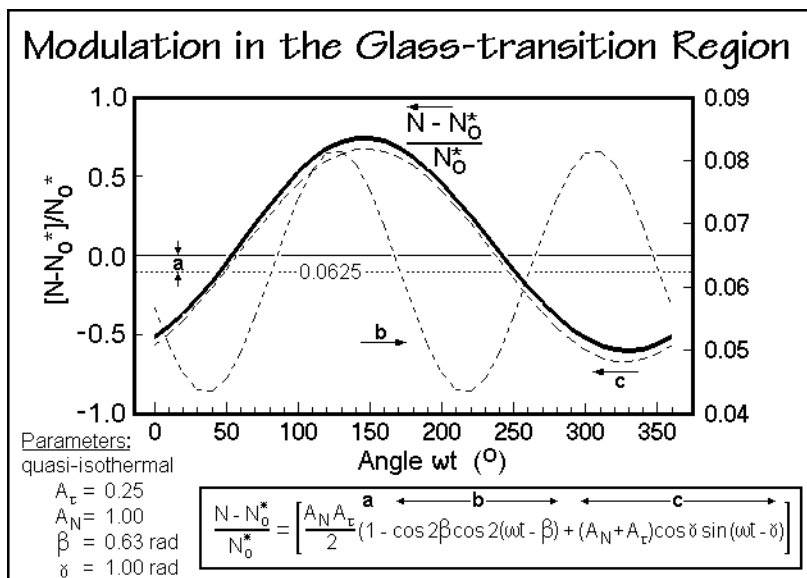


**Fig. 4.131**

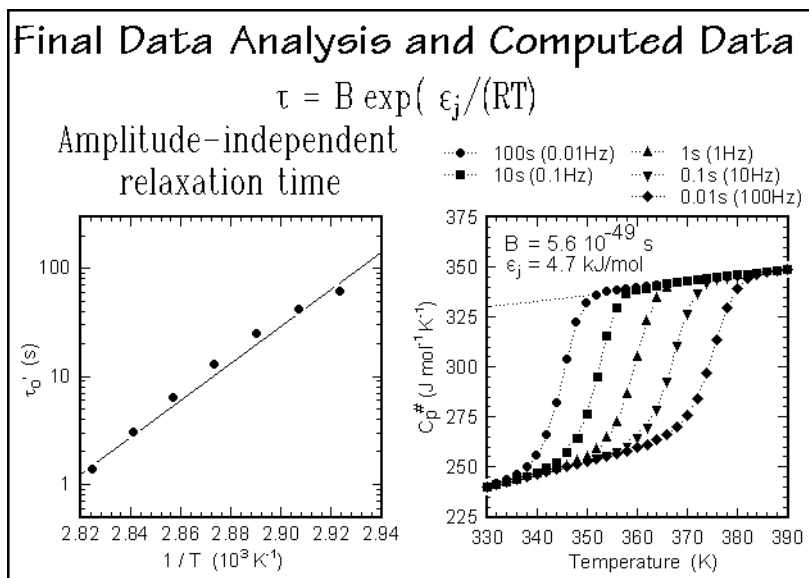


Fig. 4.132

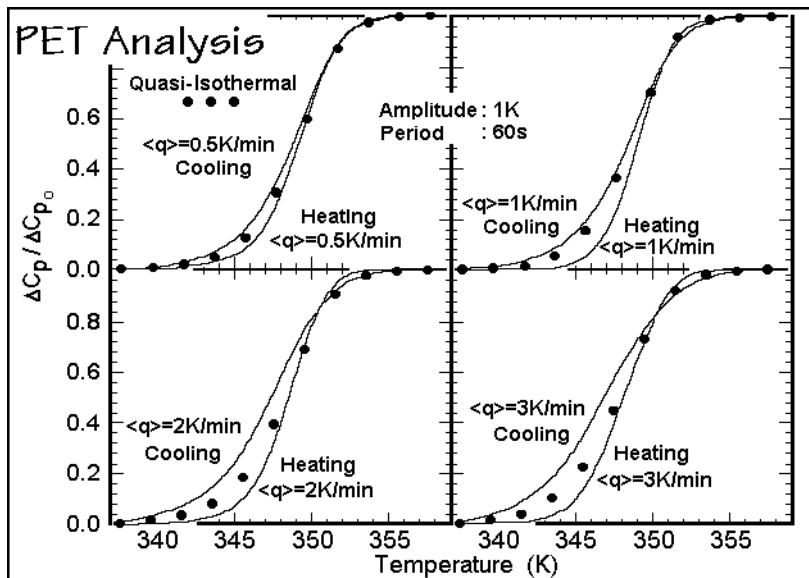


Fig. 4.133

heating and cooling data are different and separate from the quasi-isothermal data taken after a steady state had been reached. The reason lies in the incomplete separation of the apparent, reversing heat capacity from the total heat capacity. An attempt at a more detailed separation of the various contributions is given in Sect. 6.1 by numerical solution of the rather complicated kinetic equations.

The small difference of the data sets at  $\langle q \rangle = 0.5$  K prove the usefulness of TMDSC in separating reversing and nonreversing contributions to the glass transition (for the latter see Fig. 4.127). Furthermore, a quantitative kinetic analysis is possible that lets us model the behavior of the glass transition. And finally, the remaining small discrepancies in Fig. 4.126 and Fig. 4.133 can be quantitatively assessed.

#### 4.4.7 First-order Transition Analysis

The analyses of the first-order transitions, such as melting and crystallization, bring a major new problems and opportunities for analysis to TMDSC. Due to the usually larger heat of transition in comparison to the heat capacity one must consider greater lags in the heat-flow rate, but can now study the closeness of the transitions to equilibrium. For example, at 400 K the heat of fusion of polyethylene,  $4.1 \text{ kJ mol}^{-1}$ , is 120 times larger than the heat capacity of the crystal,  $34.2 \text{ J K}^{-1} \text{ mol}^{-1}$ . For the standard DSC this problem was solved by the baseline method, described in Figs. 4.71 and 4.72. The sample temperature was assumed to remain at the transition temperature as long as the sample needed to add or lose heat of transition, and then approach exponentially the steady state that is characteristic of the heat capacity of the new phase. Except for very broad transitions with small heats of transition, loss of steady state is inevitable and must be dealt-with in the data interpretation. As glass transitions, first-order transitions are of major importance in thermal analysis of polymeric materials (see Sects. 2.5.7, 3.6, 4.3.7, 5.4, 5.5, 6.1, 6.2, and 7.2).

A simple analysis of an irreversible first-order transition is the cold crystallization, defined in Sect 3.5.5. For polymers, crystallization on heating from the glassy state may be so far from equilibrium that the temperature modulation will have little effect on its rate, as seen in Fig. 4.122. The modeling of the measurement of heat capacity in the presence of large, irreversible heat flows in Fig. 4.102, and irreversible melting in Figs. 3.89 and 4.123, document this capability of TMDSC to separate irreversible and reversible effects. Little needs to be added to this important application.

A second type of analysis pertains to sharp equilibrium transition, such as seen for In. Figures 4.82 and 4.83 illustrate the change of onset of melting with heating rate and the need of supercooling by about 1.0 K. On TMDSC, melting will occur as soon as the modulation reaches the melting temperature,  $T_m$ . The extent of melting will then be determined by the time  $T_s(t)$  stays at  $T_m$ , or the sensor temperature exceeds  $T_m$ , as illustrated in the time-domain recording of the heat-flow rates in Figs. 4.106 and 4.107. As soon as  $T_s(t)$  drops below  $T_m$ , recrystallization start without supercooling as long as crystal nuclei remain in the sample. The shape of the heat-flow-rate curve is, however, far from sinusoidal, so that the data treatment of Sect. 4.4.3 is not applicable. The curve must be analyzed in the time domain, as in the baseline method of Figs. 4.71 and 4.72 for the standard DSC, but modified for a sinusoidal baseline. If then steady state is approached after melting and crystallization during the modulation cycle, quantitative analysis is possible. Small sample masses and appropriate modulation are needed for such studies. Extraction of a reversing amplitude gives higher values for the apparent  $C_p$ , as seen in Figs. A.13.13 and 4.108. Its interpretation is better done by the integration of  $HF(t)$  in the time domain, as is illustrated in Fig. A.13.15 with the example of melting of the paraffin  $C_{50}H_{102}$ .

Figure 4.134 shows a magnification of the quasi-isothermal analysis of Fig. 4.109 for the melting of In with about 25% melting in each modulation cycle, followed by recrystallization on cooling. The trace reveals the high quality of present-day scanning calorimeters. Using instead a TMDSC which does increase its block-temperature, modulation on melting yields lower heat-flow rate amplitudes, but can be treated similarly. Figure 4.135 shows Lissajous figures (see Figs. 4.113 and 4.114) at three

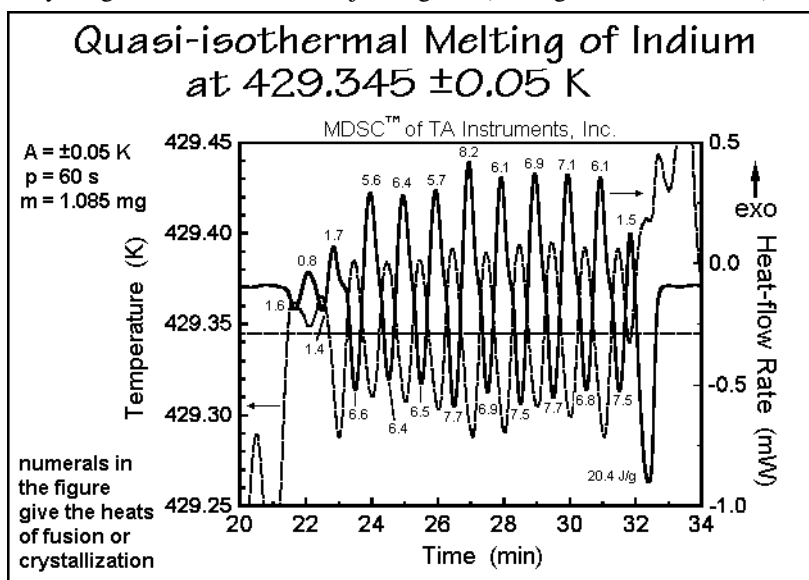


Fig. 4.134

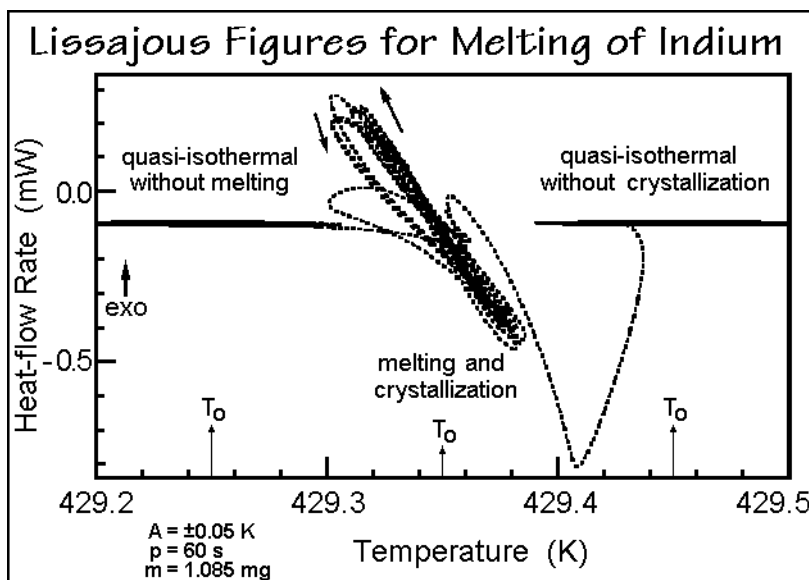


Fig. 4.135



sequential values for  $T_0$  for the same quasi-isothermal TMDSC of the melting of indium as shown in Figs. 4.109 and 4.134. Without melting and crystallization, the almost horizontal Lissajous ellipses are so flat that they are only slightly thicker horizontals on the left and right of the center figure. The continuity of melting and crystallization with a slope determined by the heat conductivity of the calorimeter is obvious in the center modulation. It is evident that steady state is lost as soon as melting starts. The melting of the remaining 75% of indium on increasing the base temperature shows also clearly. The heat capacities of solid and liquid indium are almost identical, so that the heat-flow rate before and after melting is the same. It is apparent from this discussion indium that, although the analysis of the heat of fusion is best and more precisely done by standard DSC, the check with TMDSC teaches much about the quality and limitations of the calorimeter on hand. No TMDSC should be used for quantitative measurements without testing its limits on the melting and crystallization of a reversibly melting substance like indium.

It remains to introduce the thermal characterization of semicrystalline polymers with incompletely irreversible melting. While separation of cold crystallization from heat capacity was from the beginning one of the premier applications of TMDSC, as illustrated in Fig. 4.122, and the inability to improve on the quantitative analysis of sharp melting substances one of its biggest detractors, polymer melting, being intermediate in reversibility, caused most confusion. A schematic plot of melting and crystallization rates based on a large volume of kinetic data on large, intermediate, and small molecules (polymers, oligomers, and monomers, respectively) is given in Fig. 3.76, together with details of the kinetics in Sects. 3.5 and 3.6. Melting is usually rather fast. In calorimetry, it is often sufficient to assume melting is limited only by heat conduction. Also, many small molecules show continuity of melting through the equilibrium melting temperature,  $T_m$ . Flexible, longer molecules, however, lose on melting their shape and become conformationally disordered. It was suggested that each flexible molecule must undergo a molecular nucleation step before it can crystallize, leading to the 5–15 K region of metastability in which neither melting nor crystallization is possible, even in the presence of crystal nuclei.

From the analysis of the melting and crystallization kinetics of polymers, one would expect no contribution of melting to the reversing heat capacity. Indeed, this could be documented on well-crystallized poly(oxyethylene) with Figs. 3.89 and 4.123. With help of Fig. 3.76 it can be seen that whenever the sample sensor reached or exceeded the melting temperature, some melting occurred, but during the cooling cycle no recrystallization reverses the melting. Using the quasi-isothermal mode, the remaining small effect of the melting spike due to loss of stationarity, as modeled in Fig. 4.100, appears only in the first cycle and is not included in the analysis when using only the last 10 min of a 20-min experiment. Again, as in the indium melting, the actual melting is best analyzed by standard DSC or in the time domain of TMDSC under conditions of regaining steady state within each modulation cycle.

A similar analysis of a melt-crystallized poly(ethylene terephthalate), PET, of the typical molecular mass of a polyester showed a surprising reversing melting peak, as seen in Fig. 3.92. On comparison with an amorphous PET, one finds that the reversing peak depends on crystallization history, as is shown in Fig. 4.136. The change of the glass transition with crystallization is typical for polymers. It shows a

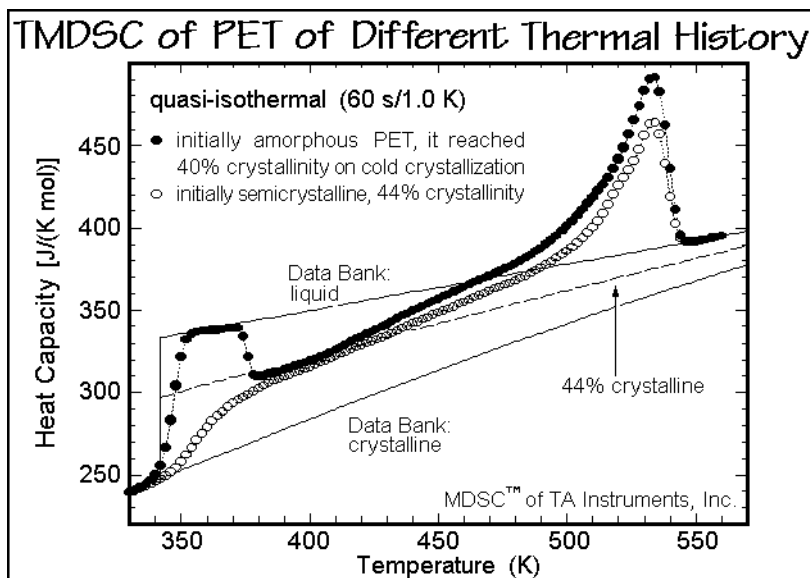


Fig. 4.136

broadening towards higher temperature. The cold crystallization, visible in the total heat-flow rate of Fig. 4.122, does not show at all in the quasi-isothermal analysis. Furthermore, by extending the time of quasi-isothermal analysis in the melting region, it could be observed that the magnitude of the peak in the reversing heat capacity decreases with time and the kinetics can be followed. Figure 4.137 reveals that after about six hours, the reversing melting and crystallization had decreased considerably,

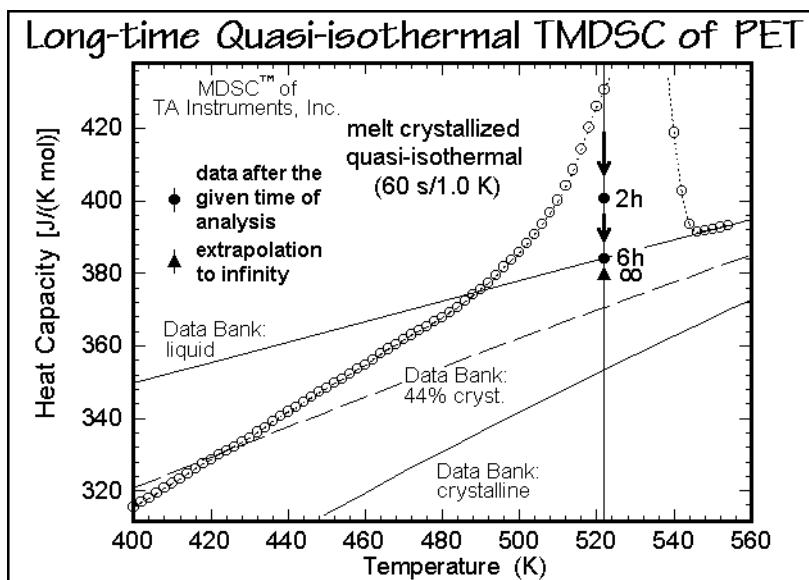


Fig. 4.137

but ultimately a reversible portion remains at very long time. These experiments were interpreted as showing that the melting of polymers is basically irreversible, but specific details of crystal melting had been uncovered that were never before seen by calorimetry. To show reversible melting and crystallization, some polymer molecules must melt only partially. On cooling, these partially melted molecules do not need to undergo any molecular nucleation and can recrystallize close to reversibly (see Sects. 3.5 and 3.6). Some reversibility of melting and crystallization is thus maintained on a sub-molecular level. Once a molecule melts completely, it cannot recrystallize without supercooling beyond the region of metastability of Fig. 3.76. A new tool for the assessment of the morphology of semicrystalline polymers has thus been found in TMDSC. It is likely that the partially meltable molecules can be linked to decoupling of parts of molecules on the crystal surfaces, as is discussed in Sect. 6.2.

The melting range of polymers, in addition, is much broader than the sharp melting standards, such as indium. Most of this broadening is due to two causes, a wide distribution of crystal sizes, and the possible presence of lower melting oligomers or the existence of a distribution of lengths of crystallizable sequences in copolymers. Indications of small amounts of oligomers that may have a sufficiently small gap of metastability in polymer samples were found in low-molar-mass poly(oxyethylene). Figure 4.114 shows the Lissajous figures of a long-time quasi-isothermal experiment of such a sample in the melting range. In this case the amount of melting and crystallizing crystals increases with time. The analysis can be carried out with varying modulation amplitude, so that the metastable melting/crystallization gap can be assessed quantitatively. Since the low-molar-mass crystals melt at the low-temperature side of the melting peak, they can be easily distinguished from the partially melted crystals of high molar mass.

A final topic in polymer melting concerns reorganization, recrystallization, or annealing of crystals during melting, a process very difficult to study with standard DSC. In the past, measurements with different heating rates or on chemically altered crystals were necessary for the study of reorganization as described in Chaps. 5 and 6. Figure 4.138 shows a qualitative proof of such reorganization on PET. Despite loss of steady state in the melting range, it is possible by using a modulation that never permits cooling described in Fig. 4.86, to show a substantial exothermic heat flow in the melting region. The loss of steady state in the experiment of Fig. 4.138 is indicated by the variation of heating rate, but the reorganization exotherm is also seen at temperatures where the heating rate is zero. Any heat evolved, thus, must come from crystallization or from crystal perfection, recrystallization, or annealing. In Fig. 4.139 one can see that the reversing melting endotherm is larger than the total melting endotherm, indicating that the exotherm is not additional, new crystallization. Again, a quantitative analysis must rely on time-domain data because of the loss of steady state.

Converting the data of Fig. 4.138 to the reversing and total contributions without considering the time-domain analysis, reasonable data are obtained only up to the beginning of melting, as seen in Fig. 4.139 (see also Fig. 4.122). Following the endotherms and exotherms of Fig. 4.138 gives for the chosen time scale a picture of the two processes. Figure 4.116 shows the change in reversing melting with modulation period for the example of nylon 6 and its possible analysis through the

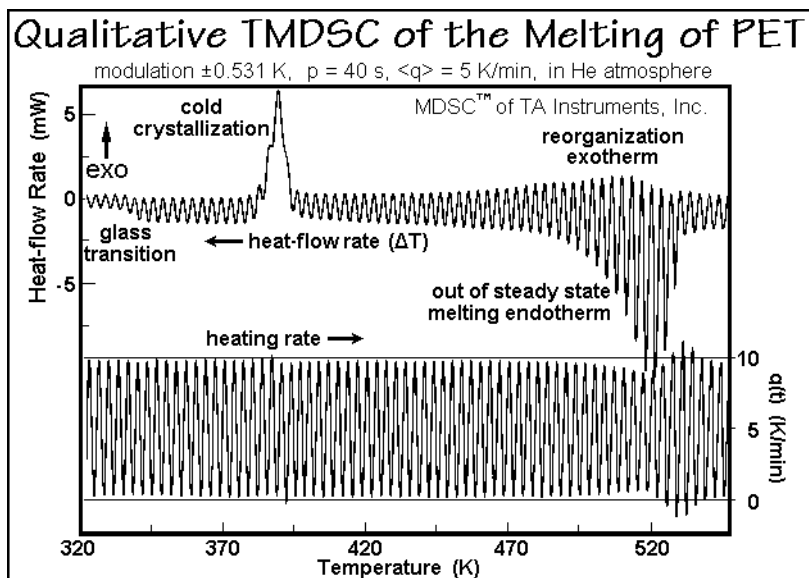


Fig. 4.138

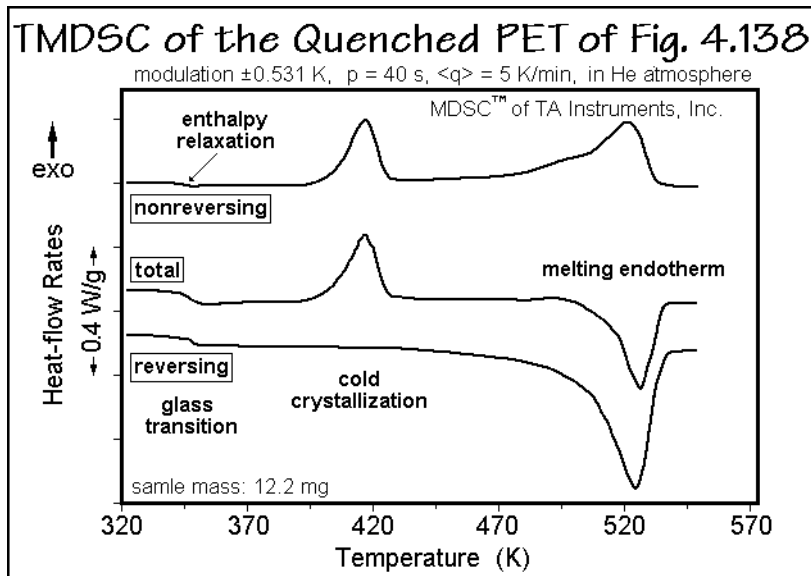


Fig. 4.139

model in Fig. 4.117. In this example, as for the TMDSC of poly(ethylene terephthalate) in Fig. 4.138, only irreversible melting with a temperature-dependent rate was analyzed by avoiding cooling of the sample. The quasi-isothermal analyses in Figs. 4.136 and 4.137, in contrast, test the reversibility by applying fully symmetric heating and cooling cycles and give proof that true reversibility exists, but is only a small fraction of the reversing melting peak of Fig. 4.139.

#### 4.4.8 Chemical Reactions

In the description of applications of TMDSC, heat capacity is the most subtle effect, followed by the glass transition which manifests itself in a time-dependent step in the heat capacity with a possible additional small enthalpy-relaxation. The next larger step is the first-order transitions with heat flows up to 100 times those experienced in heat capacity measurements. The topic of this section can bring even larger heat flows. The main point is, as before, to distinguish between reactions that are close enough to equilibrium to be influenced by the modulation amplitudes and fully irreversible reactions. The fully irreversible reactions are naturally best studied by standard DSC. By TMDSC it is, however, possible to study simultaneously reversing effects, not possible with a DSC. Figure 4.140 shows the apparent heat capacity of a fullerene,  $C_{70}$ , measured while the sample underwent considerable oxidation. The first two small endotherms in the vicinity of 300 K are rather broad, reversible mesophase transitions of the type crystal to plastic crystal and can be seen in both, the heat capacity and the total heat-flow rate. The huge exotherm starting at about 575 K does not seriously affect the reversing heat capacity measurement. One can conclude safely, that up to almost 700 K, no further phase transitions exist.

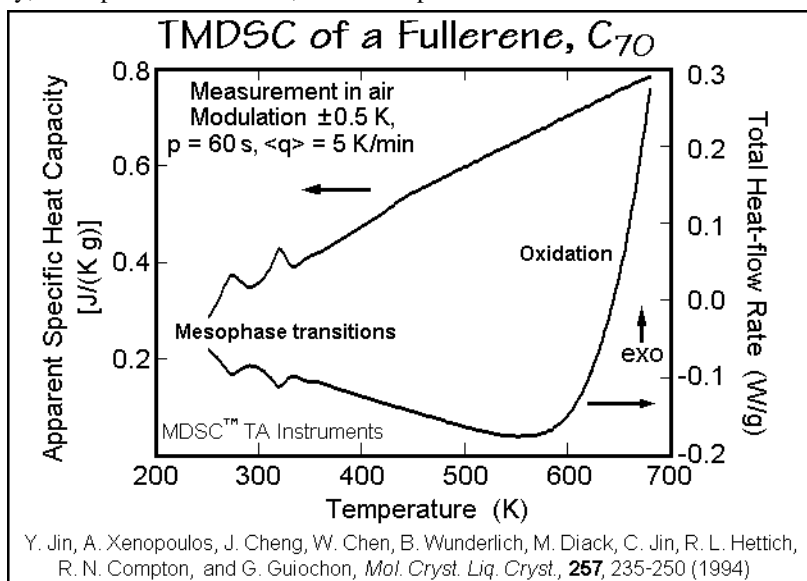


Fig. 4.140

A second example of a chemical reaction during TMDSC is the analysis of the cure of an epoxide. In this case both the exotherm and the change in heat capacity could be used to analyze the cure kinetics as shown in Fig. 4.141. The exothermic, nonreversing heat-flow rate is a measure of the progress of the cross-linking, and the reversing  $C_p$  indicates the development of the glass with time. A full TTT (time-temperature-transition) diagram of the liquid-gel-glass transitions is thus established by TMDSC to the control the curing of such materials [42], as shown in Fig. 4.142.

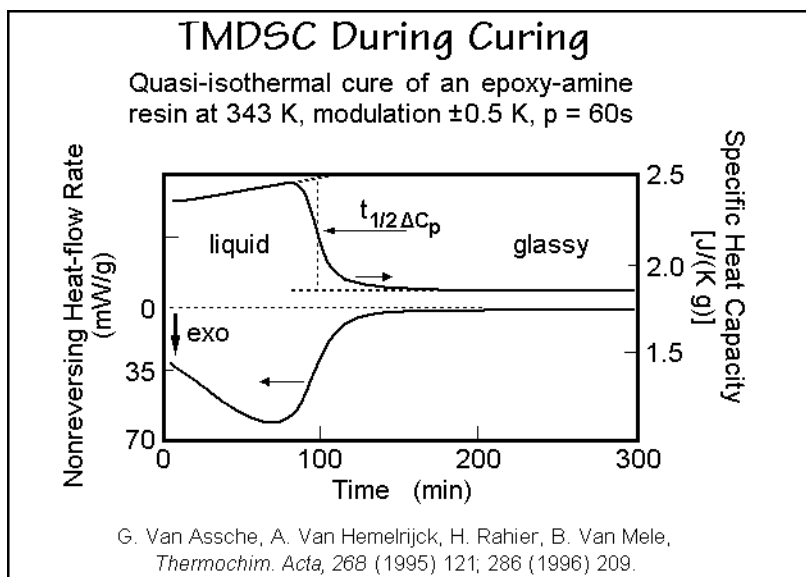


Fig. 4.141

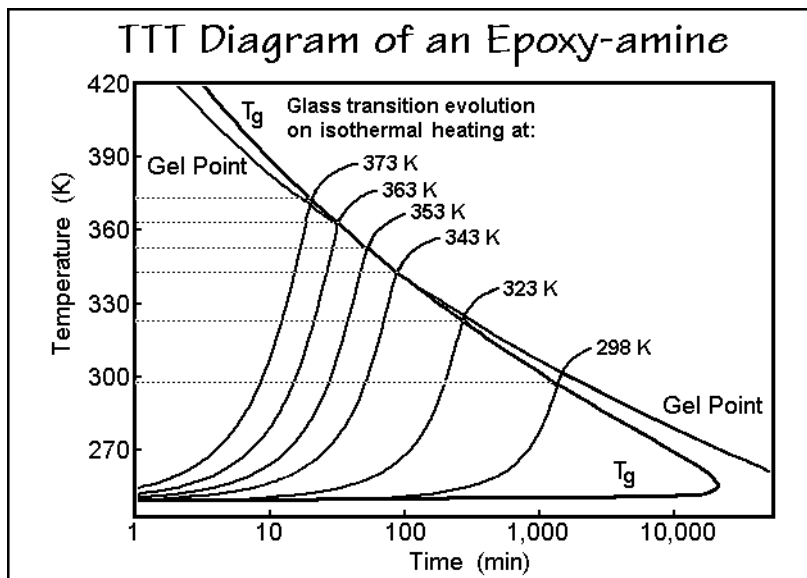


Fig. 4.142

In summary, the applications of TMDSC look quite different from those of DSC. Many important applications can only be solved by TMDSC. A good number of others are, however, still better, and sometimes only, solvable by DSC. Fortunately any TMDSC can also be run without modulation under DSC conditions. The development of TMDSC has also led to long-awaited progress in the hardware and software improvements of DSC as illustrated with Fig. 4.54 and Appendix 11.

## 4.5 Thermomechanical Analysis, DMA, and DETA

### 4.5.1 Principle of TMA

The variables of state for thermomechanical analysis are deformation (strain) and stress. The SI units of deformation are based on length (meter, m), volume, (cubic meter, m<sup>3</sup>) and angle (radian, rad, or degree) as listed in Fig. 4.143 (see also Fig. 2.3). Stress is defined as force per unit area with the SI unit newton m<sup>-2</sup>, also called by its own name pascal, Pa. Since these units are not quite as frequently used, some conversion factors are listed below.<sup>1</sup> The stress is always defined as force per area,

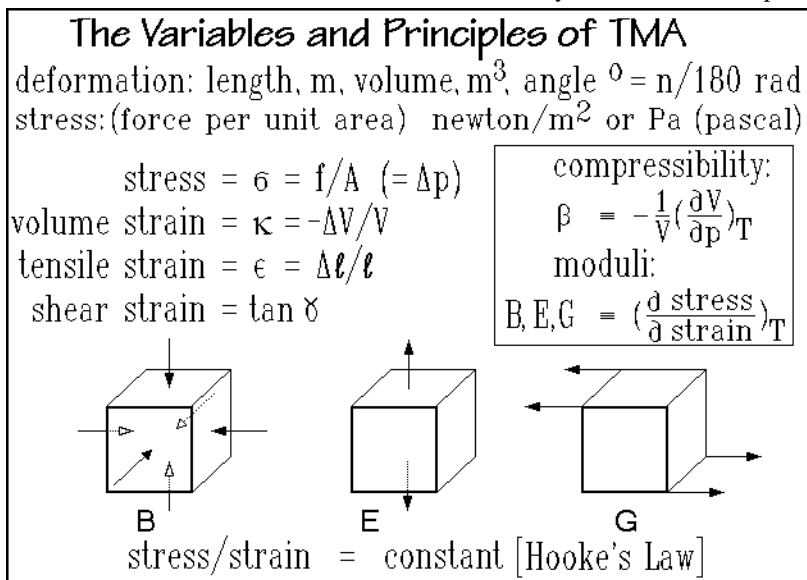


**Fig. 4.143**

while the strain is the fractional deformation, as is also shown in Fig. 4.143. The shear strain and tensile strain cause increasing strain with increasing stress. The volume strain is defined with a negative sign to account for the fact that increasing pressure causes always a decrease in volume. The derived function of the volume with respect to pressure is the compressibility,  $\beta$ , as shown by the boxed equation in Fig. 4.143. The inverse of compressibility is the bulk modulus, also called the isothermal elasticity coefficient. The second equation in the box gives a general expression for three different isothermal elasticity coefficients, known as bulk modulus, B, tensile or Young's modulus, E, and shear modulus, G. They represent the differential coefficient of stress with respect to the three different types of strain sketched at the bottom of the figure. The bottom equation in Fig. 4.143 represents

<sup>1</sup> 1 atm = 101,325 Pa  $\approx$  0.1 MPa; 1 bar = 100,000 Pa; 1 mm Hg = 1 torr = 133.3224 Pa; 1 dyne = 0.1 Pa; 1 lb in<sup>-2</sup> = 6,894.76 Pa.

Hooke's law, which holds for the ideal, reversible, linear, elastic response of a system to an applied stress. All elastic materials follow Hooke's law when the stress is sufficiently small.

Figure 4.144 shows a list of some typical bulk moduli, illustrating the large range possible for different materials. The elastic spring shown, is the symbol of an elastic response of a material. The sketch in the center illustrates the extension of a rigid macromolecule on an atomic scale. Each atom of the network polymer undergoes a reversible, affine deformation, i.e., it is strained by the same amount as the macroscopic sample. At larger stresses, the deformation becomes plastic, meaning the sample deforms beyond the elastic limit and does not regain its original shape on removal of the stress.

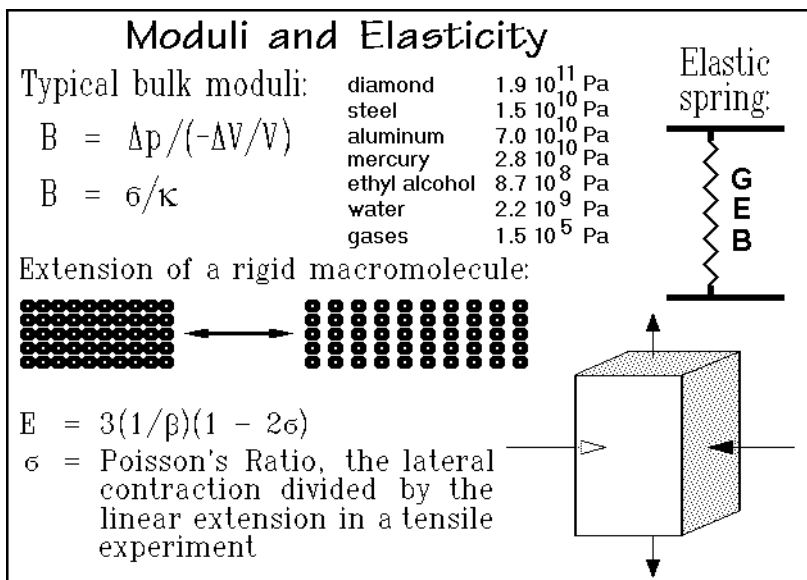


**Fig. 4.144**

The bulk modulus  $1/\beta$  and Young's modulus  $E$  are related through the equation at the bottom of Fig. 4.144. The symbol  $\sigma$  represents Poisson's ratio, the linear, lateral contraction divided by the linear extension in a tensile experiment. One can compute that a value of 0.5 for Poisson's ratio leads to a constant volume on extension, a situation often achieved in rubbery materials. Most crystals and glasses have a Poisson's ratio between 0.2 and 0.35. Note that a value of  $\sigma$  close to 0.5 makes Young's modulus much smaller than the bulk modulus, a case realized by rubbery macromolecules which can change their shape on extension at constant volume (see Sect. 4.6.5). The bulk modulus of small-molecule liquids and solids decreases normally with increasing temperature, while increasing pressure causes an increase.

The graph in Fig. 4.145 illustrates Young's modulus,  $E$ , for atactic polystyrene. This graph shows that for linear macromolecules, the modulus changes in a complicated manner with temperature. In addition, one finds that the modulus depends on time, a topic which is taken up in Section 4.5.5 when discussing DMA.



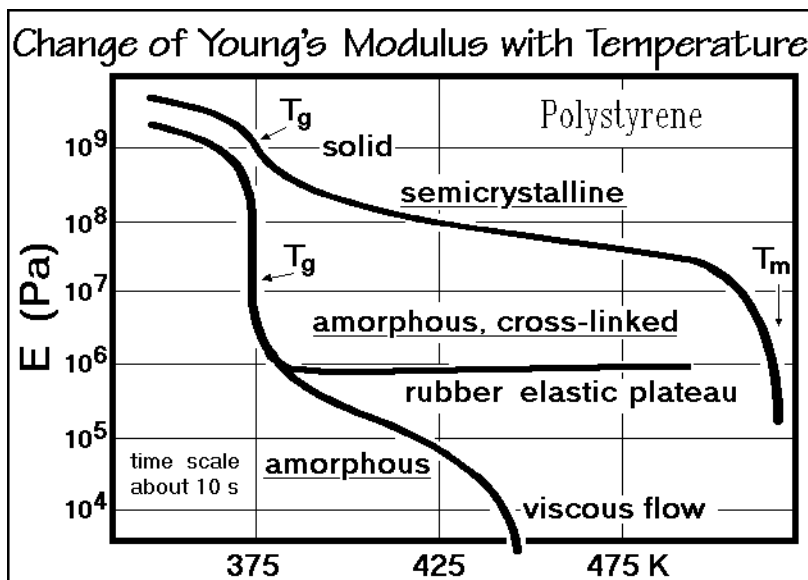


Fig. 4.145

The present graph refers to a time scale of about 10 s for any one measurement and is to be compared, for example, to a DSC scan at  $6 \text{ K min}^{-1}$ . On the left-hand side of the graph, the high moduli of the glassy and semicrystalline solid are seen and can be compared to the table of bulk moduli in Fig. 4.144. At the glass transition, Young's modulus for amorphous polystyrene starts dropping towards zero, as is expected for a liquid. The applied stress causes the molecules to flow, so that the strain increases without a limit when given enough time. Before very low values of  $E$  are reached, however, the untangling of the macromolecular chains requires more time than the 10 s the experiment permits. For a given time scale, the modulus reaches the so-called rubber-elastic plateau. Only at higher temperature ( $>450 \text{ K}$ ) is the molecular motion fast enough for the viscous flow to reduce the modulus to zero. Introducing permanent cross-links between the macromolecules by chemical bonds, the rubber-elastic plateau is followed with a gradual increase in  $E$ .

The data for a semicrystalline sample of polystyrene are also shown in the graph of Fig. 4.145. They show a much higher  $E$  than the rubbery plateau. Here the crystals form a dense network between the parts of the molecules that become liquid at the glass transition temperature. This network prohibits flow beyond the rubber elastic extension of the liquid parts of the molecules. Unimpeded flow is possible only after the crystals melt in the vicinity of 500 K.

#### 4.5.2 Instrumentation of TMA

A schematic diagram illustrating a typical thermomechanical analyzer is shown in Fig. 4.146. This instrument was produced by the Perkin-Elmer Co. Temperature is controlled through a heater and the coolant at the bottom. Atmosphere control is possible through the sample tube. The heavy black probe measures the position of the

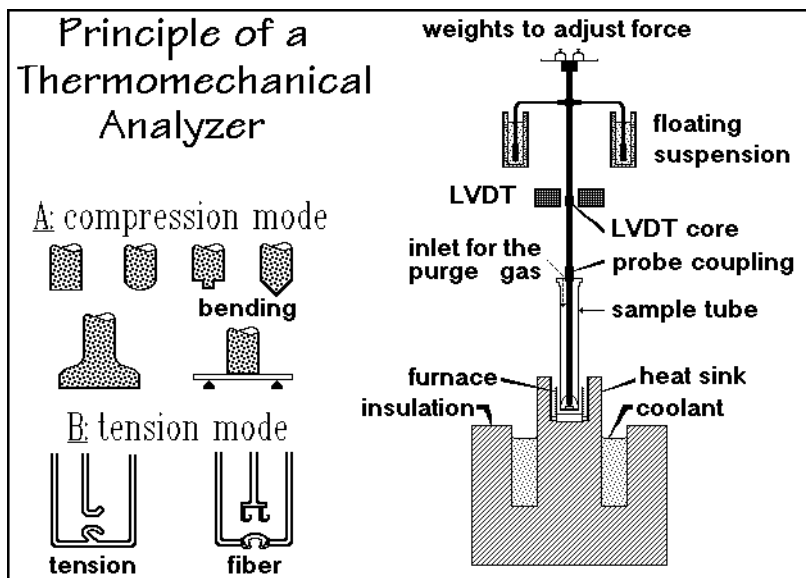


Fig. 4.146

sample surface with a linearly variable differential transformer, LVDT (see Fig. 4.13). The floating suspension, combined with added weights at the top, controls the force on the sample. The measurement can be carried out in various modes of sample-configuration. The simplest application uses a negligible downward compression force to study the sample dimension. A wide foot in contact with the sample, applied with a minimal downward force, yields the linear expansivity and is an example of a one-dimensional dilatometer. By enclosing the sample in a dilatometer flask with fixed wall, one may also obtain data on volume expansion and compression. The problem in the volume dilatometer probe is, naturally, to find a filling medium which is a properly hydrostatic medium and is easily sealed without friction. More details on general dilatometry are discussed in Sect. 4.1.

When the force on the sample is increased, the just described dilatometer becomes a thermomechanical analyzer, proper. The four types of probes at the top of A in Fig. 4.146 are being used to act in a penetration mode. A rod of well-defined cross section or geometry presses with a known force on the sample, and its penetration is measured as a function of temperature. The sharp, conical probe on the right is also used to characterize the sample by producing a plastic indentation. The setup at the bottom of A is designed to test the elastic modulus in a bending experiment. The deflection is followed at fixed loads with changing temperature. The two setups in B, finally, show special arrangements to put tension on a film or fiber sample. The measurement consists then of a record of force and length versus temperature. Measurements of shrinkage and expansion are important to analyze the performance of fibers and films.

Thermomechanical analyzers are available for temperatures from as low as 100 K to as high as 2,500 K. Basic instruments may go from 100 to 1,000 K with one or two furnaces and special equipment for liquid N<sub>2</sub> cooling. For higher temperatures,

different designs with thermally stable materials are needed. The linear range of the LVDT may be several millimeters. The maximum sensitivity is as high as a few tenths of a micrometer. A typical mass on the weight tray or force on the spring may be as much as 200 g. The dimensions of the sample are typically 0.5 cm in diameter and up to a few centimeters in height. The data acquisition and treatment through electronics and computer is as varied as in DTA and calorimetry. Direct recording of length and derivative of length is most common. The heating rates range from perhaps  $0.1 \text{ K min}^{-1}$  to as high as  $40 \text{ K min}^{-1}$ . They depend on the sample size and holder configuration. Even faster heating and cooling rates are often used to accomplish quick, uncontrolled temperature changes.

### 4.5.3 Applications of TMA

Data from a thermomechanical analysis are usually plotted as linear expansivity or length of the sample as a function of temperature. Figure 4.147 illustrates eight different TMA experiments. The top graphs show solid-solid transitions for potassium ethylsulfate,  $\text{K}(\text{C}_2\text{H}_5)\text{SO}_4$ , and dichlorodipyridylcobalt(II),  $\text{Co}(\text{C}_5\text{NH}_5)_2\text{Cl}_2$ . The organic compound acetanilide,  $\text{CH}_3\text{CONHC}_6\text{H}_5$ , which has a melting temperature of about 388 K, shows premelting shrinkage. The barium chloride,  $\text{BaCl}_2 \cdot 2\text{H}_2\text{O}$ , decreases in volume when it loses its crystal water, but continues afterwards with a normal, positive expansivity. All these measurements were done in the compression or penetration mode. In this configuration melting registers as a decrease in length, despite an increase in volume of the sample, because the material starts flowing.

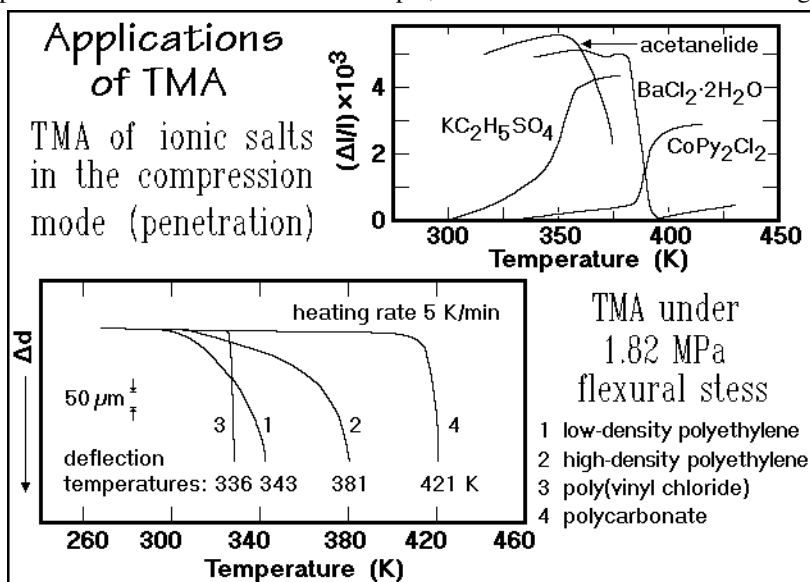


Fig. 4.147

The graphs at the bottom of Fig. 4.147 display results gained in the flexure mode under conditions that satisfy the ASTM (American Society for Testing and Materials). The deflection temperature is taken where the sample has been deformed by 0.010 in

(0.254 mm). For polycarbonate and poly(vinyl chloride) the deflections occur abruptly, close to the glass transition temperature, as is expected. For the two polyethylenes, the deflection is more gradual and can be related to the melting ranges of the semicrystalline polymers.

In the next series of applications schematic TMA traces of polymeric fibers in the tension mode are compared to DTA traces. The analyzed fibers could, for example, be poly(ethylene terephthalate), PET (see Sects. 4.3, 4.4, and 5.2). As extruded, the fibers are largely amorphous with some orientation. The TMA in Fig. 4.148 shows the usual expansion below the glass transition, followed by shrinkage as soon as the glass transition is reached. The partially drawn molecules relax to smaller dimensions as soon as sufficient mobility is gained at the glass transition. When equilibrium is established in the liquid (rubbery) state, a gradual decrease in expansivity is observed as the sample crystallizes. The crystallization is clearly evident in the DTA experiment through its exotherm. On melting, the sample becomes liquid and starts flowing. The recording stops when the fiber ultimately breaks. The DTA trace illustrates the full melting process.

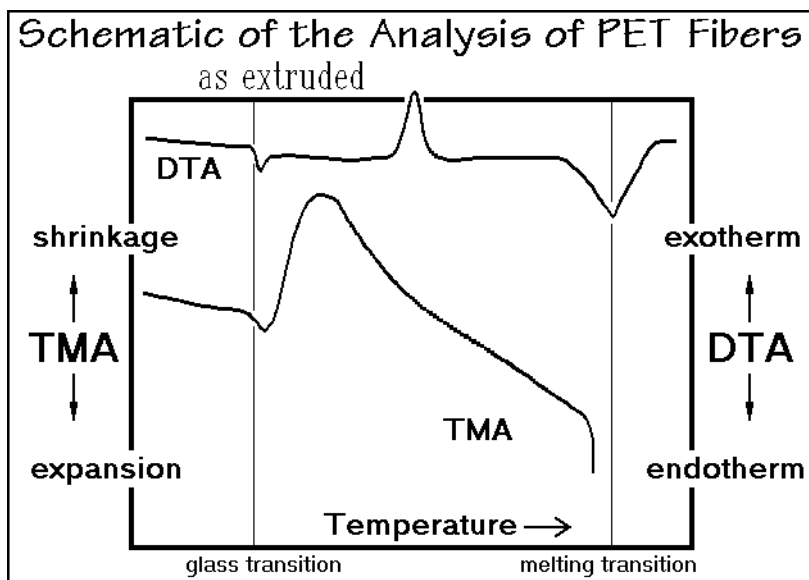


Fig. 4.148

Drawing causes higher orientation of the fiber, as is illustrated by Fig. 4.149. At the glass transition much larger shrinkage is observed than in Fig. 4.148. Subsequent crystallization occurs at lower temperature due to the better prior orientation. Since the DTA crystallization peak is smaller than the subsequent melting peak, one would conclude that the original drawn sample was already somewhat crystalline.

Annealing the drawn fiber, as shown in Fig. 4.150, introduces sufficient crystallinity to cause the shrinkage to occur continually between the glass and melting temperatures. One would interpret this behavior in terms of the existence of a rigid amorphous fraction that gradually becomes mobile at temperatures well above the

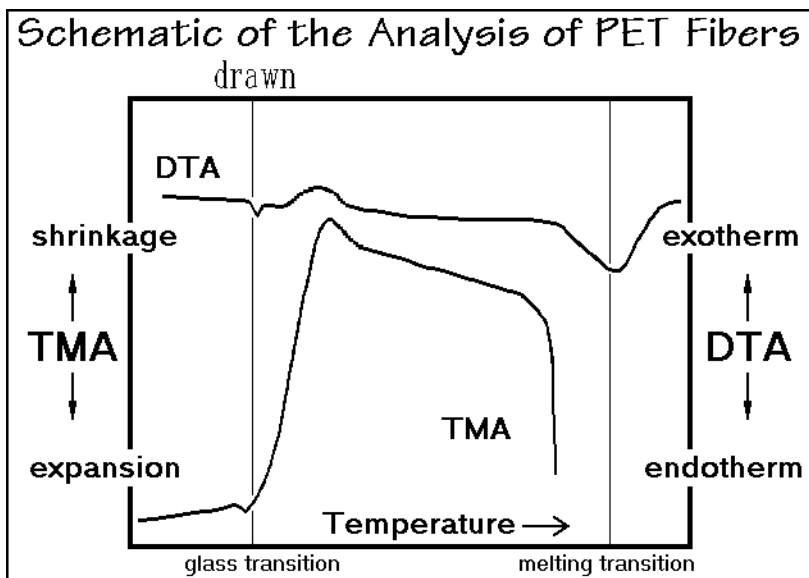


Fig. 4.149

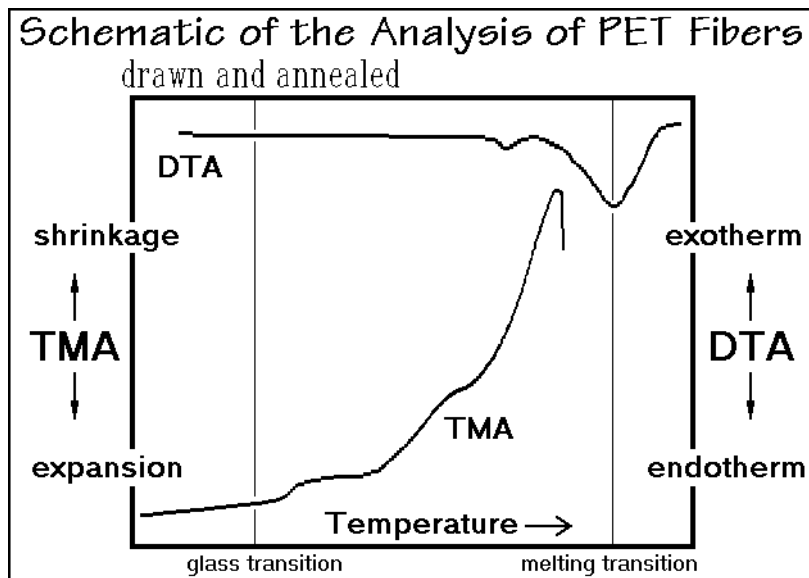


Fig. 4.150

glass transition. The TMA is thus a key tool in characterizing the various steps of fiber formation, particularly, if it is coupled with DSC and the analysis of molecular structure and mobility as discussed with Figs. 5.68–72 and 5.113–115.

Even more detailed are the DTA traces reproduced in Fig. 4.151 for PET. The broken lines show the melting at constant length. The continuous lines show melting

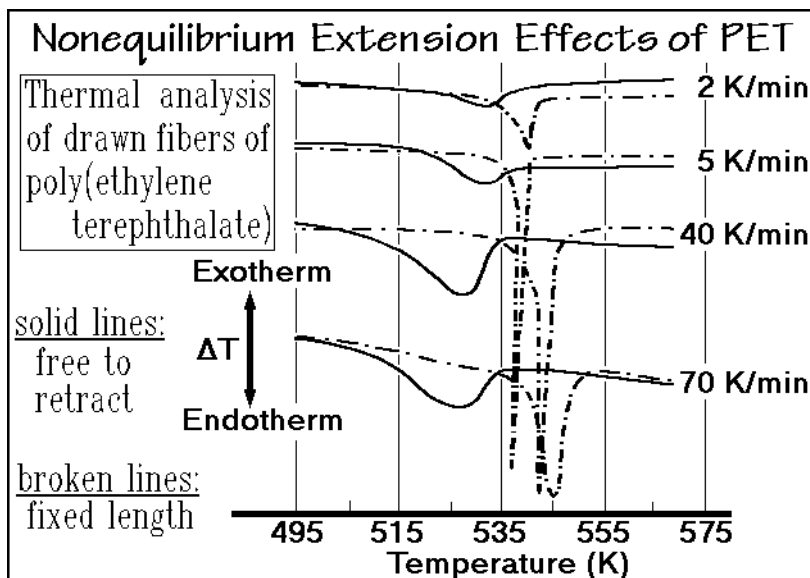
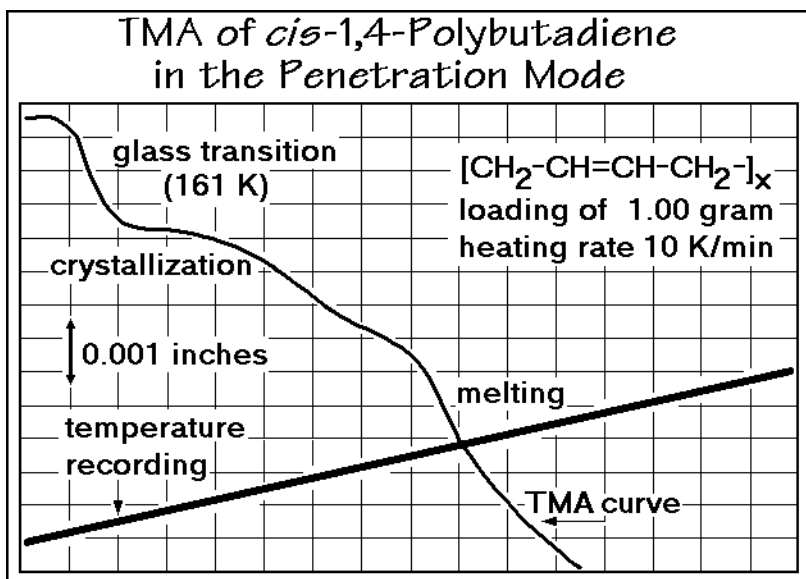


Fig. 4.151

of samples allowed to shrink freely. One can see from the changing of the melting peak with heating rates that equilibrium conditions were not fulfilled. The fact that the samples kept at fixed length, melt more sharply than the freely shrinking ones, is also in need of an explanation. The crystals are connected to the amorphous chains in the arrangement of the fibers. Any portion of the amorphous chains which is not fully relaxed after crystallization will increase the local melting temperature, as discussed in Chaps. 5–7. The degree of stretch is, however, determined by the crystals that set up a rigid network to maintain the strain in the amorphous chains. As the first crystals melt, the amorphous chains can start relaxing and thus decrease the melting temperature of the crystal portions to which they are attached, as shown in Fig. 4.151. There is, thus, a complicated sequence of melting and chain relaxation. In the PET case shown, there is a wide distribution of crystalline and intermediately ordered material (see Sect. 6.2), which causes the broad melting range of the samples. The fibers analyzed under the condition of fixed length, melt more sharply and increase in melting temperature with the heating rate. In the low-heating-rate samples, one can even detect a tilt of the peak toward low temperatures. This must mean that the collapse of the crystal network occurs so suddenly that it lowers the melting temperature faster than the heating rate increases the temperature. At a high heating rate, this decrease in melting temperature occurs less sudden, and the melting occurs at higher temperature and over a wider temperature range. In Figs. 4.148–150 the TMA and DTA curves don't show this decrease in temperature on melting because of the different experimental conditions and time scales.

This discussion documents that various forms of thermal analyses have to be brought together, and combined with knowledge from thermodynamic theory, to begin to understand the often complicated melting and crystallization behavior of polymeric materials (see Chaps. 5–7).

A final TMA example is shown in Fig. 4.152. It reproduces a penetration experiment with a rubbery material, *cis*-1,4-polybutadiene ( $\text{CH}_2\text{-CH=CH-CH}_2\text{-}$ )<sub>x</sub>. The glass transition occurs at 161 K. It softens the material to such a degree that the TMA probe penetrates abruptly. The quantitative degree of this penetration depends on the probe geometry, loading, and heating rate. At higher temperature the rate of penetration is then slowed somewhat by crystallization. At the melting temperature of the crystals grown during heating, the penetration is speeded up again.



**Fig. 4.152**

Thermomechanical analysis, thus, permits a quick comparison of different materials. As long as instrumental and measuring parameters are kept constant, quantitative comparisons are possible.

#### 4.5.4 Principles and Instrumentation of DMA

The study of elastic and viscoelastic materials under conditions of cyclic stress or strain is called dynamic mechanical analysis, DMA. The periodic changes in either stress or strain permits the analysis of the dynamic response of the sample in the other variable. The analysis has certain parallels to the temperature-modulated differential thermal analysis described in Sect. 4.4, where the dynamic response of the heat-flow rate is caused by the cyclic temperature change. In fact, much of the description of TMDSC was initially modeled on the more fully developed DMA. The instruments which measure stress versus strain as a function of frequency and temperature are called dynamic mechanical analyzers. The DMA is easily recognized as a further development of TMA. Its importance lies in the direct link of the experiment to the mechanical behavior of the samples. The difficulty of the technique lies in understanding the macroscopic measurement in terms of the microscopic origin. The

technique and application of DMA has developed to such a degree that a separate textbook is necessary to cover it adequately. In this section only a brief introduction is given to show the ties to TMA and TMDSC. A detailed description of DMA can be found in the list of general references to this section. A major application lies in the analysis of flexible, linear polymers.

Figure 4.153 shows a schematic drawing of a torsion pendulum. It was used for some of the first DMA experiments that were carried out as a function of temperature [43]. The pendulum is set into vibrations of small amplitude ( $\approx 3^\circ$ ) and continues to

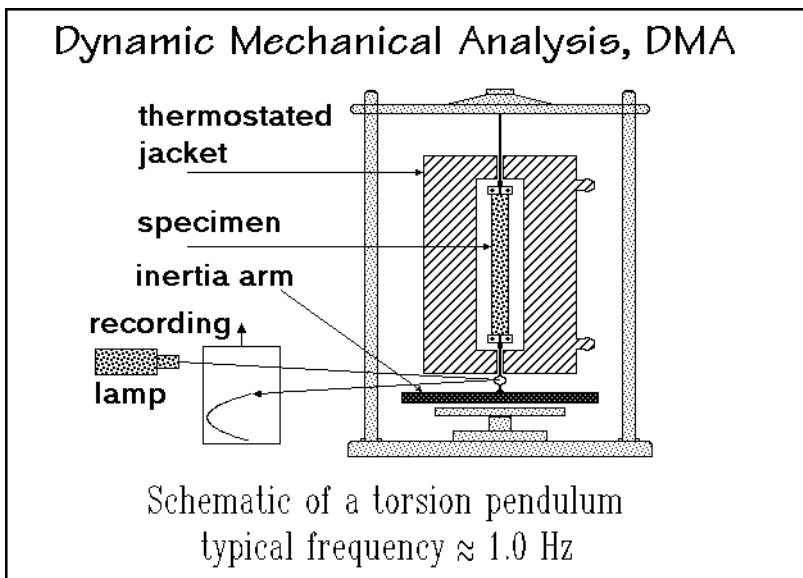


**Fig. 4.153**

oscillate freely with a constant, characteristic resonant frequency of decreasing amplitude, recorded by a lamp and mirror arrangement. The viscoelastic properties are then computed from the frequency and the logarithmic decrement,  $\Delta$ , of the amplitude. A typical torsional oscillation and a plot of the logarithm of the maximum amplitudes versus their ordinal numbers are shown in Fig. 4.154. The slopes of the curves A to D represent the logarithmic decrements.

Dynamic mechanical analyzers can be divided into resonant and defined frequency instruments. The torsion pendulum just described is, for example, a resonant instrument. The schematic of a defined-frequency instrument is shown in Fig. 4.155. The basic elements are the force generator and the strain meter. Signals of both are collected by the module CPU, the central processing unit, and transmitted to the computer for data evaluation. The diagram is drawn after a commercial DMA which was produced by Seiko. At the bottom of Fig. 4.155, a typical sample behavior for a DMA experiment is sketched. An applied sinusoidal stress,  $\sigma$ , is followed with a phase lag,  $\delta$ , by the strain,  $\epsilon$ . The analysis of such data in terms of the dynamic moduli (stress-strain ratios, see Fig. 4.143) at different frequencies and temperature is the subject of DMA.



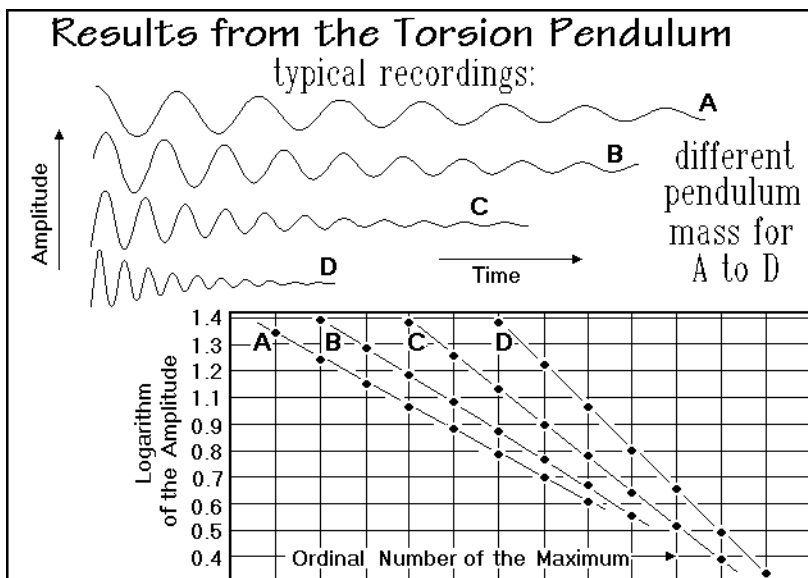


Fig. 4.154

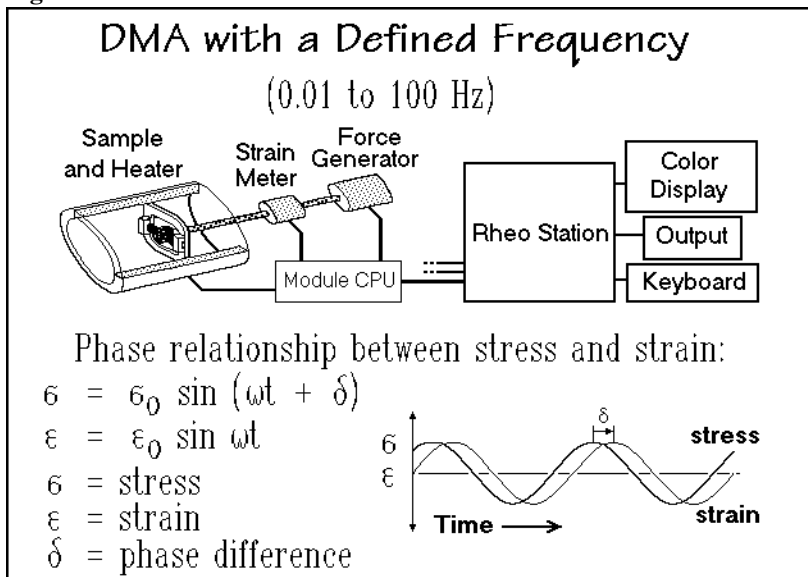


Fig. 4.155

Figure 4.156 illustrates the detailed technical drawing of a dynamic mechanical analyzer by TA Instruments. The sample is enclosed in a variable, constant-temperature environment, not shown, so that the recorded parameters are stress, strain, time, frequency, and temperature. This instrument can be used for resonant and defined-frequency operation. Even creep and stress relaxation measurements can be performed. In creep experiments, a constant stress is applied at time zero and the

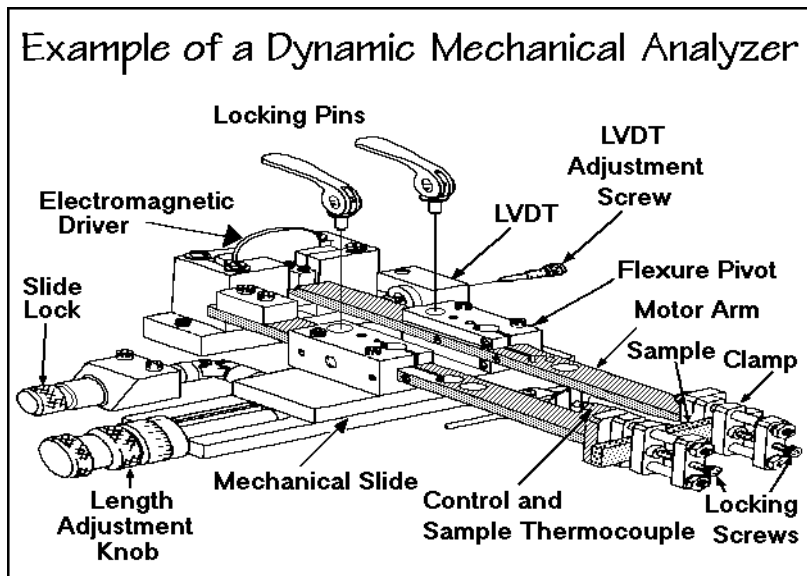


Fig. 4.156

strain of the sample measured as a function of temperature. In stress-relaxation a constant strain is applied to the sample and the relaxation of the stress is followed.

In the description of the basics of thermomechanical analysis in the first part of this section the mechanical properties were assumed to result from perfect elasticity, i.e., the stress is directly proportional to the strain and independent of the rate of strain. Hooke's law expresses this relationship with a constant modulus as sketched at the top of Fig. 4.157 for the example of tensile stress and strain.

The theory of hydrodynamics similarly describes an ideal liquid behavior making use of the viscosity (see Sect. 5.6). The viscosity is the property of a fluid (liquid or gas) by which it resists a change in shape. The word viscous derives from the Latin *viscum*, the term for the birdlime, the sticky substance made from mistletoe and used to catch birds. One calls the viscosity Newtonian, if the stress is directly proportional to the rate of strain and independent of the strain itself. The proportionality constant is the viscosity,  $\eta$ , as indicated in the center of Fig. 4.157. The definitions and units are listed, and a sketch for the viscous shear-effect between a stationary, lower and an upper, mobile plate is also reproduced in the figure. Schematically, the Newtonian viscosity is represented by the dashpot drawn in the upper left corner, to contrast the Hookean elastic spring in the upper right.

The idealized laws just reviewed can, however, not describe the behavior of matter if the ratios of stress to strain or of stress to rate of strain is not constant, known as stress anomalies. Plastic deformation is a common example of such non-ideal behavior. It occurs for solids if the elastic limit is exceeded and irreversible deformation takes place. Another deviation from ideal behavior occurs if the stress depends simultaneously on both, strain and rate of strain, a property called a time anomaly. In case of time anomaly the substance shows both solid and liquid behavior at the same time. If only time anomalies are present, the behavior is called linear

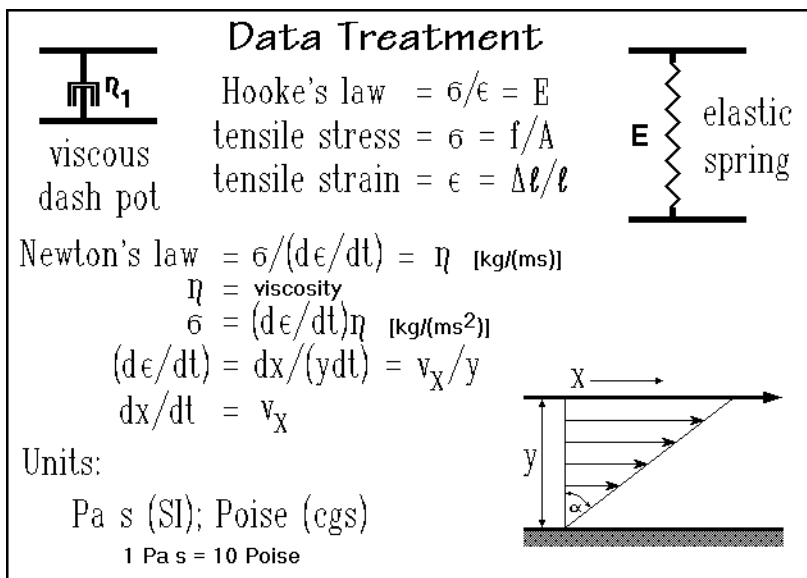


Fig. 4.157

viscoelasticity. In this case the ratio of stress to strain is a function of time alone, and not of the stress magnitude.

Two models that can duplicate viscoelastic behavior are the Voigt model with a spring and a dashpot coupled in parallel, and the Maxwell model with a spring and a dashpot coupled in series. Both are shown schematically in Fig. 4.158. The ratio of viscosity to modulus of one element of the Voigt model is called the retardation time

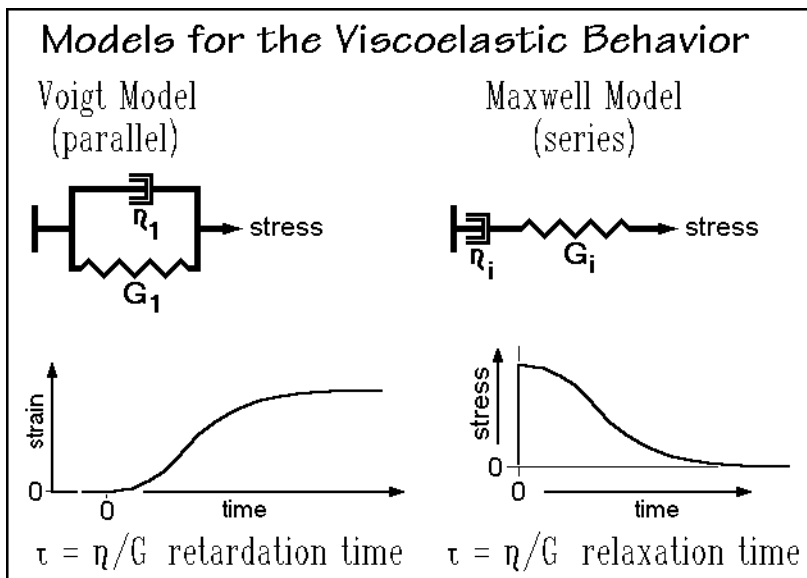
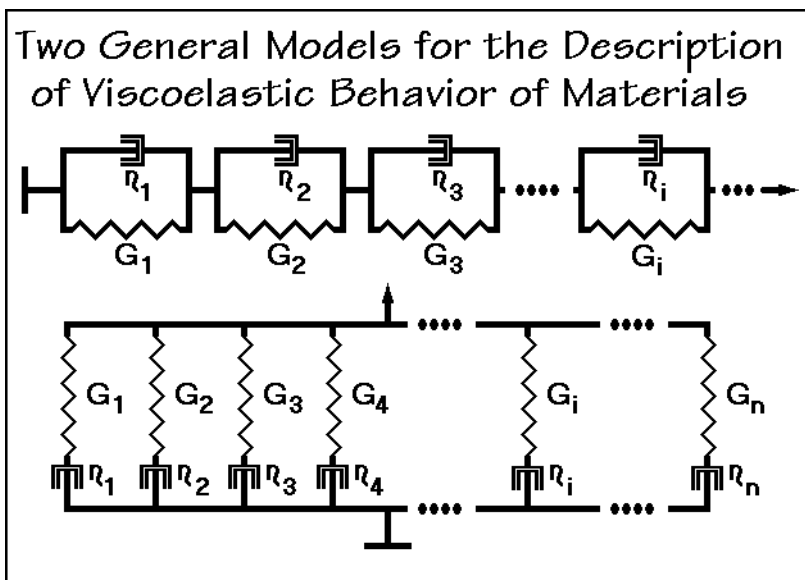


Fig. 4.158

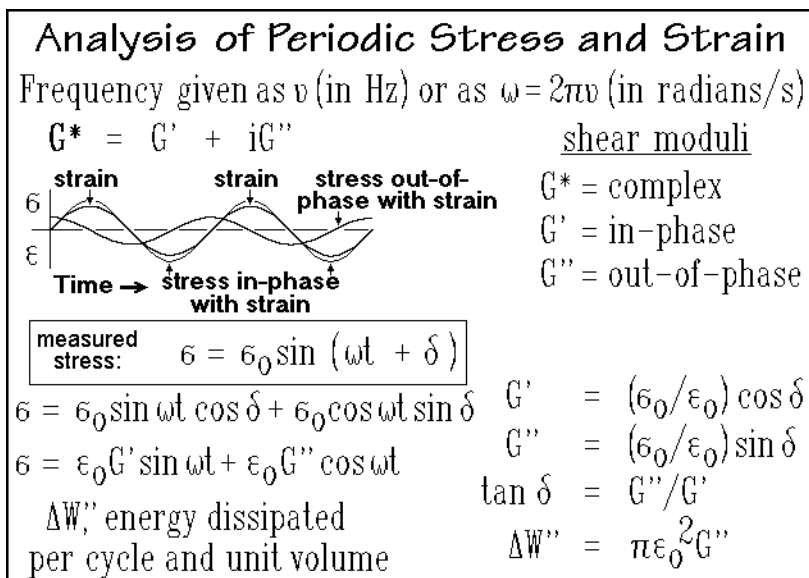
and for the example of a shear experiment is a measure of the time needed to extend the spring to its equilibrium length, as shown in the graph. The rise of the strain caused by the application of the stress to the parallel spring and dashpot is retarded, but ultimately the full equilibrium extension is reached. For the Maxwell model the same ratio is called its relaxation time and is a measure of the time needed for the initially applied stress to drop to zero, as shown on the right of Fig. 4.158. Description of the macroscopic behavior of a material would be simple if the spring in the Voigt or Maxwell models could be identified with a microscopic origin, such as a bond extension or a conformational change in an entropy elastic extension, and the dash pot with a definite molecular friction. One can imagine, however, that there must be many different molecular configurations contributing to the viscoelastic behavior of the sample. For this reason the simple models are expanded to combinations of many elements “*i*” as shown in Fig. 4.159. These combinations of the elements of the model are linked to retardation and relaxation time spectra. Naturally, there may also be combinations of both models needed for the description.



**Fig. 4.159**

For most polymeric materials, viscoelastic behavior can be found for sufficiently small amplitudes of deformation. Rigid macromolecules and solids, in general, show relatively little deviation from elasticity and behave approximately as indicated in Fig. 4.144. The major application of DMA is to flexible, linear macromolecules from the glass transition to the rubbery state.

The analysis of DMA data is illustrated in Fig. 4.160 with the example of shear deformation. The periodicity of the experiment is expressed in frequency, either in hertz,  $\nu$ , (dimension:  $s^{-1}$ ), or in  $\omega$  (dimension: radians per second). Periodic experiments at frequency  $\omega$  in DMA, as also in TMDSC, are comparable to a nonperiodic, transient experiment with a time scale of  $t \approx 1/\omega = 0.159$  s.

**Fig. 4.160**

To describe the stress and strain caused by the modulation, as given by the instrument of Fig. 4.155, one defines a complex modulus  $G^*$  as shown in Fig. 4.160. Analogous expressions can be written for Young's modulus and the bulk modulus. The real component  $G'$  represents the in-phase component, and  $G''$  is the out-of-phase component. The letter  $i$  represents, as usual, the square roots of  $-1$ . In order to evaluate  $G^*$ , the measured stress is separated into its two components, one in-phase with the strain, and one out-of-phase. The simple addition theorem of trigonometry links  $\sigma$  to the complex terms of the modulus. Also given are the equations for  $G'$ ,  $G''$ , and the tangent of the phase difference  $\delta$ . Since the in-phase portions of the stress are only a part of the measured total stress, there is a loss in the recovered mechanical energy in every cycle. This energy, dissipated as heat over one cycle,  $\Delta W''$ , is given at the bottom of Fig. 4.160.

A strain-modulated DMA parallels the temperature-modulated DSC discussed in Sect. 4.4. Figure 4.161 shows a comparison to the results in Figs. 4.90, written for a common phase lag  $\theta$ . Note that the measured heat-flow rate  $HF(t)$  lags behind the modulated temperature, while the measured shear stress advances ahead of the modulated strain. Besides modulation of strain, it is also easily possible to modulate the stress, and even temperature-modulation is possible and of interest for comparison of DMA to TMDSC, as was established recently [44].

The data are further analyzed mathematically. In particular, it is of interest to establish retardation and relaxation time spectra that fit the measured data using Voigt or Maxwell models. Adding the temperature dependence of the data leads to the interesting observation that time and temperature effects are often coupled by the time-temperature superposition principle. Effects caused by an increase in temperature can also be produced by an increase in time scale of the experiment. The ratio of modulus to temperature, when plotted versus the logarithm of time for different temperatures,

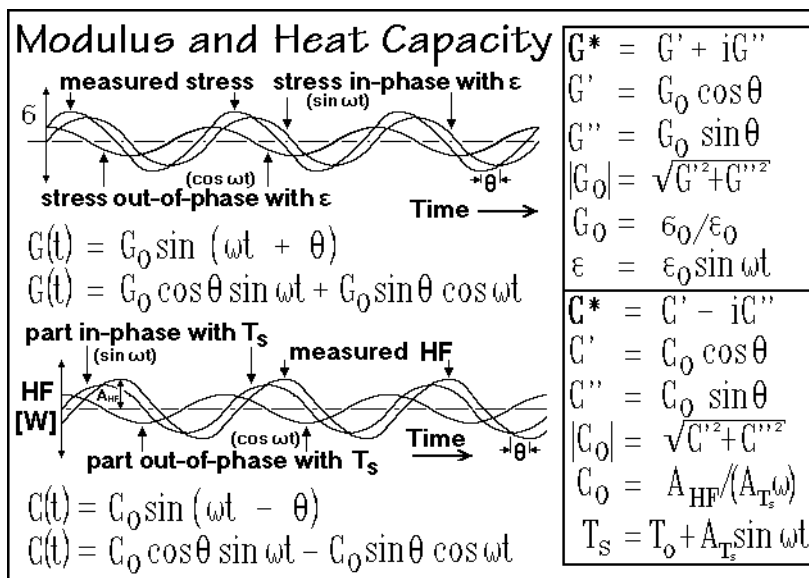


Fig. 4.161

can be shifted along the time axis by  $a_T$  and brought to superposition. The shift factor  $a_T$ , is the ratio of corresponding time values of the modulus divided by the respective temperatures  $T$  and  $T_0$ . A great variety of amorphous polymers have in the vicinity of the glass transition a shift factor  $a_T$  that is described by the approximately universal Williams-Landel-Ferry equation (WLF equation):

$$\log a_T = [17.44(T - T_g)] / [51.6 + (T - T_g)].$$

The mechanical spectra and temperature dependencies derived from DMA provide, as such, no immediate insight to their molecular origin. Qualitatively the various viscoelastic phenomena are linked to the energy-elastic deformation of bonds and the viscous effects due to large-amplitude movement of the molecular segments. The latter are based on internal rotation causing conformational motion to achieve the equilibrium entropy-elastic response.

### 4.5.5 Applications of DMA

The application of DMA to the study of the glass transition of poly(methyl methacrylate) is shown in Fig. 4.162. The graph illustrates the change in Young's storage modulus  $E'$  as a function of frequency. Measurements were made on an instrument as in Fig. 4.155 with frequencies between 0.03 and 90 Hz. The low-temperature data (below 370 K) show the high modulus of a glass-like substance. At higher temperature this is followed by the glass transition region, and the last trace, at 413 K, is that of a typically rubber-elastic material (see also Fig. 4.145). With the proper shift  $a_T$ , as described in Sect. 4.4.4, the master curve at the bottom of Fig. 4.163 can be produced. The shift factors  $a_T$  are plotted in the upper right graph in a form

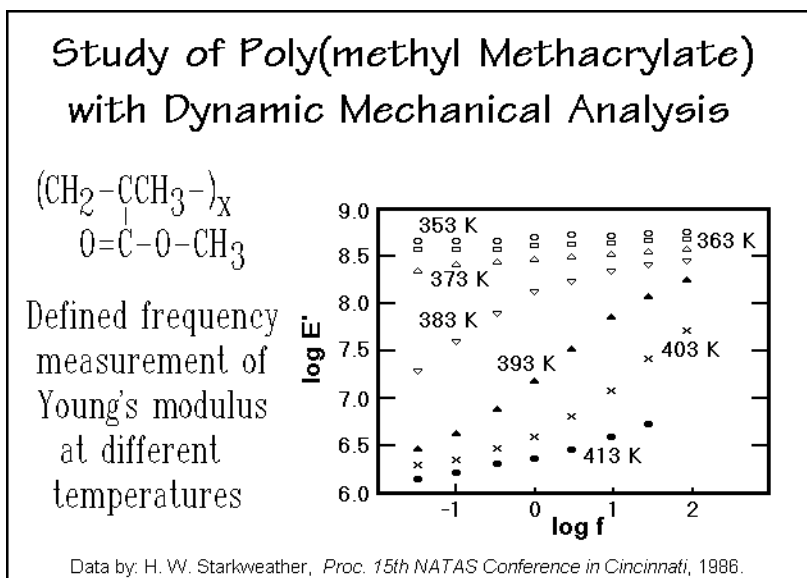


Fig. 4.162

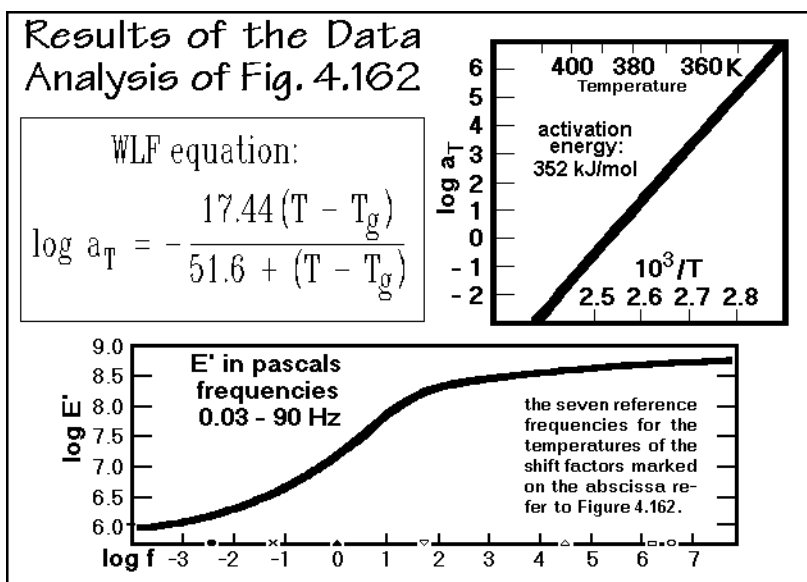


Fig. 4.163

which indicates a logarithmic dependence on the inverse of temperature as expected from the WLF equation. An activation energy of  $352 \text{ kJ mol}^{-1}$  can be derived from the plot. Figures 4.164 and 4.165 show the same treatment for  $\tan \delta$ . The glass transition is marked by the maximum in the plot of  $\tan \delta$  versus frequency or temperature. The reference temperature chosen for the shift is 393 K.

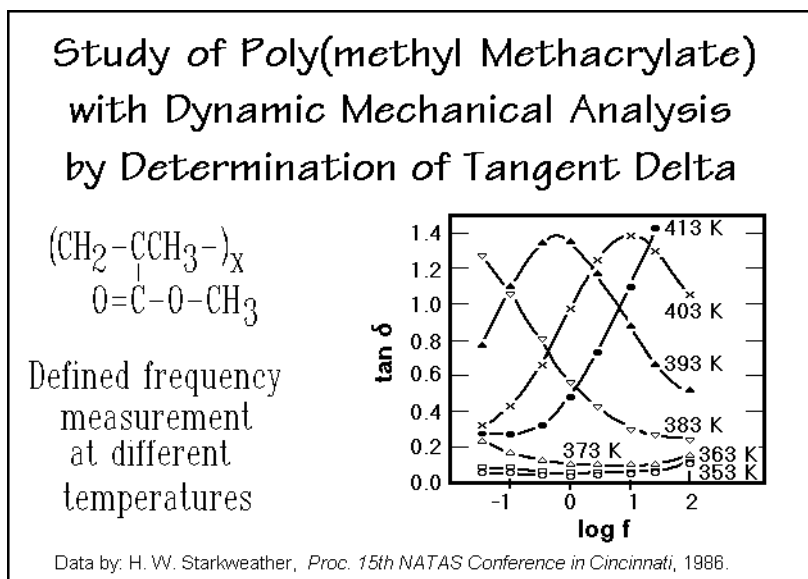
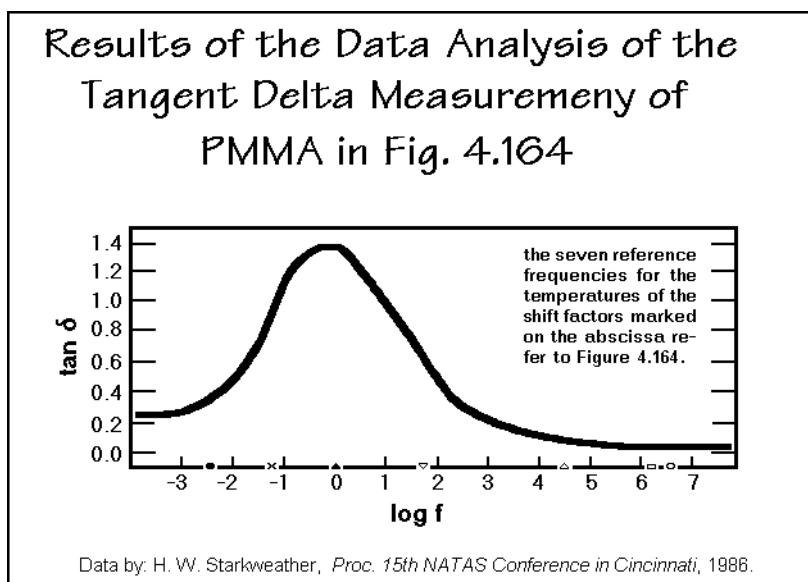
**Fig. 4.164****Fig. 4.165**

Figure 4.166 shows a DMA analysis of an amorphous polycarbonate, poly(4,4'-isopropylidenediphenylene carbonate). These data were taken with an instrument like that seen in Fig. 4.156. Measurements were made at seven frequencies between 0.01 and 1 Hz at varying temperatures. Again, the glass transition is obvious from the change in flexural storage modulus, as well as from the maximum of the loss modulus.



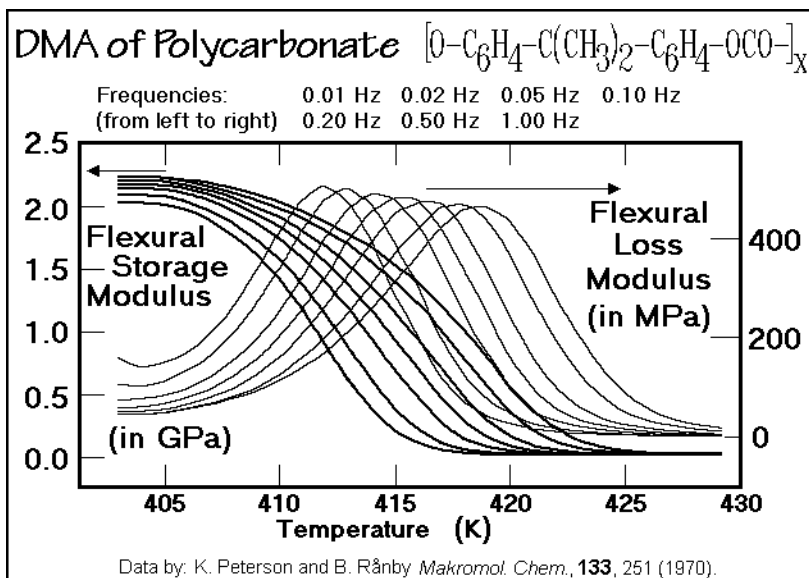


Fig. 4.166

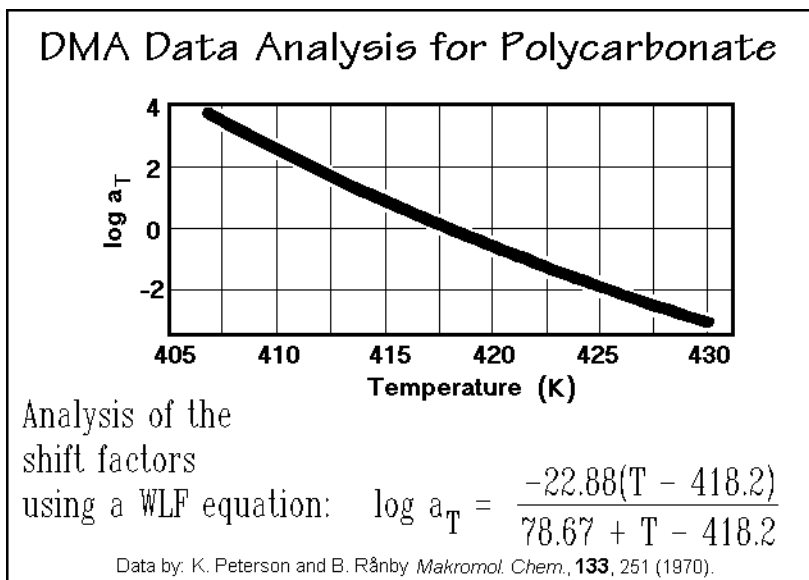


Fig. 4.167

Figure 4.167 illustrates the analysis of the shift factors using the WLF equation as given in Fig. 4.163 with of the constants fitted for the polycarbonate. Finally, in Figs. 4.168 and 169 the master curves are generated by shifting the data for the loss and storage moduli, as given in Fig. 4.166. The master curves represent the full data set of Fig. 4.166.

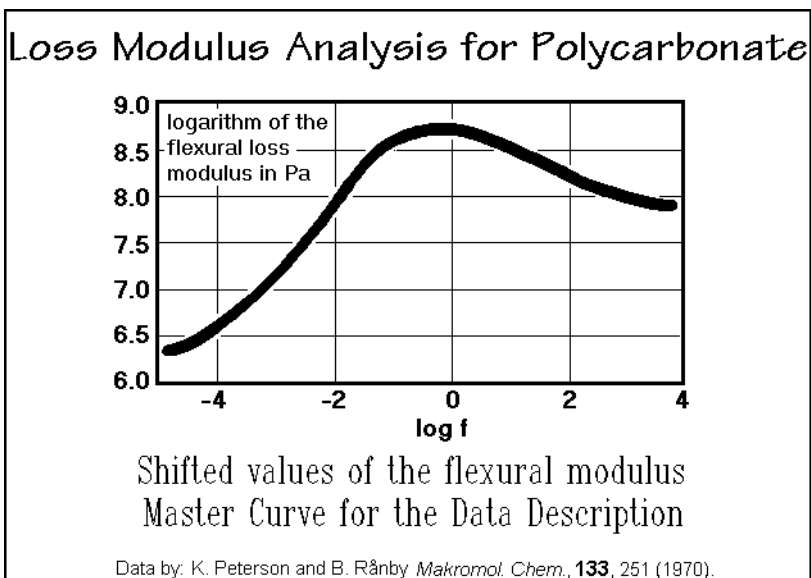


Fig. 4.168

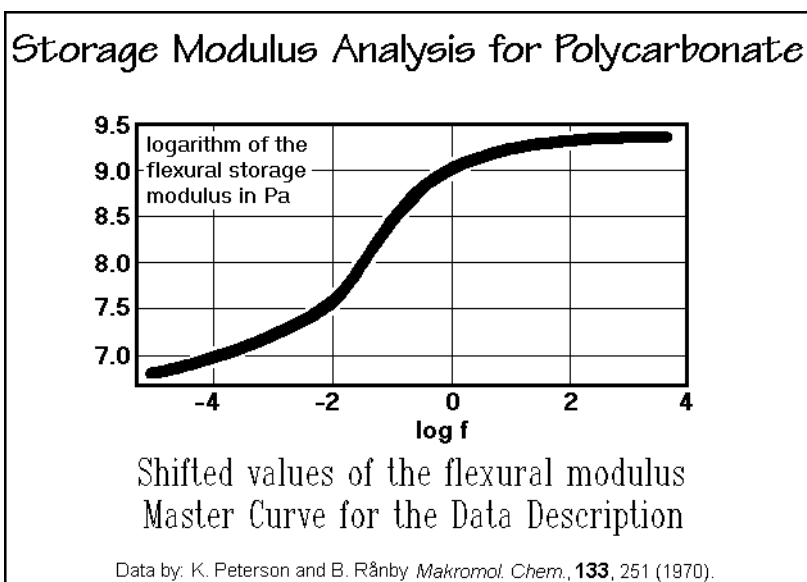


Fig. 4.169

Another DMA analysis is shown in Fig. 4.170 for poly(vinyl chloride),  $[-\text{CHCl}-\text{CH}_2]_x$ . The data for  $G'$ ,  $G''$ , and  $\tan \delta$  are given as a function of temperature for one frequency. The glass transition occurs at about 300 K, as indicated by the drop in  $G'$  and the peaks in  $G''$  and  $\tan \delta$ . In addition, there is a broad peak in  $G''$  and in  $\tan \delta$ , indicating a secondary, local relaxation in the glassy state. Semicrystalline

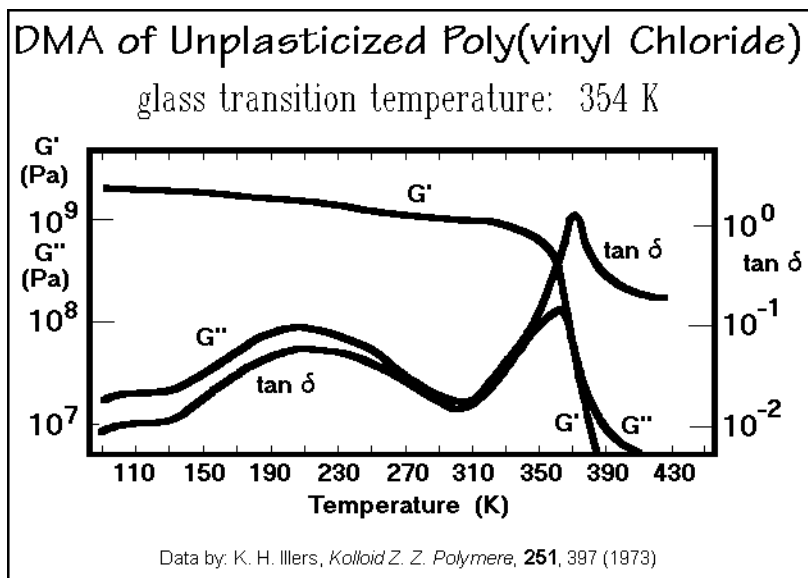


Fig. 4.170

polymers show a more complicated DMA picture (see Fig. 4.145) because of the additional melting transition and a considerable broadening of the glass transition (see Chaps. 6 and 7).

#### 4.5.6 Dielectric Thermal Analysis, DETA

The mechanism of dielectric effects of interest to DETA involves permanent dipoles<sup>1</sup> which exist within the sample and try to follow an alternating electric field, but may be hindered to do so when attached to segments of molecules with limited mobility. The fundamental analogy of dielectric and mechanical relaxation has been pointed out already in 1953 [45].

An electric field in a material causes polarization,<sup>2</sup> as summarized in Fig. 4.171. The polarization may have different origins: (1) Electron polarization, an interaction that shifts the electrons with respect to the center of the atom. (2) Atom polarization, caused by shift of relative positions of bonded atoms. (3) Dipole or orientation polarization, the effect to be discussed. The first two types of polarization involve fast displacement of positive and negative charges relative to each other within a time-scale of about  $10^{-15}$  s. Both are usually treated together as induced polarization and are related to the refractive index,  $n$ , by the equation of Maxwell (see also the discussions of light scattering, Sect. 1.4.2 and Appendix 3). The time scale of dipole polarization is  $10^{-12}$  to  $10^{-10}$  s for mobile dipoles, but may become seconds and longer

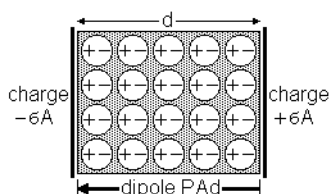
<sup>1</sup> In SI-units the dimension of the dipole moment  $\mu$ , is C m (C = coulomb or A s, see Fig. 2.3).

<sup>2</sup> Polarization is the charge introduced per unit surface area, identical to the average dipole moment per unit volume. The SI-unit has the dimension  $C m^{-2}$ , C = coulomb or A s.

### Brief Discussion of the Polarizability

The electric polarizability of a molecule is defined by the induced electric dipole  $p = \alpha E$ , where  $E$  is the electric field strength (in V/m). The SI unit of  $\alpha$  is  $C\ m^2\ V^{-1}$ .

The macroscopic polarization of a dielectric,  $P$ , is the average dipole moment per unit volume or charge per unit area. The connection between the definitions can be gained from the sketch:



where  $d$  is the separation between the two electrodes of a capacitor,  $A$  is the area of each electrode, and  $\epsilon$  is the charge per unit area.

The molecular dipoles of the dielectric align in the applied field and give rise to the opposing charges ( $-PA$  on the right and  $+PA$  on the left), but cancel in the bulk.

The polarization  $P$  is connected to the permittivity\*  $\epsilon$  as follows: The electric field between the plates in vacuum is  $E_0 = \epsilon/\epsilon_0$ , but with the dielectric it is reduced to  $E = \epsilon/\epsilon$ ; furthermore, one can see that the dielectric reduces the surface charge to  $E = (\epsilon - P)/\epsilon_0$ . Eliminating  $\sigma$  between the two equations yields  $P = E(\epsilon - \epsilon_0)$ .

\* The relative permittivity  $\epsilon_r$  (earlier called dielectric constant) is given by  $\epsilon_r = \epsilon/\epsilon_0$ .

Fig. 4.171

for less mobile dipoles. In case the sample contains freely migrating charges, such as small ions, a space-charge or ion polarization exists which interferes with the measurement of dipole polarization and must be avoided.

The polarization of a material is measured via its relative permittivity (dielectric constant),  $\epsilon_r$ , by placing it between the plates of a condenser as shown schematically in Fig. 4.172. The three-electrode arrangement has the goal to confine the field in the

### Dielectric Thermal Analysis

#### Schematic of Sample and Capacity Bridge for DETA

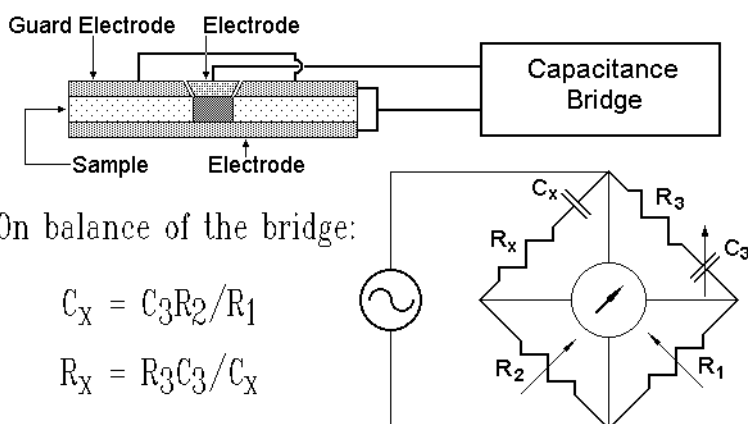


Fig. 4.172

densely shaded area of the sample. The capacitance can then be determined with a Schering capacity bridge by adjusting the resistances  $R_1$ ,  $R_2$ , and the capacitance  $C_3$  as indicated in the figure.

The Debye equation gives the link to the molar polarizability:

$$P_m = \frac{(\epsilon - 1)M}{(\epsilon + 2)\rho} = \frac{N_A}{3\epsilon_0} \left( \alpha_o + \frac{\mu^2}{3kT} \right) \quad (1)$$

where  $M$  is the molecular mass,  $\rho$  the density,  $N_A$  the number of molecules per mole (Avogadro's number),  $\alpha_o$  the induced molecular polarizability, and  $\mu$  the permanent dipole moment. Changing now from a stationary electric field to one that changes sinusoidally, the time scale of the experiment becomes important as in DMA. Figure 4.173 shows in its dotted upper curve the change in relative permittivity as a function of frequency of a simple polar material that shows only one dispersion region. At high frequency, the permanent dipoles cannot follow the changing alternating electric field, i.e., they do not contribute to the polarization and Eq. (1) consists of only the first part of the right-hand side. As the frequency approaches a time scale that permits the permanent dipoles to align, one reaches the dispersion region and the permittivity (dielectric constant) increases, until a low frequency limit is reached for the assumed single relaxation mechanism.

The time-dependent behavior of the permittivity is treated analogously to the DMA data in Sect. 4.5.4. A complex permittivity,  $\epsilon^*$ , is written as:

$$\epsilon^* = \epsilon' + i\epsilon'' \quad (2)$$

where  $\epsilon'$  and  $\epsilon''$  are the in-phase and the out-of-phase components of the permittivity, respectively. As in DMA,  $\epsilon''$  represents the loss factor or dielectric loss. The dotted

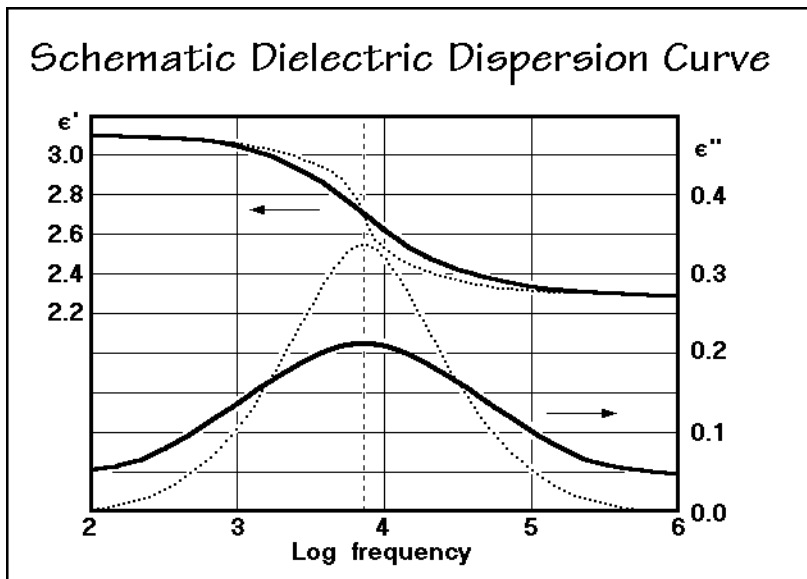


Fig. 4.173

curve at the bottom of Fig. 4.173 shows its change with frequency. At both, high and low frequencies  $\epsilon''$  approaches zero, in the dispersion region it reaches a maximum.

Debye derived the classical equations for the complex permittivity:

$$\epsilon^* = \epsilon'_\infty + \frac{\epsilon'_{\text{zero}} - \epsilon'_\infty}{1 + i\omega\tau}; \quad \epsilon' = \epsilon'_\infty + \frac{\epsilon'_{\text{zero}} - \epsilon'_\infty}{1 + \omega^2\tau^2}; \quad \epsilon'' = \frac{(\epsilon'_{\text{zero}} - \epsilon'_\infty)\omega\tau}{1 + \omega^2\tau^2} \quad (3)$$

where  $\tau$  is the relaxation time. The loss reaches its maximum at  $\tau\omega$ . At this point  $\epsilon' = (\epsilon'_{\text{zero}} + \epsilon'_\infty)/2$  and  $\epsilon'' = (\epsilon'_{\text{zero}} - \epsilon'_\infty)/2$ . Analogous to DMA a loss tangent can be defined ( $\tan \delta = \epsilon''/\epsilon'$ ). Actually measured dispersion curves are, however, flattened and extend over wider frequency ranges, as shown by the solid curves in Fig. 4.173. As in the DMA case, this can be accounted for by assuming a relaxation-time spectrum. If several distinct relaxation mechanisms occur with sufficiently widely separated relaxation times, Eqs. (1) and (3) need to be expanded by additional terms describing the added processes. As with DMA, temperature and frequency are related, permitting a similar time-temperature superposition of the data.

A convenient way to represent the experimental data at constant temperature is in a Cole-Cole plot shown in Fig. 4.174, making use of the following equation:

$$\epsilon^* = \epsilon'_\infty + \frac{\epsilon'_{\text{zero}} - \epsilon'_\infty}{1 + (i\omega\tau_0)^{1-\alpha}} \quad (4)$$

where  $\tau_0$  is the most probable relaxation time at which  $\epsilon''$  shows the maximum. The empirical fitting parameter  $\alpha$  is zero if the relaxation process follows simple Debye behavior as described by Eq. (3) and tends toward one for broader relaxation time spectra. On plotting of  $\epsilon''$  versus  $\epsilon'$ , a circle is obtained with  $\epsilon'_\infty$  and  $\epsilon'_{\text{zero}}$  as

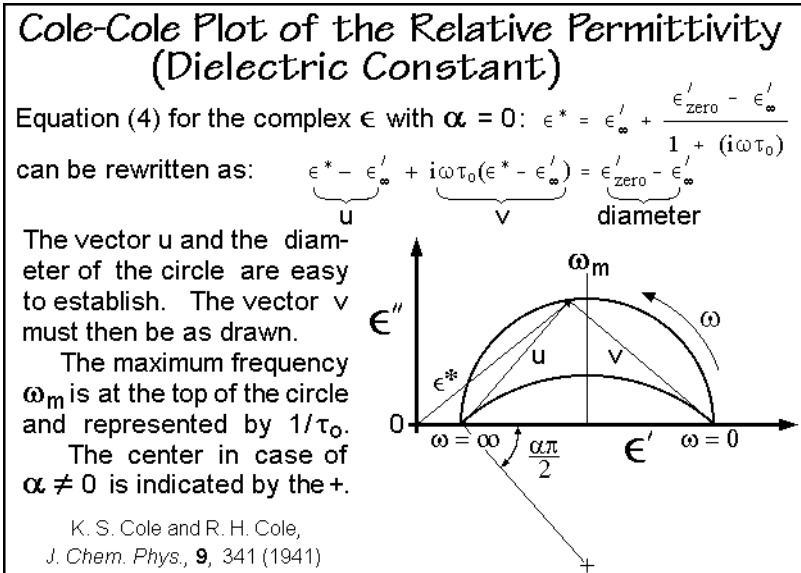


Fig. 4.174

intercepts with the abscissa. For  $\alpha = 0$  the center of the circle lies on the abscissa at  $(\epsilon_{\infty}' + \epsilon_{\text{zero}}')/2$ . With increasing  $\alpha$ , the center moves below the abscissa and a diameter from  $\epsilon_{\text{zero}}$  encloses the angle  $\alpha\pi/2$  with the abscissa. The data in Fig. 4.174 were drawn with an  $\alpha$  of about 0.25.

## 4.6 Thermogravimetry

### 4.6.1 Principle and History

The additional variable of state for thermal analysis by thermogravimetry is mass, as suggested in Fig. 4.175. The SI unit of mass is the kilogram [kg], which is the mass of an international prototype in form of a platinum cylinder and is kept at the International Bureau of Weights and Measures near Paris, France (see also Fig. 2.3). The last adjustment was made for the 1990 SI scale. Originally, that is in 1795, the gram was chosen as mass standard. It was to represent the mass of 1 cm<sup>3</sup> of H<sub>2</sub>O at its freezing temperature. In 1799 the mass standard was changed to 1,000 cm<sup>3</sup> of water at its maximum of density at 277.13 K, since the larger mass could be measured more precisely. At present, this connection is only approximate, but the difference from the old size is hardly noticeable for practical applications. Today the mass standard is independent of the volume of water.

The basic mass determination is simple. It consists in a comparison of the force exerted by gravity on the two masses to be compared, using for example a beam balance as is shown schematically in Fig. 4.175. For practically all thermal analyses, changes in temperature, pressure, volume, or chemical bonding do not change the total mass. The main calculation from a direct measurement of mass is to establish the number of moles of the compound or element in question. This is achieved by division through the molar mass, MW. With the general use of SI units, one must remember that the molar masses must be entered in kg, not g! The mole is defined as the number of atoms in exactly 12 g (0.012 kg) of the isotope 12 of carbon. The number of particles per mole is  $6.02214 \times 10^{23}$ , Avogadro's number.

The principles of thermogravimetry are also illustrated in Fig. 4.175. The sample, indicated by number 3, is kept in a controlled furnace, 2, whose temperature is monitored by the thermocouple, 4, via the millivoltmeter, 5. The balance, 1, allows continuous mass determination. A plot of mass as a function of temperature, T, or time, t, represents the essential thermogravimetry result. The definitions of the temperature units [K] and time units [s] are given in Sect. 4.1 with Fig. 4.2.

In gravimetry the sample represents, according to the definition of Sect. 2.1, an open system. The mass-flow across the boundaries of the sample holder is continuously monitored by the balance. One can suggest immediately two logical extensions of thermogravimetry. In order to identify the mass flux, an analysis technique, such as mass spectrometry or exclusion chromatography can be coupled to the furnace. The other extension involves the simultaneous measurement of the heat flux by calorimetry. Instruments that couple all three techniques have been built and can fully characterize an open system. Since one should, however, always be able to precisely repeat scientific experiments, it should be possible to separately measure mass change,

## Units and Principle of Thermogravimetry

Analysis of Mass: The SI-unit is the kilogram, kg. (One gram was originally chosen to be equal to 1 cm<sup>3</sup> of H<sub>2</sub>O at the freezing point, then 1000 cm<sup>3</sup> of H<sub>2</sub>O at 277.13 K = 1 kilogram, now the mass of the Pt standard without reference to H<sub>2</sub>O volume).

Schematic for a thermogravimetric experiment:

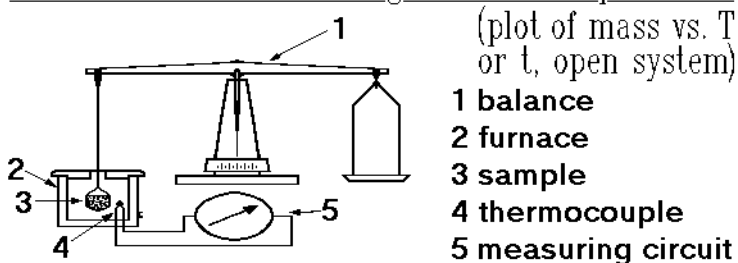


**Fig. 4.175**

composition of the evolved gases, and heat flux. Frequently the dedicated instruments that focus on one measurement are more precise and easier to handle than the combination thermal analysis.

The wood-block print reproduced in Figs. 4.176 suggests that thermogravimetry was already possible a long time ago. Mass, temperature, and time determinations are among the oldest measurements of general interest. Looking into the alchemist's

## Alchemist's Laboratory of the 15<sup>th</sup> Century



Weighing and experimentation with heating of various forms of matter stood at the beginning of quantitative science.

**Fig. 4.176**



laboratory of the fifteenth century in Fig. 4.176, one can see that respectable balances and furnaces were available already at that time. Accurate temperature determination would have been somewhat more difficult then, as was discussed in Sect. 4.1.

It took considerable time until what one might call modern thermogravimetry was developed. Early analyses by Hannay and Ramsey in 1877 may have been the first of the more modern thermogravimetry experiments. They studied the rate of loss of volatile constituents of salts and minerals during drying. Most definitive, however, was the thermobalance designed by Honda in 1915. An interesting review of thermogravimetry was published by Duval [46]. A note about nomenclature, although the ICTAC suggests the name thermogravimetry in favor of the older term thermogravimetric analysis, it permits the old abbreviation TGA since TG would lead to confusion with the abbreviation of the glass transition temperature,  $T_g$ .

#### 4.6.2 Instrumentation

The schematic of a typical thermogravimetric system is illustrated based on the classical, high-precision instrument, the Mettler Thermoanalyzer [47]. The block diagram of Fig. 4.177 gives a general overview of the instrumentation and control, and Fig. 4.178 is a sketch of a basic thermoanalyzer installation. The center table provides space for the high temperature furnace, the balance, and the basic vacuum equipment. The cabinet on the right houses the control electronics and computer. On the left is the work bench and gas-cleaning setup.

The weighing principle is shown in the upper right diagram in Fig. 4.178. At the center is the beam balance with a sapphire wedge support. The operation is based on the substitution principle. As a sample is added to the balance pan, an equivalent mass is lifted off above the pan to keep the balance in equilibrium. In this classical balance

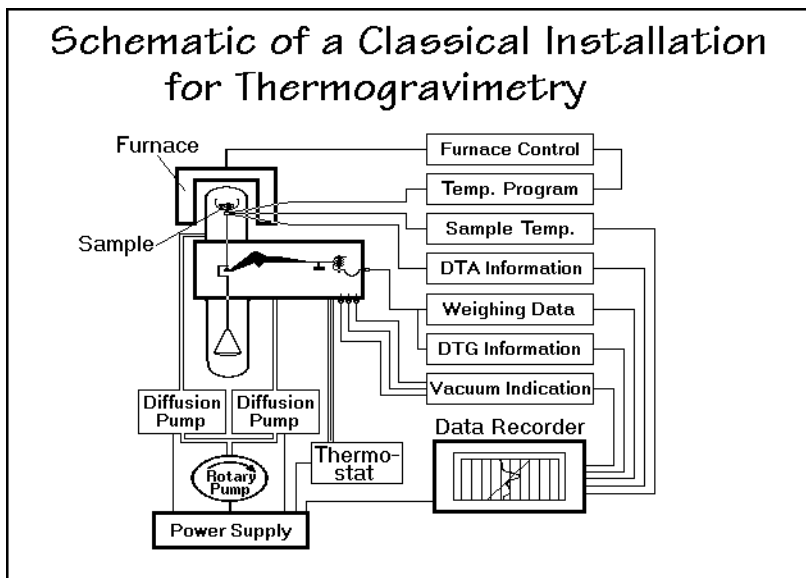


Fig. 4.177

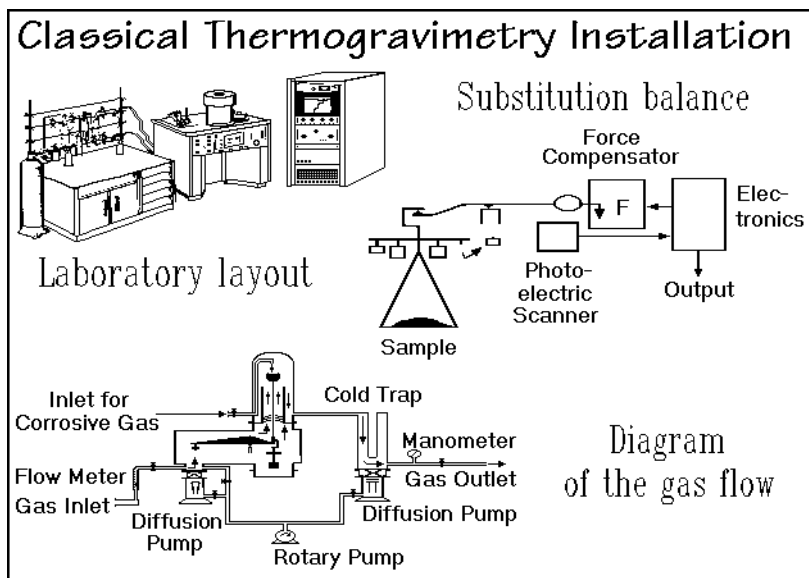


Fig. 4.178

the main weights still are moved manually, as in standard analytical balances (15.99 g). For continuous recording, there is compensation by an electromagnetic force that acts on the right balance beam. A photoelectric scanning system detects any imbalance and adds an electromagnetic force to compensate the pull of gravity. This electromagnetic force can correct imbalances between 0 and 1,000 mg, and is recorded with an accuracy of 50  $\mu\text{g}$  over the whole 16 g weighing range. Modern instruments cover more, or all of the weighing range electromagnetically.

The gas flow diagram is illustrated in the bottom diagram of Fig. 4.178. The pumping system produces a vacuum of about  $10^{-3}$  Pa ( $\approx 10^{-5}$  mm Hg). After evacuation of the balance, a chosen inert gas can be added through the left inlet. A flow rate as high as 30 L  $\text{h}^{-1}$  is possible without affecting weighing precision. Corrosive gases are entered separately through the top inlet. This second gas flow is arranged so that corrosive gases added to or developed by the sample cannot diffuse back into the balance compartment. A cold trap and a manometer are added on the right side, located at a point just before the gas outlet. At this position one can add further analysis equipment to identify the gases evolved from the sample.

Figures 4.179 and 4.180 illustrate two furnaces for TGA for different temperature ranges. The figures are self-explanatory. Several different sample holders are shown in the bottom portions of the figures. The multiple holders can be used for simultaneous thermogravimetry and DTA, the single crucibles are used for simple thermogravimetry. The major problem for the combined thermogravimetry and DTA technique is to bring the thermocouple wires out of the balance without interference with the weighing process. Even the temperature control of the sample holder may be a major problem in vacuum experiments since the thermocouple does not touch the sample. The crucibles are made of platinum or sintered aluminum oxide. Typical sample masses may vary from a few to several hundred milligrams.

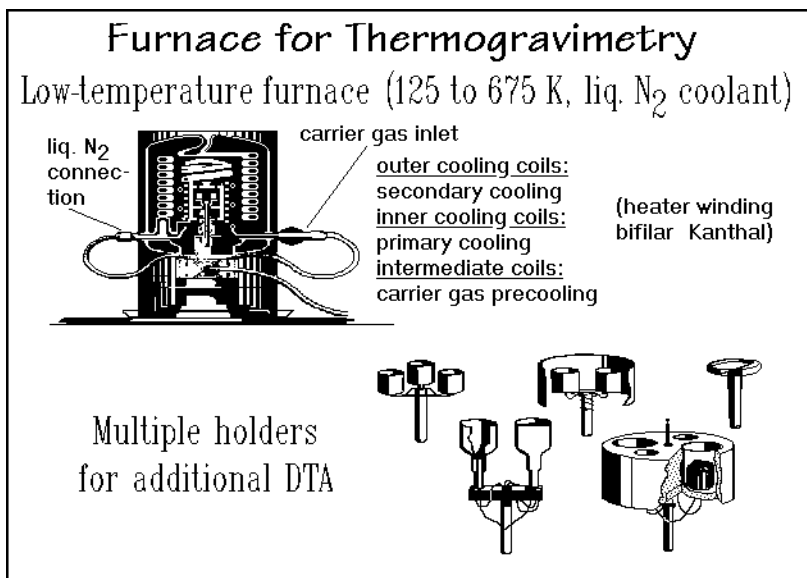


Fig. 4.179

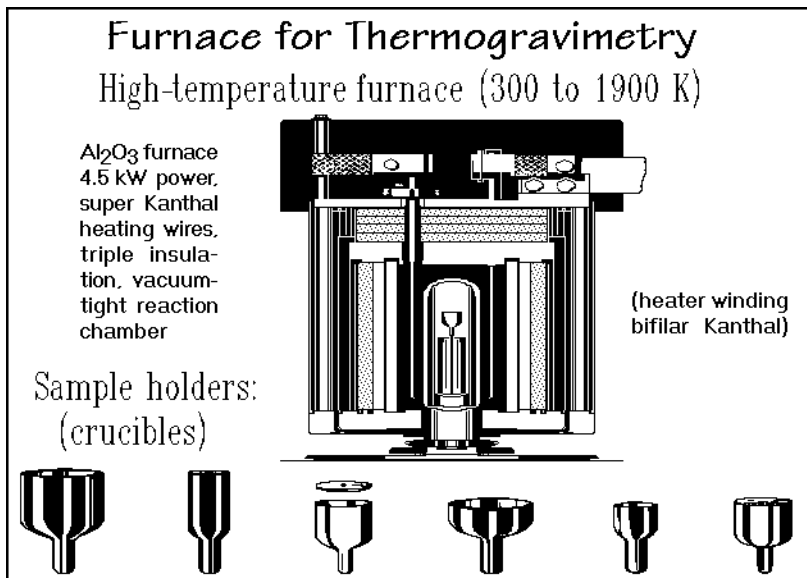


Fig. 4.180

Later developments include desktop thermogravimetry. A typical apparatus is shown in Fig. 4.181. The readability of this balance is 1  $\mu\text{g}$ . The electrical range of mass compensation is from 0 to 150 mg, and the overall capacity of the balance is 3,050 mg. The temperature range is room temperature to 1,250 K with heating rates from 0 to 100 K  $\text{min}^{-1}$ .

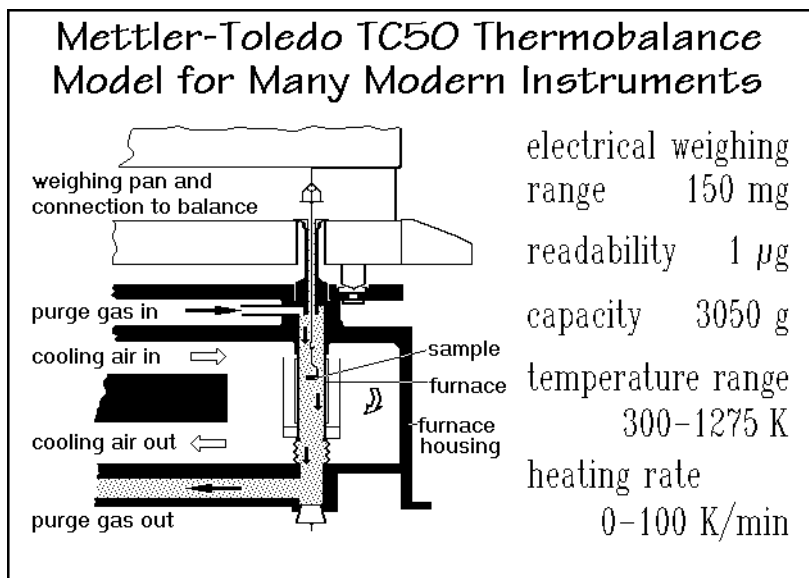


Fig. 4.181

Figure 4.182 illustrates the Seiko TG/DTA300 combined thermogravimetry and differential thermal analyzer. The mass compensation is governed completely electromagnetically by the optical deflection sensor. The change of current in the balance mechanism is used directly as the thermogravimetry signal. The DTA setup consists of an additional reference holder with detection of the temperature difference by beam-mounted sensors. The reliability of the balance is claimed to be  $\pm 100 \mu\text{g}$  at

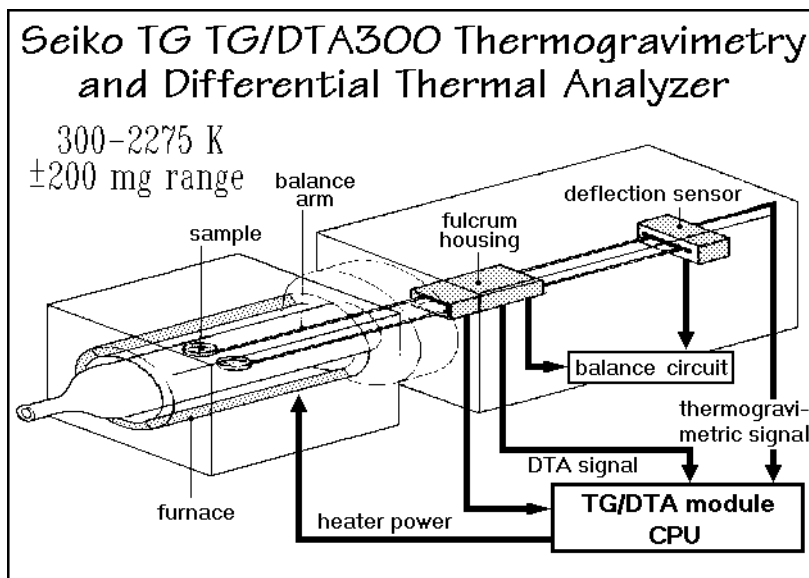


Fig. 4.182

a maximum sample mass of 200 mg. The temperature range is room temperature to 1,750 K.

Figure 4.183 reproduces the schematic of the TA Instruments 951 Thermogravimetric Analyzer, a table-top instrument first described in 1968 in connection with mass-spectrometric product analysis [48]. The balance is fully electromagnetic, with photoelectric detection of the null position. The sample, E, is suspended from a quartz beam, D, connected to the balance beam. A taut-band electric meter movement, B, balances the forces. Position F allows for a tare. The left-hand envelope is a quartz tube and fits into a horizontal, moveable furnace, outlined in the diagram. The right-hand envelope, K, is cold. The center-housing of the balance, A, is of aluminum. The O-rings, M, make the instrument vacuum-tight. Gases can be led over the sample via the connection on the left which can be connected to standard glassware. The sample temperature, finally, is measured by a floating thermocouple, J, in the vicinity of the sample. The accuracy of the balance is  $\pm 5 \mu\text{g}$  with a sample capacity of 1 g. The temperature range is from room temperature up to 1,500 K.

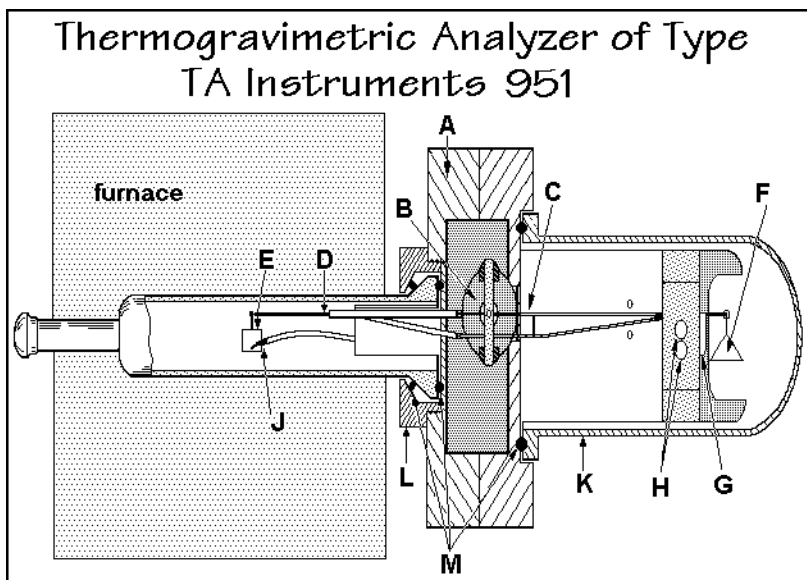
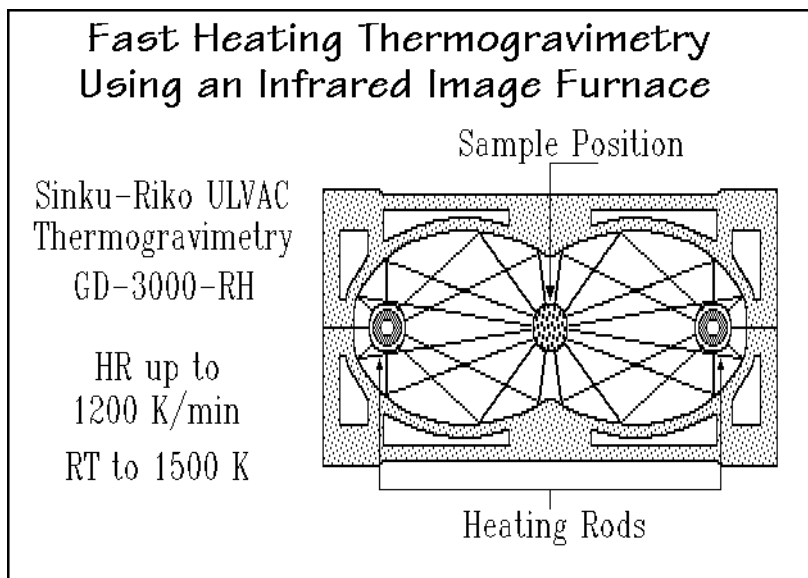


Fig. 4.183

In Figs. 4.184 an infrared image furnace by Sinku Riko is illustrated. For fast heating of the furnace one uses radiation from two 150-mm-long infrared heaters, focused by the two elliptical surfaces onto the sample. The sample is in a platinum/rhodium cell (5×5 mm), which is surrounded by a transparent, protective quartz tube. A thermocouple for temperature measurement and control touches the sample cell. The weighing system consists of a quartz-beam torsion balance that is kept at equilibrium by an electromagnetic force. Equilibrium is, as usual, detected photoelectrically. The infrared furnaces can provide heat almost instantaneously, so that heating can be done at rates as fast as  $1,200 \text{ K min}^{-1}$ . Control of temperature is achieved by regulating the current through the furnace according to the output of the

**Fig. 4.184**

sample thermocouple. With such a fast temperature rise, accurate isothermal thermogravimetry can be performed. The constancy of temperature is claimed to be  $\pm 0.5$  K. The temperature range goes up to about 1,500 K. Besides single sample cells, double cells capable of giving simultaneously DTA signals can be used in this instrument. Outside of the sample cell, little heating occurs throughout the apparatus, so that cooling from 1,000 K to room temperature is quick.

Other specialized heating methods include microwave heating, which has been suggested for uniform heating of larger samples, laser heating for in situ analysis of bulk materials, and heating with high-frequency electromagnetic fields to reach high temperatures.

The Derivatograph Q-1500 D is shown in Fig. 4.185. Its principle was first described in 1958 [49]. The two furnaces are operable from 300 to 1300 K. They permit fast sample changes without the need to wait for a furnace to cool. The balance is an analytical beam-balance with automatic weight changes and continuous weight recording through an LVDT that detects the deviation of the balance beam (see Sect. 4.1). In addition, the instrument measures the derivative of the mass change by sensing the movement of an induction coil suspended from the balance arm inside a magnet. Today derivatives are routinely available by external computation. This derivative is used for quasi-isothermal and quasi-isobaric measurements. The sample is in this case heated with a constant heating rate until a non-zero derivative in sample weight is sensed. Then, heating is switched to a very small temperature increase to record the quasi-isothermal loss of mass. After completion of the first step of the reaction, the normal heating is resumed. The quasi-isobaric environment is created by a special labyrinth above the sample holder that maintains the self-generated atmosphere during the decomposition range. With double holders, simultaneous DTA is possible as illustrated in Figs. 4.188 and 4.190

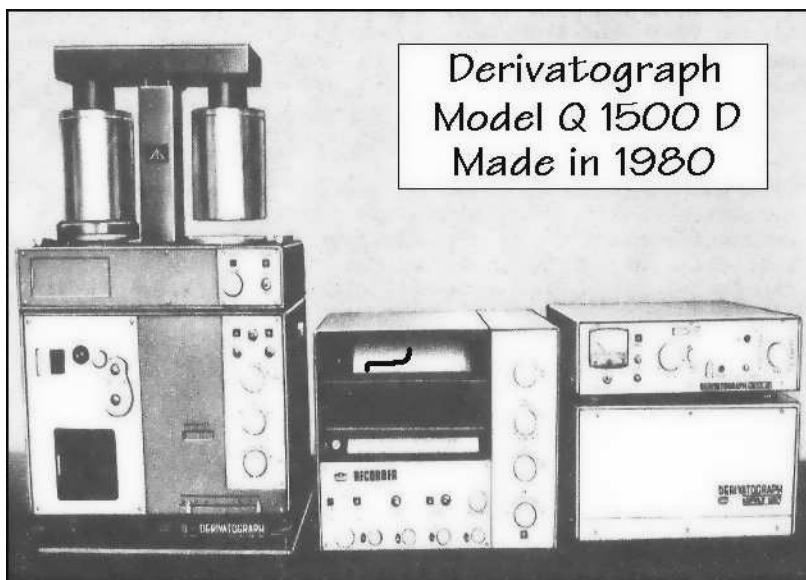


**Fig. 4.185**

A general variation of thermal analysis involves a feedback from the sample to control its heating or cooling rates, commonly known under the name sample-controlled thermal analysis [50] (SCTA, ICTAC nomenclature, 1996). The SCTA can lead to an improved resolution of overlapping processes, more homogeneous transformations, and better data for the study of the kinetics. A property that can most easily be used for SCTA is the rate of weight change in TGA, as pointed out in connection with the discussion of the Derivatograph of Fig. 4.185. Similarly, the evolved gas analysis, mentioned in Sect. 2.1.3, can be controlled by coupling the pressure and temperature signals.

Another method of SCTA in TGA is the stepwise isothermal thermogravimetry. During the first step, the heating rate is kept constant until the derivative of the mass reaches a pre-set threshold. The second step is then run at constant temperature until the continuing change of mass decreases below a second threshold. This triggers again the first step to continue the temperature program.

A third mode of SCTA applied to TGA is the HiRes™ method of TA Instruments. Its main objective is to obtain a high resolution of overlapping processes in an experiment of short duration. The method makes simultaneous use of the information on the rate of change of mass and temperature. Between transitions the heating rate is increased, within a transition it slows, allowing any desired resolution by changing the coupling between the rates of mass and temperature change.

Besides the standard weighing methods, it has also been proposed to use the piezoelectric properties of quartz for mass determination. Change in the weight of a sample that has been deposited directly on the quartz surface, causes a change in the oscillation frequency of the quartz crystal. Mass changes as small as  $10^{-12}$  g can be determined by this method. The changes in frequency with temperature must be established by calibration, or the experimentation must be done isothermally.

### 4.6.3 Standardization and Technique

Thermogravimetry needs a check of the accuracy of temperature, mass, and time measurements. Practically all thermobalances are capable of producing good data with only infrequent checks of the calibration via a standard mass. Since changes in volume of the sample take place, a buoyancy correction should be done routinely. The mass,  $m$ , of the displaced gas can easily be calculated from the ideal gas law ( $m = pM\Delta V/RT$ ).

The packing of the sample is of importance if gases are evolved during the experiment because they may seriously affect the equilibrium. Questions of gas flow and convection effects should be addressed, and, if needed, eliminated by proper baffling. Noise in a thermogravimetric curve can often be attributed to irregular convection currents.

To establish the true sample temperature is difficult since in most cases the temperature sensor is removed from the sample, in contrast to the principles of thermometry (see Sect. 4.1). In addition, sample masses are often larger than those used in a DSC, so that the sample may develop excessive internal temperature gradients (see Sect. 4.3). All these problems are aggravated because heat transfer in thermogravimetry is usually across an air or inert gas gap from the furnace, and an additional separation exists between sample and temperature sensor. Further temperature imbalances may occur during transitions. Chemical reactions, as are frequently studied by thermogravimetry, have heat effects typically 10 to 100 times greater than heat effects during phase transition.

This short summary leads to the conclusion that the mass axis, customarily drawn as the ordinate, is much better defined than the temperature abscissa. As in DSC, thus, careful calibration of temperature is necessary. For a simple calibration, one might suggest to check a standard material for its weight loss under reproducible conditions of sample mass, packing, heating rate, sample holder configuration, and atmosphere type, flow, and pressure. Efforts to establish international standards, however, were abandoned when it was found that it was not possible to fix all these instrumental and experimental variables satisfactorily. One has to develop one's own standards of weight loss under carefully controlled conditions to check the reproducibility of the equipment. The thermogravimetry of calcium oxalate, described in Figs. 4.194–196, below, may give a standard trace.

The most successful temperature calibration is obtained by the analysis of a ferromagnetic material. A pellet of the reference sample is placed within the field of a magnet so that the resulting magnetic force adds to or subtracts from the gravity effect on the thermobalance. At the Curie temperature of the standard, the magnetic force vanishes, and an equivalent mass increase or decrease is registered by the instrument. The thermogravimetry curve at the top of Fig. 4.186 shows such an experiment with increasing and decreasing temperature,  $T$ . As in other thermal analysis curves, various characteristic temperatures,  $T_1$ ,  $T_2$ , and  $T_3$ , can be chosen and compared between laboratories. Certified reference materials for thermogravimetry are available from the National Institute for Standards and Technology. A typical calibration curve is shown at the bottom in Fig. 4.186. The three characteristic calibration points are marked on the mass trace and on the temperature curve for



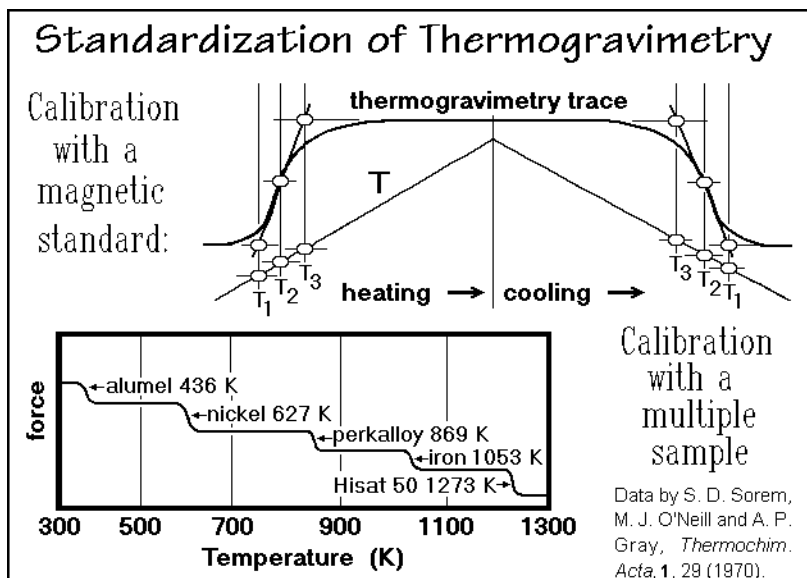


Fig. 4.186

heating and cooling experiments. As with the reporting of data for DSC, thermogravimetry is much in need of standard practices. The ICTAC recommendations are listed together with the recommendations for the differential thermal analysis in Appendix 9. One should read these recommendations every time before one writes a research report.

Time-calibration, as discussed in Sect. 4.1, poses little problems. Any good watch or stop watch, as well as the internal clocks of computers, are usually adequate for the relatively slow heating rates used in thermogravimetry. For standard of time, see Fig. 4.3.

#### 4.6.4 Decomposition

An analysis of black praseodymium dioxide,  $\text{PrO}_2$ , in a variety of atmospheres is shown in Fig. 4.187 as an example of decomposition reactions. The measurements were carried out with a Mettler Thermoanalyzer as described in Figs. 4.178–180 with a gas-flow rate of  $10 \text{ L h}^{-1}$ . The TGA-curves are recalculated in terms of the chemical composition. The left two curves show the large shifts of the temperatures of oxygen loss in the presence of reducing atmospheres ( $\text{H}_2$  and  $\text{CO}$ ). The reaction goes to the yellow  $\text{Pr}_2\text{O}_3$  almost without formation of intermediates. In a vacuum,  $\text{PrO}_2$  is much more stable and several intermediates can be identified. The compounds are listed on the right-hand side of the graph. The  $\text{Pr}_7\text{O}_{12}$ , with 1.714 oxygen atoms per praseodymium atom is particularly stable. Note also the little maximum at the beginning of the decomposition trace in a vacuum. It is caused by the recoil of the leaving oxygen. The stability of  $\text{Pr}_7\text{O}_{12}$  is increased in oxygen, nitrogen, or air. The oxygen effect is expected, since it will directly influence the chemical equilibrium. The influence of  $\text{N}_2$ , which is not a reaction partner, is caused by the reduction of the rate of diffusion

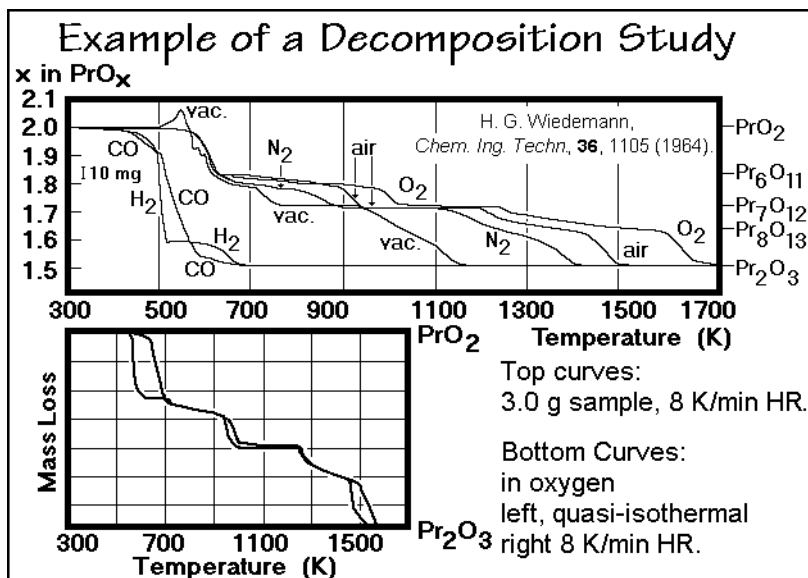


Fig. 4.187

out of the sample of the oxygen that is generated in the reaction. This self-generated oxygen atmosphere retards the decomposition. The decomposition temperature is, thus, dependent on pressure, sample packing, and sample geometry, making the TGA qualitative (quantitative in mass determination only, not in time and temperature).

The PrO<sub>2</sub> analysis can also serve as an example of the influence of heating rates. The bottom graph in Fig. 4.187 is a comparison of the PrO<sub>2</sub> decomposition in O<sub>2</sub> at constant heating rate to quasi-isothermal runs. The left-hand curve was obtained by stopping the heating as soon as a mass loss was detected until one practically reached equilibrium. The changes in decomposition temperatures are substantial, as much as 50–100 K.

A number of decompositions of polymers are also described in Sect. 3.4 (Fig. 3.49). It is possible not only to use thermogravimetry to measure the thermal stability and life-time (see Sect. 4.6.6), but also to identify polymers by their degradation parameters such as temperature, degradation products, char residue, evolved gases, differences in reaction with O<sub>2</sub> and other gases, etc.

#### 4.6.5 Coupled Thermogravimetry and Differential Thermal Analysis

The next examples illustrate the greater detail that can be obtained when thermogravimetry and DTA are combined. The experiments can be carried out either simultaneously or successively. Figures 4.188–191 are copies of pages from the Atlas of Thermoanalytical Curves. The measurements were made with the Derivatograph depicted in Fig. 4.185 and carried out at different heating rates and with varying masses. The derivative of the sample mass,  $dm/dt$  is also shown in the graphs and labeled DTGA. If DTGA and DTA identify both the same transition or reaction, the plots of  $dm/dt$  and  $\Delta T$  versus  $T$  are similar.

Figure 4.188 shows curves for salicylic acid, a small organic molecule. The DTA curve is reproduced at the top of the figure, followed by the differential thermogravimetric data. The TGA-curve is given in Fig. 4.189. Two widely different masses are analyzed at different heating rates. Both samples are run in air in open platinum crucibles. Peak 1 of the DTA has no counterpart in TGA, it refers to the melting of

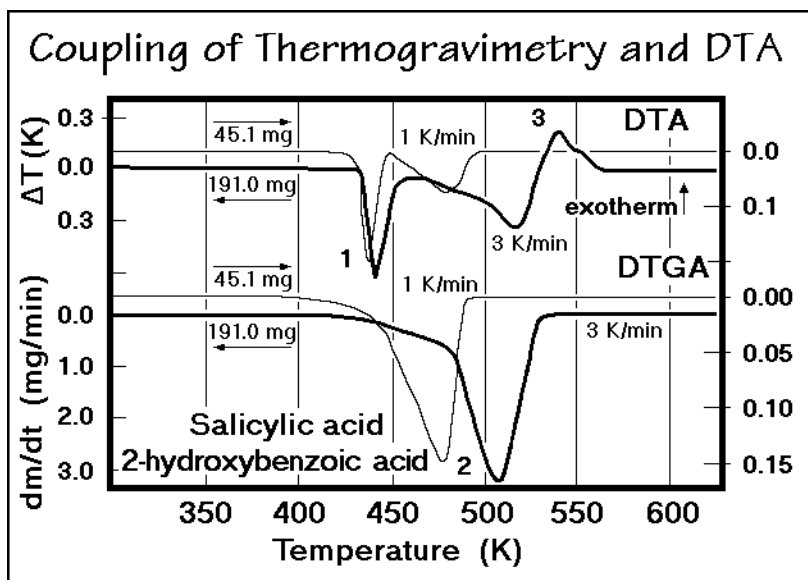


Fig. 4.188

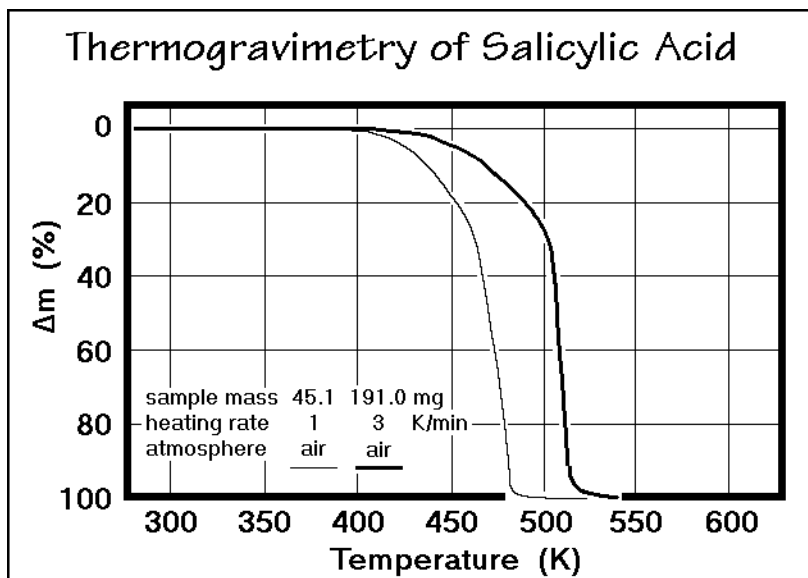


Fig. 4.189

the salicylic acid. Melting is followed by slow evaporation. In fact, it can be seen from the sensitive DTGA trace that before the crystals melt, some of the mass has already been lost by sublimation. After the evaporation endotherm, the exotherm 3 is visible. It indicates the oxidation of the remaining salicylic acid. The smaller sample mass, measured at a somewhat slower heating rate, was fully evaporated before the oxidation started, as can be seen from the missing DTA peak 3 in the thin-line curve. This example shows the higher power of interpretation that is possible if DTA and TGA are available simultaneously. Full information would require chemical analysis of the gases evolved from the sample and an attempt at the elucidation of the kinetics.

Figures 4.190 and 4.191 show the analysis of the hexahydrate of praseodymium nitrate. The DTA and DTGA curves are complicated. From TGA, one can see the stages of the reaction. The first step, 1, is the melting endotherm, showing only in the DTA trace. Then water is lost, giving even larger endotherms and the corresponding steps in the TGA. The praseodymium nitrate is stable up to about 675 K, where it undergoes an endothermic reaction to praseodymium oxynitrate, losing  $\text{N}_2\text{O}_5$ . The reaction is given by the peaks labeled 4. The last step shown is 5, the change to the oxide, listed as  $\text{Pr}_6\text{O}_{11}$ . From Fig. 4.187 it can be deduced, however, that  $\text{Pr}_6\text{O}_{11}$  is not stable in air beyond 725 K. It slowly goes to  $\text{Pr}_7\text{O}_{12}$ , reached at about 975 K. Checking the mass loss, one finds that  $\text{Pr}_6\text{O}_{11}$  should occur at a 60.8% mass loss, while  $\text{Pr}_7\text{O}_{12}$  shows a slightly larger loss of 61.4%.

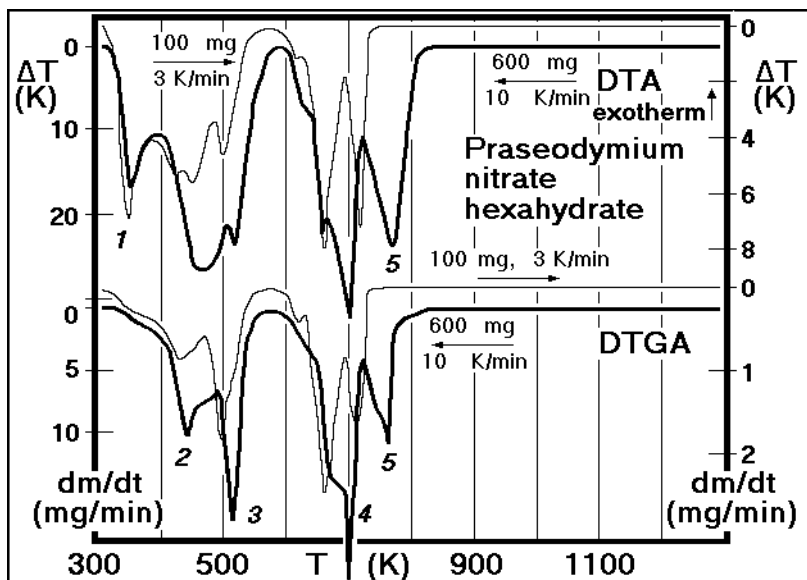


Fig. 4.190

Figures 4.192 and 4.193 represent a series of curves obtained with a Mettler Thermoanalyzer similar to the one shown in Fig. 4.181. Each graph represents two TGA traces, TG1 and TG2, of low and high sensitivity, and a DTA curve. The top of Fig. 4.192 is of a kaolinite from South Carolina. Between 700 and 1000 K, water is

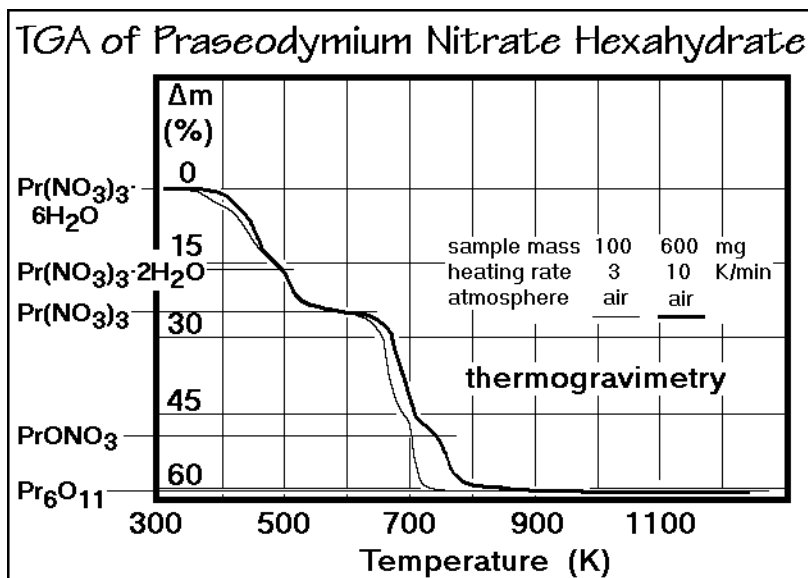


Fig. 4.191

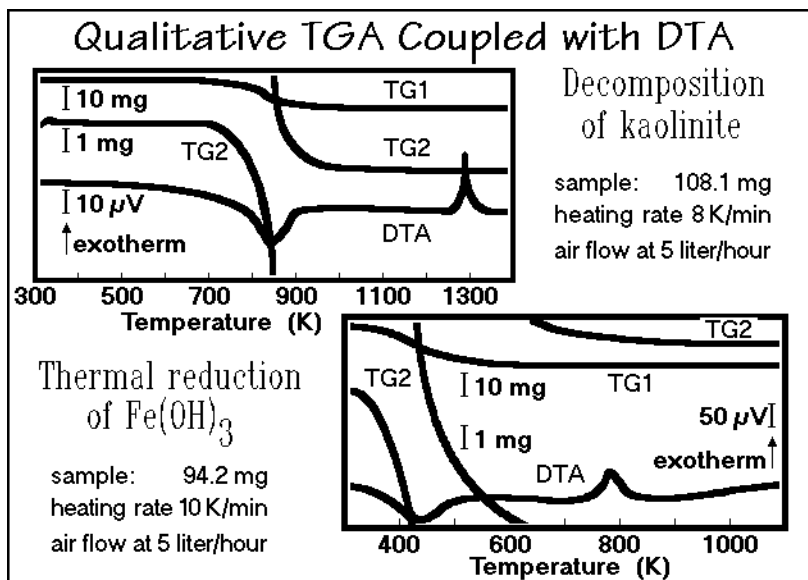


Fig. 4.192

released, to give a mixture of aluminum oxide and silicon dioxide. At about 1275 K, mullite, which has a formula composition of  $3 \text{Al}_2\text{O}_3$  and  $2 \text{SiO}_2$ , crystallizes. The excess of  $\text{SiO}_2$  remains as cristoballite. The mullite is the characteristic material in porcelain ware. Since during this crystallization, there is no mass lost, it could not have been studied by thermogravimetry alone.

The bottom of Fig. 4.192 provides information on iron(III) hydroxide, an amorphous, brown, gel-like substance. Loss of water takes place over the whole temperature range up to 1,075 K. No distinct intermediate hydrates occur until hematite,  $\text{Fe}_2\text{O}_3$ , is obtained. The crystallization exotherm of the hematite is visible in the DTA curve at about 775 K.

Figure 4.193 illustrates in its top graph the fast, explosive decomposition of ammonium picrate. At 475 K the fast, exothermic reaction takes place. The study of explosives by thermogravimetry and DTA is possible because of the small sample masses that can be used. An important branch of thermal analysis is thus the study of chemical stability of compounds that are used industrially.

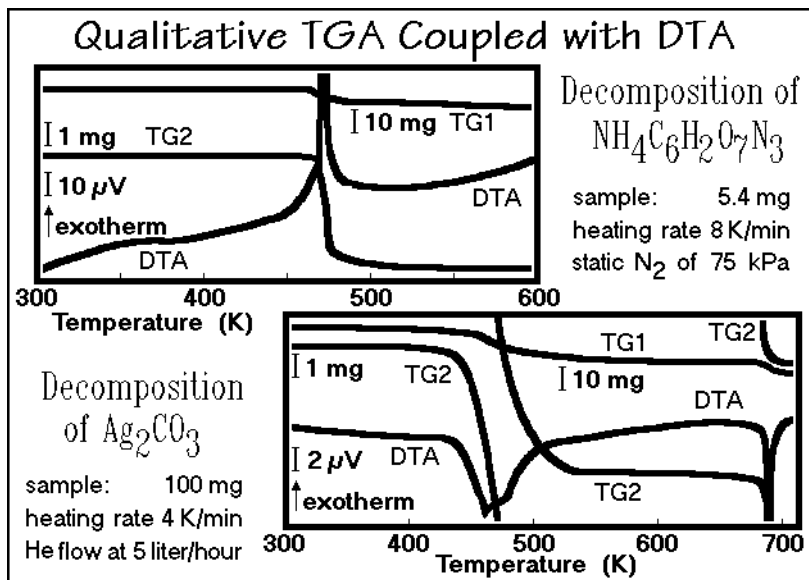


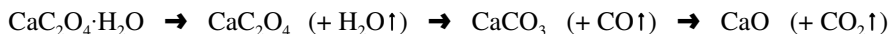
Fig. 4.193

The bottom example in Fig. 4.193 represents the thermal decomposition of a silver carbonate,  $\text{Ag}_2\text{CO}_3$ , in helium. At about 400–550 K, the carbonate loses carbon dioxide and changes into the oxide  $\text{Ag}_2\text{O}$ . A second, smaller loss of mass begins at a temperature of 675 K. Both mass losses are accompanied by an endotherm in the DTA trace, meaning that the reactions are entropy driven. The final decomposition product is metallic silver.

#### 4.6.6 Applications of Thermogravimetry

Three detailed applications of thermogravimetry are described with more quantitative interpretations, i.e., efforts are made to develop information on the kinetics and equilibrium. The calcium oxalate/carbonate decomposition is treated first. The lithium hydrogen phosphate polymerization has been discussed above as a step-reaction in Sect. 3.1 (Figs. 3.16–22). Finally, the method and some examples of life-time determinations based on TGA are shown at the end of this section.

*Calcium oxalate/carbonate decomposition* follows the chemical reactions:



These reactions have been frequently analyzed and also often used as a calibration standard. The TGA curves are taken with the infrared image furnace shown in Fig. 4.184. A general kinetics equation can be written as:

$$dp/dt = k(T) f(p) g(T,p)$$

The progress of the reaction,  $dp/dt$ , at a given time is expressed as a product of three terms: 1) A rate constant,  $k(T)$ , which is dependent only on temperature and can be expressed by the Arrhenius equation shown in Fig. A.7.2. 2) A function  $f(p)$ , which should contain all concentration dependence. 3) A function  $g(T,p)$ , which sums all other factors that influence the indicated reaction rate such as changes in buoyancy, turbulence, heating rate, momentum transfer on evaporation in vacuum experiments, or changes in physical structure of the sample, such as breakage of grains, crust formation, changes in rates of diffusion of gases, etc. Naturally, one usually assumes as first approximation that  $g(T,p)$  may be 1.0. The present example illustrates the more common case that the first two factors alone do not represent the kinetic data.

The curves of Fig. 4.194 were taken on 14 mg of the monohydrate at a nitrogen flow rate of  $90 \text{ cm}^3 \text{ min}^{-1}$  with a quite fast heating rate. The first step is assigned to the water loss, the second, to the conversion of the oxalate to carbonate, the last step is the loss of  $\text{CO}_2$  in the reaction that forms calcium oxide. From the DTA trace the first and last reactions seem to be simple, endothermic reactions. The DTA trace of the loss of CO indicates an initial exothermic reaction onto which an endothermic

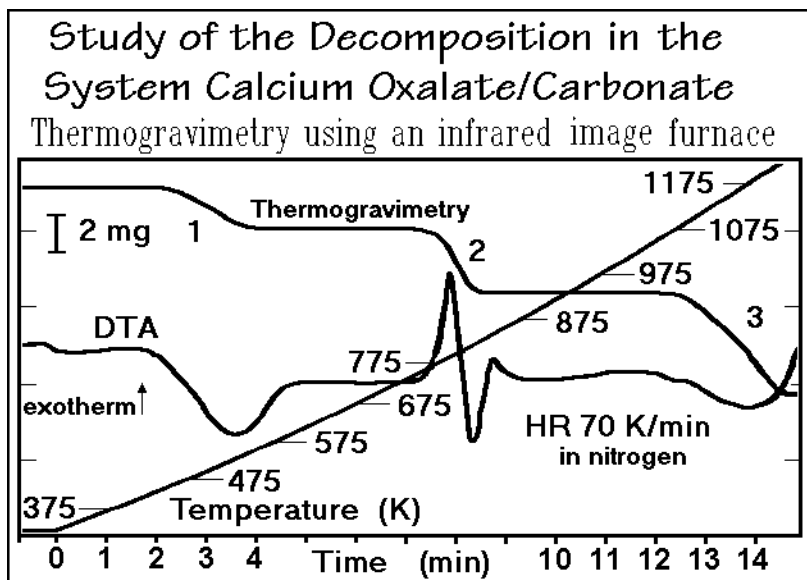


Fig. 4.194

reaction is superimposed. The recorded mass-changes agree well with the assumed overall reaction. The temperatures for the change from one plateau to the other are, however, variable.

For the analysis of the data of the first step of the reaction with a nonisothermal kinetics one can make use of the Freeman-Carroll method described in Sect. 3.6.6 with Fig. 3.87. In such an attempt, one finds for different heating rates, different activation energies and an order of about one for the reaction, which does not fit the assumed kinetics. The plot of the data is shown in Fig. 4.195, together with the results of the Freeman-Carroll analysis. Comparing the heating-rate-dependent data with isothermal data on the same thermogravimetric balance, one finds different values for both,  $n$  and the activation energy. This is a clear indication that the assumptions of the analysis using the Freeman-Carroll plot are not satisfied.

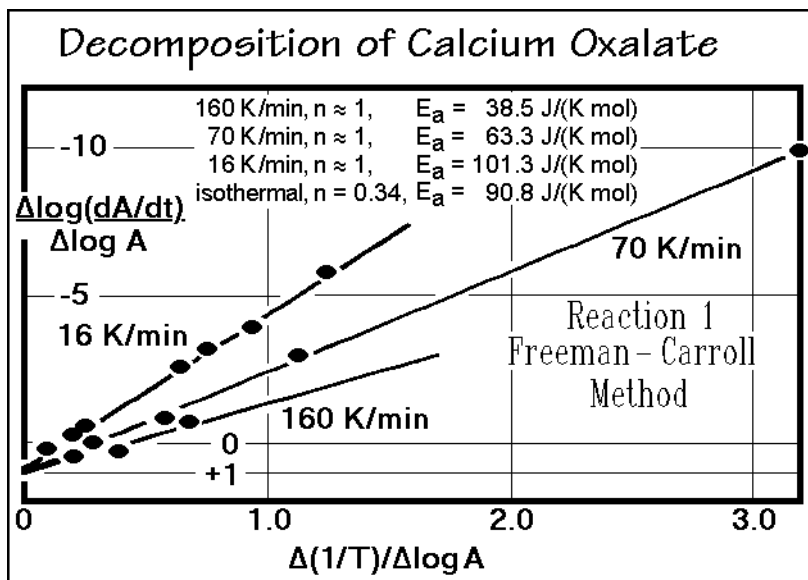


Fig. 4.195

It is even more difficult to analyze the second step, where the DTA in Fig. 4.194 already shows a two-stage reaction. In the literature, one may find suggestions that the reaction is purely exothermic, as well as suggestions that the reaction is purely endothermic. Thus, even in often-analyzed systems, surprises are still possible.

The carbonate decomposition, step 3, has been studied separately. Well-defined  $\text{CaCO}_3$  crystals were analyzed by electron microscopy, surface area measurement, and particle counts. The TGA data of Fig. 4.196 show qualitatively the effects of sample mass and heating rate. Three of five sets of data were analyzed with the Freeman-Carroll method. Again, there were large changes in the kinetic parameters with sample mass and heating rate, indicating that such analysis is not permissible. To get more information on the kinetics, isothermal runs were made using a Cahn balance with a controlled furnace and otherwise similar reaction conditions. Isothermal data were collected between 1 and 32 mg and temperatures between 600 and 700 K. Using



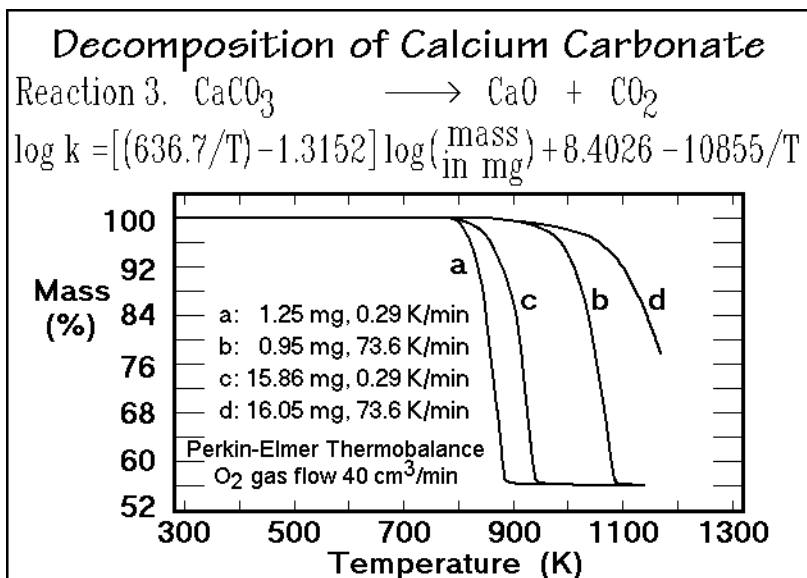


Fig. 4.196

18 different functions to represent the data, it was found that the equation in Fig. 4.196 gives the best fit. This equation can be justified if one assumes that the mass loss is governed by the contracting geometry of the particles.

**Lifetime prediction** is an applied technique, which is frequently needed in industry to find out the probable performance of a new material. The philosophy of lifetime prediction is to identify the critical reaction which limits the life of a material, then to measure its kinetics quantitatively at high temperature where the reaction is fast. Finally, using proper kinetic expressions, one extrapolates the kinetics to the much longer reaction times expected at the lower temperatures at which the sample will be in service. Naturally, the reverse process, extrapolating the kinetics to higher temperatures, could also be carried out to find shorter lifetimes—as for example, for ablation processes.

In the present discussion it is tacitly assumed that the thermal analysis technique identifies the proper life-determining reaction and that the detailed chemistry and physics of the various failure mechanisms are as assumed. The example materials chosen for the discussion of lifetime determination are linear macromolecules. The example technique is mass loss, despite the fact that the useful life of a material may have ended long before a loss of mass is detected. If, for example, the material fails due to embrittlement caused by cross-linking, there would be no mass loss; only the determination of the glass transition by DSC or DMA at different times could help in such case.

There are two common methods of kinetic analysis based on the kinetics equations derived in Sects. 3.1 and 3.2. The first method is the steady-state parameter-jump method. As illustrated in Fig. 4.197, the rate of loss of mass is recorded while jumping between two temperatures,  $T_1$  and  $T_2$ . At each jump time,  $t_j$ , the rate of loss of mass is extrapolated from each direction to  $t_j$ , so that one obtains two rates at

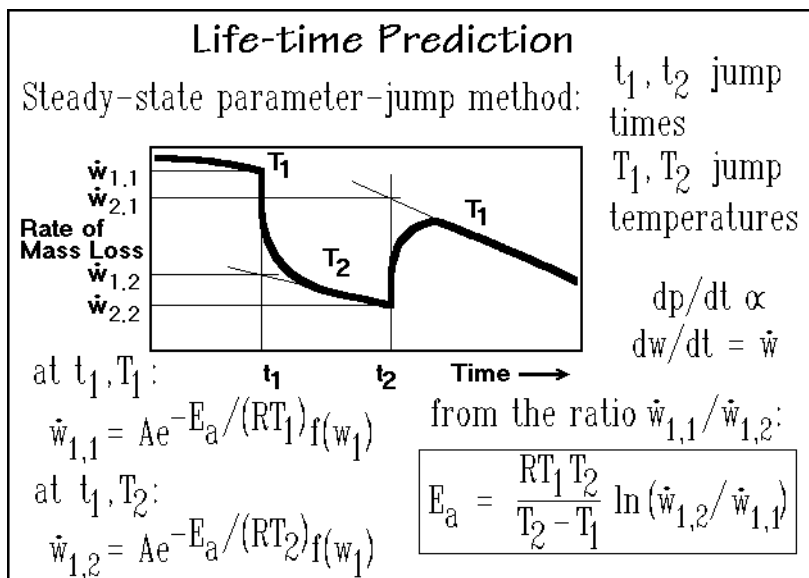


Fig. 4.197

different temperatures at the same reaction time. Other reaction-forcing variables, such as atmospheric pressure, could similarly be used for the jump. Figure 4.197 gives an easy experimental value for the activation energy,  $E_a$ . If  $E_a$  should vary with the extent of reaction, this would indicate the presence of other factors in the rate expression [see factor  $g(T,p)$ , discussed above]. Figure 4.198 lists as example 1 results on the lifetime of polystyrene by this steady-state parameter jump method.

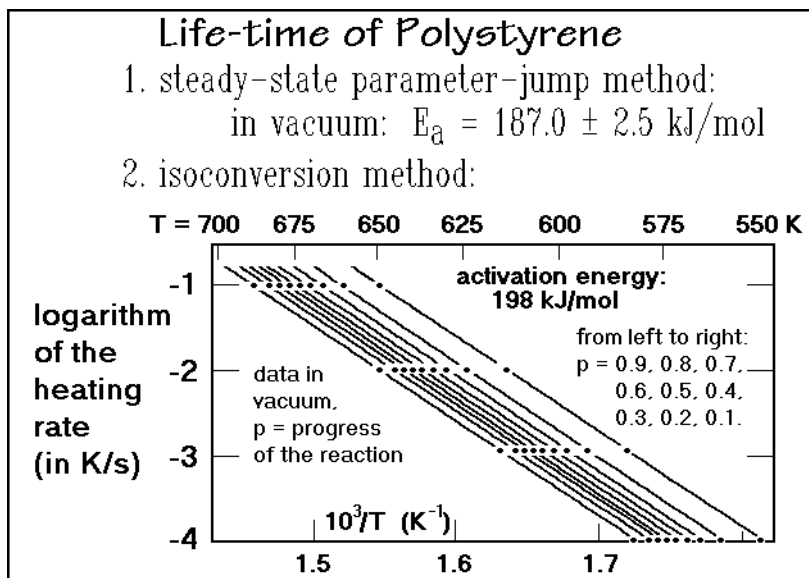


Fig. 4.198

The second method makes use of data on mass loss, collected in a series of different constant-heating-rate experiments as outlined in Fig. 4.198 for polystyrene. Isoconversion occurs at different temperatures for different heating rates. As one reaches the point of isoconversion, the integrated, mass-dependent functions  $f(p)$  must be identical. Thus, one has again achieved information about  $k(T)$  at different temperatures. Naturally this analysis is only valid if the kinetics has not changed over the range of temperature and conversion.

The Arrhenius equation of Appendix 7 (Fig. A.7.2) can be inserted in the general rate expression from above with  $g(T,p) = 1$  for the present application, and then integrated.

$$dp/dt = A e^{-E_a/(RT)} f(p)$$

The constant heating rate  $q$  is  $dT/dt$  and can be used to change time into temperature and obtain:

$$dp/f(p) = (A/q) e^{-E_a/(RT)} dT$$

Integrating to constant conversion  $p$  gives, for the left-hand side, a constant value, while the right-hand side is somewhat more difficult. Either, one carries out numerical integrations, or it may be sufficient to notice that the logarithm of the integral portion in the center can be approximated as a linear function of  $1/T$  so that one arrives at the final equation:

$$\log q_2 - \log q_1 \approx -0.4567(E_a/R)[(1/T_2) - (1/T_1)]$$

The prediction of the lifetime of polystyrene in Figs. 4.198 seems to give similar activation energies for both, the parameter-jump method and the isoconversion method. It is of interest to judge how precise this lifetime prediction is. The error introduced by two standard deviations, to reach a 95% confidence level, gives for the steady-state parameter-jump method an estimate ranging from  $2.7 \times 10^8$  to  $1.3 \times 10^9$  years at 300 K, an error of about 80%. One can see from this estimate that relatively small errors in activation energy can produce large errors in the lifetime.

Polystyrene is, however, a relatively ideal case. In Fig. 4.199, data on the isoconversion of decomposition of a segmented polyurethane are reproduced. Only the first 10% of decomposition in vacuum give parallel lines with activation energies between 145 and 170 kJ mol<sup>-1</sup>. Perhaps it may still be possible to describe this early decomposition as a single process. At higher conversion, the kinetics is much more complex and no interpretation is possible with thermogravimetry alone.

**Summary of Chapter 4.** At the end of this discussion of thermal analysis tools it may be worthwhile to attempt a brief summary. The basic theory of thermal analysis is well represented by macroscopic equilibrium and nonequilibrium thermodynamics, and the connection to the microscopic description is given by statistical thermodynamics and kinetics. All of these theories are highly developed, but they have not been applied to their fullest in the description of materials. The reason for this failure to

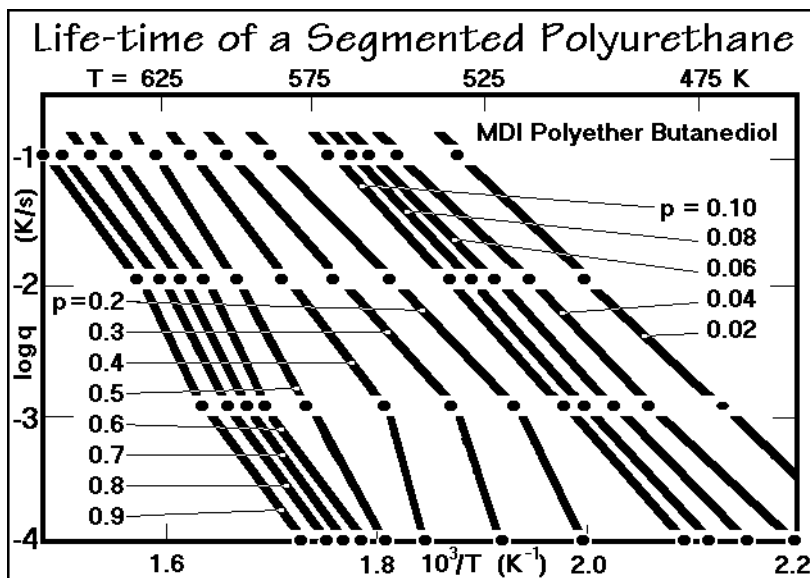


Fig. 4.199

develop thermal analysis into a well-rounded field of scientific enquiry is not necessarily a lack of precision in measurement, but rather the fact that these theories were developed before many of the present-day measuring tools were available. Traditional courses in physical chemistry and engineering often do not contain the material needed to understand the application of thermal analysis, but do treat topics that unnecessarily complicate the subject. In turn, many thermal analyses are carried out at less than optimum precision, since the operators are often unaware of the added information that could be obtained and used for interpretation. On the other hand, as shown in the discussion of thermogravimetry, data can also easily be over-interpreted because of a lack of detailed understanding of the microscopic processes. Finally, it should be remarked that the field of thermal analysis goes far beyond the basic techniques described here and is constantly growing. Almost any measurement which can be done at different temperatures can be expanded into thermal analysis, and any series of thermal analysis techniques can be combined for valuable multiple-parameter measurements. With the understanding of the basic techniques presented here, one should be able to expand one's knowledge to the practically unlimited opportunities of thermal analysis.

## References

### **General References**

**Sect. 4.1.** Much information on temperature can be found in the proceedings of Symposia on Temperature, sponsored by the American Institute of Physics, the Instrument Society of America, and the National Institute for Standards and Technology. Also, see the treatise: by various eds *Temperature: Its Measurement and Control in Science and Industry*. Vol 1, 1944; Vol 2, 1955; Vol 3, 1962; Reinhold, New York. Vol 4, 1972–73, Inst Soc America, Pittsburgh; Vol 5, 1982; Vol 6, 1992, Am Inst Physics, New York.

General references on temperature measurement are: Schooley JF (1987) *Thermometry*. CRC Press, Boca Raton, FL; Quinn TJ (1983) *Temperature*. Academic Press, New York; Sturtevant J M (1971) *Temperature Measurement*. In Weissberger A, Rossiter BW, *Physical Methods of Chemistry*. Wiley-Interscience, New York, Vol I, Part V, Chap I.

For a general introduction into metrology see, for example: Klein AH (1974) *The World of Measurement*. Simon and Schuster, New York.

Thomson GW, Douslin DR (1971) *Determination of Pressure and Volume*. In Weissberger A, Rossiter BW, *Physical Methods of Chemistry*. Wiley-Interscience, New York, Vol I, Part V, Chap II.

A Series of biannual reviews in the journal *Anal Chem* covers all thermal analysis: Wendlandt WW (1982) 54: 97R; (1984) 56: 250R. (1986) 58: 1R; Dollimore D, 60: 274R; (1990) 62: 44R; (1992) 64: 147R; (1994) 66: 17R; (1996) 68: 63R; Dollimore D, Lerdkananaporn S, (1998) 70: 27R; Dollimore D, Phang P (2000) 72: 27R; Vyazovkin S (2002) 74: 2749; (2004) 76: 3299.

**Sect. 4.2.** Basic textbooks for this section are: Wunderlich B (1990) *Thermal Analysis*. Academic Press, Boston; Hemminger W Höhne G (1984) *Calorimetry*. Verlag Chemie, Weinheim, Germany.

Some classical texts on calorimetry are: White WP (1928) *The Modern Calorimeter*. Chem Catalog Co, New York. Swietoslawski W (1946) *Microcalorimetry*. Reinhold Publ, New York. Sturtevant JM (1971) *Calorimetry*. In: Weissberger A Rossiter BW, eds, *Techniques of Chemistry* Vol I, Part V. Wiley-Interscience, New York.

Tables of calorimetric data are found in: **a.** Landolt–Boernstein (1956–71) *Zahlenwerte und Funktionen*. Springer, Berlin, 6<sup>th</sup> ed, Vol II, Parts 1–5; continued as Hellwege KH, ed. New Series Group IV: Macroscopic and Technical Properties of Matter. **b.** Am Pet Inst Research Proj 44 Selected Values of Properties of Hydrocarbon and Related Compounds. Thermodynamics Res Center, Texas A&M University, College Station, TX. **c.** Touloukian YS, Ho CY, eds (1970–1979) *Thermophysical Properties of Matter*, The TPRC Data Series. Vols 4–6, Specific Heat. IFI/Plenum, New York, NY. **d.** NBS Technical Notes 270–3 to 270–7 (1968–1973) *Selected Values of Chemical Thermodynamic Properties*. Institute for Basic Standards, National Bureau of Standards, Washington, DC. **e.** Karapet'yants MKh, Karapet'yants ML (1970) *Thermodynamic Constants of Inorganic and Organic Compounds*. Humphrey Sci Publ, Ann Arbor. Translated by Schmork J. **f.** Lide DR (annual editions) *CRC Handbook of Chemistry and Physics*. CRC Press, Boca Raton, FL.

**Sect. 4.3.** The main reference for DSC of Materials is the two-volumes compendium: Turi E (1997) *Thermal Characterization of Polymeric Materials*. Academic Press, San Diego.

Books documenting the history and principles of DTA and DSC are: Smothers WJ, Chiang Y (1966) *Handbook of Differential Thermal Analysis*. Chem Publ, New York; Mackenzie RC (1970,1972) *Differential Thermal Analysis*, Vols 1 and 2. Interscience Publ, New York; Wunderlich B (1971) *Differential Thermal Analysis*. In Weissberger A, Rossiter BW, *Physical Methods of Chemistry*, Vol 1, Part V, Chap 8. Wiley, New York; Wendlandt WW (1986) *Thermal Analysis*, 3<sup>rd</sup> edition. Wiley-Interscience, New York.

The earliest DTA-related research papers are: LeChatelier H (1887) *Z Phys Chem* 1: 396; Roberts-Austen WC (1899) *Metallographist* 2: 186; Kurnakov NS (1904) *Z anorg Chem* 42: 184; Saladin E (1904) *Iron and Steel Metallurgy Metallography* 7: 237; see also: LeChatelier H (1904) *Rev Met* 1: 134.

A number of Reference DTA and TGA curves can be found in: Liptay G (1971–76) *Atlas of Thermoanalytical Curves*, Vols 1–5. Heyden, London; Sadtler (1965) *DTA Reference Thermograms*, Vols 1–7. Sadtler, Philadelphia, PA.

Newer books on DSC are: Wunderlich B (1990) *Thermal Analysis*. Academic Press, Boston; Höhne G, Hemminger W, Flammersheim HJ (2003) *Differential Scanning Calorimetry*, 2<sup>nd</sup> edn. Springer, Berlin; Brown ME, Gallagher PK, Cheng SZD, eds (1998, 2002) *Handbook of Thermal Analysis and Calorimetry*. Vol 1, Principles and Practice, Vol 3, Applications to Polymers and Plastics. Elsevier Science, Amsterdam.

For information about the identification of the glass transition see: Seyler RJ, ed (1994) *Assignment of the Glass Transition*. Am Soc Testing and Materials, Philadelphia; the analysis of polymer melting is discussed in Wunderlich B (1980) *Macromolecular Physics*, Vol 3, *Crystal Melting*. Academic Press, New York.

**Sect. 4.4.** A general review of TMDSC is found in: Reading M, ed (2004/5) *Basic Theory and Practice for Modulated Temperature Differential Scanning Calorimetry*. Kluwer, Dordrecht. The Proceedings of the last five Lahnwitz Seminars in 1996, 1998, 2000, 2002, and 2004, focusing on TMDSC, discussed authoritatively: (1997) *Temperature-modulated Calorimetry*. *Thermochim Acta* Vol 304/305; (1999) *Investigation of Phase Transitions by Temperature-modulated Calorimetry*. *Ibid* Vol 330; (2001) *Frequency and Time Dependent Heat Capacity*. *Ibid* Vol 377; (2003) *Thermodynamics and Calorimetry of Small Systems*. *Ibid* Vol 403; (2005) *Thermodynamics and Calorimetry of Thin Films*. *Ibid*, to be published. For early publications see: Reading M, Hahn BK, Crowe BS (1993) *Method and Apparatus for Modulated Differential Analysis*. US Patent 5,224,775, July 6. Reading M, Elliot D, Hill VL (1993) *J Thermal Anal* 40: 949; Wunderlich B, Jin Y, Boller A (1994) *Thermochim Acta* 238: 277; Boller A, Jin Y, Wunderlich B (1994) *J Thermal Anal* 42: 307.

**Sect. 4.5.** Wendland WW (1986) *Thermal Analysis*, 3<sup>rd</sup> ed. Wiley, New York; Gallagher PG (1997) Chap 1 in Turi E, ed. *Thermal Characterization of Polymeric Materials*. Academic Press, San Diego; Barth HG, Mays JW (1991) *Modern Methods of Polymer Characterization*. Wiley-Interscience, New York.

For the measurement of length, pressure, and volume, see: Thomson GW, Douslin DR, (1971) *Determination of Pressure and Volume*. In Weissberger A, Rossiter BW, eds. *Physical Methods of Chemistry*, Vol 1, Part V. Wiley-Interscience, New York. See also Riga AT, Neag CM, eds (1991) *Materials Characterization by Thermomechanical Analysis*. ASTM STP 1136, American Society for Testing and Materials, Philadelphia, 1991.

For further study of DMA see, for example: Ferry JD (1980) *Viscoelastic Properties in Polymers*, 3<sup>rd</sup> edition. J. Wiley, New York; Ward IM (1983) *Mechanical Properties of Solid Polymers*, 2<sup>nd</sup> edn. Wiley, New York; Meier DJ (1978) *Molecular Basis of Transitions and Relaxations*. Gordon and Breach, New York; McCrum NG, Read BE, Williams G (1967) *Anelastic and Dielectric Effects in Polymeric Solids*. Wiley, New York; Aklonis JJ, MacKnight WJ (1967) *Introduction to Polymer Viscoelasticity*. Wiley, New York; Matsuoka S (1992) *Relaxation Phenomena in Polymers*. Hanser Publ, Munich.

For dielectric measurements, see for example: Karasz FE, ed (1972) *Dielectric Properties of Polymers*. Plenum Press, New York; Blythe AR (1979) *Electrical Properties of Polymers*.

Cambridge University Press, Cambridge. A related technique, that of thermally stimulated current analysis is described by Ibar JP (1993) *Fundamentals of Thermal Stimulated Current and Relaxation Map Analysis*. SLP Press, New Canaan.

**Sect. 4.6.** Descriptions of thermogravimetry are given by: Gallagher PG (1997) Chap 1 in Turi E, ed. *Thermal Characterization of Polymeric Materials*. Academic Press, San Diego; Wunderlich B (1990) *Thermal Analysis*. Academic Press, Boston; Duval C (1963) *Inorganic Thermogravimetric Analysis*, 2<sup>nd</sup> ed. Elsevier, Amsterdam. (For decomposition of polymers see Refs to Sect 3.4).

Early thermogravimetry: Agricola G (1556) *De re metallica*. Translated from the 1556 edition by Hoover HC, Hoover LH (1912) Dover Publ, New York; Hannay JB (1877) *J Chem Soc* 32: 381; Ramsey W (1877) *ibid* 395; Honda K (1915) *Sci Rep, Tohoku Univ* 4: 97.

For tables of the integrated functions and general discussions of calculations of TGA, see Doyle, CD (1966) *Quantitative Calculations in Thermogravimetric Analysis*. In Slade PR, Jr, Jenkins LT, eds. *Techniques and Methods of Polymer Evaluation*. Marcel Dekker, New York, pp 113–216.

Typical TGA and DTA curves are collected by: Liptay L (1971–76) *Atlas of Thermo-analytical Curves*, Vols 1–5. Heyden, London.

For lifetime determination, the jump method is described by: Flynn JH, Dickens B (1976) *Thermochim Acta* 15: 1–16. The isoconversion method, by: Ozawa T (1965) *Bull Chem Soc, Japan* 38: 1881–1886.

### ***Specific References***

1. The Proceedings of the International Conferences on Thermal Analysis (and Calorimetry) can be found in book form under the title: *Thermal Analysis*. Various publ and edts, 1965, 1969, 1972, 1975, 1977, 1980, 1982. More recent proceedings are published in: *Thermochim Acta* (1985) 92/93; (1988) 133/135; *J Thermal Anal Cal* (1993) 40, (1997) 49, (2001) 64.
2. Proceedings of the annual NATAS Conferences, changing eds, for example: . Kociba KJ, Kociba BJ, eds (2002) *Proc. 30<sup>th</sup> NATAS Conf in Pittsburgh, PA, Sept 23–25, vol 30*. Since 2003 the proceedings are issued on CD.
3. The ITS 90 was initiated on Jan 1, 1990 and is described by Preston–Thomas H, Quinn TJ (1992) *The International Temperature Scale of 1990: Parts I and II*. In: Murray TP, Shepard RL, eds (1992) *Temperature: Its Measurement and Control in Science and Industry, Vol 6, Part 1*. Am Inst Physics, New York pp 63–74. See also Preston–Thomas H (1990) *Metrologia* 27: 3. See there also for the conversion of the IPTS 68 and earlier scales to the ITS 90.
4. Lavoisier AL (1789) translated by Kerr R (1790) *Elements of Chemistry*. Part III, Chap III. Edinburgh. Frequently reprinted, for example, printed as a facsimile: (1965) Dover Publications, New York.
5. For the original paper on the ice calorimeter, see: Bunsen R (1870) *Ann Phys* 141: 1.
6. Updyke J, Gay C, Schmidt HH (1966) Improved Precision Ice Calorimeter. *Rev Sci Instr*, 37: 1010–1013.
7. Southard JC (1941) A Modified Calorimeter for High Temperatures. The Heat Content of Silica, Wollastonite and Thorium Dioxide above 25°. *J Am Chem Soc* 63: 3142–3146.
8. Sunner S, Manson M (1979) *Experimental Chemical Thermodynamics, Vol 1, Combustion Calorimetry*. Pergamon, Oxford, 1979.
9. Nernst W (1911) *Der Energieinhalt fester Stoffe*. *Ann Phys* 36: 395–439; see also Lindemann FA, Koref F, Nernst W, (1910) *Untersuchungen an spezifischen Wärmen bei tiefen Temperaturen. I and II*. *Sitzber kgl preuss Akad Wiss* 12(13): 247–292.
10. Tasumi M, Matsuo T, Suga H, Seki S (1975) Adiabatic Calorimeter for High-resolution Heat Capacity Measurements in the Temperature Range from 12 to 300 K. *Bull Chem Soc, Japan* 48: 3060–3066.

11. Oetting FL, West ED (1982) An Adiabatic Calorimeter for the Range 300 to 700 K. *J Chem Thermodynamics* 14: 107–114.
12. Chang, SS (1976) A Self-balancing Nanovolt Potentiometer System for Thermometry and Calorimetry. *J Res Natl Bur Stand* 80A: 669–675.
13. Gmelin E, Rödhammer P (1981) Automatic Low Temperature Calorimetry for the Range 0.3–320 K. *J Phys E, Instrument* 14: 223–238.
14. Tian A (1933) Researches on Calorimetry. Generalization of the Method of Electrical Compensation. *Microcalorimetry*. *J Chim Phys* 30: 665–708; and Calvet E (1948) Compensated Differential Microcalorimeter. *Compt rend* 226:1702–1704.
15. Palermo E, Chiu J (1976) Critical Review of Methods for the Determination of Purity by Differential Scanning Calorimetry. *Thermochim Acta* 14: 1–12.
16. Moros SA, Stewart D (1976) Automated and Computerized System for Purity Determination by Differential Scanning Calorimetry. *Thermochim Acta* 14: 13–24.
17. Sarge SM, Bauerecker S, Cammenga HK (1988) Calorimetric Determination of Purity by Simulation of DSC Curves. *Thermochim Acta* 129: 309–324.
18. Plato C, Glasgow AR, Jr (1969) Differential Scanning Calorimetry as a General Method for Determining the Purity and Heat of Fusion of High-purity Organic Chemicals. Application to 95 compounds. *Anal Chem* 41: 330–336 (1969).
19. Wunderlich B, Jin Y (1993) Thermal Properties of the Four Allotropes of Carbon. *Thermochim Acta* 226: 169–176.
20. Jin Y, Wunderlich B (1991) The Heat Capacity of *n*-Paraffins and Polyethylene. *J Phys Chem* 95: 9000–9007.
21. Watson ES, O'Neill MJ, Justin J, Brenner N (1964) Differential Scanning Calorimeter for Quantitative Differential Thermal Analysis. *Anal Chem* 36: 1233–1238.
22. Gill PS, Sauerbrunn SR, Reading M (1993) Modulated Differential Scanning Calorimetry. *J Thermal Anal* 40: 931–939.
23. Wunderlich B (1987) Development Towards a Single-Run DSC for Heat Capacity Measurement. *J Thermal Anal* 32: 1949–1955.
24. Jin Y, Wunderlich B (1993) Single-run Heat Capacity Measurement by DSC: Principle, Experimental and Data Analysis. *Thermochim Acta* 226: 155–161.
25. Jin Y, Wunderlich B (1990,1992) Single Run Heat Capacity Measurements. *J Thermal Anal* 36: 765–789; II. Experiments at Subambient Temperatures. *Ibid* 36: 1519–1543; III. Data Analysis. *Ibid* 38: 2257–2272.
26. Höhne G, Hemminger W, Flammersheim, HJ (2003) *Differential Scanning Calorimetry*, 2<sup>nd</sup> edn, Sect 5.4. Springer, Berlin
27. Lau SF, Suzuki H, Wunderlich B (1984) The Thermodynamic Properties of Polytetrafluoroethylene. *J Polymer Sci, Polymer Phys Ed* 22: 379–405.
28. Mathot VBF, Pijpers MFJ (1989) Heat Capacity, Enthalpy, and Crystallinity of Polymers from DSC Measurements and Determination of the DSC Peak Baseline. *Thermochim Acta* 151: 241–259.
29. Wunderlich B, Androsch R, Pyda M, Kwon YK (2000) Heat Capacities by Multi-frequency Saw-tooth Modulation. *Thermochim Acta* 348: 181–190.
30. Moon I, Androsch R, Wunderlich B (2000) A Calibration of the Various Heat-conduction Paths for a Heat-flux-type Temperature-modulated DSC. *Thermochim Acta* 357/358: 285–291.
31. Androsch R, Moon I, Kreitmeyer K, Wunderlich B (2000) Determination of Heat Capacity with a Sawtooth-type, Power-compensated Temperature-modulated DSC. *Thermochim Acta* 357/358: 267–278.
32. Androsch R, Wunderlich B (1999) Temperature-modulated DSC Using Higher Harmonics of the Fourier Transform. *Thermochim Acta* 333: 27–32.
33. Pak J, Wunderlich B (2001) Heat Capacity by Sawtooth-modulated, Standard Heat-flux Differential Scanning Calorimeter with Close Control of the Heater Temperature. *Thermochim Acta* 367/368: 229–238.



34. Kwon YK, Androsch R, Pyda M, Wunderlich B (2001) Multi-frequency Sawtooth Modulation of a Power-compensation Differential Scanning Calorimeter. *Thermochim. Acta* 367/368: 203–215.
35. Pyda M, Kwon YK, Wunderlich B (2001) Heat Capacity Measurement by Sawtooth Modulated Standard Heat-flux Differential Scanning Calorimeter with Sample-temperature Control. *Thermochim Acta* 367/368: 217–227.
36. Wunderlich B (1997) Modeling the Heat Flow and Heat Capacity of Modulated Differential Scanning Calorimetry. *J Thermal Anal* 48: 207–224.
37. Merzlyakov M, Wurm A, Zorzut M, Schick C (1999) Frequency and Temperature Amplitude Dependence of Complex Heat Capacity in the Melting Region of Polymers, *J Macromolecular Sci, Phys* 38: 1045–1054.
38. Toda A, Tomita C, Hikosaka M (1998) Temperature Modulated DSC of Irreversible Melting of Nylon 6 Crystals. *J Thermal Analysis* 54: 623–635.
39. Wunderlich B (2003) Reversible Crystallization and the Rigid Amorphous Phase in Semi-crystalline Macromolecules. *Progr Polym Sci* 28: 383–450.
40. Wunderlich, B, Bodily, DM, Kaplan MH (1964) Theory and Measurement of the Glass-transformation Interval of Polystyrene. *J Appl Phys* 35: 95–102.
41. For a series of publications on the glass transitions of polystyrene and poly(ethylene terephthalate) see: Modulated Differential Scanning Calorimetry in the Glass Transition Region, written by: Thomas LC, Boller A, Kreitmeier S, Okazaki I, Wunderlich B (1997) *J Thermal Analysis* 49: 57–70; *Thermochim Acta* 291: 85–94; (1996) *J Polymer Sci, Part B: Polymer Phys* 34: 2941–2952; *J Thermal Analysis* 47: 1013–1026; *Thermochim Acta* 284: 1–19.
42. van Mele B, Rahier H, van Assche G, Swier S (2004) The Application of Modulated Temperature Differential Scanning Calorimetry for the Characterization of Curing Systems. In Reading M, ed, *Basic Theory and Practice for Modulated Temperature Differential Scanning Calorimetry*. Kluwer, Dordrecht, The Netherlands, pp 72–152.
43. Schmieder K, Wolf K (1952) The Temperature and Frequency Dependence of the Mechanical Properties of Some High Polymers. *Kolloid Z* 127: 65–78.
44. Wurm A, Merzlyakov M, Schick C (2000) Reversible Melting During Crystallization of Polymers Studied by Temperature Modulated Techniques (TMDSC, TMDMA). *J Thermal Anal Calorimetry* 60: 807–820; see also: (1998) Reversible Melting Probed by Temperature Modulated Dynamic Mechanical and Calorimetric Measurements. *J Colloid Polymer Sci* 276: 289–296.
45. Schmieder K, Wolf K (1953) Mechanical Relaxation Phenomena in High Polymers. *Kolloid Z* 134: 149–189.
46. Duval C (1951) Continuous Weighing in Analytical Chemistry. *Anal Chem* 23: 1271–1286.
47. Details on the TGA of Figs. 4.177–180 are described in: Wiedemann HG (1964) *Thermogravimetric Investigations. VI. Universal Device for Gravimetric Determinations under Variable Conditions*. *Chemie Ing Tech* 36: 1105–1114.
48. Zitomer F (1968) Thermogravimetric Mass Spectrometric Analysis. *Anal Chem* 40: 1091–1095.
49. Paulik F, Paulik J, Erdely L (1958) The “Derivatograph.” I. An Automatic Recording Apparatus for Simultaneously Conducting Differential Thermal Analysis, Thermogravimetry, and Derivative Thermogravimetry. *Z anal Chem* 160: 241–252. For standardization, quasi-isothermal and isobaric analyses and some example research with the Derivatograph see also: (1966) *Anal Chim Acta* 34: 419–426; Paulik F, Paulik J (1973) *J Thermal Anal* 5: 253–270; (1975) 8: 557–576.
50. Sørensen OT, Rouquerol J, eds (2003) *Sample-controlled Thermal Analysis (SCTA): Origin, Goals, Multiple Forms, Applications, and Future*. Kluwer, Amsterdam.

## Structure and Properties of Materials

In this Chap. 5 of the book on Thermal Analysis of Materials, the link between microscopic and macroscopic descriptions of crystals is given in Sects. 5.1–3. This is followed by a thermodynamic analysis of melting of crystals and isotropization of mesophases in terms of entropy and enthalpy in Sects. 5.4 and 5.5. The final section deals with the properties of liquids and glasses (Sect. 5.6).

### 5.1 Crystal Structure

#### 5.1.1 Introduction

Crystals have always fascinated man. To this day crystals are not only treasured because of their beauty [1], but there remain some of the ancient beliefs of possible magic. Huygens' drawing of a  $\text{CaCO}_3$  crystal in Fig. 2.101 was first prepared to explain the occurrence of the birefringence more than 100 years before Dalton's proof of the existence of atoms (see Sect. 1.1.1). Even earlier suggestions exist of links between the external regularity of crystals, depicted in Fig. 3.77, and the atomic structure. Kepler analyzed in 1611 the hexagonal structure of snow flakes, as shown in Fig. 5.1 in terms of regularly packed balls, and Hooke (1665) used bullets to understand the shapes of diamonds. The correct NaCl structure could be derived 100 years ago purely from packing consideration of spheres of different radius and charge, as reproduced in Fig. 5.2. All leads to the conclusion that motifs must repeat themselves regularly in space. Today we know about the details of the structure of the motifs and their arrangement in the crystals through X-ray diffraction, as can be seen in Fig. 5.81, below, and electron microscopy, as illustrated in Fig. 2.102.

To characterize a crystal, one must describe the motif and find the repetition scheme that generates the crystal. There are an unlimited number of different motifs, i.e., represented by atoms, ions, parts of molecules, molecules, or even groups of many molecules, but for the resulting crystals, there are only a limited number of repetition schemes. They are represented by the 230 space groups. The motifs and repetition-schemes in crystals and helices are discussed in Sects. 5.1.1–6.

The combination of motifs and repetition schemes is the second topic of this section. The space group of the lattice is the scheme that acts on motifs placed into the unit cell and generates the crystal structure. The space group is determined by X-ray diffraction or, less frequently, by electron or neutron diffraction. Typically one to 18 repeating units of a macromolecule exist within one unit cell, but helices with long translational repeats may place many more repeating units into one unit cell. For example, poly(*m*-methylstyrene)s with a  $2 \times 40/11$  helix form a four-chain unit cell with

## Examples of Morphologies Found in Crystals of Ice and Snow

A small selection of the over 2000 photographs of W. A. Bentley of snow crystals as seen in Vermont, ranging from close to single-crystalline hexagonal to dendritic.

W. A. Bentley and W. J. Humphreys, "Snow Crystals." McGraw-Hill, New York, 1931.

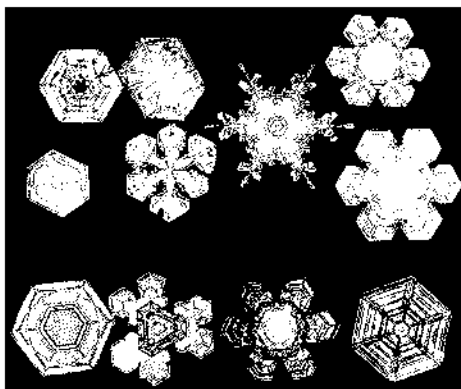
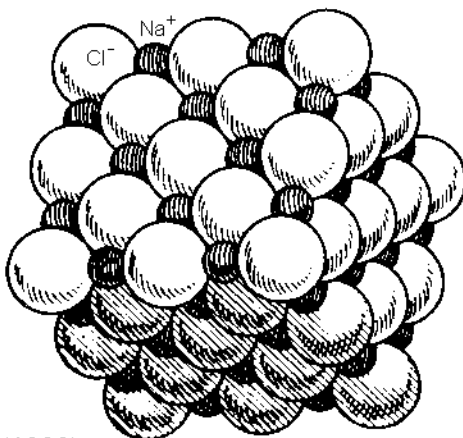


Fig. 5.1

## Close Packing of Two Types of Spheres

Illustration of the close-packing of two types of motifs, such as the  $\text{Na}^+$  and  $\text{Cl}^-$  ions in NaCl as proposed in 1898 just before it became possible to analyse crystal structures by X-ray diffraction.



W. Barlow, *Z. Krist.*, **29**, (1898)

Fig. 5.2

160 repeating units, compared to the similar poly(*o*-methylstyrene) of Fig. 5.29, below, which has the similar  $2\frac{1}{2} \times 4/1$  helix and 16 repeating units. Central for the understanding of a crystal structure is the packing of its motifs.

The closest packing without distorting motifs will usually yield the most stable crystals with lowest free enthalpy, as discussed in Sects. 5.1.7 and 5.1.8. The packing

fraction, as described in Fig. 4.24, should be a maximum. These principles are analyzed on a series of examples of macromolecular crystals in Sects. 5.1.9 and 5.1.10. Crystals with less-well-defined motifs are described in Sect. 5.1.11.

### 5.1.2 Lattice Description

The space-lattice of Fig. 5.3 helps in the description of crystals. One must, however, observe that the lattice is only a mathematical abstraction and not the actual crystal. The lattice points may or may not coincide with actual motif positions. All motifs, however, have a fixed relationship to the lattice. The lattice descriptor is the *unit cell*, drawn in heavy lines. The three non-coplanar axes of the unit cell have the lengths:  $a$ ,  $b$ ,  $c$ , and the angles:  $\alpha$ ,  $\beta$ ,  $\gamma$ . One lattice point occupies the corners of the unit cell. Since for any given unit cell only 1/8 of its corners lies inside the unit cell, each primitive unit cell shown, contains only one lattice point.

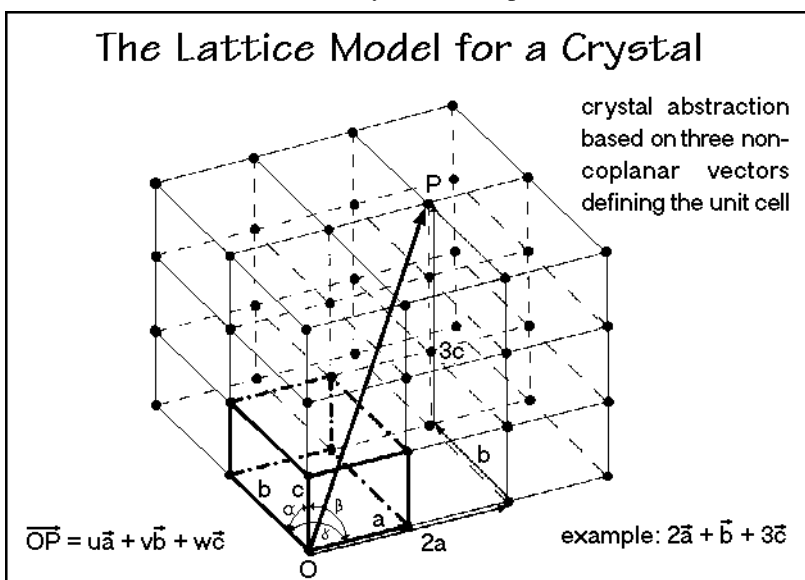


Fig. 5.3

The vectors identifying any lattice point,  $P$ , relative to the origin  $0,0,0$  can be written with three integers, as indicated in the figure. The example chosen corresponds to 2,1,3. Note also that the chosen axis system is a *right-handed system*, meaning that if one looks along the vector  $\vec{c}$ , the rotation from  $\vec{a}$  to  $\vec{b}$  is clockwise.

### 5.1.3 Unit Cells

Crystals are also described by *unit cells*, similar to lattices. All unit cells can be grouped into seven crystal systems, as listed in Fig. 5.4. The cubic system has the highest symmetry, the triclinic system has the lowest. The seven unit cells of the crystals can be linked to a total of 14 different lattices, called the Bravais lattices. The

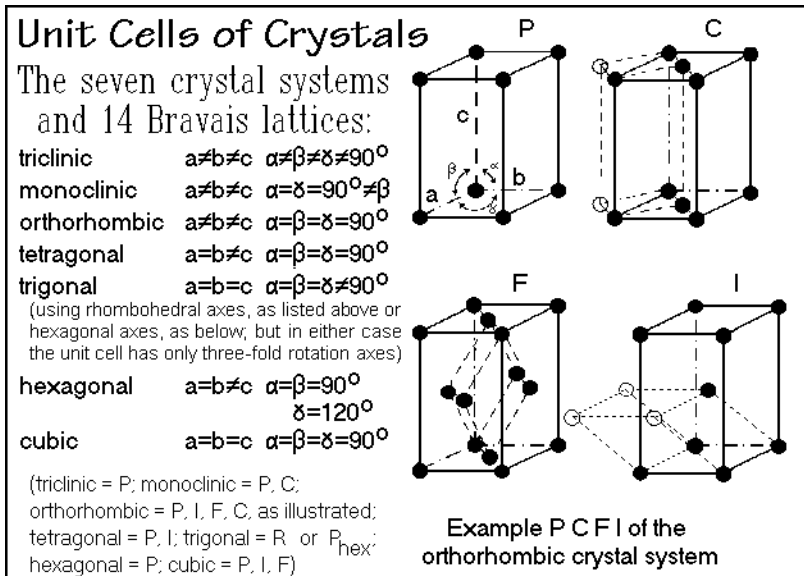


Fig. 5.4

unit cells of the Bravais lattices are also listed in Fig. 5.4. To identify the lattices by their external crystal symmetry, it is customary to sometimes give a somewhat larger unit cell than the primitive unit cell (P). The unit cell I (for German “innenzentriert,” body-centered) has two lattice points; the unit cell F, (face-centered) has four; and C, has two (base-centered, face ab). The orthorhombic crystal system with its four possible Bravais lattices is drawn as an example in Fig. 5.4. The primitive unit cells that belong to the larger unit cells are indicated by dashed lines. It is quite obvious that from the primitive cells, it is not possible to identify the crystal systems.

### 5.1.4 Miller Indices

To navigate throughout a crystal, a set of indices has been devised, the Miller indices. Figure 5.5 illustrates the construction necessary to find the Miller index of a plane. The plane to be described may be a macroscopic, naturally occurring crystal surface, or it may be a specific lattice plane needed to describe a microscopic, atomic-scale problem. Once the axes and the plane are identified, the plane is moved parallel to itself towards the origin of the axis system until the least set of whole-numbered multiples of the reciprocals of the intercepts with the axes in units of  $a$ ,  $b$ , and  $c$  is reached. All planes parallel to the original plane are given the same Miller index ( $h$   $k$   $l$ ). In the microscopic descriptions of two planes that are parallel, but refer to different occupancies with motifs, it is permitted to use larger than the least multiples to distinguish differences in packing of motifs inside a crystal, i.e., the (111) and (222) planes may be different and are then given these different indices.

Fortunately, indices higher than 3 are rare, so that it is easy to visualize the various planes without calculation. Figure 5.5 shows the difference between a rare (232) plane, and the more frequent (111) planes. Planes parallel to a unit cell axis intersect

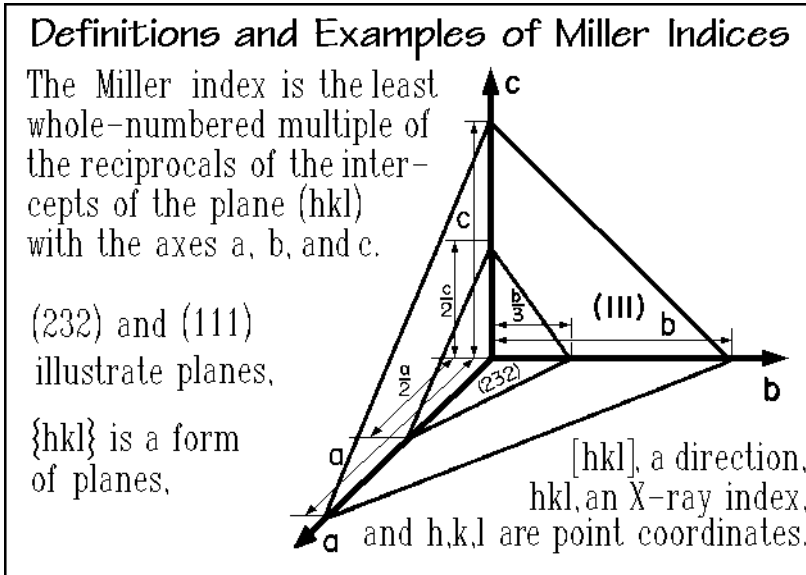


Fig. 5.5

at  $\infty$ , and, as shown in Fig. 5.6, the index is 0, its reciprocal. Planes that intersect an axis with a negative intercept receive a bar over the corresponding index, as in  $(0\bar{1}0)$ . A form of planes is a group of planes that is related by symmetry. Its simplest Miller index is enclosed in braces  $\{ \}$ , as in the example the form  $\{100\}$ , shown in Fig. 5.6 to include all surfaces of a cube.

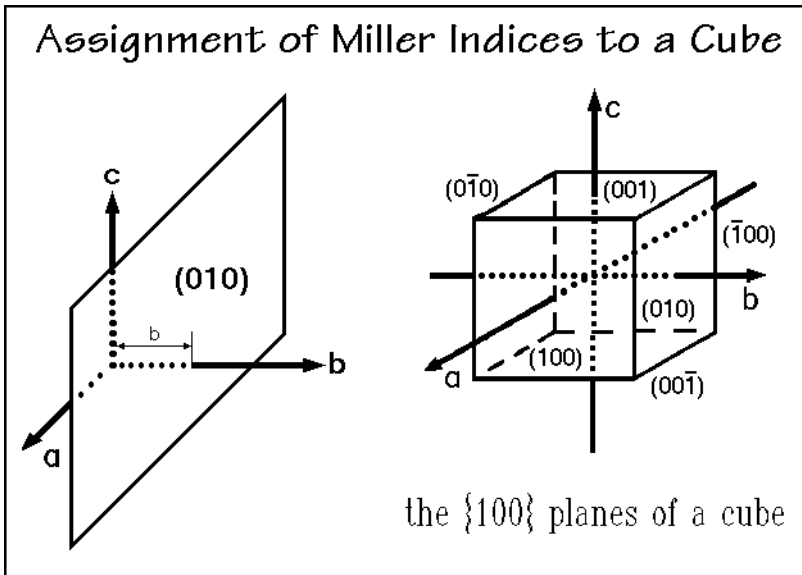


Fig. 5.6

Similar to the planes, directions can be named by specifying in brackets [ ] the smallest integer of multiple lattice-spacings  $u$ ,  $v$ ,  $w$  which is met by a line from the origin in the chosen direction. In Fig. 5.3, the direction  $\vec{OP}$  is [213]. The X-ray diffraction peak due to a plane ( $hkl$ ) is given by specifying  $hkl$  (no parentheses), and a lattice point is given by its coordinates. Point P in Fig. 5.3 is described as 2,1,3. A summary of these definitions is given in Fig. 5.5. They allow a precise description of surfaces, directions, and points within crystals and lattices.

### 5.1.5 Symmetry Operations

Basic to the representation of crystals, lattices, and motifs is their symmetry. Group theory, summarized in Appendix 14 with Fig. A.14.1, is the branch of mathematics dealing with interrelationships between the symmetry elements. Some elementary group theory is needed for the operations, described next.

Point groups are made up of an internally consistent set of symmetry operations that leave at least one point unchanged when operating on an object to give a closed operation. Figure 5.7 illustrates the simplest, closed symmetry operations. The unit operation "1" is represented by the Statue of Liberty. Only a full rotation about the axis of symmetry will reproduce the original statue. There is no other symmetry in

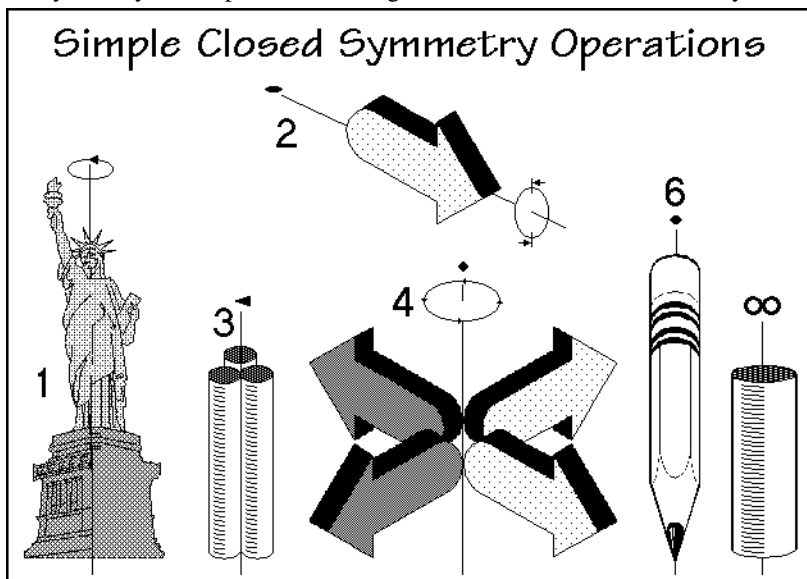


Fig. 5.7

this figure, as is also observed in most other things one sees. Each body will have this symmetry 1. Additional symmetry is exceptional, and always worth mentioning in the description of an object.

The arrow at the top in Fig. 5.7 has a twofold axis of symmetry. It is indistinguishable after rotation about this axis by  $180^\circ$ . The operation 2 reproduces the same arrow after half a turn. Naturally this is only true if the surface which is not seen in the

drawing is identical to the dotted surface. In addition, we will see below that there is additional symmetry in the arrow, namely two mirror planes.

The other possible rotation axes  $2\pi/n$  in crystals are analogously labeled by “n” and their symbols are indicated in the center in form of polygons. Axes with  $n > 6$  cannot describe a space-filling lattice, and even a fivefold axis of symmetry is not possible. Motifs, on the other hand, may have any symmetry. The rotation axis  $\infty$  is, for example, exhibited by the cylinder shown on the right of Fig. 5.7. It is also shown that the stacking of cylinders as motifs in a crystal cannot make use of this high symmetry, their crystal symmetry is only 3, 4, or 6. The pencil of Fig. 5.7 has a sixfold rotation axis which is not disturbed by the higher symmetry of the rounded sections. The group of arrows in the center of Fig. 5.7 has fourfold symmetry, assuming that the two sides of each arrow are different in the same way as indicated.

A final, sixth, symmetry-element of the point groups is the center of inversion, i, marked by an open circle ( $\circ$ ). Its operation involves a projection of each point of the object through its center to a point equally distant on the other side. The projection is illustrated by the letter A in Fig. 5.8.

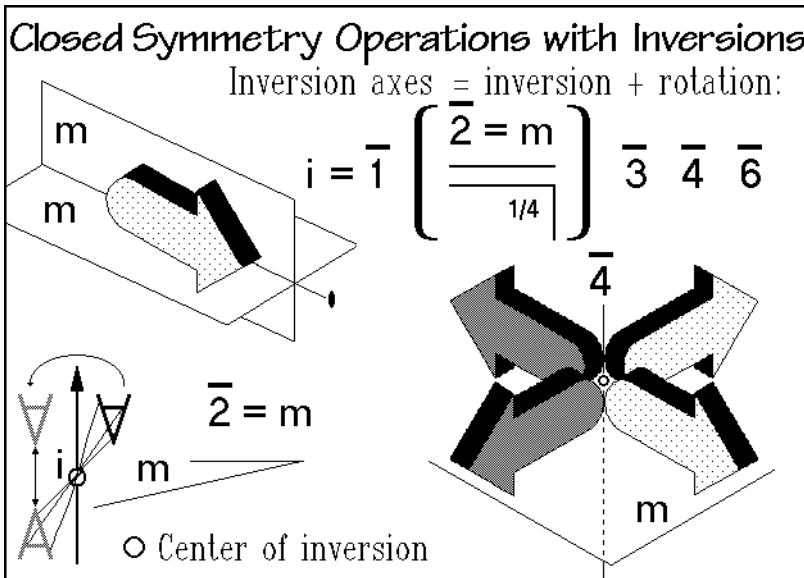


Fig. 5.8

Note that the letter is different in front and back. The other symmetry elements of the letter A are also indicated. The six basic point-symmetry elements (1, 2, 3, 4, 6, and i) can describe the crystal symmetry as it is macroscopically recognizable by inspection, if needed, helped by optical microscopy.

The basic symmetry elements can also be carried out in sequence. This combination is called the product of the elements (see Appendix 14). Two fourfold rotations about the axis of symmetry are thus equal to one twofold rotation, two sixfold rotations, a threefold one, and three sixfold rotations, a twofold one. When the element i is included in the products, one can generate the inversion axes  $\bar{1}$ ,  $\bar{2}$ ,  $\bar{3}$ ,



$\bar{4}$ ,  $\bar{5}$ , and  $\bar{6}$ , as listed in Fig. 5.8. The onefold inversion axis,  $\bar{1}$ , is identical to the inversion center  $i$  alone, while  $\bar{2}$  is equivalent to a mirror plane at right angles to the inversion axis, as illustrated by the construction with the letter A. Similarly, the single arrow from Fig. 5.7, also shown in Fig. 5.8, has two mirror planes at right angles to each other, in addition to the twofold axis of symmetry, assuming front and back are identical. The  $1/4$  in the mirror plane symbol indicates the distance  $m$  lies below the plane of reference as fraction of the unit cell dimension. The line, drawn above, is used if one observes the mirror plane side-on. The set of four arrows of Fig. 5.7 shows in Fig. 5.8 that it has an inversion center in the middle, making the symmetry axis an inversion axis,  $\bar{4}$ , and since a fourfold rotation contains also twofold symmetry, there must be a mirror plane running through the tips of the arrows, as indicated. This example of four arrows shows that it belongs to a group of four simple symmetry elements:  $1, i, 2, 4$ , with the simple products  $\bar{1}, \bar{2} = m$ , and  $\bar{4}$ . The group in itself is self-consistent, no other than the shown set of symmetries are possible. Only 32 point groups can be generated from the six basic point-symmetry elements possible for the description of crystals.

The internal structure of a crystal or its space lattice needs a seventh symmetry operation for its description: the translation in the directions of the unit cell axes, as illustrated with Fig. 5.9. This operation fills the space with points removed from the initial point and is called open, in contrast to the closed operations discussed until now. The most important combined open operations are the screw axes, combining translations and rotations, and glide planes, combining translations and mirror planes. Adding the seventh basic symmetry operation leads to 230 space groups which cover all possible crystals. Fortunately, due to packing considerations only space groups are needed to describe most crystals. Screw axes and glide planes, as open operations, are the two products that permit the generation of all motifs in a crystal.

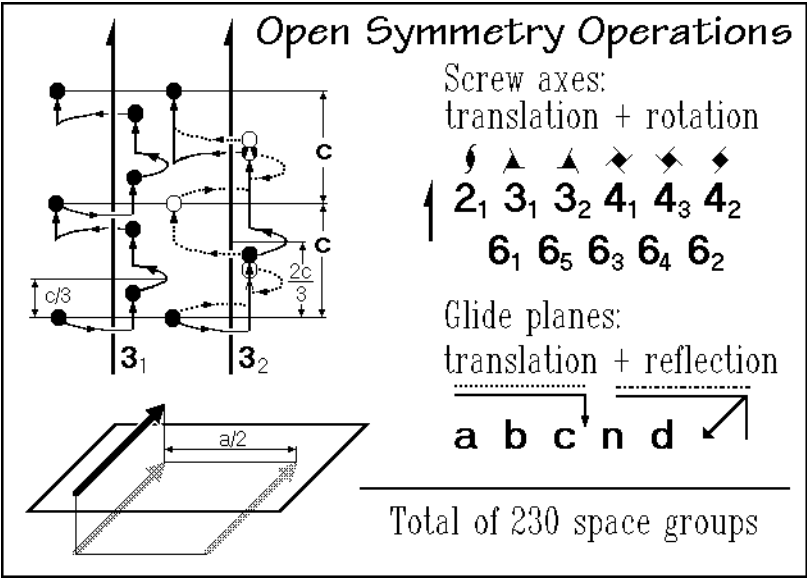


Fig. 5.9

Figure 5.9 shows on the upper left the operation of a screw axis  $3_1$  on a lattice point. After a rotation of  $2\pi/3$ , a translation by  $1/3$  in the direction  $c$  is carried out. After two more of such  $3_1$  operations, the identical point of the lattice in the next unit cell is reached. Three  $3_1$  operations, thus, are identical to one unit cell translation,  $c$ . Again, the symbol indicating a screw axis  $3_1$  is drawn next to the axis indication. The also shown action of a screw axis  $3_2$  has a rotation of  $2\pi/3$  followed by a translation of  $2c/3$ . Figure 5.9 shows that identity of the filled circle is reached two unit-cell lengths away from the initial point. Filling-in the missing points, by translation back by  $c$  for each point to reach the open circles, gives a screw axis that is identical to  $3_1$ , except that it rotates counterclockwise instead of clockwise as can be seen by following the dotted path with six counterclockwise rotations by  $2\pi/3$  and a translation  $1c/3$ . The other possible screw axes are listed together with their symbols. As in threefold screw axes,  $4_1$  and  $4_3$ ,  $6_1$  and  $6_5$ , as well as  $6_2$  and  $6_4$  are of opposite handedness, they are enantiomorphs (Gk. *ἐναντίος* and *μορφή*, of opposite form, as in stereoisomers, see Appendix 14).

Glide planes are also shown in Fig. 5.9. Shown is the glide plane  $a$ , the product of a mirror operation followed by a glide of  $a/2$ . The glide planes with glides along  $b$  and  $c$  are analogous to  $a$ , with glides of  $b/2$  and  $c/2$ . The glide planes  $n$  have a diagonal glide  $(a + b)/2$ ,  $(b + c)/2$ , or  $(c + a)/2$ . The glide plane  $d$  is the so-called diamond glide, found in centered lattices with a  $1/4$  glide along the diagonal. The total of 230 space groups represents the possible repetition schemes that act on the motif(s) placed in the unit cell and generate the crystal.

### 5.1.6 Helices

Crystallization of flexible linear macromolecules is only possible if the molecule assumes an ordered conformation of low energy. In the treatment of the size and shape of random coils of macromolecules in Sects. 1.3.3–5 it is found that the backbone bonds of the molecules have only few conformations with low energy, the rotational isomers, illustrated in Figs. 1.36 and 1.37. A conformation is defined in Fig. A.14.3 and distinguished from a configuration. Repeating low-energy conformations along the chain commonly leads to helices. Based on lowest-energy, the helices may result in any rotational symmetry and are not necessarily rational in their repetition along their axis. For the description of rational and irrational numbers, see Fig. A.14.4. The screw-axes in crystals, in contrast, as described in Sect. 5.1.5, are limited to 1-, 2-, 3-, 4-, or 6-fold rotations with rational repeats in the direction of the axes. In addition, screw axes do not necessarily recognize the continuity of the molecule, as illustrated by the  $3_2$  screw axis, described in Fig. 5.9. To rectify this problem, polymer scientists have developed the helix-lattice concept [2,3].

Figure 5.10 explains the helix notation for simple  $1*3/1$  helices which are equal to the  $3_1$  screw axes of Fig. 5.9. The class of the helix,  $A$ , indicates the number of chain atoms that are placed in relation to a lattice point of the single helix, as will be shown below. For the description of the simple helix shown in Fig. 5.10, the class is by its definition the number 1 and as such can be omitted, i.e., one may just write  $3/1$  as the helix notation to show the identity to the screw axis  $3_1$  of the crystal lattice. At the bottom of the helix of Fig. 5.10, the projection of the helix is drawn.

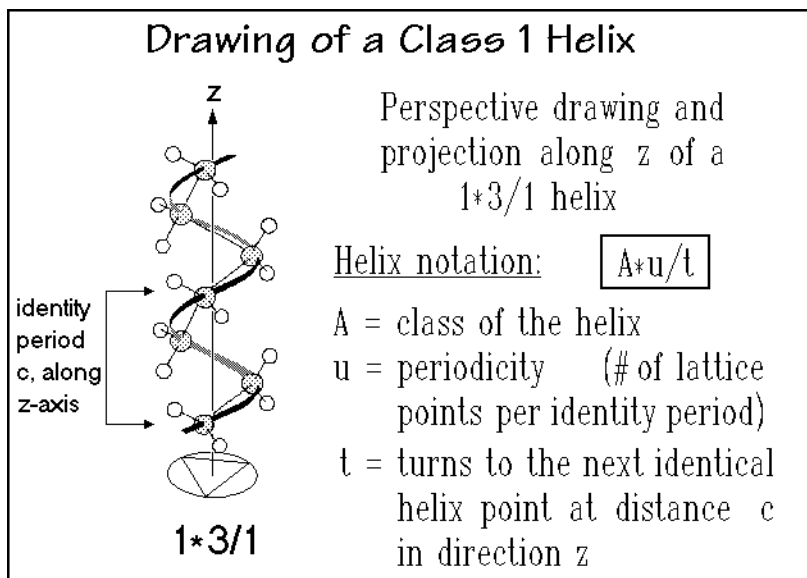


Fig. 5.10

Figure 5.11 contains a selection of projections of rational helices that correspond to the indicated screw axes. If there is no equivalent screw axis indicated, it does not exist in space-lattice symmetry. The helix lattice generates the complete molecule starting with the first motif, but one must specify whether the helix rotation is left- or right-handed. While the screw axis  $3_1$  corresponds to a right-handed  $3/1$  helix, the  $3_2$  screw axis generates a left-handed  $3/1$  helix, but every second lattice point is generated

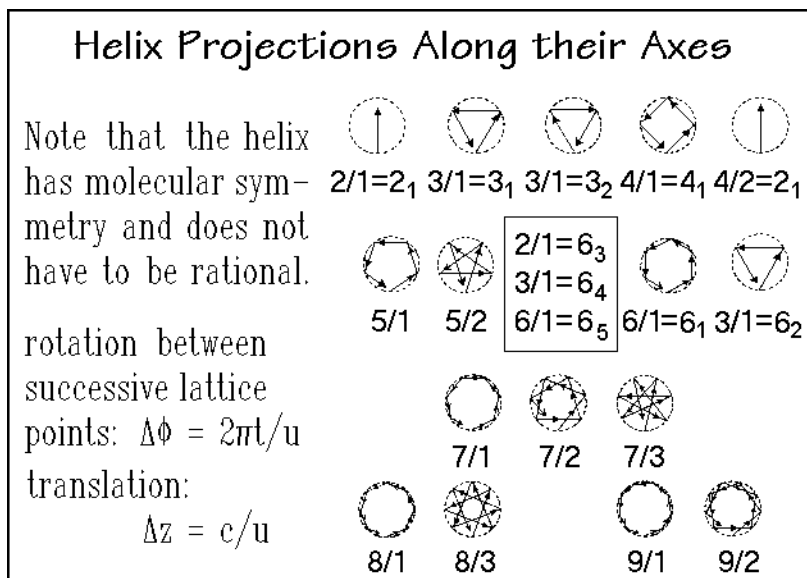
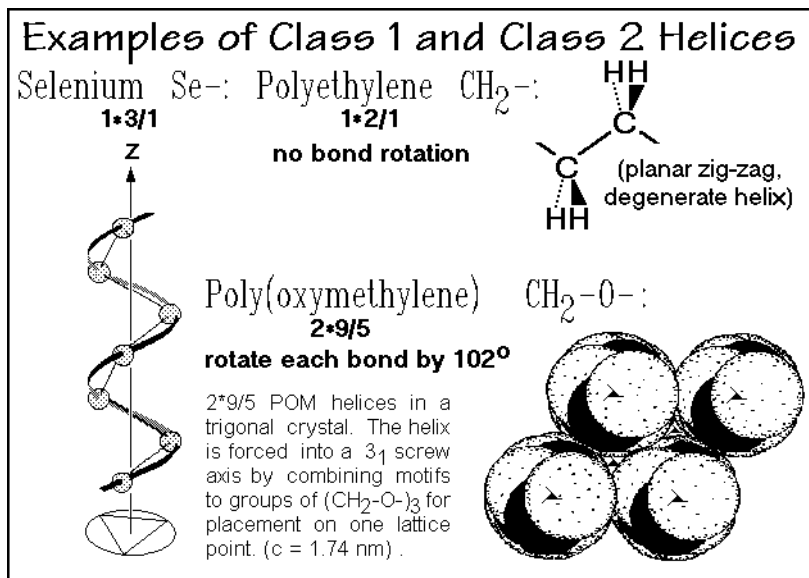


Fig. 5.11

by translational symmetry, as shown in Fig. 5.9. The left-handed nature of a molecule when described with a  $3_2$  helix is not obvious and the helix symmetry operations do not follow the progression of the molecule. Of special interest are the equivalencies for the sixfold screw axes listed in Fig. 5.11.

Finally, one must observe that polymer helices may have any symmetry, but already of the shown helices in Fig. 5.11, the 5-, 7-, 8-, and 9-fold screw axes are not permitted as crystal symmetry, as are any not shown screw axes. Finally, the positions of the lattice points of a polymer helix can be computed from the definitions and equations in Fig. 5.11.

Selenium is an example of a class 1 helix. It is given on the left side in Fig. 5.12. Since the  $1\frac{1}{3}/1$  helix is identical to the  $3_1$  screw axis, there is no difficulty to describe its crystal structure in Fig. 5.20, below. Next, planar zig-zag chains can be looked upon as degenerated helices of either no bond rotation, or a  $180^\circ$  rotation according to two conventions to assign the zero rotation angle, which are followed by different researchers. One must, thus, check for any helix description the zero rotation angle



**Fig. 5.12**

chosen! Figure 5.12 also illustrates on the top right the  $1\frac{1}{2}/1$  helix of polyethylene with its CRU of  $\text{CH}_2$ - (see Sect. 1.2). A class 2 helix is illustrated at the lower right with the example of poly(oxymethylene), POM. It can be visualized by rotation of each backbone bond by a  $102^\circ$  angle, not far from the all-*gauche* conformation of  $120^\circ$ . The helix  $2\frac{9}{5}$  is found in a trigonal crystal, the unit cell of which is indicated in Fig. 5.12. In order to fit the helix  $2\frac{9}{5}$  to the  $3_1$  or  $3_2$  screw axis with three lattice points per identity period, required by the trigonal crystal, the motif per lattice point is increased to three monomer units. The corresponding helix lattice is  $6\frac{3}{1}$  with the three monomers per lattice point having  $5/3$  rotation about the helix axis by themselves, so that the three steps of rotation of the  $3_1$  screw axes total the five

rotations of the helix  $2^*9/5$ . Small adjustments in the POM helix do not take a large amount of energy. Thus, closing the rotation angle to  $117^\circ$ , leads to an only slightly less stable orthorhombic crystal with a  $2^*2/1$  helix and results in a second possible crystal structure ( $2^*2/1 \approx 2^*10/5$ ). It has even been proposed that  $2^*29/16$  or even irrational helices may be more stable than the helix  $2^*9/5$  of POM. Experimentally such small local changes are difficult to establish by X-ray diffraction.

For the isotactic polypropylene helix of Fig. 5.13, two bond-rotation angles must be specified. The planar zig-zag at  $\phi_1 = \phi_2 = 0$ , the all-*trans* conformation, is sterically hindered by contact between two successive  $\text{CH}_3$  groups. The stable  $2^*3/1$  helix consists of close to alternating *gauche* and *trans* conformations. When looking along one repeating unit of the chain, two stereoisomers can be recognized, marked as *d* and *l* configurations. The chirality of the  $(\text{LC})\text{HC}^*(\text{CH}_3)(\text{RC})$  grouping, however, is negligible since the left chain end (LC) and the right chain end (RC) are hardly distinguishable (see also Appendix 14). On packing *d* and *l* configurations in a crystal, however, largely different energies result, as discussed in Sect. 5.1.8.

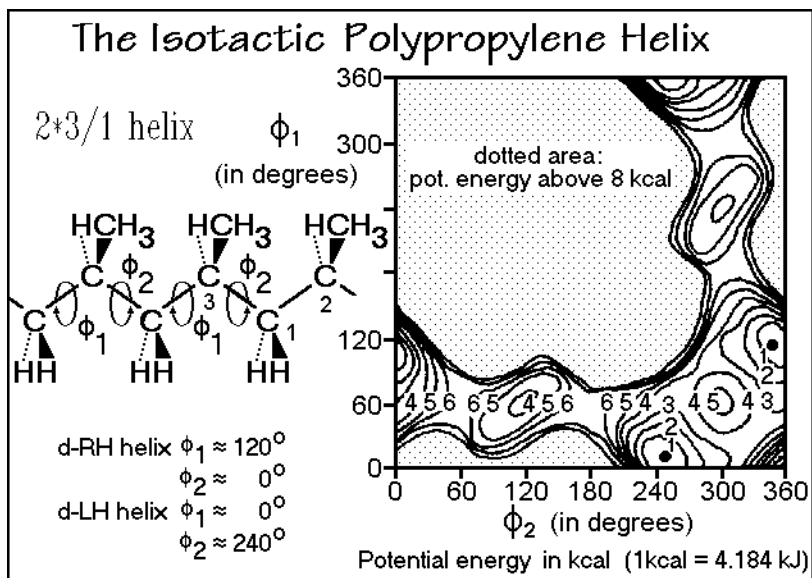


Fig. 5.13

The diagram of the potential energy on the right in Fig. 5.13 illustrates the change in energy on bond-angle rotation for isotactic polypropylene. Alternate rotation directions are chosen for  $\phi_1$  and  $\phi_2$ . Both the left- and right-handed helices are energetically equally stable and can interchange their handedness along a narrow path as seen in the figure.

A perspective drawing of a  $2^*3/1$  helix observed for several vinyl polymers is given on the left of Fig. 5.14 [4]. The helix is drawn as a right-handed helix, but of the *l*-configurations, as defined in Fig. 5.13, above. The side-groups,  $\bullet$ , are chosen as lattice points. The other two helices in Fig. 5.14 show that increasing bulkiness opens the helix from  $2^*3/1$  to  $2^*7/2$ , and finally to  $2^*4/1$  by decreasing  $\phi_1$  and  $\phi_2$  by

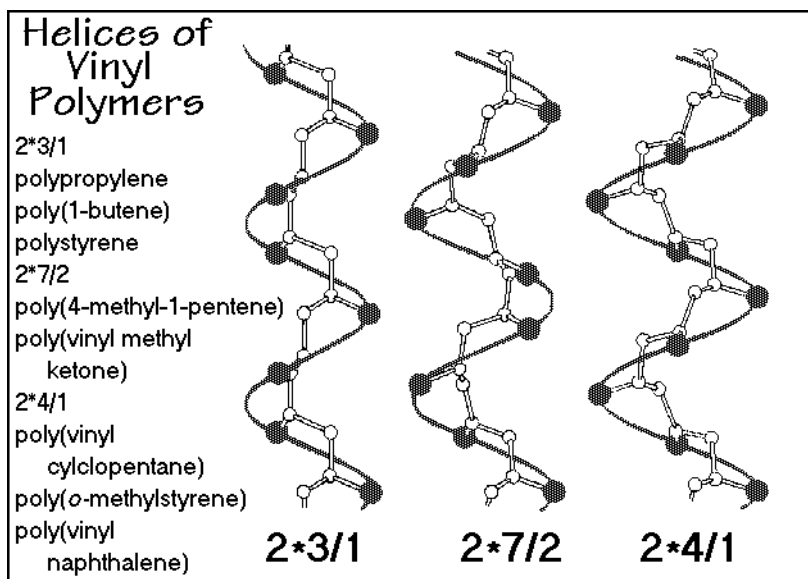


Fig. 5.14

about  $20^\circ$ . Mathematical formulas exist to generate the helix parameters from the molecular backbone rotation angles.

Examples of class 3 helices are the poly(amino acid)s, illustrated in Fig. 5.15 with poly(L-alanine). The helix also can be described with only two bond rotation angles since the third rotation, about CO-NH, is sufficiently hindered in position  $0^\circ$  due to resonance stabilization. The potential energy diagram shows only a few angular

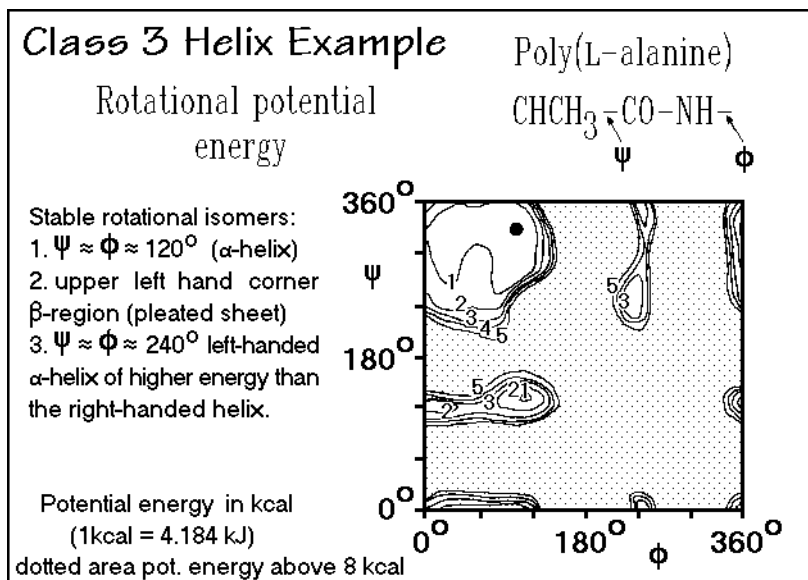


Fig. 5.15

regions of stability. Also, since the poly(L-alanine) is truly optically active (see Appendix 14). The symmetry about the  $360$  to  $360^\circ$  diagonal in the potential-energy diagram, present for polypropylene, is disturbed. The right-handed helix (RH) has a lower energy than the left-handed helix (LH).

Poly(L-alanine) can stabilize the RH  $3 \times 18/5$  helix, the well-known  $\alpha$ -helix, by intramolecular hydrogen bonds, indicated by the dotted lines in Fig. 5.16 A. Another stable conformation, called the pleated sheet, must make the H-bonds inter-

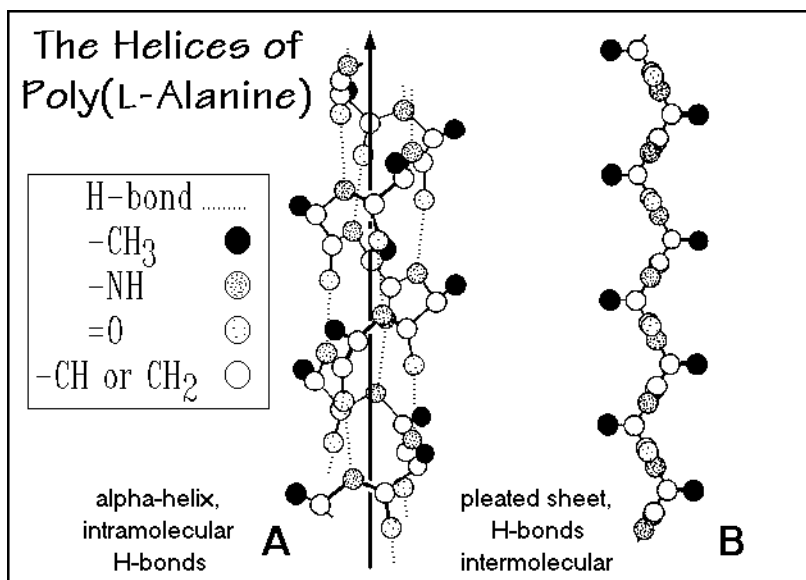


Fig. 5.16

molecularly, as shown by the sketch in Fig. 5.16 B. The different conformations of the amino acid residues have a marked influence on their structural functioning in biological systems, such as in globular and structural proteins.

It is of interest to note that one may change the translation lattice of Fig. 5.3 by replacing the translation lattice vector  $\vec{c}$  with the molecular helix lattice, keeping the translation symmetries  $\vec{a}$  and  $\vec{b}$ . This would lead to a match of the molecular helix symmetry with the crystal symmetry and even for irrational helices, a crystal structure symmetry would be recognized. In fact, a whole set of new lattices can be generated replacing all three translation symmetry operations by helix symmetry operations [5]. Since a  $1 \times 1/1$  helix has a translational symmetry, this new space lattice description with helices would contain the traditional crystallography as a special case.

### 5.1.7 Packing in Crystals

To produce crystals of lowest free enthalpy, a hierarchy of steps is necessary, involving a decreasing amount of interaction energy [6]. First, all strong bonds of the motif must be given proper length and angle (see Sect. 1.1). Next, the lowest-free-enthalpy helix is produced by minimizing conformational energy and steric

interaction. Finally, the helices are packed densely, taking care of any possible H-bonds, dipoles and possibly even isolated ionic charges.

The packing fraction,  $k$ , of solid rods, described in Fig. 4.24, can be easily derived from Fig. 5.17. As indicated,  $k$  is larger than possible for the three-dimensionally closely-packed spheres (CN = 12), or for the lower coordination number of rods in two dimensions (CN = 4). The closer approach of the covalently bound atoms along the chain is the reason for these high packing-fractions of rod-like motifs.

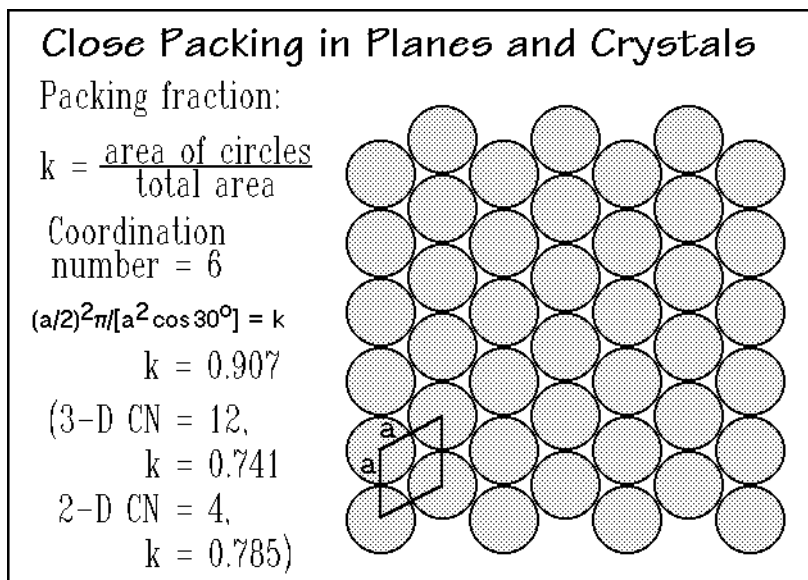


**Fig. 5.17**

The closest approach of polyethylene molecules in a crystal is probed in Fig. 5.18. The packing has a CN = 6. Four of the chains approach more closely (triple contacts) than the other two (single contacts). The packing fraction,  $k$ , of 0.70 is based on the experimental data listed, and the corresponding van der Waals radii defined in Fig. 4.23. Several crystals with zig-zag chains result in an average of 0.72 for  $k$ , to which the data on crystals with true helices in Sect. 5.1.8 have to be compared.

The unit cell of polyethylene is drawn in Fig. 5.19 in two projections. The zig-zag chains are represented such that the carbon atoms are located at the intersections of the backbone bonds and the hydrogen atoms are located at the ends of the heavy lines. All symmetry elements are marked by their symbols as also given in Figs. 5.7–9. With help of the symmetry elements all atom-positions can be fixed in both projections. The symbols are standardized and will be used for the description of all the other crystal structures. Since the structure in the chain direction is best known, most projections will be made parallel to the chain axis which is also the helix axis. Before continuing with the study, it is of value to take the time to check the operation of every symmetry element in Fig. 5.19 with respect to its operation, since the later examples will similarly be displayed and a facility of three-dimensional visualization of crystal structures is valuable for the understanding of the crystal structures.



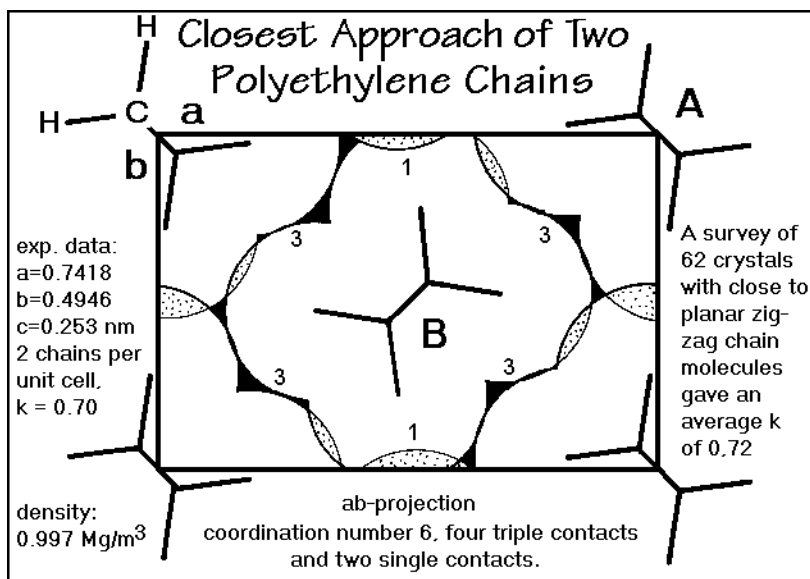


Fig. 5.18

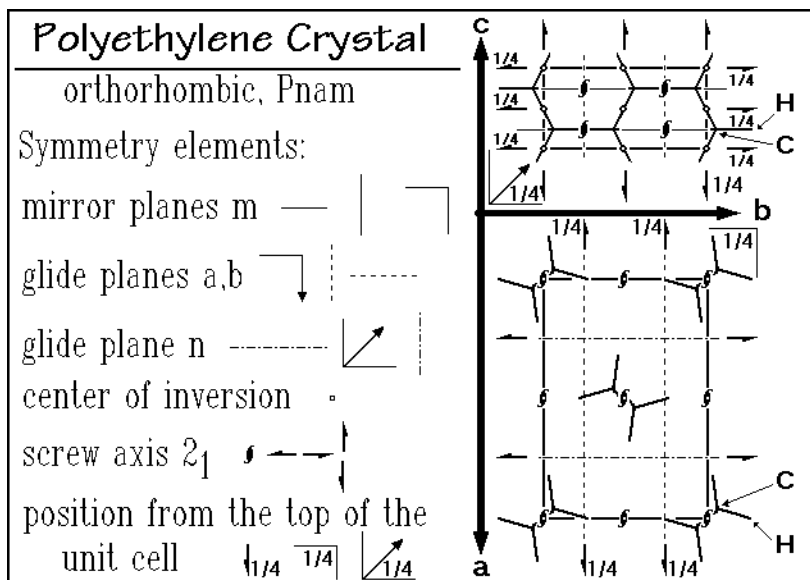


Fig. 5.19

The orthorhombic space group for polyethylene has been given the symbol  $Pnam$  by Bunn in 1939 [7]. The  $P$  indicates a primitive space group,  $n$ ,  $a$ , and  $m$  indicate the characteristic symmetry elements that determine the nature of the space-group. There are two chains in the unit cell and along the  $c$ -axis each chain repeats with two  $\text{CH}_2$ -units, i.e., the unit cell contains four  $\text{CH}_2$ -units.

Polyethylene has two other crystal structures, one is monoclinic and somewhat less stable, the other is hexagonal and represents a mesophase (condis crystal, see Sect. 2.5). The mesophase is stable only at elevated pressure and temperature, as discussed in Sect. 5.5. The monoclinic crystal structure (formerly erroneously called triclinic) is frequently found in drawn polyethylene, and then identified by its different X-ray reflections. Its zig-zag planes are all parallel and angle  $\beta = 107.9^\circ$ .

### 5.1.8 Packing of Helices

To pack a helix closely is more involved than the packing of spheres. The density depends on the degree of overlap that can be achieved between neighboring helices, i.e., the interpenetration that can be achieved by having the turns of the helix intermesh.

An example of a very close pack is metallic selenium, shown in Fig. 5.20. One can look upon the polymeric chains in the trigonal crystal as being related to a close packing of metallic atoms with a coordination number  $CN = 12$  that overlap along the

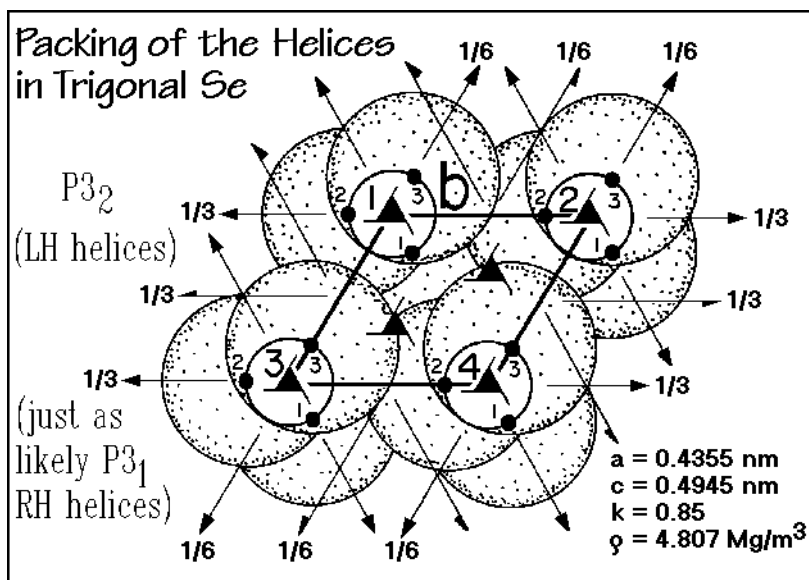
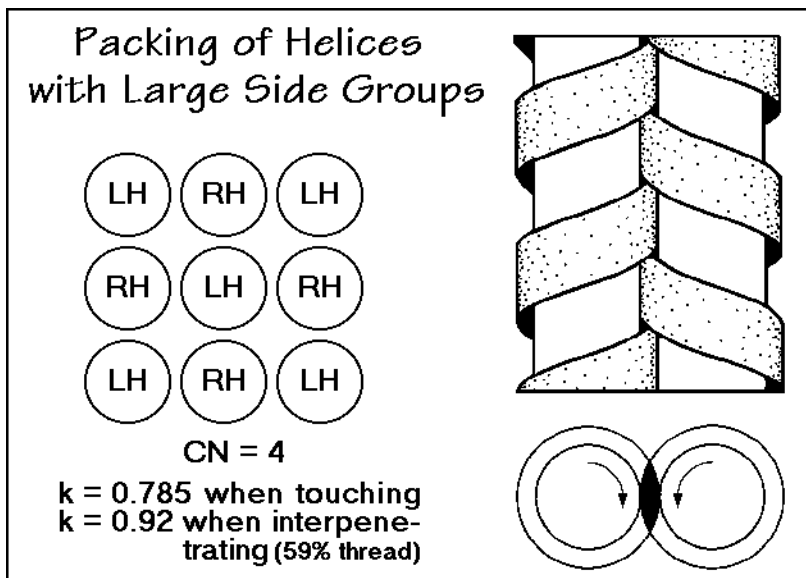


Fig. 5.20

path of the helix by formation of the much shorter covalent bonds. The low-energy helix of selenium is of type  $1\frac{1}{3}/1$ , as is illustrated in Fig. 5.12. The crystal-structure parameters are listed in Fig. 5.20. Its trigonal symmetry lets the helices intermesh and gives each Se, in addition to the normal six laterally nonbonded neighbors, four nonbonded neighbors with shorter secondary bonds, two each in the higher and lower layers. The remaining two neighbors are the very short-distance covalently bonded atoms of the helix proper. Overall, this gives the  $CN$  of 12 as in a close pack of spheres. The unit cell of Fig. 5.20 shows the shortened van der Waals bonds from atom 2 of chain 2 to atoms 1 of chains 1 and 4. These less favorable shorter van der

Waals bonds are offset by the six lateral neighbors. The only other choice of packing would have been to reduce the neighboring chains from six to four, as shown for the organic polymers with more complicated helix geometries.

The helices of organic macromolecules have their side-groups stick out sufficiently without matching the lattice symmetry that intermeshing as in Se is not possible. In these cases the coordination number must be reduced to four, as shown in Fig. 5.21. The raised part of the schematic screws, the threads, can only intermesh (approx-



**Fig. 5.21**

mately) if the contacting screws are of opposite hand, as illustrated in the right-hand sketch of Fig. 5.21. With a coordination number  $CN = 6$ , at least two of the neighboring helices must be of the same hand. A further reduction to  $CN = 3$  is observed for some of the vinyl polymers with helix symmetry three, where a  $CN$  of three permits more regular and denser packing due to the symmetric intermeshing. The same type of reduction of coordination number occurs on packing of ions. Instead of a  $CN$  of 12, that is possible on packing of the atoms of a metal, the  $CN$  is reduced to eight seen for the CsCl structure. With a larger difference in the radii of the two ions,  $CN$  decreases to six to the NaCl structure shown as Fig. 5.2. The directive covalent bonds as in carbon, naturally, fix the  $CN$  to four, the number of permitted covalent bonds. In addition, the covalent bond is directive as pointed out in Fig. 1.5. It directs the positions of the neighbors into the corners of the circumscribed tetrahedron with bond angles to its corners of 109 degrees.

Inspecting the helical molecules of isotactic polypropylene, as discussed with Figs. 5.13 and 5.14 (see also Fig. 1.20), one finds that in crystals the same helix can assume the four different shapes drawn in Fig. 5.22. For closest packing, any given crystal position can accommodate only one of these shapes, not the other three. To produce the four helices of Fig. 5.13, one can orient a polypropylene molecule so that

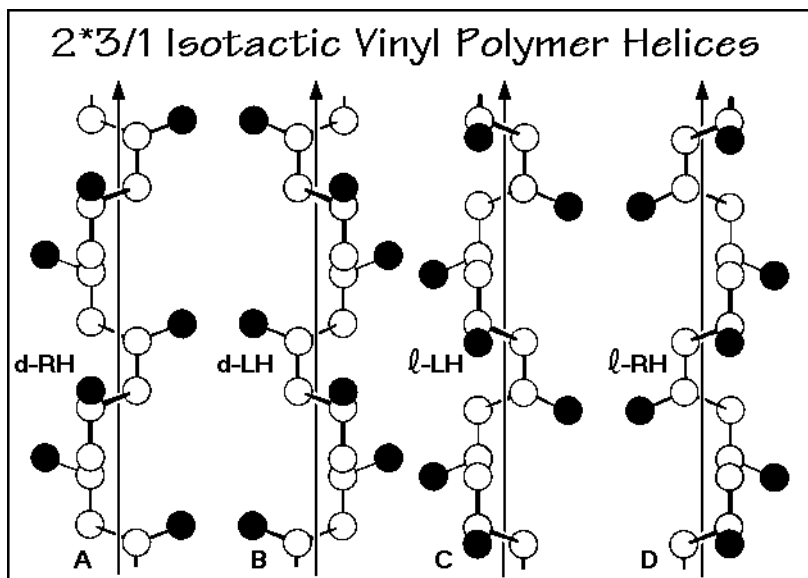


Fig. 5.22

all CH<sub>3</sub>-groups point to the right or to the left. One can place, for example, the molecule of Fig. 5.13 so that all CH<sub>3</sub>-groups point to the right which yields the d-arrangement when progressing in direction C-1 → C-2 or to the left, giving the ℓ-arrangement in the opposite direction C-1 → C-3. A horizontal rotation normal to the plane of the paper by 180 degrees interchanges the two alignments. Next, each of the two differently aligned chains can be wound into a right- or a left-handed helix of equal energy (RH or LH). The equal energetics of the interchange of the handedness of the helix can be seen from the potential energy diagram of Fig. 5.13.

Once a given shape is included in a crystal, a rewinding of the helix with different handedness is possible without changing the helix direction. Such reorganization of the helix can change a polypropylene condensation crystal (see Fig. 2.107) to a crystal, or remove on annealing similar, isolated helix defects in crystals. In both cases a more stable crystal results. The mesophase is described in Sect. 5.5.5 as an aggregate of helix segments of improper handedness. The annealing becomes possible above the glass transition of the mesophase at about 380 K (see Fig. 5.146).

To change the helix direction from d to ℓ, however, takes melting and recrystallization with turning of the molecule or finding some suitable position elsewhere within the crystal. One expects, thus, that quickly grown crystals may show both types of defects, annealed crystals may improve the perfection of the handedness (for polypropylene the larger defect), but only slow crystallization or recrystallization can lead to truly perfect crystals with both, proper directiveness and helicity.

Further inspection of Fig. 5.22 reveals that the d-RH/d-LH and ℓ-LH/ℓ-RH helix pairs have a plane of symmetry between them, i.e., they are enantiomorphous (see Sect. 5.1.5), and the two d-chains have all CH<sub>3</sub>-groups pointing up, while the ℓ-chains have their CH<sub>3</sub>-groups pointing down. All four alignments may occur in crystals, and examples are discussed in the next section.

### 5.1.9 Selected Unit Cells

A number of selected crystal structures of polymers are shown in this section in projection along the helix axes. The poly(ethylsilylethylene) of Fig. 5.23 has its silicon atoms marked by solid circles. Neighboring helices are related by a center of symmetry, so that they must be enantiomorphous and also anticlinal, i.e., the helix pairs have different handedness (d-RH and *l*-LH helices) and opposite inclinations of side-groups (up- and down-helices) as discussed in Sect. 5.1.8. The coordination number for the helices is three instead of the expected four because the  $3_1$  and  $3_2$  screw axes of the  $2^*3/1$  helices match the trigonal lattice symmetry and permit a closer overall packing with CN = 3 rather than 4 (see Fig. 5.21).

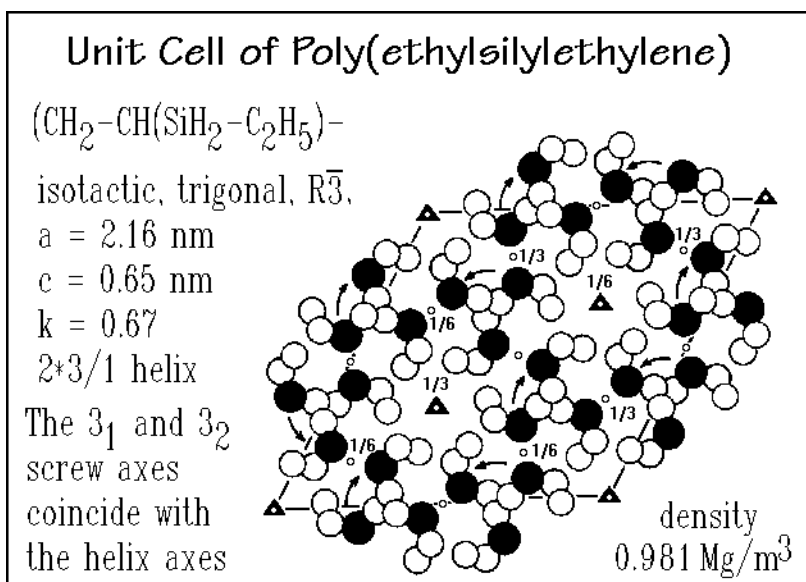


**Fig. 5.23**

The unit cell of poly(*o*-fluorostyrene) crystals is represented in Fig. 5.24. The three visible carbon atoms of the vinyl helix are dotted. Note that, as in all  $2^*3/1$  vinyl helices, the not substituted  $\text{CH}_2$ -group is located directly underneath the CHR-group and does not show on projection into the *ab*-plane (see Fig. 5.14). The fluorine-substituted phenyl group can be used to easily locate the chains. The neighboring helices are separated by glide planes, i.e., the helix pairs must be enantiomorphous and isoclinal. Note that all side-groups in the figure point downwards. A comparison of the packing fraction of the two similar structures of Figs. 5.23 and 5.24 shows a somewhat better packing of the second. This is due to the phenylene groups that can better fill the space between the helices.

Figure 5.25 shows the unit cell of isotactic poly(1-butene). It illustrates a special problem to polymer crystallography. Its space group requires simultaneous presence of centers of inversion and glide planes between the chains. One produces isoclinal neighbors, the other anticlinal neighbors, an obvious impossibility. One solution to

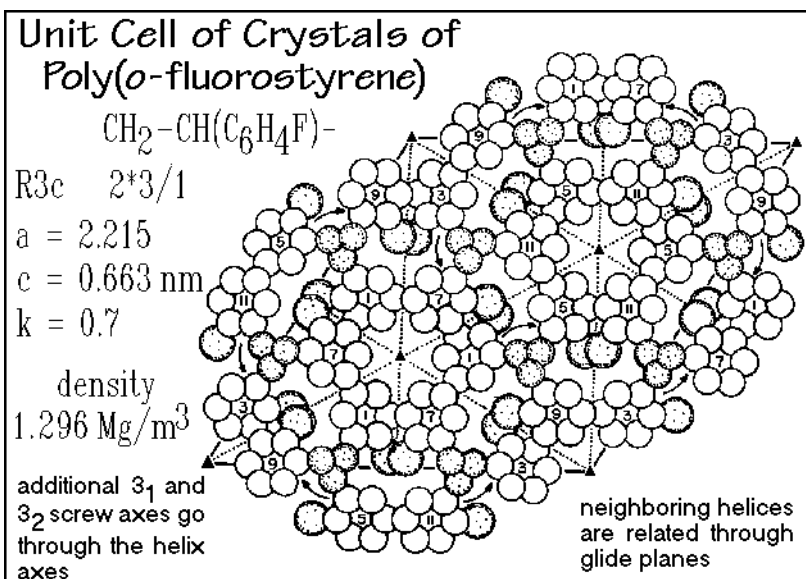


Fig. 5.24

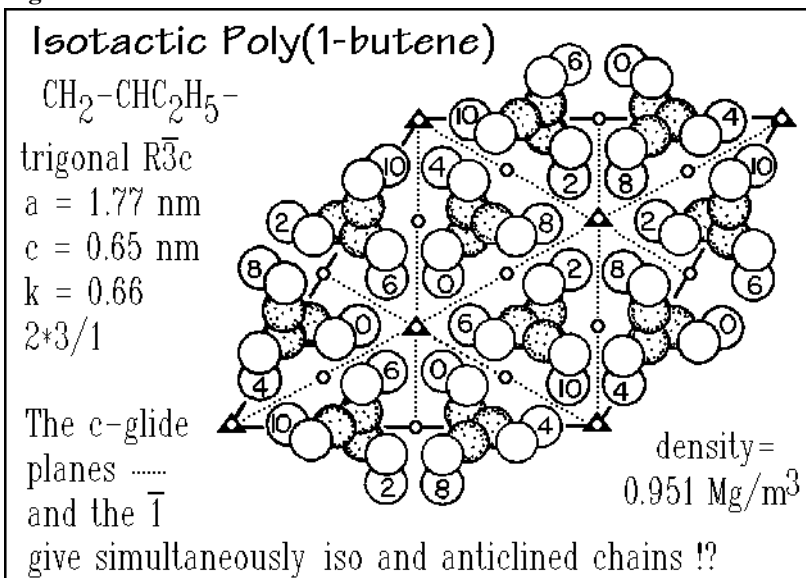
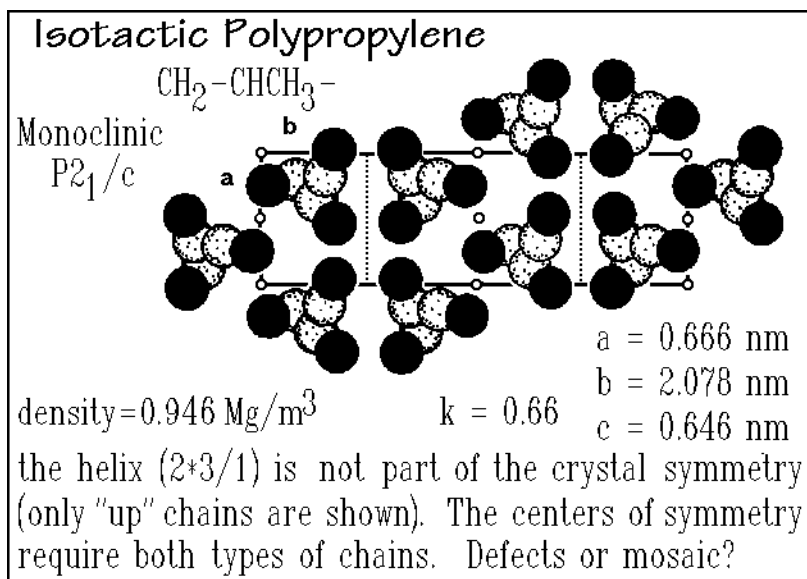


Fig. 5.25

this puzzle is to assume that the crystals consist of mosaics of sufficiently small domains of the different inclinations, so that the X-ray probing the lattice averages over both substructures and records the higher symmetry. Another possibility is that the crystal has complete disorder in inclination of the side groups. Only a detailed discussion of the packing density for the two cases may resolve the actual structure of isotactic poly(1-butene) and similar vinyl polymers.

**Fig. 5.26**

The crystal structure of polypropylene of Fig. 5.26 is closely related to that of the poly(1-butene) of Fig. 5.25. By shortening the  $-\text{CH}_2-\text{CH}_3-$  group to  $-\text{CH}_3$ , the helices can pack more closely and do not need to interpenetrate as much. The pairs of polypropylene helices that are related through the glide planes are then able to touch the next-neighbor pairs because of the smaller side chains, in contrast to the poly(1-butene) in Fig. 5.25. The CN increases, as a result, from three to five, a CN rarely found in crystals. The chains drawn in the figures are all isoclined up-chains. Across the glide planes, the helices are enantiomorphous (LH facing RH and vice versa). The centers of inversion ( $\circ$ ) require, as for the poly(1-butene), that pairs of helices on either side of the center of inversions are anticlined. One assumes, as before, that the actual crystal contains a mosaic of domains of opposite orientation, or a random mixture of the inclination of the chains. Either arrangement is averaged by the X-ray beam and mimics the shown, higher symmetry. The crystal structure of polypropylene is monoclinic, i.e., one of the angles of the unit cell is  $\neq 90^\circ$ . Crystallographic convention makes this the  $\beta$  angle and the unique axis  $b$  (see Fig. 5.4). For polymers, however, one frequently breaks this tradition and keeps the  $c$ -axis parallel to the unique helix axis, as shown for polypropylene ( $\beta = 99.6^\circ$ ). A final point to recognize is because of this choice polypropylene cannot include the helix symmetry  $2*3/1$  as part of the crystal symmetry. This provides the reason for the lower overall symmetry which, in turn, permits the higher and unusual CN of five. Two of the five neighboring chains have, in addition, the same handedness.

Figure 5.27 illustrates the crystal structure of  $\beta$ -*trans*-1,4-poly(2-methyl butadiene), also known as *trans*-polyisoprene or gutta-percha. The  $\alpha$ -crystal is more stable, but not fully identified. The  $-\text{CH}_3$ -group is attached to position 2 in the helix  $4*1/1$ , drawn in the sketch of Fig. 5.27. The methyl group is in this case on the carbon atom that has undergone a right-handed rotation out of the planar zig-zag by about

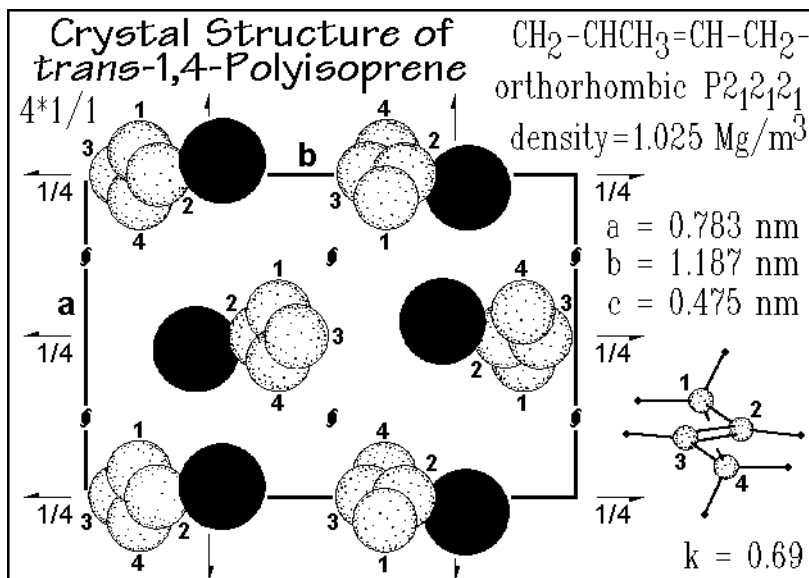


Fig. 5.27

$+75^\circ$  around  $\text{C}_1\text{-C}_2$ . To keep the chain conformation straight, a similar rotation by  $-75^\circ$  occurs around  $\text{C}_3\text{-C}_4$ . Identical crystals can be grown with all  $-\text{CH}_3$  on position 3. A typical sample of  $\beta$ -*trans*-1,4-poly(2-methyl butadiene) should be a mixture of both crystals.

Figure 5.28 shows the unit cell of *cis*-1,4-poly(2-methyl butadiene), also known as *cis*-polyisoprene or natural rubber. This second isomer of polyisoprene (see

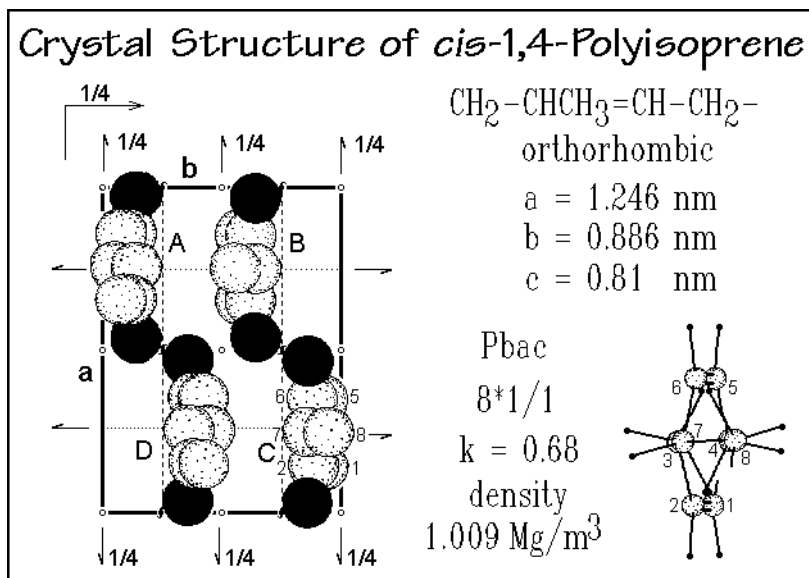
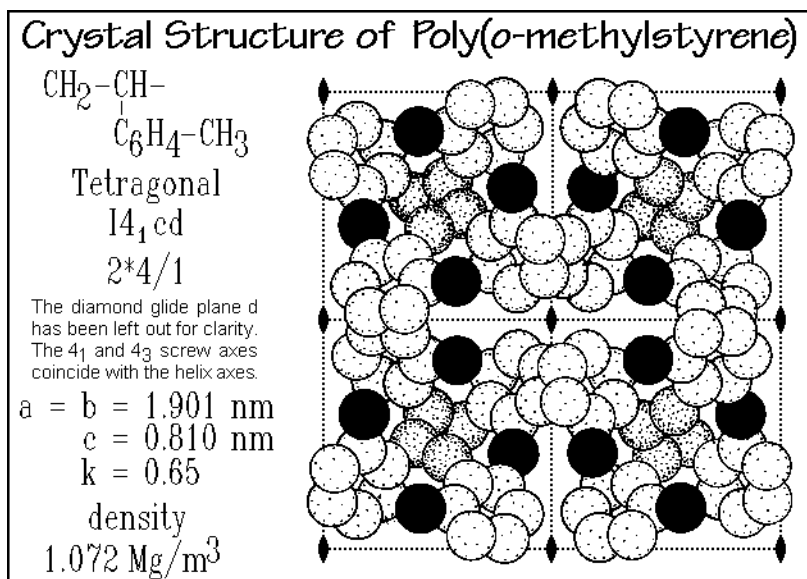


Fig. 5.28



Sect. 1.2) has a less extended chain because of the more compact *cis*-configuration of the double bond. To arrive at an extended chain, the translational repeat has to be doubled, as illustrated in the sketch in Fig. 5.28. Chains A and B have the methyl groups substituted on carbon atoms 3 and 5, but have their chain axes reversed. Chains C and D have the methyl groups substituted on carbon atoms 2 and 6, and again, the action of the screw axis in the *ab*-plane turns the chain in going from C to D. These four possible arrangements of the same chain lead to disorder in the crystals, as in the vinyl helices of Fig. 5.22. The most frequent disorder occurs when pairs A-B and C-D do not alternate regularly.

A coordination number of four is demonstrated by isotactic poly(*o*-methylstyrene) crystals, as shown in Fig. 5.29. The neighboring  $2^*_4/1$  helices are created by the indicated glide planes *c* and are of opposite handedness, but isoclined (drawn are the up chains). Many of the vinyl helices with larger side-groups have  $2^*_4/1$  helices in their crystal structures (see also Fig. 5.14).



**Fig. 5.29**

The polyamides or nylons represent a different type of polymer crystals. Besides the question of packing of the chain, a major energetic advantage is possible by proper placement of the hydrogen bonds  $\text{---N---H}\cdots\text{O=C---}$ . More energy is gained by making one H-bond than by several dispersion bonds. In addition, the H-bonds are directive, severely limiting their placement in the crystal. The crystal structure of nylon 6,6, represented in Fig. 5.30, is characterized by H-bonded sheets in the *ac* crystal plane. Depending on how these sheets are stacked, the  $\alpha$  or  $\beta$  crystal form results. Characteristic is also the placement of the  $\text{CH}_2$ -groups. The crystal is a compromise between the packing of paraffin sequences and amide groups. The crystal structure of nylon 7,7 in Fig. 5.31 can be characterized by tilted H-bonds relative to the chain axis. This aligns the  $\text{CH}_2$ -groups horizontally with the indicated mirror planes. Both

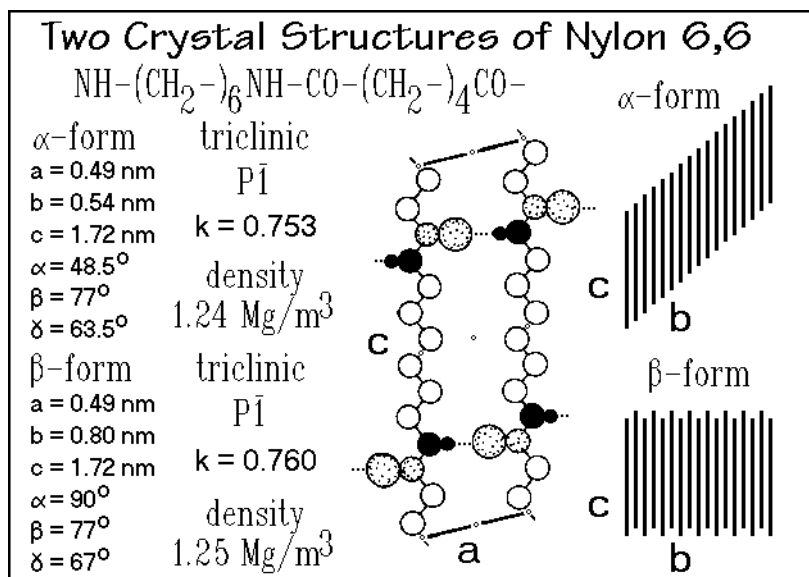


Fig. 5.30

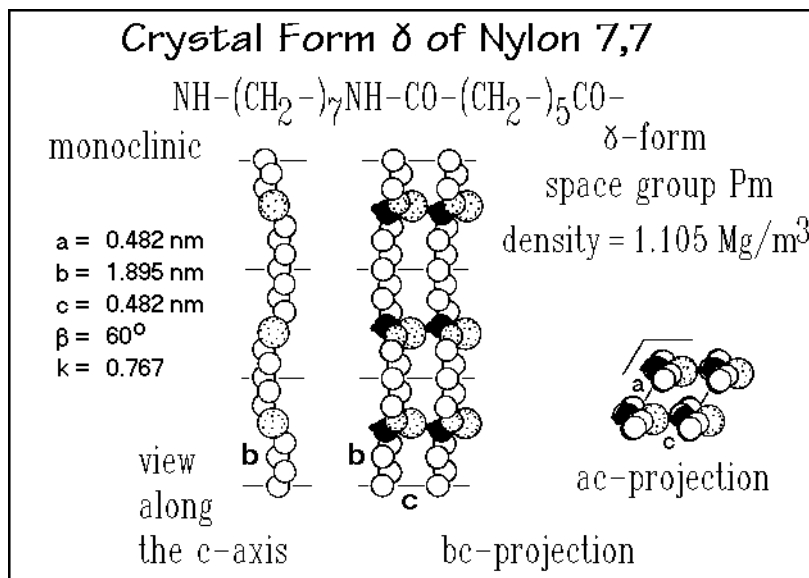


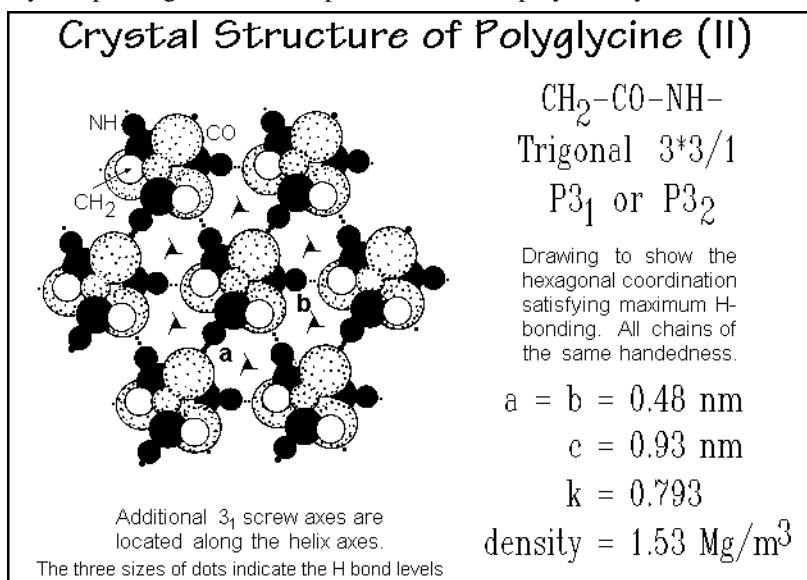
Fig. 5.31

the nylon 6,6 and nylon 7,7 can be looked upon as polyethylenes with inserted amide groups. Due to the effect of the amide groups, the polyethylene substructure is not orthorhombic in packing, but rather triclinic and monoclinic, respectively.

Following the chains of the nylons, one can observe, that in nylon 6,6 and nylon 7,7 there is no difference in direction with respect to the encountered structures. This

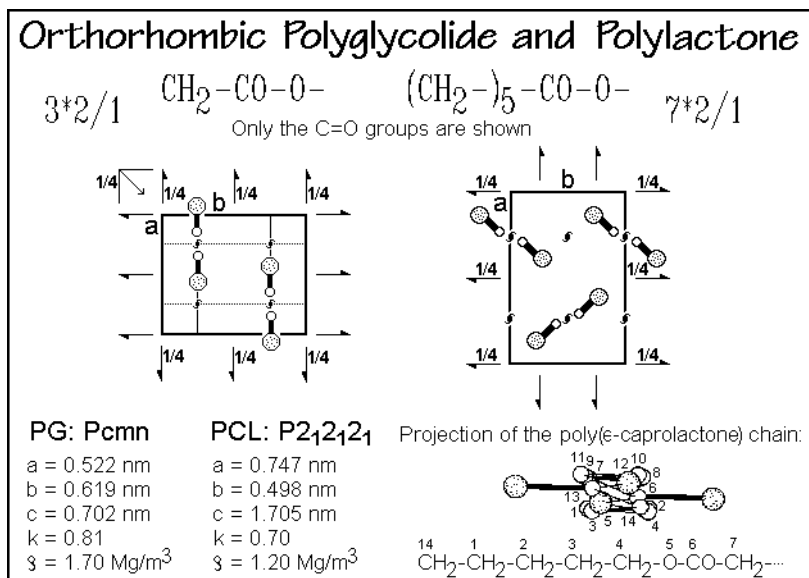
type of structure is called nonpolar. The nylons a, on the other hand, are polar as in nylon 6, see Fig. 1.18 as well as Fig. 3.10. In one direction one always encounters first the NH-group, in the other, first the CO-group. It is possible to classify the nylons according to this polarity and the even or odd number of chain atoms in the a and b sequences. The seven possible combinations distribute themselves in preference for either triclinic or monoclinic crystal structures, as shown above (even, polar, and nonpolar chains prefer triclinic crystals).

Nylon 2 or polyglycine is the homopolymer of the simplest poly(amino acid). It is, thus, also related to the proteins, which are copolymers of the 20 naturally occurring amino acids (see, for example, Sect. 3.1 and Fig. 3.1). Polyglycine is the parent substance of fibrous proteins. The structure of its crystal form II is shown in Fig. 5.32. It is trigonal with closely packed  $3 \times 3/1$ , polar helices containing intermolecular hydrogen bonds. Polyglycine II crystals, thus, are different from the scheme of nylons of Figs. 5.30 and 5.31, and do not assume the intramolecular  $\alpha$ -helix of Fig. 5.16, prominent in proteins. The undistorted, planar, intermolecular pleated-sheet-structure of Fig. 5.16 is only seen in polyglycine I crystals. Such exceptions are common in first members of homologous series where the influence of the paraffin chains is secondary to the stronger polar and hydrogen bonds. Note the rather high density and packing fraction, compared to the other polymer crystals.



**Fig. 5.32**

Figure 5.33 illustrates the same change in crystal structure from the first to latter compounds in a homologous series of polyesters. Polyglycolide contains a three-atom planar zig-zag chain, different from all known polyethylene structures. Neighboring chains in the ac planes form sheets of molecules in the same direction, while neighboring sheets have opposite directions. Noteworthy is the high packing density possible by alignment of the ester groups. In polycaprolactam the  $\text{CH}_2$ -sequences are

**Fig. 5.33**

close to polyethylene, as shown in the sketch of Fig. 5.33. The total length of the chain is, however, somewhat shorter than expected for a full planar zig-zag. It is caused by a tilt of the ester group.

### 5.1.10 Isomorphism

The crystal in Fig. 5.34 illustrates the concept of *isomorphism*, the possibility that two different motifs fit into the same crystal. For polymers isomorphism of repeating units is most important. Isomorphism of complete chains is seldom possible. Poly(vinyl fluoride) that fits into a crystal of poly(vinylidene fluoride) provides a rare exception. The repeating-unit isomorphism can be separated into three types: Type 1 occurs when both homopolymers have the same crystal structure, and a smooth change of the lattice parameters occurs on changing the concentration. An example of type 1 repeating-unit isomorphism is poly(vinylidene fluoride-*co*-vinyl fluoride). Type 2 is also called isodimorphism and occurs if the homopolymers have different crystal structures. A change in structure occurs at an intermediate concentration. Type 3 occurs if one homopolymer does not crystallize by itself, but participates in the crystal of the other.

Figure 5.34 indicates the repeating-unit isomorphism of atactic poly(vinyl alcohol). The  $-\text{OH}$  group on every second chain-atom occurs randomly along the chain, in contrast to isotactic vinyl polymers. Two positions are available for the  $-\text{OH}$ , i.e., in the actual crystal half of these positions remain filled by the smaller  $-\text{H}$ . Only because the size difference between  $-\text{H}$  and  $-\text{OH}$  is sufficiently small, is such a compromise possible.

Figure 5.35 demonstrates the changes in the  $a$ -dimension of polyethylene copolymers with side-chain concentrations. The  $b$ - and  $c$ -dimensions are little affected. Although these results seem to indicate that all groups may be accommo-

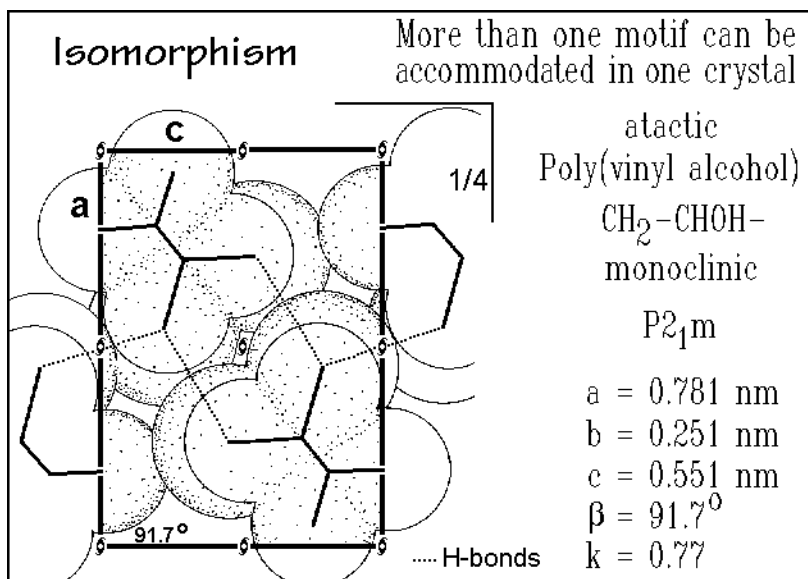


Fig. 5.34

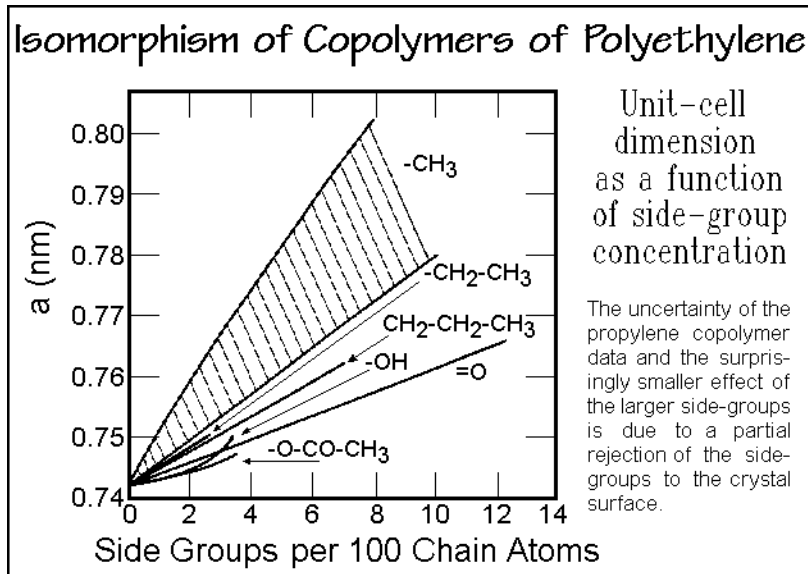


Fig. 5.35

dated, the fact that larger side-groups have smaller effects suggests that the change in  $a$  is produced at the surface of the only nanometer-size crystals. True isomorphism and isodimorphism is limited to  $-\text{OH}$  and  $-\text{CO}$ . Figure 5.36 shows the change in lattice parameters of poly(4-methyl-1-pentene) with inclusion of other side chains (tetragonal crystals, helices  $2 \times 7/2$ , see Fig. 5.14). The crystal structure does not

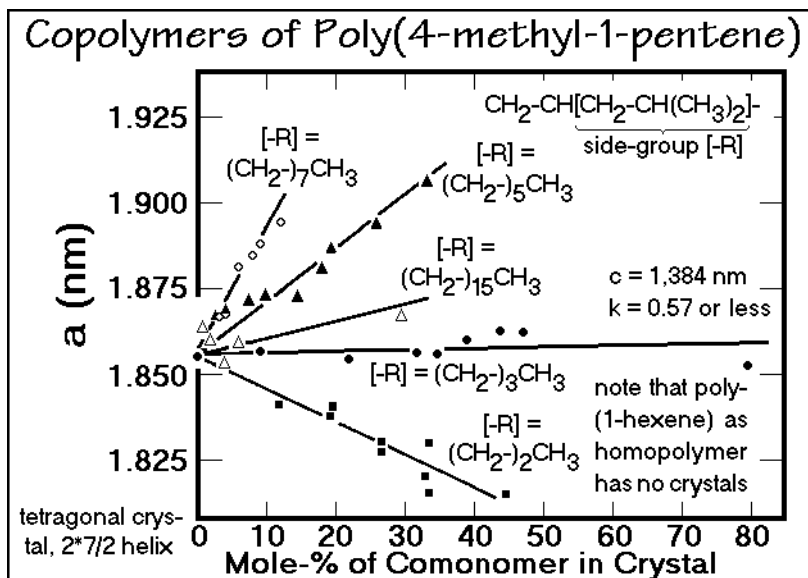


Fig. 5.36

change over the analyzed concentration range (isomorphism). The small influence of  $-(CH_2)_{15}-CH_3$  is explained by exclusion of most copolymer units. Poly(1-hexene) does not crystallize on its own, its isomorphism is thus of Type 3.

### 5.1.11 Crystals with Irregular Motifs

Very large and irregular motifs may also produce a regular, crystalline arrangement. The electron micrograph of the virus, seen in Fig. 2.102 is an example (triclinic, space group P1, with 21.4% water). Similarly, globular proteins may have a sufficiently compact shape to crystallize with the whole molecule being the motif (often orthorhombic and with 10 to 50% water). The motifs of these examples are of such sizes that the spaces between them are too large to be bridged by the van der Waals forces, and large enough to hold small molecules. In the biological molecules these spaces are usually filled with water. Much of the energetics of the crystal structure is then not supplied by packing of the motif itself, but by the interaction with the interstitial water. Similarly, fullerenes, which are still large when compared to the repeating units of many linear polymers, can cocrystallize with small solvent molecules placed in the interstices left between the large motifs. An example is drawn in Fig. 5.37 for  $C_{60}$ . A comparison of this fullerene  $C_{60}$  with other allotropes of carbon is shown on Fig. 2.109.

Block copolymers are another group of molecules with a crystalline-like order with irregular motifs [8,9] (see also Sect. 5.5). Figure 5.38 is a schematic of the triblock copolymer poly(styrene-*block*-1,4-butadiene-*block*-styrene). The two chemically different segments are incompatible and try to segregate as much as possible. The stable structure that arises is a packing of spheres which collect the junction points of the different blocks at their surfaces. The sizes of the motifs are determined by the

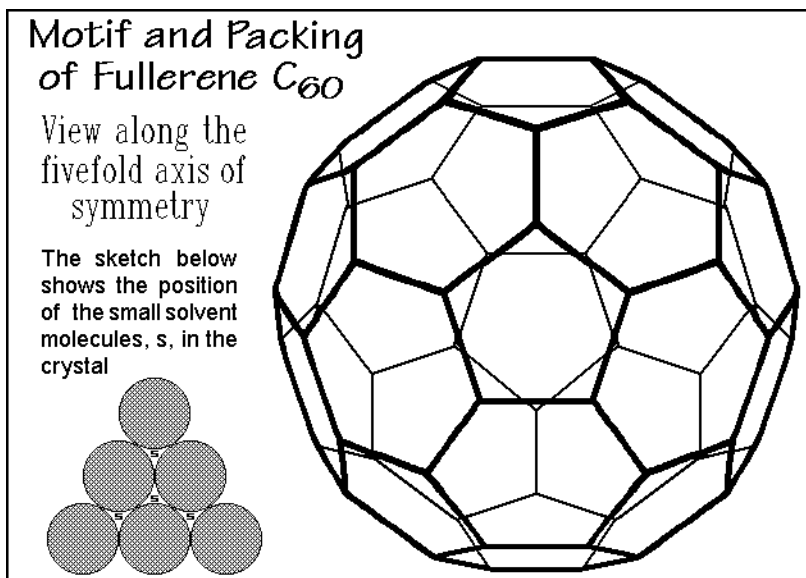


Fig. 5.37

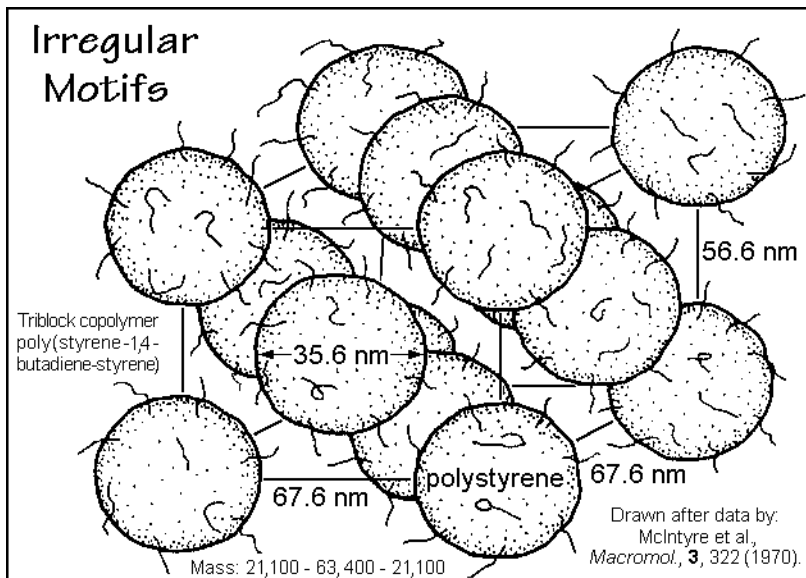


Fig. 5.38

lengths of the sequences. The regular structure is caused by the drive to reach a minimum of the surface free energy, not from packing considerations. Some distance from the interface the polystyrene spheres as well as the 1,4-polybutadiene matrix have their normal, amorphous glassy or liquid homopolymer structure. A triblock copolymer oriented by drawing is illustrated by the electron micrographs reproduced

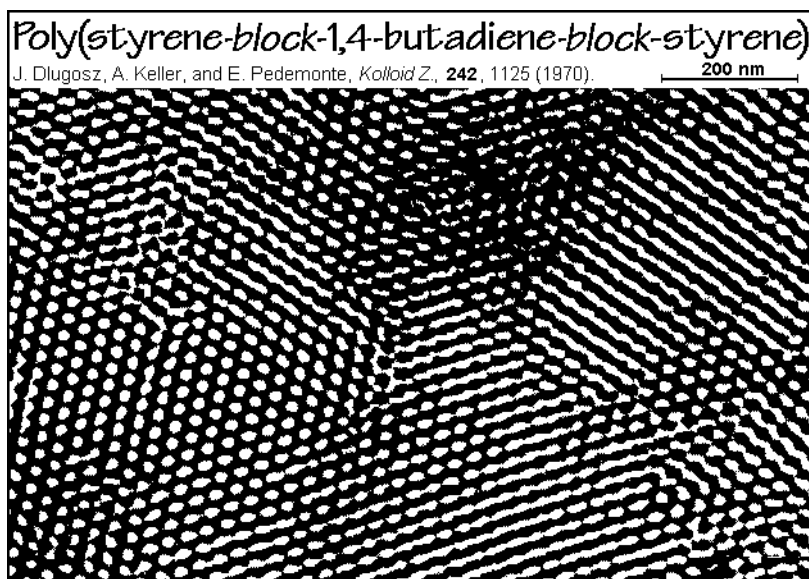


Fig. 5.39

in Figs. 5.39 and 5.40. The contrast is produced by staining the 1,4-polybutadiene, which is above its glass transition temperature, with a heavy metal oxide ( $\text{OsO}_4$ ). Figure 5.39 represents a perpendicular and Fig. 5.40 a parallel cut to the draw-direction. A hexagonal packing of the rods is obvious. See also Sect. 5.5 for more details on these structures which also have been called amphiphilic liquid crystals.

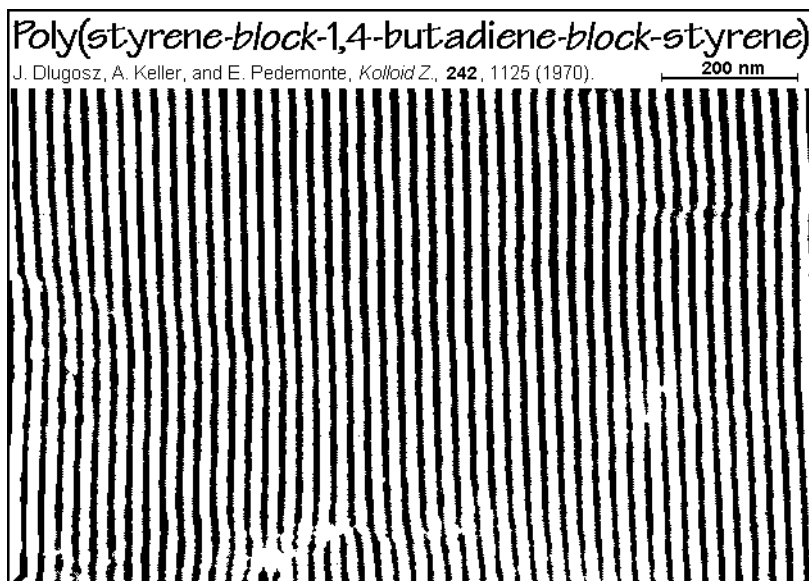


Fig. 5.40



## 5.2 Crystal Morphology

### 5.2.1. Crystal Habit

Crystal morphology refers to the external appearance or shape of a crystal (Gk. μορφή, form, shape). It will be discussed at the level of the appearance of the crystal, its habit (L. *habitus*, appearance) and the conformation of the overall polymer chain within the crystal, the macroconformation of the molecule. A selection of basic habits is given in Fig. 5.41. These terms and their later expansions should be used in the identification of crystal shapes.

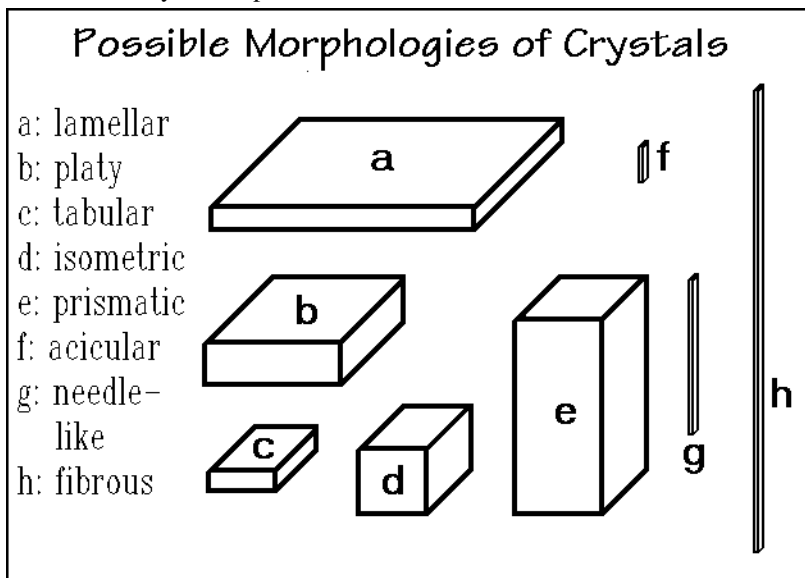


Fig. 5.41

It is not surprising that macromolecules can assume fibrous habits with the long chains aligned parallel to the fiber axis as described in Sect. 5.2.6, but frequently they are also lamellar, with the chain close to normal to the surface of the lamella, as discussed in Sect. 5.2.4. The names fibrous and lamellar habits have in addition to an indication of the shape of the crystal a connotation of flexibility. The isometric habit, i.e., crystals with close to equal dimensions in all directions are rare for the macromolecular crystals, but common for atoms and small molecules (see Sect. 5.2.7).

### 5.2.2 Molecular Macroconformation

The macroconformation is a representation of the overall molecular shape, in contrast to the local conformations, discussed in Sect. 1.3.5 and describes the shape on a repeating unit scale (see also Appendix 14). In the description of crystals, the macroconformation must fit the crystal habit and it must be recognized that polymer crystals are usually small, so that the chain often extends beyond the crystal.

The amorphous macromolecules are entangled *random coils* (see Sects. 1.3). At low temperature these are frozen to glassy solids. Above the glass transition temperature they are viscous liquids (see Sects. 2.5 and 5.6). Corner A of Fig. 5.42 gives a schematic representation of the amorphous macroconformation of a polymer in the solid (glassy) or liquid state.

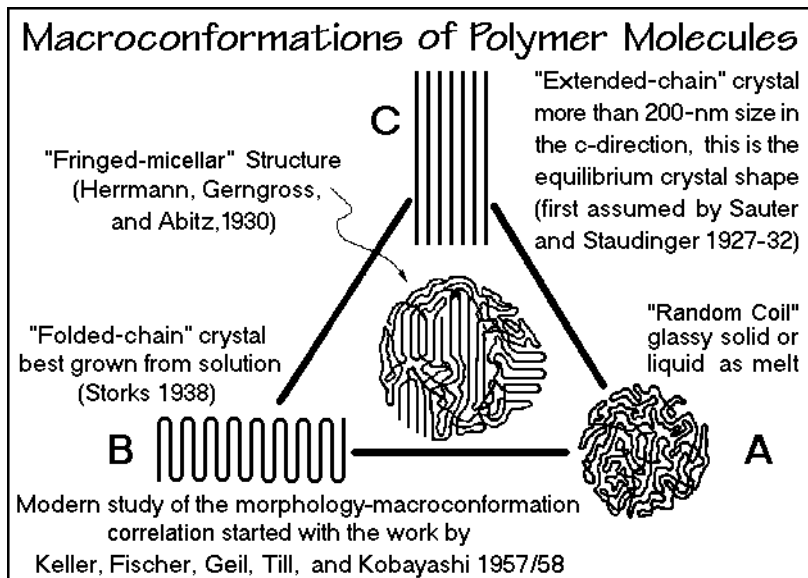


Fig. 5.42

To identify the macroconformation of an equilibrium crystal, one must first find the helix of lowest energy and then pack such helices densely, side-by-side as described in Sect. 5.1.8. Such crystals are of an *extended-chain* macroconformation, as illustrated schematically at corner C of Fig. 5.42. Two problems prevent the common occurrence of extended-chain crystals. First, unlike in short, small molecules, macromolecules are not all of the same length. They could, thus, not produce a smooth, low-energy surface with their chain ends. Second, flexible molecules in the melt or in solution are not sufficiently extended to immediately go to the equilibrium crystal. To produce the extended-chain macroconformation, a substantial reduction of its entropy is necessary, producing a barrier of positive free enthalpy of extension ( $\Delta G = -T\Delta S$ , see the discussion of entropy elasticity in Sect. 5.6.5). The ultimate compensation of the entropy of extension can occur only after the packing of the molecule into the crystal is achieved and all heat of crystallization has been absorbed ( $\Delta H_{\text{cryst}} = T_m \Delta S_{\text{cryst}}$ ). If the major disentanglement and close packing do not occur in close succession, i.e., are decoupled processes, the nonequilibrium path to the crystal leads to arrested, metastable states.

A path with a lower positive free-enthalpy barrier to crystallization than to the extended-chain crystals involves a *folded-chain* macroconformation and leads to the *chain-folding principle*. Crystallization occurs first with shorter, chain-folded segments of the molecules, as shown schematically at B of Fig. 5.42 (A  $\rightarrow$  B). From

the most mobile amorphous state with separated macromolecules, the dilute solution, rather perfect lamellar crystals have been grown as is illustrated in Sect. 5.4. The path  $A \rightarrow C$ , in contrast, is not possible for flexible macromolecules. After the initial folding, extended-chain crystals result only, if there is sufficient mobility in the folded-chain crystal to permit annealing with chain extension, as is documented in Sect. 5.7. The mobility is linked to a *sliding diffusion* within the crystal [10]. Frequently, such mobility is found in conformationally disordered mesophases (condensed crystals, see Sects. 2.5 and 5.5). Another path to extended chain crystals is crystallization during polymerization. In this case the mobile monomer goes directly to the polymer crystals, i.e., the randomly coiled amorphous phase is bypassed. Examples of crystallization during polymerization can be found in Fig. 5.77, below for polydiynes, Fig. 3.104 and 3.105 for poly(oxymethylene), and Figs. 3.86 and 3.16–22 for lithium polyphosphate. On crystallization from the most mobile state, the gas phase, rather perfect extended-chain single-crystals have been grown. A typical example is Se, which can easily be grown into large, equilibrium crystals [11]. For the crystal structure of Se see Fig. 5.20.

The corners A, B, and C in Fig. 5.42 form the three limiting molecular macroconformations. All three were described in the 1930s [12 and 13], but applied only in the 1960s and 1970s, following the fundamental work of Keller (UK), Fischer (Germany), Geil and Till (USA), and Kobayashi (Japan) [14–18].

A *fringed-micellar structure* was proposed in 1930 for the structures of colloids and gels [19]. By adding the possibility of chain-folded crystals, as illustrated in the center of Fig. 5.42, all three limiting macroconformations are combined. Semicrystalline polymers, thus, are a system consisting of folded-chain crystals, intercrystalline amorphous, and possibly extended-chain subsystems (see Fig. 2.80). The latter are expected particularly in fibers drawn to large extension. Most samples have a macroconformation somewhere within the triangle of Fig. 5.42.

The dimensions of the crystal and amorphous subsystems vary from nanometers to micrometers, i.e., polymeric materials are nanophase- or microphase-separated and have only a partial crystallinity. If we treat homopolymers as one-component systems, the phase rule of Sect. 2.5.7 does not permit equilibrium between two phases, except at the transition temperature. Partially crystalline homopolymers are, thus, not in equilibrium. The properties of semicrystalline polymers are critically influenced by the interactions between the amorphous and crystalline domains, as is seen in the formation of rigid amorphous fractions, discussed in Sect. 6.1.3 and 6.3.4.

### 5.2.3 Fold Length

The lamellar thickness of the crystal, and with it the fold length of the macroconformation, is a function of the crystallization conditions. Figure 5.43 illustrates the temperature dependence of the lamellar thickness on the example of polyethylene crystallized from various solvents. The curves in the figure shift proportionally with the temperatures of dissolution of equilibrium crystals and reveal that the supercooling of the solution is the main factor determining the fold length. On approaching the longer fold lengths at higher crystallization temperatures, the crystallization rate slows and finally it becomes impossible to wait for crystallization.

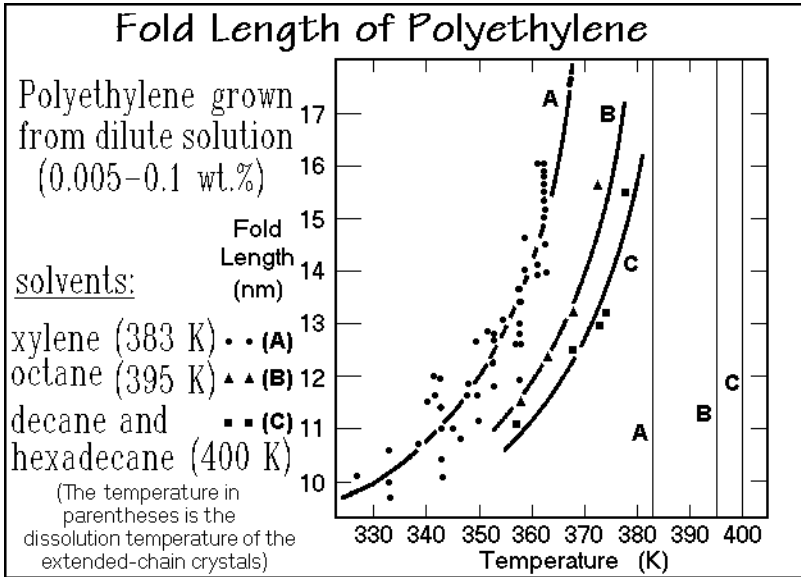


**Fig. 5.43**

Crystallizing of polyethylene from the melt increases the crystallization temperatures, as shown in Fig. 5.44. Up to about 400 K the curve is similar to the solution case, except that at higher temperature, the fold length increases strongly. The crystal growth-rate is small at this temperature and the main mechanism for the increase in fold length is an annealing in the solid state, i.e., the chains extend by longitudinal diffusion within the already grown crystal, called sliding diffusion [10].

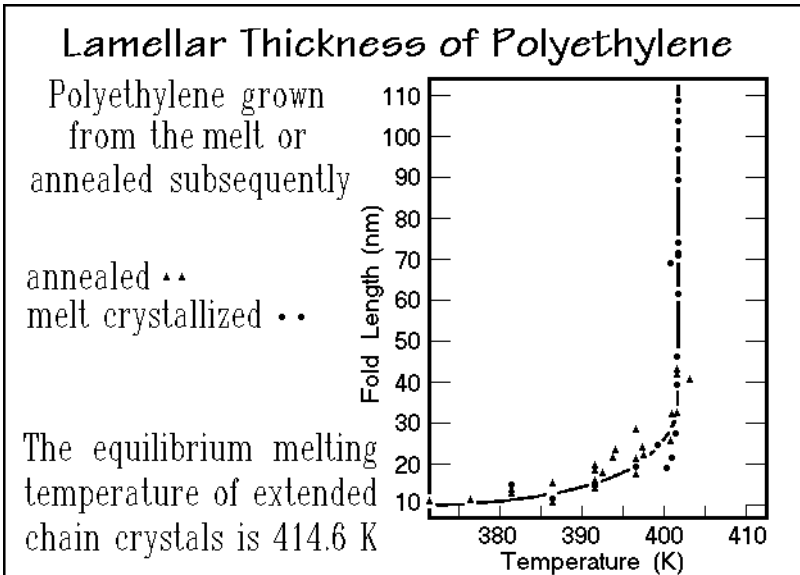


**Fig. 5.44**

The fact that the lamellar thickness is not mainly a function of temperature, but of the degree of supercooling, expressed by  $T_m - T_c$ , can also be deduced from Fig. 5.45 which shows the results of crystallization of polyethylene from dilute solution at increasing pressure. The crystallization temperatures were chosen at about equal supercoolings, but increasing temperatures. On going from atmospheric pressure to 500 MPa, the crystallization temperature was increased from 360 K to 445 K. The

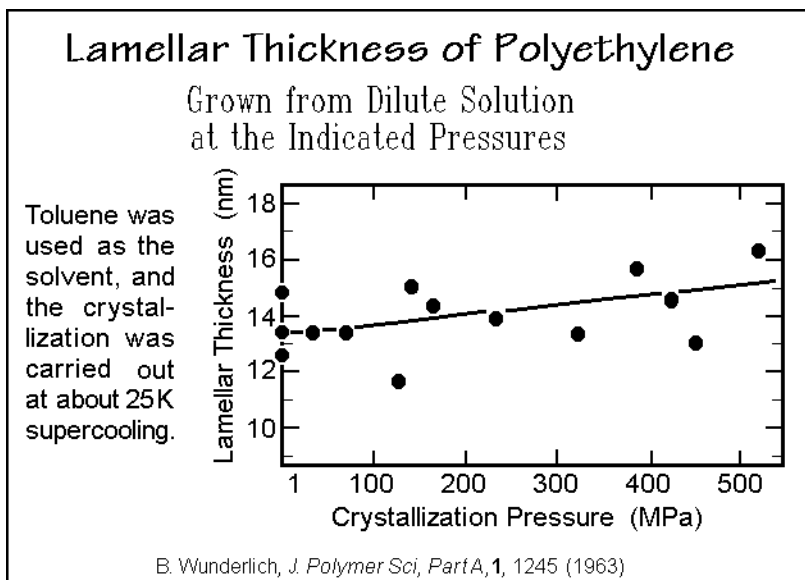


**Fig. 5.45**

increase in thickness on crystallization under higher pressures under these conditions is small and approximately proportional to  $1/T$ , in contrast to the atmospheric-pressure data of Fig. 5.43.

Crystallization of polyethylene from the melt under elevated pressure of more than 300 MPa leads to crystals that are initially folded, but extend increasingly faster with temperature because of the existence of a hexagonal mesophase, discussed in Sect. 5.5 and shown also in Sect. 5.7. In Fig. 5.46 one can see that at higher temperature the subsequent thickening at 500 MPa increases quickly at higher temperature, reaching practically full extension at about 500 K. The data in Fig. 5.47 illustrate lesser rates of thickening at atmospheric pressure. In all cases the annealing of polyethylene to greater thickness is a process which accelerates with temperature, in contrast to the initial crystallization rate, which decreases as one approaches the melting temperature (see Sect. 3.6).

The question of the length of a flexible macromolecule before it folds on crystallization was first measured on oligo-urethanes:



Figure 5.48 documents that the short-chain oligomers crystallize fully extended. As the chain length increases to the fold-length of the polyurethanes, the molecules fold,

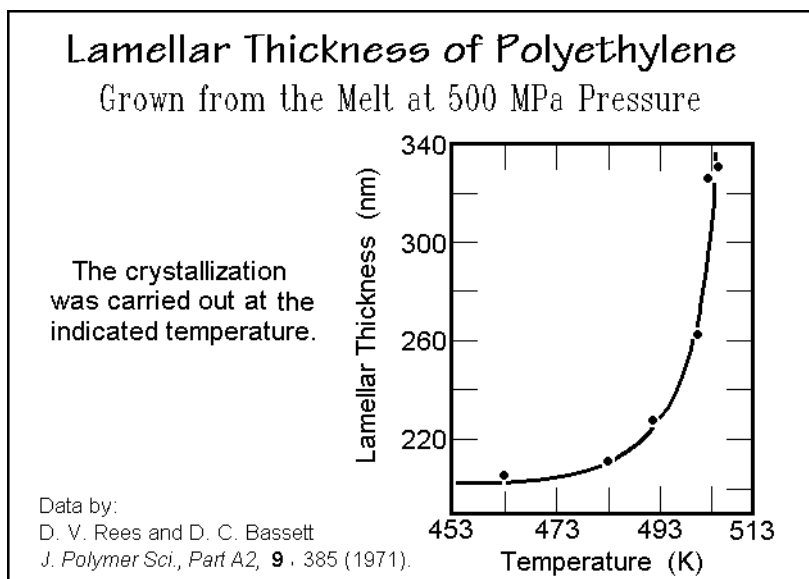


Fig. 5.46

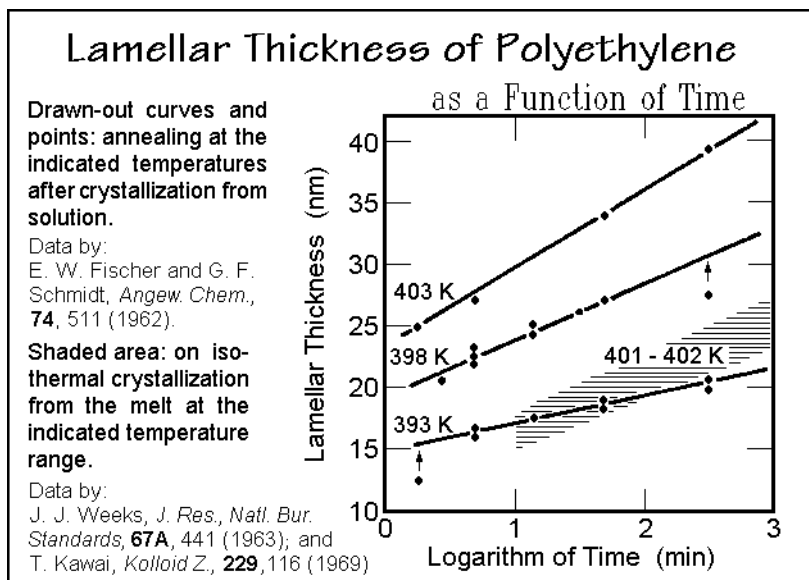


Fig. 5.47

as expected from the larger entropy of chain extension. For paraffins the limit of growth in the extended-chain form has been reported to be 37 nm ( $C_{294}H_{590}$ , molar mass 4,100) [20]. When rather sharp, low-molar-mass fractions of poly(oxyethylene) molecules became available, it was found that, depending on supercooling, molecules could grow as extended chain, once, and multiply folded crystals. Figure 5.49 displays the data for 10,000 and 25,000 molar masses. The high-molar-mass sample

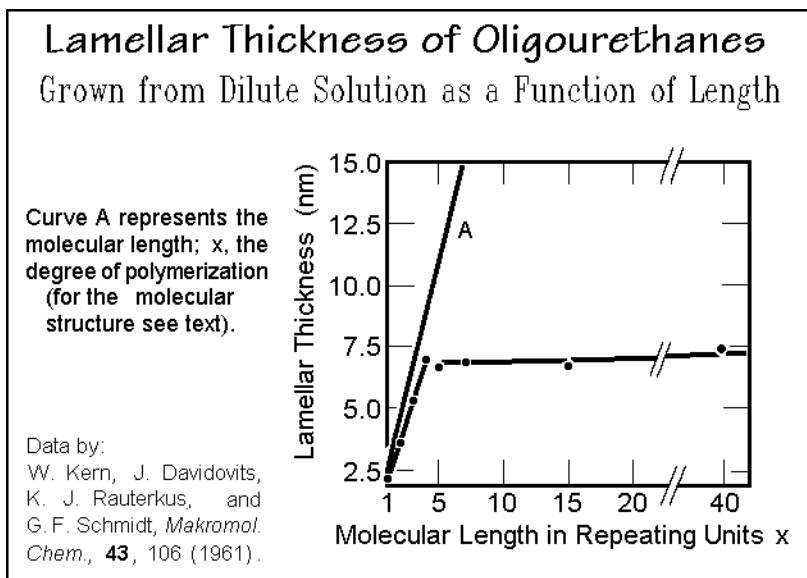


Fig. 5.48

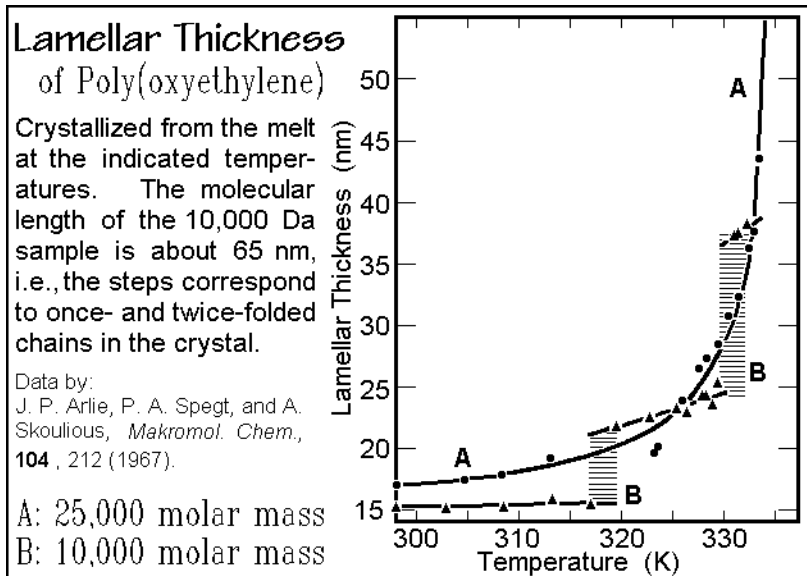


Fig. 5.49

has a fold length which changes continuously with supercooling, while the low-molar-mass sample shows the step-wise change due to integral folding, with the high-temperature crystallization leading to once-folded molecules.

Theories about the details of the fold-length dependence of lamellar crystals have gone through many steps, but are not fully resolved at present. References to some

of the more detailed discussions are listed in the general references to this section. A theory of polymer crystallization must explain not only the fold length, but also the rejection of different molecular masses on crystallization, the reasons for the larger supercooling than even necessary for chain folding, the increases and decreases of the initial fold length on annealing at the crystallization temperature, the attainment of integral folds for molar masses, and the regularity of folds (see also Sect. 3.6).

### 5.2.4 Lamellar Crystals

In the following figures the morphology of folded-chain single-crystals is shown with a series of electron and optical micrographs [21]. The regular hexagonal lamellae of poly(oxymethylene) in Fig. 5.50 permits the easy recognition of trigonal crystal symmetry and an assignment of the Miller indices for the crystal structure indicated in Fig. 5.12. The folds are aligned in the  $\{001\}$  lamellar surfaces. The  $(\text{CH}_2-\text{O})_x$  chains have  $2\frac{9}{5}$  helices with bond rotations of  $102^\circ$ , close to a continuous succession of *gauche* conformations.

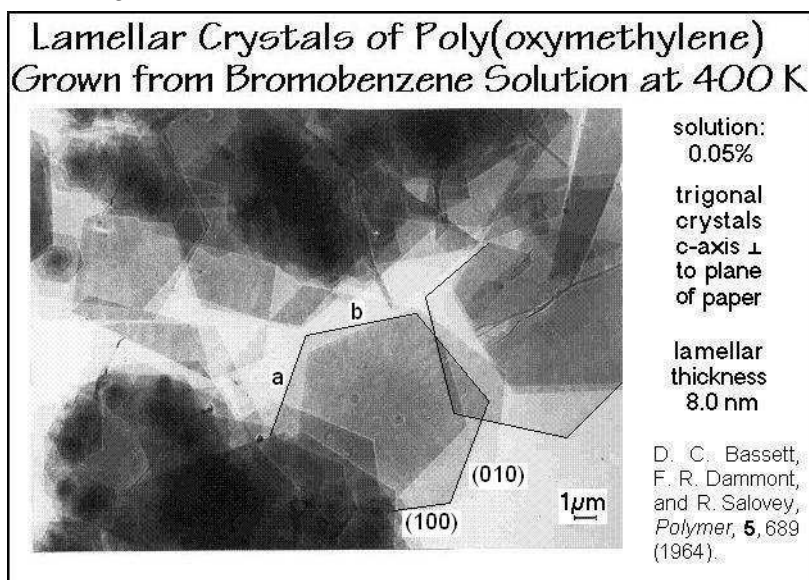


**Fig. 5.50**

Figures 5.51 and 5.52 show the special features of polyethylene grown from dilute solution. The two folded-chain lamellae in Fig. 5.51 can easily be recognized as orthorhombic crystals. The fast-growing faces on crystallization, causing the lamellar morphology, are of type  $\{110\}$ . These are the active growth faces where new folded chains are added on crystallization. The top and bottom faces should then be  $\{001\}$ . The crystals in Fig. 5.52 display additional  $\{100\}$  faces. These develop often on crystallization at higher temperature and are prominent on crystallization from the melt. Also, one can see that the lamellae develop growth spirals, defects that permit thickening along  $c$ . Otherwise the fold surfaces preclude growth in direction  $[001]$  (see Sects. 3.6 and 5.3). Some special features are the pleats in the crystals, which are



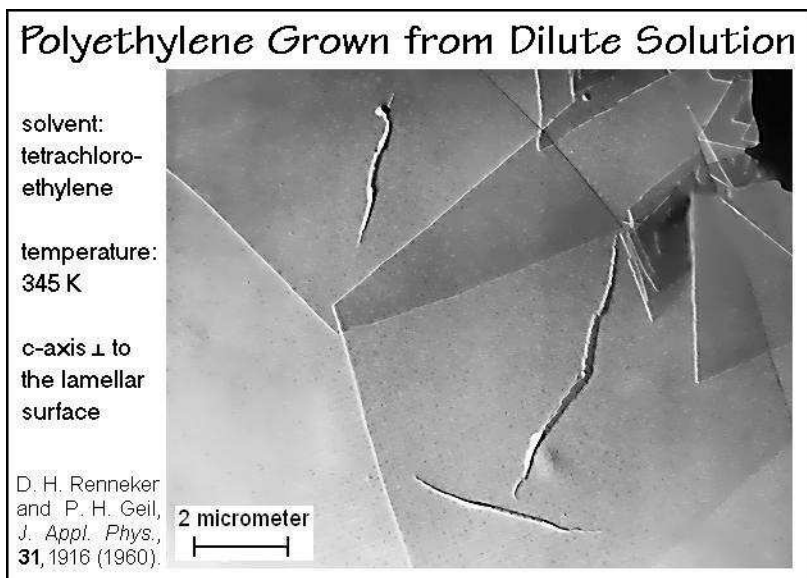


Fig. 5.51

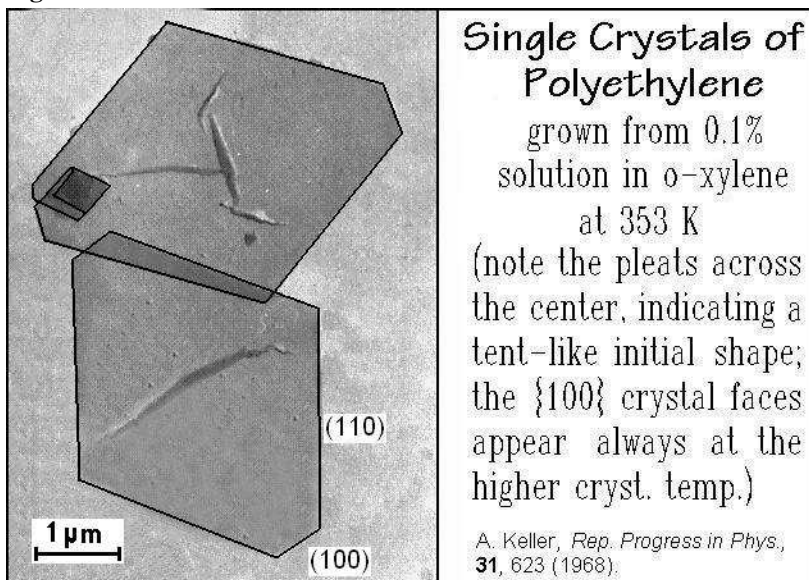
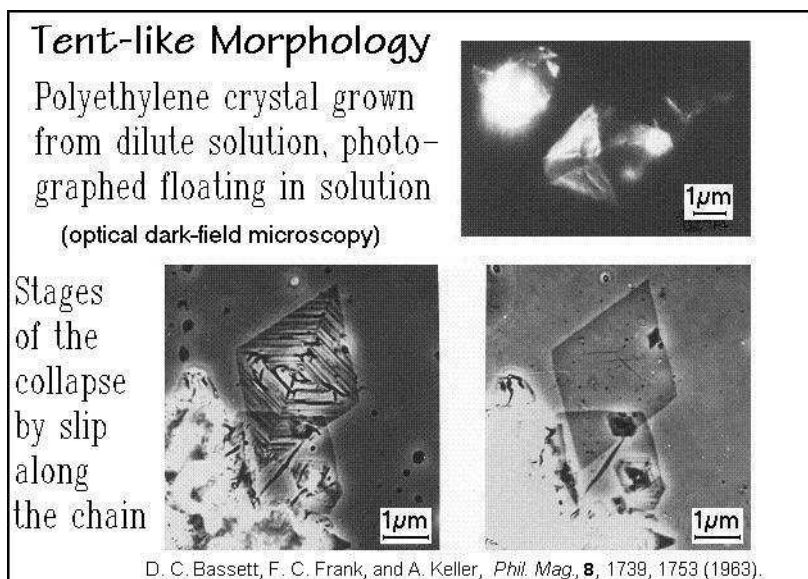


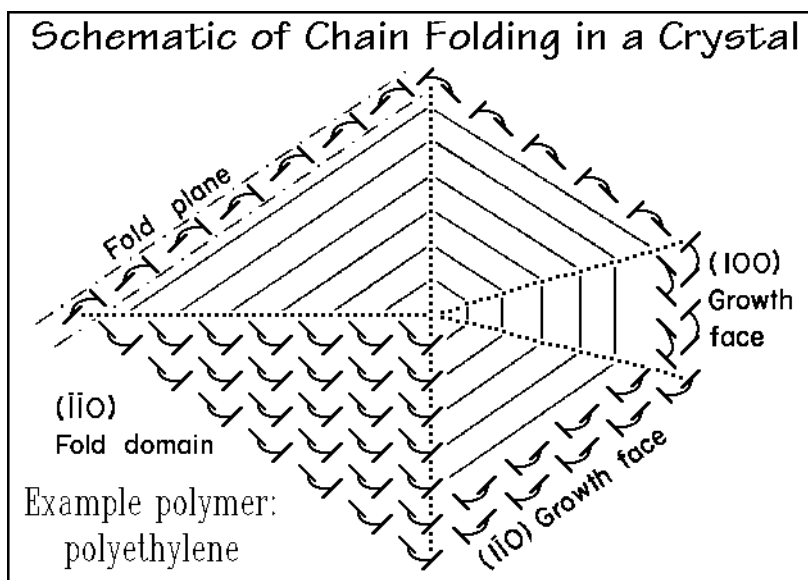
Fig. 5.52

roughly parallel to the a- and b-axes. The optical micrographs in Fig. 5.53 reveal the origin of the pleats. They indicate that, while floating in solution, the crystals are not actually flat, but are tent-like, as is actually seen in the upper optical micrograph for a crystal of the type seen in Fig. 5.52. The floating crystal displays sloping lamellar surfaces of indices  $\{312\}$  for the faces leading to the  $\{110\}$  growth faces, and  $\{201\}$  adjacent to  $\{100\}$ . The pleats are produced on collapse of the tent. The two bottom

**Fig. 5.53**

micrographs show two stages of the collapse of tent-like crystals of polyethylene of the type illustrated in Fig. 5.51. The collapse shows first a development of pleats, then a complete slip to an almost flat lamellar surface. The type of pleat that ultimately develops depends on crystal size and substrate.

The schematic of the crystal in Fig. 5.54 represents a composite of the two growth morphologies illustrated in Fig. 5.51–53 [21]. The left half shows two {110} growth

**Fig. 5.54**

faces, the right half displays an additional (100) growth face. The zig-zag planes are marked by the short straight-lines, the upper folds by the arcs. The crystallographic b-axis is represented by the dotted vertical (the upward direction is +), the a-axis is the horizontal (with the direction to the right being +). In order to make the coordinates right-handed, the c-axis points up, out of the plane of the paper (compare to Fig. 5.19). For simplicity, the crystal is taken not to be tent-like. The growth sequence can now be read from the drawing. Once a chain is attached by molecular nucleation, as outlined in Sect. 3.6 with Fig. 3.74, additional chain segments follow in sequence along the fold plane with alternating chain folds at the top (shown) and at the bottom (not shown, connecting the open space between two adjacent chains). This growth sequence develops four or six separate growth domains in each crystal, unique for polymer crystals. The fold-domain boundaries are recognizable only at the surface. In the interior, the crystal lattice is continuous. The full description of the folded-chain single-crystals can, thus, either be done by specifying the unit cell of the repeating unit and adding the surface structure as a defect, or by treating each growth domain as a separate lattice with a unit cell that includes the fold. In the latter case, the c-dimension of the unit cell would be the lamellar thickness, and the domain boundaries would act as twin boundaries. A *twin boundary* connects two lattices of the same type symmetrically. The macroscopic twin crystal shows an added symmetry element. In the case of the fold-domain boundary across (010), it is a glide plane, macroscopically recognized as a mirror plane. The glide distance is of the repeating unit dimension ( $a/2$ ).

Twin crystals based on the lattice of the repeating unit are also common in the growth of macromolecular crystals, as shown, for example, in the poly(oxyethylene) crystal of Fig. 5.55. It grew out of a small droplet of a melt. The multiple twin has its chain axis tilted to the a-axis by  $126^\circ$ , so that the axis shown in the figure is the

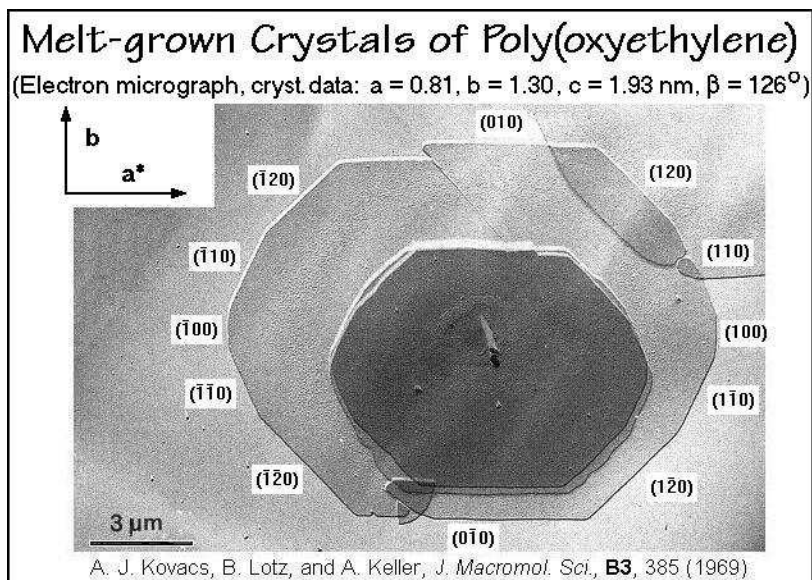


**Fig. 5.55**

projection to  $90^\circ$ , labeled  $a^*$ . The chain consists of a  $3\frac{7}{2}$  helix. Again, the growth in direction  $c$  was possible via growth spirals or screw dislocations as shown in Fig. 3.72. The growth spirals in Fig. 5.55 are visible in the center in form of a terrace, a combination of two growth spirals of opposite handedness as described in Sect. 5.3, and at the lower edge as a standard left-handed spiral.

### 5.2.5. Dendrites and Spherulites

Only on relatively slow crystallization do folded-chain single crystals grow. As the crystallization speeds up, problems arise in solution with the diffusion of molecules to the growth front, and in the melt with conduction of the heat of crystallization away from the growth front, as is discussed in Sect. 3.6. Instead of large, flat crystal surfaces, skeletonized, serrated surfaces are produced by a decrease of the polymer concentration in front of large, flat growth faces, as illustrated in Figs. 3.80–82. Well-known dendrites are the snowflakes illustrated in Fig. 5.1. Similar looking dendrites of polyethylene are illustrated in Fig. 5.56. The picture is an interference micrograph, so that the dark interference fringes signify the increasing thickness of the dendrite towards the center. The increase in thickness between two interference fringes is about  $1\text{ }\mu\text{m}$  or the thickness of 100 lamellar crystals. Screw dislocations allow the

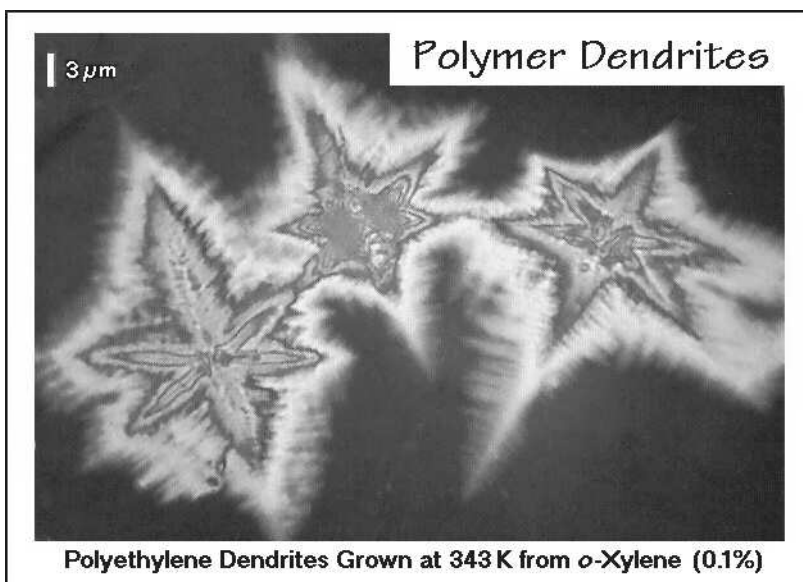


Fig. 5.56

thickening in the  $c$ -direction which is normal to the plane of the paper. Figure 5.57 gives the molecular mass and supercooling-dependence of dendritic and single crystal growth. At the boundary between single-crystal lamellae and dendrites, one can find intermediate morphologies, such as single crystals or growth spirals with sharpened edges as shown in Fig. 3.81. On entering the area of dendritic growth, branches develop which ultimately change to dendrites as seen in Fig. 3.82.

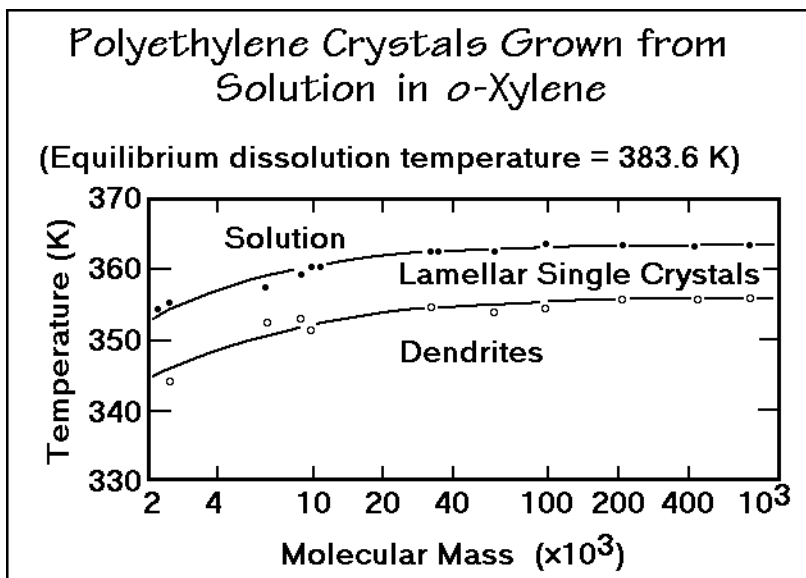


Fig. 5.57

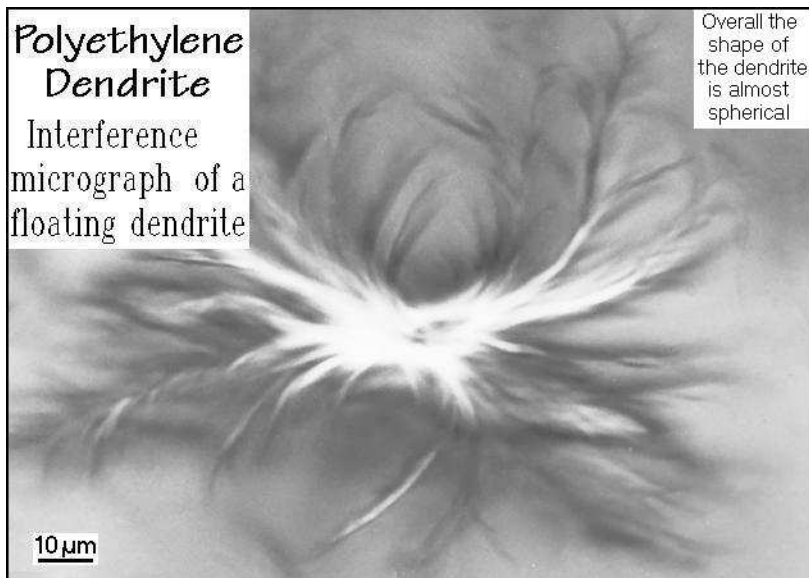
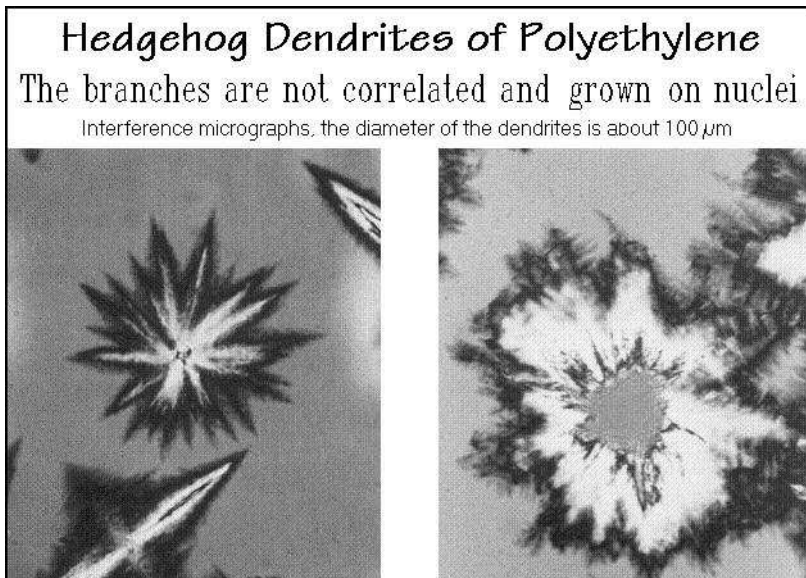


Fig. 5.58

Figure 5.58 represents a polyethylene dendrite still floating in the solvent out of which it was grown (causing the reduced contrast). It reveals that dendrites do not grow flat, as the snow flakes of Fig. 5.1, but splay apart from a common center, the crystal nucleus. Only on settling on the microscope slide is the regular nature of the dendrite shown as seen in Fig. 5.56. Similar three-dimensional shapes are also found

in single crystals with growth spirals due to the tent-like structure, illustrated in Fig. 5.53. Continued twinning is the ultimate cause of the growth of a dendrite, coupled with the creation of many growth spirals to thicken the crystal.

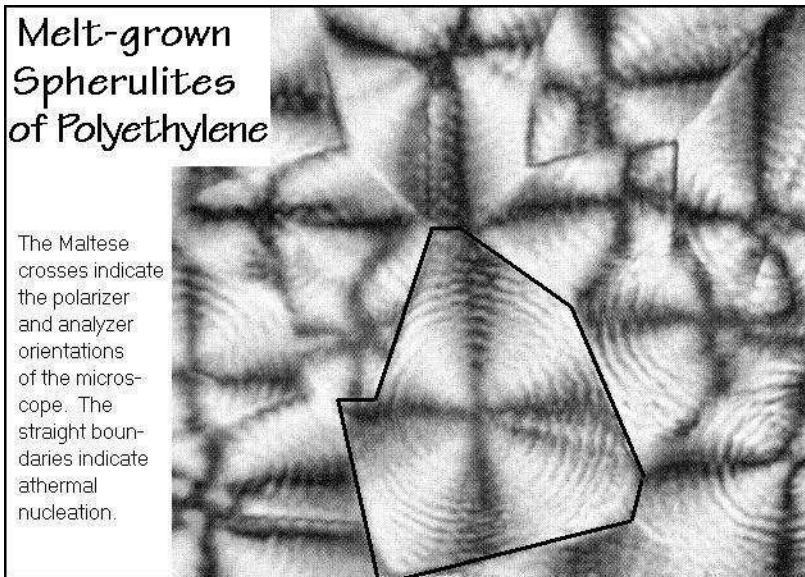
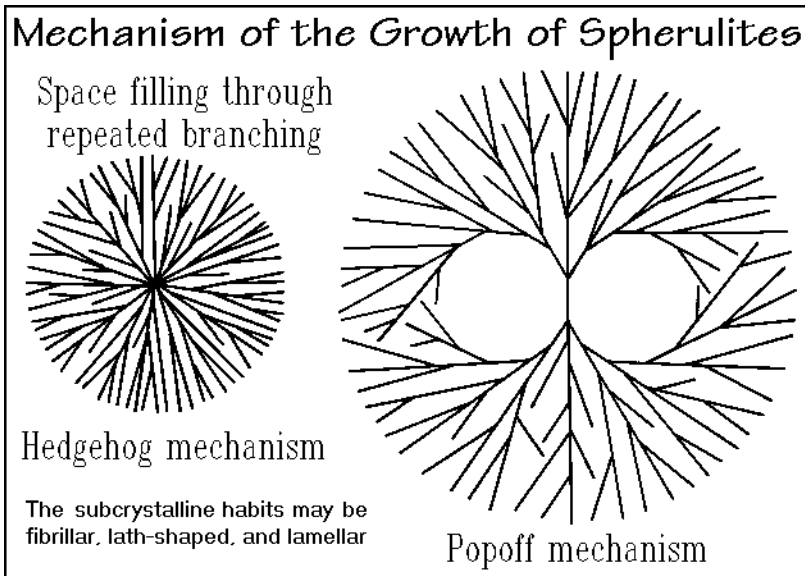
Hedgehog dendrites as shown in Fig. 5.59 are a special class of dendrites. They lack the special symmetry between the branches of the dendrites in Fig. 5.56. An explanation is their start from heterogeneous nuclei, described Sect. 3.5. Indeed, nucleating material added to the solution was found to reside in the center of the hedgehog dendrites. The regular dendrites of Fig. 5.56 grow from an initial, small single crystal that cannot keep straight growth surfaces because of the fast crystal growth. Observing crystal morphology may thus reveal the type of nucleation.



**Fig. 5.59**

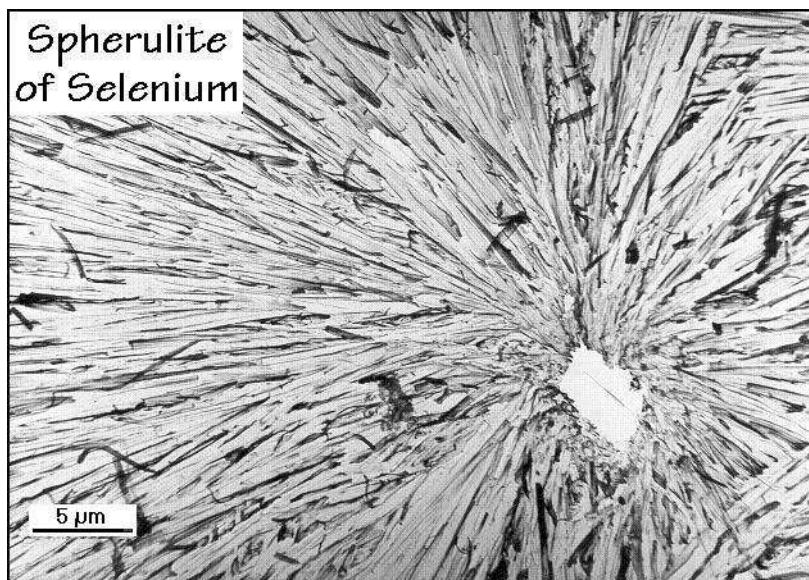
Fast growth of crystals from the melt produces spherulites, as shown schematically in Figs. 3.55–57 and illustrated by the micrograph in Fig. 5.60. In most of these spherulites one expects also a dendritic morphology. The high polymer concentration in the melt, however, hinders the separation of the branches. The birefringence of the polymer crystals gives the spherulites their characteristic appearance under the polarizing microscope illustrated in Fig. 5.60. The birefringence and polarizing microscopy are discussed in Appendix 15. Although the spherulites look like solid spheres that grow from a nucleus in the center, one finds that the polymer molecules within and between the spherulites are only partially crystalline. The link to nucleation kinetics is given by the shape of the interfaces between adjacent spherulites as they grow. Details of spherulitic crystallization kinetics are discussed in Sect. 3.6.5 using the Avrami treatment.

The two sketches in Fig. 5.61 illustrate different paths to a spherulitic crystal morphology. These paths create a spherical overall appearance, despite the fact that the basic crystals are polyhedra, i.e., the spherulites are aggregates of polyhedral

**Fig. 5.60****Fig. 5.61**

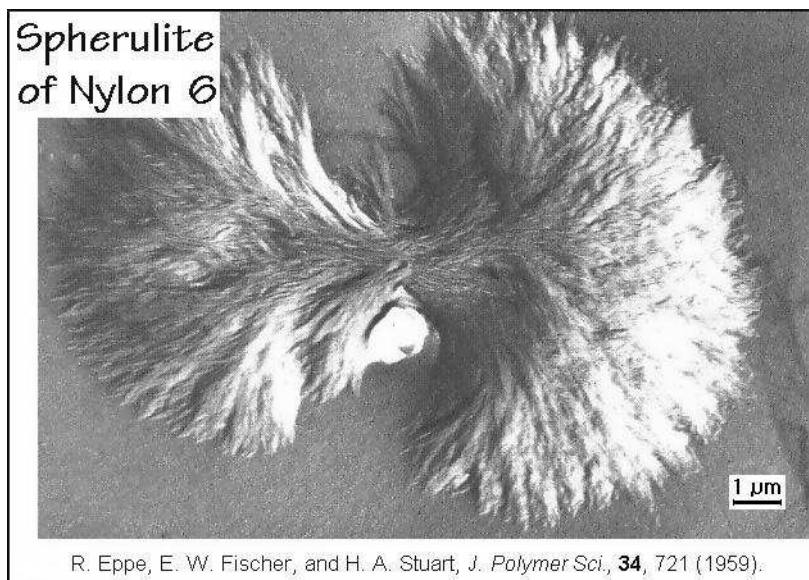
crystals or dendrites growing out of a common nucleus. Hedgehog spherulites are found, for example, in crystalline selenium as shown in the electron micrograph of Fig. 5.62. The crystal structure is shown in Fig. 5.20.

During the preparation for electron microscopy the heterogeneous (?) nucleus in the center was not replicated and is missing from the fracture surface. The molecules

**Fig. 5.62**

of  $(\text{Se-})_x$  are sufficiently close to the ceiling temperature, explained with Fig. 3.30, when crystallizing from the melt that they depolymerize and repolymerize during crystallization and avoid, thus, the presence of many chain folds by undergoing chemical annealing.

The electron micrograph of Fig. 5.63 gives an example of a Popoff-type spherulite [22] for nylon 6. In the center all lamellae are approximately parallel. Their



R. Eppe, E. W. Fischer, and H. A. Stuart, *J. Polymer Sci.*, **34**, 721 (1959).

**Fig. 5.63**



subsequent thickening due to the growth spirals splay the lamellae apart, so that ultimately a spherical crystal growth front results. Compare the length scale to that of Fig. 5.60 to judge that the eyes in the center of the spherulite cannot be visible by optical microscopy. They will, in time, fill with less-well arranged lamellae.

Figure 5.64 is an electron micrograph of the replica of a fracture surface of a melt-grown polyethylene spherulite. It gives another proof that polymer spherulites can be made of lamellae. In addition, it shows that there is a regular twist that permits an

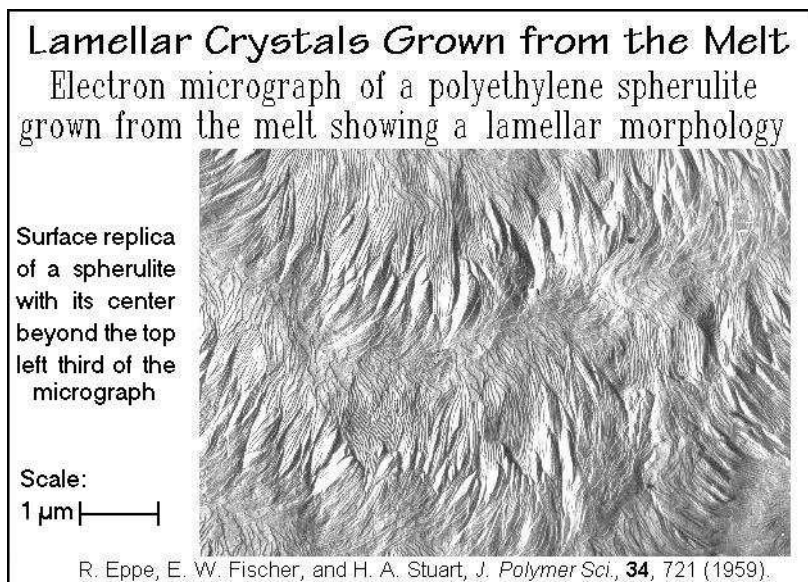


**Fig. 5.64**

alternation of circular interference rings inside the spherulite, as can also be seen in optical micrographs such as Fig. 5.60. One can see from the lamellar orientation that the molecular chains are aligned tangentially to the spherulite surface. Observation of the birefringence of the spherulites under the optical microscope can similarly establish the orientation of the molecules within the spherulites.

The analysis of melt-grown crystals is often difficult because a large part of the semicrystalline polymers is made up of the amorphous material that does not show any structure under the polarizing microscope (see Appendix 15). Poly(ethylene terephthalate) is a typical example. Its crystal morphology becomes visible only after the amorphous phase is etched away by hydrolysis as described in Sect. 3.4.5 and Fig. 3.52. The crystals hydrolyze more slowly and, thus, remain for analysis when most or all of the amorphous polymer segments are etched away. The morphology of the remaining debris from melt-crystallized poly(ethylene terephthalate) is shown in Fig. 5.65. Another method of analysis involves the staining of the noncrystalline molecules. Above the glass transition temperature, heavy metal compounds, such as involving of Os, Ru, can still diffuse into the amorphous areas of the polymer and make them opaque to electrons and outline the crystals which are more transparent to the electrons.

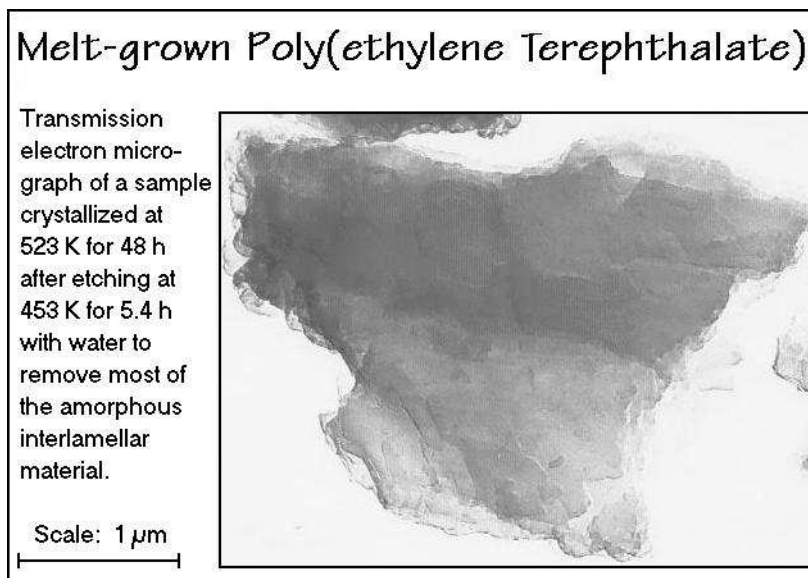


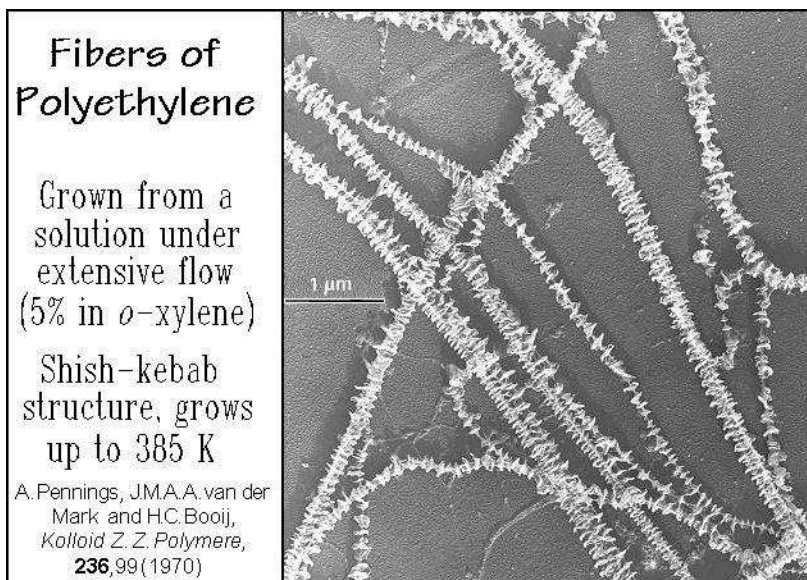
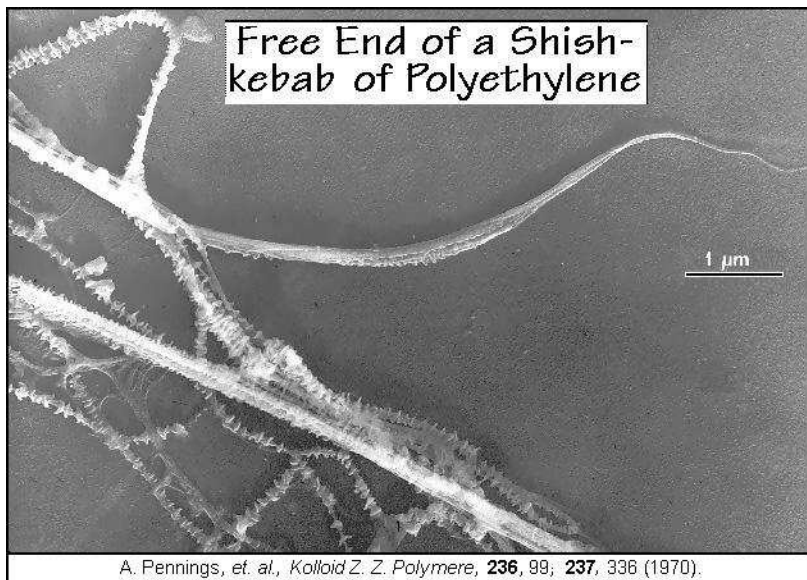
Fig. 5.65

### 5.2.6 Fibers

A different, frequent crystal morphology of flexible, linear macromolecules is that found in fibrils, as shown in Fig. 5.41. The fibers are usually drawn from prior crystallized lamellae, or from the amorphous state in form of a melt, gel, or solution. Most progress has been made in the analysis of fibers grown from solution in a flow-field that continuously stretches the long molecules by extensive flow as described in Sect. 5.6. Figure 5.66 shows, as an example, polyethylene fibers grown by stirring a solution of the polymer. The fibers have a so-called shish-kebab, double morphology. The name originates from the Turkish, *sis* = skewer, and *kebab* = mutton. The fibers consist of two components, fibrillar, extended-chain (defect) crystals are coupled with an overgrowth of lamellae. The shish of the structure is made up of the fraction of the polymer of the highest molar mass which is most susceptible to extension, as is discussed further in Sect. 5.6. The kebabs are lamellae that nucleate subsequently on the shish at more or less regular distances and grow into the double morphology. Both parts are joint to an integral structure and can change in proportion, depending on the amount of flow, the molar-mass distribution, concentration, and the temperature of crystallization.

Figure 5.67 illustrates that the ends of the fibers are often tapered. This special structure is an indication that growth in the fiber direction seems to occur by long molecules caught on the fiber surface which are then smoothed by the flow past the fiber and give rise to the longitudinal growth.

Fibers drawn from prior grown lamellar crystals must undergo a major rearrangement of the morphology on drawing. This mechanism is discussed with the properties of the defects in crystals in Sect. 5.3.

**Fig. 5.66****Fig. 5.67**

Details of the structure of fibers grown from the melt have been derived from an X-ray fiber analysis for the example of poly(ethylene terephthalate) [23–25]. The basic X-ray scattering technique is summarized in Appendix 16. The full-pattern fiber analysis used in this analysis, the Rietveld method, is given in [26]. The triclinic crystal structure of poly(ethylene terephthalate) is illustrated in Fig. 5.68. The unit cell

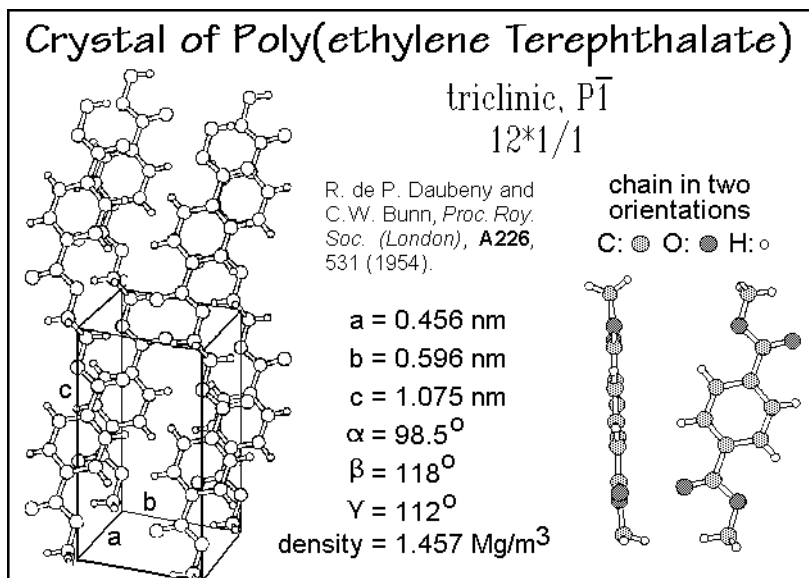


Fig. 5.68

is shown in the lower left of Fig. 5.68 and two views of the repeating unit of the molecule as they appear in the crystal are illustrated on the lower right. The molecules are stacked flat into close packing. The Rietveld analysis is shown in Figs. 5.69–72. On drawing, the crystal parameters change only little from the undrawn structure of Fig 5.68, but their diffraction pattern in Fig. 5.70 and that of the amorphous, undrawn fiber in Fig. 5.71 cannot be added to give the observed pattern of Fig. 5.69

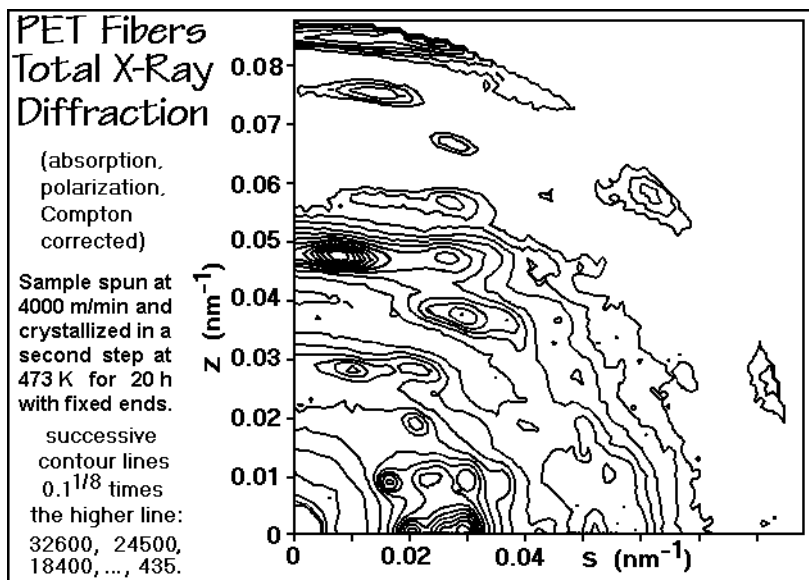


Fig. 5.69

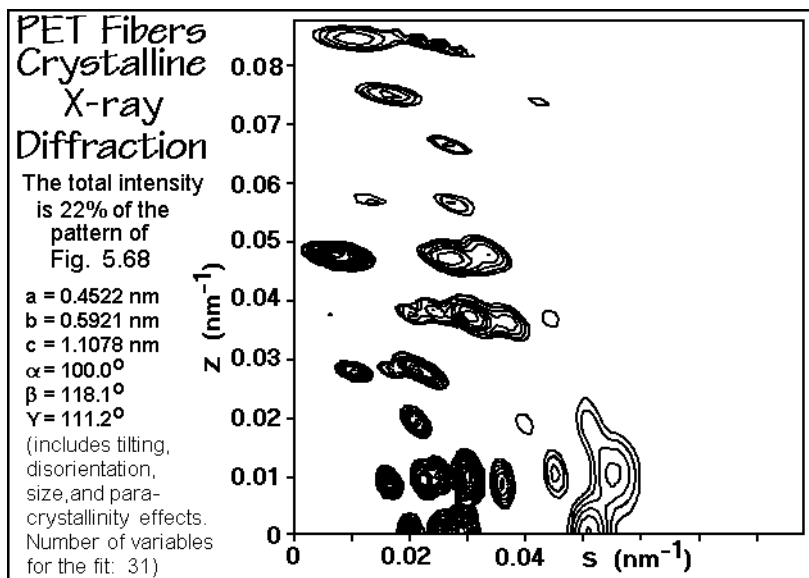


Fig. 5.70

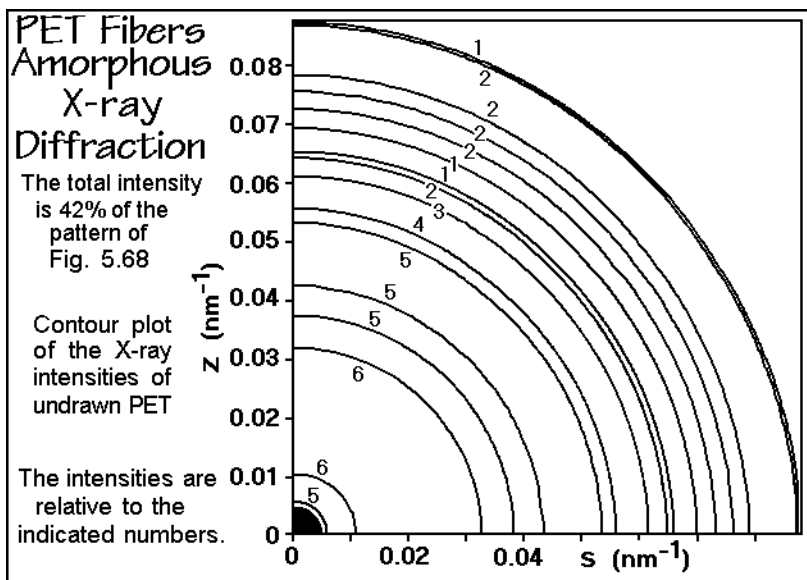


Fig. 5.71

The crystal diffraction-pattern in Fig. 5.70 was computed from the observed pattern in Fig. 5.69 by fitting the structure of the crystal in Fig. 5.68 considering all possible defects. An additional, third phase must be present as shown by Fig. 5.72. The third phase has the character of a liquid-crystalline mesophase and determines much of the fiber properties, as discussed in Sect. 5.3.6 with Figs. 5.113–115.

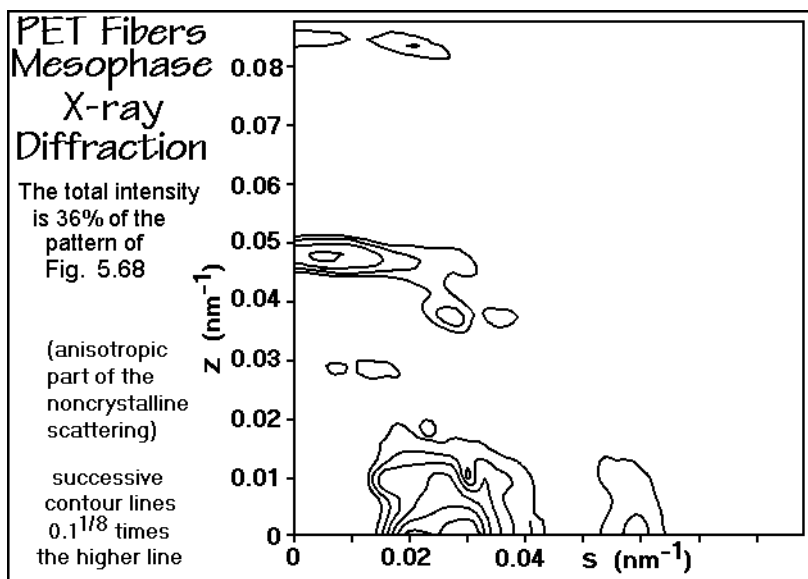


Fig. 5.72

The macroscopic fiber morphology may be compared to that of the native cellulose in the form of cotton which is displayed in Fig. 5.73. The internal structure of the cotton fiber is made visible by removal of most of the less-ordered phase by hydrolytic etching, as described for the poly(ethylene terephthalate) crystals in Fig. 5.65. Small, acicular crystals are imbedded in a matrix of less-ordered material and tied to the global structure by the macromolecules that traverse the phases of different order.

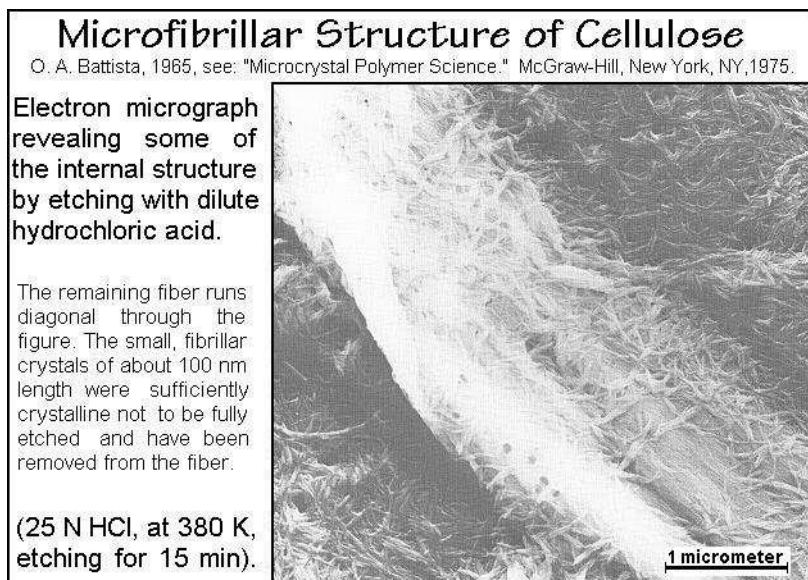
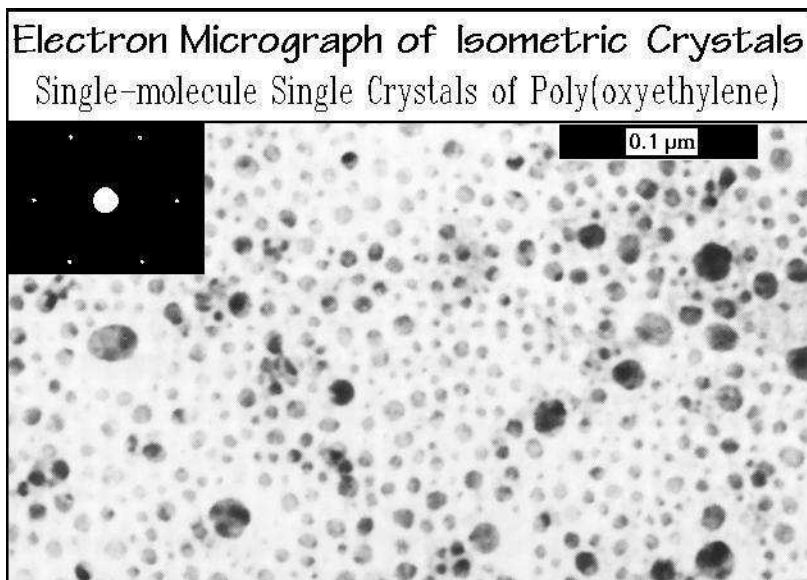


Fig. 5.73

### 5.2.7 Isometric Crystals

To obtain isometric crystals as described in Fig. 5.41, one must restrict the width of the thin lamellae. This is illustrated in Fig. 5.74 with single-molecule single crystals grown from droplets of a very dilute solution of poly(oxyethylene) in benzene. Each of the crystals contains only one molecule [27]. The poly(oxyethylene) was of a broad

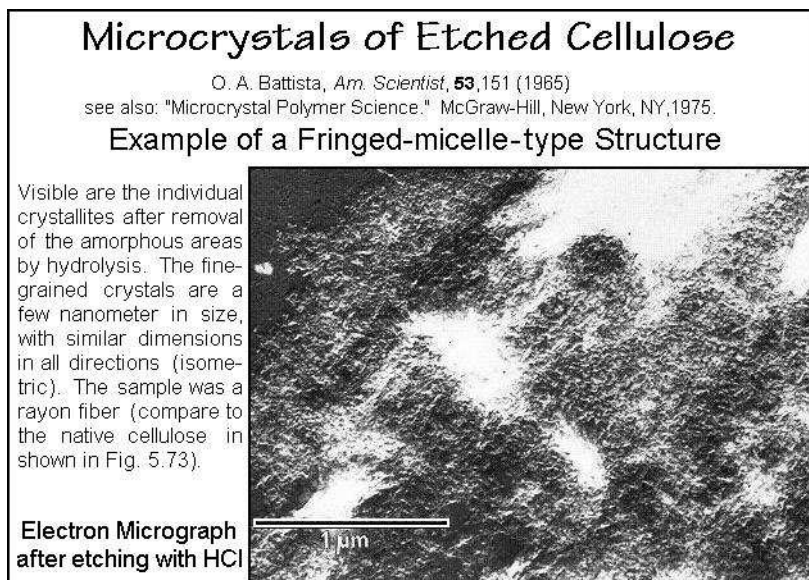
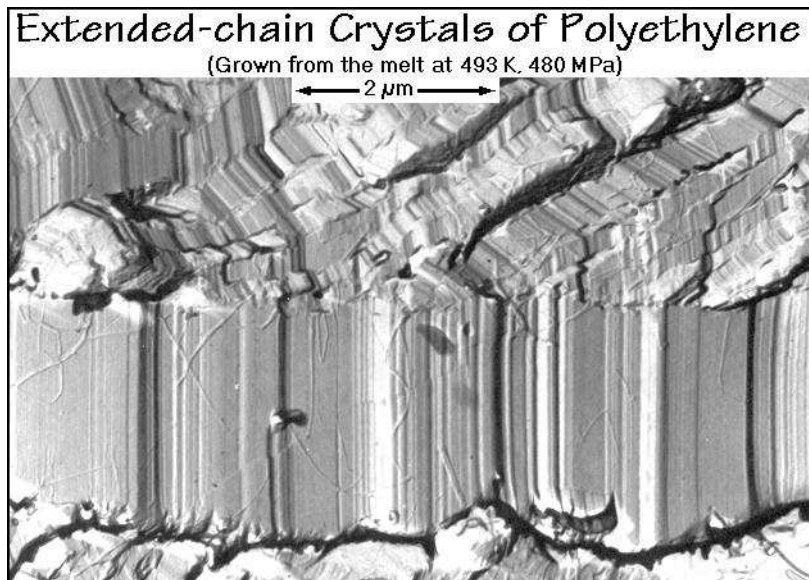


**Fig. 5.74**

molar-mass distribution with a viscosity average of  $2.2 \times 10^6$  Da. The mass-estimates of the crystal shapes in Fig. 5.74 agree well with the molar-mass distribution and the electron-diffraction pattern of a single crystal in the upper left of Fig. 5.74 proves the single-crystal structure. Details of the crystal morphology correspond to the description of Fig. 5.55 [28].

On fast cooling of melts, one approaches isometric crystals of nanophase dimensions with the fringed-micellar macroconformations displayed Fig. 5.42. Similar structures are also obtained in poorly crystallized fibers. Figure 5.75 illustrates the close-to-isometric, but small fringed-micellar crystals for cellulose from rayon fibers. This figure is in contrast to the crystals of the native cotton fibers of Fig. 5.73 which are much larger and show for their larger crystals an acicular rather than an isometric morphology (see Fig. 5.41).

Extended-chain crystals of large size are seen in Fig. 5.76, an electron micrograph of a surface replica of polyethylene [29–31]. Their morphology is still lamellar, or better called platy when using the nomenclature of Fig. 5.41. The plates and lamellae have a broad distribution of thickness. The chains run parallel to the major striations seen. In the largest lamella, the chain extension is macroscopic, almost  $2 \mu\text{m}$ , which equals a molar mass of  $\approx 225,000$  Da. Crystals of such magnitude are large enough to be considered equilibrium crystals. The smaller lamellae grew at a later time. To

**Fig. 5.75****Fig. 5.76**

some degree they have a lower molecular mass, as will be discussed in Sect. 7.1. Intersections between two extended-chain lamellae are shown in Fig. 5.77. They are common features. From the narrowing at the center of such intersections it was concluded that the plates grew first as thin lamellae and then extended on annealing, as discussed in Sect. 5.2.3. The conditions of growth of these extended-chain crystals



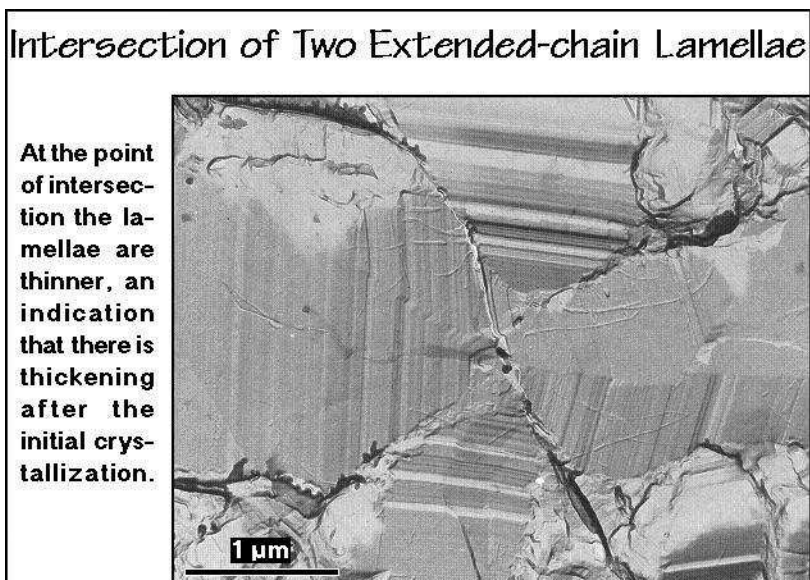


Fig. 5.77

were high pressure and high temperature (see Fig. 5.46). These conditions lead to the mesophase of hexagonal condic crystals in the phase diagram of Fig. 5.156, below. In this phase sliding diffusion [10] is facile and permits fast chain extension (for polymeric mesophases see Sects. 2.5, 5.5, and 6.2).

The morphology which is illustrated with Fig. 5.78 is a rare example of a truly macroscopic isometric single crystal, that of a polyacetylene. To avoid chain folding,

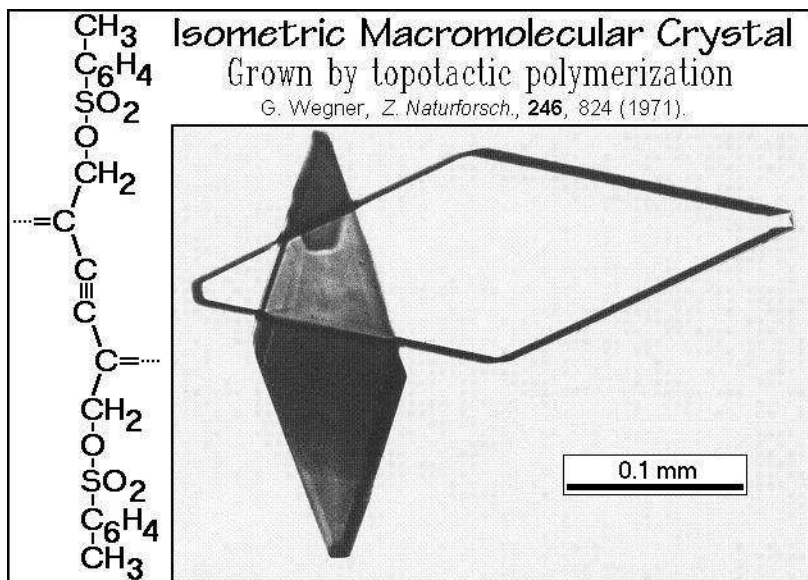


Fig. 5.78

it was grown from a monomeric single crystal without ever leaving the crystal constraint in a topotactic polymerization, a crystallization during polymerization (see also Sect. 3.6.7, Fig. 3.104 and Sect. 5.2.2). One can see from the chemical structure that the monomer has most of its bulk in the side chains, so that the crystals of monomer and polymer change little in volume on polymerization and can be isomorphous (see Sect. 5.4.10). Of special interest in this crystal are its optical and electrical properties.

Large domains of macroscopic order can also be produced by amorphous liquids, as is illustrated in Fig. 5.79 for an amphiphilic block copolymer. Such large-domain structures are illustrated in Figs. 5.38–40, and are discussed in Sect. 7.1.6. The driving force to produce this liquid-crystalline-like structure is the need to collect the junction points between the blocks in well-defined surfaces of minimal area.

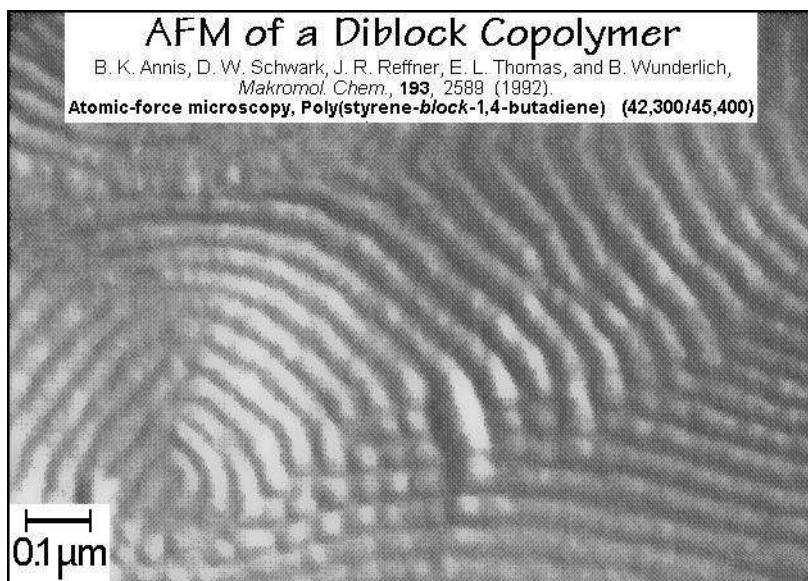


Fig. 5.79

### 5.3 Defects in Polymer Crystals

In this section it will be shown that many properties of crystalline materials do not have a simple correlation to the ideal crystal structure, as described in Sect. 5.1. Rather, minor microscopic defects may have a major influence on the material's properties. For example, if one calculates the strength of a crystal by assuming that failure occurs when all bonds across a chosen surface break, one is usually wrong by a factor of 100 to 1,000. For crystals other than macromolecules, the knowledge about the importance of the defect structure and the details of the mechanisms involving microscopic defects was developed starting in the 1930s. For polymer crystals, this understanding is still in its beginning.

### 5.3.1 Materials Properties

To understand the importance of defects in polymer crystals, one must distinguish structure-insensitive properties from structure-sensitive properties. For crystals of small molecules and rigid macromolecules (see Fig. 1.6), the structure-insensitive properties often can be derived directly from the ideal crystal structure as summarized in Fig. 5.80. The density, for example, can be calculated from the unit cell dimensions (see Sect. 5.1). The polymeric materials in form of flexible macromolecules are, in

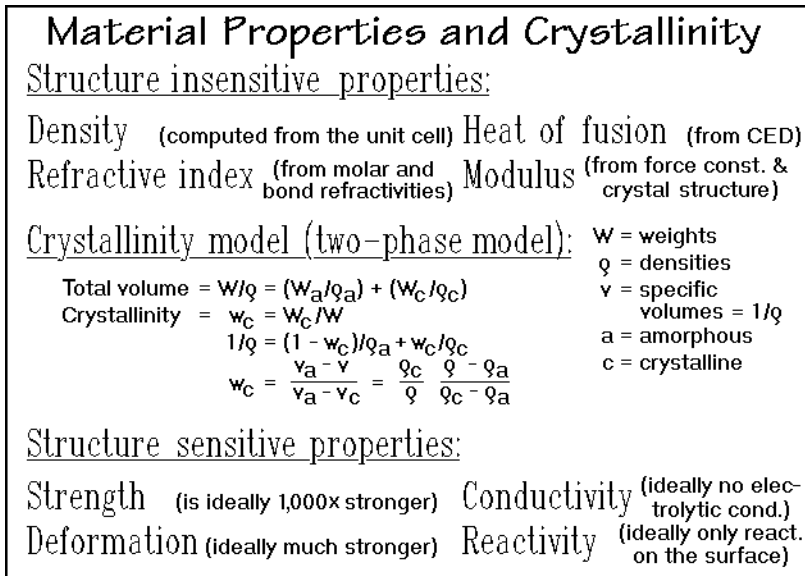


Fig. 5.80

contrast, usually semicrystalline and their structure-insensitive properties are given by the sum of contributions from the crystalline and amorphous phases, using an appropriate crystallinity parameter. Figure 5.80 illustrates how to calculate the weight fraction crystallinity,  $w_c$ , from the volumes of the assumed two phases. The corresponding volume fraction crystallinity,  $v_c$ , is derived in Fig. 3.84. The correlation between both can easily be derived to be  $w_c = (\rho_c/\rho)v_c$ . Many structure-insensitive properties can, in turn, serve to find the weight-fraction or volume-fraction crystallinity, as is shown in Sect. 5.3.2.

Several structure-sensitive properties are listed at the bottom of Fig. 5.80. They need, in contrast to structure-insensitive properties, a detailed defect mechanism to be understood, as is discussed in Sects. 5.3.3–6. The structure-sensitive properties are at the center of most of the important material properties.

### 5.3.2 Crystallinity Analysis

To determine the crystallinity of a sample, many structure-insensitive properties can be used, since they can be separated into contributions from the amorphous and the crystalline phase. Three examples are given in this section: X-ray, infrared, and

calorimetric analyses. The calculation of crystallinity from dilatometry (see Sect. 4.1) is already given in Fig. 5.80.

Figure 5.81 shows an X-ray diffraction pattern for polyethylene. The separate contributions from the amorphous and crystalline parts of the fiber are clearly visible and have to be quantitatively separated. The equation given in Fig. 5.81 is the Bragg equation that links diffraction angle and wavelength of the X-rays to the crystal-plane

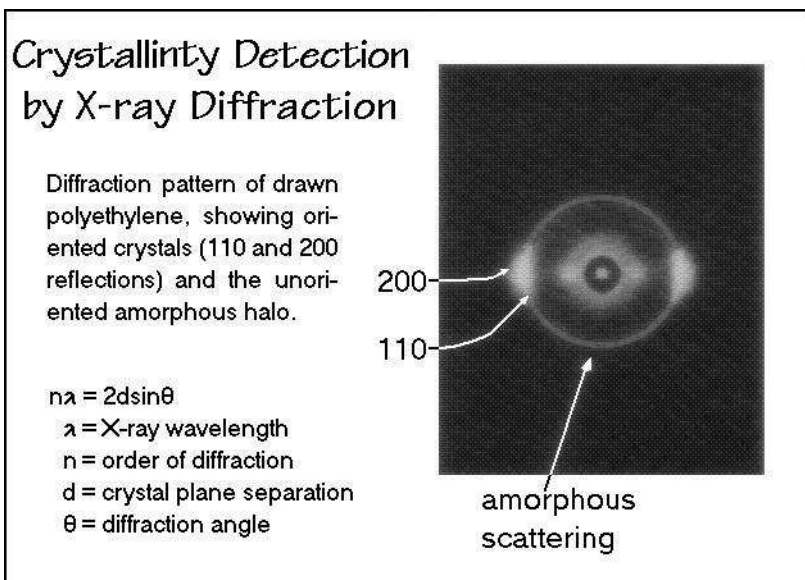


**Fig. 5.81**

separations, as described in Appendix 16. To separate the amorphous scattering from the crystalline, the properly integrated intensities must be compared. The total diffraction intensity of a given sample mass is constant, but not so easy to assess because diffraction into all angles must be considered. An often used approximate technique is illustrated in Fig. 5.82 for polypropylene crystallized from the melt. The separation of the amorphous and crystalline X-ray scattering over a limited diffraction-angle range is chosen as indicated. Although only a part of the range of scattering angles is used for the analysis, a crystallinity can be deduced, once the calibration constant  $k$  in the boxed equation is evaluated. A plot of areas in the diffraction diagram versus specific volumes for different polyethylenes is given in Fig. 5.83. It yields proper crystalline and amorphous specific volumes at 100% and zero crystallinity, indicating the validity of the analysis. The density of the crystal is known from its structure, as discussed in Sect. 5.1, and the amorphous density is available by extrapolation of dilatometric data from the melt at temperatures above the glass transition. For oriented samples this process is not as easy to carry out because of difficulties in the accounting for all scattering intensities. Similarly, when a third, an intermediate phase is present, one needs to introduce different techniques to explain even the structure-insensitive properties. The Figs. 5.69–72 show such a three-phase separation for fibers of poly(ethylene terephthalate).

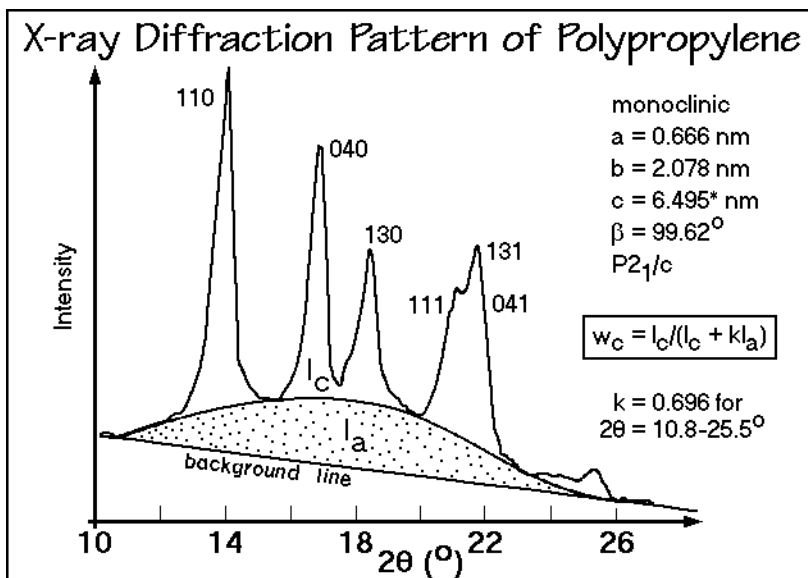


Fig. 5.82

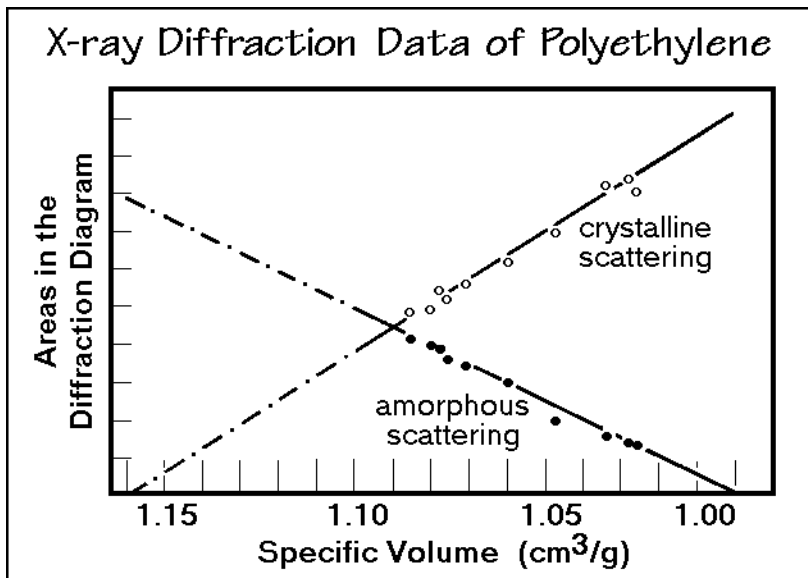


Fig. 5.83

A technique that leads to quantitative data for the determination of the volume-fraction crystallinity is the infrared analysis. As an example, in Fig. 5.84 one can see the two areas in the IR spectrum of polyethylene where amorphous and crystalline samples are largely different (frequencies A and C). The equation in the upper right-hand corner permits now a quantitative evaluation, as is documented in Fig. 5.85 for

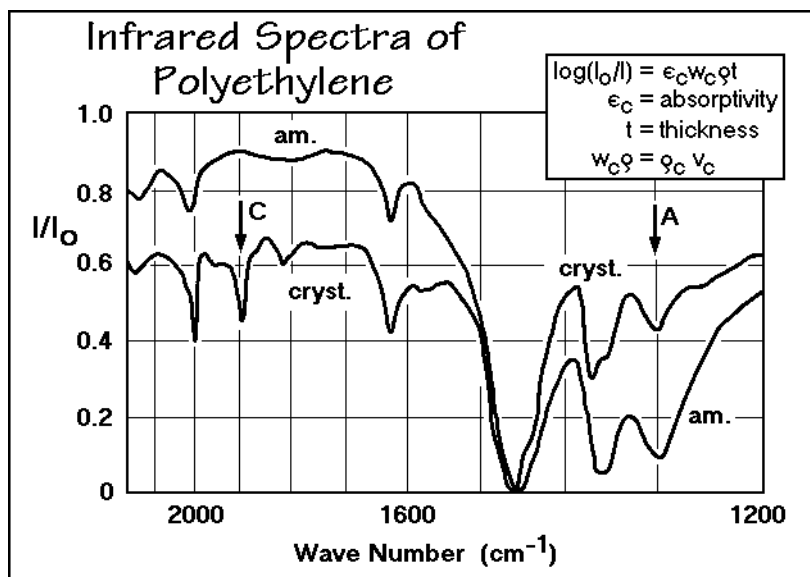


Fig. 5.84

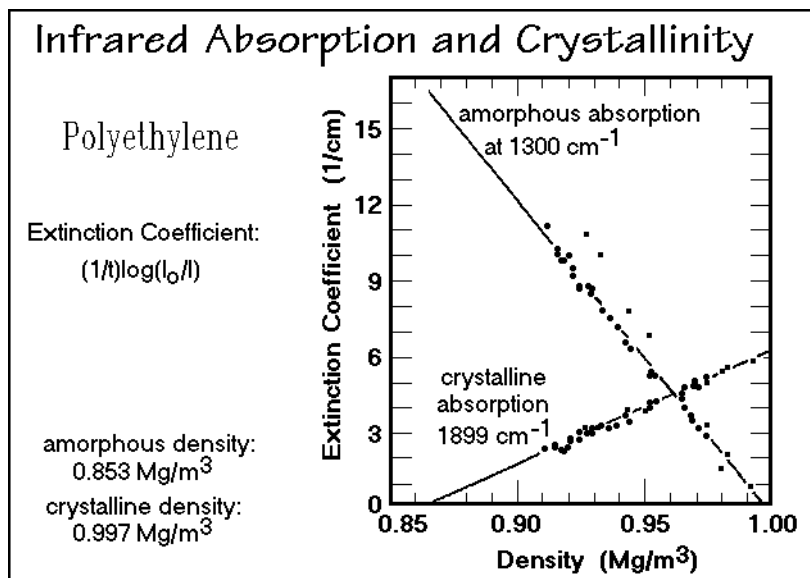


Fig. 5.85

a number of bulk samples of different crystallization history. By plotting the ratio  $I/I_0$  versus the density, a straight line results. Again, the extrapolation to fully crystalline and amorphous samples yields the expected densities, suggesting an internal consistency of the two-phase or crystallinity model for the structure-insensitive properties of bulk polyethylene.



The noncrystalline region in a semicrystalline polymer, measured by crystallinity, is itself a typical polymer-specific defect. It is also called an *amorphous*, or three-dimensional crystal defect. As shown schematically in Fig. 5.87, the chain molecules are connected to the neighboring crystals, permitting to assign the defect to the surrounding crystals. The strain within the molecules bridging the crystals keeps the amorphous regions from crystallizing and broadens the glass transition with a shift to

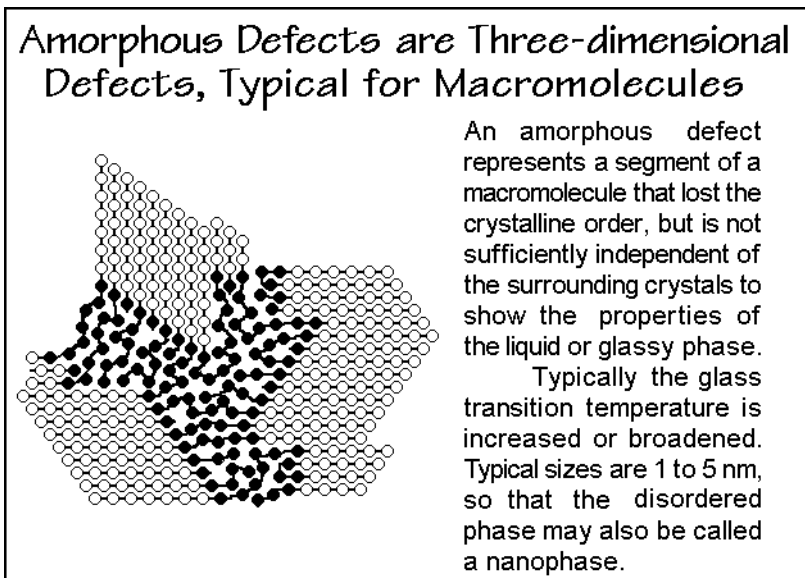


Fig. 5.87

higher temperatures. The rigid amorphous fraction, described in Sect. 6.1, has most likely its origin at the interface of the amorphous defect with the crystal. In crystals of small and rigid macromolecules such amorphous defects are also found in grain boundaries, but only in semicrystalline, flexible polymers do these defects become truly three-dimensional and take on a nanophase dimension, as suggested already in the 1960s along with many other polymer-specific defects, redrawn in Fig. 2.98.

Figure 5.88 is an illustration of two-dimensional defects in the form of surfaces and *grain boundaries*. They either terminate a crystal or separate it from the three-dimensional defects. In polymer crystals, these surfaces and grain boundaries are rarely clean terminations of single-crystalline domains, as one would expect from the unit cell descriptions in Sect. 5.1. The surfaces may contain folds or chain ends and may be traversed by tie molecules to other crystals and cilia and loose loops that enter the amorphous areas, as is illustrated in Figs. 5.87 and 2.98. The properties of a polycrystalline sample are largely determined by the cohesion achieved across such surfaces and the mechanical properties of the interlamellar material, the amorphous defects.

One-dimensional or line-defects are added to the list of defects in Fig. 5.86. They are commonly known as *dislocations* and are prominently involved in deformation mechanisms of metals and salts. In polymers, they have a more restricted function.



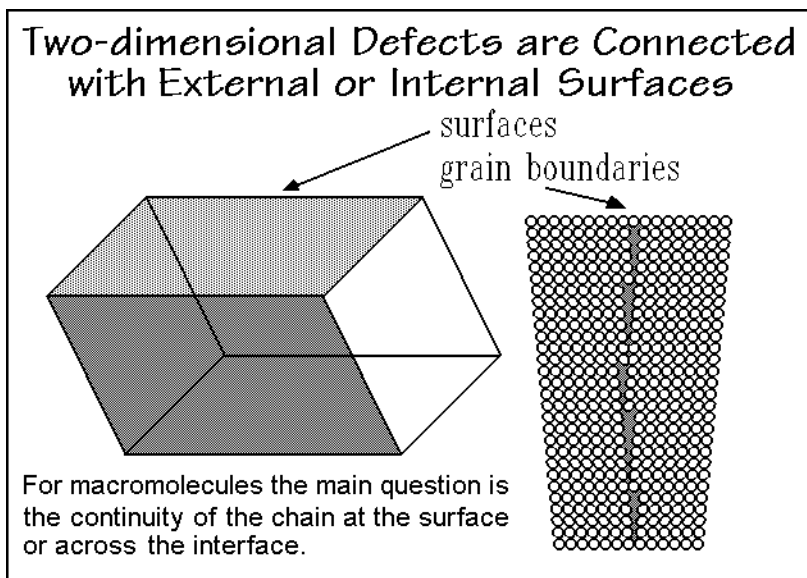


Fig. 5.88

The connection between the chain atoms cannot easily be broken in flexible polymers. On deformation, the chains react by slip of the whole chain, rather than by movement of dislocations.

Figure 5.89 illustrates how the presence of chain ends within the crystal must lead to dislocations. Three superimposed layers of chain molecules of a crystal are sketched schematically. Without chain-ends, one only would expect parallel lines, as

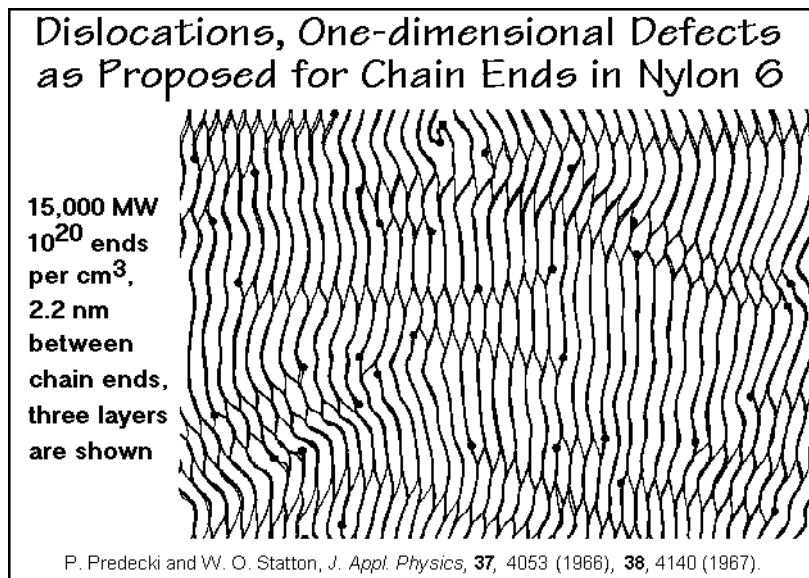


Fig. 5.89

seen in limited areas of the illustration. Any chain end is marked by a filled circle (●). At these positions the neighboring chains slip into the vacancies created by the chain-ends and distort their own, as well as their neighbor's chains. In this simple schematic, the distortions which take the form of line-defects continue until they reach a compensating second chain end or the surface. Obviously in the illustrated nylon 6 of low molar mass, the crystal is sufficiently distorted to be not recognizable as a crystal, or thermodynamically stable (see Fig. 5.30 for the ideal crystal structure). This analysis gives support to the arguments that chain ends are often expelled to the crystal surfaces, and strains are dissipated within limited distances and not propagated as far as drawn in Fig. 5.89.

Zero-dimensional defects or *point defects* conclude the list of defect types with Fig. 5.87. Interstitial electrons, electron holes, and excitons (hole-electron combinations of increased energy) are involved in the electrical conduction mechanisms of materials, including conducting polymers. Vacancies and interstitial motifs, of major importance for the explanation of diffusivity and chemical reactivity in ionic crystals, can also be found in copolymers and on co-crystallization with small molecules. Of special importance for the crystal of linear macromolecules is, however, the *chain disorder* listed in Fig. 5.86 (compare also with Fig. 2.98). The ideal chain packing (a) is only rarely continued along the whole molecule (fully extended-chain crystals, see the example of Fig. 5.78). A most common defect is the chain fold (b). Often collected into fold surfaces, but also possible as a larger defect in the crystal interior. Twists, jogs, kinks, and ends are other polymer point defects of interest.

Next, somewhat more detail is given for the line and point defects. The latter will be the major topic in connection with their occurrence in computer simulations displayed in Sect. 5.3.4. Figure 5.90 gives a schematic representation of the two basic dislocations. The cubes of the illustrated crystals represent the motifs. In the screw

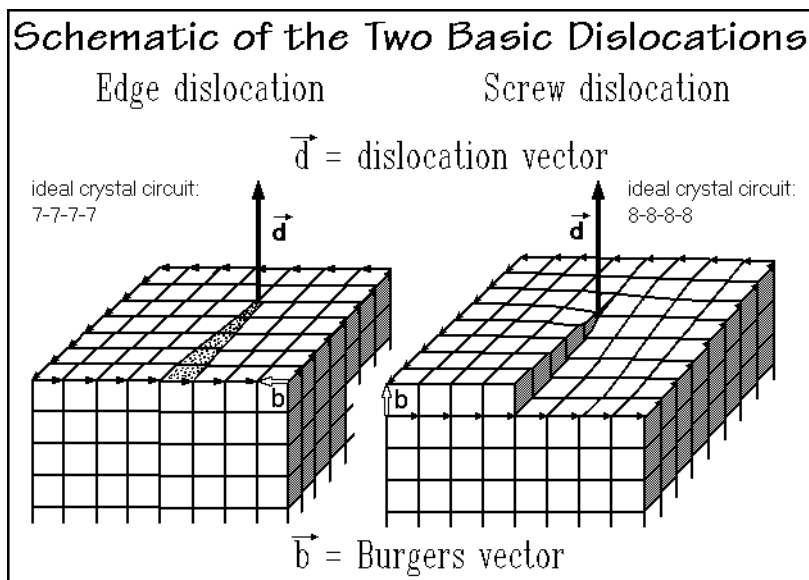


Fig. 5.90

dislocation on the right, the dislocation vector  $\vec{d}$  is parallel to the Burgers vector  $\vec{b}$  which connects the ends of a Burgers circuit that would meet in an ideal crystal. In the screw dislocation a slip of one cube has occurred in the Burgers circuit, giving rise to a spiral. The line defect is shown on the left of Fig. 5.90. In this case the dislocation vector is at right angles to the Burgers vector. One can visualize the edge dislocation as an extra layer of motifs that terminates, causing a strained region within the crystal along the direction of the dislocation vector.

In crystals of small molecules and rigid macromolecules the dislocations are primarily involved in deformation mechanisms, as is illustrated in Fig. 5.91. For the edge dislocation, a glide can occur only parallel to the Burgers vector in the glide

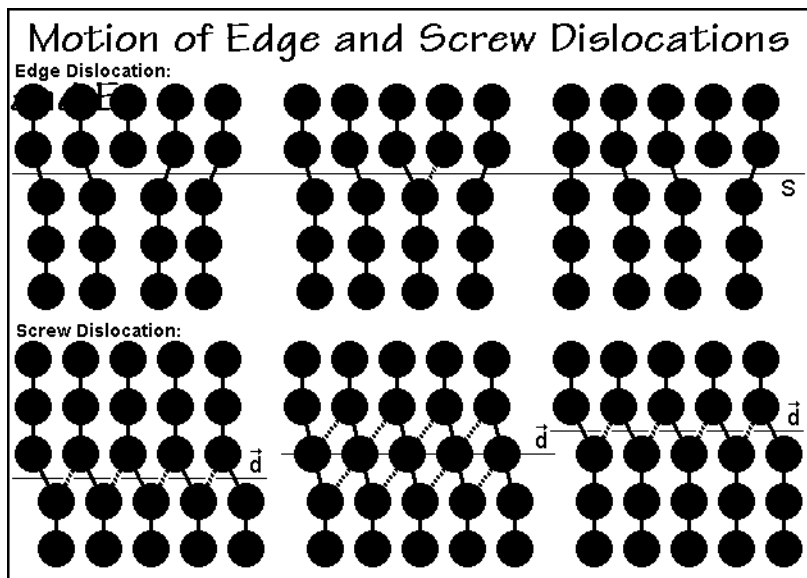


Fig. 5.91

plane S, defined by  $\vec{d}$  and  $\vec{b}$ . The screw dislocation, in contrast, can glide in any plane parallel to the dislocation vector  $\vec{d}$ . In trying to transfer this deformation mechanism to flexible macromolecules, one finds that many dislocations are sessile, i.e., they do not move. If we assume that the heavy lines in Fig. 5.91 represent the covalent backbone bonds, the glide of the edge dislocation would have to involve breakage of bonds, which does not happen in flexible macromolecules. Glide planes in polymers must thus be parallel to the chain direction. Before bonds break, flexible macromolecules will be able to slip, involving point defects rather than dislocations, as will be discussed below. The glide of the screw dislocation would be possible, but macromolecules have often screw dislocations of such large Burgers vectors, that a glide does not occur. Furthermore, the motion of a single dislocation produces a deformation of a magnitude of only one Burgers vector, so that a continuous generation of new dislocations is necessary for larger deformations. Such sources exist within crystals of small molecules and rigid macromolecules and produce continuous streams of defects on application of small stresses. They need, however,

crystal domains of micrometer in size. In crystals of flexible polymers such dimensions rarely available making the generation of new dislocations unlikely (see Sect. 5.2).

Screw dislocations are also of help in developing crystal thickness by providing a continuous, indestructible secondary nucleus (see Sect. 3.5). In chain-folded crystals of flexible, linear macromolecules, crystal growth in direction of the chain axis is limited by the chain folds. The screw dislocations, however, can provide a mechanism for continuous growth in the chain direction via screw dislocations with a Burgers vector of the enormous length of the thickness of the lamellar crystal instead of the unit cell dimension. The example on the right of Fig. 5.92 has screw dislocations with left- as well as right-handed rotations when looking along the dislocation vector. The terrace, close to the center of the figure, is caused by two screw dislocations of

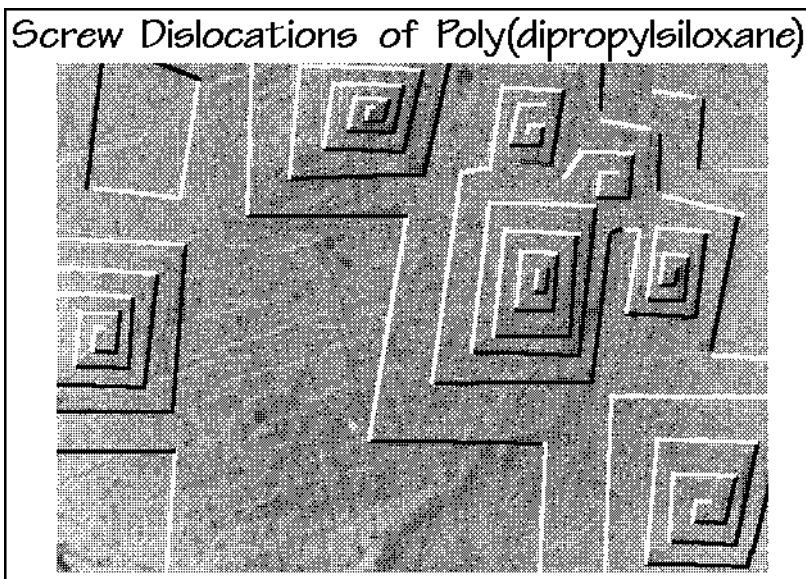


Fig. 5.92

opposite handedness, generated in close proximity. Whenever the layers of the two screw dislocations meet, a new terrace layer is generated (see also Fig. 3.72). The screw dislocations with large Burgers vectors can be generated by reentrant crystal growth faces or a tear or slip of a lamella.

Edge dislocations with their extra planes of motifs as seen in Fig. 5.90 can be made visible on magnification by double diffraction, illustrated by the optical analog of Fig. 5.93. Two lamellae are represented by the parallel lines, with each line representing the projection of a growth plane of Fig. 5.54. At the point of the missing portion of the extra growth plane, the rotation angle changes and a new fringe is created, as described in more detail in Appendix 17. The additional fluctuations in the fringes in Fig. 5.93 are due to minor variations in line separation of the drawing.

A similar picture is created when two superimposed polymer crystals are viewed in the electron microscope, as shown in Fig. 5.94. The changes in rotation angle and

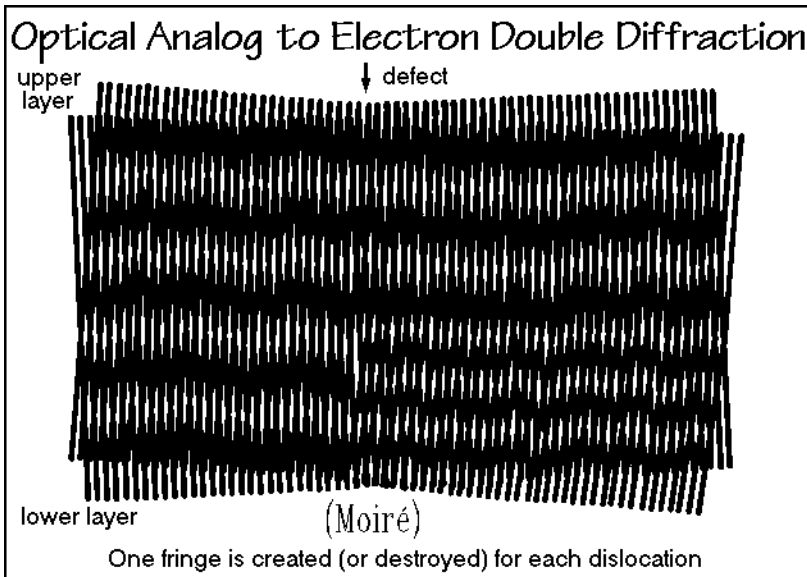


Fig. 5.93

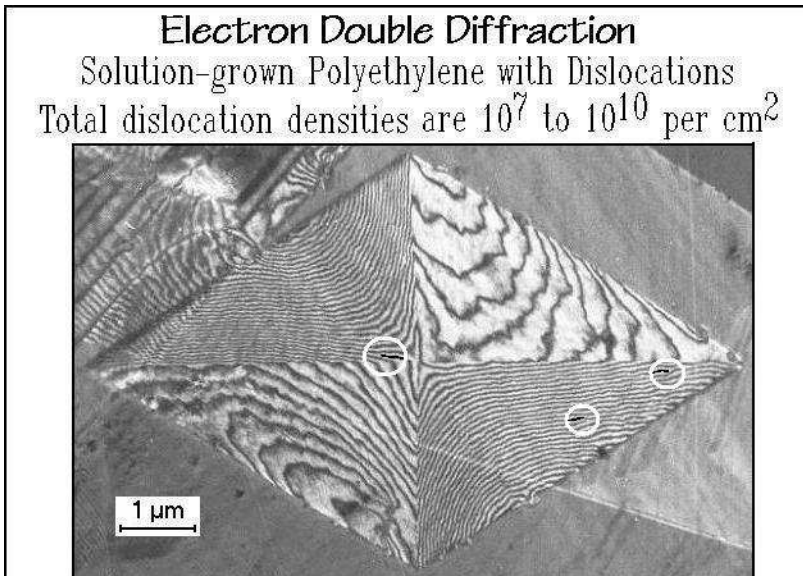


Fig. 5.94

separation of the planes of motifs in the interior of the crystal cause the more complicated patterns. By following the Moiré lines, one discovers the three terminating fringes, caused by three dislocations.

Some more insight in plastic deformation can be gained by molecular dynamics (MD) simulation of a crystal that was enclosed on three sides in a rigid box of too

small volume, so that in order to reach the equilibrium density, the crystal had to expel several of the chains. Figures 5.95 and 5.96 show such a simulation and a model of a paraffin with a kink. The simulation shows the initial, perfect crystal, compressed within the three rigid surfaces. After 4 ps, a ripple runs over the top layer of chains. Then, a slip plane develops parallel to the (102) plane and a dislocation ( $\perp$ ) is produced within a few picoseconds ( $10^{-12}$  s). The crystal is projected along the chain

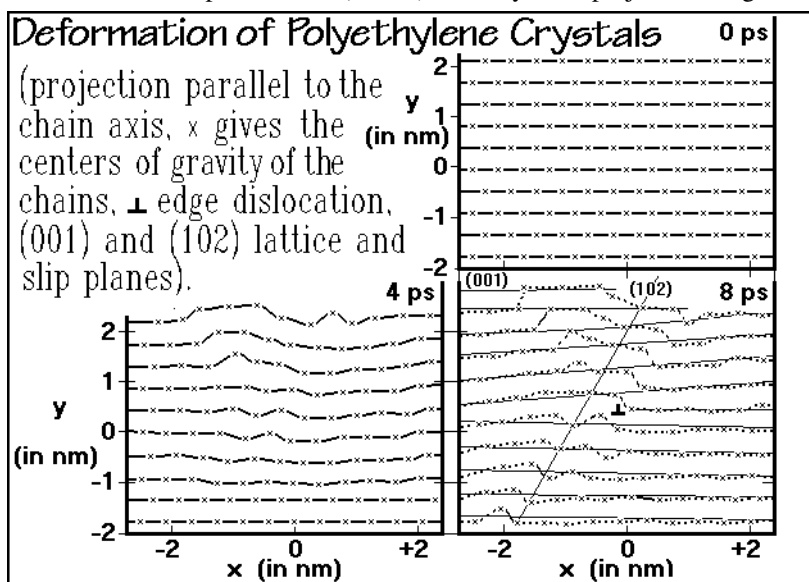


Fig. 5.95

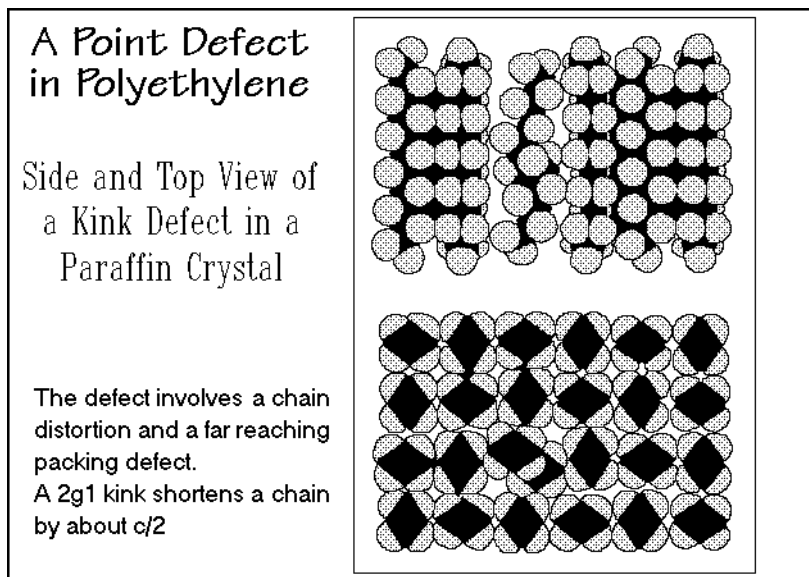


Fig. 5.96

axes, as it is also introduced in Sect. 5.2. Details on the MD simulations are given in Sects. 1.3 and 2.1 and in the figures given in Sect. 5.3.4. Note that the initial crystal was monoclinic, so that the chain axes are parallel to the b-axes, which are the z axes in Fig. 5.95 (the a-axis is x, and the c-axis is the diagonal of the crystal).

Point defects cannot be seen directly in crystals of flexible macromolecules, but have been deduced from calculations and models. The defect in Fig. 5.96 in the third chain from the left consists of a sequence of *gauche*, *trans*, and *gauche* conformations and is called a 2g1 kink (see also Fig. 5.86). This disruption of the crystal is small, but it will be shown to assist in the motion of chains in annealing and deformation, as well as contribute to the change in heat capacity beyond the vibrational contributions.

### 5.3.4 Supercomputer Simulation of Crystal Defects

Major progress in the understanding of point defects in polymers listed in Fig. 5.86 became possible when sufficiently large segments of crystal could be simulated on supercomputers for a time sufficiently long to show the approach to equilibrium in what one might consider super-slow motion to bridge the enormous jump from the atomic to the macroscopic time scale [32,33] (see Sects. 1.3.4 and 5.3.5). Figure 5.97 details a 180° twist in a polyethylene crystal. The bottom-portions of seven chains of a simulation are shown, as in Fig. 1.47. At time zero the twist is centered in the

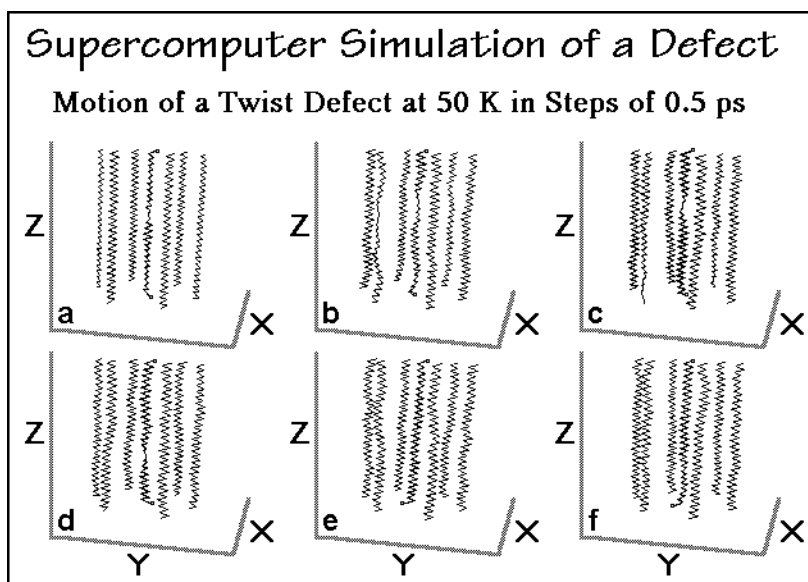


Fig. 5.97

middle chain and forces the bottom portion of the chain to be out of register with the other chains. The twist has the extremely short life time of  $\approx 2$  ps and quickly diffuses to the nearest crystal surface, as seen by the complete turning of the marked chain end between steps d and e. If such twists are to cause large-scale motion, as are involved in deformation, there must be a continuous source of new twists.

A point defect that does not lead to a full rotation of the chain by  $180^\circ$  is a single *gauche* conformation as illustrated in Fig. 1.37 which is equivalent to a single bond being rotated by  $120^\circ$  and accommodating the distortion of the chain by a twist in either direction away from the all-*trans* chain. The tracking of such simple *gauche* defects at high temperature is shown in Fig. 5.98. A defect is marked by a heavy line for the time of its existence which is defined by a bond with a rotation angle of more than  $90^\circ$  away from the stable *trans* conformation. From Fig. 5.98, one can deduce

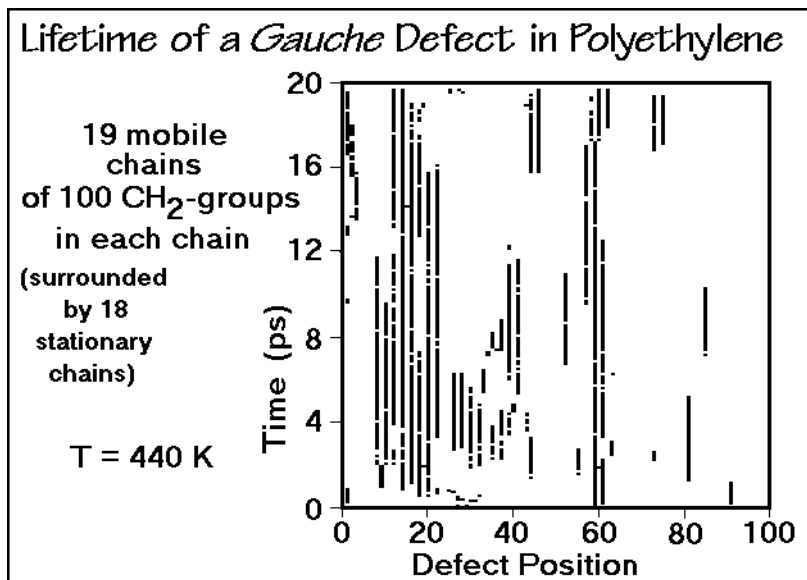


Fig. 5.98

more or less random appearances of defects, an extremely short life time, and a tendency to cluster in kinks (see Fig. 5.96). Changing the temperature, crystal size, and restrictions changes the life times of the defects, their concentration, and also their distribution (see also Fig. 1.48).

The results of many MD simulations are summarized in Fig. 5.99. The rate of attainment of defects is computed for the whole chain, so that for every bond in the crystal of polyethylene one expects at room temperature,  $\approx 300$  K, about  $10^{10}$  brief excursions to a *gauche* conformation in every second! The polymer crystals have thus much more mobility and disorder than is conveyed by the drawings of the crystal structures in Sect. 5.1. The short life times connected with the high rate of formation and destruction gives the concentrations plotted in Fig. 5.100 (see also the simulations of Figs. 2.14 and 2.15). At room temperature, the concentration is only a fraction of one percent, in agreement with the infrared data shown in the figure and the increase of heat capacity beyond the vibrational contributions (see Fig. 2.65). Close to melting, the *gauche* concentration reaches about 2% of all bonds.

The details of the mechanism of formation of a kink can be deduced from Fig. 5.101, where one chain that develops a kink has been drawn in a sequence of snapshots, spaced 0.1 ps apart. The perspective is as before in Figs. 1.47 and 5.97.



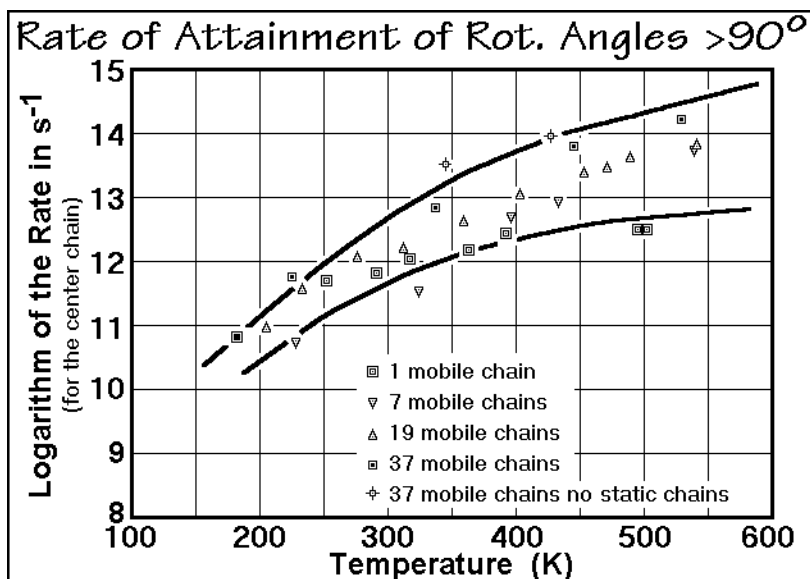


Fig. 5.99

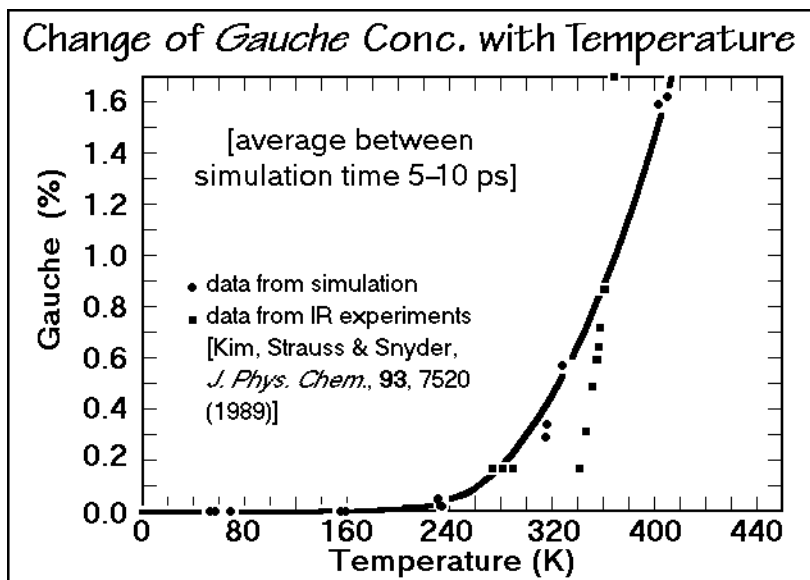


Fig. 5.100

By inspection, one can see that the kink is the result of the collision of a transverse (A), torsional (B), and longitudinal vibration (C) between 0.5 and 1.1 ps (see also Fig. 1.47). After formation, this particular kink defect had a life time of about 2 ps.

The mechanism of twisting of a single chain is illustrated in Fig. 5.102. One can see a very gradual twist starts at about 1.5 ps, and is completed after 2.3 ps. After this

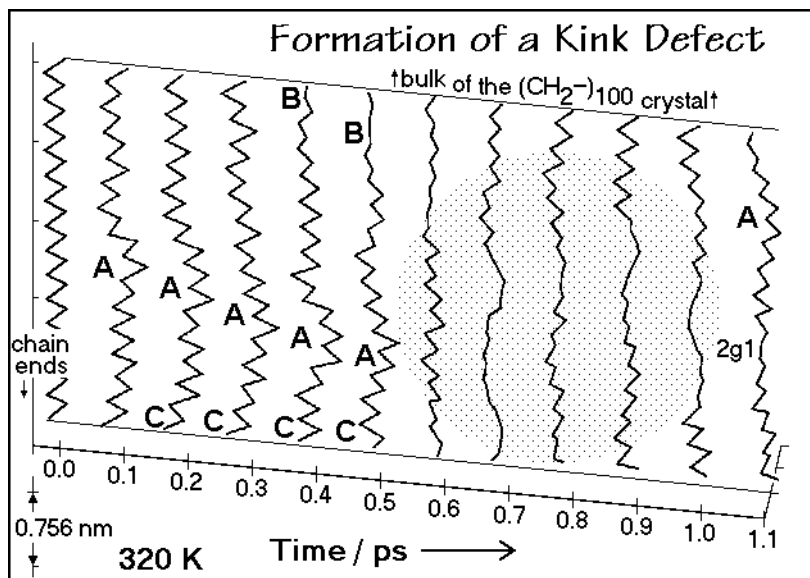


Fig. 5.101

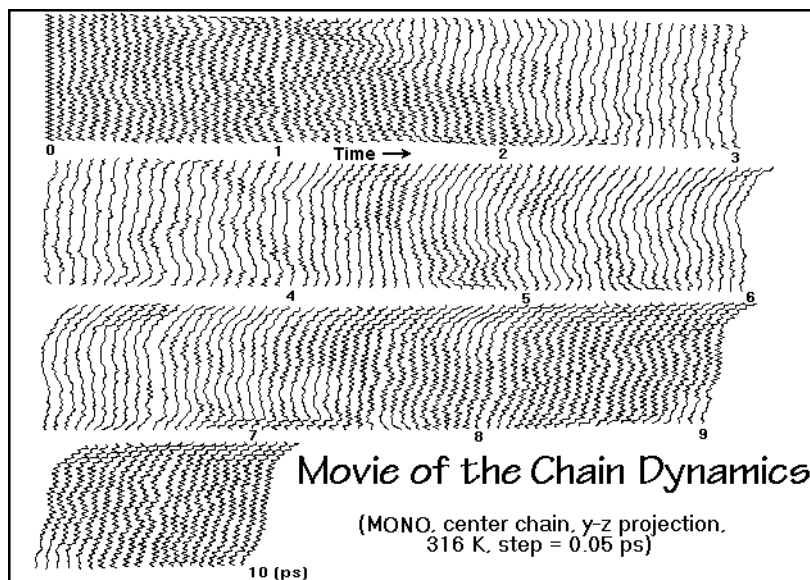


Fig. 5.102

twist, the whole chain has been rotated by about  $90^\circ$ . It remains with minor fluctuations in this position until 7 ps when the rotation reverses. The twist is so gradual that no *gauche* conformations are necessary for its occurrence.

The sequence of Figs. 5.103–105 illustrates the details of the diffusion of a chain through the crystal. The figures refer to a chain that was driven into the direction of

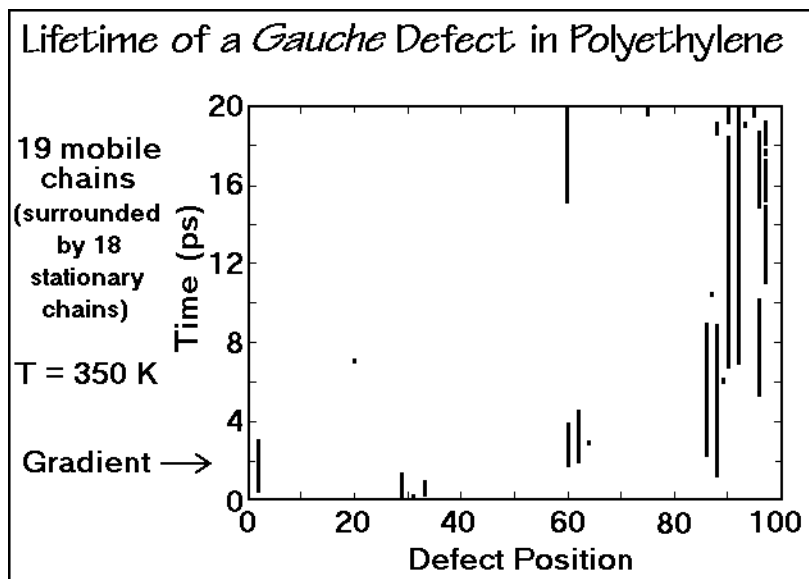


Fig. 5.103

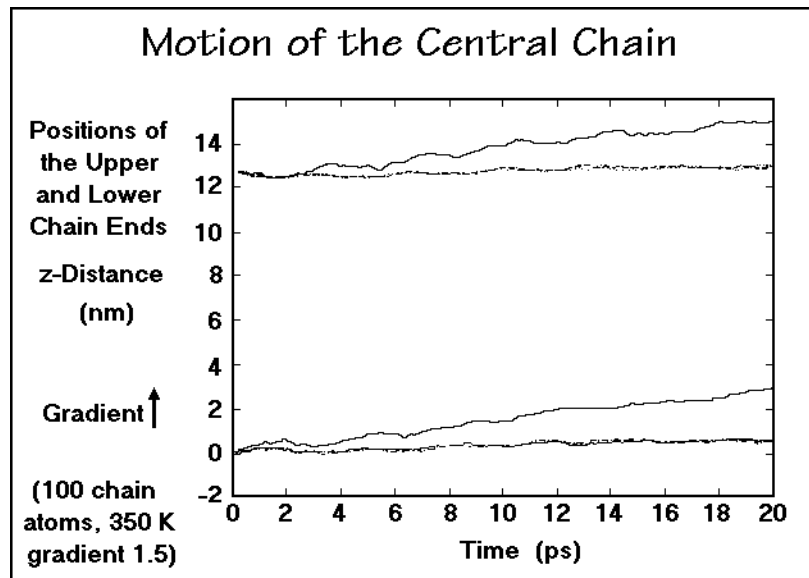


Fig. 5.104

the indicated gradient by application of an external force. Figure 5.103 illustrates the *gauche* conformations that appear during the diffusion (compare to Fig. 5.98). There is no direct involvement of the *gauche* defects in the motion. At later time, the increase in *gauche* bonds is connected with the chain having moved out of the crystal in the positions above 85.

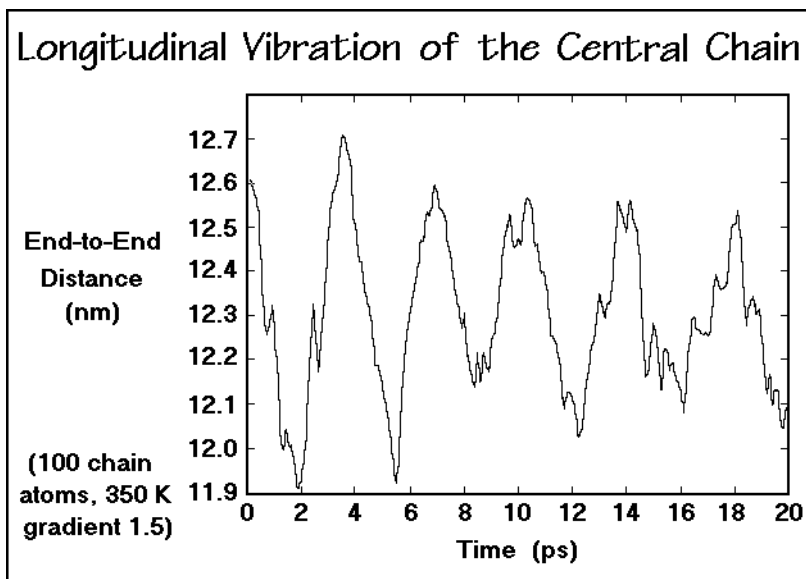


Fig. 5.105

Figure 5.104 shows more details how the chain moves. The almost horizontal, dotted lines represent the non-moving chains which surround the chain being moved out of the crystal by the force gradient. One should note the initial pulling of the lower chain-end into the crystal at 0–2 ps. This is followed by an expulsion of the upper chain-end out of the crystal between 2 and 4 ps.

The mechanism of the diffusion of the chain is shown even better in the enlarged plot of the end-to-end distance of the moving chain in Fig. 5.105. The longitudinal acoustic mode of vibration (LAM) is clearly visible. From the LAM frequency one can extract a sound velocity in the chain direction which agrees with experiments. On this LAM vibration a series of spikes is superimposed which occur on motion of the chain into or out-of the crystal as seen in Fig. 5.104. The sliding diffusion of the chain through the crystal is, thus, coupled strongly with the skeletal vibrations and does not involve diffusion of the point defects themselves, but rather seems to be connected with the twisting motion of the chain which is illustrated in the movie of the chain dynamics of a single chain in Fig. 5.102.

The change of the rate of diffusion with temperature is illustrated in Fig. 5.106. Although point defects are not directly involved in the motion, they help in the motion of the chain. The motion decreases towards zero in the temperature range where the concentration of *gauche* bonds reaches zero in Fig. 5.100, i.e., with *gauche* defects present, the diffusion is more facile.

Instantaneous projections of segments of  $C_{50}H_{100}$  within a crystal at different temperatures are shown in Fig. 5.107. The MD simulation represents the hexagonal polymorph. One can see that the crystal is divided in nanometer-size domains and has increasingly averaged chain cross-sections at higher temperatures. Both yield on macroscopic X-ray analysis hexagonal, average symmetry. At higher temperature, chains start to leave the surface of the crystal, indicating the first stages of fusion.

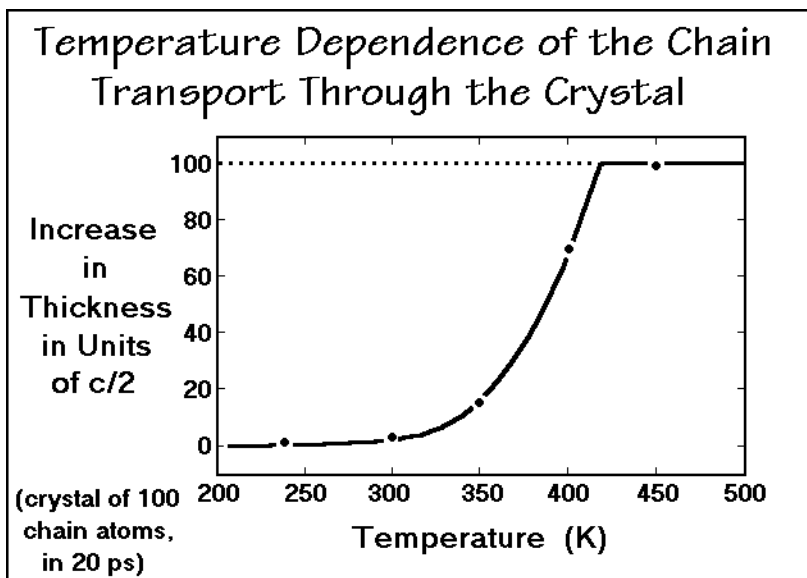


Fig. 5.106

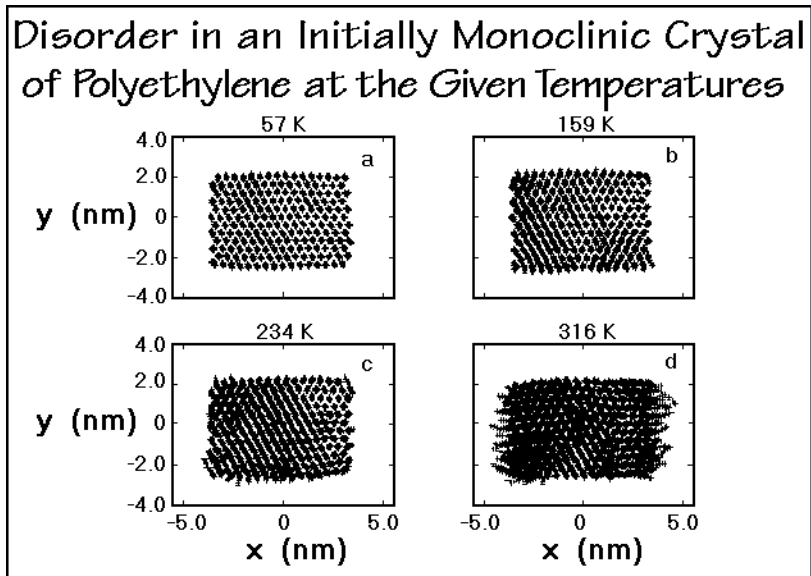


Fig. 5.107

### 5.3.5 Deformation of Polymers

Turning to the macroscopic deformation of polyethylene, as experienced on drawing of fibers, one observes frequently the formation of a neck at the yield point, as illustrated in Fig. 5.108. The stress-strain curve in Fig. 5.108 illustrates a typical

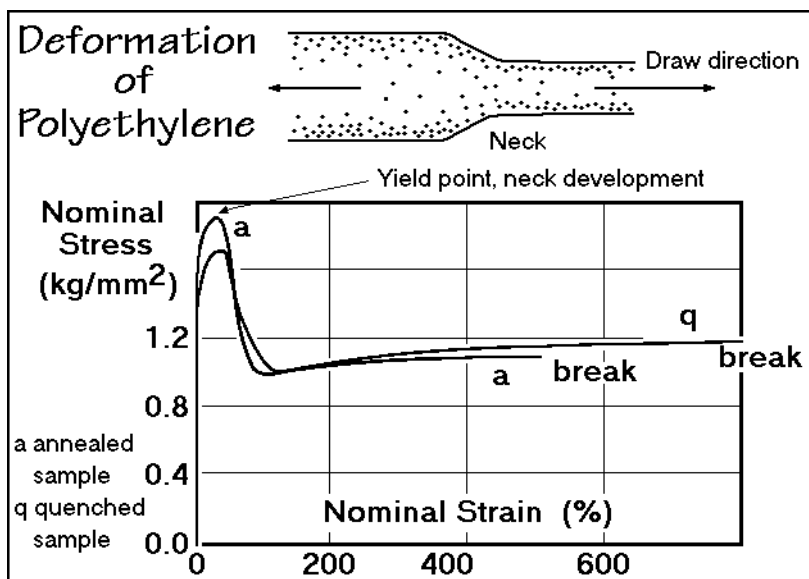


Fig. 5.108

drawing of quenched polyethylene. During plastic deformation in the neck, the cross-section is drastically reduced, so that the true stress and strain are actually increasing instead of decreasing.

Figure 5.109 illustrates a calculation of the true draw ratio by following the changes of the cross-section at various positions along the fiber, starting at the point of initial necking. In Fig. 5.110 the true stress-strain curves are plotted as calculated

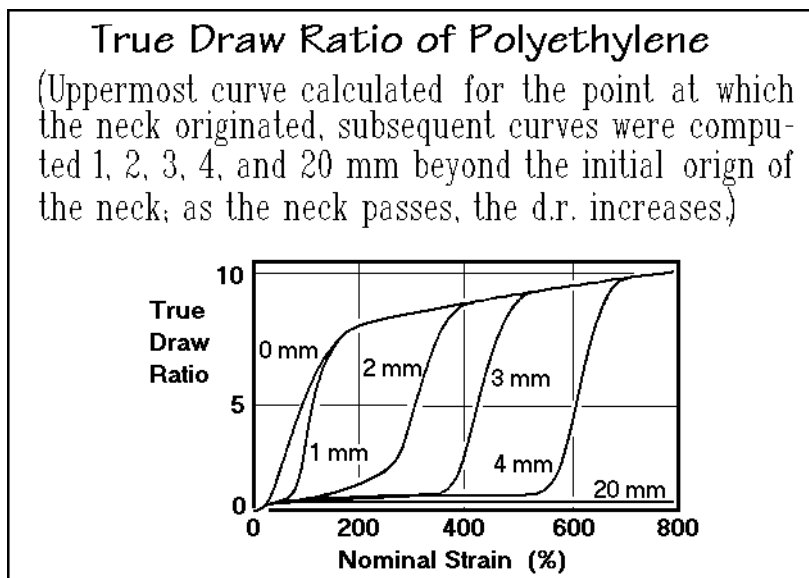


Fig. 5.109

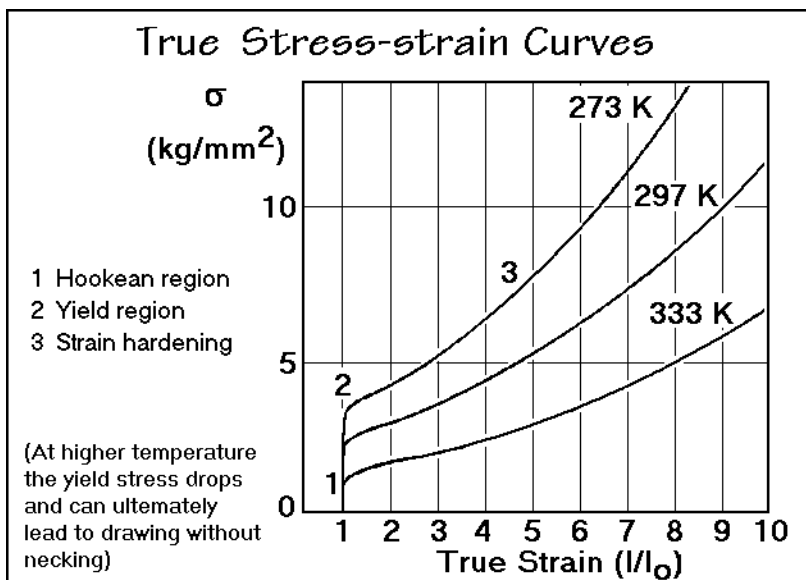
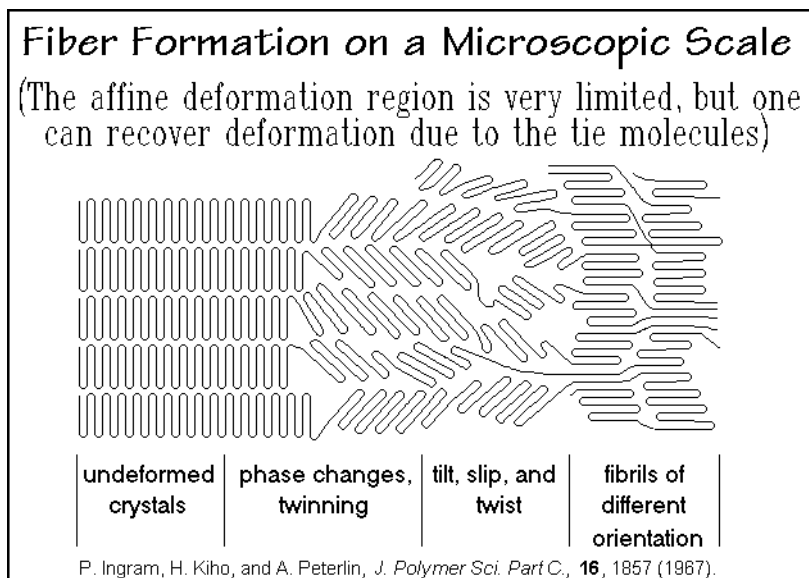


Fig. 5.110

from the actual cross-section at the moment of stress measurement for experiments on drawing at different temperatures. Figure 5.110 shows three regions of different behaviors. Region (1) is the Hookean region. It indicates elastic deformation with a constant Young's modulus as defined in Fig. 4.143. In the scale of the stress in the figure the slope appears almost vertical, i.e., Young's modulus is rather large. This region of elastic deformation decreases with increasing temperature parallel to the increase of *gauche* defects seen in Fig. 5.100. In the region of the neck of Fig. 5.108, a catastrophic change occurs, the polymer yields as marked by (2). Rather than breaking, the modulus increases in parallel with the production of a stronger fiber morphology in a process called strain hardening (3). At the ultimate break, most molecules are arranged along the fiber axis in fibrillar crystals and inter-fibrillar, oriented intermediate-phase material. The oriented, noncrystalline material can often be described as a mesophase. Its structure was derived in Sect. 5.2 on the example of poly(ethylene terephthalate) in Figs. 5.68–72. A more detailed deformation mechanism is schematically given in Fig. 5.111. It was suggested already in 1967 by Peterlin and coworkers (see also [34]).

The simulations discussed in the previous Section begin to explain some of the details of the drawing process. In particular, they show the enormous speed that is possible on a molecular scale for the sliding of the chain within the crystal. The ratio between macroscopic time scales of about 1.0 s and the molecular time scale of 1.0 ps is  $10^{12}$ ! The simulations indicated that the initiation of the diffusion seems to come from a sessile *gauche* defect or kink. On application of an external force, this can lead to a moving of the chains, catastrophically deforming the crystal morphology with the possible creation of a metastable mesophase as an intermediate, as indicated schematically in Fig. 5.111 and shown sometimes to be able to remain as a third phase in Fig. 5.69–72. On annealing, part or all of the initial structure may be regained.

**Fig. 5.111**

### 5.3.6 Ultimate Strength of Polymers

To use flexible linear macromolecules as high-strength materials, the molecular chains should be arranged parallel to the applied stress and be as much extended as possible. The resulting modulus is then dependent on the properties of the isolated chain and the packing of the chains into the macroscopic cross-section. The properties of the chain can be derived from the same force constants as are used for the molecular dynamics calculation in Sect. 5.3.4 with Figs. 1.43 and 1.44. The ultimate strength, also called tenacity or tensile strength, in turn, depends on the defects in form of chain ends and other defects that produce the slipping mechanism and reduce the ultimate number of chains available at break to carry the load. The moduli, thus, are close-to structure insensitive, while the ultimate strengths are structure sensitive as was suggested in the summary discussion of Fig. 5.80 of Sect. 5.3.1.

Figure 5.112 compares the specific tensile strengths and moduli of a number of strong materials. The specific quantities are defined as shown in the figure as the modulus divided by the density. This quantity is chosen to emphasize the materials of high strength at low weight. For these properties most desirable are the materials found in the upper right corner of the plot. Many rigid macromolecules as defined in Fig. 1.6 collect along the drawn diagonal with a rather small ratio of strength-to-modulus because of the above-mentioned deformation mechanism followed ultimately by a crack development that breaks the crystals by separating a few crystal layers at a time needing much less stress. In flexible polymers, the covalent backbone bonds are stronger than metallic or ionic bonds (see Sect. 1.1). High-strength fibers result when chains of a proper mesophase gradually orient parallel to the stress and the molecules become fully extended in large numbers over a small deformation limit.



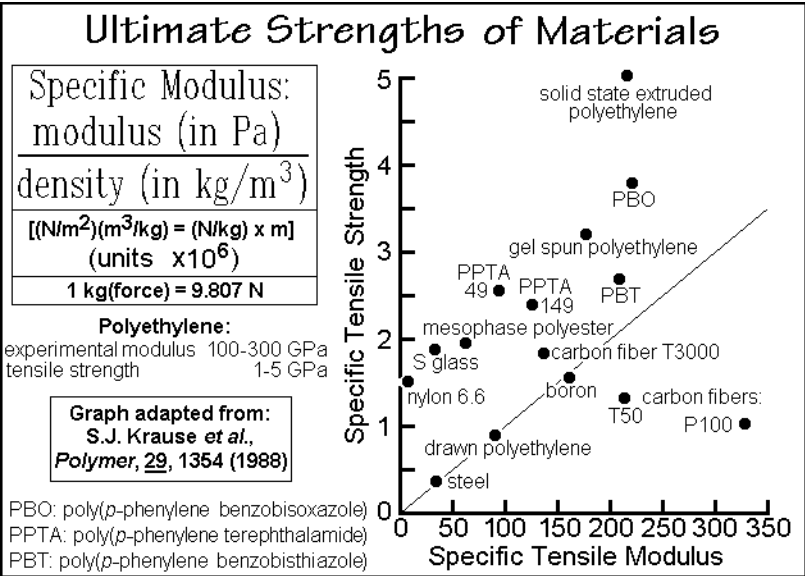


Fig. 5.112

Figures 5.113–115 illustrates the need to parallelize the chains of poly(ethylene terephthalate) applying the three-phase structure, identified in Figs. 5.69–72 [25]. Figure 4.113 shows the model for the combination of the three phases [35,36]. The orientation in the mesophase matrix, measured by its average orientation function (OF) obtained from the X-ray diffraction pattern [24], is of most importance for the modulus and, surprisingly, also for the ultimate strength, as indicated by the left curves

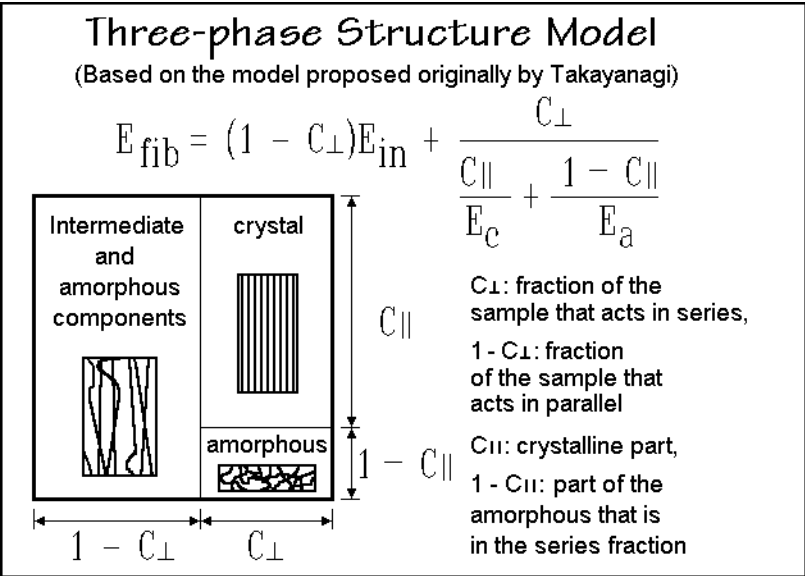


Fig. 5.113

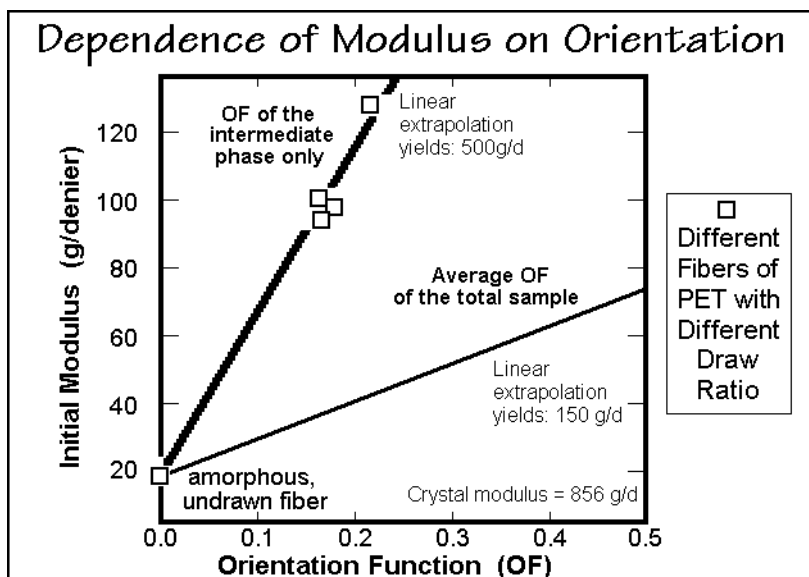


Fig. 5.114

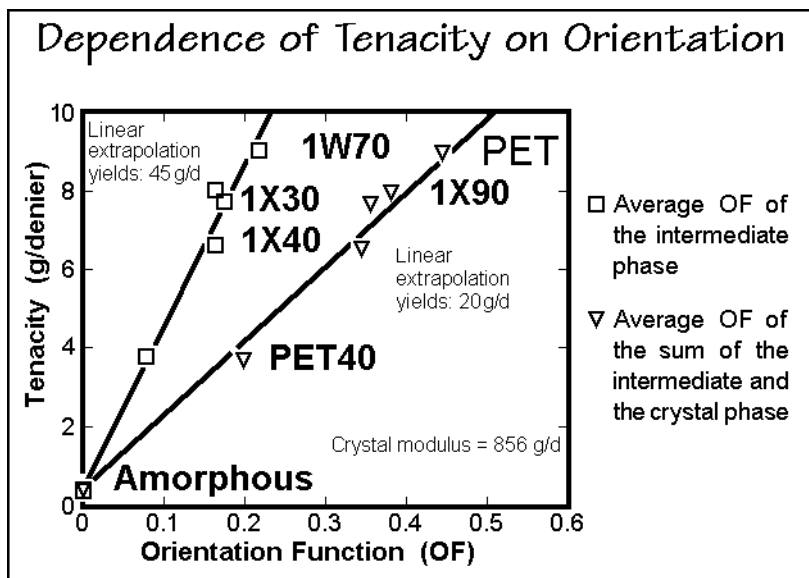


Fig. 5.115

of Figs. 4.114 and 4.116. The right curves are computed assuming the fibers consist only of two phases and, using the total orientation, were summed over all chains. Only the left curves extrapolate within a factor of two to the known ultimate modulus of the crystal of poly(ethylene terephthalate). The extrapolated tenacity is, as expected, smaller than the extrapolated modulus.

## 5.4 Transitions and Prediction of Melting

The discussion in this chapter has dealt in Sects. 5.1 to 5.3 with the description of structure and properties of crystals, perhaps the best-known branch of material science of polymers. Complications arise, however, since most crystallizing polymers do not reach equilibrium. The metastable, multiphase structures will be discussed in Chaps. 6 and 7. They represent the most complex structure and need for their description all tools of thermal analysis of polymeric materials.

In this section, the upper temperature limit of the crystalline state is explored on the basis of experimental data on the thermodynamics of melting, extrapolated to equilibrium. The more common nonequilibrium melting will see its final discussion in Sects. 6.2 and 7.2. The other condensed states of macromolecules, the mesophases, glasses, and melts are treated in Sects. 5.5 and 5.6. Much less is known about them than about the crystals.

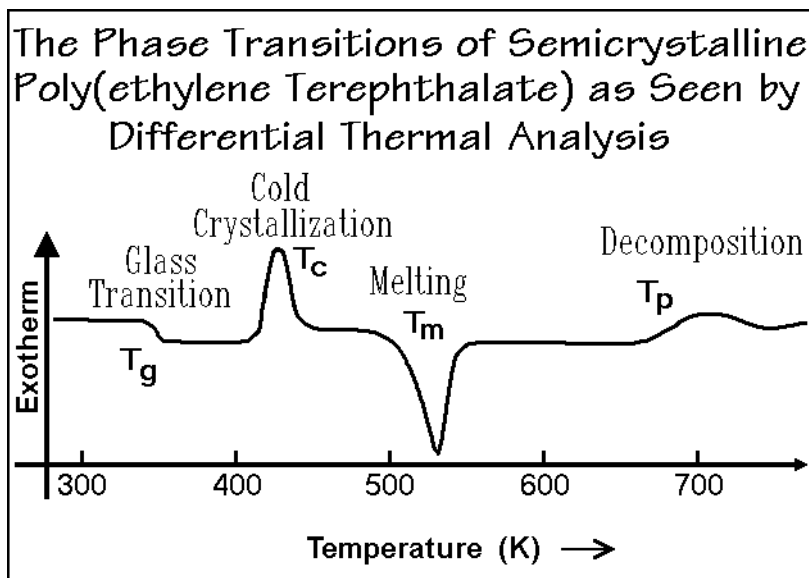
### 5.4.1 Transitions of Macromolecules

The transitions in flexible linear macromolecules are distinguished by their non-equilibrium nature. Figure 5.116 gives a schematic overview of the possible transitions, modeled on the thermal analysis of a quenched, amorphous poly(ethylene terephthalate) presented as a fingerprint DSC in Fig. 4.74. Examples of more quantitative TMDSC analyses of PET are given in Figs. 3.92, 4.122, and 4.136–139. A special review of TMDSC of the glass transition of PET is seen in Figs. 4.129–133. In Fig. 5.116, the glass transition temperature is labeled  $T_g$  and characterized by an increase in heat capacity (see Sects. 2.3 and 2.5) and marks the change of the brittle, glassy solid to a supercooled, viscous melt. More details on glass transitions are discussed in Sects. 5.6, 6.1, and 6.3.

Next is the exothermic crystallization transition at  $T_c$ . Such crystallization on heating above the glass transition temperature is called cold crystallization [37]. It contrasts to crystallization on cooling from the melt, see also Figs. 4.122, 4.136, and 4.138. After cold crystallization, the sample is semicrystalline with about 40% crystallinity, as indicated in Fig. 4.136.

The following melting range is rather broad and indicated by the endotherm, centered about  $T_m$ . Most of the breadth is produced by the wide range in lamellar crystal perfection and thickness (see Sects. 5.2 and 5.3), and additional reorganization occurs during the melting experiment which will be addressed in Sect. 6.2. The resulting melt is stable up to over 600 K, and finally shows an exothermic peak that signals decomposition. The appearance of decompositions of other polymers in thermogravimetry is illustrated in Fig. 3.49.

The main object in the present section is to gain a quantitative understanding of the equilibrium melting temperature and the changes in enthalpy and entropy during the transition. The melting transition assigns the upper temperature limit of the solid state of the crystalline polymers, as pointed out in Fig. 1.6, just as the glass transition alone limits the solid state of amorphous and mesophase polymers (see Sects. 5.5 and 5.6). Beyond these temperatures, polymers cannot be used as bulk structural materials, fibers, or films.

**Fig. 5.116**

Before an analysis of the more common, nonequilibrium melting is possible in Sect. 2.4 and Chap. 6, the empirical information that can be extracted from equilibrium melting of small and large molecules in crystals needs to be understood. For such a discussion, equilibrium data have first to be extrapolated from nonequilibrium. For the equilibrium values of the structure-insensitive, thermodynamic functions, such as enthalpy, volume, and heat capacity, it is sufficient to extrapolate to 100% crystallinity, as discussed in Sect. 5.3.2. The equilibrium melting temperature,  $T_m^\circ$ , is more difficult to obtain with precision. Equilibrium crystals have been made and measured only for few macromolecules, such as polyethylene in Fig. 4.18, some polyoxides, and polytetrafluoroethylene. Extrapolations of melting temperatures with increasing perfection as linked to fold lengths or crystallization temperatures are often chosen as approximation for  $T_m^\circ$ . The final quantity considered is the entropy of melting ( $\Delta S_{\text{fusion}} = \Delta H_{\text{fusion}} / T_m^\circ$ ). The enthalpy of fusion is structure insensitive and the melting temperatures of polymers are typically in the range of 300 to 600 K, errors of 5–20 K in  $T_m^\circ$  are, thus, acceptable for entropy estimates since most thermodynamic functions are known only with errors of  $\pm 3\%$ . The often heard argument that equilibrium information is not available for polymers is not valid in this range of precision, and it will be shown in this section that valuable information can be deduced from a discussion of the equilibrium entropy of fusion.

The discussion of  $T_m^\circ$  must involve four independent variables, namely the enthalpies and entropies of both the melt and the crystal. It, however, will be shown that good estimates of  $T_m^\circ$  can be made by using empirical rules for  $\Delta S_{\text{fusion}}$ , to be derived next. For similar macromolecules  $\Delta H_{\text{fusion}}$  is usually also similar and derivable from the chemical structure. For aliphatic polyesters, for example,  $\Delta H_{\text{fusion}} \approx 2.3 \text{ kJ (mole of backbone atoms)}^{-1}$ . For a summary of extrapolated equilibrium data the ATHAS Data Bank, summarized in Appendix 1, should be consulted.

### 5.4.2 Crystals of Spherical Motifs

The melting of crystals of spherical motifs is the easiest to describe. It is assumed that before melting, the crystal is in perfect order in a cubic or hexagonal close-pack with long-range order and undergoes only vibrational motion. The melting can then be broken into three steps: (1) An increase to the usually larger volume of the melt. (2) The disordering of the crystalline arrangement to the liquid which shows short-range order only. (3) The introduction of additional defects into the liquid structure which, at least for spherical motifs, is often a quasi-crystalline structure and can have defects of the type described for crystals in Sect. 5.3. Of the three types of disorder of Fig. 2.102 which can be introduced on melting of different molecules, spherical motifs can gain only positional disorder. If the motifs are not spherical, rotation adds the orientational disorder. Finally, after fusion, flexible molecules may carry out internal rotations that lead to conformational disorder.

Figure 5.117 lists as the first four substances the entropy of melting of monatomic noble gases. Quite clearly, all noble gases have close to the same entropy of fusion. A simple corollary of this observation is that the value of the melting temperature is linked mainly to the heat of fusion. This, in turn, suggests that the packing for different noble gases is not only similar in the crystals, but also in the melts, so that the increase in interaction energy for atoms with larger number of electrons via the

Melting Temperatures and Entropies of Melting of Crystals with Spherical Motifs					
Motif	$T_m$ (K)	$\Delta S_f$ [J/(K mol)]	Motif	$T_m$ (K)	$\Delta S_f$ [J/(K mol)]
Neon	24.6	13.6	Nickel	1725	10.2
Argon	83.8	14.0	Calcium	1124	8.3
Krypton	116.0	14.1	Lead	601	8.5
Xenon	161.4	14.2	Cadmium	594	10.3
			Platinum	2043	9.6
Silver	1234	9.2	Cobalt	1736	8.6
Lithium	452	10.2	Tin	505	14.2
Aluminum	932	11.5	Chromium	2163	7.1
Molybdenum	2895	9.5	Strontium	1030	8.9
Gold	1336	9.5	Cesium	301	6.9
Sodium	371	7.1	Titanium	2073	10.1
Barium	998	7.7	Copper	1356	9.6

Fig. 5.117

London dispersion forces is the cause of the higher  $T_m^\circ$ . To explain the similar entropies of fusion, one can assume that the entropy of going from positions fixed in the crystal lattice to full access for the motifs to the liquid volume is  $R$ , the gas constant of  $8.31 \text{ J K}^{-1} \text{ mol}^{-1}$ , the communal entropy [38]. An additional  $0.7 R$  was estimated for the two other stages of melting [39]. Assuming that the latter

contributions to the entropy of fusion are approximately proportional to the introduced disorder, one can include all within the rather wide, empirically derived, limits of the positional entropy of fusion. Similar proportionalities are assumed for the other types of disorder included in Fig. 2.103.

The metals in Fig. 5.117 expand the table of entropies of fusion. Perhaps it is not surprising that the metals have an entropy of melting similar to the noble gases. Their crystal structures are frequently also hexagonal or cubic and closely packed with a coordination number of 12 as mentioned in Sect. 1.1.2. A comparison of chromium and sodium in Fig. 5.117 shows that in metals, enormous differences in melting temperatures can be produced with the same entropy of fusion. The maximum in variation of entropies of melting is illustrated between tin and sodium. Some additional metals are shown in Fig. 5.118. In all cases shown, the wide variation of melting temperatures is based mainly on differences of the intermolecular forces and demonstrated by the comparison of the metals tungsten and potassium.

Melting Temperatures and Entropies of Melting of Crystals with Spherical Motifs					
Motif	$T_m$ (K)	$\Delta S_f$ [J/(K mol)]	Motif	$T_m$ (K)	$\Delta S_f$ [J/(K mol)]
Uranium	1406	11.0	CO	68.2	12.2
Iron	1803	8.3	N <sub>2</sub>	63.2	11.4
Vanadium	2190	8.0	H <sub>2</sub>	13.9	13.9
Mercury	234	10.0	O <sub>2</sub>	54.4	8.1
Tungsten	3660	9.6	HBr	186.2	12.9
Potassium	337	7.1	P <sub>4</sub>	317.2	7.9
Zinc	693	9.6	HCl	158.8	12.5
Lanthanum	1193	8.4	PH <sub>3</sub>	139.4	8.0
Zirconium	2130	10.8	HI	222.2	12.9
			SiH <sub>4</sub>	88.5	8.4
CF <sub>4</sub>	84.5	8.4	CH <sub>4</sub>	90.7	10.3
H <sub>2</sub> S	187.6	12.7	CH <sub>3</sub> OH	371.0	8.6

Fig. 5.118

Larger changes in entropies of fusion can be discussed in terms of changes in coordination number between the crystal structure and the quasi-crystalline structure in the melt. The changes in heat of fusion, in turn, are to be linked to the bond energies that will change with coordination number, CN, the changing number of electrons in the conduction band, as well as changes of the character of the bonds from the metallic CN (usually 12) to the covalent CN (often 4, see Fig. 1.5).

The rule of constant entropy of melting was first observed by Richards [40], and should be compared to the rule of constant entropy of evaporation of  $90 \text{ J K}^{-1} \text{ mol}^{-1}$  by simple liquids as proposed by Trouton (see Sects. 1.1 and 2.5.7). Both rules are helpful in developing an understanding of the differences of transition temperatures for different materials. A general application of Richards's rule requires, however,

modification whenever other than positional disorder is produced on melting. Before exploring the melting of such different molecules, Fig. 5.118 shows also some entropies of melting of larger, but close to spherical motifs (molecules). Surprisingly, they still seem to follow Richards's rule. A more detailed investigation, however, reveals that most of these molecules have one or more additional transitions at lower temperatures where the molecules take on a mesophase structure in form of a plastic crystals as defined in Sect. 2.5. At the melting temperature, or better, the isotropization temperature, the motifs rotate within the crystal and, thus, average to a sphere, and satisfy Richards's rule.

Figure 5.119 extends the list of almost spherical motifs to much larger, organic molecules with a molecular structure which is still close to spherical. Again, these molecules are plastic crystals and have gained orientational mobility before ultimate

Melting Temperatures and Entropies of Melting of Crystals with Spherical Motifs			
Motif	$T_m$ (K)	$\Delta S_f$ [J/(K mol)]	Remarks:
Neopentane $C(CH_3)_4$	256.5	12.6	The only possible disorder introduced on fusion is the positional disorder (not quite spherical motifs are able to rotate in the crystal and have an additional transition at lower temp.)
Pseudo-cumene 1,2,4-trimethyl benzene	279.8	13.4	
<i>cis</i> -1,2-Dimethyl cyclohexane	223.2	7.4	
Cyclohexane	279.8	9.4	
Camphor $C_{10}H_{16}O$	451.6	14.3	
			$\Delta S_f = 7 - 14$ [J/(K mol)] [independent of motif size]

Fig. 5.119

isotropization. For the discussion of the entropies of fusion these results indicate that the size of the motif does not significantly influence the entropy of fusion. All data treated up to now, thus, can be summarized by stating that under the given conditions the entropy of fusion, or better isotropization, is made up of mainly positional disordering, and that the entropy of disordering varies little among all these almost spherical and truly spherical molecules.

Figure 5.120 presents, next, the entropy of melting of 20 alkali halides. All of these crystals have the  $F_m3_m$  space group of the NaCl structure which is depicted in Fig. 5.2. The average entropy of fusion of these 20 salts is  $24.43 \pm 1.7$  J K<sup>-1</sup> mol<sup>-1</sup>. Since their formula mass refers to two ions, the average positional entropy of fusion is 12.2 J K<sup>-1</sup> mol<sup>-1</sup>, in good accord with Richards's rule. A total of 76 other salts, with up to four ions per formula, was similarly analyzed [41]. The majority of these salts follow the same rule of constant entropy of fusion per mole of ions, irrespective of the

Melting Temperatures and Entropies of Melting of Ionic Crystals (per Formula Mass)					
Motif	$T_m$ (K)	$\Delta S_f$ [J/(K mol)]	Motif	$T_m$ (K)	$\Delta S_f$ [J/(K mol)]
LiF	1121	24.1	LiBr	823	21.5
NaF	1268	25.9	NaBr	1020	25.6
KF	1131	25.0	KBr	1007	25.4
RbF	1068	24.1	RbBr	965	24.1
CsF	986	22.3	CsBr	909	25.9
LiCl	883	22.6	LiI	742	19.7
NaCl	1073	26.1	NaI	933	25.3
KCl	1043	25.4	KI	954	25.2
RbCl	995	23.8	RbI	920	24.0
CsCl	918	22.6	CsI	899	26.2

**Fig. 5.120**

charge of the ions. There are, however, a reasonable number of exceptions. Smaller as well as larger entropies of fusion have been reported. Lower entropies of fusion can be observed, for example, if the melt is made up of covalently bonded dimers, or if the crystal is disordered at lower temperatures. Higher entropies of fusion are possible if the aggregates in the melt attain more orientational freedom than in the crystal with its correspondingly higher entropy of fusion, as will be discussed next. Excluding 14 such special salts from consideration permitted the analysis of 82 salts and yielded an average of  $10.9 \pm 2.0 \text{ J K}^{-1} \text{ mol}^{-1}$  for the entropy of fusion per mole of ions, in good accord with Richards's rule.

### 5.4.3 Crystals of Non-spherical Motifs

Non-spherical motifs that do not rotate in the crystal before melting, in contrast, should gain an orientational contribution to  $\Delta S$  in addition to the positional disorder. Figure 5.121 illustrates the rather sizable increase on examples of small molecules. This observation of a different, but again largely constant entropy of fusion, was made by Walden [42]. Increasing the size of the motifs, as shown in Fig. 5.122, does not seem to affect the entropy of melting much, as observed also in Fig. 5.119 for the rotating large organic motifs. Assuming now that the entropy of fusion is made of two major contributions, leads to the range for Walden's rule listed in Fig. 5.122.

Finally, one can derive from Richards's and Walden's rules combined that  $\Delta S_{\text{orientational}}$  should be about 10 to  $50 \text{ J K}^{-1} \text{ mol}^{-1}$ . This uncertainty of the entropy change is larger than for  $\Delta S_{\text{positional}}$ , but the rotational degrees of freedom have a larger variation of rotational motion. The rotation may require different amounts of volume, be coupled between neighboring molecules, and, depending on the symmetry of the molecules, may have a reduced entropy contribution.



Melting Temperatures and Entropies of Melting of Crystals with Non-spherical, Rigid Motifs					
Motif	$T_m$ (K)	$\Delta S_f$ [J/(K mol)]	Motif	$T_m$ (K)	$\Delta S_f$ [J/(K mol)]
HCF <sub>3</sub>	118.0	34.4	C <sub>2</sub> H <sub>6</sub>	89.9	31.8
CO <sub>2</sub>	216.5	38.7	SO <sub>2</sub>	197.6	37.4
N <sub>2</sub> O	182.3	35.9	CHCl <sub>3</sub>	210.0	45.2
COS	134.3	35.2	SiCl <sub>4</sub>	203.4	37.9
CS <sub>2</sub>	161.1	27.2	C <sub>6</sub> H <sub>6</sub>	278.5	35.3
Br <sub>2</sub>	267.0	40.4	SF <sub>6</sub>	218.0	21.8
Cl <sub>2</sub>	172.1	37.2	H <sub>2</sub> O	273.2	22.0
C <sub>2</sub> N <sub>2</sub>	245.3	33.1	NH <sub>3</sub>	195.4	28.9
HCN	259.8	32.3	NO	109.4	21.0
C <sub>2</sub> H <sub>4</sub>	104.0	32.2	CH <sub>3</sub> CF <sub>3</sub>	161.9	42.5
Walden's Rule, proposed 1908					

Fig. 5.121

Melting Temperatures and Entropies of Melting of Crystals with Non-spherical, Rigid Motifs			
Motif	$T_m$ (K)	$\Delta S_f$ [J/(K mol)]	Remarks
Diphenyl C <sub>6</sub> H <sub>5</sub> C <sub>6</sub> H <sub>5</sub>	438.6	44.7	The non-spherical motifs have a distinctly higher entropy of fusion, ranging from 20 to 60 J/(K mol). Again the entropy of fusion is size-independent. The additional contribution to $\Delta S$ is "orientational":
Phenanthrene C <sub>14</sub> H <sub>10</sub>	369.4	50.5	
Anthracene C <sub>14</sub> H <sub>10</sub>	489.6	58.9	
Thiophene C <sub>4</sub> H <sub>4</sub> S	233.8	21.2	
2-Methyl-naphthalene	238.8	50.1	
Dioxane [(CH <sub>2</sub> ) <sub>2</sub> O] <sub>2</sub>	284.2	45.2	
			$\Delta S_f = \Delta S_{\text{positional}} + \Delta S_{\text{orientational}}$

Fig. 5.122

#### 5.4.4 Crystals of Linear Hydrocarbons

Flexible molecules have an additional, size-dependent entropy contribution that can also be derived from the molar entropy of fusion. Figure 5.123 shows the melting temperatures and entropies of melting of the homologous series of normal paraffins

Melting Temperatures and Entropies of Melting of <i>n</i> -Paraffin Crystals					
Motif	$T_m$ (K)	$\Delta S_f$ [J/(K mol)]	Motif	$T_m$ (K)	$\Delta S_f$ [J/(K mol)]
Methane CH <sub>4</sub>	90.7	10.3 (10.3)	Heptane C <sub>7</sub> H <sub>16</sub>	182.6	77.6 (11.1)
Ethane C <sub>2</sub> H <sub>6</sub>	89.9	31.8 (15.9)	Octane C <sub>8</sub> H <sub>18</sub>	216.4	95.4 (11.9)
Propane C <sub>3</sub> H <sub>8</sub>	91.5	38.5 (12.9)	Nonane C <sub>9</sub> H <sub>20</sub>	219.6	70.5 ( 7.8)
Butane C <sub>4</sub> H <sub>10</sub>	134.8	34.6 ( 8.6)	Decane C <sub>10</sub> H <sub>22</sub>	243.4	118.2 (11.8)
Pentane C <sub>5</sub> H <sub>12</sub>	143.5	58.7 (12.3)	Undecane C <sub>11</sub> H <sub>24</sub>	247.6	90.1 ( 8.1)
Hexane C <sub>6</sub> H <sub>14</sub>	177.8	73.6 (12.3)	Dodecane C <sub>12</sub> H <sub>26</sub>	263.6	138.8 (11.6)

**Fig. 5.123**

$C_nH_{2n+2}$ . The first three members of the series with  $n = 1-3$  illustrate Richards's rule with methane, a close to spherical molecule, and Walden's rule with ethane and propane, two non-spherical, rigid molecules. The threefold increase in the entropy of fusion of ethane and propane is caused by the added orientational motion. The linear increase of mass with the number of C-atoms also increases the interaction-energy and, thus, keeps  $T_m$  almost constant.

The special change that occurs with the longer molecules ( $n \geq 4$ ) is connected with their flexibility, i.e., the possible rotation about the interior bonds of the molecule. It becomes first possible in butane with its three conformational isomers, as illustrated in Fig. 1.37. Figure 5.123 shows that for the paraffins with even  $n$  from hexane ( $n = 6$ ) to dodecane ( $n = 12$ ), there is an increase in  $\Delta S \approx 20 \text{ J K}^{-1} \text{ mol}^{-1}$  for each pair of additional bonds around which rotation is possible. Similar observations can be made for the paraffins with odd numbers of carbon atoms. The difference in absolute level of  $\Delta S$  between the odd and even series arises from differences in crystal packing as was analyzed with thermodynamic parameters in Fig. 4.52 for decane. The few paraffins with exceptionally low  $\Delta S$  are, at present, not fully understood. Their low  $\Delta S$  may be caused by experimental error caused by incomplete crystallization, mobility in the crystal through mesophase formation, or by differences in the packing in the crystal or structure in the melt.

The entropy of melting per carbon atom is given in Fig. 5.123 in parentheses and approaches the entropy of melting of polyethylene which is  $9.91 \text{ J K}^{-1} \text{ mol}^{-1}$ . For polyethylene and other flexible polymers the positional and orientational contributions to the melting process are negligible because of the many bonds about which rotation is possible in contrast to a single translational and rotational contribution for the molecule as a whole. This simplification allows for an easy assessment of the chain flexibility, as is shown in Section 5.4.5.

From entropy data on polymers discussed in the next section and the just presented small molecules, one can derive that  $\Delta S_{\text{positional}} \approx 7\text{--}14 \text{ J K}^{-1} \text{ mol}^{-1}$ ,  $\Delta S_{\text{orientational}} \approx 20\text{--}50 \text{ J K}^{-1} \text{ mol}^{-1}$ , and  $\Delta S_{\text{conformational}} \approx 7\text{--}12 \text{ J K}^{-1} \text{ mol}^{-1}$ . Only the last contribution is size-dependent, i.e., it is proportional to the number of rotatable bonds in the molecule or, for polymers, the repeating unit. The proportionality of the conformational entropy of melting to the number of bonds that allow rotation is also the reason for dividing flexible macromolecules into beads of which each contributes  $7\text{--}12 \text{ J K}^{-1} \text{ mol}^{-1}$  to the conformational entropy. These empirical limits of entropy gain on disordering can also be used for the discussion of mesophases, as is shown in Fig. 2.103 (see also Sects. 2.5 and 5.5).

### 5.4.5 Crystals of Macromolecules

Turning to macromolecules with Figs. 5.124–126, the positional and orientational contributions to the entropy of melting can be neglected for the present discussion since they contribute only little when considering that the total molecule of thousands of chain atoms can have only one positional and one orientational contribution (see Fig. 2.103). To discuss the remaining conformational contributions one can divide the molecules into beads, defined by the bonds causing molecular flexibility. The data in the tables were calculated per mole of beads, with the number of beads indicated in

Melting Data for Some Macromolecules				
Macromolecule	$T_m$	$\Delta S_f$	Packing Fraction	CED
	(K)	[J/(K mol)]	$\Delta(\%)$ $k_l$	(kJ/mol)
Polyethylene	414.6	9.91 (1)	14 0.60	4.18
Polytetrafluoroethylene	605.0	6.78 (1)	15 0.68	3.35
Selenium	494.2	12.55 (1)	11 0.76	9.71
Polypropylene*	460.7	7.55 (2)	9 0.60	4.74
Poly(1-butene)*	411.2	8.50 (2)	9 0.60	4.60
Poly(1-pentene)*	403.2	7.80 (2)	9 0.59	4.52
Poly(4-methyl-1-pentene)*	523.2	9.50 (2)	-2 0.59	4.74
Poly(4-phenyl-1-pentene)*	439.3	5.00 (2)	3 0.64	4.14
Polystyrene*	516.0	9.70 (2)	6 0.63	4.13
Poly(vinylidene fluoride)	483.2	6.93 (2)	11 0.70	3.77
1,4-Polybutadiene, <i>cis</i>	284.7	10.77 (3)	10 0.61	4.18
1,4-Polybutadiene, <i>trans</i>	437.0	2.85 (3)	13 0.60	4.18
Polyisoprene, <i>cis</i>	301.2	4.80 (3)	9 0.62	3.93
* isotactic polymers				

Fig. 5.124

parentheses in the column for  $\Delta S_f$ . The tables include also information on packing fractions in the liquid,  $k_l$  (see Fig. 4.24), and the change of packing fractions on melting,  $\Delta$ , as well as cohesive energy densities, CED. The cohesive energy density is calculated per mole of interacting groups, i.e., per mole of  $\text{CH}_2$ -,  $\text{NH}$ -,  $\text{O}$ -,  $\text{CO}$ -, which may be different from the number of beads. The CED is derived from the heat

Melting Data for Some Macromolecules				
Macromolecule	$T_m$	$\Delta S_f$	Packing Fraction	CED
	(K)	[J/(K mol)]	$\Delta(\%) k_f$	
Polyisoprene, <i>trans</i> $\alpha$	352.7	12.13 (3)	14 0.61	3.93
Polyisoprene, <i>trans</i> $\beta$	356.2	9.90 (3)	12 0.61	3.93
Polyoxymethylene	457.2	10.70 (2)	10 0.70	5.23
Poly(oxyethylene)	342.0	8.43 (3)	10 0.65	4.88
Poly(oxytetramethylene)	330.0	8.74 (5)	11 0.62	4.60
Poly(oxyoctamethylene)	347.0	9.38 (9)	13 (0.60)	4.41
Penton	476.0	10.25 (4)	7 0.65	7.04
Polyglycolide	506.2	11.0 (2)	11 0.72	5.86
Poly- $\beta$ -propiolactone	366.0	9.28 (3)	6 0.71	5.44
Poly(dimethyl propiolactone)	518.2	9.6 (3)	11 0.63	5.02
Poly- $\epsilon$ -caprolactone	342.2	9.25 (6)	9 0.64	4.90
Poly(ethylene adipate)	338.2	7.8 (8)	11 0.67	5.19
Poly(ethylene sebacate)	356.2	7.5 (12)	12 0.64	4.90

Fig. 5.125

Melting Data for Some Macromolecules				
Macromolecule	$T_m$	$\Delta S_f$	Packing Fraction	CED
	(K)	[J/(K mol)]	$\Delta(\%) k_f$	
Poly(ethylene suberate)	348.2	7.7 (10)	11 0.66	5.02
Poly(ethylene terephthalate)	553.2	9.7 (5)	9 0.68	5.02
Polycarbonate	568.2	11.8 (5)	10 0.65	4.51
Nylon 6, $\alpha$	533.2	8.1 (6)	12 0.66	11.7
Nylon 8, $\delta$	491.2	4.5 (8)	8 0.65	10.0
Nylon 6,6, $\alpha$	574.0	8.4 (12)	12 0.66	11.7
<p>Since the macromolecules are so large, the positional and the orientational contributions to the entropy of fusion are negligible. By dividing the molecule into "mobile" beads (given in parentheses) the conformational entropy of fusion per mobile bead can be estimated to be:</p> <p style="text-align: center;">7 – 12 J/K mol</p>				

Fig. 5.126

of evaporation of small model compounds or the heat of solution into solvents of known CED and corrected for volume changes. Out of such tables, omitting the obvious exceptions, the conformational entropy of melting per bead was derived, as shown in Figs. 5.124–126 and mentioned already in the discussion of paraffins in Sect. 5.4.4.

Combining the results of all presented data, a number of valuable conclusions can be drawn about polymers from their melting characteristics. Furthermore, this experience helps to predict the melting properties from information about the chemical structure. Adding this information about melting to the predictions possible from the heat-capacity analysis (see Sect. 2.3 and Appendix 1), a rather complete profile can be developed for the thermal properties of a given chemical structure.

Some examples of the discussion of melting transitions of flexible macromolecules are given next. For polyethylene and a number of all-carbon-and-hydrogen vinyl polymers in Fig. 5.124 one observes that the short side-groups do not contribute to  $\Delta S$ . Next, one can see that going from polyethylene to polypropylene adds one more interacting unit, i.e., it increases the heat of fusion. As a result, the melting temperature increases, yielding a material useable to higher temperature. For poly(1-butene) and poly(1-pentene), the added  $\text{CH}_2$ -groups in the side chain do not seem to be able to increase the interaction in the crystal as derivable from Figs. 5.25 and 5.26, so that the melting temperature decreases again. Of special interest is the poly(4-methyl-1-pentene). The second methyl group at the end of the side chain interacts in this case sufficiently to increase the heat of fusion and melting temperature. Also, it can be derived from Fig. 5.124 that all these polymers have the same packing density in the melt,  $k_r$ , and that the helical polymers pack less-well in the crystal, as was already found in Sect. 5.1.8 when analyzing their crystal structure.

The top three polymers in Fig. 5.124 show a large variation in properties. Polytetrafluoroethylene, PTFE, has a much higher  $T_m$  due to the low  $\Delta S$ . A more detailed analysis shows that at lower temperature PTFE becomes a conformationally mobile mesophase, as is discussed in Sects. 2.5 and 5.5 and illustrated in Fig. 2.63. Adding the entropy of disordering of PTFE of  $2.85 \text{ J K}^{-1} \text{ mol}^{-1}$  at the lower transitions at 292 and 303 K, leads to a similar total  $\Delta S$  as for polyethylene. The somewhat higher  $\Delta S$  of Se is linked to the chemical depolymerization equilibrium in the melt, analyzed with Fig. 2.69. The much higher CED of Se, listed in the last column of Fig. 5.124 is largely compensated by the higher entropy, so that the densely packed Se, whose crystal structure is shown in Fig. 5.20, melts at only 494 K.

Figure 5.124 shows also the similarity between polyethylene and *cis*-1,4-polybutadiene when representing the chains by their bead structure. The C=C-group is a rigid single bead. The reason of the low melting point of the *cis*-1,4-polybutadiene is, however, not obvious. The solution of this puzzle lies with the large intramolecular contribution on melting of polyethylene from the change of the *trans* to *gauche* conformations, not present in *cis*-1,4-polybutadiene.

The series of five polymers with particularly low entropies of melting in Fig. 5.124 show crystals that are disordered, most likely to condense crystals (see Sect. 2.5), as shown above for PTFE. Of special interest is the difference between *cis*- and *trans*-1,4-polybutadiene. Their entropies are shown in Fig. 2.113.

Figure 5.125 illustrates the changes in the homologous series of polyoxides. As always in such series, the first member can have a more suitable packing for the chemically different groups. In this case, the higher melting temperature is due to the higher CED. A similar effect can be seen in the polyesters in Fig. 5.125. Note how the two added methyl groups in poly(dimethyl propiolactone) increase the melting point because of better packing in the crystal.

The three polyesters in Fig. 5.126 show that the reason for the low melting of the aliphatic poly(ethylene suberate) is the larger number of beads. The two aromatic polyesters contain one and two phenylene groups of six carbons linked into rigid rings, losing considerable entropy relative to the all flexible aliphatic chain. The aliphatic nylons, finally, have higher melting temperatures than the corresponding esters because of the higher CED.

Once these empirical rules have been established, it is possible to link the melting temperatures of polymers to chain flexibility, interactions (cohesive energy densities), internal heats of fusion, and the possible presence of mesophases (see Fig. 2.103). Such analyses are of importance for the design of new polymers and of changes in existing polymers when there is a need to alter thermal stability.

## 5.5 Mesophases and Their Transitions

Mesophases are intermediate phases between rigid, fully ordered crystals and the mobile melt, as explained in the introductory discussion of phases in Sect. 2.5, and summarized in Figs. 2.103 and 2.107. The quantitative analysis of melting in Sect. 5.4 shows that with a suitable molecular structure, three types of disorder and motion can be introduced on fusion: (1) positional disorder and translational motion, (2) orientational disorder and motion, and (3) conformational disorder and motion [43]. In case not all the possible disorders and motions for a given molecule are achieved, an intermediate phase, a mesophase results. These mesophases are the topic of this section. Both structure and motion must be characterized for a full description of mesophases.

### 5.5.1 Multiple Transitions

First experimental evidence for mesophases is often the presence of more than one first-order transitions in DSC curves on heating from the crystal to the melt. The disordering of a crystal to its mesophase causes a substantial endotherm. Much smaller endotherms may indicate solid-solid transitions which only involve changes in crystal structure without introduction of large-amplitude motion. Figure 5.127 illustrates the behavior of poly(oxy-2,2'-dimethylazoxybenzene-4,4'-dioxycydecenoyl), DDA-12, a mesophase-forming macromolecule. Before analysis, the sample was quenched to a LC glass, i.e., a solid with liquid-crystalline order, but without large-amplitude motion (see Fig. 2.103). On cold crystallization above the glass transition temperature at about 345 K, metastable condic crystals grow with an exotherm to a partial crystallinity. At about 395 K, the CD crystals again disorder with an endotherm to the liquid crystal. The second endotherm in Fig. 5.127 is the isotropization to the melt. The isotropization is reversible, the disordering is not, as can be tested with TMDSC. Low-molar-mass analogs behave similarly. For example, *p*-butyl-*p*'-methoxyazoxybenzenes can be quenched to a semicrystalline LC glass and shows then a DSC-trace, as displayed in Fig. 5.128, which can be compared to Fig. 5.127. The difference is that the cold crystallization of the small molecules yields close to equilibrium crystallinity instead of the polymeric semicrystalline sample.

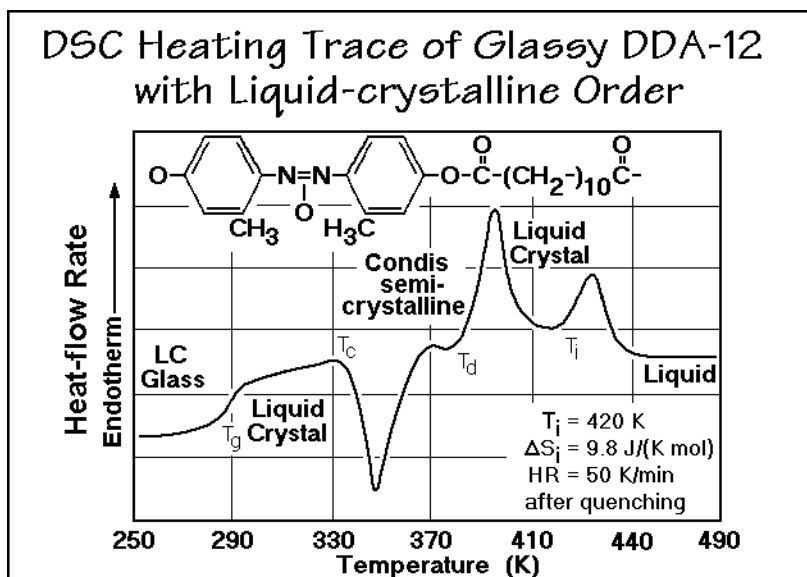


Fig. 5.127

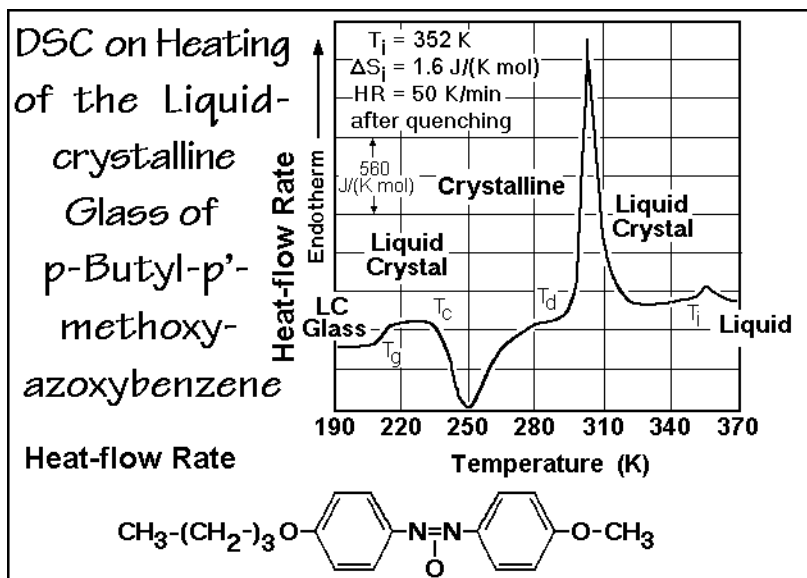


Fig. 5.128

Another example of mesophase calorimetry is shown in Fig. 5.129. On the left, DSC traces are given for poly(dimethyl siloxane), PDMS, which does not exhibit a mesophase, on the right, for poly(diethyl siloxane), PDES, with a stable mesophase. The samples A were quenched with liquid  $N_2$  to the amorphous state, samples B, cooled at  $10 \text{ K min}^{-1}$ , and samples C, slowly cooled or annealed. The quickly cooled

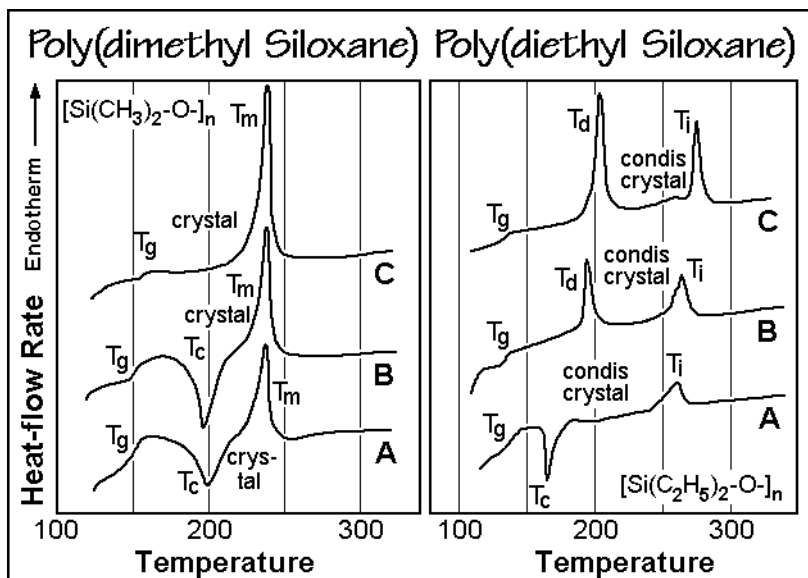


Fig. 5.129

samples, A, show cold crystallization at  $T_c$  (see Sect. 3.5.5). The samples C show only weak glass transitions, and PDMS displays one, PDES two relatively sharp endotherms. On cold crystallization, A, PDES forms only the condis phase with partial crystallinity. The semicrystalline PDES of samples B and C disorder to the condis phase at about 200 K. The condis phase was shown to be able to be annealed to extended-chain crystals.

In Sect. 2.5 a similar two-step melting was discussed for the condis state of *trans*-1,4-polybutadiene. The *cis*-isomer shows in Fig. 2.113 complete gain of the entropy of fusion at a single melting temperature, while the *trans* isomer loses about 2/3 of its entropy of transition at the disordering transition. The structure of the *trans* isomer is close to linear, so that conformational motion about its backbone bonds can support a condis crystal structure with little increase in volume of the unit cell.

The existence-range of the condis crystal of poly(tetrafluoroethylene), PTFE, can be seen from the phase diagram of Fig. 5.130. The calorimetric heat capacity analysis of PTFE is described as an example of the ATHAS applications in Fig. 2.63, and the entropies of transition, which lead to the high isotropization temperature, are discussed in Sect. 5.4.3.

A TMDSC analysis at different frequencies and amplitudes reveals in Fig. 5.131 that the solid-solid transition which changes the  $1 \times 13/6$  helix to the  $1 \times 15/7$  helix is irreversible, while the transition to the condis state is reversible [44]. The conformational disorder consists mainly of a mobility of the  $1 \times 15/7$  helix from left- to right-handed, averaging the structure of the backbone chain so that it fits into the trigonal symmetry. The low-temperature crystals are triclinic with a fixed left- or right-handed  $1 \times 13/6$  helix (see Sects. 5.1 and 5.2). Crystal form III is a high-pressure phase with a close-to-planar chain conformation, and form IV, located between the two endotherms of Fig. 5.131, is made up of rigid  $1 \times 15/7$  helices.



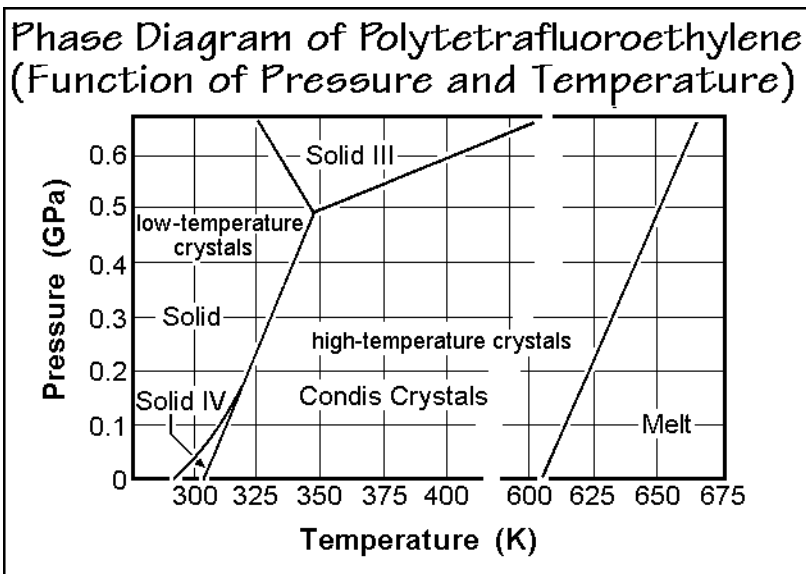


Fig. 5.130

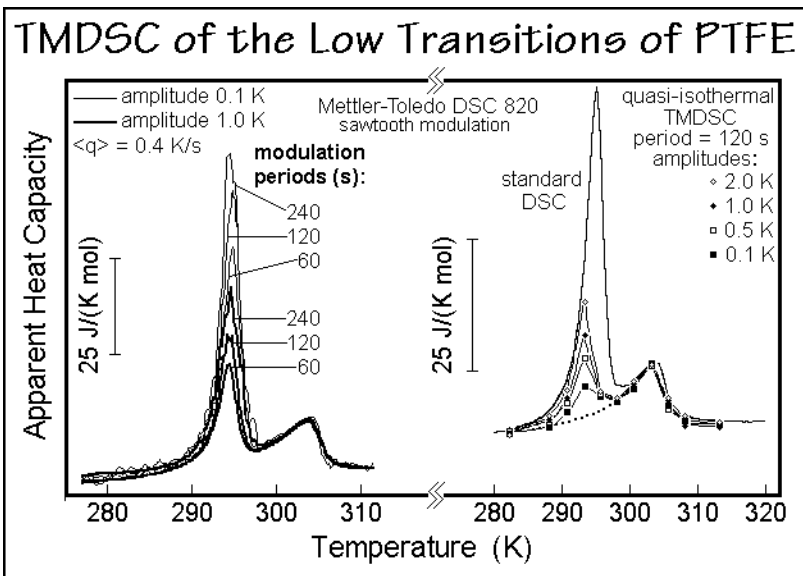
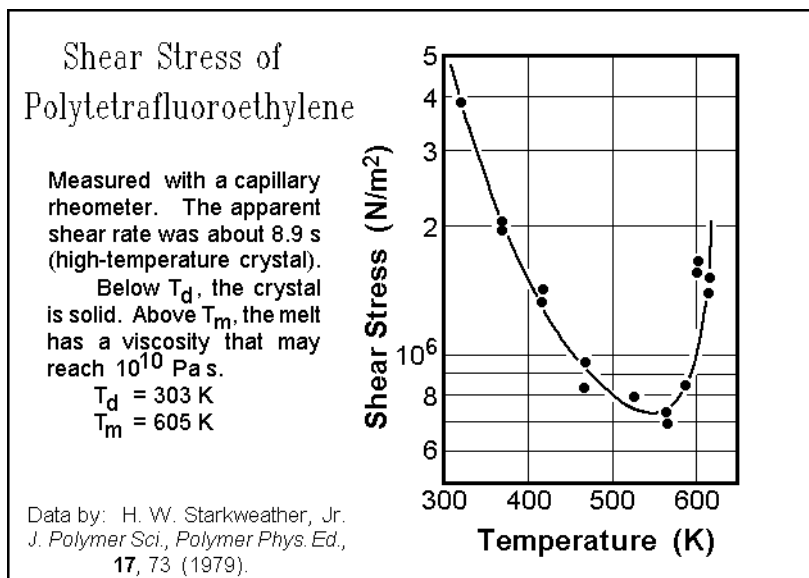


Fig. 5.131

Figure 5.132 illustrates that mesophases can also be identified by rheological properties. The crystals of PTFE show a highly anisotropic flow parallel to the molecular axes, a property often found in smectic liquid crystals. As soon as the molecules start to melt, however, the shear-stress increases abruptly because of the chain-entanglement that occurs during melting. On a microscopic basis, PTFE

**Fig. 5.132**

crystallizing in the condis state can, given enough time, extend their initially chain-folded crystals, and yield extended-chain, equilibrium crystals (see Sect. 5.2).

On a molecular scale, mesophases are most easily detected by direct determination of the mobility of their molecules. An example is shown for *trans*-1,4-polybutadiene in Fig. 2.112 by measurement of the second moment of the line-width of the proton NMR signal [45]. At the glass transition, the usual gradual narrowing of the line-width is observed, while disordering to the condis-phase shows a further decrease. On isotropization, the NMR signal becomes a very narrow line.

A listing of the typical properties that distinguish the different mesophases is also given in Sect. 2.5 with Fig. 2.107. Furthermore, Sect. 2.5 contains examples for low-molar-mass liquid crystals and plastic crystals in Figs. 2.108–111, important model compounds for polymers.

### 5.5.2 Classes of Mesophases

The three different classes of mesophases are characterized in Fig. 2.107. Their disorder, and large-amplitude motion are at the root of their characteristic properties [43]. The change from an ideal crystal to a defect crystal, and finally to a plastic crystal can be understood as follows: The defects in the ideal crystal do not disturb the long-range order and concentrate at the surface. The motion of the defects is largely localized, as described in Sect. 5.3. The plastic crystal, in contrast, has all motifs rotating, averaging the shape of the close-to-spherical mesogen in time and over locations. A concerted rotation of nearest neighbors permits closer approach of the motifs than needed for free rotation.

The condis crystal motion results in a similar rotation as in the plastic crystal, but the molecules do not rotate as a whole, rather they undergo segmental motion and

remain largely parallel [46]. This segmental motion is indicated by the molecular dynamics simulation reproduced in Fig. 5.133 (see also Fig. 5.102). Again, time and position averages yield a higher symmetry that usually leads to hexagonal, columnar crystals with the molecular chain direction parallel to the c-axis.

The two main liquid-crystal polymorphs, nematic and smectic, of disc- and rod-like mesogens are compared in Fig. 5.134 to their ideal crystals. Possible flexible

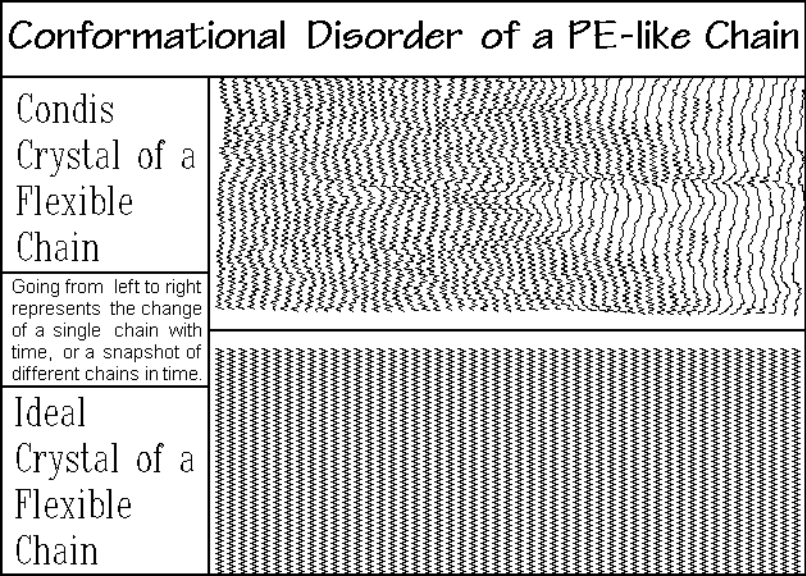


Fig. 5.133

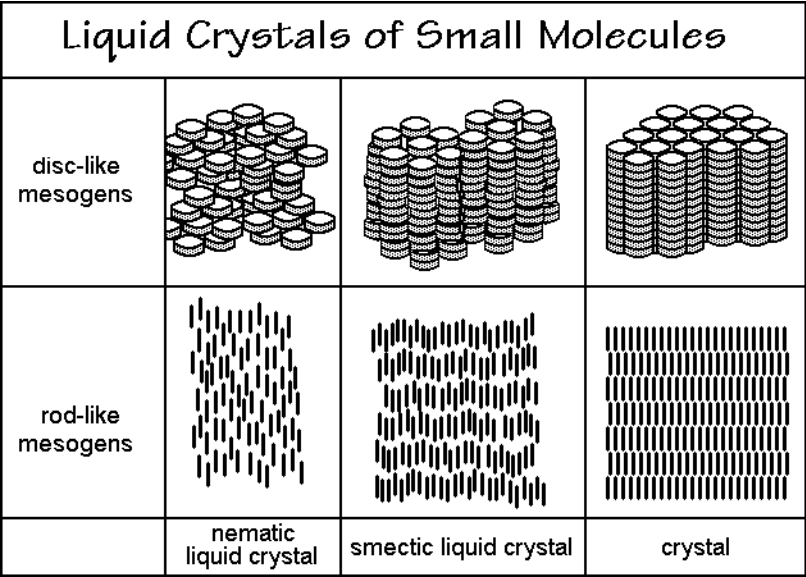


Fig. 5.134

appendages are not shown. These flexible appendages in the nematic liquid crystal are fully interspersed with the mesogen, i.e., they form a solution. For the smectic LC, however, the two parts of different flexibility, and often also different polarity, are nanophase-separated. At lower temperatures, many smectic LCs remain separated in their two nanophases, as shown in Fig. 5.135 for 4-*n*-octyloxybenzoic acid. Solubility and nanophase-separation are also implied in Fig. 5.136 for polymeric LCs.

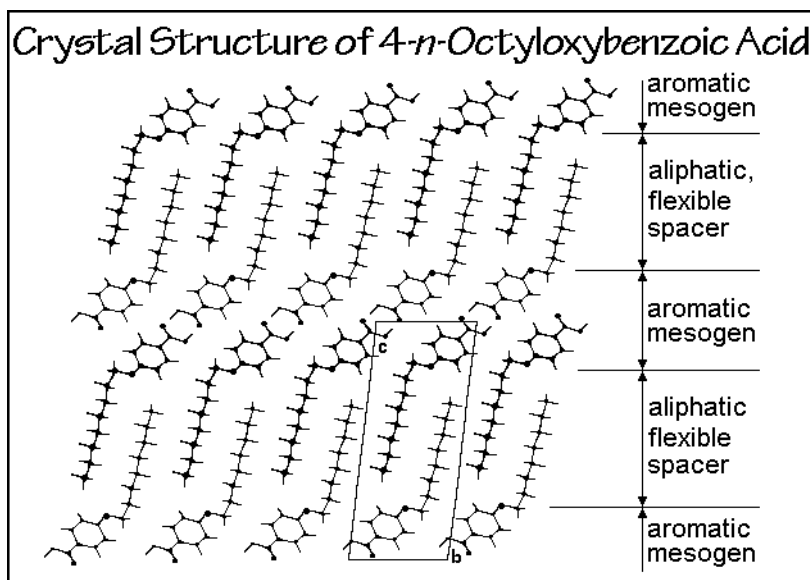


Fig. 5.135

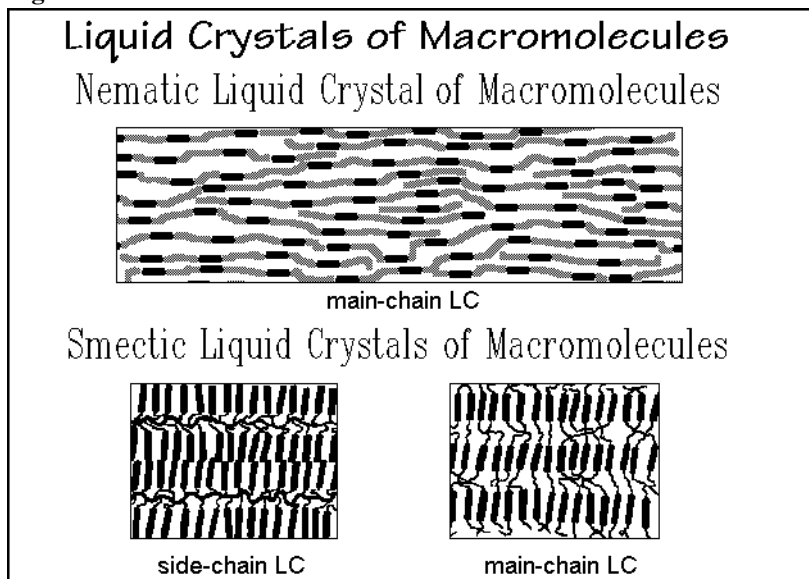


Fig. 5.136

With the help of the entropy discussion of Sect. 5.4, the scheme of mesophases and their transitions can now be made more quantitative. Figure 2.103 is a summary of the scheme of phases including the entropy contributions for the possible changes in large-amplitude motion and order. The isotropization entropy of the least-ordered nematic and smectic liquid crystals is much smaller than  $\Delta S_p + \Delta S_o$ . A summary of 279 nematic mesophases of small molecules gave an average  $\Delta S_i$  of only  $2.3 \pm 1.5 \text{ J K}^{-1} \text{ mol}^{-1}$  and 188 smectic mesophases, of  $11.7 \pm 7.8 \text{ J K}^{-1} \text{ mol}^{-1}$ , less than the positional disordering of a single atom of Sect. 5.4. Polymeric liquid crystals do not show much increase from these values. Side-chain LCs led to  $3.5 \pm 2.5 \text{ J K}^{-1} \text{ mol}^{-1}$  and  $9.8 \pm 5.6 \text{ J K}^{-1} \text{ mol}^{-1}$ , respectively, while the nematic main-chain LCs led to  $15.6 \pm 7.5 \text{ J K}^{-1} \text{ mol}^{-1}$  (with 67 examples) [43]. Only longer flexible segments between the rigid mesogens increase the entropies of isotropization, as one would expect from a certain degree of ordering imparted on the flexible chains as can be seen in Fig. 5.136.

Plastic crystals always show the expected  $\Delta S_c$  on isotropization as deduced from Figs. 5.118 and 5.119, while condic crystals have the highest entropy of isotropization. Figure 2.103 indicates a value of  $n' \Delta S_c$  for polymers, and  $n' \Delta S_c + \Delta S_o + \Delta S_p$  for small molecules with  $n'$  representing the number of remaining conformationally ordered bonds in the condic crystal ( $n' < n$ ) [43,46].

A broadening of a transition can result not only from decreasing crystal size as shown in Sect. 2.4, but also from decreasing cooperativity of the large-amplitude motion. The Ising model, summarized in Fig. 5.137 has been used for its description. It is based on the assumption that the introduction of two defects in neighboring chains takes less energy than for two isolated defects. An example, derived for the description of a paraffin that can develop 11 defects per chain is given in Fig. 5.138 [46]. The intermolecular energy of an isolated defect is taken to be  $3.35 \text{ kJ mol}^{-1}$ , and the intramolecular, conformational energy, to be  $2.55 \text{ kJ mol}^{-1}$ , as indicated in the

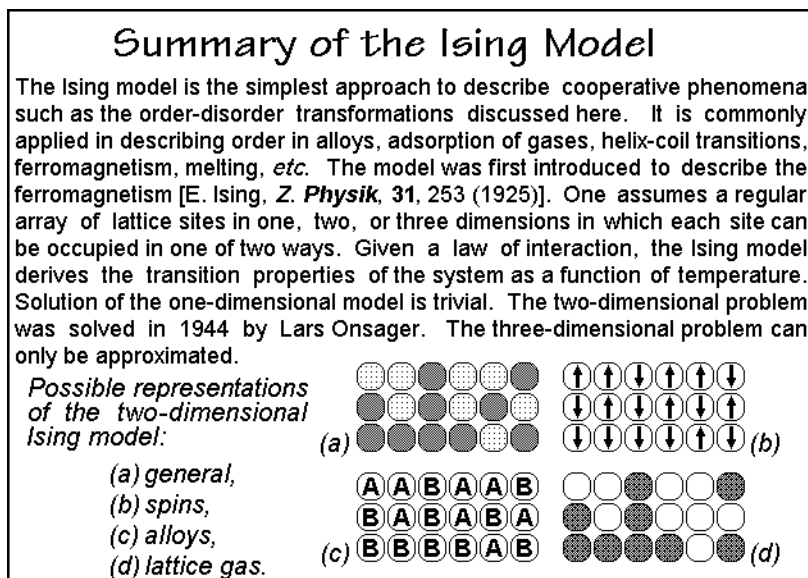


Fig. 5.137

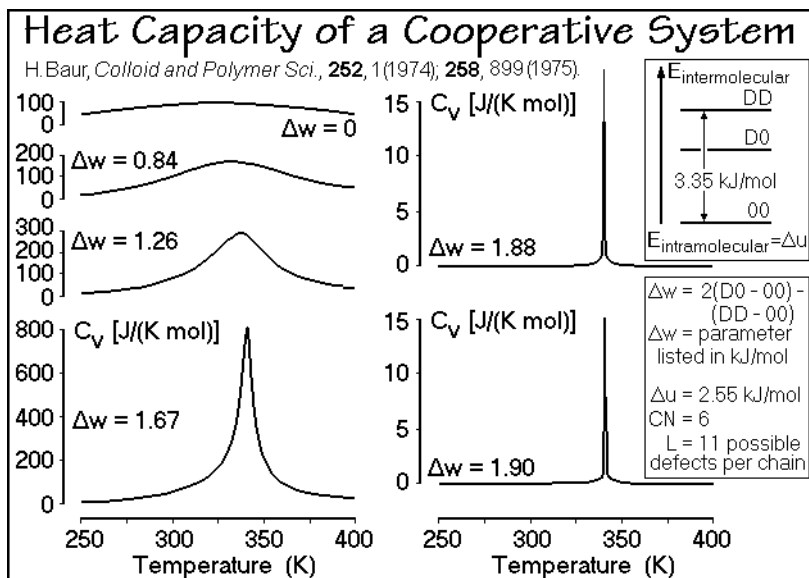


Fig. 5.138

energy-level diagram on the upper right. The character of the increasing excitation depends on the parameter  $\Delta w$ , which is a measure of the cooperativity. If  $\Delta w$  is zero, the beginning of the motion is spread over a wide temperature range, as shown in the heat-capacity curve derived in Fig. 2.33. The figure illustrates the change in sharpness as  $\Delta w$  increases. A true first-order transition is reached with a critical value for  $\Delta w$  of 1.89 when the condition of Fig. 2.119 is reached.

### 5.5.3 Jump-motion in Crystals

The main molecular motion in crystals is vibrational, as described in detail in Sect. 2.3. Heat capacity is the macroscopic tool of choice for its evaluation. Comparing, however, the heat capacity of polymer crystals and glasses with the contributions expected from vibrations, one finds deviations at elevated temperatures, as already noted in Figs. 2.51 and 2.65 for polyethylene. The deviations are linked in Sect. 5.3 to isolated, large-amplitude defect motion. Similarly, the large-amplitude motion accessible in mesophases causes entropy changes which are not always collected in the well-defined transitions, as is discussed in Sect. 5.5.4, below. In the present section, the often overlooked large-amplitude jump-motion is added to the better-known vibrations and large-amplitude motion as a cause of molecular mobility. A jump-motion usually does not register a measurable entropy of disordering if it represents an exchange between states of equal symmetry. In this case disorder exists only during the short time of the actual jump which is usually negligible. If the states before and after jumps are distinguishable and of different degree of overall order, entropies of disordering are measurable.

A jump-motion about an axis of symmetry is a common example of initial large-amplitude motion on the path from a rigid crystal to the melt. It could be identified

only after the development of solid-state NMR as a quantitative tool to probe molecular motion [45]. Since after the jump, the molecule is indistinguishable from its initial state, and the molecule spends only a very short time in transition, there is hardly any increase in disorder (entropy) or change in X-ray structure expected at the onset of this motion. As an example, Fig. 5.139 displays the heat capacity of a cyclopropane. For the crystals, there is little indication of any heat capacity

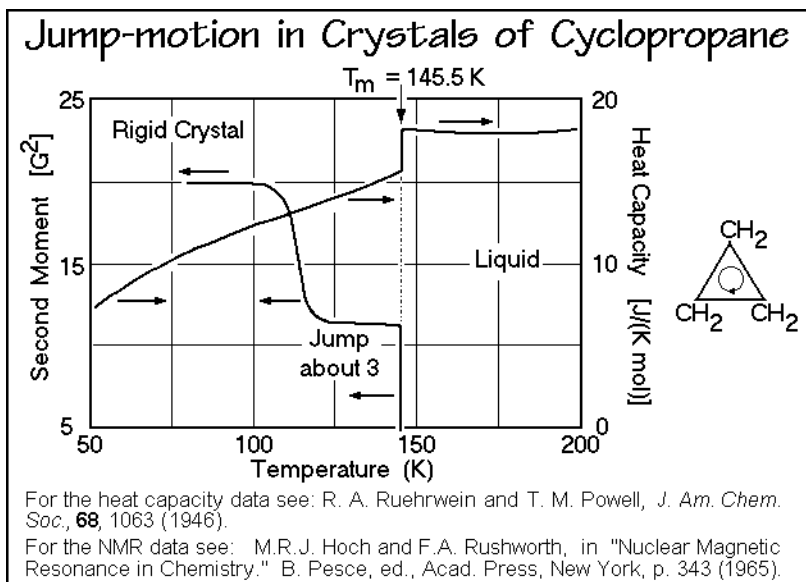


**Fig. 5.139**

contributions besides vibrational. Also, all the expected heat of fusion of the rigid molecule is absorbed at 145.5 K. The second moment of the proton NMR linewidth, however, proves the existence of motion about the threefold axis of rotation, as illustrated in the figure. Good agreement between calculated and measured second moment is achieved with the assumption that at low temperature the crystal shows vibrations only, i.e., it is rigid. The second moment between 120 and 140 K is, in turn, that of  $\text{C}_3\text{H}_6$ , averaged about the threefold axis. In order to be observed, this jump-motion must reach the NMR frequency of 10–100 kHz. This happens at  $\approx 150 \text{ K}$ , 30 K below the melting temperature. This is a much different picture of the motion in the crystal above 125 K from that of a vibrations-only solid.

Figure 5.140 shows a similar analysis for crystals of benzene. Again, rapid jumps about the sixfold axis are possible much below the melting temperature. Closer to the melting point even jumps about the twofold axes are possible. It is of interest that furan,  $\text{C}_4\text{H}_4\text{O}$ , also a planar, rigid, cyclic molecule, but without the symmetry of benzene, shows a transition with entropy  $13.6 \text{ J K}^{-1} \text{ mol}^{-1}$  at 150 K where rotational jumping becomes possible. In this case the jumping occurs to positions with different symmetry, so that an entropy of transition is observed on losing long-range order.

More complicated motions are found in the flexible cycloalkanes of larger size [46]. The molecules possess two endotherms between crystal and melt. Figure 5.141

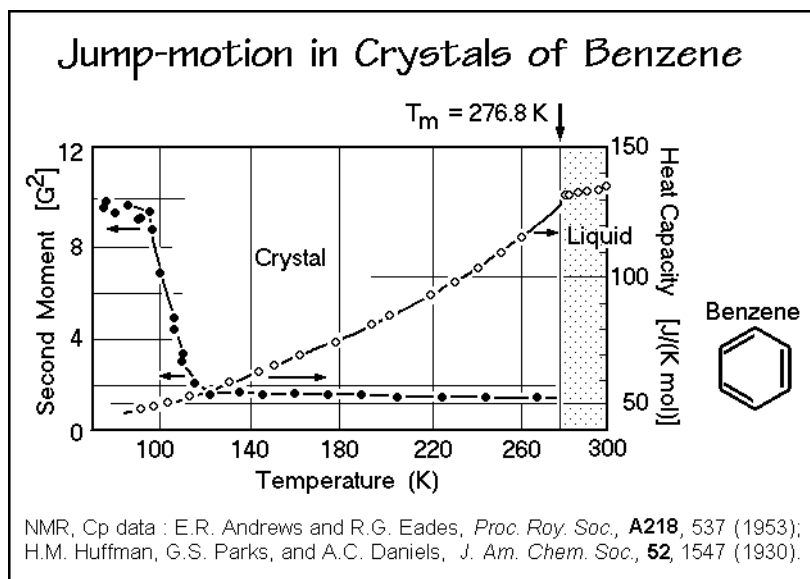


Fig. 5.140

shows the chemical shift for the carbon atoms of the rings of cyclododecane. Below  $T_d$  the crystals have two distinguishable carbon atoms, marked a and b in the graph. On disordering at  $T_d$ , solid-state NMR reveals the equivalence of all carbon atoms of the rings, i.e., the chains must rotate so that the carbon atoms can exchange their positions a and b within the crystal. On melting, only little further change occurs in the NMR spectrum. The ring structure of cyclotetraeicosane ( $C_{24}H_{48}$ ) is more

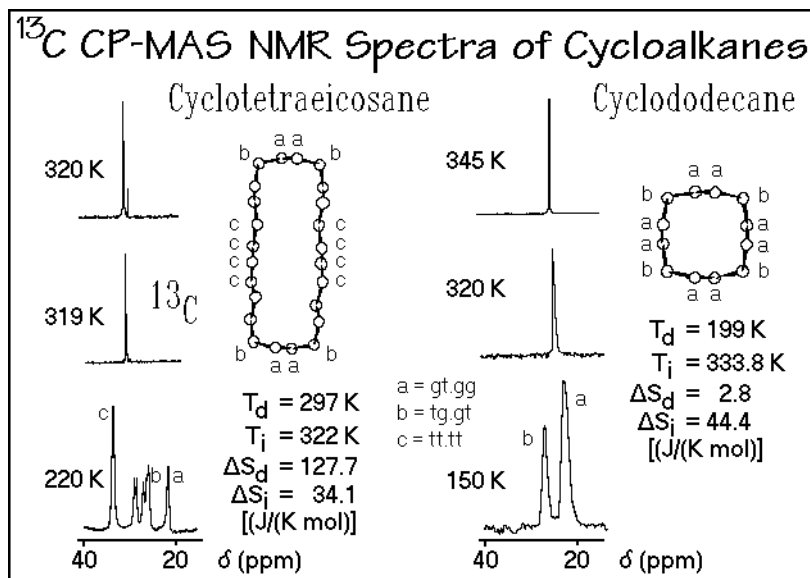


Fig. 5.141



complicated. Three positions could be identified in the NMR spectrum. Again, above the disordering transition only one type of carbon exists. The differences in entropies of transition listed in Fig. 5.141 are linked to defects indicated by the two conformations of the bonds before and after the  $\text{CH}_2$ -groups a, b, and c. The specific jump-motion is discussed next.

### 5.5.4 Conformational Disorder

From the entropies of disordering in Fig. 5.141, one notes that cyclododecane gains almost no disorder in the low-temperature transition, while cyclotetraeicosane may develop 11 to 18 conformational isomers [calculated from  $127.7/(7 \text{ to } 12)$ , based on Fig. 2.103]. The conclusion reached is that cyclododecane may undergo rotoreptation, a rotation with simultaneous change of conformational isomers. This motion leads to little disorder, particularly in a jump-like motion. Schematically, this jump process is shown in Fig. 5.142 for cyclodoeicosane. One can treat this rotoreptation similar to the jump-rotation, seen in cyclopropane and benzene [46].

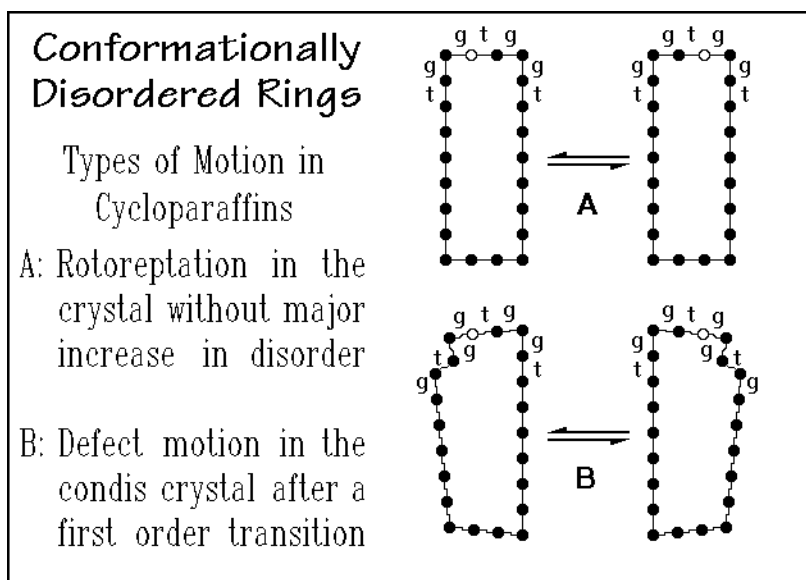


**Fig. 5.142**

The cyclotetraeicosane, in contrast, has a sufficiently large conformational entropy-gain at  $T_d$  to support a defect motion, utilizing most of the bonds, as illustrated in Fig. 5.142. The marked carbon atom  $\circ$  changes in the shown concerted process by one position. Continuation of the process allows interchange of all carbon atoms, as required by the NMR results in Fig. 5.141.

A small molecule that exhibits many mesophases and may serve as a model for molecular motion is *N,N'*-bis(4-*n*-octyloxybenzal)-1,4-phenylenediamine, OOBPD, mentioned already in Sect. 2.5. An overview of its heat capacity and transitions is given in Fig. 2.108. Figure 5.143 represents the same transitions on a more expanded

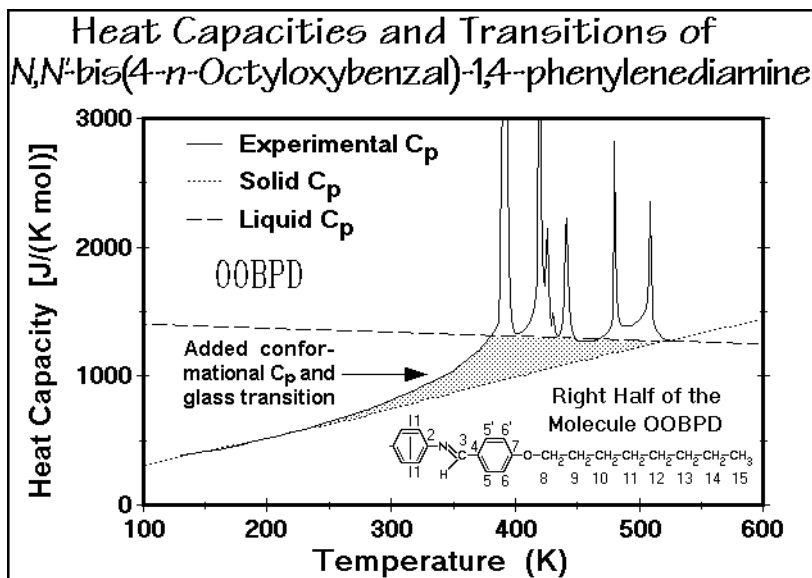


Fig. 5.143

heat capacity scale. The molecular structure consists of the central mesogen and two flexible appendages. Its isotropization transition and, for reference, the data bank values for its liquid and solid heat capacities are shown as the last transition in the heating scan. The transition is rather broad, but the temperature-modulated DSC proves full reversibility of the transition, as illustrated in Fig. 5.144. The nematic liquid crystal has a higher heat capacity than the liquid, a sign of additional ordering

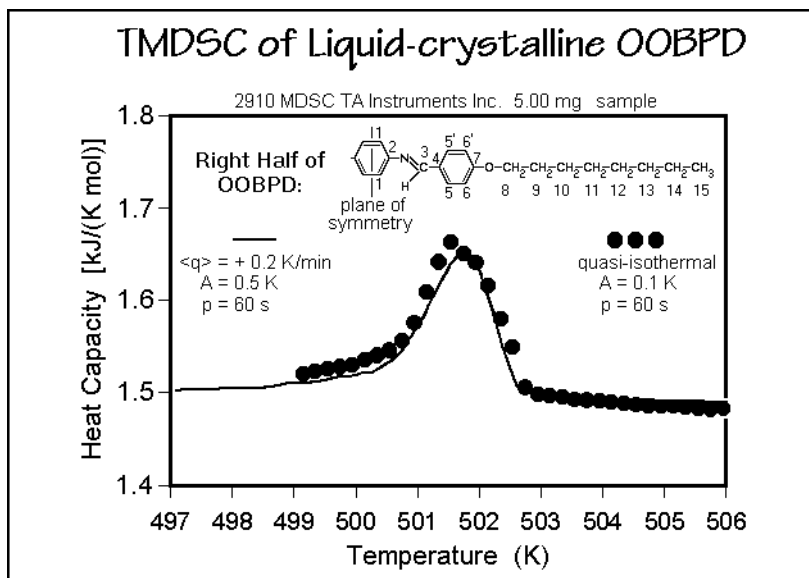


Fig. 5.144

on cooling. This continuous increase in order after the initial, reversible formation of the nematic liquid crystal, N, is typical for the highly mobile liquid crystals. The entropy change at the transition is summarized in Fig. 5.145. The four additional smectic liquid crystals, called H', G', I, and C have a lamellar structure and the mesogens are nanophase-separated from the appendages, although considerable translational motion is still possible. Note that the heat capacity of the smectic state is very close to liquid-like. In contrast to the nematic phase, changes in order occur only close to the transitions. Some of the transitions between the smectic polymorphs are very small and account only for small changes in the molecular order.

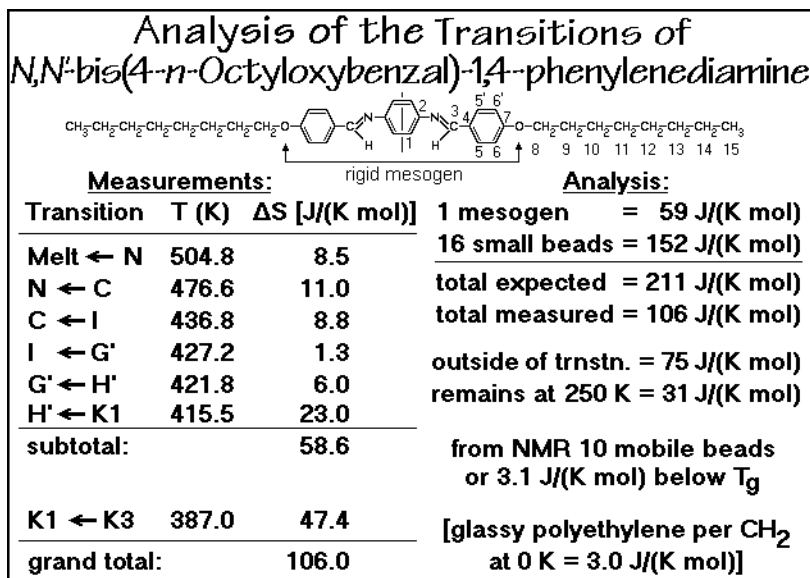


Fig. 5.145

Figure 5.143 shows also the transition to the K<sub>3</sub> and K<sub>1</sub> phases which were originally identified as crystals. The entropies of transition on going from K<sub>1</sub> to the melt amount, when added, to only 59 J K<sup>-1</sup> mol<sup>-1</sup>, as listed in Fig. 5.145, close to the gain expected for positional and orientational disordering of the mesogen alone, leaving all CH<sub>2</sub>- and CH<sub>3</sub>-groups largely mobile and disordered. The transition from K<sub>3</sub> to K<sub>1</sub>, on the other hand, is only 47 J K<sup>-1</sup> mol<sup>-1</sup>, also not enough to order the 16 flexible groups which should take  $\approx 152$  J K<sup>-1</sup> mol<sup>-1</sup>. The crystal K<sub>3</sub> must, thus, still have considerable conformational disorder and be a condis phase. Solid-state NMR could prove this interpretation of the calorimetry of OOBPD.

There is no further transition on cooling the K<sub>3</sub> condis crystal of OOBPD. The shaded area in Fig. 5.143 accounts for some of the difference between expected and measured entropy assessed in Fig. 5.145. The total entropy accounting agrees well with the assessment of the motion by NMR. The overall interpretation of the sequential mesophases of OOBPD is then as follows: At T<sub>i</sub> the melt changes on cooling reversibly to a nematic phase with some gain of orientational order. Four smectic mesophases are produced on further cooling. These have a lamellar structure

and can be considered nanophase-separated mesogens. The condic phase  $K_1$  has fixed a mesogen without orientational and translational motion (but jump-like motion about the twofold axes of the phenylene groups). The nanophases of the flexible appendages are still conformationally mobile, but change order on cooling. The motion slows with decreasing temperature and can be described as a broad glass transition that reaches the solid state at  $\approx 250$  K. At this temperature only vibrational motion remains (see Fig. 5.143).

Besides the stages of freezing, changes of entropy outside the transition region could be documented with OOBPD. With sufficient symmetry, some large-amplitude jump-like motion may go undetected by calorimetry, but is revealed by NMR. Without this symmetry, disordering endotherms are seen in the same temperature region.

### 5.5.5 Examples

To illustrate the enormous breadth of behavior and properties of mesophases, a series of examples is described in this section, in addition to those mentioned in Sect. 2.5 and above. Mesophases may well be the most important source of new materials and are easily recognized by thermal analysis [43,46].

Rapidly quenched polypropylene, PP, is an example of metastable condic crystals. The fast crystallization prohibits the development of proper handedness of the helices of Fig. 5.26. The X-ray diffraction-scan in Fig. 5.146 shows the disorder caused by random assembly of left- and right-handed helices. The two broad diffraction maxima at room temperature correspond to the spacings along and between the chains. The state is a glass, since no conformational mobility is detectable. As soon as the sample is heated to about 360 K, conformational mobility permits perfection of the helices.

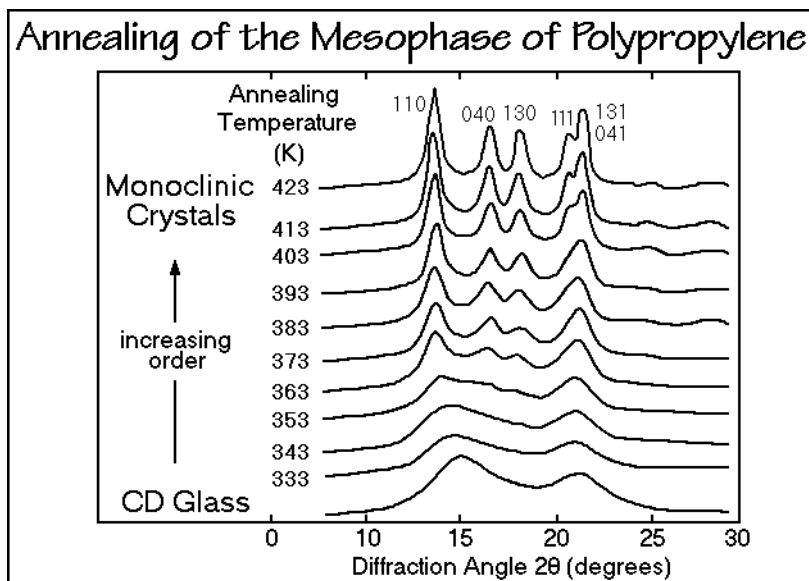


Fig. 5.146

Calorimetry detects an exothermic heat effect of about  $600 \text{ J mol}^{-1}$ . The glass transition of the CD glass must occur at about  $350 \text{ K}$ . The mesophase of polypropylene is not stable under any known condition, it appears only as an intermediate on crystallization, similar to the mesophases found in the fibrous poly(ethylene terephthalate) of Fig. 5.72. Often these metastable mesophases determine the mechanical properties of the materials as demonstrated with Figs. 5.113–115.

Soap-like molecules are examples of condic crystals of small molecules. This is illustrated on the case of the homologous series of thallium carboxylates, TIX, in Fig. 5.147. These soaps are amphiphilic molecules and form lamellar, smectic liquid crystals without the help of a mesogen by ordering on both sides of the interface between the polar and nonpolar parts of the nanophase-separated molecules. The only regular increases of entropy with chain-length  $n$  occur, when adding all transition

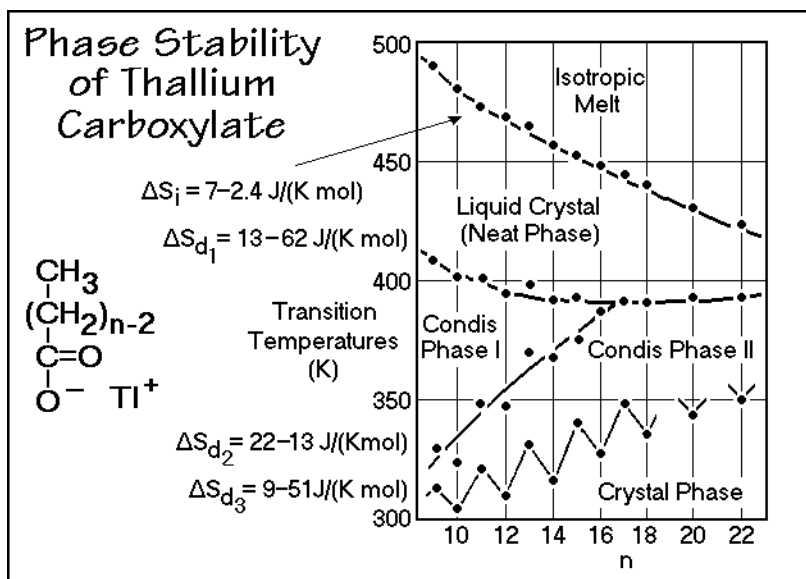
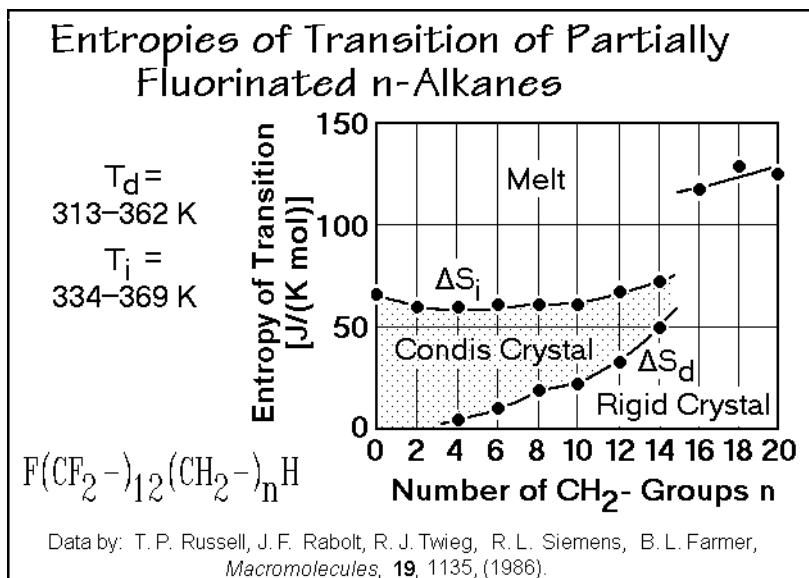


Fig. 5.147

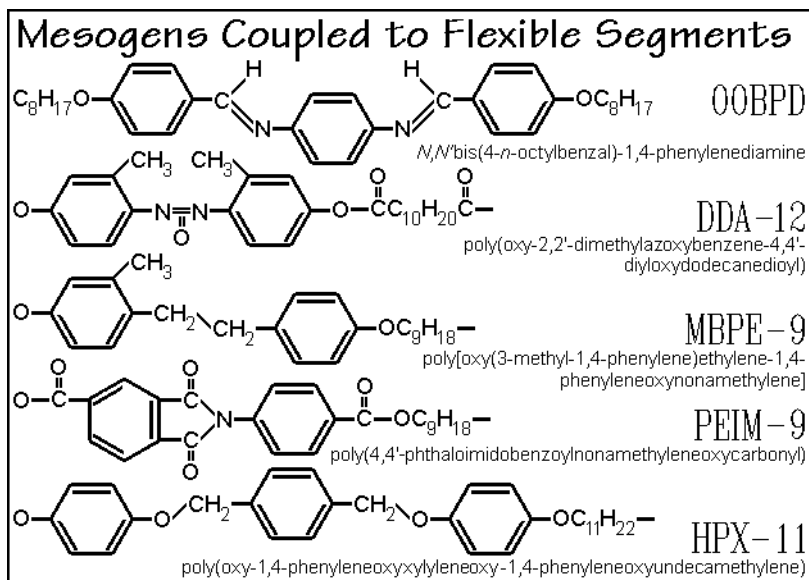
entropies, up to the neat phase. For  $n = 22$  this leads to  $120 \text{ J K}^{-1} \text{ mol}^{-1}$ , still too low to account for the entropy of isotropization expected when melting a completely ordered crystal. From the data of Fig. 2.103 one would expect  $185-300 \text{ J K}^{-1} \text{ mol}^{-1}$ . The deficits of the total entropies of transition may have three reasons: 1) Some disorder remains in the state, erroneously called a crystal phase. 2) Some disordering may occur on heating before reaching the transition regions. Such disordering outside the sharp transition regions has been found for other condic crystals of small molecules such as OOBPD in Fig. 5.145. 3) Some order may be left in the melt. The different polymorphs are labeled condic crystals since they have different degrees of conformational mobility. On isotropization of the liquid crystalline phase only little of the orientational mobility is gained.

Partially fluorinated paraffins are another interesting group of small-molecule model-compounds for mesophase polymers and shown in Fig. 5.148. The condic

**Fig. 5.148**

crystals have conformationally mobile  $CH_2$ -groups because of the lower melting temperature of the paraffins. As the perfluorinated paraffin melting (isotropization) temperature is approached by longer paraffin segments, both phases melt together.

Molecules can be made of alternating amphiphilic segments (Gr.  $\alpha\mu\phi\iota$  = both sides;  $\phi\iota\lambda\omicron\varsigma$  = liking). They have a tendency to phase-separate into different crystals. The similarity of the structure of a number of such molecules is shown in Fig. 5.149.

**Fig. 5.149**

Nematic liquid crystals are found for DDA-12, as illustrated in Fig. 5.127, and for OOBPD, as illustrated in Figs. 2.108 and 5.143–145. In these cases the aromatic groups are sufficiently long and rigid to serve as mesogens. As required for nematic liquid crystals, the two different segments are soluble in the LC and isotropic phases. Both compounds form condisc crystals on cooling with nanophase-separated mesogens and flexible segments. The MBPE and PEIM compounds are at the borderline to liquid crystals, while HPX forms only two condisc polymorphs on cooling from the melt. A few of the special properties of MBPE, PEIM and HPX are illustrated next on hand of experimental data.

The isotropization enthalpy of the homologous series of MBPEs is compared in Fig. 5.150 with DDA with flexible spacers. One notes immediately that the aromatic sequence of MBPE, in contrast to DDA, does not seem to contribute to the ordering

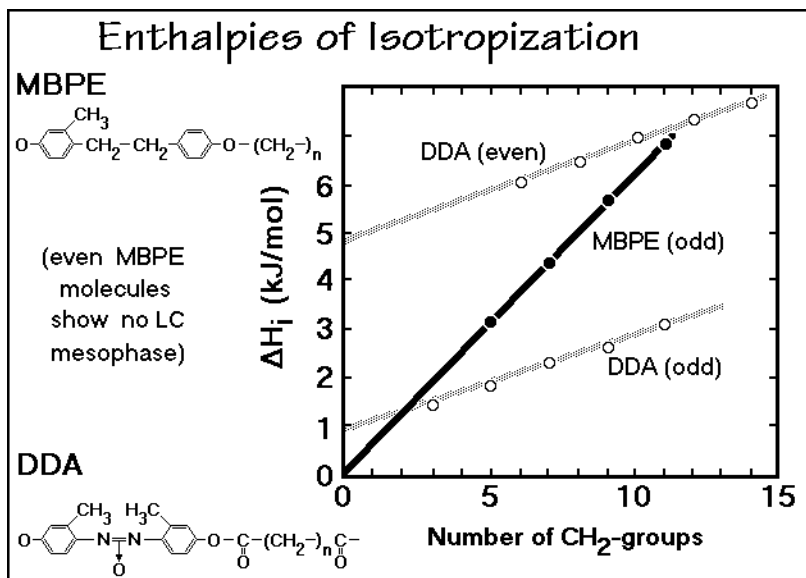


Fig. 5.150

transition. A DSC analysis of MBPE-9 is shown in Fig. 5.151. The high-temperature ordering does not supercool. The DSC curves of MBPE-9 on the right side of Fig. 5.151 reveal that on annealing between the two exotherms on the left, an even more stable phase is generated using up the entire ordered phase formed on cooling and melting at 350 K, only little above the ordering temperature. The more stable phase is identified by the higher melting temperature of about 360 K. One cannot assume that a once-grown, single-phase liquid crystal will revert back to a metastable, amorphous phase and then change to a semicrystalline, two-phase structure where only the crystal phase is more stable. It is much more likely that the ordering is an example of Ostwald's law of successive states. A semicrystalline, less stable condisc phase 1 forms first at 340 K, and not a liquid crystal. This condisc crystals of type 1 convert on annealing to a more stable condisc phase 2 with similar crystallinity as 1 in a process similar to PP in Fig. 5.146, where the condisc phase converts into a stable crystal.

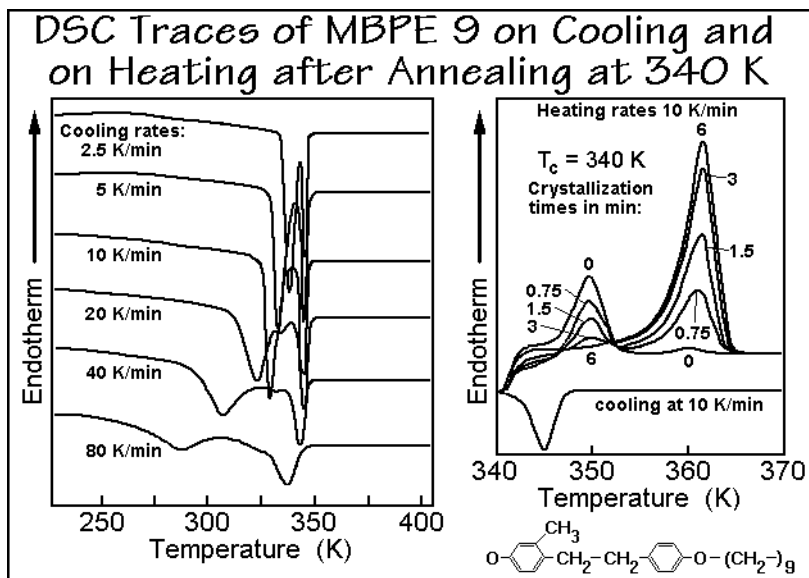


Fig. 5.151

In order to substantiate these assumptions about the phase structures of MBPE-9, the molecular motion was studied by solid state NMR, as shown in Fig. 5.152. The three chosen temperatures are just before initial ordering in the melt, between the two exotherms of Fig. 5.151, and below the second exotherm after completed cooling. Two spectra are shown at each temperature. One is sensitive to mobile atoms, as found in the melt, the other is sensitive to the less mobile atoms as in condic crystals.

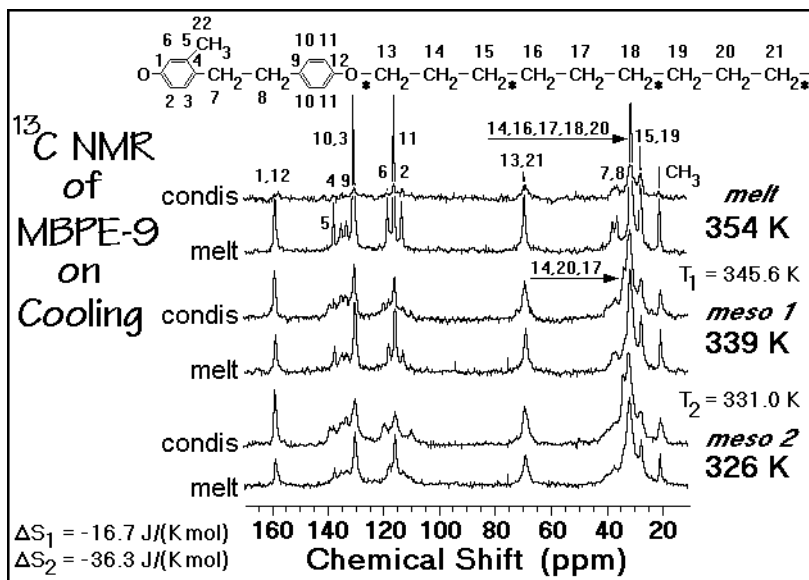


Fig. 5.152



In the melt, there is practically no condensation spectrum. At the two lower temperatures most types of carbon atoms contribute comparably to both spectra, suggesting a partial crystallinity, not observed by liquid crystals. The details of the different spectra reveal that the order of the MBPE-9 observed on cooling between the two exotherms is realized by partial change of the  $\text{CH}_2$ -sequences to *trans* conformations at the four bonds marked by \* in Fig. 5.152. In the more stable room-temperature phase, melting at 360 K, the methyl-substituted phenylene ring also participates in creating increased order without a further increase in the order of the  $\text{CH}_2$ -sequences. The observed transition entropies by DSC could be linked to the transition of polyethylene from the melt to the condensation phase, and of polyparaxylylene from the melt to its crystal phase. The model that has been proposed for this crystallization with little or no nucleation involves a local nanophase-separation or cluster formation between the methylene spacers and the phenylene groups. The interface that develops between the two nanophases keeps the flexible spacers in a more extended conformation and also introduces some orientational order to the aromatic nanophase. No or only little supercooling should then be necessary for the MBPEs to order, while locally undergoing a spinodal phase separation (see Chap. 7).

Finally, quantitative thermal analysis of MBPE-9 was carried out for the mesophase present at low temperature. It was used as an example mesophase in Sect. 2.3.10 in Fig. 2.68. At low temperature the heat capacity agrees with a vibration-only motion. This is followed at higher temperature by three major events: 1) a glass transition, 2) a slow unfreezing of the condensation crystals (shaded area) as in the OOBPD of Fig. 5.143, and 3) the isotropization endotherm. A comparison of the increase in heat capacity at the glass transition and the heat of isotropization reveals a rigid-amorphous fraction, i.e., an amorphous fraction that does not become mobile at the glass transition described in Sect. 6.1. At room temperature the composition is 40% melt, 17% of a rigid-amorphous phase, and 43% CD glass.

The fourth example of molecules with short, alternating rigid and flexible segments in Fig. 5.149 is a series of poly(ester imide)s, PEIMs. It was concluded from a number of investigations that the PEIMs always form layered, supermolecular structures, in both, crystalline and glassy states. According to the discussion above, the nanophase-separated, layered structures could result either from the formation of both, a smectic LC, driven by the mesogen orientation *and* the phase separation, or *only* by the phase-separation of the segments, due to their amphiphilic character, without any LC formation. In the latter case, the layer structure and its molecular order in the immediate vicinity of the interface is based on the need to maintain minimal interfacial energy, no additional ordering is involved. The molecular orientational order that might exist in one or both of the phase volumes is, then, introduced by the geometric restrictions caused by the interface, and not by the intervention of orientational ordering of the mesogen. Small changes of the aromatic segment of the PEIMs by reversing of the carbonyl groups led to a loss of the amphiphilic character due to the shortening the rigid sequence. In this case, stable, nematic, single-phase LC mesophases are observed. Furthermore, by increasing the length of the mesogenic group in PEIMs by the addition of an ethyne group,  $-\text{CH}=\text{CH}-$ , to the mesogen between phenylene and carboxyl groups, a third set of PEIMs results, but now with stable, two-phase, thermotropic, smectic-LC mesophases.

Finally, increasing the polarity of the flexible spacer by replacing the methylene spacer with an ethylene-oxide sequence prohibits again the amphiphilic phase separation, and results on cooling in amorphous glasses, this time without meso-phase ordering. These big changes in the phase behavior on slight modification in the molecular structure demonstrate the importance of nanophase separation and analysis of the phase types.

The thermal behavior of the PEIMs can be judged from the DSC traces in Fig. 5.153. The figure on the left shows a large supercooling before crystallization for the polymer with 12  $\text{CH}_2$ -groups (PEIM-12), but much less for PEIM-9 on the right with 9  $\text{CH}_2$ -groups. The difference may be caused by small changes in the phase

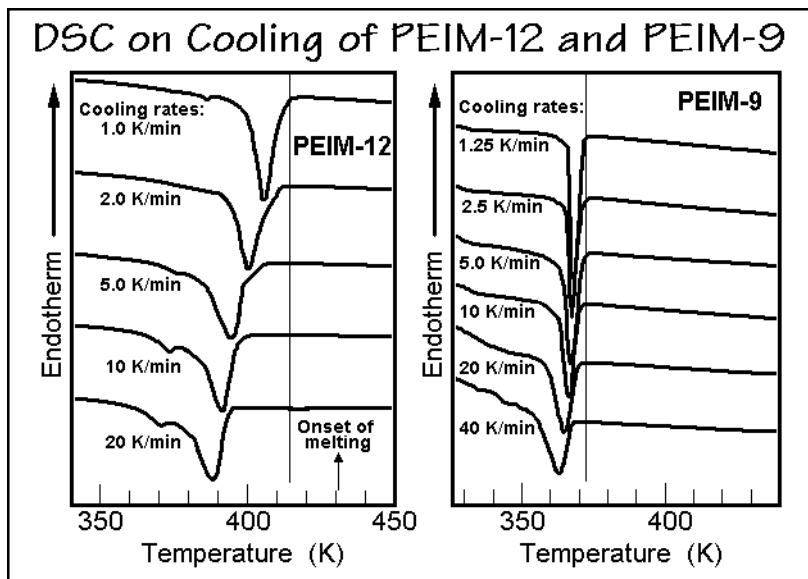


Fig. 5.153

equilibria, with PEIM-9 behaving more like a liquid crystal. Figure 5.154 shows from the temperature-modulated DSC experiments described in Sect. 4.4 that PEIM-12 behaves fully irreversibly, in contrast to a typical LC polymer DHMS-7,9, which has a fully reversible transition. The irreversible behavior of PEIM-12 is similar to a typical polymer crystal or condensation crystal. No contribution is seen for the reversible, quasi-isothermal experiment, as also demonstrated in Fig. 3.89 for an extended chain poly(oxyethylene), POE. The reversible behavior of the DHMS-7,9, a copolyether, synthesized by coupling 4,4'-dihydroxy- $\alpha$ -methylstilbene with a 1:1 molar mixture of 1,7-dibromoheptane and 1,9-dibromononane) is similar to OOBPD, discussed with Figs. 2.108 and 5.143–145. All TMDSC analysis methods, quasi-isothermal, and with an underlying heating and cooling rate (see Fig. 4.88) follow the reversible liquid-crystal transition.

The HPX polymer of Fig. 5.149 has a rather flexible aromatic sequence, and, indeed, the polymer behaves like a typical semicrystalline polymer, just that the aromatic and aliphatic sequences cannot interdigitate in a satisfactory crystal structure

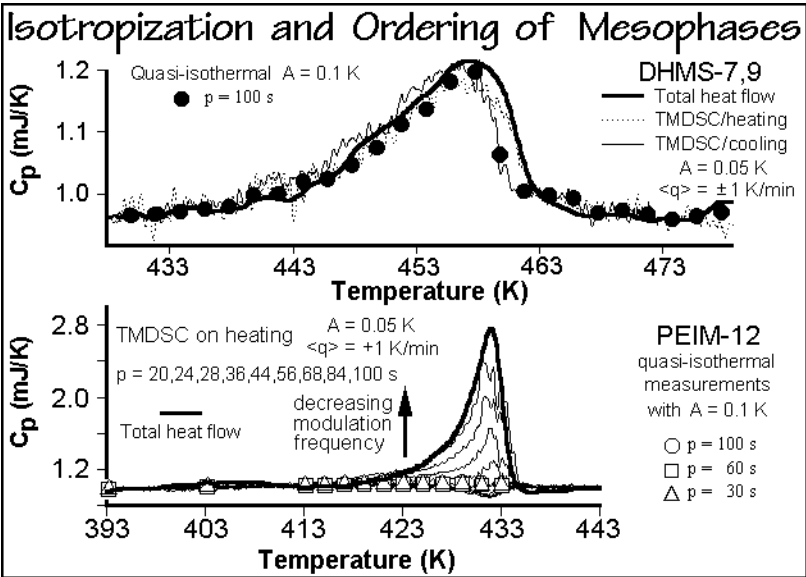


Fig. 5.154

which leads to the condis polymorphs. Figure 5.155 documents the DSC traces on cooling. The onsets of ordering of the isotropic melt to the mesophase show substantial supercooling. Furthermore, the entropies of isotropization are too large to be isotropization entropies of a smectic phase. Solid state NMR could identify the bond conformations of the  $\text{CH}_2$ -sequence below about 437 K as (starting from the ether oxygen):

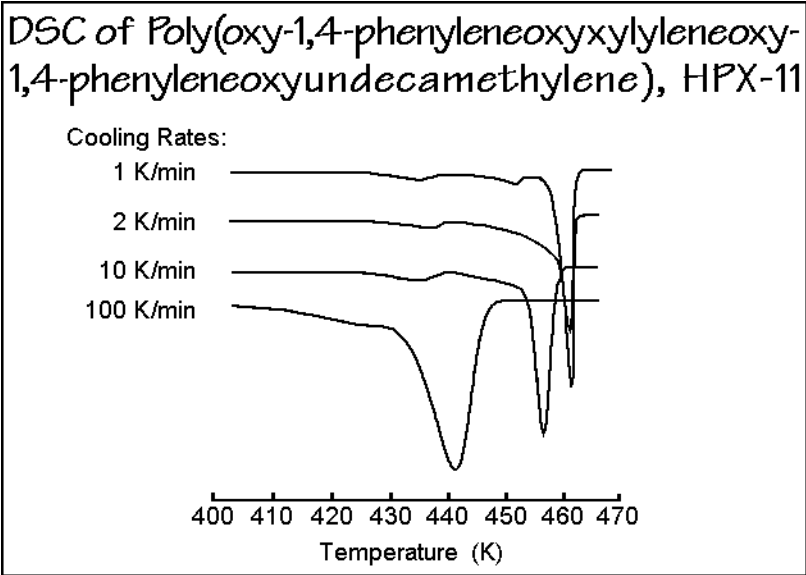
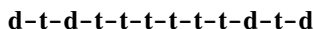
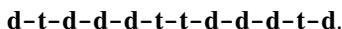


Fig. 5.155



where d stands for disordered, and t, for *trans*. In the high-temperature phase, the flexible spacer has four more disordered bonds with an overall bond conformation of:



The two HPX crystalline polymorphs are, thus, most appropriately classified as condic crystals. At even lower temperatures, the solid state changes to the condic glass, as seen for OOBPD, above.

The final example of a mesophase is the hexagonal polyethylene. The equilibrium phase diagram of Fig 5.156 reveals the stable hexagonal condic phase at high pressure. This condic phase has absorbed more than 50% of  $\Delta S_f$  and has almost as many *gauche* conformations as in the melt. The mesophase mobility gives the reason for the very

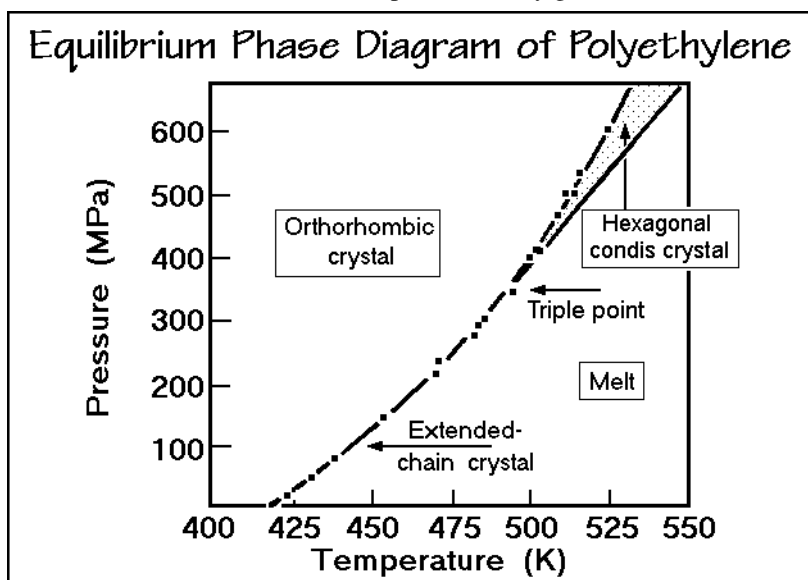


Fig. 5.156

large increase in fold length on crystallization at elevated pressure described in Sect. 5.2. Although not all condic phases analyzed yield extended-chain crystals, all extended-chain crystals grown from polymer melts grew as a chain-folded condic phase first, followed by chain-extension in the mobile condic phase. The orthorhombic phase which is stable at room temperature and atmospheric pressure is described in Sect. 5.1 with Fig. 5.19.

Spinning ultrahigh-molar-mass polyethylene fibers from a gel, as described in Sect. 3.4.3. The gel must have sufficient molecular entanglements to avoid excessive slipping on drawing, but not too many entanglements to restrict the chain extension. The enhanced mobility of such gel of a high-molar-mass polymer results, on drawing, in highly-extended, strong fibers. Their thermal analysis with a DSC showed a

crystallinity of about 70%, not much more than seen in normally-drawn fibers, described in Sect. 5.2. When looking for the amorphous fractions by X-ray diffraction, however, there were only 3–10% of amorphous content seen.

The solution to this puzzle could be found from an analysis with solid-state  $^{13}\text{C}$  NMR. Figure 5.157 shows, using the technique applied to the analysis of MBPE-9 with Fig. 5.152, that in gel-spun polyethylene fibers there are two signals from the

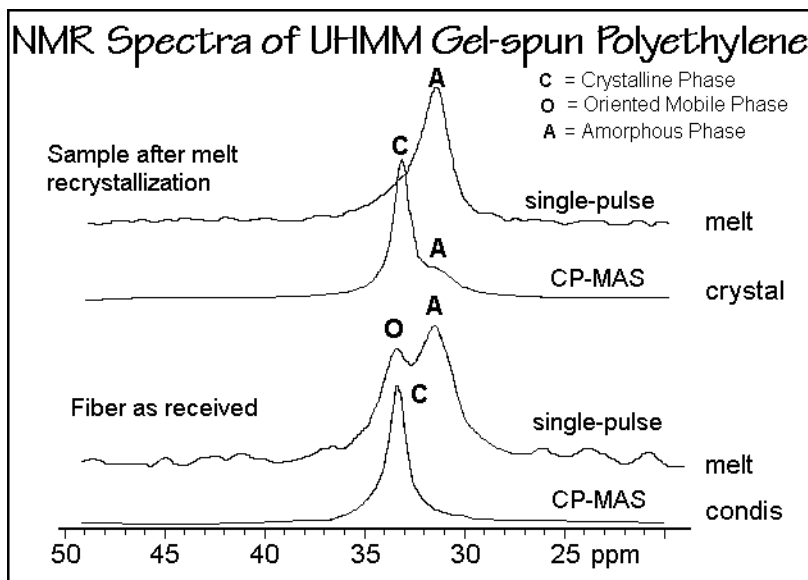


Fig. 5.157

close-to-*trans* conformation, the expected rigid one from the crystal, marked as C in the figure, and a second one at an identical position in the spectrum detecting high-mobility conformations as seen in the melt marked O. The mobile-amorphous part can also be seen in the melt spectrum at the positions A. Note that the intensity scales of the two spectra are not the same and, as such, cannot be taken for evaluation of the sample fractions. On recrystallization, the orientation of the fiber is lost and normal polyethylene results as shown in the two upper curves of Fig. 5.157.

The oriented, mobile phase in the fibers, O, is kept in its metastable state by being connected to the crystal as tie molecules. The relaxation times for the motion involved can be gained from the experiments displayed in Fig. 5.158. A series of 32 successive spectra is shown after different times of spin reorientation. The faster is the recovery of the original peak, the higher is the mobility in the indicated conformation. The relaxation times are listed in the figure. At the shortest time, the amorphous fraction is already fully relaxed, and the oriented mobile phase of the *trans*-component 1 also has reached almost maximal signal intensity, as indicated, while the *trans*-component 2 is just beginning its relaxation.

The condis phase in fibers contributes considerably to the modulus and strength, as was discussed for poly(ethylene terephthalate) in terms of structure and properties in Figs. 5.68–72 and 5.113–115, respectively. The gel-spun polyethylene has little

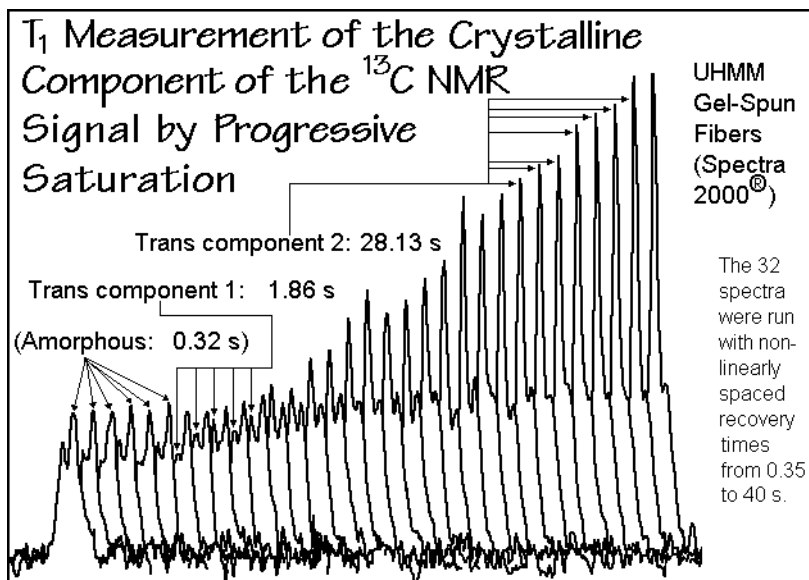


Fig. 5.158

amorphous content and since the chains in the condic phase are parallel to the chains in the crystals, the fibers have moduli not far from the value for the ideal crystal. These examples of metastable mesophases in fibers of polyethylene and PET show that a major difference between small molecules and macromolecules is the ease of formation of metastable nanophases in one-component systems by molecules that link the nanophase-separated system. Adding the ease of inducing molecular orientation in macromolecular fibers makes knowledge of mesophases and nanophases key issues for the understanding of the structure-processing-property triangle. Focusing only on the amount and orientation of the crystals for the properties of fibers has led to limited success. Major contributors to polymer properties are the mobile- and rigid-amorphous nanophases and their orientation. The rigid-amorphous phase may take on the structure of an oriented mesophase when it is drawn, and be the major factor in optimizing fiber moduli and strengths.

*To summarize this section on mesophases*, one must conclude that for the description of any material, its phase structure must be established. Structure *and* large-amplitude motion define the nine basic phases of condensed matter, six of which are mesophases. Structure alone is insufficient to identify a given phase. For flexible macromolecules the most notable mesophase is the condic phase. Metastable, nanophase separation is common in semicrystalline polymers. Specific points are that smectic liquid crystals are nanophase-separated with coupled, high translational mobility in both phases, while nematic liquid crystals are solutions of the two or more molecular segments. Amphiphilic liquid crystals with a lamellar superstructure may have similar phase behavior to the thermotropic, smectic LC if the incompatible molecular segments become small. Their orientational order may be created by the interface, not rod-, disc-, or board-like mesogens. Liquid crystals and condic crystals can be distinguished by the list of attributes given in Fig. 2.107.

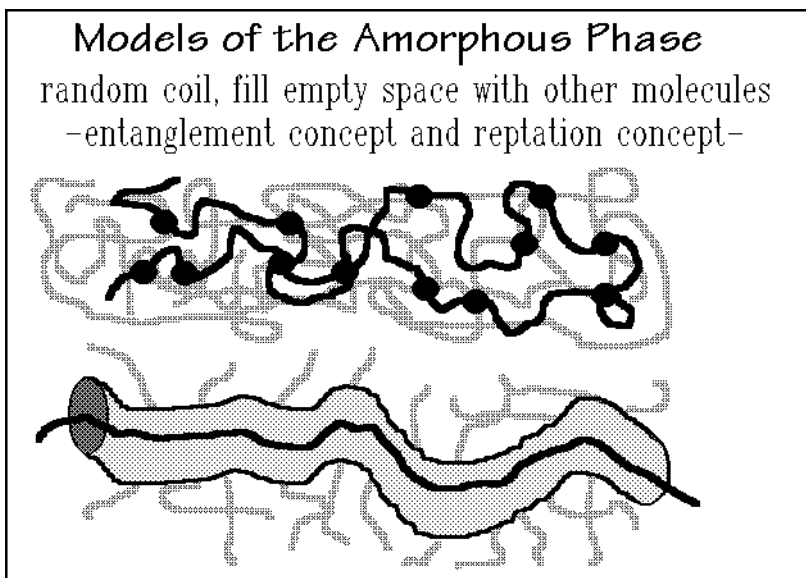
## 5.6 Melts and Glasses

In this chapter on “Structure and Properties of Polymeric Materials,” crystals were treated first. Much is known about their highly ordered structure and morphology, as demonstrated with Sects. 5.1 and 5.2. Actual samples turned out, however, to be semicrystalline, i.e., the regular structure consists of more than one phase and, thus, cannot be in thermodynamic equilibrium. To accommodate this fact, the study of defects in crystals in Sect. 5.3 had to include the amorphous defects which represent the amorphous nanophase, attached by tie-molecules to the crystal. Progress in understanding structure-property relations is possible only by the study of this complicated, metastable, biphasic structure. The thermodynamic description of the melting equilibrium in Sect. 5.4 gave, next, a macroscopic, quantitative tool to assess the change in order and molecular motion on a transition from crystal to melt. The intermediate states of order, the mesophases, were treated in Sect. 5.5. They are of major importance for the understanding of polymer structure and properties. The present section closes the discussion with an analysis of melts and glasses, the two amorphous phases. Knowledge of the structure of the melt and glass as it relates to the properties is less advanced than just shown for the crystals. The structure and properties of the amorphous phase are treated in Sects. 5.6.1–2. The mechanics of the coiled macromolecules, which has contributed much to the understanding of viscosity and elasticity of polymers, is described in Sects. 5.6.3–6.

### 5.6.1 Structure of the Amorphous Phase

In macroscopic terms, melts and glasses are the two amorphous, condensed phases shown in Fig. 2.103. At the glass transition temperature, these two phase areas meet, as illustrated in Fig. 2.117 and 2.118. The melt is the liquid phase, the glass is the solid phase. Extrapolated to the glass transition temperature, the two phases have the same structure, i.e., there is no heat or entropy of transition. Inspecting the liquid heat capacity, one finds that on cooling its disorder (entropy) initially decreases faster than that of the crystal, but it seems not to reach zero before one reaches the temperature of zero kelvin, as discussed for polyethylene with Figs. 2.71 and 2.72. The main characteristics of melts and glasses is a macroscopically isotropic structure that persists as long as the molecules remain fully relaxed.

Microscopically the liquid (or melted) molecules are mobile, i.e., they can undergo large-amplitude motion in addition to vibrations. For polymers, most important is the conformational motion. In the glassy state, this large-amplitude motion is frozen-in, rendering the glass a solid which shows at sufficiently low temperature only vibrational motion. The special, irreversible nature of the glass transition enables the study of the sample history and will be described in Sects. 6.1 and 6.3 for pure phases, and in Sect. 7.3 for multiple component systems. The models developed for the microscopic structure of the amorphous state involve knowledge of the random-coil macroconformation, expected for the molecule in the melt at the theta temperature as mentioned in Sect. 1.3, and the packing needed to make up the proper density of the condensed phase. The number of entanglements of the molecules and their space-filling nature is difficult to assess, but is needed to understand, for example, viscous

**Fig. 5.159**

flow as discussed in Fig. 3.5. At the top of Fig. 5.159 a schematic polymer structure with entanglements is depicted (●). It must be characterized by the number of entanglements, their separation along the chain, and their structural nature. The seemingly impossible problem of describing individual entanglements is reduced in the reptation concept, proposed by de Gennes [47]. The individual molecules are assumed to diffuse along a tube, set up by the neighboring chains, as shown in the bottom schematic of Fig. 5.159. Lateral motion is restricted by the walls of the tube, leading to reptation, a snake-like motion of curvilinear diffusion along its own contour. The motion within the tube is determined by the average diameter and length of the tube and the characteristic mobility of the molecule along the tube. There are two characteristic relaxation times for such chain motion, one is the equilibration time for the defect concentration, proportional to the square of the molar mass, the other is the time required for the complete renewal of the macroconformation of the chain, proportional to the cube of the molar mass.

To be in equilibrium, the amorphous phase must be properly entangled and relaxed. For high molar masses this takes long times (seconds to hours?). Little information is available about this problem to date. Qualitatively it has been observed, for example, that the time of injection molding of high-molar-mass pellets of an amorphous polymer is not enough to erase the history of the shape of the pellet from the finished product. Similar effects are expected on inter-diffusion across surfaces on welding of films and on melting of well-ordered crystals. Also, a reasonable time should be needed to re-entangle on melting the single-molecule crystals shown in Fig. 5.74 and to fully fuse isolated, droplets of few molecules which are illustrated in Fig. 5.160. The molecules are separated in dilute solution and then sprayed, precipitated, or freeze-dried to particles of single or few molecules. The diagram in the upper left corner allows to estimate the number of molecules per particle [48].



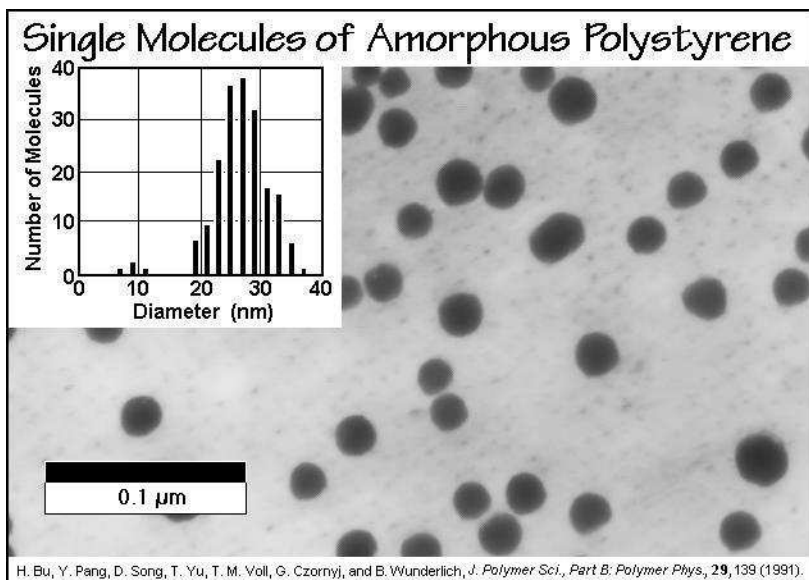


**Fig. 5.160**

### 5.6.2 Properties of the Amorphous Phase

When discussing crystal defects in Sect. 5.3, the properties of materials were divided into structure-sensitive and structure-insensitive. The same is true for the amorphous phases, the liquids and glasses. For the liquid state, the special structure-sensitive property is the viscosity, as treated in Sect. 5.6.3. To represent the structure-insensitive properties of semicrystalline materials, a simple two-phase model is often sufficient, as pointed out in Sect. 5.3. The weight fraction crystallinity is then the only additional parameter to model the average properties of the metastable two-phase material. In amorphous materials consisting of a single phase, the structure-insensitive heat capacity, density, and refractive index, are additive from their constituent groups of the molecular composition [49]. Typical examples of the additivity of liquid heat capacities are given in Sect. 2.3 for the aliphatic polyoxides, nylons, and polyesters in Figs. 2.59–61.

The change of heat capacity with temperature over the full temperature range for amorphous polyethylene is given in Fig. 2.46. This figure shows that below the glass transition temperature the heat capacity of the glass is almost identical to that of the crystal, shown in Fig. 2.51. Deviations toward a higher heat capacity of the glass are seen below about 50 K in the graph at the right side of Fig. 2.45. The same behavior can be seen in Appendix 1 for other polymers when comparing  $\Theta$ -temperatures. A typical dilatometric result for polyethylene is given by Fig. 4.18, and changes in volume of liquid polypropylene with pressure and temperature are given in Fig. 4.19.

For the representation of the structure-sensitive properties, it is necessary to develop an even more detailed model on the molecular level. A key example treated in Sect. 5.3 is the description of the strength of semicrystalline fibers. The properties

of these fibers could be described only with a model that combined three nanophase-separated phases, as illustrated in Fig. 5.113. The additional, third phase was non-crystalline, but oriented due to the strain imparted during the drawing of the fiber and described in Figs. 5.68–72 for poly(ethylene terephthalate) and Figs. 5.156–158 for polyethylene. Similar models are needed for the structure-sensitive properties of the amorphous phases, such as the viscosity, to be described next.

Important structure-sensitive properties of glasses limit the ultimate strength. A description must describe the crack-propagation, crazing, and fibrillation on fracture and plastic deformation. All of these create new external or internal surfaces, which are critically dependent on the conformation and large-amplitude motion of the macromolecules in relation to the new interfaces. Little more is discussed about this topic. The continually changing special literature on this rather empirical topic must be checked for further information.

### 5.6.3 Viscosity

The main structure-sensitive characteristic of a liquid polymer is its viscosity. Figure 5.161 lists a definition for a liquid in terms of viscosity,  $\eta$ , the ratio of the tangential or shear-stress  $\sigma$  to the rate-of-shear,  $d\epsilon/dt$ . The sketch relates the various quantities for an experiment consisting of a stationary base plate over which a mobile

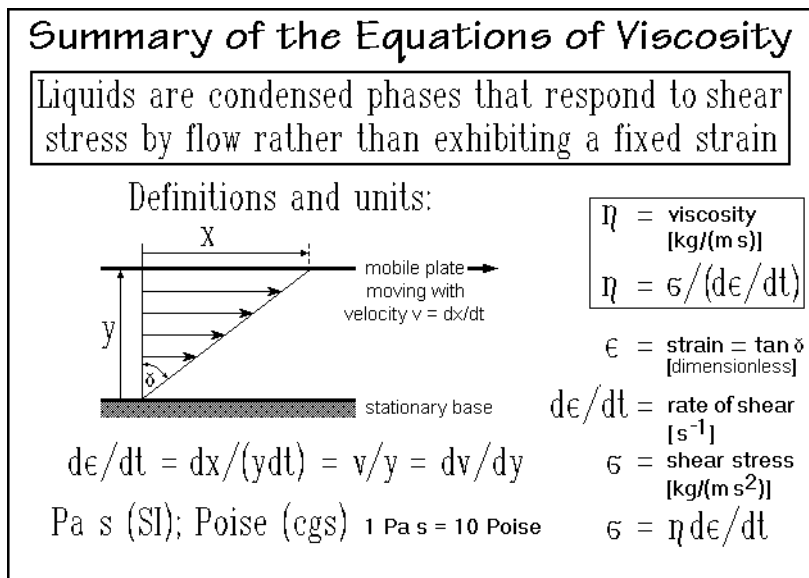


**Fig. 5.161**

plate is moved (see also Sect. 4.54 and Fig. 4.157). Some experimental tools for the measurement of viscosity are summarized in Fig. 5.162. For the capillary viscometers the empirical calibration equation is given in Fig. 1.70 together with a schematic of the Ubbelohde viscometer. The viscosity is also numerically equal to the energy dissipated per m<sup>3</sup> per second as can be gathered from the dimensions in Fig. 5.162.

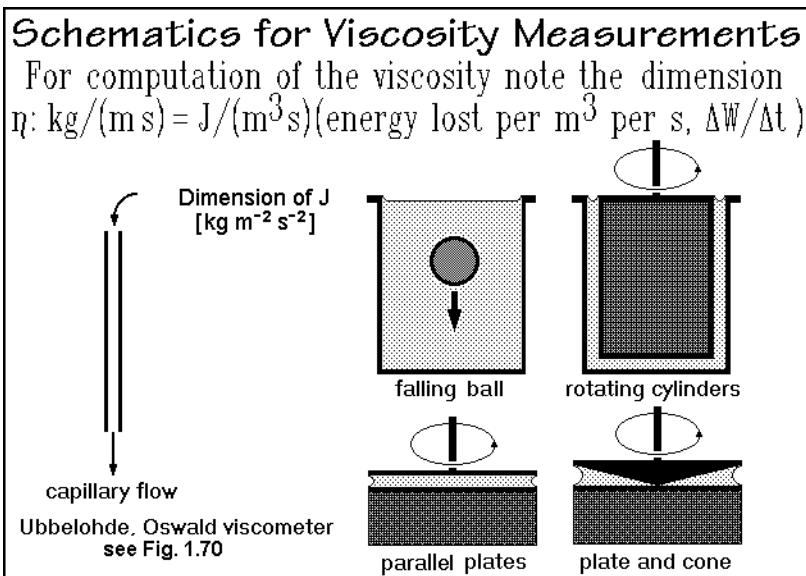


Fig. 5.162

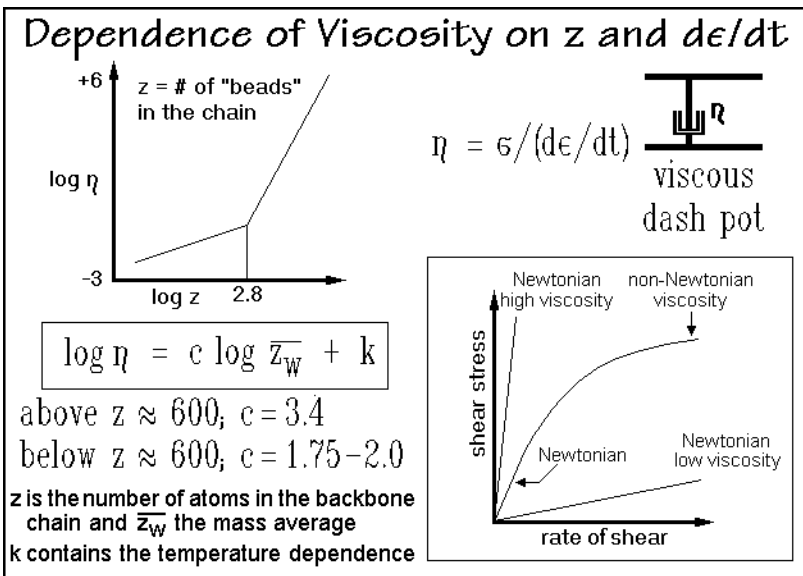


Fig. 5.163

The change of viscosity with molar mass (chain length) of a flexible macro molecule is shown in Fig. 5.163 as it is also presented in Fig. 3.5. The graph indicates a strong increase of the viscosity with chain length when the molecule reaches the so-called entanglement limit. It occurs when the mass-average number of chain atoms reaches about 600. Typical viscosities that demonstrate the broad range of possible

different materials are listed below with polymer melts falling between viscous oils and glasses:

gases	$\mu$ Pa s ( $10^{-6}$ Pa s)	pitch	G Pa s ( $10^9$ Pa s)
water	m Pa s ( $10^{-3}$ Pa s)	ice at 273 K	T Pa s ( $10^{12}$ Pa s)
light oil	Pa s ( $10^0$ Pa s)	glasses at $T_g$	T Pa s ( $10^{12}$ Pa s)

The equations in Fig. 5.161 suggest that the viscosity should be independent of shear-rate. If this condition holds, one calls the viscosity Newtonian. The insert in Fig. 5.163 shows examples of plots of low and high Newtonian viscosities. Polymers, in turn, show a shear-thinning at high shear-rates and become then non-Newtonian. An example of Newtonian behavior at low shear-rate, followed by shear-thinning is also shown in the insert of Fig. 5.163. The higher shear-rates cause the flexible macromolecules to deform from their equilibrium random coil and elongate. A dashpot, representing schematically the viscosity is given on the right of Fig. 5.163. It is used in describing samples that show viscous as well as elastic responses as treated in Sects. 4.5 and 5.6.6.

Some understanding of the viscosity of flexible macromolecules can be gained from analyzing the intrinsic viscosity of solutions as defined in Fig. 1.70. The contribution of the macromolecule to the solution viscosity can be estimated from the energy dissipated in the solution by the polymer molecule, as discussed in Sect. 1.4.5 in connection with the determination of molar masses. Figure 5.164 illustrates the random coil conformation of a macromolecule in a solvent with a shear-gradient. It is assumed that the molecule is freely-draining, i.e., the solvent can flow freely through the polymer, subject only to friction between polymer and solvent. This model treats the polymer molecule as a string of beads. One bead is marked at P. The

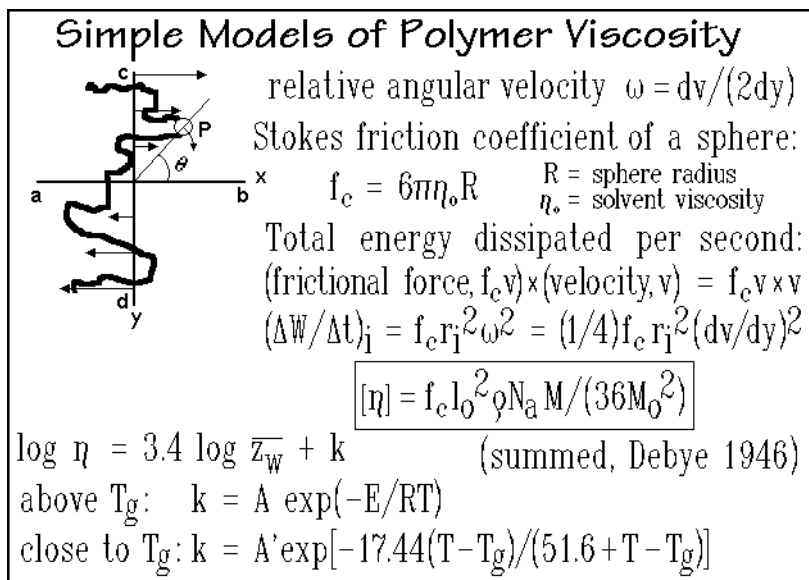


**Fig. 5.164**

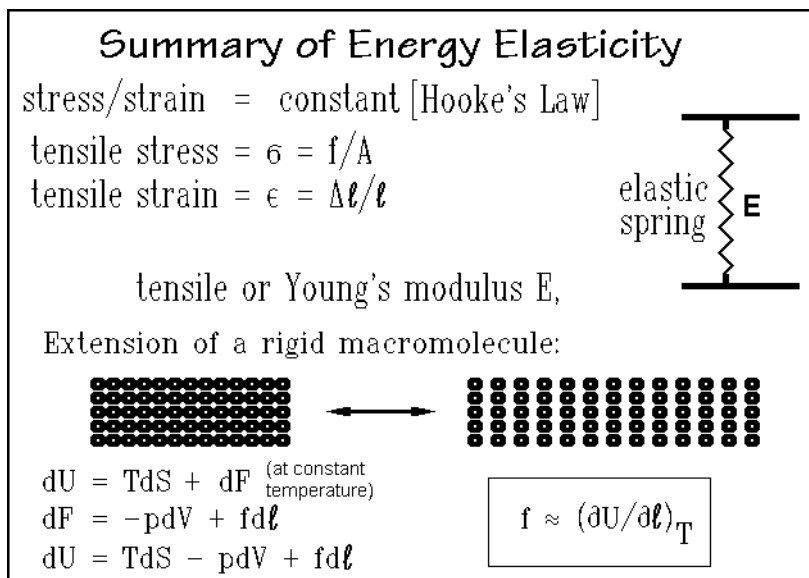
macromolecule must be at its  $\theta$ -temperature so that there is no expansion of the random coil due to polymer-solvent interaction as described in Sects. 1.3 and 1.4 (the expansion coefficient  $\alpha = 1.0$ ). At sufficiently low shear-rate, there will be Newtonian behavior, i.e., no deviation from the random coil due to the friction is expected. The energy dissipated due to the frictional force of the macromolecule can then be calculated by summing the contributions arising from all beads  $P$ . The shear-gradient in the volume occupied by the molecule causes tumbling. In addition, the tumbling molecule is carried along with the velocity of the solvent at the center of rotation of the macromolecule.

Figure 5.164 lists the frictional coefficient of one bead moving through the medium of viscosity  $\eta_0$ , approximated by the Stokes expression for a sphere of radius  $R$ . The equation for  $(\Delta W/\Delta t)_i$  represents then the energy dissipated per second by bead  $i$  of the molecule on rotation in the shear-gradient indicated. The viscosity contribution due to the tumbling random coil of the molecule was summed by Debye as explained in Sect. 1.4.5, and is given in the boxed equation with  $l_0$  representing the segment length of the random coil;  $\rho N_A/M$ , the number of molecules per unit volume,  $\rho$  = polymer density,  $M$  = molar mass,  $N_A$  = Avogadro's number, and  $M_0$ , the molar mass of one bead. This result gives only a first-power dependence of viscosity on molar mass. To correct this wrong exponent it was suggested in Sect. 1.4.5 to use the equivalent-sphere approach. To reach an understanding of more concentrated solutions, and ultimately the melt, the entanglement effect or the reptation behavior has to be assessed.

The bottom three equations of Fig. 5.164 return to the melt viscosity  $\eta$  and its temperature dependence through the factor  $k$  which is introduced in Fig. 5.163. Above the glass transition, a standard Arrhenius expression, as is used for the description of chemical and crystallization kinetics in Chap. 3 can be used to express the temperature dependence, as summarized in Appendix 7. As the glass transition temperature,  $T_g$ , is approached on cooling, the motion becomes more cooperative and the viscosity increases much more rapidly than given by a simple exponential expression. At the glass transition, the viscosity reaches often about  $10^{12}$  Pa s, a value also characteristic of the plastic deformation of solids. The general WLF equation, given as the last equation in Fig. 5.164 and introduced in Sect. 2.5.5 can be used for the description of the viscosity in this temperature region.

### 5.6.4 Energy Elasticity

The definitions needed for the description of the elastic behavior of a solid are summarized in Fig. 5.165 together with its symbolic spring. The connection to other types of deformation and compressibility is given in Figs. 4.143 and 4.144. For a constant stress-strain ratio, the deformation is reversible and follows Hooke's law. Hookean behavior is achievable for solids when the deformation is small, usually less than 1%. On a molecular level, the load-bearing network of atoms is assumed to extend proportional to the external strain, i.e., it undergoes an affine deformation by extending the appropriate bonds as sketched in the figure and also depicted in Fig. 4.144. The energy of extension  $f d\ell$ , thus, is stored as energy of bond deformation, and the system is said to be energy elastic.

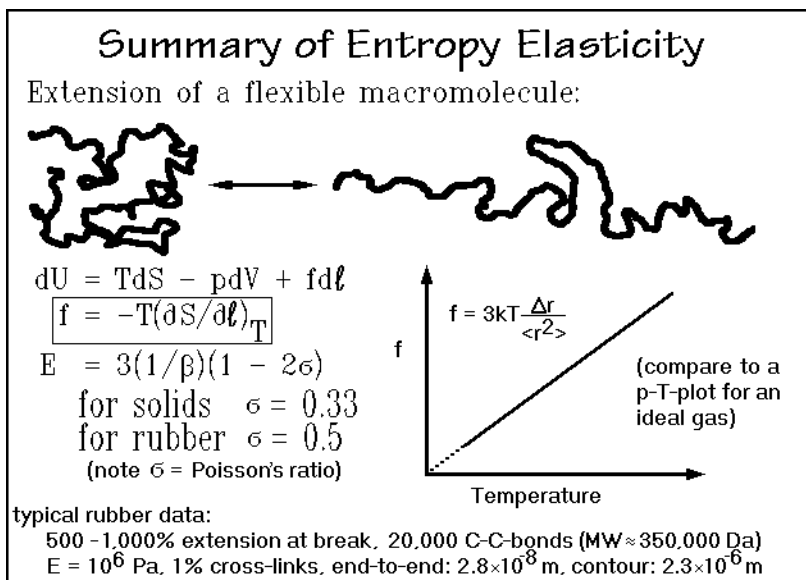
**Fig. 5.165**

The thermodynamic description of energy elasticity is easily assessed with the equations at the bottom of Fig. 5.165, using the expressions of Fig. 2.17. The free energy,  $dF (= dw_{\text{reversible}})$ , gained on extension has two contributions. A small amount comes from a minimal increase in volume ( $-pdV$ , due to a Poisson's ratio  $< 0.5$ , see Fig. 4.144). The major amount is linked to the work of extension,  $fd\ell$ . Since the order changes little, there is little change in entropy. The boxed thermodynamic equation states that the extensive force,  $f$ , for energy elasticity is caused mainly by the change of  $U$  with  $\ell$ .

### 5.6.5 Entropy Elasticity

The tensile deformation of polymers is more complicated than described in Fig. 5.165. Only below the glass transition temperature and for small strain is the response similar to the energy elasticity of Sect. 5.6.4. At higher strain, the deformation becomes plastic, i.e., irreversible. To describe such plastic deformation, the detailed molecular deformation mechanism must be known. A typical example is treated in the discussion of drawing of crystalline fibers or films which involves necking, as seen in Figs. 5.108–111. Above the glass transition, however, polymers are highly viscous liquids, as described in Sect. 5.6.3. Liquids should respond to a stress with viscous flow and not be elastic. In this section, it is described that liquid macromolecules have special elasticity, the entropy or rubber elasticity [50].

On tensile deformation above the glass transition, the flexible macromolecule reacts differently from the rigid macromolecule. It changes its random coil to a more extended conformation, as shown in Fig. 5.166. This contrasts also the rotation on shear deformation, illustrated in Fig. 5.164. The main effect on extension is a decrease in conformational disorder, i.e., a decrease in entropy. This property was made use

**Fig. 5.166**

of by applying extensive flow to grow more extended crystalline fibers from solution. The extension of the molecule also reduces the barrier to molecular nucleation, as discussed with Figs. 5.66 and 67. To change the viscous to an elastic response, it is necessary to arrest the slip of the molecules. Otherwise, the initial, external retracting force will reduce either time to zero, as seen in Fig. 4.145. Even the ever present entanglements can retard this slip. More permanent are chemical cross-links which produce a network with an elastically responding mesh. One must think of the molecule of Fig. 5.166 as being attached at the entanglement or cross-link points of the network. The following discussion of the entropy elasticity is simplified by using only the single chain depicted in the figure, and furthermore, by dealing with an ideal rubber which shows no energy elasticity, but only the change in entropy.

The thermodynamic expression for the extension of an ideal rubber is given in Fig. 5.166. It can be easily derived from Fig. 2.17 (see also Fig. 5.165). In contrast to the energy elasticity, there is no change in energy  $U$ , but a change in entropy. To fulfill the conditions of an ideal rubber, all conformations must have the same energy, only then can the force be solely entropic. In any real case one expects, thus, some energy contribution. The condition of no volume work is approached by most rubbers. Since the rubber is liquid, it does not change its volume on deformation, i.e., Poisson's ratio is very close to 0.5 (see Fig. 4.144).

A typical entropy-elastic material is cross-linked natural rubber, *cis*-poly(1-methyl-1-butenylene) or *cis*-1,4-polyisoprene, as summarized in Fig. 5.166 (see also Fig. 1.15). Its extensibility is 500 to 1,000%, in contrast to the 1% of typical energy-elastic solids. Natural rubber has a molar mass of perhaps 350,000 Da (about 5,000 isoprene monomers or 20,000 carbon backbone bonds) and is then vulcanized to have about 1% cross-links (see Fig. 3.50). A rubber with a Young's modulus of  $10^6$  Pa (depending on cross-link density) must be compared to its bulk modulus ( $= 1/\beta$ ,

inverse of the compressibility) of about  $10^9$  Pa (see Fig. 4.143). This leads by insertion into the equation of Fig. 5.166 to a Poisson's ratio of 0.4998 for this specific rubber. A typical Poisson's ratio for a solid ( $\sigma = 0.33$ ) would, in contrast, yield similar bulk and Young's moduli.

Kinetically one can compare the rubber elastic extension to the compression of a gas, as illustrated in Fig. 5.167. The thermodynamic equations reveal that reversible rubber contraction can just as well drive a heat pump as reversible gas expansion. Raising temperature, increases the pressure of a gas, analogously it takes a greater force to keep a rubber band extended at higher temperature. The two equations for this fact are known as the ideal gas law  $p = p_0 TV_0/(T_0 V)$  with  $p_0 V_0/T_0 = R$ , the gas

### Gas Expansion versus Rubber Contraction

At constant temperature the change of internal energy is zero for ideal gas and rubber

The gas (left) does no elastic work, the rubber (right) no volume work, as given in the two equations written

$$dU = \underbrace{TdS}_{\text{reversible heat exchange}} - \underbrace{pdV}_{\text{reversible volume work}} + \underbrace{fd\ell}_{\text{reversible elastic work}}$$

GAS:

$$p \approx T \left( \frac{\partial S}{\partial V} \right)_T$$

RUBBER:

$$f \approx -T \left( \frac{\partial S}{\partial \ell} \right)_T$$

Since  $p$  and  $f$  are always +,  $S$  increases with  $V$  and decreases with  $\ell$ , gases cool on reversible expansion at const.  $T$  and rubber heats on reversible extension at const.  $T$

Using the relations of Fig. 2.19, one can write the equations:

GAS:

$$p \approx T \left[ \frac{\partial - \left( \frac{\partial F}{\partial T} \right)_V}{\partial V} \right]_T = T \left( \frac{\partial p}{\partial T} \right)_V$$

RUBBER:

$$f \approx -T \left[ \frac{\partial - \left( \frac{\partial F}{\partial T} \right)_\ell}{\partial \ell} \right]_T = T \left( \frac{\partial f}{\partial T} \right)_\ell$$

Pressure,  $p$ , is due to translational, force  $f$  to conformational motion. The two equations show that both  $p$  and  $f$  increase at constant  $V$  and  $\ell$  with temperature

**Fig. 5.167**

constant (see Figs. 2.8 and 2.9) and the analogous ideal rubber equation which is written  $\sigma = E_0 T \ell / (T_0 \ell_0)$ . The graph in Fig. 5.166 gives the results of a kinetic model of an ideal rubber molecule with  $\langle r^2 \rangle$  representing the mean-square end-to-end distance between cross-link points, and  $\Delta r$ , the extension of the random coil.

The change of the melting temperature of crystals of macromolecules as a function of tensile force  $f$  can be treated the same as the effect of pressure which is described by the well-known Clausius-Clapeyron equation. Figure 5.168 lists at the top the change of free enthalpy with changes in pressure and extension, as can be derived from Fig. 2.19. Equation (a) is the Clausius-Clapeyron equation and Eq. (b) the ideal rubber equation. The ratios of the changes of volume and length on fusion over the corresponding entropies of fusion give information of the change in melting temperature. On melting, the volume of most substances increases, while a molecule of a macromolecular, extended-chain crystal shrinks to the random coil on fusion. Considering the opposite signs of the two equations, one finds that both, increasing pressure and extension, will increase the melting temperature. For crystallizable



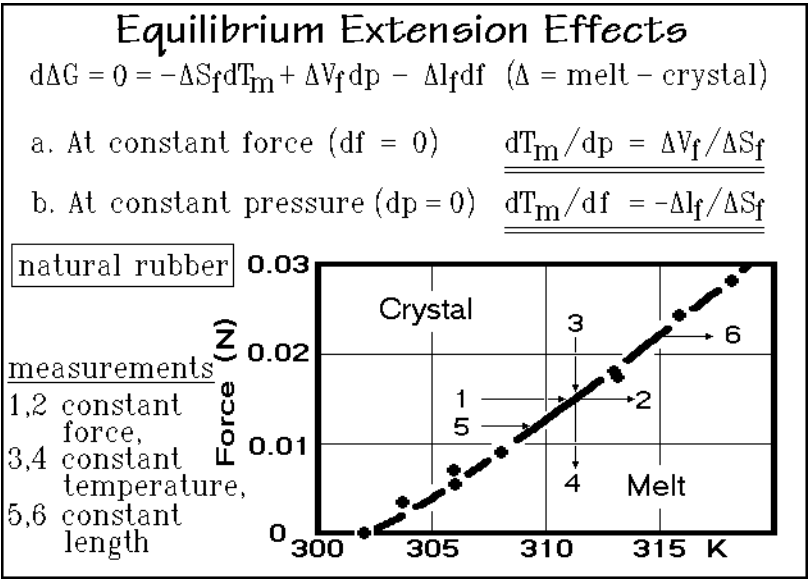


**Fig. 5.168**

rubber materials this means that on extension somewhat above the melting temperature, crystallization can be induced, increasing the heat evolved on extension.

Experimental data on natural rubber are illustrated in the phase diagram of Fig. 5.168 and expanded to length versus temperature plots in Fig. 5.169. As usual with polymer crystals, the experimental phase diagram is not an equilibrium phase diagram. Still, it can be used to illustrate the possible experiments of melting and

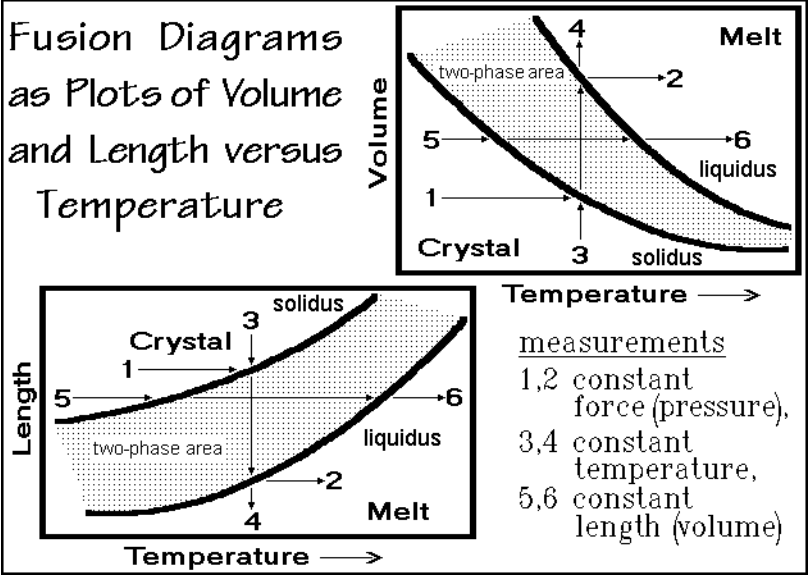


**Fig. 5.169**

crystallization of polymer molecules when the corresponding liquid phase is under strain. In Fig. 5.168 the liquidus line is drawn. Representing the last crystals melting, it should be closer to equilibrium. Three marked paths are distinguishable for further discussion. Path 1,2 indicates melting at constant force, path 3,4, at constant temperature. Both paths lead to a constant melting temperature. At constant length, path 5,6, one finds a melting range,  $\Delta T$ . The same paths are shown more clearly in Fig. 5.169 a schematic length-temperature phase diagram, which is compared to the analogous V-T plot. More detailed p-V-T plots are shown in Fig. 4.20–22. Such diagrams permit the description of the behavior of a polymer under different conditions of force, pressure, length, and volume. A second set of experimental data is shown in Fig. 5.170. At not too high extensions, the phase diagram looks as

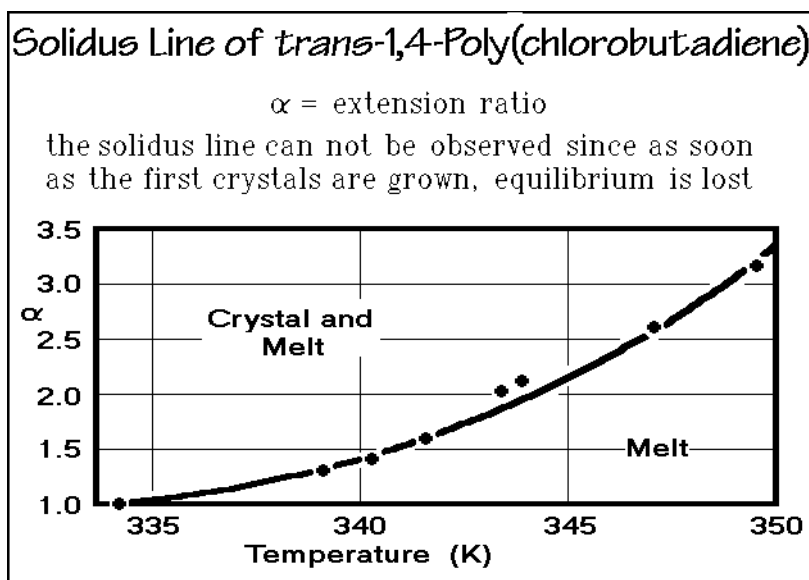


Fig. 5.170

expected, but only the liquidus line is identified, the phase boundary indicating the end of melting. The solidus line would mark complete crystallization, a state that is never reached in polymers.

### 5.6.6 Viscoelasticity

The analyses of several polymers by dynamic mechanical analysis, DMA, are described in Sect. 4.5 in connection with the brief description of the DMA equipment. It was observed in such experiments that neither the viscosity nor the modulus are constant, as is assumed for the discussion of energy and entropy elasticity, outlined in Sects. 5.6.4 and 5.6.5, respectively. One finds a stress anomaly when the elastic limit of a material has been exceeded and plastic deformation occurs. Other deviations have the stress depend both on strain *and* rate of strain. Finally, a time anomaly exists whenever the stress/strain ratio depends only on time and not on the stress magnitude.

A sample which shows such time anomaly only is said to be viscoelastic and can be analyzed as described in this section. At small strains most polymers show such viscoelastic behavior.

Based on the measurement of the stress,  $\sigma$ , resulting on the application of periodic strain,  $\epsilon$ , with equipment as shown in Fig. 4.155, one can develop a simple formalism of viscoelasticity that permits the extraction of the in-phase modulus,  $G'$ , the storage modulus, and the out-of-phase modulus,  $G''$ , the loss modulus. This description is analogous to the treatment of the heat capacity measured by temperature-modulated calorimetry as discussed with Fig. 4.161 of Sect. 4.5. The ratio  $G''/G'$  is the loss tangent,  $\tan \delta$ . The equations for the stress  $\sigma$  are easily derived using addition theorems for trigonometric functions. A complex form of the shear modulus,  $G^*$ , can be used, as indicated in Fig. 4.160.

A number of DMA analyses are discussed in Sect. 4.5.5. They deal with amorphous poly(methyl methacrylate) and a polycarbonate and their frequency dependencies as functions of temperature (Fig. 4.162–165 and Fig. 4.166–169, respectively); and poly(vinyl chloride) with a glass transition ( $T_g = 370$  K) and some local motion at about 200 K (see Fig. 4.170).

A typical example of a DMA experiment on a series of semicrystalline polyethylenes is shown in Fig. 5.171 [51]. The peaks in the  $\tan \delta$  plot are labeled  $\alpha$ ,  $\beta$ , and  $\gamma$ . From the changes of the amplitudes of  $G'$  and  $G''$  with crystallinity in

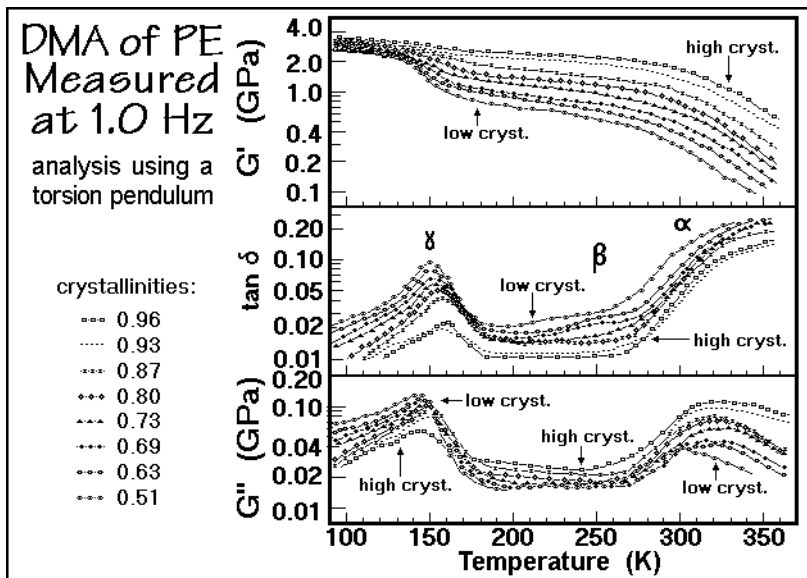


Fig. 5.171

Fig. 5.171 one can see that the  $\alpha$ -transition is connected to the crystals and begins at about 260 K. The  $\beta$ -transition is best seen in the  $\tan \delta$  plot. The  $\tan \delta$  increases with decreasing crystallinity and, thus, has been linked to the glass transition of the amorphous part of the semicrystalline samples. Its maximum can be placed at about 250 K. Calorimetrically, the glass transition of polyethylene is rather difficult to

establish because of its breadth, seen in the heat-capacity plot of Fig. 2.46. The  $\gamma$ -transition increases in amplitude of  $G''$  and  $\tan \delta$ . It marks the first drop in the storage modulus  $G'$  from the value of the solid and increases with decreasing crystallinity. Its temperature range in Fig. 5.172 falls into the low-temperature region of the extended range of the glass transition when measured by heat capacity, which stretches in Fig. 2.46 from 120–200 K. The interpretation of the dynamic mechanical analyses of the three relaxation regions in semicrystalline PE [51] can now be combined with the knowledge gained by the calorimetric experimentation, which is assembled in Chaps. 2 and 5 and was first summarized in [52].

Based on evidence as shown in Fig. 5.171, the  $\alpha$ -relaxation is linked to local mobility in the crystalline lamellae, which mobilizes the chain translationally, and affects the amorphous regions tied to the crystals. Similarly, the increase in heat capacity beyond the vibrational  $C_p$  of crystalline PE and paraffins starts at about 250–300 K and can be discerned from Figs. 2.52 and 2.65. It was linked in Sects. 2.1.6 and 5.3.4 (Fig. 5.100) to the increase in *gauche* conformations in the crystal. The conformational defects are also at the root of the diffusion of the chains within the crystal which were simulated using the molecular dynamics calculations shown in Figs. 5.103–106. This motion of the chain within the crystals is now generally referred to as sliding diffusion [10] and is also at the root of the chain-extension of the crystals on annealing.

The  $\gamma$ -transition is a broad relaxation in the temperature- or frequency-domain, interpreted as a localized crankshaft-like motion of the backbone of the chain. This interpretation of the DMA result [51] agrees well with the calorimetry. The calorimetric results were interpreted already in 1962 based on an energy estimation as a local relaxation of *gauche* conformations in the amorphous phase [53,54]. The broad increases in the heat capacity beyond the vibrational  $C_p$  of amorphous PE seen in Fig. 2.46 were interpreted as a gradual, local unfreezing of the *gauche-trans* equilibrium.

On further heating, the  $\gamma$ -transition is followed by the major part of the cooperative glass transition, the  $\beta$ -relaxation. Again, the calorimetry agrees with the DMA interpretation, but allowing several more quantitative statements. The mid-point of the glass transition in Fig. 2.46 is at 237 K [53]. The end of the glass transition is reached at about 250 K, with an overall  $\Delta C_p$  of  $10.5 \text{ J K}^{-1} \text{ mol}^{-1}$  (see Appendix 1), in agreement with the expected value of Fig. 2.103. Further broadening of the glass transition up to about 300 K was seen for gel-spun fibers of polyethylene (see Sect. 6.2.6), as is expected for the strained noncrystalline fraction of the fibers. The properties of high-molar-mass, gel-spun polyethylenes are discussed further in Sect. 5.5.5 with Figs. 5.156–158.

## References

### General References

**Sect. 5.1.** The fundamental tabular summary of crystallography is: Henry NFM, Lonsdale K, eds (1969) *International Tables for X-Ray Crystallography*, Vol I. The International Union of Crystallography, Publ Kynoch Press, Birmingham, see also later reprints.

Specific books treating the crystal structures of linear macromolecules are: Wunderlich B (1973) *Macromolecular Physics*, Vol I, Crystal Structure, Morphology, Defects. Academic Press, New York; Alexander LE (1969) *X-Ray Diffraction Methods in Polymer Science*. Wiley-Interscience. New York; Tadokoro H (1979) *Structure of Crystalline Polymers*. Wiley, New York; Miller RL (1989) *Crystallographic Data for Various Polymers*. In Brandrup J, Immergut EH, *Polymer Handbook*, 3<sup>rd</sup> edn. Wiley, New York, Sect VI, pp 1–277.

Proteins are special macromolecules. For their crystal structure see, for example,: Blundell TL, Johnson, LN (1976) *Protein Crystallography*. Academic Press, New York.

Specific books of interest to the history of crystallography are: Burke JG (1966) *Origins of the Science of Crystals*. University of California Press, Berkeley; Kepler J (1611) *Strenua seu, de nive sexangula*. Frankfurt. Reprint in English (1966) *The Six-cornered Snowflake*. Oxford Univ Press (Clarendon), London; Hooke R (1665) *Micrographia, or some Physiological Descriptions of Minute Bodies Made by Magnifying Glasses with Observations and Inquiries Thereupon*. London.

The first enumerations of the 14 translation lattices, 32 point groups, and 230 space groups can be found in: Bravais A (1850) *Mémoire sur les systèmes formés par des points distribués régulièrement sur un plan ou dans l'espace*. J Ecole Polytech 19: 1–128, English translation by Shaler A (1949) *Cryst Soc Amer Memoir*, Vol 1; Hessel JFC (1831) *Kristallometrie oder Kristallonomie und Kristallographie*. Leipzig; Schoenflies A (1891) *Kristallsysteme und Kristallstruktur*. Leipzig. A general text on symmetry groups is: Flurry RL, Jr (1980) *Symmetry Groups, Theory and Chemical Applications*. Prentice Hall, Englewood Cliffs.

**Sect. 5.2.** The main reference on which this Sect was developed is: Wunderlich B (1973) *Macromolecular Physics*, Vol I, Crystal Structure, Morphology, Defects. Academic Press, New York. A more recent source of excellent pictures and brief discussions of polymer morphology is given by Woodward AE (1988) *Atlas of Polymer Morphology*. Hanser, München.

The first major treatise on polymer crystallization is the three volume series: Stuart HA, ed (1955) *Die Physik der Hochpolymeren*. See Vol 3 *Ordnungserscheinungen und Umwandlungserscheinungen in festen hochpolymeren Stoffen*. Springer, Berlin.

General books on optical microscopy, a technique often sufficient to evaluate the morphology of polymers and general crystal morphology are: Hemsley DA (1989) *Applied Polymer Light Microscopy*. Elsevier, New York; Sawyer L, Grubb DT (1987) *Polymer Microscopy*. Chapman and Hall (Methuen), New York.

Discussions of the problems of chain folding are published in the following places: (1979) Special issue of the *Farad Disc Chem Soc* 68; Dosié M, ed (1993) *Crystallization of Polymers*. NATO ASI Series C, Volume 405, Kluwer, Dordrecht; (2002) *Proceedings of the International Symposium on Polymer Crystallization in Mishima, Japan, June 9–12*, also published in part in a special issue (2003) *J Macromolecular Science B*42.

**Sect. 5.3.** The main reference on which this section was developed with updates is: Wunderlich B (1973) *Macromolecular Physics*, Vol I, Crystal Structure, Morphology, Defects, Chap 4. Academic Press, New York.

For a summary of the history and development of defect concepts of non-polymeric defects see: Nabarro FRN (1967) *Theory of Crystal Dislocations*. Oxford University Press (Clarendon), London; Friedel J (1964) *Dislocations*. Pergamon, Oxford [translation of (1956) *Les Dislocations*. Gauthiers-Villars, Paris]; Frank FC (1949) *Disc Farad Soc* 5: 48–54; Frank FC, Read WT, Jr (1950) *Phys Rev* 70: 722–723.

Discussion of dislocations in polymers is given by: Keith HD, Passaglia E (1964) *J Res Natl Bur Stand* 68A: 513–518; Predecki P, Statton WO (1966) *J Appl Phys* 37: 4053–4059; (1967) *Appl Polymer Symp* 6: 165–181; (1967) *J Appl Phys* 38: 4140–4144; Lindenmeyer PH (1966) *J Polymer Sci, Part C* 15: 109–127; Peterson JM, Lindenmeyer PH (1966) *J Appl Phys* 37: 4051–4053.

Early discussions of polymer point defects are given by: Holland VF, Lindenmeyer PH (1965) *J Applied Phys* 36: 3049–3056; *Science* 147: 1296–1297; Pechhold W (1968) *Kolloid Z Z Polym* 228: 1–38; Reneker DH (1962) *J Polymer Sci* 59: S39–42.

For updates on defects by molecular dynamics simulations see the Refs to Sects 1.3 and 2.1 and: Wunderlich B, Kreitmeier SN (1995) *MRS Bulletin*, September issue, pp 17–27; Suter U, Monnerie L, eds (1994) *Atomistic Modeling of Physical Properties of Polymers*, Springer, Berlin (*Adv Polymer Sci*, Vol 116).

Early ideas about deformation of polymers are found in: Frank FC, Keller A, O'Connor A (1958) *Phil Mag* 3: 64–74; Bonart R (1969) *Kolloid Z Z Polym* 231: 438–458; Hay IL, Keller A (1965) *Kolloid Z Z Polym* 204: 43–74.

**Sect. 5.4.** The main references with which this section was developed are: Wunderlich B (1980) *Macromolecular Physics*, Vol 3, Crystal Melting. Academic Press, New York; (1990) *Thermal Analysis*. Academic Press, Boston; (1997) *The Basis of Thermal Analysis*. In Turi E ed, *Thermal Characterization of Polymeric Materials* 2<sup>nd</sup> edn. Academic Press, New York, pp 205–482; Ubbelohde, AR (1965) *Melting and Crystal Structure*. Oxford University Press, London, and also (1978) *The Molten State of Matter, Melting and Crystal Structure*. Wiley, New York.

For a larger summary of melting data see, for example: Wunderlich B, Pyda, M (2004) *Thermodynamic Properties of Polymers*, in Kroschwitz JI, ed, *Encyclopedia of Polymer Science and Engineering*, 3<sup>rd</sup> edn, John Wiley & Sons, New York; see also (1990) 2<sup>nd</sup> ed, Vol 16, pp 1188–1192. Also available via: [www.mrw.interscience.wiley.com/epst](http://www.mrw.interscience.wiley.com/epst).

**Sect. 5.5.** For general literature on the discussions of mesophases and their transitions see also Sect 2.5. Many of the here discussed examples are reviewed in: Gordon M, ed (18983/84) *Liquid Crystal Polymers I–III*. Springer, Berlin (*Adv Polymer Sci*, Vols 59–61).

Specific references to the materials discussed in some detail are as follows:

DDA, MBPE, PEIM, and HPX: Chen W, Wunderlich B (1999) *Macromol Chem Phys* 200, 283–311.

DDA-12: Yandrasits MA, Cheng SZD, Zhang A, Cheng J, Wunderlich B, Percec V (1992) *Macromolecules* 25: 2112–2121; Cheng SZD, Yandrasits MA, Percec V (1991) *Polymer* 32: 1284–1292; Blumstein RB, Thomas O, Gauthier MM, Asrar J, Blumstein A (1985) in Blumstein A, ed *Polymeric Liquid Crystals*. Plenum Press, New York p 239.

PDES: Varma-Nair M, Wesson JP, Wunderlich B (1989) *J Thermal Anal* 35: 1913–1939. OOBPD: Cheng J, Chen W, Jin Y, Wunderlich B (1994) *Mol Cryst Liq Cryst* 241: 299–314; Cheng J, Jin Y, Liang G, Wunderlich B, Wiedemann HG (1992) *Mol Cryst Liq Cryst* 213: 237–258; Wiedemann HG, Grebowicz J, Wunderlich B (1986) *Mol Cryst Liq Cryst*: 140: 219–230.

PP: See the extensive list of references and summary of the properties in [46] pp 57 and 58.  
 TLX: Lindau J, Diele S, Krüger H, Dörfler HD (1981) *Z phys Chem (Leipzig)* 262: 775–784;  
 Lindau J, König HJ, Dörfler HD (1983) *Colloid Polymer Sci* 261: 236–240.  
 PE: Hu W, Buzin A, Lin JS, Wunderlich B (2003) *J Polymer Sci, Part B: Polymer Phys* 41: 403–417; Kwon YK, Boller A, Pyda M, Wunderlich B (2000) *Polymer* 41: 6237–6249;  
 Boller A, Wunderlich B (1997) *J Thermal Analysis* 49: 343–349; Fu Y, Chen Y, Pyda M, Londono D, Annis B, Boller A, Habenschuss A, Cheng J, Wunderlich B (1996) *J Macromol Sci, Phys B35*: 37–87; Chen W, Fu Y, Wunderlich B, Cheng J (1994) *J Polymer Sci, Part B: Polymer Phys* 32: 2661–2666 (1994).

**Sect. 5.6.** The basic references for the description of polymer melts are: Flory PJ (1953) *Principles of Polymer Chemistry*. Cornell University Press, Ithaca, NY; Bueche F (1962) *Physical Properties of Polymers*. Wiley, New York; de Gennes PG (1979) *Scaling Concepts in Polymer Physics*. Cornell University Press, Ithaca, NY; Doi M, Edwards SF (1988) *The Theory of Polymer Dynamics*. Oxford University Press, New York; de Gennes PG (1990) *Introduction to Polymer Physics*. Cambridge University Press, Cambridge.

More details about physical properties of amorphous polymers can be found in: Ferry JD (1980) *Viscoelastic Properties of Polymers*, 3<sup>rd</sup> edn. Wiley, New York; Ward IM (1983) *Mechanical Properties of Solid Polymers*, 2<sup>nd</sup> edn. Wiley, New York; Matsuoka S (1992) *Relaxation Phenomena in Polymers*. Hanser, München.

### **Specific References**

1. See, for example the collections of beautiful crystals in: DeMichele V (1969) *Kristalle; ein farbenfrohes Bild geheimnisvoller und gesetzmäßiger Kunstformen der Natur*. Südwest Verlag, München (125 color reproductions); Roberts WL, Rapp GR, Jr, Weber J (1974) *Encyclopedia of Minerals*. Van Nostrand, New York.
2. Klug A, Crick FHC, Wyckoff HW (1958) *Diffraction by Helical Structures*. *Acta Cryst* 11: 199–213.
3. Shimanouchi T, Mizushima S (1955) *On the Helical Configuration of a Polymer Chain*. *J Chem Phys* 23: 707–711.
4. G. Natta G, Corradini P (1960) *General Considerations on the Structure of Crystalline Polyhydrocarbons*. *Nuovo Cimento, Suppl* 15: 9–39.
5. McCoullough RL (1962) *Representation of Ordered Systems*. *Polymer Preprints* 3(2): 53–57.
6. The classical book dealing with the packing of motifs in crystals is: Kitaigorodskii AI (1955) *Organicheskaya Kristalloghimiya*. Press of the Acad Sci USSR. Moscow; revised English translation (1961) by the Consultants Bureau, New York.
7. Bunn CW (1939) *The Crystal Structure of Long Chain Normal Hydrocarbons*. *The Shape of the >CH<sub>2</sub>-group*. *Trans Farad Soc* 35: 482–491.
8. Hajduk DA, Harper PE, Gruner SM, Honeker CC, Kim G, Thomas EL, Fetters LJ (1994) *The Gyroid: A New Equilibrium Morphology in Weakly Segregated Diblock Copolymers*. *Macromolecules* 27: 4063–4075.
9. Matsen MW, Bates FS (1996) *Unifying Weak- and Strong-segregation Block Copolymer Theories*. *Macromolecules* 29: 1091–1098; and Matsen MW, Bates FS (1997) *Block Copolymer Microstructures in the Intermediate-segregation Regime*. *J Chem Phys* 106: 2436–2448.
10. Hikosaka M (1987) *Unified Theory of Nucleation of Folded-chain and Extended-chain Crystals of Linear-chain Polymers*. *Polymer* 28: 1257–1264.
11. Wunderlich B, Shu HC (1980) *The Crystallization and Melting of Selenium*. *J Crystal Growth* 48: 227–239; see also: *Crystallization during Polymerization of Selenium from the Vapour Phase*. *Polymer* 21: 521–524.

12. Staudinger H, Johner H, Signer R, Mie G, Hengstenberg J (1927) Der polymere Formaldehyd, ein Modell der Zellulose. *Z phys Chem* 126: 425–448; see also: Staudinger H, Signer R (1929) Über den Kristallbau hochmolekularer Verbindungen. *Z Krist* 70: 193–210; Sauter, E. (1932) Röntgenographische Untersuchungen an hochmolekularen Polyoxymethylenen. *Z Phys Chem B18*: 417–435.
13. Storks KH (1938) An Electron Diffraction Examination of Some Linear High Polymers. *J Am Chem Soc* 60: 1753–1761.
14. Keller A (1957) A Note on Single Crystals in Polymers: Evidence of a Folded Chain Conformation. *Phil Mag* 2: 1171–1175.
15. Fischer, EW (1957) Stufen und spiralförmiges Kristallwachstum bei Hochpolymeren. *Z Naturforsch* 12a: 753–754.
16. Geil PH (1958) Polyhedral Structures in Polymers Grown from the Melt. In Doremus, RH, Roberts BW, Turnbull DW, eds. *Growth and Perfection of Crystals*. Wiley, New York, p 579.
17. Till PH, Jr (1957) The Growth of Single Crystals of Polyethylene. *J Polymer Sci* 24: 301–306.
18. Kobayashi K (1958) Fourth Int Congress for Electron Microscopy in Berlin, Germany. Published in (1962) *Properties and Structure of Polymers*. Kagaku (Chem) 8:203, Kagaku Dojin, Kyoto.
19. Herrmann K, Gerngross O, Abitz W (1930) Zur röntgenographischen Strukturermorschung des Gelatinemicells. *Z phys Chem* 10: 371–394.
20. Bassett DC, Olley RH, Sutton SJ, Vaughan AS (1966) On Sperulite Growth in a Monodisperse Paraffin. *Macromolecules* 29: 1852–1853; On Chain Conformations and Sperulitic Growth in Monodisperse  $n\text{-C}_{294}\text{H}_{590}$ . *Polymer* 37: 4993–4997.
21. A first and quite comprehensive discussion of chain-folded crystals was given by Geil PH (1963) *Polymer Single Crystals*. Interscience, New York.
22. Popoff B (1927) Die Erscheinung der Strahlungskristallisation. *Fortschr Mineal Krist Petr* 11: 320–321.
23. Fu Y, Busing WR, Jin Y, Affholter KA, Wunderlich B (1993) Poly(ethylene Terephthalate) Fibers 1. Crystal Structure and Morphology Studies with Full-pattern X-ray Diffraction Refinement. *Macromolecules* 26: 2187–2193.
24. Fu Y, Busing WR, Jin Y, Affholter KA, Wunderlich B (1994) Structure Analysis of the Noncrystalline Material in Poly(ethylene Terephthalate) Fibers. *Macromol Chem Phys* 195: 803–822.
25. Fu Y, Annis B, Boller A, Jin Y, Wunderlich B (1994) Analysis of Structure and Properties of Poly(ethylene Terephthalate) Fibers. *J Polymer Sci, Part B: Polymer Phys* 32: 2289–2306.
26. Busing WR (1990) X-ray Diffraction Study of Disorder in Allied Spectra-1000 Polyethylene Fibers. *Macromolecules* 23: 4608–4610.
27. Bu H, Pang Y, Song D, Yu Y, Voll T, Czornyj G, Wunderlich B (1991) Single Molecule Single Crystals. *J Polymer Sci, Part B: Polymer Phys* 29: 139–152.
28. Bu H, Shi S, Chen E, Hu H, Zhang Z, Wunderlich B (1996) Single-molecule Single Crystals of Poly(ethylene Oxide). *J Macromol Sci, Phys B35*: 731–747.
29. Geil PH, Anderson FR, Wunderlich B, Arakawa T (1964) Morphology of Polyethylene Crystallized from the Melt under Pressure. *J Polymer Sci, Part A 2*: 3707–3720.
30. Wunderlich B, Melillo L, Cormier CM, Davidson T, Snyder G (1967) Surface Melting and Crystallization of Polyethylene. *J Macromol Sci B1*: 485–516.
31. Wunderlich B, Melillo L (1968) Morphology and Growth of Extended Chain Crystals of Polyethylene. *Makromolekulare Chemie* 118: 250–264.
32. Sumpter BG, Noid DW, Liang GL, Wunderlich B (1994) Atomistic Dynamics of Macromolecular Crystals. *Adv Polymer Sci* 116: 27–72.



33. Sumpter BG, Noid DW, Wunderlich B (1992) Computational Experiments on the Motion and Generation of Defects in Polymer Crystals. *Macromolecules* 25: 7247–7255.
34. Peterlin A (1971) Molecular Model of Drawing Polyethylene and Polypropylene. *J Mater Sci* 6: 490–508.
35. Takayanagi M, Imada K, Kajiyama T (1966) Mechanical Properties and Fine Structure of Drawn Polymers. *J Polymer Sci Part C* 15: 263–280.
36. Kamezawa M, Yamada K, Takayanagi M (1979) Preparation of Ultrahigh Modulus Isotactic Polypropylene by Means of Zone Drawing. *J Appl Polymer Sci* 24: 1227–1236.
37. Wunderlich B (1958) Theory of Cold Crystallization of High Polymers. *J Chem Phys* 29: 1395–1404.
38. Hirschfelder J, Stevenson D, Eyring, H (1937) A Theory of Liquid Structure. *J Chem Phys* 5: 896–912.
39. Lennard-Jones, JE Devonshire AF (1939) Critical and Cooperative Phenomena. III. A Theory of Melting and the Structure of Liquids. IV: A Theory of Disorder in Solids and Liquids and the Process of Melting. *A Proc Roy Soc, London, Ser A* 169: 317–338; 170: 464–484.
40. Richards JW (1897) Relations between the Melting Points and the Latent Heats of Fusion of the Metals. *Chem News* 75: 278–279.
41. Xenopoulos A, Cheng J, Yasuniva M, Wunderlich B (1992) Mesophases of Alkylammonium Salts. I. First-order Transitions. *Molecular Crystals and Liquid Crystals* 214: 63–79.
42. Walden P (1908) Über die Schmelzwärme, spezifisch Kohäsion und die Molekulargröße bei der Schmelztemperatur. *Z Elektrochem* 14: 713–724.
43. Wunderlich B, Grebowicz, J (1984) Thermotropic Mesophases and Mesophase Transitions of Linear, Flexible Macromolecules. *Adv Polymer Sci* 60–61: 1–59.
44. Androsch R (2001) Reversibility of the Low-temperature Transition of Polytetrafluoroethylene as Revealed by Temperature-modulated Differential Scanning Calorimetry. *J Polymer Sci, Part B: Polym Phys* 39: 750–756.
45. Fyfe CA (1983) *Solid State NMR for Chemists*. C.F.C Press, Guelph, CN.
46. Wunderlich B, Möller M, Grebowicz J, Baur H (1988) Conformational Motion and Disorder in Low and High Molecular Mass Crystals. Springer, Berlin (*Adv Polymer Sci*, Vol 87).
47. de Gennes PG (1971) Reptation of a Polymer Chain in the Presence of Fixed Obstacles. *J Chem Phys* 55: 572–579 (1971).
48. Festag R, Alexandratos SD, Cook KD, Joy DC, Annis B, Wunderlich B (1997) Single- and Few-chain Polystyrene Particles by Electrospray. *Macromolecules* 30: 6238–6242.
49. van Krevelen DW ed (1997) *Properties of Polymers: Their Correlation with Chemical Structure; Their Numerical Estimation and Prediction from Additive Group Contributions*, 3<sup>rd</sup> edn. Elsevier, Amsterdam.
50. Roberts AD, ed (1988) *Natural Rubber Science and Technology*. Oxford University Press, New York.
51. Boyd RH (1985) Relaxation Processes in Crystalline Polymers: Experimental Behavior; Molecular Interpretation—A Review. *Polymer* 26: 323–347 and 1123–1133.
52. Wunderlich, B (1997) The Basis of Thermal Analysis. In Turi E ed, *Thermal Characterization of Polymeric Materials* 2<sup>nd</sup> edn. Academic Press, New York, pp 387–389.
53. Wunderlich B (1962) Motion in Polyethylene. III. The Amorphous Polymer. *J Chem Phys* 37: 2429–2432.
54. Wunderlich B (1963) Motion in the Solid State of High Polymers. *J Polymer Sci, Part C* 1: 41–64.

## Single Component Materials

In the last two chapters of the book on Thermal Analysis of Polymeric Materials the link between microscopic and macroscopic descriptions of macromolecules will be discussed with a number of examples based on the thermal analysis techniques which are described in the prior chapters. Chapter 6 deals with single-component systems, Chap. 7 with multiple-component systems. It is shown in Sect. 6.2, as suggested throughout the book, that practically all partially crystalline polymers represent nonequilibrium systems, and that thermodynamics can establish the equilibrium limits for the description. It was found, however, more recently, that equilibrium thermodynamics may be applied to local areas, often small enough to be called nanophases [1]. These local subsystems are arrested and cannot establish global equilibrium.

Amorphous polymers are easier to treat as equilibrium systems as long as they consist of single components above their glass transition temperature and are without extensive surfaces that introduce significant local stresses, as shown in Sect. 6.3. For macromolecules, in general, the meaning of the term component was relaxed to account for the fact that macromolecules are sufficiently large, so that small changes in their length do not affect their properties significantly, i.e., all macromolecules in a distribution are considered to be one component. Note, that this is not true for distributions that contain oligomers, defined in Sect. 3.1 as molecules below 1,000 atoms in size. Similarly, decoupled segments of a polymer chain may change the accounting for components, as is shown in Sect. 6.2. Section 6.1 is a review and extension of the prior, basic thermodynamic description of phases and transitions.

### 6.1 The Order of Transitions

#### 6.1.1 Review of Thermodynamics, Motion, and Reversibility

A concise review of the relative order, mobility, density, and possible types of phase transitions of one-component systems is presented by the schematic of Fig. 2.115, along with the dictionary definition of the word transition. This schematic is discussed in Sect. 2.5 in connection with an initial description of phases and their transitions. More details of the structure and properties of crystals, mesophases, and amorphous phases are given in Chap. 5. Some characteristics of the three types of mesophases are given in Fig. 2.107. Quantitative information on the thermodynamic parameters of the transitions between the condensed phases is summarized in Fig. 2.103 and described in more detail in Sect. 5.5. The dilute phases in Fig. 2.115, the gases, are of lesser interest for the present description, although the ideal gas law in Figs. 2.8 and

2.9 and the extension to nonideal gases in Figs. 2.99 and 2.100 are the basic equations to which the thermodynamics of most systems is based.

The link of the various glasses in Fig. 2.103 goes only to their corresponding mobile, condensed phases. The omission of the connections of the glassy areas to the phases of higher order indicates that such direct transitions are not possible. This point needs some elaboration, in particular, since a definition of devitrification as a transition from a glass to the crystal is still popular. Polymeric glasses crystallize frequently by cold crystallization, i.e., above the glass transition, as shown in Fig. 5.116, i.e., they change first to a supercooled liquid before crystallization. A typical example is the well-known cold crystallization of amorphous poly(ethylene terephthalate) on heating, as shown in Figs. 4.122, 4.136, 4.138 and 4.139. For more symmetric and flexible macromolecules, such as polyethylene or poly(oxyethylene), the motion needed to crystallize is so little, that crystallization can occur at the very beginning of the glass transition so that glass transition and cold crystallization overlap. The glass transition is then masked by the big exotherm of crystallization, and the increase in heat capacity, characteristic of a glass transition, is missing, because the sample is solid again after it gained temporarily enough mobility for crystallization. Similarly, metals and minerals with close to spherical motifs need only minor rearrangements to crystallize and can often do so at the beginning of large-amplitude, cooperative motion. To describe all the mentioned cases, it is suggested with Fig. 2.103 that the devitrification to the states of higher order or the crystal is always a two-step transition, step one is the glass transition to gain mobility, to be followed by step two, the ordering or ultimate crystallization.

Straight-forward definitions of transitions are available only for the first-order and glass transitions. The basic definitions of both transitions are given in Sect. 2.5 and experimental information is summarized in Sects. 5.4–6. As the dictionary definition of Fig. 2.115 indicates, even subtle changes may be, and have been, called transitions. The observation of gradual changes without transitions have been documented with some examples in Sect. 5.5 (see Fig. 2.108 and 5.143). The definition of the order of thermodynamic transitions, finally is discussed with Fig. 2.119 [2].

Any thermodynamic definition needs special caution before being applied to polymeric systems. It is shown in Sect. 2.5 with the free enthalpy diagram of Fig. 2.118 that the glass transition, although superficially similar to a second-order transition, is time- and frequency-dependent, and thus, is not a thermodynamic transition. Many of the polymer transitions that exhibit a heat of transition, and thus fit the criterion for a first-order transition ( $\Delta S \neq 0$ ), are also not equilibrium transitions because of the chain-folding principle and semicrystalline behavior described in Chap. 5. Before discussing the transitions in polymeric single-component systems, in Sect. 6.2, it is necessary to look at the large increase in number of phase areas caused by irreversibility, as shown schematically in Fig. 2.120.

Figure 6.1 shows schematically a diagram of phase areas of different degrees of metastability [3]. The diagram is drawn under the assumption of a one-component polymeric system which is limited to one crystal polymorph and one mesophase in addition to the liquid and glassy phases. Different sequences of transition occur on heating the seven possible low-temperature structures represented by areas #3, #10, #14, #8, #15, #6, and #11. The transitions are indicated by the densely dotted, narrow

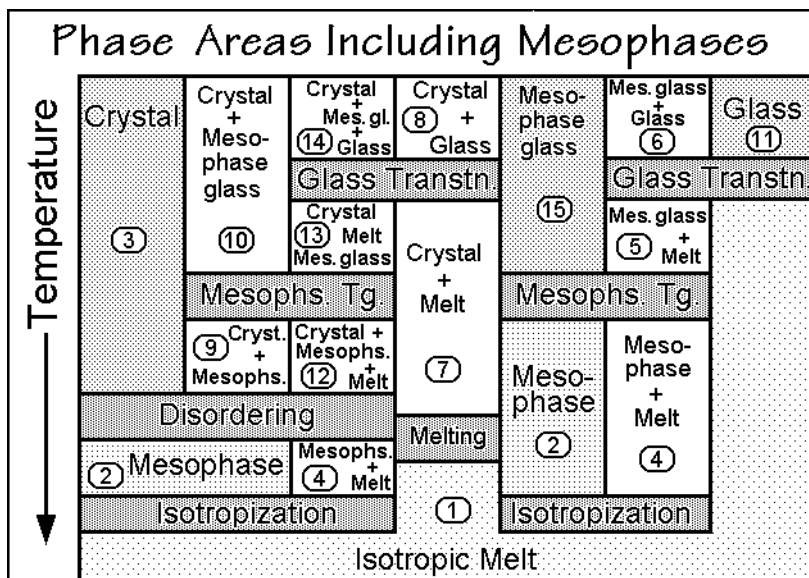


Fig. 6.1

boxes. All one-phase areas are marked by the remaining dotted boxes. The boxes without shading represent two- and three-phase areas. Only the left side of the diagram, structures #1–#3, can be in equilibrium. This is judged from the phase rule which permits at constant pressure only one phase in a given phase area, and two at the boundaries, as pointed out in Sect. 2.5.7, and from the frozen-in nature of the single-phase areas of the glasses discussed in Sect. 2.5.6. The importance of this phase-diagram lies in the illustration of the large variety of metastable phase structures. Increasing the number of possible polymorphs of crystals and mesophases, naturally, increases the number of combinations and the analysis becomes more complicated. All of the 15 different phase-combinations in Fig. 6.1 have been observed. Examples of several polymer systems will be discussed next.

### 6.1.2 First-Order Phase Transitions

For polyethylene, the most studied polymer, all of the 15 phase areas shown in Fig. 6.1 seem to be possible, and most have, indeed, been realized. The sequence of phases seen on heating of extended chain crystals, represented by the phase area #3 in Fig. 6.1, to mesophase, area #2, and melt #1 is seen in the equilibrium phase diagram of linear polyethylene under high hydrostatic pressure in the upper left of Fig. 6.2. Condis crystals of close to 100% crystallinity have been grown on isobaric crystallization above the triple point. The hexagonal condis-crystal phase is sufficiently mobile to permit chain extension after folding on initial crystallization, as required by the chain-folding principle described in Sect. 5.2.2. On cooling from the melt, however, the transitions do not occur at the equilibrium temperatures because of the need of crystal and molecular nucleation described in Sect. 3.5. Other examples of the possibility of equilibrium melting of extended-chain equilibrium crystals that were

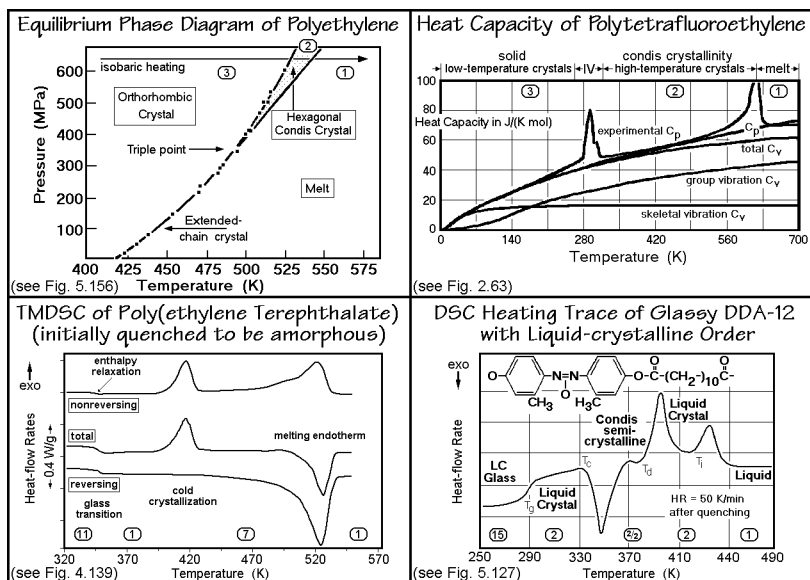


Fig. 6.2

grown after chain extension of the crystals in the condic phase are polytetrafluoroethylene, as illustrated in the upper right of Fig. 6.2, and *trans*-1,4-polybutadiene and polydiethylsiloxane. For the latter two polymers DSC traces are shown in Figs. 2.112 and 5.129, respectively. For polytetrafluoroethylene the phase IV in Fig. 6.2 disappears at somewhat higher pressure (for the phase-diagram, see Fig. 5.130). For *trans*-1,4-polybutadiene and polydiethylsiloxane the DSC traces indicate partial crystallinity. A glass transition is easily detected, arising from the amorphous fractions of *trans*-1,4-polybutadiene and polydiethylsiloxane. The phase sequence is, thus, better described by the sequence #14→#13→#12→#4→#1. On better crystallization, this non-equilibrium sequence approaches the equilibrium sequence #3→#2→#1, with a possible intermediate of #10→#9→#2→#1.

Just as partial crystallization of the condic crystals of *trans*-1,4-polybutadiene and polydiethylsiloxane from the melt results in the metastable phase area #4, sufficiently quick cooling of phase area #4 may yield areas #5 and #6 which contain the corresponding glasses. It must be observed, however, that the glass-transition temperatures of mesophase and melt are not necessarily fixed in the sequence given in Fig. 6.1. If the mesophase permits easier large-amplitude motion than the melt, as observed in some liquid crystals, the mesophase glass transition temperature,  $T_g$ , may be lower than the glass transition of the melt. The existence of a metastable mesophase together with melt or glass, is also found in quenched polypropylene, as seen in Fig. 5.146. The metastable mesophase of polypropylene has been known for many years, but no condition of elevated pressure was found that stabilizes the conformationally disordered crystals. The conformational disorder consists mainly of helix reversals. When the CD glass of polypropylene reaches its glass transition temperature, at about 350 K, the condic crystal orders to the monoclinic crystal with an exotherm of about 600 J mol<sup>-1</sup>.

The phase area #4 in Fig. 6.1 is less likely for liquid crystals than for condensation crystals since the small increase in order that is needed to change a mobile melt into a mobile liquid crystal occurs fast and is usually completely reversible as seen in the reversible transition shown in TMDSC of Fig. 5.144 for a small molecule and the upper curves of Fig. 5.154 for a macromolecule. Once in phase area #2, the polymeric liquid crystals will, however, not crystallize completely on cooling, but rather become a semicrystalline material. In the present scheme, they will produce metastable phase areas #9, followed by #10.

On crystallization of polyethylene at atmospheric pressure, the structure typical for a semicrystalline polymer results. It usually consists of nanophase-separated crystalline/amorphous phase structures, as described in Chap. 5, and is represented by phase areas #7 and #8 of Fig. 6.1. A zero-entropy production path on heating, discussed in Sect. 2.4, permits to evaluate the free enthalpy distribution in areas #7 and #8, as shown in Fig. 6.3 [4] (see also schematics of  $G$  in Figs. 2.88 and 2.120).

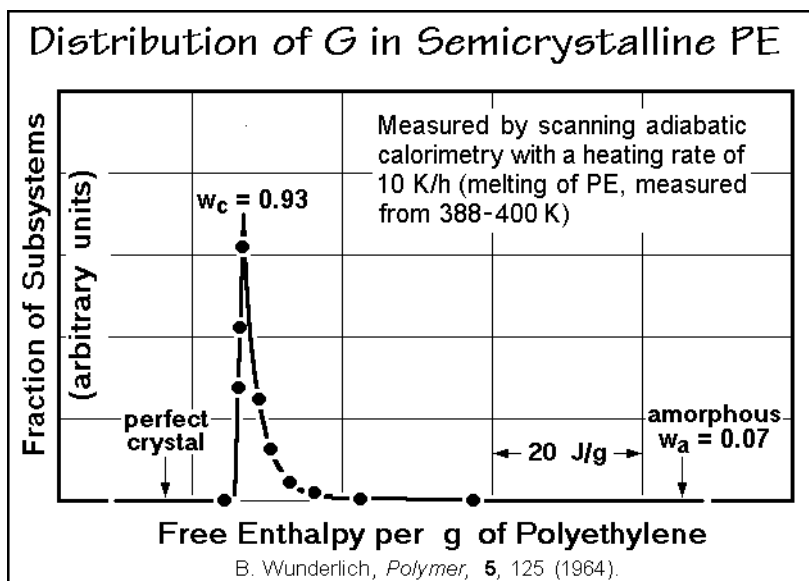


Fig. 6.3

The glass transition of the amorphous phase can be used to estimate the strain introduced into the metastable, amorphous nanophases by the interfaces with the crystals. The local strain manifests itself in an increase of the glass-transition temperature and the possible presence of a rigid amorphous fraction that does not show a contribution to the increase in heat capacity at  $T_g$ , as is discussed in Sect. 6.1.3. Most bulk-crystallized macromolecules which do not exhibit intervening mesophases are described by the phase areas #7 and #8 of Fig. 6.1.

The lower left TMDSC traces in Fig. 6.2 illustrate the special case of poly(ethylene terephthalate) as also documented with Figs. 4.122, 4.136–139, and 5.116. At low temperature, this quenched sample is fully glassy-amorphous, i.e., it is represented by area #11. At the glass transition, it changes simply to area #1, as a supercooled,

metastable equilibrium. Further heating causes cold crystallization to area #7, and on completing the DSC trace, reaching again the area #1 after melting. The complications expected from rigid amorphous content, described in Sect. 6.3, are not included in Fig. 6.1, but could be added by increasing the number of possible phase areas by at least eight, and adding the glass transition for the rigid-amorphous fraction.

A metastable, hexagonal condisc phase of polyethylene was also found at atmospheric pressure in gel-spun, ultra-high-molar-mass polyethylene, yielding areas #9 and #10 or with some amorphous phases present, #12, #13, and #14. Figure 6.4 illustrates the superposition of the orthorhombic X-ray diffraction pattern given by the drawn-out lines on the left, extracted from the two-dimensional diagram on the right. The experimental results are given by the crosses on the intensity plot along the layer lines on the left [5]. The more intense experimental reflection in the 002 area indicates the presence of an additional disordered mesophase which is more mobile than the crystals, as described in more detail in Sect. 5.5 with Figs. 5.157 and 5.158.

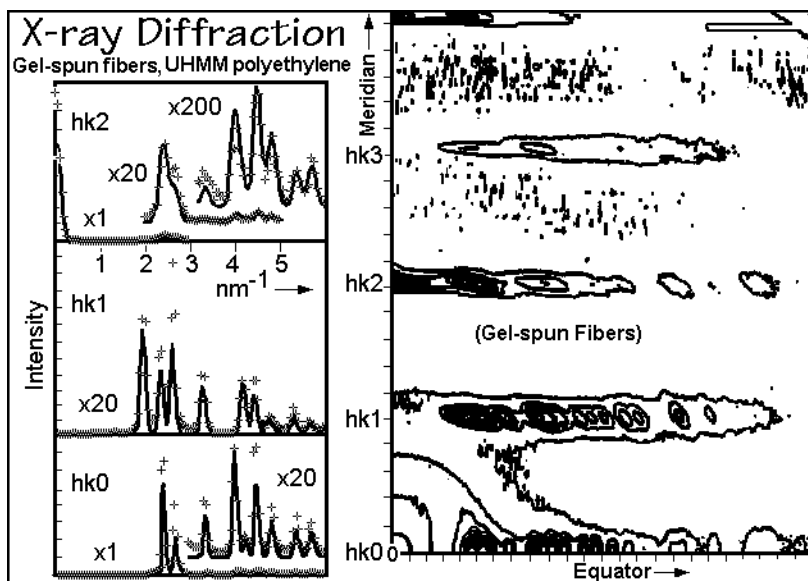


Fig. 6.4

Fully amorphous polyethylene is rather difficult to make because of its fast crystallization. By superfast quenching it was, however, possible to make small amounts of polyethylene glass of phase area #11 [6]. Glassy polymers are much more easily available for macromolecules that crystallize slowly, such as poly(ethylene terephthalate) and poly(oxy-1,4-phenyleneoxy-1,4-phenylenecarboxy-1,4-phenylene) or macromolecules that have structural irregularities which prohibit crystallization completely, such as atactic polystyrene and poly(methyl methacrylate). More details about the special properties of the transition #11→#1 are discussed in Sect. 6.3.

In polyethylene alone one has found, thus, most of the 15 different phase structures of Fig. 6.1. The majority of them is metastable. The remaining phase area #15 may well also be possible for polyethylene by quenching of phase area #2.

The three-phase structures #12, #13, and #14 are of particular interest because of the even more severe violation of the phase rule. At constant pressure, in equilibrium, only one-phase areas should be stable. Drawn fibers of poly(ethylene terephthalate) (PET) are discussed as three-phase structure with Figs. 5.68–72 and 5.113–115. As in polyethylene, the drawing to fibers or films orients the amorphous nanophase and achieves an arrested mesophase order, proven with Fig. 5.72. Since the drawing of PET fibers is much less efficient in extending the molecules than gel-spinning, there remains a sizeable portion of the amorphous phase, as shown in Fig. 5.71. The mobile mesophase of PET has not been found as a stable phase, as in polyethylene. Copolymers of PET with stiffer repeating units, such as oxybenzoate, however, have stable mesophases (see Chap. 7).

The final phase area #15 of Fig. 6.1 is quite common for macromolecular mesophases that do not crystallize well. It is, for example, easily possible to quench poly(oxy-2,2'-dimethylazoxybenzene-4,4'-dioxydodecanedioyl), DDA-12, from the liquid state (#1) to the LC glass (#15). The lower-right DSC trace of Fig. 6.2 reproduces the subsequent DSC heating trace. Above the glass transition temperature, the supercooled mesophase, the liquid crystalline area #2, crystallizes partially to a condic crystal, another mesophase which is more similar to a crystal (see Fig. 2.103). This phase arrangement of two mesophases is not described in the scheme of Fig. 6.1, which was restricted to one mesophase only. In Fig. 6.2 this new area is marked as #2/2, to indicate the simultaneous presence of two mesophases. This condic crystal/liquid crystal state is similar to area #9. Further heating produces the stable liquid crystalline state #2 and, on isotropization, the melt #1. This example indicates the rather complicated paths on heating low-temperature structures when larger numbers of polymorphs are possible.

The large multiplicity of phases, of which many are mesophases, is typical for macromolecules. The old two-phase model for semicrystalline polymers is in need of considerable extension. Most of the phase areas are metastable and have, in addition, only nanometer dimensions [7]. Only when a full characterization has been completed, can an attempt be made to link structure and properties, the central goal of thermal analysis of materials.

As a final point, one must remember that first-order phase transitions are based on equilibrium and require a sharp transition at the intersection of the free enthalpy curves as seen in Figs. 2.84–88. As indicated in Fig. 2.120, the observed broadness comes mainly from a distribution of areas of different size and perfection causing the distributions of subsystems in Fig. 6.3 (for the definition of subsystems see Fig. 2.80). Combining the different types of molecules, phases, and sizes with the range of metastable phase structures yields an enormous number of materials that must be explored to find the perfect match for the application on hand.

### 6.1.3 Glass Transition

The glass transition is much more subtle than the first-order transition. As is illustrated in Sect. 2.5.6. The classical glass transition occurs in a sample that can undergo large-amplitude motion, i.e., liquids or mesophases (see Fig. 2.103). On cooling, the large-amplitude motion freezes cooperatively, and the sample becomes



glassy over a relatively narrow temperature range. A glass transition with its seven characteristic parameters as measured by DSC is shown in Fig. 2.117. A typical free-enthalpy diagram for two glasses cooled at different rates is given in Fig. 2.118. The experimental analysis of glass transitions as a function of frequency can also be done with a temperature-modulated DSC, as illustrated in Sect. 4.4.5. Dilatometry can identify glass transitions as shown in Fig. 4.27, and the effects of glass transitions on mechanical measurements are discussed with Figs. 4.170 and 5.171. Details of the DSC analyses are described next. This is followed by a discussion of the changes that occur when glassy phase-areas are restricted in size and if there are constraints on the amorphous phase so that there remains an amorphous, rigid phase above  $T_g$  of the unrestrained amorphous material.

**The hole model of the glass transition.** To get a better feeling for the nature of the glass transition to polymers, the simple, 70-year old hole-model of the liquid [8,9] was used for its description [10,11]. The model is shown schematically on the upper right of Fig. 6.5. The main distinction between liquid and solid is the low viscosity of the liquid (see Sect. 5.6). This low viscosity is linked to the long-range mobility of the holes through their ability to diffuse or, after collapse, to reform elsewhere.

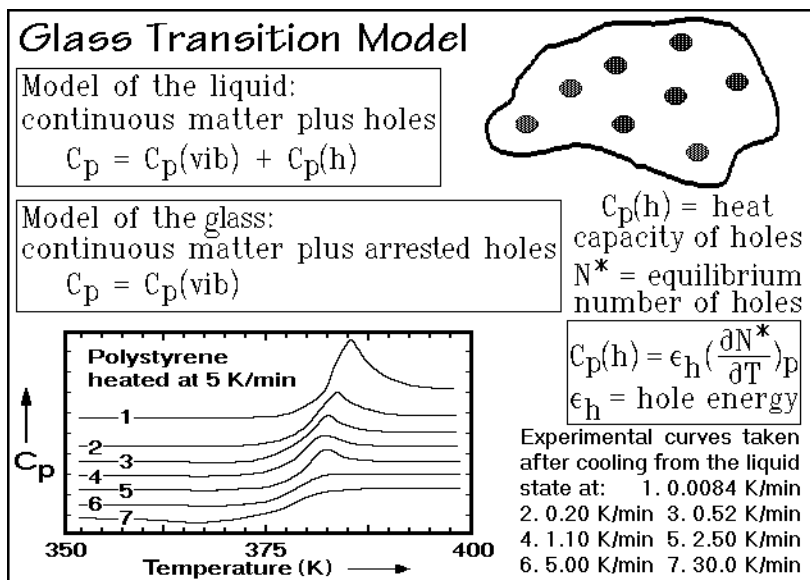


Fig. 6.5

The model is linked easily to the heat capacity of the liquid, as seen in the upper box of Fig. 6.5. The  $C_p$  arises mainly from vibrations,  $C_p(\text{vib})$ , and a contribution from the holes,  $C_p(\text{h})$ . In  $C_p(\text{h})$  one finds the energy needed to change conformational isomers to accommodate the hole, as well as the potential energy required to create the extra volume of the holes that permits the large-amplitude molecular motion. Below  $T_g$ ,  $C_p(\text{h})$  is zero, as shown in the second box, because the hole-equilibrium is arrested. Above  $T_g$ , it contributes the hole energy,  $\epsilon_h$ , multiplied with the change in equilibrium number of holes with temperature  $\partial N^*/\partial T$  at constant pressure. The equations can be

fitted to the experimental heat capacities of the equilibrium liquid and the metastable glass. In the intermediate region,  $C_p$  is time dependent, as shown in Sect. 4.4.6.

**Enthalpy Relaxation.** On cooling, a measurement of the heat capacity through the glass transition will always look like the curve in Fig. 2.117. The decrease in heat capacity occurs at a temperature uniquely fixed by the cooling rate, being caused by the freezing of the hole equilibrium. On heating, one observes a hysteresis that depends on the thermal history of the sample, i.e., the manner how the glassy state was reached on prior cooling. Figure 6.5 shows some experiments on polystyrene [12]. Exothermic and endothermic effects can be seen in the heat capacity on heating of the sample. If the glass was cooled more slowly than its subsequent heating, an endotherm is seen prominently in the upper temperature region of the glass transition and obliterates to some degree the response due to the unfreezing of the holes. It was shown in Figs. 4.125–127 that, at least approximately, TMDSC can separate the unfreezing of the holes from this enthalpy relaxation or hysteresis. If the samples in Fig. 6.5 were cooled faster, one would see a hysteresis exotherm on slow heating at the beginning of the glass transition. Such exotherms have not been studied extensively. Only when cooling and heating rates are alike, is the hysteresis small and glass transition temperatures can be established on cooling as well as on heating. Annealing a glass within the glass transition region creates a similar endothermic hysteresis as seen on slow cooling. An example for polystyrene is given in Fig. 4.127.

Figure 6.6 shows schematically with curve 1 how on slow cooling a system deviates at  $T_g$  from equilibrium of V, H, and S (heavy line, compare also to Fig. 4.128). The indicated fictive temperature points to the equilibrium liquid with the identical number of holes as are frozen in the glass. The derivative quantities, heat capacity and expansivity, are shown in the lower curve of Fig. 6.6. Following the slow cooling with fast heating, curve 1 cannot be followed in the glass-transition

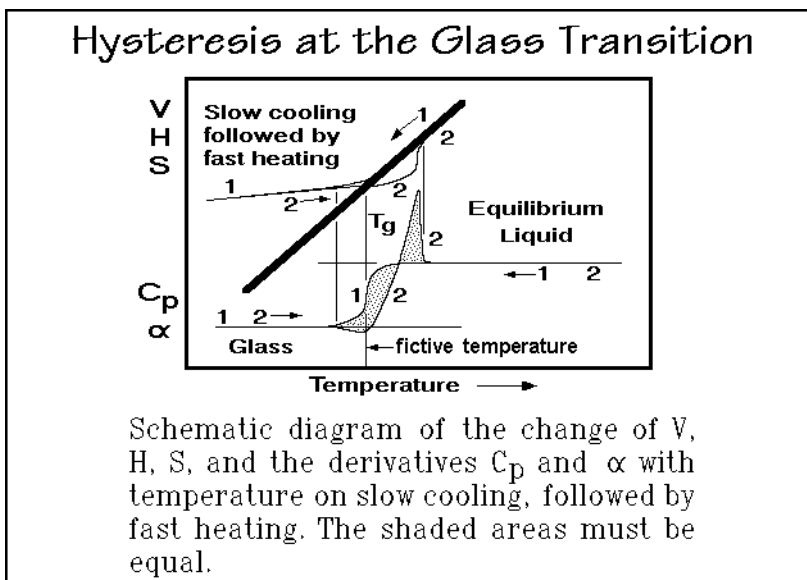


Fig. 6.6

region. The glass superheats and follows the V, H, and S of the glass beyond the liquid equilibrium along curve 2 and catches up only above  $T_g$  with a higher slope in H and a peak in  $C_p$ . This endothermic hysteresis peak is heating-rate dependent and must not be mistaken for a first-order transition. It can be made to disappear by matching cooling and heating rates, as is shown in the experiments of Fig. 6.5. The two dotted areas in the lower curve of Fig. 6.6 are equal, as required by the first law of thermodynamics for any cyclic process that starts and ends with the same equilibrium state which, in the present case, is the liquid (see also Sects. 2.1 and 2.2).

**The kinetics of the change in number of holes.** The glass-transition range with its gradual change in heat capacity from the value of the solid to that of the liquid can be based on the differential equation of Fig. 6.5. The number of holes refers then not to the equilibrium number of holes,  $N^*$ , which changes only with temperature, but to the actual change of holes,  $N$ , with time during heating or cooling with rate  $q$ . The solution of this equation is given in Sect. 4.4.6 with Fig. 4.131 under the assumption of first-order kinetics, and applied to the analysis of TMDSC experiments on polystyrene [13]. Figure 6.7 illustrates a collection of TMDSC data with underlying heating and cooling rates and under quasi-isothermal conditions. The discrepancies

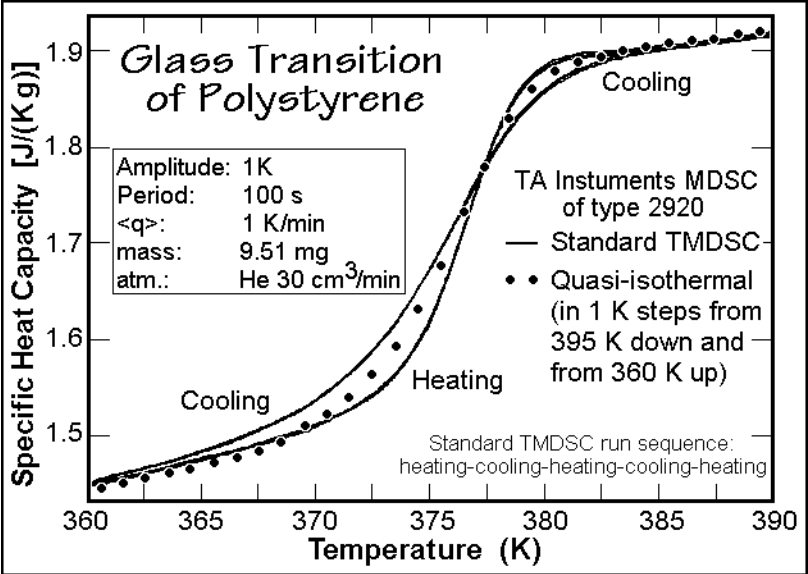


Fig. 6.7

between the three analysis methods are to be resolved next. For this purpose quasi-isothermal polystyrene and poly(ethylene terephthalate) data were generated [14] and analyzed as indicated in Fig. 4.131 and 6.118 [15].

As indicated in Fig. 6.5, the equilibrium number of holes at a given temperature is  $N^*$ , and its contribution to  $C_p$  is listed in the boxed equation on the right. Creation, motion, and destruction of holes in the glass-transition region lead to deviations if the measurement is carried out faster than the kinetics allows. Applied to the glass transition, one can write the simple first-order kinetics expression given in Sect. 4.4.6:

$$\left( \frac{dN}{dt} \right) = \frac{1}{\tau} (N^* - N) \quad (1)$$

with  $\tau$  representing the relaxation time for the change in number of holes. Due to the modulation of temperature, the values of  $N^*$  and  $\tau$  are also time dependent and solutions could only be found for quasi-isothermal analyses and, as usual, for the conditions that steady state could be maintained [15]. Figure 4.113 illustrates that steady state could be kept at the glass transition under typical analysis conditions [14]. The activation energies  $\epsilon_i$  of Fig. 4.132 could be evaluated as 345.5 and 328 kJ mol<sup>-1</sup> for polystyrene and poly(ethylene terephthalate), respectively. The corresponding values for the pre-exponential coefficients were 1.876×10<sup>-46</sup> and 5.59×10<sup>-49</sup> s, the hole energies,  $\epsilon_h$  6.00 and 4.70 kJ mol<sup>-1</sup>, respectively. With these results, the coefficients of the equation in Fig. 4.131 could be evaluated.

To attempt to describe the TMDSC data with an underlying cooling and heating rate, it turns out that the above kinetics equation is best solved numerically with the parameters derived from the quasi-isothermal analyses. Each of a series of short intervals, running from 0 to  $i$ , is integrated with a constant  $N^*$ , appropriate for the instantaneous temperature, and an average value of  $\tau$  is set equal to  $[\tau_i \times (\tau_i - 1)]^{1/2}$  and lead to:

$$\Delta N_i = N_i^* - (N_i^* - N_{i-1}) e^{-\frac{t}{\sqrt{\tau_i \times (\tau_i - 1)}}} \quad (2)$$

For a heating experiment,  $N_0^*$  at  $i = 0$  is chosen at the fictive temperature for the given prior thermal history. The fictive temperature identifies the temperature at which the actual hole concentration equals equilibrium. It is also found at the intersection of the heavy line of the enthalpy of the equilibrium liquid with the thin lines for the glass in Fig. 4.128. For a cooling experiment  $N_0^*$  is the equilibrium value at  $T_o$ , the starting temperature in the liquid region.

Typical results for the number of holes for cooling through vitrification and on heating, illustrating devitrification are shown in Figs. 6.8 and 6.9. The glass transitions are modeled on data for the polystyrene shown in Fig. 6.7. For the calculation, data were calculated in intervals of one second. Figure 6.8 shows that the fast modulation with a frequency of 0.01 Hz freezes first. The fastest rates of temperature change for modulations are  $\pm 3.8$  K min<sup>-1</sup>, to be compared to the slow, underlying rate of cooling or heating of 1.0 K min<sup>-1</sup>. In the glass-transition region, the amplitude of the changing number of holes due to modulation decreases rapidly. This is followed by the drift to the constant  $N$ , characteristic of the glass, caused by the underlying cooling rate  $\langle q \rangle$ . Stopping the cooling within the glass transition region also yields annealing, discussed qualitatively with Fig. 4.128. The simulation of the modulation with an underlying heating rate in Fig. 6.9 is started at the same number of holes reached on cooling in Fig. 6.8. From Fig. 6.5, one expects the small exotherm before  $T_g$  and a small endotherm above. Indeed, this is observed. Overall, on heating, the changes on modulation are more asymmetric than on cooling.

The next step after evaluation of the change of hole numbers with time (and temperature) is to calculate the heat capacities obtained from the reversing signal.

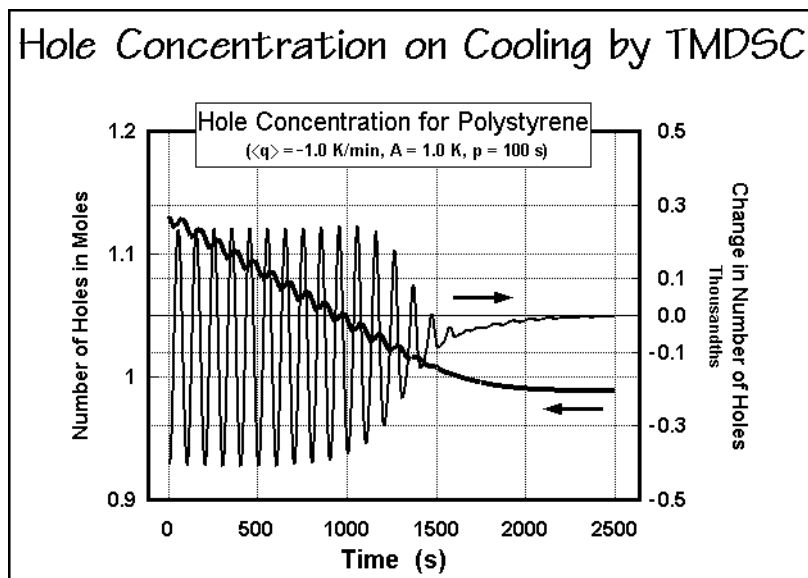


Fig. 6.8

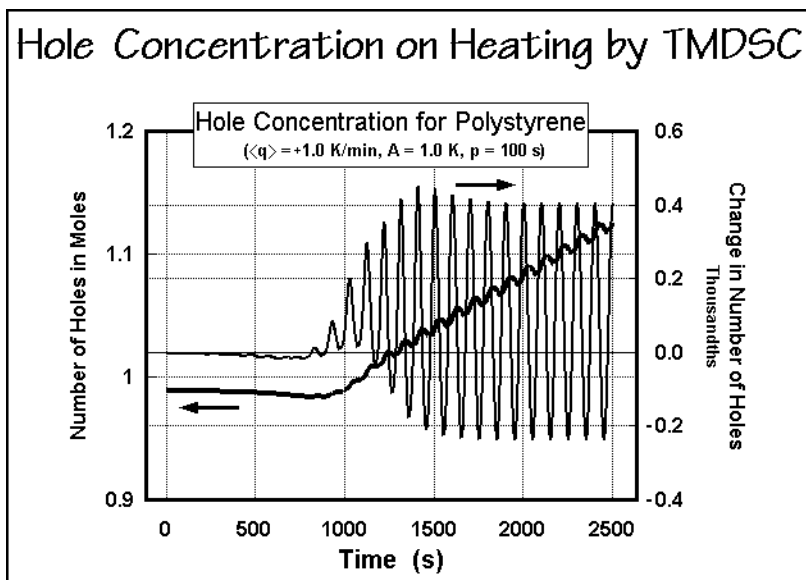


Fig. 6.9

Again, it is assumed that all instrument lags are minimized and steady state is maintained. The number of holes is multiplied with the hole energy for polystyrene of  $\approx 6 \text{ kJ mol}^{-1}$  and entered in a spread sheet which can calculate instantaneous heat-flow rates,  $\text{HF}(t)$ . Figures 6.10 and 6.11 represent the total, reversing, and non-reversing heat capacities due to the glass transition on cooling and heating.

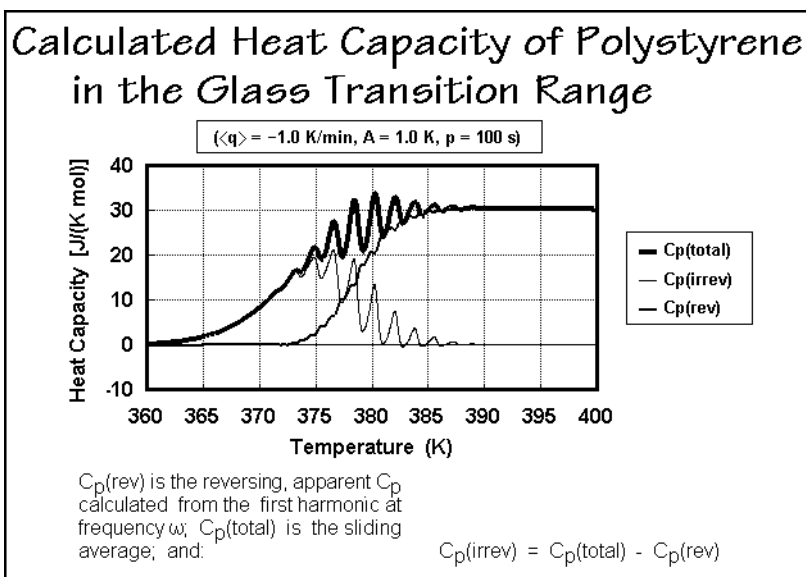


Fig. 6.10

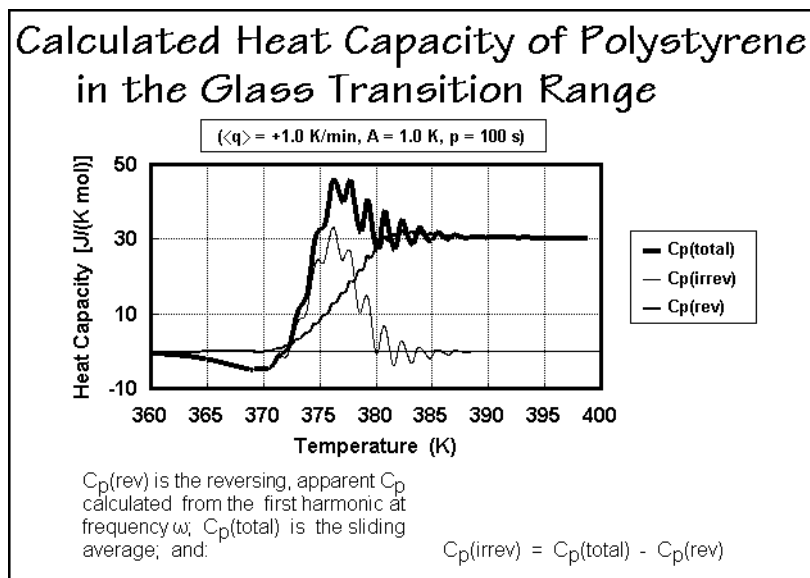


Fig. 6.11

The initial observation is that the deconvolution of the HF(t) as outlined in Figs. 4.97–99 does not remove all the modulation in the glass transition region. By counting the cycles in a given time, one finds that the linear temperature change and the modulation cause a change in frequency, a Doppler-like effect, similar to the change in frequency of a moving source of sound relative to a stationary observer.

The irreversible contribution shows a maximum in heat capacity, as is expected from the difference in time scale of the modulation and the underlying change in temperature. While cooling, there are gradual changes in hole concentration and irreversible heat capacity, as displayed in Figs. 6.8 and 6.10. On heating, there are a minimum and an asymmetry in hole concentration in Fig. 6.9, and the heat capacity in Fig. 6.11 mirrors this change with an exotherm at low temperature followed by an endothermic enthalpy relaxation. At least qualitatively, the simulations have thus duplicated the experiments. The remaining differences are pointed out next.

Figure 6.12 displays the calculations of the change in heat capacity of polystyrene in the glass-transition region for comparison with the experiments in Fig. 6.7. The changes in frequency in the glass-transition region, which cause the remaining

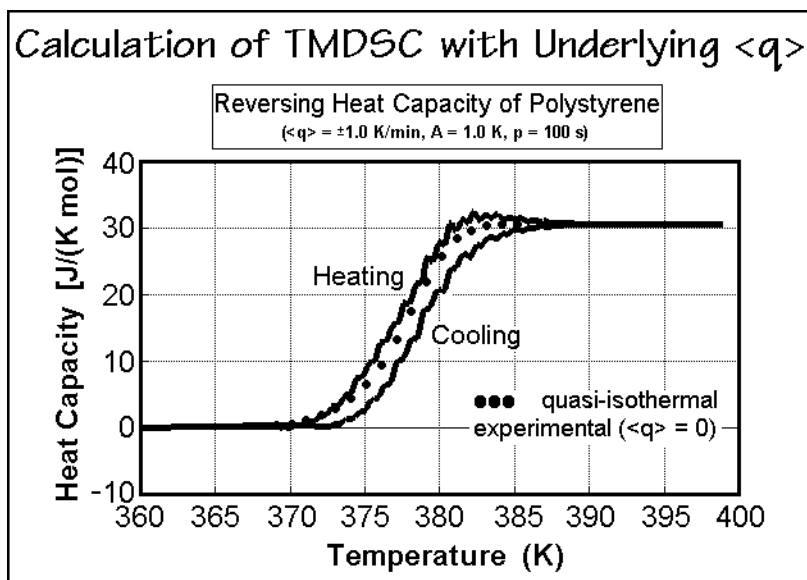


Fig. 6.12

modulation of the results in Figs. 6.10 and 6.11 are not obvious in the experiments of Fig. 6.7. One reason is a further smoothing done in the evaluation of the experiment, as discussed in Figs. 4.98–102 (curves I). Another difference in Fig. 6.7 is the cross-over between heating and cooling with underlying changes of temperature. Only close to the liquid state is the calculation comparable to the experiment. Clearly the relaxation time,  $\tau$ , is shorter on cooling than on heating. This observation was already made early when following the glass transition with dilatometry [16]. Combining all DSC data, which reach from the early efforts to model the glass transition as measured in Fig. 6.5 with the hole theory [12] to the results in Fig. 4.126 [17] and the extensive measuring and modeling efforts of Figs. 6.7–12 [13–15], one must reach the conclusion that the relaxation time is not only temperature-dependent, but also dependent on the hole concentration itself, i.e., it shows the cooperative character pointed-out throughout the discussion of the glass transition. Some discussion of cooperativity based on DMA can also be found, for example in Ref. [18].

**Effect of the size of the phase on the glass transition.** Changing the size of the amorphous phase from macrophase to microphase, and finally to nanophase dimensions, has a strong influence on the glass transition. A free surface allows the large-amplitude motion to occur at a lower temperature and broadens the glass transition range because of a gradual change to the bulk sample. If molecules cross the interface,  $T_g$  increases in case the adjacent phase has a higher  $T_g$ , and it decreases in case of a lower  $T_g$ . Examples of such changes of the glass transition are discussed in Sect. 7.3 for immiscible block copolymers. In semicrystalline polymers the strong interaction across the interface causes also a higher glass transition in the interface [19]. In case the interaction is strong, a rigid amorphous phase may occur and remain rigid far above  $T_g$  of the unrestrained, amorphous phase. The effect of a free surface is discussed next, followed by an analysis of rigid-amorphous fractions.

Figure 6.13 illustrates the glass transition temperature of small beads of polystyrene, measured by standard DSC [19]. One can observe, besides the glass transition with a small hysteresis peak, that on first heating, shown by the solid curves,

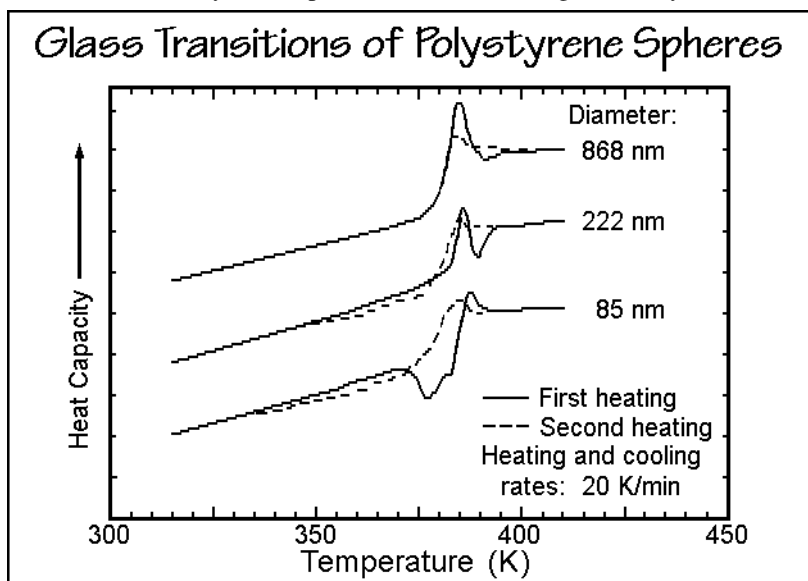


Fig. 6.13

there is a sizeable exotherm of strain release when the beads start coalescing. The dashed lines allow a comparison with the same sample after completed coalescence to a compact sample as it existed on second heating. The glass transition of the small beads can be seen to start about 30 K earlier than after the fusion to a macrophase, and the exotherm has disappeared, as expected. Increasing the bead sizes changes the glass transition on first heating, without affecting the second heating scans. The exotherm due to the coalescence of the beads moves to increasingly higher temperature, as does the beginning of the glass transition. When approaching the limit of the microphase size of one micrometer, the broadening of the glass transition to lower temperature becomes negligible.



A quantitative analysis of the data of Fig. 6.13 is attempted in Fig. 6.14 [20]. Extrapolating the increase in heat capacity to  $T_g$ , suggests that 1/3 of the total beads of 85 nm contribute to a lower glass transition. This, in turn, suggests a 5-nm-thick layer of polystyrene with a lower glass transition temperature. Figure 6.15, finally, shows that a subdivision into concentric shells of the polymer with linearly decreasing glass transition temperatures when approaching the surface, models the experiments.

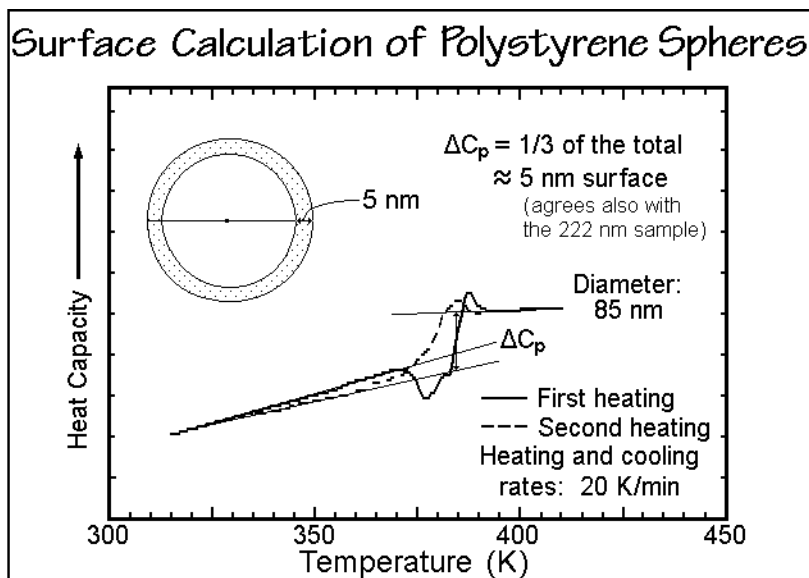


Fig. 6.14

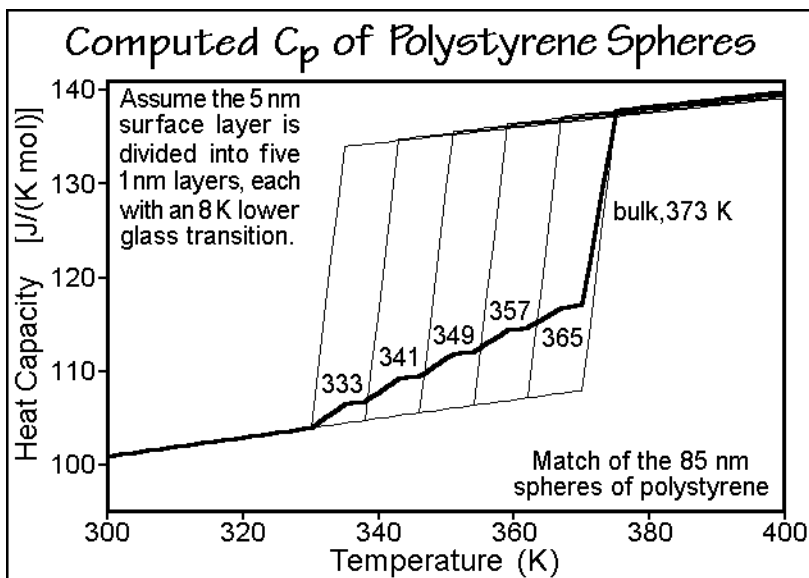


Fig. 6.15

**Rigid-amorphous fraction, RAF, in semicrystalline polymers.** The influence of interfaces with crystals on the glass transition of the amorphous phase may not only cause the commonly observed broadening and shifting of the glass-transition range to higher temperature, as shown in Figs. 4.136 and 6.132 for the reversing heat capacity from TMDSC of poly(ethylene terephthalate), it may also give rise to a rigid-amorphous fraction, RAF, that is metastable to much higher temperatures. In Fig. 4.136,  $T_g$  has shifted on crystallization by 10 K from 347 K to 357 K and the end of the glass transition reaches up to about 375 K. Between 380 and 420 K a second  $T_g$  seems to exist, attributed to a RAF (for  $T_e$ , see also Fig. 4.137).

The first quantitative analysis of RAF was carried out by analysis of the heat capacity of semicrystalline poly(oxymethylene), POM, as shown in Fig. 6.16 [20]. Clearly, the 67% of crystallinity computed from the heat of fusion, which would require a 33% amorphous fraction as indicated by the dotted line in the left trace, does

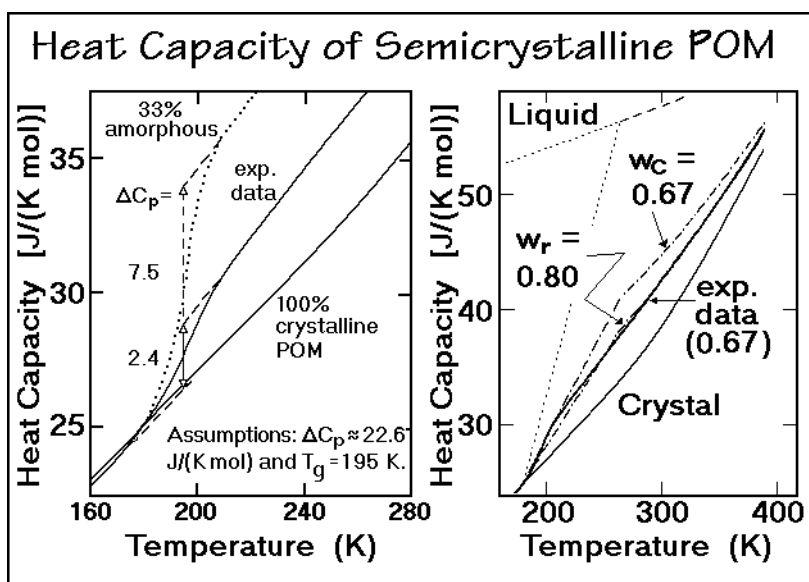


Fig. 6.16

not agree with the experimental data given by the solid line. The right trace identifies the rigid fraction,  $w_r$ , as 0.80 of the total sample, leading to a rigid-amorphous fraction,  $(w_r - w_c) = 0.13$  which does not contribute to the glass transition, but is also not crystalline. The glass transition is completed at about 210 K. In Fig. 6.17 the analysis of several POM samples is given, allowing an overview of the polymer behavior. The RAF is a significant part of the material and does not permit a description of the properties of the polymer with a two-phase model, as is often done. For every semicrystalline sample, the RAF should be analyzed as a function of temperature since it may be as important for the determination of the thermal and mechanical properties of the material as the crystallinity. The data of the right trace Fig. 6.16 show that there is no indication that for POM the RAF changes up to the melting region. In Sect. 6.3 it is shown that for other polymers, the RAF may have a glass transition below, above,

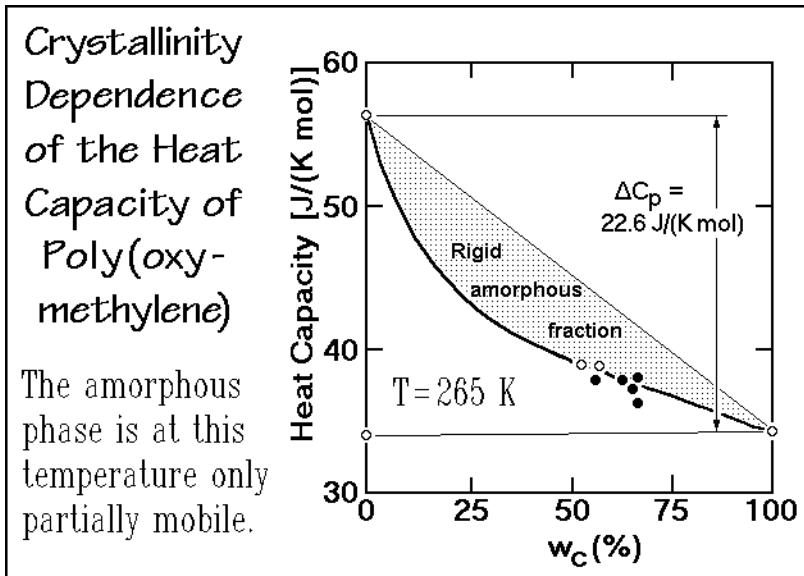


Fig. 6.17

or at the melting transition. Some polymers, such as polyethylene, show no separate glass transition, but have only a broadened glass transition. On drawing, the RAF of semicrystalline polymers can be oriented and then be the supporting structure which determines the overall modulus and even the ultimate strength (tensile strength) of the fibers and films which are discussed in Sect. 6.2.6. Proof of such structures is given in Figs. 5.68–72 and 5.113–115 for fibers of poly(ethylene terephthalate) and Figs. 5.157, 5.158, and 6.4 for gel-spun, ultra-high-molar-mass polyethylene.

The reversing heat capacity and the total heat-flow rate of an initially amorphous poly(3-hydroxybutyrate), PHB, are illustrated in Fig. 6.18 [21]. The quasi-isothermal study of the development of the crystallinity was made at 296 K, within the cold-crystallization range. The reversing specific heat capacity gives a measure of the crystallization kinetics by showing the drop of the heat capacity from the supercooled melt to the value of the solid as a function of time, while the total heat-flow rate is a direct measure of the evolution of the latent heat of crystallization. From the heat of fusion, one expects a crystallinity of 64%, the total amount of solid material, however, when estimated from the specific heat capacity of PHB using the ATHAS Data Bank of Appendix 1, is 88%, an indication of a rigid-amorphous fraction of 24%.

There are two possibilities for the production of the RAF. Either it forms at the same time as the crystallinity, or it forms later, when the crystals impinge or when secondary crystallization occurs. Figure 6.18 shows clearly that the formation of RAF goes parallel with the crystallization as long as the temperature is below the  $T_g$  of RAF. Furthermore, the analysis of PHB indicates no significant defect contribution to  $C_p$ , in contrast to polyethylene (see Fig. 2.51). The reason is that there must be at least three consecutive  $\text{CH}_2$ -groups to form *gauche-trans-gauche* defects (2g1 kinks) as in polyethylene (see Sect. 5.3), and in addition, the melting temperature of PHB is lower than for polyethylene, also keeping the  $C_p$  closer to its vibrational limit.

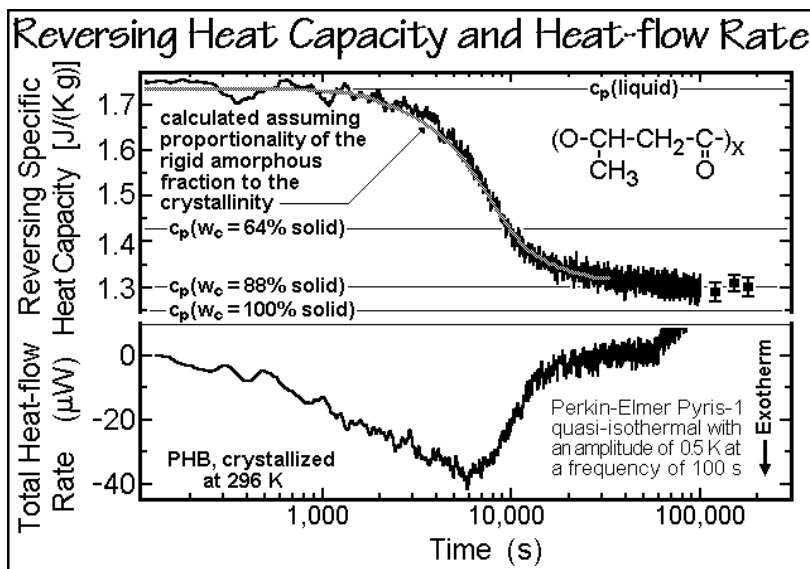


Fig. 6.18

**Differences in  $T_g$  measured by DSC and DMA.** A final topic concerns the difference between  $T_g$  measured by DMA, DSC, TMDSC, and TMA (see Sects. 4.5.4, 4.3–5, respectively and also Fig. 4.17). The operational definition of  $T_g$  by DSC (and dilatometry) requires to find the point of half-completion of the transition (see Fig. 2.117). The DMA results, in contrast, are usually reported as the maximum of  $\tan \delta$ , the ratio of the out-of-phase to the in-phase modulus (Fig. 4.160). Figure 6.19

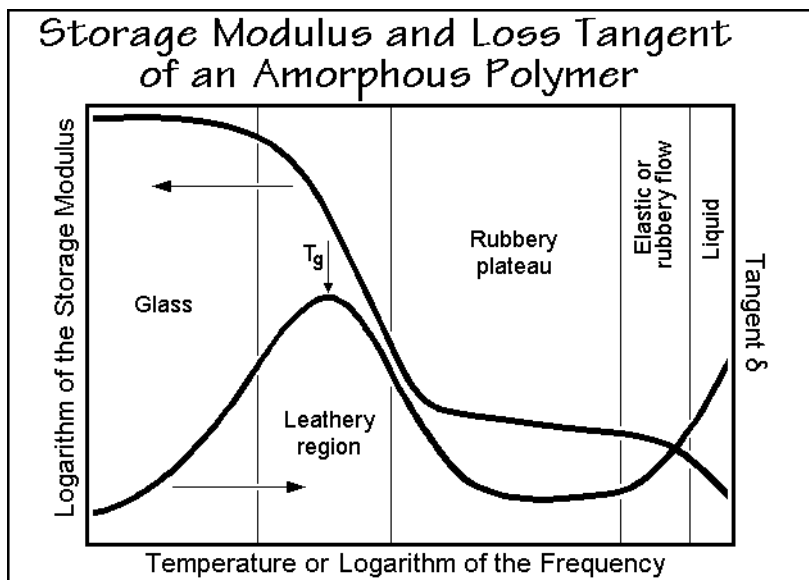
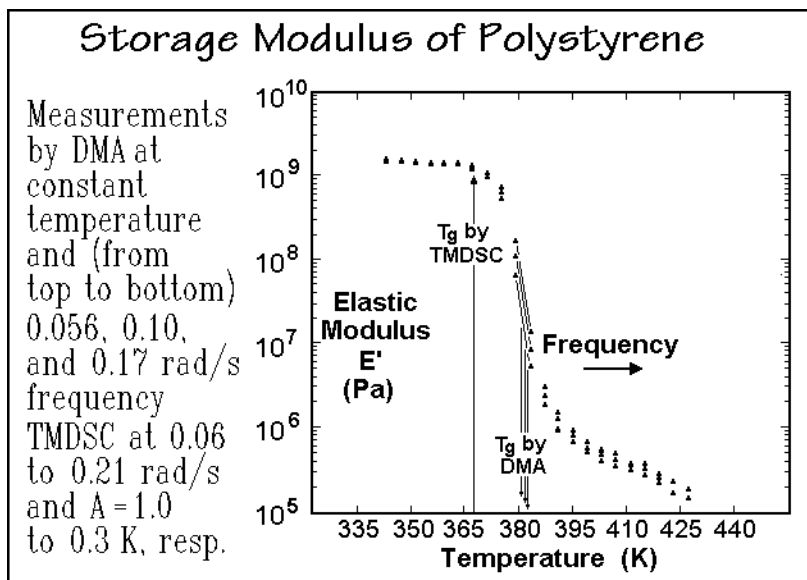


Fig. 6.19

is a schematic of the mechanical properties of an amorphous polymer as a function of temperature (at constant frequency) or frequency (at constant temperature). Note that the in-phase storage modulus is plotted logarithmically, and  $\tan \delta$  represents the linear, out-of-phase modulus, normalized to the storage modulus (see, for example Fig. 4.169), i.e., it represents the maximum energy dissipated per unit storage modulus (see Fig. 4.160). A comparison of the glass transition of polystyrene measured at equal frequencies by TMDSC and DMA is depicted in Fig. 6.20. Despite the identical



**Fig. 6.20**

frequency, the  $T_g$  by DMA is more than 10 K higher than by DSC. If one would have picked  $T_g$  where the modulus approaches 50% of its glassy value, the two values would have been much closer. Much of the difference in glass transition temperatures that may arise when not measuring with the same thermal analysis technique, thus, is caused by differences in definition of the glass transition.

## 6.2 Size, Extension, and Time Effects During Fusion

In this section the broad spectrum of melting of one-component macromolecular systems is described by means of several specific polymers. The description starts with polyethylene, the most analyzed polymer. It continues with two sections that present several special effects seen in the thermal analysis of polymers including some examples of detailed analyses by TMDSC, documenting the locally reversible melting and crystallization equilibrium within a globally metastable structure. Then illustrations of poly(oxymethylene) and PEEK are given as typical common polymeric materials. This is followed in the last section with the discussion of special effects seen in drawn polymers, as are commonly found in fibers and films.

### 6.2.1. Melting of Polyethylene

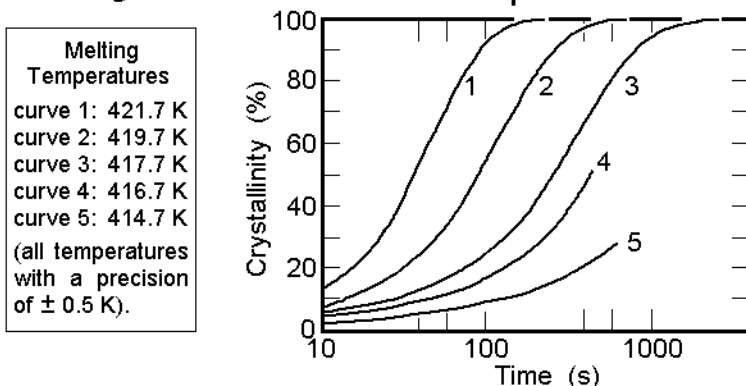
Polyethylene has experimentally been produced in many of the crystal morphologies of Fig. 5.41, including macroscopic, isometric-to-plate equilibrium crystals (Fig. 5.76 and 5.77), lamellar crystals (Fig. 5.51–53), and fibrillar structures (Fig. 5.66 and 5.67). The macroconformations of polyethylene include all areas of the diagram of Fig. 5.42. The crystal sizes (phase sizes) could be found to cover the full range from macroscopic phases to nanophases (see Sect. 2.5.2). Finally, the phases could not only be the classical glassy, crystalline, and melted phases, but also a mesophase (condensed crystal, see Fig. 2.103) and a mesophase glass have been observed in addition to a less stable, monoclinic crystal (see Sect. 5.1.7). This enormous breadth of different, mostly metastable, phase structures (see Fig. 6.1) are naturally also influencing the mechanical properties. For a specific sample, thermal analysis has, thus, the goal to identify the combination of phases and establish the link of structure to property.

Figure 4.18 represents the slow dilatometry of a strictly linear poly(methylene) with  $1.4 \times 10^7$  Da molar mass without molecules of molar mass less than  $10^6$  Da. By crystallization at elevated pressure, the sample had reached a crystallinity of 98% and an extended-chain macroconformation, i.e., it was close to equilibrium. In the melting region, one point was taken every 24 h to avoid superheating and to establish the equilibrium melting temperature of 414.6 K. Within the estimated experimental error of  $\pm 0.3$  K, the same value was found by an extrapolation of the zero-entropy-production melting temperatures of lamellar crystals as a function of the lamellar thickness, given in Fig. 2.90, and resulted also from the extrapolation of the melting temperatures of many paraffins to infinite chain length, shown in Fig. 3.4.

The kinetics of melting of a similar high-molar-mass poly(methylene) is illustrated in Fig. 6.21 for different temperatures [22]. It was measured by isothermal DSC, as illustrated in Fig. 3.98. Measurements of this type, when coupled with data for the crystallization kinetics, allow to establish the temperature region of metastability that is caused by the need of crystal and molecular nucleation, discussed in Sect. 3.6 (see Fig. 3.76). The change in the melting-peak temperature of a series of different polyethylene crystals is shown in Fig. 6.22 [23]. These data were measured with a DSC as in Fig. A.9.2D. Curve E illustrates the slow-melting of the extended-chain crystals of Fig 6.21. Characteristic for the superheating of the crystals is the constant  $T_b$  with rate of heating, while  $T_p$  and  $T_e$  increase (the temperatures  $T_b$ ,  $T_p$ , and  $T_e$  are defined in Fig. 4.62). An example of DSC curves of crystals which superheat on melting is shown in Fig. 6.92 for extended-chain crystals of poly(oxymethylene). Curve F displays data for an extended-chain polyethylene of broad molar-mass distribution as illustrated in Fig. 5.76. The crystals of Curve F have a chain extension of up to 2  $\mu\text{m}$ . Curve E, in contrast, was generated from crystals with an extension of up to 10  $\mu\text{m}$ . The superheating of the crystals of F is less than the crystals of E, and in addition, the melting range on slow dilatometry is broader because of the presence of molecules of lower molar mass which melt at a lower temperature, as is indicated in Fig. 3.76, and is documented in more detail in Sect. 7.1.

These experiments prove that crystals of the type E and F are at low temperatures, at least in part, close to equilibrium and allow the direct assessment of the equilibrium melting parameters: heat of fusion, volume change on fusion, and equilibrium melting

### Melting Kinetics at Different Superheating of Extended-chain Crystals of Polyethylene Using Isothermal DSC Experiments



Drawn after E. Hellmuth and B. Wunderlich, **36**, *J. Appl. Phys.*, 3039 (1965).

Fig. 6.21

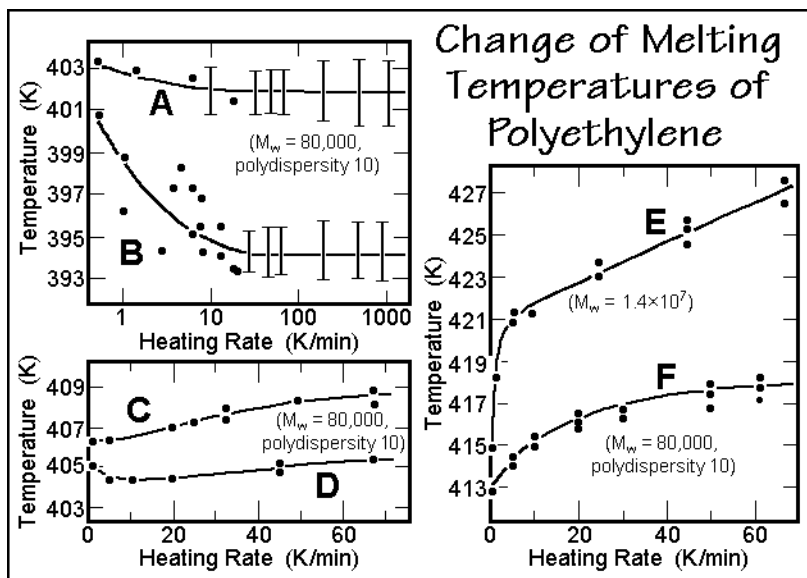


Fig. 6.22

temperature. Adding the heat capacity to these equilibrium data, as described in Sect. 2.3 (Figs. 2.46, 2.51, 2.59, and 2.65), conversion to the integral functions of Fig. 2.23, and the phase diagram of Fig. 5.156, gives a full quantitative description of the equilibrium thermodynamics of polyethylene. This is possible even though equilibrium melting cannot be reversed, and must be done slowly to avoid superheating of the crystals.

The equilibrium crystals just discussed had to be grown in the hexagonal condis phase area of the phase diagram (Fig. 5.156) to achieve the chain extension by subsequent annealing of the initially grown chain-folded crystals. On crystallization from the melt in the orthorhombic phase area, the initially produced lamellar crystals also do not correspond to the crystals that one melts in a later experiment, although the crystal perfection is less than in the condis phase area. Figure 6.23 illustrates the

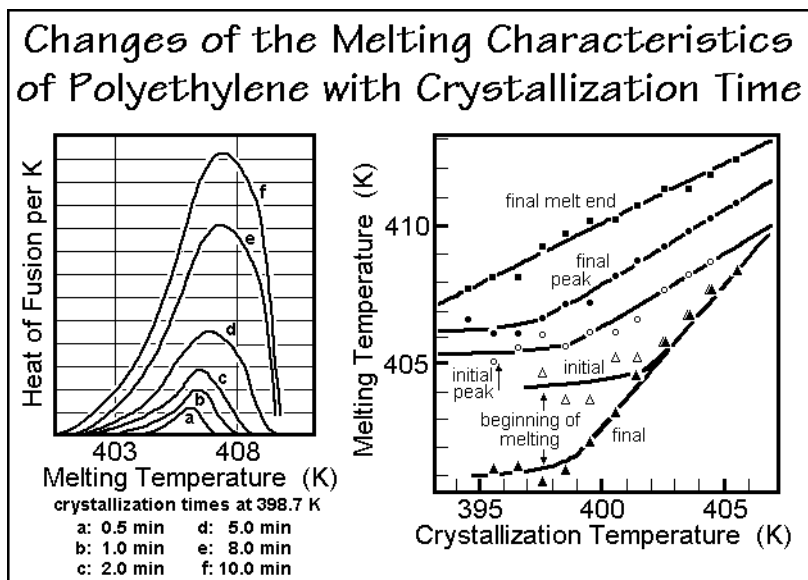


Fig. 6.23

change of the melting characteristics as a function of time of a polyethylene sample of the same molar mass as the extended-chain crystals F of Fig. 6.22, but crystallized at 398.7 K at atmospheric pressure [24]. As the crystallinity increases, melting peak and melting end shifts to higher temperature. At later times, crystals grow which are poorer and have lower melting temperatures. Even isothermally grown crystals, thus, are far from uniform and, as the melting temperatures indicate, they are also far from equilibrium ( $T_m^0 = 414.6$  K). Only at the highest crystallization temperatures is the equilibrium melting temperature approached, but at these temperatures crystallization is exceedingly slow, as illustrated by curve 9 of Fig. 3.67. Crystallizing a melt during cooling, as is often the case in industrial applications, leads to an even broader distribution of crystals of different degrees of perfection, as can be surmised from the curves on the right of Fig. 6.23 and seen from fast calorimetry of Fig. A.10.6.

Once produced, the metastable crystal distributions must be analyzed under conditions of zero-entropy-production melting (see Sect. 2.4.2 and 2.4.3). If annealing occurs during heating, the measurements do not correspond to the starting material and cannot be linked to the properties of the sample, as shown schematically in Fig. 2.86. Crystals with lamellar thicknesses  $\ell_1$  and  $\ell_2$  melt above the zero-entropy-production melting temperature of the initial thickness  $\ell$ . Figure 6.22 also shows a comparison of melt-crystallized polyethylene with a morphology as indicated in Fig. 5.64 [22,23].



Sample C was cooled at  $0.65 \text{ K min}^{-1}$ , and sample D at  $450 \text{ K min}^{-1}$ . Both had the same molar mass distribution as sample F. The melting peaks of sample C are close to zero-entropy-production melting with some reorganization or superheating. Samples of this type can be used to create a free-enthalpy map, as shown in Fig. 6.3. On faster cooling, crystallization occurs at lower temperature, as shown in Fig. A.10.6, leading to less crystal perfection and lower melting temperatures. In addition, there is a decrease in peak temperature with the rate of heating, indicating that on slow heating, the crystals improve and yield a higher melting temperature by going from  $\ell$  to  $\ell_1$  or  $\ell_2$  in the free enthalpy diagram of Fig. 2.86.

Crystallizing the same polyethylene used for generating the curves C, D, and F in Fig. 6.22 from dilute solution yields at higher temperatures rather well-defined lamellar crystals, as illustrated in Fig. 5.57. Their morphology is seen in Figs. 5.51 and 5.52. The fold lengths are 10 and 15 nm, as shown in Fig. 5.43. On faster cooling, crystallization begins at lower temperature and the lamellae change to dendrites as seen in Fig. 5.57. Melting of the well-formed lamellae and growth spirals is illustrated in Fig. 6.22 by curve B. A zero-entropy-production melting temperature could be established with the fast-heating microscopy, discussed in Fig. 3.95 for heating rates of  $100\text{--}1000 \text{ K min}^{-1}$ . The dendritic morphology is illustrated in Figs. 5.56, 5.58, and 5.59. The melting of these less perfect crystals is mirrored in curve A of Fig. 6.22. It is assumed that reorganization is even faster than for the more perfect lamellae [22,23] so that no thermodynamic evaluation of the sample is possible at the rates of Fig. 3.95. The melting characteristic of dendrites can only be assessed with very fast calorimetry as described in Appendix 10.

Comparing all observed melting-peak temperatures of Fig. 6.22, one covers values from 393 to 427 K [23]. Thermodynamic equilibrium is only reached at the temperature  $T_m^\circ = 414.6 \text{ K}$ . This range of 34 K is characterizing the various metastable and unstable crystal distributions. Since the experiments assess only the melting-peak temperatures, the actual melting range is even broader. Considering the apparent heat capacities of samples of different crystallinity in the left graph of Fig. 2.45, one can deduce that the poorest crystals may melt in the glass-transition region and melting may extend up to the nonequilibrium melting caused by superheating. Overall, this may cover temperatures from 190 to 500 K.

Before the low-temperature region of melting can be explored in more detail, it is necessary to separate the contribution of the changing equilibrium-defect concentration on the heat capacity,  $C_p$ . In polyethylene, this contribution is based on the *trans-gauche* equilibrium which also influences the mechanical properties, as discussed in Sect. 5.6.6 (see Fig. 5.171). This effect on  $C_p$  is illustrated in Fig. 2.65, and the defects are analyzed with Figs. 5.98–103. Further endothermic contributions to  $C_p$  can then be assigned to irreversible latent heats of fusion. In addition, with temperature modulation, locally reversible melting was discovered within the globally metastable structure. This adds additionally to the apparent  $C_p$  [25] (see Fig. 3.92).

For polyethylene a full homologous series of oligomers exists in form of the normal paraffins. The low-molar-mass paraffins grow at atmospheric pressure into the extended-chain macroconformation. Figure 6.24 represents standard DSC and quasi-isothermal TMDSC of pentacontane,  $C_{50}H_{102}$ . The standard DSC trace and the quasi-isothermal TMDSC with small modulation amplitude are almost identical until

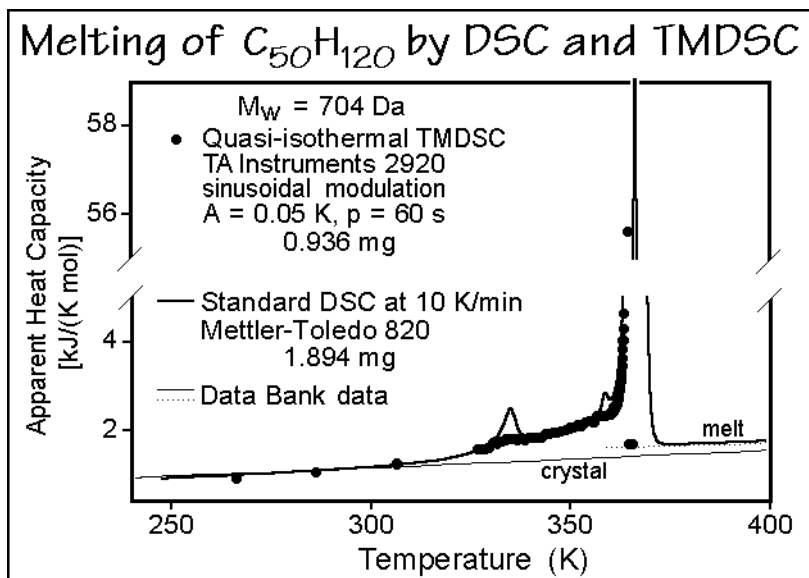


Fig. 6.24

reaching about 0.5 K from the melting end at  $365.30 \pm 0.05$  K. The broader melting peak of the standard DSC is due to instrument lag, and the lower area for the heat of fusion by TMDSC is due to incomplete melting during the modulation cycles [26], discussed in more detail with Figs. A.13.11–15. At the last point in the melting peak, over 60% of the heat of fusion should have been absorbed, making the major part of the reversible melting less than 0.1 K wide. The calorimeter, however, could not deliver that much heat of fusion at the 0.05 K amplitude, resulting in incomplete melting and crystallization. The first 13 quasi-isothermal cycles at the next temperature produced the final melting before reaching the response due to the liquid heat capacity. The first deviation of the measured  $C_p$  from the vibrational value occurs at about 250 K, as seen in Fig. 4.50. This is due to equilibrium defects in the crystal as found in polyethylene (Fig. 2.65). It gradually changes into a small amount of reversible melting of either short-chain impurities on the crystal surfaces, or a small fraction of poorly crystallized pentacontane. A small amount of irreversible melting of impurities is also seen in the standard DSC trace. The TMDSC completes 62% of the fusion within the last 0.1 K of the melting peak. The information about the reversibility of paraffins and narrow molar mass fractions of polyethylene (PE) is collected in Fig. 3.75. Up to 75 carbon atoms the crystallization can be reversible, above, a need of molecular nucleation introduces supercooling (see Sect. 3.5.6).

Changing from pure paraffins to narrow fractions of similarly low-molar-mass fractions of PE, the reversibility is largely retained, as seen from Fig. 6.25 which illustrates the melting of fraction PE560 of a weight average molar mass of 560 Da and polydispersity of 1.06. The melting temperature of 354.5 K for  $C_{40}H_{82}$  with a similar molar mass as PE560 approximates the melting end of the quasi-isothermal data, as well as the beginning of crystallization on quasi-isothermal TMDSC on cooling. The low-temperature melting peak at 332.6 K is most likely the eutectic

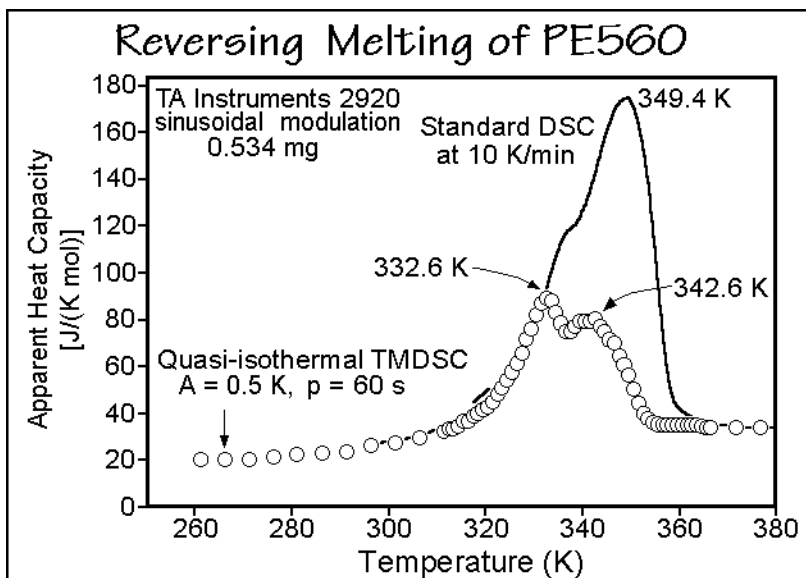


Fig. 6.25

temperature of the distribution of molecular lengths discussed in detail in Chap. 7 and may contain some of the transitions to a high-temperature mesophase which are observed in paraffins with a lower mass than that of  $C_{40}H_{82}$ . The apparent reversing heat capacity shows a sizeable contribution to the melting, but not as much as seen for the pure  $C_{50}H_{102}$  in Fig. 6.24 where all fusion is complete within 1.0 K, i.e., with a modulation amplitude of 0.5 K, the melting of  $C_{50}H_{102}$  would be fully reversing. The width of the melting region of PE560 is about 30 K. The broadening of the melting of PE560 in the quasi-isothermal measurements is due to the chain-length distribution and much of the irreversibility is due to slow diffusion and recrystallization needed to set up the eutectic crystal distributions. On quasi-isothermal TMDSC during cooling, the change in reversing crystallization due to perfection of the crystal distribution can be followed. It is similar to the slow changes observed in Fig. 6.36 for the reversing melting of a POE of similar molar mass.

Figure 6.26 illustrates the standard DSC and quasi-isothermal TMDSC of average molar mass 2,150 Da (PE2150) with a polydispersity of 1.15. This molar mass still yields largely extended-chain crystals on slow crystallization. The melting region is narrower and the reversing heat capacity is much less than for PE560 since at higher molar masses the spread of the melting temperatures of the components is less, and it exceeds the critical length of Fig. 3.75 for most of its components. The supercooling can be seen from the difference between the marked end of melting and beginning of crystallization in Fig. 6.27. Almost identical reversibility on cooling after the irreversible crystallization and on second heating characterize PE2150 and is seen in the quasi-isothermal TMDSC traces. The first heating indicates the presence of poorer crystals which result in larger and more time-dependent reversing contributions. Most likely, the slow TMDSC with modulation on cooling has led to a better separation of the various lengths of the molecules.

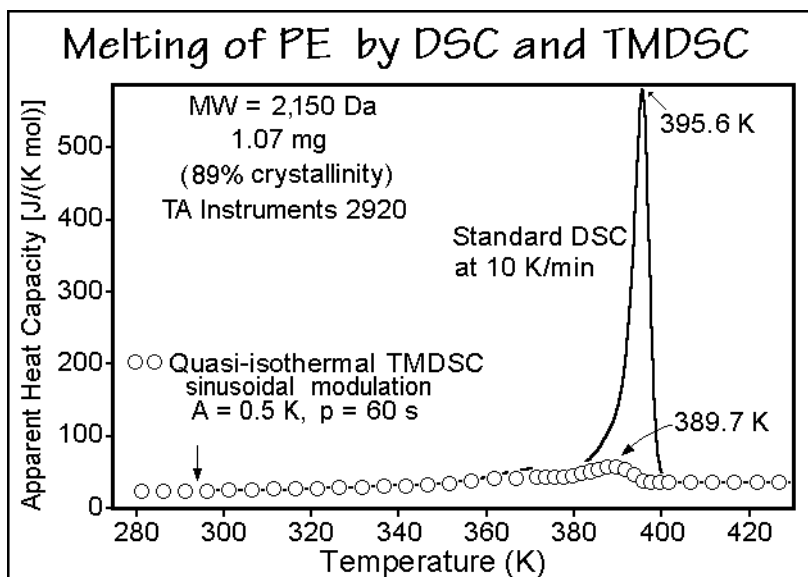


Fig. 6.26

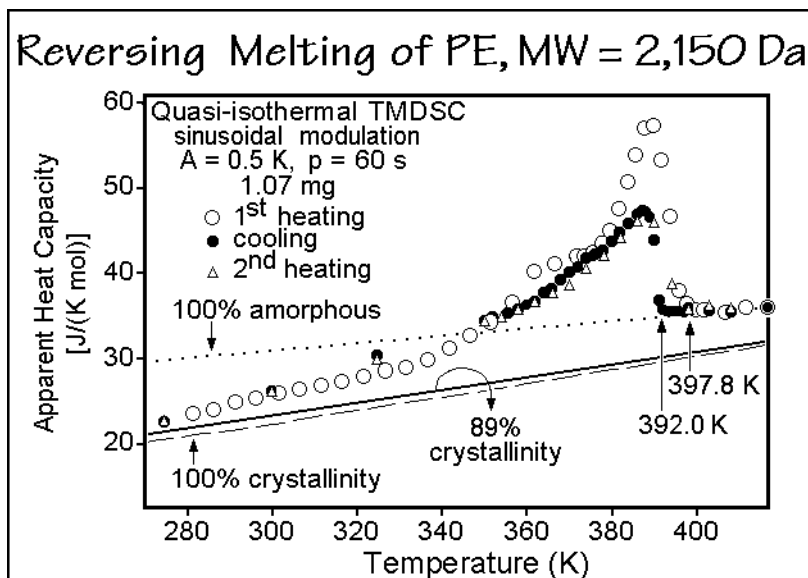


Fig. 6.27

To summarize, the analysis of the melting of oligomers illustrates cases from practically fully reversible, sharp melting (Fig. 6.24), to broad reversing melting due to the presence of multiple components and possibly incomplete phase separation. At higher mass, the extended-chain crystals decrease rapidly in reversibility, as shown in Fig. 6.26. A comparing of these data to an extended-chain fraction of lower mass and

an unfractionated polyethylene crystallized to an extended-chain sample of 98% crystallinity and an average molar mass of 130,000 Da is given in Fig. 6.28. The last shows even less reversible melting. The very small remaining amount of reversibility in PE130000 can be linked quantitatively to an equilibrium phase separation of the low-molar-mass fractions and is discussed in Chap. 7. One concludes that the extended-chain crystals of paraffins and polyethylene melt irreversibly if they have a

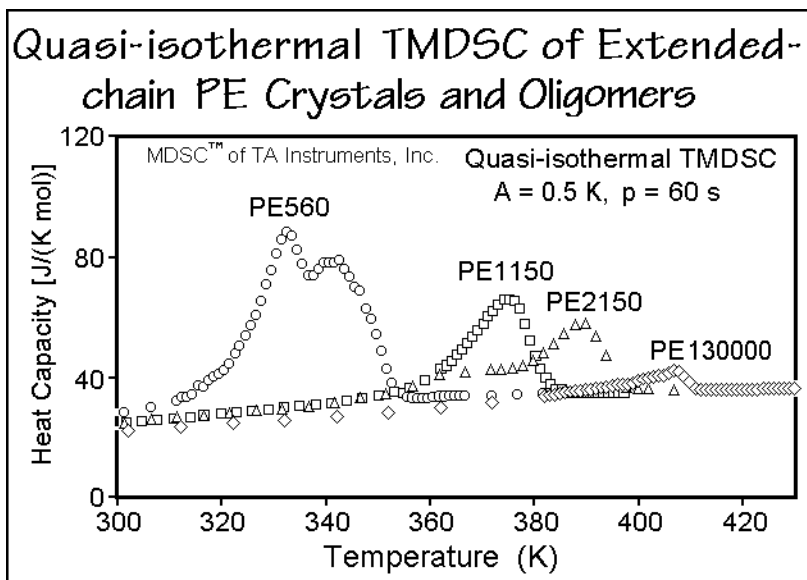


Fig. 6.28

higher molar mass than the critical length of Fig. 3.75. The data of the extended-chain crystals of poly(oxyethylene) of molar mass 5,000 Da of Figs. 3.97 and 3.98 suggest a similar absence of reversible melting in the aliphatic polyethers.

Turning to folded-chain crystals, the amount of reversing melting increases. Figures 6.29 and 6.30 illustrate TMDSC results of a rather low molar mass PE15520 of a low polydispersity of 1.08. The apparent, reversing heat capacities on cooling after irreversible crystallization and on second heating are almost identical to PE2150 in Fig. 6.27, despite the rather small crystallinity when going to the folded-chain crystals. Below 340 K the PE15520 is also characterized by a higher apparent reversing heat capacity than PE2150. The apparent reversing heat capacity of PE15520 in the melting range is less on cooling than on first and second heating. The increased reversing melting in the heating experiment seems to originate from secondary crystals grown at lower temperature during the cooling experiment within in the matrix of the primary crystals. In part, these secondary crystals have perfected by the time they were analyzed at higher temperature, and in part they crystallized reversibly in the wide temperature range  $335 \pm 40$  K. The reversing melting may involve short molecules or sections of longer molecules of lengths less than 10 nm that remain partially crystallized as expected from Fig. 3.75. On quasi-isothermal experiments of long duration, the reversing melting during the first heating reaches

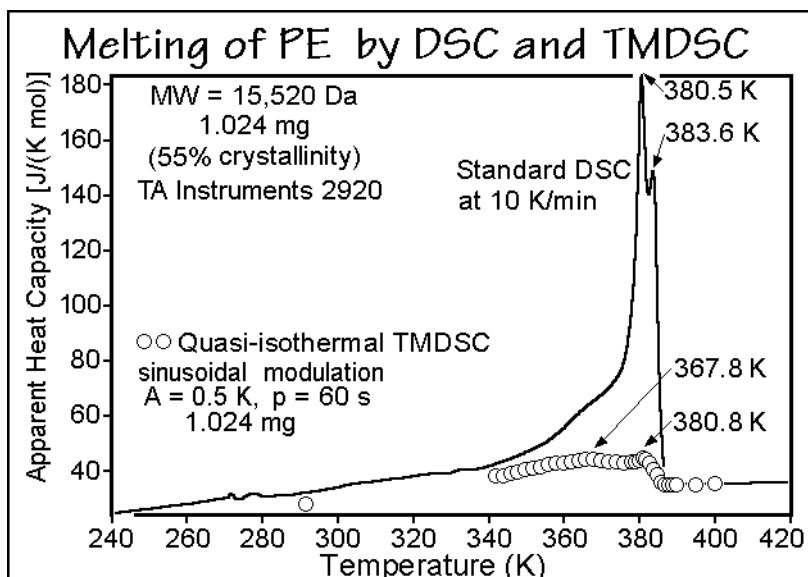


Fig. 6.29

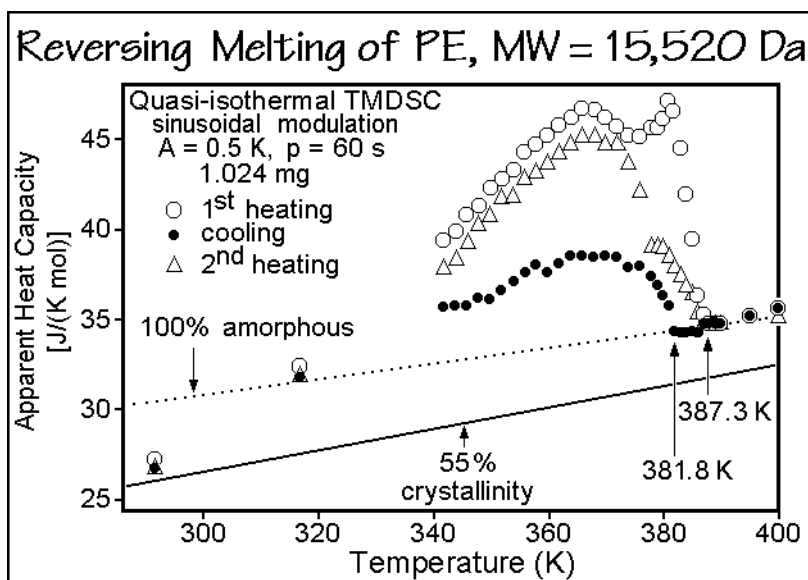


Fig. 6.30

ultimate levels of reversibility which are still above the level seen on cooling. As for all other polymers of high molar mass, discussed below, two processes are involved in the kinetics of the apparent reversing heat capacity. Their relaxation times are longer than the response of the calorimeter, and the short-time change is usually based on an exotherm. One expects, thus, that an annealing process is involved in the

decrease of the reversing heat capacity which starts with an exothermic crystal perfection or further crystallization. Each sufficiently perfected crystal has a higher melting temperature and is removed from the next melting cycle. Similarly, a fully melted molecule or molecular segment above the critical length would ultimately be removed from reversing melting since it would need a renewed molecular nucleation to recrystallize (see Sect. 3.5.6). Because of the slow perfection it takes several hundred minutes to reach steady state within the DSC, which then may be a true local equilibrium within the matrix of the metastable, higher-melting crystals. The super-cooling of the sample can be seen from the difference between the marked end of melting and beginning of crystallization in Fig. 6.30 (see also Fig. 3.75).

Other TMDSC analyses differ only little from the data presented in Figs. 6.29 and 6.30. Small changes being expected by the variation in molar mass and sample history [1]. Figure 6.31 shows the results of high-frequency modulation of polyethylene in the melting region (MW = 52,000 Da, polydispersity 2.9, modulation  $\approx 0.2$  K) [28]. Above 0.1 Hz, the reversing  $C_p$  becomes almost independent of frequency with a maximum between 38 and 41  $\text{J K}^{-1} \text{mol}^{-1}$  at 402 K. This value compares to about 30  $\text{J K}^{-1} \text{mol}^{-1}$  for the vibrational contribution in the crystal (see Fig. 2.51), 34  $\text{J K}^{-1} \text{mol}^{-1}$

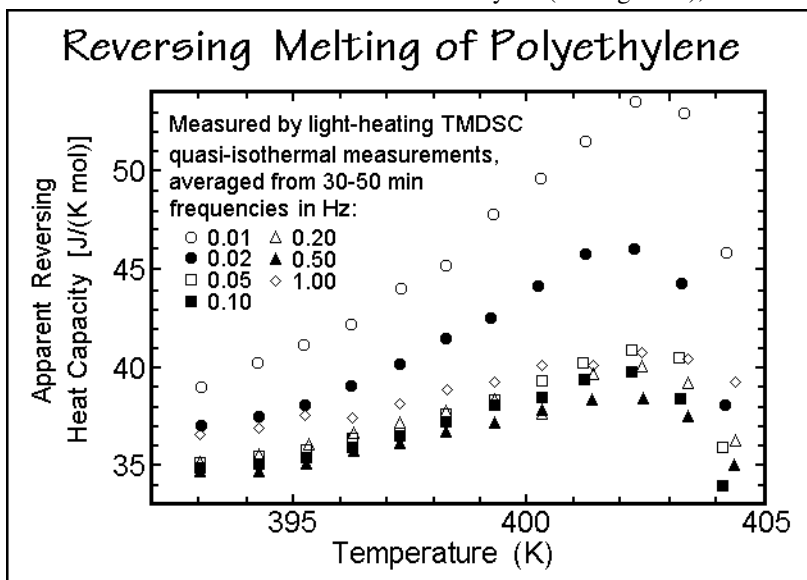


Fig. 6.31

for the experimental  $C_p$  of a sample of 99% extended-chain crystallinity, and 35  $\text{J K}^{-1} \text{mol}^{-1}$  for  $C_p$  of the liquid. Accidentally the liquid and experimental crystalline  $C_p$  are similar, so that the crystallinity is irrelevant at this temperature. Note that the maximum reversing heat capacity at low frequency is also similar to the quasi-isothermal values of Fig. 6.28. The relaxation time for the frequency-dependent part of the excess heat capacity was 14 s. Within error limits, Fig. 6.31 separates the apparent heat capacity from the frequency-dependent, slow reversible latent heat, and the faster contribution from the vibrations and *trans-gauche* equilibrium.

A combined study of TMDSC, WAXD, SAXS, and AFM of the crystallization of polyethylene with a weight-average mass of 52,300 Da and a polydispersity of 3.2 was made to study the structural changes of the reversing melting [29]. Figure 6.32 illustrates the change of the apparent reversing  $C_p$  with time. An excess  $C_p$  is generated beyond the values calculated for the proper proportion of the experimental  $C_p$  of amorphous and crystalline polyethylene (dotted line). During the primary

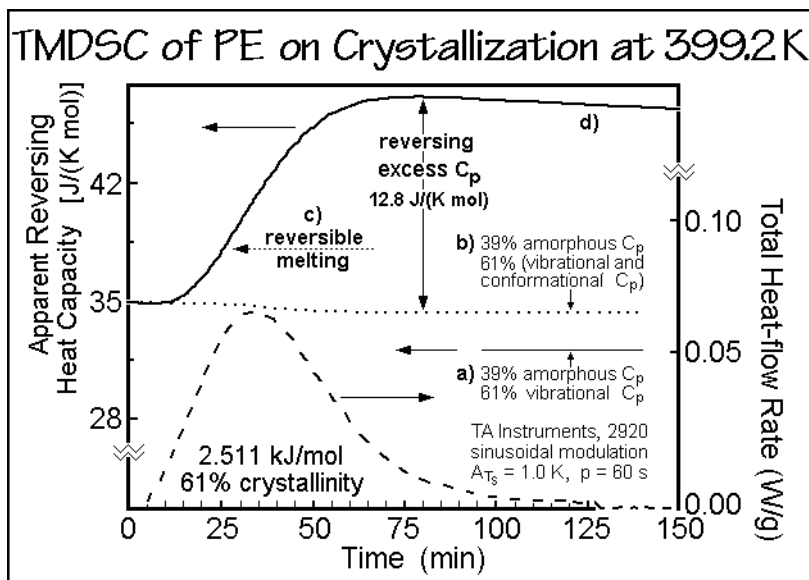
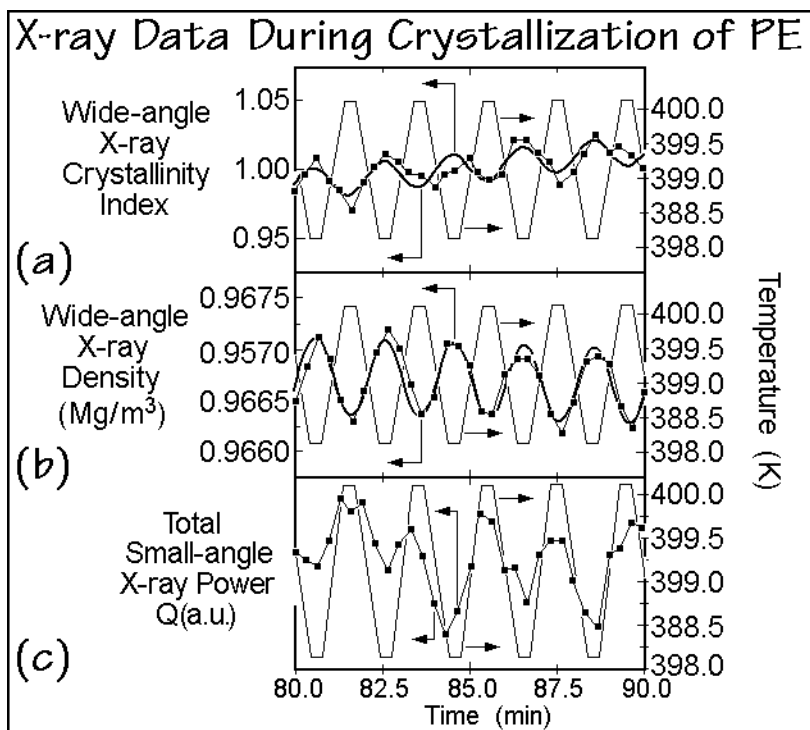


Fig. 6.32

crystallization, the excess  $C_p$  follows qualitatively the increase in crystallinity, deduced from the area under the total heat-flow-rate curve (dashed line). During the secondary crystallization phase, after about 75 min, the excess heat capacity decreases slightly, while the crystallinity still increases. The apparent, excess reversing heat capacities are close to the low frequency values of Fig. 6.31 for similar polyethylene. At higher modulation frequencies, the apparent, reversing heat capacity should drop to the reversible level of  $38 \text{ J K}^{-1} \text{ mol}^{-1}$ , as marked by the dotted line. The  $C_p$  calculated from the vibrational contribution from the crystal added to the 39% amorphous PE is marked by the thin line and arrow at  $32 \text{ J K}^{-1} \text{ mol}^{-1}$ .

The structural changes of the sample in Fig. 6.32 were followed by similar quasi-isothermal temperature modulations during WAXD and SAXS. An excerpt from the data is illustrated in Fig. 6.33. The temperature modulation is indicated by the thin lines. It consists of a cooling ramp from 400.2 to 398.2 K at  $3 \text{ K min}^{-1}$ , followed by an isotherm of 19.6 s and heating to the starting temperature and another isotherm. The curve (a) shows the change of the crystallinity index, calculated from the area of the 110 and 200 diffraction peaks above an estimated, amorphous scattering background, normalized to the 90 min value. Quite clearly, there exists a modulation out-of-phase with the temperature and the underlying increase in crystallinity due to the secondary crystallization is also noticeable. The fitted curve corresponds to a





**Fig. 6.33**

crystallinity-index change of  $2.1 \pm 0.4\%$  from maximum to minimum, about double that calculated from the calorimetric data. From the diffraction-peak positions, the change in the density of the crystals could be assessed, as shown in curve (b). The oscillation matched the known density change with temperature of polyethylene. The noticeable decrease in average density with time cannot be due to the perfection of the crystals, which would call for a density increase, but must be assigned to the later growing, less-perfect crystals. The lateral crystal dimensions from the WAXD peak widths remained constant during the modulation at a value of 35 to 40 nm, much smaller than the overall lamellar dimensions seen by AFM to be in the micrometer range, but similar in size to a mosaic substructure, also detectable by AFM. Curve (c) depicts the total SAXS power which also increases parallel to the total heat-flow rate in Fig. 6.32, i.e., with overall crystallinity. The modulation, however, is in-phase with the temperature and should be a measure of an increase in the local amorphous-crystalline volume fraction between the lamellae on increasing the temperature. This interpretation is based on a perfect lamellar structure-model of stacked crystals and amorphous material with a constant (electron-) density difference between the two phases. With further assumptions, the most probable thickness of the amorphous and crystalline layers and the total long period were computed. Figure 6.34 combines these WAXD and SAXS results, suggesting that during the modulation on increasing the temperature, the amorphous layer increases by as much as the crystalline layer decreases. Overall, the crystalline thickness increases slightly with time, as expected

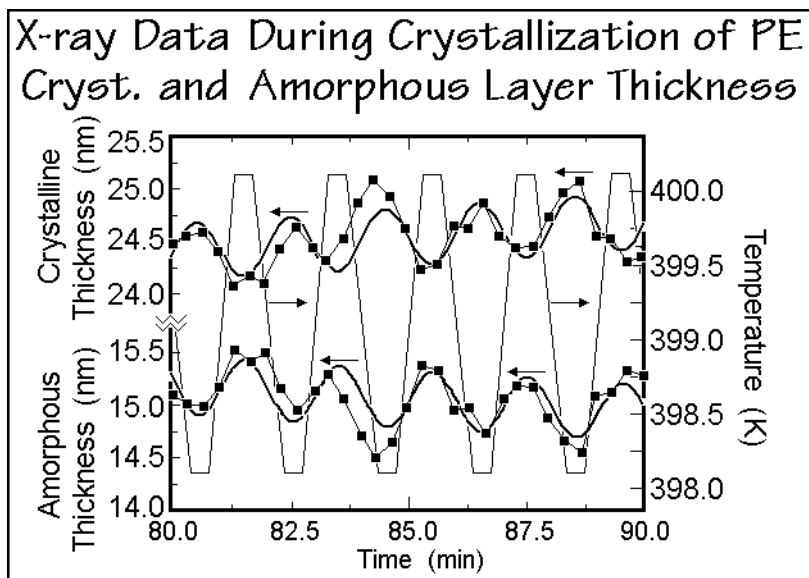


Fig. 6.34

from the annealing during secondary crystallization, and the modulation amplitude of both, the crystalline and amorphous layers is  $0.28 \pm 0.05$  nm and was proposed to coincide with model calculation of “fold-surface melting” [29].

This “fold-surface melting” was observed already some 40 years ago [30]. A comparison to annealing and lateral melting is given in Ref. [31]. The main conclusions from the study of surface melting were that the thermodynamically reversible process occurs over a wide temperature range, does not fully destroy the crystal core, and develops at a lower temperature than the lateral, irreversible melting [32]. It was proposed that this discrepancy can be accounted for by a half-as-large heat of fusion in the surface layer. Such lower heat of fusion was proven to exist for the mobile-oriented phase discovered in gel-spun fibers of polyethylene which is discussed in Sect. 6.2.6.

Although this picture placing the reversible melting exclusively at the fold surface seems possible, it would be unique for polyethylene. The “fold-surface melting” is more likely connected to the *gauche-trans* equilibrium defects which have a tendency to diffuse to the fold surface (see Sect. 5.3.4). In this case they would need little or no additional latent heat. New experiments on high-density, linear polyethylene led to information about the specific reversible melting, a quantity defined as the ratio of reversible to irreversible melting [33]. Up to 350 K, this specific reversible melting is about 0.5 and decreases toward zero at higher temperatures, within the main melting peak. This measurement is more in accord with reversible growth-face melting since it links the irreversible with reversible melting. Such reversible melting on the growth faces also can be proven for several polymers which cannot change their lamellar surface reversibly, as described in the next section. More details about the melting of polyethylene segments with similar specific reversible melting are discussed in Chap. 7 for copolymers [1]. In this case, growth-face reversibility could be proven.

## 6.2.2 Reversible Melting and Poor Crystals

The discussion of the melting of polyethylene in the previous section revealed that it is possible to establish equilibrium and metastable phase diagrams, but only from zero-entropy-production heating experiments, not on cooling. There is no reversible melting of the type that could be accomplished for nucleated indium (see Figs. 4.106 and 4.107, and 4.109 and 4.134), or studied for the isotropization of small- and large-molecule liquid crystals (see Figs. 5.144 and 5.154). The reason of this missing reversibility is the need to molecular nucleation, as seen from the plot of melting and crystallization rates in Fig. 3.76 and discussed in Sects. 3.5 and 3.6.

**Poly(oxyethylene).** The reversing melting of a poorly crystallized oligomer of poly(oxyethylene) with mass 1500 Da is analyzed in Fig. 6.35 with quasi-isothermal TMDSC. A comparison of this sample with a standard DSC trace is shown in

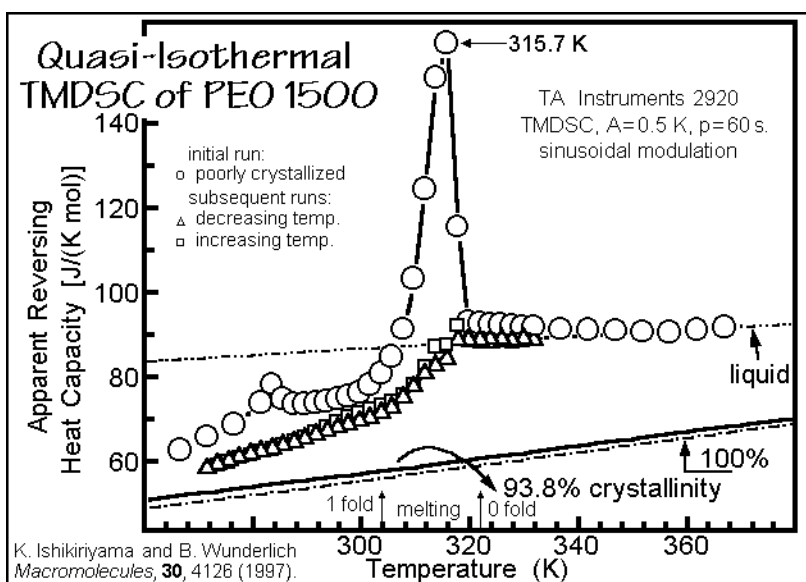


Fig. 6.35

Fig. 4.123. The reversing melting is observed in the low-temperature range, where one expects the lower-molar-mass crystals to melt. The quasi-isothermal TMDSC experiments with decreasing temperature allow more perfect crystals to grow, and only a gradually changing reversing heat capacity is observed on cooling and second heating, similar to the behavior of extended-chain crystals of paraffins and polyethylene (see Sect. 6.2.1). Only at perhaps 200 K is the vibrational  $C_p$  reached.

The following reasoning may explain the reversing melting in Fig. 6.35. Due to the position of the reversing melting on the low-temperature side of the irreversible melting peak in Fig. 4.123, one expects the reversing melting to involve molecules of lower than the average length. Well crystallized, extended-chain poly(oxyethylene) with a molar mass above 1,000 Da, the limit for reversible melting from Fig. 3.91, should melt irreversibly. Comparing the apparent, reversing  $C_p$  of POE1500 with a

higher molar mass sample POE5000, analyzed in Figs. 3.88 and 3.89, one observes that they are equal up to 300 K. This means that the increase in  $C_p$  beyond the vibrational limit is due to conformational motion (as also in polyethylene in Fig. 2.65). Above 300 K, the  $C_p$  of POE1500 increases faster than the  $C_p$  of POE5000. Thus, one expects that for the well-crystallized samples, only the additional increase of the reversing  $C_p$  is due to reversible melting of short-chain molecules within the samples. This reversible melting is limited, according to Fig. 3.91, to a length of 75 backbone-atoms. These melt at 316 K and should limit reversing melting in Fig. 6.35.

The next problem concerns the reversing melting peak in Fig. 6.35 which is observed for poorly crystallized PO1500. An interesting observation is a strong increase of the reversing melting peak with long time periods on extending the modulation, illustrated in Fig. 6.36. This is in contrast to a decrease, seen in most polymers such as the poly(ethylene terephthalate) shown in Fig. 4.137. Along the curve, a slow decrease in total crystallinity with time after raising the temperature to 315.7 K is marked. These values were obtained by standard DSC performed on

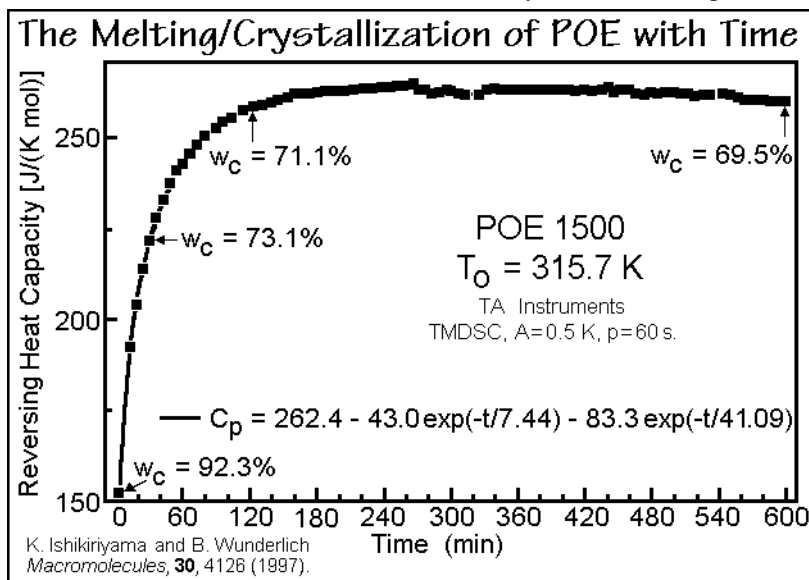


Fig. 6.36

parallel runs, stopped at the indicated times. The heat-flow rates at an early time (13 min) and at a late time (600 min) are shown separately in Fig. 6.37; in addition, Lissajous figures are depicted in Fig. 4.114 for the same run. The curve after 600 min is distinctly of larger amplitude, and the difference between the two curves reveals more melting than crystallization. While the melting which follows the crystallization is practically continuous, there is a small supercooling between melting and crystallization. Overall, then, there is a decrease in crystallinity in time, as demonstrated by Fig. 6.36. Due to the different latent-heat effects on cooling and heating, the heat-flow rate curves in the melting region are not strictly sinusoidal anymore. The calculated apparent heat capacities in Figs. 6.35 and 6.36, thus, can only be an

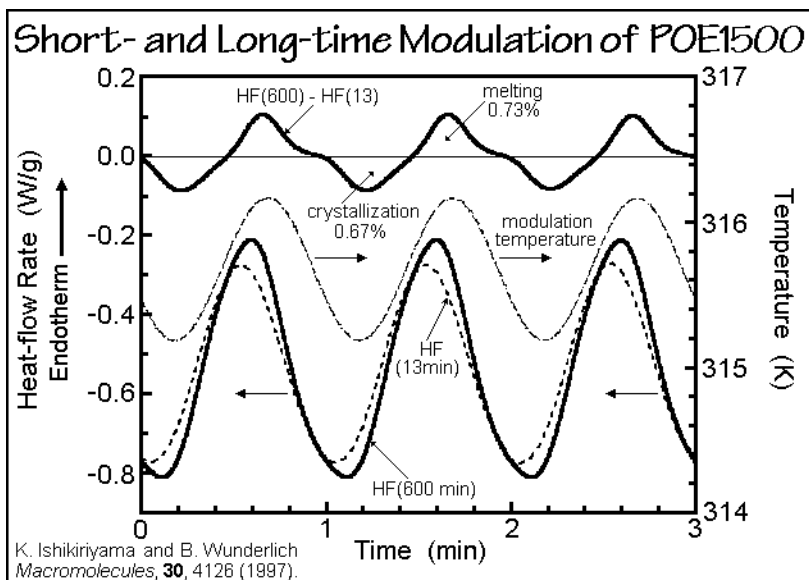


Fig. 6.37

approximation since the method of Fig. 4.92 involves the amplitude evaluation of only the first harmonic.

Lissajous figures at a temperature close to the reversing melting peak in Fig. 6.35 are plotted in Fig. 6.38 with modulation at different amplitudes,  $A$ . Larger-scale melting and crystallization can be seen as soon as  $A$  covers the region from a finite melting rate to a finite crystallization rate, as is indicated in Fig. 3.76. Closer

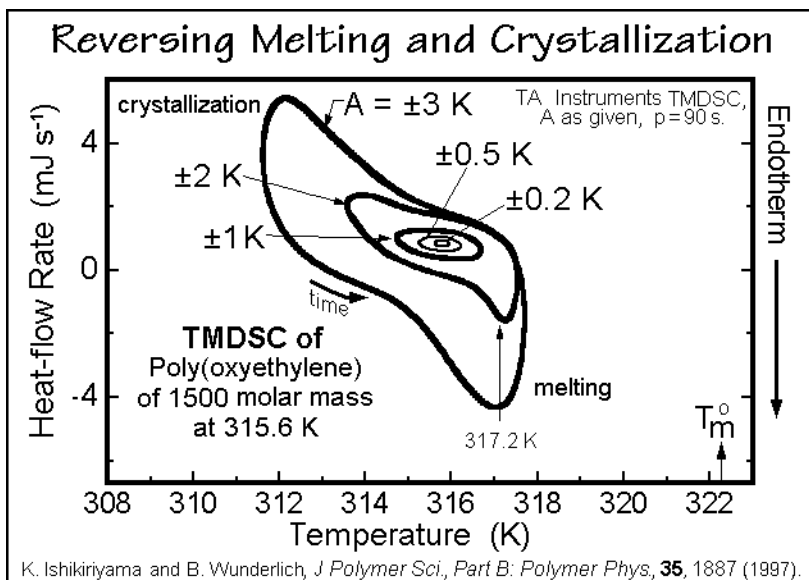
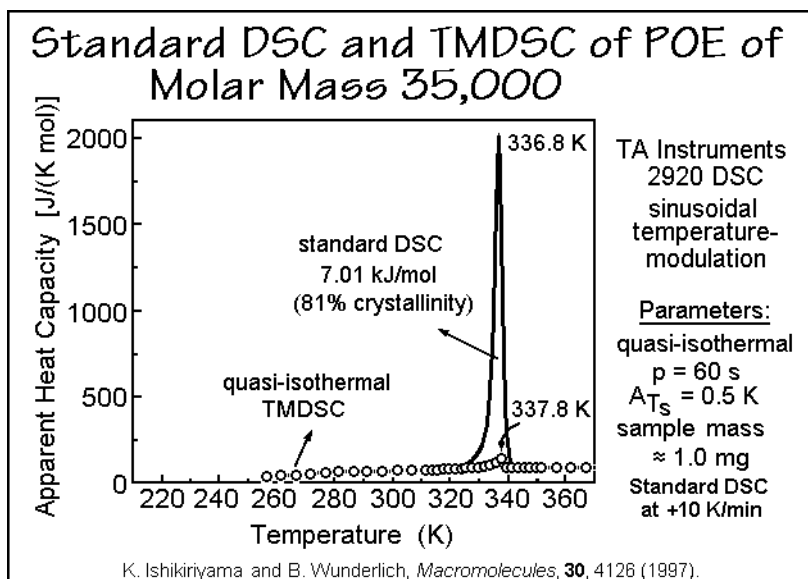


Fig. 6.38

inspection of the Lissajous figures reveals a number of details. The crystallizations with the amplitudes of  $A = 2.0$  and  $3.0$  K start at the same temperature after having reached close to steady state on completion of the prior melting. The melting, in contrast, begins earlier for the larger modulation amplitudes. On crystallization at constant frequency, but different amplitudes, the once grown crystals have more time to perfect in the case of  $A = 2.0$  K and reach, thus, a higher melting temperature than in the case of  $A = 3.0$  K. The TMDSC is thus a tool to study the shape of the growth-rate curves in Fig. 3.76.

Figure 6.39 illustrates the melting of a high-molar-mass poly(oxyethylene). Its crystal morphology is that of folded chain crystals (see Figs. 5.49 and 5.55). The behavior is similar to the poly(ethylene terephthalate), detailed in Figs. 3.92 and 4.136–139. The reversing melting peak is on the high-temperature side of the irreversible melting peak and the reversing amplitude decreases with increasing modulation time without reaching the expected thermodynamic heat capacity.



**Fig. 6.39**

The analysis of the melting of poly(oxyethylene) disclosed that for a small fraction of low molar mass poly(oxyethylene) below a molar mass of about 1,000 Da, melting and crystallization could be reversible. On poor crystallization, however, the reversing melting peak is not reversible, since melting and crystallization does not occur at the same temperature. Such processes which could be reversed, but either were not reversible or had not been analyzed with respect of their reversibility are customarily called reversing (see also Sect. 4.4). Crystal perfection is common in polymers, but for the low molar mass fractions, it is also important to consider the phase diagram, as discussed in Chap. 7 for polyethylene. The increase of reversing melting of POE1500 with time may also have a contribution from slow diffusion of the proper chain length molecules to the proper crystal, as seen in Fig. 6.25 for polyethylene.

**Polyterephthalates.** The molecular motion and their connection to the thermal parameters for the three most common members of the homologous series of polyterephthalates is summarized in Fig. 6.40. The number of vibrations and the derived  $\Theta$ -temperatures allows the calculation of a vibrational heat capacity of the solid state, as outlined in Sect. 2.3.7. The changes within the  $\Theta$ -temperatures are practically within the error limit. The specific heat capacities of the polyterephthalates are, as a result, also almost the same. The transition parameters are extrapolated to the equilibrium crystals and the fully amorphous glasses. Their values show regular changes with chemical structure. All thermal properties are next related to the vibrational baselines computed from the parameters of Fig. 6.40.

Molecular Motion in Polyterephthalates					
Vibrations:					
Total vibrations:	9x	9	30	9	Total: 48 + 9x
Group vibrations:	7x	5	25	5	35 + 7x
Skeletal vibrations:	2x	4	5	4	13 + 2x
	PET	PTT	PBT		
Heat of fusion	26.9	30.0	32.0		kJ/mol
$T_m^0$	553	510	518		K
$\Delta C_p$ at $T_g$	77.8	94	107		J/(K mol)
$T_g$	342	310	248 (315)		K
$\Theta_1$	544.7	550.5	530		K
$\Theta_3 (= \Theta_2)$	48	51	55		K
$A_0$	estimated for all three to be 0.0039 K mol / J				

Fig. 6.40

Poly(ethylene terephthalate), PET, has always been the standard polymer for thermal analysis and many thermal analyses are illustrated with help of its properties. A basic DSC trace is shown in Fig. 5.116. The first measurement of its heat capacity by adiabatic calorimetry with the calorimeter of Fig. 4.33 was published in 1956 [34], and more extensive data sets are now available in the ATHAS Datas Bank (see Appendix 1). The PET is easily quenched from the melt to an amorphous glass, and on heating shows then a narrow glass transition range, described in Sect. 4.4.6 (see Figs. 4.129–133). It is also a textbook example for the cold crystallization, which follows the glass transition on heating (see Sect. 3.5.5 and also Figs. 4.122, 4.138, and 4.139). On heating from room temperature, the samples of different thermal histories display at higher temperature varying degrees of recrystallization and one or more melting peaks. The details of the recrystallization of PET are discussed in Sect. 6.2.3, and the effects of the crystallinity on its glass transition in Sect. 6.3.4. The analysis of drawn films of PET, is summarized in Sect. 6.2.6. Typical TMDSC data in the time-domain are shown in Fig. 4.122 and 4.138, and analyzed in Fig. 4.139 [1].

Finally, detailed results on quasi-isothermal TMDSC are compared to standard DSC in Fig. 3.92, and for two thermal histories, results are given in Figs. 4.136. The approach of quasi-isothermal data to reversibility in local equilibria is seen in Fig. 6.41. These results are compared to the calculated heat capacities in Fig. 4.137.

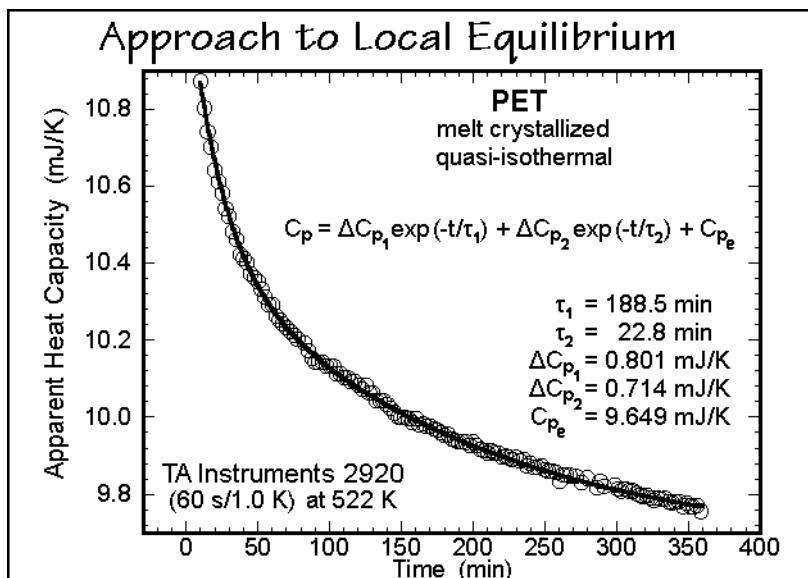


**Fig. 6.41**

Although it is known from solid-state NMR that PET crystals at 430 K can undergo 180° flips of their phenyl rings and interchanges between the *trans-gauche* conformational isomers in the O-CH<sub>2</sub>-CH<sub>2</sub>-O- chain segments [35], this has not yet been connected to increases in  $C_p$ . The reasons for this missing information are that symmetric ring flips do not change the disorder (entropy) of the crystal and, thus, do not show in  $C_p$  (Sect. 5.5.3). Also, the calculations for  $C_p$  of solid PET are mainly based on glassy, not crystalline samples and small errors in the  $C_v$ -to- $C_p$  conversion may conceal increases in the crystalline  $C_p$  due to defect contributions (see Sect. 2.31). Finally, the possible defects occur in a large repeating unit and are more difficult to measure than for polyethylene, where the changes are easily detectable (see Fig. 2.65). Thus, it is not possible to separate with certainty the initial reversible increase in  $C_p$  into latent heats of transitions and contributions from conformational mobility.

Poly(trimethylene terephthalate), PTT, with an additional methylene group has higher molecular flexibility and an increased rate of crystallization. Its melting and glass transition temperatures are also lower relative to PET, as seen in Fig. 6.40. The thermodynamic characterization by standard DSC allows a detailed interpretation of the TMDSC analyses, as illustrated with Fig. 6.42 for a melt-cooled sample [36]. The glass transition of the semicrystalline PTT is about 20 K higher than for the amorphous PTT, but in addition to the broadening of the transition, there is no indication of a RAF above about 370 K. A reversing latent heat contribution shows 25 K above the upper end of the glass transition and reaches a maximum in the



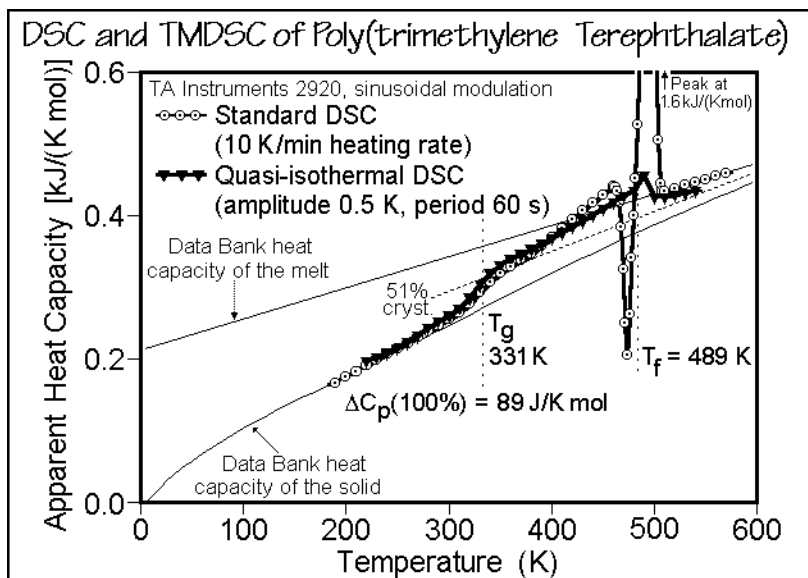


Fig. 6.42

melting region. The highest reversing  $C_p$ , however, is only half that of PET in Fig. 4.136. The sharp recrystallization peak at about 470 K is also different from PET, where recrystallization is sufficiently slow to yield only a shallow exotherm as seen for the total  $C_p$  in Fig. 4.139.

A quenched sample of PTT is analyzed in Fig. 6.43. The quenching produced a 12% crystalline polymer, rather than a fully amorphous one. At 315 K the glass

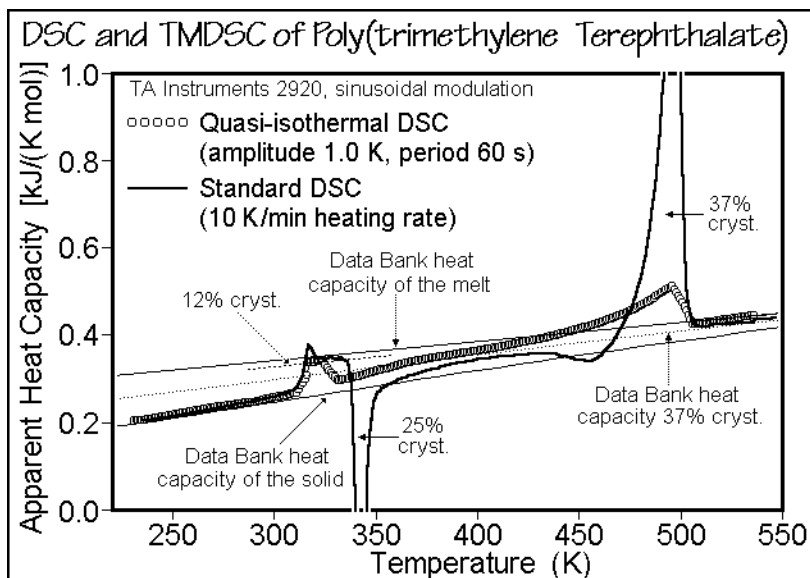


Fig. 6.43

transition is sufficiently low to produce a reasonable enthalpy relaxation due to keeping the sample at room temperature before analysis. The enthalpy relaxation is largely irreversible. The cold-crystallization exotherm is fully irreversible and decreases for the slower TMDSC to about 335 K. In contrast to the melt-crystallized sample of Fig. 6.42 and the PET of Fig. 4.136, the cold crystallization produces a large RAF (33%) which completes its softening at about 370 K. The recrystallization of quenched PTT reaches a broad exotherm at about 460 K. Figure 6.44 shows that the reversing melting peak of the quenched sample is double the size of the melt-crystallized sample. Above 450 K both samples have a larger reversible  $C_p$  than the melt, i.e., not all of the increases above the vibrational Data Bank heat capacity of the

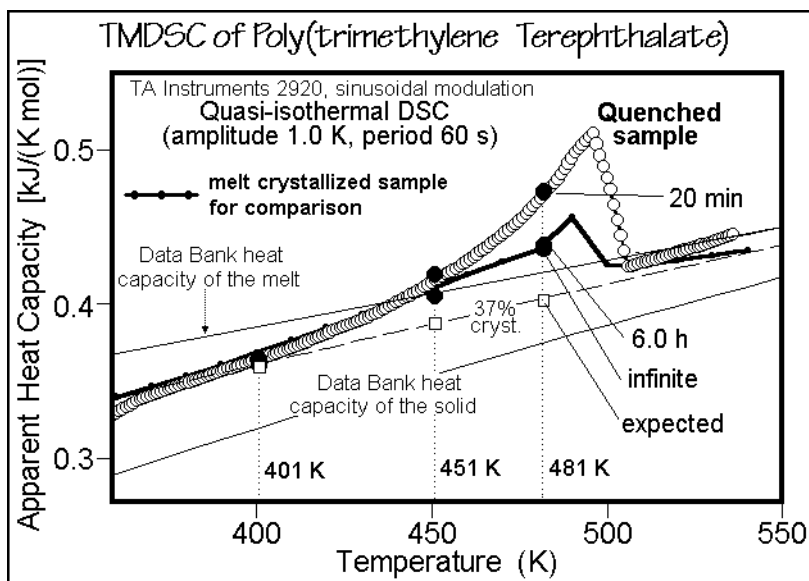


Fig. 6.44

solid can be due to conformational motion within the crystal, since the melt usually contains more conformational mobility than the crystal. When analyzing the reversing melting, in the time-domain one finds that the exotherm is larger than the endotherm before reversibility is approached. The remaining, locally reversible latent heat is similar for the samples of Figs. 6.43 and 6.44. As for PET in Fig. 4.139, the reversing melting peak of PTT with an underlying heating rate at low frequency is larger than the total melting peak by the standard DSC trace [36]. At higher frequencies the reversing melting peak decreases. This decreasing reversing heat capacity is also observed for other polymers. Measurements on PET were used as early evidence of the erroneous data that can be generated by TMDSC [37] when the conditions of steady state and stationarity are not obeyed. Model calculations and experiments by modulating the sample temperature externally with light suggest that with a high frequency, the reversing heat capacity should reach the level given by the quasi-isothermal measurement. Data for polyethylene are illustrated in Fig. 6.31, for nylon 6 in Fig. 4.119, and for a polymeric mesophase in Fig. 5.154.

Poly(butylene terephthalate), PBT, is the next member of the homologous series of polyterephthalates with its thermodynamic properties listed in Fig. 6.40. Figure 6.45 presents the crystallinity for a semicrystalline, melt-crystallized PBT sample, calculated with the method of Fig. 4.80, Eq. (3). Below the glass transition, the crystallinity reaches 36.2%. With this crystallinity function, the expected heat capacity without latent heat effects is given in Fig. 6.46.

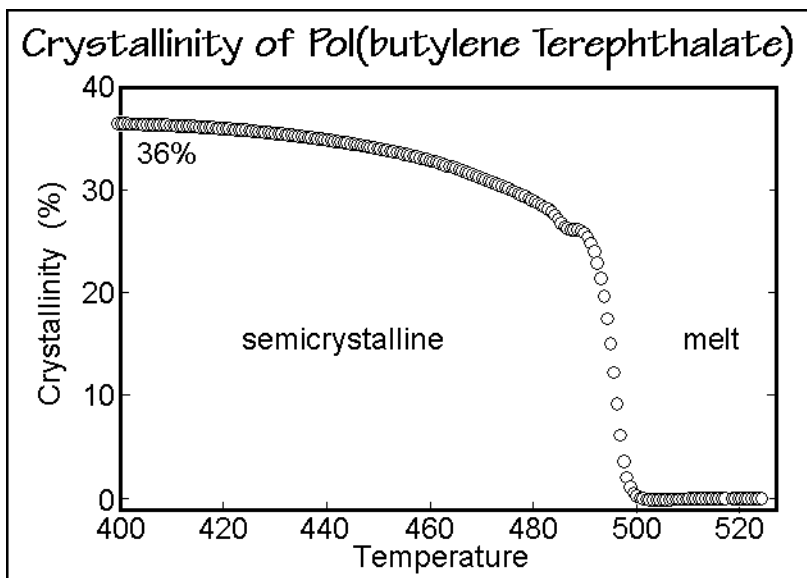


Fig. 6.45

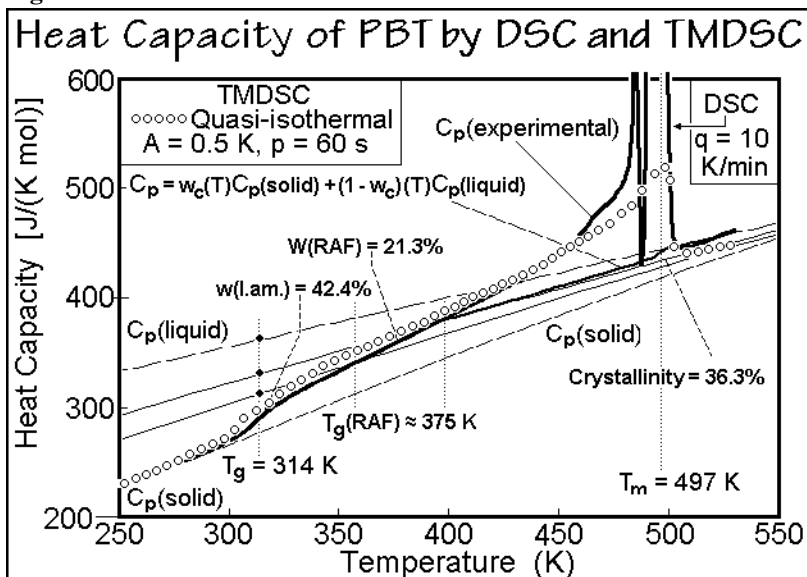


Fig. 6.46

At about 400 K the expected heat capacity for the crystallinity of 36.3% agrees with the standard DSC and the quasi-isothermal TMDSC and a mobile-amorphous fraction of 63.7%. The glass transition is seen at 314 K. It is very broad and reaches a mobile amorphous fraction of only 42.4% at about 350 K. The additional 21.3% of amorphous fraction is assigned to a rigid-amorphous fraction, RAF, and its glass transition ranges from 360 to 400 K. Up to about 460 K, the reversing heat capacity matches the irreversible melting. In the main melting area, a reversing melting is observed and a sharp recrystallization exotherm divides the melting peak. The exotherm does not register in the reversing  $C_p$ . Both of these effects are similar to those of the PTT in Fig. 6.42.

The crystallization of PBT is faster than of PET and PTT. Glassy PBT is only obtained by superquenching in a liquid-nitrogen-cooled, high-thermal-conductivity bath. Figure 6.47 shows the DSC and TMDSC results on quenched PBT. A small thermal activity occurs at low temperature. Using the standard DSC data alone, it was mistakenly assumed that this was the beginning of the glass transition, followed by cold crystallization before the heat capacity could reach the value of the liquid [38]. Since the heat capacity dropped to the value of the solid state immediately after the thermal activity, it was thought that beginning crystallization at this low temperature rendered the amorphous polymer rigid! A recent comparison with TMDSC traces suggests, in contrast, the presence of a small endotherm and only a minor glass-transition-like increase in  $C_p$ . The endotherm could be an enthalpy relaxation or a minor amount of irreversible melting. Before confirming this interpretation, one has to check for possible chemical impurities, such as sequences of tetramethylene oxide in the PBT chain, or physical additives with low-temperature transitions. Further analysis of Fig. 6.47 can be done by using the calculated crystallinity of Fig. 6.48. The expanded Eq. (2) for crystallinity of Fig. 4.80 which accounts for the influence

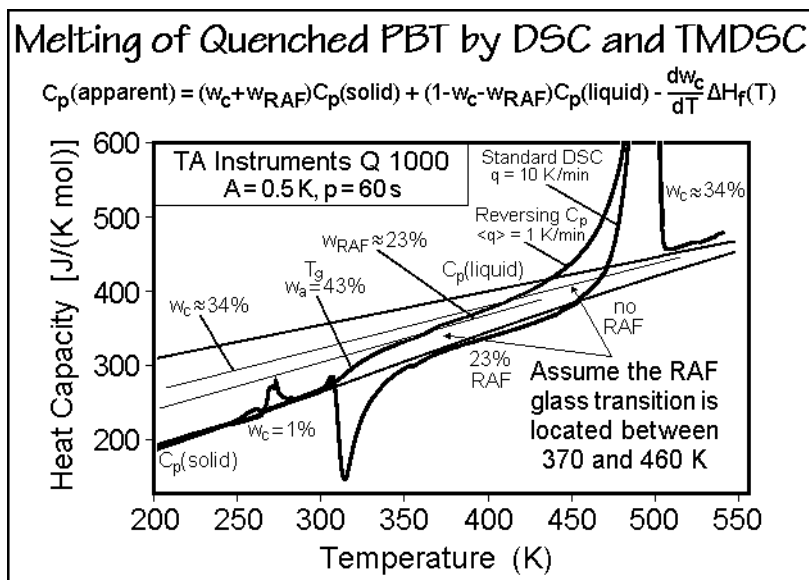


Fig. 6.47

of the RAF was used for this calculation. It is listed at the top of Fig. 6.47. This equation can account not only for the change in heat of fusion and heat capacities with temperature, but also for the change due to the glass transition of the RAF. The assumptions used are listed in Fig. 6.47. This approach allowed a full analysis of the quenched PBT, covering the whole temperature range between  $T_g$  and  $T_m$ .

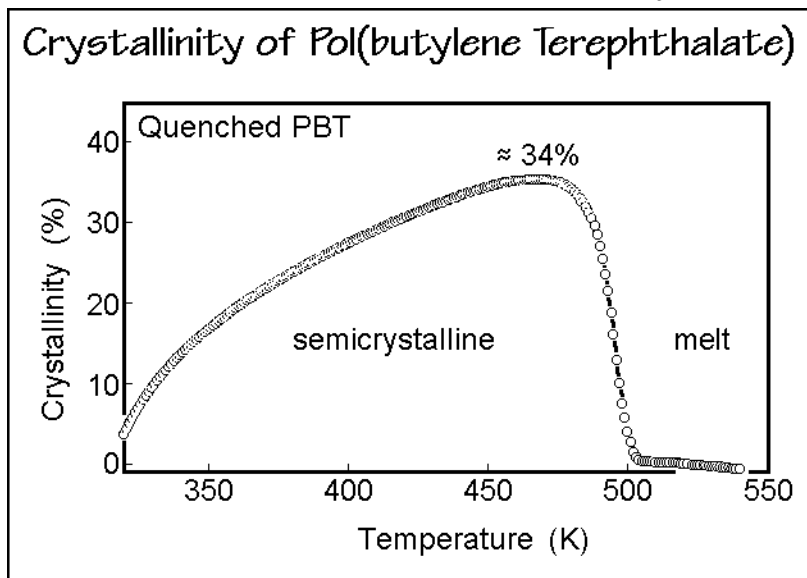


Fig. 6.48

**Polynaphthoate**, specifically the poly(ethylene-2,6-naphthalene dicarboxylate)  $(O-CH_2-CH_2-O-CO-C_{10}H_6-CO-)_x$ , PEN, is a more rigid polymer than PET due to the replacement of the phenylene ring with the larger and asymmetric naphthylene ring. The thermal properties were initially based on measurements by standard DSC as shown in Fig. 6.49 [39]. Quite similar to PET, PEN can be quenched to the amorphous state. In the amorphous state, on heating at  $10\text{ K min}^{-1}$ , it has a higher glass transition at 390 K, compared to 342 K for PET. At about 300 K, a small increase of the heat capacity may indicate some local motion of the naphthylene group, as was also reported by mechanical and dielectric measurements [40]. Similar to glassy polyethylene (Fig. 2.65), this motion gets excited over a wide temperature range. In contrast to PET, the jump or rotation about the axis of the aromatic group breaks symmetry, so that one expects that the crystals have an increase in  $C_p$  at higher temperature. The cold crystallization of PEN starts at a higher temperature than for PET and has a broader temperature range (460–510 K), with a maximum growth-rate at about 490 K. On continued heating, the exothermic cold crystallization changes directly into the melting endotherm with a peak at about 533 K.

Semicrystalline PEN increases in glass transition temperature with decreasing crystallization temperature and also develops an increasing RAF [39]. On crystallization above 490 K, the glass transition becomes constant at the value found for amorphous PEN, and the RAF decreases towards zero at somewhat higher crystalliza-

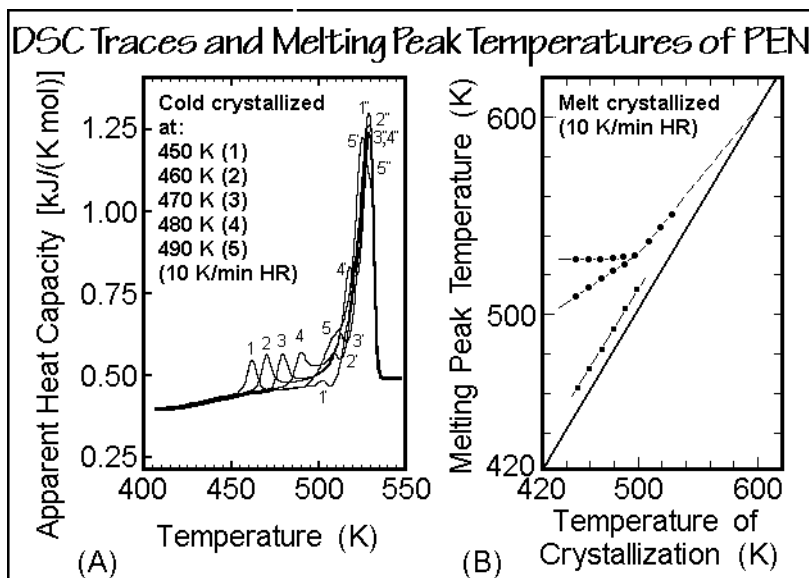


Fig. 6.49

tion temperature. Above 440–460 K, the heat capacity increases beyond that of the values calculated for the given composition of RAFs and crystallinity. This may suggest a glass transition of the RAF, at the beginning of the melting region. Insufficient TMDSC data exist to identify the major reasons for this initial increase in heat capacity, which may also be due to an increase in conformational motion.

As is common for these aromatic polyesters, isothermal crystallization can produce as many as three melting peaks in standard DSC traces, as seen in the graph A of Fig. 6.49, which is an example of isothermal cold crystallizations after heating from the glassy state. The crystallized samples were then cooled before the DSC runs and show the melting peaks labeled 1, 1', 1"; 2, 2', 2"; ... . At the higher crystallization temperatures, the three peaks fuse into a single peak. The results on crystallization after cooling from the melt are shown in the graph B of Fig. 6.49. The data closely match the graph A for the cold crystallization. At higher crystallization temperatures, the melting peak temperatures increase beyond the horizontal line, and indicate the existence of an even higher equilibrium melting temperature. The squares in graph B represent the small annealing peaks which are caused by secondary growth or annealing at the crystallization temperature. The main melting peak, marked by 1"-5", is practically constant up to 500 K and then increases. The constant level is due to rearrangement of the crystals grown at low temperatures.

The TMDSC traces shown in Fig. 6.50 are for a sample crystallized from the glassy state at 483 K for 30 min and analyzed under conditions of heating only [41]. The traces should be compared to Fig. 4.139 for PET. The three melting peaks are marked, analogously to Fig. 6.49, as A, A', and A", although peak A is barely visible. The zero-entropy-production melting temperature of the original crystals could be identified at position X by fast heating. The exotherm in the heat-only, nonreversing heat-flow-rate curve is a safe indication of major recrystallization in the vicinity of X

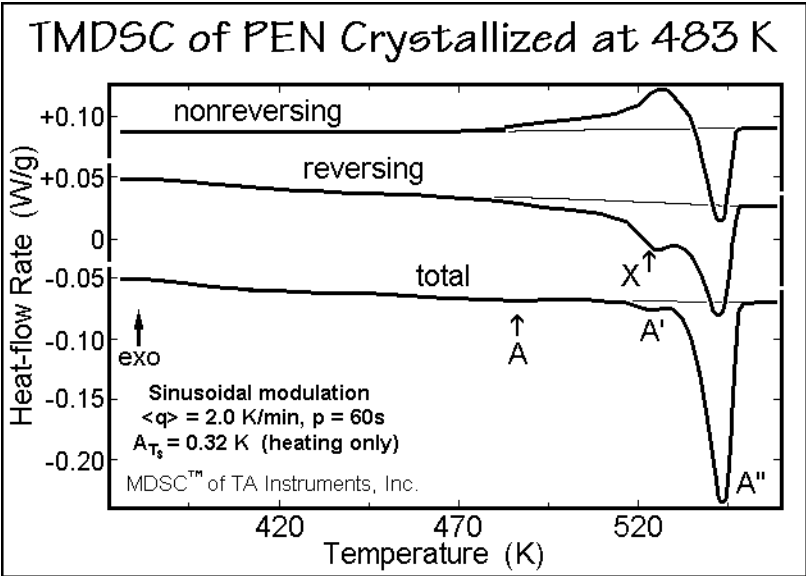


Fig. 6.50

(see also Sect. 6.2.3 for the discussion of recrystallization of PET). Small changes on longer annealing times and a change from incompatible to compatible blends with PET were linked to transesterification in the melt.

Quasi-isothermal TMDMA data for PEN are shown in Fig. 6.51 for slow cold crystallization at 418 K [42]. The method consists of dynamic mechanical analysis, DMA (see Sect. 4.5.4), to which temperature modulation was added. The insert is a

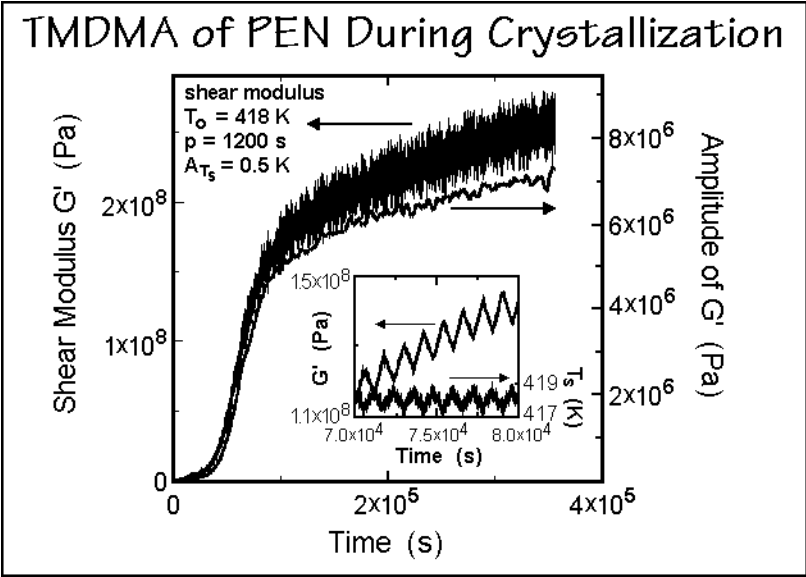
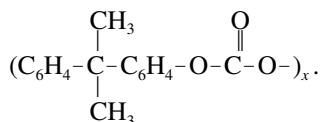


Fig. 6.51

magnified plot of the graph in the time period of fast, primary crystallization and illustrates the sawtooth-like modulation of the temperature. To interpret the data, it must be noted that the storage shear-modulus,  $G'$ , is proportional to crystallinity. The increase in crystallinity stretches over a time interval of several days. At the end of the fast, primary crystallization, the amplitude of the storage modulus, which is a measure of the reversing melting, also continues to increase, in contrast to PET, where it reaches a constant value. Analogous TMDMA experiments for melt crystallization of poly( $\epsilon$ -caprolactone) (PCL) are discussed below in Fig. 6.58 and for poly(ether ether ketone), PEEK, in Sect. 6.2.5 (Fig. 6.99).

**Polycarbonate**, specifically poly(4,4'-isopropylidenediphenylene carbonate), PC, has the repeating unit:



Its flexibility and segmental mobility are reduced so much that the crystallization of a quenched, amorphous sample of molar mass 28,000 Da needs an induction time of almost 50 h at 460 K, the temperature of fastest growth, and the half-time of crystallization is only reached after about 7 days [43]. The heat capacity of the solid PC has been analyzed, and the heat capacity of the liquid PC was measured and compared to the other aromatic polyesters.

The reversing specific heat capacity in the glass transition region is illustrated in Fig. 6.52 [21]. The analysis in terms of the ATHAS Data Bank heat capacities shows that there is no low-temperature contribution due to conformational motion below the glass transition. The glass transition of the semicrystalline sample is broadened to higher temperature relative to the amorphous sample, as found in all polymers. Of

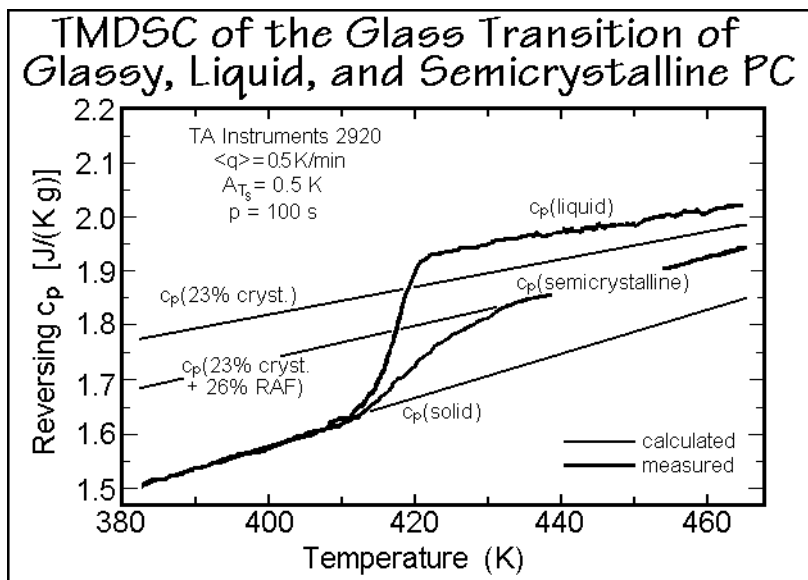


Fig. 6.52



particular interest is the sizeable RAF that is attained on crystallization. It is about equal to the crystallinity and makes up one third of the total amorphous fraction. Up to 460 K neither reversing melting nor a contribution from a glass transition of the RAF is seen for the semicrystalline of PC. The heat capacity of PC represents in this temperature range the behavior of an ideal, linear macromolecule without contributions of local large-amplitude motion.

The slow, irreversible cold crystallization is followed in Fig. 6.53 for more than 10 days with quasi-isothermal TMDSC to a fixed value of RAF. At the end of the crystallization there is no frequency dependence of the heat-capacity. The crystallization and the glass transition to the RAF occur simultaneously (see also Fig. 6.18).

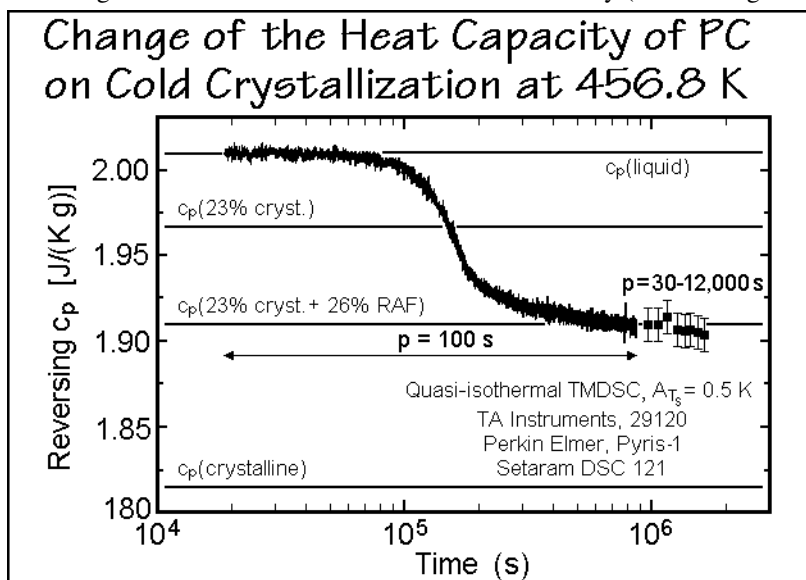


Fig. 6.53

The melting of the semicrystalline PC is shown in Fig. 6.54 [44]. The total  $c_p$ , depicted in the lower curve is similar to a standard DSC trace. It shows two melting peaks, one between 460 and 485 K for the secondary crystals, and the main melting peak at about 503 K. Single melting peaks are seen for PC of this molar mass only on crystallization above 486 K, a temperature above which no fringed-micellar, secondary crystals grow [43]. A similar change to one melting peak is seen for PEN in Fig. 6.49 at 500 K and many other polymers (see Sect. 6.2.3). The excess of  $c_p(\text{total})$  beyond  $c_p(\text{liquid})$  at the main melting peak in Fig. 6.54 is about 20 times that shown by the reversing  $c_p$  in the upper curve. In the low-temperature melting range, the reversing  $c_p$  shows an increase beyond the baseline for the semicrystalline polymer starting at about 470 K. Quasi-isothermal measurements separate the contributions. They seem to indicate increasing devitrification of the RAF with time and may be interpreted as for poly(phenylene oxide), described next. As long as some RAF surrounds a crystal, it cannot melt. The final exotherm in TMDSC may be due to loss of stationarity as often seen at a sharp end of irreversible melting (see Sect. 4.4.3).

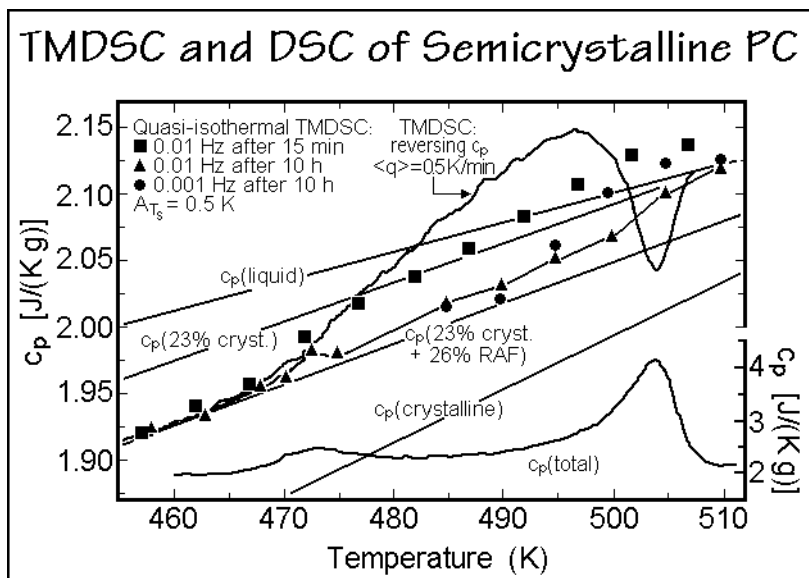


Fig. 6.54

Overall, there seems to be very little or no reversible melting for PC, a result which is reasonable, considering that the induction time for crystallization of an oligomer of a molar mass of 4,000 Da, i.e., with about 14 repeating units, is still about 200 min at 483 K [43] and may preclude sufficiently fast recrystallization of a once-melted chain segment. All excess reversing heat capacity, thus, seems to be accountable by irreversible reorganization which decays with time.

**Poly(phenylene oxide)**, of these, most common is poly(oxy-2,6-dimethyl-1,4-phenylene), better called poly(oxy-1,4-*m*-xylylene),  $[\text{O}-\text{C}_6\text{H}_2(-\text{CH}_3)_2-]_x$ , PPO<sup>TM</sup>, General Electric trademark. When analyzing the heat capacity of a 30% semi-crystalline PPO, a surprising result was obtained as represented by Fig. 6.55 [45]. Practically all of the noncrystalline material behaves as a rigid, amorphous fraction, RAF. In the center DSC trace of Fig. 6.55 there is no indication of a glass transition before melting. Annealing for increasing lengths of time at 496 and 502 K, which is above the exceptionally high  $T_g$  of amorphous PPO<sup>TM</sup>, however, causes a slow development of the glass transition, as can be seen in the left and right traces, respectively. In addition, as expected, the melting peak moves to somewhat higher temperature due to crystal perfection, but unexpectedly, the crystallinity decreases sharply. On annealing at 505 K, about 15 K below (!) the melting peak temperature, the sample becomes almost completely amorphous within 65 min. It was concluded from these experiments that the glass transition of the RAF is above the melting temperature of the original crystals and hinders the melting at the zero-entropy-production temperature of, perhaps, 500 K. The high  $T_g$  of the RAF is most likely also the reason for the difficulty in crystallization of PPO from the melt. As soon as crystals start to grow, they are surrounded by networks of rigid-amorphous materials and further growth is not possible. Usually a plasticiser or solvent must be added to crystallize PPO from the melt.

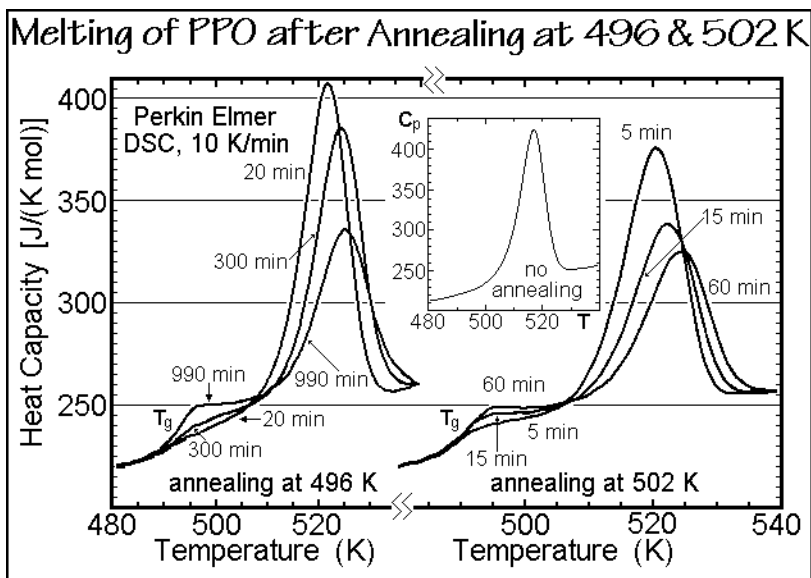


Fig. 6.55

Figure 6.56 shows quasi-isothermal TMDSC traces of an amorphous and a 30% crystalline PPO<sup>TM</sup>. The glass transitions of the two phases are clearly separated. The  $T_g(\text{amorphous})$  occurs at about 488 K, while the broadened glass transition of the RAF has a midpoint of about 502 K. Inspection of the semicrystalline trace shows no reversible melting, supporting the argument that polymer crystals surrounded by RAF show little or no melting, neither reversible nor irreversible.

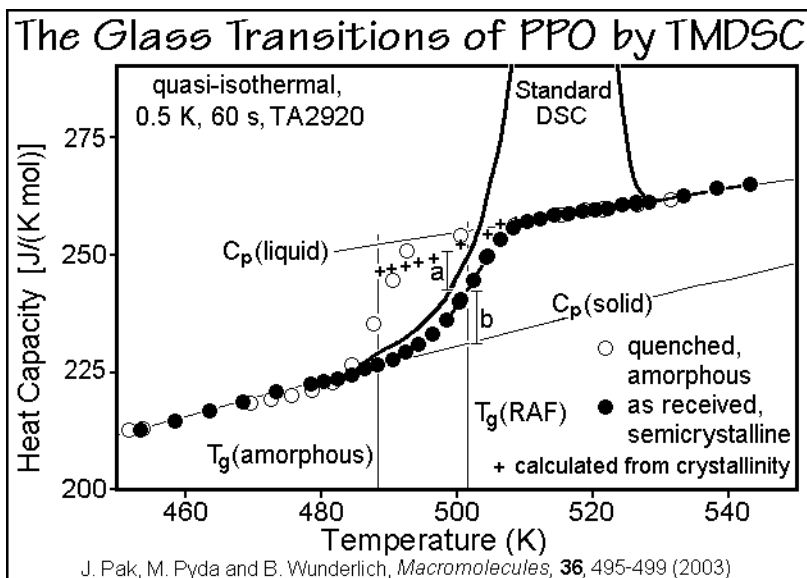


Fig. 6.56

With the known crystallinity from standard DSC, it is easy to calculate the expected  $C_p$  in Fig. 6.56 (+). The deficiency of the calculated  $C_p$  from the measured  $C_p$  is marked as the length a. The length b is then due to the RAF which has already gone through its glass transition and is now a mobile-amorphous fraction. The ratio  $a/\Delta C_p^\circ$  is the remaining rigid RAF at the given temperature. It is plotted in Fig. 6.57 together with the measured, reversing  $C_p$  and the crystallinity from a separate set of experiments. As the temperature increases, the crystallinity and the RAF initially decrease at different rates. Melting is completed at about 510 K. Up to about 495 K the crystallinity decreases very little, while the RAF loses almost 20% of its value, which is in accord with the assumption that the surrounding glass must become mobile first, before melting can occur. Between 495 and 510 K the decrease of both, the RAF and the crystallinity, is close to linear, with the RAF losing three times more solid

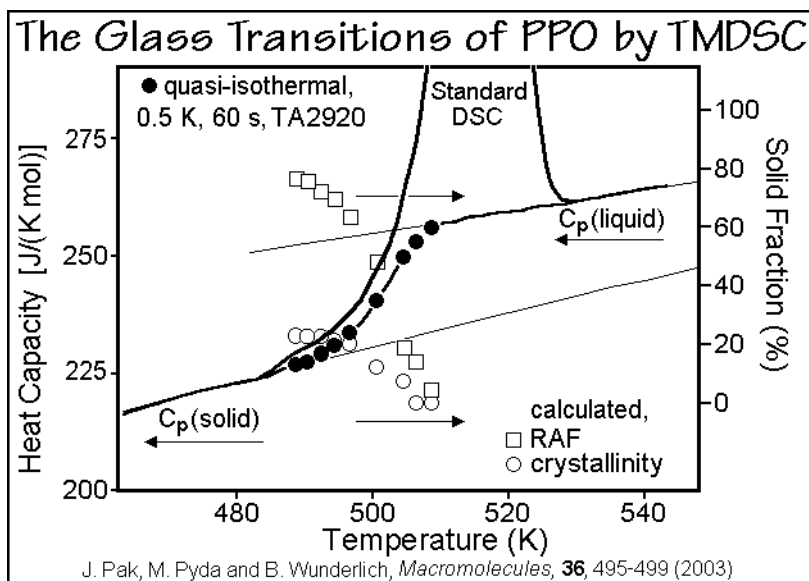


Fig. 6.57

fraction than the crystallinity. In this temperature range, the crystallinity is lost parallel to the loss of the RAF, proving that the glass transition of the RAF is coupled to the melting. This result can be compared to the parallel development of crystallinity and RAF in Figs. 6.18 and 6.53.

**Poly( $\epsilon$ -caprolactone), PCL**, is an aliphatic, linear polyester with the repeating unit  $O-(CH_2)_5CO-$ . Figure 6.58 illustrates the change of the real part of the shear modulus of PCL along with its amplitude on temperature modulation when using TMDMA [42,46,47] (see also Fig. 6.51). The sample was cooled from the melt at  $1.0 \text{ K min}^{-1}$  to the crystallization temperature and reached a crystallinity of  $\approx 50\%$ . The insert shows that during the crystallization the modulation of the temperature produces a reversible crystallization and melting. As the primary crystallization is complete at about  $2.0 \times 10^5 \text{ s}$  ( $\approx 56 \text{ h}$ ), the increase in  $G'$  slows, but indicates considerable secondary crystallization with some decrease in reversibility.

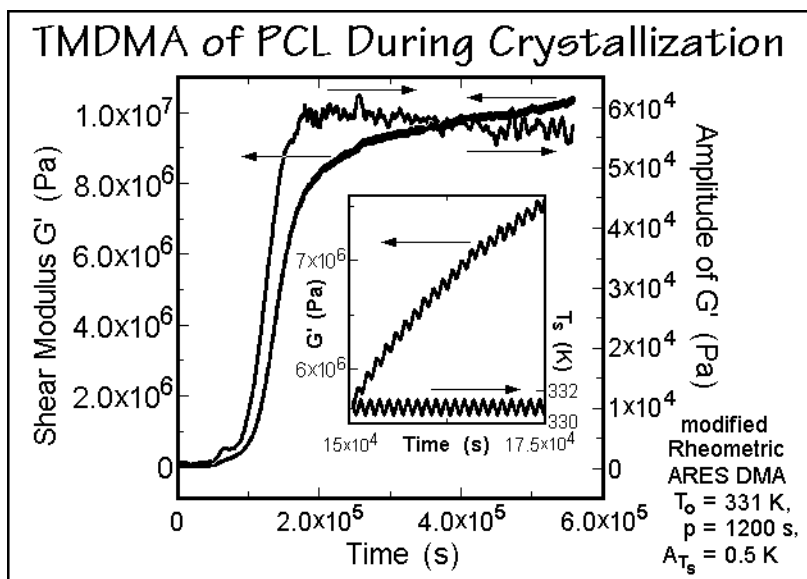


Fig. 6.58

Figure 6.59 displays the corresponding quasi-isothermal TMDSC at slightly lower temperature. The expected reversing specific heat capacity was estimated from the latent heat and the ATHAS Data Bank  $C_p$  for the crystalline PCL and the melt. The measured value, although lower than the  $c_p$  of the melt, never reaches this level. The small decrease in reversing  $c_p$  goes parallel to the small decrease of the amplitude of the storage modulus in Fig. 6.58 in the region of secondary crystallization.

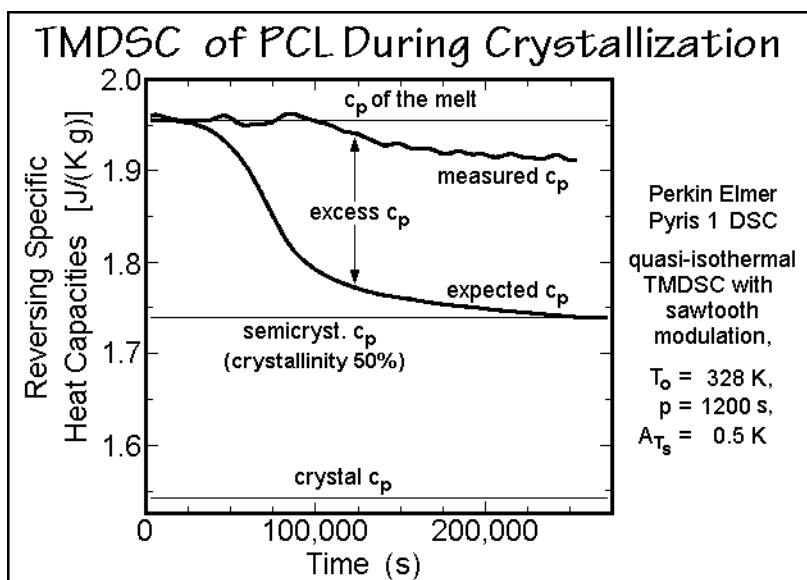


Fig. 6.59

Next, it needs to be determined whether this excess heat capacity is indicative of conformational defects or true reversible melting. To make sure that linearity was maintained in the melting range for measurement of the reversing heat capacity, its amplitude-dependence was tested by quasi-isothermal TMDSC and is shown in Fig. 4.115. The dependence of the reversing heat capacity on frequency is represented in Fig. 6.60 over a wide frequency range in terms of excess heat capacity [48]. The drawn line suggests that a sigmoidal decrease can represent the frequency dependence. For PCL it should take a frequency of more than 10 Hz to separate the reversible melting from the base heat capacity and determine how much conformational contribution is present in the measured baseline. Assuming a similar concentration of *gauche-trans* conformations as in polyethylene crystals at the same temperature (see Fig. 2.65), the defect contribution may be within the error limit of measurement. The equilibrium melting temperature,  $T_m^\circ$ , of 342 K for PCL is below  $T_m^\circ$  of polyethylene, so that one would expect fewer defects and even less than in nylon 6 and 12 with values of  $T_m^\circ$  of 533 and 500 K, respectively.

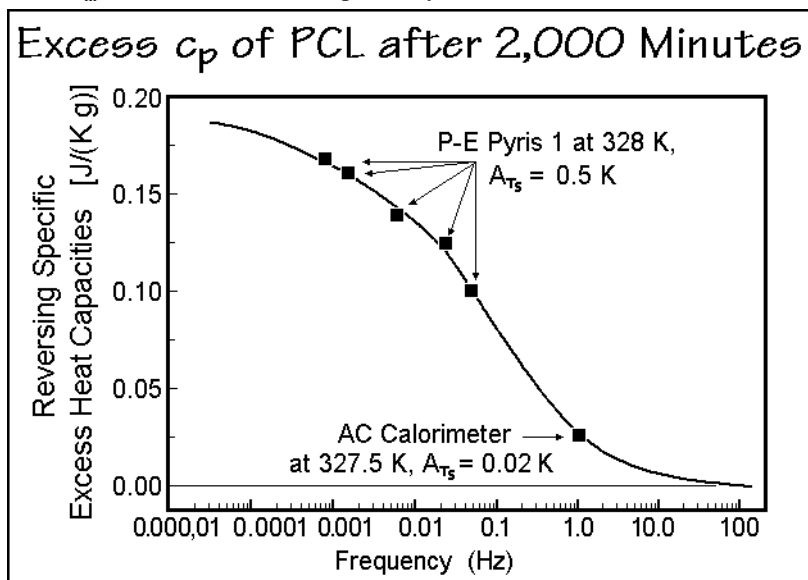
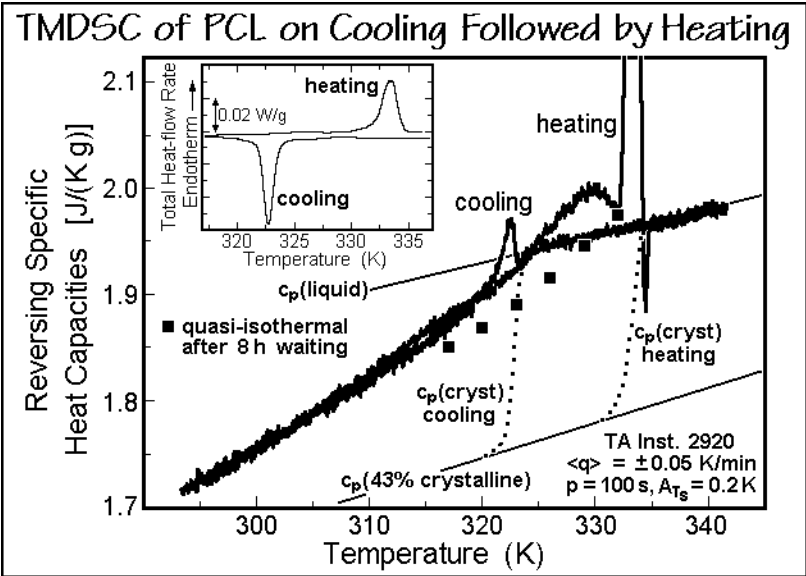


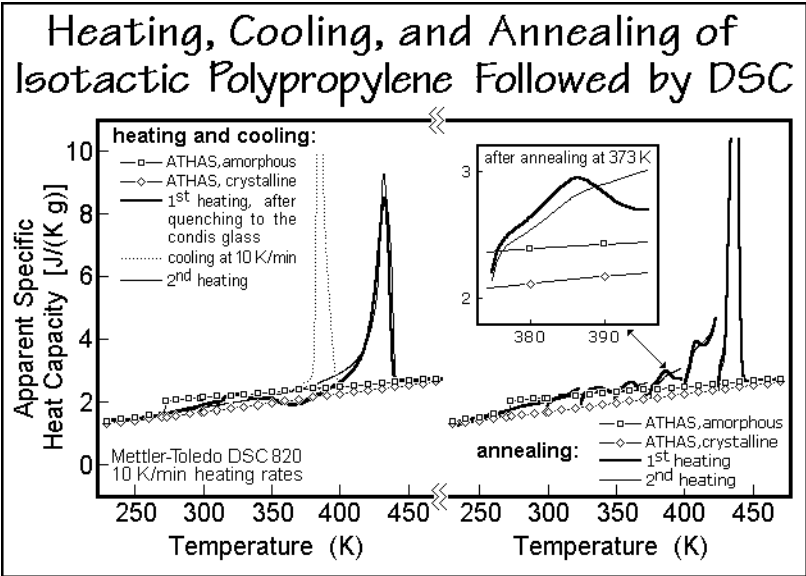
Fig. 6.60

Figure 6.61 describes the TMDSC of reversing  $c_p$  on cooling from the melt, followed by heating. Except for the small sharp endotherm at the beginning of crystallization and exotherm at the end of melting, which may be caused by errors in the deconvolution from the irreversible latent heats, the two reversing heat capacities differ little. The quasi-isothermal points give an assessment of the slow reorganization processes. Below about 300 K this reorganization seems to stop, but an excess heat capacity can be extrapolated down to about 270 K. The PCL is thus a semicrystalline polymer which has no rigid amorphous fraction. It also seems to have no significant contribution of conformational disorder to the heat capacity, so that the total apparent reversible  $c_p$  should be due to reversible melting. Another, related flexible linear polymer, poly-*p*-dioxanone, is illustrated in Fig. 4.124. It seems similar in behavior.



**Fig. 6.61**

**Polypropylenes**,  $(\text{CH}_2-\text{CHCH}_3)_x$ , PP, is commonly found as its isotactic stereoisomer, iPP. Figure 6.62 illustrates a standard DSC analysis on cooling, heating, and annealing which was subsequently studied quantitatively by TMDSC [49]. The melting and crystallization peaks in the apparent heat capacity plots on the left side of the figure show a typical supercooling of about 40 K. The first heating trace represents a sample that was cooled quickly. In this case, iPP forms a metastable,



**Fig. 6.62**

conformationally-disordered glass (condis glass) with a smectic structure, disordered mainly by helix reversals and a crystallinity of about 39% (see Fig. 5.146). On heating, the condis glass transforms after a small endotherm at 320 K with a broad exotherm centered at 367 K to the stable,  $\alpha$ -monoclinic crystal structure (see Fig. 5.46). Cooling from the melt at  $10 \text{ K min}^{-1}$  leads to a 53%  $\alpha$ -monoclinic crystallinity of lamellar morphology with a similar fold-length. An RAF of as much as 30% was observed on a different sample, cooled at  $0.5 \text{ K min}^{-1}$ . The RAF devitrified between 325 and 370 K in a broad, second step of the glass transition and led then, after quenching, to a normal glass transition on reheating, followed by cold crystallization of about 6% of the polymer and remelting with an annealing peak at about 340 K [50]. The second heating trace in Fig. 6.62 does not have enough resolution to identify the RAF, but it can be seen in Fig. 6.64, below.

The morphology and fold-length were determined on identical and similar samples as used in the calorimetry with wide- and small-angle X-ray diffraction, as well as atomic force and electron microscopy, WAXD, SAXS, AFM, and electron microscopy [49,51]. The similarity in fold-length accounts for the comparable main melting peaks seen in the left heating traces in Fig. 6.62. Next, both samples were step-wise annealed for 40–400 min, as shown in the right DSC traces of Fig. 6.62. After each step, an annealing peak (endotherm) is observed on resuming the heating which is much smaller for the melt-cooled sample (see insert). Only few kelvins later, the apparent heat capacity shown in the left curves is resumed, which suggests that only the crystals that lose their stability in the vicinity of the annealing temperature are affected by the annealing. In Fig. 6.63, the heating and annealing of the quenched iPP is followed by time-resolved X-ray diffraction. The upper figure shows changes on heating after annealing at 373 K. First, the diffraction intensity marked by '1' is constant, followed by an increase in crystallinity at '2' which corresponds to the

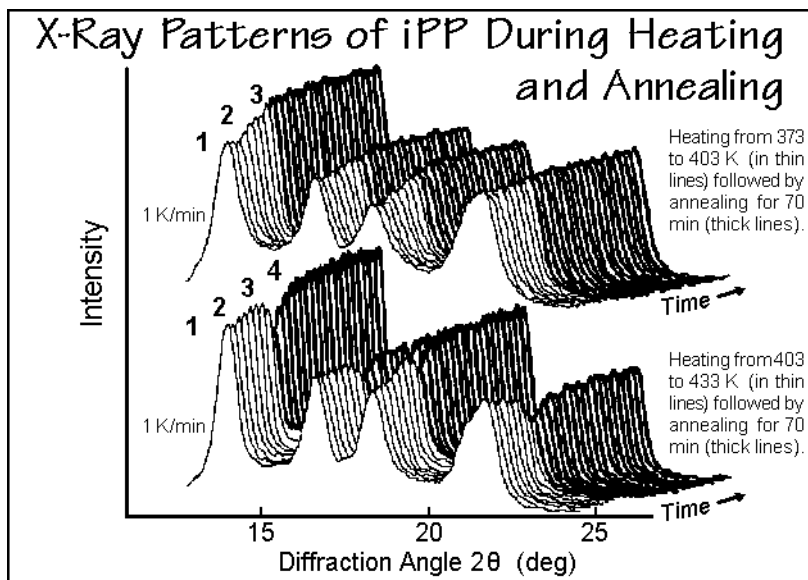


Fig. 6.63



exotherm in the insert in Fig. 6.62. The following annealing of 70 min starts at '3' with only a slight increase in diffraction intensity. The subsequent heating to 433 K is shown in the lower part of Fig. 6.63. It reveals, again, a period of constant intensity '1' followed by an increase in crystallinity '2' which leads to the beginning melting at '3', which on annealing at '4' indicates some recrystallization and a further, slight increase in crystallinity. The next heating leads to the main melting with disappearance of the crystalline diffraction pattern, in accord with the DSC trace.

Further analysis of the two samples of Fig. 6.62 is done by TMDSC, as seen in the left graphs of Fig. 6.64. A comparison of the two reversing heat capacities shows that the cold crystallization and the transition mesophase-to- $\alpha$ -monoclinic crystals do not show, i.e., they are nonreversing. There remains, however, a substantial reversing contribution which is larger for the quenched iPP than for the lamellar, melt-cooled iPP. The upper limit of the devitrification of the RAF seems to occur at 320–330 K,

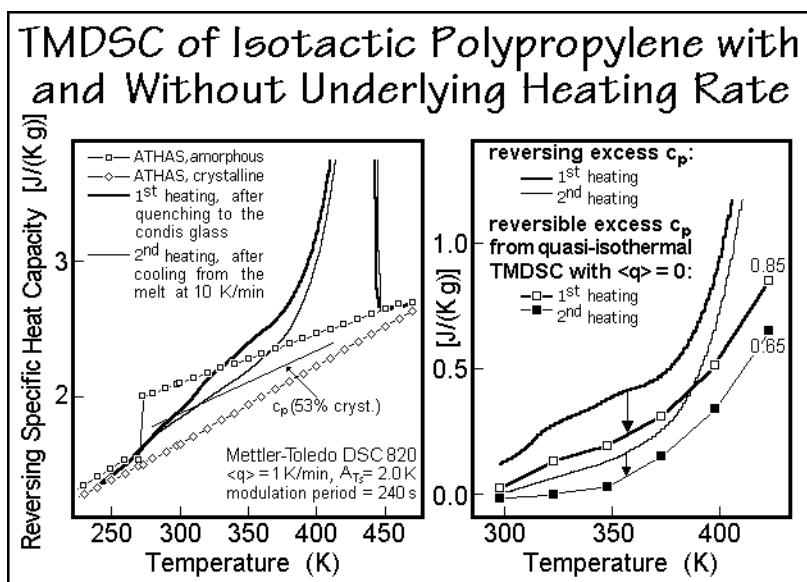


Fig. 6.64

but cannot be separated fully from the reversing melting. The curves on the right in Fig. 6.64 represent the latent-heat contributions of the apparent, reversing  $c_p$ , obtained by subtracting the expected thermodynamic  $c_p$  for the given crystallinity from the curves on the left. Results from quasi-isothermal experiments on heating are plotted also in Fig. 6.64. These are taken after the slow crystal perfection ceased and represent reversible latent heats. The slowly-cooled, lamellar sample begins to show reversible melting at 320 K, while the fast-cooled sample with globular morphology begins melting at the end of the glass transition. More qualitative data were generated throughout the melting peak and show a maximum in reversible melting on heating after fast cooling of  $3.05 \text{ J K}^{-1} \text{ mol}^{-1}$  and after slow cooling of  $2.80 \text{ J K}^{-1} \text{ mol}^{-1}$  [52]. The same thickness in the chain direction and the difference in lateral extension places the reversible melting for iPP on the growth faces of the crystals.

Figure 6.65 further supports this interpretation of reversible melting at the lateral growth face with an analysis of iPP samples annealed for long times at different temperatures. The standard DSC traces were taken after the quasi-isothermal TMDSC could detect no further decrease in the apparent reversing heat capacity and were used for a measurement of the remaining crystallinity. Then, corresponding X-ray diffraction differences were taken in a temperature range of  $\pm 1.5$  K after the metastable, global equilibrium was achieved in this temperature region. On the right side, Fig. 6.65 displays the normalized difference patterns of the X-ray diffraction experiments. Within experimental error, the increase in latent heat, marked in Fig. 6.64 as open squares, and the increased differential diffraction areas in Fig. 6.65 give the same changes in crystallinity [53], making it certain that the reversible melting refers to the same process seen in the irreversible melting and crystallization.

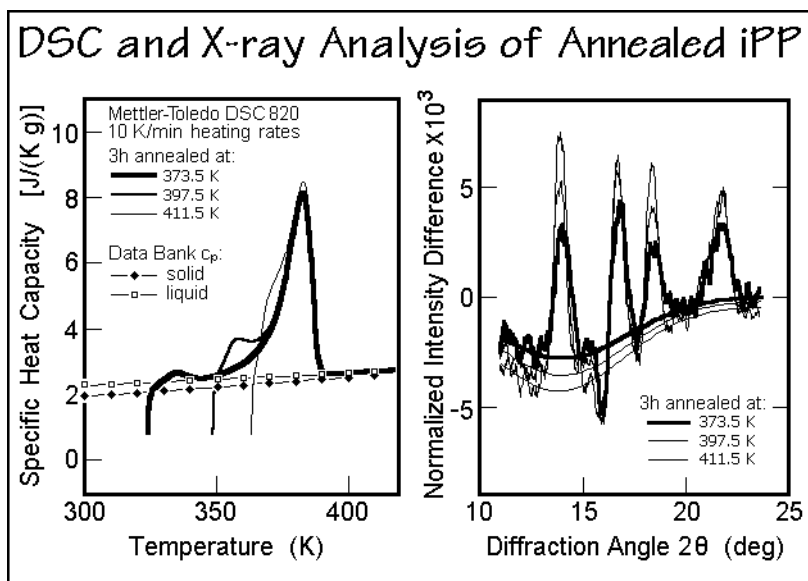


Fig. 6.65

Syndiotactic polypropylene, sPP, is known almost as long as iPP, but only became readily available with high stereospecificity after the discovery of soluble, single-site, metallocene catalysts (see Sect. 3.2.1). Several semiquantitative studies are available and have been reviewed in Ref. [1]. Figure 6.66 illustrates TMDSC traces of an sPP sample of low crystallinity (and stereospecificity). The reversing  $c_p$  of the semicrystalline state on initial cooling and on subsequent heating are identical. Above the low-temperature glass transition, the sample has a solid fraction of 59%. With a heat of fusion of 17%, this corresponds to an RAF of 42%. A broad glass transition of the RAF is indicated between 315 and 365 K. Above this glass transition, reversing melting is observed with both of the irreversible melting peaks showing a reversing component. The frequency dependence of the reversing heat capacity of sPP after isothermal crystallization at 363 K is shown in Fig. 6.67 [54]. At low frequency the sample shows reversing melting which at higher frequency reverts to a partially

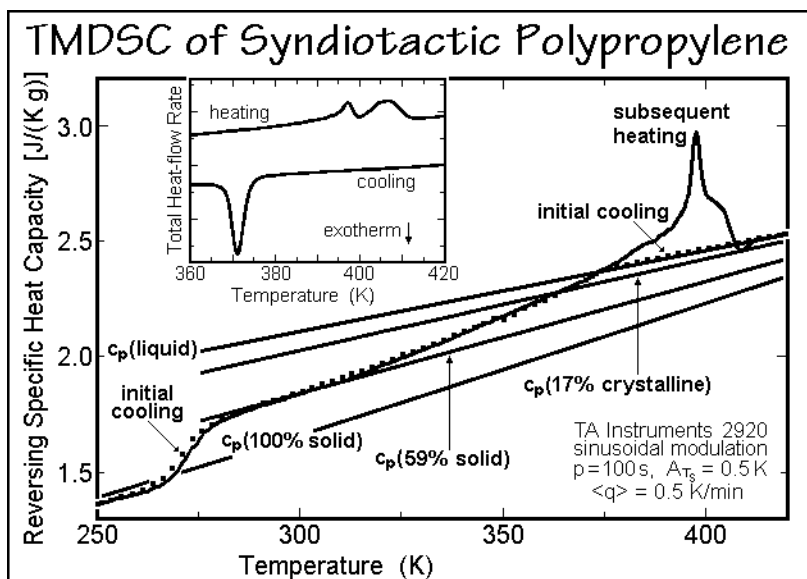


Fig. 6.66

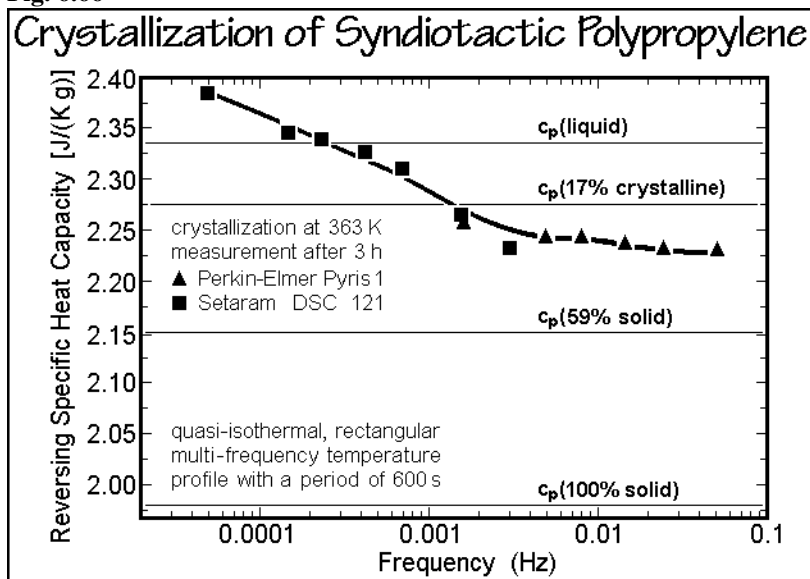


Fig. 6.67

devitrified RAF. Both iPP and sPP are thus examples with a broad devitrification of the RAF before the major melting peak. The frequency dependence of the reversing specific heat capacity of sPP over the full temperature range is displayed in Fig. 6.68 and should be compared to similar results on other polymers (see, for example, the results for nylon 6 in Figs. 4.116 and 4.119). The frequency dependence was extracted from the higher harmonics of the heating rate and heat-flow rate.

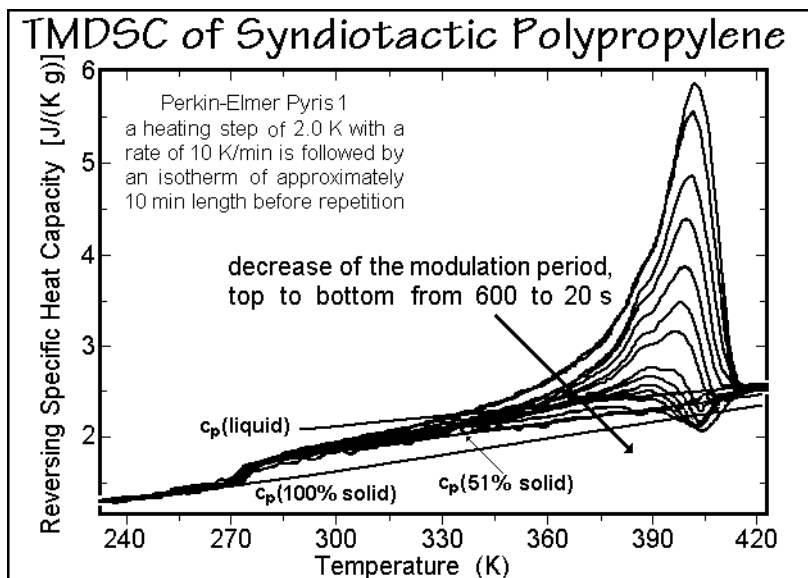


Fig. 6.68

*Decoupling of segments of polymer chains* was proposed as a mechanism for the examples of the reversing and reversible melting which are summarized with their properties in Table 6.1 [1,33]. To restate the main facts, it is shown in Figs. 3.75 and 3.91 that flexible molecules melt reversibly only up to a critical length, which for paraffins is 10 nm. Longer extended-chain crystals melt irreversibly (Figs. 3.89 and 6.28). A first observation of decoupling of melting concerns the limiting reversibility of crystals grown from a distribution of molecules of low molar mass. In this case two physical changes that should occur simultaneously are partially decoupled. The melting/mixing and crystallization/demixing are incomplete, probably due to slow diffusion in the available time. This can cause the limited reversibility seen in Figs. 6.25 and 6.35. Decoupling is also known for polymers with long side-chains, where side-chains may be largely independent of the main chain (see Sect. 7.2.3).

Locally reversing and reversible melting within a globally metastable structure of semicrystalline, flexible macromolecules also exhibit decoupling. Such decoupling allows molecular nucleation to start with crystallization of segments of the polymer chains (see Fig. 3.74). The portions of the molecules not crystallized must be considered as amorphous and belonging to a different phase. Figure 6.69 illustrates such creation of points of decoupling and a possible mechanism of reversible melting at the growth face. Figure 6.69 is linked to the molecular nucleation in Fig. 3.74. Because of the transfer of stress across the interface and along the continuing molecule, this picture also offers an explanation of the broadening of the glass transition and the creation of a separate RAF. In case  $T_g$  of the RAF is close to  $T_m$ , melting is governed by the RAF and not the crystal, as documented in Fig. 6.56.

For polyethylene, the melting point of decoupled segments can be estimated from the known  $T_m$  of folded and extended-chain crystals, given in Figs. 2.90 and 3.04, as is shown in Fig. 6.70. The bottom one of the two equations permits the computation

**Table 6.1.** The reversing behavior of the various polymers<sup>a</sup>

Polymer	cold cryst.	hot cryst.	confor- mational $C_p$	RAF ( <sup>b</sup> )	reversible melting	reversing melting
PET	✓	✓	0	$<T_m$	✓	✓
PTT	✓	–	✓	$<T_m$	✓	✓
PBT	✓	✓	?	$\leq T_m$	✓	✓
PEN	✓	–	✓	$<T_m$	✓	✓
PEEK	–	✓	✓	$<T_m$	✓	✓
PC	✓	–	0	$\leq T_m$	0(?)	✓
PPO	–	–	0	$>T_m$	0	0
PTFE <sup>c</sup>	–	✓	?	$\approx T_g$	✓	✓
nylon 12	–	✓	✓	$\approx T_g$	✓	✓
nylon 6	–	✓	✓	$\approx T_g$	✓	✓
PHB	✓	–	0	$<T_m$	✓	✓
PCL	–	✓	0	$\approx T_g$	✓	✓
POM	–	–	0	$\approx T_m$	–	–
POE	–	✓	✓	$\approx T_g$	✓	✓
POTM	–	✓	✓	$\approx T_g$	✓	✓
PPDX	✓	–	0	$\approx T_g$	✓	✓
iPP	✓	✓	0	$<T_m$	✓	✓
sPP	–	✓	0	$<T_m$	✓	✓
PE	–	✓	✓	$\approx T_g$	✓	✓
PE- <i>alt</i> -CO	✓	✓	0	$\approx T_g$	✓	✓

<sup>a</sup> ✓ indicates “yes”; 0, “no”; –, not discussed or measured; ?, “questionable.” The table has been adapted from [1].

<sup>b</sup>  $T_g$  of the RAF below ( $<$ ), up to ( $\leq$ ), at ( $\approx$ ), or above ( $>$ ) the melting temperature,  $T_m$ ;  $\approx T_g$  indicates a broadening of the glass transition only.

<sup>c</sup> Only the low temperature transitions of PTFE have been analyzed (see Fig. 5.31). See Sect. 5.5 also for TMDSC of other mesophase transitions.

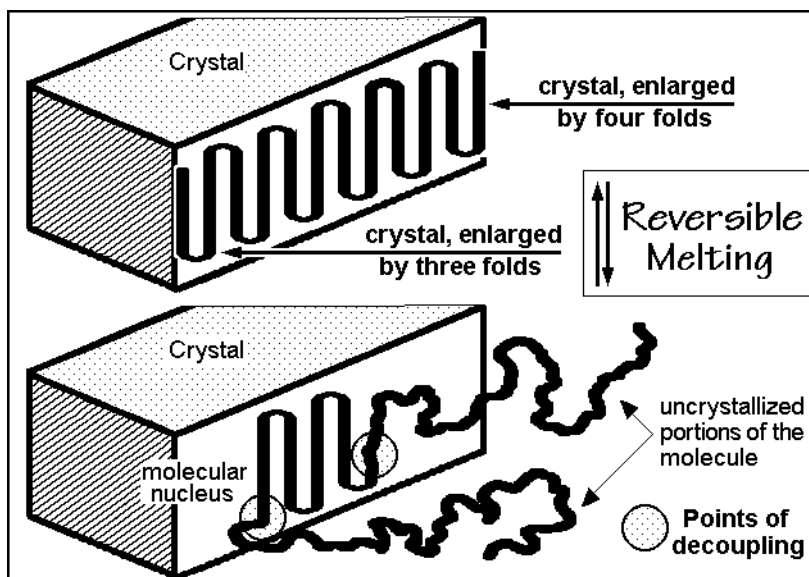


Fig. 6.69

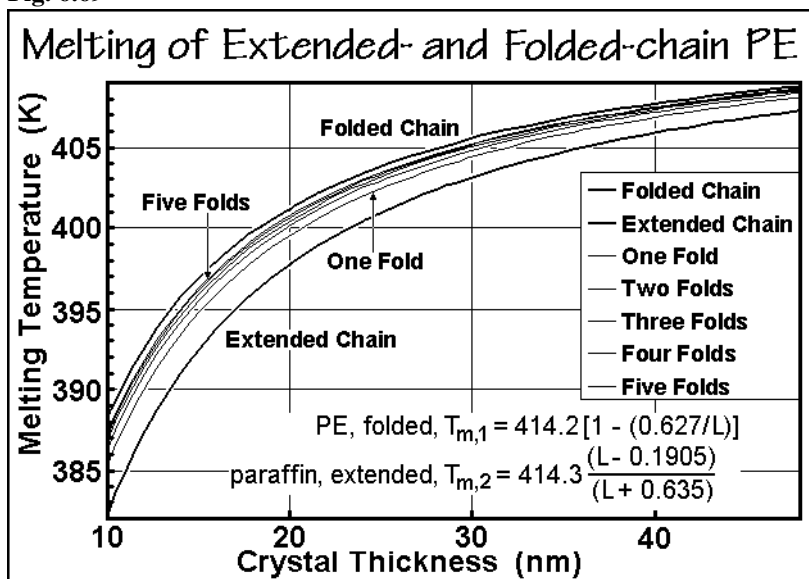


Fig. 6.70

of the extended-chain length of the decoupled segment. Inserting its melting temperature into the upper equation instead of 414.2 K (the melting temperature of the extended-chain crystal of infinite length) and correcting the melting point lowering (in brackets) for the fraction of the surface covered with chain folds, yields the shown curves. (For one fold, the correction factor for the term in brackets is 0.50, for two folds, 0.67, for three, 0.75, for four, 0.80, and for five, 0.83.)

**Poor crystals** of polymers which are susceptible to reversing melting are either small, nanophase-separated crystals, as just discussed, or may be conformationally disordered. The conformationally disordered crystals are mesophases, described in Sect. 5.5. The reversing and reversible melting of the mesophases depends on the mobility within the crystal, as seen from Figs. 5.131, 5.144, and 5.154. Liquid crystals are likely to have fully reversible transitions within the time scale of calorimetry, while the condic phases are sufficiently rigid to show less reversing behavior and are closer in their behavior to the small polymer crystals with their slow crystal perfection due to melting and recrystallization and reversibility on the growth faces.

Quenching from the melt or solution can lead directly to glasses (see Sect. 6.3), to small crystallites, dendrites, and spherulites (see Figs. 5.56, 5.60, and 5.75), or to mesophase glasses (see Fig. 5.146). Small crystals are also found on cold crystallization of a glass by growing crystals as little above the glass-transition temperature as possible and by drawing of fibers or other deformations (see Sects. 5.2.6 and 5.3.5). In addition, by partial crystallization at higher temperature it is possible to set up a network of larger crystals, separated by amorphous defects, as described by Fig. 5.87. On cooling, these amorphous defects may generate a second population of poor crystals, observed calorimetrically in the form of “annealing peaks” (see Sect. 6.2.5). In all these cases there is a chance to set up a configuration for locally reversible melting and crystallization. One expects these poorly grown crystals to be close to a fringed-micellar structure, schematically shown in Fig. 5.42, with many of the molecular chains being decoupled into crystals and amorphous segments.

A unique method to generate poor crystals is shown in Fig. 6.71. It involves the compression of crystals of poly(4-methyl-1-pentene), P4MP1, with a glass transition  $T_g = 303$  K, melting transition  $T_m^0 = 523$  K, and a heat of fusion of  $\Delta H_f = 10$  kJ mol<sup>-1</sup> (see also Fig. 5.124). At room temperature, the tetragonal crystals of P4MP1 have a

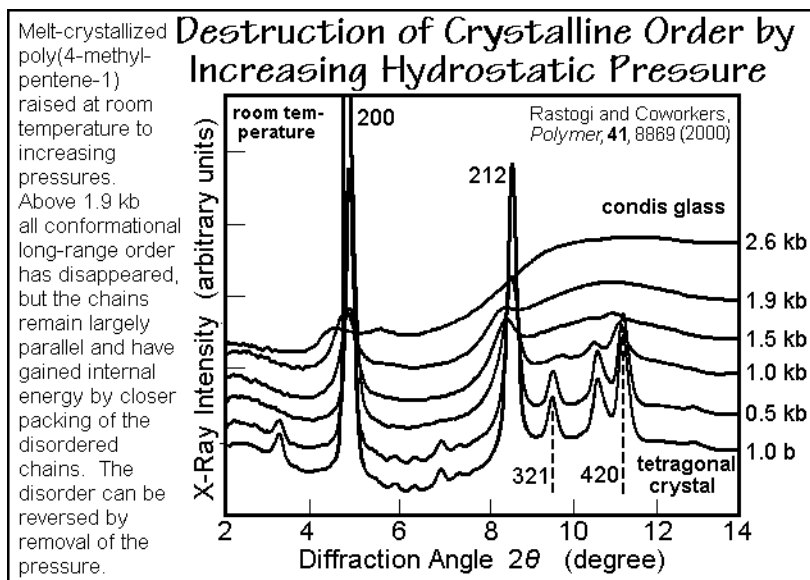


**Fig. 6.71**

lower density than the surrounding amorphous phase. The rather open helical conformation  $2\frac{1}{2}$  for P4MP1 is the reason for the poor packing in the crystals at room temperature, compared to the amorphous phase. Increasing the temperature expands the amorphous phase faster than the crystals, so that at  $T_m$  the crystals are somewhat denser. The change of  $T_m$  as a function of pressure is shown in Figs. 6.72 and 6.73. After the initial, expected increase with pressure,  $T_m$  decreases.

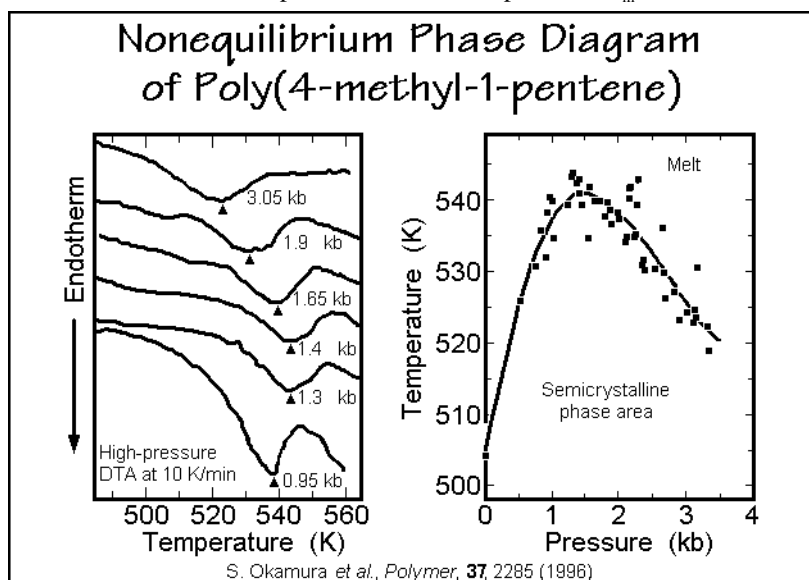


Fig. 6.72

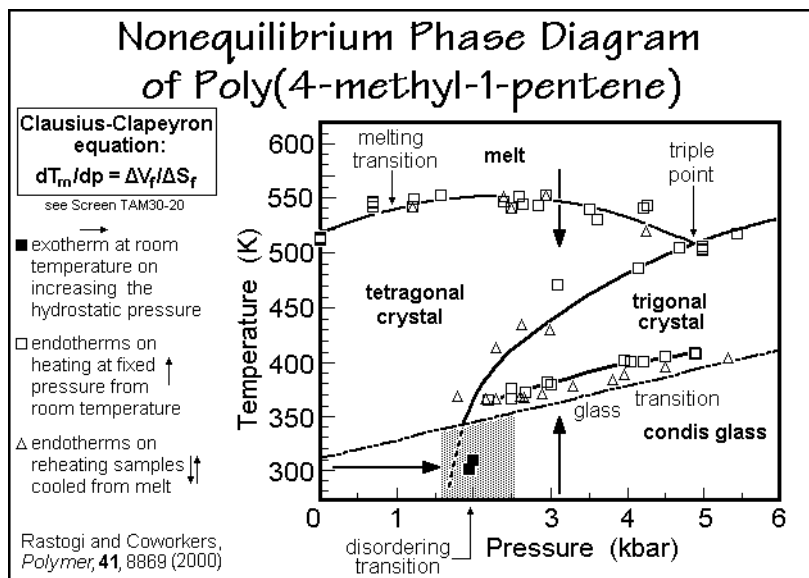


Fig. 6.73



This unique behavior of the melting temperature with pressure indicates that increasing the pressure reverses the density difference in a similar manner as decreasing the temperature. At the maximum of the  $T_m$  versus  $p$  curve in Fig. 6.73, the difference in molar volume between melt and crystal is zero, leading to a pressure of coefficient of zero in the Clausius-Clapeyron equation discussed in Sect. 5.6.5 and written in Fig. 5.168. In Fig. 6.73 a phase diagram for the various states is drawn based on high-pressure calorimetry. Only the melt appears as a true equilibrium phase. All other phase areas are semicrystalline, i.e., do not follow the phase rule (see Sect. 2.5.7). Because Fig. 6.73 does not represent equilibrium, it can mirror the actual processes. All exotherms and endotherms, except for melting, are small (0.5 to 2 J/g), indicating that at the transitions, the changes in entropy of the phases are small. Major crystallization and melting, thus, is not possible.

The nonequilibrium states were identified and seem to be initiated in close concert with the existence of the glass transition of the majority glassy phase identified in Fig. 6.73. Isothermal disordering at room temperature along the horizontal arrow causes a transition to the condis glass on the right of the extrapolated phase boundary. It seems to be a frustrated tetragonal to trigonal transition. Although superficially showing an amorphous X-ray pattern in Fig. 6.71, the condis glass retains most of its heat of fusion and acquires largely sessile backbone and side-chain conformational defects. This disordering can be reversed by reduction of pressure. Based on Fig. 6.73 one can speculate that the equilibrium phase-diagram is as given in Fig. 6.74. The tetragonal phase is the stable crystal. The trigonal crystal form with a  $2\frac{2}{3}/1$  helix conformation, common for vinyl polymers with smaller side chains (see Fig. 5.14), exists as the low-temperature, high-pressure phase. As expected from a high-pressure, low-temperature phase, it is denser than the trigonal crystals. Neither of the two equilibrium polymorphs has dynamic conformational disorder.

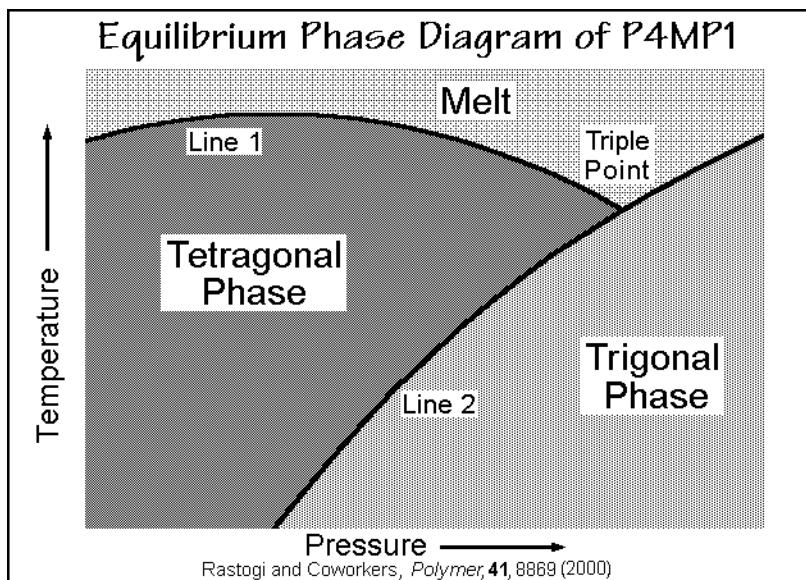


Fig. 6.74

### 6.2.3 Annealing and Recrystallization Effects

The word annealing derives from the Anglo-Saxon *aelan*, to bake or burn, and the prefix *an*, on. It was used to describe the burning-on of a glaze or enamel on ceramics and metals, and furthermore the strengthening, hardening, or toughening by heating. In the polymer field, the term implies imparting of a certain (advantageous) property by heat treatment without large-scale melting. If large-scale melting of crystals is involved in the process and renewed crystallization occurs before the whole sample turns liquid, the process is called recrystallization rather than annealing. Naturally, both processes may occur at the same time in a semicrystalline sample. Glassy polymers are mainly annealed close to the glass transition for strain release and densification (see Sect. 6.3), while crystalline polymers perfect their internal structure and their morphology on annealing (see Sects. 5.1–3). Crystal structure and morphology are best assessed by X-ray diffraction and electron microscopy, while the change in macroscopic properties is, as usual, best tested by thermal analysis.

Point defects and dislocations are shown in Sect. 5.3 to appear as nonequilibrium defects, usually introduced during crystal growth or deformation, and as equilibrium defects, generated thermally. The dislocation density can be determined by the moiré method (see Appendix 17 and Fig. 5.93). On annealing of crystals above their crystallization temperature, the nonequilibrium dislocation density increases, as is demonstrated in the left graph of Fig. 6.75. Since the number of such nonequilibrium

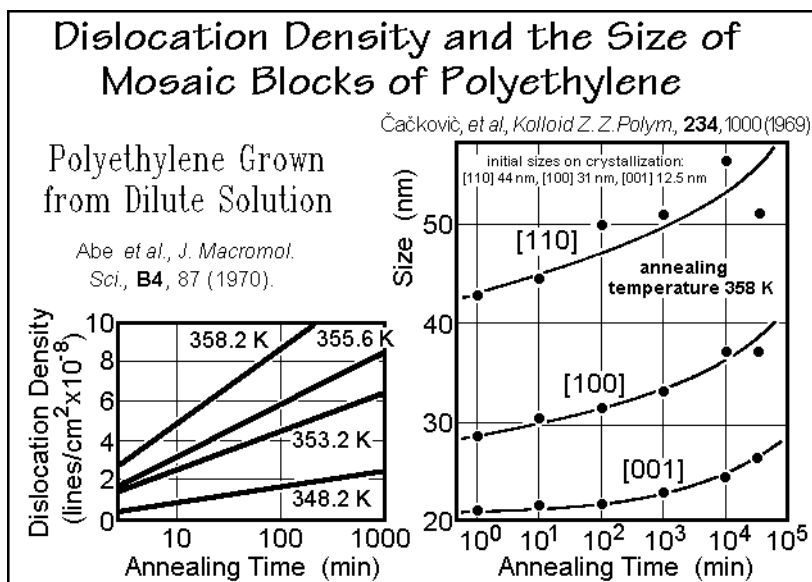
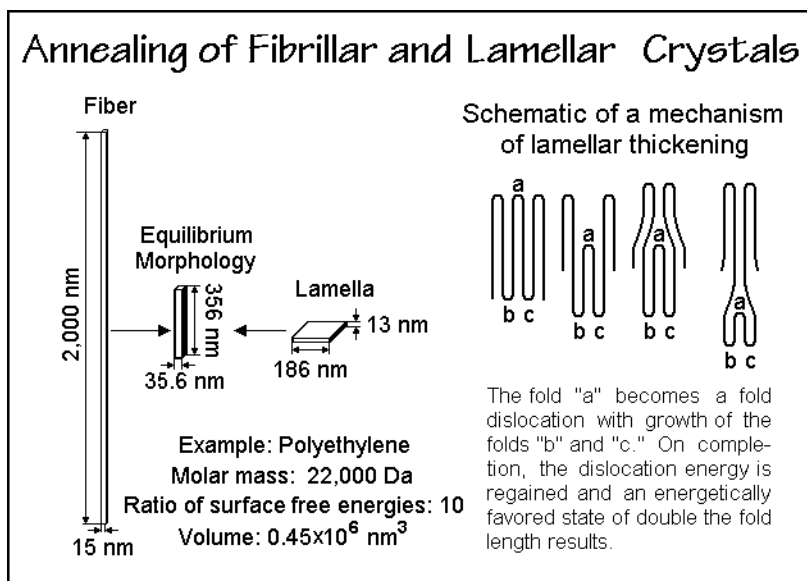


Fig. 6.75

defects cannot increase by annealing without a cause which more than compensates their metastability, one assumes that the cause is a change in the packing within the crystals or between the lamellae that cause the moiré pattern. The right graph in Fig. 6.75 illustrates, based on X-ray diffraction, that the mosaic dimensions, indeed,

increase on annealing in the crystallographic *a* and *b* directions (see Figs. 5.18 and 5.19). A fast, but small adjustment from 12.5 to 20 nm in fold length occurs within the first minute along [001] (compare to the initial dimension, and see also Fig. 6.34). The following long-time annealing affects all dimensions of the crystals.

On a larger scale, crystals of polymers were shown in Sect. 5.2 to commonly have a fibrillar or lamellar morphology. Neither of these is an equilibrium shape. Figure 6.76 illustrates how these nonequilibrium morphologies would have to change to reach an equilibrium shape. More detailed studies are available for the thickening of the lamellar crystals. It involves an increase of fold-length by a mechanism as displayed by the right-hand sketch in Fig. 6.76. The intermediate states have only a small



**Fig. 6.76**

increase in free enthalpy which acts as an activation energy for the process to the more stable state. Actual observation of the thickening is seen in Fig. 6.77. Separated lamellae develop holes with rims of about double the original thickness. From the dimension of the rims, it can be estimated that for each growth plane that crosses the hole, only one molecule thickens in the early stages of annealing. The graph in Fig. 6.77 indicates that annealing speeds up above 395 K. The crystals become more irregular and have more than twice the fold length. A hole in one lamella is naturally an ideal position for the adjacent lamella to thicken into.

The electron micrograph of Fig. 6.78 depicts melt-grown polyethylene lamellae of thicknesses of 18–22.5 nm, grown at 403 K on the surface of the (110) growth face of an extended-chain crystal, as seen in Fig. 5.76 and 5.77 [24]. This substrate lets one see the growth face of the folded-chain lamellae. In the bottom of the figure the lamellae were annealed below the melting temperature of the substrate, at 411.6 K, for 18 h. The lamellae are now irregular and show thicknesses of 27 to 45 nm. The underlying extended chain crystals are little affected by the annealing.

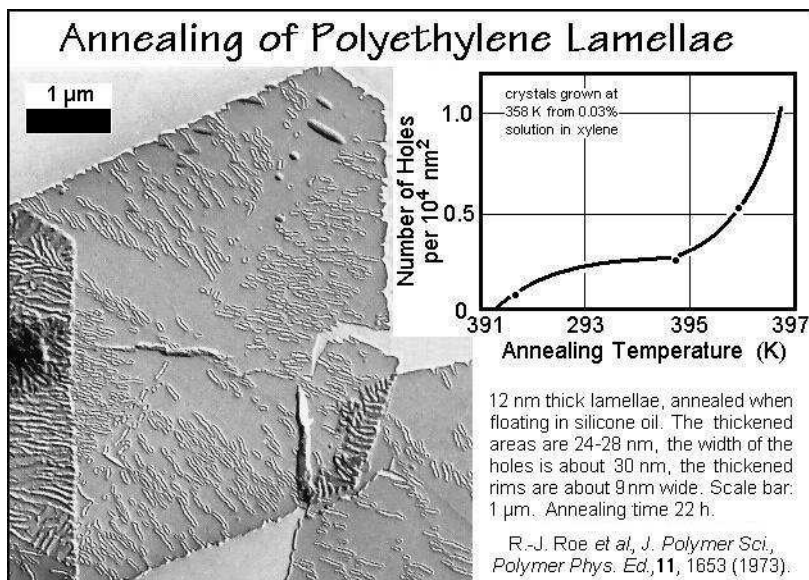


Fig. 6.77

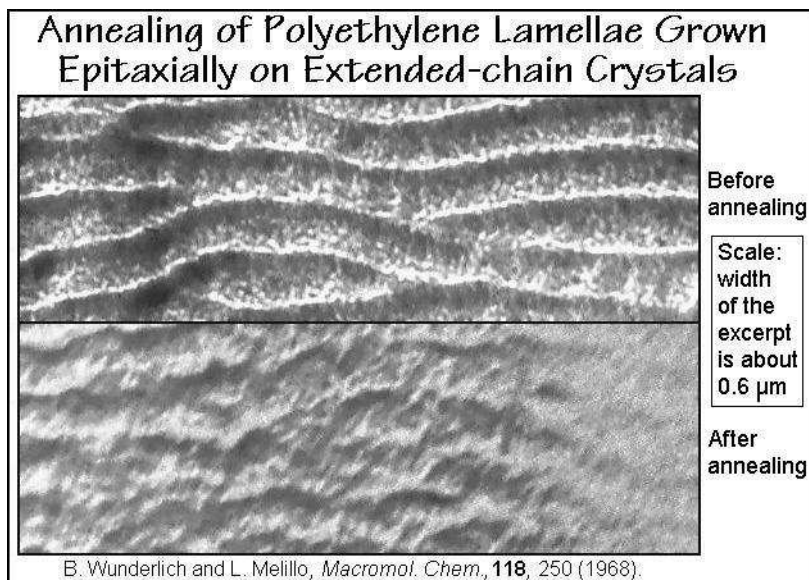


Fig. 6.78

This short summary of microscopic observations of annealing reveals that there are at least two processes that must be considered when interpreting the macroscopic annealing experiments of thermal analysis: (1) A crystal perfection within the original crystal morphology. (2) A change in crystal shape towards equilibrium, which may involve several stages of crystal thickening.

The macroscopic thermal analysis, furthermore, proves that it is also common for melting of the original crystals to be followed by recrystallization to a more stable morphology. Finally, some crystals may have different crystal structures at high temperatures and, thus, show polymorphic transitions on annealing. Annealing of polymers to a more stable state as shown in Fig. 6.79, simply expressed by a decrease in free enthalpy, may thus be a rather complicated process (compare to Sect. 2.4.2).

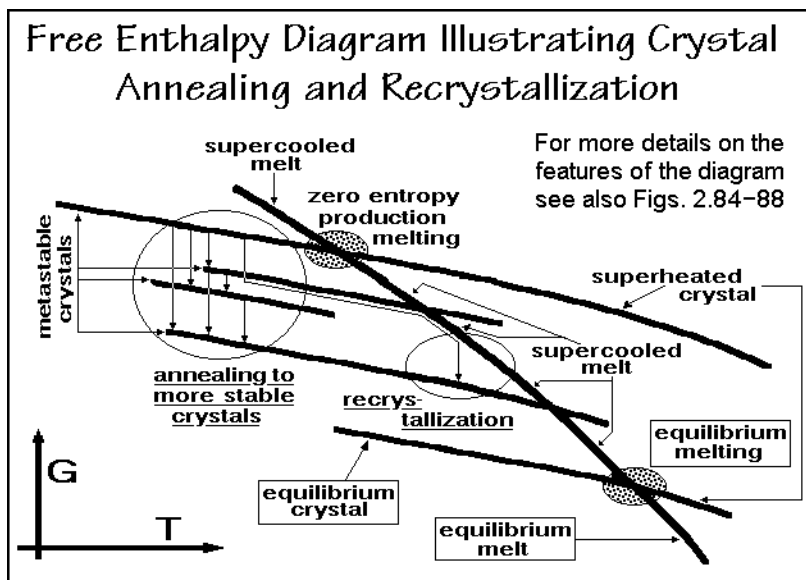


Fig. 6.79

On discussing the melting of polyethylene in Sect. 6.2.1, the annealing of samples on heating was observed in curves A and B of Fig. 6.22 to cause a decrease in melting temperature with heating rate. In case the kinetics of rearrangement of the crystals could be outrun, a constant zero-entropy-production melting temperature was obtained. At the same time, the slower heating rate experiments give some information about the annealing process. Besides using fast heating to minimize reorganization, it is possible to stop the thickening of crystal lamellae by immobilizing the amorphous phase. Two examples are shown in Fig. 6.80, one for nylon 6, the other for polyethylene. For nylon 6 the  $-NH$ -groups of the amorphous nylon (see Fig. 1.18) are methylmethoxylated to  $-N-CH_2-O-CH_3$ , so that they cannot be moved into the crystal. Figure 6.80 implies that after 4 h, the single, heating-rate independent, sharp melting peak is related to the zero-entropy-production melting. On longer reaction, this peak broadens because of reaction with the crystals. In addition, the melting point seen after 4 h has also increased by about 3 K due to the permanent change of the molecules, or possibly due to a change of the initially present  $\gamma$ -crystals to the higher melting  $\alpha$ -crystals (see also Sect. 6.2.6). For immobilizing the amorphous polyethylene, cross-linking by irradiation has been used, as also shown in Fig. 6.80. The irradiation caused a similar effect as fast heating shown in curves A and B in Fig. 6.22.

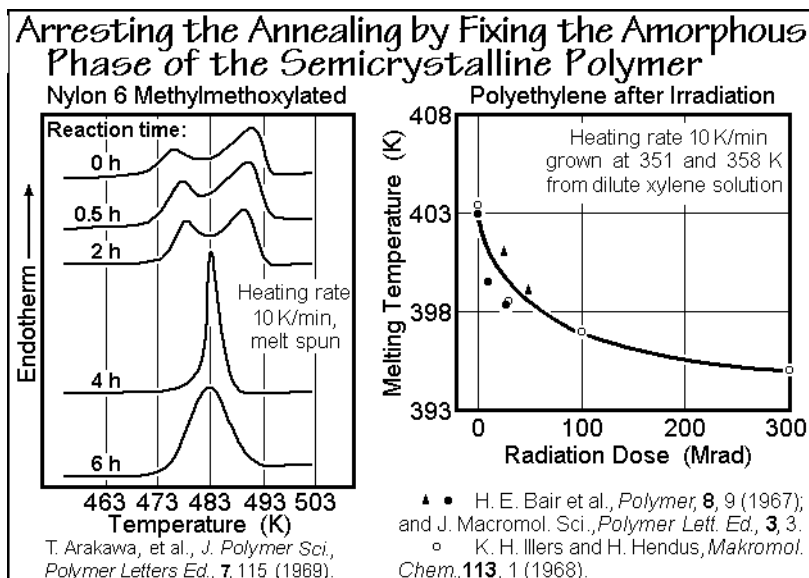


Fig. 6.80

In the following figures, further experiments are linked to the annealing and recrystallization of a number of additional polymers. In Fig. 6.81 the increase of lamellar thickness is illustrated on the example of solution-grown polyethylene. The crystals were collected in dried mats. The graph on the right side allows a comparison with data on melt-crystallized and annealed polyethylene (see also Sect. 5.2). Sufficiently mobile and flexible molecules, such as polyethylene, can thicken by chain

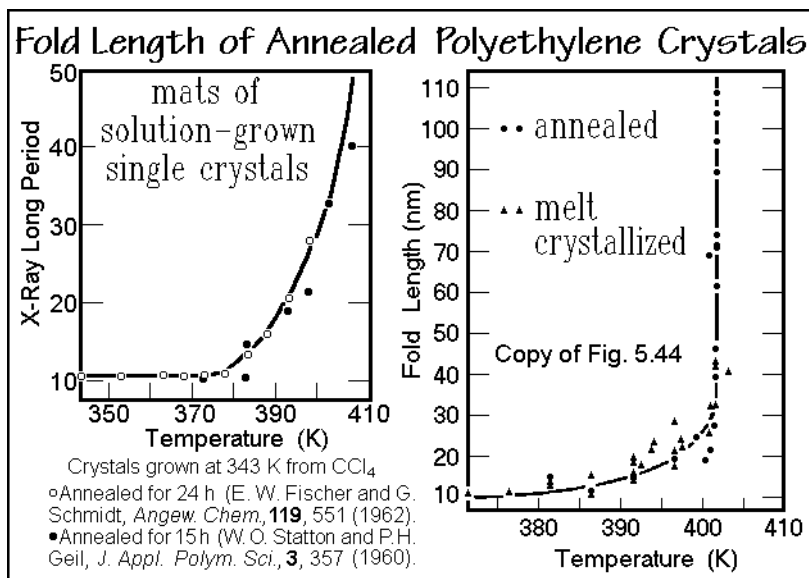
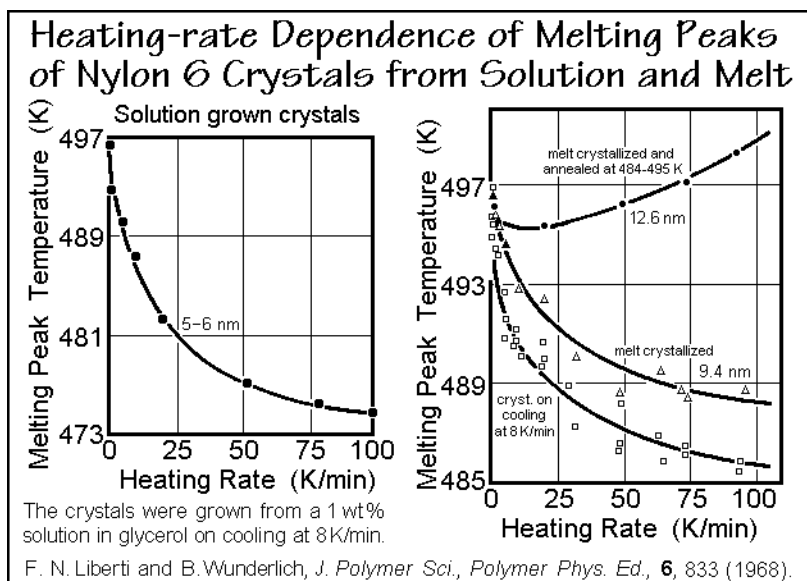


Fig. 6.81

extension, either on crystallization, or on subsequent annealing at higher temperatures. For polyethylene, long-time annealing at temperatures above about 400 K can reach thicknesses of over 100 nm. Full extension of the polyethylene crystals, however, needs the intervention of the hexagonal condic phase (see Fig. 5.156).

Of the polyamides, nylon 6 is perhaps best studied. Figure 6.82 shows the similarity of the melting of solution-grown  $\alpha$  crystals of nylon 6 lamellae with polyethylene in Fig. 6.22. The initial crystal thickness was only 5–6 nm, accounting for the larger drop in melting temperature. The melt-crystallized nylon 6 is initially about 10 nm in fold length and leads to the correspondingly higher zero-entropy-production melting temperature. On annealing, the perfection gained during slow



**Fig. 6.82**

heating leads on faster heating to a small amount of superheating. The curves in Fig. 6.82 show only the temperature of the last (major) melting peak. As many as four lower-temperature melting peaks can be observed, as are illustrated in the summary in Fig. 6.83. The  $\alpha$  form has a somewhat higher melting temperature ( $\bullet$ ) than the  $\gamma$  form ( $\circ$ ). The horizontal appearance of lines 1 and 2 are an indication of reorganization of the initially less-perfect crystals, as in Fig. 6.82 for the  $\alpha$  crystals. Lines 3 and 4 are closer to zero-entropy-production melting. Line 5, finally, refers to the “annealing peak.” It corresponds to small crystals that form between prior grown crystals. They melt somewhat above the crystallization or annealing temperature. As seen in Fig. 8.62, most melting temperatures shift when changing the heating rate. On reorganization, the peak sizes will also change. Sometimes, an attempt is made to extrapolate the assumed zero-entropy-production melting points (lines 3 and 4) to the point of intersection with the line that marks the position of  $T_m = T_c$  to estimate the equilibrium melting temperature,  $T_m^\circ$ . This is only safe on using the zero-entropy-production melting temperatures, on avoiding superheating of crystals grown at higher

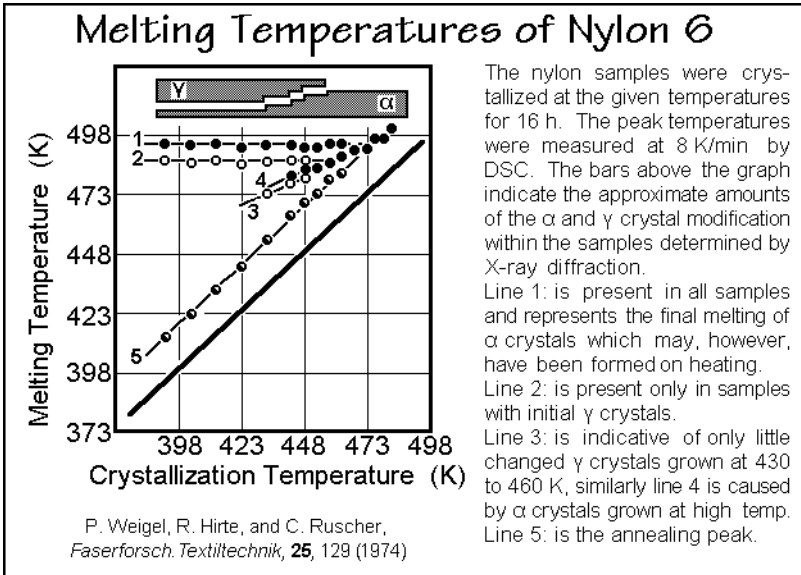


Fig. 6.83

temperature, and if it is proven that the extrapolation is linear. These limits are usually not understood, and as a result, the extrapolation to  $T_m^\circ$  is often imprecise.

In Figs. 6.84–87, summary graphs of the melting temperatures of isotactic polystyrene, poly(vinylidene fluoride), rubber, and poly(oxypropylene) are reproduced. The data were obtained by DSC and dilatometry. All graphs show characteristic horizontal lines of crystals annealed during heating, and annealing peaks close to

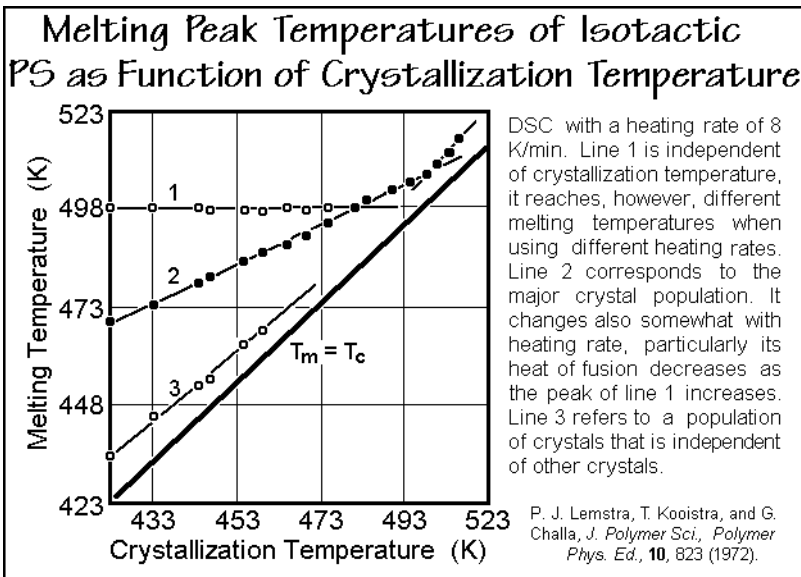


Fig. 6.84



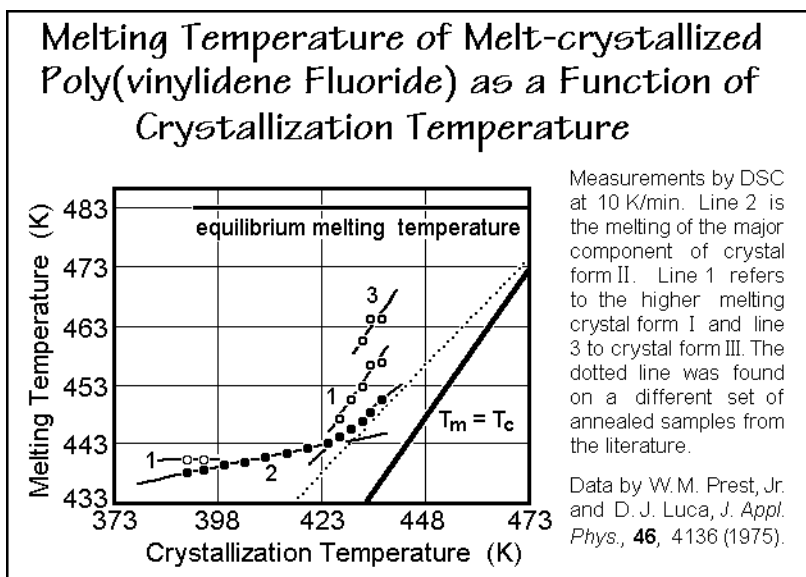


Fig. 6.85

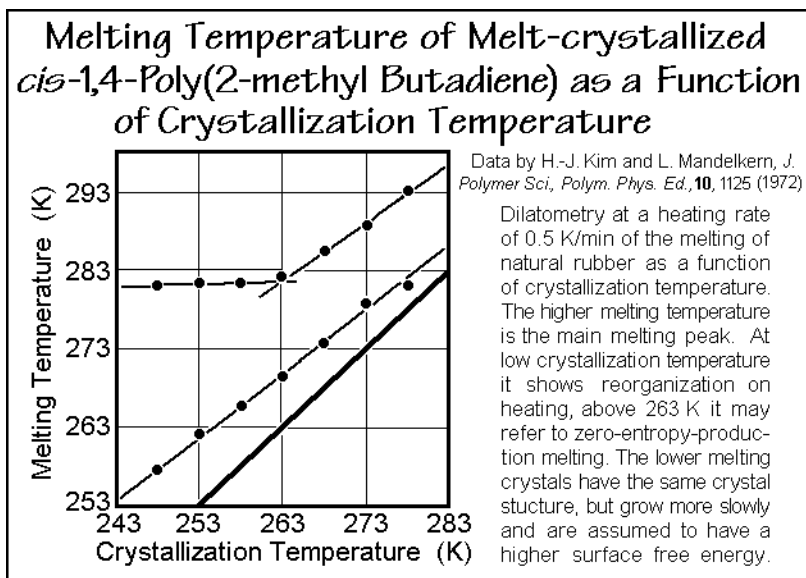
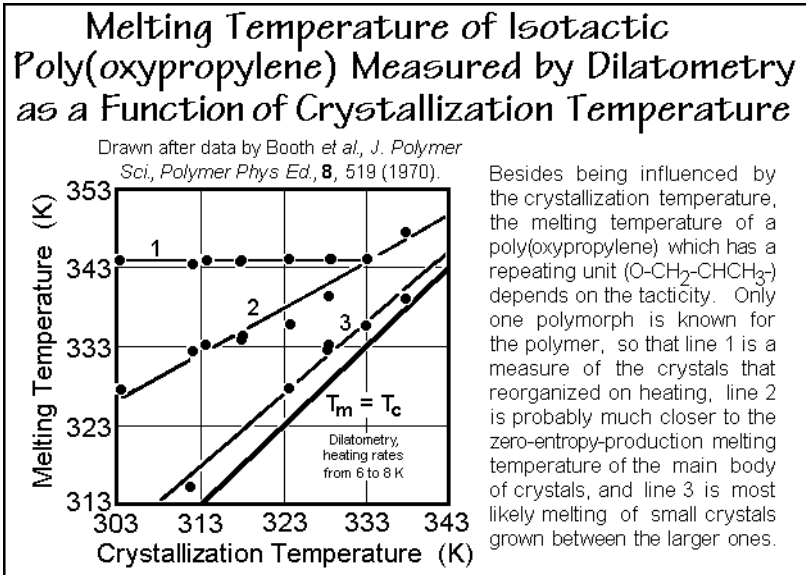


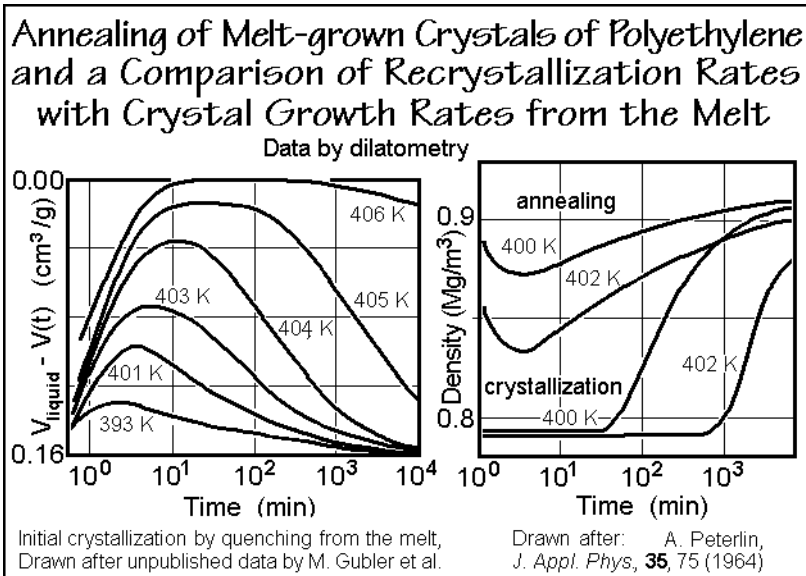
Fig. 6.86

$T_m = T_c$ . Complications arise when crystal polymorphs are possible, as seen in poly(vinylidene fluoride). The polymorphs must be identified by X-ray diffraction, as described in Appendix 15. Also, the appearance of the melting peaks closer to the zero-entropy-production condition is characteristic for different polymers and may depend on the heating rate.

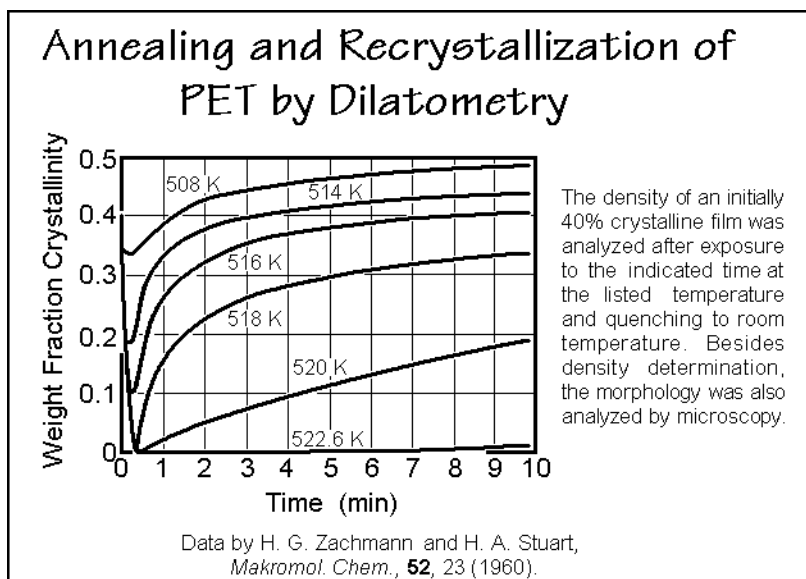


**Fig. 6.87**

To illustrate recrystallization as a frequent occurrence in addition to reorganization and lamellar thickening, the behavior of melt-grown polyethylene crystals and poly(ethylene terephthalate) are chosen as examples in Figs. 6.88 and 6.89. The free enthalpy diagram for such process is given in Fig. 6.79. The crystals melt partially or completely when reaching the annealing temperature, indicated for polyethylene in Fig. 6.88 by the increase in specific volume and decrease in density. This is followed



**Fig. 6.88**

**Fig. 6.89**

by recrystallization. The larger crystals which do not melt can still anneal and the newly grown material is enlarging the remaining crystals and also anneal. The polymer crystals undergo Ostwald ripening<sup>1</sup>. Of interest is the larger rates of recrystallization when compared to melt crystallization at the same temperature in the right graph of Fig. 6.88.

The amount of recrystallization for poly(ethylene terephthalate), PET, in Fig. 6.89 increases with annealing temperature, as in polyethylene. At 520 K, the thin film of PET could be melted almost completely by fast heating. Thin films were chosen for quick temperature equilibration at constant temperature. The analysis of crystallinity after quenching to room temperature showed that relatively quick melting is followed by recrystallization. Above 518 K practically all crystals melt first. This temperature is at the beginning of the melting peak of a standard DSC trace, as given in Fig. 3.92. A qualitative correspondence exists between the dilatometry of 1960 and the analysis of the instantaneous, complete melting of thin films pressed against a hot surface at 518 K [54]. The completion of melting was identified by the nature of the viscous flow at the high temperature and by dilatometry and DSC after quick quenching between cold plates. In the same research isothermal primary melt crystallization was shown to be followed by insertion of secondary lamellar stacks and continuous crystal perfection by time-resolved small-angle X-ray scattering and DSC at different heating rates. The major high-melting peak at 525 K was shown not to be due to the originally grown crystals, but was changed due to recrystallization and annealing.

<sup>1</sup> F. Wilhelm Ostwald (1853–1932), Professor at the University of Leipzig, Germany (1887–1906). Organized physical chemistry as a major discipline of science, Nobel Prize in 1909 (work on equilibria and reaction rates). The rule states that initial, small crystals disappear in time and energetically favorable, large ones appear [Z Phys Chem 22: 289 (1897)].

More quantitative information than by calorimetry in Fig. 6.89 could be gained recently by the use of ultra-fast, thin-film calorimeters based on integrated circuits (see Appendix 10) [55]. Figure 6.90 illustrates the faster recrystallization than crystallization from the random melt, as was also seen for polyethylene in Fig. 6.88.

A special effect in changing the melting characteristic is transesterification, illustrated in Fig. 6.91. Transesterification is found in polyesters, as described in

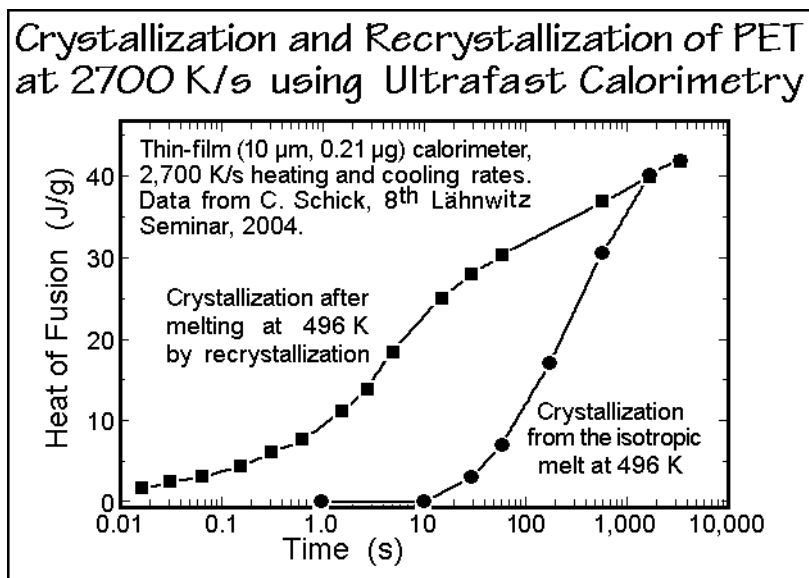


Fig. 6.90

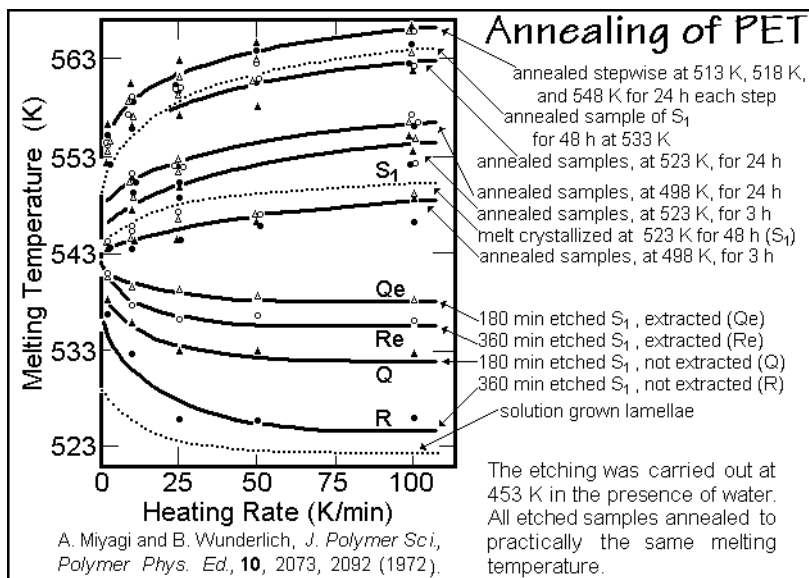
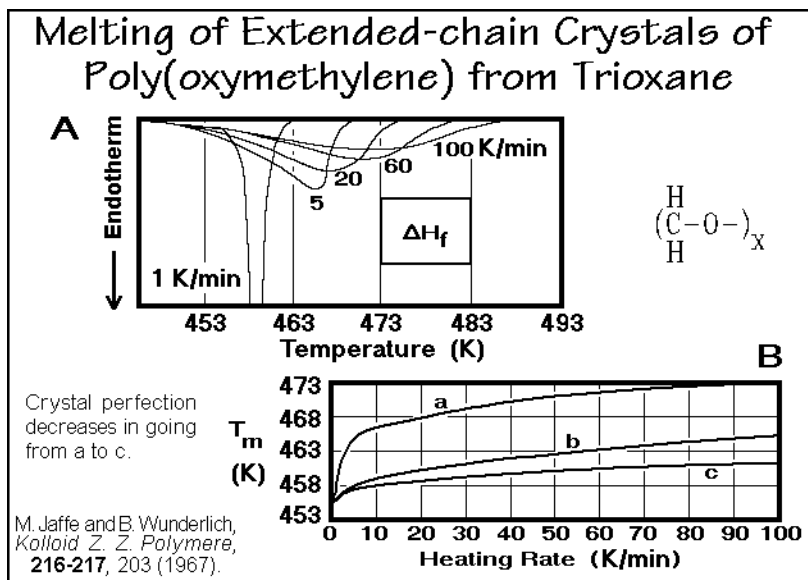


Fig. 6.91

Sects. 3.1 and 3.4 and involves the possibility to change the backbone chain structure to accommodate better crystallization. Figure 6.91 contains a collection of annealing studies by DSC, analyzed as a function of the heating rate. The dotted lines refer to standard crystals grown from solution, from the melt (isothermally grown at 523 K, sample  $S_1$ ), and obtained after annealing of sample  $S_1$  at 533 K. The three curves illustrate decreasing to increasing melting peaks with heating rates, analogous to the polyethylene and nylon 6 data in Figs. 6.22 and 6.82, respectively. In addition, the sample  $S_1$  was etched with superheated steam at 453 K to remove the amorphous segments to increasing amounts. The lamellar morphology of the remaining crystalline PET is seen in Fig. 5.65, and the thermal properties are illustrated in Fig. 6.91. Depending on the degree of etching and the remaining amount of amorphous, low-molar-mass debris, the zero-entropy-production melting temperature decreased. Annealing these etched samples R, Q, Re, and Qe, identified by different symbols, lead to repolymerization to similar high-molar-mass crystals by transesterification without intermediate melting, as seen by the upper lines. A similar industrial process is known as solid-state polymerization and used for tire-yarn improvement. Transesterification, thus, is important in annealing of PET crystals.

#### 6.2.4. Melting of Poly(oxymethylene)

Poly(oxymethylene), POM, is a polymer with well-known melting behavior [56]. Fibrous, extended chain crystals can be produced by crystallization during polymerization, as described in Figs. 3.104 and 3.105. These extended-chain crystals can superheat on melting due to their slow melting rate, as is also seen for extended-chain crystals of polyethylene in Fig. 6.21. The DSC melting endotherms in Fig. 6.92 start for all heating rates at about the same temperatures, but the peak- and melt-end



**Fig. 6.92**

temperatures increase, indicating a kinetic effect. The plot of melting-peak-temperature versus rate of heating is shown in graph B and reveals less superheating for imperfect crystals. The estimated equilibrium melting temperature is 457 K.

The next thermal analyses are for solution-grown dendrites, hedrites, and melt-grown lamellae, represented by Figs. 6.93 and 6.94. The dendrites melt at much lower temperatures than the extended-chain crystals and show multiple melting peaks.

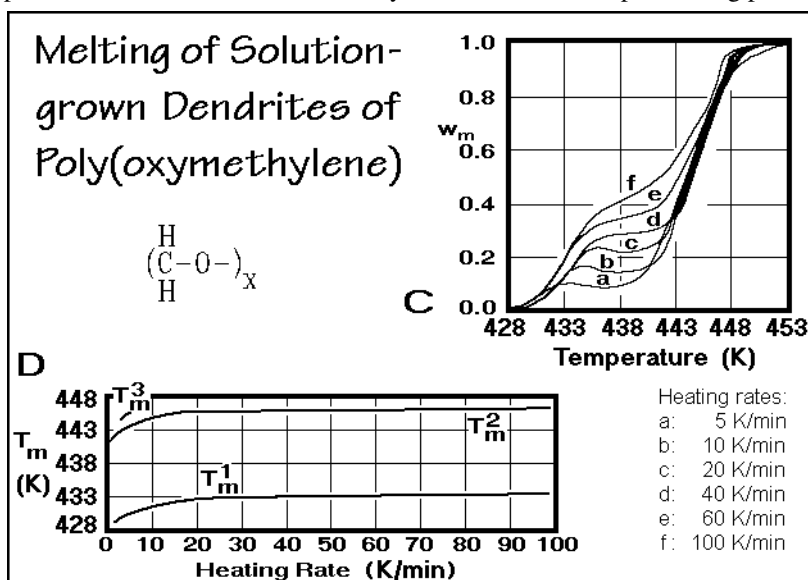


Fig. 6.93

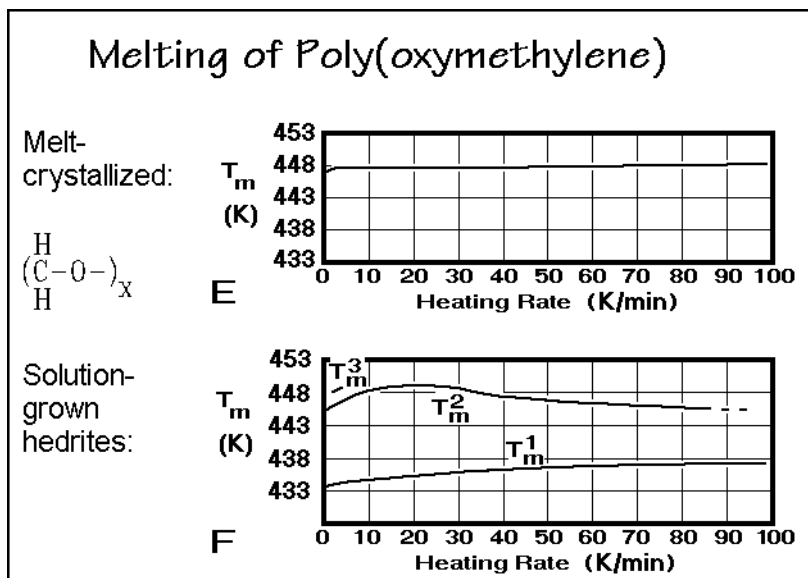


Fig. 6.94

Graph C, which shows the weight fraction of the melted polymer,  $w_m$ , illustrates that as the heating rate increases from 'a' to 'f' more melting of the not perfected crystals occurs at  $T_m^1$ . The zero-entropy-production melting can be seen at about 433 K. Melting peak  $T_m^3$  is seen only at the slowest rate which allows enough time for two recrystallizations during the analysis.

Curve E in Fig. 6.94 shows the minimal change in melting peak temperatures for crystals grown from the melt. These crystals do not reorganize significantly on heating. They remain metastable during the whole analysis. Their zero-entropy-production  $T_m$  is 448 K, close to that found for the recrystallized dendrites. Finally, the dendrites in Graph F of Fig. 6.94 are also grown from solution. Their crystal morphology is represented by stacks of lamellar single crystals as seen in Fig. 5.50. As seen in rhw dendrites, the dendrites also have triple melting peaks in their actual DSC traces. Their higher perfection is indicated by the higher  $T_m$  for zero-entropy-production melting ( $\approx 438$  K) than found for dendrites ( $\approx 433$  K). The thermal analysis of poly(oxyethylene) was an early example of a complete coverage from superheating to lamellar melting with major reorganization bracketing equilibrium and different zero-entropy-production melting temperatures.

### 6.2.5 Melting of PEEK

Poly(ether ether ketone), PEEK, poly(oxy-1,4-phenyleneoxy-1,4-phenylenecarbonyl-1,4-phenylene),  $(O-C_6H_4-O-C_6H_4-CO-C_6H_4-)_x$ , can be considered to be made up of three straight segments joined into a zig-zag structure, each with a phenylene group in its center. The one (O-)group and two (C=O-)groups which link the rigid segments allow rotations about their bonds and induce flexibility. In addition, the phenylene groups may flip about their twofold symmetry axis. As a high-temperature polymer, PEEK is often used as a matrix in composites. The overall behavior of PEEK [57] has similarities to poly(ethylene terephthalate), discussed in Sect. 6.2.2. The DSC-curve in Fig. 6.95 reveals that on quenching, crystallization can be avoided. The cold crystallization occurs above the glass transition, and crystallization and melting peaks have close to the same size. A more precise analysis would have to take into account the change of the heat capacities and the heat of fusion with temperature, as outlined in Fig. 4.80. The graph at the bottom of Fig. 6.95 represents a summary of the melting-peaks observed on crystallization at different temperatures, as detailed in Fig. 6.96. The line  $T_m = T_c$  corresponds to zero-entropy production for crystallization and melting, and was extrapolated to the experimental line of data to give an estimate of the equilibrium,  $T_m^o$ , of about 668 K (compare with other polymers in Figs. 6.83–87, but see also the mentioned cautions in the discussion of  $T_m^o$  on pp. 660 to 61). A model of primary and secondary crystallization of PEEK was developed to explain the various melting peaks [58].

The top DSC curves in Fig. 6.96 illustrate the melting behavior after cold crystallization at different temperatures. Enough time was allowed at the crystallization temperature to complete the crystallization and also to undergo annealing at the same temperature. The lower melting crystals give rise to the usual annealing peaks. They are representative of smaller crystals which may grow in the spaces left by the earlier grown, high-melting crystals. The melting peak at high temperature of the

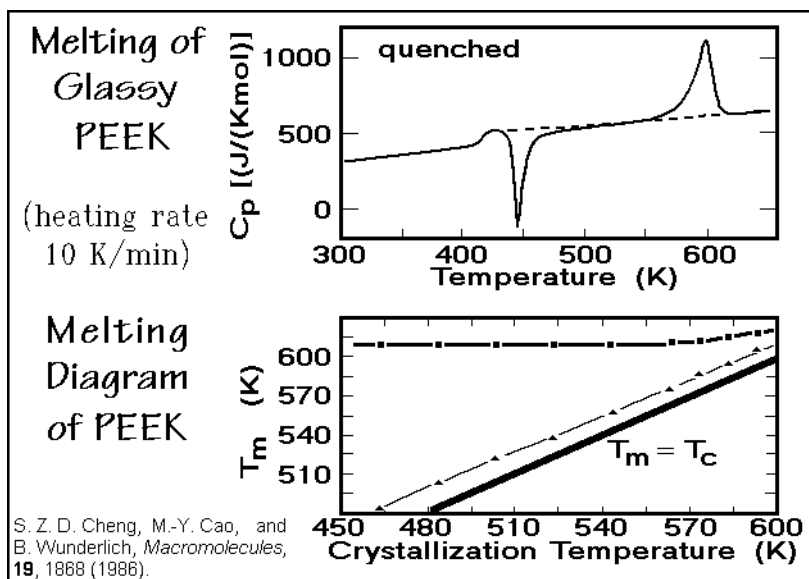


Fig. 6.95

cold-crystallized samples, seen in the upper graph of Fig. 6.96, does not change with the crystallization temperature.

The DSC curves at the bottom of Fig. 6.96 represent an analogous set of crystallization experiments, but grown from the melt. The melt-crystallized polymer shows higher perfection in both the annealing peak and the melting peak for the primary crystals. Ultimately, both peaks are expected to come together.

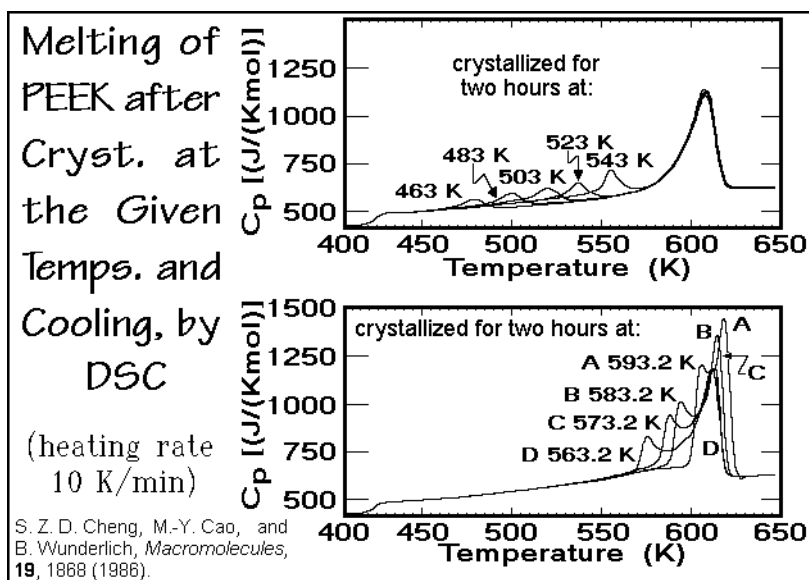


Fig. 6.96



The bottom DSC-curves in Sect. 3.6.7 (Fig. 3.98) show the DSC curves of the same sample of PEEK as analyzed in Fig. 6.96, but obtained by immediate heating after partial crystallization at a temperature close to case B. The curves indicate that the high-melting crystals grow first, the low-melting ones later, and that there is an intermediate perfection of crystals that does not show up in the DSC traces after crystallization for long times. On cooling at increasing rates, it was found that the rigid-amorphous fraction increases, as is discussed in Sect. 6.3.4.

A more detailed analysis involves DSC, TMDSC, quasi-isothermal TMDSC, and TMDMA [42,59] (for other TMDMA experiments see also Figs. 6.51 and 6.58). Figure 6.97 is a comparison of the apparent total  $c_p$  from standard DSC and the reversing  $c_p$  from TMDSC at the same heating rate, and quasi-isothermal TMDSC at short and long times after heating to  $T_o$ . All measured apparent, specific heat

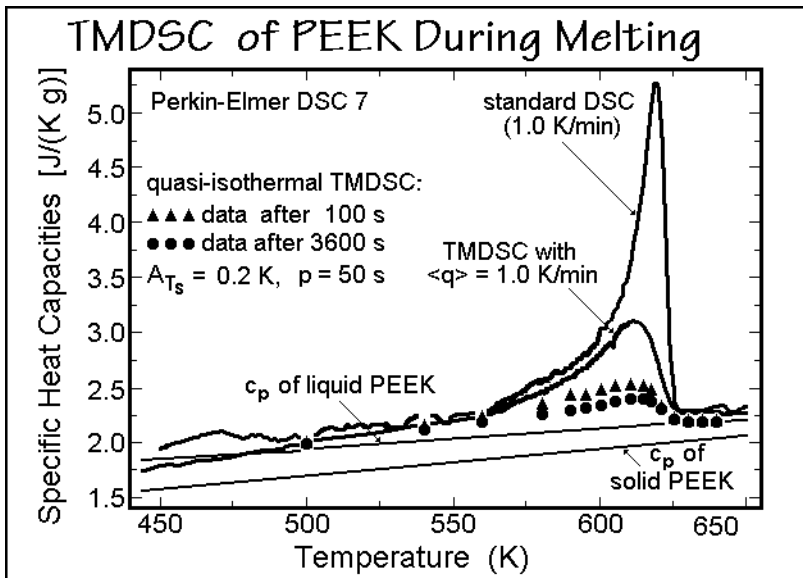


Fig. 6.97

capacities between 500 and 620 K are higher than the heat capacity of the liquid and, thus, must contain latent heat contributions. Compared to PET of Fig. 3.92, the reversing endotherm of melting is twice as high, and because of the identical heating rates for DSC and TMDSC, the melting peak positions are identical.

Slow, primary crystallization of PEEK is analyzed in Fig. 6.98 using long-time, quasi-isothermal TMDSC at 606.5 K, and in Fig. 6.99, using TMDMA at 605 K. The analysis of the TMDSC data is further illustrated in Fig. 6.100 and reveals an increase in heat capacity with time and crystallinity, instead of the decrease expected from a lower heat capacity of a semicrystalline sample. The crystallinity is derived from the integral of the total heat-flow rate,  $\langle \Phi(t) \rangle$ , with time in Fig. 6.98. From Fig. 6.99 it can be seen that the reversing melting reaches a maximum before the crystallization is complete. These data suggest that both crystallinity and crystal morphology need to be considered for the analysis of the reversing melting and crystallization.

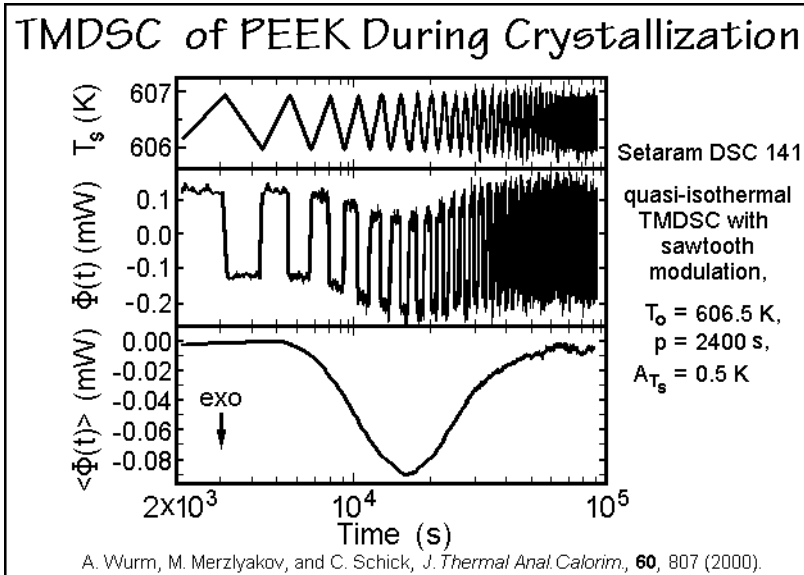


Fig. 6.98

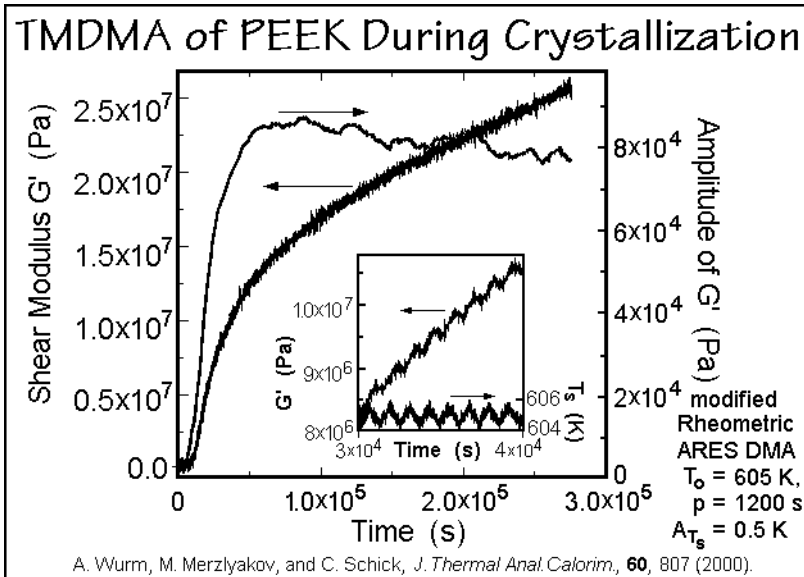
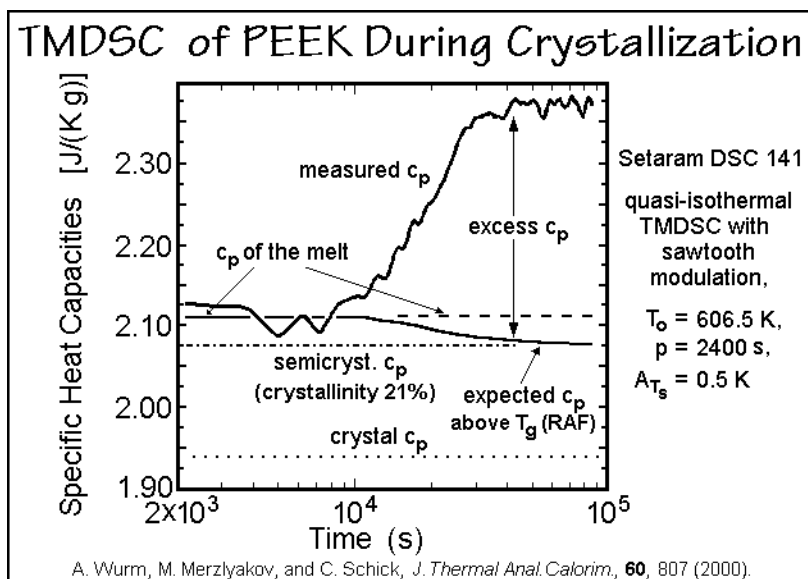


Fig. 6.99

A considerable secondary crystallization, typical for PEEK, is seen in Fig. 6.99. Only about 50% of the total crystallinity can be assigned to primary crystallization. Secondary crystallization starts at about 28 h ( $\approx 10^5$  s). At that time, the reversing amplitude of the storage modulus is almost constant. At later times, it decreases slowly, indicating very different processes for primary and secondary crystallization.



**Fig. 6.100**

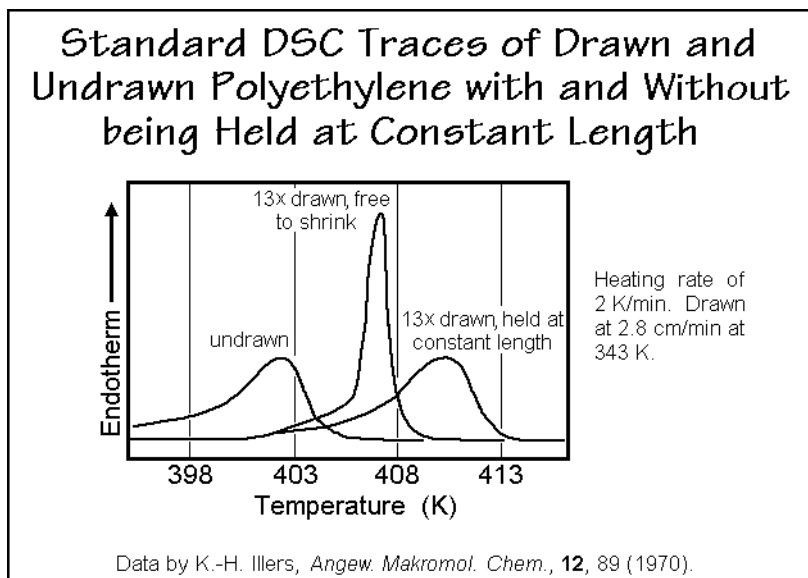
Note that this decrease in reversing melting is similar to the behavior of poly( $\epsilon$ -caprolactone) in Fig. 6.58, and contrary to the behavior of PEN seen in Fig. 6.51.

The decrease in the quasi-isothermal, apparent, reversing  $c_p$  in Fig. 6.97 was followed at 603 K and revealed that the melting endotherm reaches its steady state quicker than the crystallization exotherm. Combining kinetic information on the integral crystallinity of Fig. 6.99 derived from the storage modulus and the change of the reversing melting determined from the TMDSC, the two slow processes were proven to be independent of each other. This supports the assumption that local equilibria in an overall metastable phase structure cause the reversible melting.

## 6.2.6 Melting of Fibers

Specially difficult systems are represented by fibers of macromolecules. All the topics treated in the prior sections must be considered under the additional aspect of the presence of crystal deformations caused by the drawing process (see Sect. 5.2.6 and 5.3.6) and possible strain retained in the amorphous areas (see Sect. 6.3.3), as well as the existence of strain-induced mesophases (see Figs. 5.69–72 and 5.113–115).

An example of the changes in the thermal analysis results on drawing is given in Fig. 6.101. An undrawn sample as a reference is compared with a drawn sample, measured at constant length and free to shrink. The big difference between a drawn sample free to shrink during analysis, and one restrained can naturally only be caused by differences in the melting or/and annealing behavior since the actual polymer is the same. In fact, extensive experimentation with fibers of known crystal sizes which were either cross-linked to avoid reorganization or etched to remove the amorphous fraction, suggests that the outcome of both experiments with the drawn fibers in Fig. 6.101 is based on the increase of the melting temperature due to residual

**Fig. 6.101**

orientation in the amorphous fraction (see Sect. 5.6). The sharper melting peak of the unrestrained fiber is due to a relaxation of the oriented amorphous part while melting. The restrained fibers, in contrast, lose their orientation more gradually and keep the superheating to higher temperature (see Fig. 2.120).

The special behavior of fibers is particularly well investigated on gel-spun, ultra-high-molar-mass polyethylene, UHMPE. The as-polymerized UHMPE shows a much higher amount of reversing melting than the lower-molar-mass folded-chain crystals of PE, described in Sect. 6.2.1, or the extended chain crystals of PE and its oligomers of Fig. 6.28. Figure 6.102 displays DSC and TMDSC traces of nascent UHMPE and illustrates the changes on recrystallization from the melt and on second heating [60]. The apparent reversing heat capacity exceeds the standard DSC result on the low-temperature side of the melting peak. On crystallization from the melt, the reversing latent heat is less than on first heating, but increases on reheating, as was also seen for the lower-molar-mass PE in Fig. 6.30, just that the excess  $C_p$  on cooling and second heating is higher than for the lower-molar-mass PE, despite the likely lower crystallinity for the UHMPE. The frequency dependence of the nascent UHMPE was also analyzed. It showed a decrease in excess heat capacity reaching the heat capacity measured by standard DSC at 397 K, but at the peak temperature, at 411 K, the maximum of the reversing heat capacity retained is  $67 \text{ J K}^{-1} \text{ mol}^{-1}$  (compare to Fig. 6.31). Model calculation of the frequency dependence of the reversing excess  $C_p$  allowed in this temperature range to speculate about a number of different irreversible and reversible processes. Quantitative information may be available as soon as the morphology is known for the specific sample.

On gel-crystallization from solution, the UHMPE obtains a lamellar crystal morphology with 13-nm-thick crystals. Stretching such gel-crystallized samples below the melting temperature leads to big changes in the sample morphology.

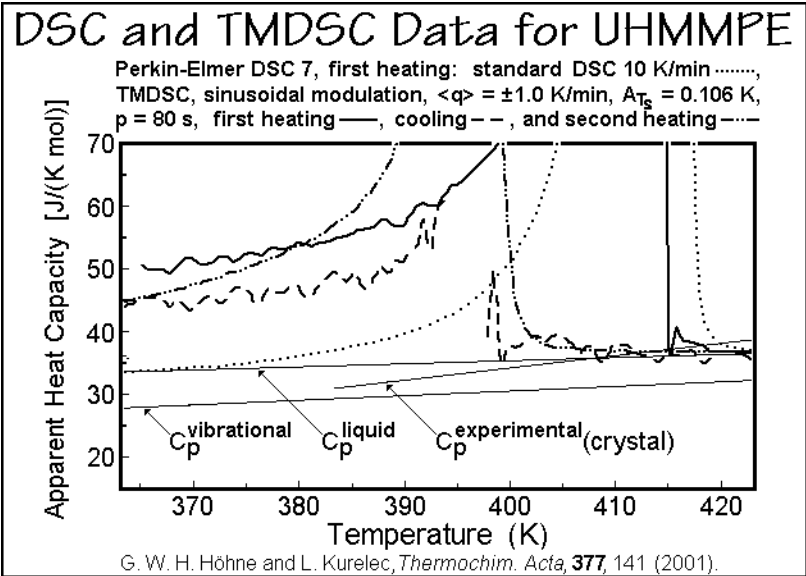


**Fig. 6.102**

Details on calorimetry coupled with information on morphology, full-pattern X-ray analysis (see Fig. 6.4), solid-state NMR (see Figs. 5.157 and 5.158), mechanical properties, and quantitative TMDSC were derived for a number of commercial gel-spun UHMMPE fibers. The structure of an UHMMPE gel-spun fiber is rather complicated and changes on heating with constraint, as seen in Fig. 6.103. It consists of a metastable system of four interconnected, recognizably different phases. At low

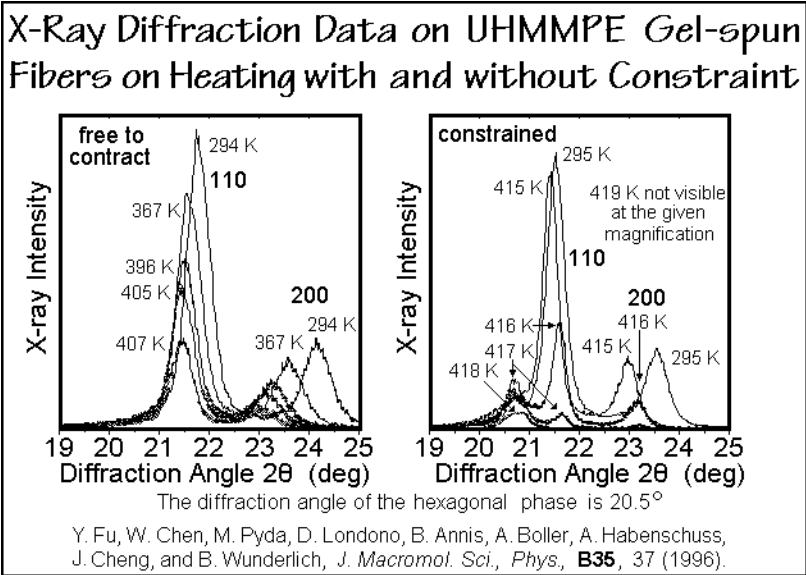


**Fig. 6.103**

temperature, the orthorhombic PE is the major and only stable phase (typically 60–80%). Also present are some monoclinic crystals of PE (5–15%). The amorphous phase is as little as 1–10%, while an intermediate, oriented phase makes up the difference. The three unstable phases are arrested in a metastable state by their molecular links to the orthorhombic crystals. The X-ray signal of the monoclinic crystals starts to disappear at 363 K. On heating of the fibers so that they are free to shrink, the whole structure collapses when the orthorhombic crystals melt at about 415 K. The intermediate, oriented phase was shown by solid-state  $^{13}\text{C}$  NMR to consist mainly of *trans* conformations which are at room temperature intermediate in mobility between the liquid and the crystal as illustrated in Figs. 5.157 and 5.158. A solid-state  $^{13}\text{C}$  NMR analysis as a function of temperature gave for typical, gel-crystallized UHMPE fibers that at room temperature 7% monoclinic phase which disappeared at about 380 K. Its 78% orthorhombic crystals and about 15% intermediate phase increase somewhat to make up the loss in monoclinic phase at 380 K. The orthorhombic phase showed melting from 393 K (75%) to 413 K (72%) while the intermediate phase still increased in amount (25% at 393 K and 28% at 413 K) [61]. The amorphous phase remained negligible throughout the experiment at  $\approx 1\%$ .

The calorimetry of the UHMPE fibers is beset by an additional difficulty due to the considerably lateral expansion on shrinking of the fibers on melting as is illustrated in Fig. 6.104. In case the fiber shrinks from an extension of 100 $\times$  to its original length, the diameter needs to expand by a factor of 10 and a lateral constraint is introduced when the lid of the DSC pan was crimped onto the fibers which is sufficient to hinder longitudinal shrinkage and may even be sufficient to deform the DSC pan and invalidate the calibration of the run [62]. In the presence of such constraints, the orthorhombic crystals superheat sufficiently and undergo the phase transition to the hexagonal mesophase, starting at about 415 K, as seen from the X-ray

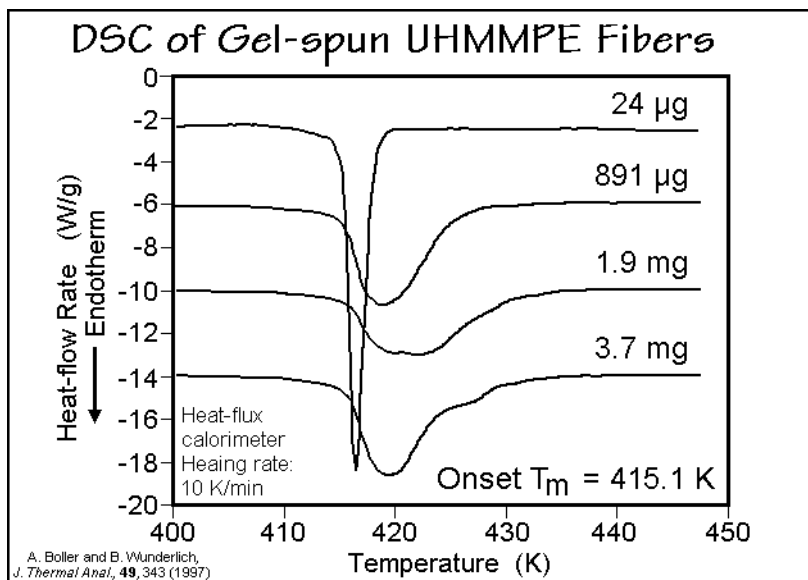


Fig. 6.104

data in Fig. 6.103. Figure 6.104 illustrates that with decreasing sample weight, the melting range decreases. For the smallest mass, finally, there is practically no constraint, and direct melting of the orthorhombic crystals is approached, in agreement with Fig. 6.103.

Figure 6.105 illustrates the heat capacity between the glass transition and the beginning of melting, as measured by DSC, using a special step-scan modulation mode of overlapping 20 K heating and cooling steps for two types of samples in a comparison with ATHAS Data Bank information [63]. The fiber A is gel-spun without post-stretch annealing, while the three fibers labeled B are typical commercial

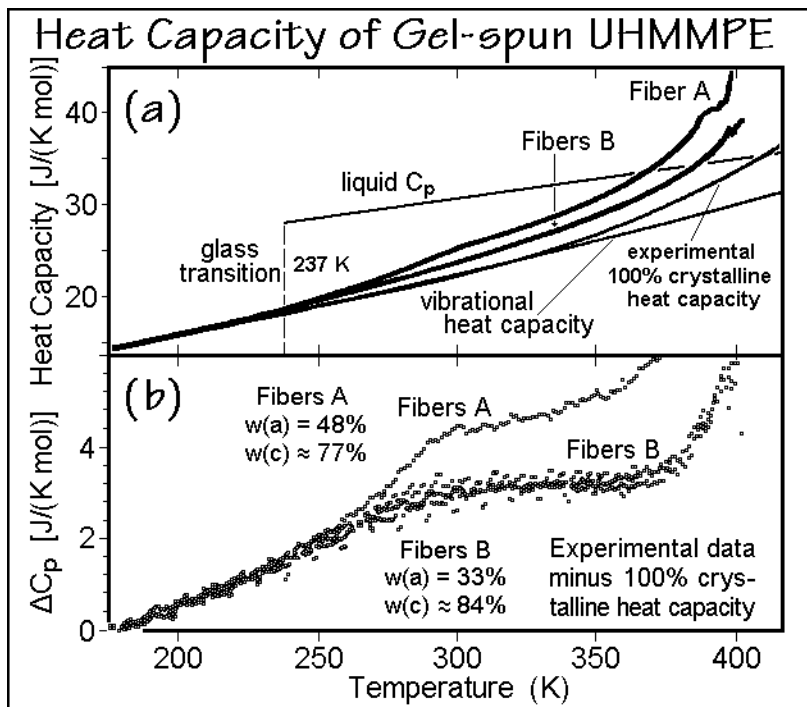


Fig. 6.105

fibers. Subtracting the heat capacity of the 100% crystalline PE (which includes the vibrational and the *trans-gauche* contributions within the crystal) from the measured  $C_p$  leads to the data in Fig. 6.105(b). As expected for drawn polymers, the glass transition, which starts at about 190 K, is broadened and extends to room-temperature. The increase in heat capacity,  $\Delta C_p$ , is a measure of the noncrystalline material, but does not agree with crystallinity from heat of fusion. To account for the discrepancy, the amorphous and the intermediate, oriented phase must contribute to  $\Delta C_p$ . To also bring the heat of fusion into agreement with the structural analyses, both the crystalline and the intermediate phase must have a latent heat. Mass, heat capacity, and energy balance suggest for fibers B and A a heat of disordering of the intermediate phase of 30 and 50% of the orthorhombic PE, respectively [63]. From Fig. 6.105, one can conclude that melting begins at about 375 K, but is initially reversible.

Figure 6.106 shows the TMDSC of fibers B using a sawtooth modulation and evaluation with the standard DSC technique described in Appendix 13. On first heating with constraint, reversibility exists to 405 K, which includes a substantial decrease in the orthorhombic crystals and compensating increase in the intermediate phase. On second heating, after recrystallization, the DSC and TMDSC traces are similar to the sample of Fig. 6.102 and contain only orthorhombic crystals. In this

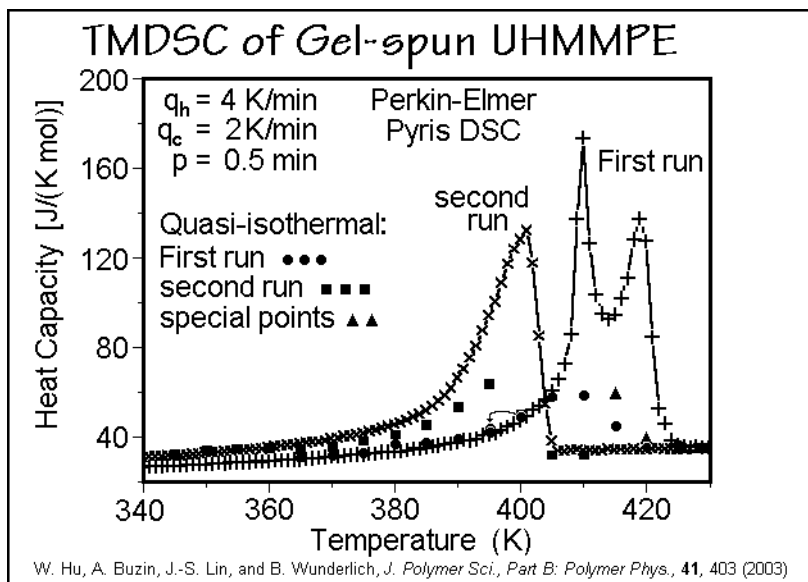


Fig. 6.106

case, complete reversibility reaches to 360 K, as can also be derived from Fig. 6.105. The maximum of the reversing excess heat capacity is double as much as for the polyethylene of lower molar mass in Fig. 6.30, and occurs at higher temperature.

As one goes into the double melting peak of Fig. 6.106, which was ascribed to melting of orthorhombic crystals, transition into the hexagonal phase, and melting of the hexagonal phase, the reversible contributions ( $\bullet$ ) are only a fraction of the reversing  $C_p$  ( $+$ ). Most of the reversibility of the transition must involve the orthorhombic, metastable morphology and employ local processes which involve the intermediate, oriented phase since the amorphous phase is still negligible at 413 K. It may even be speculated that the decrease of the reversible excess heat capacity beyond 410 K is a direct measure of the disappearance of orthorhombic and intermediate, mobile phase. The hexagonal phase is melting irreversibly. The special points in Fig. 6.106 were taken out of the experimental sequence by direct heating from room temperature. They indicate changes during the annealing through the stepwise increase in temperature. The curved arrow connects a repeat point ( $\bullet$ ) after the analysis at 400 K, proving reversibility of the structure over wider temperatures.

Another fiber with rather well-known structure is drawn poly(ethylene terephthalate), PET. Some typical DSC traces are shown in Fig. 4.151. Again, the restrained fibers melt higher, but for PET the collapse of the fibers that leads to the



loss of orientation in the mesophase is most effective for the restrained fibers. A summary of the melting peaks by DSC is given in Fig. 6.107 (compare to the undrawn PET in Fig. 6.91), and the shrinkage of the fibers is recorded by TMA in Fig. 6.108 (see Sect. 4.5 and the schematics in Figs. 4.148–150).

A study of Fig. 6.107 indicates that at slow analysis rates, both, the restrained and unrestrained fibers reorganize. The fibers which are restrained, superheat at higher

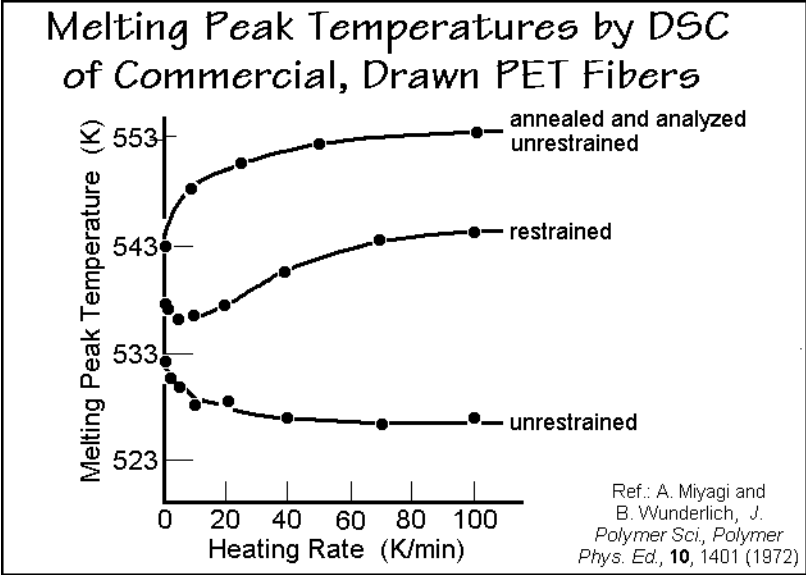


Fig. 6.107

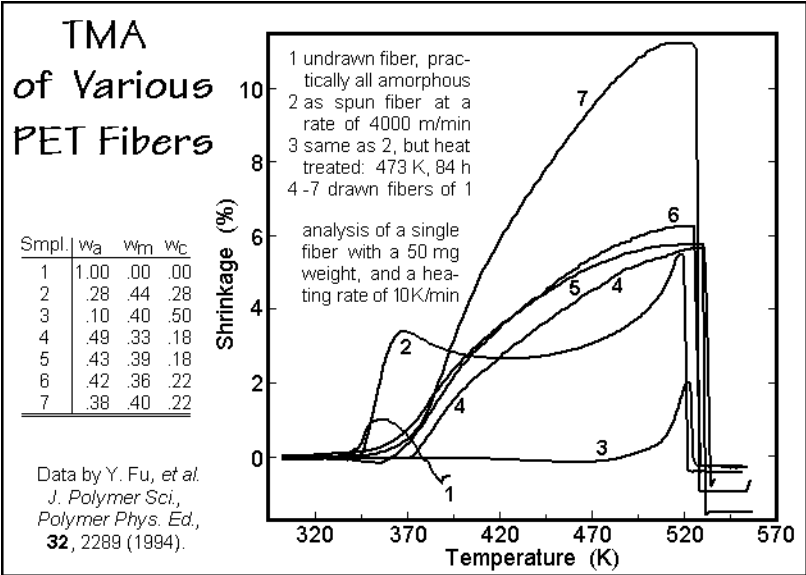


Fig. 6.108

analysis rates because of insufficient time on partial melting of the crystals to disorder the oriented, noncrystalline areas. Even more superheating and no reorganization is seen in the annealed fibers. The structure of the PET fibers was illustrated in Figs. 5.69–72 and the mechanical properties in Figs. 5.114 and 5.115. The three-phase structure, proven by X-ray diffraction and solid-state NMR, yields only one melting peak, as in the gel-spun polyethylene described above. The initial shrinkage in Fig. 6.108 is seen at the glass transition temperature. The amorphous fiber (1) loses its integrity at this temperature since it is not crystalline. Additionally, shrinkage can occur in the region where the rigid amorphous part is reduced (see Sect. 6.1.3) and/or small crystals start melting. The final step in the analysis indicates the flow of the fiber after the main body of crystals and mesophase melt (negative shrinkage).

Some more insight into the thermal properties of an oriented PET is given by the data from quasi-isothermal, temperature-modulated differential scanning calorimetry. Figure 6.109 displays a comparison of a drawn film of PET [25] with a standard bulk sample which is analyzed in more detail in Figs. 4.136–139. Compared to the 44%

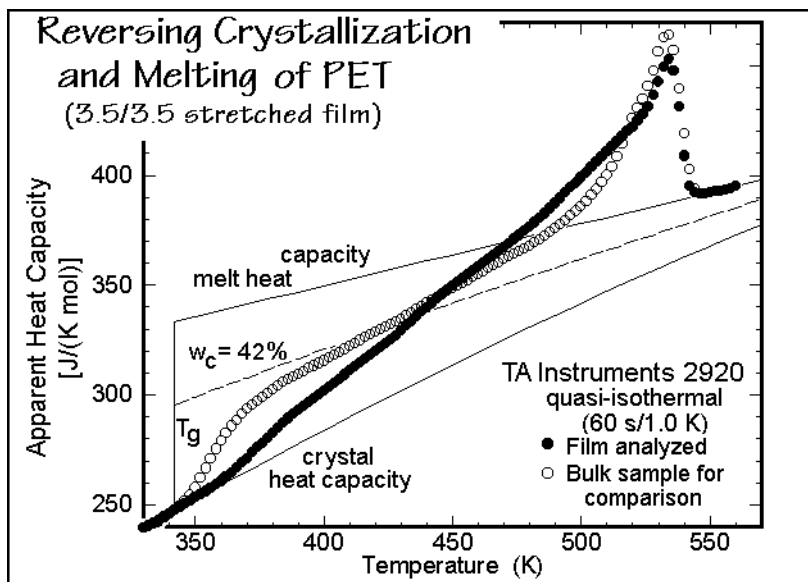
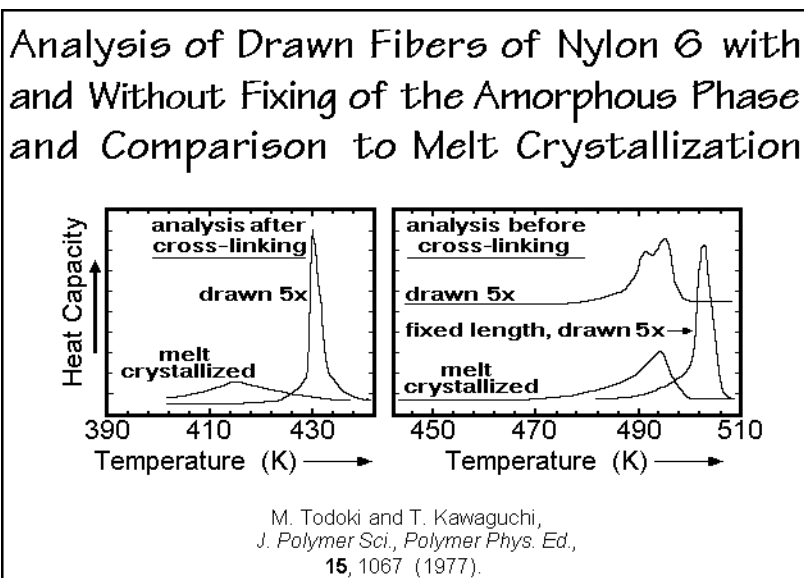


Fig. 6.109

crystalline bulk material, the 42% crystalline film has a considerably higher glass-transition temperature. The glass transition range is also broadened, and the heat capacity does not rise to the expected heat capacity for 42% crystallinity. This deficit in heat capacity indicates a rigid amorphous fraction. A reversing latent heat contribution to  $C_p$  develops towards the end of the glass transition and increases towards the melting region. These observations point to a large level of strain and orientation in the amorphous fraction, as described in detail for the PET fibers.

The final example of the DSC of fibers deals with nylon 6 [64,65]. Comparing on the right in Fig. 6.110 the DSC traces of drawn fibers before cross-linking to a melt-crystallized sample, one may conclude that there is little difference between the two

**Fig. 6.110**

samples, despite the enormous rearrangement the fiber must have undergone on drawing (see Fig. 5.111). An analysis at fixed length increases the melting peak temperature of the fibers, indicating the presence of strained, noncrystalline material that does not relax before melting. A more realistic analysis is possible after chemical cross-linking of the amorphous phase by  $\gamma$  irradiation in the presence of acetylene. After this treatment the amorphous phase prohibits the crystals from annealing and recrystallizing, as also shown in Fig. 6.80. Although the chemical reaction changes the phase-transition conditions somewhat, one can now observe an approximation to zero-entropy-production melting. Both the fiber and the melt-crystallized polymer have a much lower melting temperature after cross-linking.

The detailed analysis of this method of fixing the crystal morphology by cross-linking is documented in Fig. 6.111. The controls in traces (a) and (d) are to be compared to Fig. 6.110 (note the change from the heat-flow rate to heat capacity). The sample analyzed in (a) was next heated to 417 K, then quenched to room-temperature, cross-linked, and analyzed by DSC (curve a). Next, the same process was repeated with new samples by heating to 437, 459, 480, 485, 489, 492, 495, 498, and 501 K for curves b–j, respectively. The melting peak moves continually to higher temperature than reached before quenching and cross-linking. The quantitative analysis of the heats of fusion after the various partial annealings is depicted in Figs. 6.111(b) and (c). Graph (b) shows that the annealing starts with some new crystallization, and graph (c) reveals that by separating the contributions to the two melting peaks, one can separate annealing and recrystallization steps.

This was followed by a new set of experiments carried out at constant length, reproduced in Fig. 6.111(d). The temperatures chosen were 430, 453, 473, 483, 493, 498, 501, 503, and 507 K for curves 1–9, respectively. No high-temperature melting material is produced in this case.

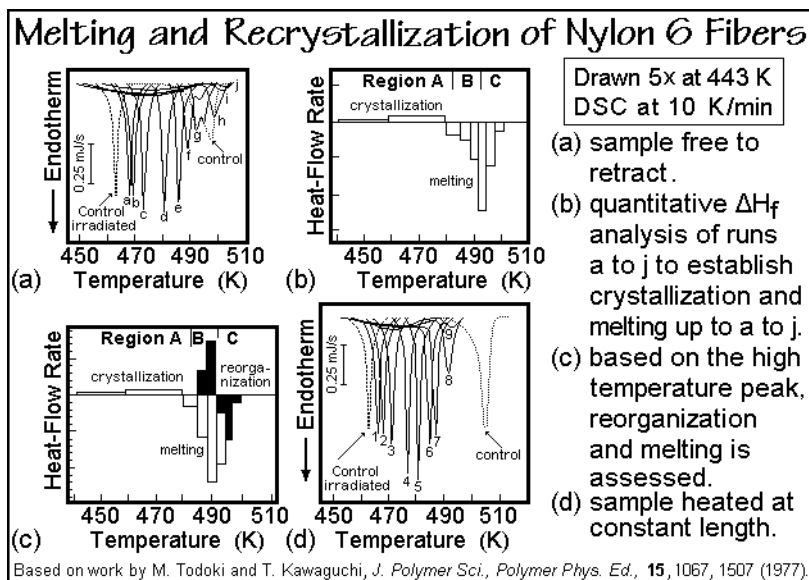


Fig. 6.111

Figure 6.112 completes the analysis with repeat experiments for different draw ratios. The peak temperatures of the directly analyzed fibers show little difference in method (A). Analyzing at constant fiber length, with method (B), gives only a measure of the relaxation of orientation in the amorphous phase. Only after arresting reorganization by cross-linking can the fibers be characterized in method (C). It is now possible to analyze the history of drawing at different temperatures with a DSC.

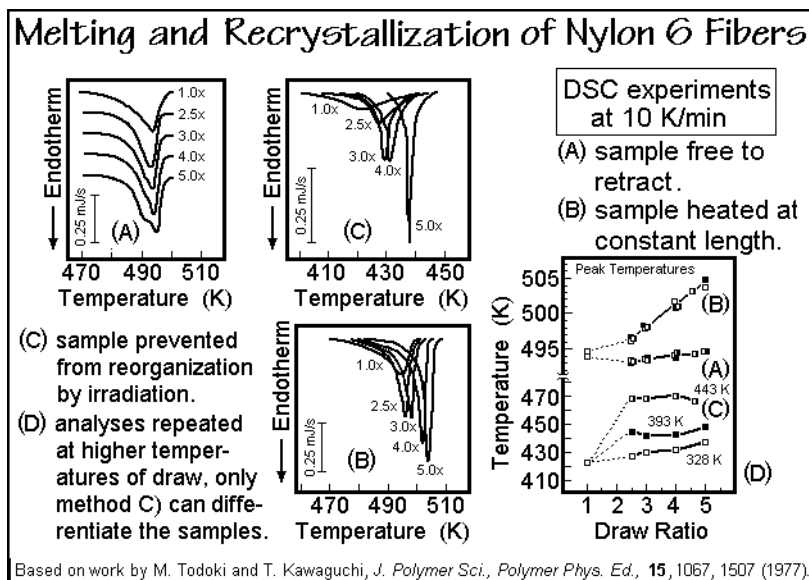


Fig. 6.112

## 6.3 Sample History Through Study of the Glass Transition

Glasses are not in equilibrium, as is discussed in more detail in Sect. 2.5.6. Every path from a liquid to the glass is unique. A description of the internal variables which characterize a particular glass can be accomplished by irreversible thermodynamics (see Sect. 2.4). These internal variables can then yield information about the sample history, i.e., determine how the final, metastable state was attained. Two common histories are easily established: (1) The initial path from the mobile to the glassy state by cooling or increasing of the pressure at given rates which produced the metastable state. (2) Annealing of a given glass close to the glass transition temperature for a specific time or plastic deformation. In both cases the sample must remain unchanged after the setting of the structure until the analysis is carried out. The first type of history is often linked to checking of manufacturing conditions, while the second may allow an analysis of storage conditions or changes that may have occurred during use of the material. Such analyses of sample history are not possible on materials in equilibrium, since all history is erased when equilibrium is reached.

The tools for the analysis of the glass transition are developed in Chap. 4 and general descriptions are given in Sect. 6.1.3. In Sect. 7.3, finally, thermal analysis is applied to the study of the glass transition in multi-component systems. In the present section time-temperature effects are reviewed first (Sect. 6.3.1). This is followed by a description of modeling by using temperature-modulated DSC (Sect. 6.3.2). Finally, applications to the study of pressure and strain, crystallization, and network formation are treated in Sects. 6.3.3–5, respectively.

### 6.3.1 Time and Temperature Effects

Six of the seven parameters describing the glass transition region in Fig. 2.117 are dependent on time. Only the overall increase in heat capacity,  $\Delta C_p$ , does not change significantly with time of measurement and thermal history. The heat capacity of the glass is based almost entirely on vibrational motion. As such, it reacts very fast to temperature changes (within picoseconds, see Sect. 2.3) and practically all of the low-frequency vibrational modes which may be different for different metastable glasses are already fully excited before reaching the glass transition temperature,  $T_g$ , i.e., they contribute the same amount to  $C_p(\text{glass})$ , namely  $R = 8.314 \text{ J K}^{-1} \text{ mol}^{-1}$  (see Sect. 2.3). The  $C_p(\text{liquid})$  reacts also sufficiently fast to temperature changes, but only as long as the sample for thermal analysis is sufficiently above  $T_g$ . In addition, as an equilibrium state, it has lost all thermal history. Since  $C_p(\text{glass})$  and  $C_p(\text{liquid})$  change differently with temperature, there is, however, a gradual change in  $\Delta C_p$  if the glass transition changes, for example, due to cross-linking (see Sect. 6.3.5), or time effects.

In order to identify the history of a glass, one heats the sample through the glass transition region and measures the enthalpy relaxation (hysteresis, see Fig. 6.6) and then relates it to the characteristic internal parameters changed on cooling or annealing given in Fig. 2.117. The experimental separation of the enthalpy relaxation and the glass transition by TMDSC is described in Sect. 4.4.6. The schematic enthalpy diagram is Fig. 4.128. The parallel, thinner lines in Fig. 4.128 are characteristic of the metastable glasses reached by different cooling rates, as indicated on fast cooling from

$T_1$  to  $T_2$ . Isothermal annealing, as seen at temperatures  $T_2$  and  $T_3$ , reaches different levels of enthalpy, characterized by “fictive temperatures,”  $T_f$ . The  $T_f$  is related to a  $T_g$  which corresponds to an appropriate cooling rate. The kinetics of annealing to lower and higher enthalpies (fictive temperatures) is asymmetric, giving one of several indications that a single internal parameter is insufficient to describe a given glass (see Sect. 2.4.4). An empirical fit of this asymmetry is given by the so-called Tool-Narayanaswamy equation:

$$\tau = \tau_0 \exp[x\Delta H_a/(RT) + (1 - x)\Delta H_a/(RT_f)] \quad (1)$$

where  $0 \leq x \leq 1$  is the nonlinearity parameter. As  $T_f$  approaches  $T$ , equilibrium is reached and  $\tau$  follows an Arrhenius expression (see Fig. A.7.2). Approaching the enthalpy of a given  $T_f$  from higher values, after quenching to temperatures lower than  $T_f$ , the parameter  $x$  increases with time, i.e., the process is self-retarding. Approaching the enthalpy of  $T_f$  from lower enthalpy, after quick heating to temperatures higher than  $T_f$ ,  $x$  decreases with time, i.e., the process is autocatalytic.

Figure 6.113 shows the glass transition of polystyrene as a function of cooling rate, measured with a dynamic DTA technique, DDTA. The glass transition temperature decreases exponentially with cooling rate  $q$  and is described with an activation energy,  $E_a$ . Since  $E_a$  is of the order of magnitude of the energy of strong bonds (see Fig. 1.4), but no strong bonds are broken at  $T_g$ , this indicates a cooperative process.

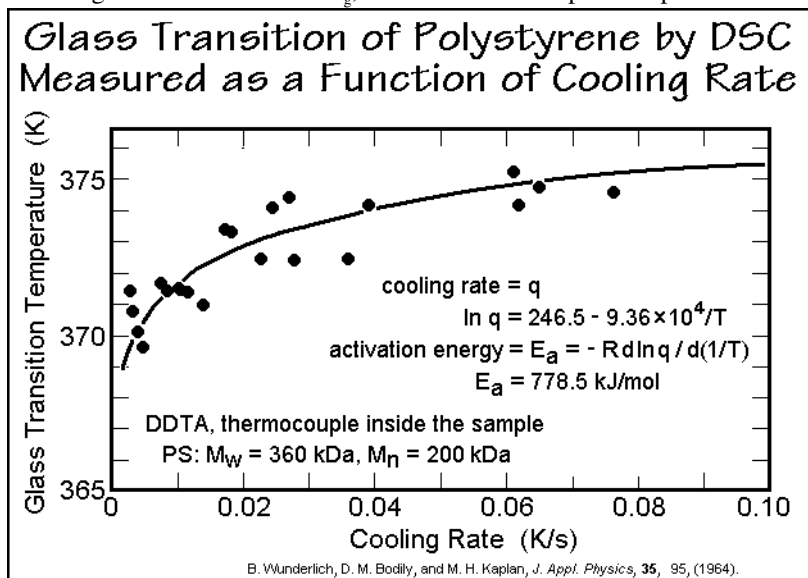


Fig. 6.113

A general evaluation of the experimental results on the glass transition is given in Sect. 4.4.6. Figures 4.125–127 illustrate the treatment of the raw data of polystyrene as obtained by TMDSC. Next, Figs. 4.129–133 are used to document the conversion of such experimental data for poly(ethylene terephthalate) to yield activation energies and extrapolated data to a wider frequency range. In Sect. 6.1.3 the glass transition is described based on the hole theory and documented for the example of polystyrene

in Figs. 6.7–12. Experimental data for polystyrene are displayed in Fig. 6.114, and the relaxation times which govern the change of the reversing  $C_p$  with frequency are illustrated in Fig. 6.115. Of interest is that the relaxation times are dependent on the amplitude of modulation because of the asymmetry of the kinetics and need, thus, to be extrapolated to zero amplitude. With these data, one can compute the frequency dependence of the reversing  $C_p$ , as shown in Fig. 6.116.

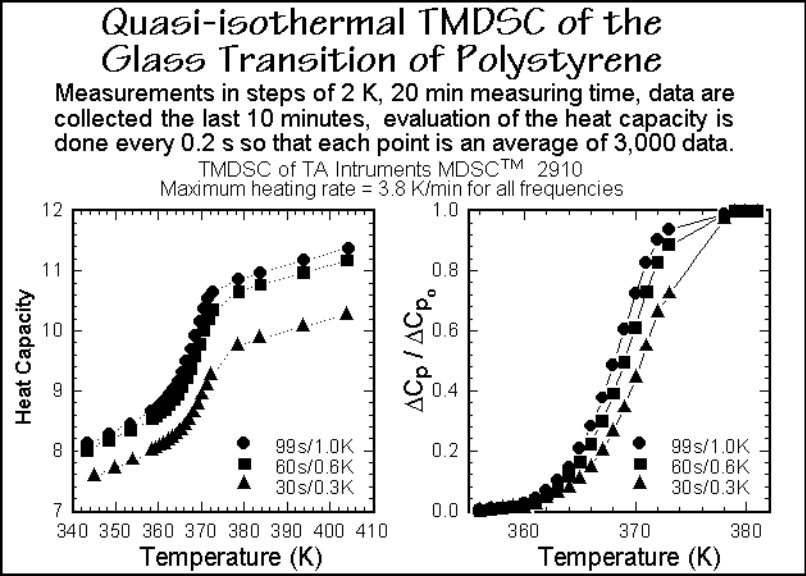


Fig. 6.114

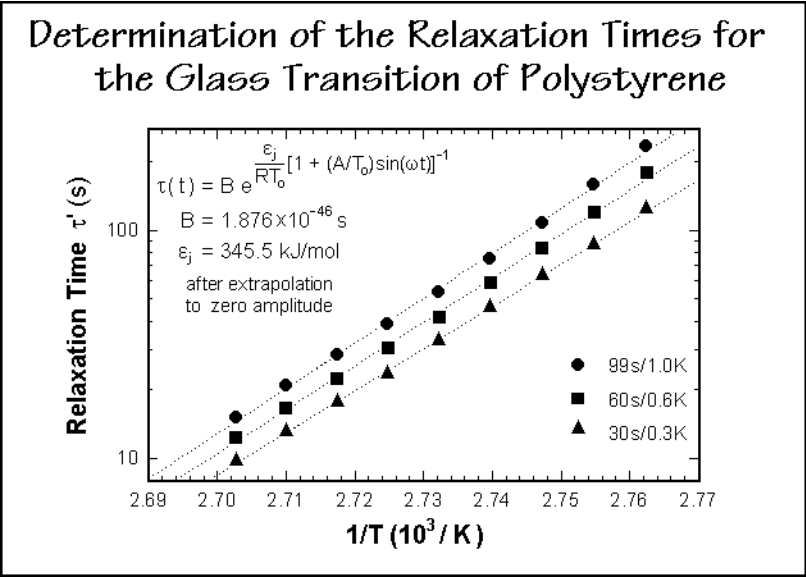


Fig. 6.115

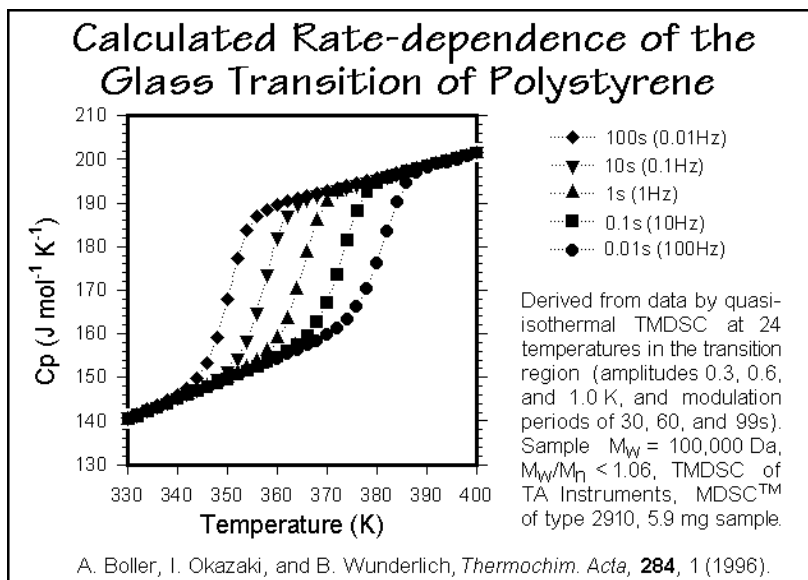


Fig. 6.116

Other thermal analysis techniques such as dilatometry in Sect. 4.1 or thermo-mechanical analysis in Sect. 4.5 can also be used to study the time dependence of  $T_g$ . Especially suited for measurement of the frequency response are dynamic mechanical analyses in Sects. 4.5.4 and 4.5.5, and dielectric thermal analyses in Sect. 4.5.6. Although the different techniques respond to different external excitations, the obtained relaxation times are similar, as shown in Fig. 6.117. Over wider temperature

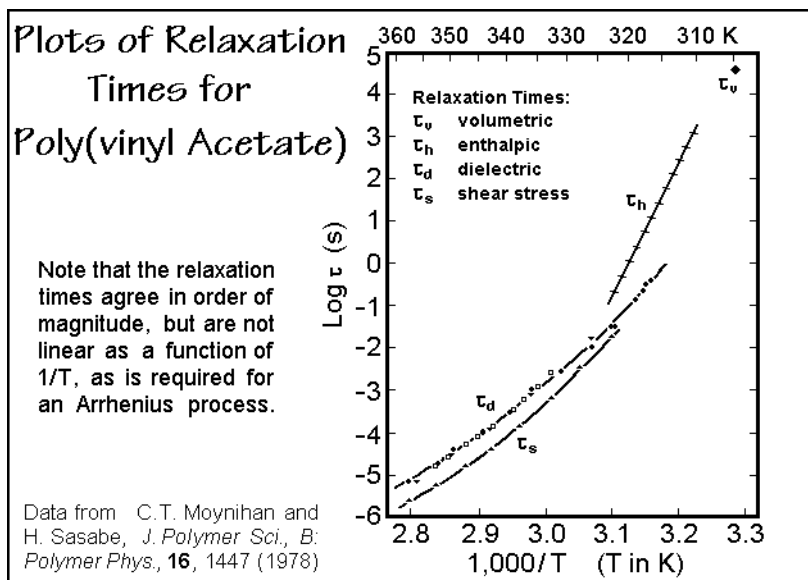


Fig. 6.117



ranges, the activation energies change, i.e., a simple Arrhenius description does not hold. The activation energy increases as temperature decreases.

In comparing glass transition temperatures, one must, furthermore, consider the differences in definition for the glass transition temperature for the different techniques. In Fig. 6.20, for example, the glass transition temperatures are compared to data obtained from DMA (using the maximum in  $\tan \delta$ ) and TMDSC (using the temperature of half-vitrification) when measured at similar frequencies.

### 6.3.2 Modeling of the Glass Transition

The simplest model to represent the glass transition is based on the hole theory which was developed by Frenkel and Eyring some 60 years ago and is described in more detail in Sect. 6.1.3 (see also Sect. 4.4.6). The equilibrium number of holes at  $T$  is  $N^*$  and each contributes an energy  $\varepsilon_h$  to the enthalpy. As given on Fig. 6.5, the hole contribution to the vibrational heat capacity  $C_{p_0}$  and its kinetics is represented by:

$$C_p(\text{liquid}) = C_{p_0} + \varepsilon_h \left( \frac{dN^*}{dT} \right) \quad (1)$$

$$\left( \frac{dN}{dt} \right) = \frac{1}{\tau} (N^* - N) \quad (2)$$

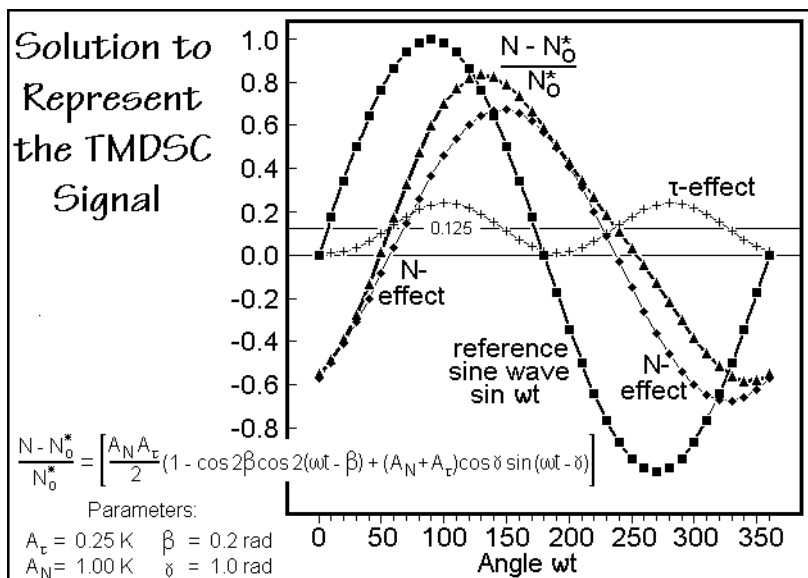
In Eq. (2),  $N$  represents the instantaneous number of holes and  $\tau$  is the relaxation time towards the hole equilibrium. During a TMDSC experiment, as outlined in Sect. 4.4.6,  $N^*$  and  $\tau$  are temperature and, thus, time dependent. First, a solution of Eq. (2) is attempted for quasi-isothermal temperature-modulated DSC, to be followed by a numerical solution for standard TMDSC. The basic solution of Eq. (2) is:

$$N(t) = N(t_0) e^{-\Phi(t)} + e^{-\Phi(t)} \int_{t_0}^t \frac{N^*(t')}{\tau(t')} e^{\Phi(t')} dt' \quad (3)$$

$$\Phi(t) = \int_{t_0}^t \frac{1}{\tau(t')} dt'$$

where  $t_0$  is the beginning of the experiment, and  $\Phi(t)$  is the time-averaged relaxation time. The evaluation of Eq. (2) is rather complicated [12]. Because of the temperature modulation, both  $\tau$  and  $N^*$  are to be inserted into Eq. (3) with their proper temperature/time dependence. In addition, the discussion in Sect. 6.3.1 revealed that  $\tau$  is also dependent on  $N$  which further compounds Eq. (3).

Figure 6.118 shows the integrated Eq. (3) for the steady state of quasi-isothermal experiments ( $\blacktriangle$ ). The measurements needed for this analysis are displayed for polystyrene in Figs. 6.14 and 6.15 and for poly(ethylene terephthalate) in Figs. 4.129 and 4.130. The parameters in Fig. 6.118 were arbitrarily chosen to clarify the three different contributions to the approximation shown in the figure. For a solution fitted to the experiments for poly(ethylene terephthalate), see Fig. 4.131. The parameters  $A_\tau$  and  $A_N$  represent the amplitude contributions due to the change in  $\tau$  and  $N^*$  with temperature, and  $\beta$  and  $\gamma$  are phase shifts. The plotted  $(N - N_0)/N^*$  is proportional to the heat flow (and thus to  $\Delta C_p$ ). The curve ( $\blacktriangle$ ), however, is not a sinusoidal response.

**Fig. 6.118**

The curve is elevated relative to zero by a constant amount (0.125) and has a contribution of  $2\omega$ , double the modulation frequency (+, second harmonic). Both these contributions are not included in the experimental reversing heat flow which contains only the contribution to the first harmonic ( $\blacklozenge$ , see Sect. 4.4.3). Accepting the present analysis, it is possible to determine  $\gamma$  and  $\tau$  from the reversing heat capacity by matching the last term of the equation in Figs. 6.118 and 4.131, and then use the parameters describing the match to compute ( $\blacktriangle$ ), the actual response of the TMDSC to the quasi-isothermal temperature modulation.

To assess standard TMDSC experiments with an underlying heating rate  $\langle q \rangle$ , a numerical analysis has to be found for Eq. (2). Intervals of one second, running from  $i = 1$  to  $n$ , are integrated with constant values for  $N_i^*$  appropriately chosen for the instantaneous temperature, and an average value of  $\tau$  is inserted in Eq. (2), as is outlined in Eq. (2) on p. 601. The various  $\Delta N_i$  are then summed over the whole temperature range of interest. For cooling experiments from above  $T_g$ ,  $N_o$  is equal to  $N_o^*$ , for heating from below  $T_g$ ,  $N_o$  corresponds to  $N^*$  at the fictive temperature,  $T_f$ . The fictive temperature identifies the temperature at which the actual hole concentration of the metastable glass would be in equilibrium, as shown in Fig. 4.128.

The results based on polystyrene for the number of holes for cooling, on vitrification, and heating, on devitrification, at the given underlying rates,  $\langle q \rangle$ , are shown in Figs. 6.8 and 6.9. For poly(ethylene terephthalate) analogous data are reproduced in Figs. 6.119 and 120. The freezing of the hole equilibrium is clearly visible in Fig. 6.119. Also, it can be seen that after the response to the fast modulation has almost stopped, a considerable further decrease in number of holes occurs due to the slow, underlying cooling rate until the glass becomes metastable after about 1,000 s. Heating, in Fig. 6.120, starts with annealing as the glass transition is approached. This leads first to an exotherm with a decrease in  $N$  up to about 500 s,

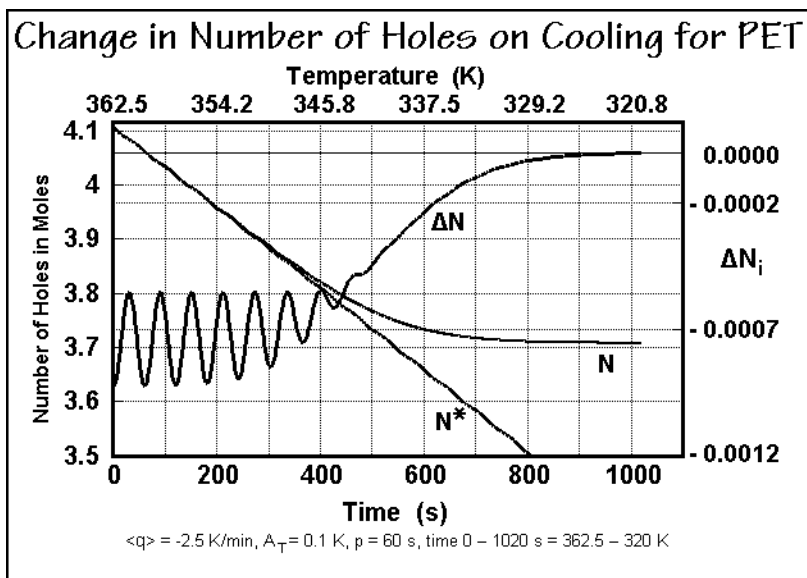


Fig. 6.119

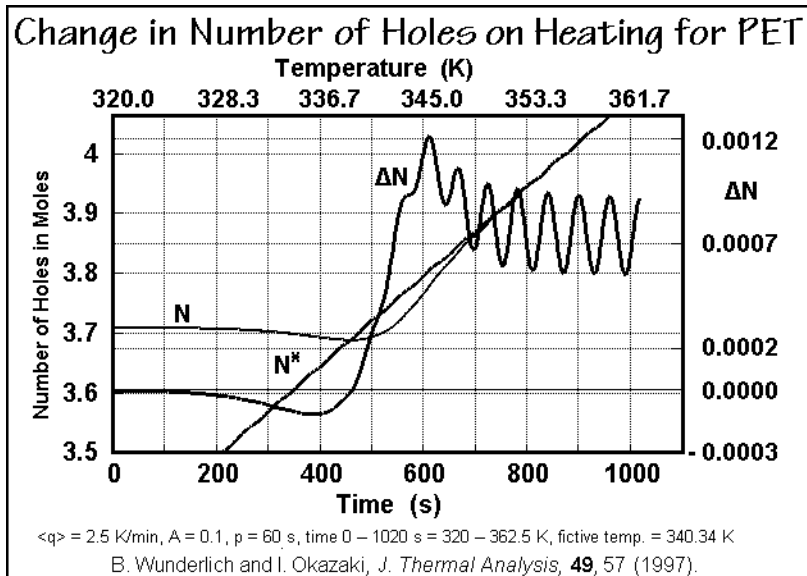


Fig. 6.120

an effect that has not been analyzed to a great extent with experiments [12]. Next, one can see the well-known, endothermic hysteresis which overlaps the beginning response to the oscillations (see also Fig. 6.6 for a schematic). Finally, the liquid state is reached after about 900 s. The analogous polystyrene data in Figs. 6.8 and 6.9 show similar responses, just that the concentrations and times are different.

The total, reversing, and nonreversing heat capacities can then be calculated as described in Sect. 4.43, with the results shown for polystyrene in Figs. 6.10 and 11 (assuming that all instrument lags have been eliminated). The abbreviated Fourier analysis used to extract the reversing part of the heat flow assesses only the first harmonic of the oscillations and only at the modulation frequency  $\omega$ , i.e., the reversing heat capacity does not correspond exactly to the apparent reversible heat capacity, as was already shown for the quasi-isothermal analysis in Fig. 6.118. The interference of the time scales of the underlying rates  $\langle q \rangle$  and  $\omega$  cause a small shift in  $\omega$  (Doppler effect) which explains the additional oscillations of the heat capacities in Figs. 6.10 and 11. The higher harmonics also can be extracted and are small, as shown in Fig. 6.121 which summarize data for poly(ethylene terephthalate) from Fig 6.119.

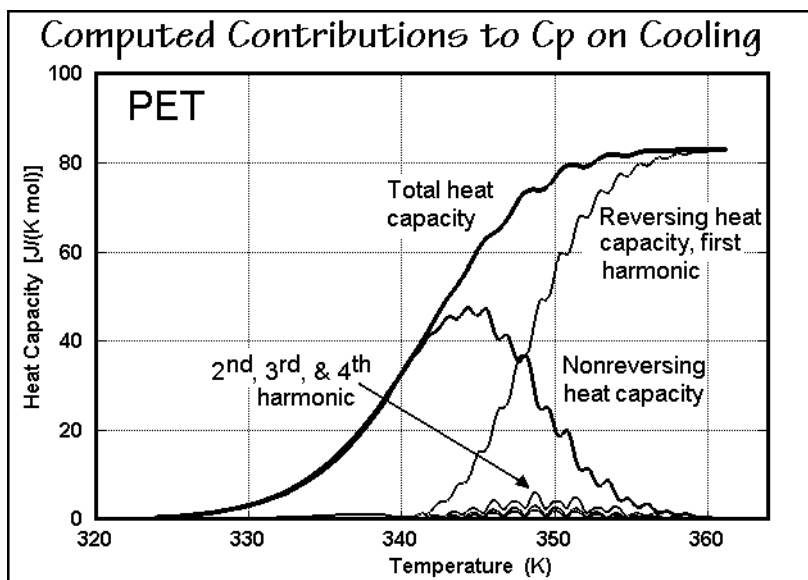


Fig. 6.121

This modeling reveals a glass-transition-like behavior in systems describable with the hole model. It also shows that the reversing heat capacity by TMDSC is only approximately the apparent reversible heat capacity. In addition, it was shown in Sect. 6.1.3 that an asymmetry exists, not treated in the simple hole model, causing a change of the relaxation time  $\tau$  with  $N$  (see also Fig. 4.126). Additional observations point to deviations from the exponential response of the first-order kinetics of Eq. (2), above. All these complications point to the fact that the glass transition is cooperative and needs a more detailed model for full representation.

### 6.3.3 Pressure and Strain Effects

The principal effect of hydrostatic pressure on a substance is an increase in density and a preference of better packed structures, in contrast to tensile strain which mainly causes a chain extension. To describe the change of melting temperature with pressure

and strain, one uses the Clausius-Clapeyron equation which is written as  $dT_m/dp = \Delta V_f/\Delta S_f$ , and  $dT_m/dp = -\Delta \ell_f/\Delta S_f$  (see Fig. 5.168). The effect of pressure on  $T_g$ , however, cannot be described by the corresponding equation for reversible second-order transitions ( $\Delta\beta/\Delta\alpha = dT_g/dp$ , where  $\Delta\beta$  is the change in compressibility and  $\Delta\alpha$  the change in expansivity, see also Sect. 2.5.6). Still, the change of  $T_g$  with pressure goes usually parallel to  $T_m$ .

The experimental increase of  $T_g$  with pressure of polystyrene is indicated in Fig. 6.122 by line BE. The liquid D cooled at elevated pressure, freezes at the higher glass transition temperature E than liquid C cooled at atmospheric pressure ( $T_g = B$ ). On releasing the pressure below  $T_g$ , the compressed sample F expands to G, not to the level A of a glass cooled at atmospheric pressure. The glass remains “pressure densified” by the amount  $AG \approx FF'$ , where F' is the volume after isothermal compression from A. This densification corresponds to a volume strain.

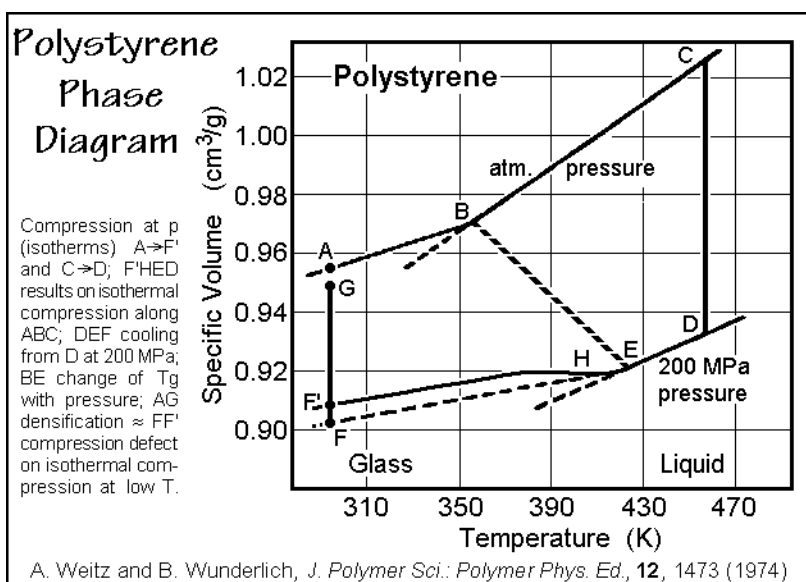


**Fig. 6.122**

Slow cooling leads to glasses of lower free enthalpy and enthalpy (see Figs. 2.118 and 4.128, respectively). Due to the same direction of changes in  $H$ ,  $S$ , and  $V$ , schematically shown in Fig. 6.6, denser glasses ought to be more stable. Surprisingly the pressure-densified glass of Fig. 6.122 does not have a lower enthalpy, but rather a higher one, as is shown in Fig. 6.123. Such higher enthalpy, however, is expected for strained samples. The relaxation kinetics depicted in the graph on the right in Fig. 6.123 indicates that the pressure-densified glass relaxes to a less dense glass (larger volume) with lower enthalpy, i.e., it is less stable than a glass of the same density obtained by annealing. In fact, on extended relaxation, the volume will decrease again and the enthalpy decrease even further. Figure 6.123 also reveals that enthalpy and volume follow different kinetics. Enthalpy relaxation is coupled with little volume relaxation and volume relaxation sees little change in enthalpy.

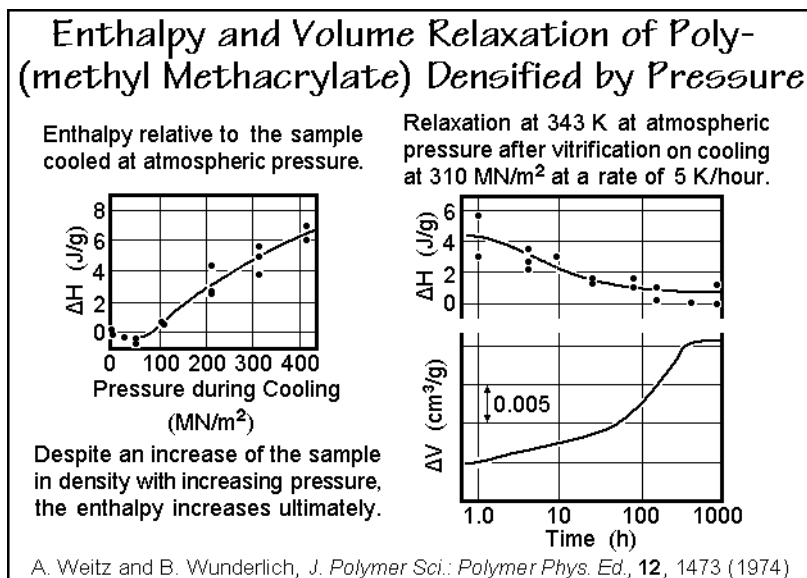


Fig. 6.123

Figure 6.124 shows for polystyrene cooled at atmospheric pressure the typical DSC trace of enthalpy relaxation for a sample cooled slowly and heated fast. This experiment represents the typical hysteresis or enthalpy relaxation described in Fig. 6.6. Carrying out the same DSC experiments with a pressure-densified glass leads to the much different response of the upper curves in Fig. 6.124. The beginning of the glass transition is shifted considerably

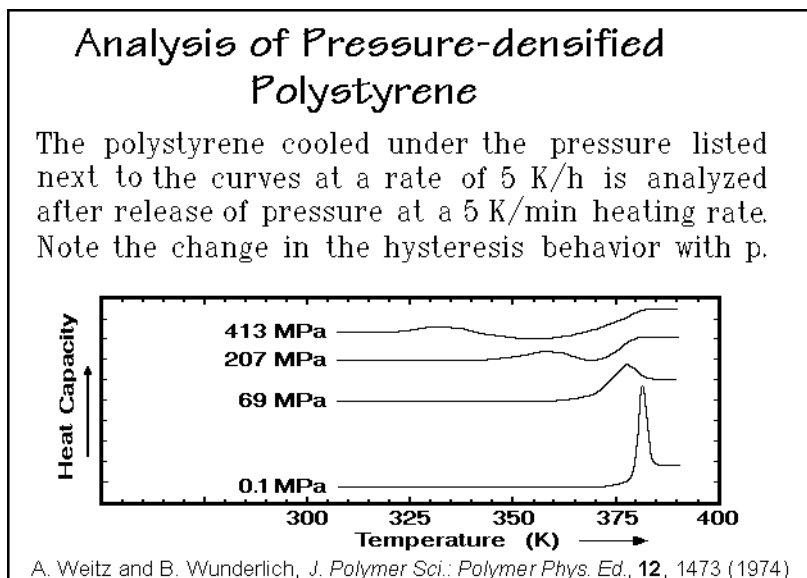
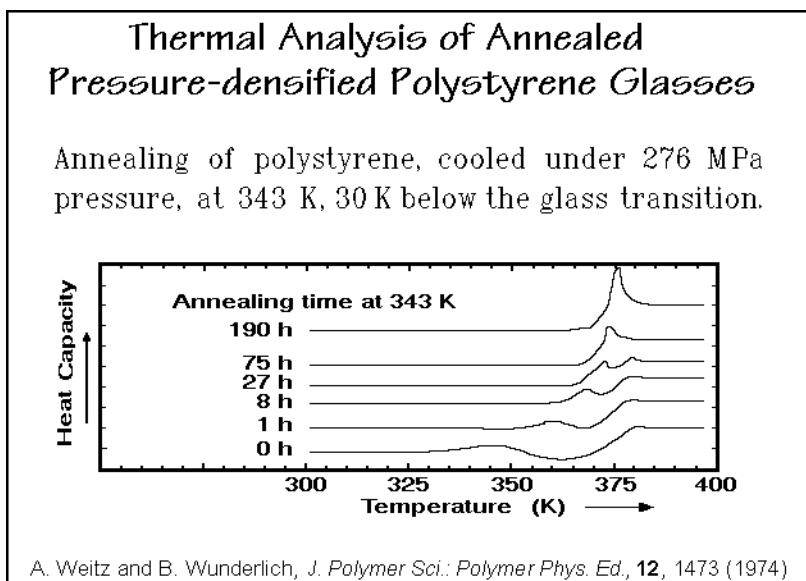


Fig. 6.124

towards lower temperature and despite the fact that the pressure-densified glasses were cooled with the same slow rate, they lose their endothermic enthalpy relaxation at  $T_g$ . Instead, they develop a broad exotherm below  $T_g$  of the samples cooled at atmospheric pressure. The annealing of a polystyrene cooled at an intermediate pressure of 276 MPa is illustrated by the DSC traces in Fig. 6.125. The annealing temperature at atmospheric pressure is chosen to be 343 K, 30 K below the  $T_g$  at atmospheric pressure of about 373 K. The integral kinetics of this annealing is similar to the data of Fig. 6.123. As the initial enthalpy decrease is completed, the exotherm in the DSC trace disappears and the standard enthalpy relaxation (hysteresis) builds up with further annealing, and the strain history, introduced by the cooling under pressure, is erased. This example of superposition of strain history and thermal history illustrates our presently poor understanding of the glass transition. No set of internal variables and no proper relaxation kinetics have been derived for these more complicated processes of pressure, three-dimensional strain, and temperature/time variations.



**Fig. 6.125**

Two other examples of the influence of strain on the glass transition are discussed in Sect. 6.1. One deals with two-dimensional surface strain, the other with molecular, one-dimensional strain. Surface strain has been detected in small particles as an exotherm that occurs below  $T_g$  for small particles and high strain and above  $T_g$  for larger particles. An example for polystyrene is given in Fig. 6.13. The molecular strain can result from molecules crossing a solid/liquid phase boundary (see Sect. 6.3.4). Its presence may broaden the glass transition to a higher temperature, or even shift the glass transition for a part of the amorphous fraction to higher temperature. Then, the affected parts of the molecules make up a rigid-amorphous fraction (see Figs. 6.16–18). The effect of macroscopic strain on the glass transition, as on linear extension of amorphous polymers, is mentioned above.

### 6.3.4. Crystallinity Effects

Partial crystallization of a linear macromolecule strongly affects the glass transition of the remaining noncrystalline portion. In fact, the strains introduced by the tie-molecules between the amorphous and crystalline fractions, together with the chain-folding principle, are the cause of the limited crystallization (see Chap. 5). The details of the melting of the semicrystalline polymer poly(oxy-1,4-phenyleneoxy-1,4-phenylenecarbonyl-1,4-phenylene), PEEK, are treated in Sect. 6.2.5. Figure 6.126, in turn, is a plot of the changes in the glass transition temperature as a function of the crystallization history which was set by crystallization at different temperatures. The crystallization at high temperature leads to a constant, relatively low glass transition temperature,  $T_g$ , indicative of a relaxed interface between crystals and melt. The achieved  $T_g$ , however, is not the glass transition of the fully amorphous PEEK, which is 419 K, four kelvins lower. The lower the crystallization temperature, the more strain remains, and the higher is  $T_g$ . The higher glass transition is mainly caused by a broadening of the glass-transition region, as is seen, for example, in poly(ethylene terephthalate), PET, and polydioxanone of Figs. 4.136 and 4.124, respectively. In both figures the amorphous sample is indicated by  $\bullet$ , the semicrystalline one, by  $\circ$ .

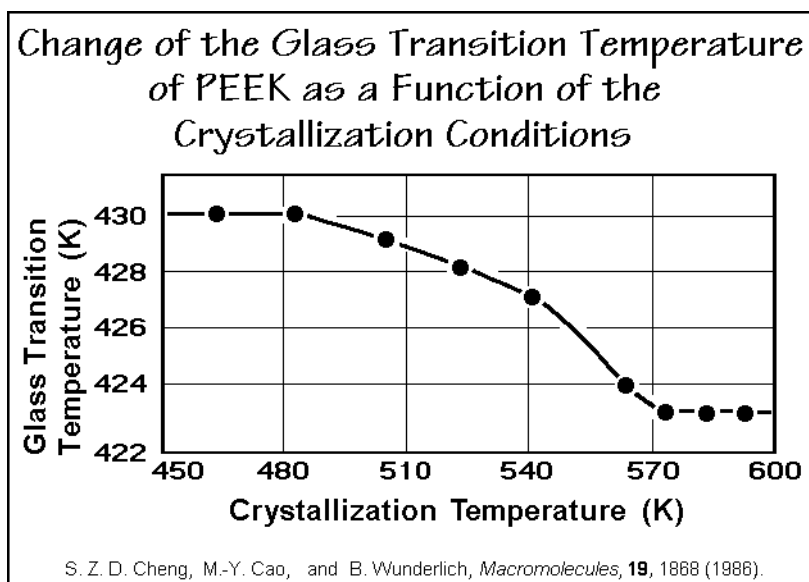


**Fig. 6.126**

Figures 6.127 and 6.128 illustrate that for the two macromolecules the strain on the amorphous fraction is so large that a portion of the amorphous phase remains rigid up to the transition region and a lower increase in heat capacity at  $T_g$  results than is expected from the fraction of the amorphous sample,  $(1 - w_c)$ . This fraction is called the rigid-amorphous fraction, RAF. The method of its evaluation is described in Figs. 6.16–18 for the case of poly(oxyethylene). For PEEK, the RAF is illustrated in Fig. 6.127. It is calculated as the ratio to the total amorphous fraction and increases



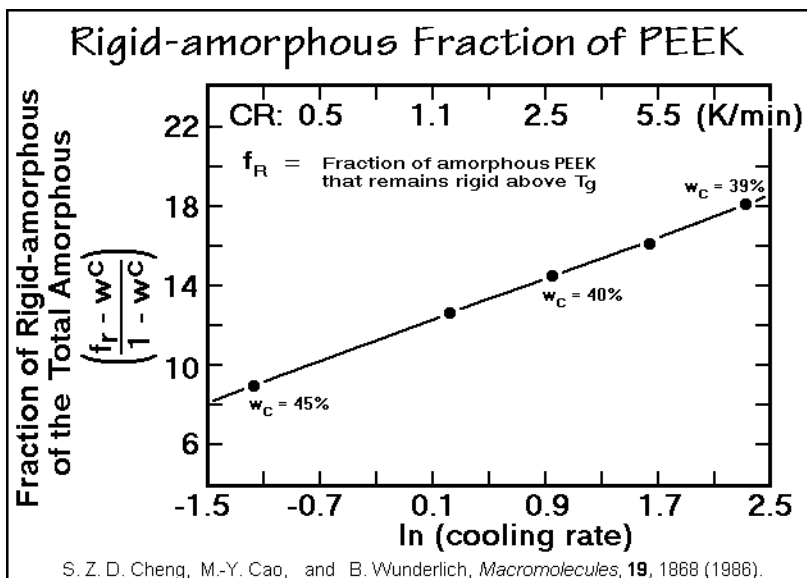


Fig. 6.127

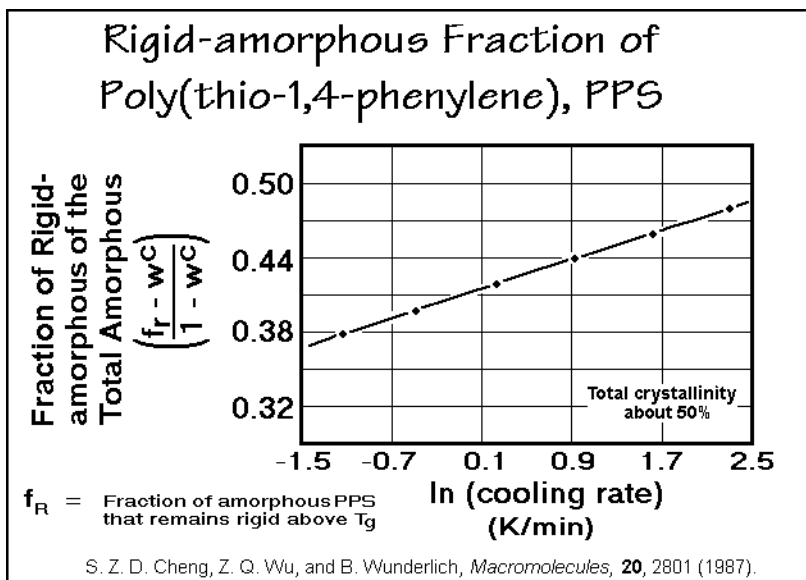
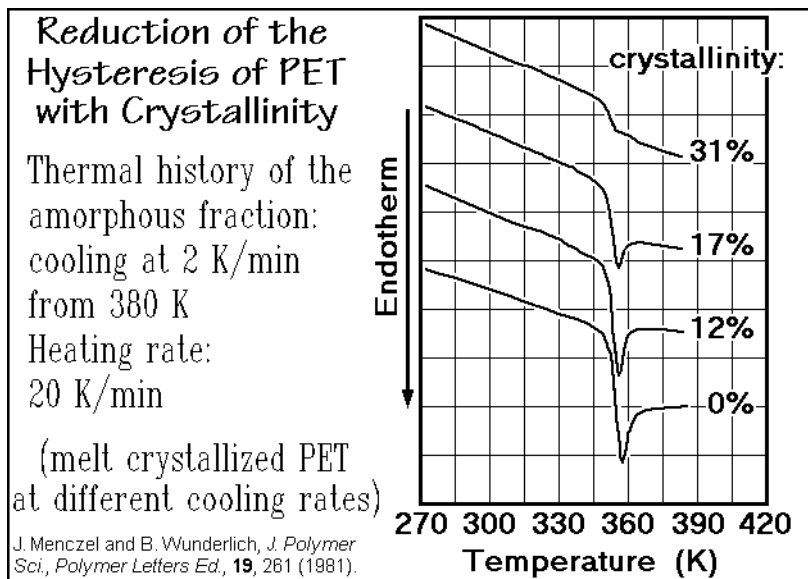


Fig. 6.128

with increasing cooling rate from 8 to 18%, while the crystallinity decreases from 45 to 39%, i.e., the overall rigid fraction does not decrease, as one might expect, but it increases from 53 to 57%. Similarly, on annealing of a macromolecule with a rigid-amorphous fraction, the overall rigid fraction may decrease since the interfaces relax on annealing by physical changes or ester interchange. Figure 6.128 illustrates a similar behavior for poly(thio-1,4-phenylene), PPS, or poly(phenylene sulfide).

Besides  $T_g$ , the breadth of the transition region, and  $\Delta C_p$ , partial crystallization affects also the hysteresis behavior (enthalpy relaxation) of the amorphous fraction. Figure 6.129 in its bottom curve depicts a typical enthalpy relaxation in amorphous PET that can be used to study the thermal history, as outlined for polystyrene in Figs. 4.125–127. The DSC curves for the samples with increasing crystallinity show that the hysteresis disappears faster than the step in  $\Delta C_p$  at the glass transition. The top sample in Fig. 6.129 of 31% crystallinity shows a smaller change in heat capacity than expected for an amorphous content of 69%, due to some rigid-amorphous fraction, but the hysteresis peak seems to have disappeared completely.



**Fig. 6.129**

Since development of the temperature-modulated DSC (see Sect. 4.4) it is possible to quantitatively describe the kinetics of the glass transition, as is illustrated in Sects. 6.3.1 and 6.3.2. Figures 6.130 and 6.131 illustrates the glass transition regions of a number of PETs with different thermal histories which leads to different crystallinities ( $w_c$ ) and rigid-amorphous fractions ( $w_r$ ) [66]. The standard DSC traces reveal that the broadening of the glass transition region and the disappearance of the hysteresis are connected to the crystallinity alone. The rigid amorphous fraction, by not taking part in the glass transition, affects only the  $\Delta C_p$ .

A drawn film was also included in the analysis [66]. The quasi-isothermal TMDSC of this drawn sample is reproduced in Fig. 6.109. It was produced out of practically amorphous PET by biaxial drawing at 368 K. The sample retains no residual cold crystallization and has a higher rigid-amorphous fraction than the semi-crystalline reference PET of Fig. 3.92. Long-time annealing causes an annealing peak of the crystals, as described in Sect. 6.22, but displays no hysteresis peak, as was also observed for the slowly cooled, undrawn PET samples with similar crystallinity used as an example in Fig. 6.129.

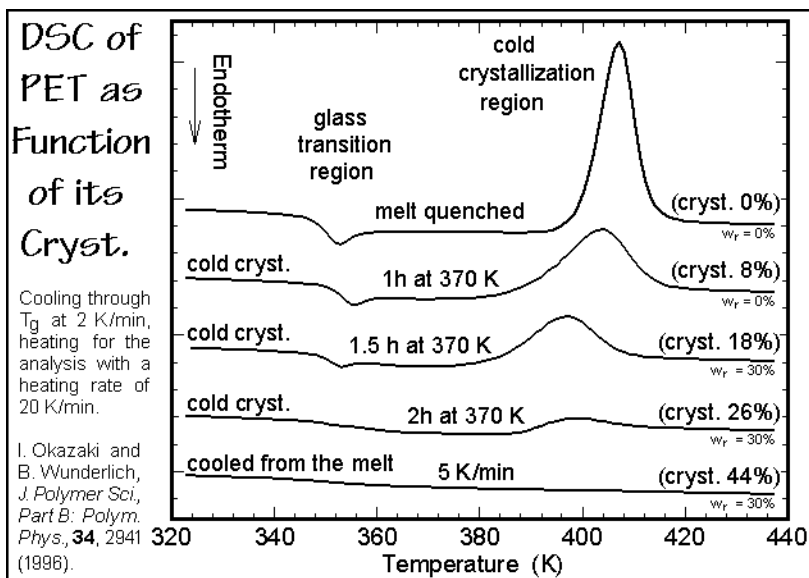


Fig. 6.130

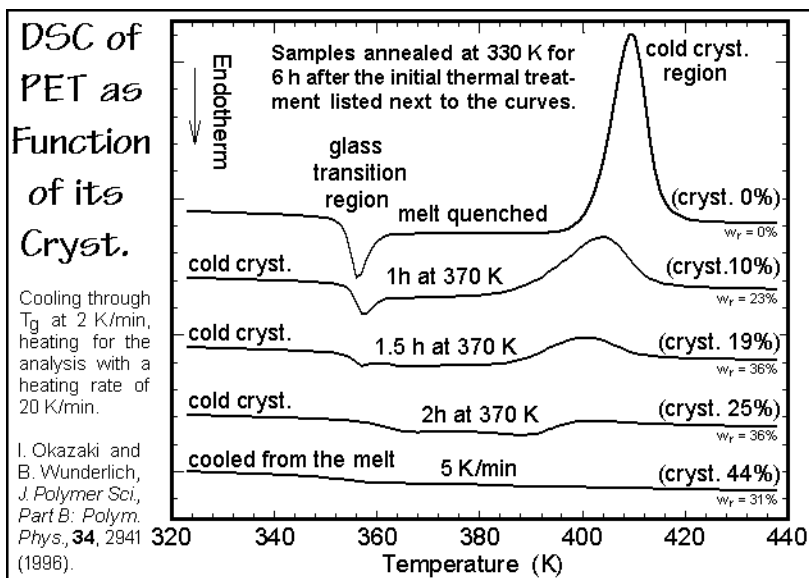


Fig. 6.131

A more detailed analysis of the kinetics of the glass transition was carried out by quasi-isothermal TMDSC [66,67]. Figure 6.132 is a representation of plots of the reversing, apparent heat capacities of some of these samples after extrapolation to zero modulation amplitude. All traces of hysteresis are absent. The same methods as described in Sects. 6.3.1 and 6.3.2 were used for the analyses of the glass transitions. For the amorphous PET, the analysis is shown in Figs. 4.129–133 and 6.119–121.

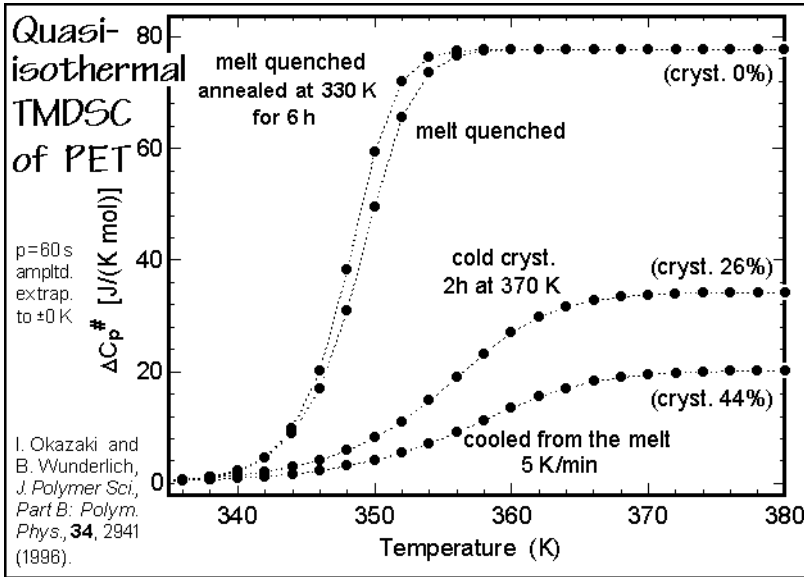


Fig. 6.132

Figure 6.133 illustrates that much of the disappearance of the hysteresis is linked to changed kinetic parameters (compare to the top and bottom curves of Fig. 6.129). Both, the broadening of the transition and the reduction of hysteresis are qualitatively seen. Figure 6.134, finally, reveals that the activation energies and preexponential factors of all the PET samples change in concert. As one would expect, the sharper the glass transition, the higher is the activation energy.

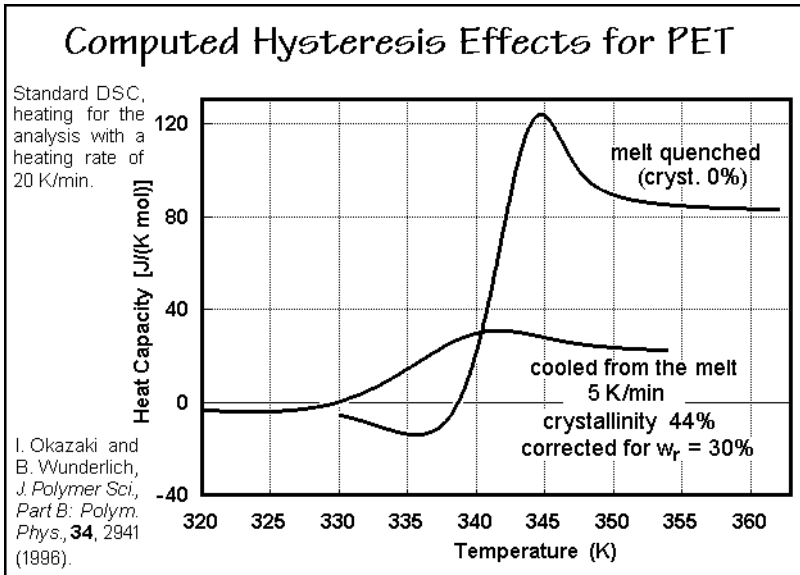


Fig. 6.133

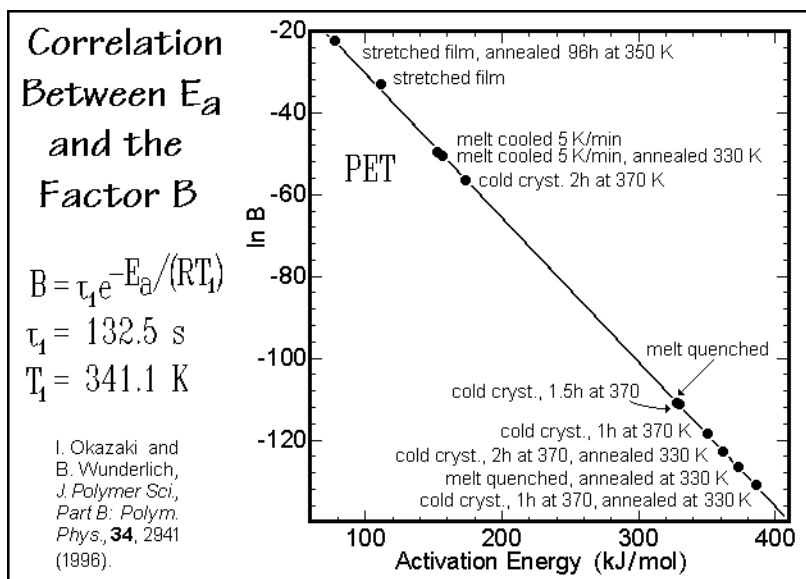


Fig. 6.134

### 6.3.5 Network Effects

Cross-linking of linear macromolecules as described in Sect. 3.4.3 and 3.4.5 hinders the large-amplitude motion similar to the presence of crystals, discussed in Sect. 6.3.4. In addition, the chemically different nature of the cross-link may lead to a solution of the two components, and for more extensive changes in the chemical nature, there may even be a phase separation with the effects described in Chap. 7. Because of the lesser mobility, one expects an increase in the glass transition temperature. A broadening of the transition may occur if the cross-links are nonuniform, or the influence of the cross-link component on the phase-structure becomes significant. At least initially, the liquid and glassy heat capacities are not affected significantly by the cross-links, but the higher glass transition temperature must ultimately lead to a lower increase in heat capacity,  $\Delta C_p$ , at  $T_g$ .

Figure 6.135 illustrates the increase of  $T_g$  of polystyrene when copolymerized with divinyl benzene for cross-linking ( $\text{CH}_2=\text{CH}_2-\text{C}_6\text{H}_4-\text{CH}_2=\text{CH}_2$ ). All samples were gels (see Sect. 3.4.3), practically without extractable polystyrene. The decrease in the change of the heat capacity at  $T_g$  on cross-linking is shown in Fig. 6.136. The curve drawn in Fig. 6.136 is calculated from the heat capacities of the liquid and glassy polymers at the measured glass transition temperature of Fig. 6.135. Considerable deviations are observed, but one may still extrapolate the data to a point where  $\Delta C_p$  becomes zero ( $\approx 50\%$  divinyl benzene,  $T_g$  500–550 K). Indeed, highly cross-linked polystyrenes with practically no  $\Delta C_p$  at  $T_g$  have been reported.

Cross-linking during curing of an epoxy resin, as observed with quasi-isothermal TMDSC, is described in Fig. 4.141. As the curing proceeds, the glass transition increases until it reaches the reaction temperature. At this point the reaction changes

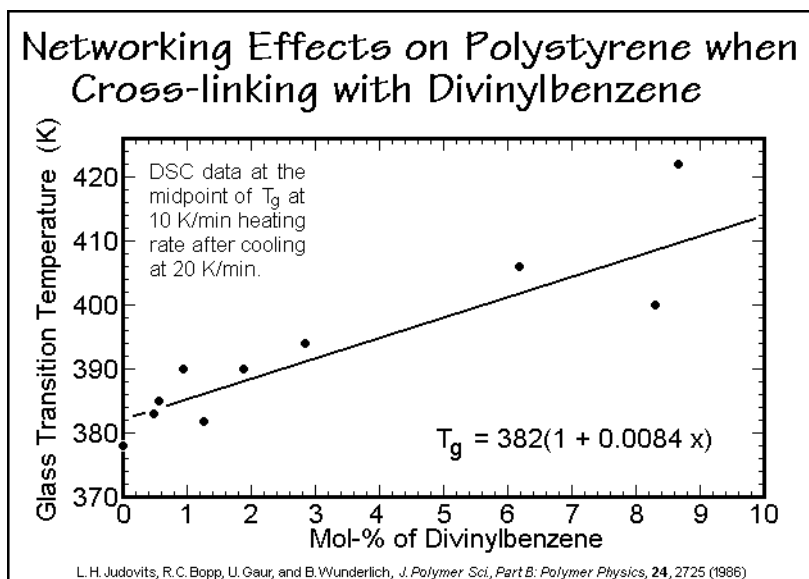


Fig. 6.135

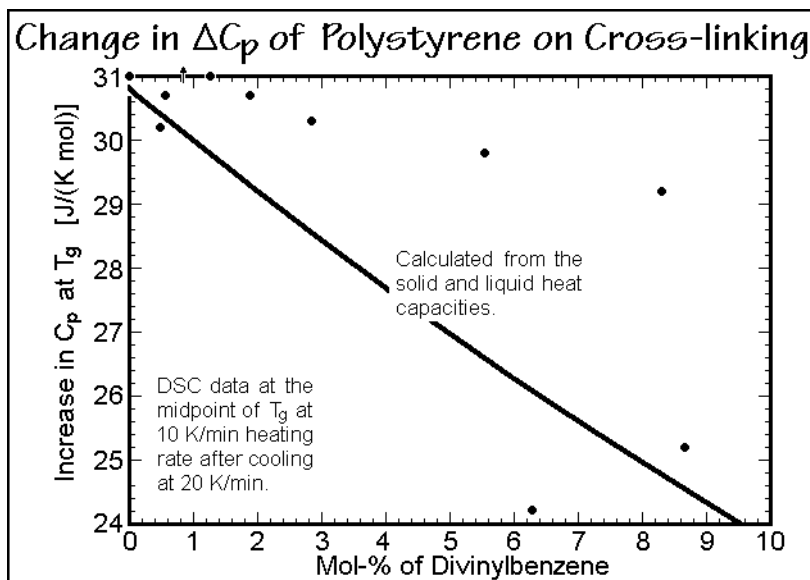
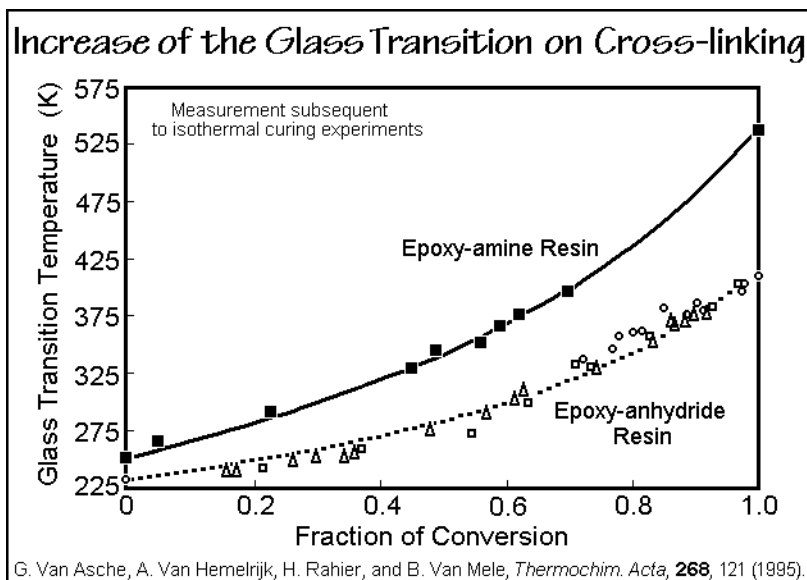


Fig. 6.136

to a diffusion-controlled, slow process. Figure 6.137 represents the change of the glass transition with the degree of curing for two epoxy systems. The glass transition is in this case a measure of the reaction history of the sample. Complete time-temperature-transformation (TTT) plots can be drawn using the quantitative changes in the glass transition temperature and following the heats of reaction by DSC and TMDSC as shown in Fig. 4.142.

**Fig. 6.137**

To summarize the observations of Sect. 6.3, one must remember that the history of a metastable sample is stored in its internal variables, i.e., for description, one must use the irreversible thermodynamics of Sect. 2.4, instead of the equilibrium thermodynamics. The internal variables that characterize the metastable state must be uniquely coupled to the history to be discovered. The evaluation of the thermal history of a glass is simple if the initial cooling of the sample is the only contributing factor to the history. In this case, a simple hysteresis determination, matched empirically to a reference, may be sufficient for the task (see Sect. 6.3.1, Fig. 6.6).

The quantitative prediction of the hysteresis can be attempted, as shown in Sect. 6.2 with Figs. 6.10 and 6.11, but is, at best, approximate. Problems in the theory of the glass transition which are not fully resolved are:

- (1) The asymmetry of the approach to equilibrium—self-retardation and autocatalysis, see Eq. (1) of Sect. 6.3.1, causing an  $N$ -dependent relaxation time  $\tau$  in Eq. (2) of Sect. 6.3.2 (see Fig. 4.126).
- (2) A cooperative kinetics with a temperature-dependent activation energy (see Fig. 6.117 and Sects. 6.3.1 and 6.3.2).
- (3) The need to handle more than one internal variable (see Fig. 6.123, Sect. 6.3.3).
- (4) The quasi-isothermal TMDSC analyses result in the reversing  $C_p$ , not the actual, apparent, reversible  $C_p$  (see Fig. 6.118, Sect. 6.3.2 and Sect. 4.4.3).
- (5) The standard TMDSC causes interactions between the rate of change of the underlying temperature and the modulation which result in differences in the reversing heat capacity with underlying temperature change and changes in the frequency of the response (see Figs. 4.133 and 6.7, and Sect. 6.3.2).
- (6) The strain, crystallinity, and cross-linking effects lead to additional internal variables that can set the history of a sample.

## References

### **General References**

**Sect. 6.1–3.** The basis for the phase scheme of equilibrium melting is based on the thermodynamic description developed by Ehrenfest [2] and later expanded to copolymers by Flory PJ (1953) *Principles of Polymer Chemistry*. Cornell University Press, Ithaca.

The discussion of metastable, semicrystalline phases of polymers and their irreversible melting is based on the two early papers: Wunderlich B (1964) A Thermodynamic Description of the Defect Solid State of Linear High Polymers. *Polymer* 5: 125–134; and: The Melting of Defect Polymer Crystals. *Polymer* 5: 611–624. A later review and expansion is given in: Wunderlich B (1997) Metastable Mesophases. *Macromol Symp* 113: 51–65.

More details about the main first-order phase transition, the melting, can be found in: Ubbelohde AR (1965) *Melting and Crystal Structure*. Oxford University Press, London. See also the sequel (1978) *The Molten State of Matter. Melting and Crystal Structure*. Wiley, New York.

The following book deals specifically with crystallization and melting of macromolecules: Wunderlich B (1976,1980) *Macromolecular Physics*, Vol 2, Crystal Nucleation, Growth, Annealing. Vol 3, Crystal Melting. Academic Press, New York.

A general discussion of the glass transition is given in: Seyler RJ, ed (1994) *ASTM Symposium on the Assignment of Glass Transition Temperatures Using Thermomechanical Analysis*. Atlanta GA, March 4–5, 1993, ASTM STP 1249, Am Soc Testing and Materials, Philadelphia; and by: Tant MR, Hill AJ, eds (1998) *Structure and Properties of Glassy Polymers*. ACS Symposium Series, 710, Am Chem Soc, Washington; see also: Matsuoka S (1992) *Relaxation Phenomena in Polymers*. Hanser, Munich. Finally see also the references to Chap 7.

### **Specific References**

1. Wunderlich B (2003) Reversible Crystallization and the Rigid Amorphous Phase in Semicrystalline Macromolecules. *Progr Polymer Sci* 28: 383–450.
2. Ehrenfest P (1933) Phase Changes in the Ordinary and Extended Sense Classified According to the Corresponding Singularities of the Thermodynamic Potential. *Proc Acad Sci, Amsterdam* 36: 153–157, Suppl 75b, Mitt Kammerlingh Onnes Inst, Leiden.
3. Wunderlich B, Grebowicz J (1984) Thermotropic Mesophases and Mesophase Transitions of Linear, Flexible Macromolecules. *Adv Polymer Sci* 60/61: 1–59.
4. Wunderlich B (1964) A Thermodynamic Description of the Defect Solid State of Linear High Polymers; and: The Melting of Defect Polymer Crystals. *Polymer* 5: 125–134 and 611–624.
5. Fu Y, Chen W, Pyda M, Londono D, Annis B, Boller A, Habenschuss A, Cheng J, Wunderlich B (1996) Structure-property Analysis for Gel-spun Ultra-high Molecular-mass Polyethylene Fibers. *J Macromol Sci, Phys* B35: 37–87.
6. Jones JB, Barenberg, S, Geil PH (1977) Amorphous Linear Polyethylene: Electron Diffraction, Morphology, and Thermal Analysis. *J Macromol Sci, Phys* B15: 329–335.
7. Chen W, Wunderlich B (1999) Nanophase Separation of Small And Large Molecules. *Macromol Chem Phys* 200: 283–311.



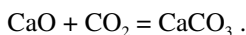
8. Eyring H (1936) Viscosity, Plasticity, and Diffusion as Examples of Absolute Reaction Rates. *J Chem Phys* 4: 283–291.
9. Frenkel J (1946) *Kinetic Theory of Liquids*. Clarendon, Oxford.
10. Hirai N, Eyring H (1958) Bulk Viscosity of Liquids. *J Appl Phys* 29:810–816.
11. Hirai N, Eyring H (1959) Bulk Viscosity of Polymer Systems. *J Polymer Sci* 37: 51–70.
12. Wunderlich B, Bodily DM, Kaplan MH (1964) Theory and Measurement of the Glass-transformation Interval of Polystyrene. *J Appl Phys* 35: 95–102.
13. Thomas LC, Boller A, Okazaki I, Wunderlich B (1997) Modulated Differential Scanning Calorimetry in the Glass Transition Region, IV. Pseudo-isothermal Analysis of the Polystyrene Glass Transition, *Thermochim Acta* 291: 85–94.
14. Wunderlich B, Boller A, Okazaki I, Kreitmeier S (1996) Modulated Differential Scanning Calorimetry in the Glass Transition Region II. The Mathematical Treatment of the Kinetics of the Glass Transition. *J Thermal Anal* 47: 1013–1026.
15. Boller A, Okazaki I, Wunderlich B (1996) Modulated Differential Scanning Calorimetry in the Glass Transition Region, III. Evaluation of Polystyrene and Poly(ethylene terephthalate). *Thermochim Acta* 284: 1–19.
16. Kovacs AJ (1964) Glass Transitions in Amorphous Polymers. Phenomenological Study. *Adv Polymer Sci* 3: 394–508.
17. Boller A, Schick C, Wunderlich B (1995) Modulated Differential Scanning Calorimetry in the Glass Transition Region. *Thermochim Acta* 266: 97–111.
18. Matsuoka S (1992) *Relaxation Phenomena in Polymers*. Hanser, Munich.
19. Gaur U, Wunderlich B (1980) Study of Microphase Separation in Block Copolymers of Styrene and  $\alpha$ -Methylstyrene in the Glass Transition Region using Quantitative Thermal Analysis. *Macromolecules* 13: 1618–1625.
20. Suzuki H, Grebowicz J, Wunderlich B (1985) The Glass Transition of Polyoxymethylene. *Brit. Polymer J* 17: 1–3.
21. Schick C, Wurm A, Mohammed A (2001) Vitrification and Devitrification of the Rigid Amorphous Fraction of Semicrystalline Polymers Revealed from Frequency-dependent Heat Capacity. *Colloid Polymer Sci* 279: 800–806.
22. Hellmuth, E, Wunderlich B (1965) Superheating of Linear High-Polymer Polyethylene Crystals. *J Appl Phys* 36: 3039–3044.
23. First published: Wunderlich B (1965) Zeitabhängige Vorgänge des Kristallisierens und Erstarrens bei linearen Hochpolymeren. *Kunststoffe* 55: 333–334.
24. Wunderlich B, Melillo L, Cormier CM, Davidson T, Snyder G (1967) Surface Melting and Crystallization of Polyethylene. *J Macromol Sci B1*: 485–516.
25. Okazaki I, Wunderlich, B (1997) Reversible Melting in Polymer Crystals Detected by Temperature Modulated Differential Scanning Calorimetry. *Macromolecules* 30: 1758–1764.
26. Pak J, Wunderlich B (2000) Thermal Analysis of Paraffins as Model Compounds for Polyethylene. *J Polymer Sci, Part B: Polymer Phys* 38: 2810–2822.
27. Pak J, Wunderlich B (2001) Melting and Crystallization of Polyethylene of Different Molar Mass by Calorimetry. *Macromolecules* 34: 4492–4503.
28. Saruyama Y (1999) Quasi-isothermal Measurement of Frequency Dependent Heat Capacity of Semicrystalline Polyethylene at the Melting Temperature using Light Heating Modulated Temperature DSC. *Thermochim Acta* 330: 101–107.
29. Goderis B, Reynaers H, Scherrenberg R, Mathot VBF, Koch MHJ (2001) Temperature Reversible Transitions in Linear Polyethylene Studied by TMDSC and Time-resolved, Temperature-modulated WAXD/SAXS. *Macromolecules* 34: 1779–1787.

30. Nukuchina Y, Itoh Y, Fischer EW (1965) Nachweis des partiellen Schmelzens von Polyäthylen Einkristallen mit Hilfe der Röntgenkleinwinkelstreuung. *J Polymer Sci B3*: 383–387.
31. Fischer EW (1972) Effect of Annealing and Temperature on the Morphological Structure of Polymers. *Pure Appl Chem* 31: 113–131.
32. Schultz JM, Fischer EW, Schaumburg O, Zachmann HA (1980) Small-angle X-ray Scattering Studies of Melting. *J Polymer Sci, Polymer Phys Ed* 18: 239–240.
33. Androsch R, Wunderlich B (2003) Specific Reversible Melting of Polyethylene. *J Polymer Sci, Part B: Polymer Phys* 41: 2157–2173.
34. Smith CW, Dole M (1956) Specific Heat of Synthetic High Polymers. VII. Poly(ethylene Terephthalate). *J Polymer Sci* 20: 37–56.
35. English AD (1984) Macromolecular Dynamics in Solid Poly(ethylene Terephthalate):  $^1\text{H}$  and  $^{13}\text{C}$  Solid State NMR. *Macromolecules* 17: 2182–2192.
36. Pyda M, Wunderlich B (2000) Reversible and Irreversible Heat Capacity of Poly(trimethylene Terephthalate) Analyzed by Temperature-modulated Differential Scanning Calorimetry. *J Polymer Sci, Part B: Polymer Phys* 38: 622–631.
37. Sichina WJ (1995) Examination of the Use of Dynamic DSC in the Melting Region, Proc. 24<sup>th</sup> NATAS Conf in San Francisco, Sept. 10–13, Mikhail SA, ed 24: 123–129.
38. Cheng SZD, Pan R, Wunderlich B (1988) Thermal Analysis of Poly(butylene Terephthalate), its Heat Capacity, Rigid Amorphous Fraction and Transition Behavior. *Makromolekulare Chemie* 189: 2443–2458.
39. Cheng SZD, Wunderlich B. (1985) Glass Transition and Melting Behavior of Poly(ethylene-2,6-naphthalene Dicarboxylate). *Macromolecules* 21: 789–797.
40. Blundell DJ, Buckingham KA (1985) The  $\beta$ -Loss Process in Liquid Crystal Polyesters Containing 2,6-Naphthyl Groups. *Polymer* 26: 1623–1627.
41. Sauer BB, Kampert WG, Neal-Blanchard E, Threefoot S, Hsiao BS (2000) Temperature Modulated DSC Studies of Melting and Recrystallization in Polymers Exhibiting Multiple Endotherms. *Polymer* 41: 1099–1108.
42. Wurm A, Merzlyakov M, Schick C (2000) Reversible Melting During Crystallization of Polymers Studied by Temperature Modulated Techniques (TMDSC, TMDMA). *J Thermal Anal Cal* 60: 807–820.
43. Alazideh A, Sohn S, Quinn J, Marand H (2001) Influence of Structural and Topological Constraints on the Crystallization and Melting Behavior of Polymers: 3. Bisphenol A Polycarbonate. *Macromolecules* 34: 4066–4078.
44. Schick C, Wurm A, Merzlyakov M, Minakov A, Marand H (2001) Crystallization and Melting of Polycarbonate Studied by Temperature-modulated DSC (TMDSC). *J Thermal Anal Cal* 64: 549–555.
45. Cheng SZD, Wunderlich B (1987) Glass Transition and Melting Behavior of Poly(oxy-2,6-dimethyl-1,4-phenylene). *Macromolecules* 20: 1630–1637.
46. Wurm A, Merzlyakov M, Schick C (1999) Crystallization of Polymers Studied by Temperature-modulated Techniques (TMDSC, TMDMA). *J Macromolecular Sci, Physics* 38: 693–708.
47. Wurm A, Merzlyakov M, Schick C (1999) Isothermal Crystallisation of PCL Studied by Temperature Modulated Dynamic Mechanical and TMDSC Analysis. *J Thermal Anal Cal* 56: 1155–1161.
48. Schick C, Merzlyakov M, Minakov AA, Wurm A (2000) Crystallization of Polymers Studied by Temperature-modulated Calorimetric Measurements at Different Frequencies. *J. Thermal Anal Cal* 59: 279–288.
49. Androsch R, Wunderlich B (2001) Reversible Crystallization and Melting at the Lateral Surface of Isotactic Polypropylene Crystals. *Macromolecules* 34: 5950–5960.

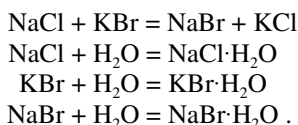
50. Grebowicz J, Lau S-F, Wunderlich B (1984) The Thermal Properties of Polypropylene. *J Polymer Sci Symp* 71: 19–37.
51. Wang ZG, Hsiao BS, Srinivas S, Brown GM, Tsou AH, Cheng SZD, Stein RS (2001) Isothermal Crystallization and Melting of Isotactic Polypropylene Analyzed by Time- and Temperature-dependent Small-angle X-ray Scattering Experiments. *Polymer* 42: 7561–7566.
52. Hu WB, Albrecht T, Strobl G (1999) Reversible Surface Melting of PE and PEO Crystallites Indicated by TMDSC. *Macromolecules* 32: 7548–7554.
53. Androsch R, Wunderlich B (2001) The Heat of Reversible Crystallization and Melting of Isotactic Polypropylene. *Macromolecules* 34: 8384–8387.
54. Schick C, Mohammed A, Wurm A (2001) Vittrification and Devitrification of the Rigid Amorphous Fraction in Semicrystalline Polymers Revealed from Frequency Dependent Heat Capacity. *Proc 29<sup>th</sup> NATAS Conf in St. Louis*, eds Kociba KJ, Kociba BJ, 29: 639–644.
54. Wang ZG, Hsiao BS, Sauer BB, Kampert WG (1999) The Nature of Secondary Crystallization in Poly(ethylene Terephthalate). *Polymer* 40: 4615–4627.
55. Adamovsky SA, Minakov AA, Schick C (2003) Scanning Microcalorimetry at High Cooling Rate. *Thermochim Acta* 403: 55–63.
56. Jaffe M, Wunderlich B (1967) Melting of Polyoxymethylene. *Kolloid Z Z Polym* 216–217: 203.
57. Cheng SZD, Cao M-Y, Wunderlich B (1986) Glass Transition and Melting of PEEK. *Macromolecules* 19: 1868–1876.
58. Marand H, Alizadeh A, Farmer R, Desai R, Velikov V (2000) Influence of Structural and Topological Constraints on the Crystallization and Melting Behavior of Polymers. 2. Poly(arylene Ether Ether Ketone). *Macromolecules* 33: 3392–3403.
59. Wurm A, Merzlyakov M, Schick C (1998) Reversible Melting Probed by Temperature-modulated Dynamic Mechanical and Calorimetric Measurements. *J Colloid Polymer Sci* 276: 289–296.
60. Höhne GWH, Kurelec L (2001) Temperature-modulated Differential Scanning Calorimetric Measurements on Nascent Ultra-high Molecular Mass Polyethylene. *Thermochim Acta* 377: 141–150.
61. Cheng J, Fone M, Fu Y, Chen W (1996) Variable-temperature Study of a Gel-spun Ultra-high-molecular-mass Polyethylene Fiber by Solid State NMR. *J Thermal Analysis* 47: 673–683.
62. Pak J, Wunderlich B (2004) Reversible Melting of Gel-spun Fibers of Polyethylene. *Thermochim Acta* 421: 203–209.
63. Kwon YK, Boller A, Pyda M, Wunderlich B (2000) Melting and Heat Capacity of Gel-spun, Ultra-high-molar-mass Polyethylene Fibers. *Polymer* 41: 6237–6249.
64. Todoki M, Kawaguchi Y (1977) Origin of Double Melting Peaks in Drawn Nylon 6 Yarns. *J Polymer Sci, Polymer Phys Ed* 15: 1067–1075.
65. Todoki M, Kawaguchi Y (1977) Melting of Constrained Drawn Nylon 6 Yarns. *J Polymer Sci, Polymer Phys Ed* 15: 1507–1520.
66. Okazaki I, Wunderlich B (1996) Modulated Differential Scanning Calorimetry in the Glass Transition Region, V. Activation Energies and Relaxation Times of Poly(ethylene terephthalate)s. *J Polymer Sci Part B: Polymer Phys* 34: 2941–2952.
67. Okazaki I, Wunderlich B (1997) Modulated Differential Scanning Calorimetry in the Glass Transition Region, VI. Model Calculations Based on Poly(ethylene Terephthalate). *J Thermal Anal.* 49: 57–70.

## Multiple Component Materials

In this last Chapter of Thermal Analysis of Polymeric Materials, the link between microscopic and macroscopic descriptions of multi-component macromolecules is discussed, based on the thermal analysis techniques which are described in the prior chapters. The key issue in polymeric multi-component systems is the evaluation of the active components in the system. The classical description of the term component was based on small-molecule thermodynamics and refers to the number of different molecules in the different phases of the system (see Sect. 2.2.5). If chemical reactions are possible within the system, the number of components may be less than the different types of molecules. It then represents the species of molecules that can be varied independently. For example, the three independent species  $\text{CaO}$ ,  $\text{CO}_2$ , and  $\text{CaCO}_3$  represent only two components because of the equation that links their concentrations:



More complicated is the mixture of the eight independent species in the four chemical equations:



Together with the material-balance equation, this system is described by only three components in the phase rule given in Sect. 2.5.7.

For macromolecules, the meaning of the term component was already relaxed to account for the fact that small changes in their length do not affect their properties, as discussed in Chap. 6. Similarly, decoupled segments of a polymer chain at a phase boundary may change the accounting for components, as is shown in Fig. 6.69. The main issues in Chap. 7 are the additional problems arising from the size of the macromolecule when one treats it as a single component in phase diagrams with components of smaller size (Sect. 7.1). Additionally, the flexibility of the macromolecules after copolymerization allows a decoupling of different repeating-unit sequences, leading to phase separation into domains of micrometer and nanometer dimensions without changing of the molecular structure. This may, for example, allow the treatment of copolymers as a multiple-component system (Sect. 7.2), even if the reactions that lead to the copolymer are fully arrested. Finally, Sect. 7.3 deals with the effect of multiple components in polymers on the glass transition.

## 7.1 Macromolecular Phase Diagrams

### 7.1.1 Phase Diagrams

The thermodynamics of the phase diagrams of multi-component systems of small molecules are described in Sects. 2.2.5 and 2.2.6. The key equations and the eutectic phase diagram are reviewed in Figs. 2.24–27. Applications of these equations are found in the molar-mass determinations described in Sect. 1.4. One-component pVT-phase diagrams are discussed in Sect. 4.1.7.

To review a general phase diagram in the condensed state with two components, a series of DSC heating-traces, labeled A–F, are shown in Fig. 7.1 with a vertical temperature axis and a horizontal heat-flow-rate axis. The phase diagram derived from these DSC curves is indicated by the dotted line using the same temperature axis and a horizontal concentration axis [1]. The DSC trace A is for a sample with a concentration somewhat beyond the pure component,  $x_1$ . The single, broad, melting peak suggests a solution of the two components. The beginning and end of melting indicate the positions of the solidus and liquidus, as represented by the dotted lines. Both change with variations in the overall concentration. When analyzing run B, a second endotherm can be seen, a peritectic transition. It is best identified together with run C at a higher mole fraction of component 2. At the peritectic temperature, a second solid solution that exists at larger  $x_2$  turns unstable. This becomes obvious when completing the full phase diagram, as is shown in area 6 of Fig. 7.2, below. The DSC runs D, E, and F reveal a simple eutectic phase diagram of crystals of component 2 with an intermediate compound (point 5 in Fig. 7.2). The phase diagram is interpreted in Fig. 7.2. Proof of the assumed phases usually needs a detailed X-ray structure analysis of all the indicated phase areas.

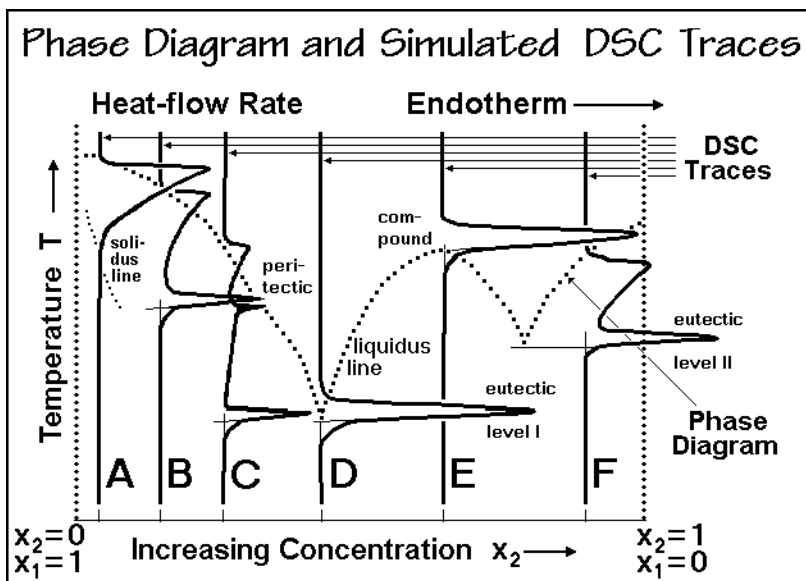


Fig. 7.1

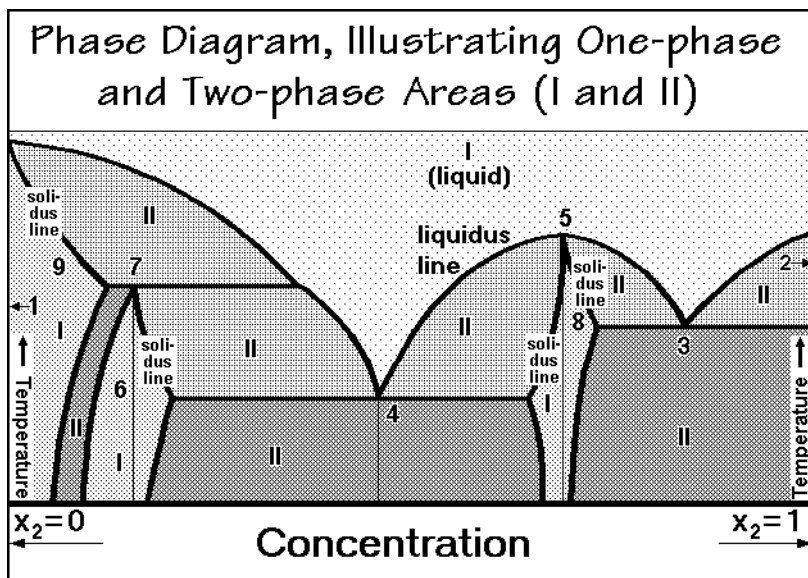


Fig. 7.2

Only the eutectic portion on the far right of Fig. 7.2 fulfills the conditions of complete solubility in the liquid phase and complete separation in the crystals, as was assumed in Fig. 2.27. The pure crystals, marked by the concentration  $x_1 = 1$ , and the compound "5," participating in the eutectic "3," have a small solubility in their crystals, the areas "9" and "8," respectively. All the solid solutions indicated in the diagram need additional specification of the concentration-dependence of the chemical potential of the components in the single phase areas (I) of limited solubility ("8," "6," and "9"). The solid solution "6" decomposes above the peritectic temperature "7" into the solid solution "9" and the liquid solution. All two-phase areas (II) consist of the two phase-separated compositions given at any chosen temperature by the points of intersections of a horizontal with the boundaries of the phase-areas. At equilibrium, the possible numbers of phases are governed by the phase rule:  $P + F = C + 2$  (see Sect. 2.5.7). In Fig. 7.2, three of the condensed phases are in contact at the eutectic temperatures "3" and "4," and the peritectic temperature "7." Adding the gas phase, omitted in the present discussion, leads to four phases (P) and no degrees of freedom (F). These quadruple points are thus the points of sharp transitions in the two-component phase diagram of Fig. 7.2 ( $C = 2$ ).

The next step towards the description of phase diagrams that include macromolecules is to change from the just discussed ideal solution to the real solutions, mentioned in Sect. 2.2.5. For this purpose one can look at the phase equilibrium between a solution and the corresponding vapor. The simplest case has a negligible vapor pressure for the second component, 2. The chemical potentials for the first component, 1, in solution and in the pure gas phase are written in Fig. 7.3 as Eqs. (1–3), following the discussion given in Fig. 2.26. For component 1, the chemical potential of the solvent,  $\mu_1^\circ$ , is defined in Eq. (1) for its pure state,  $x_1 = 1.0$ , but at its vapor pressure,  $p_1^\circ$ , not at atmospheric pressure. It must then be written as

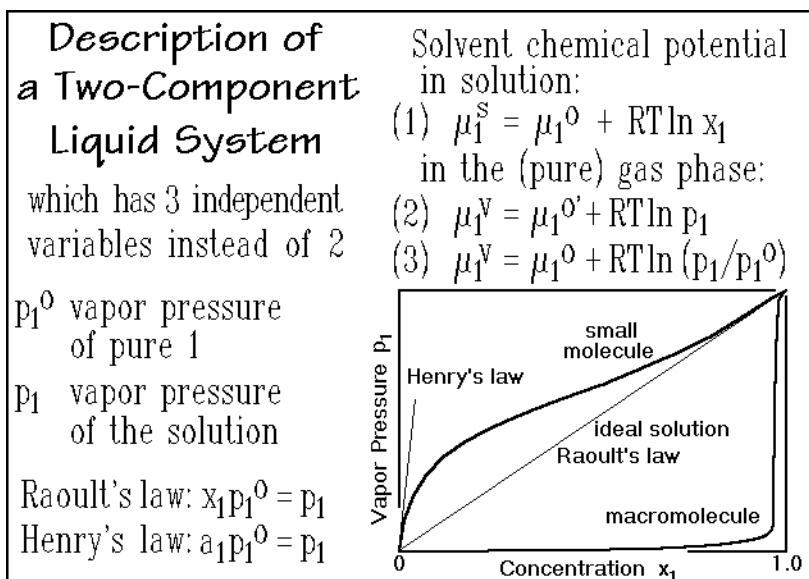


Fig. 7.3

Eq. (2) for the gas phase, but with its chemical potential  $\mu_1^0$  defined at atmospheric pressure  $p = 1.0$  atm. Equation (3) expresses then the chemical potential of the (pure) solvent vapor over the solution. Note, that in these expressions one always uses atm as unit of pressure, a non-SI unit of pressure (see Fig. 2.3, for conversion factors see Sect 4.5.1). At equilibrium, the two logarithmic terms in Eqs. (1) and (3) must be equal,  $\mu_1^s = \mu_1^v$ , and produce Raoult's law. Raoult's law is indicated by the diagonal in the graph of Fig. 7.3. At concentrations approaching the pure solvent,  $x_1 \rightarrow 1.0$ , this equation must always hold.

At higher solute concentrations ( $x_2 = 1 - x_1$ ), however, deviations occur for real solutions and must be evaluated in detail. The deviations from the ideal solution are often treated by introduction of an activity  $a_1$  replacing the concentration  $x_1$ . A well-known interpretation of the activity for the strong interactions, as are found for ions dissolved in water, is given by the Debye-Hückel theory [2]. Clusters of water are bound to the solute and reduce  $p_1$ . Repulsions, on the other hand, reject the solvent from the solution into the pure gas phase and increase  $p_1$ , as is shown in the example of Fig. 7.3. At high solute concentration  $x_2$ , the indicated tangent can approximate the vapor pressure and is called Henry's law.

For macromolecules the vapor pressure of a the low molar solvent is decreased so much that the Henry's law activity,  $a_1$ , remains practically zero for a wide concentration range. Only close to  $x_1 = 1.0$  does the vapor pressure approach Raoult's law, i.e., a large mole fraction of low-molar-mass solvent dissolves in a polymer melt without producing a noticeable vapor pressure. Perhaps, this should not be surprising if one remembers that  $x_1$  must be large compared to  $x_2$ , the mole fraction of the polymeric solute, to achieve comparable masses for the two components. The Flory-Huggins equation, to be described next, will resolve this problem and describes the vapor pressure in Fig. 7.3 for cases such as natural rubber dissolved in benzene.

### 7.1.2. Flory-Huggins Equation

To assess the influence of size on chemical potentials, one first searches, as in Sect. 2.2.5, for an ideal entropy of mixing, but now for macromolecules and small molecules. In Fig. 7.4, the description for a eutectic equilibrium between a pure polymer crystal and an amorphous solution is attempted as in Fig. 2.26 with Eqs. (1) and (2). The large-molecule component is 2, the small-molecule solvent, 1. Next, one tries to find expressions for the RHS and LHS of the differences in chemical potential, as before. The RHS is identical to the prior case and written on the right in Eq. (2). One needs to remember that  $\Delta H_f$  refers to one mole of large molecules, i.e., it has a much bigger effect than for small molecules, perhaps by a factor of 1,000! The left-hand side, the mixing expression, will be given by the Flory-Huggins equation.

**Derivation of the Flory-Huggins Equation**

(1)  $\mu_2^S - \mu_2^O = \mu_2^C - \mu_2^O$

(2)  $(\partial \Delta G_{\text{mix}} / \partial n_2) = -\Delta G_f = -\Delta H_f \Delta T_m / T_m^O$

(3)  $\Delta G_{\text{mix}} = -T \Delta S_{\text{ideal}} + \Delta G^*$  2 = macromolecular component  
1 = low-molecular-mass component

a. ideal mixing ( $\Delta G^* = 0$ )  $\Delta H_f$  per mole of macromolecule

(4)  $\Delta S_{\text{ideal}} = -n_1 R \ln v_1 - n_2 R \ln v_2$  volume fractions:

(5)  $v_1 = n_1 / (n_1 + n_2 x)$   
 $v_2 = n_2 x / (n_1 + n_2 x)$

b. including interaction (6)  $x = \text{volume ratio} = v_2 / v_1$

(7)  $\Delta G^* = \underbrace{(z - 2) x n_2 v_1}_{\substack{\text{total \# of} \\ \text{macromolecular} \\ \text{sites}}} \underbrace{\Delta w_{1,2}}_{\substack{\text{interaction parameter} \\ \text{site fraction} \\ \text{occupied, } \approx v_1}}$  n = number of moles of molecules

$z = \text{coordination number}$   $\Delta w_{1,2} = \text{interaction parameter}$

**Fig. 7.4**

The free enthalpy of mixing,  $\Delta G_{\text{mix}}$ , will first be treated by considering a new ideal entropy of mixing that depends on molecular size. Then, it will be expanded to a real solution by adding the interaction term,  $\Delta G^*$ , seen in Eq. (3). Easiest is the Hildebrand derivation [3]. One assumes that ideal liquids have a universal free volume fraction,<sup>1</sup>  $v_f$ . On mixing, the molecules expand into the available free volume, as in an ideal gas. They change from the free volumes in the pure states,  $V_{f1} = V_1 v_f$  and  $V_{f2} = V_2 v_f$ , to the total free volume  $V_{f1,2} = V_{\text{total}} v_f$  with a change in the entropy of  $\Delta S_{\text{ideal}} = -n_1 R \ln (V_{f1,2} / V_{f1}) - n_2 R \ln (V_{f1,2} / V_{f2})$ , where  $n_1$  and  $n_2$  are the moles of the respective molecules. Since the free volume fraction is assumed to be constant during the mixing, this leads to Eq. (4) in Fig. 7.4 with the definition of the volume fractions

<sup>1</sup>Fraction of empty space, for the related concepts of packing fractions, see Figs. 4.24 and 5.17, and for the hole model, see Sects. 6.13 and 6.23, as well as Fig. 6.5.



written as Eq. (5) and Eq. (6). An identical expression can be derived by placing the solution on a lattice where the solvent molecules occupy one unit cell each, and the macromolecules use  $x$  unit cells each ( $x = V_2/V_1$ ) [4,5]. Note that with  $x = 1$ , i.e., for equal sizes of both components, the equation describing the mixing reverts back to the result for the ideal gas in Fig. 2.24 ( $v_1 = x_1$  and  $v_2 = x_2$ ).

A simple calculation clarifies the effect of molecular size. Assuming two types of molecules mixed to a fixed volume  $V$  with fractions  $v_1 = v_2 = 0.5$ . Allowing large and small molecules of ratio 1,000:1, Eq. (4) yields a  $\Delta S = 693 R$  when both molecules are small ( $x = 1.0$ , and  $n_1 = n_2 = 500$ ), when one molecule is large and the other one small,  $x = 1,000$ , and now  $\Delta S = 347 R$  ( $n_1 = 500$  and  $n_2 = 0.5$ ), and when both molecules are large,  $x$  is again 1.0, but this time  $\Delta S = 0.7 R$  ( $n_1 = n_2 = 0.5$ ). One concludes that for small molecules the positive entropy strongly drives the dissolution and may overcome the endothermic heat of solution which usually exists in the absence of specific dipole or H-bond interactions between solvent and solute. Large molecules still may dissolve in a small molecular solvent for entropic reasons. Macromolecules, in contrast, will not dissolve other macromolecules, unless the overall free enthalpy is negative, i.e., the heat-of-dissolution is exothermic (see Sect. 2.2.3).

The last step in the derivation involves the evaluation of  $\Delta G^*$ , the interaction term, which may help the dissolution of a macromolecule by becoming exothermic. Equation (7) in Fig. 7.4 and the sketch in Fig. 7.5 show how one can assess  $\Delta G^*$  from the number of contacts a macromolecule can make with its low-molar-mass neighbors. If the interaction parameter,  $\Delta w_{1,2}$  per contact pair, is taken to be an enthalpy, the resulting mixing expression applies to a regular solution (ideal entropy and a non-zero enthalpy of mixing). Making it a free enthalpy by including a correction to the ideal entropy into  $\Delta w_{1,2}$ , the mixing expression for a real solution of unequal molecular sizes results. The equivalence in Eq. (8) allows one to eliminate  $x$  from Eq. (7), and

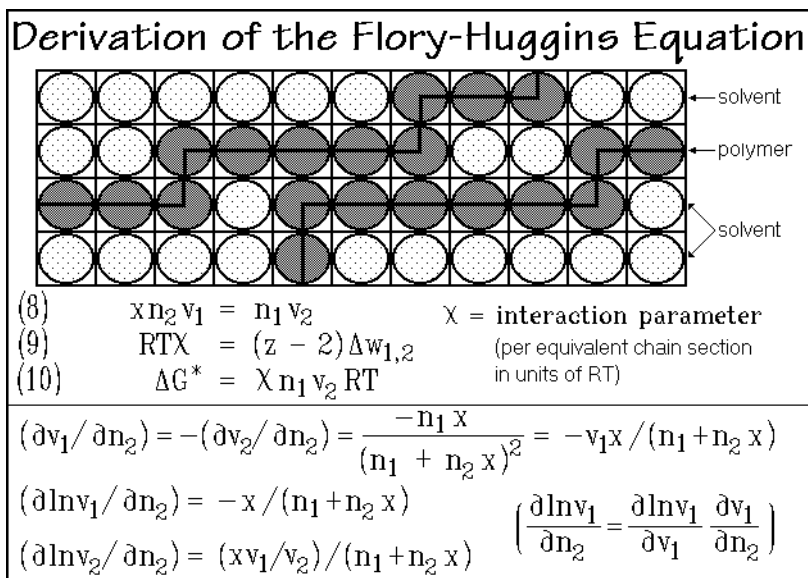


**Fig. 7.5**

the introduction of the interaction parameter  $\chi$ , expressed in units of  $RT$ , yields Eq. (9) and allows, finally, to change Eq. (7) in Fig. 7.4 to Eq. (10) of Fig. 7.5, and yields with Eq.(3) the Eq. (11) in Fig. 7.6. The new interaction parameter  $\chi$  is central to the description of the polymer solutions. The bottom equations in Fig. 7.5 help in the derivation of the operation suggested by Eq. (2). The result is the Flory-Huggins equation, Eq. (12). The boxed Eq. (13) is the equation for  $\Delta T_m$ , which describes the freezing-point lowering of polymer crystals in the presence of a solvent under equilibrium conditions, with the solvent being rejected from the polymer crystal (eutectic phase diagram). Examples are given in Sects. 7.1.5 and 7.1.6.

**Solution for the Freezing-point Lowering**

(3)  $\Delta G_{\text{mix}} = -T\Delta S_{\text{ideal}} + \Delta G^*$

(11)  $\Delta G_{\text{mix}} = +\chi n_1 v_2 RT + n_1 R \ln v_1 + n_2 R \ln v_2$

(2)  $(\partial \Delta G_{\text{mix}} / \partial n_2) = -\Delta G_f = -\Delta H_f \Delta T_m / T_m^0$

(12)  $(\partial \Delta G_{\text{mix}} / \partial n_2) = RT [\ln v_2 + (1-x)(1-v_2) + \chi x (1-v_2)^2]$

(13)  $\Delta T_m = -RT T_m^0 [\ln v_2 + (1-x)(1-v_2) + \chi x (1-v_2)^2] / \Delta H_f$

for  $x = 1$  and small  $v_1$  ( $v_1 = \text{mole fraction } x_1$ )

(14)  $\Delta T = RT^2 x_1 / \Delta H_f$

for  $x \gg 1$  and small  $v_1$

(15)  $\Delta T = RT^2 v_1 x / \Delta H_f$       (16)  $\Delta T = RT^2 v_1 / \Delta H_u$

**Fig. 7.6**

At equal sizes of the two components and with a small  $v_1$ , the ideal  $\Delta T_m$  of Fig. 2.26 is recovered, as is indicated by Eq. (14) of Fig. 7.6. With a macromolecular component 2, i.e., a very large  $x$  and also for a small concentration  $v_1$ , the heat of fusion of the macromolecule in Eq. (15) of Fig. 7.6 can be replaced by  $\Delta H_f/x$ , the heat of fusion of the macromolecule per reference volume of the low-molar-mass component 1, which is often written with Eq. (16) as  $\Delta H_u$ .

Quite analogous to the phase equilibrium of the macromolecular component 2 in Eq. (13), one can also write the Flory-Huggins expression for the small-molecule component 1 (see Fig. 2.26) to complete a eutectic phase diagram (see Fig. 2.27):

$$\mu_1^s - \mu_1^o = \mu_1^c - \mu_1^o,$$

with the RHS representing the  $\Delta H_f$  of the small solvent molecules, which have a much smaller effect than the macromolecules (factor of  $1/x$ ). The left-hand sides of the equations, representing the partial molar mixing, which are available for both components from the overall expression for  $\Delta G_{\text{mix}}$  by differentiation with respect to the component under consideration,  $n_1$ . The result is used in Fig. 7.7, below.

### 7.1.3. Upper and Lower Critical Temperatures

Liquid-liquid phase separations are treated in this section. The top equation in Fig. 7.7 repeats the Flory-Huggins equation for the chemical potential of a macromolecular component 2 dissolved in a low-molar-mass solvent 1, as derived in Fig. 7.6, Eq. (12). By analogy, the chemical potential of component 1 is written in the second equation. From Fig. 7.4, one can, furthermore, state that for the phase separation into solutions I and II, the equations in the center of Fig. 7.7 must hold. The condition for a phase separation is thus that the system must have two concentrations,  $x_2^I$  and  $x_2^{II}$ , with the same slopes  $\partial\Delta G/\partial x_2$ , as shown.

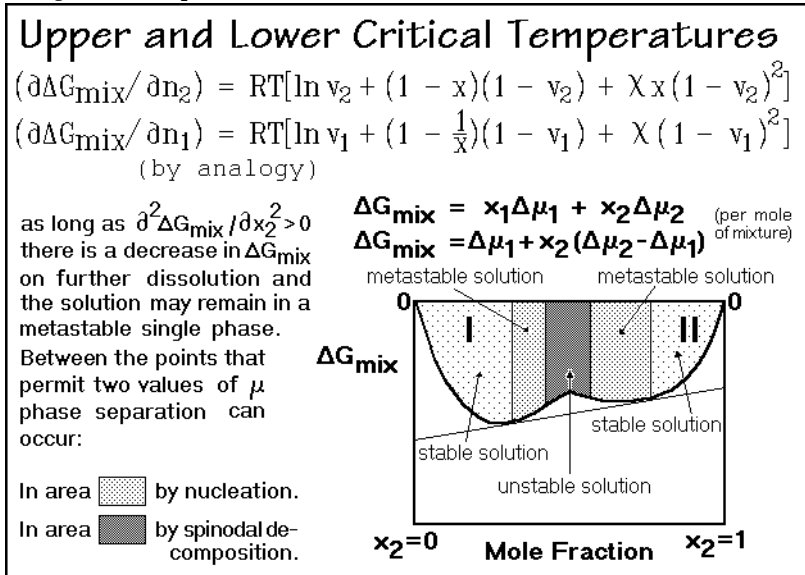


**Fig. 7.7**

The equation in the center of Fig. 7.7 is analogous to the evaluation of the partial molar quantities in Fig. 2.25 for volume and leads to the constructions shown. The limiting two concentrations share the same tangent to the  $\Delta G_{\text{mix}}$  curve. Between the two areas of stable solutions lies the two-phase area. A system in the two-phase range separates into two different concentrations, set by the limits of the two-phase area. Its total  $\Delta G_{\text{mix}}$  is less than the heavy line in Fig. 7.7 (more negative). The sum of the free enthalpies of mixing of the two solutions is given by the tangent to the two concentrations of phase separation. On gradually entering the region of phase separation by changing the concentration, one notes that the free enthalpy of mixing still decreases as long as  $\partial^2\Delta G_{\text{mix}}/\partial x_2^2 \geq 0$ , i.e., starting the phase separation needs a nucleation event to overcome an interfacial free energy. The single phase may remain metastable. The limiting value  $\partial^2\Delta G_{\text{mix}}/\partial x_2^2 = 0$  is reached at the point of inflection. From this point on, phase separation is spontaneous, one has reached the spinodal decomposition concentration. Changing the concentration along the tangent of inflection causes no change in  $\Delta G_{\text{mix}}$  for concentration fluctuations, and the two phases given by the phase limits (the binodals) can grow continuously without nucleation.

The phase diagrams expressed in temperature versus volume fraction  $v_2$  are shown in Fig. 7.8 for a series of different molar masses of polystyrene dissolved in diisobutyl ketone (the lower curves correspond to lower molar masses). Lower molar masses dissolve at lower temperature and yield a narrower two-phase area. To find the upper critical temperature of phase separation, the UCST, one can insert for low polymer concentrations  $v_2$  the first few terms of the series-expansion for  $\ln v_1 = \ln(1 - v_2)$  given in Fig. 7.8 into the expression for  $\partial\Delta G_{\text{mix}}/\partial n_1$  (given in Fig. 7.7). With the first two terms of the expansion this leads to the equation listed for  $\ln a_1$ , the activity of the component 1 ( $\partial\Delta G_{\text{mix}}/\partial n_1 = \Delta\mu_1$ , see also Fig. 7.3).

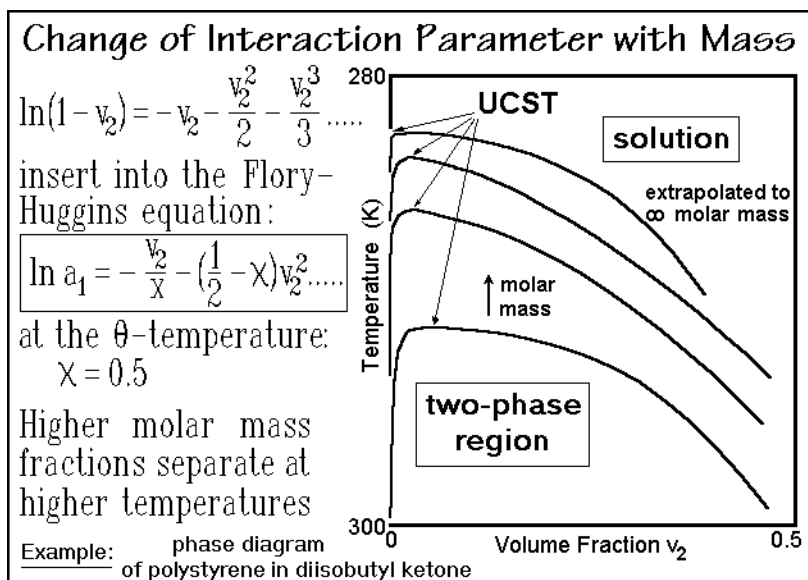


Fig. 7.8

First, one notices that when the interaction parameter  $\chi$  reaches a value of 0.5, the term in parentheses, the second virial coefficient, becomes zero and the term in  $v_2^2$  vanishes. The temperature where this condition is met is called the  $\theta$ -temperature. It is easy to see that, in analogy to the non-ideal gases, this is the temperature where the repulsive effect of the interaction between the large and small molecules overcomes the excluded volume and the system behaves as if it were ideal. For macromolecules and small molecules this condition is discussed in Figs. 1.33 and 1.34 and methods to measure the second virial coefficient are found in Sect. 1.4.2.

The second observation is that a horizontal tangent and tangent of inflection for incipient phase separation (UCST) is obtained at  $\partial\Delta\mu_1/\partial v_2 = \partial^2\Delta\mu_1/\partial v_2^2 = 0$ . Carrying out the differentiations with the appropriate equation of Fig. 7.7, leads first to the result  $(1 - v_{2c})^{-1} - (1 - x^{-1}) - 2\chi v_{2c} = 0$  and then to  $(1 - v_{2c})^{-2} - 2\chi = 0$ . The solution for the UCST is thus  $v_{2c} = (1 + x^{1/2})^{-1}$ , i.e.,  $v_{2c}$  is close to zero for large molar masses. Similarly, the critical  $\chi_c$  is  $\approx 0.5 + x^{-1/2}$ .

Figure 7.9 shows the phase diagram for two polystyrenes of different molar masses with acetone. It illustrates that the value of  $\chi$  can be separated into an enthalpy effect,

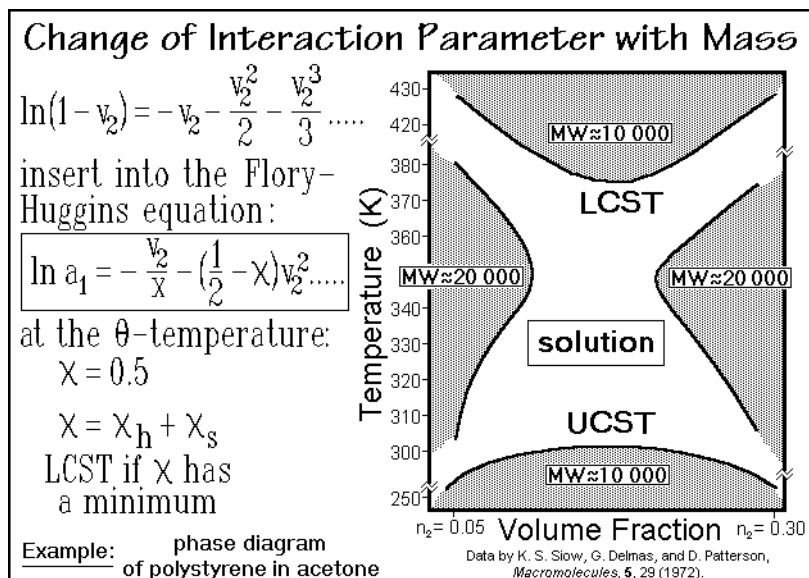


Fig. 7.9

$\chi_h$ , and an entropy effect,  $\chi_s$ . If  $\chi$  has a minimum in its temperature-dependence, an LCST, lower critical solution temperature, is possible in addition to the UCST, as exhibited by the lower-molar-mass polystyrene. The same equations as derived above for the UCST apply for the case of an LCST.

#### 7.1.4. Phase Diagrams with Low-mass Compounds

In this section, phase diagrams of systems with two components are discussed, one of low and one of high molar mass. Only the case is treated where both components crystallize in a eutectic-like manner. The top equation in Fig. 7.10 describes the liquidus line for the macromolecule located on the right side of a eutectic phase diagram. It applies to equilibrium, and represents Eq. (13) of Fig. 7.6, the Flory-Huggins equation. The second equation applies to the left, low-molar-mass side and can similarly be derived from the appropriate equations of Fig. 7.4–7. The phase diagram for polyethylene and 1,2,4,5-tetrachlorobenzene (TCB) at the bottom of Fig. 7.10 looks, indeed, like a eutectic phase diagram. The data points were obtained by DSC, as outlined in Sect. 7.1.1. To minimize nonequilibrium effects, the results were extrapolated to a heating rate of zero. The volume fraction is assumed to be close to the weight fraction. The low-molar-mass side is close to equilibrium, but polyethylene should show a  $T_m^\circ$  of 414.6 K at  $w_2 = 1.0$ , i.e., the phase diagram follows at best, a zero-entropy-production curve, paralleling equilibrium (see Fig. 6.79).

The equations at the lower right in Fig. 7.10 express the freezing point lowering for the pure solvents on adding small amounts of the solute, i.e., the tangents to zero concentrations. The top equation is the ideal solution limit ( $a_1 = x_1 = 1 - x_2$ , Raoult's law, see Fig. 7.3). It arises from the second of the top equations for the low-molar-mass solvent in Fig. 7.10 if the polymer solution is so dilute that the macromolecules

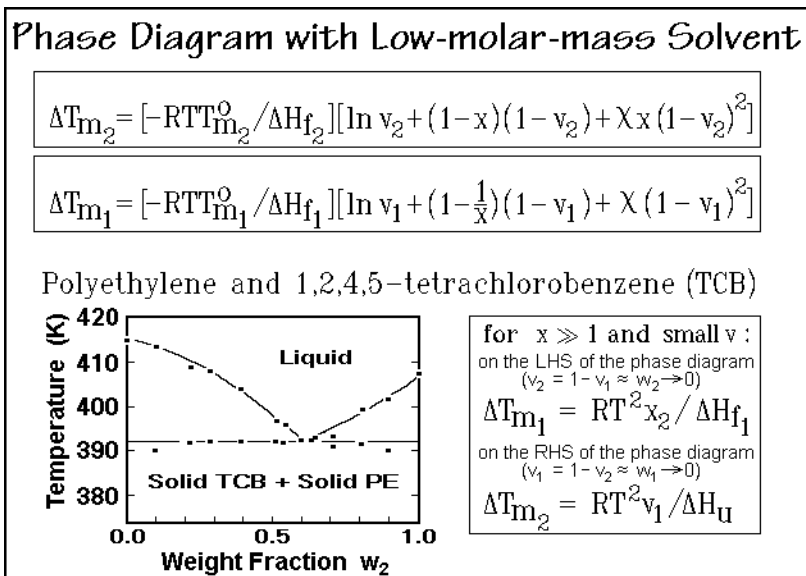


Fig. 7.10

are isolated from each other (compare to Fig. 7.6). This equation is used to determine molar masses of polymers in Fig. 1.63 and 6.64 (see Sect. 1.4.3). The data points from the right-hand side of the eutectic phase diagram can be used with the second equation which is identical to Eq. (16), derived in Fig. 7.6.

The method of adding small amounts of a low-molar-mass compound to the polymer can be used to determine  $\Delta H_u$  from the freezing point lowering, measured by DSC or dilatometry, and is known as the diluent method. The slope  $\partial \Delta T / \partial v_1$  allows the evaluation of  $\Delta H_u$ . Some typical experimental values for the heat of fusion of polyethylene with the diluent method are 3.89, 3.91, 4.14, and 4.06 kJ mol<sup>-1</sup> for the solvents ethyl benzoate, *o*-nitrotoluene, 1,2,3,4-tetrahydronaphthalene (tetralin), and  $\alpha$ -chloronaphthalene, respectively [6,7]. The method is not absolute, since polymer crystals are usually not in equilibrium. The measurements rely, thus, on analyzing crystals of identical lamellar thickness (identical metastability) for the different concentrations. A distinct advantage of the diluent method is that the crystallinities of the samples needs not to be known. The reasonable agreement with the established equilibrium heat of fusion (4.11 kJ mol<sup>-1</sup>) suggests, furthermore, that the free enthalpy curves of crystals of different metastability are often parallel, as assumed, for example, for the schematic in Figs. 2.86–88 and Fig. 6.79.

Figure 7.11 illustrates the irreversible behavior of the same TCB and polyethylene, but under nonequilibrium conditions. The DSC data were collected after quenching to 354 and 388 K for crystallization. Comparing with Fig. 7.10 shows reasonable agreement for TCB. For polyethylene, crystallization at the higher temperature, 378 K, raises the eutectic and melting temperatures relative to crystallization at 354 K. The cooling traces, in contrast, show even lower crystallization temperatures for the polymer and at higher concentration, the TCB phase diagram is also affected. It is of particular interest that both the eutectic temperatures and the eutectic concentrations

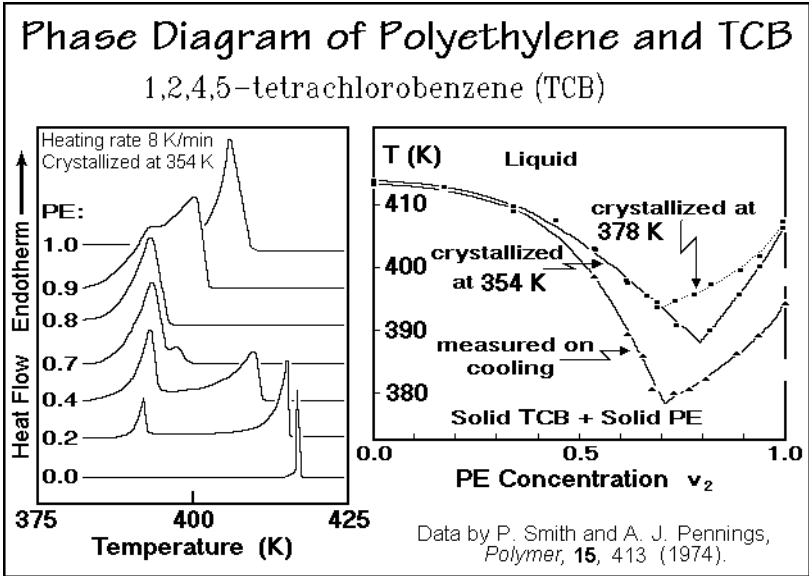


Fig. 7.11

change with different degrees of perfection of the crystals. These experiments indicate that crystal perfection plays a considerable role in the phase diagram obtained. While there is only one equilibrium phase diagram, a system may have an unlimited number of nonequilibrium phase diagrams.

A second phase diagram of a polymer with a low-molar-mass compound is displayed in Fig. 7.12. The system consists of polypropylene, PP, and pentaerythrityl

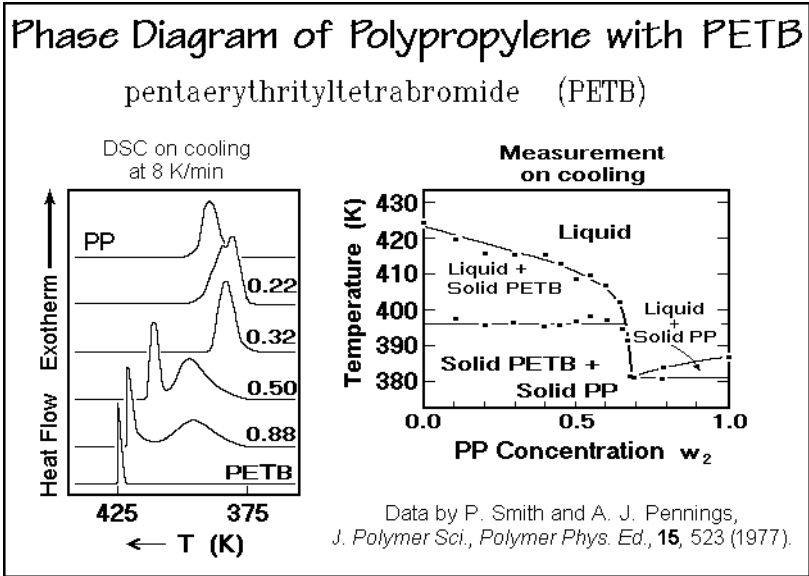


Fig. 7.12

tetrabromide, PETB. Again, cooling curves are used for the analysis and large deviations from equilibrium are obvious. Two eutectic temperature levels develop. One on the PETB side which, as a small molecule, is expected to be closer to equilibrium. The other one, on the PP side, is displaced by about 15 K to lower temperature. The reason for this lower eutectic temperature is an enhanced nucleation of the polymer by the PETB that crystallizes before the polymer on the low PP concentration side of the phase diagram. The two data points on the right indicate that PP may not nucleate PETB.

### 7.1.5. Phase Diagrams with Low-mass Homologs

A polymer sample with some low-molecular-mass fraction is expected to show a broader melting peak due to early melting of low-molar-mass homologs (see Fig. 6.25). Now an attempt will be made to describe the melting peak of polyethylene crystallized in the extended-chain, equilibrium macroconformation using the Flory-Huggins treatment of Sect. 7.1.2. Under such conditions it is possible to approach equilibrium for a wider range of molar mass. It is known that paraffins of different lengths follow the eutectic crystallization behavior, i.e., they are soluble in the melt, and segregated into different crystals on solidification. Only on quenching are metastable solid solutions formed.

Figure 7.13 displays a eutectic phase diagram when both components have large sizes and possess identical melting temperatures ( $T_{m1}^{\circ} = T_{m2}^{\circ}$ ). One, then, can use the Eq. (13) in Fig. 7.6 for calculation of both liquidus lines of the eutectic phase diagram. A substantial lowering of the melting temperature occurs only when the volume fractions approach zero, and  $\ln v_2$ , respectively  $\ln v_1$ , approach infinity because of the high molar entropy of fusion ( $\Delta H_f/T_m^{\circ}$ ) and a value of  $x = 1$  in Eq. (13).

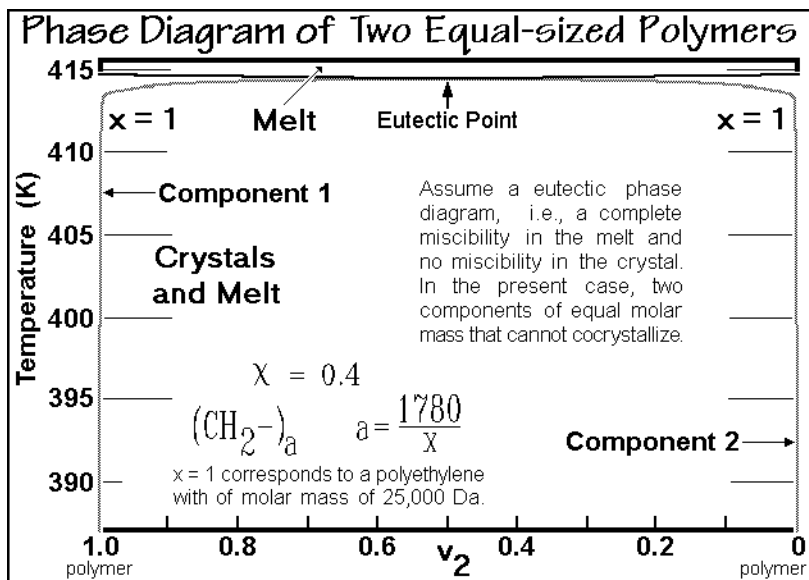


Fig. 7.13



The eutectic point is located at  $v_2 = v_1 = 0.5$  as long as the two values of  $T_m^\circ$  are taken to be identical. As soon as the melting temperatures of the two components are different, the eutectic moves to the ordinate of the lower-melting component, i.e., the higher melting component is practically independent of the lower melting component, a typical behavior of macromolecules.

Figure 7.14 contrasts the liquidus line of a polyethylene with a molar mass of 25,000 Da with those of its oligomers. A paraffin  $C_{20}H_{42}$ , for example, would cause a value of  $x = 200$  in Eq. (13) of Fig. 7.6, and has an equilibrium melting temperature of 219.6 K. Such low melting temperature is still far below any reasonable concentration of paraffin,  $v_1$ , in the phase diagram, and the eutectic point lies on the ordinate at  $v_1 \approx 1.0$  or  $v_2 \approx 0$ . The melting curve of the polymer, however, is considerably broadened due to the dissolution of the polymer into the liquid paraffin.

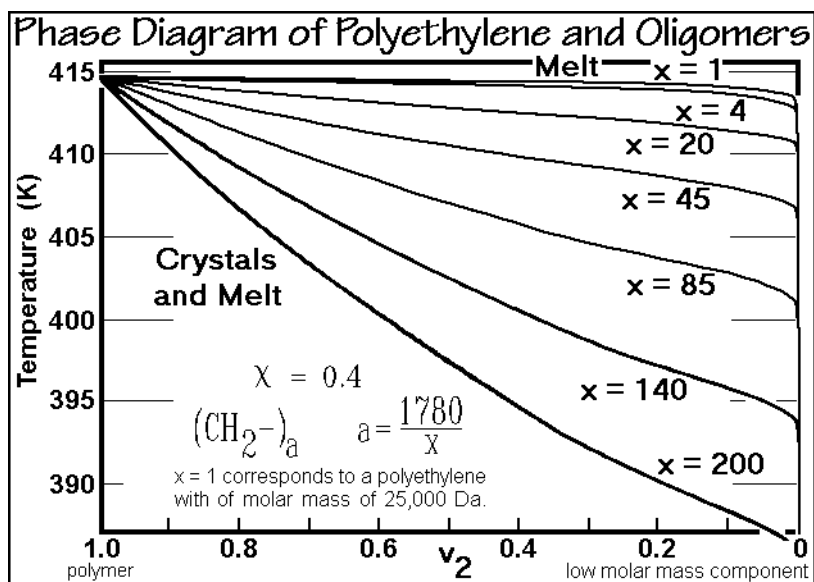


Fig. 7.14

The other curves in Fig. 7.14 complete the phase diagrams for a series of oligomers. The eutectic points are still located at the right ordinate. The  $T_m^\circ$  of the lower mass components are for  $x = 4$ , 408 K, and for  $x = 85$ , 311 K.

High-molar-mass, extended-chain crystals melt sharply, as is discussed with Figs. 3.89, 4.18, and 6.28. Broader molar-mass distributions crystallized under conditions of chain extension can be checked for attainment of equilibrium using the phase diagrams displayed in Fig. 7.14 after adjustment for the change from a two-component system to multi-components. Equations (1) and (2) of Fig. 7.15 indicate the needed alterations [8]. The equations are derived from the Flory-Huggins equation of Fig. 7.6 by using suitable averages for  $x$  in Eq. (13) to handle the multiple components in the melt. With the larger number of components, the phase diagram can only be calculated using numerical iteration, as shown in the flow sheet of Fig. 7.15. The first step is to approximate the composition of the polymer by division

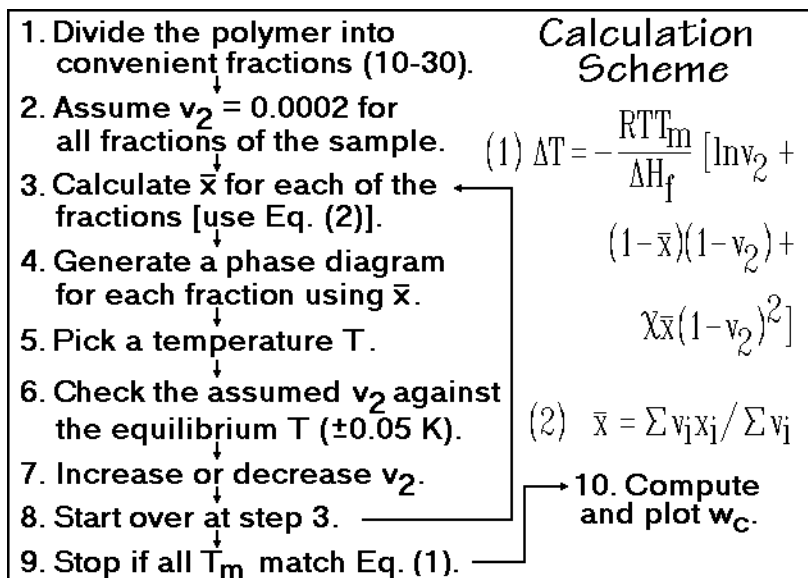
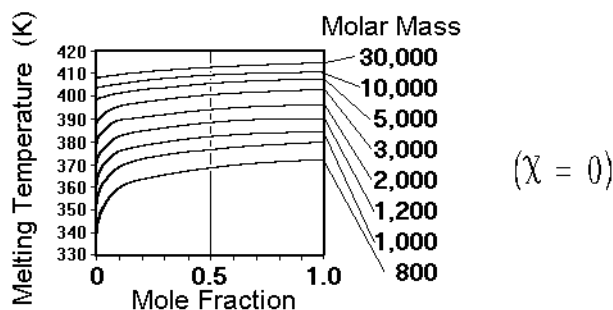


Fig. 7.15

into typically 10 to 30 components, rather than using the continuous distribution function. Next, a low concentration limit of  $v_2$  is chosen to be 0.0002 to avoid the very large negative values for  $\ln v_2$  which would occur in Eq. (1) as  $v_2$  approaches zero. After setting up this description of the melt, an experiment with increasing temperature is simulated. At low temperature, all polymer fractions are crystallized. As soon as on raising the temperature, an intersection of any of the phase diagrams calculated with Eq. (1) and shown in Fig. 7.16 occurs at  $v_2 > 0.0002$ , its fraction in the melt is iteratively increased until it matches the phase diagram. If the sample does not contain enough crystals of the given fraction, all is assumed to have melted.

Going through all fractions and temperatures, leads to the melting curves, illustrated in Fig. 7.17. Comparisons with the experiments on samples of close to 100% crystallinity show that the low-molar-mass fraction, FR1, follows the calculation throughout the melting range within the limits of error. One concludes that all components in this distribution follow an equilibrium phase diagram. For the two other samples, the match between experiment and calculation stops after partial melting. The crystals melt sharper than predicted for eutectic crystallization, an indication that solid solutions were formed with shorter molecules. The first deviations from equilibrium can be traced to the melting temperatures of molecules with a molar mass of about 20,000. One concludes that under the given crystallization conditions, eutectic separations can occur below a molar mass of 20,000. Above, non-equilibrium, mixed crystals grow. It is of interest that similar separations into solid solutions of different, high-molar-mass components and eutectic crystallization of components with low-molar-mass components occurs also on melt and solution crystallization to lower crystallinity into the folded-chain macroconformations. The reasons for this behavior are linked to the need of molecular nucleation (see Sect. 3.5.6) and the chain-folding principle, discussed in Sect. 5.22.

### Phase Diagrams for Polyethylene and its Oligomers in Contact with a Melt of Molar Mass 2,500 Da



For details see: B. Prime and B. Wunderlich,  
*J. Polymer Sci., Polymer Phys. Ed.*, **7**, 2073 (1969)

Fig. 7.16

### Comparison of the Computed Phase Diagrams with Experiments on Extended-chain Polyethylene

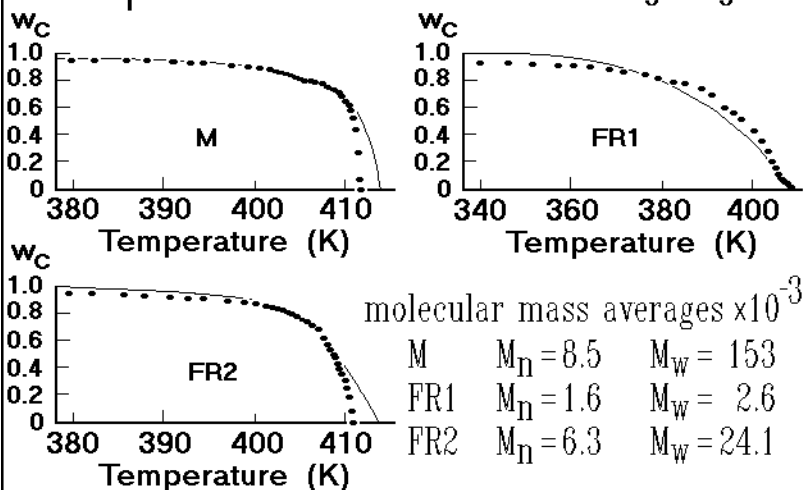


Fig. 7.17

The analysis by TMDSC of the melting of extended-chain crystals of polyethylene of low-molar-mass oligomers, and paraffins is discussed with Figs. 6.24–28. It is concluded in Sect. 6.2.1 that the melting transition of extended-chain crystals is irreversible as long as their molar mass exceeds 1,000 Da. This lower limit of irreversible melting is established with experiments depicted in Fig. 3.75 and linked to the need for molecular nucleation for the longer chain lengths in Sect. 3.5.6. Such

molecular nucleation is not needed for melting, so that on heating, the melting temperature is usually observed at the zero-entropy-production condition, as discussed in Sect. 2.4.2. Only for large, extended-chain crystals is the melting sufficiently slow that superheating is observed in DSC experiments, as shown in Fig. 6.22. To document all these effects, Fig. 7.18 presents a comparison of standard DSC and quasi-isothermal TMDSC for the extended-chain crystals M of Fig. 7.17 [9]. Their morphology is illustrated in Fig. 5.76 [10]. On first heating, when the extended-chain macroconformation is still intact, the reversing melting by quasi-isothermal TMDSC is minimal, almost all crystals melt irreversibly. A comparison to the lower-molar-mass samples of extended-chain macroconformation is shown in Fig. 6.28. Quite clearly, the reversible melting decreases with molar mass.

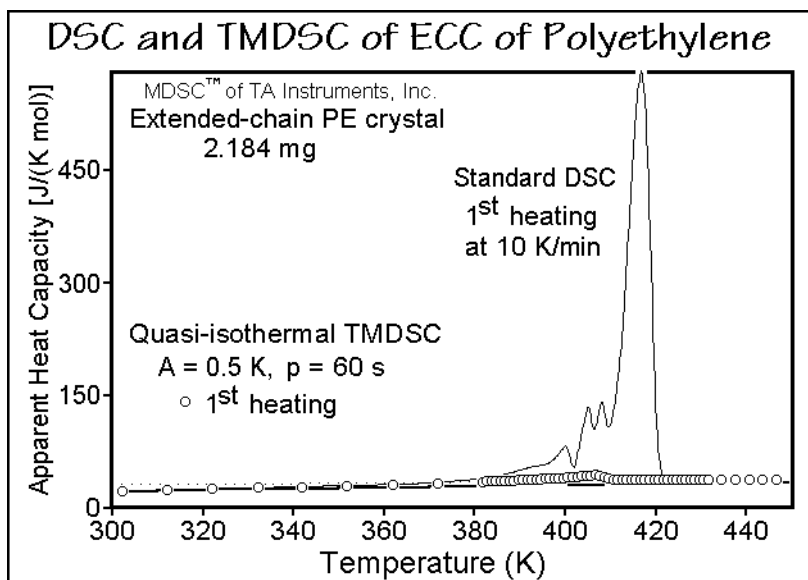


Fig. 7.18

The crystal structure and perfection of the extended-chain crystals was measured by X-ray diffraction, the crystal size distribution was assessed by electron microscopy and compared to the molar mass distribution determined by size-exclusion chromatography. The melting, finally was followed by slow dilatometry to avoid superheating which is common for extended-chain crystals of more than one micrometer thickness [8,11,12]. The slow dilatometry, free of superheating, and the long-time corrected reversible melting on quasi-isothermal TMDSC yield a baseline for the reversible melting, as shown in Fig. 7.19 [9]. The reversible heat of fusion is indicated by the shaded area. It is only about 7% of the total heat of fusion. Figure 7.20, finally, illustrates the molar-mass distribution, as obtained from size-exclusion chromatography (see Sect. 1.44), and crystal-size distribution from electron microscopy [12].

From Fig. 6.20, the limits of molecular nucleation of Fig. 3.75, and the phase diagram evaluated from dilatometry, a separation of the various contributions to the reversible melting is possible. The polyethylene of Fig. 7.18 has 3% of its molar-mass

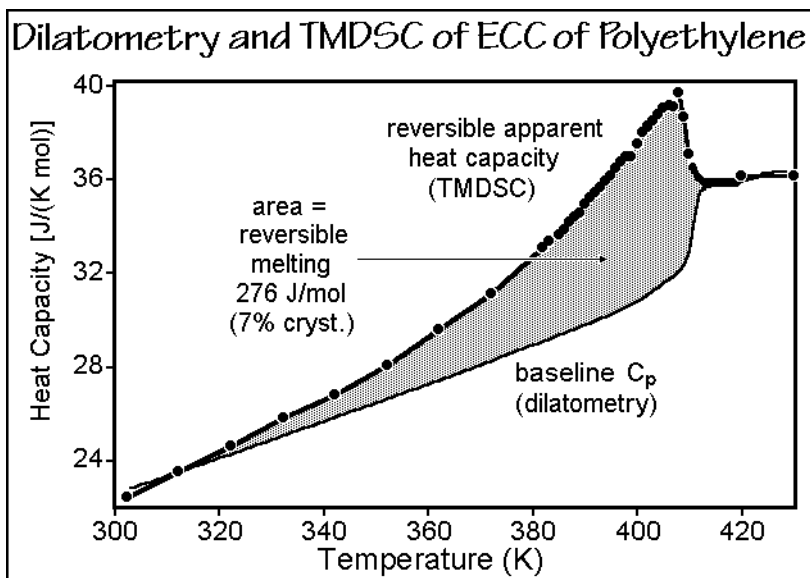


Fig. 7.19

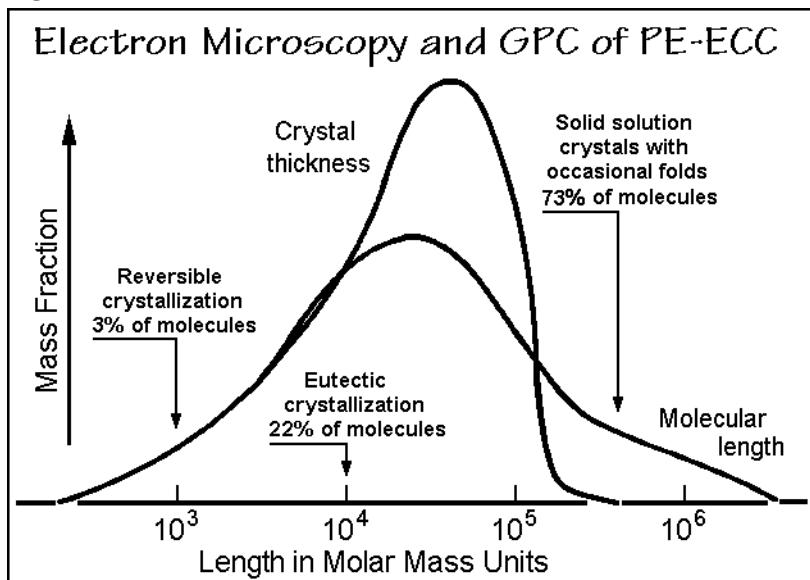


Fig. 7.20

distribution shorter than the critical length given in Fig. 3.75 ( $\approx 1,000$  Da). These 3% of the crystals melt fully reversibly at temperatures below 385 K, i.e., the ratio of reversible latent heat absorbed per kelvin of change of temperature to the total is one, DSC and reversing TMDSC give the same apparent heat capacities. This small low-molar-mass fraction accounts for about 40% of the reversible melting seen in

Fig. 7.19. The next portion of the molecules, up to about 10,000 Da in molar mass, accounts for 22% of the polyethylene, and still segregates on crystallization at elevated pressure into separate crystals of uniform mass (see the marking in Fig. 7.20). This second fraction agrees also with the number of crystals of the same length which have a known melting range up to 408 K. In this temperature range between 385 and 408 K, the amount of reversible melting decreases rapidly as also seen in Fig. 6.28. The percentage of reversible latent heat absorbed per kelvin of change of temperature decreases from 75% K<sup>-1</sup> to 7% K<sup>-1</sup> of the total latent heat per kelvin in this temperature range. Beyond 408 K, 73% of the total crystallinity remain. This large fraction melts sharply and gives rise to the major irreversible DSC peak in Fig. 7.18. In this fraction, the crystals consist of a solid solution of different molar masses and lamellar thicknesses between 100 and 4,000 nm, as deduced from Fig. 7.20. The TMDSC experiments display very little reversible melting, going to zero at about 409.5 K, while the dilatometry shows the last melting at about 411 K, i.e., the highest melting, most perfect, extended-chain crystals show no reversibility. On cooling after melting of the extended-chain crystals, normal folded-chain crystals grow and the reversing melting reaches the higher levels discussed in Sect. 6.2.1 with Figs. 6.29–34.

### 7.1.6. Block Copolymers

The effect of a second component in the phase structure is treated in this chapter in several stages. First, it was assumed that both components were of identical size and behaved ideally, i.e., they do not interact. Assuming further that there is no cocrystallization, the typical eutectic phase diagram of Fig. 2.27 results. The discussion of the experimental evaluation of phase diagrams indicated the effect of formation of solid solutions, as seen in Fig. 7.2. The deviation from an ideal solution can be treated by introduction of an activity as in Fig. 7.3. Next, in Sect. 7.1.2 the shape-difference of two components was treated using the free-volume argument of Hildebrandt, and finally, the interaction parameter  $\chi$  was introduced to treat real solutions in Fig. 7.4–6. The examples treated in Sects. 7.1.3–5 dealt then with components that were isolated molecules.

In this section the case of two components being part of a single molecule is treated with the example of a block copolymer as described in Fig. 1.19 and Sect. 3.4. The treatment of shape effects and the consideration of parts of the same molecule as different components are typical for such polymeric systems. Multi-component molecules are of interest if the different components phase separate without breaking the molecular integrity and yield phase boundaries that contain the intramolecular junctions between the components. There exists a full spectrum of systems in the treatment of phases of large molecules. Each molecule may either need to be described as the constituent part of a component, as in Sects. 7.1–5, or it may be separated into its smallest identities, the constitutional repeating units (CRU), which are then the constituent parts of the components, as discussed in Sect. 7.2. Finally, it is possible to introduce variable or fixed points of decoupling into the molecule, which can locate at phase boundaries. For semicrystalline polymers, variable points of decoupling were useful for the description of the rigid-amorphous fractions. The points of decoupling are in this case located at the crystal-amorphous interface,

enabling stress-transfer between the phases (see Sect. 6.1.3). Similarly, it was suggested that reversible melting, seen in folded-chain polymers, may need points of decoupling as illustrated in Figs. 6.69 and 6.70. In the present section, the concept of fixed points of decoupling is explored, caused by a change in chemical structure along the molecule at positions which are determined by the synthesis.

Typical phase morphologies of block copolymers are illustrated in Figs. 5.38–40 and 5.79. In the classification of phases, the phase-separated block copolymers are considered to be amphiphilic liquid crystals despite the fact that inside the phase areas the typical liquid-crystalline order is missing (see Sect. 5.5). In this section the question will be addressed what happens when the usually micro- or nano-phase separated block copolymers show solubility, i.e., when the amphiphilic liquid crystal becomes thermotropic, i.e., dissolve at a given temperature.

Figure 7.21 illustrates a phase diagram of an AB-diblock copolymer with two amorphous segments, joined at the fixed point of decoupling. The interaction due to lateral contact between the repeating units of A and B are represented by the Flory-

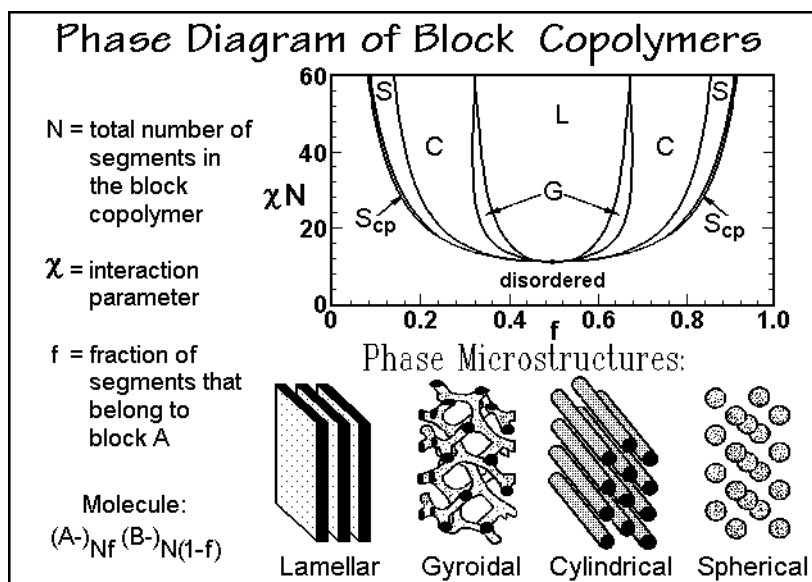


Fig. 7.21

Huggins parameter  $\chi$ , with positive values signifying unfavorable interaction. Changes in the phase diagram are caused by changes in  $\chi$ , the length of the molecular segment,  $N$  (ordinate), and the fraction of A in the molecule,  $f$  (abscissa). Of special interest is the limit of phase separation for small values of  $\chi N$ . Depending on the strength of interaction  $\chi$  and the length of the decoupled segments, the phases may dissolve for small lengths,  $N$ , as indicated in the phase diagram. Since  $\chi$  is also temperature-dependent, amphiphilics of such short-segment lengths may also act thermotropically, i.e., they may lose their liquid crystalline structure at a well-defined transition temperature. The typical different phase morphologies exhibited by the amphiphilic liquid crystals are shown at the bottom of Fig. 7.21.

By changing from diblock copolymers of two, micrometer-long segments A and B to alternating block copolymers of many shorter repeating segments of A and B, the short-range order introduced by the interfaces may become a significant fraction of the sample. When the segment lengths reach nanometer size, the orientational and conformational order caused by the interface may persist throughout the phases. A truly liquid crystalline phase structure results in this case from the molecular-level nanophase separation, not from the orientational ordering of mesogens, just as for low molar mass soaps and lipids[13]. Naturally, in all these molecules one must identify the type of phase or mesophase and realize that there are also intermediate cases where both mesogen *and* interface can stabilize a liquid-crystal-like structure.

## 7.2 Melting Transitions of Copolymers

### 7.2.1. Theory of Copolymer Melting and Crystallization

In the copolymers described in Sect. 3.4, the multiple components of the system are joined by chemical bonds and demixing, needed for complete phase separation of the components, is strongly hindered and may lead to partial or complete decoupling from crystallization. The resulting product is then a metastable micro- or nanophase-separated system with arrested, local equilibria. In some cases, however, it is possible to change the copolymer composition during the crystallization or melting by chemical reactions, such as trans-esterification or -amidation. In this case, the chemical and physical equilibrium must both be considered and a phase separation of the copolymer into either crystalline homopolymers or block copolymers is possible.

The thermodynamics of macromolecular solutions with small molecules is described in Sect. 7.1. A term frequently used to describe solutions of macromolecules is: *blend*. The word is obviously derived from the mixing process and should only be used when the resulting system is not fully analyzed, i.e., one does not know if a dissolution occurred or the phases remained partially or fully separated. The term blend should best be used only if a phase-separated system has changed by vigorous mixing to a finer subdivision, containing micro- or nanophases. The differences between nanophase separation and solution can be rather subtle, as is seen, for example, in the thermodynamic description of block copolymers (see Sect. 7.1). Micro- and nanophase-separated systems can often be stabilized by compatibilizers that may be block copolymers of the two components. Their properties can be considerably different from macrophase separated systems or solutions and, thus, of considerable technical importance.

The problems of nonequilibrium crystallization and melting discussed in Chap. 6 and Sect. 7.1 for single-component systems, are even more pronounced for multi-component systems. The additional problem of separating the components by diffusion into phases of different concentration complicates the description of multi-component systems even further. Usually equilibrium concentrations cannot be achieved at the moment of crystallization or melting, i.e., the processes of component diffusion and crystallization/melting are not molecularly coupled. One must thus always consider two deviations from equilibrium. One is the formation of non-



equilibrium crystals, the other, the added influence of limited mixing or demixing of the components. As discussed in Chap. 6, the results of incomplete equilibration are local equilibria, critically dependent on sample history.

Figure 7.22 represents a typical DSC trace of copolymer melting. The poly(ethylene-*co*-vinyl acetate) is expected to follow a eutectic phase diagram. The melting temperature decreases from the value of the homopolymer, but the crystallinity decreases much more than expected from the small amount of noncrystallizable comonomer. Also, the crystallization of a eutectic component, required by an equilibrium phase diagram, seen for example in Fig. 7.1, is rarely observed in random copolymers with short repeating units, as in vinyl polymers.

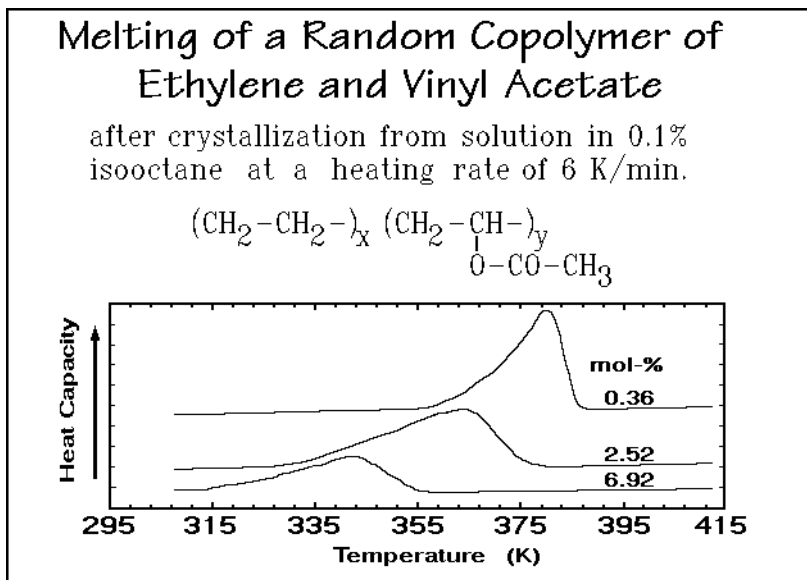


Fig. 7.22

Three limiting theories are outlined next. The first is an equilibrium theory of the eutectic phase diagram of copolymers as developed by Flory which has been widely used, even for systems not in equilibrium. The second is the corresponding theory for the formation of solid solutions. The third is the application of cold crystallization to copolymers as a limiting, nonequilibrium theory of melting and crystallization.

The derivation of the melting equation for the eutectic of copolymers is similar to low-molar-mass materials as described by Figs. 2.24–27. The molar mass of the molecule itself is of little concern since the crystallization cannot extend beyond the length of the sequences of crystallizable components. Naturally, one expects a result similar to the eutectic of low molar mass. The main modification in the equation describing the phase diagram is a term accounting for the length of the crystallizable repeating units, usually designated as  $G_k$ , zeta,  $\zeta$ .

For an ideal, random copolymer of repeating units A and B which shows no heat of mixing or demixing, one can write the top two equations in Fig. 7.23. The sequences of consecutive, crystallizable A-units have the length  $\zeta$ . The term

equivalent to  $RT \ln x_1$  in Fig. 2.26 is replaced by  $RT \ln p_\zeta$ . The mole fraction of the low-molar-mass component,  $x_1$ , is the probability of occurrence of component 1 in solution. Similarly,  $p_\zeta$  is the probability of the occurrence of a crystallizable sequence of A-units of length  $\zeta$ . This probability must take cognizance that any sequence of length  $\zeta$  or longer contributes to  $p_\zeta$ . In addition, the heat of fusion must be adjusted to  $\zeta \Delta H_u$  to account for the full sequence. Finally, one must add the surface free energy  $2\gamma_e$  to account for the termination of the crystal on both ends of the crystallized sequence. The lateral surface of the crystal is considered small, and has been neglected. The crystal would then take the shape given by the sketch of Fig. 7.23. The ends of the crystallized sequence can be either of type A or B, as shown.

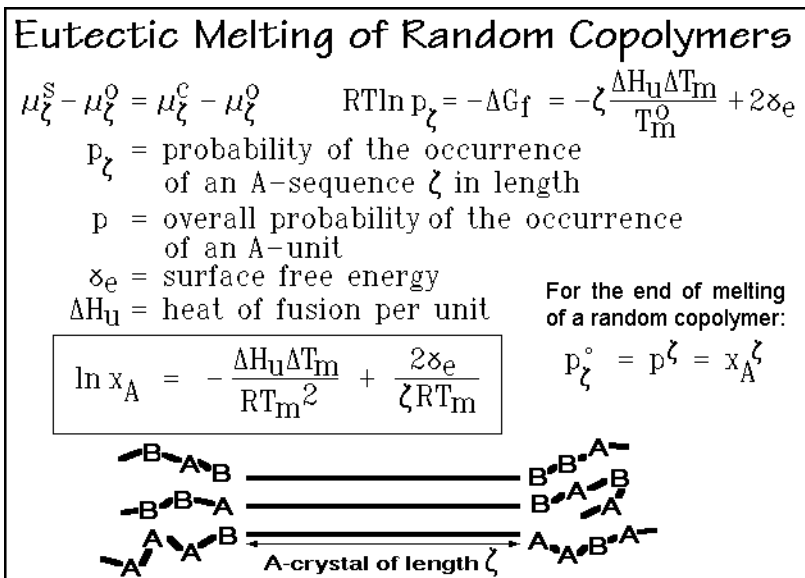


Fig. 7.23

In Fig. 7.24 the equilibrium weight fractions of crystallinity of length  $\zeta$ ,  $w_\zeta$ , are displayed, calculated from the top right equation of Fig. 7.23 with parameters approximating polyethylene. The dotted line represents a random distribution of sequences assuming equal sizes for A and B (molar and weight fractions  $x_A = 0.9$ ). As soon as the equilibrium line crosses the dotted line, at  $\zeta^*$ , the longer sequences may crystallize and reduce their concentration in the melt, as marked by the shading for the curve representing the crystallization temperature of 339.4 K.

At a sufficiently low temperature, at the eutectic, all A-sequences have been sorted into separate crystals for complete crystallization of all A-units. At the end of melting, at the liquidus line, the concentration in the melt must be equal to the initial sequence-distribution,  $w_\zeta^O$ , as obtained on polymerization. If this distribution is random, as shown in Fig. 3.46, the simple correlation given in Fig. 7.23 holds, and the boxed equation can be derived. At the liquidus line, a remaining trace of an extended chain crystal of a long sequence of A-units is in equilibrium with the solution. For the example of Fig. 7.24 this temperature is 368.9 K.

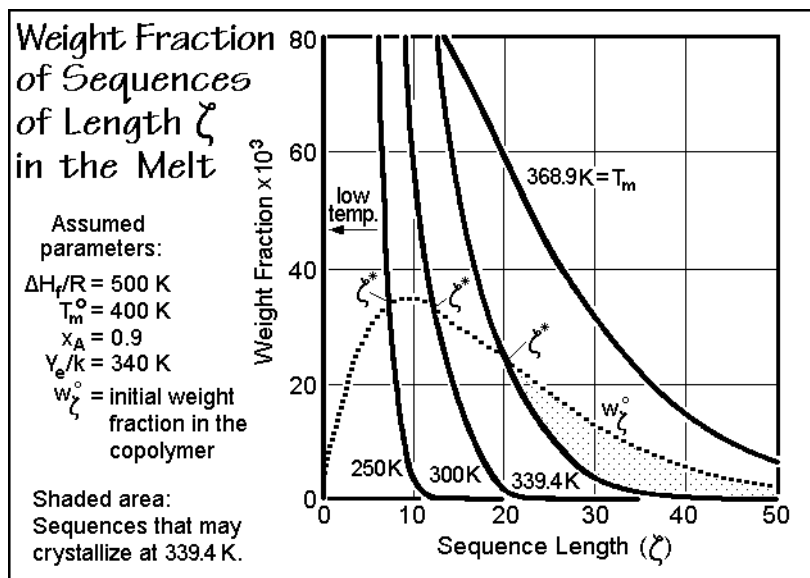


Fig. 7.24

In most copolymers the fraction of large sequences is small, and in addition, long sequences would chain-fold and not reach equilibrium. The calculated end of melting of a copolymer, if measurable at all, would thus have to be corrected for chain folding by typically 10–20 K (see Fig. 2.90).

The difficulty to reach equilibrium is further illustrated in Fig. 7.25. The change of the concentration of sequences of crystallizable A-units is calculated by following

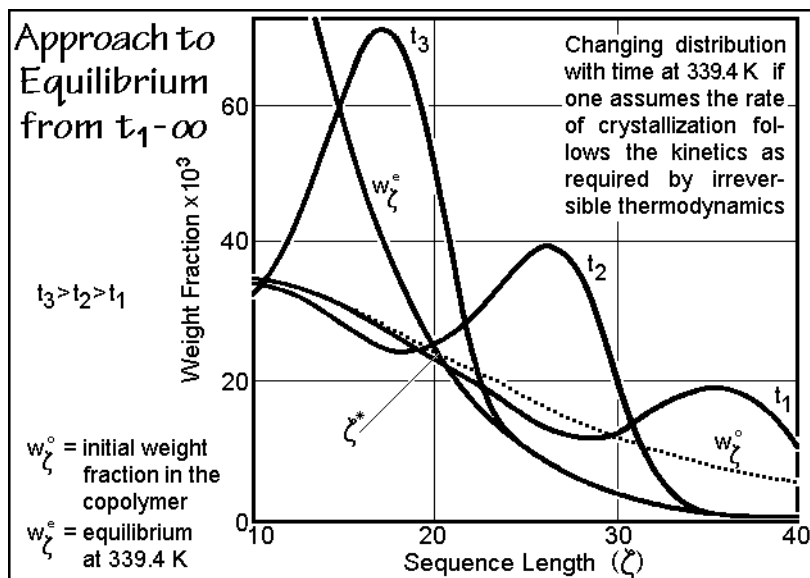


Fig. 7.25

the isothermal kinetics, as is derivable from irreversible thermodynamics in Sect. 2.4 with  $dp_\zeta/dt = -L_\zeta \Delta G_\zeta/T$  when disregarding the retardations due to any type of nucleation described in Sect. 3.5. In the initial time interval that leads to  $t_1$ , all sequences longer than  $\zeta^*$  are beginning to crystallize, but initially not necessarily to a crystal matching their length. The crystallization to a smaller crystal, but larger than  $\zeta^*$ , is faster and may create one or two short A-ends. This partial crystallization distorts the concentration of the uncrystallized sequences. At time  $t_2$ , crystallization has progressed to equilibrium up to the length  $\zeta \approx 34$ . Overall, the approach to equilibrium takes the shape of a wave approaching  $w_\zeta^e$ . It is obvious that the process of readjustment of sequence-distributions will be arrested long before equilibrium is reached, leaving a large concentration of crystallizable ends in the melt. Experimental detection of these chain ends will be shown below.

Sets of data for the liquidus line of poly(ethylene terephthalate-*co*-sebacate) and poly(ethylene terephthalate-*co*-adipate) are shown in Fig. 7.26. Because of the greater lengths of the repeating units, both components crystallize and the qualitative appearance of the melting-end temperatures is that of a eutectic phase diagram. As in homopolymer crystallization, however, there is little chance that equilibrium is reached. The equilibrium melting of poly(ethylene terephthalate) occurs at 553 K, not at 515 K. At best, the liquidus line and the corresponding eutectic point refer to zero-entropy-production conditions and additional internal variables have to be known to describe the system and account for the lowering of the liquidus line to the eutectic-like temperature (see Sect. 2.4).

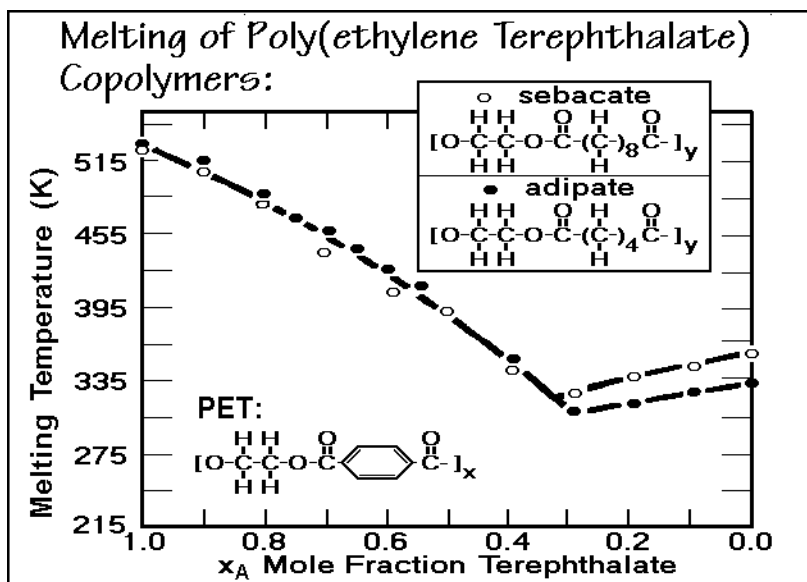
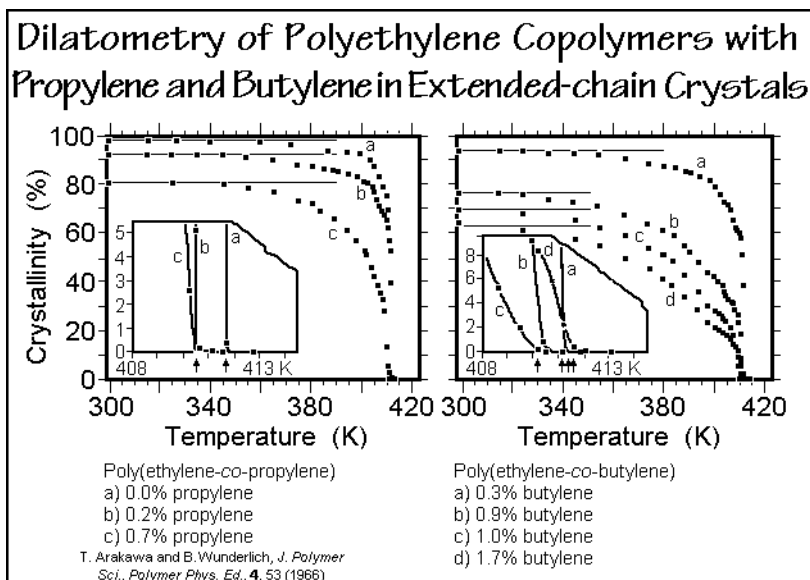


Fig. 7.26

The melting-point lowering in ideal solutions is caused solely by the entropy of mixing. For copolymers, it has additional restrictions due to small crystal sizes and chain folding. Often this additional reduction of the melting point is larger than the

mixing effect. Furthermore, the demixing on crystallization is usually incomplete. The B-units rejected by the A-crystals do not mix fully with the surrounding melt, but accumulate at the interface, causing a change in the entropy of mixing on fusion, as is also seen from the sketch in Fig. 7.23. Figure 7.27 shows an example of the end of melting of poly(ethylene-*co*-propylene)s and poly(ethylene-*co*-butene)s, crystallized to the extended-chain morphology under elevated pressure to eliminate the chain-folding effect. The crystallinities of these copolymers decrease strongly with the comonomer concentration, given in side-groups per 100 chain atoms. The temperature of the melt end, however, seems not to change from the base polymer. All seven samples melt at  $411.2 \text{ K} \pm 0.6 \text{ K}$ . This observation suggests that the mixing process either does not occur at all, or is decoupled from the melting (melting is governed by a local equilibrium without major changes in the concentration in the melt).



**Fig. 7.27**

More complicated is the description of the melting of copolymers with full or partial isomorphism or isodimorphism (Sect. 5.1.10). The changes in concentration in the mixed crystals as well as the melt must be considered and the change of the lattice energy with cocrystallization must be known. The simplest description assumes that there is no difference in concentration between melt and crystal, and there is a linear change of the heat of fusion,  $\Delta H_u$ , with concentration. This leads to:  $T_m = [1 - x_B(\Delta H_u/\Delta H_u)]T_m^\circ$ , where  $\Delta H_u$  is the heat of fusion per repeating unit of the homopolymer.

Figure 7.28 illustrates a solid solution of poly(ethylene terephthalate-*co*-isophthalate). The liquidus curve is taken at the end of melting and the solidus curve was calculated from the changes in lattice spacings with temperature and concentration of the comonomer. The minimum in the phase diagram corresponds to the change in crystal structure from terephthalate to isophthalate.

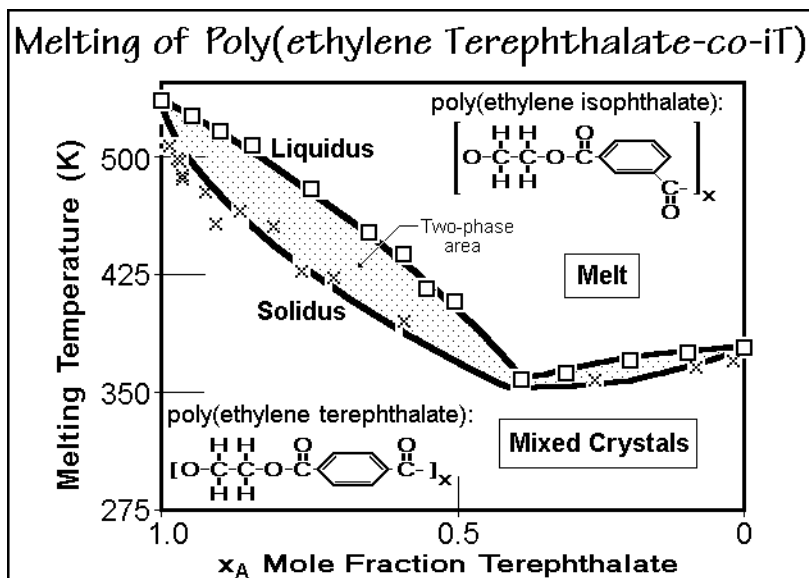


Fig. 7.28

Cold crystallization is the third possible crystallization mode for copolymers. Crystallization occurs at sufficiently low temperature so that the mobility of the repeating units can align only the smallest crystals that are stable at this large distance from the melting temperature. In Fig. 7.29 cold crystallization is modeled in two dimensions with 12 chains that have been moved into register. Crystallization is only possible by neighboring sequences of two or more A-units, indicated by the shading.

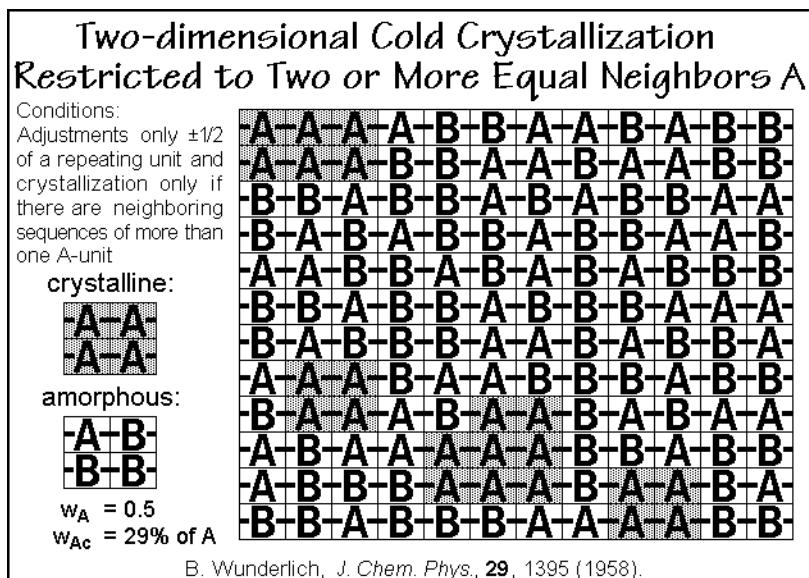


Fig. 7.29

The example had a fraction of A-units,  $w_A$ , of 0.5. It is quite obvious that small deviations from randomness can drastically influence the crystallinity. Besides finding an overall limit of the crystallinity, it is also possible to evaluate the size- and shape-distribution of the crystals, as well as the surface areas. In reverse, a measured melting curve can be used to fit these parameters as long as the melting occurs under zero-entropy-production conditions, outlined in Sect. 2.4.

Figure 7.30 illustrates the limits from equilibrium to cold crystallization. They are based on a computer calculation for three-dimensional cold crystallization. It is assumed in this case that sequences of less than three A-units do not crystallize, and that at least two out of the four neighboring chains must match the sequence of three repeating units to make the central sequence crystalline. If all four lateral neighbors are crystalline, the repeating unit is in the interior of the crystal, if only three are crystalline, it is on the surface, and if only two are crystalline, it is part of an edge. With this critical sequence length and two surface free energies, experimental data of poly(ethylene terephthalate-co-sebacate) can be discussed, as is shown in Fig. 7.31. The experimental phase diagram of the same copolymer, but after slower cooling, is displayed in Fig. 7.26.

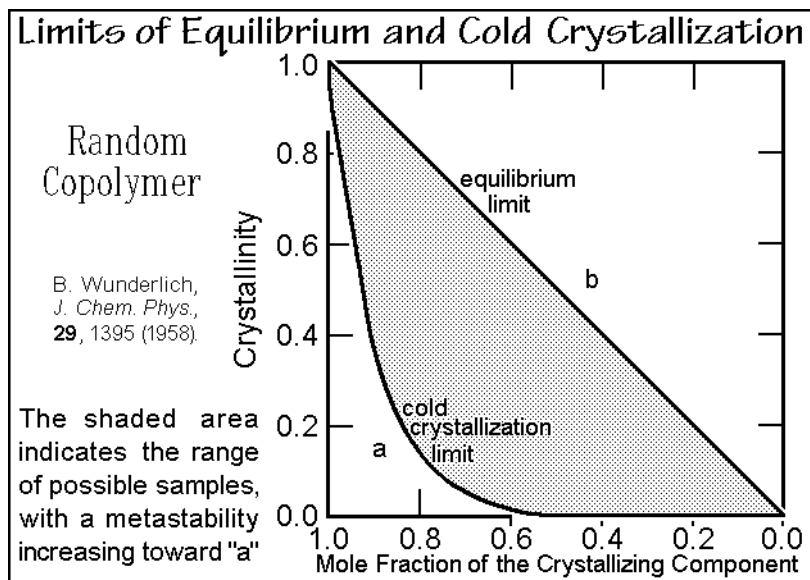


Fig. 7.30

With this brief summary of some basic descriptions of copolymer systems, it is clear that beyond concentration, detailed structural and thermodynamic information is needed for a full description. As seen in Chap. 6, semicrystalline polymers are globally nonequilibrium systems. Local equilibria may determine the premelting behavior and give information about the crystal morphology and crystallization history. Since copolymers crystallize less than the corresponding homopolymers, the defect structure is of overriding importance and the possible decoupling from the demixing produces additional, arrested internal parameters.

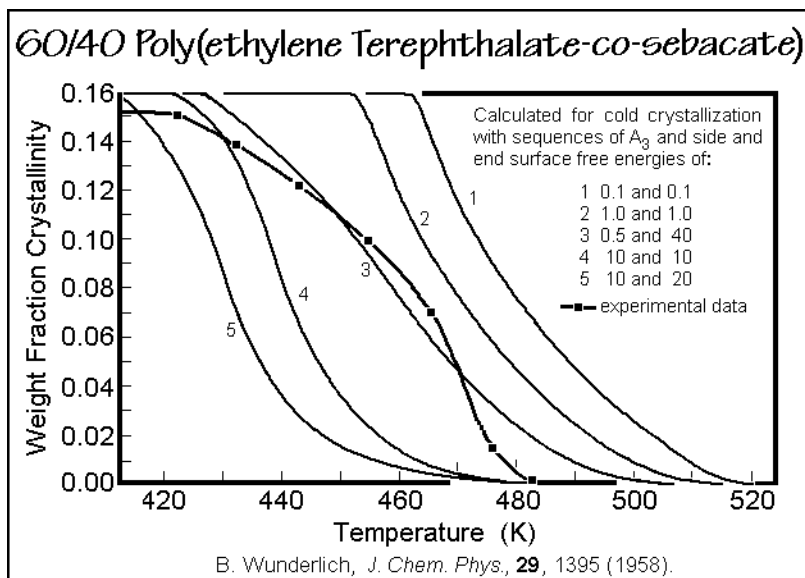


Fig. 7.31

## 7.2.2. Applications

In this section, copolymers of polyethylene are discussed, starting with low-density, branched polyethylene and culminating with crystallization, melting, and annealing of poly(ethylene-*co*-octene-1), also described as linear-low-density polyethylene, LLDPE. Furthermore, partial phase diagrams of poly(ethylene terephthalate-*co*-oxybenzoate), PETcoOB, and poly(oxybenzoate-*co*-oxynaphthoate), POBcoON, are presented. The latter systems are examples of increasing chain stiffness by cocrystallization which leads to mesophase behavior (see Sect. 5.5).

**LLDPE.** Figure 7.32 displays results of an early study of the change in the crystals of branched, low-density polyethylene as a function of branch content (see Fig. 1.22). The X-ray data of a number of copolymers in Fig. 5.35 revealed limited isomorphism of the polyethylene crystals for a number of branch types. In accord with these data, the unit cell volume in Fig. 7.32 increases with branch content. The low-angle X-ray data indicate a gradual decrease of the long period. The lamellar crystal thickness can be separated from the long period with help of the crystallinity information in Fig. 7.33. All of these changes in volume and length should be compared to the average sequence length of crystallizable  $\text{CH}_2$ -groups, also shown in Fig. 7.32. It decreases rather rapidly with increasing number of branches. The discrepancy between the average sequence length and crystal thickness can be brought into accord by considering the decrease in crystallinity (which suggests increasingly only less prominent longer  $\text{CH}_2$ -sequences crystallize) and the isomorphism (which suggests increasing numbers of branches are included in the crystals).

The plot on the right of Fig. 7.32 proves that only occasional branches can be included into the crystals. Next, the defect concentration in the crystals was calculated, assuming that 2g1 kinks cause the change in the unit cell volume (see



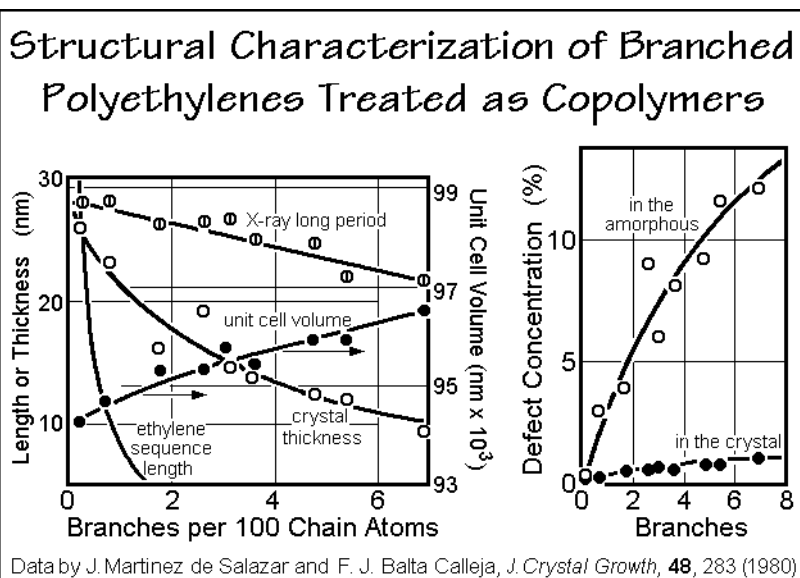


Fig. 7.32

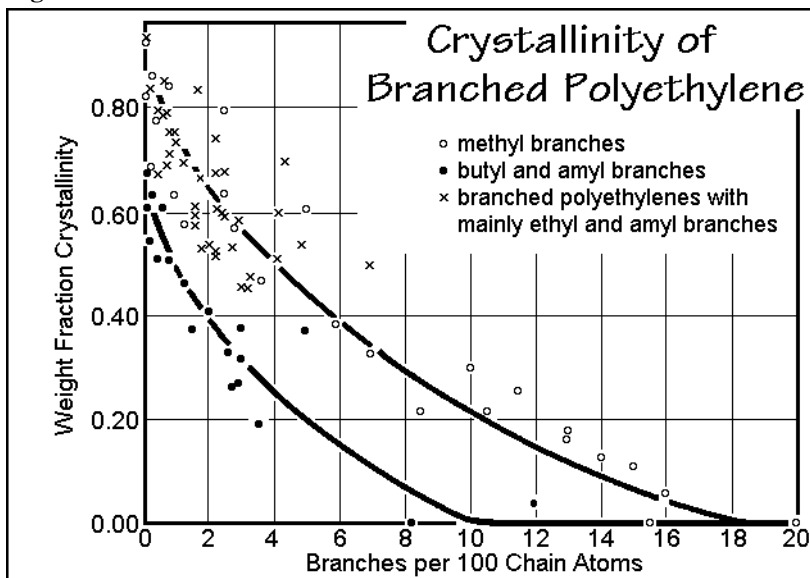


Fig. 7.33

Sect. 5.3.3). Figure 7.34, finally, is a plot of data of the melting end as a function of branch concentration. Although one might extrapolate the data to the marked equilibrium melting temperature of the homopolymer, the influence of the fold limit is obvious.

The more recently available linear-low-density polyethylenes allow more precise analyses. In LLDPE, for example, ethylene and octene are reacted using a homoge-

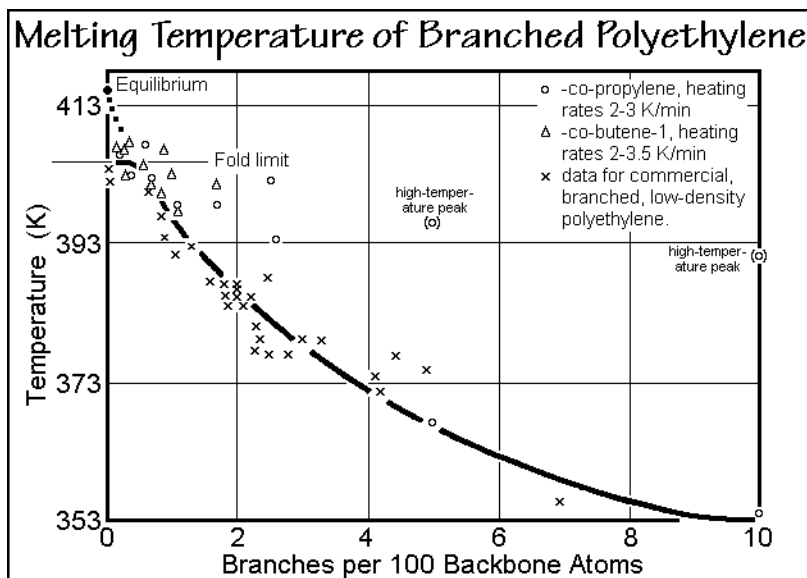


Fig. 7.34

neous, single-site catalyst which results in a uniform distribution of the comonomers and a very narrow molar mass distribution (see Sect. 3.2.1). In Fig. 7.35 heat capacity measurements and the transition behavior of LLDPE with an octene content of 7.3 mol-% are displayed (24 wt-%) [14–17]. On heating, the crystallinity is 24% at 240 K and decreases continuously to a value of 14% at 298 K and reaches the melt-end at 355 K. The crystallization process during cooling begins at 323 K (onset) and covers

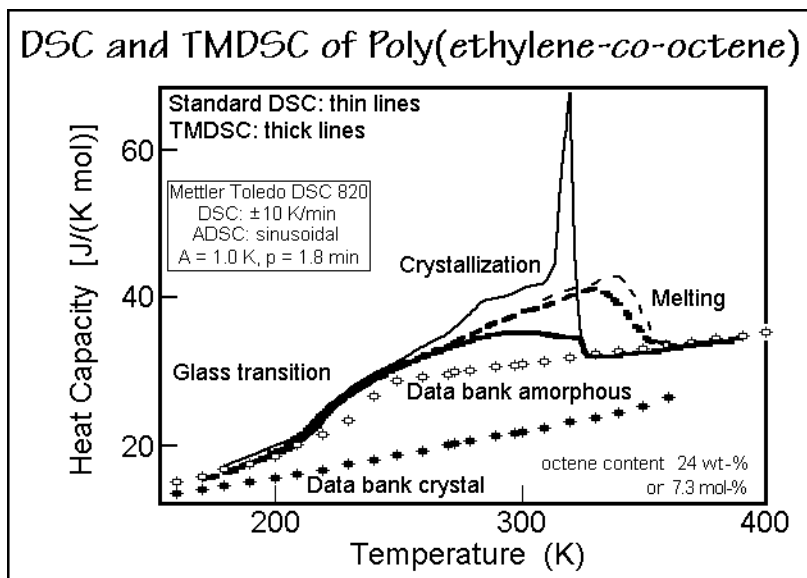
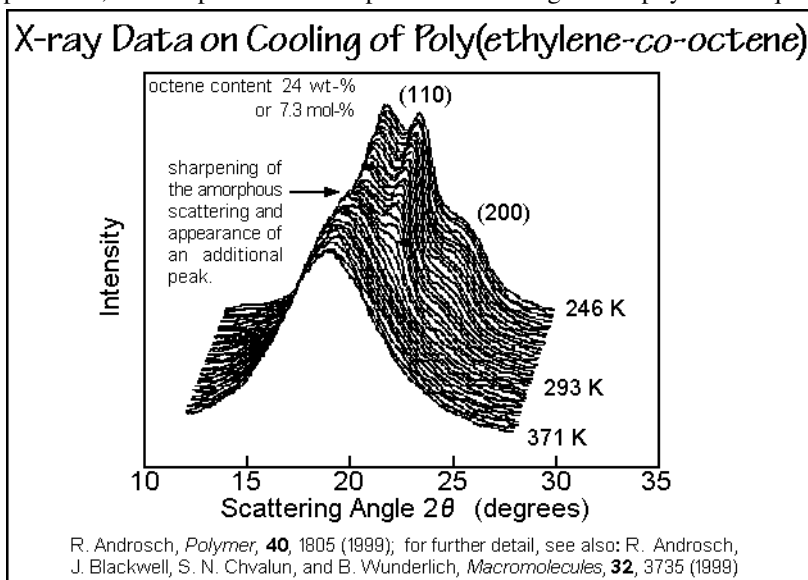


Fig. 7.35

the temperature range down to the glass transition. Crystallization consists of at least two different processes, one gives rise to the sharp peak at 318 K, the other is a more continuous process that extends to low temperatures.

These DSC data are compared in the figure to TMDSC results. The crystallization peak appears only in the total heat capacity and not in the reversing heat capacity, i.e., this process is irreversible and continues to ca. 255 K. At approximately 328 K, the reversing heat capacity also signals an exothermic process which dominates when approaching the glass transition temperature. On heating, larger deviations between the underlying and reversing heat capacity can be seen as a separate shoulder during the end of the melting process. It is straightforward to assume that the high-temperature melting correlates to the sharp crystallization peak.

Temperature-resolved X-ray experiments on cooling are presented in Fig. 7.36. The first scans show only an amorphous halo. The copolymer is melted. At 321 K, the 110 and 200 orthorhombic crystal interferences appear. The peaks are shifted to lower values compared to the polyethylene homopolymer. The calculated lattice constant  $a_0$  of 0.766 nm is expanded, as discussed with Fig. 7.32. At slightly lower temperatures, the shape of the amorphous halo changes abruptly and acquires a



**Fig. 7.36**

superimposed peak, indicative of the hexagonal phase. Cooling the sample further, results in an increase of the 110 and 200 orthorhombic interferences, as well as the hexagonal diffraction peak. At low temperature the LLDPE consists, thus, of at least three phases, orthorhombic and hexagonal crystals and amorphous glass or melt. More details of the LLDPE system were generated by studying a wider range of compositions, as shown in Figs. 7.37 and 7.38. Again, the structure was first set by cooling and analyzed by standard DSC.

To estimate the ratio of the reversing to irreversible melting at a chosen temperature, the specific reversibility, TMDSC results were compared to standard

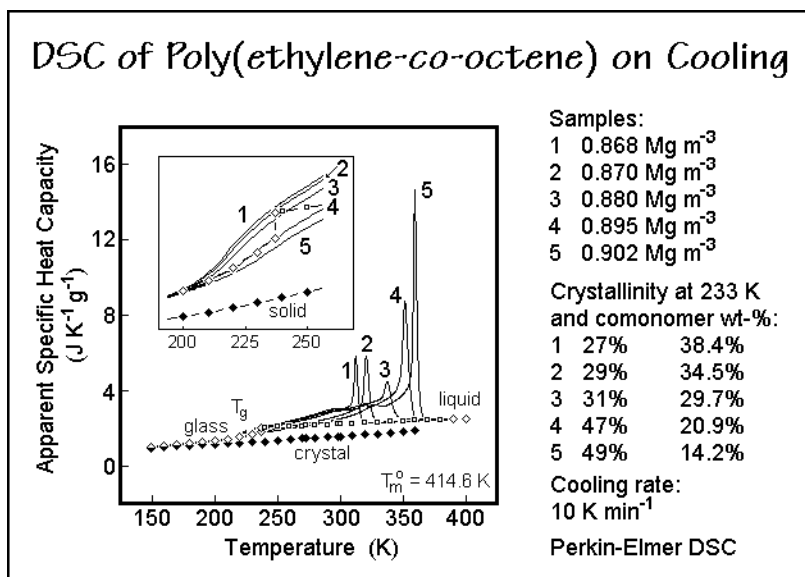


Fig. 7.37

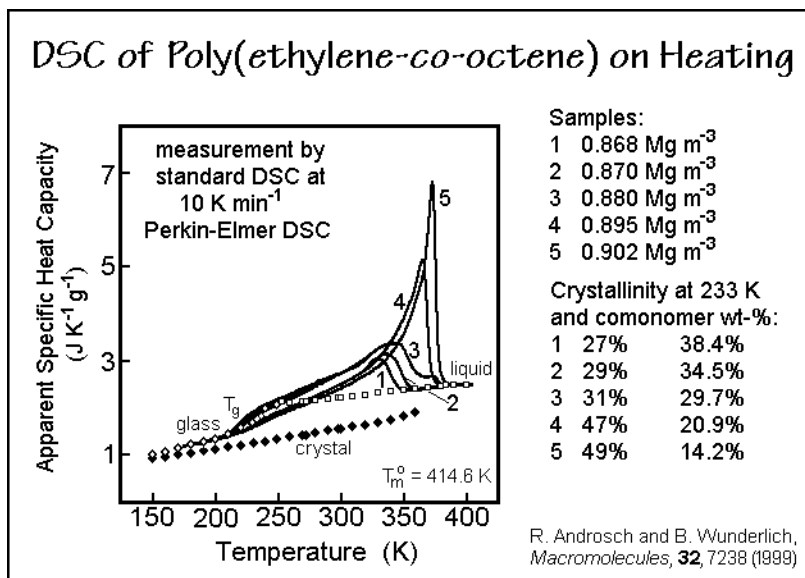


Fig. 7.38

DSC, as given in Fig. 7.39. It is noted, that reversing melting occurs always along with irreversible melting and is absent far from irreversible melting, suggesting the same basic process for both, different from the reversible changes in fold-length seen in polyethylene in Fig. 6.34. At low temperature, the specific reversibility of LLDPE reaches 70%, at higher temperature, this fraction decreases. Only close to the glass transition does the cooling and heating yields similar specific reversibility.

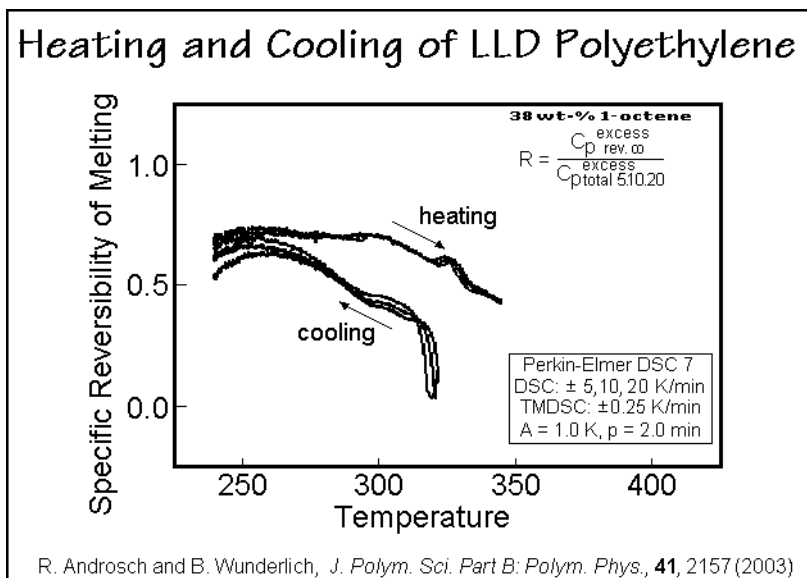


Fig. 7.39

Since Fig. 7.39 shows an increase on the reversing melting, just as illustrated in Fig. 6.30, the annealing of LLDPE was followed for different lengths of time after cooling to a given crystallinity and temperature. The results are shown in Fig. 7.40. The time-development of this annealing for one example is reproduced in 7.41. Finally, the annealed samples for the different times shown in Fig. 7.41 are reheated for analysis of the crystallinity distribution. The results are displayed Fig. 7.42.

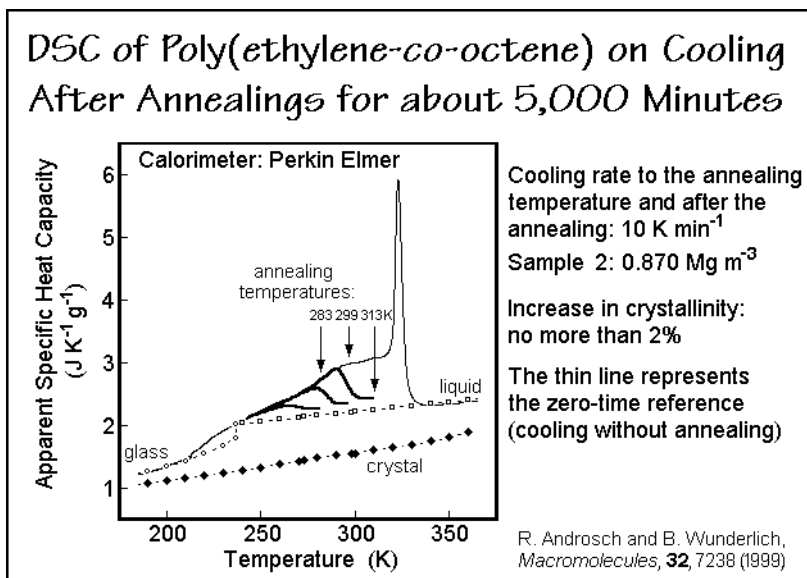


Fig. 7.40

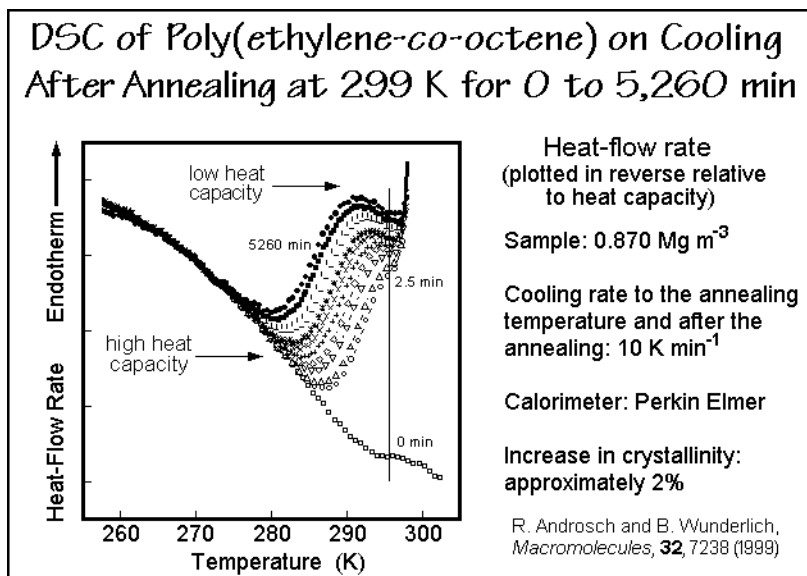


Fig. 7.41

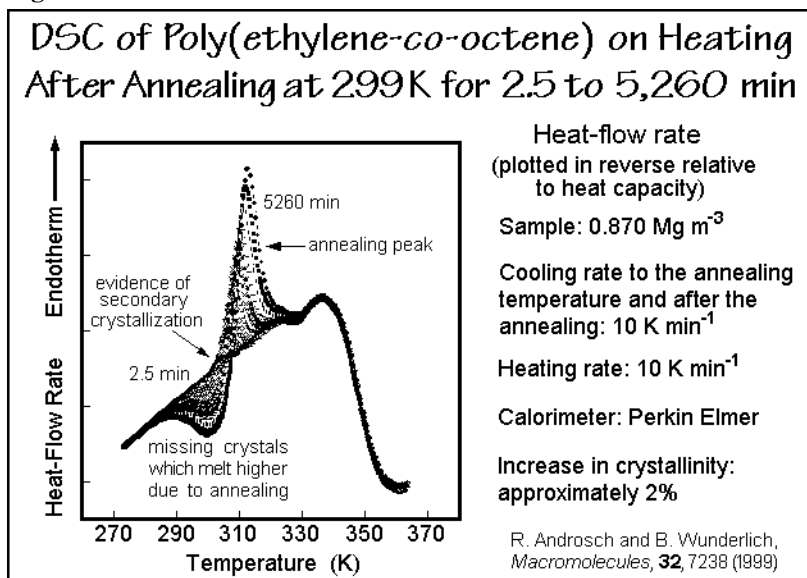
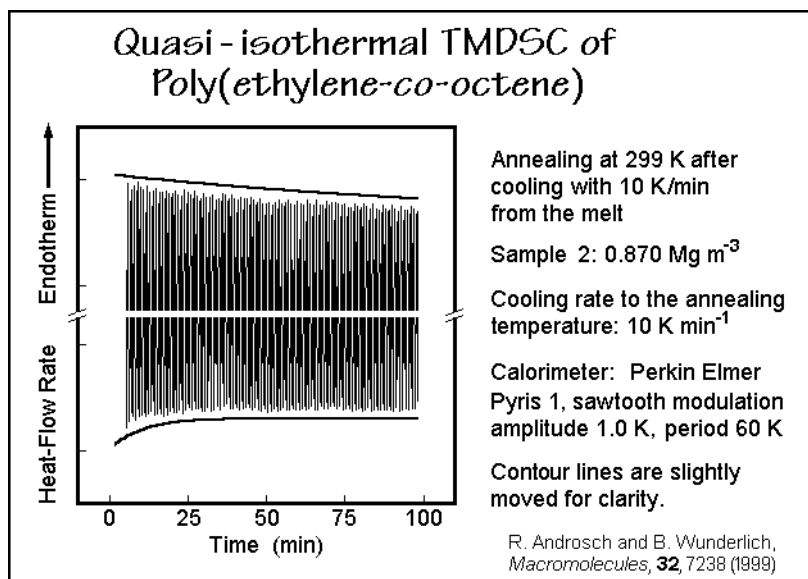


Fig. 7.42

This large volume of data shows that the apparent reversing specific heat capacity increases with comonomer content. This is seen best immediately above the glass transition temperature, as displayed in the insert in Fig. 7.37. The amount of irreversible crystals, which are identified as the normally grown folded-chain crystals, decreases with increasing comonomer composition, as expected (see Figs. 7.37 and 7.38 and compare to Fig. 7.35).

The nature of the crystals, identified by the reversing heat capacity, yields for all analyzed samples similar specific reversibility, as seen in Fig. 7.39. Even normal linear polyethylene has a similar specific reversible melting [18]. One expects that both, the orthorhombic as well as the hexagonal phase contribute to the reversible melting, as can be discerned from the annealing experiments. Figure 7.40 indicates that after long-time annealing much, but not all of the excess heat capacity has disappeared by crystal perfection, as revealed by the higher-temperature endotherm in Fig. 7.41. It is also obvious that only local improvement is possible by annealing at anyone temperature. Figure 7.40 indicates that further cooling reaches again, the same high value of the total and reversing heat capacity.

Using quasi-isothermal TMDSC, the kinetic changes on annealing can be followed even more quantitatively. Figure 7.43 illustrates the first 100 min of annealing with



**Fig. 7.43**

the heat-flow-rate output, and Fig. 7.44, with the heat capacity. The final time plot includes the frequency correction and a comparison to data in the melt region which show no time dependence. The results are given in Fig. 7.45. From Figs. 43–45 one can see two changes with annealing time. First, there is a residual crystallization or crystal perfection, marked by the excess exotherm in the first few modulation cycles of Fig. 7.43. Its relaxation time is about 5 min as seen in Fig. 7.44. It causes a decrease in the reversing signal due to either the growth of higher melting crystals, or an improvement of crystals still unmelted in the crystallization cycle. Next, there is a slowly decreasing excess endotherm of the heat-flow rate stretching over the whole time shown in Fig. 7.43. Its relaxation time is derived from Fig. 7.44 to be about 100 min. In this case, it seems that some of the crystallizing polymer segments improve sufficiently on crystallization, so that on the next heating cycle they do not melt again. Despite of this slow decrease in reversing melting, considerable reversibility remains

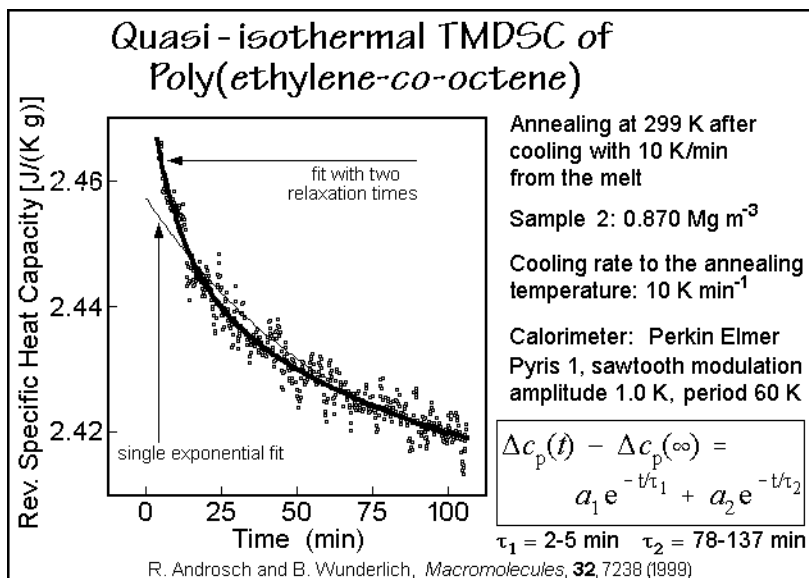


Fig. 7.44

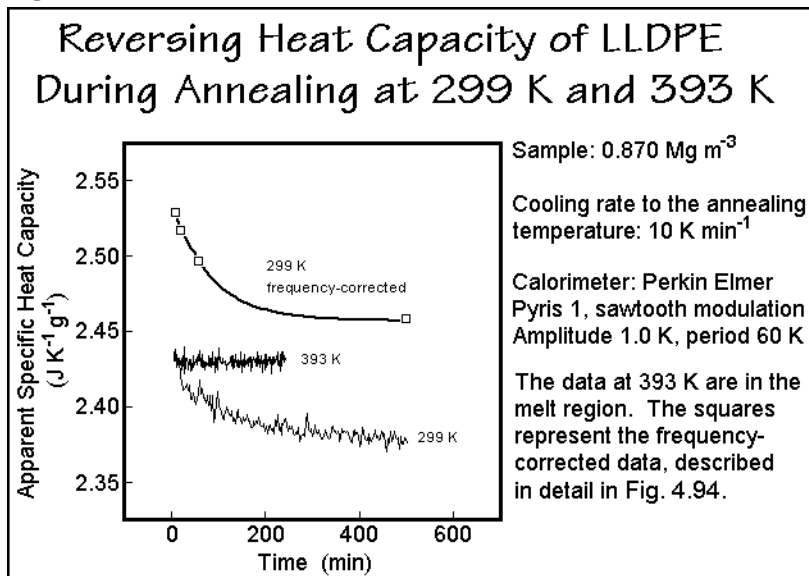
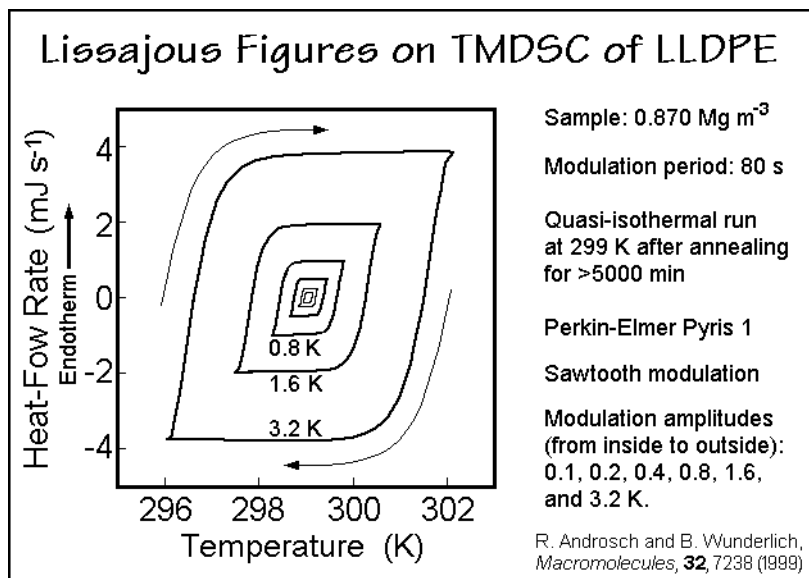


Fig. 7.45

when the kinetic data are extrapolated to infinite time. The corrected heat capacity in Fig. 7.45 at 500 min is still above that of the liquid polymer and the crystal, as can be seen from Fig. 7.40. The proof of full reversibility after long time annealing is further documented by the perfect Lissajous figures of the sawtooth modulation in Fig. 7.46. The response of the calorimeter is linear, stationary, and reaches steady state for all amplitudes (see Sect. 4.4).



**Fig. 7.46**

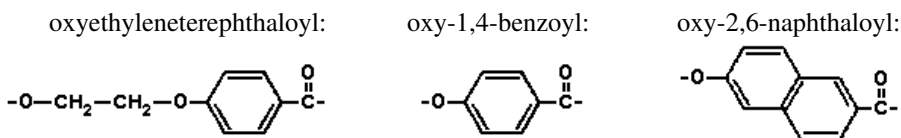
This analysis of the crystallization, melting, and annealing of LLDPE, has a rather wide application to crystallization of polymers. Its advantage is the rather large concentration of the specific reversing contribution to melting, crystallization, and annealing. This reversing contribution in the melting range varies from polymer to polymer and changes also depending on thermal, mechanical, and chemical history. Quite similar observations were made for a number of homopolymers discussed in Chap. 6. Clearly, there are at least six different contributions to the apparent heat capacity of the copolymers, and under proper circumstances also in homopolymers. The first three contributions are truly reversible:

1. Vibrational heat capacity, as described in Sect. 2.3 for solids and liquids.
2. *Gauche-trans* equilibrium or other conformational changes which produce an increase beyond the vibrational heat capacity of the solid polymers, as documented with Fig. 2.65 and described in Sect. 5.3 for polyethylene.
3. Fully reversible melting, as just shown for LLDPE and many other polymers. This reversible melting is either caused by short, decoupled segments of the molecules (see Figs. 3.75 and 3.91) or indicates remaining molecular nuclei.

The second three contributions are increasingly more irreversible:

4. Crystal perfection with the relaxation time of ca. 100 min in Fig. 7.44 is often observed on reheating a sample for annealing or recrystallization (see Sect. 6.2.3).
5. Secondary crystallization, which has a time constant of approximately 5 min for the LLDPE. The contributions 4 and 5 contribute to the annealing peak, usually characterized by an endotherm at 5–15 K higher temperature (see Fig. 7.42).
6. The primary crystallization and melting which commonly is the biggest effect and shows temperature differences between crystal growth and melting of usually 10 to 30 K due to crystal and molecular nucleation (see Sect. 3.5).

**PETcoOB and POBcoON.** A second example of thermal analysis of copolymers involves the two systems, poly(ethylene terephthalate-*co*-oxybenzoate), PETcoOB, and poly(oxybenzoate-*co*-oxynaphthoate), POBcoON. The structural formulas of the CRUs are as follows:



Of special importance is in this case that the backbone of the copolymer can change chemically by trans-esterification (see Fig. 3.47). In fact, heating poly(ethylene terephthalate) and acetoxibenzoic acid in the melt is a common synthetic route to PETcoOB. The inclusion of oxybenzoate groups makes poly(ethylene terephthalate) increasingly stiffer (see Fig. 1.50). In POBcoON, oxynaphthoate adds an additional off-set of the large zig-zag of the benzoate. As a result of this chain stiffening, the PETcoOB with more than 30 mol-% oxybenzoate shows an anisotropic melt, as for a nematic main-chain liquid crystal (see Fig. 5.136) and the system POBcoON has a mesophase character over the whole concentration range.

Figure 7.47 illustrates the change of the glass transition of PETcoOB with concentration. Surprisingly, the glass transition temperatures stay rather constant. In addition, there is a wide concentration region where two glass transitions can be seen (see also Sect. 7.3 for the normal copolymer behavior). The only simple explanation for such behavior is that locally two different aggregations of stiffer and more flexible segments are possible, each with a practically constant glass transition temperature, almost 100 K apart. The sketch in Fig. 5.136 suggests how such separation, perhaps of nanophase-size, may be possible in a basically liquid-crystal-like structure.

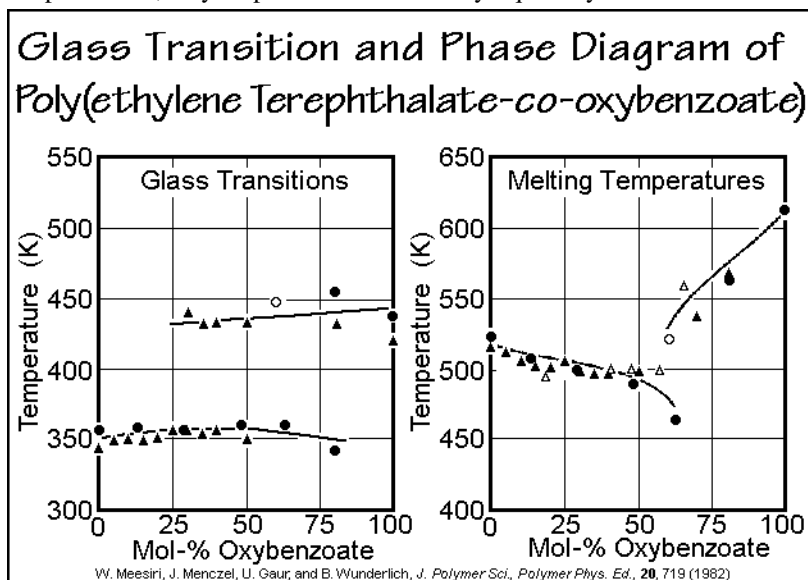
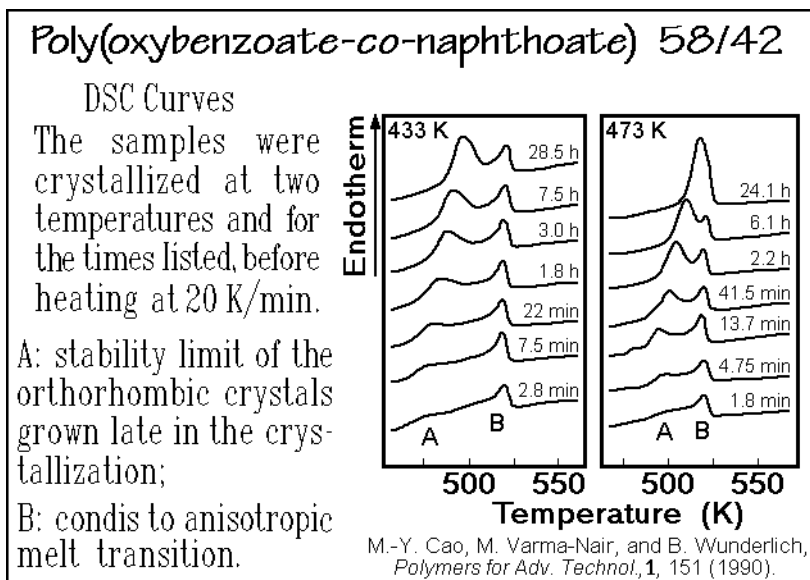


Fig. 7.47

The melting or disordering transition shown on the right of Fig. 7.47 changes with concentration without noticeable effect from the change in the melt from isotropic to the anisotropic melt (liquid crystal?). Although the diagram looks like a eutectic diagram, it may be showing a partial solid solution (isodimorphism). When comparing to the normal copolymers of poly(ethylene terephthalate) of Figs. 7.26 and 7.28, the changes of the transition temperatures are much smaller than expected for full demixing and remixing of the components and the heats of transition do not decrease below 30% of that of the corresponding homopolymers, which also supports the existence of a nanophase-separation in the melt. In the benzoate-rich region of the phase diagram, macroscopic phase separation becomes noticeable by optical microscopy, particularly for polymers that are not fully randomized. A full characterization has not yet been completed for this interesting copolymer.

The POBcoON is even more intriguing. These copolymers are commercially available under the trade name Vectra™. In contrast to PETcoOB, the melt of POBcoON is over a wide temperature range an anisotropic, but homogeneous solution. On cooling, the copolymer becomes semicrystalline with rather low crystallinity in the mid-range of concentrations. Figure 7.48 illustrates the thermal analysis of the 58/24 copolymer, crystallized at two temperatures for different lengths of time [19]. A very small amount of hexagonal condic crystals forms first (peak B), to be followed by an orthorhombic phase (peak A) which perfects with crystallization temperature and time and ultimately may exceed the stability of the hexagonal phase. On crystallizing above 490 K, the endotherm of the orthorhombic phase disorders directly into the anisotropic melt, as is illustrated in Fig. 7.49. The heat capacity of this copolymer is discussed in Sect. 2.3.10 and reveals a very broad glass transition region, typical for semicrystalline polymers with small crystals (see also Sects. 7.3 and 6.3, for the glass transition, see Figs. 2.64 and 7.50).



**Fig. 7.48**

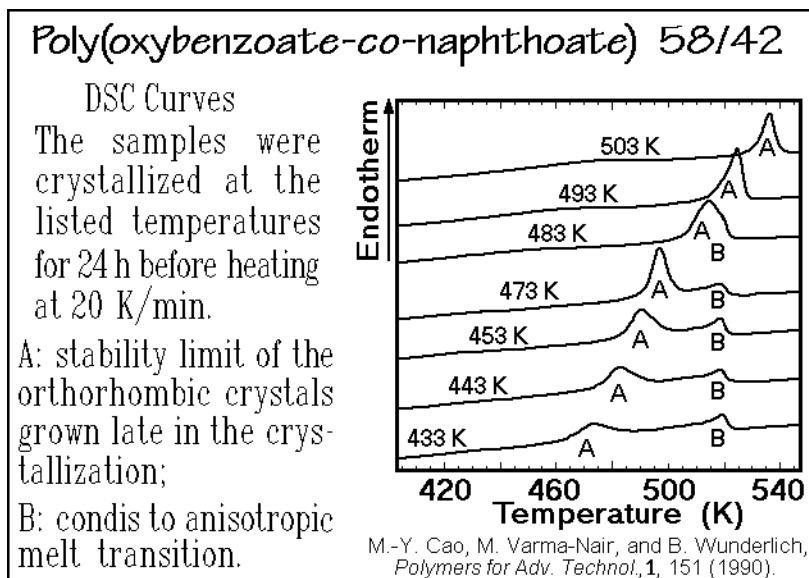


Fig. 7.49

Figure 7.50 displays heat capacities for a high concentration of oxybenzoate, and Fig. 7.51 presents the corresponding X-ray-diffraction results. Two models have been developed for the description of the small crystals. One is called the nonperiodic layer model. In it, one assumes that the ordered domains are formed by the lateral register of similar, but nonperiodic repeating units [20,21] in a fashion similar to the cold crystallization model (see Fig. 7.29). In this case, at least a nanophase separation is

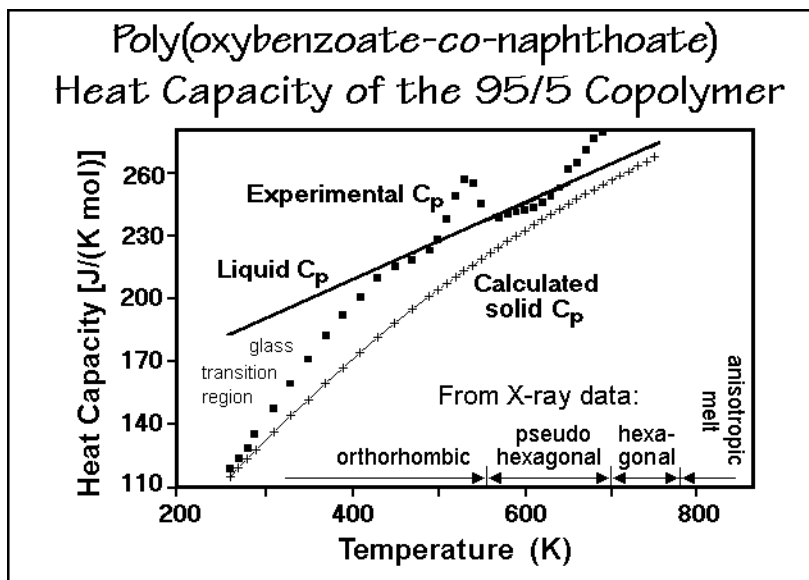


Fig. 7.50

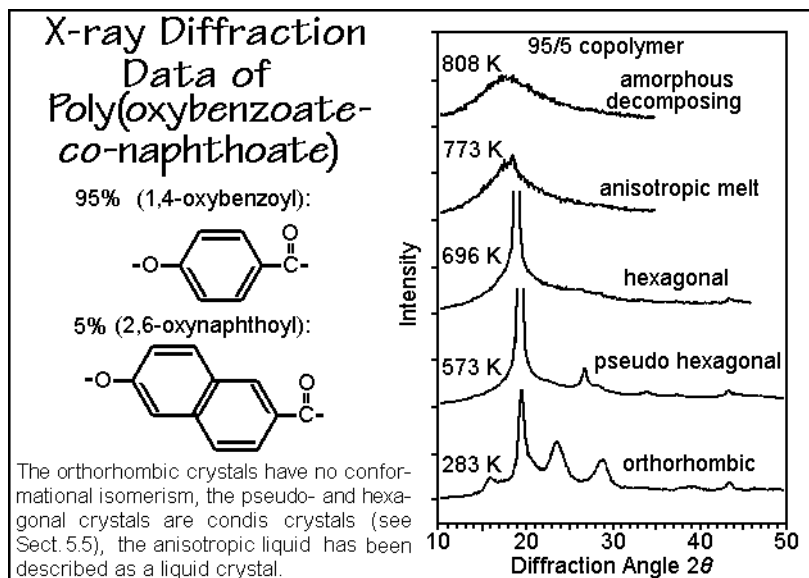


Fig. 7.51

required. The second model is called the paracrystalline lattice model. In this model, ordered domains are formed without sequence matching by the presence of conformational correlations between the different repeating units [22]. In the common scheme of phase diagrams this corresponds to a solid solution. Detailed X-ray patterns have been computed for the latter model and agree well with the observed patterns [23]. Most likely, the actual crystallization requires elements of both models, a certain amount of phase separation, and some solid solution formation.

The results of thermal analysis and X-ray structure analysis are next combined in Fig. 7.52 to a nonequilibrium phase diagram for samples that were crystallized quickly [24]. Large areas of the diagram are still not fully explored and change considerably for different thermal histories, as outlined above. At least in the orthorhombic areas, one expects a normal semicrystalline structure with nanophase separation, causing the broad glass transition. In the hexagonal and anisotropic melt, however, there seems to be, in contrast to PETcoOB, only a single phase structure. The limit of existence of this copolymer system is set by decomposition, marked in Fig. 7.52 by the symbols ♦ at about 750 K from data based on thermogravimetry.

The observations on the examples of the close-to-random copolymers in the last two sections show that a number of arrested equilibria can be superimposed and give rise to different local nanophases. The chemical equilibrium may be totally arrested, as in most vinyl polymers, or actively drifting towards an equilibrium distribution, as in the described polyesters. The transesterification starts below the melting temperature. Furthermore, there may be equilibria of the different sequences of repeating units which are driven by crystallization or liquid-liquid phase separation. In addition, these phase separations are coupled to the physical diffusion to minimize the free enthalpy. The diffusion of the segments, in turn, is hindered by the chemical connectivity of the macromolecules and the high viscosity which at the glass transition temperature stops

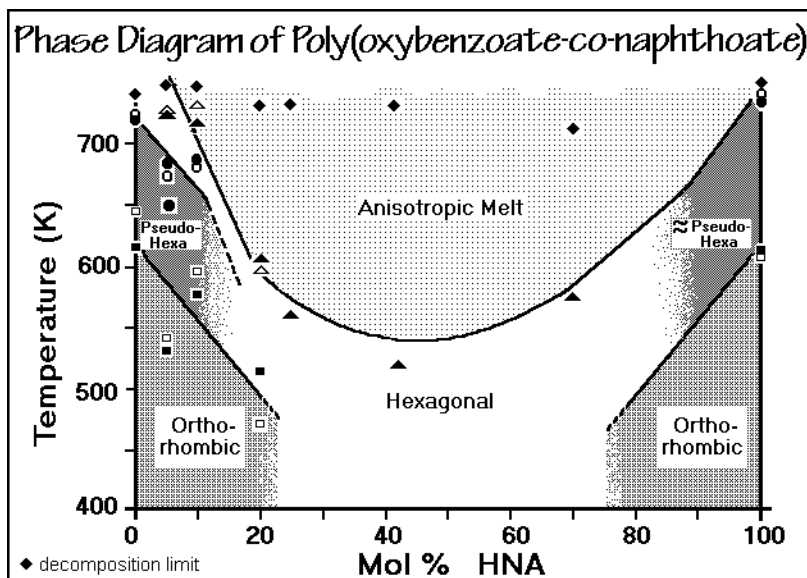


Fig. 7.52

all large-amplitude motion. This combination of the various arrested equilibria gives rise to several internal variables, which are, however, often not available.

### 7.2.3. Melting Transitions of Block Copolymers

The chemical structure of block copolymers is given by the number of blocks, their sequence, and their length, as is discussed in Fig. 1.19 and Sect. 3.4.1. The structure of a diblock copolymer poly(styrene-*block*-1,4-butadiene) of type AB, for example, can have the following chemical structure:



with the corresponding segment lengths of molar masses 42,300, and 45,400 Da. At sufficiently large molar mass, the segments can phase separate under the restriction that the junctions between the different repeating units define the interfaces, as is described in Sect. 5.1.11 (see also the phase diagram Fig. 7.21). The liquid-liquid phase diagram is discussed in Sect. 7.1.6, and the lamellar structure of the chosen example of poly(styrene-*block*-1,4-butadiene) is reproduced in the AFM picture of Fig. 5.79. The lamellar spacing is 50 to 60 nm. At the chosen large molar mass, the phase structure is over the whole temperature range that of an amphiphilic liquid crystal (see Sect. 5.5).

A microphase structure as shown in Fig. 5.79 is sufficiently large to allow molecular mobility within the different lamellae which is hindered only close to the interfaces. The glass transitions of such block copolymers are described in Sect. 7.3. Depending on the nature of the segment, crystallization is possible within the lamellar superstructure. Depending on the space available, the typically nanometer-size crystals, described in Sect. 5.2 are unaffected and experience no restriction.

A well studied example is given by the poly(oxyethylene-*block*-styrene). In case of atactic sequences of polystyrene, only the poly(oxyethylene), POE, can crystallize. A typical morphology of the POE is shown in Fig. 5.55. Single crystals of the copolymer can be grown from a common solvent which keeps both components mobile up to the time of crystallization of the POE-component. Figure 7.53 illustrates a growth spiral out of poly(oxyethylene-*block*-styrene), grown at 293 K from a solution of ethylbenzene (AB diblock, 28 wt-% oxyethylene block with a molar mass of about 10,000 Da). The crystal is comparable to the lamellar crystals of Fig. 5.55, i.e., the poly(oxyethylene) crystals are chain-folded with about 2.5 nm amorphous polystyrene layers at the interfaces.

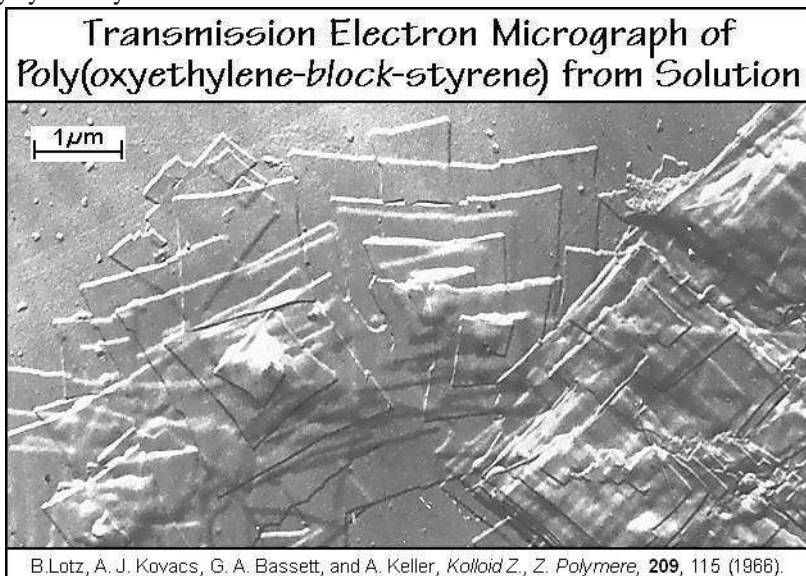


**Fig. 7.53**

By shortening the length of the crystallizable segment, extended chain, once-folded, or twice-folded crystals of poly(oxyethylene), the component  $A_x$ , could be grown from the melt for poly(oxyethylene-*block*-oxypropylene) [25]. Table 7.1 gives a list of the crystallinity and the length of the amorphous and crystalline lengths,  $\ell_a$ , and  $\ell_c$ , respectively, for di- and symmetric tri-block copolymers.

Certain conclusions can be drawn about the changes in melting temperature with the presence of the second component. The poly(oxyethylene) homopolymer segments did not reach full crystallinity. The amorphous oxypropylene component is added to the intercrystalline layers in order to account for the amorphous layer thickness. The influence of the chain folding results in an increase in the surface area, but also allows for a larger crystallinity by reducing the crystalline layer thickness, and causes an additional decrease in the melting temperature. A comparison between the AB and BAB copolymers suggests that the entropic effect of mixing on fusion is not simply proportional to the oxypropylene concentration of the block copolymer, but is also influenced by the length of the crystallizable segments, and the achieved fold characteristics.

**Table 7.1.** Characteristics of poly(oxyethylene-*block*-oxypropylene) crystals

$A_xB_y$ or $B_yA_xB_y$	$w_c$ (fraction)	$\ell_a$ (nm)	$\ell_c$ (nm)	$T_m$ (K)
$x = 40, y = 0$	0.68	3.7	7.4	323.8 (extended)
$x = 40, y = 2$	0.69	4.3	7.0	323.2 (extended)
$x = 40, y = 3$	0.69	4.8	7.1	323.0 (extended)
$x = 40, y = 5$	0.69	5.6	7.0	321.8 (extended)
$x = 40, y = 8$	0.69	6.7	7.8	320.5 (extended)
$x = 40, y = 11$	0.69	7.4	6.8	320.2 (extended)
$y = 0, x = 48, y = 0$	0.68	4.6	8.9	328.2 (extended)
$y = 1, x = 48, y = 1$	0.67	5.6	9.0	327.2 (extended)
$y = 2, x = 48, y = 2$	0.69	6.1	8.5	322.0 (extended)
$y = 5, x = 48, y = 5$	0.77	4.7	6.2	314.6 (once folded)
$y = 6, x = 48, y = 6$	0.78	5.0	5.9	314.0 (once fld.) 311.0 (twice fld.)
$y = 7, x = 48, y = 7$	0.78	5.1	5.8	312.6 (once fld.) 310.2 (twice fld.)

The melting temperature, measured at the melt-end by dilatometry, is proportional to the concentration of the crystallizing units, A, whenever the ratio of the of the B-sequence length,  $y$ , to the number of B-sequences in the molecule,  $n + 1$ , is less than 2.5. For larger B-sequence lengths the concentration effect decreases, most likely due to increasing phase separation in the melt. Figure 7.54 represents a plot of the changes in melting temperature observed when the short blocks are linked to an overall higher-molar-mass copolymer  $B_y(A_xB_y)_n$ . A full assessment of the data is difficult since the initial steep decrease in melting point is due to chain folding (see Table 7.1).

The overall behavior of poly(oxyethylene-*block*-styrene) was also studied when crystallization was carried out from cooling of the melt. In case the polystyrene phase separates before crystallization of the poly(oxyethylene) component, the glassy lamellae restrict the crystal morphology. Figure 7.55 illustrates the global phase structure as evaluated by small-angle X-ray diffraction, SAXD, electron microscopy, and standard DSC. For the chosen sequence-lengths of the components, a liquid-liquid phase separation occurs on cooling at 422 K, yielding a lamellar structure as illustrated in the electron micrograph (compare with Fig. 5.40 and the phase diagram of Fig. 7.21). This lamellar structure gets fixed at the glass transition of the polystyrene component.



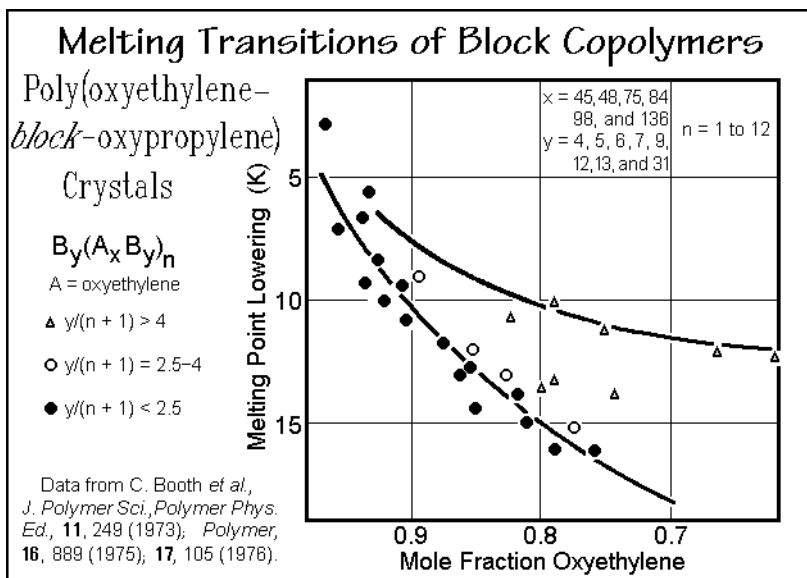


Fig. 7.54

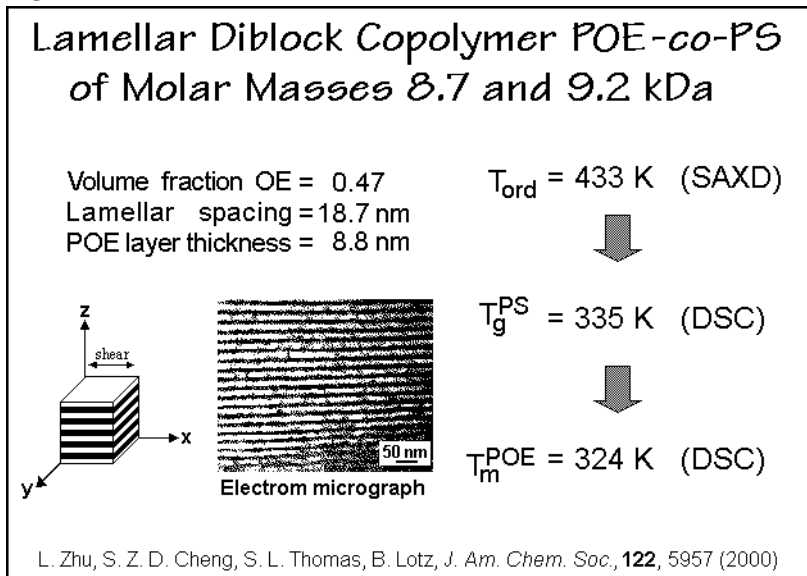


Fig. 7.55

The poly(oxyethylene component can, however, still crystallize at 324 or lower temperatures. Figure 7.56 illustrates such restricted crystallization. At the lowest temperature, the resulting crystals are small and are more or less randomly arranged. Between 223 and 263 K, the orientation changes and the crystallized chains are arranged parallel to the global lamellae. Above 308 K, finally, enough mobility exists to orient the chains at right angles to the glassy polystyrene lamellae.

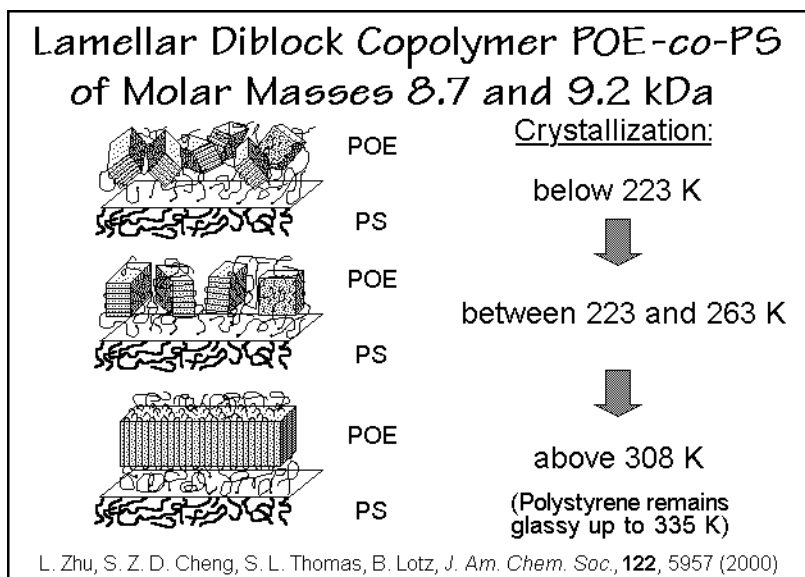


Fig. 7.56

In copolymers with even shorter blocks, considerable additional hindrance exists for the crystallizing component if the other component undergoes earlier solidification at a higher temperature by a glass transition or separate crystallization. Figures 7.57 to 7.61 illustrate the interactions of two crystallizing sequences for poly[oligoimino(1-oxododecamethylene)-*alt*-oligooxytetramethylene] [26]. The two components are identified by their weight ratios of amide to ether, A/E. The components are

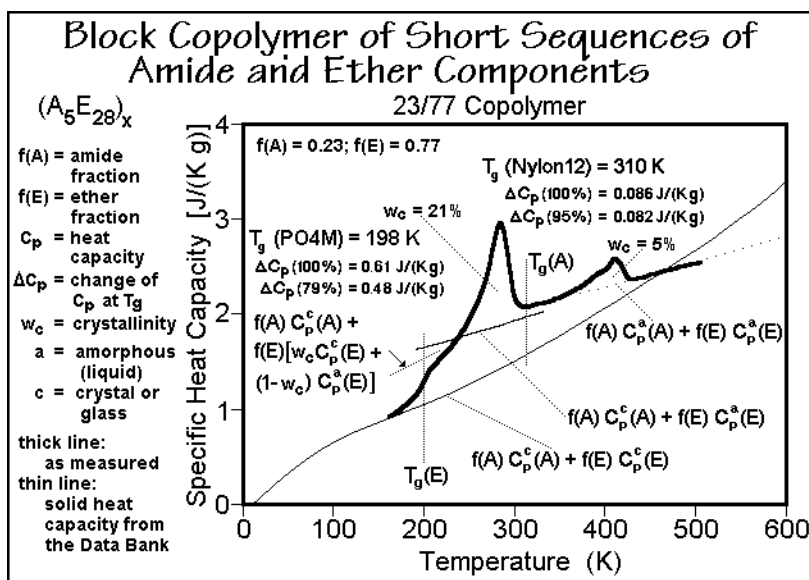


Fig. 7.57

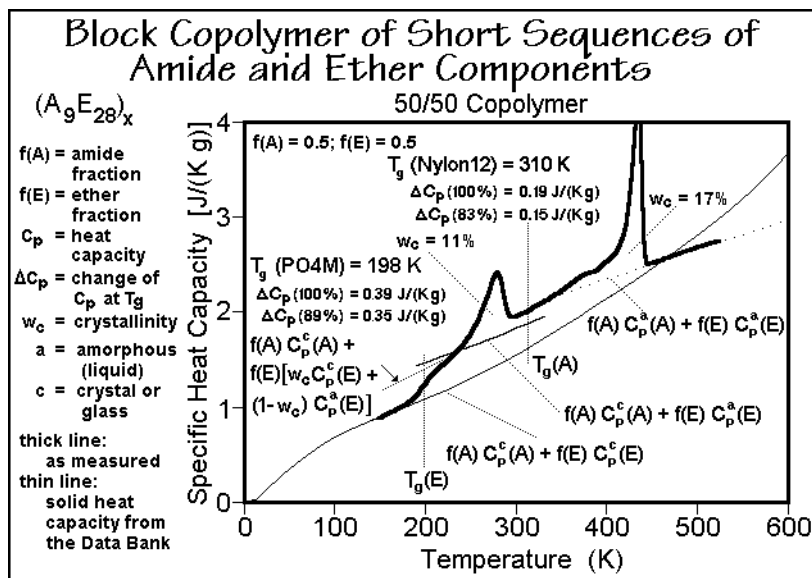


Fig. 7.58

immiscible and show two separate glass transitions, not far from the transitions of the two homooligomers, related to nylon 12 and poly(oxytetramethylene). The structure of the copolymer is  $\{[-\text{CO}(-\text{CH}_2)_{11}(-\text{NH}-\text{CO}(-\text{CH}_2)_{11})_{m-1}-\text{CO}[-\text{O}(-\text{CH}_2)_n]_n\}_x$ , PEBA. The polymer is known commercially as Pebax™ (trademark of Atofina Chemicals). The glass transitions are broadened because of the existing crystallinity and the smallness of the phase regions, as is discussed in Sect. 6.3.4.

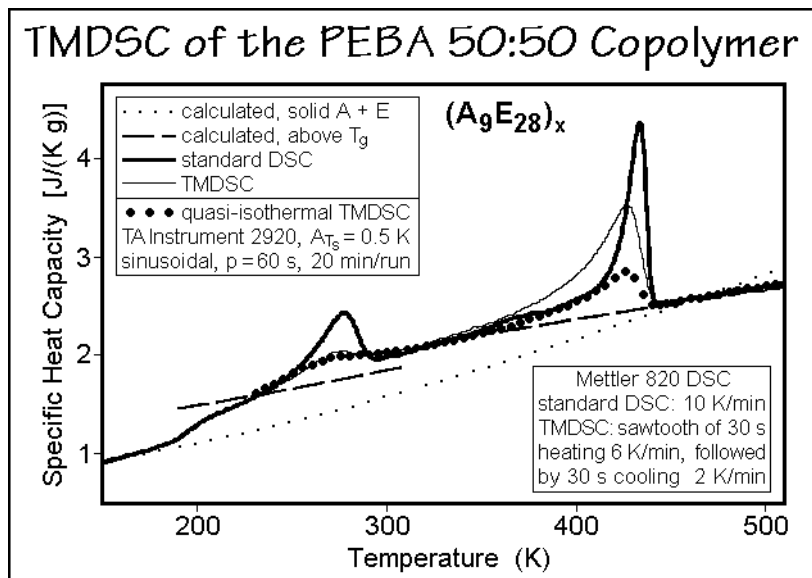


Fig. 7.59

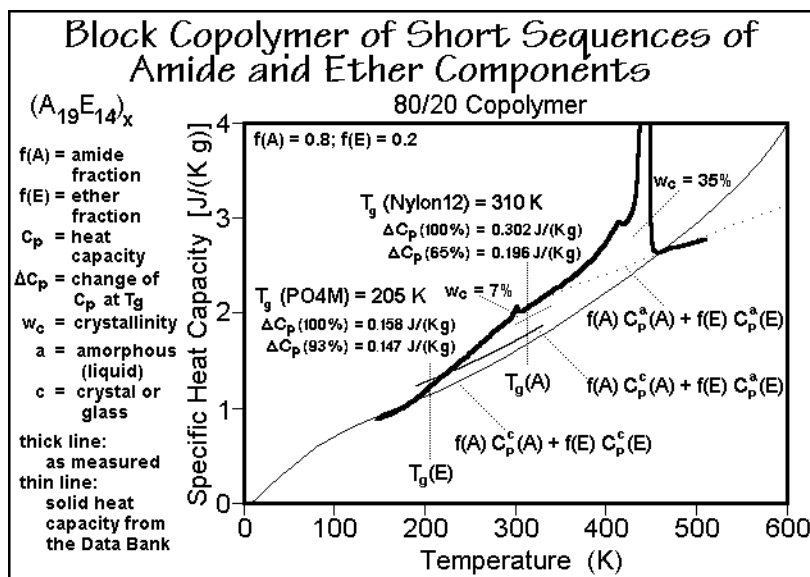


Fig. 7.60

The ether sequences, E, in Fig. 7.57 are 17 nm long and permit a crystallinity of only 21% in the E-phase, while the A component is only 5% crystalline with chain sequences of five nanometers. Both are much less than is typical for polymers of the same repeating units. For the E oligomer this low crystallinity is due to the need to crystallize within the layers of solid, partially crystalline A, for A, the sequence length is too short for more extensive crystallization.

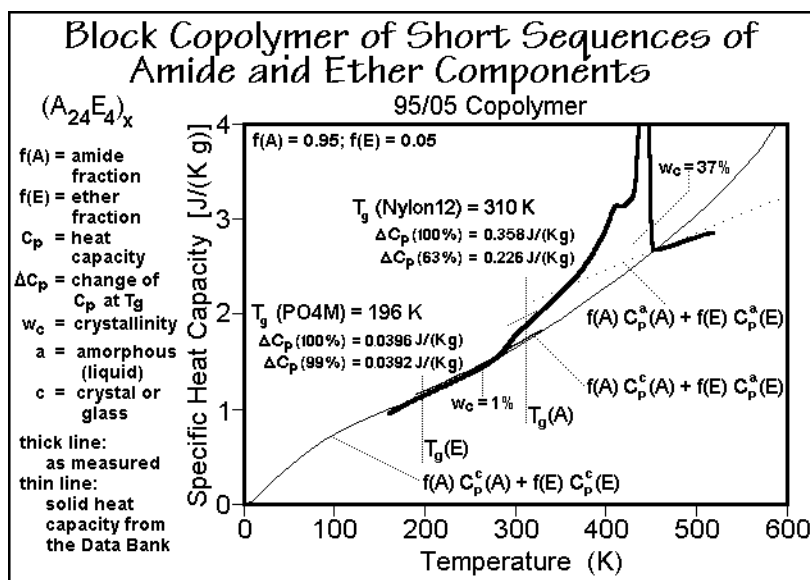


Fig. 7.61

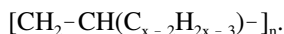
Figure 7.59 illustrates the temperature-modulated DSC of the 50:50 PEBA [27]. The standard DSC trace is identical to the curve in Fig. 7.58, i.e., the crystallinity of E is 11%, and of A is 17%, as is expected for the changes in sequence lengths compared to Fig. 7.57. As in most other polymers, the heating traces show a certain amount of reversing melting which is frequency-dependent. The ether crystallinity has a melting temperature of 278 K, which compares to the pure oligomer of similar chain length ( $E_{28} \approx 2000$  Da) which is about 55% and melts with a peak temperature of about 296 K. Both changes are indications of fewer and smaller (or less perfect) crystals. The amount of reversing melting for both the amide and ether crystals, normalized to crystallinity, increases with decreasing crystal perfection. The ether crystals have a higher reversibility than the pure oligomer crystals, which have practically none, since they are above the critical length of Fig. 3.91 (POTM2000) and yield an extended-chain crystal morphology on annealing.

The crystallinities of the various phase regions in the two-component systems in Figs. 7.57 to 7.61 are calculated using an adaptation of the method described in Fig. 4.80 for one component, considering the temperature dependence of all heat capacities and heats of fusion [26]. The two limiting heat capacities are the contribution of the two fractions,  $f(A)$  and  $f(E)$ , multiplied with their crystalline and liquid heat capacities,  $C_p^c$  and  $C_p^a$ , respectively, as illustrated in Fig. 4.81. In Figs. 7.57 and 7.58 all semicrystalline heat capacities are marked, starting from the all-solid range up to the glass transition of the amorphous fraction of E, where  $(1 - w_c)$  of E becomes liquid. Next is the melting region of E at which the remaining  $w_c$  of E also turns liquid. Shortly thereafter, at the glass transition of A the amorphous fraction of A turns liquid. Finally, beyond the melting of A, the whole sample is liquid.

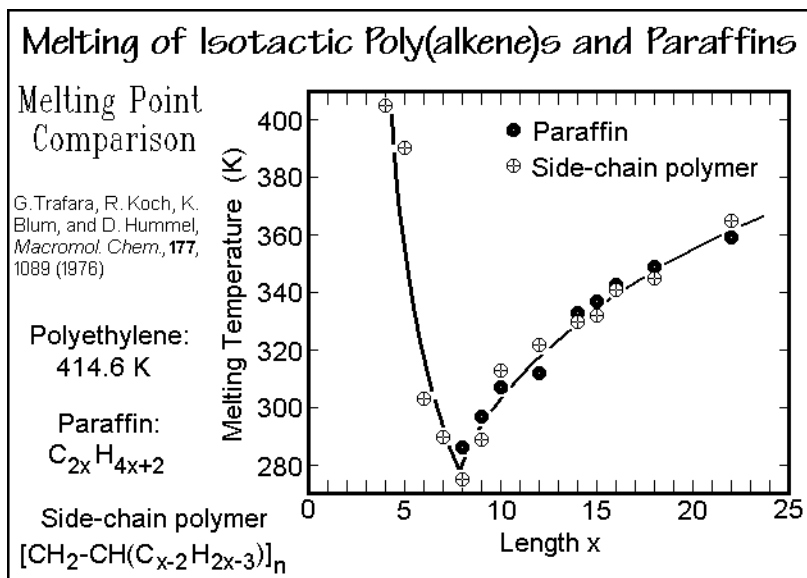
Increasing the amide concentration, as seen in Figs. 7.60 and 7.61, the copolymer amide crystallinities of 35 and 37% exceed that of the corresponding nylon 12 of 30%. The copolymer melting peaks at about 436 K are about 10 K lower than seen for nylon 12. The amide crystals of the copolymers with enhanced crystallinity have less total reversibility than those of the homopolymer and the copolymers of less amide content have more [21]. One interprets these data by assuming that close to the phase boundary the ether blocks give an additional mobility to the crystallizing amide blocks. The higher reversibility of poorer crystals, in turn, seems to be a general observation for chain-folded polymers [28].

The ether-sequences, E, in Fig. 7.61 are only about 3 nm long and the crystallinity in the E-phase is only 1% due to restrictions by the surrounding glassy and 37% crystalline amide-phase, A, of 40 nm molecular chain length. The crystals seem to be located close to the phase boundary.

A different type of block copolymer can be produced by the introduction of long side chains into the polymer which by themselves may decouple and crystallize independently. Figure 7.62 displays the change of melting temperature of isotactic poly(1-alkene)s as a function of side-chain length:



These polymers are usually classified as homopolymers, but can be considered as block copolymers as soon as the side chains become sufficiently long to decouple. The polymers with short side chains have a crystal structure with a  $2\frac{1}{3}/1$  helix, as

**Fig. 7.62**

discussed in Sect. 5.1. 6 and 5.1.8. The side chain is part of the helix symmetry, as shown for example by the poly(1-butene) crystal structure of Fig. 5.25. As the side chain lengthens, the close packing of the side chain around the helix becomes more difficult. The polymers do not crystallize well, and the melting temperature decreases rapidly because of a decrease in heat of fusion. The minimum in the melting temperature coincides with a change in crystal structure which now permits a paraffin-like packing of the side chain and forces the backbone into a  $2^*4/1$  helix. Each macromolecule is arranged in a plane with the side chains extending to both sides of the backbone. As a result, the melting points with the paraffin-like packing of the side-chain are identical of the paraffins with double the chain length, as can be derived from Fig. 7.62. On quenching such long-side-chain polymers from the melt, the side chains decouple and crystallize by themselves in a metastable crystal structure with a much lower melting temperature, leaving the entire backbone of the polymer in the amorphous portion. On annealing, recrystallization to crystals that include backbone and side chains is possible.

Figure 7.63 illustrates the change in melting temperatures of atactic side-chain polymers. As soon as the side chains are long enough, they crystallize, leaving the backbone in a decoupled, amorphous layer on top of the crystals. The melting temperatures are intermediate to paraffins of single and double the side-chain lengths. Figure 7.64, finally, shows the changes that occur by copolymerizing of the long side-chain polymers with short chain monomers. The poly(vinyl stearate)s show signs of phase separation and perhaps a blocky chemical structure. Poly(*n*-octadecyl acrylate-*co*-*n*-dodecyl acrylate)s form mixed crystals over the whole concentration region, while the three other acrylates show a reduction of the melting temperature as expected for compatible melts. Overall, these side-chain polymers behave more like decoupled small molecule systems than polymers.

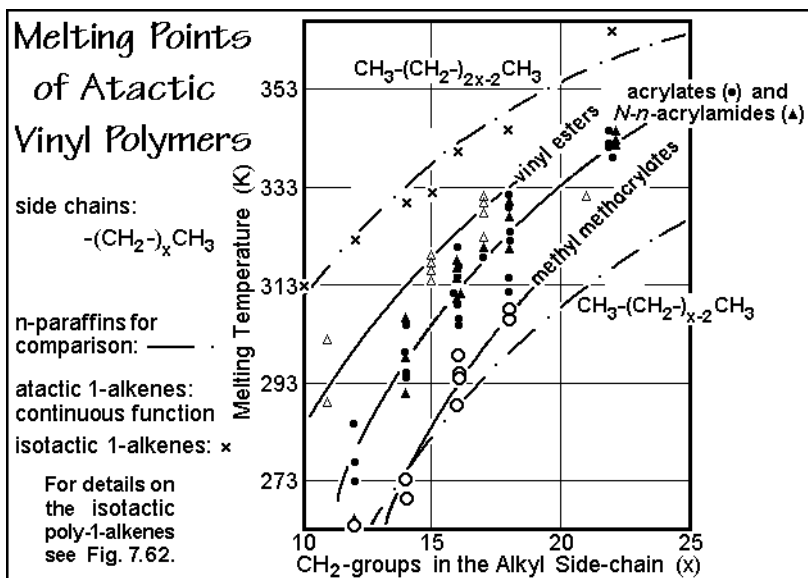


Fig. 7.63

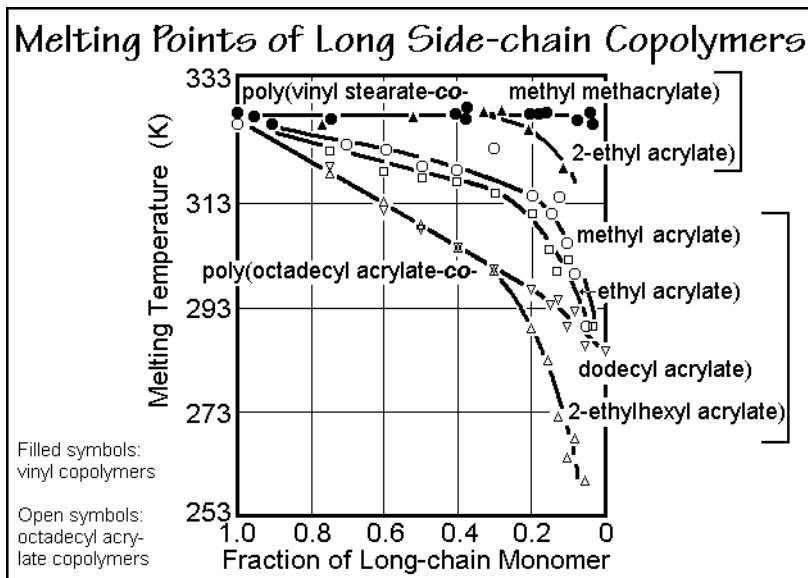


Fig. 7.64

#### 7.2.4. Melting Transitions of Regular Copolymers

The discussion of block copolymers in the last section included already a number of regular copolymers. An alternating block copolymer of type  $A_xB_y$  may well be considered a homopolymer, as illustrated by the example of nylon 6,6 [A is

$\text{CO}-(\text{CH}_2)_4\text{CO}-$ ; and B is  $\text{NH}-(\text{CH}_2)_6\text{NH}-$ ] (see Fig. 1.18). Naturally, nylon 6,6 could also be broken into even more blocks, namely to  $(\text{CD}_4\text{CED}_6\text{E})_n$ , with each of the letter representing a different chain atom. As the component segments get sufficiently long, one can expect phase separation. Since the segments are part of the polymer backbone, the typical macromolecular properties are anticipated.

The melting temperatures of the polyureas and polyamides in Figure 7.65 look like parts of a phase diagram of polyethylene, interrupted regularly by urea and amide groups. In the crystal, interruption of longer sequences of identical groups with molecular structures of different polarity or geometry can lead to nanophase separation as is illustrated in Figs. 2.106 and 5.135, discussed in the formation of mesophases in Sects. 2.5.3 and 5.5.2. The distinct odd-even difference in the melting temperatures is linked to the changes in packing and entropy with odd and even-numbered  $(\text{CH}_2)_x$ -sequences, as is illustrated by the schematics VV and V\A for three and four  $\text{CH}_2$ -groups (see also Fig. 5.123 and 5.147). The small polar groups will become three-dimensionally disordered on melting due to the random coil formation of the backbone

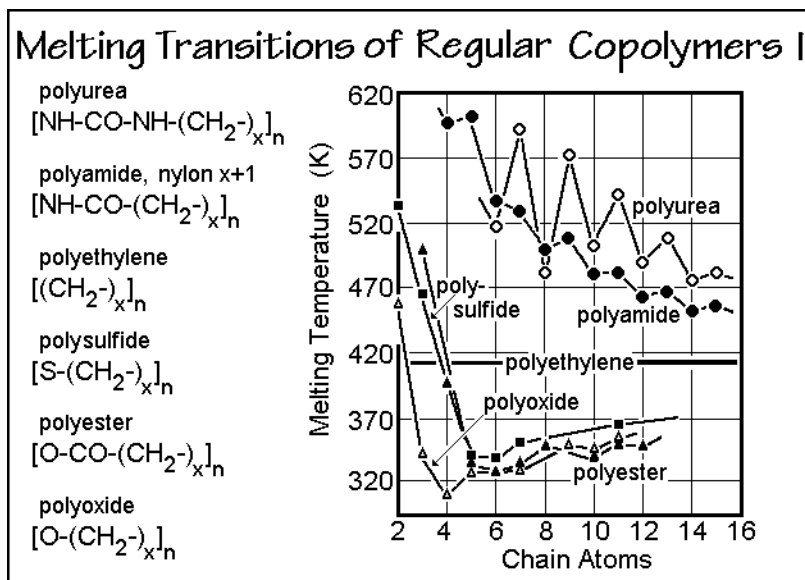
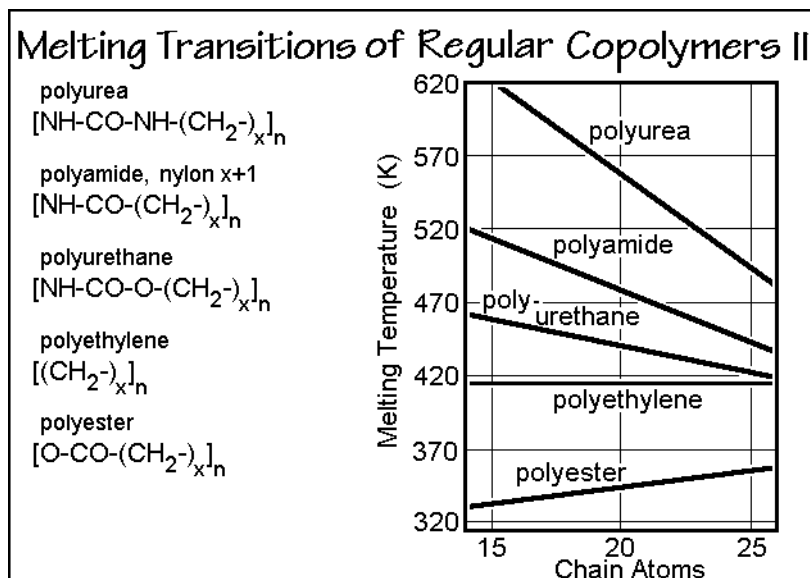


Fig. 7.65

chain, but the chains stay in sequence along the chain. Even in the melt can the polar interaction and hydrogen bonds give a sufficient driving force for aggregation (phase separation) which may ultimately lead to the formation of amphiphilic liquid crystals, as discussed in Sect. 7.1.6. The bottom-half of Fig. 7.65 adds a number of regular copolymers that show a minimum in melting temperature at short  $\text{CH}_2$ -sequence length. Both groups of polymers ultimately approach the polyethylene melting temperature. The higher melting polymers, however, may have also a shallow minimum before approaching the polyethylene values. Furthermore, this diagram is drawn on the basis of irreversible melting temperatures. The further extension to larger values of  $x$  is shown in Fig. 7.66.





**Fig. 7.66**

The almost 30 examples of phase diagrams of this section show that equilibrium is rare in copolymers. Nanophase separation is found frequently when partial crystallization occurs. Dissolutions are possible by randomizing the conformations and by chemical reaction.

### 7.3. Glass Transitions of Copolymers, Solutions, and Blends

The change of the heat capacity and free enthalpy during the glass transition are discussed in Sect. 2.5.6 (see Figs. 2.117 and 2.118, respectively). In Chap. 4, the different methods of thermal analysis sensitive to the glass transition are described. One-component systems are then examined in Sect. 6.1.3, using the hole model to analyze the enthalpy relaxation. Also discussed are the effects of small phase-size and the presence of a strongly coupled second phase that may produce a rigid amorphous fraction. Section 6.3, finally, contains a detailed examination of several one-component systems. In this Sect. 7.3, a review of the glass transition of multiple component systems of copolymers, solutions, and blends is presented.

The main issues in describing polymeric materials are decoupling of chain segments and nanophase morphology (see Sects. 6.2 and 7.2). The hole theory in Sects. 6.1 and 6.3 allow the estimation of a hole volume. It is about 1/5 of the “mobile bead” volume which determines the  $\Delta C_p$  at  $T_g$  (see Figs. 2.103 and 2.117). Assuming the affected mobile units in the first surrounding sphere of the hole as four, and about 16 in the second, leads to a volume of about 20 “beads” being affected by a hole. For polystyrene, this is a volume of about  $1.66 \text{ nm}^3$ , or a sphere of a radius of 0.6 nm (two beads per repeating unit, 104.2 Da, density =  $1.04 \text{ Mg m}^{-3}$ ). The glass transition is thus an ideal tool to check the properties of a nanophase structure.

The multi-component systems, to be discussed next, may have a much more complex glass transition than the single-component systems. First, in solution, the glass transition changes with concentration from that of one homopolymer to the other. The change with the mole fraction may be linear for some mixtures, but deviations due to specific interactions and packing problems between the components are possible and may be positive or negative. Multiple glass transitions are possible on incomplete mixing under equilibrium or nonequilibrium conditions. Finally, when nanophase structures exist, the glass transitions may be broadened due to interactions across the interfaces, as illustrated by rigid-amorphous phases (see Sect. 6.1.3).

### 7.3.1. Theory of Glass Transitions

Copolymers combine multiple components within one molecule, i.e., the mixing within the molecules is set by the chemical reaction (see Sect. 3.4). Solutions, in contrast, consist of separate molecules, mixed only physically (see Sect. 7.1). Although the effects of these two mixing types may yield different distributions, the same expressions are usually applied erroneously to describe glass transitions of copolymers and solutions as a function of composition.

Copolymers are often sufficiently irregular not to be able to crystallize. Random copolymers of short repeating units, such as vinyl polymers, and mass fractions of 0.3–0.7 are normally amorphous since sequences of identical repeating units must commonly be two to five nanometers long to crystallize, and cocrystallization of different repeating units is not very frequent (see Sect. 5.1.10).

The glass transitions of amorphous copolymers change smoothly with concentration from one pure component to the other, as is shown in Fig. 7.67 for poly(acrylamide-*co*-styrene), poly(methyl acrylate-*co*-styrene), and poly(styrene-*co*-

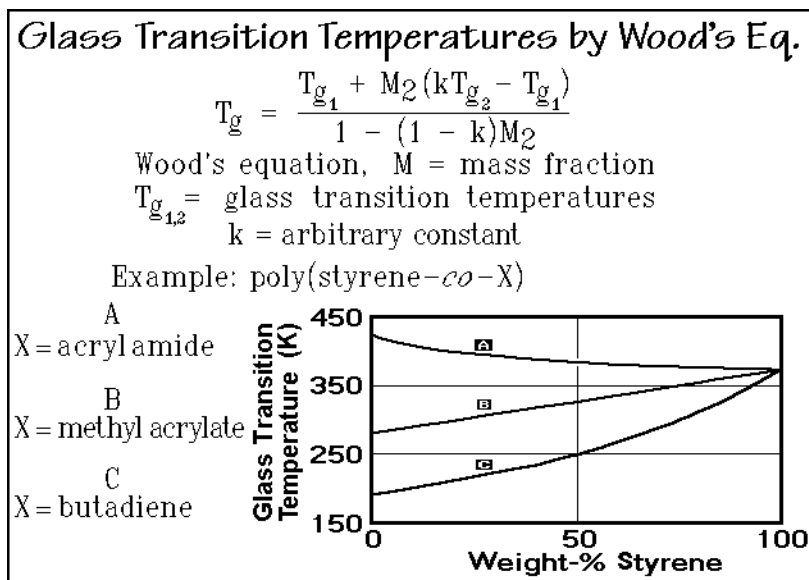
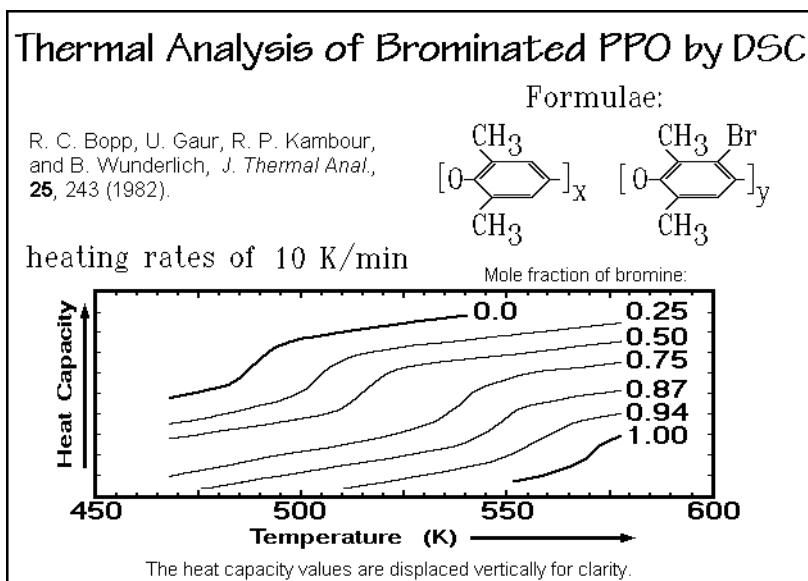


Fig. 7.67

1,4-butadiene). Wood's equation, listed in the figure, empirically describes such concentration dependence with a single, empirical fitting parameter,  $k$ .

Another example of the glass transitions of copolymers is given by brominated poly(oxy-2,6-dimethyl-1,4-phenylene) in Fig. 7.68. In this case the backbone structure and distribution of molecular lengths are the same for all copolymer samples. The first bromine introduced into the phenylene group adds in the meta position relative to the methyl group and deactivates the second meta position, so that only one bromine adds per phenylene [29]. The glass transition of the copolymers moves smoothly from that of one homopolymer to the other. The value of  $\Delta C_p$  at  $T_g$  decreases with the amount of bromination, an indication of stiffening of the backbone which accelerates at high bromine fractions. Note that there is no significant change in the breadth of the glass transition region with composition.



**Fig. 7.68**

Turning to polymer solutions, an identical equation to Wood's equation is the Gordon-Taylor equation, as written in Fig. 7.69 ( $W_1 \equiv M_1$ ,  $1 - W_2 = M_1$ , etc.). This equation was proposed to account for the glass transition in case of volume-additivity of the homopolymers. If this condition holds, the constant  $k$  should be  $\rho_1 \Delta \alpha_2 / \rho_2 \Delta \alpha_1$ , where  $\rho$  represents the densities and the  $\Delta \alpha$  the change in expansivity at the glass transition of the homopolymers.

Assuming the conformational entropy is responsible for the glass transition, one can write the change of the glass transition temperature as a function of the fractions of flexible bonds,  $B$ , as is given in the Gibbs-Di Marzio equation. This equation can be connected to the Gordon-Taylor equation by linking the constants in the two equations. The Gordon-Taylor equation is recovered from the Gibbs-Di Marzio equation if  $k$  assumes the value  $\gamma_2 w_1 / \gamma_1 w_2$ , where the  $\gamma$  is the number of flexible bonds in the respective components, and  $w$ , the mass, both per mole of repeating units.

### The Glass Transition of Polymer Solutions

$$T_g = \frac{W_1 T_{g1} + W_2 k T_{g2}}{W_1 + W_2 k} \quad \text{(Gordon-Taylor equation)}$$

$$T_g = B_1 T_{g1} + B_2 T_{g2} \quad \text{(Gibbs-Di Marzio equation)}$$

$$1/T_g = (W_1/T_{g1}) + (W_2/T_{g2}) \quad \text{(Fox equation)}$$

$$\frac{T_g - T_{g1}}{T_{g2} - T_{g1}} = (1 + K_1) W_{2c} - (K_1 + K_2) W_{2c}^2 + K_2 W_{2c}^3 \quad \text{(Schneider equation)}$$

$W_{1,2}$  = mass fractions

$T_{g1,2}$  = glass transition temperatures

$B_{1,2}$  = flexible bond fractions

$K_{1,2}$  = interaction constants

**Fig. 7.69**

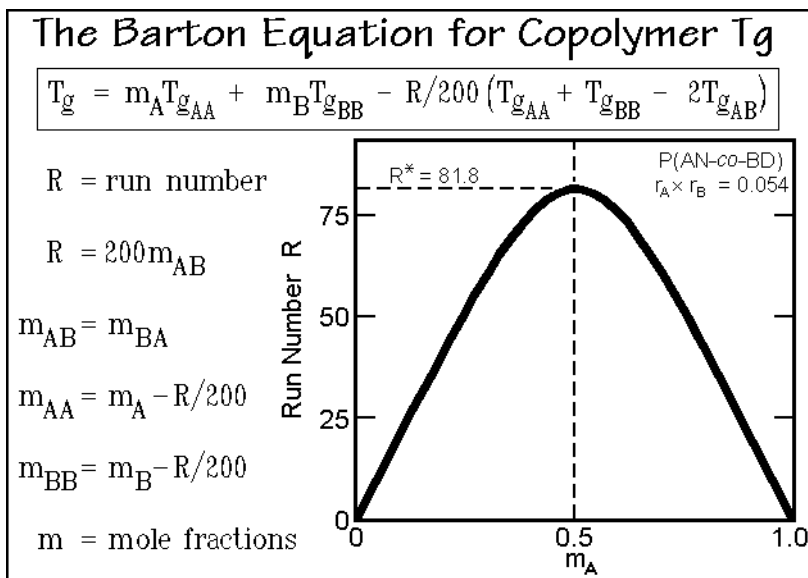
A different equation results if one assumes that the product of the change in expansivity with the glass transition temperature,  $\Delta\alpha T_g$ , is a constant, known as the empirical Simha-Boyer rule  $\Delta\alpha T_g = 0.113$ . The well-known and simple Fox expression for the glass transition temperature results on insertion of the Simha-Boyer rule into the Gordon-Taylor equation. The Gibbs-Di Marzio and the Fox equations are easily generalized to SVT or pVT equations of state when assuming that the solution can be based on simple additivity of the homopolymer properties.

To add effects of specific interactions, the Gordon-Taylor expression can be expanded into a virial expression, as in the Schneider equation, listed in Fig. 7.69 [30]. The variable  $W_{2c}$  is the expansivity-corrected mass fraction of the Gordon-Taylor expression:  $W_{2c} = kW_2 / (W_1 + kW_2)$ . The Schneider equation can be fitted with help of the constants  $K_1$  and  $K_2$  to many polymer/polymer solutions, as is illustrated in Sect. 7.3.2. The parameter  $K_1$  depends mainly on differences in interaction energy between the binary contacts of the components: A-A, B-B, and A-B, while  $K_2$  accounts for effects of the rearrangements in the neighborhood of the contacts.

While these equations are often used indiscriminately for homopolymer solutions and for copolymers, it can be shown that sequence distributions of copolymers, given by the reactivity ratios  $r_1$  and  $r_2$  of Sect. 3.4.1, can affect the glass transition. Different chain stiffness can result for other reactivity ratios at the same overall concentration.

In Fig. 7.70 the Barton equation for copolymer glass transitions is listed. It is based on the assumption that the four possible dyads in a copolymer, poly(A-co-B), have the following glass transitions: AA ( $T_g = T_{gAA}$ ), BB ( $T_g = T_{gBB}$ ), AB, and BA ( $T_g = T_{gAB} = T_{gBA}$ ). Inserting these three different glass transitions into the Gibbs-Di Marzio equation for the intermolecular effects, leads to:

$$T_g = m_{AA} T_{gAA} + m_{BB} T_{gBB} + 2m_{AB} T_{gAB} ,$$

**Fig. 7.70**

where the  $m_{ij}$  represent the appropriate mole fractions [31]. Similarly, the Fox equation can be used as base to describe intermolecular effects. The resulting equation is written in terms of the inverse of the glass transition and is called the Johnston equation.

The reactivity ratios for a copolymer poly(A-co-B) can be written as  $r_A = k_{AA}/k_{AB}$  where  $k_{AA}$  and  $k_{AB}$  are the rate constants of the chain terminating in A continuing with another A or B unit, respectively (see Figs. 3.45 and 3.46). Out of these reactivity ratios one can calculate the run number,  $R$ , which is defined as the average number of consecutive A- and B-sequences per 100 chain units:

$$R = 400m_A m_B / [1 + \{1 + 4m_A m_B (r_A r_B - 1)\}^{1/2}].$$

For a homopolymer, this number is zero (no run is completed). For an alternating copolymer, poly(A-alt-B),  $R = 100$ . Each run is linked by an A-B or B-A dyad, with the dyads being equal to each other, i.e., one writes:  $R = 100(m_{AB} + m_{BA})$  and  $m_{AA} = m_A - m_{AB} = m_A - (R/200)$ . The Barton equation in terms of the run number is shown in Fig. 7.70. The curve is drawn with data derived for  $R$  for poly(acrylonitrile-co-1,4-butadiene) with a value of  $r_A r_B = 0.054$ . The run number is symmetrical to  $m_A = 0.5$ , with a maximum run number  $R^* = 81.8$  [31].

Figure 7.71 illustrates the change of the glass transition for poly(styrene-co-acrylonitrile) as a function of the run number, defined in Fig. 7.70. The branches of the Barton equation ( $m_A > m_B$ , and  $m_A < m_B$ ) are symmetric to the line which extends to the alternating copolymer. This treatment of  $T_g$  can also be applied to triads, and one can use the other equations of Fig. 7.69 as base, but with an increase in complexity. Stereo-specific copolymers consisting of meso and racemic dyads can be treated if the samples of different tacticity have different glass transitions [32].

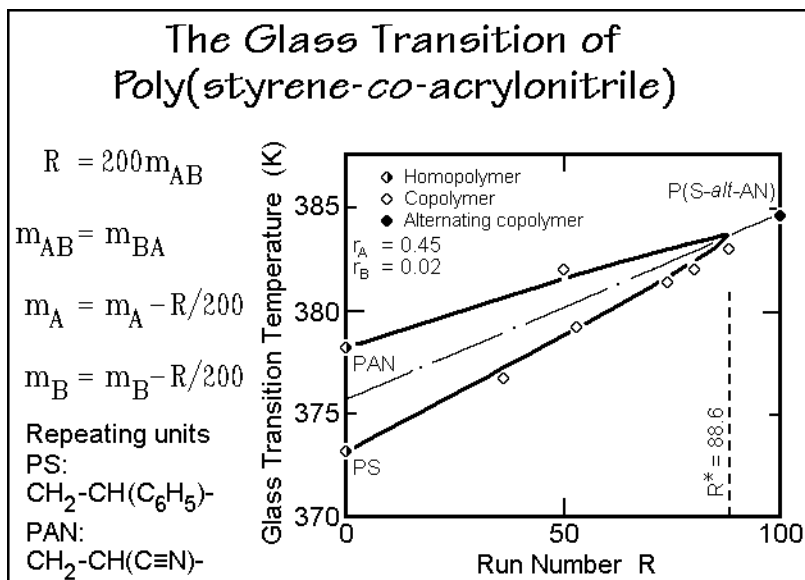


Fig. 7.71

### 7.3.2. Glass Transitions of Solutions

Solutions of flexible, linear macromolecules are thermodynamically described by the Flory-Huggins equation of Sect. 7.1.2. The glass transition intervenes at low temperatures by terminating the equilibrium phase diagram. Once the temperature decreases below the glass transition, phase changes, such as crystallization or liquid-liquid phase separation, are frozen. The glassy system is then a solid and can exhibit sufficiently large-amplitude motion for phase transitions only in special cases.

Figure 7.72 illustrates a large number of glass transition data of polymer solutions with comparisons to the Gibbs-DiMarzio (DM), Fox (F), and Schneider (S) equations described in Fig. 7.69 [30]. The upper left displays two sets of literature data on poly(vinylidene fluoride)-poly(methyl methacrylate) solutions (■,▲). The glass transition shows a positive deviation from simple additivity of the properties of the pure components, which can only be represented with the help of the indicated interaction parameters of the Schneider equation. The lower left set of data illustrates poly(oxyethylene)-poly(methyl methacrylate) solutions (●,○). They are well described by all three of the equations, indicating rather small specific interactions and great similarity between volume and entropy descriptions.

The upper right curves in Fig. 7.72 display data of solutions of two aliphatic polyesters with polyepichlorohydrin. A large  $K_2$  is needed in S to account for the negative deviation of the solution with poly(butylene adipate), PBA, while the solutions with poly(ethylene adipate), PEA, show little redistribution in the contact neighborhood ( $K_2 \approx 0$ ). The lower right curves demonstrate that solutions of poly(vinyl chloride) and poly( $\epsilon$ -caprolactone) can be fitted with all equations. The rather large  $K_1$  and  $K_2$  must cancel, since  $K_1 = K_2 = 0$  leads to the Gordon-Taylor

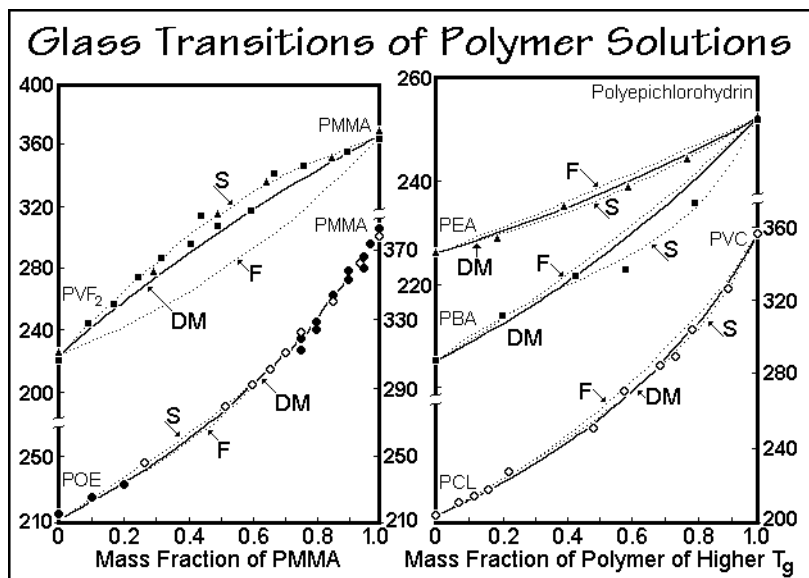


Fig. 7.72

equation. This overview of the five polymer pairs shows that volume additivity (Gordon-Taylor equation) and additivity of flexible bonds (Gibbs-Di Marzio equation) are not sufficient to describe all polymer solutions. Specific interactions must be considered. Unfortunately, the Schneider equation accounts for the interactions only with empirical constants. The broadening of the glass transition in Fig. 7.73 indicates that mixing of polymer chains may cause additional effects.

A series of thermal-analysis traces of solutions of polystyrene of 37,000 molar mass in poly( $\alpha$ -methylstyrene) of molar mass 90,000 is shown in Fig. 7.73 [33]. The two pure polymers show a small amount of enthalpy relaxation. The three solutions indicate a considerable broadening of the glass transition region, in contrast to the practically constant broadness with concentration in copolymers (see Fig. 7.68). Solutions of polymers are commonly characterized by such a broadened glass-transition region. The same is also seen for solutions of polymers with small molecules, such as plasticizers. The homopolymers in Fig. 7.73 display a  $T_2 - T_1$  of about 7 K and a  $T_g - T_b$  of 30 K, with the temperatures defined in Fig. 2.117, while the 50/50 solution reaches 33 and 75 K, respectively. As outlined in Sect. 7.3.1, this broadening is most likely connected with an incomplete mixing of the homopolymer sequences along the chain. It may be possible to describe this inhomogeneity as a nanophase separation of regions with nonrandom chain segments.

Plotting the glass transition temperatures of Fig. 7.73 as a function of concentration, yields Fig. 7.74. Only the Gordon-Taylor equation with a fitted constant represents the data. Similarly it is possible to fit with the Schneider equation with its two constants. Two additional equations, not in Fig. 7.69, are compared in Fig. 7.74 to the data; one, is the Couchman equation, based on additivity of the products of  $\Delta C_p$  with the logarithm of  $T_g$ , the other uses a molar additivity of the logarithm of  $T_g$ . All equations without adjustable parameters do not fit the experimental data ( $\circ$ ).

### Solution of Polystyrene and Poly( $\alpha$ -methylstyrene)

Thermal analysis curves of solutions of polystyrene and poly( $\alpha$ -methylstyrene) at a heating rate of 20 K/min.

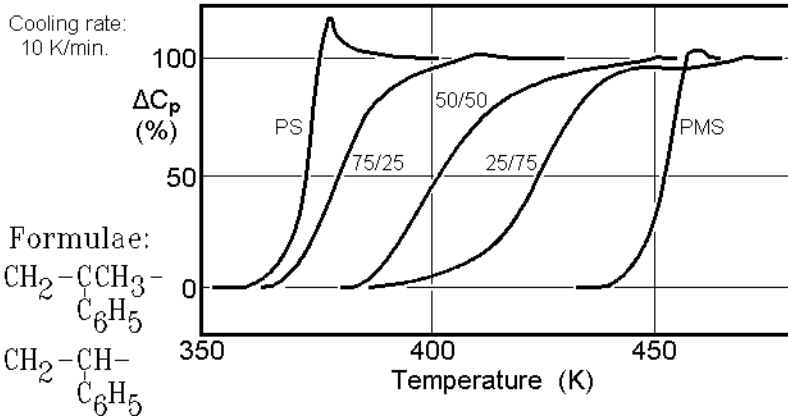


Fig. 7.73

### Solution of Polystyrene and Poly( $\alpha$ -methylstyrene)

Equations from  
top to bottom:

1. Gibbs-Di Marzio
2. Logarithmic eq.
3. Fox
4. Couchman
5. Gordon-Taylor  
with fitted constant  
 $k = 0.14$  (Wood  
equation)

Formulae:

$$\text{CH}_2-\text{C}(\text{CH}_3)(\text{C}_6\text{H}_5)- \quad \text{PMS}$$

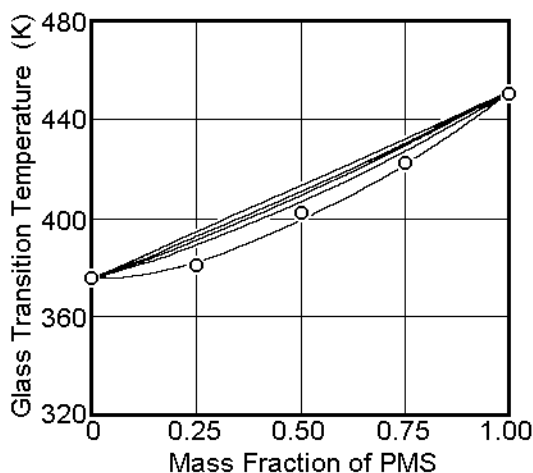
$$\text{CH}_2-\text{CH}(\text{C}_6\text{H}_5)- \quad \text{PS}$$


Fig. 7.74

The next figure illustrates partial solubility of the same polymers as in Figs. 7.73 and 74 by increasing the molar mass of the polystyrene. Figure 7.75 represents DSC curves of a 50/50 blends with the high molar mass poly( $\alpha$ -methylstyrene). For the low molar mass two glass transitions are seen, but not with values of  $\Delta C_p$  that correspond to a complete phase separation. In addition, the high-temperature glass transition of the poly( $\alpha$ -methylstyrene) is considerably broadened compared to the homopolymer



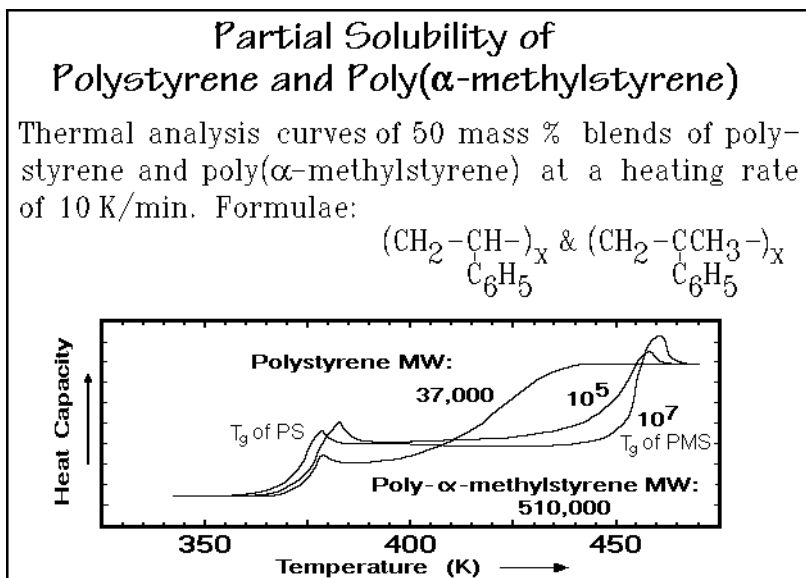


Fig. 7.75

in Fig. 7.73 [33]. The straight-forward interpretation is that some, but not all of the low-molar-mass polystyrene is dissolved in the poly( $\alpha$ -methylstyrene). The solubility can be reduced by increasing the molar mass of the polystyrene component. The higher glass transition is then much sharper and approaches the proper  $\Delta C_p$ . With even higher molar mass, one can reach complete immiscibility, as shown.

### 7.3.3. Glass Transitions of Copolymers

While for solutions of homopolymers the mixing of the chain segments may be incomplete when compared to the intermolecular mixing, the distribution of the chain segments of the copolymers are fixed by the polymerization reaction, as described in Sect. 3.4, i.e., the same concentration can yield different segment distributions and glass transitions. The change of the glass transition with composition and randomness of the repeating units along the chain is demonstrated in Fig. 7.71 for poly(styrene-*co*-acrylonitrile) based on the Barton equation. Two further examples are given in Figs. 7.76 and 7.77 for poly(acrylonitrile-*co*-1,4-butadiene) and poly(styrene-*co*-methyl methacrylate) [34], respectively. As expected, the average  $T_g$  of the two homopolymers, the  $T_g$  for the critical run number  $R^*$  ( $= 81.8$ , see Fig. 7.70), and the alternating copolymers ( $R = 100$ ) lie on a straight line. The usually inaccessible region between the alternating copolymer and the value for  $R^*$  was achieved with special control of the sequence regularity. The data in Fig. 7.77 exhibit a minimum in  $T_g$  at an  $R$ -value of 65.2, corresponding to a styrene mole fraction of 0.57.

Special complications arise when the stereospecific homopolymers show different glass transitions for isotactic (I), syndiotactic (S), and heterotactic (H) chains. An example is the poly(methyl methacrylate). The iso- and syndiotactic stereoisomers of PMMA have glass transition temperatures of 315 and 400 K, respectively. Treating the stereoisomers as copolymers with a modified Barton equation of Fig. 7.70:

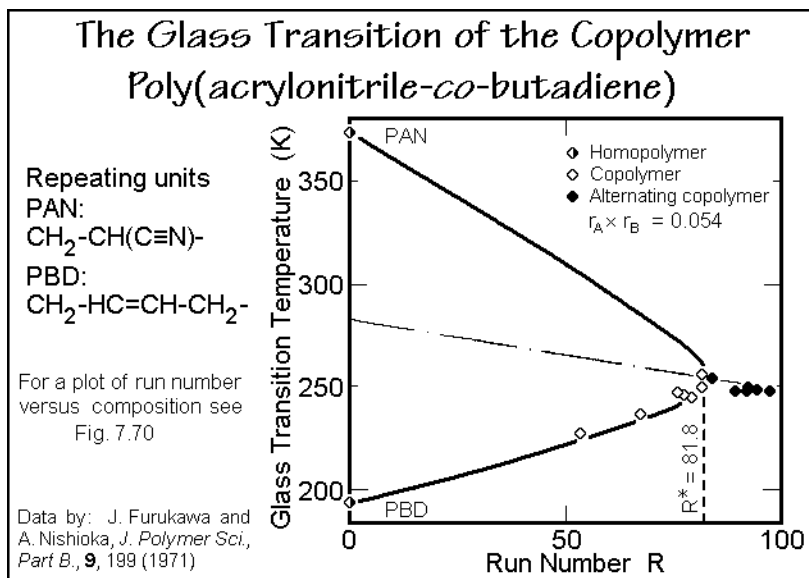


Fig. 7.76

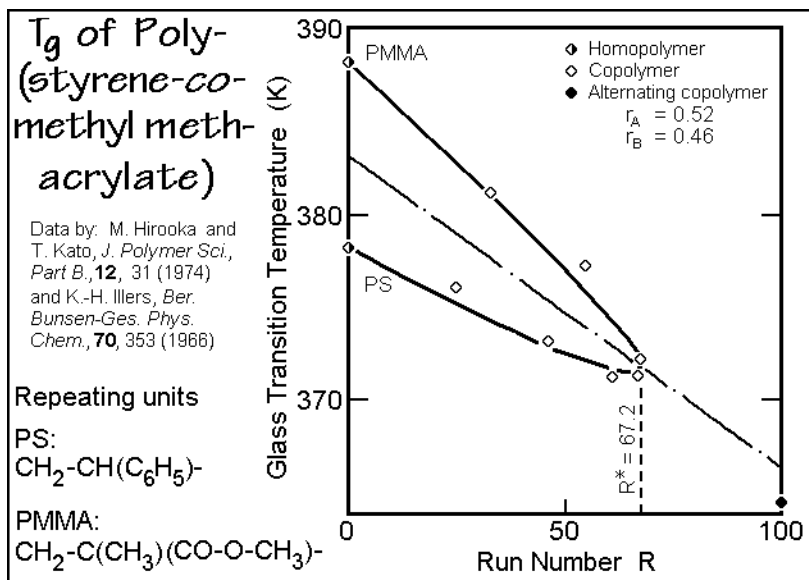


Fig. 7.77

$$T_g = m_I T_{gI} + m_S T_{gS} + m_H T_{gH},$$

the heterotactic glass transition was estimated as 391 K. The different possible PMMA polymers should thus be found in a triangle defined by these three limiting glass transitions. The truly atactic polymer is specified by the parameters  $m_I = m_S = 0.25$  and  $m_H = 0.5$ , at 374 K.

Another aspect of thermal analysis concerns the thermodynamic functions based on heat capacity. Obviously, the number of possible copolymers is so large, that complete measurements for all copolymers are not possible. Fortunately, the heat capacity of glassy and liquid copolymers over wide temperature ranges are not structure sensitive (for a discussion of structure-sensitive properties see Sect. 5.3.1). A simple additivity rule based on the molar composition of the components is suggested in Fig. 2.70 for the copolymers of styrene and butadiene (see also the addition scheme of heat capacities in Fig. 2.77).

Improvements beyond the empirical, direct additivity of heat capacities is needed at low temperatures, where skeletal vibrations govern the heat capacities. With only few measured points it is possible to establish the functional relationship of the  $\Theta_1$  and  $\Theta_3$  temperatures with concentration for the inter- and intramolecular vibrations (see Sect. 2.3). The group-vibration frequencies are strictly additive, so that heat capacities of complete copolymer systems can be calculated using the ATHAS, as discussed in Sect. 2.3.7. In Fig. 2.70 the glass transition changes with concentration, to reach 373 K for the pure polystyrene, as for the previously discussed copolymer systems with polystyrene. Below  $T_g$ , the solid  $C_p$  of both components needs to be added for the heat capacity of the copolymer, above, the liquid  $C_p$  must be used. The glass transition retains the same shape and width as seen in Fig. 7.68 on the example of brominated poly(oxy-2,6-dimethyl-1,4-phenylene) [29].

To summarize the basic information of the first three sections of this chapter, one recognizes that the glass transitions for multicomponent systems must take into account the mixing between and within the macromolecules. The first is described by one of the equations in Fig. 7.69, the latter by combination of contributions of dyads or triads which affect the chain stiffness with the intermolecular effects as by the Barton equation in Fig. 7.70. The broadening of the glass-transition region in case of solutions in Fig. 7.73, in contrast to random copolymers of Figs. 2.70 and 7.68, is taken as an indication of nanophase separation. The change in the sharpness of the glass-transition region is an important, often neglected tool for the characterization of polymeric materials and will be further explored in the discussion of the next two sections.

### 7.3.4. Glass Transitions of Block Copolymers

The chemical structure of block copolymers is given by the number of blocks, their sequence, and their length, as discussed in Sect. 3.4.1 and Fig. 1.19. A diblock copolymer poly(styrene-*block*- $\alpha$ -methylstyrene) (S/MS) of molar masses 312,000, and 354,500 Da, for example, has the following approximate chemical structure:



For such large molar masses, the segments will separate into microphases, with the junctions between the different repeating unit sequences defining the interfaces, as is described in Sect. 5.1.11. The liquid-liquid phase diagram is discussed in Sect. 7.1.6 (see Fig. 7.21). The phase areas of such diblock copolymers are often sufficiently large to allow independent, large-amplitude molecular mobility on both sides of the point of decoupling of the components. Depending on the nature of the components,

glass transitions and ordering are possible within the separate phases. The crystallization of the block copolymers is described in Sect. 7.1.6, the glass transitions are discussed next.

Figure 7.78 represents the heat capacities of the homopolymers polystyrene and poly( $\alpha$ -methyl styrene) with sharp glass transitions at 375 and 443 K, respectively [35]. On copolymerization to a triblock molecule, MS-S-MS(45), a much broader glass transition results. It stretches from the polystyrene to the poly( $\alpha$ -methylstyrene) glass transition and could indicate a solution, but the molar mass seems too high for solubility when compared to Fig. 7.75 in Sect. 7.3.2 ( $M_w \approx 10^6$  Da). Similarly, the figure indicates broad transition regions for the other copolymers.

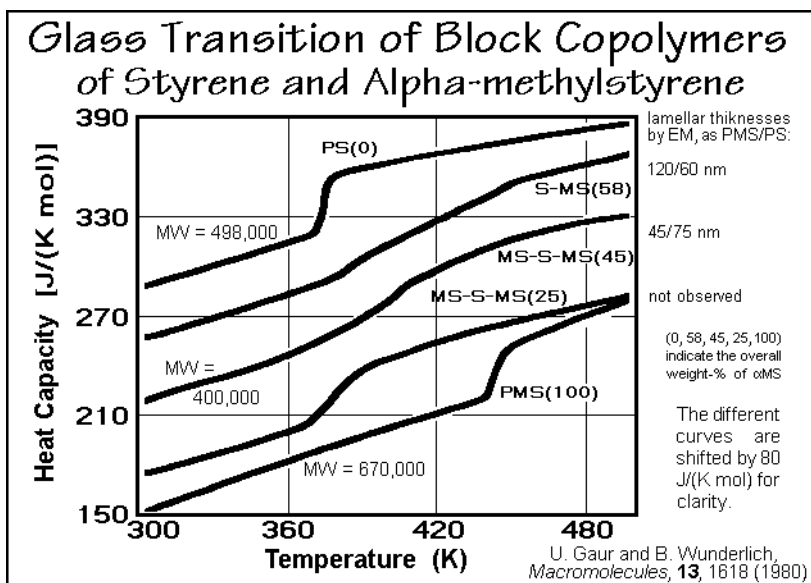


Fig. 7.78

The interpretation of these data becomes clearer when introducing an entropy relaxation by slow cooling before an analysis with a faster heating rate (see Sect. 6.1.3). Figure 7.79 documents that the enthalpy relaxation centers at the glass transitions of the homopolymers with a reduction in peak amplitude on copolymerization that is larger than expected from the reduction in concentration. This is the typical behavior of phase-separated polymers. Even more conclusive is that electron microscopy on the same samples reveals that all these high-molar-mass S/MS block copolymers are microphase-separated.

Separate experiments on small spheres of polystyrene indicate that the glass transition broadens as the radius of the spheres decreases as shown in Figs. 6.13–15 [35]. The broadening of the glass transitions in Fig. 7.79 results, thus, from the smallness of the phase areas. Figure 7.80 combines the data of Figs. 13–15 together with information on two of the block copolymers of Fig. 7.78 which have an overall lamellar structure. The plot shows that the broadening of the glass transition is related to the specific surface area of the phases. The indicated temperature difference is then

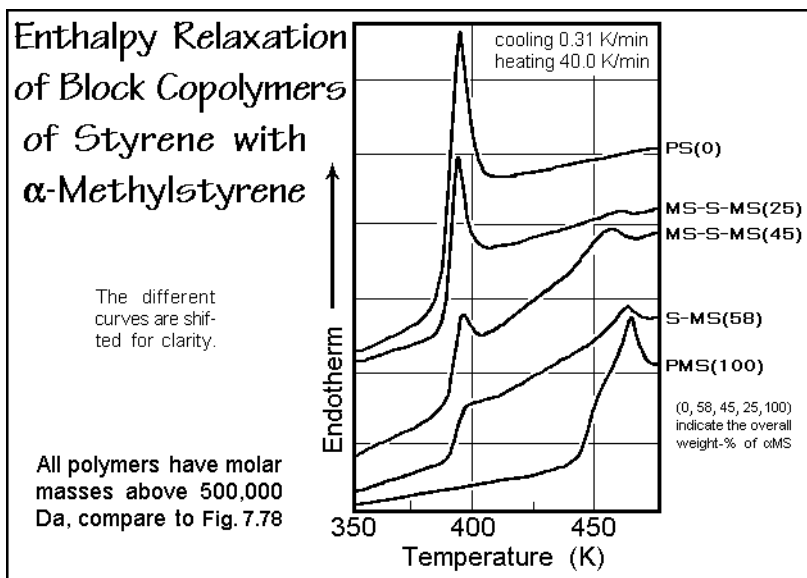


Fig. 7.79

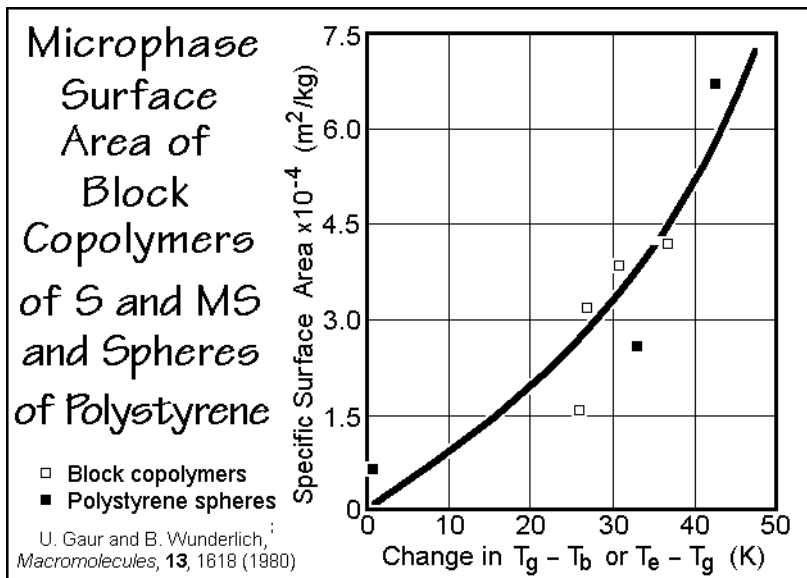


Fig. 7.80

$\Delta T = T_g - T_b$  or  $T_e - T_g$ , where  $T_b$  and  $T_e$  are the beginning and the end of the glass transition regions, respectively, defined in Fig. 2.117. The value of  $\Delta T$  increases sharply with the surface area of the microphase. For the transition of the phases surrounded by a surface that connects to a phase of lower glass transition, the glass transition starts at lower temperature (spheres of polystyrene in air and MS surrounded

by S), while a surrounding surface coupled strongly to a phase of higher glass transition extends to higher temperatures (S surrounded by MS). In the block copolymers of Fig. 7.78, this effect broadens the glass transition to such a degree that the two transitions practically fuse. It is of interest to note that the broadening in solutions of polymers, which was linked to the inability to completely mix the homopolymer chains with the solvent, extends symmetrically to both sides (see Sect. 7.3.2) rather than to one side, as in the surface effect of Fig. 7.78. Thermal analysis is, thus, able to distinguish incomplete mixing from surface effects.

Comparing the block copolymers of high molar mass to solutions of the same polymers described, as in Sect. 7.3.2, one expects solubility at lower block lengths. Indeed, Fig. 7.81 shows that this is so, and that Barton's equation describes the data for the block copolymer solutions (run number  $R = 0$ ), blocky copolymers (indicated run numbers  $R = 6$  and 30), as well as random copolymers ( $\circ$ ) [36].

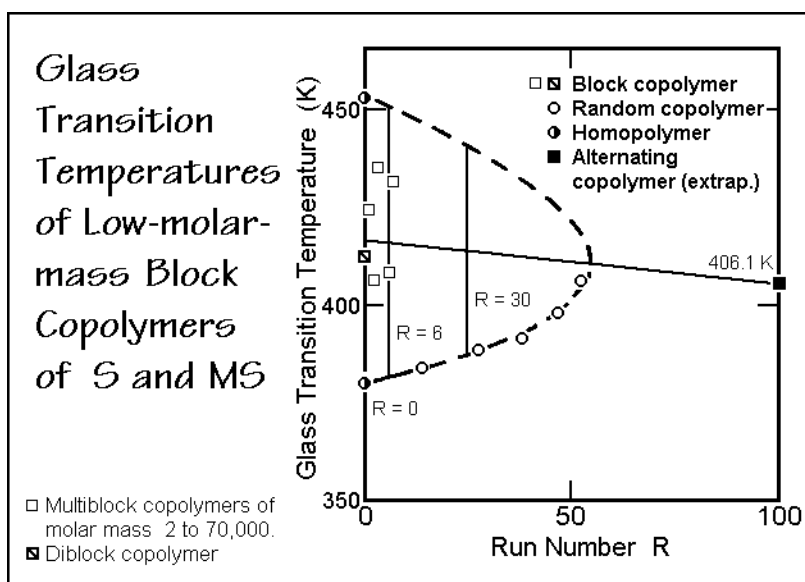


Fig. 7.81

A quantitative thermal analysis of a series of tapered block copolymers was carried out with poly(*n*-butyl acrylate-*block-gradient-n*-butyl acrylate-*co*-methyl methacrylate) [37], i.e., one of the blocks was copolymerized from both components with changing composition from one end to the other. Such block copolymers show, in addition to the size and strain effects, a partial solubility. A third phase due to the gradient in concentration was not discovered for the analyzed samples.

To summarize all copolymers, Fig. 7.82 reproduces a three-dimensional plot of the Barton equation, as it was used throughout this chapter. This graph allows the correlation between the three types of projections possible and shown in various parts of this chapter. The two effects that must be added for a full description are the specific interactions (see Fig. 7.69, Schneider equation) and the broadening of the glass transition, available from heat capacity analysis.

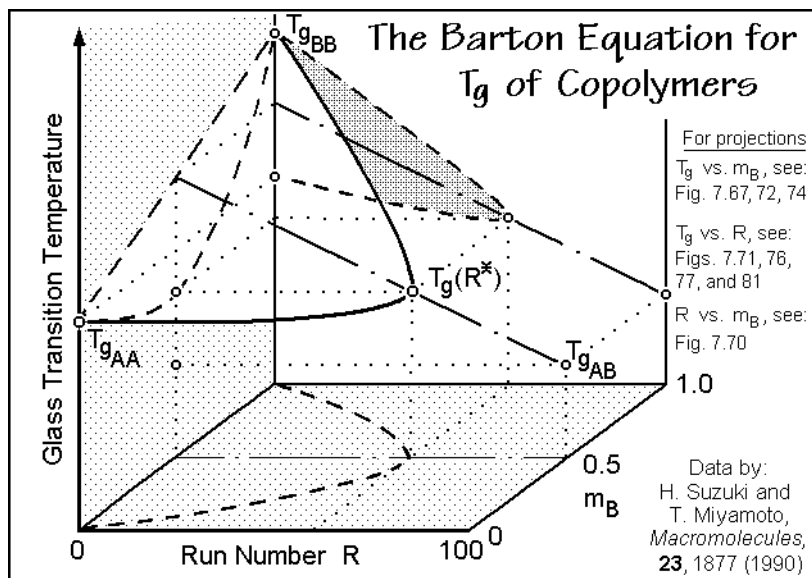


Fig. 7.82

### 7.3.5. Glass Transitions of Multi-phase Systems

Multi-phase systems have been discussed throughout the last two chapters and it became increasingly clear that thermal analysis of the glass transition region gives important information for the description of materials. Every one of the seven characteristics of the glass transition of Fig. 2.117 contains information on the nature of the phase to be analyzed. Copolymers, solutions, and blends can be classified as solutions or as macro-, micro-, or nanophase-separated systems by measuring  $T_g$ ,  $\Delta C_p$  and the broadness of the glass transition region.

The broadening of the glass transition, prominently featured in this section, is qualitatively linked to the loss of cooperativity of the large-amplitude motion. Without cooperative behavior, the torsional oscillations about flexible bonds gradually lead at sufficiently high temperature to motions of larger amplitude, ultimately reaching rotational isomers of higher internal energy,  $\Delta E$ . This motion leads to an endothermic contribution to the heat capacity, as discussed in Fig. 2.33. Interactions between the molecules hinder this motion and force a narrower glass transition range with a  $T_2 - T_1$  in Fig. 2.117 of typically 3 to 10 K. The early initiation of such molecular isomerism as a gradual endotherm of little cooperativity is seen for polyethylene in Fig. 2.65 for the glass as well as the crystal, and is discussed in Sects. 2.3.10, 2.1.6, and 5.3.4. The main reason for the gradual initiation of conformational isomerism in polyethylene is the rather small volume requirement for internal rotation which decreases the cooperativity of neighboring segments.

The broadening of glass transitions in polymer solutions, as in Fig. 7.73, and on partial ordering, as in Fig. 2.64, reaches the 50 and 100 K range of  $T_g - T_b$  or  $T_c - T_g$  of Fig. 2.117. It certainly is not a negligible effect. In this case, one again assumes,

that nanophases of different structure increase or decrease their glass transitions from the average value. Only if sufficiently large phases of fully intra- and intermolecularly randomized mobile repeating units (beads) are present, does the glass transition get sharper. This size-effect is illustrated in Fig. 7.80 and is expected to change with the nature of the system.

Besides calorimetry, one has several other, quite sensitive thermal analysis techniques for the analysis of the glass transition, such as dilatometry, TMA, DMA, and DETA, all described in Chap. 4. A detailed analysis of the DMA of polyethylene is given in Sect. 5.6.6 by means of Fig. 5.171. The so-called  $\gamma$ -transition is linked to the gradual increase of heat capacity that leads ultimately to the glass transition. The DMA is very sensitive to this early softening in the glassy region, but up to the present, only DSC data have seen a quantitative description, as discussed above. The (broadened) glass transition is only poorly recognized in Fig. 5.171 by DMA as the  $\beta$ -transition and by DSC it is only obvious in the heat capacity. Quantitative analysis is possible after extrapolation to fully amorphous polyethylene (see Fig. 2.46). The polyethylenes of lower crystallinity are commonly copolymerized, as demonstrated in Figs. 7.37 and 7.38. An additional observation is that melting can begin within the glass transition region. Finally, the  $\alpha$ -transition in Fig. 5.171 is most likely linked to the *gauche-trans* equilibrium in the crystal and on the interface of the crystals which could be studied in more detail in gel-spun polyethylenes, described in Sect. 6.2.6, Figs. 5.157, 5.158, and 6.4. Most recently the glass transition of these fibers could be analyzed by quantitative DSC, as documented in Fig. 6.105 and 6.106. The glass transition must belong to the metastable mesophase of the polyethylene fibers and is broadened considerably to higher temperatures.

The glass transitions of crystals that can be treated as two-phase structures with at least one phase being a mesophase are illustrated by OOBPD, treated in Sect. 5.5.4 (see Fig. 5.143). The mesophase glass transition is broadened because of lack in cooperativity (dotted area). A similar, but macromolecular mesophase is shown in Fig. 2.68. In this case one can describe the sample as a multi-block copolymer. A normal, only slightly broadened amorphous glass transition occurs at about 275 K and is decreased in  $\Delta C_p$  by the presence of some rigid amorphous fraction (see Sect. 6.1.3). This is followed by the shaded area which is the mesophase glass transition. As discussed in Sect. 5.5, many of such two-part repeating units can be considered nanophase-separated (Figs. 2.106 and 5.135). The broadening of glass transitions, thus, is an important characteristic for the description of polymers.



## References

### General References

**Sect. 7.1.** The general references for the equilibrium thermodynamics of polymers are as follows: Flory PJ (1953) *Principles of Polymer Chemistry*. Cornell University Press, Ithaca (and later reprints); Billmeyer FW (1984) *Textbook of Polymer Science*, Chaps 7 and 8. Wiley-Interscience, New York; Morawetz H (1979) *Macromolecules in Solution*. Wiley, New York.

References to many interaction parameters  $\chi$  are given in: Barton AFM (1990) *Handbook of Polymer-Liquid Interaction Parameters and Solubility Parameters*. CRC Press, Boca Raton.

**Sect. 7.2.** The main reference for this part of the course is: Wunderlich B (1976,1980) *Macromolecular Physics*, Volume II, Crystal Nucleation, Growth, Annealing, and Volume III, Crystal Melting. Academic Press, New York (look for the chapters on copolymer crystallization and melting).

A general summary of the topic phase diagrams of polymers is given by: Porter RS, Jonza JM, Kimura M, Desper CR, George ER (1989) *A Review of Phase Behavior in Binary Blends: Amorphous, Crystalline, Liquid Crystalline, and On Transreaction*. *Polymer Eng Sci*: 29: 55–62.

For the description of the eutectic phase diagram with and without the interaction parameter  $\chi$ , see: Flory PJ (1949) *Thermodynamics of Crystallization in High Polymers*. IV. A Theory of Crystalline States and Fusion in Polymers, Copolymers, and their Mixtures with Diluents. *J Chem Phys* 17: 223–240; and (1955) *Theory of Crystallization in Copolymers*. *Trans Farad Soc* 51: 848–857.

The details on the time dependence of the eutectic crystallization are given by: Baur H (1965) *Zur Theorie der Kristallisation von Copolymeren*. *Kolloid Z Z Polymere* 203: 97–107; (1966) *Zur Frage nach der geordneten Selektion von Sequenzen bei der Kristallisation von Kopolymeren*. *Ibid* 212: 97–112; (1968) *Bemerkungen zur Kinetik der Kristallisation von Polymeren*. *Ibid* 224: 36–46; (1967) *Zur Dynamik des Schmelzens und Kristallisierens in Mischungen (Teil I)*. *Ber Bunsenges* 71: 703–711.

The solid solution crystallization is first described by: Sanchez IC, Eby RK (1975) *Thermodynamics and Crystallization of Random Copolymers*. *Macromolecules* 8: 638–642.

The theory of cold crystallization is derived on the basis of copolymers by: Wunderlich B (1958) *Theory of Cold Crystallization of High Polymers*. *J Chem Phys* 29: 1395–1404. Further applications of such computer-generated matching of chemical structure and crystals were shown by: Hanna S, Windle AH (1988) *Geometrical Limits to Order in Liquid-crystalline Random Copolymers*. *Polymer* 29: 207–223.

**Sect. 7.3.** 7.3 For general discussions of the glass transitions of polymer solutions and copolymers see: Turi E, ed (1997) *Thermal Characterization of Polymeric Materials*, 2<sup>nd</sup> ed. Academic Press, San Diego.

A Summary of solubility data for polymers is given by: Krause S, in Brandrup J, Immergut EH, Grulke GA, eds (1999) *Polymer Handbook*, 4<sup>th</sup> ed. Wiley, New York.

A discussion of the “hole volume” and the rule of constant  $\Delta C_p$  at  $T_g$  can be found in: Wunderlich B (1960) Study of the Change in Specific Heat of Monomeric and Polymeric Glasses During the Glass Transition. *J Phys Chem* 64: 1052–1056.

The description of the historic Gordon-Taylor and Wood equations for the glass transition of solutions and copolymers can be found in: Gordon M, Taylor JS (1952) Ideal Copolymers and the Second-order Transitions of Synthetic Rubbers. I. Noncrystalline Copolymers. *J Appl Chem* 2: 493–500; Wood LA (1958) Glass Transition Temperatures of Copolymers. *J Polymer Sci* 28: 319–330; for the relationship to the volume changes, see Kovacs AJ (1964) Glass Transition in Amorphous Polymers. Phenomenological Study. *Fortschr Hochpolym Forsch* 3: 394–508.

### **Specific References**

1. Wunderlich B (1971) Differential Thermal Analysis. In Weissberger A, Rossiter BW, eds *Physical Methods of Chemistry*, Vol 1, Part V, Chapter 8, pp 427–500. Wiley, New York.
2. Debye P, Hückel E (1923) The Theory of Electrolytes. I. Lowering of Freezing Point and Related Phenomena. *Physikal. Z* 24: 185–206; see also your favorite Physical Chemistry texts, such as are listed on pg VIII.
3. Hildebrand JH (1947) The Entropy of Solution of Molecules of Different Sizes. *J Chem Phys* 15: 225–228.
4. Huggins ML (1942) Some Properties of Solutions of Long-chain Compounds. *J Phys Chem* 46: 151–158; Thermodynamic Properties of Solutions of Long-chain Compounds. *Ann NY Acad Sci* 43:1–32; Theory of Solution of High Polymers. *J Am Chem Soc* 64: 1712–1719.
5. Flory P (1942) Thermodynamics of High-polymer Solutions. *J Chem Phys* 10: 51–61.
6. Quinn FA, Jr, Mandelkern L (1958) Thermodynamics of Crystallization in High Polymers: Polyethylene. *J Am Chem Soc* 80: 3178–3182.
7. Quinn FA, Jr, Mandelkern L (1959) Thermodynamics of Crystallization in High Polymers: Polyethylene, (correction of the of Table I for the heat of fusion of polyethylene by the diluent method). *J Am Chem Soc* 81: 6533.
8. Prime RB, Wunderlich B (1969) Extended-chain Crystals. IV. Melting under Equilibrium Conditions. *J Polymer Sci, Part A-2* 7: 2073–2089.
9. Pak J, Wunderlich B (2002) Reversible Melting of Polyethylene Extended-chain Crystals Detected by Temperature-modulated Calorimetry. *J Polymer Sci, Part B: Polymer Phys* 40: 2219–2227.
10. Wunderlich B, Melillo L (1968) Morphology and Growth of Extended Chain Crystals of Polyethylene. *Makromol Chem* 118: 250–264.
11. Prime RB, Wunderlich B, Melillo L (1969) Extended-Chain Crystals. V. Thermal Analysis and Electron Microscopy of the Melting Process in Polyethylene. *J Polymer Sci, Part A-2* 7: 2091–2097.
12. Prime RB, Wunderlich B (1969) Extended-Chain Crystals. III. Size Distribution of Polyethylene Crystals Grown under Elevated Pressure. *J Polymer Sci, Part A-2* 7: 2061–2072.
13. Chen W, Wunderlich B (1999) Nanophase Separation of Small And Large Molecules. *Macromol Chem Phys* 200: 283–311.
14. Androsch R, Wunderlich B (1998) Melting and Crystallization of Poly(ethylene-*co*-octene) Measured by Modulated DSC and Temperature-resolved X-ray Diffraction. *Proc 26<sup>th</sup> NATAS Conf in Cleveland, OH*. Williams KR, ed 26: 469–474.
15. Androsch R, Wunderlich B (1999) A Study of the Annealing of Poly(ethylene-*co*-octene)s by Temperature-modulated and Standard Differential Scanning Calorimetry. *Macromolecules* 32: 7238–7247.

16. Mathot VBF, Scherrenberg RL, Pijpers MFJ, Bras W (1996) Dynamic DSC, SAXS and WAXS on Homogeneous Ethylene-propylene and Ethylene-octene Copolymers with High Comonomer Contents. *J Thermal Anal* 46: 681–718.
17. Mathot VBF, ed (1993) *Calorimetry and Thermal Analysis of Polymers*. Hanser Publishers, Munich, 1993.
18. Androsch R, Wunderlich B (2003) Specific Reversible Melting of Polyethylene. *J Polymer Sci, Part B: Polymer Phys* 41: 2157–2173.
19. Cao M-Y, Varma-Nair M, Wunderlich B (1990) The Thermal Properties of Poly(oxy-1,4-benzoyl), Poly(oxy-1,4-naphthoyl) and its Copolymers. *Polymers for Adv Technol* 1: 151–170.
20. Hanna S, Lemmon T, Spontak RJ, Windle AH (1992) Dimensions of Crystallites in a Thermotropic Random Copolyester. *Polymer* 33: 3–10.
21. Langelaan HC, Posthuma de Boer A (1996) Crystallization of Thermotropic Liquid Crystalline HBA/HNA Copolymers. *Polymer* 37: 5667–5680.
22. Biswas A, Blackwell J (1988) Three-dimensional Structure of Main-chain Liquid-crystalline Copolymers, Parts 1–3. *Macromolecules* 21: 3146–3164.
23. Blackwell J, Biswas A, Cheng HM, Cageao RA (1988) X-ray Analysis of Liquid Crystalline Copolyesters and Copolyamides. *Molecular Cryst Liq Cryst* 155: 299–312.
24. Varma-Nair M, Habenschuss A, Wunderlich B (1992) Phase Transitions in Poly(4-hydroxybenzoic acid), Poly(2,6-hydroxynaphthoic acid) and their Copolymers. *Proc 21<sup>st</sup> NATAS Conf in Atlanta GA*, 21: 343–348.
25. Ashman PC, Booth C (1975) Crystallinity and Fusion of Ethylene Oxide–Propylene Oxide Block Copolymers. 1. Type PE Copolymers. *Polymer* 16: 889–896.
26. Di Lorenzo ML, Pyda M, Wunderlich B (2001) Calorimetry of Nanophase-separated Poly(oligoamide-*alt*-oligoethers). *J Polymer Sci, Part B: Polymer Phys* 39: 1594–1604.
27. Di Lorenzo ML, Pyda M, Wunderlich B (2001) Reversible Melting in Nanophase-separated Poly(oligoamide-*alt*-oligoether)s and its Dependence on Sequence Length, Crystal Perfection, and Molecular Mobility. *J Polymer Sci, Part B: Polymer Phys* 39: 2969–2981.
28. Wunderlich B (2003) Reversible Crystallization and the Rigid Amorphous Phase in Semicrystalline Macromolecules. *Progress in Polymer Sci* 28: 383–450.
29. Bopp RC, Gaur U, Kambour RP, Wunderlich B (1982) Effect of Bromination on the Thermal Properties of Poly(2,6-dimethyl-1,4-phenylene Oxide). *J Thermal Anal* 25: 243–258.
30. Schneider HA, Di Marzio EA (1992) The Glass Temperature of Polymer Blends: Comparison of Both the Free Volume and the Entropy Predictions with Data. *Polymer* 33: 3453–3461.
31. Suzuki H, Mathot VBF (1989) An Insight into the Barton Equation for Copolymer Glass Transition. *Macromolecules* 22: 1380–1384.
32. Suzuki H, Kimura N, Nishio Y (1994) A Note on Analysis of Glass Transition Temperature Data of Steric Copolymers. *Polymer* 35: 5555–5559.
33. Lau S-F, Pathak J, Wunderlich B (1982) Study of Phase Separation in Blends of Polystyrene and Poly- $\alpha$ -methylstyrene in the Glass Transition Region. *Macromolecules* 15: 1278–1283.
34. Suzuki H, Nishio Y, Kimura N, Mathot VBF, Pijpers MFJ, Murakami Y (1994) Effects of Sequence Length Distribution on Heat Capacity and Glass Transition Temperature of Styrene–Methyl Methacrylate Copolymers. *Polymer* 35: 3698–3702.
35. Gaur U, Wunderlich B (1980) Study of Microphase Separation in Block Copolymers of Styrene and  $\alpha$ -Methylstyrene in the Glass Transition Region using Quantitative Thermal Analysis. *Macromolecules* 13: 1618–1625.
36. H. Suzuki H, Miyamoto T (1990) Glass Transition Temperatures of Compatible Block Copolymers. *Macromolecules* 23: 1877–1879.
37. Buzin AI, Pyda M, Matyjaszewski K, Wunderlich B (2002) Calorimetric Study of Block-copolymers of Poly(*n*-butyl Acrylate) and Gradient Poly(*n*-butyl Acrylate-*co*-methyl Methacrylate). *Polymer* 43: 5563–5569.

## Table of Thermal Properties of Linear Macromolecules and Related Small Molecules—The ATHAS Data Bank<sup>a</sup>

1.	Poly(alkene)s . . . . .	780
2.	Poly(vinyl)s and Related Polymers . . . . .	781
3.	Aliphatic Poly(oxide)s . . . . .	783
4.	Poly(acrylate)s and (methacrylate)s . . . . .	784
5.	Aliphatic Poly(ester)s . . . . .	785
6.	Poly(itaconate)s . . . . .	786
7.	Aliphatic Poly(amide)s . . . . .	787
8.	Poly(amino Acid)s . . . . .	787
9.	Phenylene-containing Polymers . . . . .	789
10.	Poly(silylene)s . . . . .	792
11.	Poly(siloxane)s . . . . .	792
12.	Aliphatic and Aromatic Poly(sulfone)s . . . . .	793
13.	Inorganic Polymers . . . . .	793
14.	Paraffins and Perfluoroparaffins . . . . .	793
15.	Tetraalkylammonium Salts . . . . .	797
16.	Other Small Molecules . . . . .	798
17.	References . . . . .	799

**In the table the following symbols are used:** The glass transition temperature is listed as  $T_g$ ;  $\Delta C_p$  is the change of the heat capacity at  $T_g$  for the fully amorphous sample;  $T_m$  is the equilibrium melting temperature;  $\Delta H_f$ , the heat of fusion for the 100% crystalline sample; S, H, and G are the entropy, enthalpy, and free enthalpy (Gibbs function), respectively;  $S_0$  represents the residual entropy at absolute zero based on the presented data;  $\Theta_3$  and  $\Theta_1$  are the characteristic temperatures for the contributions of the skeletal vibrations to the heat capacity; N represents the number of skeletal vibrations per repeating unit (the total number of vibrations is given by the number of degrees of freedom = three times the number of atoms in the repeating unit);  $C_p$  denotes the heat capacity at constant pressure. The last line of each entry (*in italics*) gives the filename and the references, starting at p. 799.

### Footnotes for the Table

<sup>a</sup> This table includes all data collected, measured, and updated as of **November 1994**. Please correspond with us about improvements, new data, errors, etc. In the column of the table labeled #, (a) represents the amorphous sample, and (c) represents the 100% crystalline sample; the mark \*\* represents heat capacities for semicrystalline polymers; the mark \* next to the reference numbers, given in italics, indicates that an update is available only in the ATHAS Data Bank. The last line for each entry lists the abbreviation under which data can be retrieved in the computer version of the data bank, available in our web-site, and also listed the reference number to the last update on the given entry. At this reference, information on the source of the experimental data can be found.

<sup>b</sup> The change in the heat capacity at  $T_g$ , listed in  $J K^{-1} mol^{-1}$ , as derived from the ATHAS recommended, experimental data. A \* in this column indicates that the data were derived

instead from the difference between experimental, liquid  $C_p$  and the calculated, solid  $C_p$ . The first numeral in parentheses refers to the number of small, mobile beads in the repeating unit (like  $\text{CH}_2^-$ ,  $\text{O}^-$ , or  $\text{CHCH}_3^-$ ). The average increase in  $C_p$  at  $T_g$  of all listed molecules per small bead is  $11.5 \pm 1.7 \text{ J K}^{-1} \text{ mol}^{-1}$ . The second numeral refers to large beads (like  $\text{C}_6\text{H}_4^-$ ). The increase in  $C_p$  of a large bead at  $T_g$  is double or triple that of a small bead.

**c** The melting temperature is an estimate of the equilibrium melting temperature, and the heat of fusion in  $\text{kJ mol}^{-1}$  of repeating unit is computed for 100% crystallinity.

**d** An X in this column indicates that enthalpy, entropy, and free enthalpy are available, based on the ATHAS recommended data.

**e** Residual entropy in the glassy state at zero temperature, in  $\text{J K}^{-1} \text{ mol}^{-1}$ .

**f** The number of skeletal vibrational modes used in the Tarasov equation with the theta temperatures of the previous two columns. Values of theta temperatures in parentheses are estimates based on data from polymers of similar backbone structure. The group vibration frequencies are usually tabulated in the listed references.

**g** Temperature range of the ATHAS recommended experimental heat capacity data. The computations of heat capacities of solids are based on these data and are usually carried out from 0.1 to 1,000 K, to provide sufficiently broad ranges of temperature for the addition schemes and for analysis of superheated polymers, as in laser ablation studies. For the references, *in italics*, see the list starting on p. 799.

**h** The PTFE has additional crystal-crystal-condis crystal transitions at 292 K and 303 K; their combined heats of transition are  $850 \text{ J mol}^{-1}$  [13].

**i** Properties of the metastable, monoclinic selenium are also analyzed and described in detail in [3,39].

**j** The *trans*-PBUT has an additional condis state at lower temperature. The crystal-condis crystal transition is at 356 K, and the heat of transition is  $7.8 \text{ kJ mol}^{-1}$  [18, 41].

**k** The PPX has two lower first-order transitions, leading to condis crystals at 504 K and 560 K with heats of transition of 5.0 and  $1.5 \text{ kJ mol}^{-1}$  [32].

**l** For deuterated, amorphous, solid polystyrene and ring-only deuterated polystyrene, heat capacities lead to Tarasov  $\Theta_3$  and  $\Theta_1$  temperatures of 55, 244 K and 49, 278 K, respectively. The thermodynamic functions S, H, and G are in [22]. For other data, see [23].

**m** The PDES has an additional condis state at a lower temperature. The crystal-condis crystal transition is at 206.7 K; its heat of transition is  $2.72 \text{ kJ mol}^{-1}$  [52,55].

**n** The POB shows a disordering transition at 616.5 K with a heat of transition of  $3.8 \text{ kJ mol}^{-1}$  [51].

**o** The PON shows a disordering transition at 614.5 K with a heat of transition of  $0.4 \text{ kJ mol}^{-1}$  [51].

**P** The glass transition temperature of semicrystalline PBT is seen at  $T_g$  from 310 to 325 K. In addition, it shows the existence of a rigid-amorphous fraction [53]. The quenched sample shows some small transition at 248 K which is probably not the  $T_g$ , as assumed earlier [72].

**q** The listed glass transition temperature has been assigned to relaxation processes of the *n*-alkyl/cycloalkyl side groups. Another,  $T_g^U$  has been assigned to the backbone [29].

**r** Semicrystalline PPO shows the existence of a rigid-amorphous phase which governs the thermal properties from  $T_g$  to  $T_m$ . Fusion, superheating and annealing are directly affected by the rigid-amorphous phase [42].

**s** Above  $T_g$ , poorly crystallized samples show a rigid-amorphous fraction that does not contribute to the increase in heat capacity at  $T_g$  [35].

**t** Between  $T_g$  and  $T_m$ , the  $C_p$  of the liquid cannot be extrapolated from melt since the liquid heat capacities of the fluorinated polymers are nonlinear [19].

**u** The PDMSi shows two small transitions. One is at 240 K with a heat of transition of  $0.1 \text{ kJ mol}^{-1}$  and the other at 432.5 K with a heat of transition of  $0.56 \text{ kJ mol}^{-1}$  is probably a transition from one crystal form to another [59].

**v** The PDPSi shows a disordering transition from condic crystal I to condic crystal II at 338.3 K with a heat of transition of  $1.4 \text{ kJ mol}^{-1}$  [59].

**w** The PDHSi shows a disordering transition at 323.2 K with a heat of transition of  $14.84 \text{ kJ/mol}$  [59].

**x** Estimated glass transition temperature and change in heat capacity at  $T_g$  for PTDSi [59].

**y** The PTDSi shows a disordering transition at 329 K with a heat of transition of  $39.2 \text{ kJ/mol}$  [59].

**z** All these paraffins and perfluoroparaffins have additional crystal-mesophase transitions [57], [62] and [66].

**aa** For ammonium salts, the temperature listed is the isotropization temperature. TA3Br and TA3I decompose immediately after isotropization. All the tetra-*n*-alkylammonium salts have additional crystal-mesophase transitions. In addition, no heat capacities for the liquid could be measured due to decomposition [67].

**ab** The transition temperature listed corresponds to a change of a nematic liquid crystal to the melt; OOBPD has several mesophase transitions below this temperature [68].

**ac** The glass transition and  $\Delta C_p$  in both amino acids PLSER and PLMET are estimates obtained for the main chain [69].

#	T <sub>g</sub>	ΔC <sub>p</sub> <sup>b</sup>	T <sub>m</sub> <sup>c</sup>	ΔH <sub>f</sub> <sup>c</sup>	SHG <sup>d</sup>	S <sub>o</sub> <sup>e</sup>	Θ <sub>1</sub>	Θ <sub>3</sub>	N <sub>s</sub> <sup>f</sup>	C <sub>p</sub> <sup>g</sup>
<b>1. Poly(alkene)s</b>										
Polymethylene [commonly called poly(ethylene)]										
(c)	-	-	414.6	4.11	X	0	519	158	2	0.1-410
(a)	237	10.5(1)	-	-	X	3.0	519	80	2	0.1-600
<i>PE</i>	37	37	38	38	1*	1*	25	25	25	1,29
Polypropylene										
(c)	-	-	460.7	8.70	X	0	714	91	7	10.0-460
(a)	270	19.2(2)*	-	-	X	5.2	633	78	7	10.0-600
<i>PP</i>	49	15*	4,10	50	4,15*	50*	15	15	15	4,29
Poly(1-butene)										
(c)	-	-	411.2	7.00	X	0	618	93	9	10-249**
(a)	249	23.1(2)	-	-	X	6.4	618	(80)	9	249-630
<i>PB</i>	2	2	2	2,10	57	57	17	17	17	2
Poly(1-pentene)										
(c)	-	-	403.2	6.30	X	0	580	(93)	11	200-233**
(a)	233	27.0(2)	-	-	X	(0.9)	580	(80)	11	233-470
<i>PPEN</i>	2	2	2,10	2,10	57	57	17	17	17	2
Poly(1-hexene)										
(a)	223	25.1(2)	-	-	X	?	563	86	13	20-290
<i>PHEX</i>	2	2			57		17	17	17	2
Polycyclopentene										
(a)	173	28.9(4)	-	-	X	?	582	88	10	10-320
<i>PCPEN</i>	2	2			57		45	45	45	2
Poly(4-methyl-1-pentene)										
(c)	-	-	523.2	9.96	X	0	660	(93)	14	80-303**
(a)	303	30.1(1+1)	-	-	?	?	660	?	14	303-540
<i>P4MIP</i>	2	57	2,10	10	57		16*	16*	16	2,57
Polyisobutylene										
(c)	-	-	317	12.0	X	0	850	?	10	?
(a)	200	21.3(2)	-	-	X	?	850	103	10	15-380
<i>PIBUT</i>	2	2	2	2	2*		17	17	17	2
Poly(1-butenylene), <i>cis</i>										
(c)	-	-	284.7	9.20	X	0	589	87	8	30-171**
(a)	171	27.2(3)*	-	-	X	17.5	589	?	8	171-350
<i>PBUT cis</i>	18	18*	2,10	2,10	18*	18*	18	18	18	2,29
Poly(1-butenylene), <i>trans</i>										
(c)	-	-	437	3.73 <sup>j</sup>	X	0	599	95	8	30-190**
(a)	190	28.0(3)*	-	-	X	16.2	599	?	8	190-500
<i>PBUT trans</i>	18	18*	2,41	2,41	18*	18*	18	18	18	2,29

#	T <sub>g</sub>	ΔC <sub>p</sub> <sup>b</sup>	T <sub>m</sub> <sup>c</sup>	ΔH <sub>f</sub> <sup>c</sup>	SHG <sup>d</sup>	S <sub>o</sub> <sup>e</sup>	Θ <sub>1</sub>	Θ <sub>3</sub>	N <sub>s</sub> <sup>f</sup>	C <sub>p</sub> <sup>g</sup>
1,4-Poly-(2-methyl butadiene), <i>cis</i>										
(c)	-	-	301.2	4.35	?	0	647	(120)	11	?
(a)	200	30.9(3)	-	-	X	?	647	58	11	2-360
<i>PMB cis</i>	2	2	2,10	2,10	2*		45	45	45	2

## Poly(2-methyl-1,3-pentadiene)

(a)	278	34.3(?)	-	-	?	?	?	?	?	230-320
<i>PMP</i>	29	29								29

**2. Poly(vinyl)s and Related Polymers**

## Poly(vinyl alcohol)

(c)	-	-	538	7.11	X	0	495	119	4	60-300**
(a)	358	?(2)	-	-	?	?	495	?	4	?
<i>PVA</i>	2		10	10	57		45	45	45	2

## Poly(vinyl acetate)

(a)	304	40.7(?)	-	-	X	?	600	(86)	11	80-370
<i>PVAC</i>	2	45*			57		45*	45	45	2,45

## Poly(vinyl fluoride)

(c)	-	-	503.2	7.54	X	0	440	105	4	80-314**
(a)	314	17.0(2)*	-	-	X	9.4	440	?	4	480-530 <sup>i</sup>
<i>PVF</i>	2	19*	2	2	19*	19*	20	20	20	2,29

## Poly(vinylidene fluoride)

(c)	-	-	483.2	6.70	X	0	346	66	4	5-212**
(a)	212	21.2(2)*	-	-	X	5.1	346	?	4	450-580 <sup>i</sup>
<i>PVF2</i>	19	19*	2,10	2,10	19*	19*	20	20	20	2,29

## Polytrifluoroethylene

(c)	-	-	495.2	5.44	X	0	315	56	4	25-280**
(a)	280	13.8(2)*	-	-	X	13	315	?	4	480-600 <sup>i</sup>
<i>PTRIF</i>	19	19*	19	19	19*	19*	20	20	20	2,29

## Polytetrafluoroethylene

(c)	-	-	605	4.10 <sup>h</sup>	X	0	250	54	2	0.3-280
(a)	200	9.4(1)	-	-	X	3.3	250	?	2	180-700
<i>PTFE</i>	12	12	13	13	13*	13*	13	13	13	13,29

## Poly(vinyl chloride)

(c)	-	-	546.0	11.0	X	0	354	(90)	4	?
(a)	354	19.4(2)	-	-	X	2.4	354	45	4	5-380
<i>PVC</i>	2	2	2	2	19*	19*	21	21*	21	2

## Poly(vinylidene chloride)

(c)	-	-	463	?	X	0	308	119	4	60-255**
(a)	255	?(2)	-	?		?	308	?	4	?
<i>PVC2</i>	2		2		57		21	21	21	2



#	T <sub>g</sub>	ΔC <sub>p</sub> <sup>b</sup>	T <sub>m</sub> <sup>c</sup>	ΔH <sub>f</sub> <sup>c</sup>	SHG <sup>d</sup>	S <sub>o</sub> <sup>e</sup>	Θ <sub>1</sub>	Θ <sub>3</sub>	N <sub>s</sub> <sup>f</sup>	C <sub>p</sub> <sup>g</sup>
Poly(chlorotrifluoroethylene)										
(c)	-	-	493	5.02	X	0	215	42	4	1-325**
(a)	325	?(2)	-	-	?	?	215	?	4	?
<i>PCTFE</i>	2		2	2	19*		21	21	21	2
Poly(vinyl benzoate)										
(a)	347	69.5(?)	-	-	X	?	541	(50)	10	190-500
<i>PVB</i>	2	2			57		45	45	45	2
Poly(vinyl- <i>p</i> -ethyl benzoate)										
(a)	330	56.9(?)	-	-	X	?	411	(50)	15	190-500
<i>PVEB</i>	2	2			57		45	45	45	2
Poly(vinyl- <i>p</i> -isopropyl benzoate)										
(a)	335	66.6(?)	-	-	X	?	567	(50)	18	190-500
<i>PVIPB</i>	2	2			57		45	45	45	2
Poly(vinyl- <i>p</i> - <i>tert</i> -butyl benzoate)										
(a)	394	60.4(?)	-	-	X	?	512	(50)	21	190-500
<i>PVTBB</i>	2	2			57		45	45	45	2
Polystyrene										
(c) <sup>l</sup>	-	-	516.2	10.0	X	0	284	110	6	?
(a)	373	30.8(1+1)	-	-	X	4.4	284	48	6	0.1-600
<i>PS</i>	5	5	5,10	5,10	22*	23*	23	23	23	5,29
Poly( <i>p</i> -fluorostyrene)										
(a)	384	33.3(1+1)	-	-	X	?	284	(48)	6	130-384
<i>PFS</i>	29	29			22*		23	23	23	29
Poly( <i>p</i> -chlorostyrene)										
(a)	406	31.1(1+1)	-	-	X	?	284	(48)	6	300-550
<i>PCS</i>	29	29			22*		23	23	23	29
Poly( <i>p</i> -bromostyrene)										
(a)	410	31.6(1+1)	-	-	X	?	284	(48)	6	300-550
<i>PBS</i>	29	29			22*		23	23	23	29
Poly( <i>p</i> -iodostyrene)										
(a)	424	37.9(1+1)	-	-	X	?	284	(48)	6	300-550
<i>PIS</i>	29	29			22*		23	23	23	29
Poly( <i>p</i> -methylstyrene)										
(a)	380	34.6(1+1)	-	-	X	?	284	(48)	6	300-500
<i>PMS</i>	29	29			22*		23	23	23	29
Poly(α-methylstyrene)										
(a)	441	25.3(1+1)	-	-	X	?	450	48	9	1.4-490
<i>PAMS</i>	5	5			22*		23	23	23	5

#	T <sub>g</sub>	ΔC <sub>p</sub> <sup>b</sup>	T <sub>m</sub> <sup>c</sup>	ΔH <sub>f</sub> <sup>c</sup>	SHG <sup>d</sup>	S <sub>o</sub> <sup>e</sup>	Θ <sub>1</sub>	Θ <sub>3</sub>	N <sub>s</sub> <sup>f</sup>	C <sub>p</sub> <sup>g</sup>
<b>3. Aliphatic Poly(oxide)s</b>										
Poly(oxymethylene)										
(c)	-	-	457.2	9.79	X	0	232	117	2	0.1-390
(a)	190	28.2(2)*	-	-	X	3.4	232	?	2	190-600
<i>POM</i>	24	24*	10	10	6,24*	24*	25	25	25	6,29
Poly(oxyethylene)										
(c)	-	-	342	8.66	X	0	353	114	4	10-342
(a)	206	38.2(3)*	-	-	X	8.1	353	?	4	206-450
<i>POE</i>	24	24*	10	10	6,24*	24*	25	25	25	6,29
Poly(oxymethyleneoxyethylene)										
(c)	-	-	328	16.7	X	0	317	114	6	10-328**
(a)	209	62.1(5)*	-	-	X	27	317	?	6	209-390
<i>POMOE</i>	6	24*	6	6	6,57	57	25	25	25	6
Poly(oxytrimethylene)										
(c)	-	-	308	9.44	X	0	433	100	6	1.0-308
(a)	195	46.8(4)*	-	-	X	7.8	433	40	6	1.0-330
<i>PO3M</i>	6	24*	6	6	6,57	24*	25	25	25	6
Poly(oxytetramethylene)										
(c)	-	-	330	14.4	X	0	436	90	8	5-189**
(a)	189	57.0(5)*	-	-	X	17	436	?	8	189-340
<i>PO4M</i>	6	24*	6	6	57*	57*	25	25	25	6
Poly(oxyoctamethylene)										
(c)	-	-	347	29.3	X	0	480	137	16	14-255**
(a)	255	83.1(9)*	-	-	X	63	480	?	16	350-360
<i>PO8M</i>	6	24*	6	6	57	57	25	25	25	6
Poly(oxymethyleneoxytetramethylene)										
(c)	-	-	296	14.3	X	0	392	122	10	10-296
(a)	189	83.8(7)*	-	-	X	15	392	?	10	189-360
<i>POMO4M</i>	6	24*	6	6	6,57	57	25	25	25	6
Poly(oxypropylene)										
(c)	-	-	348	8.40	X	0	494	112	7	80-198**
(a)	198	32.1(3)*	-	-	X	9.4	494	?	7	198-370
<i>POPR</i>	6	57	6	6	57	57	45	45	45	6
Poly[oxy-2,2'-bis(chloromethyl)trimethylene]										
(c)	-	-	463	32	X	0	463	?	12	10-390**
(a)	278	17.8(?)	-	-	?	?	463	44	12	?
<i>POCMM</i>	6	6	6	6	57		45	45	45	6

#	T <sub>g</sub>	ΔC <sub>p</sub> <sup>b</sup>	T <sub>m</sub> <sup>c</sup>	ΔH <sub>f</sub> <sup>c</sup>	SHG <sup>d</sup>	S <sub>o</sub> <sup>e</sup>	Θ <sub>1</sub>	Θ <sub>3</sub>	N <sub>s</sub> <sup>f</sup>	C <sub>p</sub> <sup>g</sup>
<b>4. Poly(acrylate)s and (methacrylate)s</b>										
Poly(methyl acrylate)										
(a)	279	42.3(?)	-	-	X	?	552	86	11	10-500
<i>PMA</i>	7	7			57		17	17	17	7
Poly(ethyl acrylate)										
(a)	249	45.6(?)	-	-	X	?	543	89	13	90-500
<i>PEA</i>	7	7			57		17	17	17	7
Poly( <i>n</i> -butyl acrylate)										
(a)	218	45.4(?)	-	-	X	?	518	88	17	80-440
<i>PBA</i>	7	7			57		17	17	17	7
Poly(isobutyl acrylate)										
(a)	249	36.6(?)	-	-	X	?	(524)	(90)	18	230-500
<i>PIBA</i>	7	7			57		45*	45	45	7
Poly(octadecyl acrylate)										
(a)	?	?(?)	-	-	?	?	520	84	45	130-500
<i>PODA</i>							17	17	17	7
Poly(methacrylic acid)										
(a)	501	?(?)	-	-	X	?	653	107	11	60-300
<i>PMAA</i>	7				57		17	17	17	7
Poly(methyl methacrylate)										
(c)	-	-	450	9.60	X	0	680	(140)	14	?
(a)	378	32.7(?)	-	-	X	7.1	680	67	14	0.2-550
<i>PMMA</i>	7	17	26	26	17*	57	17	17	17	17,29
Poly(ethyl methacrylate)										
(a)	338	31.7(?)	-	-	X	?	622	(60)	16	80-380
<i>PEMA</i>	7	7			57		17	17	17	7
Poly( <i>n</i> -butyl methacrylate)										
(a)	293	27.9(?)	-	-	X	?	559	58	20	80-440
<i>PBMA</i>	7	7			57		17	17	17	7
Poly(isobutyl methacrylate)										
(a)	326	39.0(?)	-	-	X	?	595	(60)	21	230-400
<i>PIBMA</i>	7	7			57		45	45	45	45
Polyacrylonitrile										
(a)	378	?(?)	-	-	X	?	980	62	6	60-370
<i>PAN</i>	7				7,57		17*	17	17	7
Poly( <i>p</i> -methacryloyloxybenzoic acid)										
(a)	316	60.0(?)	-	-	?	?	631	89	18	10-310
<i>PMAB</i>	29	29					57	57	57	29

#	T <sub>g</sub>	ΔC <sub>p</sub> <sup>b</sup>	T <sub>m</sub> <sup>c</sup>	ΔH <sub>f</sub> <sup>c</sup>	SHG <sup>d</sup>	S <sub>o</sub> <sup>e</sup>	Θ <sub>1</sub>	Θ <sub>3</sub>	N <sub>s</sub> <sup>f</sup>	C <sub>p</sub> <sup>g</sup>
<b>5. Aliphatic Poly(ester)s</b>										
Polyglycolide										
(c)	-	-	501	9.74	X	0	521	98	6	10-318**
(a)	318	31.8(2)	-	-	X	7.6	521	?	6	318-550
PGL	8	57	28	57	46	46	27	27	27	8,29
Poly(ethylene oxalate)										
(c)	-	-	450	23	?	0	533	?	12	?
(a)	306	56.2(4)	-	-	X	?	533	89	12	10-360
PEOL	44	29	44	44	46		27	27	27	29
Poly(β-propiolactone)										
(c)	-	-	366	10.9	X	0	522	85	8	10-249**
(a)	249	42.9(3)	-	-	X	15.2	522	?	8	249-400
PPL	28	57	28	57	46	46	27	27	27	29
Poly(L-lactic acid)										
(c)	-	-	480	6.55	X	0	574	(52)	9	190-470**
(a)	332.5	43.8(2+1)	-	-	X	1.7	574	52	9	5.0-250
PLA	71	71	71	71	71	71	71	71	71	71
Poly(γ-butyrolactone)										
(c)	-	-	337.5	14.0	X	0	474	96	10	10-214**
(a)	214	52.0(4)	-	-	X	20.6	474	?	10	214-350
PBL	28	57	28	57	46	46	27	27	27	29
Poly(δ-valerolactone)										
(c)	-	-	331	18.8	X	0	502	101	12	10-207**
(a)	207	60.9(5)	-	-	X	32	502	?	12	207-350
PVL	28	57	28	57	46	46	27	27	27	29
Poly(ε-caprolactone)										
(c)	-	-	342.2	17.9	X	0	491	101	14	10-209**
(a)	209	67.4(6)	-	-	X	23	491	?	14	209-350
PCL	8	57	28	57	46	46	27	27	27	8,29
Polyundecanolactone										
(c)	-	-	365	39.5	X	0	528	105	24	10-227**
(a)	227	102.7(11)	-	-	X	68	528	?	24	227-400
PUDL	28	57	28	57	46	46	27	27	27	29
Polytridecanolactone										
(c)	-	-	368	50.6	X	0	519	112	28	10-229**
(a)	229	115.8(13)	-	-	X	92	519	?	28	229-370
PTDL	28	57	28	57	46	46	27	27	27	29
Polypentadecanolactone										
(c)	-	-	370.5	63.4	X	0	525	114	32	10-251**
(a)	251	124(15)	-	-	X	128	525	?	32	251-370
PPDL	28	57	28	57	46	46	27	27	27	29

#	T <sub>g</sub>	ΔC <sub>p</sub> <sup>b</sup>	T <sub>m</sub> <sup>c</sup>	ΔH <sub>f</sub> <sup>c</sup>	SHG <sup>d</sup>	S <sub>o</sub> <sup>e</sup>	Θ <sub>1</sub>	Θ <sub>3</sub>	N <sub>s</sub> <sup>f</sup>	C <sub>p</sub> <sup>g</sup>
Poly(pivalolactone)										
(c)	-	-	513.0	14.8	X	0	585	(98)	14	150-267**
(a)	267	37.6(3)	-	-	X	16.5	585	?	14	267-550
<i>PPVL</i>	61	61	61	61	61	61	61	61	61	61
Poly(trimethylene succinate)										
(c)	-	-	?	?	?	0	495	(141)	18	?
(a)	240	93(7)	-	-	?	?	495	?	18	320-360
<i>PTMS</i>	46	46					46	46	46	46
Poly(trimethylene adipate)										
(c)	-	-	?	?	?	0	(514)	(141)	22	?
(a)	?	?	-	-	?	?	(514)	?	22	320-360
<i>PTMA</i>							46	46	46	46
Poly(butylene adipate)										
(c)	-	-	328.8	?	X	0	514	(108)	24	80-199**
(a)	199	140.0(?)	-	-	?	514	?	24	199-450	
<i>PBAD</i>	29	29	29		57		27	27	27	29
Poly(ethylene sebacate)										
(c)	-	-	356.2	31.9	X	0	514	(158)	28	120-245**
(a)	245	127.0(12)	-	-	X	(26)	514	(80)	28	245-410
<i>PES</i>	29	57	10	10	46	46	27	27*	27	8,29
Poly(hexamethylene sebacate)										
(c)	-	-	?	?	?	0	(519)	(158)	36	?
(a)	?	?	-	-	?	(?)	(519)	(80)	36	340-400
<i>PHMS</i>							46	46	46	46
<b>6. Poly(itaconate)s</b>										
Poly(dimethyl itaconate)										
(a)	377	54.2(?)	-	-	X	?	557	(67)	20	110-450
<i>PDMI</i>	29	29			57		57	57	57	29
Poly(di- <i>n</i> -propyl itaconate)										
(a)	304	57.8(?)	-	-	X	?	428	(67)	28	110-410
<i>PDPI</i>	29	29			57		57	57	57	29
Poly(di- <i>n</i> -heptyl itaconate)										
(a)	172 <sup>q</sup>	45.6(?)	-	-	X	?	582	(67)	44	110-170
<i>PDHI</i>	29	29			57		57	57	57	29
Poly(di- <i>n</i> -octyl itaconate)										
(a)	178 <sup>q</sup>	99.1(?)	-	-	X	?	518	(67)	48	110-170
<i>PDOI</i>	29	29			57		57	57	57	29
Poly(di- <i>n</i> -nonyl itaconate)										
(a)	187 <sup>q</sup>	183.4(?)	-	-	X	?	589	(67)	52	110-180
<i>PDNI</i>	29	29			57		57	57	57	29

#	T <sub>g</sub>	ΔC <sub>p</sub> <sup>b</sup>	T <sub>m</sub> <sup>c</sup>	ΔH <sub>f</sub> <sup>c</sup>	SHG <sup>d</sup>	S <sub>o</sub> <sup>e</sup>	Θ <sub>1</sub>	Θ <sub>3</sub>	N <sub>s</sub> <sup>f</sup>	C <sub>p</sub> <sup>g</sup>
Poly(dicyclooctyl itaconate)										
(a)	390 <sup>q</sup>	67.5(?)	-	-	?	?	?	?	?	110-440
<i>PDCYOI</i>	29	29								29

## 7. Aliphatic Poly(amide)s

### Nylon 6

(c)	-	-	533	26.0	X	0	544	(67)	14	70-313**
(a)	313	53.7(6)*	-	-	X	37	544	?	14	313-600
<i>NYLON6</i>	8	11	10	10	11	11	11	11	11	8

### Nylon 11

(c)	-	-	493	44.7	X	0	420	(67)	24	230-316**
(a)	316	68.4(11)*	-	-	X	78	420	?	24	316-550
<i>NYLON11</i>	11	11	11	11	11	11	11	11	11	11

### Nylon 12

(c)	-	-	500	48.4	X	0	455	(67)	26	230-314**
(a)	314	74.3(12)*	-	-	X	82	455	?	26	314-540
<i>NYLON12</i>	11	11	11	11	11	11	11	11	11	11

### Nylon 6,6 α

(c)	-	-	574	57.8	X	0	614	84	28	0.3-323**
(a)	323	115.5(12)*	-	-	X	77	614	?	28	323-600
<i>NYLON6,6</i>	8	11	11	11	11	11	11	11	11	8

### Nylon 6,9

(c)	-	-	500	69	X	0	579	(84)	34	230-331**
(a)	331	109.5(15)*	-	-	X	114	579	?	34	331-590
<i>NYLON6,9</i>	11	11	11	11	11	11	11	11	11	11

### Nylon 6,10

(c)	-	-	506	71.7	X	0	543	(84)	36	230-323**
(a)	323	118.0(16)*	-	-	X	120	543	?	36	323-590
<i>NYLON6,10</i>	11	11	11	11	11	11	11	11	11	11

### Nylon 6,12

(c)	-	-	520	80.1	X	0	533	(84)	40	230-319**
(a)	319	141.4(18)*	-	-	X	124	533	?	40	319-600
<i>NYLON6,12</i>	8	11	11	11	11	11	11	11	11	8,11

### Polymethacrylamide

(c)	-	-	590	?	?	0	523	?	10	?
(a)	?	?	-	-	X	?	523	(193)	10	60-300
<i>PMAM</i>			11		11		11	11	11	7

## 8. Poly(amino acid)s

### Polyglycine I

(c)	-	-	?	?	X	0	(750)	(81)	6	150-370**
<i>PGLYI</i>					57		58	58	58	8

#	T <sub>g</sub>	ΔC <sub>p</sub> <sup>b</sup>	T <sub>m</sub> <sup>c</sup>	ΔH <sub>f</sub> <sup>c</sup>	SHG <sup>d</sup>	S <sub>o</sub> <sup>e</sup>	Θ <sub>1</sub>	Θ <sub>3</sub>	N <sub>s</sub> <sup>f</sup>	C <sub>p</sub> <sup>g</sup>
Polyglycine II										
(c)	-	-	?	?	X	0	750	81	6	1.4-390**
<i>PGLYII</i>					57		58	58	58	8,58
Poly(L-alanine)										
(c)	-	-	?	?	X	0	634	58	9	1.6-390**
<i>PLALA</i>					57		58	58	58	8,58
Poly(L-valine)										
(c)	-	-	?	?	X	0	664	65	14	2.0-390**
<i>PLVAL</i>					57		58	58	58	8,58
Poly(L-serine)										
(c)	-	-	?	?	X	0	685	(68)	10	220-390**
(a)	(400) <sup>ac</sup>	(30.0) <sup>ac</sup>	-	-	X	?	685	?	10	?
<i>PLSER</i>	69	69			57		58	58	58	58
Poly(L-leucine)										
(c)	-	-	?	?	X	0	625	(68)	16	220-390**
<i>PLLEU</i>					57		58	58	58	58
Poly(L-aspartic acid) sodium salt										
(c)	-	-	?	?	X	0	597	(68)	14	220-390**
<i>PLASPNa</i>					57		58	58	58	58
Poly(L-glutamic acid) sodium salt										
(c)	-	-	?	?	X	0	907	(68)	16	220-390**
<i>PLGLUNa</i>					57		58	58	58	58
Poly(L-phenylalanine)										
(c)	-	-	?	?	X	0	610	(68)	11	220-390**
<i>PLPHEA</i>					57		58	58	58	58
Poly(L-tyrosine)										
(c)	-	-	?	?	X	0	729	(68)	13	220-390**
<i>PLTYR</i>					57		58	58	58	58
Poly(L-asparagine)										
(c)	-	-	?	?	X	0	569	(68)	12	220-390**
<i>PLASN</i>					57		58	58	58	58
Poly(L-tryptophan)										
(c)	-	-	?	?	X	0	793	(68)	13	220-390**
<i>PLTRP</i>					57		58	58	58	58
Poly(L-proline)										
(c)	-	-	?	?	X	0	691	(68)	11	220-390**
<i>PLPRO</i>					57		58	58	58	58

#	T <sub>g</sub>	ΔC <sub>p</sub> <sup>b</sup>	T <sub>m</sub> <sup>c</sup>	ΔH <sub>f</sub> <sup>c</sup>	SHG <sup>d</sup>	S <sub>o</sub> <sup>e</sup>	Θ <sub>1</sub>	Θ <sub>3</sub>	N <sub>s</sub> <sup>f</sup>	C <sub>p</sub> <sup>g</sup>
Poly(L-lysine) hydrogen bromide										
(c)	-	-	?	?	X	0	636	(68)	20	220-390**
<i>PLLYSHBr</i>					57		58	58	58	58
Poly(L-methionine)										
(c)	-	-	?	?	X	0	691	(68)	15	220-390**
(a)	(400) <sup>ac</sup>	(61.0) <sup>ac</sup>	-	-	X	?	691	?	15	?
<i>PLMET</i>	69	69			57		58	58	58	58
Poly(L-histidine)										
(c)	-	-	?	?	X	0	808	(68)	13	220-390**
<i>PLHIS</i>					57		58	58	58	58
Poly(L-histidine) hydrogen chloride										
(c)	-	-	?	?	X	0	745	(68)	16	220-390**
<i>PLHISHCl</i>					57		58	58	58	58
Poly(L-arginine) hydrogen chloride										
(c)	-	-	?	?	X	0	610	(68)	23	220-390**
<i>PLARGHCl</i>					57		58	58	58	58
<b>9. (Phenyl)ene-containing Polymers</b>										
Poly( <i>p</i> -phenylene)										
(c)	-	-	>1000	?	X	0	544	(54)	3	80-300**
(a)	?	?(0+1)	-	-	?	?	544	(40)	3	?
<i>PPP</i>			30		57		30	30	30	29
Poly(thio-1,4-phenylene)										
(c)	-	-	593	8.65	X	0	566	(54)	5	220-363**
(a)	363	29.2(0+1)	-	-	X	(4.2)	566	(40)	5	363-600
<i>PTP</i>	31	31	31	31	47*	47*	30	30*	30	31,29
Poly( <i>p</i> -xylylene)										
(c)	-	-	700	10.0 <sup>k</sup>	X	0	562	(54)	7	220-410**
(a)	286	37.6(1+1)*	-	-	?	?	562	(40)	7	(286-410)
<i>PPX</i>	32	32	32	32	57		30	30	30	32,29
Poly(oxy-1,4-phenylene)										
(c)	-	-	535	7.82	X	0	555	(54)	5	300-358**
(a)	358	21.4(0+1)	-	-	X	(10)	555	(40)	5	358-620
<i>POP</i>	6	6	6	6	47*	47*	30	30	30	6
Poly(oxy-2,6-dimethyl-1,4-phenylene)										
(c)	-	-	580	5.95	X	0	564	(54)	5	80-482**
(a)	482 <sup>r</sup>	31.9(1+1)	-	-	X	(7.5)	564	(40)	5	482-570
<i>PPO</i>	6	6	42	42	47	47	30	30	30	6,30



#	T <sub>g</sub>	ΔC <sub>p</sub> <sup>b</sup>	T <sub>m</sub> <sup>c</sup>	ΔH <sub>f</sub> <sup>c</sup>	SHG <sup>d</sup>	S <sub>o</sub> <sup>e</sup>	Θ <sub>1</sub>	Θ <sub>3</sub>	N <sub>s</sub> <sup>f</sup>	C <sub>p</sub> <sup>g</sup>
Poly(oxy-3-bromo-2,6-dimethyl-1,4-phenylene)										
(a)	559	18(?)	-	-	?	?	(564)	(40)	5	310-559
<i>PPBO</i>	29	29					57	57	57	29
Poly(oxy-2,6-diphenyl-1,4-phenylene)										
(c)	-	-	753	12.2	?	0	?	?	?	180-493**
(a)	493	76.6(?)	-	-	?	?	?	?	?	493-820
<i>PDPPPO</i>	6	6	6	6						6
Poly[oxy-2,6-bis(1-methylethyl)-1,4-phenylene]										
(c)	-	-	426	17.6(?)	?	0	793	(54)	21	270-426**
<i>PPPRO</i>	29	29					57	57	57	29
Poly(ethylene terephthalate)										
(c)	-	-	553	26.9	X	0	(545)	(48)	17	1.0-10
(a)	342	77.8(4+1)	-	-	X	22	544.7	48	17	1.0-590
<i>PET</i>	8	8	10,43	10	8,57	33*	70	70	30,70	8,29
Poly(trimethylene terephthalate)										
(c)	-	-	510	30.0	X	0	550	51	19	5.0-300**
(a)	315	94(5+1)	-	-	X	31.4	550.5	(51)	19	320-570
<i>PTT</i>	70	70	70	70	70	57	70	70	70	70
Poly(butylene terephthalate)										
(c)	-	-	518	32.0	X	0	530	55	21	150-310**
(a)	314 <sup>p</sup>	77(6+1)	-	-	X	(10)	(530)	(40)	21	248-570
<i>PBT</i>	72	72	53	53	72	57	53,72	53,72	72	53,29,72
Poly(4-hydroxybenzoic acid)										
(c)	-	-	-	- <sup>n</sup>	X	0	823	(54)	7	170-434**
(a)	434	33.2(1+1)	-	-	X	?	823	(25)	7	-
<i>PHBA</i>	29	51*		51	56		56	56	56	29
Poly(2,6-hydroxynaphthoic acid)										
(c)	-	-	-	- <sup>o</sup>	X	0	640	(54)	9	170-399**
(a)	399	46.5(1+1)	-	-	X	?	640	(27)	9	399-650
<i>PHNA</i>	29	56		51	56		56	56	56	29
Poly(ethylene-2,6-naphthalene dicarboxylate)										
(c)	-	-	610	25.0	X	0	600	(54)	17	220-390**
(a)	390	81.6(4+1)	-	-	X	(10)	600	(30)	17	390-600
<i>PEN</i>	48	47,29	48	48	47*	47*	57	57	57	48,29
Poly(4,4'-iso-propylidene diphenylene carbonate)										
(c)	-	-	608.2	33.6	X	0	569	(54)	14	?
(a)	424	48.8(2+2)	-	-	X	25	569	40	14	0.4-750
<i>PC</i>	33	9,33	34	9	9,57	33*	30	30	30	9,29

#	T <sub>g</sub>	ΔC <sub>p</sub> <sup>b</sup>	T <sub>m</sub> <sup>c</sup>	ΔH <sub>f</sub> <sup>c</sup>	SHG <sup>d</sup>	S <sub>o</sub> <sup>e</sup>	Θ <sub>1</sub>	Θ <sub>3</sub>	N <sub>s</sub> <sup>f</sup>	C <sub>p</sub> <sup>g</sup>
Poly(oxy-1,4-phenylene-oxy-1,4-phenylene-carbonyl-1,4-phenylene)										
(c)	-	-	668.2	37.4	X	0	560	(54)	15	130-419**
(a)	419 <sup>s</sup>	78.1(1+3)	-	-	X	(17)	560	(40)	15	419-680
PEEK	33	33,35	36	36	33*	33*	30	30	30	33,29
Poly[oxyethylene-oxy-(1,3-phenylene)-(4,4'-oxy-diphthalimide)-1,4-phenylene]										
(c)	-	-	613	72.5	X	0	580	(54)	34	230-450**
(a)	450	172.7	-	-	X	73	580	(40)	34	450-600
ODPA1	60	60*	60	60	57*	57*	60	60	60	60
Poly[dioxyethylene-oxy-(1,3-phenylene)-(4,4'-oxy-diphthalimide)-1,4-phenylene]										
(c)	-	-	577	80.2	X	0	590	(54)	40	230-418**
(a)	418	204.7	-	-	X	86	590	(40)	40	418-600
ODPA2	60	60*	60	60	57*	57*	60	60	60	60
Poly[trioxyethylene-oxy-(1,3-phenylene)-(4,4'-oxy-diphthalimide)-1,4-phenylene]										
(c)	-	-	541	88.0	X	0	(600)	(54)	46	230-385**
(a)	385	246.8	-	-	X	97	(600)	(40)	46	385-580
ODPA3	60	60*	60	60	57*	57*	60	60	60	60
Poly[oxy-1,4(3-methylphenylene)ethylene-1,4-phenyleneoxytetramethylene]										
(c)	-	-	470	46.5	X	0	574	(54)	25	230-298**
(a)	298	142.8	-	-	X	61	(574)	(40)	25	298-470
MBPE4	65	65	65	65	65,57	65	65	65	65	65
Poly[oxy-1,4(3-methylphenylene)ethylene-1,4-phenyleneoxypentamethylene]										
(c)	-	-	385	29.7	X	0	576	(54)	27	120-289**
(a)	289	151.7	-	-	X	44	(576)	(40)	27	289-400
MBPE5	65	65	65	65	65,57	65	65	65	65	65
Poly[oxy-1,4(3-methylphenylene)ethylene-1,4-phenyleneoxyhexamethylene]										
(c)	-	-	461	41.9	X	0	578	(54)	29	230-291**
(a)	291	165.6	-	-	X	41	(578)	(40)	29	291-470
MBPE6	65	65	65	65	65,57	65	65	65	65	65
Poly[oxy-1,4(3-methylphenylene)ethylene-1,4-phenyleneoxyheptamethylene]										
(c)	-	-	372	29.7	X	0	580	(54)	31	230-277**
(a)	277	173.5	-	-	X	39	(580)	(40)	31	277-410
MBPE7	65	65	65	65	65,57	65	65	65	65	65
Poly[oxy-1,4(3-methylphenylene)ethylene-1,4-phenyleneoxyoctamethylene]										
(c)	-	-	407	34.8	X	0	581	(54)	33	230-261**
(a)	261	202.7	-	-	X	19	(581)	(40)	33	261-470
MBPE8	65	65	65	65	65,57	65	65	65	65	65
Poly[oxy-1,4(3-methylphenylene)ethylene-1,4-phenyleneoxynonamethylene]										
(c)	-	-	376	37.8	X	0	583	(54)	35	120-272**
(a)	272	200.6	-	-	X	48	(583)	(40)	35	272-400
MBPE9	65	65	65	65	65,57	65	65	65	65	65

#	T <sub>g</sub>	ΔC <sub>p</sub> <sup>b</sup>	T <sub>m</sub> <sup>c</sup>	ΔH <sub>f</sub> <sup>c</sup>	SHG <sup>d</sup>	S <sub>o</sub> <sup>e</sup>	Θ <sub>1</sub>	Θ <sub>3</sub>	N <sub>s</sub> <sup>f</sup>	C <sub>p</sub> <sup>g</sup>
Poly[oxy-1,4(3-methylphenylene)ethylene-1,4-phenyleneoxydecamethylene]										
(c)	-	-	405	61	X	0	584	(54)	37	230-269**
(a)	269	214.7	-	-	X	89	(584)	(40)	37	269-410
<i>MBPE10</i>	65	65	65	65	65,57	65	65	65	65	65
Poly[oxy-1,4(3-methylphenylene)ethylene-1,4-phenyleneoxyundecamethylene]										
(c)	-	-	385	61	X	0	586	(54)	39	230-277**
(a)	277	215.8	-	-	X	112	(586)	(40)	39	277-400
<i>MBPE11</i>	65	65	65	65	65,57	65	65	65	65	65
Poly[oxy-1,4(3-methylphenylene)ethylene-1,4-phenyleneoxydodecamethylene]										
(c)	-	-	402	63	X	0	587	(54)	41	230-272**
(a)	272	231.4	-	-	X	91	(587)	(40)	41	272-410
<i>MBPE12</i>	65	65	65	65	65,57	65	65	65	65	65

### 10. Poly(silylene)s

#### Poly(dimethylsilylene)

(c)	-	-	?	- <sup>u</sup>	X	0	342	(68)	8	160-490**
(a)	?	?	-	-	X	?	342	?	8	?
<i>PDMSi</i>					57		59	59	59	59

#### Poly(dipentylsilylene)

(c)	-	-	?	- <sup>v</sup>	X	0	320	(68)	24	160-490**
(a)	227	71.3	-	-	X	?	320	?	24	?
<i>PDPSi</i>	59	59			57		59	59	59	59

#### Poly(dihexylsilylene)

(c)	-	-	?	- <sup>w</sup>	X	0	413	(68)	28	160-500**
(a)	221	97.3	-	-	X	?	413	?	28	?
<i>PDHSi</i>	59	59			57		59	59	59	59

#### Poly(ditetradecylsilylene)

(c)	-	-	?	- <sup>y</sup>	X	0	593	(68)	60	160-500**
(a)	(250) <sup>x</sup>	(250) <sup>x</sup>	-	-	X	?	593	?	60	?
<i>PTDSi</i>	59	59			57		59	59	59	59

### 11. Poly(siloxane)s

#### Poly(dimethyl siloxane)

(c)	-	-	219	2.75	X	0	509	68	10	8-146**
(a)	146	27.7(2)	-	-	X	3.5	509	?	10	146-340
<i>PDMS</i>	9	9	52	52	55,57	55	55	55	55	9,52

#### Poly(diethyl siloxane)

(c)	-	-	282.7	1.84 <sup>m</sup>	X	0	480	87	14	10-135**
(a)	135	30.2(2)	-	-	X	8.4	480	?	14	135-360
<i>PDES</i>	52	29	55	55	55,57	55	55	55	55	29

#	T <sub>g</sub>	ΔC <sub>p</sub> <sup>b</sup>	T <sub>m</sub> <sup>c</sup>	ΔH <sub>f</sub> <sup>c</sup>	SHG <sup>d</sup>	S <sub>o</sub> <sup>e</sup>	Θ <sub>1</sub>	Θ <sub>3</sub>	N <sub>s</sub> <sup>f</sup>	C <sub>p</sub> <sup>g</sup>
<b>12. Aliphatic and Aromatic Poly(sulfone)s</b>										
Poly(1-propene sulfone)										
(c)	?	?	?	?	X	?	685	89	13	20-300**
<i>PIPS</i>					57		54	54	54	9
Poly(1-butene sulfone)										
(c)	?	?	?	?	X	?	669	89	15	100-300**
<i>PIBS</i>					57		54	54	54	9
Poly(1-hexene sulfone)										
(c)	?	?	?	?	X	?	587	95	19	20-300**
<i>PIHS</i>					57		54	54	54	9
Poly(1,4-phenylene-sulfonyl)										
(a)	493	12.3(0+1)	-	-	X	?	495	(46)	9	150-620
<i>PAS</i>	54	54			57		54	54	54	54
Poly(oxy-1,4-phenylene-sulfonyl-1,4-phenylene)										
(a)	497	39.1(0+2)	-	-	X	?	800	(46)	14	150-620
<i>PPES</i>	54	54			57		54	54	54	54
Poly[oxy-1,4-phenylene-sulfonyl-1,4-phenylene-oxy-1,4-phenylene-(1-methyldiene)-1,4-phenylene]										
(a)	458	126.6(0+5)	-	-	X	?	778	46	30	10-620
<i>PBISP</i>	54	54			57		54	54	54	54
<b>13. Inorganic Polymers</b>										
Selenium										
(c)	-	-	494.2	6.20	X	0	350	98	3	0.1-500 <sup>i</sup>
(a)	303	13.3(1)	-	-	X	3.6	343	54	3	0.1-1000
<i>SE</i>	3	3	40	40	3	3	14	14	14	3
Buckminsterfullerene										
(c)	-	-	>1000	?	X	0	?	?	6	120-560
(a)	-	-	-	-	X	?	?	?	6	?
<i>C60B</i>			57		57				64	64
<b>14. Paraffins and Perfluoroparaffins</b>										
Propane										
(c)	-	-	85.5	3.52	X	0	360	128	9	15-80
(a)	-	-	-	-	X	?	360	(128)	9	90-230
<i>C3</i>			57	57	57		62	62	62	57
Butane										
(c)	-	-	134.9 <sup>z</sup>	4.66	X	0	402	120	11	15-100
(a)	-	-	-	-	X	?	402	(120)	11	140-270
<i>C4</i>			57	57	57		62	62	62	57

#	T <sub>g</sub>	ΔC <sub>p</sub> <sup>b</sup>	T <sub>m</sub> <sup>c</sup>	ΔH <sub>f</sub> <sup>c</sup>	SHG <sup>d</sup>	S <sub>o</sub> <sup>e</sup>	Θ <sub>1</sub>	Θ <sub>3</sub>	N <sub>s</sub> <sup>f</sup>	C <sub>p</sub> <sup>g</sup>
<b>Pentane</b>										
(c)	-	-	143.5	8.39	X	0	438	97	13	10-140
(a)	-	-	-	-	X	?	438	(97)	13	150-300
<i>C5</i>			57	57	57		62	62	62	57
<b>Hexane</b>										
(c)	-	-	177.8	13.0	X	0	449	109	15	10-170
(a)	-	-	-	-	X	?	449	(109)	15	180-300
<i>C6</i>			57	57	57		62	62	62	57
<b>Heptane</b>										
(c)	-	-	182.6	14.0	X	0	449	115	17	10-180
(a)	-	-	-	-	X	?	449	(115)	17	190-370
<i>C7</i>			57	57	57		62	62	62	57
<b>Octane</b>										
(c)	-	-	216.4	20.7	X	0	465	121	19	10-210
(a)	-	-	-	-	X	?	465	(121)	19	220-300
<i>C8</i>			57	57	57		62	62	62	57
<b>Nonane</b>										
(c)	-	-	219.7 <sup>z</sup>	15.5	X	0	474	119	21	10-210
(a)	-	-	-	-	X	?	474	(119)	21	220-320
<i>C9</i>			57	57	57		62	62	62	57
<b>Decane</b>										
(c)	-	-	243.5	28.7	X	0	481	126	23	10-240
(a)	-	-	-	-	X	?	481	(126)	23	250-320
<i>C10</i>			57	57	57		62	62	62	57
<b>Undecane</b>										
(c)	-	-	247.6 <sup>z</sup>	22.2	X	0	489	122	25	10-230
(a)	-	-	-	-	X	?	489	(122)	25	250-310
<i>C11</i>			57	57	57		62	62	62	57
<b>Dodecane</b>										
(c)	-	-	263.6	36.8	X	0	494	128	27	10-260
(a)	-	-	-	-	X	?	494	(128)	25	270-320
<i>C12</i>			57	57	57		62	62	62	57
<b>Tridecane</b>										
(c)	-	-	267.8 <sup>z</sup>	28.5	X	0	498	125	29	10-250
(a)	-	-	-	-	X	?	498	(125)	29	270-310
<i>C13</i>			57	57	57		62	62	62	57
<b>Tetradecane</b>										
(c)	-	-	279.0	45.1	X	0	501	130	31	10-270
(a)	-	-	-	-	X	?	501	(130)	31	280-300
<i>C14</i>			57	57	57		62	62	62	57

#	T <sub>g</sub>	ΔC <sub>p</sub> <sup>b</sup>	T <sub>m</sub> <sup>c</sup>	ΔH <sub>f</sub> <sup>c</sup>	SHG <sup>d</sup>	S <sub>o</sub> <sup>e</sup>	Θ <sub>1</sub>	Θ <sub>3</sub>	N <sub>s</sub> <sup>f</sup>	C <sub>p</sub> <sup>g</sup>
Pentadecane										
(c)	-	-	283.1 <sup>z</sup>	34.6	X	0	504	128	33	10-270
(a)	-	-	-	-	X	?	504	(128)	33	290-310
C15			57	57	57		62	62	62	57
Hexadecane										
(c)	-	-	291.3	53.4	X	0	507	132	35	10-290
(a)	-	-	-	-	X	?	507	(132)	35	300-320
C16			57	57	57		62	62	62	57
Heptadecane										
(c)	-	-	295.1 <sup>z</sup>	40.2	X	0	506	131	37	10-280
(a)	-	-	-	-	X	?	506	(131)	37	300-390
C17			57	57	57		62	62	62	57
Octadecane										
(c)	-	-	301.3	61.7	X	0	512	134	39	10-300
(a)	-	-	-	-	X	?	512	(134)	39	310-380
C18			57	57	57		62	62	62	57
Eicosane										
(c)	-	-	309.8 <sup>z</sup>	69.9	X	0	510	135	43	100-270
(a)	-	-	-	-	X	?	510	(135)	43	?
C20			57	57	57		62	62	62	57
Tetracosane										
(c)	-	-	323.8 <sup>z</sup>	54.9	X	0	513	137	51	80-290
(a)	-	-	-	-	X	?	513	(137)	51	?
C24			57	57	57		62	62	62	57
Pentacosane										
(c)	-	-	326.7 <sup>z</sup>	57.7	X	0	514	135	53	100-280
(a)	-	-	-	-	X	?	514	(135)	53	?
C25			57	57	57		62	62	62	57
Hexacosane										
(c)	-	-	329.5 <sup>z</sup>	59.5	X	0	513	138	55	10-320
(a)	-	-	-	-	X	?	513	(138)	55	330-360
C26			57	57	57		62	62	62	57
Dotriacontane										
(c)	-	-	342.5 <sup>z</sup>	?	X	0	516	140	67	80-300
(a)	-	-	-	-	X	?	516	(140)	67	?
C32			57		57		62	62	62	57
Tritriacontane										
(c)	-	-	344.3 <sup>z</sup>	?	X	0	516	138	69	100-300
(a)	-	-	-	-	X	?	516	(138)	69	?
C33			57		57		62	62	62	57

#	T <sub>g</sub>	ΔC <sub>p</sub> <sup>b</sup>	T <sub>m</sub> <sup>c</sup>	ΔH <sub>f</sub> <sup>c</sup>	SHG <sup>d</sup>	S <sub>o</sub> <sup>e</sup>	Θ <sub>1</sub>	Θ <sub>3</sub>	N <sub>s</sub> <sup>f</sup>	C <sub>p</sub> <sup>g</sup>
Hexatriacontane										
(c)	-	-	349.1 <sup>z</sup>	88.8	X	0	513	(141)	75	130-340
(a)	-	-	-	-	X	?	513	(141)	75	360-430
C36			57	57	57		62	62	62	57
Tetratetracontane										
(c)	-	-	359.6 <sup>z</sup>	140.1	X	0	511	(142)	91	130-350
(a)	-	-	-	-	X	?	511	(142)	91	370-430
C44			57	57	57		62	62	62	57
Pentacontane										
(c)	-	-	365.3	158.1	X	0	513	(143)	103	130-360
(a)	-	-	-	-	X	?	513	(143)	103	380-430
C50			57	57	57		62	62	62	57
Perfluoropropane										
(c)	-	-	125.4 <sup>z</sup>	3.8	X	0	148	60	9	20-125.4
(a)	-	-	-	-	X	?	148	(60)	9	125.4-230
FC3			66	66	57		66	66	66	66
Perfluoroheptane										
(c)	-	-	221.8 <sup>z</sup>	28.0	X	0	210	40	17	20-221.8
(a)	-	-	-	-	X	?	210	(40)	17	221.8-310
FC7			66	66	57		66	66	66	66
Perfluorododecane										
(c)	-	-	347.9 <sup>z</sup>	68.8	X	0	227	48	27	5-347.5
(a)	-	-	-	-	X	?	227	(48)	27	347.5-380
FC12			66	66	57		66	66	66	66
Perfluorotetradecane										
(c)	-	-	376.2 <sup>z</sup>	83.0	X	0	230	47	31	5-377.4
(a)	-	-	-	-	X	?	230	(47)	31	377.4-410
FC14			66	66	57		66	66	66	66
Perfluorohexadecane										
(c)	-	-	400.1 <sup>z</sup>	93.3	X	0	232	48	35	5-400
(a)	-	-	-	-	X	?	232	(48)	35	400-440
FC16			66	66	57		66	66	66	66
Perfluoroeicosane										
(c)	-	-	438.1 <sup>z</sup>	109.7	X	0	235	(49)	43	120-428.9
(a)	-	-	-	-	X	?	235	(49)	43	428.9-470
FC20			66	66	57		66	66	66	66
Perfluorotetracosane										
(c)	-	-	463.5 <sup>z</sup>	136.8	X	0	240	(50)	51	120-461.7
(a)	-	-	-	-	X	?	240	(50)	51	461.7-500
FC24			66	66	57		66	66	66	66

#	T <sub>g</sub>	ΔC <sub>p</sub> <sup>b</sup>	T <sub>m</sub> <sup>c</sup>	ΔH <sub>f</sub> <sup>c</sup>	SHG <sup>d</sup>	S <sub>o</sub> <sup>e</sup>	Θ <sub>1</sub>	Θ <sub>3</sub>	N <sub>s</sub> <sup>f</sup>	C <sub>p</sub> <sup>g</sup>
<b>15. Tetra Alkylammonium Salts</b>										
Tetra- <i>n</i> -propylammonium bromide										
(c)	-	-	553.0 <sup>aa</sup>	-	X	0	596	(130)	34	130-370
TA3Br			67		57		67	67	67	67
Tetra- <i>n</i> -butylammonium bromide										
(c)	-	-	393.9 <sup>aa</sup>	14.8	X	0	633	(130)	42	130-350
TA4Br			67	67	57		67	67	67	67
Tetra- <i>n</i> -pentylammonium bromide										
(c)	-	-	374.0 <sup>aa</sup>	36.5	X	0	567	(130)	50	130-350
TA5Br			67	67	57		67	67	67	67
Tetra- <i>n</i> -hexylammonium bromide										
(c)	-	-	374.9 <sup>aa</sup>	16.0	X	0	(689)	(130)	58	130-240
TA6Br			67	67	57		67	67	67	67
Tetra- <i>n</i> -heptylammonium bromide										
(c)	-	-	366.5 <sup>aa</sup>	36.4	X	0	615	(100)	66	130-340
TA7Br			67	67	57		67	67	67	67
Tetra- <i>n</i> -octylammonium bromide										
(c)	-	-	374.1 <sup>aa</sup>	44.1	X	0	595	(170)	74	130-310
TA8Br			67	67	57		67	67	67	67
Tetra- <i>n</i> -decylammonium bromide										
(c)	-	-	363.4 <sup>aa</sup>	37.3	X	0	597	(130)	90	130-330
TA10Br			67	67	57		67	67	67	67
Tetra- <i>n</i> -dodecylammonium bromide										
(c)	-	-	362.6 <sup>aa</sup>	75.0	X	0	602	(170)	106	130-340
TA12Br			67	67	57		67	67	67	67
Tetra- <i>n</i> -hexadecylammonium bromide										
(c)	-	-	377.7 <sup>aa</sup>	95.1	X	0	(588)	(130)	138	130-350
TA16Br			67	67	57		67	67	67	67
Tetra- <i>n</i> -octadecylammonium bromide										
(c)	-	-	379.9 <sup>aa</sup>	124.8	X	0	551	(100)	154	130-350
TA18Br			67	67	57		67	67	67	67
Tetra- <i>n</i> -propylammonium iodide										
(c)	-	-	554 <sup>aa</sup>	-	X	0	630	(130)	34	130-210
TA3I			67		57		67	67	67	67
Tetra- <i>n</i> -butylammonium iodide										
(c)	-	-	420.6 <sup>aa</sup>	8.96	X	0	623	(130)	42	130-360
TA4I			67	67	57		67	67	67	67



#	T <sub>g</sub>	ΔC <sub>p</sub> <sup>b</sup>	T <sub>m</sub> <sup>c</sup>	ΔH <sub>f</sub> <sup>c</sup>	SHG <sup>d</sup>	S <sub>o</sub> <sup>e</sup>	Θ <sub>1</sub>	Θ <sub>3</sub>	N <sub>s</sub> <sup>f</sup>	C <sub>p</sub> <sup>g</sup>
Tetra- <i>n</i> -pentylammonium iodide										
(c)	-	-	412.1 <sup>aa</sup>	38.7	X	0	604	(100)	50	130-390
TA5I			67	67	57		67	67	67	67
Tetra- <i>n</i> -hexylammonium iodide										
(c)	-	-	378.7 <sup>aa</sup>	16.6	X	0	(589)	(130)	58	130-330
TA6I			67	67	57		67	67	67	67
Tetra- <i>n</i> -heptylammonium iodide										
(c)	-	-	398.7 <sup>aa</sup>	39.0	X	0	644	(170)	66	130-350
TA7I			67	67	57		67	67	67	67
Tetra- <i>n</i> -dodecylammonium iodide										
(c)	-	-	388.7 <sup>aa</sup>	47.5	X	0	647	(170)	106	130-320
TA12I			67	67	57		67	67	67	67

## 16. Other Small Molecules

<i>N,N'</i> -bis(4- <i>n</i> -Octyloxybenzal)-1,4-phenylenediamine										
(c)	-	-	505.4 <sup>ab</sup>	2.3	X	0	593	(80)	55	130-260
(a)	-	-	-	-	X	?	(593)	(80)	55	530-550
OOBPD			68	68	57		68	65	68	68
4,4'-(2,2'-Propylidene)diphenol										
(c)	-	-	434.7	30.9	X	0	293	(54)	14	140-313
(a)	313	161.3	-	-	X	23.1	293	(40)	14	313-470
BPA	63	63	63	63	63,57	57	63	63	63	63
2,2'-Propylidene-bis(1,2-epoxy-3-phenoxypropane)										
(c)	-	-	322.5	27.1	X	0	552	(54)	34	140-254
(a)	254	173.8	-	-	X	52.6	552	(40)	34	254-410
EPA	63	63	63	63	63,57	57	63	63	63	63
2,2'-Propylidene-bis(1,2-epoxy-2-phenoxyethane)										
(c)	-	-	320.3	20.0	X	0	523	(54)	30	140-258
(a)	258	179.0	-	-	X	20.2	523	(40)	30	258-370
EPB	63	63	63	63	63,57	57	63	63	63	63
Methylene-bis(1,2-epoxy-2-phenoxyethane)										
(c)	-	-	-	-	X	0	742	(54)	24	140-252
(a)	252	218.8	-	-	X	?	742	(40)	24	252-370
EPC	63	63			63,57		63	63	63	63
[2,2',6,6'-Tetramethyl-1,1'(2-oxy-1,2-epoxyethane)]4,4'-biphenyl										
(c)	-	-	382.1	19.9	X	0	639	(54)	34	140-267
(a)	267	236.7	-	-	X	?	639	(40)	34	267-430
EPD	63	63	63	63	63,57		63	63	63	63
Prepreg of 2,2'-propylidene-bis(1,2-epoxy-3-phenoxypropane) polymerized with 0.2 moles of 1,2-epoxy-3-phenoxypropane-(1-methylidene)-1,4-phenylene-oxy(2-propanol)										
(c)	-	-	-	-	X	0	743	(54)	39.2	140-260
(a)	260	213.9	-	-	X	?	743	(40)	39.2	260-290
EPE	63	63			63,57		63	63	63	63

## References to Appendix 1

1. Gaur U, Wunderlich B (1981) *J Phys Chem Ref Data* 10: 119.
2. Gaur U, Wunderlich BB, Wunderlich B (1983) *J Phys Chem Ref Data* 12: 29.
3. Gaur U., Shu PH-C, Mehta A, Wunderlich B (1981) *J Phys Chem Ref Data* 10: 89.
4. Gaur U, Wunderlich B (1981) *J Phys Chem Ref Data* 10: 1051.
5. Gaur U, Wunderlich B (1982) *J Phys Chem Ref Data* 11: 313.
6. Gaur U, Wunderlich B (1981) *J Phys Chem Ref Data* 10: 1001.
7. Gaur U, Lau S-F, Wunderlich BB, Wunderlich B (1982) *J Phys Chem Ref Data* 11: 1085.
8. Gaur U, Lau S-F, Wunderlich BB, Wunderlich B (1983) *J Phys Chem Ref. Data* 12, 65.
9. Gaur U, Lau S-F, Wunderlich B (1983) *J Phys Chem Ref Data* 12: 91.
10. Wunderlich B (1980) *Macromolecular Physics*, vol 3, Crystal Melting. Academic Press, New York, NY.
11. Xenopoulos A (1990) dissertation, Rensselaer Polytechnic Institute, Troy, NY.
12. Lau S-F, Wesson JP, Wunderlich B (1984) *Macromolecules* 17: 1102.
13. Lau S-F, Suzuki H, Wunderlich B (1984) *J Polym Sci Polym Phys Ed* 22: 379.
14. Cheban YuV, Lau S-F Wunderlich B (1982) *Colloid Polym Sci* 260: 9.
15. Grebowicz J, Lau S-F. Wunderlich B (1984) *J Polym Sci Polym Symp* 71: 19.
16. Aycock W (1988) dissertation, Rensselaer Polytechnic Institute, Troy, NY; incomplete, for data, request printout from ATHAS.
17. Bu HS, Aycock W, Wunderlich B (1987) *Polymer* 28: 1165.
18. Grebowicz J, Aycock W, Wunderlich B (1986) *Polymer* 27: 575.
19. Loufakis K (1986) dissertation, Rensselaer Polytechnic Institute, Troy, NY.
20. Loufakis K, Wunderlich B (1985) *Polymer* 26: 1875.
21. Loufakis K, Wunderlich B (1986) *Polymer* 27: 563.
22. Judovits LH (1985) dissertation, Rensselaer Polytechnic Institute, Troy, NY.
23. Judovits LH, Bopp LH, Gaur U, Wunderlich B (1986) *J Polym Sci Polym Phys Ed* 24: 2725.
24. Suzuki H, Wunderlich B (1985) *J Polym Sci Polym Phys Ed* 23: 1671.
25. Grebowicz J, Suzuki H, Wunderlich B (1985) *Polymer* 26: 561.
26. O'Reilly JM, Bair HE, Karasz FE (1982) *Macromolecules* 15: 1083.
27. Lim S, Wunderlich B (1987) *Polymer* 28: 777.
28. Lebedev B, Yevstropov A (1984) *Makromol Chem* 185: 1235.
29. Varma-Nair M, Wunderlich B (1991) *J Phys Chem Ref Data* 20: 349.
30. Cheng SZD, Lim S, Judovits LH, Wunderlich B (1987) *Polymer* 28: 10.
31. Cheng SZD, Wu ZQ, Wunderlich B (1987) *Macromolecules* 20: 2801.
32. Kirkpatrick DE, Wunderlich B (1985) *Makromol Chem* 186: 2595.
33. Cheng SZD, Wunderlich B (1986) *J Polym Sci Polym Phys Ed* 24: 1755.
34. Jonza JM. Porter RS (1986) *J Polym Sci Polym Phys Ed* 24: 2459.
35. Cheng SZD, Cao M-Y, Wunderlich B (1986) *Macromolecules* 19: 1868.
36. Blundell DJ, Osborn BN (1983) *Polymer* 24: 953.
37. Gaur U, Wunderlich B (1980) *Macromolecules* 13: 445.
38. Wunderlich B, Czornyj G (1977) *Macromolecules* 10: 906.
39. Judovits L, Wunderlich B (1985) *J Thermal Anal* 30: 895.
40. Wunderlich B, Shu PHC (1980) *J Crystal Growth* 48: 227.
41. Fintner J, Wegner G (1981) *Makromol Chem* 182: 1859.
42. Cheng SZD, Wunderlich B (1987) *Macromolecules* 20: 1630.
43. Mehta A, Wunderlich B (1978) *J Polym Sci Polym Phys Ed* 16: 289.

44. Lebedev BV, Kulagina TG, Lyudwig YeB, Ovchinnikova TN (1982) *Polym Sci USSR* 24: 1695.
45. Bu HS, Aycock W, Cheng SZD, Wunderlich B (1988) *Polymer* 29: 1485.
46. Varma-Nair M, Pan R, Wunderlich B (1991) *J Polym Sci Polym Phys Ed* 29: 1107.
47. Cheng SZD, Pan R, Bu HS, Wunderlich B (1988) *Makromol Chem* 189: 1579.
48. Cheng SZD, Wunderlich B (1988) *Macromolecules* 21: 789.
49. Bair HE, Schilling FC (1986) *Proc. 15<sup>th</sup> Natas Conf* 15:, 32.
50. Bu HS, Cheng SZD, Wunderlich B (1988) *Makromol Chem Rapid Commun* 9: 75.
51. Cao M-Y (1988) dissertation, Rensselaer Polytechnic Institute Troy, NY.
52. Wesson JP (1988) dissertation, Rensselaer Polytechnic Institute Troy, NY.
53. Cheng SZD, Pan R, Wunderlich B (1988) *Makromol Chem* 189: 2443.
54. Varma-Nair M, Jin Y, Wunderlich B (1992) *Polymer* 33: 5272.
55. Varma-Nair M, Wesson JP, Wunderlich B (1989) *J Thermal Anal* 35: 1913.
56. Cao M-Y, Varma-Nair M, Wunderlich B (1990) *Polym Adv Technol* 1: 151.
57. ATHAS Data Bank update.
58. Roles K (1991) dissertation, University of Tennessee, Knoxville, TN.
59. Varma-Nair M, Cheng J, Jin Y, Wunderlich B (1991) *Macromolecules* 24: 5442.
60. Cheng SZD, Heberer DP, Lien HS, Harris FW(1990) *J Polym Sci Polym Phys Ed* 28: 655.
61. Grebowicz J, Varma-Nair M, Wunderlich B (1992), *Polym Adv Techn* 3: 51.
62. Jin Y, Wunderlich B (1991) *J Phys Chem.* 95: 9000.
63. Varma-Nair M, Wunderlich B, Grebowicz J, Bauer R (1993) *Thermochim Acta* 226: 99.
64. Jin Y, Cheng J, Varma-Nair M, Liang G, Fu Y, Wunderlich B, Xiang XD, Mostovoy R, Zettl AK, Cohen ML (1992) *J Phys Chem* 96: 5151.
65. Jin Y, Cheng J Wunderlich B, Cheng, SZD, Yandrasits M (1994) *Polym Adv Technol* 5: 785.
66. Jin Y, Boller A, Wunderlich B, Lebedev BV (1993) *Thermochim Acta* 234: 103.
67. Xenopoulos A, Cheng J, Wunderlich B (1993) *Mol Cryst Liq Cryst* 226: 87.
68. Cheng J, Jin Y, Liang G, Wunderlich B, Wiedemann H (1972) *Mol Cryst Liq Cryst* 213: 237.
69. Xenopoulos A, Roles K, Wunderlich B (1993) *Polymer* 34: 2559.
70. Pyda M, Boller A, Grebowicz J, Chuah H, Lebedev BV, Wunderlich B (1998) *J Polymer Sci, Part B: Polymer Phys* 36: 2499.
71. Pyda M, Bopp, Wunderlich B (2004) *J Chem Thermodynamics* 36: 731.
72. Pyda M, Nowak-Pyda E, Mays J, Wunderlich B (2004), *J Polymer Sci Part B: Polymer Phys* 42: 4401.

## Radiation Scattering, Yesterday's Cinderella, Today's Prima Donna

Excerpts from an article by Wilfried Heller<sup>1</sup>

In 1870 and 1871 the Franco-Prussian war was raging on the continent of Europe and many Englishmen were deeply concerned about the effect of the outcome on the continental balance of power. One Englishman, J. W. Strutt, however, was concerned about an entirely different matter. He was wondering why the sky is blue during the day since in absence of any reflecting matter in the atmosphere one would have expected it to be pitch black. While Wilhelm I and Napoleon III tried to make political history, Mr. Strutt made real history by developing a theory intended to solve the mystery of the sky's coloration. Now, more than 120 years later, one realizes how tremendously a breakthrough Strutt's theory represented. It is to the credit of Queen Victoria that, here again, she proved to be very farsighted because Mr. Strutt was soon to be knighted, i.e., he was allowed, in 1873, to assume the title of his father, Lord Rayleigh.

Rayleigh had postulated a new phenomenon in order to account for the blue of the sky: light scattering. He assumed that the individual molecules in the atmosphere on being illuminated by the sun, scatter in all directions a minute fraction of the radiation received. Assuming that each molecule behaves, under the influence of incident radiation, like a single induced dipole, he calculated the nature of the effect to be expected and found it to be essentially in agreement with the facts. According to his theory, which he later refined, the intensity of the light scattered from an incident light beam should increase with the inverse fourth power of the wavelength of the latter, with the sixth power of the radius of the scattering material—assuming it to be spherical in shape—and should increase also with the refractive index ratio of the scatterer and its surroundings.

Since the sun emits essentially a continuous spectrum, the inverse fourth power law shows at once that scattered blue sunlight (450 nm) will be more than three times as intense as scattered red sunlight (600 nm) on assuming spectral invariance of the sun's brightness. The blue color of the sky was thus explained quantitatively. In addition, if anyone had asked Lord Rayleigh in 1871 as to what the earth would look like from outer space he probably would have answered without hesitation that the earth must look like a ball surrounded by a very beautiful bluish violet halo, whenever direct sunlight does not interfere with the observation. This in fact has been observed by John Glenn on his orbital flight in 1962 and by the others who preceded and followed him. An obvious corollary of this preferential blue scattering is the fact, well known to all of us, that the sun itself may look reddish during the sunset or sunrise, i.e., if it is viewed through thick enough layers of scattering material. This better penetration of long wavelength radiation through haze is the simple reason for

---

<sup>1</sup> Wilfried Heller, 1903–1982, Professor at the Department of Chemistry since 1947, Wayne State University, Detroit, MI. Excerpted with permission by the Author, 1965.

using infrared photography for objects obscured by haze or clouds. The strong increase of Rayleigh-scattering with particle size explains readily why the relatively small number of tiny smoke particles rising from the burning end of a cigar or cigarette viewed laterally in ordinary daylight gives rise to a relatively intense beam of scattered blue light, while on the other hand, a tremendously large number of molecules of nitrogen and oxygen in the atmosphere, i.e., an appreciable atmospheric thickness, are required to lead to the same effect on viewing the sky. The importance of the refractive index difference between scatterer and environment may also be demonstrated by a simple experiment which every one of us has carried out, involuntarily, at one time or another. A sheet of typewriter paper soiled with a speck of butter from a sandwich becomes transparent where it has been touched. Typewriter paper is opaque due only to the scattering of light by a dense network of fully transparent fibers. By substituting fat for air as the medium in which the fibers are embedded, the ratio of the refractive indices is reduced from 1.55 to 1.06 and this, in turn, reduced the scattering appreciably. The refractive indices are for cellulose, 1.55, for butterfat, 1.46, and for air  $\approx 1.00$ .

Those who have performed, before reading this far, the scattering experiment with cigar or cigarette smoke may have noticed that the exhaled smoke and the smoke coming out from the end opposite to the burning end have a grayish or brownish color. While one has, here again, an effect of light scattering, it does clearly not fall within the range of the Rayleigh theory. The smoke particles in this instance are far too large to be considered as single dipoles. As a rule of thumb one can say that the Rayleigh theory will fail if the longest dimension of the scatterers exceeds about  $1/20$  of the wavelength of the radiation used. While the blue smoke, therefore, consists of particles smaller than  $2.25 \times 10^{-6}$  cm, the particles in the gray smoke are appreciably larger. (This is the result of particle aggregation and absorption of the smaller particles during the transport of smoke through the tobacco and the lungs.) Another common example of the scattering by relatively large particles is the grayish ray of light coming through a tall church window. Here, the scattering particles are dust particles. While gray coloration of the scattered light is the phenomenon generally observed if the relatively large particles are present in various sizes, singularly striking colors of any hue in the spectrum are likely if they all have approximately the same size. This, for instance, is the cause and the prerequisite of the beautiful multicolored sunsets occasionally observed, particularly if the lower layers of the atmosphere and peripheral areas around clouds contain a large number of tiny water droplets of about the same size. These larger particles in the lower atmosphere are, of course, also responsible for the red, yellow, and gray bands which are seen from outer space between the blue Rayleigh halo and the boundary of the earth. It is fairly easy to anticipate that these non-blue bands will be more prominent over heavily populated areas than over desolate areas and oceans.

In addition to the complicated spectral variation of scattered light, one observes with relatively large particles several other characteristically different scattering properties. Among them, three are particularly noteworthy. First, the light scattered in the forward direction, i.e., in the same direction traveled by the incident radiation is larger than that scattered in the backward direction. This lopsidedness increases rapidly with size. (In a contradistinction, Rayleigh Scattering in the forward and

backward direction are equal.) The next time you are driving in misty weather up toward the crest of a hill you want to verify this preferential forward scattering by the following simple observation: a car which is traveling toward you, but is still out of sight below the crest of the hill, sends up an impressively bright beam of light; a car traveling ahead of you in the same direction in which you are going will also send a beam of light up into the sky but his scattered beams, viewed by you of course, in the backward direction, is incomparably weaker. The second noteworthy difference in the scattering by relatively large particles is that the total amount of light scattered by a system of given concentration of scatterers per unit volume reaches a maximum value at a very specific intermediate particle size. For this phenomenon also one can cite a common experience: The brightness of a distant light source or the visibility of a distant illuminated object is minimal in fog while they are better both in misty weather and in heavy drizzle. The average water droplet size in fog is intermediate between that in the two other instances and it is such that it produces the maximal hiding power. The implications for the production of smoke screens of maximum efficiency are obvious. The third interesting difference in the scattering by relatively large particles is the fact that the scattered light observed at an angle of  $90^\circ$  with respect to the incident beam will be found to be only partially polarized while Rayleigh Scattering is, for the same angle of observation, fully polarized. This phenomenon is outside of the realm of easy, everyday experience, but its practical significance and importance rank with the other enumerated.

The problem of the theory of the scattering by particles which are not small compared to the wavelength can be divided into two cases. The first is that of spheres. All possible contingencies that may arise here are taken care of by a theory developed by Mie in 1908. The second case is that of the non spherical particles. Here also a most useful theory exists, again initiated by Rayleigh (1911).

The great importance of light-scattering derives from the fact that it allows one to investigate quantitatively an amazingly large number of problems in many fields of human endeavor. This can be done without interfering in any way with the system investigated. One of the reasons for this unique position of the light scattering method as an analytical tool is the fact that there is, in principle, no limitation as to the wavelength that may be used. The phenomena tractable by the existing theories are the same no matter whether the radiation is that of visible light, or is of shorter wavelengths (ultra violet, X-rays, gamma radiation), or longer wavelengths (infrared, far infrared, radar or broadcasting waves). This is due to the fact that the absolute size of particles does not matter, only the size relative to the wavelength is important. Thus, hollow aluminum spheres one inch in diameter strewn into the atmosphere will scatter, i.e., attenuate radar waves quantitatively exactly like tiny aluminum spheres will scatter visible light provided only that differences in the refractive indices at the two wavelengths are taken into account.

On reviewing the development of science and technology during the last fifteen years, it is amazing to see how large a contribution the understanding and the application of radiation scattering have made. The space available here allows one to give only a few significant examples. The amazing progress in the fields of polymer chemistry and biochemistry is to a large extent due to the fact that light scattering has provided a rapid, reliable and precise method for determining molecular

masses and approximate molecular shapes and has allowed one, what no other method is capable of doing, to follow the kinetics of changes in these qualities. Noteworthy here is the pioneering work by Zimm and by Doty in the late forties. In all these areas, it is primarily Rayleigh scattering which has, at last, taken its place as a tool in scientific research which it so fully deserves. A large part of the credit for this goes to Debye who, in 1943, put the final touches to a theory developed by Einstein in 1910. This theory, though based upon an entirely different approach, is fully equivalent to Rayleigh's theory.

The science of light-scattering holds the promise of a more fruitful investigation of fogs and smogs. A full understanding that thus may be achieved, certainly will be the decisive step toward eventual control or complete eradication. Fog and smog are the ultimate result of a large accumulation in the lower atmosphere of dust and debris from combustion which act as nuclei for water condensation. However, the conclusion that the upper atmosphere is pure and clean would not be justified. Light scattering experiments quite recently showed that dust may be carried by eddy currents as high as 25,000 m. This finding, incidentally, leads to a solution of the puzzling problem as to why the sky is brighter than one would expect from Rayleigh's theory. Investigations by space probes gave exactly the same results on the pollution of the upper atmosphere, the only difference being that light scattering gave this information at a considerably smaller cost.

The sky, however, is not the limit for scattering enthusiasts. Returning to earth and proceeding in the opposite direction, i.e., entering the microcosmic world of the atomic nucleus, it is common knowledge that much of the progress made here is due to experiments with the cloud bubble chambers. Here light scattering makes visible convincingly, though indirectly, the paths taken by  $\alpha$ -particles, protons, electrons, positrons, mesons, and to follow the interactions of the so-called "strange particles" of nuclear physics. Phenomena such as neutron scattering also are treated by means of theories which in many respects are related to the scattering of electromagnetic waves. An application of scattering which is of particular concern to many of us is its use as a potentially powerful tool in medical diagnosis. One successful example is the examination of donor blood for the degree of non-sphericity of red blood cells by a rapid experiment on the deviation of lateral scattering from symmetry.

Rapidly developing also are the theory and practical application of light scattering of transparent or translucent solids. Here light scattering may be due to a dispersion, within the solid, gases or of liquids or, it may be due to the formation of tiny regions of molecular orientation within the matrix or it may, simply result from internal strain or from cavities. In all these cases, internal refractive index differences arise and the resulting optical inhomogeneity leads to light scattering and, consequently, to more or less pronounced opaqueness. A good example of a solid rendered opaque by the entrapment of tiny droplets of water is the pearl. Its delicate bluish gray color originates exclusively from light scattering. (Therefore, you should never heat a pearl above the boiling point of water.) An example of light scattering due to differences in molecular orientation within a solid is the scattering by polymer films, studied in this country at present primarily by Stein and collaborators. It gives valuable information on the internal structure of polymer films. A lesson learned from the fact that inhomogeneities in solids may make them opaque, due only to refractive index

differences, is that one now can make glasses, particularly plastic glasses, more transparent than before by simply eliminating or matching refractive index differences. Into this category of light scattering phenomena belongs also the finite, although extremely weak scattering by liquids where it is due to local statistical density differences caused by the thermal motion of the molecules which make up the liquid. Of potentially far reaching theoretical importance here is the use of this phenomenon in order to obtain in liquid mixtures information on the range of molecular forces [Debye (1961)].

The radiation scattering by molecules, particles, or inhomogeneities has thus far been considered for being unaffected by that scattered by neighbors. Actually there is an interference between the individual scattered wavelets, more so the smaller the distances of neighbors, relative to the dimension of the wavelength. A whole host of theoretically interesting and practically most important phenomena can result from such interferences. Some of them belong in an area which the uninquiring mind may wish to classify as a part of the “twilight zone.”

When you drive along a highway on a hot summer day, you may see dark patches on it in the distance which look just like water. Then, when you come closer, they vanish. The next time you make this observation, stop while you see these patches and wait until a car passes you and drives over those patches. You will be amazed to see that the car seems to lift itself a few inches off the ground and to travel in air. Moreover, you may see its under structure reflected on the patches. What is the reason? Within 5–10 cm off the ground, the temperature is 30–50 K higher than further up. Due to the resulting refractive index differences, the thin hot air layer scatters quite differently than the air above it. This results in refraction and reflection. The practical result, in the present instance, is the macroscopic effect of (a) invisibility of the ground proper and (b) reflection from the upper border of the hot air layer, provided only that the angle which the particular area on the highway makes with respect to both the sun and the direction of your vision is just right. Flying saucers also belong into this category of phenomena, although here the diffuse reflection and refraction originate at surfaces of vortices of the air which differ in density from the rest of the air. They are generally circular and, according to Helmholtz, may be extremely long lived. They may, therefore, have traveled far from the place where they were generated, for instance by a jet breaking the sound barrier. Unquestionably, photographs of this phenomenon can be taken if and when the density differences are large enough. Another phenomenon which is even more closely related to our “flying automobile” and which turned out to be of extreme practical usefulness, is that of trans-horizon wave propagation, due to diffuse reflection on stratifications in the upmost sections of the atmosphere. The closely related, but optically more perfect phenomena of a Fata Morgana require special temperature gradients, similar to those which lead to the car riding in the air. We all have felt sympathy with the man lost in the Sahara desert who becomes elated on suddenly seeing the mirage of an oasis in the distant sky. Alas, we cannot control these phenomena yet, but eventually we may. If that happens, there is no way of predicting how real estate agents may then be able to include in their package deal a permanent Fata Morgana in the backyard allowing a choice view of a selected section of Yosemite National Park.



## Derivation of the Rayleigh Ratio

The turbidity,  $\tau$ , expressed in  $\text{m}^{-1}$ , is a measure of the total intensity of light,  $I$ , scattered in all directions from an incoming beam of intensity  $I_0$ . A typical data table and the mathematical equation are shown in Fig. A.3.1, where  $\ell$  is the distance traversed by the incoming light within the scattering medium. Also given is the competing Raman scattering, which represents the scattered light of changed wavelengths, in contrast to the here described Rayleigh scattering with an unchanged wavelength. The scattering of light increases by a factor 100,000 in going from a clear crystal, such as quartz, to a 1% polymer solution, i.e., the Raman intensity originating from the polymer is negligible relative to the Rayleigh scattering.

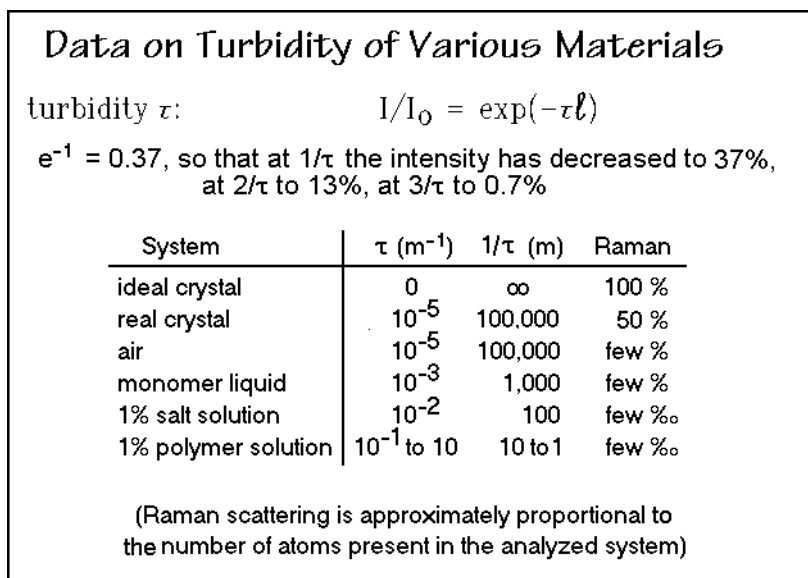


**Fig. A.3.1**

In Fig. A.3.2 the two basic proportionalities describing light scattering are added to the turbidity equation. They concern the electric moment,  $p$ , induced in the scattering center, and the amplitude of the scattered light. The scattering center is initially assumed to be of negligible size, i.e.,  $< \lambda/20$ . The polarizability is given the symbol  $\alpha$ , and  $E_0$  is the electric field strength of the incoming light. The light is characterized by its speed in vacuum,  $c = 2.998 \times 10^8 \text{ m s}^{-1}$ , and its wavelength is  $\lambda$ , the wavelengths of visible light = 400–750 nm. The amplitude of the scattered light,  $s$ , is recorded at a distance  $r$ , and the angle  $\phi_z$  from the vibration direction of the electric field,  $z$ , as shown in the schematic for plane-polarized light.

The equation for the scattered light in direction  $P$  at distance  $r$  is expressed by the superscript 1. It refers to the scattering from one scattering center only. The scattering angle is given as subscript. Using the maximum amplitude for the computation eliminates the time-dependence which is available from the frequency and the phase-

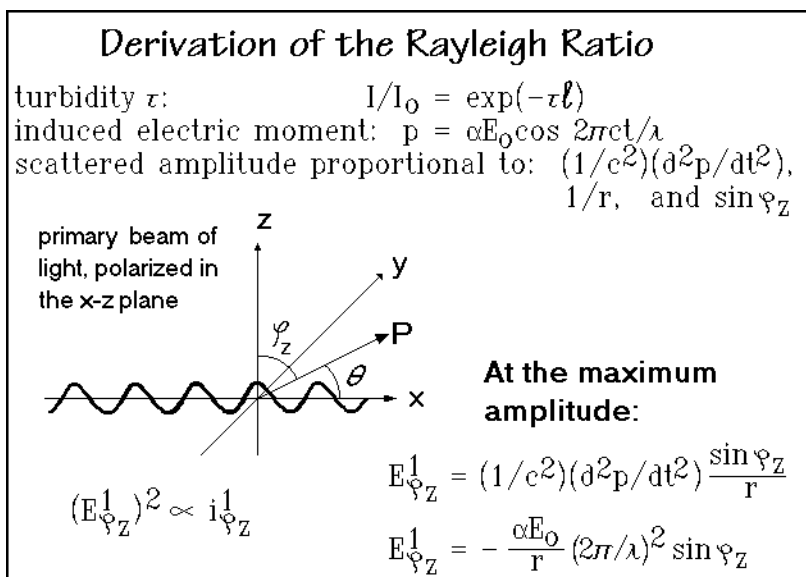


Fig. A.3.2

angle. Equation (1) in Fig. A.3.3 combines the equations of Fig. A.3.2. The analysis of Eq. (1) is drawn in form of a polar diagram of the intensity of the scattered light. The length of each of the lines of the doughnut-shaped, three-dimensional figure indicates the intensity of scattered light in the direction of the line, i.e., the largest intensity is normal to the vibration direction  $z$  of the induced dipole, the smallest is zero, seen along direction  $z$ . All other intensities change as indicated in the figure.

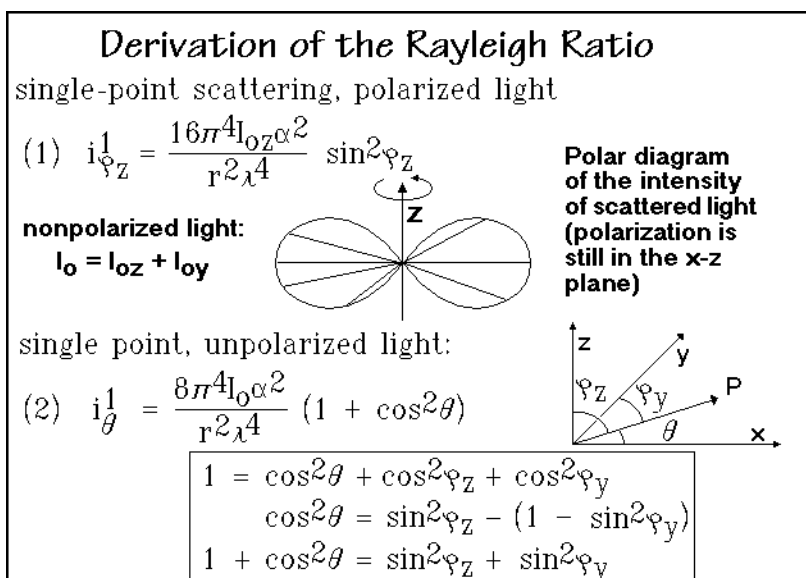


Fig. A.3.3

The change which occurs when going from the scattering of the polarized light, just derived in Eq. (1), to unpolarized light is also shown in Fig. A.3.3 with Eq. (2). The derivation of the equation involves the addition of the scattering intensities from two identical light beams traveling in the same direction, but being polarized at right angles in the  $xz$  and  $xy$  planes. Using the simple relationship  $\sin^2\phi_z - \cos^2\phi_y = \cos^2\theta$  and division by 2, because each polarized component contributes only half the total scattered light, leads from Eq. (1) to Eq. (2).

The final equation adds the intensities from all scattering points (assuming no interference) as shown in Eq. (3) of Fig. A.3.4. The value  $N_2$  is the total number of scattering centers, and  $V$  is the volume in which the scattered light is generated. The last part of Eq. (3) is linked to the experimentally available quantities. The measured quantities and known constants are expressed by introducing the concentration  $c_2$  in  $\text{Mg m}^{-3}$ , Avogadro's number  $N_A = 6.02 \times 10^{23}$ , and the molar mass  $M_2$ . The subscript 2 is used for quantities referring to macromolecules.

To summarize the derivation given so far, Eq. (1) explains already the strong wavelength dependence of the scattered light (fourth power, blue light scatters more than red), indicates that scattering is zero in direction of the  $z$ -axis ( $\sin\phi_z = 0$ ), and shows rotational symmetry about the  $z$ -axis. Next, going from Eq. (1) for the scattering of plane-polarized light to unpolarized light is done with Eq. (2). The addition of the second beam of light for Eq. (2) superimposes an identical symmetry of scattered light about the  $y$ -axis, but with opposite polarization. At  $\theta = 90^\circ$  the angular dependence of Eq. (2) is 1.0 and the scattered light changes in polarization on going from the direction of the  $y$ -axis to the direction of the  $z$ -axis. At  $\theta = 0$  and  $180^\circ$  the last factor of Eq. (2) is 2, its maximum, accounting for the strong forward and reverse scattering. Finally, adding scattered light from all centers leads to Eq. (3). Because one assumed no interference between the different, coherently

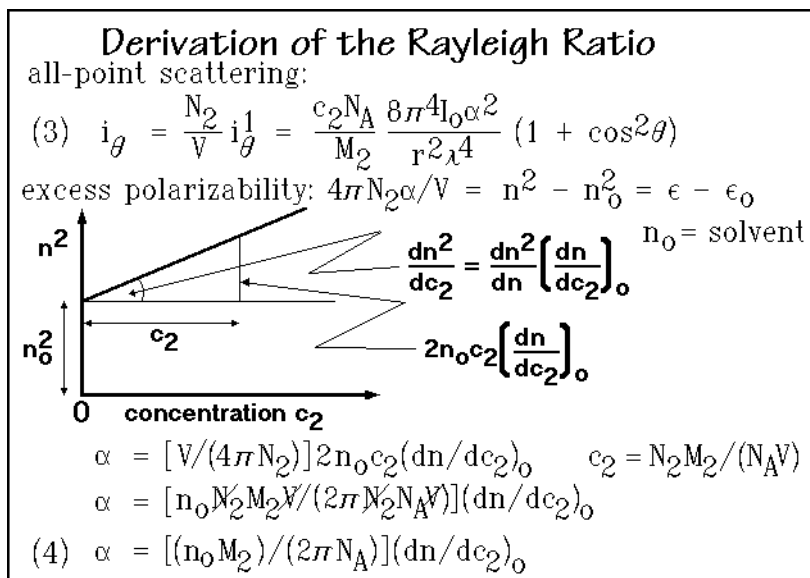


Fig. A.3.4

scattered rays, Eq. (3) is limited to dilute solutions. Experiments at higher concentration have to be extrapolated to infinite dilution.

The next step of interpretation of Eq. (3) is the development of an expression for the excess polarizability,  $\alpha$ , caused by the dissolution of the polymer in the solvent. This is done by remembering that the polarizability at the frequency of light is related to the squares of the refractive index,  $n^2$  (as well as the permittivity, the dielectric constant,  $\epsilon$ ). The connection between  $\alpha$  and  $n$  is written at the top of Fig. A.3.4. Its background can be found in any physical chemistry text. Assuming the square of the refractive index changes linearly with concentration, one can draw the sketch in the figure. The refractive index  $n_0$  refers to the pure solvent, while  $n$  is the refractive index of the solution of concentration  $c_2$ .

The angle and amplitude of the change of the refractive index with concentration can next be changed to a differential expression at concentration zero. Note that at zero concentration  $dn^2/dc_2 = 2n_0(dn/dc_2)_0$  is a quantity that can be measured with a differential refractometer using a series of concentrations of the polymer to be analyzed and extrapolation to concentration zero. Naturally, the solution must change sufficiently in  $n$  with increasing concentration to achieve measurable light scattering. The polarizability  $\alpha$  is needed for the evaluation of Eq. (3). The insertion of the expression for the concentration  $c_2$ , and the final simplification to Eq. (4) is shown at the bottom of Fig. A.3.4.

The insertion of Eq. (4) into Eq. (3) and the simplification of the expression for  $i_\theta$  is indicated at the top of Fig. A.3.5. The Rayleigh ratio of the light which is scattered into the direction  $\theta$  is the main outcome of the present derivation. It is shown at the bottom as Eq. (5). The Rayleigh ratio eliminates the influence of the measuring distance  $r$  and the incident light intensity. Both are instrumental calibration parameters. When all of the constants of the to-be-analyzed system are

### Derivation of the Rayleigh Ratio

$$i_\theta = \frac{c_2 N_A}{M_2} \frac{2\pi^2}{r^2 \lambda^4} \frac{I_0 (n_0 M_2)^2}{(2\pi N_A)^2} (dn/dc_2)_0^2 (1 + \cos^2\theta)$$

Rayleigh Ratio:

$$(5) \quad R_\theta = \frac{i_\theta}{I_0} r^2 = \frac{2\pi^2 n_0^2}{N_A \lambda^4} (dn/dc_2)_0^2 (1 + \cos^2\theta) M_2 c_2$$

$R_\theta = K (1 + \cos^2\theta) M_2 c_2$

Dimensional analysis:  
 $i_\theta/I_0$  is dimensionless  
 $R_\theta = \text{m}^{-1}$  and  $K = \text{m}^2\text{mol/kg}^2$

Fig. A.3.5

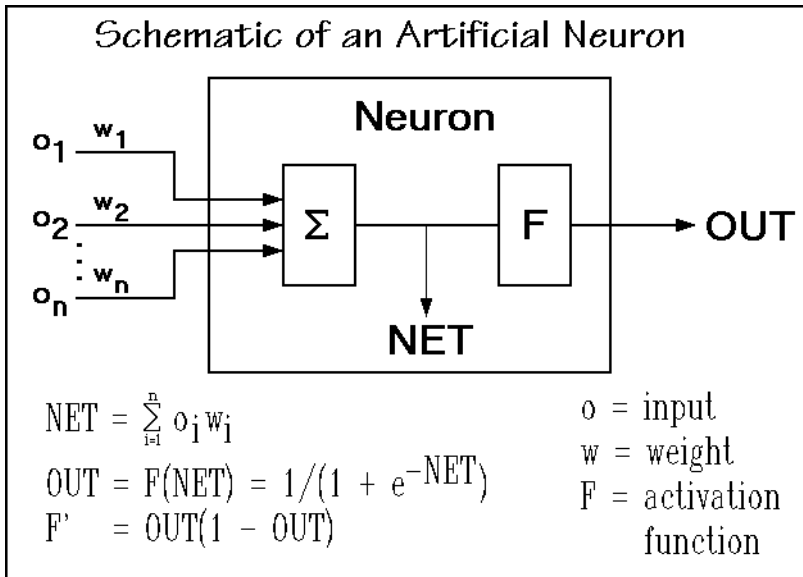
combined into a new constant,  $K$ , the Rayleigh ratio takes on the simple form listed in the box of Fig. A.3.5. Figure 1.56 starts the discussion of the light-scattering experiments in Chap. 1 using the Eq. (5) of Fig. A.3.5. A simple measurement after extrapolation to zero concentration gives the molar mass  $M_2$  looked for. With additional effort, the molecular size, shape, and also the solvent-polymer interaction can be assessed as is shown in Figs. 1.56–61. Similar expressions as given for the Rayleigh ratio just derived for the scattering of light, apply also to all other electromagnetic radiations which are summarized in Fig. 1.51 in Chap. 1. Furthermore, matter-waves such as neutrons and electrons can be similarly treated as the scattering of light. Figure 1.72 contains some additional information about the scattering of neutrons and electrons.

## Neural Network Predictions

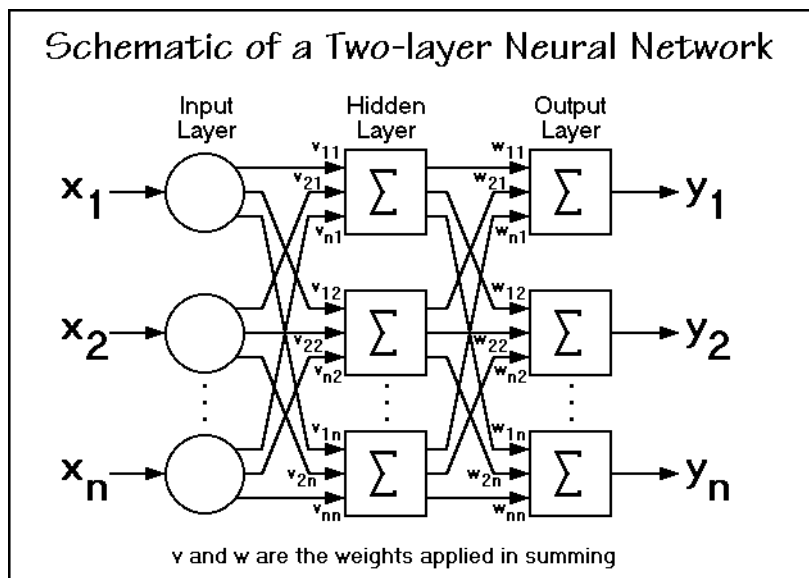
Neural net computation is a technique of data handling that is quickly gaining importance. A neural network can be thought of as a mathematical function with generalized estimation and prediction capabilities. It is a computational system made up of a number of simple, yet highly connected, layered processing elements called nodes or neurons. The neurons process information by their dynamic response to external information.

Neural networks, as the name implies, were originally biologically inspired to perform in a manner analogous to the basic functions of neurons. The network is specified by its architecture, transfer functions, and learning laws. Figure A.4.1 illustrates that the input from the net to a given neuron (NET), is the sum of the inputs,  $o_i$ , each multiplied with its corresponding weight,  $w_i$ . Before the NET is passed on to the subsequent network layers, it is multiplied with a nonlinear transfer function,  $F$ , as indicated in the figure. The architecture of a simple network is given in the Fig. A.4.2. If needed, additional layers can be added to the network, complicating the schematic of the structure.

Before the network can be used, it must undergo a learning step. The network learns in a computation-intensive step by establishing the weights that, when applied to the inputs of the nodes, will yield the required output. Note that the derivative of  $F(\text{NET})$  with respect to the output,  $\text{OUT}$ , is rather simple in the chosen example ( $F'$  in Fig. A.4.1). Since only the learning step of the network takes a considerable amount of computer time, it is possible to have the learning done on a larger and faster computer and transfer the once established weights to a desktop computer for everyday use in one's own and other laboratories. One may also speculate that it may



**Fig. A.4.1**

**Fig. A.4.2**

be possible to have the network learn the contents of a whole data base, such as the ATHAS Data Bank of heat capacities of macromolecules (Sect. 2.3), and predict unknown heat capacities by making use of the collective knowledge gained over the years in many laboratories.

## Legendre Transformations, Maxwell Relations, Linking Entropy and Probability, and Derivation of $dS/dt$

The title topics are represented in the Figs. A.5.1–4, shown below:

### Legendre Transformations

Total differentials of the different thermodynamic functions can be related to each other through the Legendre transformations:

$$df = f_1 dx_1 + f_2 dx_2 + \dots + f_n dx_n$$

where  $f$  is the dependent variable,  $x_1, x_2, \dots, x_n$  are the independent variables, and  $f_i = (\partial f / \partial x_i)_{x_2, \dots, x_n}$ , etc.

Considering the new function:

$$g = f - f_1 x_1$$

one gets on differentiation:

$$dg = df - f_1 dx_1 - x_1 df_1$$

or with the help of the top equation:

$$dg = -x_1 df_1 + f_2 dx_2 + \dots + f_n dx_n$$

i.e., the independent variable  $x_1$  has changed to  $f_1$  and the dependent one from  $f$  to  $g$ .

Applied to  $dU = -pdV + TdS$  the Legendre transformation leads to:

$$H = U - \left( \frac{\partial U}{\partial V} \right)_S V = U + pV, \text{ and}$$

$$dH = Vdp + TdS.$$

Similarly, since  $T = (\partial U / \partial S)_V$  and also  $T = (\partial H / \partial S)_p$ , one can write:

$$F = U - \left( \frac{\partial U}{\partial S} \right)_V S \text{ and } G = H - \left( \frac{\partial H}{\partial S} \right)_p S.$$

This leads to the total differentials:

$$dF = dU - TdS - SdT = -pdV - SdT$$

and:

$$dG = dH - TdS - SdT = Vdp - SdT.$$

Mathematically  $H, F$ , and  $G$  are thus Legendre transformations of the basic function of state  $U(S, V)$ .

**Fig. A.5.1**

### Maxwell Relations

From the differentials derived by the Legendre transformations of the basic equation  $dU = TdS - pdV$ :

$$dH = Vdp + TdS$$

$$dF = -pdV - SdT$$

$$dG = Vdp - SdT,$$

one can obtain, by equating with the partial differential coefficients like:

$$dU = \left( \frac{\partial U}{\partial V} \right)_S dV + \left( \frac{\partial U}{\partial S} \right)_V dS,$$

the following relationships:

$$(\partial U / \partial V)_S = -p \quad (\partial U / \partial S)_V = T$$

$$(\partial H / \partial p)_S = V \quad (\partial H / \partial S)_p = T$$

$$(\partial F / \partial V)_T = -p \quad (\partial F / \partial T)_V = -S$$

$$(\partial G / \partial p)_T = V \quad (\partial G / \partial T)_p = -S.$$

The Maxwell equations derive from the Euler reciprocity relationship:

$$\frac{\partial}{\partial y} \left( \frac{\partial f}{\partial x} \right)_y = \frac{\partial}{\partial x} \left( \frac{\partial f}{\partial y} \right)_x$$

which applies if  $f$  is a function of state and  $x$  and  $y$  are two independent variables.

The following relationships can then easily be written:

$$\left( \frac{\partial T}{\partial V} \right)_S = - \left( \frac{\partial p}{\partial S} \right)_V$$

$$\left( \frac{\partial T}{\partial p} \right)_S = \left( \frac{\partial V}{\partial S} \right)_p$$

$$\left( \frac{\partial p}{\partial T} \right)_V = \left( \frac{\partial S}{\partial V} \right)_T$$

$$\left( \frac{\partial V}{\partial T} \right)_p = - \left( \frac{\partial S}{\partial p} \right)_T$$

**Fig. A.5.2**



### Linking Entropy and Disorder

The easiest way to observe the connection between entropy and disorder is to study ideal gases. First, one defines the disorder as the thermodynamic probability  $W$ , the number of ways a system can be arranged (in contrast to the normally chosen probability that would be a fraction). Next, one notices that  $W$  is multiplicative. The combined probability of systems one and two is  $W = W_1 \times W_2$ . The entropy, in contrast, is extensive, i.e.  $S = S_1 + S_2$ . Any connection between the two must thus be:

$$S = a \ln W + b$$

where  $a$  can be obtained by finding the change of  $S$  on expanding one mole of gas from  $V_1$  to a larger  $V_2$ .

The thermodynamic probability ratio of finding all molecules of the gas ( $N_A$  molecules) in  $V_2$ , rather than in the smaller  $V_1$  is:

$$W_2/W_1 = \left( \frac{V_2}{V_1} \right)^{N_A}$$

The analogous equation for  $\Delta S$  is:

$$\Delta S = S_2 - S_1 = k \ln \left( \frac{V_2}{V_1} \right)^{N_A}$$

where  $k$  is Boltzmann's constant (with  $R = k \times N_A$ ). Comparison of the two equations gives the relationship sought after that was first given by Boltzmann in 1896:

$$\Delta S = k \ln (W_2/W_1)$$

Fig. A.5.3

### Derivation of $(dS/dT)$

Under equilibrium conditions in closed systems ( $dn = 0$ ), the entropy can be written  $dS = dQ/T$  according to Fig. 2.2.6. On insertion of  $TdS$  into the first-law equation for  $dU$  [ $= dQ - pdV$ ] and  $dH$  [ $= dU + pdv + Vdp$ ] one can easily derive the following equations:

$$dU = -pdV + TdS \quad \text{and} \quad dH = Vdp + TdS$$

Since  $U$  and  $H$  are functions of state, one can write:

$$dU = (\partial U/\partial V)_S dV + (\partial U/\partial S)_V dS \quad \text{and} \quad dH = (\partial H/\partial p)_S dp + (\partial H/\partial S)_p dS$$

By comparison of coefficients, one sees that at constant  $V$  and  $n$   $dU/dS$  is  $T$ , and at constant  $p$  and  $n$   $dH/dS$  is  $T$ . Under these conditions  $dU = C_V dT$  and  $dH = C_p dT$ . Integration of  $dS$  from zero (at  $T = 0$ ) to  $S$  (at  $T$ ) gives, then, the to be proven relationships:

$$S = \int_{0K}^T (C_V/T) dT \quad \text{and} \quad S = \int_{0K}^T (C_p/T) dT$$

Fig. A.5.4

## Boltzmann Distribution, Harmonic Vibrations, Complex Numbers, and Normal Modes

The title topics are represented in the Figs. A.6.1–4, shown below:

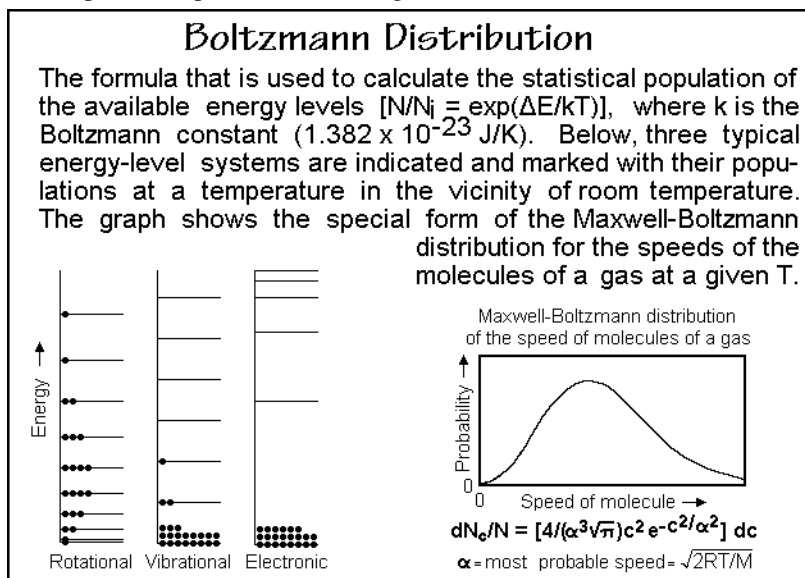


Fig. A.6.1

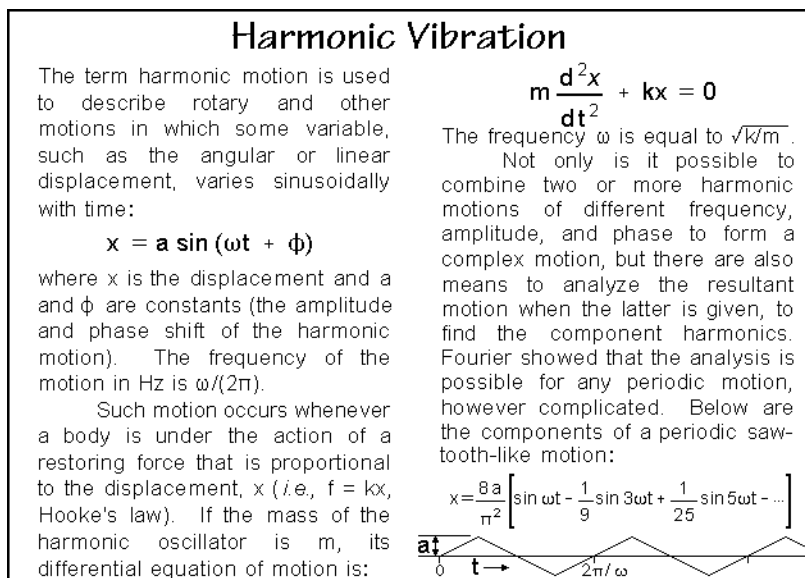


Fig. A.6.2

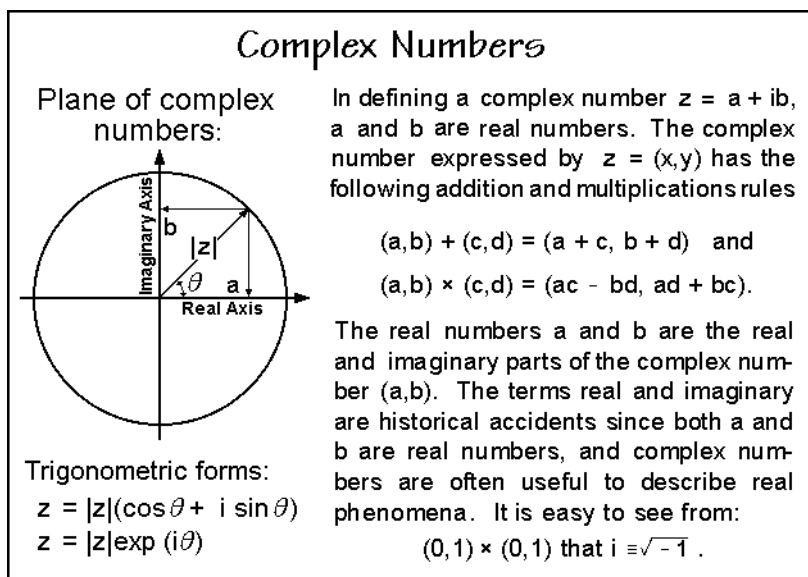


Fig. A.6.3

### Normal Mode Analysis of the Motion of Coupled Vibrators, as Needed for the Computation of Heat Capacities

A mechanical system composed of coupled oscillators, such that each oscillator is subject to an elastic restoring force, can be described when displaced from its equilibrium in terms of normal coordinates  $Q_n$  and normal velocities  $\dot{Q}_n$  with  $n$  representing the degrees of freedom of the system.

The total energy of the system is:

$$U = \sum_{i=1}^n (\alpha_i Q_i^2 + \beta_i \dot{Q}_i^2)$$

with  $\alpha_i$  and  $\beta_i$  representing arbitrary constants, depending only on the initial conditions. The normal coordinates are independent of each other and can be excited while the others remain at rest.

A vibration in which only one normal coordinate is excited is called a **normal mode**. A normal mode of a crystal (designated by vector  $\mathbf{q}$ , index  $n$ , and frequency  $\omega_{\mathbf{q}n}$ ) leads to the displacement of the  $j^{\text{th}}$  atom (in the  $l^{\text{th}}$  unit cell at a position described by the vector  $\mathbf{r}^l$ ) by vector:

$$\mathbf{u}_\mu^l(\mathbf{k}, n) = \text{Re} \{ A_\mu^i(\mathbf{q}, n) e^{i(\mathbf{q} \cdot \mathbf{r}^l - \omega_{\mathbf{q}n} t)} \}$$

where  $\mathbf{u}^l$  is the displacement of the atom from equilibrium and  $\text{Re}$  designates the real part of the expression in  $\{ \}$ . The index  $n$  takes on  $3s$  values corresponding to the  $3s$  branches of the vibrational spectrum, where  $s$  is the number of atoms in the unit cell.

Fig. A.6.4

## Summary of the Basic Kinetics of Chemical Reactions

The title topic is represented in the Figs. A.7.1 and A.7.2, shown below:

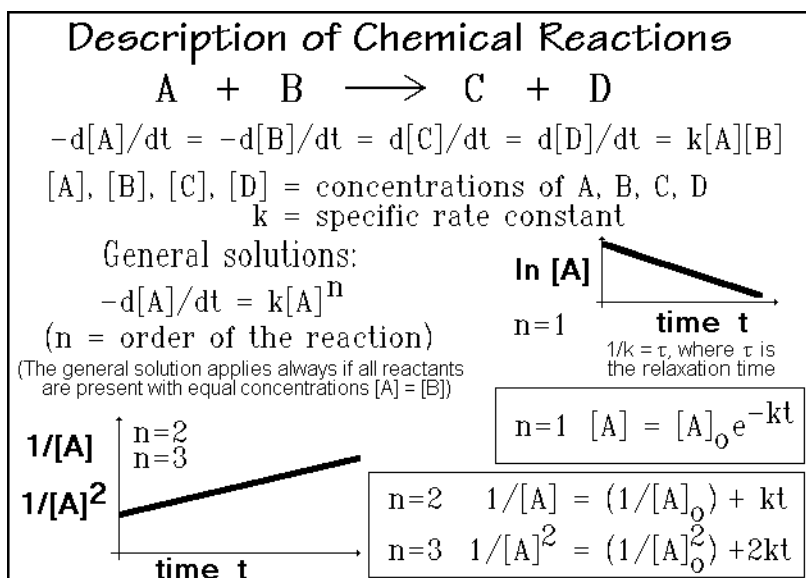


Fig. A.7.1

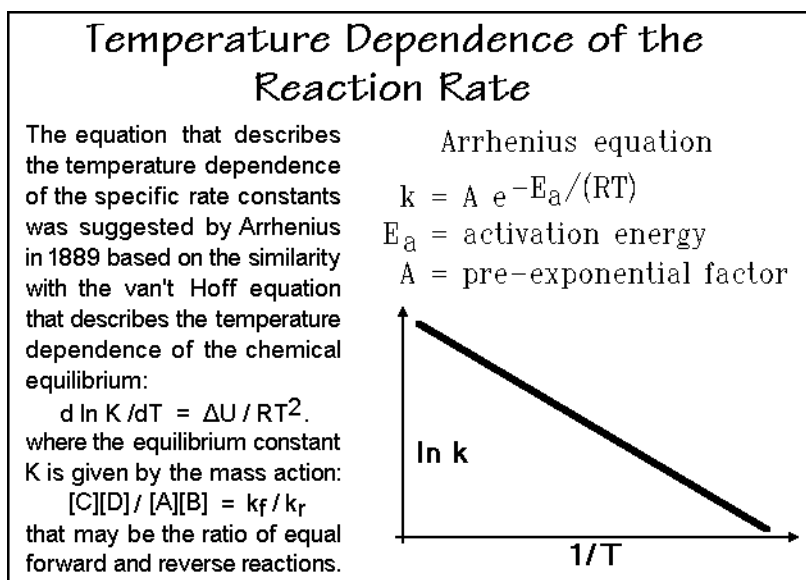


Fig. A.7.2

## The ITS 1990 and the Krypton-86 Length Standard

The thermodynamic or kelvin scale gives an absolute temperature. The origin of the kelvin scale is at absolute zero. To set the size of the subdivision of the scale, one kelvin, there must be one more fixed temperature. International agreement fixes the kelvin scale at the triple point of water, the point of equilibrium between water, ice, and water vapor. This triple point is set to be 273.16 K, about 0.01 K above the freezing point of water at atmospheric pressure.

An internationally agreed upon secondary, empirical temperature scale is described in Fig. A.8.1. It is called the International Temperature Scale of 1990, in short, the ITS 1990 ( $T_{90}$  in kelvin, K;  $t_{90}$  in degrees celsius, °C). It makes use of the higher precision possible with secondary thermometers. The given fixed points have been agreed upon internationally to achieve as close a match to the kelvin scale as possible. The values for the fixed points are to be corrected when better absolute measurements become available. Earlier international temperature scales were accepted in 1927 (ITS 27), 1948 (ITS and IPTS 48), and 1968 (IPTS) (IPTS is the abbreviation for "International Practical Temperature Scale", the second version of the 1948 scale and the 1968 scale).

Besides values for the fixed point temperatures, the ITS 1990 provides also for the maintenance of the temperatures between the given fixed points. The most important temperature range for thermal analysis reaches from about 13 to 1235 K. It is based on the platinum resistance thermometer (see Sect. 4.1.3). The platinum resistance thermometer must be constructed of pure, strain-free platinum.

<b>The International Temperature Scales 1990</b>		
Kelvin Scale: The triple point of water is set at 273.16		
ITS 1990:	$T_{90}(\text{K})$ :	$t_{90}(^{\circ}\text{C})$ :
triple point of $\text{H}_2$ at equilibrium.....	13.8033	-259.3467
triple point of Ne .....	24.5561	-248.5939
triple point of $\text{O}_2$ .....	54.3584	-218.7916
triple point of Ar .....	83.8058	-189.3442
triple point of Hg .....	234.3156	-38.8344
triple point of water .....	273.16	0.01
equilibrium M of Ga .....	302.9146	29.7646
equilibrium F of In .....	429.7485	156.5985
equilibrium F of Sn .....	505.078	231.928
equilibrium F of Zn .....	692.677	419.527
equilibrium F of Al .....	933.473	660.323
equilibrium F of Ag .....	1234.93	961.78
equilibrium F of Au .....	1337.33	1064.18
equilibrium F of Cu .....	1357.77	1084.62

**Fig. A.8.1**

At higher temperatures, monochromatic radiation pyrometers maintain the ITS 90. They can be calibrated at the freezing points of Ag, Au, or Cu. The evaluation is based on Planck's radiation law. At lower temperatures, vapor-pressure-temperature relationships for  $^3\text{He}$  and  $^4\text{He}$  are used.

With the ITS 90, one achieves the ultimate in temperature precision. Thermal analysis is usually far from such precision. Root-mean-square deviations of  $\pm 0.1\text{ K}$  are the typical goals.

***The krypton length standard.*** From the late 18<sup>th</sup> century until the middle of the 20<sup>th</sup> century, the reference meter was a particular bar of alloyed platinum and iridium, stored and protected in a site in Sèvres, outside Paris. Duplicates were kept by the industrialized nations and compared periodically. The meter bar had a cross section shaped like  $\mathbf{H}$ , to resist deformation, and it bore two marks at right angles to its length to indicate the meter. The distance was chosen to represent 1/10,000 of the pole-to-equator distance as closely as possible, to reproduce the 18<sup>th</sup> century definition of the meter. In 1960, the 11<sup>th</sup> General Conference of Weights and Measures chose the reddish-orange krypton-86 emission as the defined meter instead: "The meter is the length equal to 1,650,763.73 wavelengths in a vacuum, corresponding to the transition between the levels  $2p^{10}$  and  $5d^5$  of the krypton-86 atom."

The precision of the Pt/Ir meter was about 1 part in  $10^6$ . The krypton-86 meter can be reproduced in 1 part in  $10^8$ . A remaining drawback of the krypton-86 meter is that the emitted light is not sufficiently coherent to produce measurable interference fringes past 80 cm. Ultimately, lasers with greater coherence should replace the krypton-86 meter.

## Development of Classical DTA to DSC

The principle of heat-flux calorimetry is illustrated with a schematic of a classical DTA in Fig. A.9.1. The reference (Rfc) and sample (Spl) materials have immersed thermocouples for precise temperature measurement. An identical environment with a temperature that increases linearly in time is created by the DTA-furnace and a programmer. The furnace-control thermocouple checks the furnace (block) temperature,  $T_b$ , against the program temperature. Any difference is used to adjust the power to the heater. Additional cooling may be introduced by placing the DTA furnace in a cold bath and regulating the heating. The symmetrically placed Rfc and Spl should have the same heat flux for the same temperature difference from the furnace  $T_b - T_r$  and  $T_b - T_s$ , making the temperature difference,  $\Delta T = T_r - T_s$ , proportional to the differential heat-flow rate, HF. The reference temperature for both thermocouples is provided by an ice bath (see Fig. 4.8). For higher precision one uses an automatic reference cell with Peltier cooling and heating that can establish the triple point of water to better than 0.01 K. Commercial instruments provide internal, electronic reference junctions.

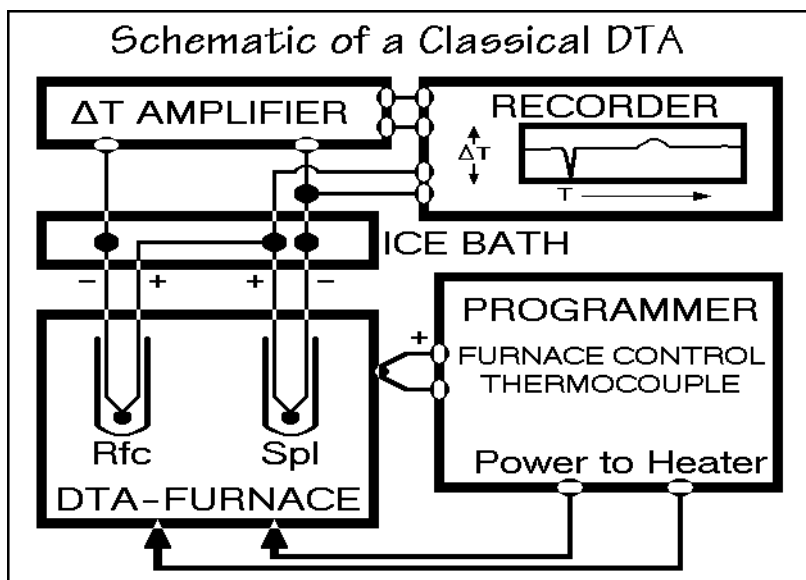
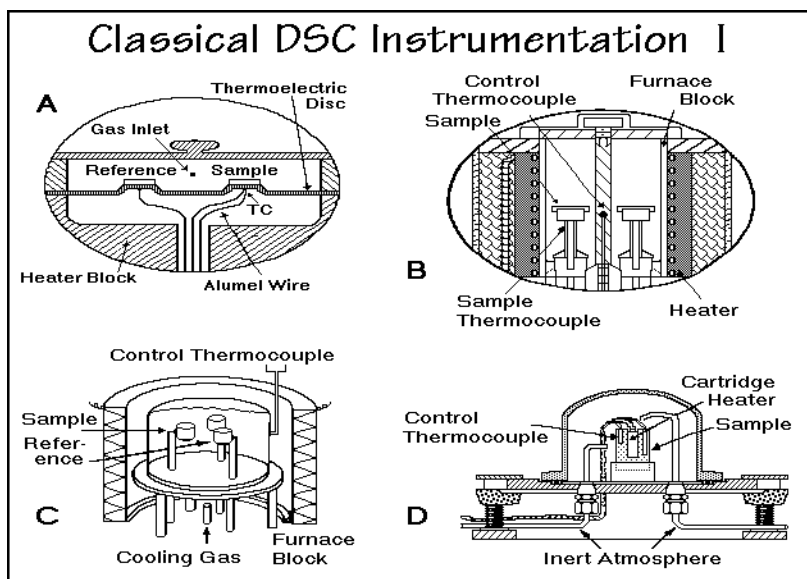


Fig. A.9.1

The thermocouple voltage due to  $\Delta T$  is only 1% or less than the voltage due to the absolute temperatures and must, thus, be preamplified before recording. Both  $\Delta T$  (proportional to heat flow HF), and  $T_s$  are then recorded either directly, as illustrated in Fig. A.9.1, or both are given as a function of time,  $t$ . Whenever the DTA trace can be used for the quantitative evaluation of caloric variables, such as heat capacities and heats of transition, the experiment is called DSC, differential scanning calorimetry. Many traditional DTAs are capable of measuring heat, and thus can be called DSC.

In contrast, one finds many DSCs which are used only for qualitative DTA work on transition temperatures. The often-posed question of the difference between DTA and DSC is therefore easily answered: DTA is the general term covering all differential thermal analysis techniques, while DSC must be reserved for scanning experiments that yield calorimetric information.

Eight schematics of classical DTA instruments of the last 50 years are illustrated in Figs. A.9.2 and 3 (A–H). The sketches are more or less self-explanatory. Sample sizes range from as much as one gram (E) down to a few milligrams (G). The latter is a micro-DTA with the thermocouples serving as sample and reference cups. Equipment (D) and (F) is distinguished from all others by having direct contact between the metal block and the sample and reference holders; i.e., heat is directly



**Fig. A.9.2**

transferred from the metal of the furnace to the sample holder in form of a glass capillary. This design is often thought to be less quantitative, but this does not have to be so, as long as a reproducible thermocouple placement is achieved, or the temperature gradient within the sample is small. In fact, the sample temperature can be determined most precisely in such instruments. An intermediate design is (A), in which much of the conduction of heat goes through a metal bridge as a controlled thermal leak. All other designs rely largely on the surrounding atmosphere for the transfer of heat. The conduction of heat through the atmosphere is, however, difficult to control because of the ever-present convection currents. The compromise (A) of a well-proportioned heat leak has found the widest application in modern DSC design. Figure 4.54 displays an updated version of this DSC and Fig. 4.55 the present, modern heat-flux DSC based on the same heat-flux principle. A number of conditions for good quality thermal analyses have been developed over the years and apply as well for modern scanning calorimetry. A summary is given below.



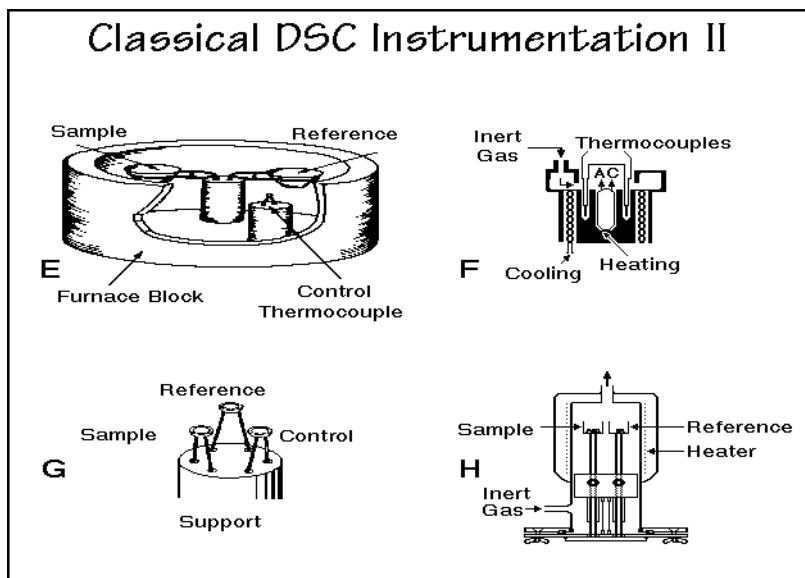


Fig. A.9.3

Typical additional conditions for the design of early DTA instrumentation and its environment are:

1. Smooth and linear furnace temperature change.
2. Draft-free environment, closely regulated room temperature.
3. High-thermal-conductivity furnace (silver, gold, or high-purity Al).
4. Control of conduction, radiation, and eliminate convection.
5. Proper heating and cooling design (direction sample→heater→cooling).

For detailed references to the equipment and design criteria see: Wunderlich B (1971) *Differential Thermal Analysis*. In: Weissberger A, Rossiter BW (1971) *Physical Methods of Chemistry*, Vol I, Part V. Wiley-Interscience, New York.

Based on recommendations of the Committee on Standardization of ICTAC, Fig. 2.5, one should always give the following information which are excerpts with updates published by: Mackenzie RC (1969) *Talanta* 16: 1227; (1972) *ibid.* 19: 1079.

1. Identification of all substances (sample, reference, diluent) by their IUPAC name and formula, empirical name and formula, or equivalent compositional data (see Sect. 1.2).
2. A statement of the source of all substances, details of their histories, pretreatments and chemical purities, for polymers also molar masses and distributions.

3. Measurement of the average rate of linear temperature change over the temperature range involving the phenomena of interest.
4. Identification of the sample atmosphere by pressure, composition, and purity.
5. A statement of the dimensions, geometry, and materials of the sample holder, and furthermore, the method of loading the sample holder and the sample, where applicable.
6. Identification of the abscissa scale in terms of time or of temperature at a specified location.
7. A statement of the methods used to identify intermediates or final products.
8. Faithful reproduction of all original records.
9. Wherever possible, each thermal effect should be identified and supplementary supporting evidence stated.

On DTA traces, the following specific details should be presented:

10. Sample weight and dilution of the sample.
11. Identification of the apparatus, including the geometry and materials of the thermocouples and the locations of the differential and temperature-measuring thermocouples, as well as their calibration.
12. The ordinate scale should indicate deflection in kelvins or heat-flow rate with the exothermic or endothermic direction clearly marked.

## Examples of DTA and DSC under Extreme Conditions

For this summary, forms of thermal analyses under extreme conditions are described for the measurement of heat and temperature, as dealt within Sects. 4.1–4. The distinction between DTA and DSC seen in these methods is described in Appendix 9. In Appendix 10, DTA or DSC at very low and high temperatures and DTA at very high pressures are mentioned. This is followed by a discussion of high-speed thermal analysis which, in some cases, may simply be thermometry. Finally, microcalorimetry is treated. One might expect that these techniques will develop in this century [1]. The numbers in brackets link to references at the end of this appendix.

**Low-temperature DTA and DSC** needs special instrumentation [2]. In Fig. A.10.1 a list of coolants is given which may be used to start a measurement at a low temperature. From about 100 K, standard equipment can be used with liquid nitrogen as coolant. The next step down in temperature requires liquid helium as coolant. A differential, isoperibol, scanning calorimeter has been described for measurements on samples of 10 mg in the 3 to 300 K temperature range [3]. To reach even lower temperatures, especially below 1 K, one needs again another technique [4], but it is

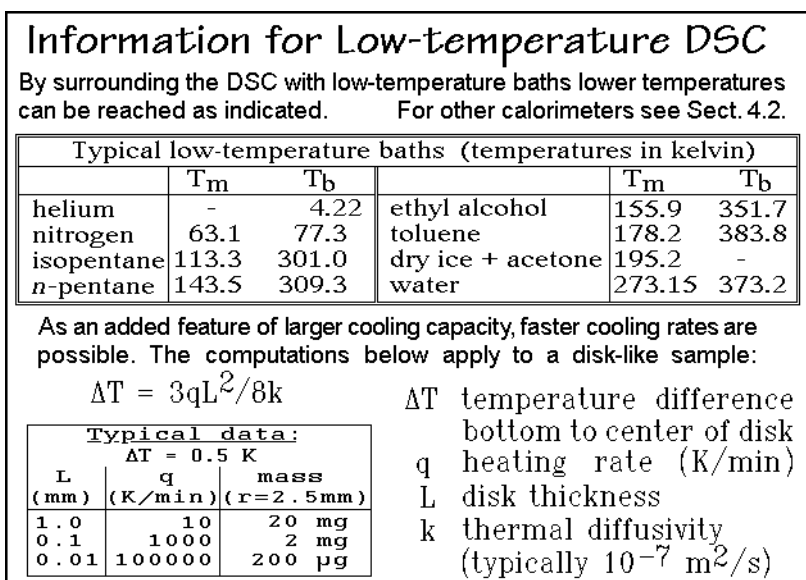


Fig. A.10.1

possible to make thermal measurements even at these temperatures. Usually heat capacities and thermal conductivities are obtained in this temperature range by time-dependent heat leak measurements.

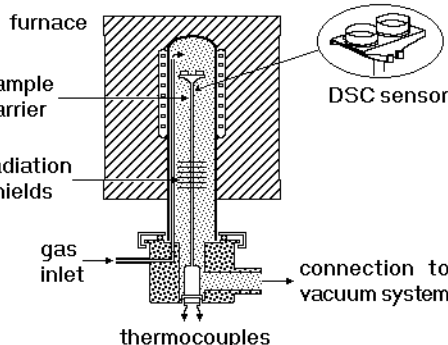
**High temperature and pressure DSC and DTA** needs special materials for the construction of the calorimeter, as is shown in Figs. A.10.2 and A.10.3. At high temperature, the control of heat loss and gain by radiation becomes important, at high pressure the strength and high mass of the enclosure must be considered.

## High-temperature DSC

The schematic on the right illustrates a typical high-temperature DSC. Main differences are the use of high-temperature resistant materials throughout and a more extensive insulation to preserve the isoperibol conditions (Gr.  $\text{ἰσο}$  = equal, and  $\text{περιβολή}$  = enclosure).

With small changes this DSC can also be used for simultaneous thermogravimetry.

## Netzsch DSC 404



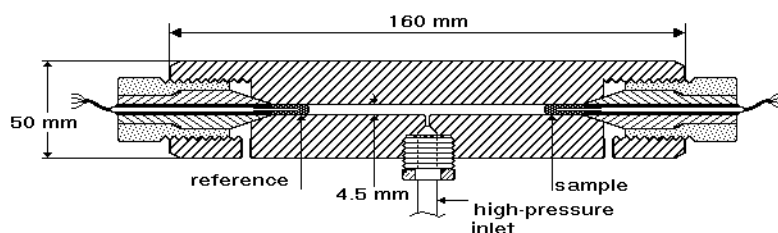
Performance data:  
 110–2700 K  
 0.1–1000 K/min  
 noise  $\pm 6 \mu\text{W}$   
 35–250 mm<sup>3</sup> sample

Fig. A.10.2

## High Pressure Differential Thermal Analysis

High-pressure calorimetry has to solve problems due to the presence of the massive pressure vessel, contact with a pressure medium (oil or a highly compressed gas), and wiring of sensor and heater connections. Note that gases such as N<sub>2</sub> under high pressure are often soluble in polymers. For other instrumentation see also: O. Yamamuro, M. Oguni, T. Matsuo, H. Suga, *Thermochim. Acta*, **121**, 73 (1988).

DTA apparatus usable up to 500 MPa pressure



T. Davidson, B. Wunderlich, *J. Polymer Sci., Part A-2*, **7**, 337 (1969).

Fig. 10.3

The diagram in Fig. A.10.2 displays an instrument based on the classical design of a heat flux DTA (see Appendix 9). With a related design, differential calorimetry and thermogravimetry can be carried out simultaneously. Figure A.10.3 illustrates a typical high-pressure DTA setup which is usable up to 500 MPa of pressure, 5,000 times atmospheric pressure. The pressure is transmitted by a gas, such as nitrogen,

or a liquid, such as silicon oil. Reference and sample are placed around their respective thermocouples inside the high-pressure container. The thermocouple output is recorded for the measurement of temperature and temperature difference. Special safety precautions must be observed when using high-pressure DTA. Particularly, special enclosures must be in place to contain the DTA in case of failure if the pressure-transmitting agent is gaseous or can easily evaporate.

**High-speed thermal analysis** is possible, as shown for example in Fig. 3.95 (see also Sect. 6.2). Many industrial processes are very fast. Spinning of fibers, for example, may be done at rates of 100 to 10,000 m min<sup>-1</sup>. A temperature change of 60 K over a length of 1 m in the thread-line, then, causes rates of temperature change of 6,000–600,000 K min<sup>-1</sup> (100–10,000 K s<sup>-1</sup>). Such heating rates must be compared to times for large-amplitude molecular motion, such as rearrangements of polymer chains by conformational adjustments, described in Sects. 1.3.5–8 and 5.3.4. The conformational motion may have a picosecond timescale (10<sup>-12</sup> s), i.e., in the time the fiber goes through the above temperature gradient, each backbone bond may rearrange billions of times, sufficient to cause intricate changes to various useful structures, particularly when, in addition, strains are imparted on the fiber.

Most DTA and DSC equipment can be adjusted to measure at rates from about 0.1 K min<sup>-1</sup> to perhaps 100 K min<sup>-1</sup>. With some modification, changes of sample size and altering of heater size, etc., this can be brought to a range of 0.01 K min<sup>-1</sup> to 1,000 K min<sup>-1</sup>. One can cover in this way five orders of magnitude in heating rates. Even faster DTA needs special considerations. Permitting a temperature gradient of  $\pm 0.5$  K in a disc-like sample, the equation in Fig. A.10.1 can be used to calculate the maximum sample dimensions for given cooling or heating rates (see also Figs. 4.65 and 4.66). Obviously the limit of fast-heating DTA has not been reached. Just dipping samples in cooling baths or heating baths can produce rates up to 10,000 K min<sup>-1</sup> with reasonable control [5].

A unique solution to fast DTA is the foil calorimeter, shown schematically in Fig. A.10.4. A copper-foil is folded in such a way that two sheets of the sample (also very thin, so that the mass remains small) can be placed between them. The copper foil is used as the carrier of electrical current for fast heating. Between the inner portion of the stack of copper foil and sample, a thin copper–constantan thermocouple is placed. Only three folds of the stack are shown. In reality, many more folds make up the stack so that there are no heat losses from the interior and measurements can be made under adiabatic conditions. Heating rates of up to 30,000 K min<sup>-1</sup> (500 K s<sup>-1</sup>) have been accomplished. Measured is temperature, time, and the-rate-of-change of temperature for a given heat input. With such fast heating rates it becomes possible to study unstable compounds by measuring faster than the decomposition kinetics of the compound. This super-fast calorimeter has seen little application, likely because it requires a new calorimeter for each sample.

A more recent step to speed up DSC was taken in connection with a commercial power-compensation DSC (High Performance DSC) [6] and is now available as HyperDSC® from the Perkin-Elmer Inc. It is claimed to reach 500 K min<sup>-1</sup>. For a pan of a diameter of 5 mm, the heating rates calculated in Fig. A.10.1 corresponds to sample masses of 20, 2, and 0.2 mg, showing that it is the heating and cooling capacity of the DSC that limits fast calorimetry, not the properties of the sample.

### Foil Calorimeter for Fast Measurement

To speed-up calorimetry, sample sizes must be reduced, as estimated in the discussion of low-temperature calorimetry. Microgram samples can easily be heated with 10,000 K/min. The foil calorimeter, below, is a unique instrument.

#### Foil Calorimeter

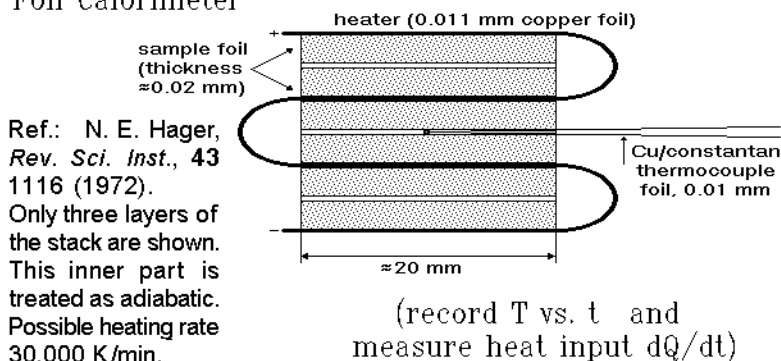


**Fig. A.10.4**

To accomplish and exceed the fast calorimetry just suggested, one can turn to integrated circuit calorimetry. The measuring methods may be modulated calorimetry, such as AC calorimetry or the  $3\omega$ -method [7,8], thin-film calorimetry as shown in Fig. A.10.4, or may involve standard heating or cooling curves as well as DSC configurations as illustrated in Chap. 4. Modern versions of such fast heating calorimeters are based on silicon-chip technology for measuring heat flow using thermopiles integrated in the chip and resistors for heating. Increasingly more numerous chips have become available based on free-standing membranes of  $\text{SiN}_x$ , produced by etching the center of a properly coated Si-chip, as illustrated in Figs. A.10.5 and A.10.6, which contain each a schematic of the calorimeter.

Figure A.10.5 illustrates the performance of several integrated circuit thermopiles, ICT, by Xensor Integration. The calibration without sample shows a constant output voltage of the sensor, decreasing at higher frequency, depending on the membrane used. The phase-angle response shows an analogous change at higher frequency. A linearity-check revealed that dynamic heat capacity measurements should be possible over the frequency range of 1 mHz to 100 Hz, compared to the 0.1 Hz limit typical for TMDSC of Sect. 4.4. This allows to analyze nanogram samples deposited from solution on the position shown in Fig. A.10.5. Similar chips for the measurements of heat capacity of samples of below 1 mg, contained in small aluminum pans, showed time resolutions well below 1 s when using heat-pulses [9].

Finally, Fig. A.10.6 illustrates the change in the crystallization rate when going from slow cooling, measured by standard DSC, to fast standard DSC, and to, ultimately, a chip calorimeter with  $5,000 \text{ K s}^{-1}$  ( $300,000 \text{ K min}^{-1}$ ) [10]. The cooling rates were varied over five orders of magnitude by using different calorimeters. The cooling rates in the figure from right to left are: for 4 mg in a standard DSC, 0.02, 0.03, 0.08, 0.2, and  $0.3 \text{ K s}^{-1}$ ; for 0.4 mg in a fast DSC: 0.3, 0.8, 3, and  $8 \text{ K s}^{-1}$ ; for

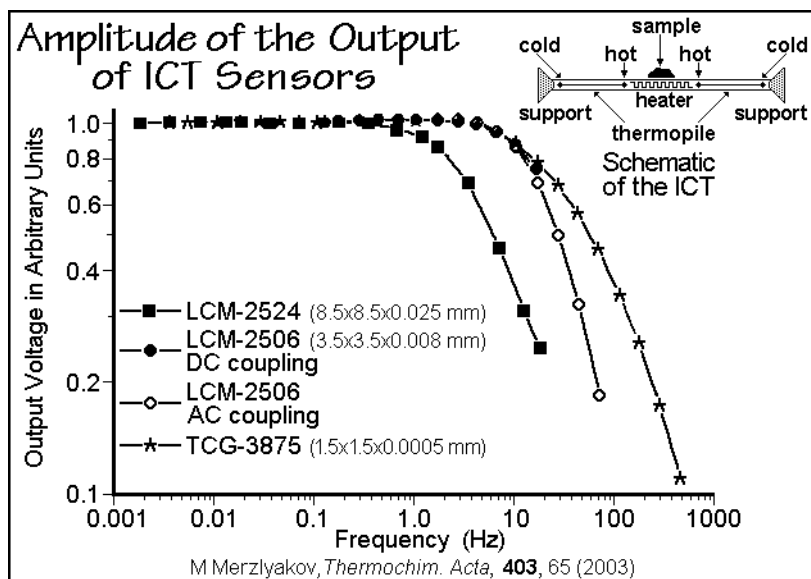


Fig. A.10.5

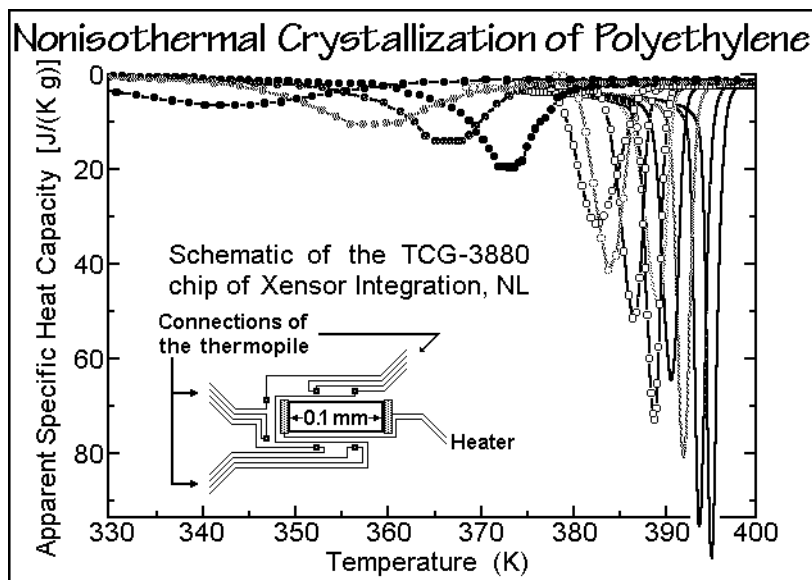
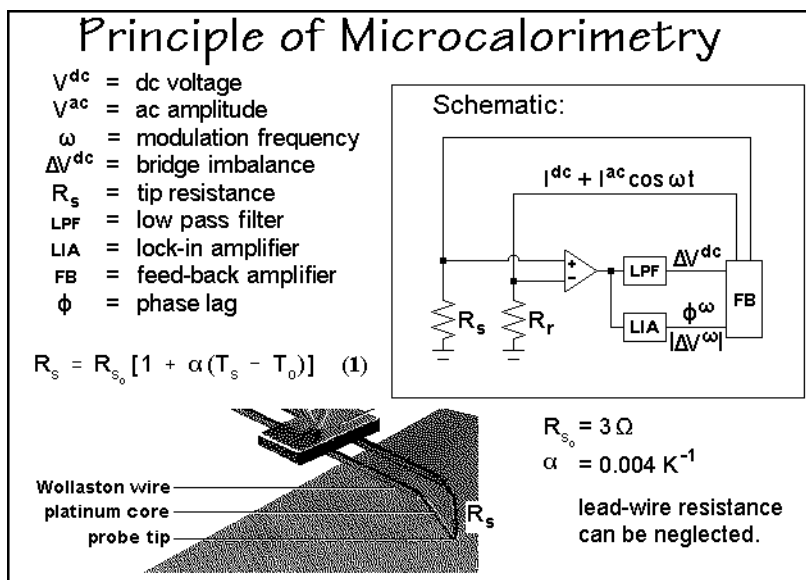


Fig. A.10.6

0.1  $\mu\text{g}$  in an IC calorimeter as shown in the sketch: 0.45, 0.9, 2.4, and 5  $\text{kK s}^{-1}$ . In this chip-calorimeter, the  $\text{SiN}_x$  film, supported by the Si-chip frame was about 500 nm thick. The cooling was achieved by overcompensating the heater power with a cooled purge gas. The heating experiments could also be used to study the reorganization, as discussed in Sect. 6.2.

**The principle of microcalorimetry** is illustrated with Fig. A.10.7 ( $\mu$ TA™ of TA Instruments, Inc.). The tip of an atomic force microscope, AFM, is replaced by a Pt-wire that can be heated and modulated, as is illustrated in detail with Fig. 3.96. A typical resolution is about 1.0  $\mu\text{m}$  with heating rates up to 1,000  $\text{K min}^{-1}$ . A temperature precision of  $\pm 3$  K and a modulation frequency up to 100 kHz has been reached. The figure shows the control circuit for localized thermal analysis. In this case the probe contacts the surface at a fixed location with a programmed force, controlled by the piezoelectric feedback of the AFM. A reference probe is attached next to the sample probe with its tip not contacting the sample, allowing for



**Fig. A.10.7**

differential measurements. Equal dc currents are applied to both probes and are controlled by the temperature-feedback circuit to achieve a constant heating rate. The temperature of the sample,  $T_s$ , can be determined, after calibration from the resistance of the probe. Since the resistance of platinum has an almost linear dependence on temperature between 300 and 600 K,  $R_s$  can be expressed as shown in Fig. A.10.7, where  $R_{s_0}$  and  $\alpha$  are the resistance and the temperature coefficient of the platinum wire at  $T_0$ . The resistance of all lead wires and the heavy Wollaston-portion of the sensor are neglected. Their resistance is small when compared to the V-shaped platinum tip. In addition to the dc current, an ac current can be superimposed on the tip to obtain a temperature-modulation. The dc difference of power between the sample and reference probes is determined by measuring the dc voltage difference between two probes after low-pass filtering (LPF) and the ac voltage difference is measured by the lock-in amplifier (LIA). This arrangement permits an easy deconvolution of the underlying, dc and the reversing ac effects (see also Sect. 4.4). An example which illustrates a qualitative local thermal analysis with a microcalorimeter is given in Fig. 3.97, the limits were probed in [12].



## References for Appendix 10

1. Wunderlich B (2000) Temperature-modulated Calorimetry in the 21<sup>st</sup> Century. *Thermochim Acta* 355: 43–57.
2. White GK (1979) *Experimental Techniques in Low Temperature Physics*. Clarendon, Oxford, 3<sup>rd</sup> edn.
3. Gmelin E (1987) Low-temperature Calorimetry: A particular Branch of Thermal Analysis. *Thermochim Acta* 110: 183–208.
4. Lounasma OV (1974) *Experimental Principles and Methods below 1 K*. Academic Press, London; see also Bailey CA, ed (1971) *Advanced Cryogenics*. Plenum Press, New York.
5. Wu ZQ, Dann VL, Cheng SZD, Wunderlich B (1988) Fast DSC Applied to the Crystallization of Polypropylene. *J Thermal Anal* 34: 105–114.
6. Pijpers TFJ, Mathot VBF, Goderis B, Scherrenberg RL, van der Vegte EW (2002) High-speed Calorimetry for the Study of the Kinetics of (De)vitrification, Crystallization, and Melting of Macromolecules. *Macromolecules* 35: 3601–3613.
7. Jeong Y-H (2001) Modern Calorimetry: Going Beyond Tradition. *Thermochim. Acta* 377: 1–7.
8. Jung DH, Moon IK, Jeong Y-H (2003) Differential 3 $\omega$  Calorimeter. *Thermochim. Acta* 403: 83–88.
9. Winter W, Höhne WH (2003) Chip-calorimeter for Small Samples. *Thermochim. Acta* 403: 43–53.
10. Adamovsky SA, Minakov AA, Schick C (1003) *Thermochim. Acta* 403: 55–63. Figure modified from a presentation at the 8<sup>th</sup> Lahnwitz Seminar of 2004, courtesy of Dr. C. Schick.
11. Moon I, Androsch R, Chen W, Wunderlich B (2000) The Principles of Micro-thermal Analysis and its Application to the Study of Macromolecules. *J Thermal Anal and Calorimetry* 59: 187–203.
12. Buzin AI, Kamasa P, Pyda M, Wunderlich B (2002) Application of Wollaston Wire Probe for Quantitative Thermal Analysis, *Thermochim Acta*, 381, 9–18.

## Description of an Online Correction of the Heat-flow Rate

A basic analysis of the heat-flow rate in a DSC was derived in Sect. 4.3.6 with Figs. 4.69 and 4.70. To use these equations, special baseline calibrations are necessary, as illustrated in Fig. 2.29. With the development of data analysis by computer, it has become possible to make a number of corrections online, i.e., during the run. The Tzero™ method is the first of such programs [1]. Figure A.11.1 illustrates a conventional DSC baseline over an extensive temperature range of 450 K. Considerable improvement arises from the correction with the Tzero™ method before recording the data. The main correction concerns the asymmetry of the instrumentation which is not likely to change from run to run. An initial calibration sets the instrument parameters and leads to such a much improved performance. In this appendix the Tzero™ method of TA Instruments will be summarized [2].

To analyze the instrument performance, the DSC shown in Fig. 4.54 is used. Note that in the literature cited to this appendix the used quantities are represented by different symbols than used here [2,3]. The furnace or block temperature  $T_b$  is called often  $T_o$  (hence Tzero™ method). The heat-flow rate called  $dQ/dt = \Phi$  is called  $\dot{q}$  in [2], and should not to be confused with the here used rate of temperature change  $dT/dt = q$ . The temperature difference used in Chap. 4 and maintained here is written as  $\Delta T = T_r - T_s$ , a positive quantity on heating of a sample run versus an empty pan, giving a positive differential heat flow into the sample. (In [2,3], in contrast,  $\Delta T$  is set equal to  $T_s - T_r$ , making  $\Phi$  proportional to  $-\Delta T$ ).

Next, the true sample and reference temperatures which determine the actual heat-flow rates into the sample and reference pans are computed by modeling the DSC of Fig. 4.54 by an electric circuit which behaves analogously, as described in [4], for

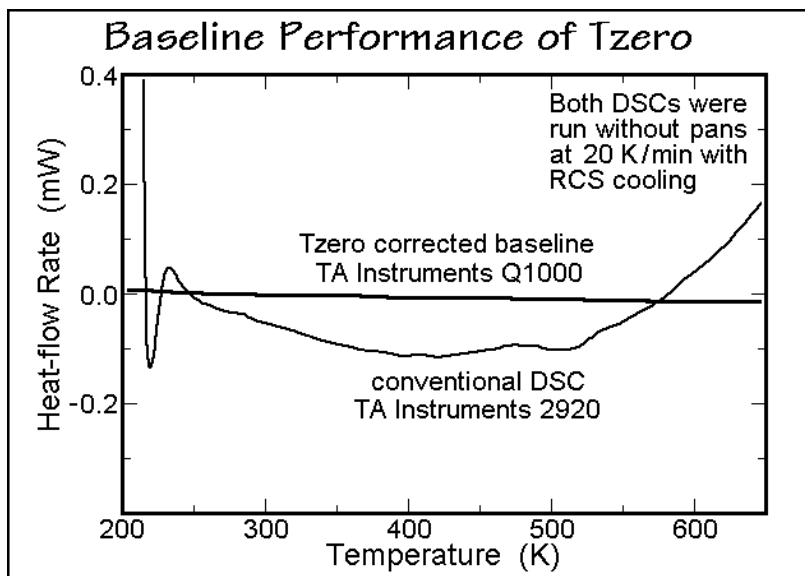


Fig. A.11.1

example. The thermal resistances are equated to electrical resistances and the heat capacities with capacitors. The heat-flow rates are then given by electrical currents calculated from Ohms law and lead to similar answers as in Figs. 4.64–72.

In the sketch A of Fig. A.11.2 the equivalent electrical circuit for a conventional DSC measurement is drawn. The heat-flow rate into the sample calorimeter (pan + sample) is represented by  $\Phi_s$ , and  $\Phi_r$  is the heat-flow rate into the empty pan which is the reference calorimeter. The heat-flow rate into the sample itself should then be  $\Phi = \Phi_s - \Phi_r$  and matches Eq. (3) of Fig. 4.69 when assuming the thermal resistances from the furnace to the measured temperatures are equal ( $R_{spl} = R_{rpl} = R$ ):

$$\Phi = \frac{T_r - T_s}{R} = \frac{\Delta T}{R} \quad (1)$$

Including also the heat capacities of the sample and reference platforms,  $C_{spl}$  and  $C_{rpl}$ , into the model leads to the bottom sketch in Fig. A.11.2. The heat-flow rate into the sample needs now a four-term heat-flow-equation making use of a second temperature difference  $\Delta T_b = T_s - T_b$  besides  $\Delta T = T_r - T_s$ :

$$\Phi = \frac{\Delta T}{R_{rpl}} + \Delta T_b \left( \frac{1}{R_{spl}} - \frac{1}{R_{rpl}} \right) + (C_{rpl} - C_{spl})q_s + C_r \frac{d\Delta T}{dt} \quad (2)$$

The second and third terms express the imbalance of the thermal resistances and heat capacities outside the calorimeters. The fourth term, the effect of different heating rates between reference and sample calorimeter. This last term is of importance when a transition occurs in the sample and does not follow the assumptions made for Figs. 4.71 and 4.72 [3]. (Note the differences to [2] from changed symbols and signs,  $\Phi = \dot{q}$ ,  $\Delta T = -\Delta T$ ,  $\Delta T_b = \Delta T_b$ ,  $q_s = dT_s/dt$ , as well as from expanded subscripts).

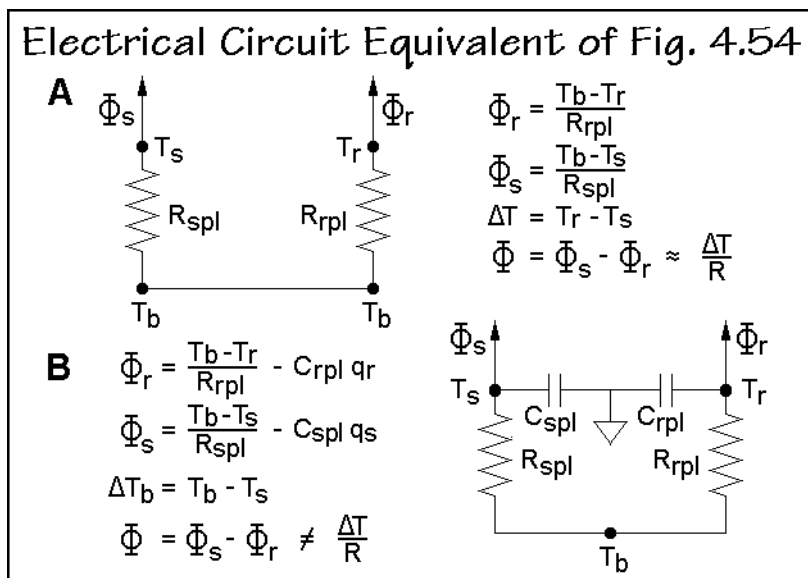
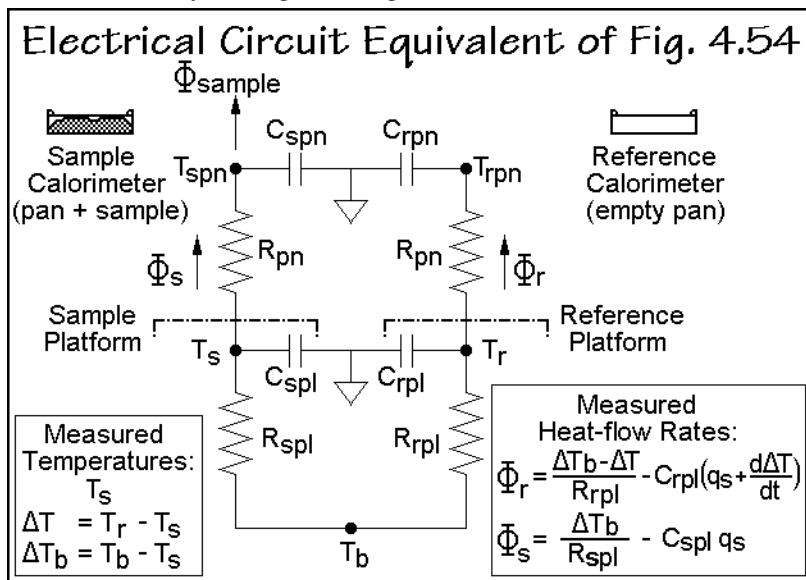


Fig. A.11.2

The use of the corrections B in Fig. A.11.2 needs two calibration runs of the DSC of Fig. 4.54. The heat capacities of the calorimeter platforms,  $C_{spl}$  and  $C_{rpl}$ , and the resistances to the constantan body,  $R_{spl}$  and  $R_{rpl}$ , must be evaluated as a function of temperature. First, the DSC is run without the calorimeters, next a run is done with sapphire disks on the sample and reference platforms without calorimeter pans. From the empty run one sets a zero heat-flow rate for  $\Phi_s$  and  $\Phi_r$ . This allows to calculate the temperature-dependent time constants of the DSC, written as  $\tau_s = C_{spl}R_{spl}$  and  $\tau_r = C_{rpl}R_{rpl}$ , and calculated from the equations in the lower part of Fig. A.11.2. For the second run, the heat-flow rates are those into the sapphire disks, known to be  $mc_p q$ , as suggested in Figs. 4.54 and 4.70. The heat-capacity-correction terms are zero in this second calibration because no pans were used. From these four equations, all four platform constants can be evaluated and the DSC calibrated.

As the next step, the effect of the pans must be considered. The differences between sample and reference pan cause similar heat-flow problems as the platforms and can be assessed by the diagram of Fig. A.11.3. The dash-dotted lines indicate the



**Fig. A.11.3**

sample and reference platforms from which  $\Phi_s$  and  $\Phi_r$ , contained in Eq. (3), enter into the calorimeters. The heat-flow rate into the sample,  $\Phi_{\text{sample}}$ , however, is modified by the heat resistance between pan and platform,  $R_{pn}$ , and the heat capacity of the pan  $C_{spn}$ . The actual sample temperature inside the calorimeter pan, in turn, is not  $T_s$ , but the temperature  $T_{spn}$ . For the reference side, one assumes the same thermal resistance  $R_{pn}$ , but because of the possibly different mass of the reference pan, a different  $C_{rpn}$ . Assuming further that the reference calorimeter is empty, as is the usual operation procedure, there is no  $\Phi_{\text{reference}}$ .

Using the two measured temperature differences  $\Delta T$  and  $\Delta T_b$  listed in Fig. A.11.3 and inserting them into the heat-flow rate expressions of sketch B of Fig. A.11.2 yields the two heat-flow rates of Fig. A.11.3 and their difference, expressed in

Eq. (2), above. To obtain the actual heat-flow rate into the sample,  $\Phi_{\text{sample}}$ , one has to compute the heat-flow rates into the two pans. Since both pans are out of the same material  $C_{\text{spn}} = m_{\text{spn}} c_{\text{pan}}$  and  $C_{\text{rpn}} = m_{\text{rpn}} c_{\text{pan}}$ , where  $c_{\text{pan}}$  is the specific heat capacity of the pan material and  $m$  represents the corresponding mass. Since all  $\Phi_r$  goes into the empty pan, one can use its value to compute  $\Phi_{\text{sample}}$ :

$$\Phi_{\text{sample}} = \Phi_s - \Phi_r \left( \frac{m_{\text{spn}} (dT_{\text{spn}}/dt)}{m_{\text{rpn}} (dT_{\text{rpn}}/dt)} \right) \quad (3)$$

Insertion of the measured values for  $\Phi_s$  and  $\Phi_r$ , contained in Fig. A.11.3, leads to an overall equation for  $\Phi_{\text{sample}}$ . The needed sample and reference pan temperatures in Eq. (3) can be calculated with some simple assumptions about the contact resistance between pan and platform  $R_{\text{pn}}$  [2]:  $T_{\text{spn}} = T_s - \Phi_s R_{\text{pn}}$  and  $T_{\text{rpn}} = T_r - \Phi_r R_{\text{pn}}$ . The commercial software includes typical values derived from data given in [5], considering geometry, purge gas, and pan construction.

To summarize, the correction for asymmetry of the measuring platforms in Fig. 4.54 due to their thermal resistances and their heat capacities with Eq. (3) eliminates the main effect of the baseline curvature with temperature, as is shown in Fig. A.11.1. Further corrections include the mass differences of the pans and the thermal resistance between calorimeters and measuring platforms.

Remaining problems are the temperature gradients within the sample and their changes on heating or cooling, deformations of the sample pan and the accompanying changes in contact resistances which occur when samples expand or shrink. Also, the position of the calorimeters should be fixed and must not be altered during measurement, as can happen by vibrations or mechanical shocks. Changes of heat transfer due to radiation can be caused by fingerprints on calorimeters, platforms, and furnace cavity since fingerprints are easily converted at high temperatures to carbon specks with higher emissivity and absorptivity. Once cleaned, it is helpful to use dust-free and clean nylon gloves and to touch the calorimeters with tweezers only. The purge gas must not change in flux and pressure from the calibration and must not develop turbulent flow or convection currents. Finally, the room temperature must not fluctuate and set up changing temperature gradients within the DSC. Avoidance of all these potential errors is basic to good calorimetry.

## References to Appendix 11:

1. Waguespack L, Blaine RL (2001) Design of A New DSC Cell with Tzero™ Technology. Proc 29<sup>th</sup> NATAS Conf in St. Louis, MO, Sept 24–26, Kociba KJ, Kociba BJ, eds 29: 721–727.
2. Danley RL (2003) New Heat-flux DSC Measurement Technique. *Thermochim Acta* 395:201–208.
3. Höhne G, Hemminger W, Flammersheim HJ (2003) *Differential Scanning Calorimetry*, 2<sup>nd</sup> edn. Springer, Berlin.
4. Holman JP (1976) *Heat Transfer*, 4<sup>th</sup> edn. McGraw-Hill, New York, pp 97–102.
5. Madhusudana CV (1996) *Thermal Contact Conductance*. Springer, New York.

## Derivation of the Heat-flow-rate Equations

The heat flow across any surface area,  $A$ , is given in Fig. A.12.1 by the heat-flow rate per unit area  $dQ/(A dt)$  in Eq. (1), a vector quantity in  $\text{J m}^{-2}\text{s}^{-1}$ . It is equal to the negative of the thermal conductivity,  $\kappa$  in  $\text{J m}^{-1}\text{s}^{-1}\text{K}^{-1}$ , multiplied by the temperature gradient ( $dT/dr$ ). Equation (2) represents the differential heat flow into the volume

<p style="text-align: center;"><b>Fourier Equation of Heat Flow</b></p> <p style="text-align: center;"><u>Heat flow across a surface:</u></p> <p>(1) <math>\left(\frac{d\vec{Q}}{A dt}\right) = -\kappa \text{ grad } T</math></p> <p style="margin-left: 40px;">heat flow across the surface <math>A</math> [in <math>\text{J}/(\text{m}^2\text{s})</math>]  <math>A</math> = area, <math>\kappa</math> = thermal conductivity [<math>\text{J}/(\text{m s K})</math>]  <math>\text{grad } T = dT/dr</math> (vector, magnitude in <math>\text{K/m}</math>)</p> <p>(2) <math>dQ = V \rho c_p dT</math></p> <p style="margin-left: 40px;">heat flow into the volume <math>V</math> (in <math>\text{J}</math>)</p> <p>(3) <math>dT/dt = k \nabla^2 T</math></p> <p style="margin-left: 40px;">Fourier equation of heat flow (in <math>\text{K/s}</math>)  <math>k</math> = thermal diffusivity = <math>\kappa/(\rho c_p)</math> in <math>\text{m}^2/\text{s}</math>  <math>\nabla^2</math> = Laplacian operator,  in one dimension  <math>\nabla^2 T = d^2T/dr^2</math></p>
--

**Fig. A.12.1**

$V$  and can be derived from the definition of the heat capacity  $dQ/dT = mc_p$ . The symbols have the standard meanings;  $\rho$  is the density and  $c_p$ , the specific heat capacity per unit mass, so that  $m = V\rho$ .

Standard techniques of vector analysis allow to equate the heat flow into the volume  $V$  to the heat flow across its surface. This operation leads to the linear and homogeneous Fourier differential equation of heat flow, given as Eq. (3). The letter  $k$  represents the thermal diffusivity in  $\text{m}^2 \text{s}^{-1}$ , which is equal to the thermal conductivity  $\kappa$  divided by the density and specific heat capacity. The Laplacian operator is  $\nabla^2 = \partial^2/\partial x^2 + \partial^2/\partial y^2 + \partial^2/\partial z^2$ , where  $x$ ,  $y$ , and  $z$  are the space coordinates. In the present cylindrical symmetry, the Laplacian, operating on temperature  $T$ , can be represented as  $d^2T/dr^2$  reducing the equation to one dimension. Equations (1)–(3) form the basis for the further mathematical treatment of differential thermal analysis, as is given, for example by Ozawa T (1966) Bull. Chem. Soc. Japan 39: 2071.

The superposition principle is obeyed by the solutions of Eq. (3), i.e., the combined effect of a number of causes acting together is the sum of the effects of the causes acting separately. This allows the description of phase transitions by evaluating several separate solutions and adding them, as suggested in Fig. A.12.2. For a modeling of the glass transition in a DSC with  $R_i = 4$  mm, see Fig. A.12.3.

### Solution for the Approach to Steady State

Since the Fourier Equation (3) is a linear and homogeneous differential equation, one can write:

$$(4) \quad T = T_1 + T_2 + T_3 \quad \begin{array}{l} T_1 = \text{steady state, Eq. (4) Fig. 4.65} \\ T_2, T_3 = \text{initial and final transients} \end{array}$$

The solution of Eq. (3) starting at  $T = 0$  at  $t = 0$  is:

$$T_2 = \frac{qR_i^2}{4k_s} [1.108e^{-5.783k_s t/R_i^2} - 0.140e^{-30.47k_s t/R_i^2} + \dots]$$

approximating  $T = T_1 + T_2$  at  $r = 0$  with Eq. (4) for  $T_1$  gives:

$$(5) \quad T = qt - \frac{qR_i^2}{4k_s} (1 - e^{-5.78k_s t/R_i^2}) \quad (\text{exponential approach to steady state})$$

and on stopping at  $t = t'$ ,  $T = T_1 + T_2$  becomes:

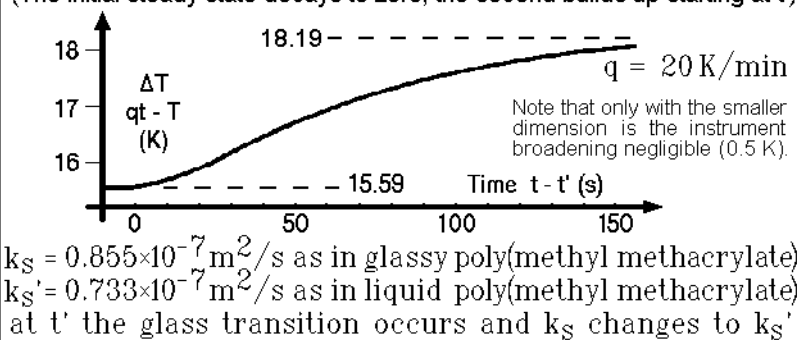
$$(6) \quad T = qt' - \frac{qR_i^2}{4k_s} e^{-5.78k_s t'/R_i^2} \quad (t^* = t - t') \quad (\text{exponential approach to constant } qt')$$

Fig. A.12.2

Initially one finds the steady state of the glass with Eq. (4) of Fig. 6.65. At time  $t'$  the heat flux into the glass stops and it approaches the constant temperature  $T = qt' [= T_1(R_i) \text{ at } t']$  with the transient  $T_2$  of Eq. (6), but at the same time  $t'$  there also begins a new transient,  $T_3$ , for the liquid which reaches the new steady state at time  $\infty$ , as described by Eq. (5) with  $t = t^*$ . Note, that  $k_s$  refers to the thermal diffusivity of the glass, and  $k_s'$  to that of the liquid.

### Application to Model the Glass Transition

Example: Effect of a glass transition on the steady state of a DSC trace. (The initial steady state decays to zero, the second builds up starting at  $t'$ )



$$T = qt - \frac{qR_i^2}{4k_s} e^{-5.78k_s (t-t')/R_i^2} - \frac{qR_i^2}{4k_s'} (1 - e^{-5.78k_s' (t-t')/R_i^2})$$

For  $R_i = 0.4 \text{ mm}$ , multiply abscissa and ordinate by 0.01!

Fig. A.12.3

In this Appendix a number of applications of sawtooth modulations are described with modeling and actual results, starting with the sawtooth modulation by utilizing a standard DSC and analysis without Fourier analysis, followed by the analysis of the sawtooth-modulation data after fitting to a Fourier series. Such temperature modulation can be done with any standard DSC which can be programed for a series of consecutive heating and cooling steps.

**Sawtooth Modulation**  
with an Underlying Heating Rate of 1 K/min

The graph plots Temperature Change ( $T - T_0$ ) (K) on the y-axis (0.0 to 3.0) against Time (min) on the x-axis (0 to 2.0). A solid line represents the modulation, which is a sawtooth wave with a period of 1.0 min and a peak change of 3.0 K. Dashed lines represent the underlying heating rates: 4 K/min, -2 K/min, 1 K/min, and -3 K/min. A horizontal dotted line is at  $T_1$  and a horizontal solid line is at  $T_0$ .

underlying temperature increase by  $1.0 \text{ K min}^{-1}$  and the reversing change by  $\pm 3 \text{ K min}^{-1}$ . Within each cycle, the upper and lower limits of the heat-flow rates,  $\text{HF}_h$  and  $\text{HF}_c$  (proportional to the temperature differences  $\Delta T$ ), are read from the measured temperature-difference response, shown in the lower graph of Fig. A.13.2 for an idealized, instantaneously reacting calorimeter and a sample without latent heat contributions. The response  $\text{HF}(t)$  is represented by the heavy line, jumping from zero to the heating response in heat-flow rate,  $\text{HF}_h$ , to the cooling response  $\text{HF}_c$ . If the response were not instantaneous, one would have had to wait until the steady states were reached and then extrapolate the steady-state response back to the beginnings of the heating and cooling segments to produce a result similar to the one shown in Fig. A.13.2. For a heat capacity that changes linearly with temperature, the analysis shown next is still possible for the slow response, but a nonlinear change in heat capacity would destroy the stationarity. The reversible heat-flow rate can be



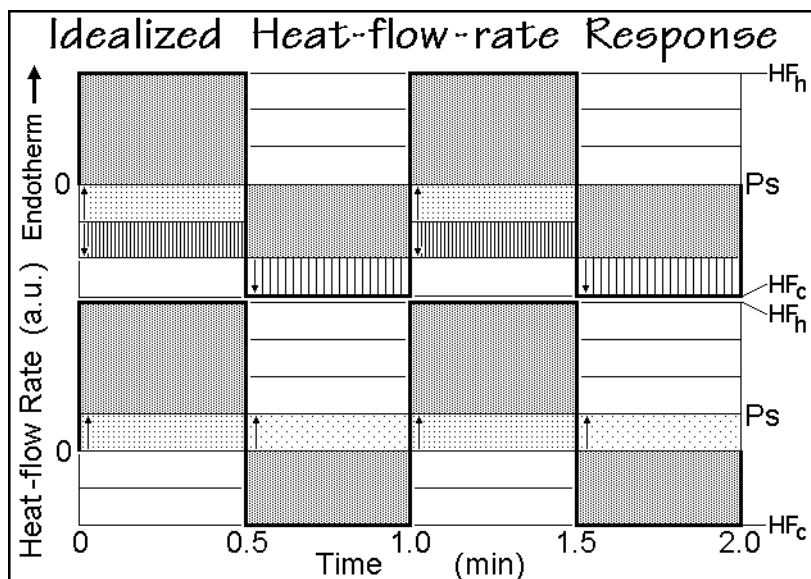


Fig. A.13.2

deconvoluted by subtracting  $\langle HF(t) \rangle$  from  $HF(t)$  as shown in the lower graph of Fig. A.13.2. During the heating segment, the lightly, vertically dotted area, is part of the positive heat-flow rate  $HF_h$ . During the cooling segment, the underlying portion of the lightly diagonally dotted area is opposite in direction and must be added to  $HF_c$  to define the raised pseudo-isothermal baseline level ( $Ps$ ).

Next, a constant, irreversible thermal process with a latent heat is added to the modulation cycles, as is found on cold crystallization of PET (see Figs. 4.74 and 4.136–139). A latent heat does not change the temperatures of Fig. A.13.1, so that the heat-flow rates need to be modified, as is shown in the upper graph of Fig. A.13.2. The constant latent heat is indicated by the vertically shaded blocks and is chosen to compensate the effect of the underlying heating rate, so that the level of  $Ps$  is moved to zero. The reversing specific heat capacity is given by:

$$mc_{p,rev} = (HF_h - HF_c) / (q_h - q_c) \quad (1)$$

Note that under the linearity condition of thermal response,  $HF$  is positive (endothermic) on heating and negative (exothermic) on cooling. Analogously, the rates of temperature change  $q_h$  and  $q_c$  change their sign on going from heating to cooling.

In TMDSC the nonreversing contribution can only be assessed indirectly by subtracting the reversing  $C_p$  from the total  $C_p$ , or by an analysis in the time domain. Any error in the reversing or total heat capacity will be transferred to the nonreversing heat capacity. The analysis using the standard DSC method, however, allows a direct measurement of the nonreversing effect by determining the difference in the heat capacities on heating and cooling at steady state. This quantity is called the imbalance in heat capacity, and can be written as:

$$mc_{p,imbalance} = (HF_h/q_h) - (HF_c/q_c) \quad (2)$$

The irreversible heat-flow rate is calculated from Eq. (2) by separating  $HF_h$  and  $HF_c$  into their reversible, underlying, and irreversible parts for heating and cooling. Assuming linear response among the heat-flow rates, caused by the true heat capacity and a constant, irreversible heat-flow rate, one can derive the following equation:

$$HF_{\text{irreversible}} = mc_{p,\text{imbalance}} / [(1/q_h) - (1/q_c)] \quad (3)$$

The cold crystallization of PET was analyzed by running the series of quasi-isothermal experiments at 388 K and evaluated as shown in Fig. A.13.3. The reversing  $C_p$  (●) decreases, as expected from the lower  $C_p$  of the crystallized sample. The same decrease can be calculated from the integral of the total heat-flow rate over

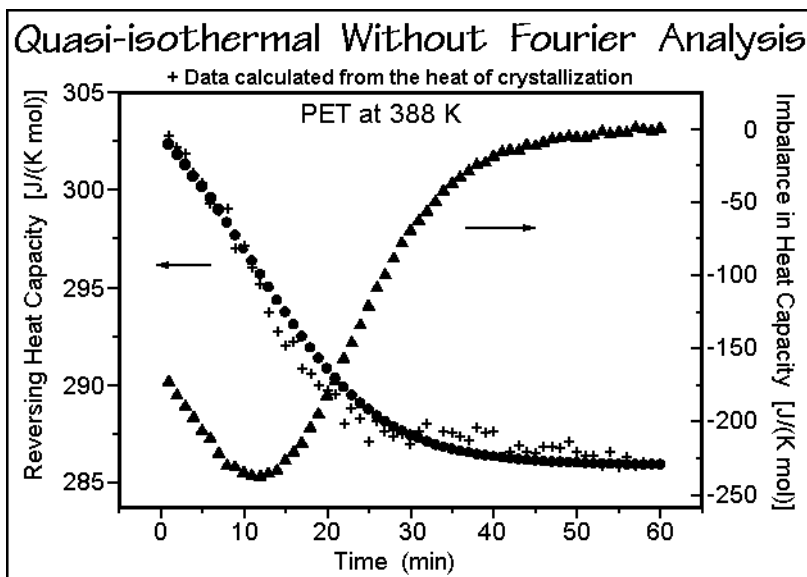


Fig. A.13.3

time, the latent heat, and used to estimate the heat capacity as sum of contributions of amorphous and crystalline fractions (+). As expected, both data sets agree, but the reversing heat capacity has smaller fluctuations. The imbalance in  $C_p$  (▲) is calculated from Eq. (3). It is a measure of the kinetics of the cold crystallization by assessing the evolution of the latent heat. It speeds up until about 12 min into the quasi-isothermal experiment, and then slows to completion at about 60 min.

An example of modulation cycles of PET at 450.8 K (before major melting) and 512.2 K (at the melting peak) is displayed in Fig. A.13.4. The measurements at 450.8 K reach steady state on both, heating and cooling, the ones at 512.2 K, only on cooling. On heating at 512.2 K, the heating is interrupted at 0.5 min by the cooling cycle, but melting continues from (a) to (b) despite of the beginning of cooling. Comparing the heat-flow rates to the data taken at 450.8 K allows an approximate separation of the melting, as marked by the shadings. Comparing the heating and cooling segments suggests an approximate equivalence of (b) and (c), so that the

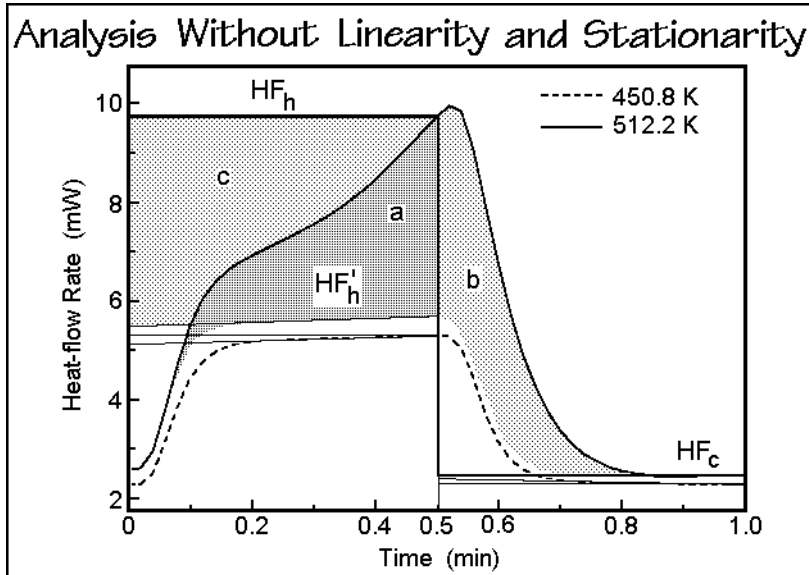


Fig. A.13.4

marked  $HF_h$  accounts for practically all irreversible melting ( $a + b$ ) and the reversible heat capacity. The cooling segment when represented by  $HF_c$ , contains almost no latent heat, and similarly, the heat-flow rate  $HF'_h$  is a measure of the heat-flow rate on heating without latent heat.

Turning to the analyses of periodic functions, such as the modulated heat-flow rate  $HF(t)$ , using Fourier series, one can find in any mathematics text the derivation of the following recursion formula [2]:

$$HF(t) = b_0 + \sum_{v=1}^{\infty} \left[ a_v \sin \frac{2\pi v}{p} t + b_v \cos \frac{2\pi v}{p} t \right] \quad (4)$$

where  $v$  is a running integer starting from 1, and the constant  $b_0$  and the maximum amplitudes  $a_v$  and  $b_v$  are given by:

$$b_0 = \frac{1}{p} \int_{-p/2}^{+p/2} HF(t) dt \quad (5)$$

$$a_v = \frac{1}{2p} \int_{-p/2}^{+p/2} HF(t) \sin \left( \frac{2\pi v}{p} t \right) dt \quad b_v = \frac{1}{2p} \int_{-p/2}^{+p/2} HF(t) \cos \left( \frac{2\pi v}{p} t \right) dt \quad (6)$$

The data deconvolution for  $v = 1$  starts with the evaluation of  $b_0$ , equal to the total heat-flow rate,  $\langle HF(t) \rangle$ , and is completed with determination of  $a_1 = 2\langle HF_{\sin}(t) \rangle$  and the value of  $b_1 = 2\langle HF_{\cos}(t) \rangle$ , the first harmonic terms of the Fourier series described in Sect. 4.4.3. A sinusoidal curve has no further terms in Eq. (4). Higher harmonics need to be considered if the sliding average  $b_0$  is not constant over the modulation

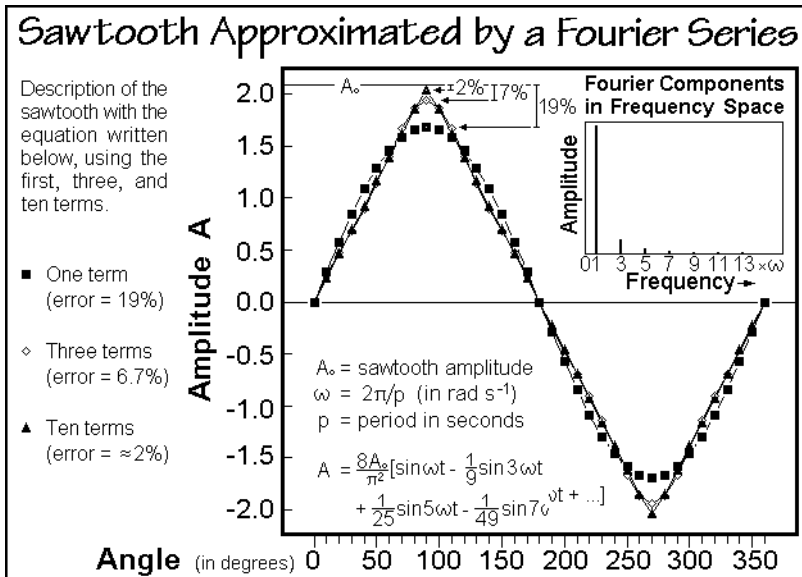


Fig. A.13.5

period (loss of stationarity) or if the frequency is not constant. The Fourier series for a sawtooth which is symmetric about  $\langle q \rangle t$  is given in Fig. A.13.5.

Figure A.16.6 illustrates the attainment of steady state after the beginning of sawtooth modulation and on changing from a heating to a cooling segment. Based on these equations, the following curves are computed for Figs. A.13.7–10 by using the same conditions as in the equations shown in Figs. 4.67 and 4.68.

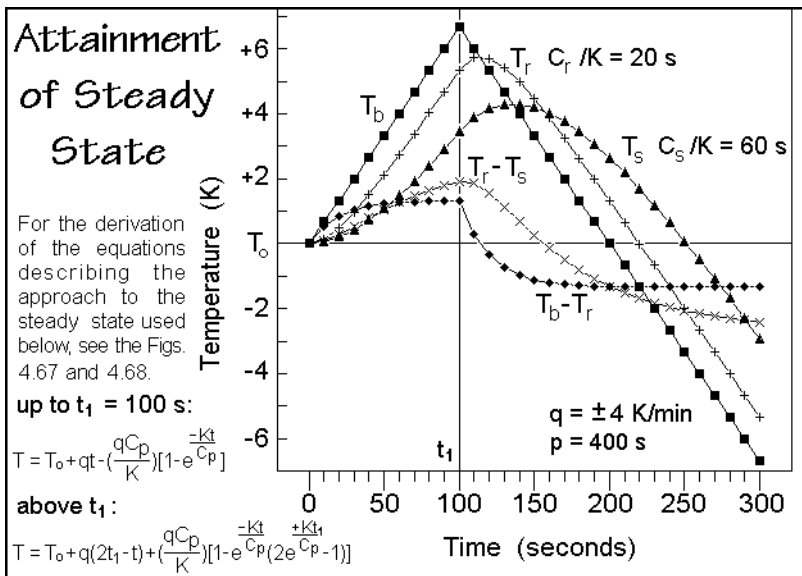


Fig. A.13.6

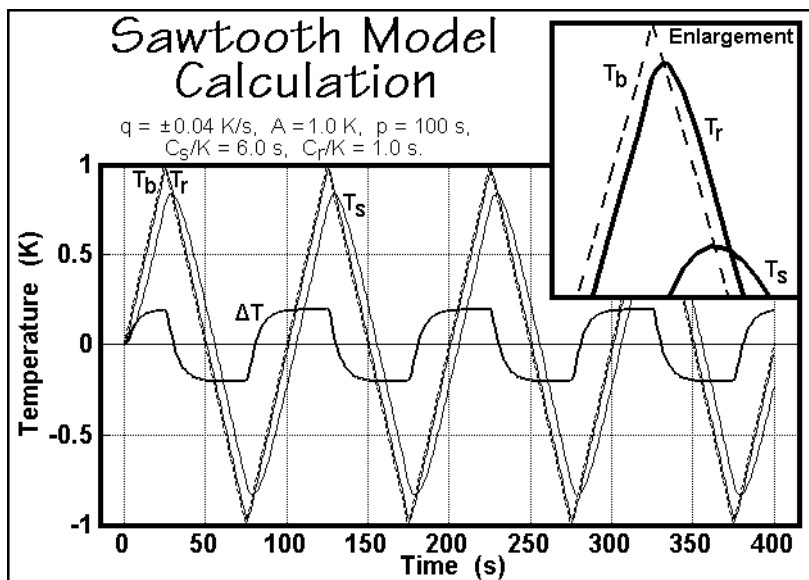


Fig. A.13.7

Figure A.13.7 illustrates the temperature modulation and resulting heat-flow rate,  $\Delta T$ , for a case that reaches steady state before changing the direction of the change in temperature, similar to the case of Fig. A.13.4 at 450.8 K. Figure A.13.8 illustrates the case that steady state is not reached. Figures A.13.9 and A.13.10 show enlarged graphs of  $\Delta T$  and their various harmonic components.

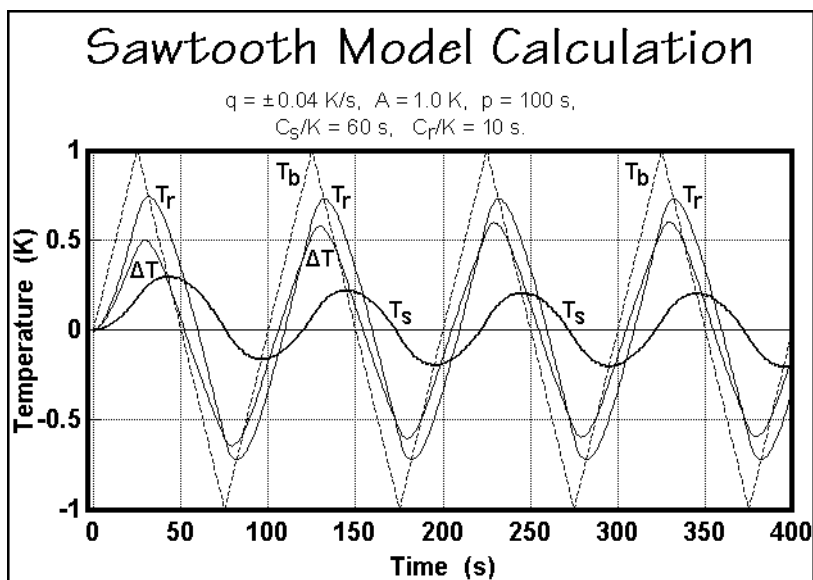


Fig. A.13.8

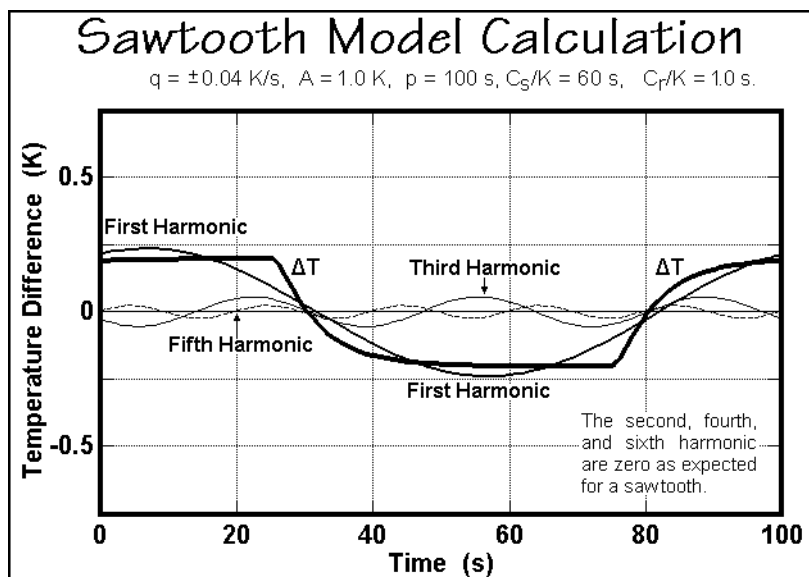


Fig. A.13.9

The data calculated from Figs. A.13.7 and A.13.9 by the standard DSC method given in Fig. 4.54, using the response after steady state has been reached at the end of each cycle give the proper heat capacity, as listed in Table A.13.1, below. The data from Figs. A.13.8 and A.13.10 cannot be analyzed in this way since in this case, steady state is never reached. For Figs. A.13.8 and A.13.10 the evaluation methods illustrated with Figs. 4.54 and 4.92 for the frequency of the first harmonic must be

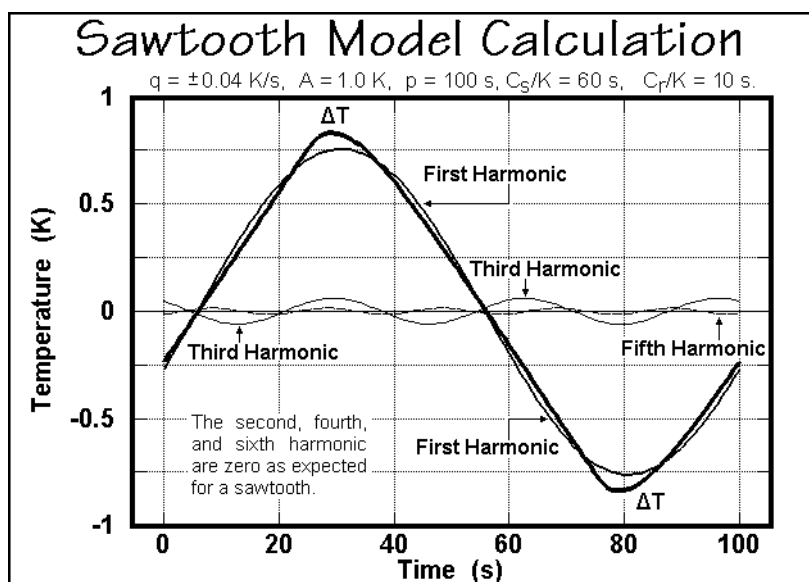


Fig. A.13.10

considered. Doing so, the last column in the table shows that, again, the proper answer is obtained for the first harmonic as long as stationarity is preserved. Every higher harmonic will under the chosen conditions also give the correct results.

Table A.13.1

Results of the Calculation of Heat Capacity				
Figures:	$C_s/K - C_r/K$	Standard DSC	Deviation (%)	TMDSC
A.13.7 and 9	$6 - 1 = 5$	4.997	-0.06	5.00
A.13.8 and 10	$60 - 10 = 50$	14.916	-70.2	50.00

**Footnote to the table:** The heat capacities  $C_s$  and  $C_r$ , when divided by the Newton's Law constant  $K$ , are given in seconds, s; the linear heating and cooling rates of the sawtooth  $q$  are  $0.04 \text{ K s}^{-1}$ ; the temperature amplitude set for the sawtooth,  $A$ , is  $\pm 1.0 \text{ K}$ ; the period  $p$  is  $100 \text{ s}$ ; the frequency  $\omega = 2\pi/p = 0.062832 \text{ rad s}^{-1}$ ; at the time  $t = 0$ :  $T_s = T_r = T_0$ ;  $C_p(\text{standard DSC})/K = \Delta T/q$ . The calculation for the first harmonic gives:  $C_p(\text{TMDSC})/K = [A_s/(A\omega)] \times [1 + (C_s\omega/K)^2]^{1/2}$ ; the total length of analysis is  $400 \text{ s}$ , one point is calculated every second; for the standard DSC,  $\Delta T$  is taken at the maximum or at the steady state of  $\Delta T/K$ ; for the quasi-isothermal TMDSC the last 100 points of the first harmonic of the maximum modulation amplitude were averaged (the 4<sup>th</sup> modulation cycle in Figs. A.13.7 and 8).

The next five figures show experimental results on the melting of pentacontane,  $C_{50}H_{102}$ , a paraffin which melts practically reversibly [3]. Figure A.13.11 illustrates the comparison of a standard DSC trace and a quasi-isothermal analysis with a

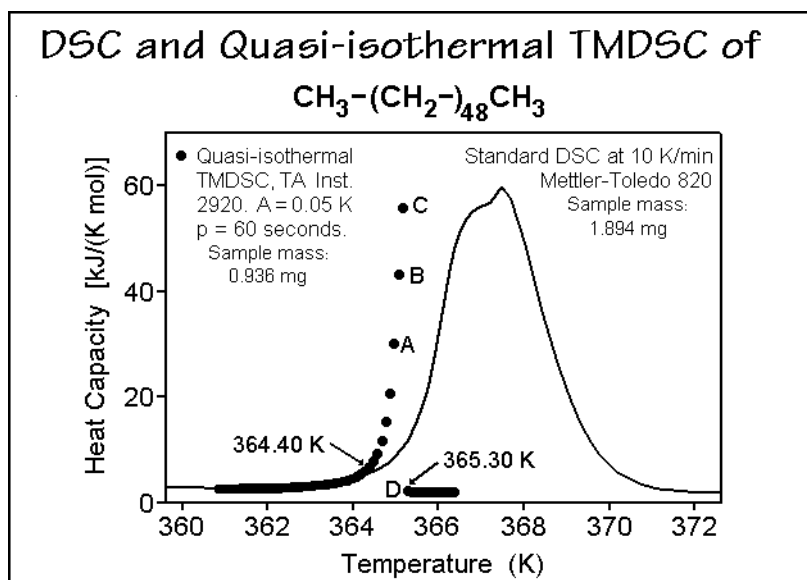


Fig. A.13.11

$\pm 0.05$  K sinusoidal modulation amplitude. The main part of the melting of  $C_{50}H_{102}$  is clearly reversible. The standard DSC shows the expected broadening in the melting peak due to the lag of the instrument. The extrapolated onset of the melting temperature, as defined for the standard DSC in Fig. 4.62, agrees with point D of the quasi-isothermal TMDSC. Lissajous figures of the heat-flow rate plotted versus the sample temperature in Fig. A.13.12 for points A to D indicates that the final heat of fusion is too large for complete melting in one modulation cycle, as was also seen for the reversibly melting indium in Fig. 4.109, 4.134 and 4.135. At point A in Figs. A.13.11 and A.13.12 the reversing heat-flow rate is already considerably larger

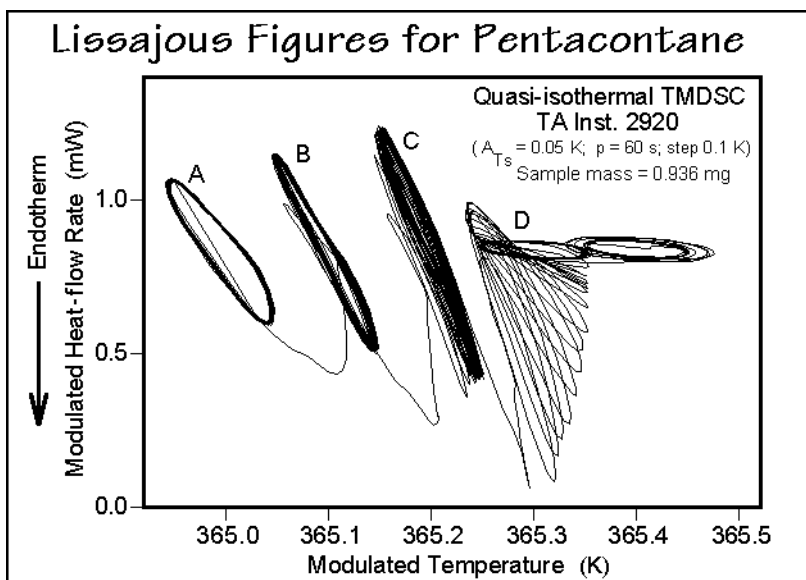


Fig. A.13.12

than expected for the crystals as can be judged from the Lissajous figure for the melt at the highest temperature indicated. The deviation from a perfect ellipse indicates further, that the response is not symmetric in the heating and cooling cycle. The melting and crystallization have either different rates over the modulation cycle, or the mechanisms are more complicated than just melting and crystallization, they may involve, for example, growth of metastable crystals on cooling, followed by annealing to stabler crystals before reaching their melting temperature. The missing area of the explained by the major melting which is not completed within the modulation cycle, as seen at temperatures C and D. Even if there were enough time within the modulation cycle to complete melting and crystallization, the simulated response of a single reversible cycle of melting followed by crystallization in Fig. A.13.13 shows that a straight-forward analysis of the heat-flow rate  $HF(t)$ , as outlined in Sect. 4.4.3, would not lead to a good representation of the melting and crystallization process. The main reason for the deviations is the nonstationary response.

The sawtooth modulation shown in Fig. A.13.14 allows an easy interpretation of the actual data for a similar pentacontane sample as in Figs. A.13.11 and A.13.12.



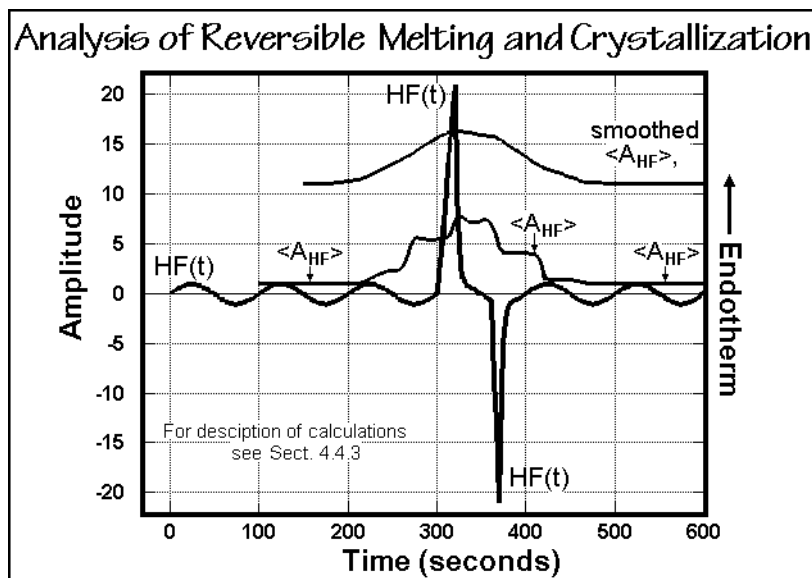


Fig. A.13.13

The first melting at (1) is incomplete and recrystallizes immediately at (2). The next melting, recrystallization, and renewed melting at (3), (4), and (5) are practically complete, and are followed by partial recrystallization (6) and final melting (7). Quantitative analyses of the various stages of this process using standard DSC baselines are shown in the integral analysis of the heat-flux rates in Fig. A.13.15. This analysis bypasses the nonstationarity problems of the Fourier analysis.

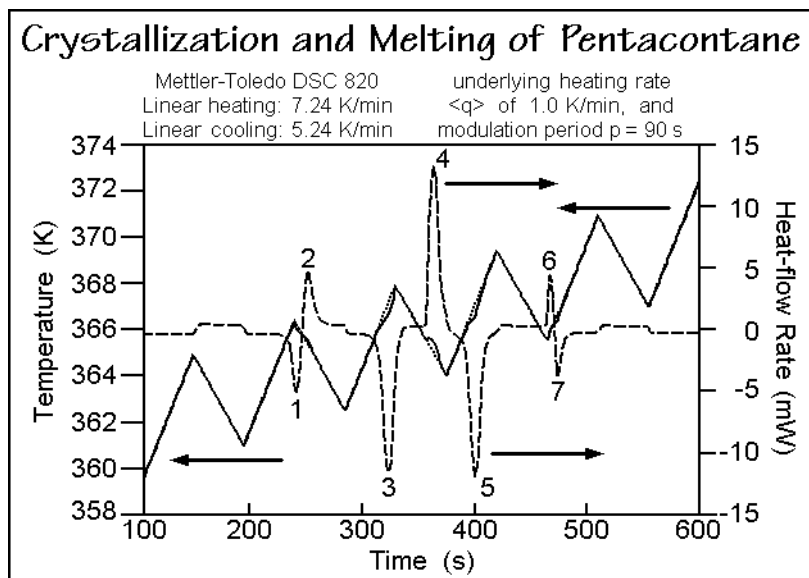


Fig. A.13.14

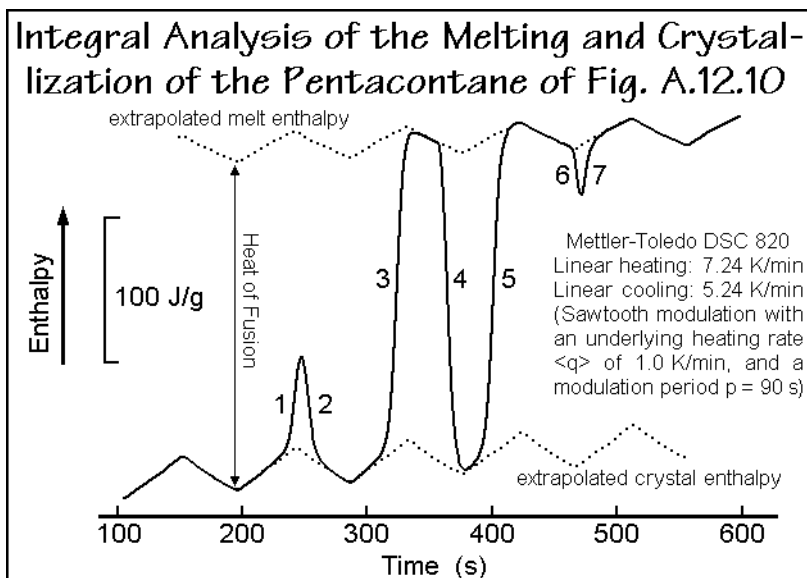


Fig. A.13.15

## References to Appendix 13

1. Details about the data analysis without Fourier transformation for sawtooth-type temperature-modulated DSC are given in: Hu W, Wunderlich B (2001) Data Analysis Without Fourier Transformation for Sawtooth-type Temperature-modulated DSC. *J Thermal Anal Calorim* 66: 677–697.
2. A collection of Fourier series for different curves can be seen, for example in: Lide DR, ed (2002/3) *Handbook of Chemistry and Physics*, 83<sup>rd</sup> ed. CRC Press, Boca Raton.
3. The TMDSC with Fourier analysis of the melting pentacontane and the calculations using saw-tooth analysis methods are given in the publication: Wunderlich B, Boller A, Okazaki I, Ishikiriya K, Chen W, Pyda W, Pak J, Moon, I, Androsch R (1999) Temperature-modulated Differential Scanning Calorimetry of Reversible and Irreversible First-order Transitions. *Thermochim Acta* 330: 21–38.

## An Introduction to Group Theory, Definitions of Configurations and Conformations, and a Summary of Rational and Irrational Numbers

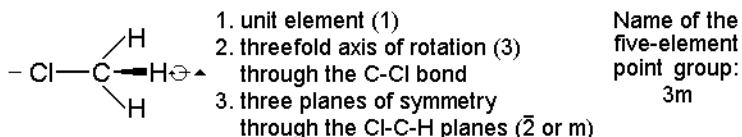
The four title topics are represented in the Figs. A.14.1–4, shown below:

### Short Introduction to Group Theory

The interrelationships of the symmetry properties of an object define a mathematical group. A group must follow the conditions:

1. Each pair of elements A and B of the group  $\mathbf{G}$  is associated with an element C of  $\mathbf{G}$  such that  $C = AB$  and called the product. (Note that this "product" does not have to be a multiplication, but may be any defined operation, such as carrying out the two symmetry operations A and B in sequence. Once defined, the operation is, however, fixed).
2. The associative law holds for any three elements of the group:  
 $(AB)C = A(BC) = ABC$
3. There exists a unit element E such that  $EA = A$  for every element of  $\mathbf{G}$ .
4. For each element there is a reciprocal  $A^{-1}$ , so that  $A^{-1}A = E$ .

As an example one can look at the symmetry of methyl chloride  $\text{CH}_3\text{Cl}$ :



Note that the nomenclature of groups and symmetry elements used in this section are preferred in crystallography. You may find differences when describing molecules.

Fig. A.14.1

### Definition of the Term "Stereoisomer"

A stereoisomer has a structure that is not superimposable on its mirror image without breaking and remaking of the bonding. The most common stereoisomers involve a chiral carbon atom  $\text{C}^*$  that contains four different substituents as for example 2-butanol:

χειρὸς = Gk. for hand

Pure isomers rotate the plane of polarization of light. The two configurations are chemically identical, but do not fit the same position in a crystal.

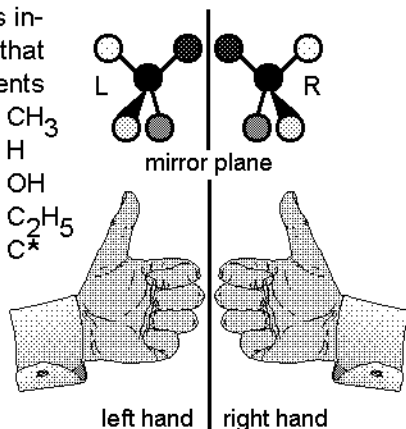
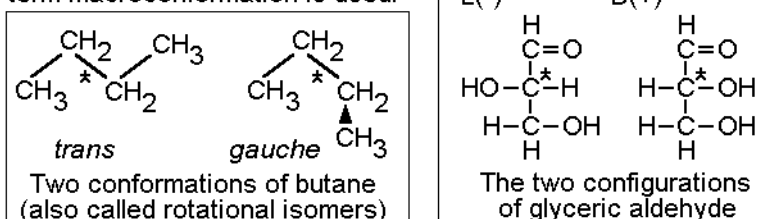


Fig. A.14.2

### Definition of the Term "Conformation"

In polymer science one distinguishes a conformation (from the Latin *conformatio*, forming, fashioning) from a configuration with a similar word origin (from the Latin *configere*, to join together). Different conformations of a molecule can be attained by rotation about bonds as shown below. Configurations need breaking of chemical bonds, as in the attainment of stereoisomers. In case we like to characterize the overall shape of a macromolecule, the term macroconformation is used.

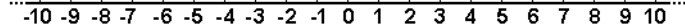


(For more about conformations and macroconformations see Sect.1.3 and Chapt. 5)

Fig. A.14.3

### Rational and Irrational Numbers

All positive and negative whole numbers and zero can be marked on the number line:



This system of numbers can be extended by the numbers  $p$  which represent the division of two whole numbers  $a$  and  $b$  ( $p = a/b$ , where  $b \neq 0$ ). All numbers that can be obtained by division are called "rational numbers." Of particular importance are the decimal fractions, written for example as:

$$24.5693 = 24 + 5/10 + 6/100 + 9/1000 + 3/10,000$$

One can prove that every fraction has either a finite or an infinite, but periodic number of decimal places. All rational numbers fill the number line densely with an infinity of points. Between these densely arranged points, one finds the also infinite number of "irrational numbers" which are represented by an infinite, not periodic number of decimal places and can thus not be represented by fractions (such as  $e = 2.7182\dots$ ,  $\pi = 3.1415\dots$ , or  $\sqrt{2} = 1.4142\dots$ ). Since the rational numbers are densely placed, one can always approximate the irrational numbers with unlimited precision by rational numbers. The total of rational and irrational numbers are called the real numbers. The real numbers must be expanded with the complex numbers which occur, for example, in efforts to solve quadratic equations. [i.e.,  $(x-5)^2 = -4$  has the solution  $x = 5 \pm 2i$ ]. For complex numbers see also Sect. 2.3.5 and Fig. A.6.3.

Fig. A.14.4

## Summary of Birefringence and Polarizing Microscopy

The title topic is represented in the Figs. A.15.1 and A.15.2, shown below:

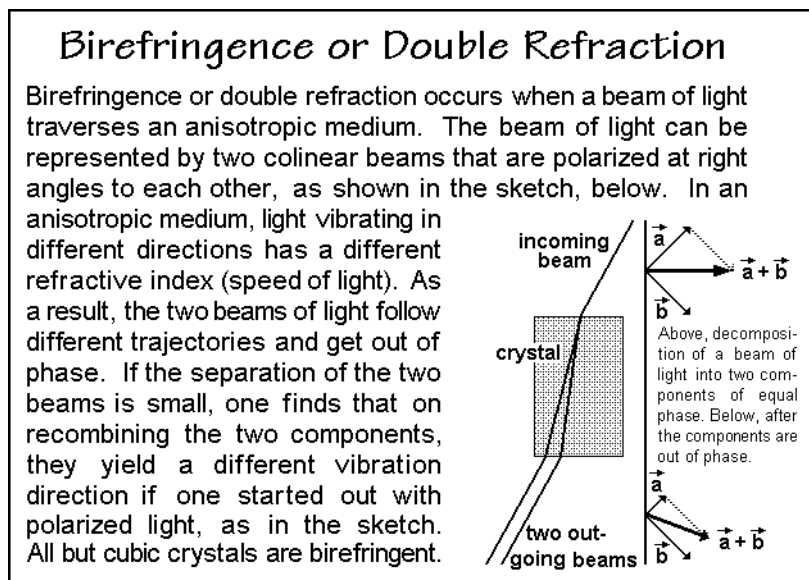


Fig. A.15.1

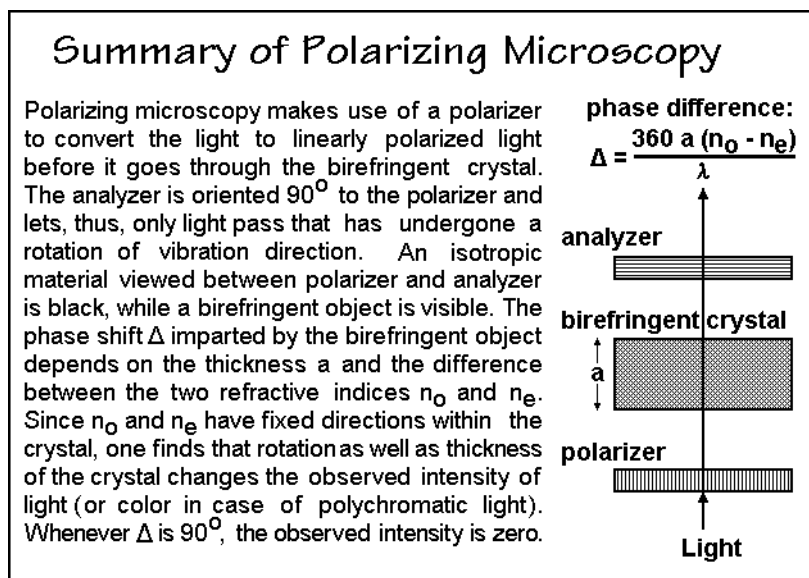


Fig. A.15.2

## Summary of X-ray Diffraction and Interference Effects

X-ray diffraction and, analogously, the diffraction of other electromagnetic waves, as detailed in Fig. 1.51 is summarized in Fig. A.16.1. A detailed drawing of the constructive and destructive interference is outlined in Fig. 1.54. A variety of typical diffraction patterns are depicted in Figs. 5.69–72, 5.81, 5.82, 6.4, 6.33, 6.63, 6.103, 7.36, and 7.51. Correspondent constructions can be applied to waves of small particles of matter, such as electrons and neutrons. An electron-diffraction pattern is reproduced in Fig. 5.74. Even sound and water waves follow the same principles of diffraction and interference.

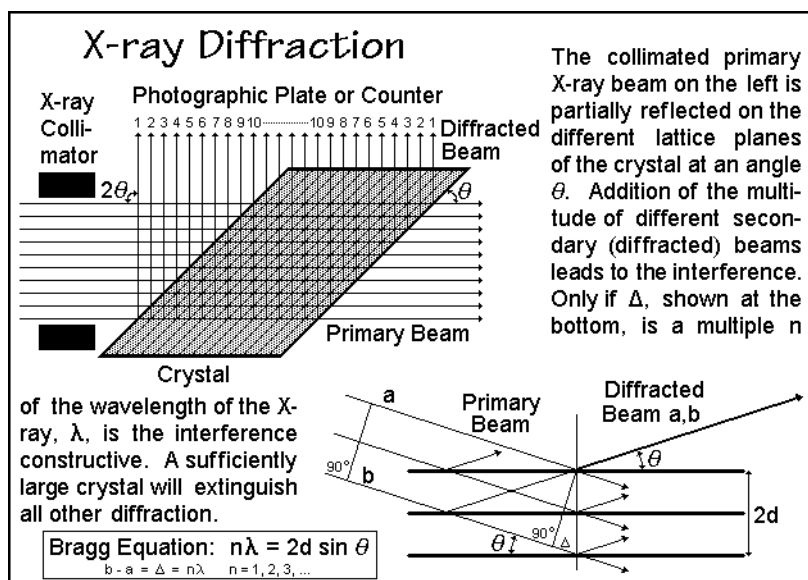


Fig. A.16.1

## Optical Analog of Electron Double Diffraction to Produce Moiré Patterns

To produce an optical analog of the electron double diffraction pattern one can draw two line lattices, as shown in Figs. A.17.1 and A.17.2. Next, Fig. A.17.3 shows the

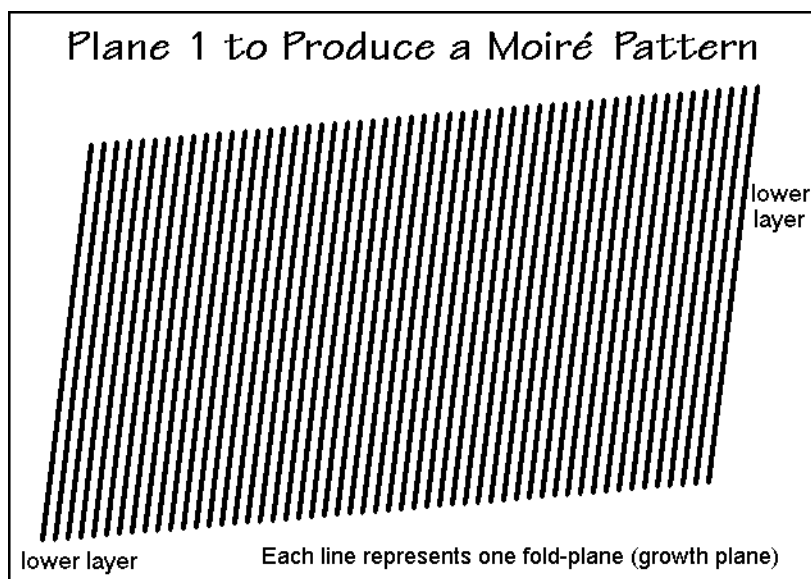


Fig. A.17.1

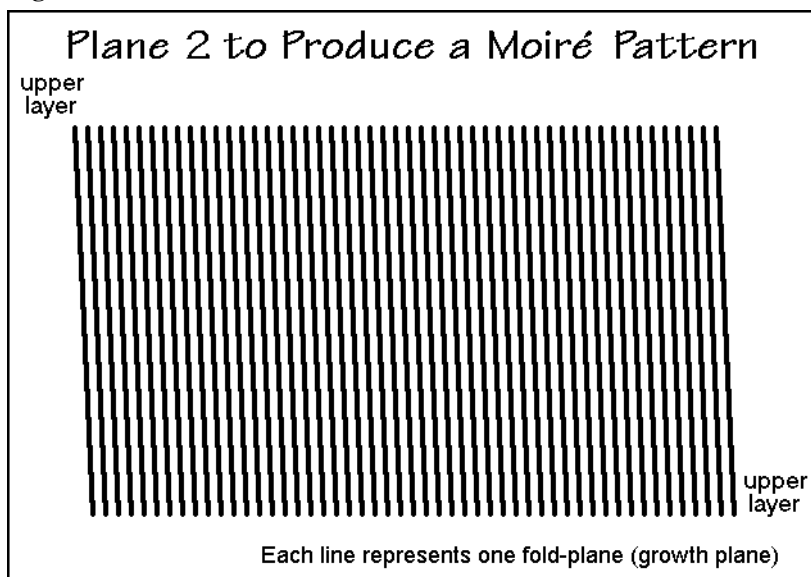


Fig. A.17.2

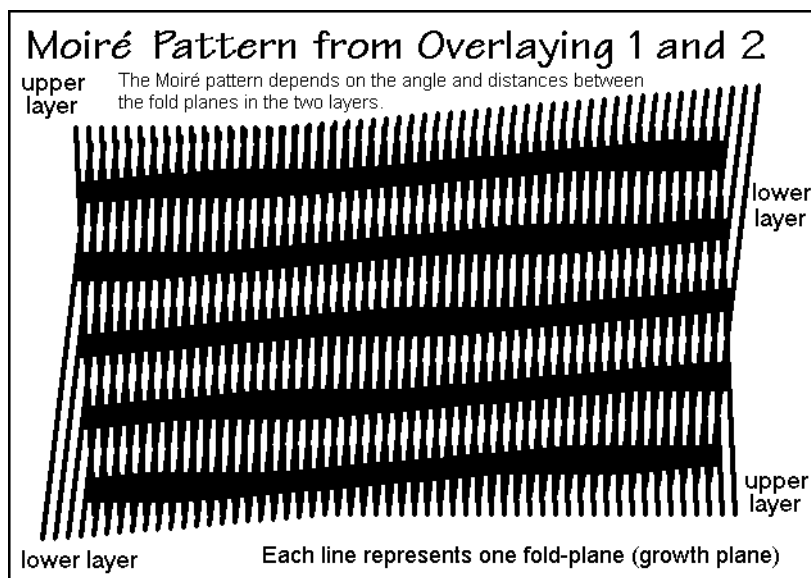


Fig. A.17.3

Moiré pattern which is produced by superposition of Figs. A.17.1 and A.17.2. The Moiré lines are related to the spacings of the basis lines and their angle of rotation. Adding a “defect,” as is illustrated in Fig. A.17.4 to the lower layer, the pattern of Fig. 5.93 results, based on the distortion of the line lattice caused by the edge dislocation. An analogous interpretation is possible for the double layer of folded-chain crystals of polyethylene lamellae, shown in Fig. 5.94.

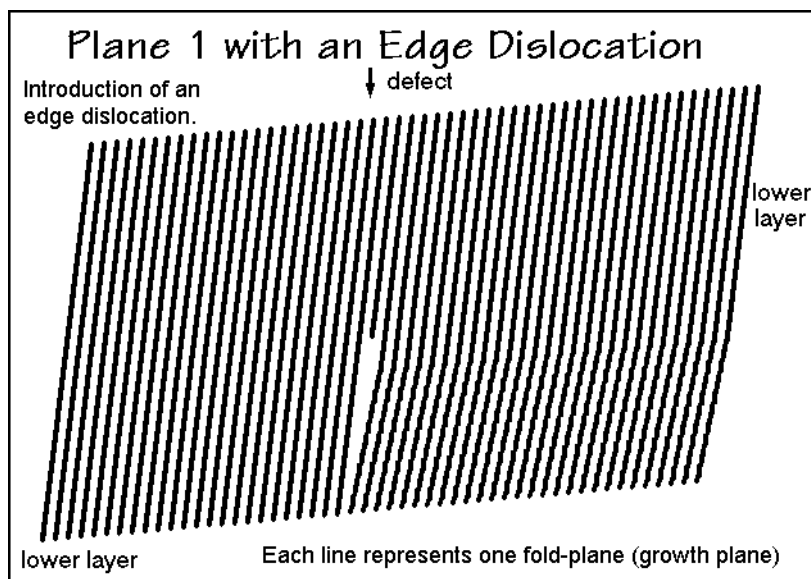


Fig. A.17.4



---

## Substance Index

The entries of the Substance Index leading to the chemical structure are underlined, figures are marked in *italics*, and table entries are written in **bold** numerals. (Note that the references to the ATHAS Data Bank on pp. **780–798** contains information on glass transition temperatures, heat-capacity changes at the glass transition, equilibrium melting temperatures, heat of fusion, information on availability of heat capacity and integral thermodynamic functions and parameters with corresponding references to the literature on pp.799–800. These entries are not listed separately in the index.)

### A

abbreviation of polymer names **17**  
ABS rubber, see: poly(acrylonitrile-*co*-1,4-butadiene-*co*-styrene)  
acetanilide, TMA of 408, 408  
acetone, reaction with *p*-phenylhydrazine analyzed by DTA 351–354, 353  
acetylene, thermochemical data **323**  
acrylic ester, reaction type **212**  
acrylonitrile, reaction type **212**  
acryloyloxybenzoic acid 175  
ADP, see: adenosine phosphate  
adenosine phosphate, (mono-, di-, and triphosphate) 218, 219  
aldehydes, reaction type **212**  
aluminum **111**  
    bulk modulus **405**  
    melting parameters **538**  
    oxide, see: sapphire  
    thermochemical data **323**  
    TMDSC 365–367, 366, 367  
ammonia, melting parameters **542**  
amyl alcohol, fingerprinting by DTA 350, 350  
ammonium cyanate 6  
ammonium picrate, TGA and DTA 443, 443  
AMP, see: adenosine phosphate  
anthracene, heat of fusion **339**

    melting parameters **542**  
argon, class of molecule 8  
    melting parameters **538**  
atactic polymers 24  
ATP, see: adenosine phosphate  
azobisisobutyronitrile 208  
*p*-azoxybenzene 170

### B

ball-and-chain polymer 26, 26  
barium, chloride, fingerprinting by DTA 351, 352  
    TMA of 408, 408  
    melting parameters **538**  
    zincate, pyrosynthesis by DTA 354, 354  
benzene, jump-motion within the crystal 556, 557  
    melting parameters **542**  
benzoic acid, heat of fusion **339**  
    expansivity **295**  
beryllium, bonding 3  
*N,N'*-bis(4-*n*-octyloxybenzal)-1,4-phenylenediamine **798**  
    glass transition 559, 560  
    heat capacity 171, 172, 172, 559  
    mesogen 563  
    transition entropies 560, 561, 560  
    TMDSC of LC isotropization 559  
boron, bonding 3

nitride 25  
 $\Theta$ -temperature **111**  
 ultimate strength **534**  
 bromine, atomization, heat of **324**  
 melting parameters **542**  
 buckminsterfullerene, see: fullerene  
 1,3-butadiene polymerization, reaction type **212**  
 butane **793**  
   heat capacity of solid 327  
   isomers, rotational **39**  
   melting parameters **543**  
 2-butanol **848**  
 butene, reaction type **212**  
*p*-butyl-*p*-methoxyazoxybenzene meso-phase transitions 547, **548**

## C

cadmium, melting parameters **538**  
 calcium, thermochemical data **323**  
   melting parameters **538**  
   carbonate, crystal structure, as proposed by Huygens in 1690 166  
   thermochemical data **323**  
   oxalate monohydrate, decomposition, by TGA and DTA **444–446, 444–446**  
   kinetics 445, 446, **445, 446**  
   oxide, thermochemical data **323**  
   sulfate dihydrate, crystal growth and morphology 256, 257  
 camphor, melting parameters **540**  
 carbon, see also the three allotropes:  
   diamond, graphite, and fullerene  
   atomization, heat of **324**  
   bond energy **324**  
   bonding **3**  
   coordination number 472  
   dioxide, class of molecule **8**  
   melting parameters **542**  
   thermochemical data **323**  
   disulfide, melting parameters **542**  
   fiber, formation **234, 235**  
   ultimate strength **534**  
   monoxide, melting parameters **539**  
   thermochemical data **323**  
   tetrafluoride, melting parameters **539**

thermodynamic functions of 325–327  
 carbonyl sulfide, melting parameters **542**  
 cellulose 235  
   graft 235  
   native, crystal morphology 507, 507  
   rayon, crystal morphology 508, 509  
   triacetate, letter abbreviation **17**  
 cerebroside **170**  
 cesium, atomic diameter **3**  
   bromide, melting parameters **541**  
   chloride, coordination number 472  
   melting parameters **541**  
   fluoride, melting parameters **541**  
   iodide, melting parameters **541**  
   melting parameters **538**  
 chain end, naming 16, 16  
 chalcogenide, two- and three-dimensional Debye functions for the description of the heat capacity **116**  
 chirality **848**  
 chlorine, atomization, heat of **324**  
   melting parameters **542**  
   thermochemical data **323**  
 chloroform, see: trichloromethane  
 $\alpha$ -chloronaphthalene, diluent for polyethylene 715  
 chromel-alumel, thermocouple emf **288**  
 chromium, melting parameters **538**  
 $\alpha$ -chymotrypsinogen, heat capacity and  $\Theta$ -temperature 127, **127, 128**  
 cobalt, melting parameters **538**  
 copper, thermochemical data **323**  
   constantan, thermocouple emf **288**  
   melting parameters **538**  
   oxide, thermochemical data **323**  
   sulfate, thermochemical data **323**  
 cyanogen, melting parameters **542**  
 cyclododecane, ring motion 557, **558**  
 cyclohexane, class of molecule **8**  
   melting parameters **540**  
 cyclopentane, transition temperatures **340**  
 cyclopropane, jump-motion within crystal 556, 556  
 cyclotetraeicosane, jump motion within crystal **557, 558, 557, 558**

**D**

- DDA-12, see: poly(oxy-2,2'-dimethylazoxybenzene-4,4'-dioxydodecanoyl)
- decane **794**  
heat capacity of solid *327*  
melting parameters **543**  
thermodynamic functions, plot of H, TS, G *329*
- DHMS-7,9, liquid crystalline copolyester **567**,  
TMDSC traces *568*
- diamond *25*, *172*  
bulk modulus **405**  
class of molecule *8*  
expansivity **295**  
frequency spectrum *115*  
heat capacity of *325*, *325*, *326*  
Θ-temperature **111**, **115**  
thermochemical data **323**
- dichlorodipyridylcobalt(II), TMA of **408**, *408*
- dichloroethane, steric hindrance *35*
- cis*-1,2-dimethyl cyclohexane, melting parameters **540**
- dimyristoyl phosphatidic acid *170*
- dioxane, melting parameters **542**
- diphenyl, melting parameters **542**
- divinyl benzene *698*
- dodecane **794**  
heat capacity of solid *327*  
melting parameters **543**
- dotriacontane **795**

**E**

- eicosane **795**
- elements, Debye temperatures and heat capacities *114*, **115**
- epoxide *25*  
curing *402*, *403*  
glass transition, change with cross-link density *700*
- ester, reaction rate and mechanism *200*, **200**, *201*  
interchange *229*, *230*, *230*
- ethanol, bulk modulus **405**  
class of molecule *8*  
thermochemical data **323**
- ethane, heat of formation *322*, *322*

- isomers, rotational *38*  
melting parameters **542**, **543**  
thermochemistry of combustion *322*, *322*
- ethyl alcohol, see: ethanol
- ethyl benzoate, diluent for polyethylene *715*
- ethylene, melting parameters **542**  
reaction type **212**

**F**

- fluorine *4*, *5*  
atomization, heat of **324**  
bonding *3*
- fullerene *3*, *172*, *483*, *484*, **793**  
crystals with solvent *484*  
heat capacity of *325*, *325*, *326*  
thermal analysis and NMR *172*–*174*, *173*  
thermodynamic functions, plot of H, TS, G *326*, *326*  
TMDSC (C<sub>70</sub>) *402*, *402*
- furan, jump-motion **556**

**G**

- gallium, melting temperature **340**
- gases, bulk modulus **405**
- glucose, heat capacity and glass transition analysis *142*
- gold, density *5*  
melting parameters **538**
- graphite *25*, *172*  
atomization, heat of **324**  
bond energy **324**  
frequency spectrum *115*  
Θ-temperature **111**, **115**  
heat capacity of *325*, *325*, *326*  
thermochemical data **323**  
thermochemistry of combustion *322*, *322*
- gutta percha, see: 1,4-poly(2-methylbutadiene), *trans*
- gypsum, see: calcium sulfate dihydrate

**H**

- helium, atomic diameter *3*  
class of molecule *8*  
use in calorimetry *312*

use as purge gas 351, 443  
heptadecane **795**  
heptane **794**  
    melting parameters **543**  
hexacosane **795**  
hexadecane **795**  
    heat capacity of solid 327  
hexane **794**  
    heat capacity of solid 327  
    melting parameters **543**  
hexatriacontane **796**  
HIPS, see: polystyrene, high impact  
HPX-11, see: poly(oxy-1,4-phenylene-oxyxylyleneoxy-1,4-phenyleneoxyundecamethylene)  
hydrocarbon, linear, melting parameters 542–544, **543**  
    heat capacity and  
        thermodynamic functions 327–329, 327–329  
    molecular mechanics 42  
    see also: paraffins; and also:  
        specific paraffins  
hydrochloric acid, thermochemical data **323**  
2-hydroxybenzoic acid, TGA and DTA 440, 441, 440  
hydrogen, atomization, heat of **324**  
    bond energy **324**  
    bromide, melting parameters **539**  
    chloride, melting parameters **539**  
    cyanide, melting parameters **542**  
    iodide, melting parameters **539**  
    melting parameters **539**  
    phosphide, melting parameters **539**  
    sulfide, class of molecule **8**  
        melting parameters **539**  
    thermochemistry of the combustion of 320–322, **321**  
    thermochemical data **323**

## I

ice, see: water  
indium, heat of fusion **339**  
    Lissajous figure on melting 397  
    melting, temperature **340**  
        DSC, change of onset with  
            heating rate 357, 357, 358, 358

    TMDSC calibration and  
        reversibility 375–378, 376, 377, 397, 397  
Invar, expansivity **295**  
iPP, see: polypropylene, stereoisomer (isotactic)  
iodine, atomization, heat of **324**  
iridium, density 5  
iron, constantan, thermocouple emf **288**  
    fingerprinting by DTA 351, 352  
    hydroxide, III, TGA and DTA **442**, **443**  
    melting parameters **539**  
    oxide, thermochemical data **323**, **443**  
    thermochemical data **323**  
isobutene, reaction type **212**  
isoprene, reaction type **212**

## K

kaolinite, TGA and DTA 441, 442, 442  
ketones, reaction type **212**  
Kevlar®, see: poly(*p*-phenylene terephthalamide)  
krypton, melting parameters 538

## L

lanthanum, melting parameters **539**  
lead, melting, parameters **538**  
    temperature **340**  
levulinic acid and aldehyde **11**  
lipid, nanophase structure **170**  
lithium 5, **5**  
    bonding **3**  
    bromide, melting parameters **541**  
    chloride, melting parameters **541**  
    fluoride 5, **5**  
        melting parameters **541**  
    iodide, melting parameters **541**  
    melting parameters **538**  
    phosphate, Avrami plot 261, 262, 262  
        crystal, growth rate 260  
        nucleation 241, 242, 242  
        DSC 202  
        step reaction 201–206, 202–206  
        TGA 202  
LLDPE, see: poly(ethylene-co-octene-1)

**M**

MBPE-9, see: poly[oxy-1,4(3-methyl-phenylene)ethylene-1,4-phenyleneoxynona-methylene]  
 mercury, bulk modulus **405**  
     melting parameters **539**  
 methane 4, 5  
     bonding 3  
     class of molecule 8  
     melting parameters **543**  
     thermochemical data **323**  
 methacryl amide, reaction type **212**  
 methacrylic ester, reaction type **212**  
 methanol, melting parameters **539**  
     thermochemical data **323**  
 methyl alcohol, see: methanol  
 methylene-bis(1,2-epoxy-2-phen-oxyethane) **798**  
 2-methyl naphthalene, melting parameters **542**  
 $\alpha$ -methyl styrene, reaction type **212**  
 molybdenum, melting parameters **538**

**N**

naphthalene, melting temperature **340**  
 neon, bonding 3  
     class of molecule 8  
     melting parameters **538**  
 neopentane, melting parameters **540**  
 nickel, melting parameters **538**  
 nitrogen, atomization, heat of **324**  
     bond energy **324**  
     bonding 3  
     melting parameters **539**  
     monoxide, melting parameters **542**  
*p*-nitrophenylhydrazone, reactions with ketones, analyzed by DTA 351–354, **353**  
*o*-nitrotoluene, diluent for polyethylene 715  
*p*-nitrotoluene, melting temperature **340**  
 nitrous oxide, melting parameters **542**  
 nomenclature, list of frequently used abbreviations **17**  
 nonane **794**  
     melting parameters **543**  
 nylon 2, see: polyglycine  
 nylon 6 **787**, 21

chemical cross-linking **658**, **659**, **680**  
 crystal, nucleation **246**  
     melting, reversing, frequency dependence **382–384**, **382–384**  
     spherulite, Popoff-type **501**, **501**, **502**  
 fiber analysis **679–681**, **680**, **681**  
 melting, data **545**  
     heating rate dependence **660**, **660**  
     peak temperatures, dependence on crystallization temperature **660**, **661**  
     polymerization **197**, **197**  
     reversing behavior **650**  
 nylon 8, melting data **545**  
 nylon 11 **787**  
     crystal, linear growth rate **249**  
 nylon 12 **787**  
     reversing behavior **650**  
 nylon 6,6 **787**, 21  
     crystal unit cell **478–380**, **479**  
     Kuhn length **48**  
     melting data **545**  
     step reaction **197**  
     treated as regular copolymer **756**, **757**  
     ultimate strength **534**  
 nylon 6,9 **787**  
 nylon 6,10 **787**  
 nylon 6,12 **787**  
 nylon 7,7, crystal unit cell **478–380**, **479**  
 nylons x+1, regular copolymers, melting for different CH<sub>2</sub>-group length **757**, **757**, **758**

**O**

OOBPD, see: *N,N'*-bis(4-*n*-octyloxybenzal)-1,4-phenylenediamine  
 octadecane **795**  
     heat capacity of solid **327**  
 octane **794**  
     heat capacity of solid **327**  
     melting parameters **543**  
     heat capacity and transitions **171**, **172**, **172**

4-*n*-octyloxybenzoic acid, nanophase separation within the crystal, as seen from the X-ray structure 553, 553

osmium, density 5

oxygen, thermochemical data **323**

atomization, heat of **324**

bond energy **324**

bonding **3**

melting parameters **539**

## P

PAA, see: poly(acrylic acid)

PAN, see: polyacrylonitrile

P(AN-*co*-BD), see: poly(acrylonitrile-*co*-1,4-butadiene)

paraffin, comparison of melting temperatures with poly(1-alkene)s **754**, **755**, **755**, **756**

cooperative melting, described with the Ising model 554, 555, 555

even, heat capacities of C<sub>4</sub>H<sub>10</sub> to C<sub>18</sub>H<sub>38</sub> 327, 327

lower limit, of chain-folding **491**  
of molecular nucleation 254, 255

melting temperatures 192, 193

molecular dynamics calculations for, parameters 44

partially fluorinated, condis crystal of 562, 563, 563

see also the specific paraffins  
supercooling 255

thermodynamic functions of, C<sub>p</sub>, H, TS, and G 327–329, 327–329

PBA, see: poly(butylene adipate)

PBD, see: 1,4-polybutadiene

PBL, see: poly(γ-butyrolactone)

PBT, see: poly(butylene terephthalate)

PC, see: poly(4,4'-isopropylidene-diphenylene carbonate)

PCL, see: poly(ε-caprolactone)

PCTFE, see: poly(chlorotrifluoro-ethylene)

PDMS, see: poly(dimethyl siloxane)

PDES, see: poly(diethyl siloxane)

PE, see: polyethylene

PEA, see: poly(ethylene adipate)

PEBA, see: poly[oligoimino(1-oxododecamethylene)-alt-oligoxytetramethylene]

Pebax<sup>®</sup>, see: poly[oligoimino(1-oxododecamethylene)-alt-oligoxytetramethylene]

PE-*alt*-CO, see: polyethylene, copolymer, alternating with CO

PEEK, see: poly(oxy-1,4-phenylene-oxy-1,4-phenylene-carbonyl-1,4-phenylene)

PEIM-9, see: poly(4,4'-phthalimido-benzoylnonamethyleneoxy-carbonyl)

PEIM-12, see: poly(4,4'-phthalimido-benzoyldodecamethylene-oxy-carbonyl)

PEN, see: poly(ethylene-2,6-naphthalene dicarboxylate)

pentacontane **796**

heat capacity analysis 328

melting by TMDSC 614, 615, 615, 844–847, **844–847**

thermodynamic functions, plot of H, G, and TS 328

pentacosane **795**

pentadecane **795**

pentaerythrityl tetrabromide, phase diagram with polypropylene **716**, **716**, **717**

pentane **794**

melting parameters **543**

Penton<sup>®</sup>, see: poly[3,3-bis(chloromethyl)-oxacyclobutane]

perfluorododecane **796**

perfluoroeicosane **796**

perfluorotetracosane **796**

perfluorotetradecane **796**

PES, see: poly(ethylene sebacate)

PET, see: poly(ethylene terephthalate)

PETB, see: pentaerythrityl tetrabromide

PETcoOB, see: poly(ethylene terephthalate-*co*-oxybenzoate)

PEO, see: poly(oxyethylene)

PGL, see: polyglycolide

PHB, see: poly(3-hydroxybutyrate)

phenanthrene, melting parameters **542**

phenol-formaldehyde resin 25

- PHMS, see: poly(hexamethylene sebacate)
- phosphorus, atomization, heat of **324**  
melting parameters **539**
- PI, see: polyimide
- PLA, see: poly(L-lactic acid)
- platinum, density **5**  
expansivity **295**  
melting parameters **538**  
resistance thermometer **286**  
thermocouple emf **288**
- PMA, see: poly(methyl acrylate)
- PMAA, see: poly(methacrylic acid)
- PMMA, see: poly(methyl methacrylate)
- P4MP1, see: poly(4-methyl-1-pentene)
- PMS, see: poly( $\alpha$ -methylstyrene)
- POB, see: poly(4-hydroxybenzoic acid),  
as well as polyoxybenzoate
- POBcoON, see poly(oxybenzoate-co-oxy-naphthoate)
- POE, see: poly(oxyethylene)
- poly(1-acetoxyethylene), see: poly(vinyl acetate)
- polyacetylene class of molecule **8**  
topotactic polymerization, **510**, **511**
- poly(*N-n*-acrylamide)s, with long side-chains, melting of **755**, **756**
- poly(acrylamide-co-styrene), glass transitions **759**, **759**, **760**
- polyacrylates, with long side-chains, melting of **755**, **756**
- poly(acrylic acid), in polymer supported chemistry **237** **237**  
letter abbreviation **17**
- polyacrylonitrile **784**, **19**  
fiber, letter abbreviation **17**  
pyrolysis to carbon fiber **234**, **235**
- poly(acrylonitrile-co-1,4-butadiene), glass transitions, description with the Barton equation **766**, **767**  
run number for the Barton eq. **762**
- poly(acrylonitrile-co-1,4-butadiene-co-styrene), graft copolymer **235**, **235**, **236**  
letter abbreviation **17**
- poly(acryloyloxybenzoic acid), glass transition **176**
- poly(L-alanine) **788**  
helix, potential energy **467**  
structure **467**, **468**, **468**
- poly(1-alkene)s, melting of **754**, **755**, **755**
- poly(L-arginine), hydrogen chloride **789**
- poly(L-asparagine) **788**
- poly(L-aspartic acid), sodium salt **788**
- polybenzimidazole, letter abbreviation **17**
- poly[3,3-bis(chloromethyl)-oxacyclobutane], melting data **545**
- poly(*p*-bromostyrene) **782**
- 1,4-polybutadiene, copolymer with acrylonitrile, glass transition description **766**, **767**  
see also: poly(1-butenylene)
- 1,4-poly(butadiene-co-isoprene), azeotropic **229**
- poly(1-butene) **780**  
crystal, unit cell **474**, **475**  
crystallization kinetics **348**  
helix within crystals **467**  
letter abbreviation **17**  
melting data **544**
- poly(1-butene sulfone) **793**
- poly(1-butenylene) **18**, **23**, **780**  
*cis*, entropy **174**, **175**  
TMA in penetration mode **412**, **412**  
heat capacity **140**  
melting data **544**  
*trans*, condis crystal, heat capacity, solid state NMR **174**, **174**  
entropy **174**, **175**  
phase areas **594**
- poly(*n*-butyl acrylate) **784**
- poly(*n*-butyl acrylate-block-gradient-*n*-butyl acrylate-co-methyl methacrylate), glass transition of **771**
- poly(butylene adipate) **786**  
glass transitions of solutions with polyepichlorohydrin **764**
- poly(butylene terephthalate) **790**  
crystallinity **632**, **634**  
letter abbreviation **17**  
melting, by TMDSC and DSC **632–634**, **632–634**  
parameters **628**  
reversing behavior **650**

- poly(*n*-butyl methacrylate) **784**  
poly( $\gamma$ -butyrolactone) **132**, **785**  
    heat capacity, liquid **133**  
polycaprolactam, see: nylon 6  
poly( $\epsilon$ -caprolactone) **785**  
    crystal unit cell, 480, 481, **481**  
    glass transitions of solutions with  
        poly(vinyl chloride) **764**  
    melting data **545**  
    reversing behavior **650**  
    TMDSC, TMDMA **641**–644,  
        642–644  
        amplitude dependence **381**  
        frequency dependence **643**  
    step-reaction mechanism **196**  
polycarbonate, see also: poly(4,4'-  
    isopropylidenediphenylene  
    carbonate)  
    TMA of **408**, **409**, **408**  
*trans*-1,4-poly(chlorobutadiene), solidus  
    line of **583**  
poly(1-chloroethylene), see: poly(vinyl  
    chloride)  
poly(*p*-chlorostyrene) **782**  
poly(chlorotrifluoroethylene) **782**  
    crystal, linear growth rate **249**  
poly(1-cyanoethylene), see:  
    polyacrylonitrile  
polycyclopentene **780**  
poly(decamethylene sebacate), linear  
    crystal growth rate of **249**  
poly(1,1-dichloroethylene), see:  
    poly(vinylidene chloride)  
poly(dicyclooctyl itaconate) **787**  
poly(diethyl siloxane) **792**  
    mesophase transitions **548**, **549**, **549**  
    phase areas **594**  
poly(difluoromethylene), see:  
    polytetrafluoroethylene  
poly(di-*n*-heptyl itaconate) **786**  
poly(dihexylsilylene) **792**  
poly(1,1-dimethylethylene), see: poly-  
    isobutylene  
poly(dimethyl itaconate) **786**  
poly(dimethyl propiolactone), melting  
    data **545**  
poly(dimethyl siloxane) **792**  
    DSC trace **549**  
    letter abbreviation **17**  
poly(dimethylsilylene) **792**  
poly(di-*n*-nonyl itaconate) **786**  
poly(di-*n*-octyl itaconate) **786**  
poly-*p*-dioxanone, adiabatic calorimetry,  
    TMDSC, DSC **387**, **388**,  
    643  
    reversing behavior **650**  
poly[dioxyethylene-oxy-(1,3-  
    phenylene)-(4,4'-oxy-  
    diphthalimide)-1,4-phenyl-  
    ene] **791**  
poly(dipentylsilylene) **792**  
poly(di-*n*-propyl itaconate) **786**  
poly(ditetradecylsilylene) **792**  
polyepichlorohydrin, glass transitions of  
    solutions, with poly(butylene  
    adipate) **764**  
    with poly(ethylene adipate) **764**  
polyesters, regular copolymers, melting  
    for different CH<sub>2</sub>-group  
    length **757**, **757**, **758**  
poly(ether ether ketone), see: poly(oxy-  
    1,4-phenylene-oxy-1,4-  
    phenylene-carbonyl-1,4-  
    phenylene)  
poly(ethyl acrylate) **784**  
polyethylene **780**, **18**  
    branched **24**, **25**  
    structure and crystallinity **733**,  
    734, **734**  
    melting of **735**  
    chlorinated, letter abbreviation **17**  
    class of molecule **8**  
    comparison of DMA and DSC **584**,  
    584, **585**  
    computer simulation of crystal  
    defects **87**, **524**–530,  
    524–530  
    copolymer, crystal isomorphism  
    481–482, **482**  
    alternating with CO, reversing  
    behavior **650**  
    cross-linking **234**, **234**, **235**, **658**,  
    659  
    crystal, annealing and  
    recrystallization **655**–657,  
    655–657, **663**, **663**, **664**  
    condis, see: mesophase  
    dendritic **497**–499, **497**–499  
    extended-chain **508**–510, **509**,  
    510  
    fast melting **269**, **612**  
    fold-length **488**–490, **489**–492



- polyethylene, crystal, fold-length  
  increase 656, 656, 657,  
  659, 659, 660  
  linear growth rate 249,  
  257–258, 274  
  nucleation 245, 245, 255, 266  
  packing fraction 469, 470  
  recrystallization, comparison to  
  melt crystallization 663  
  selfseeding 246, 247  
  spherulitic 499, 500, 502, 502  
  structure 469–471, 470  
  tent-like structure 494, 495  
  unit cell 469, 470  
  zero-entropy-production 269  
crystallinity, by IR-analysis 514,  
  515, 515  
  by X-ray diffraction 513, 514  
crystallization, Avrami analysis of  
  272, 273  
  on fast cooling 827, 828  
decoupling of chain segments 267,  
  268, 649, 651, 651  
deformation 530–532, 531, 532  
diluent for 715  
DMA of 584, 584, 585  
draw ratio 32, 531, 531  
end-to-end distance 31  
entropy, liquid and glassy 141  
etching 235, 235  
excluded volume 35, 36, 40, 41  
expansivity **295**  
fiber 503, 504, 672–677, 673–677  
  DSC and TMDSC traces for  
  673–677  
  formation 530–532, 531  
  gel-spun 569–571, 570, 571,  
  596, 673–677, 674–677  
  glass transition 676, 676  
  NMR, solid state 570, 571  
  structure 674, 675  
  X-ray diffraction 513, 596, 596,  
  674, 674, 675  
free enthalpy at 0 K 142  
  distribution 595, 595  
glass 596  
group vibrations **125**  
heat capacity, amorphous 121  
  crystalline 121, 126  
  crystallinity dependence 119,  
  120  
polyethylene, heat capacity, large-  
  amplitude motion 136, 136  
  liquid and glassy 139–142, 141  
helix structure 465, 465  
hexagonal crystal, see: mesophase  
Kauzmann temperature 140  
Kuhn length 48  
letter abbreviations **17**  
linear-low density, see:  
  poly(ethylene-co-octene-1)  
melting 611–623, 612, 613,  
  616–623  
  by AFM 269, 270  
  data **544**  
  kinetics 256, 611, 612  
  of equilibrium crystals 298,  
  299, 611, 612, 719–723,  
  720–722  
  of fractions 615–618, 616–618  
  of lamellae 155, 612, 614  
  of the fold surface 623, 623  
  peak, dependence on  $T_c$  613  
  range of 614  
  superheating 611, 612, 612  
  temperature, extrapolation 154,  
  155, 192, 193  
mesophase 490, 510, 569–571,  
  569–571, 593, 594, 596, 596  
molar mass determination from  
  colligative properties 62  
molecular dynamics, parameters 44  
  potential energy functions 44  
molecular nucleation 254, 255  
phase areas 593, 594, 595, 595, 696  
phase diagram 569, 569  
  with 1,2,4,5-tetrachlorobenzene,  
  714–716, 715, 716  
rejection of low molar mass 253  
reversing behavior **650**  
supercooling 255  
TMA of 408, 409, 408  
thermodynamic functions of, H, TS,  
  G 96  
ultimate strength **534**  
vibrational modes 123  
  group vibrations **125**  
  simulation, constant volume 45  
  single chain 45  
  skeletal vibrations 46, 123, 126  
  spectrum 121–126, 123, 125  
  Tarasov function 126

- poly(ethylene adipate), crystal, linear growth rate 249  
glass transitions of solutions with polyepichlorohydrin 764  
melting data **545**
- poly(ethylene-*co*-butene), melting of extended chain crystals 730, 730
- poly(ethylene glycol) letter abbreviation **17**  
see: poly(oxyethylene)
- poly(ethylene-2,6-naphthalene dicarboxylate) **790**  
melting, by TMDSC, DSC and temperature-modulated DMA 634–637, 635, 636  
peak, dependence on the crystallization temperature, 634, 635, 635  
reversing behavior **650**
- poly(ethylene-*co*-octene-1), LLDPE, DSC, TMDSC, X-ray diffraction 733–742, 735–742
- poly(ethylene oxalate) **785**
- poly(ethylene oxide), see: poly(oxyethylene)
- poly(ethylene-*co*-propylene), melting of extended chain crystals 730, 730
- poly(ethylene sebacate) 132, **786**  
heat capacity, liquid 133  
melting data **545**  
step-reaction mechanism 196
- poly(ethylene suberate), melting data **545**
- poly(ethylene terephthalate) 21, **790**  
annealing and recrystallization by dilatometry 664, 664, 665  
cold crystallization, by standard DSC, sawtooth modulated 839, 839  
by TMDSC 386, 387, 400, 401  
crystal, lamellar, melt-grown 502, 503  
linear growth rate 249  
recrystallization rate, comparison to melt crystallization 665  
unit cell, 504, 505, 505  
DTA, see: fingerprinting by DTA and DSC
- fibers, analysis with the Rietvelt method 505, 506, 505–507  
modulus, initial 534, 535, 535  
nonequilibrium effects by DSC 411, 411  
tenacity 534, 535, 535  
TMA, DSC, and DTA, extruded, drawn, annealed 409–411, 409–411, 677–679, 678  
fingerprinting by DTA and DSC 350, 351, 351, 536, 537  
glass transition, analysis based on TMDSC 392–396, 392–395, 687–689, 688, 689  
enthalpy relaxation, effect of crystallization 695–697, 696–698  
parameters, activation 601  
lamellar morphology 493–496, 494, 495  
letter abbreviation **17**  
Lissajous figures 379, 380  
melting, data table **545**  
by standard DSC, sawtooth modulated 839, 840, 840  
parameters **628**  
reversible and reversing 267, 267, 398–401, 399, 401, 628, 628, 629, 629, 679, 679  
TMDSC compared to DSC 267  
mesophase 507, 507  
molar-mass distribution **196**  
phase areas 595, 596  
RAF 607  
recrystallization rate, comparison to melt crystallization 665  
reorganization 400, 401, 401  
reversing behavior **650**  
transesterification 665, 665, 666
- poly(ethylene terephthalate-*co*-adipate) eutectic melting 729, 729
- poly(ethylene terephthalate-*co*-isophthalate), solid solution phase diagram 730, 731
- poly(ethylene terephthalate-*co*-oxybenzoate), glass transition and phase diagram 743, 743
- poly(ethylene terephthalate-*co*-sebacate), crystallization 271, 272  
eutectic melting 729, 729

- poly(ethylene-*co*-vinyl acetate), melting  
by DSC 726, 726
- poly(ethyl methacrylate) **784**
- poly(ethylsilylethylene), crystal, unit cell  
474, 474
- poly(*o*-fluorostyrene), crystal, unit cell  
474, 475
- poly(*p*-fluorostyrene) **782**
- polyformaldehyde, see:  
poly(oxymethylene)
- poly(L-glutamic acid), sodium salt **788**
- polyglycine **787**, **788**  
crystal unit cell (II) 480, 480
- polyglycolide 132, **785**  
crystal unit cell, 480, 481, 481  
heat capacity, liquid 133  
melting data 545
- poly(hexamethylene sebacate) 132, **786**  
heat capacity, liquid 133
- poly(1-hexene) **780**
- poly(1-hexene sulfone) **793**
- poly(L-histidine) **789**  
hydrogen chloride **789**
- poly(4-hydroxybenzoic acid) **790**  
melting 743, 743  
phase behavior of copolymers  
743–747, 743–747
- poly(3-hydroxybutyrate) 609  
heat capacity, reversing 609  
RAF on crystallization 609, 609  
reversing behavior **650**
- poly(1-hydroxyethylene), see:  
poly(vinyl alcohol)
- poly(2,6-hydroxynaphthoic acid) **790**  
phase behavior of copolymer  
743–747, 744–747
- polyimide, decomposition by TGA, 232  
letter abbreviation **17**
- poly(iminohexamethyleneiminoadipoyl),  
see: nylon 6,6
- poly[imino(1-oxohexamethylene)], see:  
nylon 6
- Poly(imino-1,4-phenyleneiminoterephthaloyl), see: poly(*p*-phenylene terephthalamide)
- poly(*p*-iodostyrene) **782**
- polyisobutene, see: polyisobutylene
- poly(isobutyl acrylate) **784**
- poly(isobutyl methacrylate) **784**
- polyisobutylene **780**, 18  
letter abbreviation **17**
- polyisoprene, see: 1,4-poly(2-methyl butadiene)
- poly(4,4'-isopropylidenediphenylene carbonate) 197, 198, **790**  
glass transition by DMA 421, 422, 422, 423  
letter abbreviation **17**  
melting data 545  
reversing behavior **650**  
TMDSC and DSC 637–639, 637–639
- poly(L-lactic acid) **785**
- poly(L-leucine) **788**
- poly(L-lysine), hydrogen bromide **789**
- polymethacrylamide **787**
- poly(methacrylic acid) **784**  
emulsion polymerization 217  
in polymer supported chemistry  
237, 237
- poly(methacrylimide), letter abbreviation **17**  
see also: polymethacrylamide
- poly(*p*-methacryloyloxybenzoic acid)  
**784**
- poly(L-methionine) 136, **789**  
glass transition 136  
heat capacity 136, 137  
Theta temperature,  $\Theta$  137
- poly[1-(methoxycarbonyl)-1-methyl-ethylene, see: poly(methyl methacrylate)
- poly(methyl acrylate) **784**  
letter abbreviation **17**
- poly(methyl acrylate-*co*-ethylene),  
ionomer 236, 236
- poly(methyl acrylate-*co*-styrene) glass  
transition 759, 759, 760
- 1,4-poly(2-methyl butadiene), *cis* 18,  
234, **781**  
crystal, unit cell 477, 477, 478  
crystallization 273, 274  
fusion on extension 581–583, 582  
melting, data **544**  
peak, dependence on crystallization temperature 662  
rubber elasticity 580, 580, 581
- trans*, crystal,  $\beta$ , unit cell 276, 277  
melting ( $\alpha$  and  $\beta$  crystals) **544**
- poly(1-methyl-1-butenylene), see:  
1,4-poly(2-methyl butadiene)

- poly(methylene), see: polyethylene
- poly(methyl methacrylate) **784**, 20  
 decomposition by TGA 232  
 emulsion polymerization 217  
 glass transition, by DMA 419, 420,  
420, 421  
 of stereospecific isomers 766,  
767  
 solutions with poly(vinylidene  
 fluoride) 764  
 solutions with poly(oxyethylene)  
764  
 pressure effect (DSC and  
 dilatometry) 691  
 Kuhn length 48  
 letter abbreviation **17**
- poly(methyl methacrylate)s, with long  
 side-chains, melting of 755,  
756
- poly(methyl methacrylate-*co*-styrene),  
 alternating tendency 229
- poly(methylene oxide), see:  
 poly(oxymethylene)
- poly(2-methyl-1,3-pentadiene) **781**
- poly(4-methyl-1-pentene) **780**  
 helix within crystals 467  
 isomorphism of copolymers  
482–483, 483  
 letter abbreviation **17**  
 melting, data **544**  
 pressure dependency 652–654,  
652–654  
 phase diagram, equilibrium 654  
 nonequilibrium 653
- poly( $\alpha$ -methylstyrene) **782**  
 glass transition of solutions with  
 polystyrene by DSC 764,  
765  
 partial miscibility 765, 766, 766
- poly(*m*-methylstyrene) crystal, size of  
 unit cell 455, 456
- poly(*o*-methylstyrene), crystal, unit cell  
456, 478, 478  
 helix within crystal 467
- poly(*p*-methylstyrene) **782**
- polynaphthoate, see: poly(ethylene-2,6-  
 naphthalene dicarboxylate)
- poly(octadecyl acrylate) **784**  
 copolymers, with long and short  
 side-chains, melting of 755,  
756
- poly(oligoamide-*alt*-oligoether), see:  
 poly[oligoimino(1-  
 oxododecamethylene)-*alt*-  
 oligooxytetramethylene]
- poly[oligoimino(1-oxododeca-  
 methylene)-*alt*-oligooxy-  
 tetramethylene] 752  
 crystallinity 355, 356, 356  
 specific heat capacity, glass and  
 melting transitions  
751–754, 751–753
- polyoxide, copolymers, regular, melting  
 for different CH<sub>2</sub>-group length  
757, 757  
 heat capacities 128–131  
 Theta temperatures 130  
 errors 130
- polyoxybenzoate, letter abbreviation **17**
- poly(oxybenzoate-*co*-oxynaphthoate),  
134–136, 743–747, 744–747  
 glass transition, broad 135, 135,  
745  
 heat capacity 135, 135, 745, 745  
 melting by DSC 134–136, 135,  
744, 744, 745  
 phase diagram 746, 747  
 thermogravimetry 746  
 X-ray diffraction and modeling  
745, 746, 746
- poly[oxy-2,2'-bis(chloromethyl)-  
 trimethylene] **783**
- poly[oxy-2,6-bis(1-methylethyl)-1,4-  
 phenylene] **790**
- poly(oxy-3-bromo-2,6-dimethyl-1,4-  
 phenylene) **790**
- poly(oxy-2,2'-dimethylazoxy-  
 benzene-4,4'-dioxydo-  
 decanoyl), entropy of  
 isotropization 564  
 homologous series 564
- mesogen 563  
 mesophase transition 547, 548  
 phase areas 593, 594, 597
- poly(oxy-2,6-dimethyl-1,4-phenylene)  
**789**  
 reversing behavior **650**  
 TMDSC of 639–641, 640, 641
- poly(oxy-2,6-dimethyl-1,4-phenylene-  
*co*-oxy-2,6-dimethyl-3-  
 bromo-1,4-phenylene-),  
 glass transition 760, 760

- poly(oxy-2,6-diphenyl-1,4-phenylene)  
**790**
- poly(oxyethylene) 21, **783**
- crystal, fold-length of 491, 492,  
492
- lamellar 496, 497, 496
- nucleation 246
- melting and crystallization rates  
267, 268
- lamellar morphology 493, 493
- screw dislocation 252
- glass transitions of solutions with  
poly(methyl methacrylate)  
764
- heat capacity, 129, 130, 132
- historic analyses by Lourenço, about  
the polymeric nature 12
- Kuhn length 48
- letter abbreviation **17**
- Lissajous figures 379, 381
- melting, data **544**
- reversible 624–627, 624–627
- reversing and reversible 264,  
298, 624–627
- TMDSC, mass 1,500 387, 388,  
624–627, 624–626
- TMDSC, mass 5,000 264, 265,  
625
- TMDSC, mass 35,000 627, 627
- reversing behavior **650**
- single-molecule single crystal 508,  
508
- supercooling 266
- poly(oxyethylene-*block*-oxypropylene)  
748, 749, 750
- poly(oxyethyleneoxyterephthaloyl), see:  
poly(ethylene terephthalate)
- poly(oxyethylene-*block*-styrene),  
crystallization, from solution  
748, 748
- from the melt after phase separation,  
orientation 750, 750, 751
- structure and transitions 749
- poly(oxy-1-fluoroethylene), naming 15
- poly[oxyethylene-oxy-(1,3-phenylene)-  
(4,4'-oxy-dipthalimide)-1,4-  
phenylene] **791**
- poly(oxymethylene) 20, **783**
- class of molecule 8
- crystal, nucleation 246
- structure 465, 465, 466
- crystallization during polymerization  
from trioxane, mechanism  
and kinetics 273–275, 275
- epitaxy on NaCl 247
- group vibrations **129**
- heat capacity 128–132, 129–132  
error for liquid data 131
- helix structure 465, 465
- letter abbreviation **17**
- melting 666–668, 666–667  
data **544**
- RAF, 607, 608, 607, 608
- reversing behavior **650**
- Theta temperatures,  $\Theta$  **129**
- poly(oxymethyleneoxyethylene) 128,  
**783**
- heat capacity 129, 130, 132
- poly(oxymethyleneoxytetramethylene)  
128, **783**
- heat capacity 129, 130, 132
- poly[oxy-1,4(3-methylphenylene)-  
ethylene-1,4-phenyleneoxy-  
decamethylene] **792**
- poly[oxy-1,4(3-methylphenylene)-  
ethylene-1,4-phenyleneoxy-  
dodecamethylene] **792**
- poly[oxy-1,4(3-methylphenylene)-  
ethylene-1,4-phenyleneoxy-  
heptamethylene] **791**
- poly[oxy-1,4(3-methylphenylene)-  
ethylene-1,4-phenyleneoxy-  
hexamethylene] **791**
- poly[oxy-1,4(3-methylphenylene)-  
ethylene-1,4-phenyleneoxy-  
nonamethylene] **791**
- condis state 565, 566
- DSC on cooling and heating 564,  
565
- entropy of isotropization of the  
homologous series (odd)  
564
- glass transition 138
- heat capacity of 137, 138, 138
- mesogen 563
- NMR of melt and solid 565
- poly[oxy-1,4(3-methylphenylene)-  
ethylene-1,4-phenyleneoxy-  
octamethylene] **791**
- poly[oxy-1,4(3-methylphenylene)-  
ethylene-1,4-phenyleneoxy-  
pentamethylene] **791**

- poly[oxy-1,4(3-methylphenylene)-ethylene-1,4-phenyleneoxytetramethylene] **791**
- poly[oxy-1,4(3-methylphenylene)-ethylene-1,4-phenyleneoxyundecamethylene] **792**
- poly(oxyoctamethylene) **128, 783**  
 heat capacity *129, 130, 132*  
 melting data **544**
- poly(oxy-1,4-phenylene) **789, 21**  
 letter abbreviation **17**
- poly(oxy-1,4-phenylene-oxy-1,4-phenylene-carbonyl-1,4-phenylene) **791**  
 crystallization *270, 271, 271*  
 glass transition, change on crystallization **693**  
 melting by DSC, TMDSC, TMDMA **668–672, 669–672**  
 rigid-amorphous fraction *693, 694, 694*  
 reversing behavior **650**
- poly(oxy-1,4-phenyleneoxyxylyleneoxy-1,4-phenyleneoxyundecamethylene), mesogen **563**  
 condis structure **567–569**  
 DSC cooling traces **568**
- poly(oxy-1,4-phenylene-sulfonyl-1,4-phenylene) **793**
- poly[oxy-1,4-phenylene-sulfonyl-1,4-phenylene-oxy-1,4-phenylene-(1-methylidene)-1,4-phenylene] **793**
- poly(oxypropylene) **783**  
 crystal, linear growth rate *249*  
 letter abbreviation **17**  
 melting peak, dependence on  $T_c$  **663**
- poly(oxytetramethylene) **128, 783**  
 heat capacity *129, 130, 132*  
 melting, by TMDSC *266*  
 data **544**  
 reversing behavior **650**  
 supercooling *266*
- poly(oxytrimethylene) **128, 783**  
 heat capacity *129, 130, 132*
- poly(oxy-1,4-*m*-xylylene), see:  
 poly(oxy-2,6-dimethyl-1,4-phenylene)
- polypentadecanolactone **132, 785**  
 heat capacity, liquid *133*
- poly(pentamethylene terephthalate) **145**
- poly(1-pentene) **780**  
 melting data **544**
- poly(L-phenylalanine) **788**
- poly(*p*-phenylene) *24, 789*  
 class of molecule *8*  
 letter abbreviation **17**
- poly(*p*-phenylene benzobisoxazole), ultimate strength **534**
- poly(*p*-phenylene benzobisthiazole), ultimate strength **534**
- poly(phenylene oxide), see: poly(oxy-1,4-phenylene)
- poly(phenylene sulfide), see: poly(thio-1,4-phenylene)  
 letter abbreviation **17**
- poly(1,4-phenylene sulfonyl) **793**
- poly(*p*-phenylene terephthalamide) **26**  
 step reaction *197, 198*  
 ultimate strength **534**
- poly(1-phenylethylene), see: polystyrene
- poly(4-phenyl-1-pentene), melting data **544**
- poly(4,4'-phthalimidobenzoyldodecamethyleneoxycarbonyl), mesogen of **563**  
 DSC cooling trace *567*  
 mesophase structure *566, 567*  
 TMDSC isotropization analysis *568*
- poly(4,4'-phthalimidobenzoylnonamethyleneoxycarbonyl), mesogen **563**  
 DSC cooling trace *567*  
 mesophase structure *566, 567*
- poly(pivalolactone) **786**
- poly(L-proline) **788**
- poly(1-propene sulfone) **793**
- poly( $\beta$ -propiolactone) **132, 785**  
 heat capacity, liquid *133*  
 melting data **545**
- poly[(2-propyl-1,3-dioxane-4,6-diyl)methylene], letter abbreviation **17**  
 synthesis *15, 16, 16, 20*
- polypropylene **18, 780**,  
 class of molecule *8*  
 crystal, linear growth rate *249*  
 nucleation *246, 246, 717*  
 table of nucleation data *248*

- crystallinity, by X-ray diffraction 513, 514
- etching 235
- helix, 466
- potential energy 466
- within crystals 467, 472, 473, 473
- Kuhn length 48
- letter abbreviation 17
- melting, see: polypropylene, stereoisomers, melting
- mesophase glass 561, 562, 561, 644, 645
- phase, areas 594, 594
- diagram with pentaerythrityl tetrabromide 716, 716, 717
- pVT diagram 299, 299
- stereoisomers 23
- melting of iPP **544**, 644–647, 644–646
- melting of sPP 647, 648, 647–649
- reversing behavior **650**
- TMDSC, DSC, and X-ray analyses 644–648, 644–649
- poly(propylene oxide), see: poly(oxypropylene)
- poly(propylene-*co*-styrene), blocky 229
- poly(propylene terephthalate), see: poly(trimethylene terephthalate)
- polypyromellitimide 232
- poly(L-serine) **788**
- polystyrene **782**, 19
- cross-linked with divinyl benzene 698
- crystal, linear growth rate 249
- emulsion polymerization 217
- foam, letter abbreviation 17
- glass transition 140, 406
- activation parameters 601
- analysis 600–604, 602–604, 683–685, 684, 685
- by TMDSC 388–392, 389–391, 600, 684
- cooling-rate dependence 683
- hysteresis, data 598
- molar-mass dependence 193
- network effects 698, 699, 699
- of solutions with poly( $\alpha$ -methylstyrene) by DSC 764, 765
- partial solubility, and 765, 766, 766
- pressure effect 690–692, 690–692
- separation from hysteresis 389, 390, 389, 390
- size effect 605, 605, 606, 606
- heat capacity 139, 140, 140
- TMDSC 366–369, 367, 368
- helix within crystals 467
- high-impact 235
- letter abbreviation 17
- in polymer-supported chemistry 237, 237
- Kuhn length 48
- letter abbreviation 17
- lifetime, by TGA 447, 447, 448
- melting, data of **544**
- peak temperature, dependence on crystallization temperature 661, 661
- Young's modulus 405, 406, 406
- Zimm plot 56–57
- poly(styrene-*co*-acrylonitrile), glass transition, change with sequence distribution 763, 763
- letter abbreviation 17
- poly(styrene-*block*-1,4-butadiene), molar mass and amphiphilic structure 747
- lamellar superstructure 511, 511
- poly(styrene-*co*-1,4-butadiene), 229
- glass transition 140, 759, 759, 760
- heat capacity 139, 140, 140
- letter abbreviation 17
- poly(styrene-*block*-1,4-butadiene-*block*-styrene), amphiphilic liquid crystal 485
- crystal-like superstructure 483–485, 484, 485
- poly(styrene-*co*-methyl methacrylate), glass transition description with the Barton equation 766, 767
- poly(styrene-*block*- $\alpha$ -methylstyrene), glass transitions 768–771, 769–771
- size effect 669–771, 770
- polysulfides, regular copolymers, melting for different CH<sub>2</sub>-group length 757, 757

- polyterephthalates, TMDSC 628–634,  
628–634  
see also: PET, PTT, PBT, PPT
- polytetrafluoroethylene 20, **781**  
class of molecule 8  
decomposition by TGA 232  
double endotherms 134, 135, 594  
entropy of fusion 134, **544**  
heat capacity 134, 135  
letter abbreviation **17**  
melting data **544**  
mesophase transition 134, 135, 174  
549–551, 550, 551  
TMDSC of 550  
phase, areas 594, 594  
diagram 550  
reversing behavior **650**  
shear stress 550, 551  
Theta temperature,  $\Theta$  134
- poly(tetrafluoroethylene-*alt*-isobutylene)  
229
- poly(tetramethyl-*p*-silphenylene  
siloxane), crystal, linear  
growth rate 249
- polythene, see: polyethylene
- poly(thio-1,4-phenylene) **789**  
letter abbreviation **17**  
rigid-amorphous fraction 694, 694
- polytridecanolactone 132, **785**  
heat capacity, liquid 133
- polytrifluoroethylene **781**  
letter abbreviation **17**
- poly(trimethylene adipate) 132, **786**  
heat capacity, liquid 133
- poly(trimethylene succinate) 132, **786**  
heat capacity, liquid 133
- poly(trimethylene terephthalate) **790**  
letter abbreviation **17**  
melting, by TMDSC 629–631, 630,  
631  
parameters 628  
reversing behavior **650**
- poly[trioxethylene-oxy-(1,3-  
phenylene)-(4,4'-oxy-  
dipthalimide)-1,4-phenyl-  
ene] **791**
- poly(L-tryptophan) **788**
- poly(L-tyrosine) **788**
- polyundecanolactone 132, **785**  
heat capacity, liquid 133
- polyurea 197, 198  
regular copolymers, melting for  
different CH<sub>2</sub>-group length  
757, 757, 758
- polyurethane 197, 198  
lower limit of chain folding 490,  
492  
regular copolymers, melting for  
different CH<sub>2</sub>-group length  
757, 758  
segmented, lifetime by TGA 449
- poly( $\delta$ -valerolactone) 132, **785**  
heat capacity, liquid 133
- poly(L-valine) **788**
- poly(vinyl acetate) **781**, 19  
letter abbreviation **17**  
reaction (hydrolysis) to poly(vinyl  
alcohol) 233, 233  
relaxation time 683
- poly(vinyl alcohol) 19, 233, 233, **781**  
class of molecule 8  
letter abbreviation **17**  
repeating-unit isomorphism 481,  
482
- poly(vinyl benzoate) **782**
- poly(vinyl-*p-tert*-butyl benzoate) **782**
- poly(vinyl butyral), see: poly[(2-propyl-  
1,3-dioxane-4,6-diyl)-  
methylene]
- poly(vinyl chloride) **781**  
class of molecule 8  
glass transitions of solutions with  
poly( $\epsilon$ -caprolactone) 764  
decomposition by TGA 232, 232  
emulsion polymerization 217  
glass transition by DMA 423, 423,  
424  
letter abbreviation **17**  
TMA of 408, 409, 408
- poly(vinyl cyclopentane), helix within  
crystal 467
- poly(vinyl ester)s, with long side-chains,  
melting of 755, 756
- poly(vinyl-*p*-ethyl benzoate) **782**
- poly(vinyl fluoride) **781**, 19  
isomorphism in crystals 481  
letter abbreviation **17**
- poly(vinylidene chloride) 20, **781**
- poly(vinylidene fluoride) **781**  
glass transitions with solutions of  
poly(methyl methacrylate)  
764



- isomorphism in crystals 481  
letter abbreviation 17  
melting, data **544**  
  peak, dependence on  
    crystallization 661, 662  
poly(vinylidene fluoride-*co*-vinyl fluo-  
  ride), repeating unit  
  isomorphism  
poly(vinyl-*p*-isopropyl benzoate) **782**  
poly(vinyl methyl ketone), helix within  
  crystal 467  
poly(vinyl naphthalene), helix within  
  crystal 467  
poly(vinyl stearate), copolymers, with  
  long and short side-chains,  
  melting of 755, 756  
poly(*p*-xylylene) **789**  
  conformational energy 43  
  letter abbreviation 17  
  molecular mechanics calculation 42  
POM, see: poly(oxymethylene)  
PO3M, see: poly(oxytrimethylene)  
PO4M, see: poly(oxytetramethylene)  
PO8M, see: poly(oxyoctamethylene)  
POMOE, see: poly(oxymethylene-  
  oxyethylene)  
POMO4M, see: poly(oxymethylene-  
  oxytetramethylene)  
PON, see: poly(2,6-hydroxynaphthoic  
  acid) and polyoxynaphthoate  
potassium, bromide, melting parameters  
  **541**  
  chloride, melting parameters **541**  
  ethylsulfate, TMA of 408, 408  
  fluoride, melting parameters **541**  
  iodide, melting parameters **541**  
  melting parameters **539**  
POTM, see: poly(oxytetramethylene)  
PP, see: polypropylene  
PPDL, see: polypentadecanolactone  
PPDX, see: poly-*p*-dioxanone  
PPO<sup>®</sup>, see: poly(oxy-2,6-dimethyl-1,4-  
  phenylene)  
PPL, see: poly( $\beta$ -propiolactone)  
PPP, see: poly(*p*-phenylene)  
PPS, see: poly(thio-1,4-phenylene)  
PPT, see: poly(pentamethylene  
  terephthalate)  
PPX, see: poly(*p*-xylylene)  
praseodymium dioxide, decomposition,  
  TGA 438, 439, 439  
praseodymium nitrate hexahydrate,  
  decomposition, TGA 441,  
  441, 442  
propane **793**  
  estimate of the heat of formation  
    324  
  melting parameters **543**  
propene, see: propylene  
propylene, reaction type **212**  
2,2'-propylidene-bis(1,2-epoxy-2-  
  phenoxyethane) **798**  
2,2'-propylidene-bis(1,2-epoxy-3-  
  phenoxypropane) **798**  
  polymerized with 0.2 moles of 1,2-  
  epoxy-3-phenoxypropane-(1-  
  methylidene)-1,4-phenylene-  
  oxy(2-propanol), prepreg of  
    **798**  
4,4'-(2,2'-propylidene)diphenol **798**  
protein, class of molecule 8  
  crystal, of molecule of globular  
    structure 483  
  of molecules with a fibrous  
    structure 480  
  heat capacity 127, 128, 137  
  synthesis 218  
  water content in crystals 483  
PS, see: polystyrene  
P(*S-alt*-AN), see also: poly(styrene-*co*-  
  acrylonitrile)  
pseudocumene, see: 1,2,4-trimethyl  
  benzene  
PTDL, see: polytridecanolactone  
PTFE, see: polytetrafluoroethylene  
PTMA, see: poly(trimethylene adipate)  
PTMS, see: poly(trimethylene  
  succinate)  
PTT, see: poly(trimethylene  
  terephthalate)  
PUDL, see: polyundecanolactone  
PVA, see: poly(vinyl alcohol)  
PVAc, see: poly(vinyl acetate)  
PVC, see: poly(vinyl chloride)  
PVL, see: poly( $\delta$ -valerolactone)  
PVF, see: poly(vinyl fluoride)  
PVF<sub>2</sub>, see: poly(vinylidene fluoride)
- Q**
- quartz 25  
  expansivity **295**

**R**

- rayon, see: cellulose  
 ribbon polymer 26, 26  
 ribonuclease 189, 190, 190  
 rubber, natural 10, 11  
     elasticity and structure data 580  
     see also: 1,4-poly(2-methyl  
       butadiene), *cis*  
 rubidium, bromide, melting parameters  
     541  
     chloride, melting parameters 541  
     fluoride, melting parameters 541  
     iodide, melting parameters 541  
     vulcanization 233

**S**

- salicylic acid, see: 2-hydroxybenzoic  
   acid  
 salts, Debye temperatures and heat ca-  
   pacities 114, **115**  
 sapphire 339  
     heat capacity 339, 349, 340  
     Lissajous figure 386, 386  
     thermochemical data 323  
     TMDSC, mass dependence 375,  
       375  
 seeds for polypropylene crystallization  
   248  
 selenium **793**  
     crystal structure 471, 472, 471  
     heat capacity, liquid 138–139, 139  
     helix, structure 465, 465  
       packing in crystal 472  
     hole equilibrium 139, 139  
     melting data 544  
     ring-chain equilibrium 138–139,  
       139  
     spherulite, hedgehog 500, 501  
 silicate glass class of molecule 8  
 silane, see: silicon tetrahydride  
 silica gel, in polymer supported  
   chemistry 237, 237  
 silicon, disulfide 25  
     atomization, heat of **324**  
     tetrahydride, melting parameters  
       539  
 silver 443  
     for calorimetry 312, 314  
     for DSC 332, 334

- melting parameters **538**  
     nitrate, TGA and DTA 443, 443  
     oxide 443  
 sodium, bromide, melting parameters  
     541  
     carbonate, thermochemical data  
       **323**  
     chloride 8  
       melting parameters 541  
       crystal structure 456  
       coordination number in crystal  
       of 472  
       thermochemical data **323**  
     fluoride, melting parameters 541  
     iodide, melting parameters 541  
     melting parameters **538**  
     sulfate, thermochemical data 323  
     Θ-temperature **111**  
     thermochemical data **323**  
 sPP, see: polypropylene, stereoisomer  
   (syndiotactic)  
 starch, glass transition 142, 143, 143  
     heat capacity 142–144  
       dry and with water 143  
 stearate, sodium 169  
 steam distillation 101  
 steel, see also: iron  
     bulk modulus **405**  
     ultimate strength **534**  
 strontium, melting parameters **538**  
 sulfur 234  
     atomization, heat of **324**  
     glass, ultimate strength **534**  
     hexafluoride, melting parameters  
       542  
 Surlin®, see: poly(methyl acrylate-co-  
   ethylene)  
 styrene, reaction type 212  
 syndiotacticity 24

**T**

- TCB, see: 1,2,4,5-tetrachlorobenzene  
 Teflon®, see: polytetrafluoroethylene  
 tetra-*n*-butylammonium, bromide **797**  
   iodide **798**  
 1,2,4,5-tetrachlorobenzene, phase dia-  
   gram with polyethylene,  
   714–716, 715, 716  
 tetrachlorosilane, melting parameters  
     542

tetracosane **795**  
tetradecane **794**  
    heat capacity of solid **327**  
tetra-*n*-decylammonium bromide **797**  
tetra-*n*-dodecylammonium bromide **797**  
    iodide **798**  
tetrafluoroethylene, reaction type **212**  
tetrafluoromethane, melting parameters,  
    **539**  
tetra-*n*-heptylammonium bromide **797**  
    iodide **798**  
tetra-*n*-hexadecylammonium bromide  
    **797**  
tetra-*n*-hexylammonium bromide **797**  
    iodide **798**  
1,2,3,4-tetrahydronaphthalene, diluent  
    for polyethylene **715**  
tetralin, see: 1,2,3,4-tetrahydro-  
    naphthalene  
[2,2',6,6'-tetramethyl-1,1'(2-oxy-1,2-  
    epoxyethane)]4,4'-biphenyl  
    **798**  
tetra-*n*-octadecylammonium bromide  
    **797**  
tetra-*n*-octylammonium bromide **797**  
tetra-*n*-pentylammonium bromide **797**  
    iodide **798**  
tetra-*n*-propylammonium, bromide **797**  
    iodide **797**  
tetratetracontane **796**  
thallium carboxylates, phases of the  
    homologous series **562**, **562**  
thiophene, melting parameters **542**  
tin, melting, parameters **538**  
    temperature **340**  
titanium, melting parameters **538**  
TIX, see: thallium carboxylate  
trichloromethane, melting parameters  
    **542**  
tridecane **794**  
trifluoroethane, melting parameters **542**  
trifluoromethane, melting parameters  
    **542**  
1,2,4-trimethyl benzene, melting  
    parameters **540**  
tritriacontane **795**  
trioxane, crystallization during polymer-  
    ization **273–275**, **275**  
tungsten, melting parameters **539**  
two-dimensional, flexible polymers **26**

## U

undecane **794**  
    melting parameters **543**  
uranium, melting parameters **539**  
urea **6**  
    heat of fusion **339**

## V

vanadium, melting parameters **539**  
Vectra™, see: poly(oxybenzoate-co-  
    oxynaphthoate)  
*N*-vinyl carbazole, reaction type **212**  
vinyl chloride, reaction type **212**  
vinyl ester, reaction type **212**  
vinyl ether, reaction type **212**  
vinyl fluoride, reaction type **212**  
vinylidene, reaction type **212** chloride  
*N*-vinylpyrrolidone, reaction type **212**  
virus, tobacco necrosis, crystal structure  
    **166**

## W

water, bulk modulus **405**  
    crystal morphology **456**  
    class of molecule **8**  
    melting parameters **542**  
    pVT diagram **300**, **301**  
    thermochemical data **323**  
    transition temperature **340**

## X

xenon, melting parameters **538**

## Z

zinc, melting, parameters **539**  
    temperature **340**  
zirconium, melting parameters **539**

---

# Subject Index

In this Subject Index, definitions or equations are found at the underlined pages. Brief biographic information is given at the pages in **bold** numerals. The *italics* direct to information displayed in the figures. For substances, see the Substance Index, except for Sections Headings, these also are listed also in the Subject Index.

## A

acknowledgments VIII  
ADMET 197  
Advanced Thermal Analysis, see:  
    ATHAS  
affine deformation 405  
AFM 270, 829, 829  
    for local melting 269, 270  
    for mass determination 67, 508,  
        508, 573, 574  
    for surface analysis 511, 511  
    see also: microcalorimeter  
amorphous phase, see: phase,  
    amorphous  
analysis, dielectric thermal, see: DETA  
    differential thermal, see: DTA  
    dynamic differential thermal, see:  
        DDTA  
    dynamic mechanical, see: DMA  
    thermomechanical, see: TMA  
*Analytical Chemistry* 331  
anharmonicity 111, 303  
annealing 655–666, 655–665  
asymmetry correction 103  
ATHAS 79, 121–128, 144, 145  
    addition scheme of heat capacities  
        144, 145  
    applications 134–145, 134–143  
    Data Bank VII, 144, 777–800  
atom model, solid or hard-sphere 37,  
    301–303, 302  
    united 43  
atomic force microscopy, see: AFM  
Avogadro's number 428

## B

backbiting 24  
birefringence 850  
Black **306**  
blend 725  
boiling point elevation 58–62, 59–62  
    100, 100  
    solvents for 60  
boiling temperature, see: temperature,  
    boiling  
Boltzmann **94**  
    distribution 106, 106, 815  
bond, directiveness 4, 5, 5  
    chemical 4  
    strength 4  
    types 4, 5  
    weak 5, 5  
bonding, molecular 3–5, 3–5  
Bowditch curves, see: Lissajous figures  
branching coefficient 231  
Bravais lattices 457, 458, 458  
Bridgman **4**  
Bunsen **307**  
    ice calorimeter 307, 308  
burette 295, 296  
Burgers vector 519, 520

## C

calculation, dynamics, molecular  
    43–47, 44–47  
    mechanics, molecular 41–43, 42,  
        43  
Monte Carlo 40, 40, 41, 41

- caloric 1, 1, 2, 72, 73–75, 304  
calorie 304  
calorimeter, 78, 307  
    aneroid 307, 308, 310  
    adiabatic 101–104, 307, 312, 313  
        scanning 317, 317  
    bomb or reaction 309, 309  
    compensating 314–317, 315  
        see also: microcalorimeter of  
            Tian and Calvet  
    differential scanning, see: DSC  
    drop calorimeter 307–309, 308  
    ice 305, 306, 306, 308  
    isoperibol 307–310, 318, 318  
        scanning, twin 307  
    isothermal 307–310  
    liquid 308–310, 309, 318, 319  
    modern 317–319, 317–319  
    principle 304–307, 305, 306  
    scanning 307  
    twin 307  
calorimetry 77, 77  
    adiabatic 312–314, 313, 414  
        loss determination 313, 314  
    applications 319–329, 320–322,  
        324–329  
    differential scanning, see: DSC  
    loss calculation 310–312, 310, 311  
    temperature-modulated differential  
        scanning, see: TMDSC  
Carnot 74  
Carothers 197  
cathetometer 296, 297  
CD, see: condis crystal  
CED, (cohesive energy density) 183,  
    544–547, 544, 545  
Celsius 281  
chapter, summaries VI  
char formation 232  
chemical, potential 99, 99, 708, 709  
chemical reaction, analysis by TMDSC  
    402, 403, 402, 403  
    identification by DTA 351–354,  
        353, 354  
chemistry 7  
    polymer-supported 237, 237  
chiral carbon atom 848  
chromatography, size-exclusion 62–63,  
    63  
Clausius 74  
clock, atomic, or cesium-133 283, 284  
CN, see: coordination number  
cohesive energy density, see: CED  
cold crystallization 251, 386, 387  
coil, random, see: flight, random  
colloid 9–10, 167  
component, thermodynamic 705  
compressibility 105, 404, 404  
condis crystal 165–167, 167, 171, 171  
    examples 174, 174, 175  
        see also: Sect. 5.5, pp. 547–571  
    motion in 551, 552, 552  
        see also: mesophase  
conductivity, electric 285–287, 286  
configuration 463, 466, 848  
conformation 463, 849  
    *gauche* 39, 39  
        by IR spectroscopy 85, 87  
        by molecular dynamics simula-  
            tion 47, 87, 525–527,  
            525–527  
        see also: macroconformation  
    *trans* 39, 39  
conformational, disorder 552, 558–561  
    motion 121, 551, 552  
conservation, of energy 76  
    of mass 76  
cooling curve 62, 290, 290 291  
    by molecular dynamics calculation  
        85–88, 85–87  
coordination number 302, 303  
    of helices 472, 472  
    of ions 472  
copolymer 22, 22  
    azeotropic 228, 229  
    alternating 22, 228, 228, 229  
    block 22, 228, 229  
    composition, diagram 228  
        ratio 227–229, 228  
    crystallization 481–483, 482, 483,  
        727–729, 728, 731, 731, 731  
        732  
        theory, cold crystallization  
            731–733, 731, 732, 733  
        theory, eutectic 726–730,  
            727–730  
        theory, solid solution 730, 731  
equation for synthesis 227–229,  
    227, 228  
feed ratio 227  
glass transition, see: transition,  
    glass

- graft 22, 23, 235, 235, 236  
melting, see: melting, of  
    copolymers  
nomenclature 22, 22, 23, 23  
random 23, 228, 229  
reactivity ratio 227, 227  
regular 22  
synthesis, see: reaction, copolymer,  
    chain or step  
creep 414, 415  
critical temperature, see: temperature,  
    critical  
critical length for molecular nucleation  
    254, 255, 265, 266, 266  
cross-linking, chemical, to avoid crystal  
    reorganization 658, 659,  
    680, 680, 681, 681  
    for gelation 231, 231, 232  
    rubber 233, 234, 234–236  
    with ionizing radiation 234, 235,  
    658, 659, 680, 680, 681  
CRU, see: repeating unit, constitutional  
cryoscopy 61–62, 62  
crystal 165, 166, 238, 455–457, 456,  
    457  
    annealing and recrystallization  
        655–666, 655–665  
        avoiding by fast heating and  
        cross-linking 268, 269,  
        269, 612, 614, 658, 659,  
        679–681, 680, 681  
    block copolymer, irregular motifs of  
        483–485, 484, 485, 511, 511  
    chain-folded 487, 487  
    chain-folding principle, of  
        macromolecular 487, 488  
    columnar 552, 552  
    condis, see: condis crystal  
    defect 511–535  
        amorphous 517, 517  
        chain disorder 516, 519  
        computer simulation of 87,  
        524–530, 524–530  
        dislocation 251, 252, 252,  
        517–524, 519–523  
        energy 86  
        *gauche* 525–527, 525–527  
        grain boundaries 517, 518  
        kink (2g1) 516, 523, 608  
        kink, formation mechanism  
        525–527, 527  
crystal, defect, point 516, 519  
    twist 524, 524, 527  
    types 516–524, 516–522  
deformation 530–533, 531–533  
dendritic 497–499, 497–499  
elements and salts, Debye tempera-  
    tures and heat capacities  
        114, **115**  
enthalpy decrease, hierarchy 468,  
    469  
etching 502, 503  
extended-chain 487, 487, 509, 510  
fibrillar 503–507, 504–507  
fold-length, of the 488–493,  
    489–492  
    theory 493  
fringed micellar 487, 488  
growth, directional 256–257, 257  
    experiments 264–275  
    faces 493  
habit 486, 486  
helical-lattice-based 468  
helix, orientation in 472, 473, 473  
    inclination 474  
homologous series, of 480  
index, see: Miller index  
isometric 508–511, 508–510  
isodimorphism 481  
isomorphism 481–483, 482, 483  
    types of 481  
    of copolymers 481–483, 482,  
    483  
jump-motion in 555–558, 556, 557  
lamellar 493–497, 493–496  
lattice 457, 457  
liquid, see: liquid, crystal  
microscopic image 166  
melting, see: melting, of crystals  
mesophase, see: mesophase  
morphology 486–511, 586, 587,  
    589–511  
    equilibrium 487, 656  
nucleation, see: nucleation  
nanophase separation, within 169,  
    170, 553, 553  
packing, in 468–471, 469–472,  
    474–482  
plastic, see: plastic crystal  
pleated 493, 494, 494, 495  
polar and nonpolar chains, in 480,  
    481, 481

property, structure sensitive or insensitive 512, 512  
 see also: mesophase  
 shish-kebab morphology 503, 504  
 staining 502  
 structure 455–457, 456  
   with helices 471–476,  
     471–476, 478, 478, 480, 480  
   with zig-zag chains 469–471,  
     470, 476–481, 477, 479,  
     481, 482, 504, 505, 505  
 spherulite 238–240, 239, 240,  
   499–503, 500–502  
 twin boundaries 496  
 unit cells 457–458, 458  
   see also: crystal, structure  
 crystallinity, analysis 512–516,  
   513–515  
   baseline from 516  
   by calorimetry 355, 356, 632–634,  
     632, 633, 634  
   by X-ray diffraction 513, 513, 514  
   by IR analysis 514, 515, 515  
   volume fraction 261, 261  
   weight fraction 512, 512  
 crystallization, cold 251  
   during polymerization 189,  
     201–206, 202, 206, 273,  
     488, 510, 511  
   diffusion control 257–259, 258,  
     259  
   directional dependence of 256,  
     257, 257  
   free growth approximation 260,  
     261, 261  
   kinetics, by DSC 269, 271  
   nonperiodic layer model 745  
   paracrystalline lattice model 746  
   rate, comparison to recrystallization  
     663, 665  
     linear 249, 249, 255–256, 256  
     regimes 273, 274  
     reversibility 255, 256, 268  
   see also: equation, Avrami  
   similarity to chain-growth  
     polymerization 238  
   spherulitic 238–240, 239, 240,  
     259–263, 260, 261, 262,  
     497–503, 597–503  
   under strain 581–583, 582, 583  
 curing 402, 403

## D

Dalton 1  
 Davy 73  
 DDTA 683, 683  
 Debye 55  
   approximation of heat capacity  
     112–116, 111–116  
   relaxation time 117  
 Debye-Hückel theory VII, 97, 708  
 decoupling, of chain segments 649  
   connection to broadening of the  
     glass transition and  
     formation of RAF 649  
   in block and side-chain copolymers  
     754, 755, 755, 756  
   on assessment of components 591,  
     705  
   on crystallization 267, 267, 268,  
     399, 400, 649, 651, 652  
   on disentanglement, to be followed  
     by crystallization 487  
   on melting, to be followed by mix-  
     ing 730, 730, 732  
   points of, in copolymers 723–725,  
     724  
 decomposition 231, 232, 232  
   by TGA 232, 438, 439, 439  
 definition, operational 3, 4  
 deformation, affine 405  
   plastic 405, 415  
 degeneracy 106, 107  
 dendrite 497–499, 497–499  
   hedgehog 499, 499  
 dendrimer 25, 25  
 density, gradient method of measure-  
   ment 296–298, 297  
   measurement 295–298, 296, 297  
   of matter within a random coil 32,  
     33  
 DETA 424–428, 425–427  
   Cole-Cole plot 427, 428, 427  
   comparison to DMA 424, 427  
   schematic and circuit diagram 425  
 dielectric constant, see: permittivity  
 differential thermal analysis, see: DTA  
   and check also DSC  
 differential scanning calorimetry, see:  
   DSC  
 differential thermogravimetry, see  
   DTGA

- diffusion, sliding, in crystals 488, 489  
  molecular dynamics simulation  
    527–529, 528, 529  
  temperature dependence 530
- dilatometer 291, 296, 297, 407
- dilatometry 77, 77  
  Avrami analysis by 272, 273  
  application of 298–303, 298–302  
  principle of 291–293, 292
- diluent method, for determination of  
  heat of fusion 100, 100, 715, 715
- dipole 424
- diradical 15, 16
- dispersion 28, 28
- distillation, steam 100–101
- DMA 79, 412  
  analysis of data 417–419, 418, 419  
  application 419–424, 420–424  
  comparison, to periodic and non-  
    periodic experiments 417  
  with DSC and TMDSC 418,  
    419, 609, 610, 610  
  to DETA 424, 427  
  defined frequency 413, 414  
  energy dissipation 418, 418  
  principle and instrumentation  
    412–419, 415  
  resonant 413, 413  
  see also: viscoelasticity  
  temperature-modulated 418, 636,  
    636, 637, 641, 642, 670, 671  
  torsion pendulum 413, 413, 414
- draw ratio 32
- DSC 77, 329  
  applications 349–358, 359–354,  
    356–358  
  baseline, method for heat of fusion  
    determination 347, 347,  
    348, 348  
  basic equations for 346  
  calibration 338–340, 339, 340  
    for heat capacity 339, 340, 340  
    for latent heats 338, 339, 339  
    for lag 340, 355, 357, 358  
  of onset temperatures of melting  
    with heating rate 357, 358,  
    357, 358  
  of temperature 339, 340  
  standards 339, 340, 818, 818  
  comparison, with DMA 418, 419,  
    609, 610, 610  
  coupled with TGA 439–443  
  development from DTA 820–823,  
    820–822  
  difference from DTA 821  
  dual 334, 335  
  extreme conditions, see: DTA,  
    extreme condition  
  fingerprinting 350–354, 350–354  
  glass transition, measurement  
    354–355  
    calculation 835, 836, 836  
  heat capacity measurement  
    102–104, 103, 349–350  
  heat-flow-rate equation 835, 836,  
    835, 836  
  heat-flux 331–335, 820, 820  
    modern 332–335, 332, 335  
  mathematical treatment 340–348,  
    341–348  
    conditions for 341, 342  
    of heat capacity 345–347, 346  
    of heat of fusion 347, 348, 347,  
      348  
    steady state 341–343, 341, 343,  
      841, 841  
    with temperature gradient  
      341–343, 341, 343  
    without temperature gradient  
      344–348, 344  
  melting, see: melting, by DSC  
  online baseline correction  
    831–834, 831–833  
  power compensation 335–338, 336  
  principle of operation 337, 338  
  principle 329  
  standard, used for TMDSC with  
    sawtooth modulation  
    837–839, 837–839  
  signals, standard and modulated  
    333  
  steady state 333, 333, 342, 841,  
    841  
  temperature gradient 343  
  DTA, and DTGA, data 439–443,  
    440–443  
  difference from DSC 821  
  early equipment 330, 821, 822  
  extreme conditions 824–829, 824,  
    825, 828, 829  
  fast measurement 826–828  
  low temperature 824



high temperature and pressure  
825  
 see also: microcalorimetry  
 ICTAC rules 438, 822, 823  
 fast, melting without reorganization,  
 268, 269, 612  
 see also: DSC 79  
 schematic 820  
 DTGA 439  
 Dulong-Petit's rule 106, 110  
 dynamic mechanical analysis, see:  
 DMA

## E

ebulliometer 60  
 Einstein 64  
   approximation of  $C_v$  111  
   function 110, 110, 125  
   temperature 110, 110, 111, 111  
 elasticity, coefficient, isothermal, see:  
   modulus  
   energy 578, 579, 579  
     thermodynamics 579, 579  
   entropy 579–583, 580  
     comparison to gas expansion  
       581, 581  
     fusion diagram 581–583, 582,  
       583  
     rubber, data 580  
     thermodynamics 580, 580, 581  
 Hookean 415, 416, 579  
 perfect 415  
 Poisson's ratio 405, 405, 579, 580,  
   580, 581  
   see also: viscoelasticity  
 electron, affinity 3  
   valence 3, 3  
 electronegativity 3, 3  
 elements, ancient 72  
 emanation thermal analysis 79  
 emulsion polymerization 217, 217  
 enantiomorph 463  
 end-group, determination 66  
   nomenclature 14, 16, 16  
 end-to-end distance 31, 31  
   restrictions 33  
 energy 75, 76, 76  
   bond 3, 4  
     table of 324  
   conservation of 76  
   density 183  
   dissipation 418, 418  
   free 91, 92  
   ionization 3  
   level 106, 107  
   of atomization, table of 324  
     rotational 37  
   total 106, 107  
     quantum mechanical 107  
 entanglement 33, 37, 572, 573, 573  
   in gel formation 231, 570  
   limit 192, 193, 576, 577  
 enthalpy, H 83, 84  
   free 92, 93, 304, 305  
     at 0 K for polyethylene 142  
     close to equilibrium 146  
     distribution 595, 595  
     of formation, table 323  
     partial molar, see: chemical  
       potential  
     of formation 322, 322  
   reference temperatures for H 304  
   see also: heat  
 entropy, S 91, 91, 92  
   conformational 39  
   derivation of  $dS/dt$  814  
   flux and production 147, 147, 148,  
     148  
   of evaporation 182, 186, 539  
   of fusion 537–547  
     conformational, rule of 544,  
       545  
     orientational, rule of 541, 542  
     tables 538–545  
     translational, rule of 538–541,  
       540  
   of the liquid at 0 K 140–142, 141  
   of mesophase transitions 554  
   relationship to disorder 814  
 epitaxy 246, 247, 247  
 equation, Arrhenius 263, 263, 817  
   Avrami 260–263, 261, 262  
     derivation 261  
     examples 271–274, 272–274  
     general 262  
     use for lamellar and fibrillar  
       growth 263  
 Barton 761, 762, 762, 763  
 Bragg 513, 513, 851  
 Boltzmann 94, 814  
 Couchman 764, 765

- Clausius-Clapeyron 300, 581, 582,  
690
- Debye, for heat capacity, see:  
    function, Debye  
    for light scattering 55  
    for molar polarizability 426  
    for viscosity 64
- Einstein, heat capacity, see:  
    function, Einstein  
    mass-energy 76  
    viscosity 64, 65
- Flory-Huggins VII, 55, 709–711,  
709–711
- Fox 761, 761
- Freeman-Carroll 263
- Fourier, of heat flow 342, 343,  
835, 835, 836
- Gibbs, for partial molar quantities  
157
- Gibbs-Di Marzio 760, 761
- Gibbs-Duham 98, 98
- Gibbs-Thomson 154, 155
- Gordon-Taylor 760, 761
- Johnston 762
- Maxwell, relation of polarizability  
    and refractive index 424,  
    808, 809
- Nernst-Lindemann 105–106, 105  
    for organic molecules and  
    macromolecules 105, 106
- Poisson 261, 261
- Schneider 761, 761
- Tarasov 125, 126
- Tool-Narayanaswamy 683
- van der Waals 51, 163
- van't Hoff 817
- virial 55
- Williams-Landel-Ferry 419, 577,  
578
- Wood 760
- equipartition 107
- esterification, energetics 201  
    rate 200
- etching, by hydrolysis 236  
    chemical 191, 192, 236
- Euler reciprocity relationship 813
- evolved gas analysis 79
- expansivity 105, 292  
    conversion, linear-to-volume 292  
    linear 292  
    table of, for solids 295
- extensive thermodynamic quantities 75
- extension, of flexible macromolecules  
580  
    of rigid macromolecules 405, 479
- F**
- Fahrenheit 281  
    temperature scale 281
- fiber 503–507, 504–507  
    carbon 235  
    formation 530–533, 531–533  
    gel-spun, of polyethylene 569–571,  
    570, 571, 674–677, 674–677  
    of PET 409–411, 409–411, 505,  
    506, 505–507, 534, 535,  
    535, 677–670, 678, 679  
    see also: melting, of fibers  
    shish-kebab morphology 503, 504  
    X-ray diffraction, of PET 504–506,  
    505–507  
    of polyethylene 513, 596, 596,  
    674, 674, 675
- fingerprinting of materials by DTA or  
    DSC 350–354, 350–354
- flight, random 31, 31–32, 487, 487
- Flory 9
- flux of extensive thermodynamic  
    quantities 88, 147, 148,  
    148
- fold-length, in crystals 488–493
- force-times-length term in enthalpy  
    expressions 304, 305,  
    579–582
- Fourier series 840, 841, 841
- freedom, degree of 106, 112  
    slowly responding 117
- freely-jointed chain, equivalent 47, 48
- Freeman-Carroll method 263–264, 263  
445, 445
- freezing point lowering 58–62, 59, 99,  
99, 100, 711, 711  
    solvents for 60
- function, Debye 113  
    one-dimensional 111, 112, 113,  
    125  
    three-dimensional 113, 113,  
    114  
    two-dimensional 112, 113  
    for chalcogenides,  $\Theta_2$  and  $\Theta_3$ ,  
    116

Einstein 110, 110  
 Gibbs, see: enthalpy, free  
 Langevin 35  
 of state 82  
 partition 107, 107, 108  
 Tarasov 125, 126  
     fitting to heat capacity 127,  
     127

## G

gas, law, Boyle's 81  
     Gay-Lussac's 81, 281, 281  
     ideal 36, 51, 81, 163, 581, 581  
     conditions for the 163  
     van der Waals' 36, 163  
     kinetics 81, 163  
 gel 230–231, 231, 237  
 gel-permeation chromatography, see:  
     size exclusion  
     chromatography  
 Gibbs 92  
     free energy or function, see:  
         enthalpy, free  
 glass 6, 7, 165, 167  
     behavior of 180, 389–391, 391  
     motion in 572, 573  
     structure 572, 573  
     ordering of 592  
     pressure densified 690, 690  
     transition, see: transition, glass  
 glide plane 462, 463, 462  
 Goodyear 234  
 grafting 235, 235  
 gravity, center of 32, 32–33  
 Gimm's tetrahedron 5, 5  
 group theory 460, 848  
 Gay-Lussac 282

## H

heat 76, 81–84, 83  
     capacity 82, 83  
         additions scheme 131–133,  
         132, 133, 139, 140, 145  
         apparent 355, 356  
         apparent, contributions to 742  
         at arrested equilibrium 157  
         by DSC 349–350  
         by molecular mechanics calcu-  
         lation on cooling 86

heat, capacity, by TMDSC 364–369,  
     365–368, 385–388, 385–388  
     calculation, using the ATHAS  
     system 121–145, 123,  
     124–143, 144, 145  
     comparison to expansivity 303  
     complex 117–118, 118, 382,  
     384  
     crystallinity dependence  
         118–121, 119–121  
     determination of  $C_p - C_v$   
         104–106, 105  
     dissipative 117  
     equations for 101  
     for two energy levels 108  
     for harmonic oscillators 109,  
         110, 109, 110  
     imaginary 117  
     measurement 101–104, 103  
     missing, in case of symmetric  
         jump motion 555–558,  
         556, 557  
     of a liquid 131–133  
     of a solid 111–116  
     of copolymers 139, 768  
     of homologous series 128–133,  
         129, 132, 133  
     of liquid selenium 138–139,  
         139  
     of MBPE-9 137–138, 138  
     heat capacity of solid paraffins  
         327–329, 327, 328  
     of polyethylene, large-amplitude  
         motion 136, 136  
     of polymethionine 136, 137  
     relation to the thermodynamic  
         functions 95  
     of polyoxides 128–131,  
         129–132  
     of poly(oxybenzoate-*co*-  
         oxynaphthoate) 134, 135  
     of poly(styrene-*co*-butadiene)  
         139–140, 140  
     of polytetrafluoroethylene 134,  
         134, 135  
     of starch 142–144, 142, 143  
     on fast heating 157, 158  
     quantum mechanics 106–111,  
         107  
     thermodynamic theory  
         104–106

heat, content, see: enthalpy (H)  
 development of the understanding of  
     71–75, 72  
 flow rate 147, 342, 343  
     as an example of a transport  
       process 158, *158*  
 derivation of the equation for  
     835, 836, 835, 836  
 difference between reversible  
     and reversing 358  
 latent 84, 291  
 measurement of 304, 305, 305  
     see also: calorimetry  
 of combustion 309  
 of formation 322  
 of fusion, by DSC 355, 356, 356  
     diluent method 100, *100*, 715,  
     715  
 of reaction, for organic compounds  
     323, 324, 324  
 pump 581  
 reference temperature for the  
     (enthalpy) 304, 322  
 specific 82  
 unit of 304, 305  
 heating curve 290, 290, 291  
 helix 463  
     anticlinal 474  
     axes 463, 464  
     class of 463, 464  
     enantiomorphs 463  
     handedness 463  
     irrational 463  
     isoclinal 474  
     lattice 463–468  
     packing in crystals 471–473, 472  
     projection 464  
 Heller **801**  
 Helmholtz free energy, see: energy, free  
 Henry's law 708, 708  
 Hildebrand, entropy of mixing of  
     macromolecules 709, 709  
 hindrance, steric 37, 38  
 history of, calorimetry 304–307, 305  
     chemistry 1, 2, *1*, 2  
     covalent structures 9, *10*  
     crystals 165, *166*, 455–457, *456*  
     dilatometry 291–293, 293  
     DSC and DTA 329–331, *330*  
     heat and temperature 71–75, 72  
     natural polymers 9–10, *11*

synthetic polymers 11–12, *12*  
 TGA 429, 429, 430  
 thermometry 279–283, 280  
 Hooke's law 404, 405, 415, 416, 579  
 hydrodynamics 415

## I

ICTAC 77, 78, 331  
     logo 72, 73, 77, 78  
 impingement, of crystals 239, 239,  
     240, 261  
     lines of 239, 240, 242  
 induction time 239, 241, 241  
 infinitesimal changes 75, 76  
 interference effects 52, 851  
 International Confederation for Thermal  
     Analysis and Calorimetry, see:  
     ICTAC  
 international temperature standard, see:  
     ITS 1990  
 intensive thermodynamic quantities 75  
 inversion, axes 461, 462, 461  
     center of 461, 461  
 ionomer 236, 236  
 irradiation, with <sup>60</sup>Co 234  
 irreversibility 94  
 Ising model, 122, 554, 555, 554, 555  
 isometric crystal, see: crystal, isometric  
 isomer 17, 23  
     conformational 39  
     model 122  
     head-to-head 23  
     head-to-tail 23  
     rotational 37–40, 38, 39  
     positional 23  
     stereo 23, 848  
     structural 23  
 isomorphism, see: crystals,  
     isomorphism  
 isotacticity 24  
 ITS 1990 281, 818, 818, 819  
 IUPAC 13

## J

Joule **74**  
*Journal of Thermal Analysis and*  
*Calorimetry* 77, 331  
 jump-motion in crystals 555–558, 556,  
     557

**K**

Kauzmann paradox 142  
 Kauzmann temperature 140  
 Kekulé **9**  
 Kelvin **74**  
 kinetics 189, 817  
   nonisothermal 263–264, 263  
 Kossel crystal 249, 250  
 Kuhn **47**  
   length 47, 48, 48, 49  
 kurtosis 28, 28

**L**

Laplacian operator 835  
 Lavoisier **73**  
 LC, see: liquid, crystal  
 Le Chatelier **330**  
 Legendre transformation 93, 813  
 length, comparison 293–295, 294, 295  
   measurement, 291–295, 292–295  
     by interference microscopy  
       294, 819  
   standard 291  
     krypton-86 819  
   scale, macroscopic V,  
     microscopic V, 37  
 lifetime, determination by TGA  
   446–449, 447, 449  
 linearly variable differential  
   transformer, see: LVDT  
 liquid, definition 164, 165, 575  
   crystal 167, 169, 170, 171, 172  
     amphiphilic, block copolymer,  
       structure of 484, 485, 484,  
       485, 724, 724, 725  
     cold crystallization 547, 548  
     examples 171, 172, 172, 547,  
       548  
     glass transition, see: transition,  
       glass  
     gradual change of order 560  
     macromolecular 553, 553  
     nematic 169, 552, 553, 552,  
       553  
     nematic, macromolecular 553,  
       553  
     nematic, one-phase structure of  
       553, 553  
   see also: mesophase

  smectic 169, 552, 552, 553,  
     553  
   soap, transitions 562, 562  
   thermotropic 724, 724  
   glass transition, see: transition, glass  
   phase, see: phase, amorphous  
 liquidus line 100  
 Lissajous figure 379, 380, 380, 381,  
   386, 386, 397, 397  
 LVDT 294, 295, 295, 407

**M**

macroconformation 32, 486–489, 487  
   of molecules in crystals 486–488  
 macromolecule 6–7, 6  
   see: polymer  
 macrophase 162  
 mass 428, 429  
 material property 512  
 Maxwell, model, see: viscoelasticity,  
   models  
   relations 93, 813  
 Maxwell-Boltzmann distribution of the  
   speeds of molecules of a gas  
     815  
 mean, arithmetic 28, 28  
 melting 6, 165  
   broadening of range of 400, 597  
   by DSC 339, 355–358, 356–358  
   by TMDSC 396–401, 397, 399,  
     401  
   equilibrium 151  
   experiments 264–275  
   free enthalpy diagrams 152–154  
   kinetics 238  
   mechanism 538  
   temperature, change with  
     crystallization temperature  
       613, 635, 661–663  
     extrapolation to equilibrium  
       154, 155, 537, 660, 661  
   odd-even effect 327–329, 329, 543,  
     757  
   of alkali halides, table of 540, 541,  
     541  
   of copolymers 725–758, 734–748,  
     750–753, 755–758  
     block 723–725, 747–755, 748,  
       750–753, 755, 756  
     alternating 751–754, 751–753

- LLDPE 733–742, 735–742  
PETcoOB 743, 743, 744  
POBcoON 743–747, 744–747  
regular 756–758, 757, 758  
theory 725–733, 726, 727–733  
with long long and short side-chains 755, 756  
of crystals of linear hydrocarbons 542–544, 543  
of fibers 672–681, 673–681  
of lamellae 148–155, 149, 150  
of macromolecules 544–547, 544, 545  
of nonspherical motifs 541–542, 542  
of PEEK 668–672, 669–672  
of polyethylene 611–623, 612, 613, 616–623  
of polymers with long side chains 754, 755, 755, 756  
of poly(oxymethylene) 666–668, 666, 667  
of polypropylenes 644–649, 644–649  
of poor crystals 652–654, 652–654  
of spherical motifs 538–541, 538–541  
of the fold surface of polyethylene 623, 623  
of the growth face of polypropylene 646, 647, 647  
prediction of 536–547, 537–545  
rate 255–256, 256, 268  
reorganization during 400, 401, 401  
reversible, decoupling of segments of polymer chains 649–651, 651  
of poly( $\epsilon$ -caprolactone) 641–643, 642–644  
of polycarbonate 637–639, 637–639  
of polynaphthoate 634–637, 635, 636  
of poly(oxyethylene) 264–265, 264, 265, 624–627, 624–627  
of poly(phenylene oxide) 639–641, 640, 641  
of polyterephthalates 628–634, 628–634  
reversing, table 650  
surface melting 529, 530, 623, 623, 646, 647, 647  
under strain 581–583, 582, 583  
zero-entropy-production 151, 153, 154, 154  
mer 13, 191  
mesogen 169  
main- and side-chain 26  
mesophase 165, 167, 169–175, 547–571  
characteristics of the three 171  
classes of 165, 166, 551–555, 552–554  
cold crystallization 547, 548  
examples 561–571, 561–565, 567–571  
glass 166, 167, 175, 176  
transition, see: transition, glass  
gradual change of order 560  
motion in 551, 552, 552  
summary 572  
metal, heavy, density 5  
microcalorimeter, based on AFM 269, 270, 331  
principle of 829, 829  
for small amounts of heat, based on a design of Tian and Calvet 314, 315  
data and loss calculation 315–317, 316  
microcrystalline powder 236  
micrometer screw 293  
microphase 162, 167  
microscopy, polarizing 850  
Miller index 458–460, 459  
mirror plane 461, 462  
mixing, entropy of 97, 97  
free enthalpy of 97  
ideal 97, 97  
solids, liquids, and gases 96  
modulus 404  
bulk 404, 404  
table 405  
comparison to heat capacity 418, 419  
complex 418, 418  
dynamic 413  
shear 404, 404  
tensile 404, 404, 405, 406, 406  
rubber elastic plateau 406  
viscous flow

three-phase model 534, 534  
 Moiré pattern, optical analog 522,  
     852–853  
 molar quantities, partial 98, 98, 712,  
     712  
 mole 428  
 molecular mass, determination, by AFM  
     67  
     by boiling point elevation  
         58–62, 59, 60  
     by calorimetry 67  
     by dilatometry 67  
     by electron microscopy 67  
     by freezing point lowering  
         58–62, 59  
     by light scattering 54, 54  
     by melt viscosity 67  
     by membrane osmometry 65  
     by solution viscosity 63–65  
 distribution 27, 27–30, 33–37  
     examples 30  
     Gaussian 33, 34, 35  
     number average 29, 29  
     polydispersity 30  
     see also: reaction, chain and  
         reaction, step  
     weight average 29, 30  
 molecule 2, 2  
     amphiphilic 170, 563, 563, 724  
     classification scheme 6–8, 6, 8  
     pseudo 3  
     size unit of, compared to the human-  
         size unit V  
     small, definition 6, 6  
     structure 3–5  
         compared to motion V  
 moment 27–28  
     calculation of 28, 28  
 monomer 13  
 motion, compared to structure V  
     molecular, types of 121, 122  
     large-amplitude 121, 122

## N

nanophase 162, 162, 168, 169  
 NATAS, 77, 77, 331  
 Natta **209**  
 Nernst **94**  
 network, interpenetrating 26  
     neural 84, 88, 811–812

Newton **280**  
 Newton's law 290  
 normal mode analysis 121, 123, 816  
 North American Thermal Analysis  
     Society, see: NATAS  
 nucleation, athermal 241  
     critical 243, 243  
         table of dimensions 244  
     heterogeneous 240, 246–249, 246,  
         248, 249  
     homogeneous, 240, 244–246, 244,  
         245  
         rate of 244  
     induction time 238, 241, 241  
     molecular 253–255, 254, 398  
         critical length for 254, 255  
         evidence for 253  
     observation of 238, 239, 240–242,  
         241  
     primary 240, 242–246, 252  
         thermodynamics of 242, 243  
     rate, evaluation 240–242, 240  
     secondary 249–253, 250, 251, 252  
     tertiary 253  
     thermal 240  
 numbers, types of 849  
     complex 117, 816, 849  
     rational and irrational 463, 849

## O

oligomer 191  
     properties 192, 193  
     synthesis 191–192, 192  
 oscillation, see: vibration  
 osmometry, membrane 65–66, 65  
     vapor phase 61  
 Ostwald **664**  
     ripening 664  
     rule of successive states 564

## P

packing fraction 302, 302, 303  
     of rods 469  
     in polymer crystals 468–471,  
         469–472, 474–482 544, 544,  
         545  
 partial changes, infinitesimal 75, 76  
 partition function 107, 107, 108  
 PC, see: plastic crystal

- Peltier effect 314, 315  
permittivity 425  
  complex 426–428, 427  
phase 162  
  amorphous 165  
    fraction, rigid, see: RAF  
    model, 573  
    property, structure sensitive or insensitive 574, 575  
    structure 572–574, 573, 574  
    property 574, 575  
    viscosity 575–578, 575–577  
  areas of single-component systems 593, 593–597  
  condensed 167, 177  
  description V, 162–171, 163, 167, 168, 170, 171, 176–178, 177, 178, 706–709, 708  
  diagram 706–725, 706–722, 724  
    by DSC 706, 706, 707  
    by thermometry 290  
    eutectic 100, 290, 291  
    for many polymeric components 718–723, 719–722  
    irreversible, macromolecule with small molecules 715, 716, 716–717, 720, 722  
    of block copolymers 723–725, 724  
    of small molecules 99–101, 100  
  polymer and low-mass components 714–717, 715, 716  
  polymer and low-mass homologs 717–723, 717–722  
  pVT 298–301, 300, 301  
  thermodynamics 706–708, 706–708  
equilibrium, of macromolecules with macromolecules 710, 717, 717, 718  
  of macromolecules with its homologous oligomers 718–723, 718, 719–722  
  of macromolecules with small molecules 708, 708, 709–715, 709–715  
  of small molecules 99–101, 99, 100, 708, 708  
    modulus for three 534, 534  
    rule 181, 707  
    separation, liquid-liquid 712–714, 712–714  
    sizes 162, 167–169, 168  
    solid 6, 7, 176  
      see also: glass or crystal  
    transition, see: transition, phase  
pipette 295, 296  
plasma V  
plastic crystal 167, 170, 170, 171  
  examples 172–174, 172, 173, 539, 540, 540  
  see also: mesophase  
  motion in 551, 552, 552  
plastics, 7, 24, 234  
  colloquialism for the easily shaped polymeric (macromolecular) materials, for details, see: polymer  
plateau, rubber-elastic 406, 406  
point group 460  
  number of 462  
polarization 424, 425, 425  
polydispersity 30, 224  
polymer 6, 6, 7, 13  
  branched 24–26, 25, 197, 733–735, 734, 735  
  brushes 25, 25  
  characterization of 50–67, 51–57, 58–66  
  flexible 6  
  identification, with TGA 439  
    by DTA, DSC 350, 351, 351  
  ladder 24–25, 24  
  living, see: reaction, chain, without termination  
  molecule, differences to small molecules VI, VII  
    chain structure, polar and nonpolar 480  
  macroconformations, linear 486–488, 487  
  network 24–26, 25, 26  
  nomenclature, abbreviations 16, 17  
  copolymers, isomers 22–24, 22, 23  
  seniority list 14  
  source based 13–22, 13, 18–21  
  structure based 13–22, 14, 15, 18–21



reaction 233–238, 233–237  
 rigid 6, 7  
 semicrystalline 488  
 transitions 536, 537, 537  
 ultimate strength 533–535, 534,  
     535  
 polymerization, degree of 27  
   emulsion 217, 217  
   living, see: reaction, chain, without  
     termination  
   Merrifield method 190–192, 192,  
     237  
   of lithium phosphate 201–206,  
     202–206  
   see also: reaction  
   stereo-specific 207, 209  
   topotactic 510, 511  
   Ziegler-Natta 209–211, 210, 211  
 potentiometer 288  
 production, of extensive thermodynamic  
   quantities 88, 147, 148,  
     148  
   sign of 88  
 properties, colligative 51, 58, 65, 96  
   prediction of 226, 227  
 purity analysis 319–320, 320, 321  
 pycnometer 295, 296, 296  
 pyrolysis 232  
   see also: decomposition  
 pyrometer 289, 819  
 pyrosynthesis by DTA 354, 354

## R

radiation, scattering 801–805  
   electromagnetic 50  
   electron 66  
   neutron 66  
 radius, atomic 3, 302  
   van der Waals 37, 301, 302  
 RAF 138, 605, 607–609, 607–609,  
     693, 694, 694  
   formation on crystallization 608,  
     609  
   disappearance on melting 641, 641  
   glass transition, see: transition,  
     glass  
 Raoult's law 708, 708  
 Rayleigh 51  
   ratio 54, 54, 809, 809, 810  
     derivation 806–810, 807–809  
   reaction, chain, copolymer 227–229,  
     227, 228  
     emulsion polymerization, 217,  
       217  
     equilibrium 214, 214, 215  
     initiation 208  
     kinetics 212–214, 213  
     list of monomers, 212  
     mass average 225–226, 225,  
       226  
     mechanism 206–212, 207  
     number and mass fraction  
       221–223, 222, 223  
     molar mass fraction 221–223,  
       222, 223  
     without termination 215–216,  
       216  
   chemical, by TMDSC 402, 403,  
     402, 403  
   interchange, see: transamidation  
     and transesterification  
   kinetics, rate equations 817  
     molecular length dependence in  
       esters 200  
   matrix 218–219, 218  
   polymer 233–238, 233–237  
   ring-chain 138, 138, 139, 194, 199,  
     199, 219  
   step, aromatic polymers 198  
     conditions 198–199, 199  
     copolymer 229, 230, 230  
     equilibrium 219  
     examples 196–198, 196–198  
     kinetics 200, 200, 201, 201  
     lithium phosphate 201–206  
     mass average 224–225, 224  
     mechanism 193–195, 194  
     molar mass 219–221, 221  
     number and mass fraction 220  
     polydispersity 224  
     statistics 195, 196  
     poymers, produced via chain  
       reactions 216  
     stepwise 189–193, 190–192  
   recrystallization 655–666, 655–665  
   relaxation 159  
     time 159–161, 159, 160, 161  
       Debye 117, 160  
       change with temperature 685  
   process 158–159  
   see also: stress relaxation

see also: thermodynamics,  
nonequilibrium  
see also: transition, glass  
see also: viscoelasticity, relaxation  
time  
repeating unit, constitutional 14, 14,  
15, 18–21  
flexible to stiff CRUs 49  
reptation model 573, 573  
revolution, industrial 11  
Richards's rule 182, 183, 339–341, 340  
Rietveld method of X-ray diffraction  
504–506, 505–507  
rotation 122  
internal 121  
rotoreptation 558, 558  
rubber elasticity, see: elasticity, entropy  
run number 762

## S

sample history, via glass transition  
682–700, 683–685, 687–700  
saw-tooth modulation 360–362, 361,  
362, 837–847, 837–847  
SCTA, see: TGA, sample-controlled  
second, ephemeris 283  
Seebeck effect 287, 314, 315  
seed material for PP, table 248  
self seeding 246, 247, 248  
semiconductor 286, 286  
scattering of light 50–58, 52, 806–810,  
806–809  
angular dependence 56  
apparatus 53  
intensity 54  
molar mass determination 54, 54  
size and shape dependence 54–56,  
54–56,  
screw axis 462, 463 462  
relation to helix axis 463, 464, 464  
sheet network 25  
SI rules and units 75, 76  
Simha-Boyer rule 761  
skewness 28, 28  
solid, see: phase, amorphous  
see: phase, crystal  
solution, ideal, regular, real 96, 710  
space groups 462, 462  
number of 462, 462, 463  
spinodal decomposition 712, 712  
spherulite 240, 499–503, 500–502  
growth 259–260, 260  
hedgehog-type 500, 501, 500, 501  
Popoff-type 500, 501  
Staudinger 6  
state, functions of, 75  
stereoisomer 23, 848  
steric hindrance 37–40, 38, 39  
stiff chain macromolecules 47–48, 49  
strain 404, 404  
release in glasses 605, 605  
stress 404, 404  
anomaly 415  
conversion factors, table of 404  
relaxation 414, 415  
time anomaly 415, 416  
Strutt, see: Rayleigh  
substance, pure 189  
subsystem 89, 90, 146, 147  
supercooling 243, 255, 266  
superposition principle 835  
symmetry, axes 460–463, 460, 461  
elements 461  
symbols for, in crystals 469,  
470  
product 461, 848  
groups 848  
operation 460–463  
closed 460, 460  
closed with inversion 461  
open 462, 463, 462  
translation 462, 462  
system, crystal 457, 458, 458  
description 88–90, 89  
equilibria (thermal, mechanical) 89  
isolated 89  
open 89, 147, 428  
types of 89  
multi-component, ideal 96–98, 97  
nonideal 98, 98  
multi-phase, of small molecules  
98–101, 99, 100  
right-handed 457  
Système International, see: SI

## T

temperature 79–81  
Boyle 36  
critical, upper and lower 712–714,  
712–714  
van der Waals 300

- eutectic 100, 100, 290, 291, 706,  
706, 707, 707  
fictive 391, 391, 601, 683  
gas 80, 81  
isotropization 176  
Kauzmann 140  
liquidus 290, 291, 706, 706, 707  
melting, extrapolation to  
equilibrium 537  
peritectic 706, 706, 707  
scale 280  
by Celsius 281  
by Fahrenheit 281  
by Newton 280  
by Réaumur 281  
gas 282, 282  
international, see: ITS 1990  
physiological 280, 280  
thermodynamic 80, 282, 282,  
283  
solidus line 706, 706, 707  
theta ( $\theta$ ) 35, 36, 36, 64, 713, 713  
Theta ( $\Theta$ ) 110  
Debye 111, 112–116, 113  
Einstein 110, 110, 111, 111  
for crystals of 100 elements and  
salts 115  
for longitudinal and transverse  
vibrations 115, 115  
for chymotrypsinogen 122  
for polymethionine 137  
for polyoxides 130  
for PTFE 134  
transition 177  
tenacity, see: tensile strength  
tensile strength 533–535, 534, 535, 608  
TGA 77, 77  
application 443–449, 444–446  
buoyancy correction 437  
coupled with, DSC or DTA 428,  
431, 432, 433, 433, 444  
other techniques 428  
mass spectrometry 434, 434  
data combined, with DTA  
439–445, 440–444  
with DTGA 439–441, 440, 441  
decomposition 231, 232, 232, 438,  
439, 439  
of calcium oxalate 444–446,  
444–446  
fast heating 434  
HiRes™ 436  
ICTAC recommendations 438,  
822, 823  
infrared image furnace 434, 435  
instrumentation 430–436, 430–436  
kinetics, equation 444  
by isoconversionion method  
448, 447, 449  
by steady-state parameter-jump  
method 446, 447, 447  
lifetime prediction 446–449, 447,  
449  
principle 428, 429, 429  
polymer identification with 439  
recoil of evolving gases 438, 439  
reference materials 437  
sample controlled 435, 436  
standardization 437, 438, 438  
Curie temperature for mass  
437, 428  
step-wise isothermal 436  
technique 437, 438  
thermal analysis 77, 77  
by computer 84–88, 85–87  
system, advanced, see: ATHAS  
techniques 76–79  
thermal head 310  
thermoacoustimetry 79  
thermobalance 430, 437  
thermobarometry 79  
thermochemistry 320–324  
data table 323  
*Thermochimica Acta* 77, 331  
thermocouple 287–289, 288  
table of EMF 288  
thermodynamic functions, of carbon  
325, 326, 325, 326  
of paraffins 327–329, 328, 329  
thermodynamics, and motion V, 167,  
176–178, 591–593, 593  
first law 76, 81–84, 83, 90, 91  
laws, not so precisely 90, 91  
nonequilibrium 146–161, 146–150,  
151–161  
flux and production 147, 148,  
148  
internal variables 155–158,  
156, 157  
melting of lamellar crystals  
148–155, 149, 150,  
152–155  
relaxation times 159–161,  
159–161

- second law 91–94, 91
  - Thomson statement 91
  - Thomson engine 93
- third law 94–96, 95, 140
  - Nernst formulation 95
- zeroth law 90, 279
- thermoelectrometry 79
- thermogravimetry, see: TGA
- thermoluminescence 79
- thermomagnetometry 79
- thermometer 80, 279, 280
  - bimetallic 289
  - calorimetric 80
  - gas 289
  - immersion 285
  - liquid-in-glass 80, 80, 280, 280
    - 283–285, 285
  - mercury-in-glass 80, 281–285, 285
    - error correction 283–285, 285
  - noise 289
  - platinum resistance 286, 818
  - principle 279–283, 280, 282
  - quartz 289
  - resistance 285–287, 286, 287
  - semiconductor 286, 287, 286
  - thermocouple 287–289, 288
  - vapor pressure 289
- thermometry 77
  - application 290–291, 290
  - contact 279, 280
- thermooptometry 79
- thermoparticulate analysis 79
- thermophotometry 79
- Thermophysics of Polymers VII
- thermorefractometry 79
- thermosonometry 79
- thermotropic liquid crystal 724, 724
- Thomson, see: Kelvin
- effect 315
- time, scale of, macroscopic V
  - microscopic V, 37
  - temperature superposition 418, 419
  - unit, SI, 283, 284
- TMA 77, 77
  - applications 408–412, 408–412
  - instrumentation 406–408, 407
  - measurement, of the expansivity
    - 298, 298
    - of the glass transition 298, 298
  - modes of measurement 407
  - principle 404–406, 404–406
  - temperature-modulated 418
- time-temperature superposition 418, 419
- TMDMA see: DMA, temperature-modulated
- TMDSC 333, 333, 334
  - analysis, pseudo-isothermal 369
  - asymmetry correction 378–379, 379, 380
  - basic equations 363, 364, 364, 365
  - calibration with In 375–378, 276, 277, 397, 397
  - Cole-Cole plot 383, 384, 383
  - comparison, of periodic and non-periodic experiments 417
    - with DMA 418, 419, 609, 610, 610
  - complex notation 362, 363
  - data treatment and modeling
    - 369–373, 369, 370–372
    - loss of stationarity 371, 371, 372
    - using spreadsheets 371
  - Fourier transform 334, 840, 841, 841, 842
  - frequency correction,  $\tau$  332, 334, 368
  - glass transition, measurement 388–396, 389
  - heat capacity, complex 382–384, 384
    - measurement 364–369, 365–368, 385–388, 385–388
  - heat-flow rate 363, 369–373, 369–372, 386, 386
    - amplitude dependence 381, 382, 382
    - contributions on melting 383, 383
    - frequency dependence 382–384, 382–384
    - in the transition region 386–388, 387, 388
    - maximum 370
    - positive and negative 378, 378
  - in- and out-of-phase signal 362, 363
  - instrumental problems 373–384, 374–384
  - linearity 369
  - Lissajous figure 266, 379, 380, 380, 381, 386, 397, 397, 398, 626, 742

- mathematical treatment 362–369,  
363–368  
model calculation, heat-flux  
DSC 365, 366, 366  
model calculation, power-  
compensation DSC 366,  
367, 367  
tau-correction ( $\tau$ ) 367–369, 3  
modeling 369–373, 369–372  
modulation method 359, 359  
complex sawtooth 361, 362  
pseudo-isothermal 369  
quasi-isothermal 359, 360, 361  
sawtooth 359, 361, 837–847,  
837–847  
sinusoidal 359  
types 360–361  
nonreversing signal 358, 386, 389  
of chemical reactions 402, 403,  
402, 403  
of first-order transitions 396–401,  
397, 399, 401  
irreversible 264, 264, 265, 265,  
396, 387, 401, 640  
partially irreversible 267, 267  
398–401, 399, 401  
reversible 255, 255, 256,  
375–378, 376, 377,  
396–400, 397, 399,  
844–846, 844–847  
reorganization 400, 401, 401  
performance, comparison to DSC  
373, 374  
limit of amplitude and frequency  
373, 374, 374  
limit of sample mass 375, 375  
principles 359–362, 359–362  
pseudo-isothermal analysis 369  
reversing signal 334, 369, 370  
distinction from reversible 358  
stationarity 369  
total signal 334, 369, 369  
trade name 16  
transamidation 230  
transesterification 200, 229, 230, 665,  
665, 666  
transition 176, 177  
boiling 182, 183  
broadening 554, 555, 555, 597  
crystallization and melting 6  
entropy, rules of 167, 182, 182,  
186, 541, 544  
transition, first-order 181–183, 182,  
183, 593–597, 593, 594  
see: melting  
see also: TMDSC, of first order  
transition  
glass 6, 178–180, 179, 180,  
597–610, 598–610  
analyzed based on TMDSC of  
PET 392–396, 392–395,  
687–689, 688, 689  
analyzed based on TMDSC of  
polystyrene 388–392,  
389–391, 600–604,  
602–604, 683–685, 684, 685  
autocatalytic 683  
block copolymer 768–772,  
769–771,  
broadening, absence in  
copolymers 760  
broadening, due to  
conformational motion 136  
broadening, due to crystallinity  
695, 695–697, 697  
broadening, due to phase size  
(surface effects) 605, 605,  
606, 606, 769–771, 769, 770  
broadening in block copolymers  
769–771, 769, 770  
broadening in polymer solutions  
764, 765  
by quantitative DSC 354, 355  
copolymer 759–762, 759–763  
766–768, 767, 772  
cooperativity 141, 175, 393,  
507, 554, 578, 604, 772  
crystallinity effects and RAF  
607, 608, 607, 608, 609,  
693–698, 693–698  
crystallization at the 592  
differences between DSC and  
DMA 609–610, 610  
Doppler-like effect 603, 689  
enthalpy relaxation 389, 389,  
390, 599–600, 599  
enthalpy relaxation, effect of  
crystallization on 695–697,  
696–698  
equations for multiple  
components 759–762, 759,  
760, 761, 763  
free enthalpy diagram 179,  
180, 180

transition, glass, hole model 392–394,  
394, 598–600, 598,  
686–689, 687–689  
hysteresis, see: enthalpy  
relaxation  
kinetics 600–604, 602–604  
measurement by DSC 179,  
354–355,  
mesophase 166, 167, 175–177,  
176, 547, 548, 559, 560  
modeling 686–689, 687–689  
molar-mass dependence 193  
multi-phase systems 772–773  
network effects 698–700, 699,  
700  
of stereospecific polymers 766,  
767  
pressure and strain effects  
689–692, 690–692  
RAF, in semicrystalline poly-  
mers 605, 607–609,  
607–609  
ratio to melting transition 179  
relaxation time 601, 685, 686  
self-retardation 683  
seven parameters of 179, 179  
size effect 605, 605, 606, 606,  
769–771, 770  
solubility, partial and 765, 766,  
766  
solutions and 760–766,  
761–766  
thermal history evaluation 682  
time and temperature effects  
682–686, 683–685  
gradual 183  
liquid-to-gas 164, 165  
liquid-to-solid 165  
liquid-to-crystal 165  
melting, see: melting  
mesophase 165, 165–167, 167,  
547–571  
entropy summary 554  
multiple, due to mesophases  
547–551, 548–551  
order of, definition by Ehrenfest  
181–182, 182  
transport process 158–159, 158  
sign of 88  
Trouton's rule 182, 186 539  
TTT diagram 402, 403  
turbidity 51, 58, 806, 806

## U

ultimate strength, see: tensile strength  
units, human V

## V

van der Waals **163**  
constants, table of 165  
radius, see: radius, van der Waals  
volume 301  
variable, internal 155–158, 156  
of state 75–76  
variance 28, 28  
vernier 294, 294  
vibration 109–111, 109  
anharmonic 110, 111  
acoustic 125  
group 124  
box distribution 125  
harmonic 109–111, 109, 110, 815  
skeletal 123  
approximation 124–126, 125,  
126  
spectrum 121–126, 123, 125, 126  
zero-point 109  
viscoelasticity 416–419, 583–585, 584  
data analysis from DMA 417–419,  
418, 419  
example analyses 584, 584  
see also: DMA  
linear 415, 416  
models 416, 417, 416, 417  
relaxation time 417, 416  
retardation time 416, 416  
spectra 417, 417  
stress anomaly 415, 583  
time anomaly 415, 583, 584  
viscometer 576  
Ubbelohde 64  
viscosity 415  
melt 575–578, 575, 577, 578  
molar-mass dependence 193,  
576  
shear thinning 577  
Newtonian 415, 416, 577  
range of (list) 577  
solution 63–65  
freely draining model 64–65,  
577, 577, 578,  
inherent 64  
intrinsic 64

molar-mass dependence 64, 64,  
65  
relative 64  
solid sphere model 64–65  
unit of 416  
Voigt model, see: viscoelasticity,  
models  
volume, excluded 36  
calculation 40, 41, 41, 164  
for real gases 163  
for macromolecules 35, 713  
measurement 295–298  
unit 291  
historical 293  
volumetric equipment 296  
vulcanization 232, 233

**W**

Walden's rule 541, 542  
water value 309  
wave, standing 111, 112  
Wheatstone bridge 287, 287  
Wöhler **6**  
work 76  
Wulff construction 168

**X – Z**

X-ray diffraction 851  
Young's modulus, see: modulus, tensile  
Ziegler **209**  
Zimm plot 56–58, 56, 57